

# REPORT DOCUMENTATION PAGE

Form Approved  
OMB No 0704-0188

Public reporting burden for this collection of information is estimated to average 1 hour per response, including the time for reviewing instructions, searching existing data sources, gathering and maintaining the data needed, and completing and reviewing the collection of information. Send comments regarding this burden estimate or any other aspect of this collection of information, including suggestions for reducing this burden, to Washington Headquarters Services, Directorate for Information Operations and Reports, 1215 Jefferson Davis Highway, Suite 1204 Arlington, VA 22202-4302, and to the Office of Management and Budget, Paperwork Reduction Project (0704-0188), Washington, DC 20503.

1. AGENCY USE ONLY (Leave blank)		2. REPORT DATE		3. REPORT TYPE AND DATES COVERED FINAL 01 Nov 96 to 31 Oct 97	
4. TITLE AND SUBTITLE ELECTROCHEMICAL SYNTHESIS AND MODIFICATION OF MATERIALS				5. FUNDING NUMBERS F49620-97-1-0015  2303/BS 61102F	
6. AUTHOR(S)  DR ROBERT H. PACHAVIS					
7. PERFORMING ORGANIZATION NAME(S) AND ADDRESS(ES) Director of Finance Materials Research Society 9800 McKnight Road Pittsburgh PA 15237				8. PERFORMING ORGANIZATION REPORT NUMBER	
9. SPONSORING / MONITORING AGENCY NAME(S) AND ADDRESS(ES) AFOSR/NL 110 Duncan Ave Room B115 Bolling AFB DC 20332-8050  Maj Hugh C. De Long				10. SPONSORING MONITORING AGENCY REPORT NUMBER	
11. SUPPLEMENTARY NOTES					
12a. DISTRIBUTION / AVAILABILITY STATEMENT  Approved for public release; distribution unlimited.				12b. DISTRIBUTION CODE	
13. ABSTRACT (Maximum 200 words) A new kinetic model for homoepitaxial growth on a singular surface is presented. The model combines the familiar rate equations approach and the concept of a feeding zone that allows connection between the growth processes occurring in neighbouring monolayers. The model involves the irreversible 2D nucleation, growth and coalescence of islands in each growing monolayer and consists of an infinite set of coupled rate equations for the adatom and island densities and coverage in successive monolayers. The temporal evolution of the surface morphology (rms roughness and RHEED intensity) is studied with this model. It is shown that the growth mode is fully determined by a single dimensionless parameter $= D/J$ where D and J are the normalized surface diffusion coefficient and deposition flux, respectively. There exist five regions of corresponding the different growth regimes varying from smooth 2D layer-by-layer growth at sufficiently high values of ( 10 ) to very upon Poisson-like random deposition growth at 10 . The extension of the model to the case of heteroepitaxy is also discussed.					
14. SUBJECT TERMS				15. NUMBER OF PAGES	
				16. PRICE CODE	
17. SECURITY CLASSIFICATION OF REPORT (U)	18. SECURITY CLASSIFICATION OF THIS PAGE (U)	19. SECURITY CLASSIFICATION OF ABSTRACT (U)	20. LIMITATION OF ABSTRACT (UL)		

**MATERIALS RESEARCH SOCIETY**  
**SYMPOSIUM PROCEEDINGS VOLUME 451**

# **Electrochemical Synthesis and Modification of Materials**

Symposium held December 2-5, 1996, Boston, Massachusetts, U.S.A.

## **EDITORS:**

**Panos C. Andricacos**

*IBM Corporation  
Yorktown Heights, New York, U.S.A.*

**Sean G. Corcoran**

*Hysitron, Inc.  
Minneapolis, Minnesota, U.S.A.*

**Jean-Luc Delplancke**

*Université Libre Bruxelles  
Bruxelles, Belgium*

**Thomas P. Moffat**

*National Institute of Standards and Technology  
Gaithersburg, Maryland, U.S.A.*

**Peter C. Searson**

*Johns Hopkins University  
Baltimore, Maryland, U.S.A.*



**PITTSBURGH, PENNSYLVANIA**

**DTIC QUALITY INSPECTED 4**

19971002 126



This material is based upon work supported by the National Science Foundation under Grant No. DMR-9614167. Any opinions, findings, and conclusions or recommendations expressed in this material are those of the author(s) and do not necessarily reflect the views of the National Science Foundation.

Single article reprints from this publication are available through  
University Microfilms Inc., 300 North Zeeb Road, Ann Arbor, Michigan 48106

CODEN: MRSPDH

Copyright 1997 by Materials Research Society.  
All rights reserved.

This book has been registered with Copyright Clearance Center, Inc. For further information, please contact the Copyright Clearance Center, Salem, Massachusetts.

Published by:

Materials Research Society  
9800 McKnight Road  
Pittsburgh, Pennsylvania 15237  
Telephone (412) 367-3003  
Fax (412) 367-4373  
Website: <http://www.mrs.org/>

Library of Congress Cataloging in Publication Data

Electrochemical synthesis and modification of materials : symposium held  
December 2-5, 1996, Boston, Massachusetts, U.S.A. / editors,  
Panos C. Andricacos, Sean G. Corcoran, Jean-Luc Delplancke,  
Thomas P. Moffat, Peter C. Searson  
p. cm—(Materials Research Society symposium proceedings ; v. 451)  
Includes bibliographical references and index.  
ISBN 1-55899-355-X  
1. Thin films—Congresses. 2. Electroplating—Congresses.  
3. Electrochemical metallizing—Congresses. I. Andricacos, Panos C.  
II. Corcoran, Sean G. III. Delplancke, Jean-Luc IV. Moffat, Thomas P.  
V. Searson, Peter C. VI. Series: Materials Research Society symposium  
proceedings ; v. 451.

TA418.9.T45E45 1997  
621.3815'2—dc21

97-23814  
CIP

Manufactured in the United States of America

## CONTENTS

Preface .....	xiii
Materials Research Society Symposium Proceedings .....	xiv

### PART I: FUNDAMENTALS OF FILM GROWTH AND DISSOLUTION

<b>bKinetic Model for Layer-by-Layer Homoepitaxial Growth</b> .....	3
<i>V.I. Trofimov, V.G. Mokerov, and A.G. Shumyankov</i>	
<b>*Dynamical Processes at the Solid-Liquid Interface</b> .....	9
<i>M. Giesen, M. Dietterle, D. Stapel, H. Ibach, and D.M. Kolb</i>	
<b>*The Initial Stages of Metal Deposition on Metal and Semiconductor Electrodes Studied by <i>In Situ</i> STM</b> .....	19
<i>D.M. Kolb, R.J. Randler, R.I. Wielgosz, and J.C. Ziegler</i>	
<b>Embedded Atom Model of Surface Stress and Early Film Growth in Electrodeposition: Ag/Au(111)</b> .....	31
<i>Michael I. Haftel, Mervine Rosen, and Sean G. Corcoran</i>	
<b>Micromechanical Stress Sensors for Electrochemical Studies</b> .....	37
<i>T.A. Brunt, W.F. Ip, T. Kayment, S.J. O'Shea, and M.E. Welland</i>	
<b><i>In Situ</i> STM Studies on the Electrodeposition of Ultrathin Nickel Films</b> .....	43
<i>O.M. Magnussen, F.A. Möller, A. Lachenwitzer, and R.J. Behm</i>	
<b>Time-Resolved Measurements of Overlayer Ordering in Electrodeposition</b> .....	49
<i>A.C. Finnefrock, L.J. Buller, K.L. Ringland, P.D. Ting, H.D. Abruña, and J.D. Brock</i>	
<b>*Halide Electroadsorption on Single Crystal Surfaces</b> .....	55
<i>B.M. Ocko and Th. Wandlowski</i>	
<b>Lattice-Gas Models of Electrochemical Adsorption: Static and Dynamic Aspects</b> .....	69
<i>Per Arne Rikvold, Andrzej Wieckowski, and Raphael A. Ramos</i>	
<b>STM Study of the Influence of Adsorption on Step Dynamics</b> .....	75
<i>T.P. Moffat</i>	
<b>Characterization of Etching Processes on Cu Surfaces</b> .....	81
<i>C.Y. Nakakura, V.M. Phanse, G. Zheng, and E.I. Altman</i>	

\*Invited Paper

<b>Growth, Structure, and Characterization of Electrodeposited Co/Cu Ultrathin Films and Multilayers</b> .....	87
<i>Y. Jyoko, S. Kashiwabara, and Y. Hayashi</i>	
<b>An <i>In Situ</i> Small-Angle Neutron Scattering Investigation of Ag<sub>0.7</sub>Au<sub>0.3</sub> Dealloying Under Potential Control</b> .....	93
<i>Sean G. Corcoran, David G. Wiesler, and Karl Sieradzki</i>	
<b>*Structure of Monolayers of Silicotungstate Anions on Ag(111) and Au(111) Electrode Surfaces</b> .....	99
<i>Maohui Ge, Brian K. Niece, Craig G. Wall, Walter G. Klemperer, and Andrew A. Gewirth</i>	
<b>Energetics of Epitaxial Monolayers Deposited on a (111) Surface of an FCC Crystal: Application to a Cu Monolayer on Au(111)</b> .....	109
<i>F.R. Zypman, L.F. Fonseca, and L. Blum</i>	
<b>Simulation of Desorption Kinetics at a Liquid-Solid Interface</b> .....	115
<i>T.W. Scott</i>	

## **PART II: PATTERN FORMATION DURING FILM GROWTH**

<b>*Electrochemical Synthesis and Processing of Materials: From Fractal Electrodes to Epitaxial Thin Films</b> .....	123
<i>Fereydoon Family</i>	
<b>Morphological Patterns During Quasi-Two-Dimensional Electrodeposition</b> .....	141
<i>Jacob Jorne and Sen-Wei Wu</i>	
<b>The Role of Coulombic Forces in Quasi-Two-Dimensional Electrochemical Deposition</b> .....	147
<i>G. Marshall, P. Mocskos, F. Molina, and S. Dengra</i>	

## **PART III: SURFACE MODIFICATION AND CHARACTERIZATION**

<b>Self-Assembled Organic Monolayer Films on Underpotentially Deposited Metal Layers</b> .....	155
<i>G.K. Jennings and P.E. Laibinis</i>	
<b>Electrochemical Heteroepitaxial Growth of Molecular Films on Ordered Substrates</b> .....	161
<i>Julie A. Last, Daniel E. Hooks, Christopher M. Yip, and Michael D. Ward</i>	
<b>Epitaxial Growth of Organic Molecules on Vicinal Surfaces of Single Crystals</b> .....	167
<i>Toshihiro Shimada, Takafumi Sakurada, and Atsushi Koma</i>	

\*Invited Paper

<b>*STM Studies of Electrode/Electrolyte Interfaces and Silicon Surface Reactions in Controlled Atmospheres</b> .....	173
<i>Christopher P. Wade, Huihong Luo, William L. Dunbar, Matthew R. Linford, and Christopher E.D. Chidsey</i>	

<b>*Molecular Grafting on Si(111) Surfaces: An Electrochemical Approach</b> .....	185
<i>C. Henry de Villeneuve, J. Pinson, F. Ozanam, J.N. Chazalviel, and P. Allongue</i>	

<b>Characterization of the Silicon/Fluoride Solution Interface by <i>In Situ</i> Microwave Reflectivity</b> .....	197
<i>Arun Natarajan, Gerko Oskam, Douglas A. Oursler, and Peter C. Searson</i>	

<b><i>In Situ</i> Characterization of the Surface State Density by Photoluminescence During Electrochemical Treatments of Silicon Surfaces</b> .....	203
<i>T. Dittrich, V.Y. Timoshenko, and J. Rappich</i>	

<b>Electrolyte Electroreflectance of Boron Phosphide (BP)</b> .....	209
<i>E. Schrotten, A. Goossens, and J. Schoonman</i>	

<b>Influence of a Silicon Cap on SiGe Passivation by Anodic Oxidation</b> .....	215
<i>J. Rappich, I. Sieber, A. Schöpke, W. Füssel, M. Glück, and J. Hersener</i>	

#### **PART IV: ELECTRODEPOSITION AND ETCHING OF COMPOUND SEMICONDUCTORS AND ELECTRODEPOSITION OF METALS ON SEMICONDUCTORS**

<b>*Chemical and Electrochemical Heteroepitaxial Growth of Chalcogenide Semiconductors From Solutions</b> .....	223
<i>D. Lincot, M.J. Furlong, M. Froment, R. Cortes, and M.C. Bernard</i>	

<b>*Thin-Layer Electrochemical Studies of ZnS, ZnSe, and ZnTe Formation by Electrochemical Atomic Layer Epitaxy (ECALE)</b> .....	235
<i>Lisa P. Colletti, Sajan Thomas, Elvin M. Wilmer, and John L. Stickney</i>	

<b>UHV Model Experiments of Electrochemical Etching of GaAs by H<sub>2</sub>O/Br<sub>2</sub></b> .....	245
<i>O. Henrion, A. Klein, C. Pettenkofer, and W. Jaegermann</i>	

<b>Scanning-Probe Investigations of Cleaved Heterostructure Layers</b> .....	251
<i>J.L. Ebel, T.E. Schlesinger, and M.L. Reed</i>	

\*Invited Paper

<b>*Electrochemical Deposition of Metals on Semiconductors</b> .....	257
<i>Gerko Oskam, John G. Long, Maria Nikolova, and Peter C. Searson</i>	
<b>Discrete Metal Deposition on Hydrogen Terminated Silicon Surfaces: Kinetics, Morphologies, and Sensor Applications</b> .....	267
<i>Oliver Chyan, Jin-Jian Chen, Junjun Wu, Steve Chien, and Min Liu</i>	
<b>Modification of the Silicon Surface by Electroless Deposition of Platinum From HF Solutions</b> .....	275
<i>P. Gorostiza, J. Servat, R. Diaz, F. Sanz, and J.R. Morante</i>	
 <b>PART V: ELECTRODEPOSITION AND MODIFICATION OF OXIDE ELECTRODES</b>	
<b>Electrodeposition of Copper/Cuprous Oxide Nanocomposites</b> .....	283
<i>Jay A. Switzer, Eric W. Bohannon, Teresa D. Golden, Chen-Jen Hung, Ling-Yuang Huang, and Mark Shumsky</i>	
<b>*Microelectrochemical Characterization and Modification of Semiconductor Surfaces With Polycrystalline Ti/TiO<sub>2</sub> as an Example</b> .....	289
<i>A. Michaelis, S. Kudelka, and J.W. Schultze</i>	
<b>In Situ Investigation of Working Battery Electrodes Using Synchrotron X-ray Diffraction</b> .....	301
<i>N.M. Jisrawi, T.R. Thurston, X.Q. Yang, S. Mukerjee, J. McBreen, M.L. Daroux, and X.K. Xing</i>	
<b>*Preparation and Study of Conductive Polymer/High-T<sub>c</sub> Superconductor Assemblies</b> .....	307
<i>J.T. McDevitt, J.E. Ritchie, C.T. Jones, A.D. Wells, C.A. Mirkin, and F. Xu</i>	
<b>Electrochemical Modification of La<sub>2</sub>CuO<sub>4</sub>: The Role Played by Microstructure</b> .....	315
<i>E.J. Williams, A. Daridon, F. Arrouy, J. Fompeyrine, E. Mächler, H. Siegenthaler, and J-P. Locquet</i>	
<b>Electrodeposited WO<sub>3</sub> Thin Films</b> .....	321
<i>E.A. Meulen Kamp, R.J.J. de Groot, and J.M.L. de Vries</i>	
<b>Bulk Restructuring of Amorphous Tungsten Trioxide Films Due to Hydration of the Film/Electrolyte Interface</b> .....	327
<i>I.V. Shiyankovskaya</i>	
<b>Electroless Deposition of La<sub>1-x</sub>Sr<sub>x</sub>MnO<sub>3</sub> Perovskite Film on Yttria Stabilized Zirconia Substrate</b> .....	333
<i>T. Sasaki and Y. Matsumoto</i>	

\*Invited Paper

**PART VI: ELECTRODEPOSITION OF METALS AND ALLOYS FOR  
MAGNETIC AND ELECTRONIC APPLICATIONS I**

<b>Fabrication and Characterization of NiFe Thin Film Composition Modulated Alloys</b> .....	<b>341</b>
<i>S.D. Leith and D.T. Schwartz</i>	
<b>*Electrodeposited Magnetic Multilayers</b> .....	<b>347</b>
<i>W. Schwarzacher, M. Alper, R. Hart, G. Nabyouni, I. Bakonyi, and E. Toth-Kadar</i>	
<b>Nanowires Grown Electrochemically in Porous Templates</b> .....	<b>359</b>
<i>C. Schönenberger, B.M.I. van der Zande, and L.G.J. Fokkink</i>	
<b>Electrochemical Fabrication of the Nanowire Arrays: Template, Materials, and Applications</b> .....	<b>367</b>
<i>Dmitri Routkevitch, Jimmy Chan, Dmitri Davydov, Ivan Avrutsky, J.M. Xu, M.J. Yacaman, and Martin Moskovits</i>	
<b>Heterojunctions in Nanowires by Electrochemical Processing</b> .....	<b>377</b>
<i>G. Redmond, S. Gilbert, B. Doudin, and J-Ph. Ansermet</i>	
<b>Production of Magnetic Nanopowders by Pulsed Sono-electrochemistry</b> .....	<b>383</b>
<i>J-L. Delplancke, O. Bouesnard, J. Reisse, and R. Winand</i>	
<b>*Electrodeposition for Hi-MEMS With Special Reference to Fabrication of a Magnetic Mini-Motor</b> .....	<b>389</b>
<i>E.J. O'Sullivan, E.I. Cooper, L.T. Ramankiw, J. Horkans, and K.T. Kwietniak</i>	
<b>Electrodeposition of High-<math>T_c</math> Superconductor Material for Microsensor Fabrication</b> .....	<b>401</b>
<i>A. Natarajan, W. Wang, E. Ma, R.N. Bhattacharya, C. Khan-Malek, M. Paranthaman, and P.M. Martin</i>	
<b>Structure and Magnetic Properties of Electrodeposited Cobalt/Platinum Multilayers</b> .....	<b>407</b>
<i>S. Kashiwabara, Y. Jyoko, and Y. Hayashi</i>	
<b>Electrodeposition of Strained-Layer Superlattices</b> .....	<b>413</b>
<i>T.P. Moffat</i>	
<b>Magnetoresistive Properties of Quasiperiodic Metallic Multilayers</b> .....	<b>419</b>
<i>M. Shima, L. Salamanca-Riba, and L.J. Swartzendruber</i>	
<b>Electrochemical Study on the Growth of Multilayer Film Electrodes of the Conducting Polymers PPP, POT, and of the Copolymer of PPP and POT</b> .....	<b>425</b>
<i>C. Kvarnström, R-M. Latonen, and A. Ivaska</i>	

\*Invited Paper

**PART VII: ELECTRODEPOSITION OF METALS AND ALLOYS  
FOR MAGNETIC AND ELECTRONIC APPLICATIONS II**

<b>*Defect Structure and Crystallographic Texture of Polycrystalline Electrodeposits</b> .....	<b>433</b>
<i>H.D. Merchant and O.B. Giritin</i>	
<b>Atomic-Force-Microscopy Study of Surface Evolution During Electrocrystallization of Zinc-Iron Alloys</b> .....	<b>445</b>
<i>F. Czerwinski, K. Kondo, and J.A. Szpunar</i>	
<b>Study of Nucleation of Electroless Cu Deposition on Pd</b> .....	<b>451</b>
<i>R. Amster, B. Johnson, and L.S. Vanasupa</i>	
<b>Influence of Nucleation on the Crystallization Behavior of Electroless Nickel-Phosphorous Alloys</b> .....	<b>457</b>
<i>Robert Oberle</i>	
<b>Electroless CoWP Barrier/Protection Layer Deposition for Cu Metallization</b> .....	<b>463</b>
<i>S. Lopatin, Y. Shacham-Diamand, V. Dubin, P.K. Vasudev, J. Pellerin, and B. Zhao</i>	
<b>Electrochemical Processing of Layered Composite Coatings of Nickel-Aluminum-Alumina/Alumina-Yttria Stabilized Zirconia</b> .....	<b>469</b>
<i>K. Barmak, S.W. Banovic, H.M. Chan, L.E. Friedersdorf, M.P. Harmer, A.R. Marder, C.M. Petronis, D.G. Puerta, and D.F. Susan</i>	
<b>Investigation of the Codeposition of Polymer Lattices With Copper on a Rotating Disk Electrode</b> .....	<b>475</b>
<i>J. Fransaer and J.P. Cells</i>	
<b>Composite Films of Copper/Boron Nitride and Nickel/Boron Nitride</b> .....	<b>481</b>
<i>Maria Hepel, Tania Tannahill, Christopher Baxter, and Richard Stephenson</i>	
<b>Characterization of High-Strength Cu/Ag Multilayered Composites</b> .....	<b>489</b>
<i>Qing Zhai, Dan Kong, Augusto Morrone, and Fereshteh Ebrahimi</i>	
<b>Electrochemical Preparation of Amorphous FeB Films Containing a Large Quantity of Plastics</b> .....	<b>495</b>
<i>P.B. Lim, N. Fujita, P.T. Squire, M. Inoue, and T. Fujii</i>	
<b>Thermal Stability of Electrodeposited Nanocrystalline Ni-45% Fe Alloys</b> .....	<b>501</b>
<i>F. Czerwinski, H. Li, F. Megret, J.A. Szpunar, D.G. Clark, and U. Erb</i>	
<b>Electrodeposition of Metals on Conductive Polymer Films</b> .....	<b>507</b>
<i>Maria Hepel, Laura Adams, and Cynthia Rice-Belrose</i>	

\*Invited Paper

<b>Etching of Polymers by Photo-Material Processing Using an Excimer Lamp</b> .....	515
<i>Noritaka Takezoe, Atsushi Yokotani, Kou Kurosawa, Wataru Sasaki, Kunio Yoshida, Tatsushi Igarashi, and Hiromitsu Matsuno</i>	
<b>High-Resolution Displacement of Functional Groups Onto Fluorocarbon Resin Surface by Using ArF Excimer Laser</b> .....	521
<i>T. Shimizu and M. Murahara</i>	
<b>Development of a Continuous Surface Modification System of Fluorocarbon Resin for Strong Adhesion</b> .....	527
<i>K. Hatao, K. Toyoda, and M. Murahara</i>	
<b>Open Air Fabrication of Al<sub>2</sub>O<sub>3</sub> Thin Films at Room Temperature</b> .....	533
<i>T. Okamoto, K. Toyoda, and M. Murahara</i>	

#### PART VIII: CORROSION

<b>*Corrosion of Electronic and Magnetic Devices and Materials</b> .....	541
<i>Gerald S. Frankel</i>	
<b>Electrochemical Atomic-Force-Microscopy Study of the Dissolution Kinetics of 304 Stainless Steel</b> .....	549
<i>T.J. McKrell and J.M. Galligan</i>	
<b>Electrochemical Reactions of Molybdenum Nitride Electrodes in H<sub>2</sub>SO<sub>4</sub> Electrolyte</b> .....	555
<i>S.L. Roberson, D. Finello, and R.F. Davis</i>	
<b>ac and dc Polarization and Cyclic Voltammetric Behavior of Boron-Doped CVD Diamond in 0.5 M NaCl Solution</b> .....	561
<i>R. Ramesham and M.F. Rose</i>	
<b>The Effects of Carbonate-Bicarbonate Concentration on Empirical Corrosion Diagram of Mild Steel as a Material of Geological Disposal Package for High-Level Nuclear Wastes</b> .....	567
<i>Guen Nakayama, Yuichi Fukaya, and Masatsune Akashi</i>	
<b>Corrosion Protection of Particulate Aluminum-Matrix Composites by Anodization</b> .....	573
<i>Jiangyuan Hou and D.D.L. Chung</i>	
<b>In Situ Characterization of Oxide Films on Liquid Alkali Metals Using Second-Harmonic Generation (SHG)</b> .....	579
<i>H. Tostmann, D. Nattland, and W. Freyland</i>	
<b>Author Index</b> .....	585
<b>Subject Index</b> .....	589
<b>*Invited Paper</b>	



## PREFACE

The papers contained in this volume were presented in Symposium P, "Electrochemical Synthesis and Modification of Materials," at the 1996 MRS Fall Meeting in Boston, MA, December 2-5. The goal of the symposium was to bring together investigators from different communities to promote discussion of new opportunities for electrochemical synthesis in materials science.

The symposium focused on the relationship between synthesis and the structure and properties of electrochemically modified surfaces. Topics covered include: characterization of growth processes and instabilities, heteroepitaxial and homoepitaxial deposition, evolution of surface morphologies, electrodeposition of novel materials and structures, electrochemical modification of semiconductor surfaces, and electrodeposition in the electronics industry.

We would like to thank all of the participants and contributors who were responsible for the success of this symposium, as well as the authors and referees who made this proceedings volume possible. We also acknowledge the financial support from NSF, Digital Instruments, TopoMetrix, and Solartron.

Panos C. Andricacos  
Sean G. Corcoran  
Jean-Luc Delplancke  
Thomas P. Moffat  
Peter C. Searson

April 1997

## MATERIALS RESEARCH SOCIETY SYMPOSIUM PROCEEDINGS

- Volume 420—Amorphous Silicon Technology—1996, M. Hack, E.A. Schiff, S. Wagner, R. Schropp, A. Matsuda 1996, ISBN: 1-55899-323-1
- Volume 421—Compound Semiconductor Electronics and Photonics, R.J. Shul, S.J. Pearton, F. Ren, C-S. Wu, 1996, ISBN: 1-55899-324-X
- Volume 422—Rare-Earth Doped Semiconductors II, S. Coffa, A. Polman, R.N. Schwartz, 1996, ISBN: 1-55899-325-8
- Volume 423—III-Nitride, SiC, and Diamond Materials for Electronic Devices, D.K. Gaskill, C.D. Brandt, R.J. Nemanich, 1996, ISBN: 1-55899-326-6
- Volume 424—Flat Panel Display Materials II, M. Hatalis, J. Kanicki, C.J. Summers, F. Funada, 1997, ISBN: 1-55899-327-4
- Volume 425—Liquid Crystals for Advanced Technologies, T.J. Bunning, S.H. Chen, W. Hawthorne, T. Kajiyama, N. Koide, 1996, ISBN: 1-55899-328-2
- Volume 426—Thin Films for Photovoltaic and Related Device Applications, D. Ginley, A. Catalano, H.W. Schock, C. Eberspacher, T.M. Peterson, T. Wada, 1996, ISBN: 1-55899-329-0
- Volume 427—Advanced Metallization for Future ULSI, K.N. Tu, J.W. Mayer, J.M. Poate, L.J. Chen, 1996, ISBN: 1-55899-330-4
- Volume 428—Materials Reliability in Microelectronics VI, W.F. Filter, J.J. Clement, A.S. Oates, R. Rosenberg, P.M. Lenahan, 1996, ISBN: 1-55899-331-2
- Volume 429—Rapid Thermal and Integrated Processing V, J.C. Gelpey, M.C. Öztürk, R.P.S. Thakur, A.T. Fiory, F. Roozeboom, 1996, ISBN: 1-55899-332-0
- Volume 430—Microwave Processing of Materials V, M.F. Iskander, J.O. Kiggans, Jr., J.Ch. Bolomey, 1996, ISBN: 1-55899-333-9
- Volume 431—Microporous and Macroporous Materials, R.F. Lobo, J.S. Beck, S.L. Suib, D.R. Corbin, M.E. Davis, L.E. Iton, S.I. Zones, 1996, ISBN: 1-55899-334-7
- Volume 432—Aqueous Chemistry and Geochemistry of Oxides, Oxyhydroxides, and Related Materials, J.A. Voight, T.E. Wood, B.C. Bunker, W.H. Casey, L.J. Crossey, 1997, ISBN: 1-55899-335-5
- Volume 433—Ferroelectric Thin Films V, S.B. Desu, R. Ramesh, B.A. Tuttle, R.E. Jones, I.K. Yoo, 1996, ISBN: 1-55899-336-3
- Volume 434—Layered Materials for Structural Applications, J.J. Lewandowski, C.H. Ward, M.R. Jackson, W.H. Hunt, Jr., 1996, ISBN: 1-55899-337-1
- Volume 435—Better Ceramics Through Chemistry VII—Organic/Inorganic Hybrid Materials, B.K. Coltrain, C. Sanchez, D.W. Schaefer, G.L. Wilkes, 1996, ISBN: 1-55899-338-X
- Volume 436—Thin Films: Stresses and Mechanical Properties VI, W.W. Gerberich, H. Gao, J-E. Sundgren, S.P. Baker 1997, ISBN: 1-55899-339-8
- Volume 437—Applications of Synchrotron Radiation to Materials Science III, L. Terminello, S. Mini, H. Ade, D.L. Perry, 1996, ISBN: 1-55899-340-1
- Volume 438—Materials Modification and Synthesis by Ion Beam Processing, D.E. Alexander, N.W. Cheung, B. Park, W. Skorupa, 1997, ISBN: 1-55899-342-8
- Volume 439—Microstructure Evolution During Irradiation, I.M. Robertson, G.S. Was, L.W. Hobbs, T. Diaz de la Rubia, 1997, ISBN: 1-55899-343-6
- Volume 440—Structure and Evolution of Surfaces, R.C. Cammarata, E.H. Chason, T.L. Einstein, E.D. Williams, 1997, ISBN: 1-55899-344-4
- Volume 441—Thin Films—Structure and Morphology, R.C. Cammarata, E.H. Chason, S.C. Moss, D. Ila, 1997, ISBN: 1-55899-345-2
- Volume 442—Defects in Electronic Materials II, J. Michel, T.A. Kennedy, K. Wada, K. Thonke, 1997, ISBN: 1-55899-346-0
- Volume 443—Low-Dielectric Constant Materials II, K. Uram, H. Treichel, A.C. Jones, A. Lagendijk, 1997, ISBN: 1-55899-347-9

## **MATERIALS RESEARCH SOCIETY SYMPOSIUM PROCEEDINGS**

- Volume 444— Materials for Mechanical and Optical Microsystems, M.L. Reed, M. Elwenspoek, S. Johansson, E. Obermeier, H. Fujita, Y. Uenishi, 1997, ISBN: 1-55899-348-7
- Volume 445— Electronic Packaging Materials Science IX, P.S. Ho, S.K. Groothuis, K. Ishida, T. Wu, 1997, ISBN: 1-55899-349-5
- Volume 446— Amorphous and Crystalline Insulating Thin Films—1996, W.L. Warren, J. Kanicki, R.A.B. Devine, M. Matsumura, S. Cristoloveanu, Y. Homma, 1997, ISBN: 1-55899-350-9
- Volume 447— Environmental, Safety, and Health Issues in IC Production, R. Reif, A. Bowling, A. Tonti, M. Heyns, 1997, ISBN: 1-55899-351-7
- Volume 448— Control of Semiconductor Surfaces and Interfaces, S.M. Prokes, O.J. Glembocki, S.K. Brierley, J.M. Woodall, J.M. Gibson, 1997, ISBN: 1-55899-352-5
- Volume 449— III-V Nitrides, F.A. Ponce, T.D. Moustakas, I. Akasaki, B.A. Monemar, 1997, ISBN: 1-55899-353-3
- Volume 450— Infrared Applications of Semiconductors—Materials, Processing and Devices, M.O. Manasreh, T.H. Myers, F.H. Julien, 1997, ISBN: 1-55899-354-1
- Volume 451— Electrochemical Synthesis and Modification of Materials, S.G. Corcoran, P.C. Searson, T.P. Moffat, P.C. Andricacos, J.L. Deplancke, 1997, ISBN: 1-55899-355-X
- Volume 452— Advances in Microcrystalline and Nanocrystalline Semiconductors—1996, R.W. Collins, P.M. Fauchet, I. Shimizu, J.-C. Vial, T. Shimada, A.P. Alvisatos, 1997, ISBN: 1-55899-356-8
- Volume 453— Solid-State Chemistry of Inorganic Materials, A. Jacobson, P. Davies, T. Vanderah, C. Torardi, 1997, ISBN: 1-55899-357-6
- Volume 454— Advanced Catalytic Materials—1996, M.J. Ledoux, P.W. Lednor, D.A. Nagaki, L.T. Thompson, 1997, ISBN: 1-55899-358-4
- Volume 455— Structure and Dynamics of Glasses and Glass Formers, C.A. Angell, T. Egami, J. Kieffer, U. Nienhaus, K.L. Ngai, 1997, ISBN: 1-55899-359-2
- Volume 456— Recent Advances in Biomaterials and Biologically-Inspired Materials: Surfaces, Thin Films and Bulk, D.F. Williams, M. Spector, A. Bellare, 1997, ISBN: 1-55899-360-6
- Volume 457— Nanophase and Nanocomposite Materials II, S. Komarneni, J.C. Parker, H.J. Wollenberger, 1997, ISBN: 1-55899-361-4
- Volume 458— Interfacial Engineering for Optimized Properties, C.L. Briant, C.B. Carter, E.L. Hall, 1997, ISBN: 1-55899-362-2
- Volume 459— Materials for Smart Systems II, E.P. George, R. Gotthardt, K. Otsuka, S. Troler-McKinstry, M. Wun-Fogle, 1997, ISBN: 1-55899-363-0
- Volume 460— High-Temperature Ordered Intermetallic Alloys VII, C.C. Koch, N.S. Stoloff, C.T. Liu, A. Wanner, 1997, ISBN: 1-55899-364-9
- Volume 461— Morphological Control in Multiphase Polymer Mixtures, R.M. Briber, D.G. Peiffer, C.C. Han, 1997, ISBN: 1-55899-365-7
- Volume 462— Materials Issues in Art and Archaeology V, P.B. Vandiver, J.R. Druzik, J. Merkel, J. Stewart, 1997, ISBN: 1-55899-366-5
- Volume 463— Statistical Mechanics in Physics and Biology, D. Wirtz, T.C. Halsey, J. van Zanten, 1997, ISBN: 1-55899-367-3
- Volume 464— Dynamics in Small Confining Systems III, J.M. Drake, J. Klafter, R. Kopelman, 1997, ISBN: 1-55899-368-1
- Volume 465— Scientific Basis for Nuclear Waste Management XX, W.J. Gray, I.R. Triay, 1997, ISBN: 1-55899-369-X
- Volume 466— Atomic Resolution Microscopy of Surfaces and Interfaces, D.J. Smith, R.J. Hamers, 1997, ISBN: 1-55899-370-3

*Prior Materials Research Society Symposium Proceedings available by contacting Materials Research Society*

**Part I**

**Fundamentals of Film  
Growth and Dissolution**

## KINETIC MODEL FOR LAYER-BY-LAYER HOMOEPITAXIAL GROWTH

V.I.TROFIMOV, V.G.MOKEROV, A.G.SHUMYANKOV  
Institute of Radio Engineering & Electronics of RAS  
Mokhovaya str., 11, Moscow 103907, Russia, FAX : 7(095) 203 8414

### ABSTRACT

A new kinetic model for homoepitaxial growth on a singular surface is presented. The model combines the familiar rate equations approach and the concept of a feeding zone that allows connection between the growth processes occurring in neighbouring monolayers. The model involves the irreversible 2D nucleation, growth and coalescence of islands in each growing monolayer and consists of an infinite set of coupled rate equations for the adatom and island densities and coverage in successive monolayers. The temporal evolution of the surface morphology (rms roughness and RHEED intensity) is studied with this model. It is shown that the growth mode is fully determined by a single dimensionless parameter  $\mu = D/J$  where  $D$  and  $J$  are the normalized surface diffusion coefficient and deposition flux, respectively. There exist five regions of  $\mu$  corresponding the different growth regimes varying from smooth 2D layer-by-layer growth at sufficiently high values of  $\mu$  ( $>10^8$ ) to very rough Poisson-like random deposition growth at  $\mu < 10^{-4}$ . The extension of the model to the case of heteroepitaxy is also discussed.

### INTRODUCTION

In the last few years, an understanding of the mechanisms of molecular beam epitaxial (MBE) growth has attracted considerable attention due to the development of advanced nanoelectronics technology where the ultimate goal is the controlled fabrication of ultra-thin films with atomically smooth and abrupt interfaces. A rather large volume of knowledge about the specifics of growth kinetics and growth mode transitions on both singular and vicinal surfaces has been obtained [1-7]. However an exact and self-consistent picture of the relative contributions of the different MBE growth mechanisms as a function of the deposition parameters is still lacking.

In this paper a simple kinetic model for homoepitaxial growth on a singular surface that combines the familiar rate equations approach [8] with the concept of a feeding zone [9] that allows the growth processes in neighbouring monolayers is presented. The model allows the prediction of the MBE growth mode as a function of the main deposition parameters.

### MODEL

We will consider growth in the complete condensation regime characteristic of the typical conditions for semiconductor MBE. If biatomic and larger islands are stable

and immobile, the rate equations for surface densities of adatom ( $n_1$ ) and 2D islands ( $N_1$ ) in the first monolayer can be written in the form [8,9]

$$dn_1/dt = J(1 - \xi_1) - 2\sigma_{11} D n_1^2 - \langle \sigma \rangle D n_1 N_1 \quad (1)$$

$$dN_1/dt = (1 - \xi_1) \sigma_{11} D n_1^2 - 2 N_1 d\xi_1/dt \quad (2)$$

where  $J$  ( $\text{cm}^{-2}\text{s}^{-1}$ ) is the atomic flux,  $D$  ( $\text{cm}^2\text{s}^{-1}$ ) the surface diffusion coefficient,  $\xi_1$  the substrate coverage,  $\sigma_{11}$  the adatom-adatom capture number, and  $\langle \sigma \rangle$  the adatom-island capture number averaged over all the islands. In eq. (1) the first term represents the deposition flux on the uncovered substrate, the second and third terms account for the loss of adatoms due to nucleation and growth of 2D islands, respectively. In eq. (2) the first term represents the nucleation rate and the second term accounts for the coalescence of growing islands.

The atoms deposited on top of the 1st-layer islands migrate over their surface with the same diffusion coefficient  $D$  and it is the behaviour of these adatoms that ultimately determines the growth mode. If an additional energy barrier for downward diffusion at the island edge (Schwoebel barrier, [10]) is absent then some fraction of these adatoms descend onto the lower level and are incorporated into the island boundary step, thus giving rise in the island lateral size. The relative fraction of adatoms remaining in the 2nd layer versus those jumping down to the 1st layer depends on the island size and on rates of deposition  $J$  and diffusion  $D$ . On the basis of the solution to the random-walk problem for a particle on a 2D lattice with traps [9] we will suppose that if the average island size  $S$  is less than a critical value  $S_c = (D/J)^{1/2}$ , then all atoms deposited onto the island migrate onto the 1st layer and so there is no nucleation on top of the island. When  $S > S_c$  only the atoms deposited onto a ring band of width  $l = (S_c/\pi)^{1/2}$  adjoining to the island perimeter diffuse to the 1st layer; the atoms deposited onto the central part of the island remain there thus forming a feeding zone (FZ) for the 2nd layer. The specific area  $\xi_{1,a}$  of the total FZ of a growing film which accounts for the coalescence of the growing islands is given by the expression

$$\xi_{1,a} = \begin{cases} 0, & \text{if } \xi_1 < \xi_{1,c} \\ 1 - \exp[-\xi_{e1} (1 - (\xi_{1,c}/\xi_1)^{1/2})^2], & \text{if } \xi_1 > \xi_{1,c} \end{cases} \quad (3)$$

Here,  $\xi_{1,c} = N_1(D/J)^{1/2}$  is the critical substrate coverage at which a 2nd layer nucleates on top of the 1st layer and  $\xi_{e1} = -\ln(1 - \xi_1)$  the so called extended coverage. Now we can write the third needed rate equation for substrate coverage

$$d\xi_1/dt = J(1 - \xi_{1,a})/N_0 \quad (4)$$

where  $N_0$  ( $\text{cm}^{-2}$ ) is the surface lattice sites density. The second layer serves as a substrate for the third one, the third layer - for the fourth one, etc. Proceeding in this way, we obtain an infinite set of coupled equations fully describing the layered growth kinetics. Introducing the dimensionless densities  $\tilde{n} = n/N_0$  and  $\tilde{N} = N/N_0$

and time  $\tau = Jt/N_0$  having the physical meaning of the number of the monolayers deposited, we can write,

$$d\tilde{n}_k/d\tau = (\xi_{k-1,a} - \xi_k) - 2\sigma_{11}\mu\tilde{n}_k^2 - \langle\sigma\rangle\mu\tilde{n}_k\tilde{N}_k$$

$$d\tilde{N}_k/d\tau = (\xi_{k-1,a} - \xi_k)\sigma_{11}\mu\tilde{n}_k^2 - 2\tilde{N}_k d\xi_k/d\tau$$

$$d\xi_k/d\tau = \xi_{k-1,a} - \xi_{k,a}$$

$$\xi_{k,a} = \begin{cases} 0, & \xi_k < \xi_{kc} \\ 1 - \exp[-\xi_{ek}(1 - (\xi_{kc}/\xi_k)^{1/2})^2], & \xi_k > \xi_{kc} \end{cases}$$

$$\xi_{kc} = \tilde{N}_k \mu^{1/2}, \quad \xi_{ek} = -\ln(1 - \xi_k) \quad k \geq 1 \quad (\xi_{0,a} = 1)$$

where the homoepitaxial growth kinetics are fully determined by a single dimensionless parameter

$$\mu = N_0^2 D/J \quad (6)$$

that is, by the ratio of the surface diffusion and deposition rates.

## RESULTS AND DISCUSSION

In the numerical integration of the eqs. (5) we took  $\sigma_{11} = 2$  and the capture number  $\langle\sigma\rangle$  was calculated using the lattice approximation formula [12]

$$\langle\sigma\rangle = -4\pi(1-\xi)/(\ln\xi + (1-\xi)(3-\xi)/2). \quad (7)$$

The average epilayer thickness  $\langle h \rangle = \sum \xi_i(\tau)$  was calculated using obtained coverage kinetics curves  $\xi_i(\tau)$ . The latter is linear with time in the complete condensation regime  $\langle h \rangle = \tau$ . For more detailed quantitative characterization of the growth morphology the rms roughness  $\sigma$  defined as  $\sigma = [\langle h^2 \rangle - \langle h \rangle^2]^{1/2}$  where angle brackets denote the average over all surface, and the RHEED intensity  $I(\tau)$  were calculated by the formulas

$$\sigma^2 = \sum (2i-1)\xi_i - (\sum \xi_i)^2, \quad I(\tau) = [\sum (-1)^k (\xi_k - \xi_{k+1})]^2, \quad \xi_0 = 1$$

The results of calculations for several values of  $\mu$  are shown in fig.1. We suppose here that the change of  $\mu$  occurs only owing to  $D$  variations at constant  $J$ , so that the dimensionless time  $\tau \sim J$  does not depend on  $\mu$  and hence we can directly compare the growth kinetics at different  $\mu$ . At sufficiently high values of  $\mu$  one expects a layer-by-layer growth since the deposited atoms diffuse over long distances complete filling the surface before the next layer begins to form. Indeed, at  $\xi = 10^8$  the calculated kinetic curves  $\xi_i(\tau)$  (not shown) indicate that each  $i$ -layer nucleates just after the previous  $(i-1)$ -layer is almost completed and as is clearly seen in fig. 1 the rms

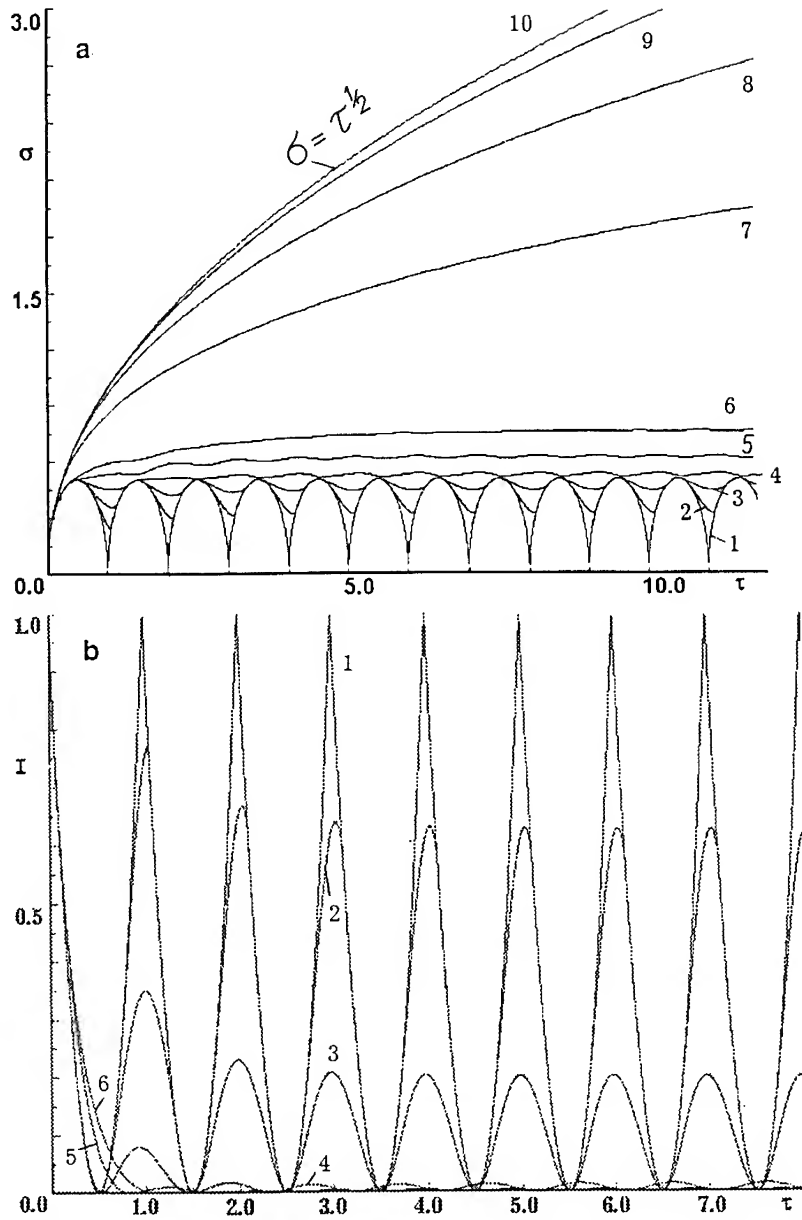


Fig.1. Temporal evolution of the rms roughness (a) and RHEED intensity (b) at different values of the parameter  $\mu$

- a) Curves 1-10 correspond to  $\mu$ :  $10^8$ ,  $10^6$ ,  $10^5$ ,  $10^4$ ,  $10^3$ , 150,  $10^{-1}$ ,  $10^{-2}$  and  $10^{-4}$ , respectively.  
b) Curves 1-6 correspond to  $\mu$ :  $10^8$ ,  $10^6$ ,  $10^4$ ,  $10^2$ , 1 and  $10^{-1}$ , respectively.



roughness  $\sigma$  and RHEED intensity oscillate with period exactly equal the time of deposition of one monolayer, and the temporal oscillations of  $s$  are very well fitted by the formula  $\sigma^2 = \xi - \xi^2$  describing an ideal layer-by-layer growth.

With decreasing of  $\mu$  the oscillation amplitude decreases steadily and at  $\mu = 10^4$ , when the growth front consists of 1-2 evolving layers, the  $\sigma$  oscillations almost vanish. With further decrease of  $\mu$  a steady growth front of 2-4 simultaneously filling monolayers persists down to  $\mu \approx 150$  and  $s$  saturates at slightly increasing level:  $\sigma_s = 0.52$  at  $\mu = 10^4$  and  $\sigma_s = 0.83$  at  $\mu = 150$ . With decreasing of  $\mu < 150$  the interface width does not saturate and diverges more and more with time, and  $\sigma(\tau)$  approaches asymptotically and eventually (at  $\mu = 10^{-4}$ ) runs into the limiting curve

$$\sigma = \tau^{1/2} \quad (8)$$

characterizing the random Poisson deposition growth process without diffusion.

In our model a new  $(i+1)$ -layer nucleates on top of the previous  $i$ -layer when its coverage reaches the critical value  $\xi_{ic} = N_i \cdot \mu^{1/2}$ . An approximate analytical dependence of  $\xi_{ic}$  can easily be obtained. Indeed, as follows from eqs.(1) and (2) the island density due to coalescence decreases as  $\tilde{N}_1 = \tilde{N}_0 \exp(-2\xi_1)$  with

$\tilde{N}_0 \sim \mu^{-1/3}$ , so  $\xi_{1c} \exp(2\xi_{1c}) = A \mu^{1/6}$ . The exact relation, obtained by fitting to the numerical data is  $\xi_{1c} \exp(2\xi_{1c}) = A \mu^{3/16}$  with  $A=0.205$ . In the next layers critical coverage decreases up to third-fourth layer and then stabilizes at some level  $\xi_{\infty c}$  that follows similar law  $\xi_{\infty c} \exp(2\xi_{\infty c}) = B \mu^{4/17}$ . It is remarkable that at extrapolation to  $\xi = 1$  both dependences yield the same critical value of  $\mu^* = 2 \cdot 10^8$  marking the onset of the perfect 2D layer-by-layer growth. It is interesting to estimate the corresponding substrate temperature,  $T^*$  through the relation (6). For example, with using data [11] on self-diffusion coefficient on a Si(001) and setting a typical value of  $J = 1$  monolayer/s for homoepitaxy of Si(001) we obtain a reasonable estimation of  $T^* = 440 - 640$  C.

Thus, the results can be summarized as shown in fig.2 where LL- and ML-growth denote the layer-by-layer and multilayer growth, respectively.

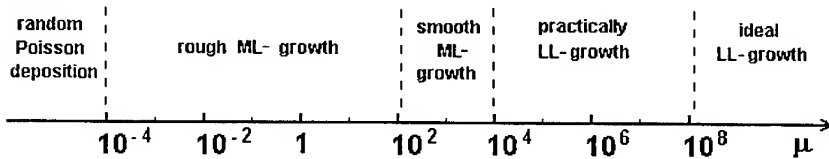


Fig.2. Diagram of the growth modes depending on  $\mu$ .

In conclusion, we discuss briefly the extension of the model to the case of the heteroepitaxy. If the lattice mismatch is negligibly small so that the strain effects can be disregarded, such an extension can be easily performed by simple introducing the different diffusion coefficients in the first ( $k=1$ ) layer (heterodiffusion with  $D_h$ ) and in all subsequent ( $k \geq 2$ ) layers (self-diffusion with  $D_s$ ). Now the model will contain two dimensionless parameters,  $\mu_h = N_0^2 D_h / J$  and  $\mu_s = N_0^2 D_s / J$ , and the set of rate eqs. (5) will of course hold with replacing  $\mu \rightarrow \mu_h$  at  $k=1$ , and  $\mu \rightarrow \mu_s$  at  $k \geq 2$ , and  $\mu \rightarrow \mu_s$  in all expressions for  $\xi_{kc}$ . The integration of eqs. (5) for a set of values of  $\mu_h$

and  $\mu_s$  shows, as expected, that in the layer - by - layer growth regime a difference between the homo- and heteroepitaxy is observed only in the first several (3-4) layers. If  $\mu_h < \mu_s$  then due to higher island density in the 1st layer and higher adatom mobility in the 2nd layer the  $\xi_{1c}$  increases and as a consequence the values of  $\sigma_{\min}$  decrease, and if  $\mu_h > \mu_s$  the result is naturally opposite. For example, as seen in Fig.3 for  $\mu_h = 10^6$  and  $\mu_s = 10^7$  the value of the  $\sigma_{\min,1}$  drops down almost to zero, and thus we obtain an ideally smooth monolayer film. It means that for growing a smoother ultra-thin film it is better to choose a substrate so that  $D_h < D_s$

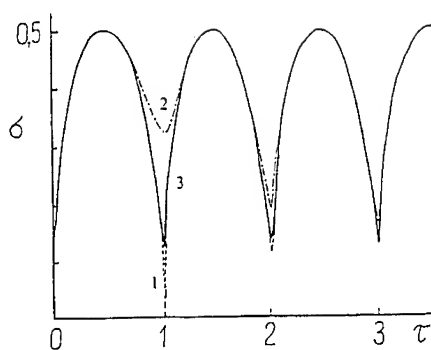


Fig.3. Comparison of roughness kinetics for (1,2) heteroepitaxy and (3) homoepitaxy: 1-  $\mu_h = 10^6$ ,  $\mu_s = 10^7$ ; 2 -  $\mu_h = 10^8$ ,  $\mu_s = 10^7$ ; 3 -  $\mu = 10^7$

## CONCLUSION

The model proposed predicts that homoepitaxial growth on a singular surface in the complete condensation regime and in the absence of Schwoebel barriers, is fully determined by a single dimensionless parameter  $\mu$  equal the ratio of the surface diffusion and deposition rates. There exist five regions of  $\mu$  corresponding different growth regimes varying from ideally smooth 2D layer-by-layer growth at sufficiently high values of  $\mu$  ( $> 10^8$ ) to extremely rough Poisson random deposition growth at  $\mu < 10^{-4}$ .

One of authors (V.I.T) gratefully acknowledges Materials Research Society for kindly presented possibility with financial support to attend the MRS 1996 Fall Meeting and International Science Foundation for travel financial support.

## REFERENCES

1. A.K.Myers-Beaghton and D.D.Vvedensky, Phys. Rev. **B42**, 5544 (1990).
2. J.Tersoff, A.W.Denier van der Gon and R.M.Tromp, Phys.Rev. **72**, 266 (1994).
3. C.Ratsch, M.D.Nelson and A.Zangwill. Phys.Rev. **B50** 14489 (1994).
4. M.D.Johnson, C.Orme, A.W.Hunt et al., Phys.Rev.Lett. **72**, 116 (1994).
5. A.Ishizaka and Y.Murata, J.Phys.:Condens.Matter **6**, L693 (1994).
6. V.I.Trofimov, B.K.Medvedev, V.G.Mokerov and A.G.Shumyankov, Physics- Doklady. **40**, 445 (1995); *ibid.*, **41**, 142 (1996).
7. Evolution of Epitaxial Structure and Morphology, edited by A.Zangwill, D.Jesson, D.Chambliss, and R.Clarke (MRS Proc. **399**, Pittsburgh, PA, 1996)
8. J.A.Venables, G.D.T.Spiller and M.Hanbuchen, Rept.Progr.Phys. **47**, 399 (1984).
9. V.I.Trofimov and V.A.Osadchenko, Growth and Morphology of Thin Films, in Russian (Energoatomizdat Moscow, 1993), 272pp.
10. R.L.Schwoebel and E.J.Shipsey, J.Appl.Phys. **37**, 3682 (1966).
11. S.Kersulis and V.Mitin, Semicond. Sci.Technol. **10**, 653 (1995).

## **Dynamical Processes at the Solid / Liquid Interface**

M. GIESEN\*, M. DIETTERLE\*\*, D. STAPEL\*, H. IBACH\*, D. M. KOLB\*\*

\*Institut für Grenzflächenforschung und Vakuumphysik, Forschungszentrum Jülich,  
D 52425 Jülich, Germany

\*\*Abteilung für Elektrochemie, Universität Ulm, D 89069 Ulm, Germany

### **ABSTRACT**

We have investigated transport processes on a stepped Ag(111) surface in an aqueous electrolyte by analyzing the equilibrium step fluctuations as a function of the electrode potential. No influence of the electrolyte and the potential was found in the regime of negative potentials with respect to the saturated calomel electrode. As the potential becomes positive and approaches the dissolution limit, the increasing magnitude of the step fluctuations and the change in the time dependence indicate a rapid exchange of silver atoms with the electrolyte long before the silver begins to dissolve.

### **INTRODUCTION**

The scanning tunneling microscope (STM) has become a powerful tool for the in-situ investigation on the structure and dynamics of electrode surfaces as this technique has allowed to view surface processes at metal-electrolyte interfaces on an atomic level. Examples are the potential-induced reconstruction of gold single crystal surfaces [1,2] and the nucleation-and-growth phenomena in electrochemical metal deposition [3,4]. Surface defects such as steps and kink sites are known to play a crucial role as nucleation centers and reactive sites in many electrochemical reactions. Their local arrangement, however, is not static, but can change at a rate that often depends strongly on the electrode potential and the electrolyte composition. The recent years have witnessed a dramatic improvement in the understanding of dynamical processes at the solid/vacuum interface by using the capacity of a variety of novel experimental techniques. Unfortunately, only a few of them can be brought to bear on the solid/liquid interface. One of these technique involves the analysis of equilibrium fluctuations of monatomic steps using the STM [5-8]. These equilibrium fluctuations arise from the movement of kink sites, caused by the rapid emission or capture of adatoms which diffuse along the step edges or on the terraces between steps. The very same phenomenon was observed also for Ag (111) surfaces in contact with an aqueous electrolyte and it was qualitatively shown that the magnitude of the fluctuations depends on the electrode potential [9].

In this paper we present the first quantitative analysis of the equilibrium step fluctuations in an electrolyte for electrode potentials which range from far below the anodic dissolution of silver up to values near the dissolution limit. A full report on the results and their analysis will be published elsewhere [10]. We find that both the magnitude and the time dependence of the equilibrium fluctuations track closely the results on the solid/vacuum interface, as long as the potential is negative with respect to the saturated calomel electrode (SCE). As the potential becomes positive and approaches the dissolution limit, the magnitude of the fluctuations increase dramatically, accompanied by a change in the time dependence. It is shown that these changes are indicative of a rapid exchange of step atoms with the terraces and with atoms dissolved in the electrolyte prior to the onset of the silver dissolution.

## EXPERIMENTAL

The STM studies were performed with an electrochemical STM which allows an independent control of sample and tip potential by a bipotentiostat. The tips were etched from polycrystalline tungsten wires and coated with Apiezon wax to reduce the area in contact with the electrolyte down to  $10^{-7}$  -  $10^{-8}$  cm<sup>2</sup> [11]. Tunneling currents were in the range of 1 to 3 nA. Two different kinds of electrolytes were used. The Cu<sup>++</sup>-containing electrolyte (A) consisted of 0.05 M H<sub>2</sub>SO<sub>4</sub> + 1 mM CuSO<sub>4</sub>, the Cu<sup>++</sup>-free one (B) of 0.05 M Na<sub>2</sub>SO<sub>4</sub> + 0.1 mM H<sub>2</sub>SO<sub>4</sub>. As has been noted previously, Cu<sup>++</sup> ions in solution can improve the tip performance significantly [9]. In addition, the Cu / Cu<sup>++</sup> redox couple constitutes a convenient, low-noise reference electrode. Therefore, solutions with Cu<sup>++</sup> ions were used whenever the presence of Cu<sup>++</sup> did not interfere with the system under study (e.g. by Cu deposition). For measurements of step fluctuations at very negative potentials, Cu<sup>++</sup> ion free solutions had been used. In experiments with electrolyte (A), a Cu wire served as a reference electrode and the tip bias  $E_{tip}$  was usually held between +20 and -20 mV vs. Cu / Cu<sup>++</sup> in the solution. For measurements in electrolyte (B), a home-made reference electrode was used which consisted of a Au wire sealed glass capillary containing a Cu wire in a  $10^{-3}$  M Cu<sup>++</sup> solution. A Pt wire served as a counter electrode in all experiments. Yet, all potentials are quoted with respect to the saturated calomel electrode (SCE). The silver crystal was cut by spark erosion, oriented by Laue reflection, mechanically and electrochemically polished. Before mounting the crystal in the electrochemical cell, the crystal was flame annealed and rapidly cooled in Ar gas. The tilt angle to the (111) surface was  $1.6^\circ \pm 0.2^\circ$  towards  $[2\bar{1}\bar{1}]$  direction. In the ideal case, the surface would consist of parallel monatomic (111)-steps along the densely packed  $[01\bar{1}]$  direction. The real surface, however, revealed occasional step pinning at residual contaminants and dislocations. We observed furthermore that the steps on the Ag(111) surface tend to merge and form double steps.

Usually, after three days with about ten cycles of flame annealing and electrochemical measurements, the crystal had to be repolished and reoriented.

## RESULTS

Due to the rapid kink motion, STM images provide spatial information as well as time information. From the spatial fluctuations one can determine the kink density of steps [8]. Whenever steps appear frizzy, the time information in the STM image is dominant. The pure time information then can be extracted from so-called "time images" where the same scan line across the steps is tracked repetitively and the lines are displayed in the normal STM image format, so that the coordinate parallel to the steps (from top to bottom of the image) represents a time scale. For the investigation of step fluctuations as a function of electrode potential we have imaged stepped areas, where no defects (other than steps) were present and no obvious step pinning occurred. Fig. 1 shows x-t images of such an area of parallel, monatomic high steps for two different electrode potentials.

Using such time images, step fluctuations can be analyzed by means of a time correlation function  $F(t)$ .

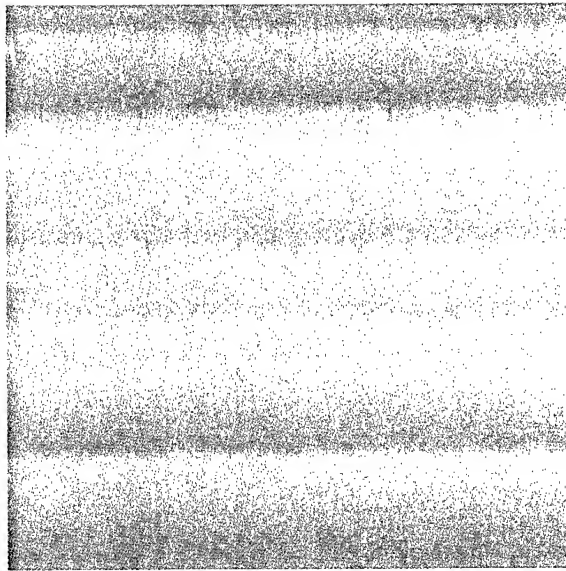
$$F(t) = \left\langle (x(t) - x(0))^2 \right\rangle \quad (1)$$

Here,  $x$  denotes the coordinate perpendicular to the steps. Using time images such as displayed in Fig. 1 we have measured the time correlation function for electrode potentials between -500 and +80 mV vs. SCE. Obviously, the fluctuations increase when the electrode potential becomes positive. Fig. 2 shows the value of the correlation function at  $t=11$  s as a function of the potential. For negative electrode potentials, the time correlation function does not depend on the potential at all. In the positive potential regime, however, we find a large increase of the fluctuations which appear to diverge as silver begins to dissolve. The solid line is a theoretical curve to be discussed below.

Theoretical analysis [13,14] shows that the correlation function obeys a power law in  $t$ . Depending on the type of process involved in the fluctuations, the correlation function can also depend on the distance between steps. The theory of step fluctuations thereby permits the determination of the type of mass transport which dominates on the surface. A detailed discussion of the various situations which could in principle be relevant to the Ag(111) surface in contact with an electrolyte is presented in [10]. Here, we consider only the two cases which actually apply to the Ag(111)/electrolyte interface.

For negative electrode potentials, we have found that  $F(t)$  obeys a  $t^{1/4}$  power law and does not depend on the step-step distance. This is indicative of a mass transport restricted to atom

$U_S = -40 \text{ mV}$



$U_S = +80 \text{ mV}$

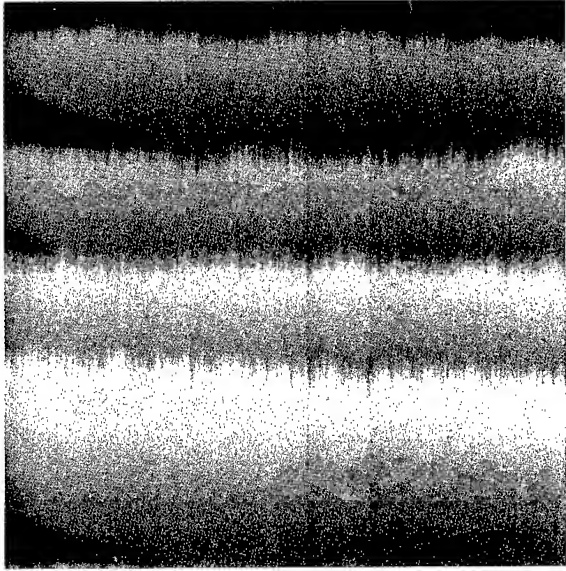


Fig. 1: Time images of stepped areas on Ag (111) for different electrode potentials. The axis perpendicular to the step direction is a spatial axis, the axis parallel is the time axis. Each image has a scan width of about 50 nm and the scan time per image is 60 s

motion along the steps. In this case the fluctuations are determined by the kink energy  $\epsilon$ , the equilibrium concentration of adatoms at steps  $c_{st}$ , and the diffusion coefficient for the motion along steps  $D_{st}$

$$F(t) = \left(2c^{-\beta\epsilon}\right)^{3/4} (c_{st} D_{st})^{1/4} t^{1/4} \quad \text{with } \beta = 1/k_B T. \quad (2)$$

where  $P_k$  is the kink concentration of steps which is related to the kink energy by

$$P_k \approx 2e^{-\beta\epsilon} \quad \text{with } \beta = 1/k_B T. \quad (3)$$

For positive potentials,  $F(t)$  was found to depend on the step-step distance  $L$  following an  $L^{1/2}$  power law. The dependence on the time changes to a  $t^{1/2}$  power law. This functional dependence proves that the mass transport involves now not only an exchange of step atoms with the terraces but also with the electrolyte. The quantitative relation in that case is

$$F(t) = \left(P_k \frac{c_s}{\tau_{sc}}\right)^{1/2} L^{1/2} t^{1/2}. \quad (4)$$

Here,  $c_s$  is the adatom concentration on the terraces and  $\tau_{sc}$  is the average time of an atom on

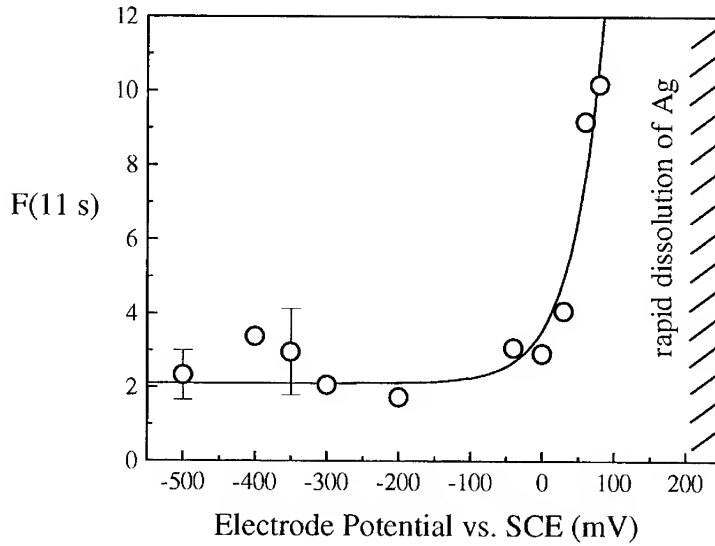


Fig. 2: Correlation value  $F(t)$  at  $t=11$  s as a function of the electrode potential. The solid line is a fit corresponding to eq. (13) for  $\lambda=1.17$ .

the surface before it is dissolved into the electrolyte.

In the regime of negative potentials (with respect to SCE), the magnitude of the correlation function does not depend on the electrode potential. Unless one assumes some compensation effects this entails that neither the kink concentration nor the concentration of adatoms along a step and their mobility is modified by the potential (eq. (2)). It would be interesting to analyze whether the presence of a liquid has an effect at all on the concentration of adatoms and kinks or on the mobility of atoms along the step edge. For that purpose we compare the fluctuations observed in the presence of an electrolyte to the fluctuations measured earlier for Ag(111) under UHV conditions [15,16]. If the experimental data for 300 K in this earlier work are analyzed using the time correlation function one finds  $F(t=1\text{ s}) = 2.1$  in good agreement with the results for negative potentials in Fig.2. We can therefore conclude that the step fluctuations and thus neither the kink concentration nor the concentration of adatoms along a step and their mobility are modified by the presence of the liquid. This is a quite remarkable result since one might have speculated that the mobility of atoms could be lowered by the presence of the liquid, the liquid providing some kind of friction. Our results show that one is not in the friction limit of diffusion and the diffusion still involves activated adatom hopping, just as known from the solid/vacuum interface.

In the regime of positive electrode potentials, the fluctuations obey the  $t$  and  $L$  dependence of eq. 4. Hence, in this case silver atoms from step sites are emitted onto the terraces between adjacent steps and subsequently either dissolved in the electrolyte or attached at a neighboring step. This is again a remarkable result since it provides evidence for the beginning of mass exchange between the solid and the liquid well below the dissolution potential of silver. We note that one has still equilibrium fluctuations of the steps with no visible loss of material and therefor no net flow of mass into the electrolyte. The observed mass exchange of silver atoms with the electrolyte is presumably confined to the immediate vicinity of the surface.

We now discuss the large increase of the fluctuations in the regime of positive electrode potential quantitatively. We write the mean time before oxidative desorption of an atom into the electrolyte,  $\tau_{se}$ , in terms of the desorption rate  $v_{se}$

$$\tau_{se} = v_{se}^{-1} = v_0 e^{-\beta E^*} \quad (5)$$

where  $v_0$  is the pre-exponential factor and  $E^*$  is the activation energy for the desorption of an atom from the solid surface into the electrolyte. Then, eq. (4) becomes

$$F(t) = \left( v_0 e^{-\beta E^*} c_s P_k \right)^{1/2} L^{1/2} t^{1/2} \quad (6)$$



If the equilibrium concentration of the adatoms on the terraces  $c_s$  are expressed in terms of the energy of formation for a vacancy-adatom pair  $E_v$ , one obtains

$$c_s = e^{-\frac{1}{2}\beta E_v} \quad (7)$$

and

$$F(t) = \left( 2v_0 e^{-\beta(E^\ddagger + \varepsilon + E_v/2)} \right)^{1/2} L^{1/2} t^{1/2} \quad (8)$$

The dramatic increase in the fluctuations suggests an exponential dependence of the fluctuations on the potential. An exponential dependence is obtained if one assumes that either one or all energies in eq. (8) decrease with increasing potential. Since  $\varepsilon$  does not depend on the potential for negative potentials we assume that it likewise does not become potential dependent in the regime of positive potentials. This leaves the energy  $E^\ddagger$  for the oxidative desorption of an atom into the electrolyte and the energy  $E_v$  for creation of an adatom-vacancy pair as candidates for the potential dependence. For both energies  $E^\ddagger$  and  $E_v$ , we make the simplest possible ansatz

$$E^\ddagger = E^\ddagger(U_S = 0) - \lambda_1 U_s \quad \text{and} \quad E_v = E_v(U_S = 0) - \lambda_2 U_s \quad (9)$$

Eq. (8) then becomes

$$\begin{aligned} F(t) &= \left( 2v_0 e^{-\beta(E_0^\ddagger + \varepsilon + E_{v0}/2)} L t \right)^{1/2} e^{\lambda U_s / 2k_B T} \quad \text{with} \quad \lambda = \lambda_1 + \frac{1}{2}\lambda_2 \\ &= C(E_0^\ddagger, t) e^{\lambda \beta U_s / 2} \end{aligned} \quad (10)$$

$E_0^\ddagger$  and  $E_{v0}$  denote the energies for zero electrode potential vs. SCE. In Fig. 2 we have fitted the data with eq. (10) and an additional constant term to account for the step fluctuations due to mass transport along the steps. This implies the reasonable assumption that the step fluctuations due to mass transport along the steps continue into the regime of positive potentials. With  $L=25$  (in atomic units), the best fit is obtained for

$$\lambda = 1.17 \pm 0.24 \quad (11)$$

and

$$C(E_0^\ddagger) = 1.44 \pm 0.48 \quad (12)$$

Assuming a typical pre-exponential factor to be  $\nu_0 = 10^{13} \text{ s}^{-1}$  we can express the energy for oxidative dissolution in terms of the experimental value for  $C(E_0^\ddagger)$  and the energy for the formation of an adatom vacancy pair and the kink energy

$$E_0^\ddagger = 0.87 \text{ eV} - \epsilon - \frac{1}{2} E_{\nu 0} \quad (13)$$

This equation is valid for  $U_s = 0$ . If one had used a different reference electrode, which is shifted by  $U_0$  with respect to SCE, i.e.  $U = U_s + U_0$ , eq. (13) would hold for  $U = U_0$  and would be insofar independent of what has been used as reference electrode. From eq. (13), one can determine an upper limit for the oxidative desorption energy  $E_0^\ddagger$ . The kink energy  $\epsilon$  and the energy for the formation of an adatom-vacancy pair  $E_{\nu 0}$  cannot vanish since we measure no net flow of mass from the solid into the electrolyte at  $U_s = 0$ . Hence, one obtains from eq. (13) an upper limit for  $E_0^\ddagger$

$$E_0^\ddagger < 0.87 \text{ eV} . \quad (14)$$

Because of the potential independence of the kink energy for negative potentials and the good agreement with the values calculated for the solid/vacuum interface there one can probably argue [17] that the energy for the creation of adatom/vacancy pairs should not bear a strong influence on the potential and should likewise correspond to the energy calculated for the solid/vacuum interface. If one inserts the corresponding numbers in eq. (13) ( $\epsilon = 0.08/0.102 \text{ eV}$ ,  $E_{\nu} = 1.03/1.10 \text{ eV}$  [18,19]) one obtains

$$E_0^\ddagger \cong 0.3 \text{ eV} \quad (15)$$

No values for  $E_0^\ddagger$  have been found in the literature to be compared with our data. However the finding that the silver surface dissolves rapidly from the step sites when the dissolution potential is approached corroborates nicely with the increasing step fluctuations and the rapidly growing exchange rate of silver atoms with the electrolyte.

## CONCLUSIONS

In summary, our results indicate that the silver-electrolyte interface is in a very dynamic state at potentials close to the dissolution of the metal. New and hitherto inaccessible information on the kinetics of electrode surface processes can be derived from the observations of step fluctuations.

## ACKNOWLEDGEMENTS

We thank U. Linke for the skilful preparation of the silver crystal. Partial support of this work by the Fond der Chemischen Industrie is gratefully acknowledged.

## REFERENCES

- [1] D. M. Kolb, *Progr. Surf. Sci.* 51, 109 (1996)
- [2] A. S. Dakkouri, *Sol. State Ionics*, in press
- [3] W. Obretenov, U. Schmidt, W. J. Lorenz, G. Staikov, E. Budevski, D. Carnal, U. Müller, H. Siegenthaler and E. Schmidt, *Faraday. Disc.* 94, 107 (1992)
- [4] T. Will, M. Dietterle and D. M. Kolb, in: *Nanoscale Probes of the Solid/Liquid Interface*, NATO-ASI, Vol. E288, eds. A. A. Gewirth and H. Siegenthaler, Kluwer, Dordrecht (1995), p. 137
- [5] M. Giesen-Seibert, R. Jentjens, M. Poensgen, and H. Ibach, *Phys. Rev. Lett.* 71, 3521 (1993); *Phys. Rev. Lett.* 73, E911 (1994)
- [6] L. Kuipers, M. S. Hoogeman, and J. W. M. Frenken, *Phys. Rev. Lett.* 71, 3517 (1993)
- [7] M. Giesen-Seibert and H. Ibach, *Surf. Sci.* 316, 205 (1994)
- [8] M. Giesen-Seibert, R. Jentjens, M. Poensgen, and H. Ibach, *Surf. Sci.* 329, 47 (1995)
- [9] M. Dietterle, T. Will and D. M. Kolb, *Surf. Sci. Lett.* 327, L495 (1995)
- [10] M. Giesen, M. Dietterle, D. Stapel, H. Ibach, and D. M. Kolb, to be published
- [11] A. S. Dakkouri, M. Dietterle and D. M. Kolb, *Festkörperprobleme / Adv. Sol. State Phys.* Vol. 36, Vieweg, Wiesbaden, in press
- [12] M. Giesen, G. Schulze-Icking-Konert, D. Stapel, and H. Ibach, *Surf. Sci.* 366, 229 (1996)
- [13] A. Pimpinelli, J. Villain, D. E. Wolf, J. J. Métois, J. C. Heyraud, I. Elkinani, and G. Uimin, *Surf. Sci.* 295, 143 (1993)
- [14] N. C. Bartelt, J. L. Goldberg, T. L. Einstein, and E. D. Williams, *Surf. Sci.* 273, 252 (1992)
- [15] M. Poensgen, J. F. Wolf, J. Frohn, M. Giesen, and H. Ibach, *Surf. Sci.* 274, 430 (1992)
- [16] M. Poensgen, PhD Thesis RWTH Aachen 1993, D82, published as report of the Forschungszentrum Jülich, Jül-2798, July 1993
- [17] A possible potential dependence of  $E_v$  could arise from the large dipole moment associated with the formation of the adatom-vacancy pair in the presence of the electric field in the Helmholtz layer. We have currently no understanding as to how large such an effect could be.
- [18] P. Stoltze, *J. Phys. Condens. Matter* 6, 9495 (1994)
- [19] R. C. Nelson, T. L. Einstein, S. V. Khare and P. J. Rous, *Surf. Sci.* 295, 462 (1993)

## THE INITIAL STAGES OF METAL DEPOSITION ON METAL AND SEMICONDUCTOR ELECTRODES STUDIED BY *IN SITU* STM

D.M. KOLB, R.J. RANDLER, R.I. WIELGOSZ, J.C. ZIEGLER  
Dept. of Electrochemistry, University of Ulm, 89069 Ulm, Germany

### ABSTRACT

The deposition of Cu onto Au(100) and of Pb onto n- Si(111) electrodes from aqueous solutions has been monitored *in situ* by scanning tunneling microscopy. In the first case, a bcc structure of the Cu overlayer is observed, which allows pseudomorphic growth on Au(100) up to the 10th layer. Then a slow structural transition to fcc begins. In contrast, Pb on Si(111) is shown to deposit as 3D crystallites with flat (111) terminated surfaces.

### INTRODUCTION

The electrolytic deposition of metal overlayers on metal or semiconductor substrates is a reaction of considerable importance in science and technology. Cu deposition onto gold single crystal surfaces has become a model system for the plating process, with which the fundamentals of nucleation and growth were elucidated by a large number of structure-sensitive methods [1-3]. In this respect the scanning tunneling microscope (STM) has come to play a central role in the study of the initial stages as it allows the imaging of electrode surfaces in an electrolytic environment in real space and with atomic resolution [4-6]. This is demonstrated in the following for Cu deposition on Au(100) from sulfuric acid solution, where the structure-determining role of the substrate in the film growth is clearly seen.

Metal deposition onto semiconductor electrodes has previously been studied for the formation of Schottky barriers [7,8] and the stabilisation of photoanodes [9-13] in photoelectrochemical solar cells. One criticism of these and other studies [14-17] is that the chemistry and surface of the semiconductor electrodes has generally not been well defined. This problem stems from the difficulties of preparing atomically flat surfaces, even from single crystal semiconductor electrodes, and avoiding chemical and electrochemical reactions which lead to corrosion of that surface. In the second part of this study results for the electrodeposition of Pb on n- Si(111) will be presented. Such electrodes when properly etched reveal an atomically flat surface [18-22] of known chemistry, which provide ideal substrates for the study of metal electrodeposition with STM.

### EXPERIMENT

The STM studies were performed with the Topometrix TMX 2010 and Molecular Imaging machines, using electrochemically etched tungsten and Pt-Ir (80:20) tips with a diameter of 0.25 mm. In order to minimize the faradaic currents the tips were coated with Apiezon wax, leaving only the very end of the tip exposed. The electrochemical STM set up contained a bipotentiostat which allowed the potentials of the tip and substrate to be varied independently of each other with respect to a reference electrode. The Au(100) working electrode was a single crystal disc of 10 mm diameter and 2 mm thickness. Before each experiment the gold crystal was carefully annealed in the flame of a Bunsen burner to red heat and then cooled down to room temperature in air. Because the electrochemical STM cell was open to air, the electrolyte was not purged with nitrogen. For the

Cu/Au(100) system, 0.05 M or 0.1 M  $\text{H}_2\text{SO}_4 + x \text{ M CuSO}_4$  (where  $x$  varied between  $5 \times 10^{-3}$  and  $10^{-4}$  M) electrolytes were used, prepared from 96%  $\text{H}_2\text{SO}_4$  (Suprapur, Merck),  $\text{CuSO}_4$  (p.a., Merck) and Milli-Q water (Millipore). For measurements in solutions with copper concentrations greater than  $10^{-3}$  M, a copper wire was used as reference electrode. Due to the problem of copper dissolution in oxygen containing electrolyte, investigations in solutions with lower copper concentrations were performed with a reference electrode consisting of a fritted glass tube containing a copper wire and electrolyte. The tunneling currents were in the order of 2 - 3 nA.

The silicon electrodes were cut from one-side polished n- Si(111) wafers (1-20  $\Omega\text{cm}$ ) supplied by Wacker Siltronic AG and Daimler-Benz. The electrodes were cleaned by refluxing with isopropanol for 2 hours and further cleaned by the RCA method [23]. Prior to assembly of the STM cell the silicon was immersed in 50% HF solution, to remove any oxide, and etched for up to 3 minutes in 40%  $\text{NH}_4\text{F}$  to produce an atomically flat monohydride terminated surface [18-20]. For the Pb / n- Si(111) system, STM measurements were performed in 0.05 M  $\text{HClO}_4$  or HCl and 0.05 M  $\text{HClO}_4$  or HCl +  $1 \times 10^{-3}$  M  $\text{Pb}^{2+}$  electrolytes, with a Pt wire counter electrode and a hydrogen charged Pd wire or SCE reference electrode.

All STM pictures were recorded in the constant-current mode and are shown as top-views or as shaded pictures (the surface appears as if it is illuminated from the left side). All potentials are quoted against the saturated calomel electrode (SCE).

## RESULTS

### Cu deposition on Au(100)

Cu deposition on gold from aqueous solutions starts with the formation of a monolayer, which occurs at potentials positive of the Nernst potential  $E_r$  for bulk Cu deposition. This so-called underpotential deposition (upd) results from a substrate-adsorbate interaction which exceeds in strength that between the adsorbate atoms [24]. The full monolayer of Cu on Au(100) in sulfuric acid electrolytes has a pseudomorphic structure, i.e., the Cu adatoms occupy gold lattice sites. At potentials negative of  $E_r$  bulk deposition starts which in most cases follows a Stranski-Krastanov mechanism: three-dimensional metal clusters with bulk lattice constants grow on top of the pseudomorphic monolayer [2]. Only in a few cases two-dimensional pseudomorphic growth is observed for the second or even third layer [25]. An extraordinary example of such a system is Cu deposition on Ag(100). Pseudomorphic growth is observed up to the 8th Cu monolayer, despite a lattice mismatch of about 12% [26]. Further, it was shown that Cu on Ag(100) initially grows with a body-centered-cubic (bcc) structure, which although energetically slightly less favourable than fcc Cu (by about 20 meV [27]), fits perfectly onto Ag(100). With the 9th layer the surface becomes buckled and a slow structural transition from bcc to fcc takes place. The transition was reported to occur over several tens of Cu layers before the emergence of a fcc structure [26].

In the following we report similar observations for Cu on Au(100) in sulfuric acid solution. Fig. 1 shows a sequence of three STM images which start with the Cu-free Au(100) surface at  $E = +0.2$  V. As the surface was initially reconstructed, monoatomic high gold islands were formed during lifting of the (hex) reconstruction, as has been demonstrated in earlier work [28, 29]. After stepping the potential from +0.2 V to -0.25 V the upd layer was formed immediately, covering the whole gold surface uniformly with a pseudomorphic layer of Cu (not seen in Fig. 1). Soon after bulk Cu deposition began with the formation of bilayers; the rims of the gold islands acting as preferred nucleation centres. Zooming into the Cu islands for atomic resolution images revealed a Cu next-neighbour distance of 0.29 nm as for gold and a step height of 0.15 nm (the step height of fcc Cu is 0.18 nm). Both observations confirmed that Cu was

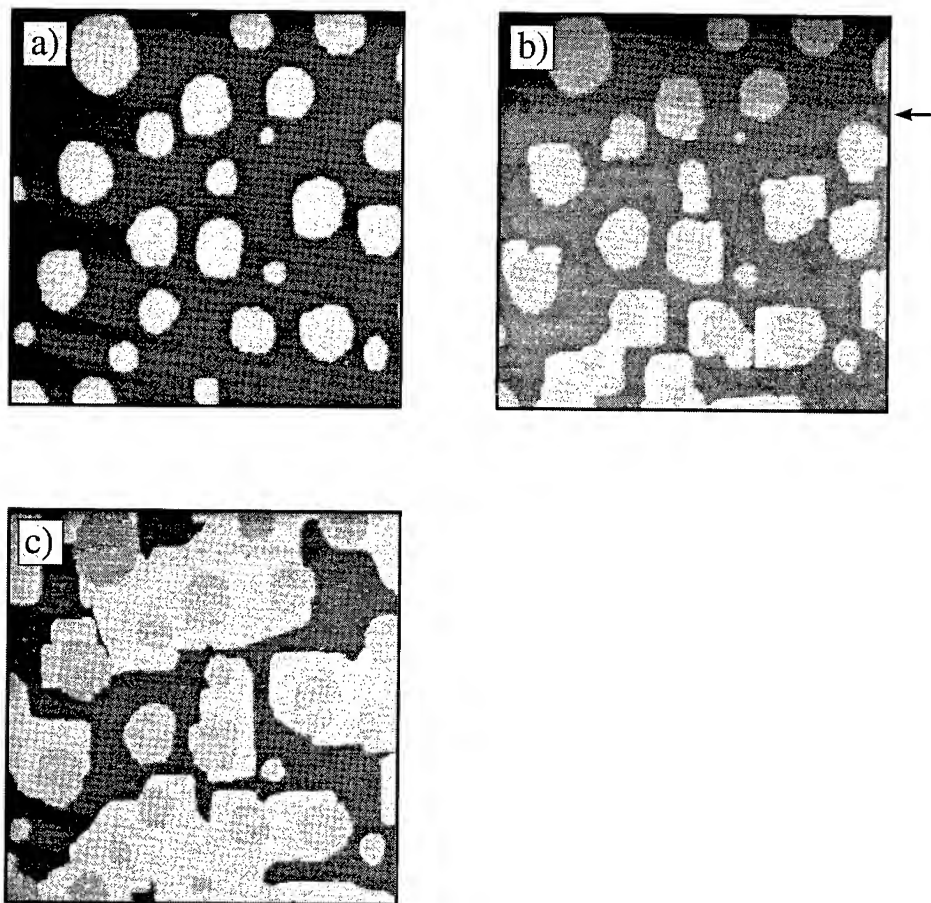


Fig. 1. STM images (220 nm x 220 nm) illustrating the copper deposition on a Au(100) surface in 0.05 M  $\text{H}_2\text{SO}_4$  + 0.1 mM  $\text{CuSO}_4$ . Image (a) shows the bare substrate surface at  $E = +200$  mV vs. SCE decorated with monoatomic high gold islands. Stepping the potential from +200 mV to -250 mV vs. SCE (see arrow, picture (b)) leads to the formation of a copper bilayer on top of the immediately preformed up film. The pictures clearly reveal that the rims of the gold islands act as nucleation sites for the bulk copper deposition.

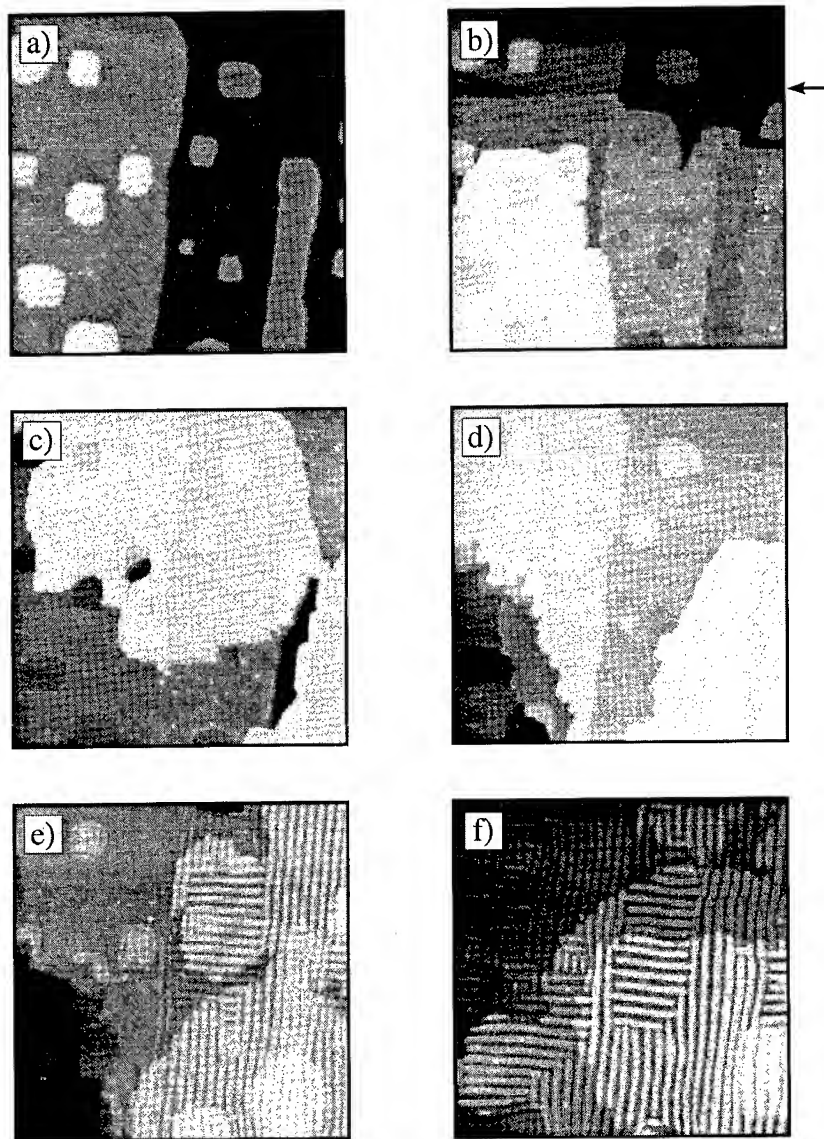


Fig. 2. Sequence of consecutive STM images (220 nm x 220 nm) showing the growth of several copper layers on a Au(100) surface in 0.1 M  $\text{H}_2\text{SO}_4$  + 0.5 mM  $\text{CuSO}_4$ . After a potential jump from +500 mV to -200 mV vs. SCE (see arrow in picture (b)) the copper deposition follows a Frank-van der Merwe-growth mode (pictures (b) - (d)). The first 10 layers form a smooth film on the gold substrate, while with the formation of the 11th copper layer a striped structure appears (pictures (e) - (f)).

deposited with a bcc structure. This was supported by the fact that only bilayers of Cu were initially formed on the upd covered gold surface, which resulted in a total of three Cu layers on Au(100) as the height necessary for a critical Cu nucleus.

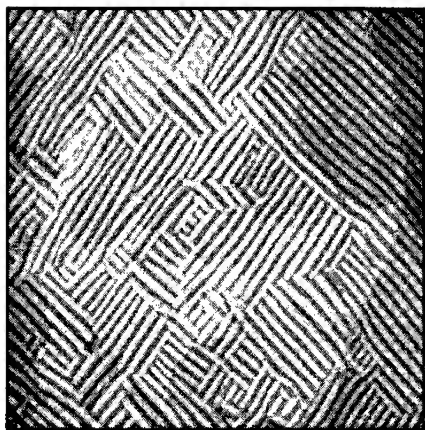


Fig. 3. STM image (350 nm x 350 nm) of the wavy copper phase on Au(100) in 1mM  $\text{CuSO}_4$  + 0.05 M  $\text{H}_2\text{SO}_4$  at -300 mV vs. SCE. The wavy structure consists of small domains rotated by  $90^\circ$  with respect to each other. As the film grows the surface morphology becomes evermore irregular, until the stripes disappear (see text for details).

Three atomic layers are indeed needed to define the crystallographic unit cell of bcc. The sequence of STM images in Fig. 2 demonstrate the layer-by-layer growth of Cu on Au(100) which could be observed up to the 10th layer. With the deposition of the 11th monolayer the surface changed abruptly. A wave like morphology was observed, the structure having a corrugation length of about 6.0 nm and a corrugation height of about 0.2 nm. Unlike Cu on Ag(100) where each terrace consisted of one single domain of the wavy structure, many small domains, rotated by  $90^\circ$  with respect to each other, are seen on Au(100). Even after deposition of 11 Cu layers the positions of the gold islands were still reflected by the defect structure of the surface. This was particularly evident at the beginning of the wave structure formation, where the 11th layer nucleated at defects which had originated from the gold islands (Fig. 2e).

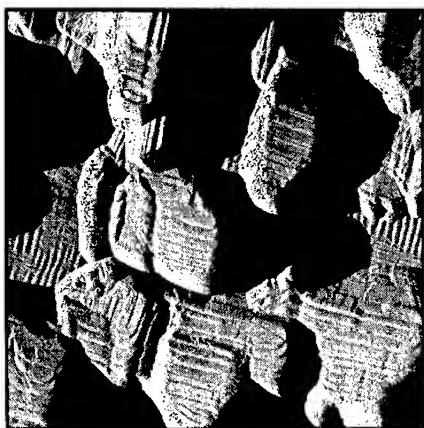


Fig. 4. STM image (470 nm x 470 nm) of a very thick copper film grown on Au(100) at -200 mV vs. SCE. The growth mode changes with increasing film thickness from a layer-by-layer fashion into growth via three-dimensional clusters. On top of these clusters atomically flat terraces are formed which are separated by monoatomic steps.



Fig. 3 shows the STM image of a Au(100) electrode covered by more than 11 Cu layers, the whole surface exhibits the wavy structure. As in the case of Cu on Ag(100), the wavy surface signals the beginning of a structural transition from bcc Cu to fcc Cu where the atoms are more closely packed. This transition region, in which the wavy structure gradually disappears, extends over many layers, until finally crystallites of fcc Cu appear (Fig. 4).

Although the lattice constants of Ag and Au are almost identical, as are the wavy structures for Cu overlayers on Ag(100) and Au(100), the maximum thickness of bcc Cu is distinctly different in both cases: 8 layers for Cu on Ag(100), but 10 layers for Cu on Au(100). The exact reasons for such a far-reaching influence of the substrate chemical properties is not yet fully understood.

#### Pb deposition on n-Si(111)

The imaging of a semiconductor surface with a STM in an electrolytic environment imposes some restrictions on the tunneling / potential conditions which can be employed. A fuller description of these considerations can be found elsewhere [30], and only a short description of the most relevant factors will be summarised here. For imaging of the n-type silicon surface the electrode was biased into accumulation conditions, with the tip potential set to a more positive value. These conditions are summarised in Fig. 5.

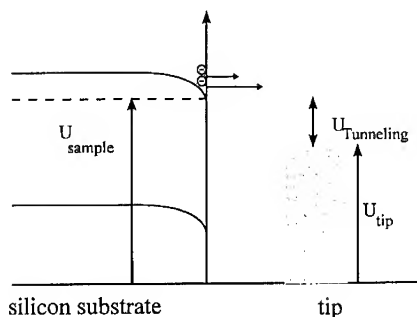


Fig. 5 Energy diagram of the conditions necessary for imaging the silicon surface with the STM. The substrate is biased into accumulation ( $U_{\text{sample}}$ ) with the tip set at a more positive value ( $U_{\text{tip}}$ ).

With the silicon electrode set to a more negative bias than its flat band potential, a density of electrons, necessary for tunneling, was present at the substrate surface. A faradaic current was observed at the substrate, presumably due to oxygen reduction. Biasing of an n-type semiconductor positive of the flat band potential was expected to reduce the concentration of the electrons at the substrate surface and cause the tip to crash. It has been reported [31] that a stable tunneling current was sustainable at the silicon substrate at potentials somewhat positive of flatband conditions. Although the effect was attributed to surface states, a band edge shift [30] or a tip induced effect [30] cannot be ruled out.

Infrared measurements [18-20] have shown that etching a (111) oriented Si surface in 40%  $\text{NH}_4\text{F}$  solution produces a monohydride terminated surface. The surface is known to be stable for periods of hours in air, in aqueous solution or an electrochemical environment with the semiconductor under accumulation conditions. STM measurements [22] have shown that the surface exhibits atomically flat terraces, with atomic bilayer step heights and triangular etch pits. The stability of the monohydride termination leads to monohydride terminated step edges [22] and a step density / morphology which is determined by the direction and degree of miscut of the wafer [32]. Fig. 6 shows a STM image of the n-Si(111) surface in 0.05 M  $\text{HClO}_4$ . The only surface

defects observed were atomic bilayer steps, 0.31 nm in height. Lateral atomic resolution of the surface was not achieved. This was believed to be due to the limited resolution of the Pt-Ir tip.

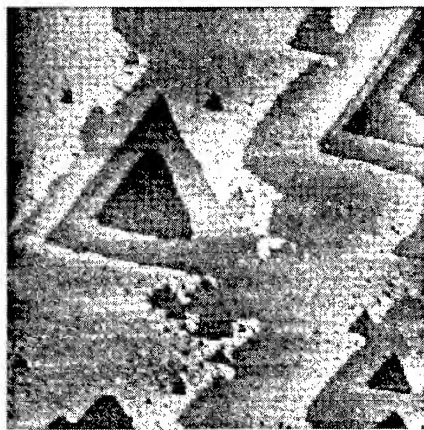


Fig. 6. STM image of a  $1\ \mu\text{m} \times 1\ \mu\text{m}$  area of the n-Si(111) surface in 0.05 M  $\text{HClO}_4$ . The sample and tip potentials were set at -610 and +240 mV vs. SCE. The tunneling current was 0.75 nA.

However, the stable tunneling conditions and surface morphology strongly suggested that the surface remained hydride terminated. The image was recorded with the semiconductor in accumulation and a tunneling voltage ( $U_{\text{Tunneling}} = U_{\text{tip}} - U_{\text{Substrate}}$ ) approaching 1V. Although tunneling was possible at less positive tip potentials, the image recorded was unstable. Stable images were only observed with these rather positive tip potentials. Imaging of the silicon surface with tungsten tips, which normally yield a higher lateral resolution, was not possible due to the reactivity of the tip at these potentials. The silicon surface showed a morphology expected for a (111) wafer with a slight miscut towards the  $[11\bar{2}]$  direction.

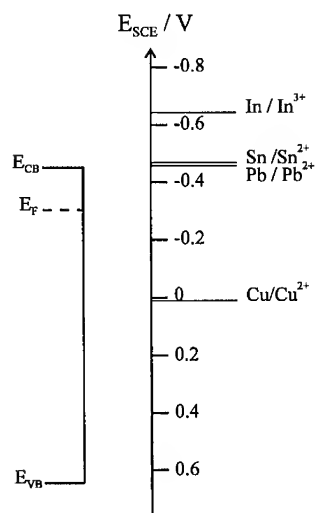


Fig. 7. Energy diagram for the n-Si(111) / electrolyte interface, in 0.05 M  $\text{HClO}_4$ .

The redox energies in solution are drawn for a  $10^{-3}$  M metal ion concentration. The band edges ( $E_{\text{CB}}$  and  $E_{\text{VB}}$ ) as well as the Fermi level ( $E_{\text{F}}$ ) at flat band conditions are shown. A doping density of  $10^{15}\ \text{cm}^{-3}$  of the silicon substrate is assumed.

The influence of the semiconductor surface on metal deposition was to be followed by observing the initial stages of deposition with the STM. This placed certain restrictions on the metal which could be studied. For the initial stages of metal deposition to be observed it would be necessary to image the bare surface prior to the start of electrodeposition. Therefore, a potential region would have to exist where the silicon surface was in accumulation but no electrodeposition was in progress. Fig. 7 shows the positions of the silicon band edges on an energy diagram relative to various metal / metal ion redox couples. The position of the band edges can be inferred from the flat band potential of silicon, the determination of which has been the subject of several studies in fluoride as well as non fluoride electrolytes [33-35]. The results obtained in both kinds of media are rather similar. A value of -300 mV vs. SCE was taken as the flat band potential, which agrees with the values reported for n- Si(111) with doping density in the order of  $10^{15} \text{ cm}^{-3}$ . The Cu/Cu<sup>2+</sup> redox couple potential lay in the bandgap of silicon, and therefore no potential window was expected, or indeed observed, which would allow the imaging of the silicon surface prior to Cu electrodeposition. From the energy diagram, it would appear that lead, tin and indium were suitable metals for study. However, in practice it was found that the instability of the Sn<sup>2+</sup> ion to oxidation in oxygen containing solutions, and a large hydrogen evolution current at the potentials necessary for indium deposition, proved problematic in the studies of the electrodeposition of these two metals.

The cyclic voltammogram of n- Si(111) in 0.05 M HClO<sub>4</sub> +  $1 \times 10^{-3}$  M Pb<sup>2+</sup> is shown in Fig. 8. The voltammogram was recorded in a standard electrochemical cell in deoxygenated solution. The voltammograms recorded in the STM cell showed a similar signature, except for a larger current prior to lead deposition, presumably due to oxygen reduction at the silicon substrate.

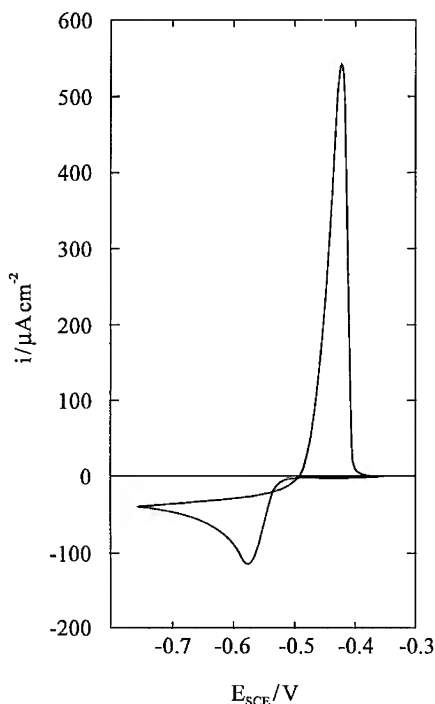


Fig. 8. Cyclic voltammogram of n- Si(111) in 0.05 M HClO<sub>4</sub> +  $1 \times 10^{-3}$  M Pb<sup>2+</sup>. Sweep rate 10 mV s<sup>-1</sup>.

The most notable feature of the curve was that both deposition and stripping peaks were observed. The stripping peak indicated that the  $\text{Pb}/\text{Pb}^{2+}$  redox couple lay above the silicon conduction band edge, so that lead dissolution could occur by the injection of electrons into the conduction band. It appeared that only a small nucleation overpotential existed for the electrodeposition of lead. There was no indication of any underpotential deposition, which suggests no strong interaction between lead and the hydride terminated silicon surface. It was evident from the voltammogram that a potential window of 200 mV or more existed where imaging of the silicon surface would be possible prior to lead deposition.

The silicon surface was imaged in  $0.05 \text{ M HClO}_4 + 1 \times 10^{-3} \text{ M Pb}^{2+}$  in a potential region prior to Pb deposition. The imaged surface was similar to that depicted in Fig. 6. On changing the potential to one more negative than for Pb electrodeposition, no change in the STM image was observed. However, the growth of a Pb layer was clearly visible to the eye. It appeared that the rather positive tip potential necessary for imaging the Si surface prevented the deposition of lead in the region of the tip. Similar effects have been observed with metal / metal systems [36], but not to such an exaggerated extent. It was, however, possible to image the lead layer, by depositing the film prior to the approach of the tip. A much smaller tunneling potential was needed for the imaging of the Pb deposit. Fig. 9 shows the STM image of lead crystallites on the Si surface.



Fig. 9. STM image of a 500 nm x 500 nm area of Pb crystallites electrodeposited onto n-Si(111) from  $0.05 \text{ M HClO}_4 + 1 \times 10^{-3} \text{ M Pb}^{2+}$ . The sample and tip potentials were -860 and -340 mV vs. SCE, respectively. The tunneling current was 2 nA. The maximum height difference measured in the image was 90nm.

The surface was imaged after the growth of the Pb crystallites had effectively stopped due to the depletion of  $\text{Pb}^{2+}$  ions from solution, and was found to be completely covered by lead at this point. Crystallites of various dimensions were observed, and interestingly they exhibited atomically flat terraces, which at first approximation lay parallel to the underlying silicon substrate. Fig. 10 shows an *in situ* STM image of such an atomically flat terrace with lateral atomic resolution. The hexagonal symmetry and interatomic spacing of  $0.35 \pm 0.02 \text{ nm}$  was consistent with that of the (111) face of lead (0.3501 nm). The individual crystallites were observed to grow in a layer-by-layer mode. On stripping the surface of Pb, the silicon surface could again be imaged with a similar morphology to that in Fig. 6. This result would suggest that the deposition and stripping of Pb did not lead to a degradation of the silicon surface.

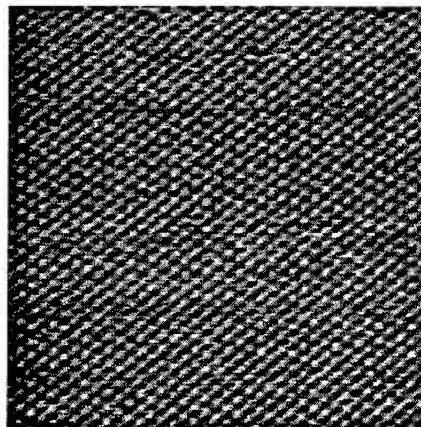


Fig. 10. STM image of a 11 nm x 11 nm region on top of a Pb crystallite (deposited onto n- Si(111) from 0.05 M HCl +  $10^{-3}$  M  $\text{Pb}^{2+}$ ). The sample and tip potentials were -580 and -550 mV vs. SCE, respectively. The tunneling current was 25 nA.

## CONCLUSIONS

We have used *in situ* STM to follow the electrodeposition of Cu on Au(100) in  $\text{CuSO}_4 / \text{H}_2\text{SO}_4$  solutions. It was found that the deposition process could be described by several steps: formation of a upd layer, pseudomorphic growth of bcc Cu up to 10 monolayers in a layer-by-layer fashion, formation of a wavy structure with the beginning of the 11th monolayer and in the end deposition of 3D fcc Cu clusters. Although the deposition of Cu on Au(100) is very similar to that observed on Ag(100) there is a strong influence of the substrate metal on the stability of the bcc Cu phase; on Au(100) the bcc Cu is stable up to a critical thickness of 10 layers, while on Ag(100) a maximum of 8 layers was found.

The silicon (111) surface has been imaged with the STM in non-fluoride solutions. It has been possible to image *in situ* a continuous film of electrodeposited Pb crystallites on the n- Si(111) surface with lateral atomic resolution. 3D Pb crystallites were observed, with flat (111) terminated faces. No upd was observed for this system. The potential / tunneling conditions necessary for imaging the silicon surface have prevented the initial stages of Pb electrodeposition from being observed due to a very strong tip shielding effect. Present efforts are directed towards *in situ* AFM measurements of the Pb / Si(111) system, in order to avoid these complications.

## ACKNOWLEDGMENT

R.I. Wielgosz presently holds a Royal Society European Exchange Programme Fellowship at the University of Ulm.

## REFERENCES

1. D.M. Kolb, Schering Lectures Publication Vol. 2, (Schering Research Foundation, Berlin (1991) p.1
2. E. Budevski, G. Staikov and W.J. Lorenz, Electrochemical Phase Formation and Growth, (VCH, Weinheim, 1996)

3. M.F. Toney, J.N. Howard, J. Richer, G.L. Borges, J.G. Gordon, O.R. Melroy, D. Yee and L.B. Sorensen, *Phys. Rev. Lett.*, 75 (1995) 4472
4. N. Batina, T. Will and D.M. Kolb, *Faraday Discuss.*, 94 (1992) 93
5. W. Obretenov, U. Schmidt, W.J. Lorenz, G. Staikov, E. Budevski, D. Carnal, U. Müller, H. Siegenthaler and E. Schmidt, *J. Electrochem. Soc.*, 140 (1993) 692
6. T. Will, M. Dietterle and D.M. Kolb, in Nanoscale Probes of the Solid/Liquid Interface Vol. E 288, edited by A.A. Gewirth and H. Siegenthaler (NATO-ASI, Kluwer, Dordrecht, 1995), p. 137
7. R. Reineke and R. Memming, *Surf. Sci.*, 192 (1987) 66
8. P. Allongue and E. Souteyrand, *J. Vac. Sci. Technol. B5* (1987) 1644
9. A. Heller, D.E. Aspnes, J.D. Porter, T.T. Sheng and R.G. Vadimsky, *J. Phys. Chem.*, 89 (1985) 4444
10. M. Szklarczyk and J.O'M. Bockris, *J. Am. Chem. Soc.*, 88 (1984) 1808
11. T. Kobayashi, Y. Tanigushi, M. Yoneyama and H. Tamura, *J. Phys. Chem.*, 87 (1983) 768
12. M.M. Kühne and J. Schefold, *Ber. Bunsenges. Phys. Chem.*, 92 (1988) 1430
13. P. Allongue, E. Souteyrand and L. Allemand, *J. Electrochem. Soc.*, 136 (1989) 1027
14. P. Allongue and E. Souteyrand, *J. Electroanal. Chem.*, 286 (1990) 217
15. P. Allongue and E. Souteyrand, *J. Electroanal. Chem.*, 362 (1993) 79
16. P. Allongue, E. Souteyrand and L. Allemand, *J. Electroanal. Chem.*, 362 (1993) 89
17. P. Bindra, H. Gerischer and D.M. Kolb, *J. Electrochem. Soc.*, 124 (1977) 1012
18. V.A. Burrows, Y.J. Chabal, G.S. Higashi, K. Raghavachari and S.B. Christman, *Appl. Phys. Lett.*, 53 (1988) 998
19. Y.J. Chabal, G.S. Higashi, K. Raghavachari and V.A. Burrows, *J. Vac. Sci. Technol. A7* (1989) 2104
20. G.S. Higashi, Y.J. Chabal, G.W. Trucks and K. Raghavachari, *Appl. Phys. Lett.*, 56 (1990) 656
21. G.S. Higashi, R.S. Becker, Y.J. Chabal and A.J. Becker, *Appl. Phys. Lett.*, 58 (1991) 1656
22. H.E. Hessel, A. Feltz, M. Reiter, U. Memmert and R.J. Behm, *Chem. Phys. Lett.*, 186 (1991) 275
23. W. Kern and D.A. Puotinen, *RCA Review*, 31 (1970) 187

- 
24. D.M. Kolb, in Advances in Electrochemistry and Electrochem. Engineering Vol. 11, edited by H. Gerischer and Ch.W. Tobias (Wiley, New York, 1978), p. 125
  25. M. Dietterle, T. Will and D.M. Kolb, *Surf. Sci.*, 342 (1995) 29
  26. M. Dietterle, T. Will and D.M. Kolb, in preparation
  27. J.R. Chelikowsky and M.Y. Chou, *Phys. Rev. B*, 38 (1988) 7966
  28. O.M. Magnussen, J. Hotlos, R.J. Behm, N. Batina and D.M. Kolb, *Surf. Sci.*, 296 (1993) 310
  29. A.S. Dakkouri, *Sol. State Ion.*, in press
  30. P. Allongue, in Advances in Electrochemical Science and Engineering Vol. 4, edited by H. Gerischer and C.W. Tobias (VCH Publishers Inc., New York, 1995) pp. 1-66
  31. E. Tomita, N. Matsuda and K. Itaya, *J. Vac. Sci. Technol. A*8 (1990) 534
  32. G.J. Pietsch, U. Köhler and M. Henzler, *J. Appl. Phys.*, 73 (1993) 4797
  33. J.-N. Chazalviel, *Surf. Sci.*, 88 (1979) 204
  34. G. Schlichthörl and L.M. Peter, *J. Electrochem. Soc.*, 141 (1994) L171
  35. J.-N. Chazalviel, in Porous Silicon Science and Technology, edited by J.-C. Vial and J. Derien (Springer-Verlag, Berlin, 1995) pp. 17-32; and references therein
  36. U. Stimming, R. Vogel, D.M. Kolb and T. Will, *J. Power Sources*, 43 (1993) 169

## EMBEDDED ATOM MODEL OF SURFACE STRESS AND EARLY FILM GROWTH IN ELECTRODEPOSITION: Ag/Au(111)

MICHAEL I. HAFTEL, MERVINE ROSEN, AND SEAN G. CORCORAN  
Naval Research Laboratory, Washington, DC. 20375-5345

### ABSTRACT

We develop an embedded-atom-model (EAM) for simulations of metallic film growth under electrodeposition. The surface charge induced by the electric field is handled as an addition to the electron density to be used in the EAM. Parameters relating the shift in electron density to the electrolytic potential are calibrated to measurements of the capacitance and of surface stress versus potential for Au. For Ag the calibration is to capacitance and local density approximation calculations of surface energy. The resulting parameters are physically realistic for the experiments performed. The model is then applied to calculating migration and step edge barriers for Ag electrodeposited on Au(111) as an explanation of the observed Stranski-Krastanov growth.

### INTRODUCTION

Scanning tunneling microscopy (STM) *in situ* observations of the underpotential electrodeposition (upd) of Ag on Au(111) indicate an unusual form of Stranski-Krastanov (SK) growth.<sup>1</sup> The first monolayer (ML), as in earlier upd work,<sup>2</sup> grows layer-by-layer, while the second also grows layer-by-layer but with 2D islanding. After 2 ML large islands nucleate at step edges whereupon 3D growth of high (~50 Å) hemispherical caps occurs on these islands when they reach a critical size (~200 Å). While Ag/Au(111) exhibits 3D (Volmer-Weber) multilayer growth in vacuum, thanks to significant step-edge barriers,<sup>3,4</sup> neither the onset after 2ML nor the extreme type of 3D growth is observed. This SK growth, not observed in vacuum deposition Ag/Au(111) either,<sup>5</sup> is unexpected since the usual mechanism for SK growth involves lattice mismatch. The authors' hypothesize that the Au substrate mediates the surface interatomic forces such that step-edge barriers (or so-called Schwoebel barriers) are markedly decreased (compared to those of Ag(111)) for coverages less than 2 ML, and a large increase after 2 ML is responsible for the 3D growth. Such an explanation critically depends on what influences the electrolytic solution may have on the step-edge barriers.

We investigate the migration and step-edge barriers for the early growth of Ag on Au(111) and to assess the influence of the electrodeposition environment on them. To do this we develop a model to incorporate the electrolytic charge deposition into the surface embedded atom method (SEAM). We then apply the model, along with previously developed SEAM potentials<sup>6</sup> to calculate site-to-site migration energies and step-edge barriers for an Ag atom moving on 1 or 2 ML of Ag electrodeposited on Au(111).

### ELECTRODEPOSITION MODEL

To treat the charge deposited in electrodeposition in the EAM



description, we picture a charge  $q$  being uniformly distributed on the surface of area  $A$  to a height  $h$ . This will lead to a change in the charge density at atomic surface sites

$$\Delta\rho = q / Ah = \sigma / h, \quad (1)$$

where  $\sigma$  is the areal charge density. An equivalent shift in the electron density ( $\Delta\rho = -q/eAh$ ) is then applied to the site electron densities in the EAM.<sup>7</sup> The total EAM energy is then expressed

$$E = \sum_{i < j} V_{ij}(r_{ij}) + \sum_i F_i(\rho_i/\rho_0 + \Delta\rho/\rho_0) + q^2 d/2\epsilon A + bN_s \Delta\rho/\rho_0, \quad (2)$$

where  $V_{ij}$  is the pair potential,  $F_i$  the embedding function,  $\rho_i$  the electron density at atomic site  $i$  produced by all other atoms, and  $A$  is the surface area under consideration. (We express  $\rho$  relative to the bulk equilibrium electron density  $\rho_0$  as the SEAM potentials are formulated in terms of this relative value). The third term on the r.h.s. is an electrostatic parallel plate contribution produced by the double layer, with  $d$  being the effective double-layer separation and  $\epsilon$  being the dielectric constant. Since  $\epsilon \approx 80$  for water, this term is negligible and will be ignored. The last term involves an ambiguity in the EAM and will be discussed shortly.

The electron density shift to be applied in the EAM is given by

$$\Delta\rho/\rho_0 = -q/\rho_0 eAh = -q/\lambda, \quad (3)$$

where  $\lambda = \rho_0 e h$ . With Eq. (3) inserted into Eq. (2) the system energy can be expressed as a function of  $q$ . From this dependence one can calculate surface energies ( $E_s$ ), surface stress ( $f$ ), the potential across the electrolyte-metal interface ( $\Phi = [\partial E/\partial q]_\lambda$ ), and the capacitance ( $C^{-1} = [\partial \Phi/\partial q]_\lambda$ ), as functions of  $q$  (depending on the value of  $\lambda$ ). At  $q=0$   $\Phi$  is related to  $\Phi_{pzc}$  - the potential of zero charge (PZC) - which is shifted (usually several volts negative) from  $\Phi(q=0)$  depending on the particulars of the electrolyte and reference electrode. The PZC of Au is about 1 volt positive of that of Ag.<sup>8</sup> While  $\Phi$  is not directly measurable, changes in  $\Phi$  should be equal to changes in the electrolytic potential.

The last term in Eq. (2) comes into play because, as is well-known, the transformation  $F(\rho/\rho_0) \rightarrow F(\rho/\rho_0) + b\rho/\rho_0$ ,  $V(r) \rightarrow V(r) - b\Phi(r)/2$ , where  $\Phi$  is the atomic electron density function, leaves the total energy  $E$  invariant in the absence of excess charge ( $q=0$ ). With the external charge this invariance is broken and the last term of Eq. (2) results if we adhere to the "standard" (untransformed) choice of having  $F'(1)=0$ . Unlike  $\lambda$ , which depends on the electrolytic environment,  $b$  is an intrinsic parameter of the interatomic potential.

We determine the  $\lambda$  and  $b$  parameters for Au by fitting the capacitance and electrocapillary measurements of surface stress ( $f$ ) versus voltage ( $\Phi$ ) of Lin and Beck<sup>9</sup>, and more recently by Raiteri and Butt.<sup>10</sup> The optimum value of  $\lambda$ , which can be determined from the capacitance alone, is  $.05 \text{ e/\AA}^2$  yielding a

capacitance (at  $q=0$  for the (100) surface as a reference) of  $33.7 \mu\text{F}/\text{cm}^2$ , in close agreement with Lin and Beck.<sup>9</sup> In this case a  $b$  value of  $0.5 \text{ eV}$  yields good agreement with the electrocapillary curves of Raiteri and Butt. Since our SEAM model does not specify an absolute value of  $\rho_0$ , we cannot specify  $h$ . If we take  $\rho_0 = .025/\text{\AA}^3$  from the EAM potential of Foiles, Daw and Baskes<sup>11</sup>, this would imply  $h=2.0\text{\AA}$ .

Since similar electrocapillary measurements are not available for Ag, we first fit  $\lambda$  to a capacitance of  $75 \mu\text{F}/\text{cm}^2$  given by Schmickler<sup>12</sup> for Ag(111) in an aqueous solution, yielding  $\lambda=.09 \text{ e}/\text{\AA}^2$ . To determine  $b$  we employ a vacuum double layer LDA calculation of Fu and Ho<sup>13</sup> of the surface energy of Ag(110), but alter the  $\lambda$  parameter to allow for the smaller interlayer spacing on the (110) surface. (Assuming  $\lambda$  scales as the interlayer spacing yields  $\lambda=.055 \text{ e}/\text{\AA}^2$  for (110).) The optimal fit yields  $b=-2.0 \text{ eV}$ . Once we know  $\lambda$  and  $b$  we can calculate  $\Phi$  as a function of  $q$  or of  $\Delta\rho$ , or invert the relation to find  $\Delta\rho$  as a function of  $\Phi$ . The electrodeposition experiments of Corcoran et al.<sup>1</sup> were run close to the pzc of Au, which is about  $+1\text{V}$  from the pzc of Ag.<sup>8</sup> In our calculation of diffusion barriers we can therefore take  $\Delta\rho_{\text{Au}}/\rho_{\text{Au}}=0$  for a Au surface. For a Ag surface  $\Delta\rho_{\text{Ag}}/\rho_{\text{Ag}}=-0.35$  corresponds to  $\Phi=\Phi_{\text{pzc-Ag}}+1\text{V}$ .

## RESULTS

Figures 1 (a) and (b) illustrate, for A and B steps, respectively, the energetics, with the  $-35\%$  shift in the surface electron density for the electrodeposition, as a single Ag atom proceeds, after 1 and 2 ML of deposition, from the eighth absorption site (counting both fcc and hcp sites) from the edge, over the step edge, and finally adsorbed along the step edge. For the step-edge both hopping and exchange processes are considered over several different paths. The energy of the last saddlepoint that appears in the figure is the minimum of the calculated step-edge barriers (usually exchange).

For an uncharged substrate (not shown) we obtain a migration energy of  $0.12 \text{ eV}$  with little site-to-site variation, for either 1 or 2 ML coverage and near either the A and B step. The additional step-edge barrier ( $\Delta E_s$ )<sup>3</sup> is  $0.18 \text{ eV}$  and  $0.11 \text{ eV}$  for 1 and 2 ML coverage, respectively, for the A step, and  $0.03$  and  $0.01 \text{ eV}$  for the B step. Obviously, in vapor deposition there is no increase in the step-edge barrier after the second monolayer is deposited.

Adding a  $-35\%$  charge shift for Ag significantly increases migration energies on the terrace and the additional step-edge barrier, and these energies are generally almost twice as high after 2ML than after 1ML. For 1ML on the A step there is a significant "downhill" tilt (Fig. 1a) to the absorption and saddlepoint energies as one approaches the step-edge. By itself, this tilt would encourage interlayer transport over the step more than otherwise would be the case. For 2 ML coverage the downward tilt goes away,  $\Delta E_s$  is larger, and large differences in site-to-site migration energies appear. The regions of high migration energy near the step edge, in effect, would inhibit interlayer transport much as the Schwoebel barrier does. The regions with high barriers would reflect adatoms away forcing them to

congregate in the "grooves" formed between these regions. These grooves are very evident for 2 ML and can serve as nucleation centers for 3D growth near the step-edge. The trends for the B step (Fig. 1b) are similar to the A step, except the downward tilt for 1 ML is not as pronounced, and the increase in  $\Delta E_s$  at 2

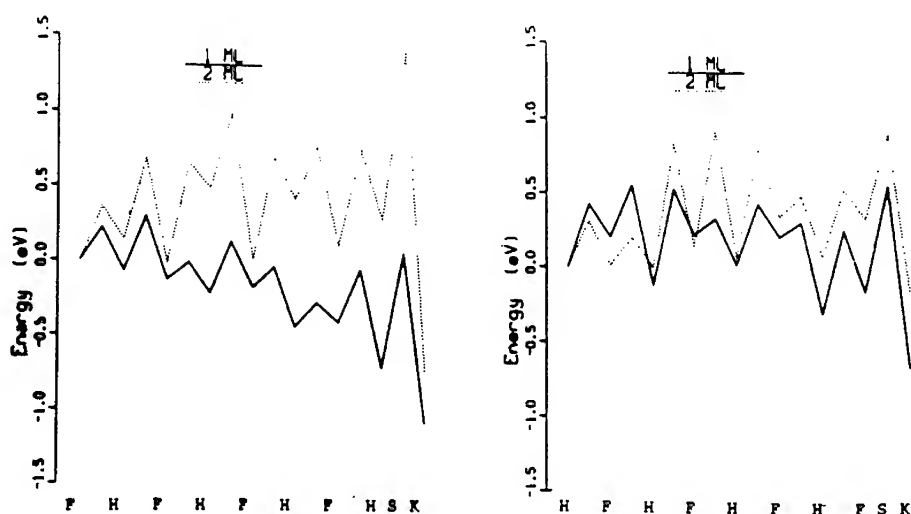


Figure 1. Energetics of an Ag adatom migrating toward an (a) A, (b) B type step edge for 1 and 2 ML Ag coverage during electrodeposition of Ag on Au(111). Minima are relative site adsorption energies, maxima are saddlepoint energies, with the lines guiding the eye. F stands for a fcc site, H for hcp, S for step-edge, and K for kink site.

ML is not as large as on the A step. The highly grooved nature of the migration energies with 2 ML coverage persists. Both the higher migration energies and step-edge barriers at 2 ML would tend toward 3D islanding, especially near the step edge where the "grooves" appear, as opposed to step flow. We estimate a diffusion length of  $\sim 1000\text{\AA}$ , comparable to terrace widths, for 2 ML coverage, versus about  $100000\text{\AA}$  for 1ML. These factors probably account for the sudden onset of 3D growth observed by Corcoran et al. after several hundred  $\text{\AA}$  diameter islands have grown during the third monolayer of deposition.

#### CONCLUSIONS

Our model of incorporating surface charge in the SEAM picture of electrodeposition accounts for the experimentally observed surface stresses, capacitance, and surface energies with

physically reasonable parameters. This model indicates that the large increase in migration and step-edge activation barriers, due to the decrease in bond saturation brought about by the deposition of positive charge on the surface, accounts for the extreme SK growth observed in electrodeposition of Ag/Au(111).

#### ACKNOWLEDGEMENTS

The authors thank Karl Sieradzki for helpful discussions. The simulations on which this investigation was carried out utilized a grant under the Department of Defense High Performance Computing (HPC) Program. Support by the Office of Naval Research is acknowledged.

#### REFERENCES

1. S.G. Corcoran, G.S. Chakarova, and K. Sieradzki, *Phys. Rev. Lett.* **71**, 1585 (1993).
2. Chen-hsien Chen, Scott M. Vesecky, and Andrew A. Gewirth, *J. Am. Chem. Soc.* **114**, 451 (1992).
3. Karsten Bromann, Harald Brune, Holger Döder, and Klaus Kern, *Phys. Rev. Lett.* **75**, 677 (1995).
4. W. Wulfhekel et al., *Surf. Sci.* **348**, 227 (1996).
5. M.M. Dovek, C.A. Lang, J. Nogami, and C.F. Quate, *Phys. Rev. B* **40**, 11983 (1989); D.D. Chambliss and R.J. Wilson, *J. Vac. Sci. Technol.* **B9**, 928 (1991).
6. Michael I. Haftel and Mervine Rosen, *Phys. Rev. B* **51**, 4426, (1995).
7. M.S. Daw and M.I. Baskes, *Phys. Rev. B* **29**, 6443 (1984).
8. J.O'M. Bockris and A.K.N. Reddy, *Modern Electrochemistry*, Plenum Press, New York, 1973, pp. 698-707.
9. K.F. Lin and T.T. Beck, *J. Electrochem. Soc.: Electrochemical Science and Technology* **123**, 1145, (1976).
10. Roberto Raiteri and Hans-Jürgen Butt, *J. Phys. Chem* **99**, 15728 (1995).
11. S.M. Foiles, M.I. Baskes, and M.S. Daw, *Phys. Rev. B* **33**, 7983 (1986).
12. Wolfgang Schmickler, *Interfacial Electrochemistry*, Oxford University Press, New York (1996), p 26.
13. C.L. Fu and K.M. Ho, *Phys. Rev. Lett.* **63**, 1617 (1989).

## MICROMECHANICAL STRESS SENSORS FOR ELECTROCHEMICAL STUDIES

T.A. Brunt<sup>1</sup>, W.F. Ip<sup>1</sup>, T. Rayment<sup>1</sup>, S.J. O'Shea<sup>2</sup> and M.E. Welland<sup>2</sup>

<sup>1</sup> Department of Chemistry, University of Cambridge, Lensfield Rd, Cambridge CB2 1EW, U.K.

<sup>2</sup> Engineering Department, University of Cambridge, Cambridge CB2 1PZ, United Kingdom

### ABSTRACT

Cantilevers developed for atomic force microscopy can be used to construct sensitive thermal and stress sensors. We have shown how the stress changes which accompany deposition and desorption may be measured on single crystal electrodes. In this work we describe the surface stress changes associated with three processes: the electrodeposition of Pb and I and desorption of self assembled thiol monolayers on the Au(111) surface.

### INTRODUCTION

Changing the electronic environment at a surface can produce large changes in the surface stress. The surface stress is related to the various lateral forces at a surface and can give an insight to the energetics of surface processes[1]. For instance, reduction of surface stress is a cause of surface reconstructions and deposition of an adsorbate can alter the surface stress dramatically. This type of adsorbate-induced surface stress change is well-documented in the UHV environment. For instance stress changes have been measured for adsorption and reconstruction processes at both metal and semiconductor [2-3] surfaces.

Less is known about surface stresses which arise at the electrode/electrolyte interface since the lateral forces which give rise to the surface stress are different and more complex than those at the metal/vacuum interface. The largest difference arises from the existence of charges at the surface which lead to long range lateral electrostatic forces. These forces give rise to the electrocapillary variation in surface energy with applied electrode potential [4-6]. As the potential is varied from the potential of zero charge (p.z.c.) in either direction, there is an increase in the compressive surface stress, due to repulsive Coulombic forces between like charges. This effect is always present in any electrochemical stress measurements and the electrocapillary curves of several different electrode surfaces have been measured[4-6]. The stress changes associated with adsorption processes can also be measured[4,7]. Although the magnitude of the stress changes is similar for both electrocapillary curves and monolayer deposition processes, the monolayer stress changes usually occur over a much narrower potential range and hence the gradient of the stress change with respect to potential is much greater for these processes. Thus it is possible to distinguish the electrocapillary and deposition stress changes.

### EXPERIMENTAL

The stress sensor is of the bending beam type and consists of an optical deflection AFM in which the Au-coated cantilever itself constitutes the working electrode. The experimental arrangement and the sample preparation has been described in detail elsewhere [4,8]. The high sensitivity of the detection system and the low force constant of the AFM cantilevers means that the system is a highly sensitive stress sensor with submonolayer sensitivity. In addition the high resonant frequency of the cantilevers allows fast surface processes to be studied.

The deflection of the free end of the cantilever is measured using a standard optical deflection AFM arrangement in which a focused optical beam strikes the free end of the cantilever, and the reflected beam impinges upon a linear photodiode detector. The deflection of the free end of the lever can be related to the geometry of our particular detection arrangement, and the difference

between the photocurrents from the two ends of the photodiode. The surface stress can be determined from Stoney's equation [9] which relates the deflection of a cantilever to the difference in the surface stress in its two faces:

$$\sigma_1 - \sigma_2 = \frac{Et^2}{6(1-\nu)R} \quad (1)$$

where  $\sigma_1$  and  $\sigma_2$  represent the surface stresses in the two faces of the cantilever and  $E, t, \nu$  and  $R$  are the Young's modulus, thickness, Poisson ratio and radius of curvature of the cantilever respectively. The Au-coated  $\text{Si}_3\text{N}_4$  cantilever is a composite cantilever so it necessary to consider the effect of the Au coating on the mechanical properties of the cantilever. Since the Au coating is thin compared to the  $\text{Si}_3\text{N}_4$ , the elastic properties can be calculated simply using the method of Sader et al. [10]. The presence of a monolayer on the lever at some stages of the experiment has a negligible effect on the mechanical properties of the cantilever. For our particular levers the appropriate values for  $E$  and  $\nu$  are  $1.47 \times 10^{11} \text{ Nm}^{-2}$  and 0.31 respectively.

## RESULTS AND DISCUSSION

### 1. Pb Underpotential Deposition on Au(111)

Figure 1 shows the cyclic voltammogram, the simultaneously-recorded surface stress changes and the derivative of the surface stress with respect to potential for the underpotential deposition (UPD) of Pb on Au (111). There are three pairs of peaks in the current curve which are labelled 1/1', 2/2' and 3/3'. The features in the current and surface stress curves are described starting at +0.8 V. In all the surface stress curves compressive surface stress is taken to be negative, so compressive surface stress increases in the negative direction on the y-axis.

1. Prior to the first deposition peak (1), the compressive surface stress decreases gradually. This is an electrocapillary effect because the p.z.c. of the Au (111) electrode surface is ~0 V with respect to the Pb/Pb<sup>2+</sup> reference.
2. The Pb deposition process begins with the formation of close-packed incommensurate islands [11]. There is no open commensurate submonolayer arrangement. Consequently, at peak (1) there is a compressive stress associated with the formation of these islands. The compressive stress in this region increases as the coverage of Pb on the surface increases.
3. The rate of compressive stress increase is a maximum at the main monolayer deposition peak (2). This peak corresponds to the formation of a complete incommensurate Pb monolayer which is compressively stressed.
4. As the potential is driven further in a negative direction more Pb is deposited. Centred on peak (3) there is a pronounced reduction in the derivative of the surface stress. This is despite the fact that more Pb is being adsorbed. This peak has been shown to correspond to a rotational phase transition of the Pb monolayer [12]. The rotation angle of the monolayer with respect to the underlying Au surface changes discontinuously at this potential (+160 mV) from 0° (at more positive potentials) to 2.5° at more negative potentials. The pronounced decrease in the surface stress derivative is a signature of this phase change and suggests that a reduction in surface stress may be the driving force for the process.

5. As the potential is scanned further towards the bulk deposition region, the compressive stress increases in reasonably linearly. This corresponds to a continuous compression of the Pb monolayer which occurs so that more Pb can be incorporated into the monolayer. This can be thought of as "maximising" the favourable Pb-Au interaction at the expense of compressing the Pb monolayer. This process has been termed "electrocompression" and has been demonstrated by measuring a continuous decrease in the Pb-Pb nearest neighbour spacing as a function of potential using Grazing Incidence X-ray Scattering (GIXS) [12]. There is a simple thermodynamic driving force for this potential-driven compression. If one imagines the equilibrium monolayer structure at some potential and then considers decreasing the potential, then the "concentration" of Pb in the monolayer is now lower than that required to maintain equilibrium with the electrolyte. Hence there is an effective overpotential which acts as the driving force for the incorporation of more Pb into the monolayer as the potential is decreased.

The stress changes can be related quantitatively to the changes in nearest neighbour spacing using a simple linear elastic model for the mechanical behaviour of the monolayer. This is explained in detail elsewhere [13]. The nearest neighbour spacings calculated from the measured stress changes agree with the values obtained by GIXS measurement to within a factor of ~50%. This discrepancy probably arises from the assumptions present in this treatment and uncertainties in the appropriate values for the monolayer thickness and elastic constant.

6. On reversal of the potential scan direction, the same qualitative features are present in the variation of surface stress with potential although there is a noticeable hysteresis particularly in the region around peaks 1 and 1'. There is some degree of hysteresis associated with all 3 pairs of current peaks (particularly the broad peak (1/1')). Irreversible adsorption of Pb in this potential region has been detected using other techniques such as the Electrochemical Quartz Crystal

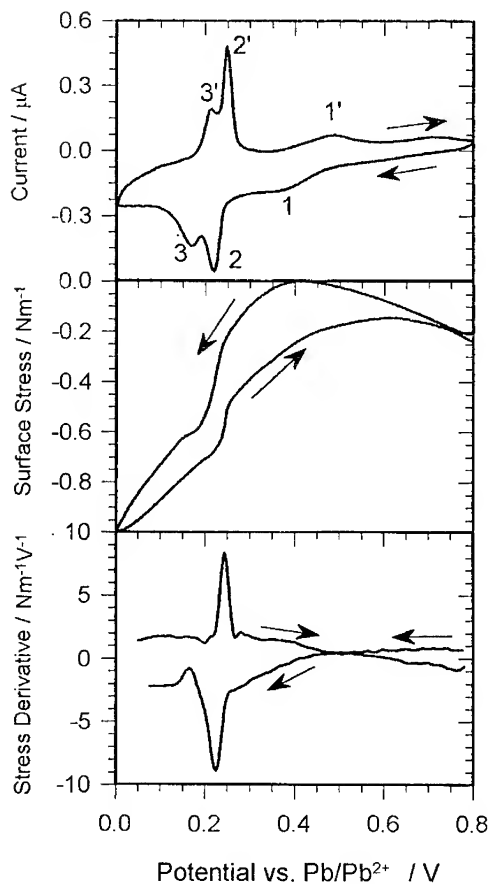


**Figure 1.** Pb UPD on Au(111); 1mM Pb(ClO<sub>4</sub>)<sub>2</sub> in 0.1M HClO<sub>4</sub>; 50 mVs<sup>-1</sup>. Top curve current; middle curve surface stress and bottom curve surface stress derivative.

Microbalance (EQCM) [14] and differences in the amount of Pb adsorbed at a given potential give rise to a significant ( $0.1\text{Nm}^{-1}$ ) difference in the surface stress in the different scan directions.

## 2. Electrodeposition of Iodine on Au (111)

Although most work upon underpotential deposition has been performed with cations, the same phenomenon exists for anions, and the best studied of all these systems is the electrodeposition of iodine on Au(111). Whilst not all results in the literature agree with each other, there seems to be a consensus that the results from a GIXS study are definitive[15]. The structural behaviour may be correlated with a typical cyclic voltammogram for this system shown in figure 2a. At negative potentials, iodine is not adsorbed and the surface displays the well-known  $23 \times \sqrt{3}$  reconstruction characteristic of a clean Au(111) surface. As the potential is swept positive there are two peaks in the voltammogram at  $-0.24\text{V}$  and  $-0.16\text{V}$  which correspond to the lifting of the reconstruction and the adsorption of a monolayer of iodine on the surface. An incommensurate  $p \times \sqrt{3}$  phase is observed from  $-0.16\text{V}$  which is compressed steadily by the adsorption of more iodine until  $+0.30\text{V}$ . At this point there is a surface phase transition forming a rotated hexagonal layer. A small peak is visible in the CV at this potential. This phase continues to be compressed until the potential is reached at which oxidation of solution iodide occurs.

Figure 2b shows the stress changes which arise during the electrodeposition of iodine, and the first derivative of the stress curve. It may be seen that there is a monotonic increase in compressive stress with increasing potential and deposition of iodine, but superimposed upon this are three features whose presence is most marked in the derivative curve, at  $-0.38, -0.24$ , and  $+0.30\text{V}$ . These features correlate well with the structural evolution of the system as described above. The overall compressive change may be explained in general terms as composed of an electrocapillary force combined with the repulsive interactions between iodine atoms incommensurately adsorbed upon the surface. However it is not possible to make even a qualitative separation for this data since the value of the pzc is not known for this system. The pzc for Au(111) surface is at  $\sim 0\text{V}$  with respect to the Ag/AgI reference electrode, but at this potential the surface is covered by a monolayer of iodine. The feature at  $-0.38\text{V}$  occurs in the region associated with the lifting of the surface

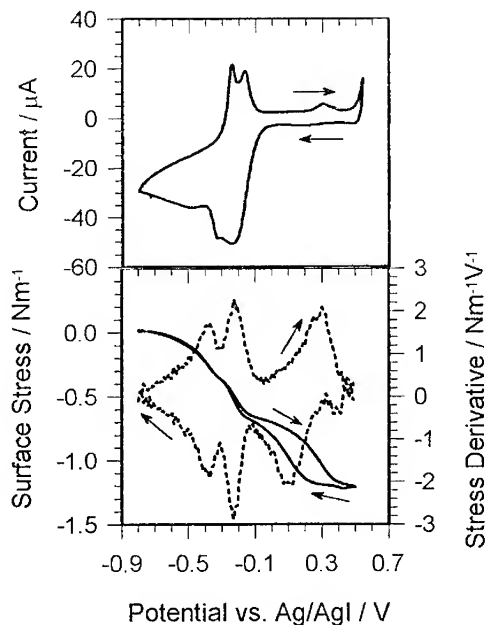


**Figure 2.** I electrodeposition on Au(111); 0.01M KI. Top curve (a) current for large area Au film electrode,  $10\text{mVs}^{-1}$ ; bottom curve (b) surface stress (solid) and surface stress derivative (dashed) measured on the sensor electrode,  $100\text{mVs}^{-1}$ .



reconstruction. The second corresponds to the deposition of a monolayer of iodine. It is not surprising that the most rapid increase of stress occurs simultaneously with the most rapid deposition of iodine on the surface. In the electrocompression region between -0.16V and +0.30V there is a linear decrease of the interatomic spacing with potential according to the GIXS data. However, the stress variation is clearly non-linear and increases rapidly with potential. This perhaps indicates increased repulsive interactions which reach a maximum at the Van der Waals separation. At +0.30V there is a phase transition to a hexagonal surface phase, and a sharp change in the stress derivative. In the new phase the interatomic distance is larger and in consequence the rate of increase of stress is smaller. However, despite this the compressive stress increases monotonically perhaps indicating the underlying influence of a small change in the electrosorption valency.

### 3. Electrochemistry of Self-Assembled Thiol Monolayers

Figure 3a shows the variation in surface stress with potential for Au(111) electrode modified with a monolayer of  $C_{12}H_{25}SH$ . Throughout this potential region the monolayer remains adsorbed on the Au surface. The surface stress changes associated with this system are much smaller than those for the clean gold surface. The reason for this 50-fold decrease in the potential-dependent surface stress is the dramatic reduction in the capacitance of the electrode which is brought about by the presence of the alkyl chains of the thiol monolayer. This reduction in the interfacial capacitance dramatically diminishes the size of the Coulombic forces within the electrical double layer which are responsible for the electrocapillary variation of surface stress with potential. This type of variation of surface energy with potential has also been demonstrated for these self-assembled systems using a Wilhelmy plate technique to measure the surface stress [16].

Figure 3b shows that at more negative potentials it is possible to irreversibly desorb the thiol monolayer. This electrochemical desorption of thiols has already been demonstrated by Porter and co-workers [17]. The peak at -1.18V in the negative-going scan direction corresponds to the reductive desorption of the surface thiol species. Whilst the mechanism of this process is not well-understood the irreversible nature of this desorption process is clear from the fact that there is no corresponding peak in the

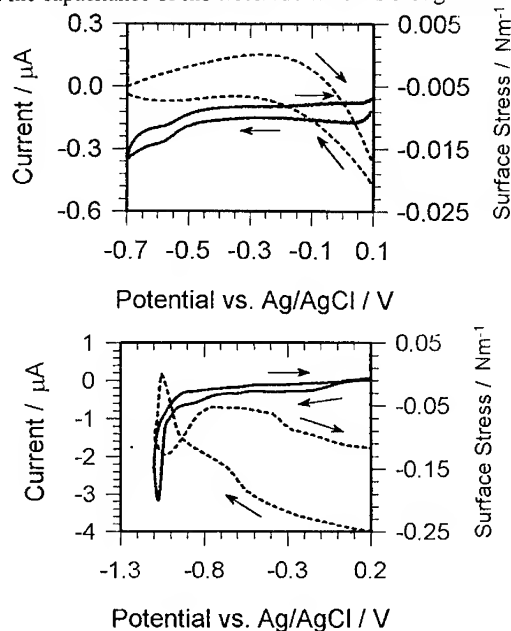


**Figure 3.** Electrochemistry of thiol self-assembled monolayer in 0.1M KOH. (a) electrocapillary curve for Au (111) electrode pre-coated with a monolayer of  $C_{12}H_{25}SH$ , 10 mVs<sup>-1</sup> (b) the irreversible electrochemical adsorption of the same thiol monolayer, 100mVs<sup>-1</sup>.

positive-going scan direction. It is clear from the surface stress data that the process is irreversible in that the surface stress after the scan differs from the starting value by over  $0.1 \text{ Nm}^{-1}$ . There are also large stress changes associated with the thiol stripping process itself. However, following the desorption of the thiol, we do not recover the electrochemistry of a clean Au surface.

## Conclusions

We have demonstrated that in during electrode processes there can be a complex variation of interfacial stress, caused by the existence of surface and double layer charges and interaction between adsorbed species. If the surface structure is known the stress changes may be shown to correlate with adsorption and phase change processes. However, a fully quantitative explanation of most the observations has not been achieved. This awaits both more experimental work and the results of *ab-initio* calculations of the electronic structure of electrode surfaces.

## References

- [1] R.C. Cammarata, Prog. Surf. Sci., **46**, p. 1-38 (1994); H.J. Ibach, Vac. Sci. Technol. A **12**, p. 2240-2243 (1994).
- [2] A. Grossmann, W. Erley, and H. Ibach, Surf. Sci. **337**, p. 183-189 (1995).
- [3] A.J. Schell-Sorokin, and R.M. Tromp, Phys. Rev. Lett. **64**, p. 1039-1042 (1990).
- [4] T.A. Brunt, E.D. Chabala, T. Rayment, S.J. O'Shea, M.E. Welland, J. Chem. Soc. Faraday Trans., **92**, p. 3807-3812 (1996).
- [5] R.A. Fredlein, A. Damjanovic, and J.O'M. Bockris, Surf. Sci. **25**, 261-264, (1971)
- [6] R. Raiteri, and H-J. Butt, J. Phys. Chem. **99**, p. 15728-15732, (1995).
- [7] W. Haiss, and J.K. Sass, J. Electroanal. Chem. **386**, p. 267-270, (1995).
- [8] S.J. O'Shea, M.E. Welland, T.A. Brunt, A.R. Ramadan, and T. Rayment, J. Vac. Sci. Technol. B **14**, p. 1383-1385 (1996).
- [9] A.J. Schell-Sorokin, and R.M. Tromp, Surf. Sci. **335**, p. 204-209 (1994)
- [10] J.E. Sader, I. Larson, P. Mulvaney, and L.R. White, Rev. Sci. Instrum. **66**, p. 3789-3798 (1995).
- [11] C.H. Chen, N. Washburn, and A.A. Gewirth, J. Phys. Chem. **97**, p. 9754-9760 (1993)
- [12] M.F. Toney, J.G. Gordon, M.G. Samant, G.L. Borges, O.R. Melroy, D. Yee, and L.B. Sorensen, J. Phys. Chem. **99**, p. 4733-4744 (1995)
- [13] T.A. Brunt, T. Rayment, S.J. O'Shea and M.E. Welland, Langmuir in press 1996
- [14] M. Hepel, K. Kanige and S. Bruckenstein, Langmuir **6**, p. 1063-1067 (1990).
- [15] B.M. Ocko, G.M. Watson and J. Wang, J. Phys. Chem. **98**, p. 897 -906 (1994).
- [16] J.A.M. Sondag-Huethorst and L.G.J. Fokkink, J. Electroanal. Chem. **367**, p. 49-57 (1994)
- [17] C.A. Widrig, C. Chung and M.D. Porter, J. Electroanal. Chem. **310**, p. 335-359 (1991)

## IN-SITU STM STUDIES ON THE ELECTRODEPOSITION OF ULTRATHIN NICKEL FILMS

O.M. MAGNUSSEN, F.A. MÖLLER, A. LACHENWITZER, AND R.J. BEHM  
Abteilung Oberflächenchemie und Katalyse, Universität Ulm, D-89069 Ulm, Germany

### ABSTRACT

An in-situ STM study of the initial stages of Ni electrodeposition on Au and Cu single-crystals is presented. On reconstructed Au(111) a complex, potential-dependent nucleation and growth process is found, involving selective Ni island formation at specific surface sites and growth of two types (compact and needle-like) of Ni monolayer islands. At higher coverages ( $1 \text{ ML} \leq \theta \leq 5 \text{ ML}$ ) an almost perfect layer-by-layer growth of a metallic Ni(111)-film was observed. Considerably rougher films were found on Au(100) and Cu(100).

### INTRODUCTION

The electrodeposition of Nickel is a well-established technical process for the production of metal coatings and for this reason it has been studied in detail by electrochemical methods and by electron microscopy on the  $\mu\text{m}$ -scale [1-3]. More recently, new interest has emerged in the electrochemical formation of thin Ni films and of Ni/metal superlattices, where the second metal is usually Cu, due to their interesting magnetic and mechanical properties [4]. Since the thickness of the Ni layers in these structures can be as low as several nm, a more fundamental understanding of the structure and the deposition process on the atomic and nanometer scale is required. We here present results of an extensive in-situ STM study of Ni electrodeposition on Au and Cu single crystal electrode surfaces [5-8], which reveal an interesting and unusual nucleation and growth behavior for Ni submonolayer deposits on the reconstructed Au(111) surface and a pronounced substrate-dependence of the morphology of the Ni film.

### EXPERIMENTAL DETAILS

A detailed description of the home-built electrochemical STM used in the experiments and of the experimental procedures is given in Ref. [9,10]. Experiments were performed in modified Watts electrolyte ( $10^{-2} \text{ M H}_3\text{BO}_3$ ,  $10^{-4} \text{ M HCl}$  and  $10^{-3} \text{ M NiSO}_4$ ) prepared from suprapure  $\text{H}_3\text{BO}_3$  and  $\text{HCl}$ , p.a. grade  $\text{NiSO}_4$ , and Milli-Q water. The Au single crystal samples were prepared by flame annealing [11], followed by subsequent immersion into the electrolyte at  $-0.2 \text{ V}$ ; the Cu(100) crystal was electropolished in phosphoric acid as described in Ref. [12]. The potentials of sample and tip were controlled potentiostatically versus an  $\text{Ag/AgCl}$  ( $\text{KCl sat.}$ ) reference electrode, with the tip potential usually kept 50-100 mV below the sample potential. STM images were obtained in constant current mode with tunneling currents between 1 and 10 nA, and are presented as topview images with lighter colors corresponding to higher surface areas.

## RESULTS AND DISCUSSION

### Cyclic Voltammetry

Prior to the STM measurements cyclic current-voltage curves (voltammograms) were recorded in a separate electrochemical cell. As can be seen in the voltammogram obtained on Au(111) in modified Watts electrolyte containing  $10^{-3}$  M  $\text{Ni}^{2+}$  (Fig. 1), the onset of nickel deposition manifests itself as a broad shoulder on the large negative current caused by hydrogen evolution. Hence Ni deposition can not be assessed from the negative potential sweep. Instead, the amount of Ni deposition was estimated by maintaining a fixed deposition potential for up to 15 minutes and then measuring the charge in the Ni dissolution peak, which is shifted to  $\approx 200$  mV more positive potentials than the  $\text{Ni}^0/\text{Ni}^{2+}$  Nernst potential ( $-0.52$  V), well above the range of hydrogen evolution. According to these stripping experiments, measurable Ni deposition starts at about  $-0.60$  V, i.e., at overpotentials  $\eta \geq 80$  mV. In particular, no underpotential deposition (UPD) is observed for Ni on Au(111). Similar cyclic voltammograms were obtained on Au(100) and Cu(100) electrodes, where overpotentials  $\eta \geq 40$  mV and  $\eta \geq 150$  mV, respectively, were found. These results are in agreement with previous electrochemical and quartz microbalance studies on polycrystalline Au, which also found large overpotentials for Ni deposition [2,13]. The overpotential is almost independent of the electrolyte composition with experiments in pure Ni sulfate or Ni nitrate solution resulting in only slightly higher overpotentials [7]. The anodic shift of the Ni dissolution peak has been attributed to stabilization of the deposit by coadsorbed (or absorbed) hydrogen [14]. In subsequent potential sweeps the cyclic voltammogram is completely reproducible, suggesting that the deposited Ni does not alter the Au(111) surface significantly.

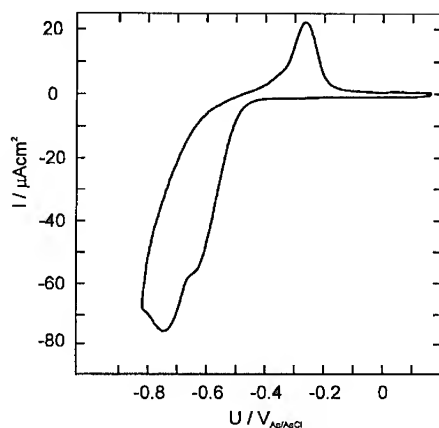


Fig. 1. Cyclic voltammogram of Au(111) in  $10^{-2}$  M  $\text{H}_3\text{BO}_3$  +  $10^{-4}$  M  $\text{HCl}$  +  $10^{-3}$  M  $\text{NiSO}_4$  (sweep rate 20 mV/s).

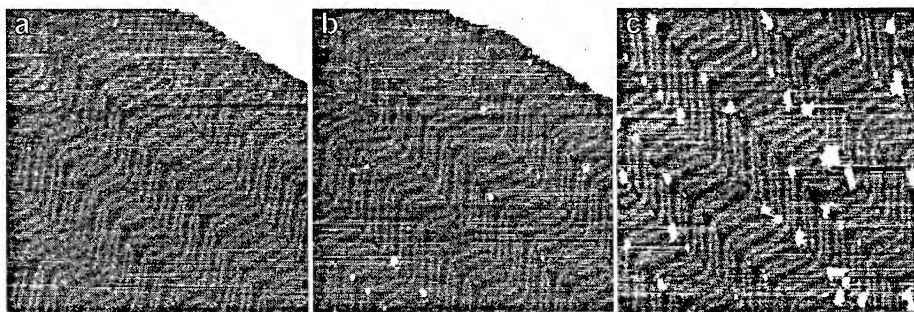


Fig. 2. STM images of Au(111) in  $10^{-2}$  M  $\text{H}_3\text{BO}_3$  +  $10^{-4}$  M  $\text{HCl}$  +  $10^{-3}$  M  $\text{NiSO}_4$  (a) directly after a potential change from  $-0.2$  V to  $-0.6$  V, (b) 3 min. at  $-0.6$  V, and (c) 20 min. at  $-0.6$  V, showing the growth of Ni islands at the "elbows" of the Au reconstruction ( $1050 \times 1050 \text{ \AA}^2$ ).

### Nucleation of Ni on Au(111)

Freshly prepared Au(111) surfaces exhibit a well-ordered herringbone reconstruction, well-known from previous UHV [15,16] and electrochemical [17,18] STM studies. The reconstruction gives rise to a characteristic long-range, vertical modulation in form of double rows arranged in a zigzag pattern, which is clearly visible on atomically flat Au terraces (see Fig. 2a). At each of the bending points ("elbows") of the modulation rows the two-dimensional lattice of the topmost Au layer exhibits a surface dislocation, resulting in a distorted surface lattice at these points [16].

The nucleation of Ni on the reconstructed surface depends strongly on the applied overpotential, as has been described in detail in Ref. [5]. Fig. 2 illustrates the growth of Ni at an overpotential  $\eta = 80$  mV, the most positive potential where growth of Ni islands *on top* of the Au surface was observed. Directly after the potential step to  $-0.6$  V (Fig. 2a) no Ni islands are found on the surface. A small but distinct change, however, is observed at the "elbows" of the Au reconstruction, which are now decorated by "holes" of about  $20$  Å in diameter and  $0.5$  Å in apparent depth. These "holes" can be attributed to substitutional Ni atoms, which have replaced the surface atoms of the distorted Au lattice at the "elbow" sites. The formation of "holes", indicating the exchange of Au surface atoms by Ni, is observed for all potentials more negative than the  $\text{Ni}^0/\text{Ni}^{2+}$  Nernst potential. After 3 minutes at  $-0.6$  V (Fig. 2b) nucleation of the first Ni islands *on top* of the Au surface is detected. At this potential the Ni islands are formed exclusively at the "elbows" of the reconstruction, i.e., *on top* of the substitutional Ni atoms. Since the "elbows" on a freshly annealed surface are regularly arranged, the islands start to form an ordered pattern. This can be seen in Fig. 2c recorded 20 min. later, where Ni islands have nucleated at about 50% of the "elbows". A very similar nucleation behavior was observed for Ni deposited on Au(111) in UHV [16,19]. No nucleation at the Au step edges was observed at  $-0.6$  V even after observation times of one hour, indicating that the "elbows" are the preferred nucleation site at this potential.

A distinctly different nucleation behavior is found at overpotentials  $\eta \geq 100$  mV. The STM images in Fig. 3a and b, recorded in the vicinity of a Au step before and after a potential step to  $-0.63$  V, show the formation of Ni monolayer islands at the lower terrace side of the Au step. Since the rate of this process is much faster than nucleation at "elbows", nucleation at Au steps becomes

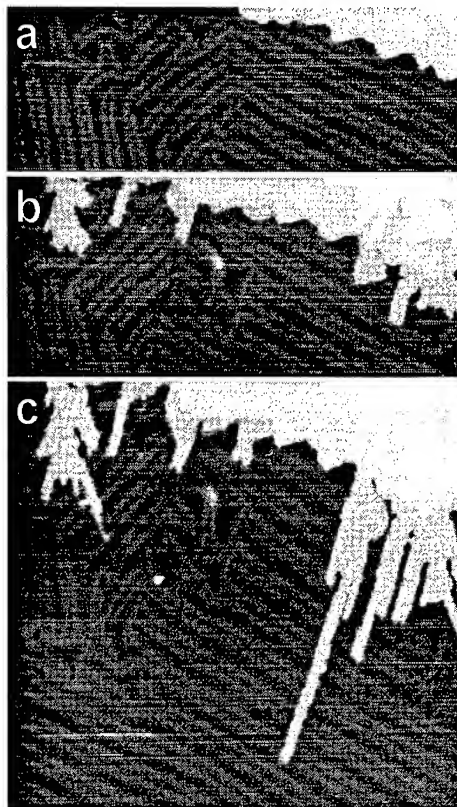


Fig. 3. STM images of Au(111) in  $10^{-2}$  M  $\text{H}_3\text{BO}_3$  +  $10^{-4}$  M  $\text{HCl}$  +  $10^{-3}$  M  $\text{NiSO}_4$  (a) at  $-0.59$  V ( $1150 \times 450$  Å<sup>2</sup>), (b) after 3 min. at  $-0.63$  V ( $1150 \times 550$  Å<sup>2</sup>), and (c) successive image recorded at  $-0.6$  V ( $1150 \times 760$  Å<sup>2</sup>), showing nucleation of Ni islands at the Au steps and the growth of anisotropic Ni needle islands.

dominant at  $\eta \geq 100$  mV. Hence, different nucleation processes and correspondingly different submonolayer morphologies can be selected by the deposition potential.

#### *Submonolayer growth of Ni on Au(111)*

Upon further deposition two different growth morphologies can be distinguished for electrodeposited Ni monolayer islands on Au(111): compact, often triangular shaped islands and strongly anisotropic, needle-like islands (Fig. 3c). The most obvious feature of the compact islands is a pronounced,  $\approx 0.6$  Å high, long-range modulation ("white dots"). From atomic-scale observations, which reveal a hexagonal lattice with a next-neighbor spacing of 2.50 Å and the same orientation as the Au substrate lattice, this modulation can be shown to originate from the mismatch between the hexagonal lattices of substrate and adlayer (Moiré pattern) [7]. Hence, the atomic arrangement in these islands is similar as in the (111)-plane of bulk Ni. This structure was also confirmed in recent in-situ x-ray diffraction experiments (unpublished data). The preferred orientation of the island steps corresponds to the close-packed direction of the Ni lattice.

More unusual is the formation of needle-like islands, which can be directly observed in the right half of the series of STM images shown in Fig. 3. This very anisotropic growth is surprising, since the reconstructed Au surface lattice is only 4.5% distorted from an ideal hexagonal arrangement. The Ni needle islands are usually less than 40 Å wide but reach lengths of several hundred Å. The needle orientation is always strictly perpendicular to the double rows of the Au reconstruction, i.e., along the direction where the reconstructed Au surface layer is contracted. A detailed analysis reveals that the width of the needles is not randomly distributed but that integer multiples of  $(11.5 \pm 1.0)$  Å are preferred. In addition, the long-range modulation pattern of the reconstruction can be observed *on top* of the Ni needles, indicating that the reconstruction of the underlying Au surface layer is maintained in the presence of the Ni deposit. All these properties of the needle islands can be understood in a simple model, where a substrate-induced structural anisotropy of the Ni lattice is assumed. Specifically, it is suggested that the Ni atoms are arranged pseudomorphically with the Au surface lattice along the needle direction, but are compressed to nearest neighbor distances of 2.5 Å in perpendicular direction. This results in a close-packed step structure for step edges parallel to the needle, but in more open step edges at the needle tip, thus explaining the preferred deposition at the needle tip. A detailed description of the Ni needle growth process and of the suggested model is given in Ref. [6].

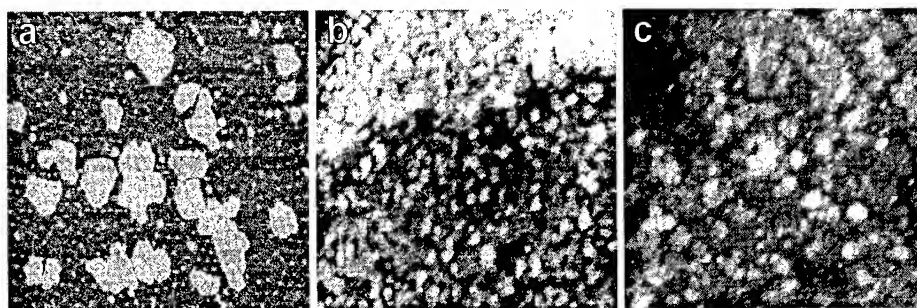


Fig. 4. STM images of a 1.3 ML deposit on (a) Au(111), (b) Au(100), and (c) Cu(100) ( $800 \times 800$  Å<sup>2</sup>), showing the considerable different surface roughness for ultrathin Ni films on different substrates.

### Morphology of Ni films on Au(111), Au(100), and Cu(100)

The microscopic morphology of ultrathin Ni films strongly depends on the structure of the underlying substrate. As an example, typical STM images of a Ni film with a coverage of about 1.3 monolayers on Au(111), Au(100), and Cu(100) are presented in Fig. 4. On Au(111) (Fig. 4a) the Au substrate surface is completely covered by a Ni monolayer on top of which several second layer Ni islands of compact, round shape are found. Substantial nucleation and growth of third layer islands starts only after the second layer is completed to more than 90%. A quantitative evaluation of series of STM images recorded during the growth of Ni on Au(111) is shown in Fig. 5, where the occupation of the individual Ni layers is plotted versus the total coverage. As can be seen in the figure, Ni is deposited in an almost perfect layer-by-layer growth on Au(111) for coverages of up to (at least) 5 ML and low deposition rates ( $80 \text{ mV} \leq \eta \leq 200 \text{ mV}$ ), resulting in a atomically smooth, metallic Ni film with a (111)-orientation.

As visible in Fig. 4b, Ni films on Au(100) are considerably rougher on a microscopic scale. Here up to four layer high Ni islands are observed at 1.3 ML coverage and the first Ni layer is completed only at coverages  $> 2 \text{ ML}$ . In addition, the typical Ni island size is very small (typical island diameter  $\approx 30 \text{ \AA}$ ), resulting in a very high defect density. This surface morphology can be rationalized by the higher surface corrugation of Au(100) as compared to the close-packed Au(111) surface, which causes a lower Ni adatom mobility and a stronger tendency of the Ni adlattice to grow in registry with the Au substrate-lattice. These effects favor a higher nucleation density and a smaller island size due to internal stress. Finally, an intermediate morphology is observed for Ni films on Cu(100) (Fig. 4c), where the lattice mismatch is close to zero. Again, this can be qualitatively explained by the corrugation potential, which falls between that of Au(111) and Au(100).

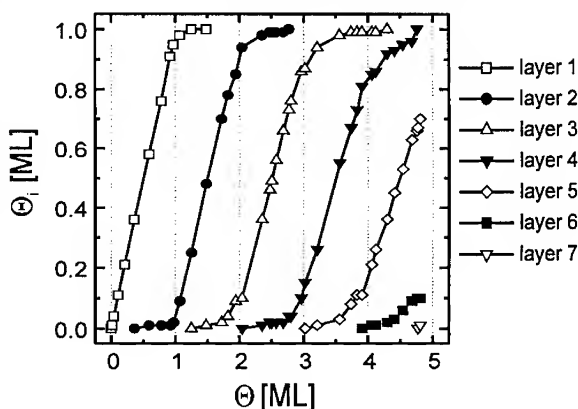


Fig. 5. Plot of the occupation  $\theta_i$  of the individual layers  $i$  ( $1 \leq i \leq 7$ ) as a function of total Ni coverage  $\theta$ , showing the almost perfect layer-by-layer growth on Au(111). The data was obtained by quantitative evaluation of series of STM images recorded on Au(111) in  $10^{-2} \text{ M H}_3\text{BO}_3 + 10^{-4} \text{ M HCl} + 10^{-3} \text{ M NiSO}_4$ .

### CONCLUSIONS

A complex nucleation and growth behavior was observed for the initial stages of growth of ultrathin Ni films on single-crystalline Au and Cu electrodes. For Ni electrodeposition on Au(111) a pronounced, potential-dependent influence of the herringbone reconstructed surface on the nucleation and submonolayer growth behavior was observed. In the future, these processes may be utilized for the controlled electrochemical formation of well-defined Ni structures on the nanometer scale. Observations at multilayer coverages found atomically smooth Ni films on

Au(111) but considerably rougher deposits on Au(100) and Cu(100), thus demonstrating the strong influence of the substrate on the morphology of the Ni deposit.

## REFERENCES

- [1] J.P. Hoare, *J. Electrochem. Soc.* **133**, 2491 (1986).
- [2] M. Zhou, N. Myung, X. Chen, K. Rajeshwar, *J. Electroanal. Chem.* **398**, 5 (1995).
- [3] J. Gómez, R. Pollina, E. Vallés, *J. Electroanal. Chem.* **386**, 45 (1995).
- [4] T.P. Moffat, *J. Electrochem. Soc.* **142**, 3767 (1995).
- [5] F. Möller, O.M. Magnussen, R.J. Behm, *Phys. Rev. Lett.* **77**, 5249 (1996).
- [6] F. Möller, O.M. Magnussen, R.J. Behm, *Phys. Rev. Lett.* **77**, 3165 (1996).
- [7] F. Möller, J. Kintrup, A. Lachenwitzer, O.M. Magnussen, R.J. Behm, unpublished.
- [8] A. Lachenwitzer, M.R. Vogt, O.M. Magnussen, R.J. Behm, submitted for publication.
- [9] O.M. Magnussen, J. Hotlos, R.J. Nichols, D.M. Kolb, R.J. Behm, *Phys. Rev. Lett.* **64**, 2929 (1990).
- [10] O.M. Magnussen, J. Hotlos, G. Beitel, D.M. Kolb, R.J. Behm, *J. Vac. Sci. Technol. B* **9**, 969 (1991).
- [11] J. Clavilier, R. Faure, G. Guinet, R. Durand, *J. Electroanal. Chem.* **107**, 205 (1980).
- [12] M.R. Vogt, C.M. Schilz, F. Möller, O.M. Magnussen, R.J. Behm, *Surf. Sci.*, **367**, L33 (1996).
- [13] M. Benje, M. Eiermann, U. Pittermann, K.G. Weil, *Ber. Bunsenges. Phys. Chem.* **90**, 435 (1986).
- [14] M. Fleischmann, A. Saraby-Reintjes, *Electrochim. Acta* **29**, 69 (1984).
- [15] J.V. Barth, H. Brune, G. Ertl, R.J. Behm, *Phys. Rev. B* **42**, 9307 (1990).
- [16] D.D. Chambliss, R.J. Wilson, S. Chiang, *Phys. Rev. Lett.* **66**, 1721 (1991).
- [17] X. Gao, A. Hamelin, M.J. Weaver, *J. Chem. Phys.* **95**, 6993 (1991).
- [18] N.J. Tao, S.M. Lindsay, *Surf. Sci.* **274**, L546 (1992).
- [19] J.A. Meyer, I.D. Baikie, E. Kopatzki, R.J. Behm, *Surf. Sci.* **365**, L647 (1996).



## TIME-RESOLVED MEASUREMENTS OF OVERLAYER ORDERING IN ELECTRODEPOSITION

A.C. Finnefrock\*, L.J. Buller†, K.L. Ringland\*, P.D. Ting‡, H.D. Abruña†, J.D. Brock‡

\*Department of Physics, Cornell University, Ithaca, New York 14853

†Department of Chemistry, Cornell University

‡School of Applied and Engineering Physics, Cornell University

### Abstract

We report *in situ* time-resolved surface x-ray scattering measurements of the underpotential deposition of  $\text{Cu}^{2+}$  on Pt(111) in the presence of  $\text{Cl}^-$  in  $\text{HClO}_4$  solution. Chronoamperometric (current vs. time) measurements indicate that after a potential step, the electrodeposition current decays to  $1/e$  of its initial value in at most 0.12 seconds. In contrast, our simultaneous time-resolved surface x-ray scattering data reveal that the overlayer requires on the order of two seconds to develop long-range periodic order. These results demonstrate that the kinetics of surface ordering can be significantly different from the kinetics of charge-transfer and illustrate the power of time-resolved surface x-ray scattering for *in situ* studies of electrodeposition.

### Introduction

The electrodeposition of a metal adsorbate onto a solid surface is a key aspect of important technological processes such as electroplating and corrosion inhibition. In a number of cases, metal overlayers can be electrodeposited onto a dissimilar metal substrate at a potential that is less negative than the Nernst potential (that required for bulk deposition). Experimentally, this "underpotential deposition" (UPD) provides a precise means for quantitatively and reproducibly controlling coverage in the submonolayer to monolayer (and in some cases multilayer) regime [1-3]. In addition to the surface coverage, both the presence of other adsorbates, especially anions, and the surface structure of the substrate can profoundly affect the structural and electronic characteristics of the deposit [4-8]. Although there is a great deal of existing work on UPD lattice formation, the early stages of deposition are not well-understood [9,10]. In much of this earlier work, the structure of a UPD overlayer was determined by depositing the overlayer followed by emerging into an ultra-high vacuum (UHV) chamber and employing established surface science techniques such as low-energy electron diffraction (LEED). However, such measurements are inherently *ex situ* and cannot provide information on the kinetics of deposition. Recently, *in situ* probes such as scanning tunneling microscopy (STM) [11-13], atomic force microscopy (AFM) [14], and surface x-ray scattering (SXS) [15-20] have been applied to UPD systems. In addition to eliminating the ambiguity of *ex situ* measurements, they offer the possibility of studying the kinetics of deposition. Kinetic studies are crucial for identifying the rate-limiting steps in the electrochemical growth.

The UPD of Cu onto Pt(111) has been extensively studied by a variety of techniques. The process is very sensitive to the presence of anions and appears to be kinetically controlled. The exact structure and nature of the overlayer, particularly at intermediate coverages, has been the subject of some controversy. Based on LEED studies, Michaelis *et al.* [21] identified

the intermediate overlayer as a  $4 \times 4$  structure. However, *in situ* anomalous x-ray diffraction measurements of the overlayer structure as a function of potential by Tidswell *et al.* [22] suggest that the intermediate overlayer structure is a more complicated incommensurate CuCl bilayer.

Time-resolved surface x-ray scattering is a nearly ideal probe for studying the time evolution of the overlayer structure during UPD. This is a noninvasive technique which can simultaneously measure from a broad area on the sample, in marked contrast to scanning probe techniques. X rays in the 0.5 to 1.5 Å region are not significantly absorbed by aqueous solutions allowing for the *in situ* study of the electrode/solution interface. In addition, the line shape of the scattered x rays can be interpreted simply in terms of well-known correlation functions, allowing direct tests of theory. Using signal averaging techniques, transient structures with lifetimes as short as a few  $\mu\text{sec}$  can be studied [23].

## Experiment

Experiments were performed at the X20A beamline at the National Synchrotron Light Source using an *in situ* reflection-geometry x-ray scattering cell. This cell is an adaptation of the design originally developed by Toney [24]. All values of the applied voltage are referenced to a Ag/AgCl reference electrode. Our sample was a single-crystal Pt(111) electrode, immersed in a solution of 1 mM  $\text{Cu}^{2+}$  and 10 mM  $\text{Cl}^-$  with 0.1 M  $\text{HClO}_4$  as a supporting electrolyte. Polypropylene film was used to cover the sample and contain the solution, as depicted in Figure 1(a). During the experiment, chronamperometric measurements were synchronized with the time base of a multi-channel scalar, which recorded the intensity of the scattered x rays. We were thereby able to acquire simultaneous *in situ* time-resolved measurements of x-ray scattered intensity and charge-transfer.

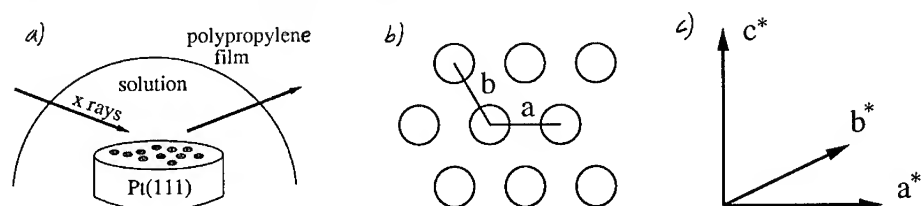


Figure 1: (a) Cartoon of the *in situ* x-ray scattering cell. X rays penetrate the polypropylene film and solution to diffract from the ordered monolayer structure on the electrode surface. (b) The Pt(111) surface with surface lattice vectors  $a$ ,  $b$ , which are perpendicular to  $c = (111)$ . (c) Reciprocal lattice vectors corresponding to the unit cell chosen in (b);  $a^*$  and  $b^*$  subtend  $60^\circ$ .

Since we will be discussing structural measurements referenced to the platinum surface, a brief description of the crystallographic notation is in order. Platinum has a face-centered cubic (fcc) crystal structure with a cubic lattice spacing of 3.9231 Å. The bulk-terminated (111) surface of platinum has sixfold symmetry; therefore, in most surface diffraction studies, the crystal lattice is described in terms of a hexagonal lattice with the  $c$  axis along the  $\langle 111 \rangle$  direction. Thus the fcc (111), (200), and (020) Bragg peaks are respectively mapped onto the (003),  $(1\bar{1}2)$ , and (012) in surface units. A more thorough description can be

found in Reference 25. Points in reciprocal space are usually indexed by  $(HKL)$ , where the momentum transfer vector is  $q = Ha + Kb + Lc$ .

Figure 2 represents the present understanding [21,22] of the UPD of Cu/Cl onto Pt(111). There are three distinct equilibrium phases, here labeled A, B, and C. At the rest potential,  $\text{Cl}^-$  is adsorbed onto the electrode in an amorphous state. As the applied potential is ramped negatively, a current peak is observed. Beyond this peak, the Cu and Cl form an incommensurate "overlayer" pattern which is well-ordered. This is phase (B). As the applied potential is again ramped negatively, the current again peaks, signalling the transition to another phase (C). Here, the Cu and Cl form a tighter overlayer structure which is commensurate with the Pt(111) electrode substrate. If the potential is ramped positively towards the rest potential, current peaks are found which correspond to transitions between the phases, now in the opposite direction.

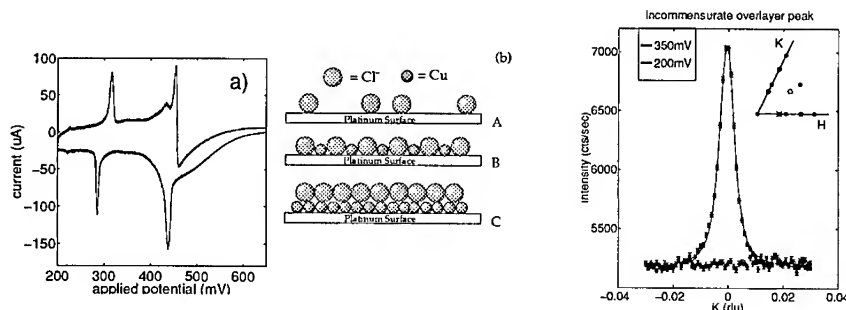


Figure 2: (a) An *in situ* (in the x-ray cell) cyclic voltammogram at 5 mV/second for Cu UPD on Pt(111) in 0.1 M  $\text{HClO}_4$  solution containing 1 mM  $\text{Cu}^{2+}$  and 10 mM  $\text{Cl}^-$ . (b) Schematic depiction of the electrodeposition process moving from a disordered chloride layer (A) to a Cu and  $\text{Cl}^-$  overlayer with long-range order (B) and finally to a full Cu monolayer (C) as the potential is made progressively more negative.

Figure 3: Comparison of the scattered x-ray intensity at the  $(0.765\ 0\ 1.5)$  incommensurate overlayer diffraction peak (shown by a cross in the inset) in the two distinct phases, corresponding to the incommensurate overlayer (350 mV) where the peak is present, and commensurate overlayer (200 mV) where the peak is absent. The solid line is a fit to a pseudo-Voigt lineshape, to guide the eye.

## Results

This paper concentrates on the transition between phases (B) and (C). That is, we are studying the transition between two ordered phases as a function of applied potential. In the former phase (B), the CuCl overlayer has a lattice spacing approximately 30% greater than the lattice spacing between Pt atoms on the (111) surface [22]. Hence, rods of scattering which are sharp in the  $a^*$  and  $b^*$  direction but diffuse in the  $c^*$  direction should be observable. The intensity along  $c^*$  is not entirely uniform; its modulation can provide information about the spacing between the Cu and Cl planes in the overlayer. In the latter phase (C), the CuCl overlayer is commensurate with the Pt(111) rod. So the rod of scattering from the overlayer

interferes with the scattering from the crystal truncation rods (CTR) of the Pt(111) surface [26]. This makes the interpretation of changes in intensity more complicated. Nonetheless, these modulations of the CTRs are easily observable and can be fit to provide structural information on this phase as well. This analysis is greatly simplified by the fact that Pt(111) is known not to reconstruct in this potential window.

Figure 3 shows the scattering found at the  $(0.765\ 0\ 1.5)$  position at two different values of the applied potential, clearly demonstrating the presence of the incommensurate overlayer structure at a higher value of the applied potential and its absence at a lower value corresponding to the commensurate structure. The full width at half maximum of this peak corresponds to a coherence length of at least  $5000\text{\AA}$ . The potential-independent background shown in this figure is due to scattering from the solution and the polypropylene film.

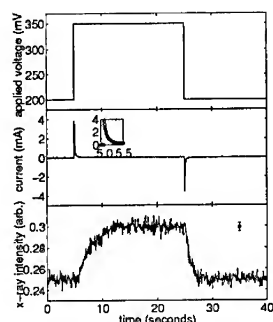


Figure 4: (a) Applied potential steps. (b) Transient currents observed when this potential step sequence is performed. (c) Simultaneous *in situ* X-ray scattered intensity of the overlayer diffraction peak as a function of time. The development of long-range periodic order in the overlayer (panel c) requires significantly more time than that required for the charge-transfer at the electrode surface (panel b).

To study the kinetics of the Cu/Cl/Pt(111) UPD process, we performed the applied potential square-wave cycle shown in Figure 4(a). Initially, the potential began at 200 mV where there is a CuCl overlayer commensurate with the Pt(111) electrode surface (phase C). Then at  $t = 5$  seconds, the potential was stepped to 350 mV, conducive to the formation of an incommensurate CuCl overlayer (phase B). At  $t = 15$  seconds, the potential was stepped back to the original 200 mV. This cycle was repeated ten times to gather statistics for the simultaneous x-ray measurement.

Figure 4(b) shows the transient currents observed when this potential step sequence is performed. These currents are generated by the stripping of  $\text{Cu}^{2+}$  and/or the adsorption of  $\text{Cl}^-$  on the positive potential step and the reverse for the negative potential step. The area under each current transient represents the total charge transferred during the process and can be used to identify the electrochemical process. For each step, the total charge transfer

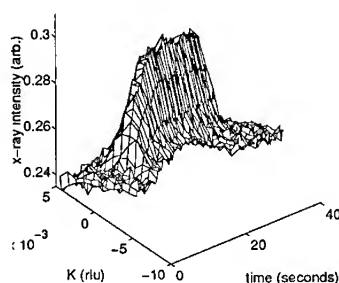


Figure 5: Scattered intensity as a function of time  $t$  and scattering vector,  $\mathbf{q} = (0.765\ K\ 1.5)$ . The peak remains centered at  $k = 0$ , ruling out the possibility that the overlayer simply shifts its periodicity in response to the voltage stimulus.

is  $\lesssim 1$  mC. The time for the current to fall to  $1/e$  of its original value is 0.08 seconds for the positive step, and 0.12 seconds for the negative step. These time scales are too slow, and the charge transfers too large, to be explained by charging of the double-layer. However, these parameters are completely consistent with the UPD processes depicted in Figure 2(b).

Time-resolved x-ray data were acquired simultaneously with these chronamperometric measurements. These data are presented in Figure 4(c) which shows the intensity of the (0.765 0 1.5) overlayer diffraction peak as a function of time. A representative error bar is displayed in the upper right-hand corner. Hence, the fluctuations in the measured intensity can be seen to arise from counting statistics. These intensities were fit to an exponential line shape for the purpose of estimating time constants. The intensity rise at  $t = 5$  seconds, due to the formation of an ordered overlayer, has a time constant of 2.3 seconds. In contrast, the intensity fall at  $t = 15$  seconds has a characteristic time constant of 0.75 seconds. This demonstrates that the ordering process for the incommensurate overlayer is slower than its disordering, an intuitively pleasing result. What is more surprising is the enormous discrepancy in time scales between the charge-transfer shown in panel (b) and the x-ray scattering signal in panel (c). Clearly, the development of long-range periodic order in the overlayer requires significantly more time than that required for the charge-transfer. Thus, charge-transfer at the electrode surface is not the rate-limiting process.

One contingency that must be allowed for is the possibility that the peak could be moving in  $H$  or  $K$ . At the (0.765 0  $L$ ) position, this would correspond to the overlayer expanding/contracting or rotating with respect to the underlying platinum lattice. Hence, it is necessary to take time-resolved  $q$ -scans, rather than simply monitoring the intensity at a single point in reciprocal space. A representative  $q$ - $t$ -scan is shown in Figure 5. From these and similar scans, the peak is simply appearing and disappearing, and not altering its periodicity in a continuous manner. This indicates the slow and uniform ordering of the incommensurate overlayer and its more rapid dissolution, in agreement with the results for the peak intensity shown in Figure 4.

## Conclusions

In summary, by combining chronoamperometric measurements with time-resolved surface x-ray scattering, we have demonstrated that the transfer of charge during the deposition and stripping process is far more rapid than the time required to form an ordered CuCl overlayer. Electrochemical measurements alone are insufficient to determine the rate-limiting steps in this UPD system. This illustrates the power of time-resolved x-ray scattering as an *in situ* probe of the kinetics of UPD processes in particular, and of interfacial growth in general.

Given the success of these experiments, we are currently carrying out further measurements to probe the height-height correlation function throughout the underpotential deposition cycle. Detailed line shape analysis will provide information on the time-dependent order parameter and correlation lengths along the surface. For instance, monitoring peak widths (such as shown in Figure 5) yields domain sizes of growing islands on the surface as a function of time. These studies will further elucidate the microscopic details of surface and interface evolution.

## Acknowledgements

This work was supported by Cornell's Materials Science Center (MRL program of the NSF under Grant No. DMR-9121654). Additional support was provided by the NSF (Grant Nos. DMR-92-57466 and CHE-94-07008) and the Office of Naval Research. The x-ray data were collected using the IBM-MIT beam line X20A at the National Synchrotron Light Source (NSLS), Brookhaven National Laboratory. LJB acknowledges support of a fellowship from the International Precious Metals Institute / Gemini Industries. ACF would like to thank the organizers of this symposium for support to attend the MRS conference, and M. Toney and B. Ocko for helpful discussions.

## References

- [1] D. Kolb, in *Advances in Electrochemistry and Electrochemical Engineering*, edited by H. Gerisher and C. Tobias (Wiley and Sons, New York, 1978), Vol. 11.
- [2] R. Adžić, *Isr. J. Chem.* **18**, 166 (1979).
- [3] S. Szabó, *Int. Rev. Phys. Chem.* **10**, 207 (1991).
- [4] D. Kolb, A. Jaaf-Golze, and M. S. Zei, in *Dechema Monographien* (VCH, Germany, 1986), Vol. 102, pp. 53-64.
- [5] J. H. White and H. D. Abruña, *J. Phys. Chem.* **94**, 894 (1990).
- [6] N. Marković and P. N. Ross, *Langmuir* **9**, 580 (1993).
- [7] J. H. White and H. D. Abruña, *J. Electroanal. Chem.* **300**, 521 (1991).
- [8] R. Gómez, J. Feliu, and H. Abruña, *Langmuir* **10**, 4315 (1994).
- [9] J. Schultze and D. Dickertmann, *Surf. Sci.* **54**, 489 (1976).
- [10] A. Bewick and B. Thomas, *J. Electroanal. Chem.* **70**, 239 (1976).
- [11] O. Magnussen *et al.*, *Phys. Rev. Lett.* **64**, 2929 (1990).
- [12] G. Edens, X. Gao, and M. Weaver, *J. Electroanal. Chem.* **375**, 357 (1994).
- [13] T. Hachiya, H. Honbo, and K. Itaya, *J. Electroanal. Chem.* **315**, 275 (1991).
- [14] S. Manne *et al.*, *Science* **251**, 183 (1991).
- [15] O. Melroy *et al.*, *Phys. Rev. B* **38**, 10962 (1988).
- [16] M. Toney *et al.*, *Phys. Rev. B* **42**, 5594 (1990).
- [17] M. Toney *et al.*, *Phys. Rev. Lett.* **75**, 4472 (1995).
- [18] J. Wang, A. Davenport, H. Isaacs, and B. Ocko, *Science* **255**, 1416 (1992).
- [19] J. Wang, B. Ocko, A. Davenport, and H. Isaacs, *Phys. Rev. B* **46**, 10321 (1992).
- [20] B. Ocko, G. Watson, and J. Wang, *J. Phys. Chem.* **98**, 897 (1994).
- [21] R. Michaelis, M. Zei, R. Zhai, and D. Kolb, *J. Electroanal. Chem.* **339**, 299 (1992).
- [22] I. Tidswell, C. Lucas, N. Marković, and P. Ross, *Phys. Rev. B* **51**, 10205 (1995).
- [23] E. Sweetland *et al.*, *Phys. Rev. B* **50**, 8157 (1994).
- [24] M. Samant *et al.*, *Surf. Sci. Lett.* **193**, L29 (1988).
- [25] A. Sandy *et al.*, *Phys. Rev. B* **43**, 4667 (1991).
- [26] I. Robinson, in *Handbook on Synchrotron Radiation*, edited by G. Brown and D. Moncton (Elsevier Science Publishers B.V., Amsterdam, 1991), Vol. 3, Chap. 7.

## Halide Electroadsorption on Single Crystal Surfaces

B.M. Ocko\* and Th. Wandlowski\*\*

\* Department of Physics, Brookhaven National Laboratory, Upton, N.Y. 11973

\*\* Department of Electrochemistry, University of Ulm, D-89069, Ulm, Germany

### ABSTRACT

The structure and phase behavior of halides have been investigated on single crystals of Ag and Au using synchrotron x-ray scattering techniques. The adlayer coverages are potential dependent. For all halides studied we found that with increasing potential, at a critical potential, a disordered adlayer transforms into an ordered structure. Often these ordered phases are incommensurate and exhibit potential-dependent lateral separations (electrocompression). We have analyzed the electrocompression in terms of a model which includes lateral interactions and partial charge. A continuous compression is not observed for Br on Ag(100). Rather, we find that the adsorption is site-specific (lattice gas) in both the ordered and disordered phases. The coverage increases with increasing potential and at a critical potential the disordered phase transforms to a well-ordered commensurate structure.

### INTRODUCTION

A true atomistic picture of the electrode interface is emerging. This development is primarily due to the introduction of *in-situ* structural methods, specifically, scanning tunneling microscopy (STM), atomic force microscopy (AFM), and X-ray techniques, including surface X-ray scattering (SXS). Studies using these techniques have shown that electrode surfaces are often very well ordered and that the sharp features observed using classical electrochemical techniques are correlated with adlayer and substrate surface phase transitions. Due to the inherently high spatial resolution of SXS, the incommensurate structures can be measured with high precision, thus permitting small potential dependent changes to be determined. Additional information is obtained by investigating the potential dependence of the scattering amplitudes.

Here we review recent SXS results of halide adsorption on the (111) and (100) faces of Au and Ag. There are several reviews of SXS studies of electrode surfaces which will guide the curious reader[1-5]. SXS studies of electrode surfaces have revealed that electrodeposited adlayers (metals and halides) may be either commensurate, uniaxially incommensurate, or biaxially incommensurate with the underlying substrate.

### RESULTS

An important finding of the present work is that the incommensurate phases are electrocompressive, that is, the distances between the neighboring atoms depend on the applied electrochemical potential. In Fig. 1 simple atomic models corresponding to these three structures on a (111) surface, hexagonally closed packed, are shown. Both panels B and C are incommensurate and electrocompressive. In panel A the adlayer is hexagonal,  $(\sqrt{3} \times \sqrt{3})R30^\circ$ , where the atomic distance are  $\sqrt{3}$  larger and the adlayer is rotated by  $30^\circ$  with respect to the underlying lattice. In panel B the adlayer is uniaxial-incommensurate, rectangular  $c(p \times \sqrt{3})$ , two atoms per unit cell, where the cell has dimensions of  $p$  and  $\sqrt{3}$ . In panel C the adlayer structure is incommensurate rotated-hexagonal. In a SXS experiment, the symmetry is uniquely determined by the characteristic diffraction pattern. Furthermore, the atomic distances can be determined to better than 0.01Å by the positions

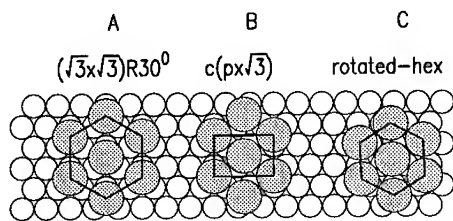


Figure 1: Atomic model of halide structures for (111) facets. These structures are (A) commensurate, (B) the uniaxial-incommensurate, and (C) rotated-hexagonal.

of the diffraction peaks in reciprocal space. The coverage,  $\theta$ , relative to the number of atoms in a underlying metal layer, is directly calculated from the distances and symmetry. The adsorption of halides can be monitored using impedance measurements, chronocoulometry and cyclic voltammetry (CV). The initial adsorption typically gives rise to a broad peak in the CV which is often followed by several sharp peaks at higher potentials[6-10]. The first sharp peak in the CV usually corresponds to a transition from a disordered adlayer to an ordered adlayer. The additional peaks correspond to transitions between different ordered structures. All of the ordered halide adlayers form over a potential regime where the underlying silver and gold lattices are unreconstructed[11]. In this report all potentials are referenced to a Ag/AgCl(3M NaCl) reference electrode.

#### A. Iodide on Ag(111) and Au(111)

In the first example we consider the adsorption of iodide on the (111) faces of Au and Ag. Iodine is the largest, most polarizable, and strongest adsorbing of the halides and exhibits ordered phases over the widest potential region. Since silver and gold have nearly identical lattice constants, a comparison of the iodide phase behavior allows us to focus on the relative role of the substrate-halide interaction. The Ag(111) surface is hexagonal, see open circles in Fig. 1., with a silver-silver nearest neighbor separation,  $a_{Ag} = 2.889\text{\AA}$ . With increasing potential, the adsorption of iodide on Ag(111) gives rise to the series of three ordered structures shown in Fig. 1[14]. The coverage extends from exactly  $1/3$  in the commensurate phase to 0.442 at the most positive potentials. In Fig. 2 the potential dependent iodide coverage on the Ag(111) surface is shown in 0.1 M NaI as open circles. The commensurate phase is stable from about -0.9 to -0.94 V. No ordered iodide phase is observed below -1.0 V. The  $c(p \times \sqrt{3})$  incommensurate phase exists between -0.92 to -0.36 V. Here  $\theta$  continuously increases from about 0.355 to 0.40. At the most positive extreme of the  $c(p \times \sqrt{3})$  phase, the structure corresponds to the  $(5 \times \sqrt{3})$  high-order commensurate unit cell with a nearest-neighbor iodide spacing of 4.39  $\text{\AA}$ . Upon a slight further increase in potential, the  $(5 \times \sqrt{3})$  phase vanishes and a rotated-hexagonal phase forms with  $\theta = 0.417$  corresponding to  $a_I = 4.59\text{\AA}$ .

We now contrast the phase behavior of I on Ag(111) with that on Au(111)[10] in 0.1 M KI, shown in Fig. 2 as filled circles, where the gold lattice constant,  $a_{Au} = 2.885\text{\AA}$  is slightly smaller than  $a_{Ag}$ . The commensurate phase is never observed on Au(111), rather it is intercepted by the disordered (fluid) phase at the potentials where it would be expected. As demonstrated in Fig. 2, similar phase behavior on the two metals is observed in the  $c(p \times \sqrt{3})$



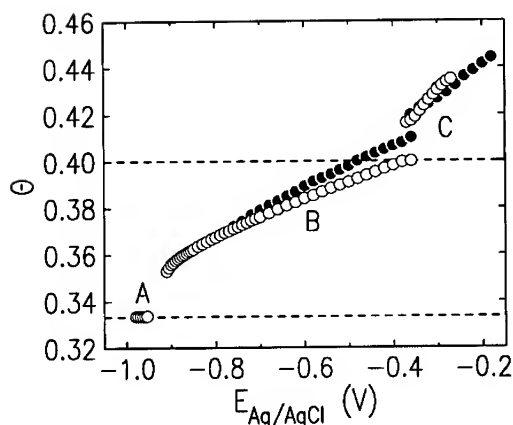


Figure 2: The potential dependent coverages,  $\theta$ , of iodide, determined from the in-plane diffraction, are shown versus the applied potential on Ag(111) in 0.1M NaI as open circles and on Au(111) in 0.1 M KI as filled circles. The potential scale of the Au(111) data has been shifted negatively by 0.5 V to facilitate the comparison with the Ag(111) data.

and the rotated-hexagonal phases. In the  $c(p \times \sqrt{3})$  phase the maximum coverage and the electrocompressibility,  $d\theta/dE$  are slightly smaller on silver than gold. Almost identical behavior is observed in the rotated-hexagonal phase which suggests that the influence of the substrate is minimal within this phase.

Many aspects of the observed phase behavior can be understood in terms of the adjustable electrochemical potential which favors increased surface densities at higher potentials, and the competition between the adsorbate-adsorbate interaction and the adsorbate-substrate interaction. In the uniaxial-incommensurate phase the adsorbates reside between the rows of the substrate atoms and this configuration has a lower interfacial energy than the rotated-hexagonal phase where some of the adsorbates must be in high energy atop sites. However, the uniaxial-incommensurate phase is slightly distorted from the hexagonal configuration and this distortion increases the adsorbate-adsorbate elastic interaction energy. With increasing potential the distortion increases and at a critical potential the uniaxial-incommensurate phase transforms to the incommensurate, rotated-hexagonal phase.

#### B. A Comparison of Chloride, Bromide and Iodide Monolayers on Au(111)

Incommensurate, hexagonal monolayers are observed for chloride[12], bromide[13], and iodide[10] on the Au(111) electrode prior to bulk electrooxidation. Whereas the bromide and iodide monolayers are rotated by several degrees with respect to the Au(111) axis, the chloride monolayer is aligned. In Fig.3 the halide-halide separations are shown for the three halides in their incommensurate hexagonal phases. With increasing potentials the separations decrease; saturation is evident for bromide at the highest potentials,  $\approx 0.7V$ . The chloride-chloride separation ranges from 3.98-4.03 Å, the bromide-bromide separation ranges from 4.03-4.22 Å, and the iodide-iodide separation ranges from 4.46-4.33 Å. These difference reflect the different intrinsic sizes of the three atoms. For all three the minimum

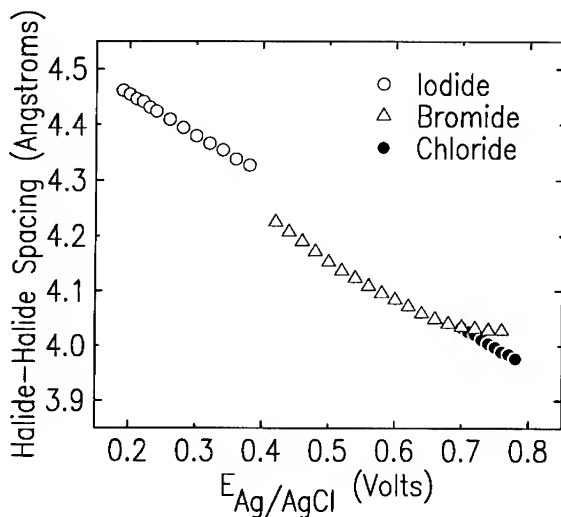


Figure 3: Comparison of halide-halide separations for chloride (0.1 M NaCl), bromide (0.1 M NaBr), and iodide (0.1 M KI) on Au(111).

spacings are close to the Van der Waals diameters and the maximum spacings are about 6% larger than that of the minimum. Despite the different intrinsic sizes of the halides and the potential range of the ordered hexagonal structures, the respective slopes,  $\partial\theta/\partial E$  are very close for all three[12]. Quantitatively, the measured electrocompressibilities are  $\partial\Gamma/\partial E$  are  $2.41 \pm 0.15$ ,  $2.95 \pm 0.07$ , and  $1.98 \pm 0.02$  ( $10^{14} \text{ cm}^2/\text{V}$ ) for chloride, bromide, and iodide, respectively, where  $\Gamma = \theta/A_{\text{Au}}$  is the absolute coverage and  $A_{\text{Au}}$  is the area per underlying gold atom. The similar slopes imply that the repulsive lateral interactions for all three halides are comparable and suggests that the fundamental nature of the repulsive interactions are similar despite the different partial charge of these species. Analysis of the electrocompression in terms of specific lateral interaction models is presented below.

### C. Bromide on Au(100)

How does the substrate structure affect the structure and coverage of the adsorbate? In order to explore this issue, we have carried out studies of the electrodeposition of Br on the Au(100) surface[15]. As shown in Fig. 4 by the open circles, this surface has an underlying square symmetry. Since the nearest-neighbor Au-Au separation is spacing of  $2.885 \text{ \AA}$  this gives  $1.20 \times 10^{15}$  gold atoms/ $\text{cm}^2$  corresponding to 86.6% of the Au(111) density. In bromide containing solutions, we find at lower potentials a commensurate  $c(\sqrt{2} \times 2\sqrt{2})R45^\circ$  phase (see Fig. 4 A) with  $\theta = 1/2$ . This commensurate structure contains two atoms in a rectangular unit cell with sides  $4.08 \text{ \AA}$  and  $8.16 \text{ \AA}$ . By construction, the nearest-neighbor separations are  $4.08 \text{ \AA}$  and  $4.56 \text{ \AA}$ . This phase is unusual since the atoms reside on bridge sites rather than the more coordinated four-fold hollows sites. The latter coordination is found for the  $(\sqrt{2} \times \sqrt{2})R45^\circ$  phase, often referred to as  $c(2 \times 2)$ , which also has  $\theta = 1/2$  and is more commonly observed on fcc (100) surfaces (see Fig. 4C). However, the symmetry of this

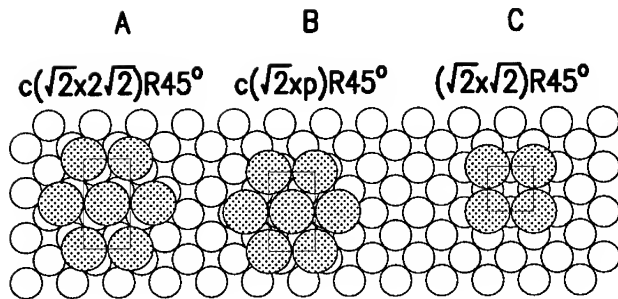


Figure 4: Atomic model of halide structures for (100) facets. These structures are (A) commensurate, (B) the uniaxial-incommensurate, and (C) commensurate.

phase is square whereas the  $c(\sqrt{2} \times 2\sqrt{2})R45^\circ$  phase is closer to hexagonal. The preference for the  $c(\sqrt{2} \times 2\sqrt{2})R45^\circ$  phase suggests that the elastic interactions between the relatively large Br adsorbates, which favor hexagonal packing, are more significant than the adsorbate-substrate interaction energy difference between the two phases. Above 0.42 V in 0.05 NaBr, the  $c(\sqrt{2} \times 2\sqrt{2})R45^\circ$  transforms to a uniaxial-incommensurate  $c(\sqrt{2} \times p)R45^\circ$  as shown in Fig. 4B, where  $p = \frac{\sqrt{2}}{1+\epsilon}$  and  $\epsilon$  is a measure of the incommensurability and varies continuously between 0 and 0.12 over the potential range 0.42 to 0.60 V, respectively. The potential dependent bromide coverage  $\Gamma$ , shown as circles in Fig. 5, is proportional to  $1 + \epsilon$ . Whereas the nearest-neighbor distance is always 4.08 Å, the next-nearest-neighbor spacing decreases from 4.56 Å for  $\epsilon = 0$  (commensurate) to 4.13 Å when  $\epsilon = 0.12$ . Thus the distortion from hexagonal symmetry, determined from the ratio between the nearest-neighbor and next-nearest-neighbor distances, decreases from 11.7 % to 1.2 % over the measured range. Despite the small distortion at this potential, the coverage at 0.60 V on the Au(111) face is still 3% higher than on the (100) face. The positive potential ranges are limited by the stability of the gold with respect to Br induced corrosion. Consequently, the more densely packed (111) face is more stable than the more open (100) face and the (111) data extends to higher potentials. The absence of satellite peaks for Br on Au(100), within the limits of the diffuse scattering background, allows us to establish that the compression is nearly uniform and not a network of locally commensurate regions separated by domain walls. The coverage in the neighborhood of the commensurate-incommensurate transition varies continuously. Accordingly, this transition is a second order phase transition. The measured critical exponent,  $\beta$ , which describes the behavior of incommensurability versus the potential, has been obtained by fitting the incommensurability to the form  $\epsilon = (E - E_0)^\beta$  in the incommensurate phase. When the entire range is used in the fitting  $\beta = 0.4 \pm 0.04$ , however systematic deviations from this form are evident. Over a range restricted to  $\epsilon < 0.06$  the data is consistent with  $\beta = 1/2$ . The dependence of  $\beta$  on the range is a direct consequence of the saturation which occur at the most positive potentials.

Over a range of coverages, between about  $6.45 \times 10^{14}$  to  $6.70 \times 10^{14} \text{ cm}^{-2}$ , the close-packed Br monolayers on Au(100) and Au(111) exhibit similar electrocompressibilities, albeit a potential shift of 0.1 V. The similarity in the potential dependences, despite the uniaxial-compression on Au(100) compared to the biaxial compression on Au(111), suggests that the

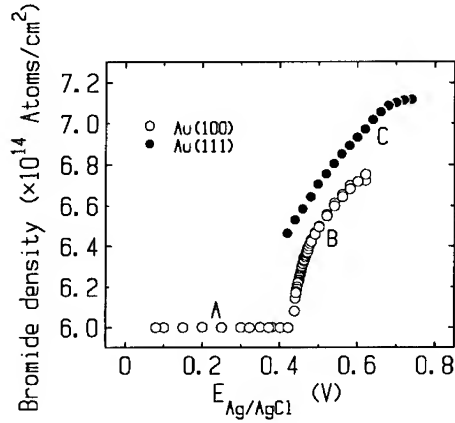


Figure 5: The potential dependent bromide coverages,  $\Gamma$ , in units of  $\text{atoms}/\text{cm}^2$ , on Au(100) and Au(111), determined from the in-plane diffraction, are shown versus the applied potential. The letters A,B and C in the figure refer to the structures given in Fig. 4. The Au(100) and Au(111) studies were carried out in 0.05 M NaBr and 0.10 M NaBr solutions, respectively. This concentration difference causes a +0.018 V shift for the Au(111) data set.

interactions between the Au and Br are similar in both cases and that the symmetry of the substrate does not play a critical role.

#### D. Bromide on Ag(100)

For bromide on Ag(100) a  $(\sqrt{2} \times \sqrt{2})R45^\circ$  structure with  $\theta = 1/2$  is formed[16] (see Fig. 4C) where the bromides reside in the four-fold hollows. This square diffraction pattern is identical to the pattern observed for vapor deposited Cl on Ag(100) using LEED[17]. The neighboring bromides are  $4.086\text{\AA}$  apart and the coverage  $\theta = 0.5$ . Below a critical potential only the integer diffraction peaks associated with a  $(1 \times 1)$  unit cell are observed. Half-order peaks, identifying the  $(\sqrt{2} \times \sqrt{2})R45^\circ$  phase, are observed above this critical potential. No incommensurate phases, such as observed for Br on Au(100)[15] is observed. The square packing arrangement of the adsorbed Br adlayer represents a large distortion from hexagonal packing. Furthermore, this arrangement is very different from the hexagonal packing formed on Ag(111)[14] and Au(111)[12], and the distorted-hexagonal pattern formed on Au(001). Electrodeposited chloride and iodide on Ag(100) exhibit the same diffraction features as that of bromide, thus they form the same  $c(2 \times 2)$  phase without regard to the different halide diameters. In contrast, these same halides exhibit very different distances of closest approach on Au(111)[12].

In Fig. 6 the cyclic voltammetry (CV) and the potential dependent x-ray scattering intensity at  $(1/2, 1/2, 0.12)$  and at  $(1, 0, 0.12)$  are shown during both sweep directions (primitive lattice coordinates). The broad weak peak in the CV at about -1.1 V has been historically attributed to the reorientation of surface water and the second, sharper peak at about (-0.75 V) to a phase transition in the adsorbate layer[18]. On the basis of the potential dependent scattering at the half-order positions and no other identifiable features below this potential,

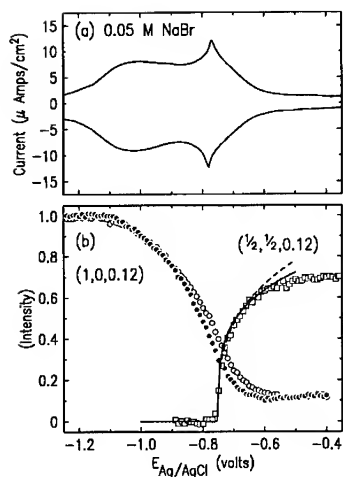


Figure 6: Comparison of the electrochemical and X-ray scans from the Ag(100) surface in 0.05 M NaBr. The cyclic voltammogram (10 mV/sec.) is shown in (a) has been obtained using a separate cell. The diffracted x-ray signals (1 mV/sec.) at  $(0.5, 0.5, 0.12)$  and  $(1, 0, 0.12)$  are shown in (b). Both intensities are normalized such that the intensity at  $(1, 0, 0.12)$  at -1.2 V are unity.

we identify the sharp peak as an order/disorder transition. At potentials more positive than -0.78 V the scattering intensity, after correcting for the diffuse component, starts to rapidly increase from zero as demonstrated by the data at  $(1/2, 1/2, 0.12)$  shown as squares in Fig. 1b. This result clearly identifies the sharp peak in the CV with the ordered phase. Saturation occurs at about -0.5V, corresponding to the potential where the CV saturates.

The x-ray intensity at superlattice positions, such as  $(1/2, 1/2)$ , measures the order parameter squared and is isomorphic to the magnetization in the Ising spin problem. Thus, the intensity should behave as  $(E - E_c)^{2\beta}$  for  $E > E_c$   $\beta = 1/8$ . This prediction, shown as the solid line in Fig. 3 for the negative potential sweep, provides a reasonable description of the critical behavior up to about 80% of the saturation value. The fit for the other sweep direction is similar, except for an offset of 30 mV (see Fig. 6). This may be due to the fact that the transition is slightly first order or to slight changes in the surface morphology with sample history. Clearly, the mean-field prediction ( $\beta = 1/2$ ) does not provide a reasonable description of the critical behavior. For Cl on Ag(100) in UHV[17],  $\beta = 0.12 \pm 0.04$ , however in this study the chemical potential was not directly measured but rather it was ascertained from the coverage.

The nature of the disordered phase is revealed by considering the potential dependent scattering intensity at  $(1, 0, 0.12)$ , see Fig. 6, which is sensitive to both the arrangement of the surface silver atoms and that of the adsorbate layer. The onset of the slow decrease with increasing potential initiates at about -1.0 V and is correlated with the broad peak in the CV but occurs after the initial increase in the current (e.g adsorption). Close to the potential where long range order in the bromide monolayer is established there is a slight increase in

the magnitude of the slope in the intensity at (1,0,0.12) but no discontinuity. This indicates that the coverage changes continuously and supports the notion that the phase transition is close to being second order. At the most positive potentials, where the ordered phase is well developed, the intensity has reached a ratio which is 11% of its value in the absence of bromide. This ratio is in perfect agreement with crystallographic calculations which take into account the Ag(100) structure, the Br adlayer structure, and the relative scattering amplitudes of Ag and Br. The continuous decrease in the scattering intensity at (1,0,0.12) results from a continuous increase in coverage from zero to one half. On this basis, we assert that the disordered phase is a "lattice-gas" corresponding to random bromide adsorbed on four-fold hollow sites. Here we note that for Br on Au(111) and Au(100) there is no corresponding interference of the bromide scattering with that of the underlying lattice, as such, there is no evidence that these systems form a lattice gas. An analysis of the potential dependent coverage, obtained from electrochemistry measurements, shows that the isotherm can be described by repulsive interactions using as a first approximation the Mean-Field (Frumkin) Isotherm.

### Theoretical Model of Electrocompression

The electrocompression of the halide lattices can be calculated from the interfacial free energy. Here we only consider the internal energy contribution and have ignored entropic effects. This assumption is justified for the high density, hexagonal close-packed adlayers but is not correct for the low density adlayers which are not of interest here. Here we include the electrochemical potentials,  $\tilde{\mu}$ , and the coverage-dependent internal interaction energies of the adsorbate,  $U(\theta)$ . The electrical potential of the adsorbed ion is not necessarily that of the electron transferred to the metal, and this complicates the derivation below and requires some additional assumptions.

In the derivation which follows, we adopt the conventions used by Schmickler[20]. The charge of the solvated ion is  $ez$  and that of the adsorbed ion is  $e(z + \lambda)$  which leaves a charge  $e\lambda$  on the metal. The electrochemical potential is given by  $\tilde{\mu}(\phi)$  which is related to the chemical potential,  $\mu$ , the potential,  $\phi$ , and the charge,  $ze$ . The electrochemical potential of the adsorbate is given by

$$\tilde{\mu}_{adsorbate} = \mu_{adsorbate} + e(z + \lambda)\phi_{adsorbate} \quad (1)$$

since the charge of the adsorbed ion is  $e(z + \lambda)$  Finally, energy conservation requires that the electrochemical potential of the solution species must equal the sum of the electrochemical potentials of the adsorbate and that of the partial electron of charge  $-e\lambda$  which is transferred. Equating these terms yields

$$\tilde{\mu}_{solution} = \mu_{adsorbate} + e(z + \lambda)\phi_{adsorbate} - e\lambda\phi_{metal} \quad (2)$$

where  $\phi_{metal}$  is the potential of the metal which need not correspond to that of the adsorbate. There is no known way to independently measure the potential of the adsorbate. The only potential which can be measured is that of the electron which is transferred to the metal surface, e.g.  $\phi_{metal}$ . However, if we assume that  $\phi_{adsorbate}$  is a constant fraction of  $\phi_{metal}$ , then Eq. 2 can be simplified. With this we reformulate Eq. 2 as

$$\mu_{solution} = \mu_{adsorbate} + e\gamma\phi + e\phi_0 \quad (3)$$

where  $\phi = \phi_{metal}$ ,  $\gamma$  is the electrosorption valence, and  $\phi_0$  is a constant. The electrosorption valence, described by Schultze and Vetter[19], is the effective charge transferred to the metal surface upon electrosorption.

The chemical potential of the of adsorbate can be expressed in terms of the derivative of the internal energy,  $U$ , with respect to the total number of adsorbed atoms,  $N$

$$\mu_{adsorbate} = \frac{\partial U}{\partial N} \Big|_{area} \quad (4)$$

Here  $U$  includes a sum over all of the lateral interaction energies and an energy of adsorption

$$U = U_{lateral} + U_0 \quad (5)$$

where we assume that these energies are not site specific. If  $U_0$  is independent of the coverage the adsorption energy can be written as

$$U_0 = Nu_0 \quad (6)$$

where  $u_0$  is the adsorption energy of a single adsorbate. The lateral energy can be written as

$$U_{lateral} = \frac{1}{2} \sum_i \left[ \sum_{j \neq i} u_{lateral}(r_{i,j}) \right] = \frac{N}{2} \sum_i u_{lateral}(r_i) \quad (7)$$

Here the double sum counts all two-particle interactions between adsorbates, independent of the separation and the factor of 1/2 is to avoid double counting. The pairwise lateral interaction energy (discussed below) between adatoms separated by  $r_{i,j}$  is  $u_{lateral}(r_{i,j})$ . Since we have assumed translational invariance, the double sum is reduced to a single sum where the pairwise lateral interaction is replaced by  $u_{lateral}(r_i)$ . In order to relate the measured change in the nearest-neighbor separation,  $r$ , with respect to the potential, the derivative with respect to  $N$  is replaced by a derivative with respect to  $r$  through use of the relation

$$dN = -\frac{2Ndr}{r} \quad (8)$$

By combining Eqs. 4-8 the chemical potential of the adsorbate is given by

$$\mu_{adsorbate} = u_0 + \left(1 - \frac{r\partial}{2\partial r}\right) \sum_i \frac{u_{lateral}(r_i)}{2} \quad (9)$$

where the first term is just the adsorption energy of a single atom and the second term is related to the lateral interactions. Given the symmetry of the adsorbate the partial derivative can be evaluated. In Eq. 9 the lateral interaction term is composed of two parts; the first is sum over all interactions for one adatom and the second is the energy to squeeze the lattice after adding an additional adatom. As we shall see below, this "squeeze" term is proportional to the radial power of the interactions.

By combining Eqs. 3 and 9, and eliminating  $\mu_{adsorbate}$  the relationship between  $\phi$  and  $u_{lateral}$  emerges as

$$-e\gamma\phi - e\phi'_0 = \left(1 - \frac{r\partial}{2\partial r}\right) \sum_i \frac{u_{lateral}(r_i)}{2} \quad (10)$$

where  $\phi'_0$  is a new constant which incorporates  $\phi_0$ ,  $u_0$ , and  $\mu_{solution}$ . Since  $\gamma$  is negative for halides, increasing the potential raises the chemical potential of the adsorbate. Here the sum over all interactions (Zucker sum) can be replaced by

$$\sum_i u_{lateral}(r_i) = Zu_{lateral}(r_{nn}) \quad (11)$$

where  $Z$  is a numerical constant which estimates the number of effective nearest neighbors and  $u_{lateral}(r_{nn})$  is the lateral interaction between nearest-neighbors. For a hexagonal lattice this constant is slightly larger than 6, the number of nearest-neighbors, when the lateral interactions fall rapidly with separation. This is because the interaction with non-nearest neighbors does not contribute significantly to the sum.

The lateral potential between adsorbed halides originates from the hard-core repulsion, Van der Waals attractive interactions, dipolar repulsion and substrate mediated repulsive interactions[23], often referred to as the "indirect interaction". The first two terms are grouped in the usually way to form the Lennard Jones (6/12) potential.

$$u_{LJ} = 4\epsilon' \left( \left[ \frac{\sigma}{r} \right]^{12} - \left[ \frac{\sigma}{r} \right]^6 \right) \quad (12)$$

where  $\epsilon'$  is the depth of the interaction well and  $\sigma$  is the position where  $u_{LJ} = 0$ . The minimum occurs at  $1.12\sigma$  which is the mean spacing between adsorbates in the absence of other interactions.

Since the adsorbed halides are partially charged, presumably with an image charge on the metal side, the neighboring halides should repel each other through dipole-dipole interactions. Here it is not possible to determine the placement of the charge, rather only the dipole moment can be determined. For dipole-dipole interactions the repulsive potential is given by

$$u_{d-d} = \frac{p^2}{2\pi\epsilon_0 r^3} \quad (13)$$

where  $p$  is the dipole moment and where we have assumed that the dielectric constant is unity. The direct dipole interactions given here do not fall off as fast with distance as the induced dipole interactions, e.g the Van der Waals  $r^{-6}$  given in Eq. 12. In practice, the dipole interactions are not infinitely long range since Debye screening from the electrolyte ions provides an exponential (Yukawa type) cut-off.

In Fig. 7 we show the Cl-Cl separation versus the potential for Au(111). Note that this is the same data as shown in Fig. 4, but here the axis have been reversed for numerical convenience. We fitted the potential to the measured separation through the relationship given by Eq. 10. The solid and dashed lines represent best fits, using the potentials given by Eqs. 12 and 13. The potential offset,  $\phi'_0$ , and the dipole moment are the only adjustable parameters. We have fixed the chloride Lennard-Jones parameters to  $\sigma = 3.5\text{\AA}$  and  $\epsilon' = 13.5\text{meV}$  as reported by McDonald [21]. In the absence of other interactions, the minimum is at  $1.12 \times 3.5 = 3.93\text{\AA}$ . This is close to, albeit slightly smaller, than the smallest Cl-Cl separation indicating that the Lennard-Jones interactions is always in the attractive regime. On the other hand, the dipolar contribution is always repulsive.



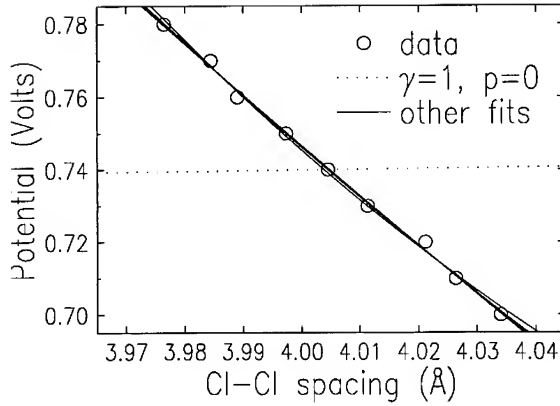


Figure 7: The measured potential versus the Cl-Cl separation for Au(111) along with various fits. Note that except for the fit with  $p = 0$  (dashed line), it is difficult to distinguish the other fits (solid lines).

In the following analysis we have fitted the data with two values of  $\gamma$ , corresponding to complete discharge ( $\gamma = -1$ ) and to the partial charge obtained via chronocoulometric measurements ( $\gamma = -0.5$ )[22]. In the latter case, the chloride still maintains half its charge when it is adsorbed.

The Cl-Cl separation can not be represented by the present formulation when  $p = 0$ , as indicated by the dotted line in Fig. 7 with  $\gamma = -1$ . The data can be equally well described by allowing the dipole moment to float in the least-squares analysis using several combinations of parameters. Fits were carried out with both values of  $\gamma$  and with  $\epsilon'$  set to zero and the value reported by McDonald. With  $\gamma = -1$ , the best fit gives  $p = 2.62$  D with  $\epsilon' = 0$  and  $p = 2.42$  D with  $\epsilon' = 13.5$  meV. The small difference between these two values demonstrates that the Lennard-Jones potential is not nearly large enough to describe the compression. With  $\gamma = -0.5$ , the best fit gives  $p = 1.85$  D with  $\epsilon' = 0$  and  $p = 1.53$  D with  $\epsilon' = 13.5$  meV.

The values obtained from the analysis above are much larger than the value of 0.7 D obtained for halides on Au in UHV derived from work function measurements[24]. We note that this UHV value would give rise to a much larger electrocompression (softer lattice) than observed in our measurements. However, we remind the reader that the dipole moment derived from the electrocompression measurements is an effective value since it also includes the effect of the solution species which are not present in the vacuum. In addition, indirect interaction[23], which is mediated by the adsorbate-substrate interactions through changes in the local electronic structure, has not been incorporated in the present model. At small distances this gives rise to a repulsive interaction which scales as  $r^{-5}$ . The absence of the indirect interaction may in part describe some of the differences between the vacuum and electrochemical results.

The surface dipole moment can also be estimated from electrochemical measurements. For Cl on Au(111)[22] the dipole moment is about 0.25 D at the highest coverages, but, the exact value depends sensitively on the surface charge and reaches a minimum of 0.04 D.

The smaller value at the electrochemical interface has been attributed to screening effects from the electrolyte. Finally, we remind the reader that electrocompression measurements are sensitive to the effects of the lateral interactions whereas the dipole moments derived from the the work function and electrochemistry measurements depend only on the surface normal charge distribution.

Further analysis and data is required to fully understand the electrocompressions observed for electrodeposited adsorbates. For adsorbates on Ag(100) we are able to deduce the coverages in both the ordered and disordered phases[16]; not just in the ordered phases as is the case for adsorbates on Au(111). Here we are able to model the isotherms using a mean-field (Frumkin type) isotherm with similar values of the dipole moment as for the halides on Au(111)[16]. At the present time we do not have a complete understanding why the dipole moment, obtained from our x-ray study, UHV work function studies and electrochemical studies do not agree. A complete understanding will require a better appreciation of the indirect interaction strength and the role of solvent-adsorbate interactions.

We greatly acknowledge the important contributions of Jia Wang to all aspect of the present work and the participation of Olaf Magnussen and Gavin Watson. The work at BNL is supported by the Division of Materials and Chemical Sciences, U.S. Department of Energy, under Contract No. DE-AC02-76CH00016. Th. Wandlowski thanks the Deutsche Forschungsgemeinschaft for support through Wa 879/2 and a Heisenberg fellowship.

## References

- [1] M.F. Toney, J.G. Gordon, and O.R. Melroy, *SPIE Proc.* **1550**, 140 (1991).
- [2] M.F. Toney and O.R. Melroy, *Electrochemical Interfaces: Modern Techniques for In-Situ Interface Characterization*, Edited by H.D. Abruna, (VCH Verlag Chemical, Publishers, Berlin, 1991), p. 57
- [3] M.F. Toney, *Synchrotron Techniques in Interfacial Electrochemistry*, Edited by C.A. Melendres and A. Tadjeddine, (Klewer, Dordrecht, 1994), p. 109.
- [4] B.M. Ocko and J. Wang, *Synchrotron Techniques in Interfacial Electrochemistry*, Edited by C.A. Melendres and A. Tadjeddine, (Klewer, Dordrecht, 1994), p. 127.
- [5] B.M. Ocko, O.M. Magnussen, J. X. Wang, and R.R. Adžić, *Nanoscale Probes of the Solid/Liquid Interface*, Edited by A.A. Gewirth and H. Siegenthaler, (Klewer, Dordrecht, 1995), p. 103.
- [6] A. Hamelin, and J.P. Bellier, *J. Electroanal. Chem.* **41**, p. 179 (1973).
- [7] D.A. Scherson, and D.M. Kolb, *J. Electroanal. Chem.* **176**, p. 353 (1984).
- [8] Gao, X.; Weaver, M. J. *J. Am. Chem. Soc.* **114**, p. 8544 (1992); Tao, N. J.; Lindsay, S. M. *J. Phys. Chem.* **96**, p. 5213 (1992).
- [9] T. Yamada, K. Ogaki, S Okubu, and K. Itaya, *Surf. Sci.*, **369**, p. 321 (1996).

- [10] B.M. Ocko, G.M. Watson, and J. Wang, J. Phys. Chem. **98**, p. 897 (1994); J. Wang, G.M. Watson, and B.M. Ocko, Physica A **200**, p. 751 (1993).
- [11] J. Wang, B.M. Ocko, A.J. Davenport, and H.S. Isaacs, Phys. Rev. B **46**, p. 10321 (1992).
- [12] O. M. Magnussen, B.M. Ocko, J. X. Wang, and R.R. Adžić, Phys. Rev. B **51**, p. 5510 (1995).
- [13] O. M. Magnussen, J. X. Wang, R.R. Adžić, and B. M. Ocko, J. Phys. Chem. **100**, p. 5500 (1996)
- [14] B.M. Ocko, O.M. Magnussen, J.X. Wang, R.R. Adžić, and Th. Wandlowski, Physica B **221**, p. 261 (1994).
- [15] B.M. Ocko, O. M. Magnussen, J. X. Wang, and Th. Wandlowski, Phys. Rev. B **53**, p. 7654 (1996); and T. Wandlowski, J. X. Wang, O. M. Magnussen, and B. M. Ocko J. Phys. Chem. **100**, p. 10277 (1996)
- [16] B.M. Ocko, J.X. Wang, Th. Wandlowski (unpublished); and Th. Wandlowski, B.M. Ocko, and J.X. Wang (unpublished)
- [17] D.E. Taylor, E.D. Williams, R.L. Park, N.C. Bartelt, and T.L. Einstein, Phys. Rev. B, **32**, p. 4653 (1985).
- [18] G. Valette, A. Hamelin, R. Parsons, Z. Phys. Chem. N.F. **113** p. 71 (1978).
- [19] J. W. Schultze and K.J. Vetter, J. Electroanal. Chem. **44**, p. 63 (1973).
- [20] W. Schmickler, **Interfacial Electrochemistry**, Oxford University Press, New York, 1996.
- [21] I.R. McDonald, D.G. Bound, and M.L. Klein, Mol. Phys. **45**, p. 521 (1982).
- [22] Z. Shi and J. Lipkowski, J. Electroanal. Chem. **403**, p. 225 (1996). Surf. Sci. **97** p. 409 (1980)
- [23] see for instance T.L. Einstein, CRC Crit. Rev. Solid State Mat. Sci. **7**, p. 261 (1978) and T.L. Einstein and J.R. Schrieffer, Phys. Rev. B **7**, 3629 (1973).
- [24] see for instance E. Bertel and F.P. Netzer, Surf. Sci. **97** p. 409 (1980)

## LATTICE-GAS MODELS OF ELECTROCHEMICAL ADSORPTION: STATIC AND DYNAMIC ASPECTS

PER ARNE RIKVOLD<sup>1,2</sup>, ANDRZEJ WIECKOWSKI<sup>3</sup>, and RAPHAEL A. RAMOS<sup>1,4</sup>

<sup>1</sup>Center for Materials Research and Technology, Supercomputer Computations Research Institute, and Department of Physics, Florida State University, Tallahassee, FL 32306

<sup>2</sup>Department of Fundamental Sciences, College of Integrated Human Studies, Kyoto University, Kyoto 606, Japan

<sup>3</sup>Department of Chemistry and Frederick Seitz Materials Research Laboratory, University of Illinois, Urbana, IL 61801

<sup>4</sup>Department of Physics, University of Puerto Rico, Mayaguez, PR 00681

### ABSTRACT

We discuss applications of statistical-mechanical lattice-gas models to electrochemical adsorption. Our strategy to describe specific systems includes microscopic model formulation, calculation of zero-temperature phase diagrams, numerical simulation of thermodynamic and structural quantities at nonzero temperatures, and estimation of effective, lateral interactions. We report applications to adsorption on single-crystal electrodes, presenting simulated and experimental coverages and voltammetric currents for urea on Pt(100) and the underpotential deposition of Cu on Au(111) in sulfuric acid. We also discuss an extension of the method to study time-dependent phenomena far from equilibrium.

### INTRODUCTION

The study of phase transitions and ordering in electrochemical adsorption contributes to our fundamental understanding of the microstructure of the solid/liquid interface, which provides the basis for a rational development of electrochemical materials synthesis techniques. The recent confluence of "traditional" electrochemistry and surface science has occasioned a two-way exchange of experimental and theoretical techniques. Here we discuss electrochemical applications of a theoretical method adapted from surface science: computational, statistical-mechanical lattice-gas modeling. We illustrate our discussion with applications to the electrosorption of urea on Pt(100) [1-3] and to the underpotential deposition (UPD) of Cu on Au(111) [3-4], both coordinated with experiments. Extension of our modeling strategy to far-from-equilibrium problems is considered, and we report Monte Carlo (MC) simulations of current transients in a model for UPD, following a potential-step experiment.

### LATTICE-GAS MODELS OF SUBMONOLAYER CHEMISORPTION

The models we discuss are defined by the two-component lattice-gas Hamiltonian [1-5],

$$\mathcal{H} = - \sum_n \sum_{\langle ij \rangle}^{(n)} \left[ \Phi_{AA}^{(n)} c_i^A c_j^A + \Phi_{AB}^{(n)} (c_i^A c_j^B + c_i^B c_j^A) + \Phi_{BB}^{(n)} c_i^B c_j^B \right] + \mathcal{H}_3 - \sum_i [\bar{\mu}_A c_i^A + \bar{\mu}_B c_i^B] \quad (1)$$

Here  $c_i^X \in \{0,1\}$  is the local occupation variable for species X;  $\sum_{\langle ij \rangle}^{(n)}$  and  $\sum_i$  run over all  $n$ th-neighbor bonds and over all adsorption sites, respectively;  $\Phi_{XY}^{(n)}$  denotes the effective lateral XY pair interaction through an  $n$ th-neighbor bond;  $\sum_n$  runs over the interaction ranges; and  $\mathcal{H}_3$  contains multi-particle interactions. The change in electrochemical potential when

one X particle is adsorbed is  $-\bar{\mu}_X$ . Particular systems differ in their binding-site geometries and the values and ranges of the lateral interactions. The thermodynamic density conjugate to  $\bar{\mu}_X$  is the surface coverage,  $\Theta_X = N^{-1} \sum_i c_i^X$ , where  $N$  is the number of surface unit cells. We relate  $\bar{\mu}_X$  to the bulk activities  $[X]$  and the electrode potential  $E$  as

$$\bar{\mu}_X = \mu_X^0 + RT \ln ([X]/[X]^0) - z_X F E, \quad (2)$$

where  $R$  is the molar gas constant,  $T$  is the absolute temperature,  $F$  is Faraday's constant,  $z_X$  is the effective electrovalence of X, and  $\mu_X^0$  and  $[X]^0$  are reference values. In the limit of vanishing potential sweep rate, the voltammetric current per unit cell is the time derivative of the charge transported during the adsorption/desorption process:  $q = -e(z_A \Theta_A + z_B \Theta_B)$ , where  $e$  is the elementary charge. The current is easily obtained in terms of the lattice-gas response functions,  $\partial \Theta_X / \partial \bar{\mu}_Y$ , and is proportional to the sweep rate [1–3].

The interactions in Eq. (1) are *effective* interactions mediated through several channels. The mechanisms include interactions between the adsorbate and the substrate electron structure, adsorbate-induced deformations of the substrate, interactions with the fluid electrolyte, and (screened) electrostatic interactions. Theoretical and computational methods are not yet sufficiently advanced to obtain these multi-source interactions from first principles.

We have developed a strategy to determine the effective interactions, providing a practical alternative to “first-principles” methods. This consists in fitting thermodynamic and structural model predictions from zero-temperature phase diagrams and numerical simulations at room temperature to experiments, considering a variety of physical quantities. Obviously, this also has its problems. The potential number of parameters is large, and there is no guarantee that a minimal set of interactions is unique. Nevertheless, previous lattice-gas studies of electrochemical systems [1–7] indicate that when all available experimental information is consistently included, this approach has considerable predictive power. When effective interactions from first-principles calculations become available in the future, results from lattice-gas models will be useful for testing their consistency with experiments.

## ADSORPTION ON SINGLE-CRYSTAL SURFACES: NEAR-EQUILIBRIUM ASPECTS

Here we discuss two systems representative of the electrosorption of small adsorbate particles on single-crystal surfaces: urea adsorbed on Pt(100) from perchloric acid [1–3] and the UPD of Cu on Au(111) from sulfuric acid [4, 6–7]. Both exhibit a dramatic peak sharpening in the cyclic voltammogram (CV) when a small concentration of the adsorbate is added to the electrolyte. Whereas the urea/Pt(100) system develops a single CV peak [8], in copper UPD two peaks are exhibited [9–10]. These peaks are associated with adsorbate phase transitions [8–10]. The voltammetric changes are much weaker or absent when the same substances are adsorbed on other crystal planes of the same metals [8–9], indicating that they depend crucially on the geometric fit between the adsorbates and the surface.

### Urea on Pt(100)

In addition to the surface-specific narrowing of the CV peak (experimental and simulated CV profiles are shown in Fig. 1a), the experimental observations are as follows.

1. The urea coverage, measured *in situ* by a radiochemical method and *ex situ* by Auger Electron Spectroscopy (AES), changes from near zero on the negative side of the CV peak to approximately 1/4 monolayer (ML) on the positive side. See Fig. 1b.

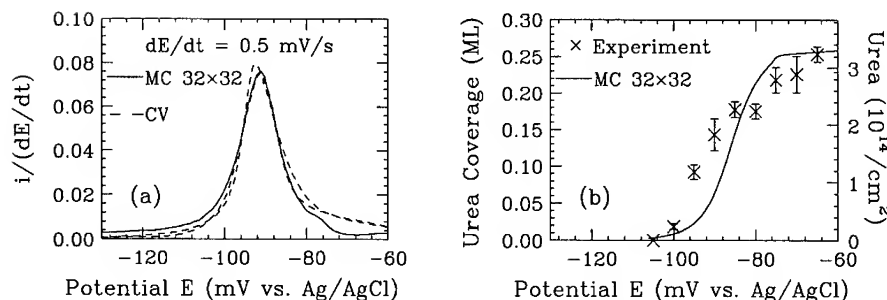


Figure 1: (a): Room-temperature CV profiles for urea on Pt(100) in 0.1 M HClO<sub>4</sub>. Experimental (dashed) and simulated (solid) normalized CV currents,  $i/(dE/dt)$ , in elementary charges per mV per Pt(100) unit cell, at 1.0 mM bulk urea. (b): Urea coverage measured radiochemically at 0.5 mM bulk urea ( $\times$ ) and simulated by MC (solid). After Ref. [2].

2. *Ex situ* Low-Energy Electron Diffraction (LEED) at potentials positive of the CV peak shows an ordered  $c(2 \times 4)$  structure, consistent with a urea coverage of  $1/4$  ML. Emersion on the negative side of the peak gives only an unreconstructed  $(1 \times 1)$  surface.

The model developed to account for these observations assumes that urea coordinates the platinum through its nitrogen atoms, with the C=O group away from the surface. This is reasonable since urea does not decompose on platinum [1], and molecular nitrogen binds more strongly to transition metals than oxygen [11]. Since the unstrained N-N distance in urea matches the square Pt(100) surface quite well, it was assumed that urea occupies two nearest-neighbor sites on the lattice. Hydrogen was assumed to adsorb in the same on-top positions as the nitrogen [12]. In the resulting model, hydrogen is adsorbed at the nodes and urea on the bonds of a square lattice. To stabilize the  $c(2 \times 4)$  phase, effective interactions are included through eighth-nearest neighbors, and were determined from ground-state calculations followed by MC simulations with a heat-bath algorithm on systems up to  $32 \times 32$  unit cells. The resulting interactions are given in Ref. [2]. The assumptions underlying this model were recently strengthened by spectroscopic studies [13], but microscopic structure determination by scanning probe microscopy remains a challenge.

#### UPD of Cu with sulfate on Au(111)

The UPD of Cu on Au(111) in sulfuric acid has been intensively studied, both experimentally and theoretically [4, 6–7]. The most striking feature in CV experiments on this system is the appearance of two peaks, 100–150 mV apart, upon addition of Cu<sup>2+</sup> ions [9–10]. Typical CV profiles are shown in Fig. 2a, together with simulation results. In the potential range between the peaks, the adsorbate layer has a  $(\sqrt{3} \times \sqrt{3})$  structure with  $2/3$  ML Cu and  $1/3$  ML sulfate [4, 7, 14], first proposed by Huckaby and Blum (HB) [6].

Our lattice-gas model for this system is an extension of the HB model with interactions through fourth-nearest neighbors (see also Ref. [7]). The models are based on the assumption that the sulfate coordinates the triangular Au(111) surface through three of its oxygen atoms, with the fourth S-O bond away from the surface. This gives the sulfate a triangular “footprint” that reasonably matches the Au(111) unit cell. The adsorption sites for the Cu and sulfur are assumed to lie on the same triangular lattice. It has been experimentally

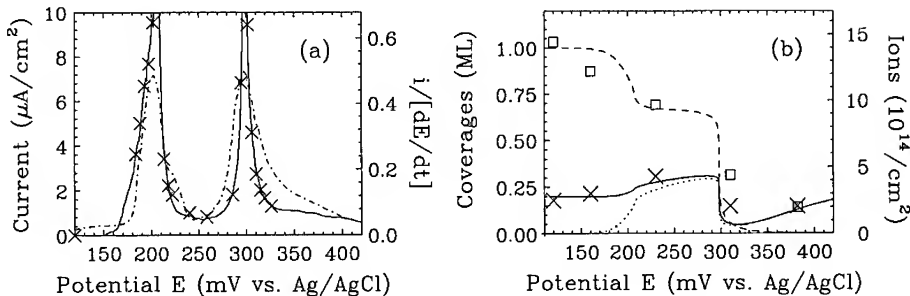


Figure 2: (a): CV profiles for UPD of Cu with sulfate on Au(111).  $dE/dt = 2\text{mV/s}$ . Experimental (dot-dashed) and simulated ( $30 \times 30$ : solid;  $45 \times 45$ :  $\times$ ) current densities. (b): Simulated coverages of Cu (dashed), first-layer sulfate (dotted), and total sulfate (solid), together with corresponding AES data,  $\square$  and  $\times$ , respectively. After Ref. [4].

observed [15–16] that sulfate is adsorbed on top of the Cu monolayer at negative potentials. A simple estimate was used for the sulfate coverage in this second layer:  $\Theta_s^{(2)} = \alpha \Theta_c (\frac{1}{3} - \Theta_s)$ , where  $\alpha$  is a phenomenological constant. Adsorption isotherms and CV currents at room temperature were obtained from MC heat-bath simulations on  $L \times L$  triangular lattices with  $L=30$  and  $45$ . The resulting parameter values are given in Ref. [4].

#### FAR-FROM-EQUILIBRIUM CURRENT TRANSIENTS IN A MODEL FOR UPD

Whereas the preceding discussion presents a near-equilibrium theory, with voltammetric currents at slow potential scan rates obtained from the adsorption isotherms, analysis of fast scans or potential-step experiments requires a true nonequilibrium treatment. In the early-time regime, mean-field rate equations are often quite satisfactory [17–18]. However, for later times, when coalescence of adsorbate islands becomes important, this approach no longer suffices [19–20]. For systems in which the phases involved are ordered (such as the Cu/Au system discussed above [21]), the microscopic adlayer structure and the dynamical details of the adsorption and lateral diffusion processes should become important, even at early times [22]. To test the domains of validity of the simpler theoretical treatments that ignore the details of microscopic structure, we have therefore initiated a study of the dynamics of electrochemical adsorption by numerical simulation of microscopic models.

In this section we present new results of simulations of current transients for a potential-step experiment, in which a model UPD system is driven through a first-order transition between a low-coverage and a high-coverage phase. We describe this process by a single-component lattice-gas model on a square lattice, with attractive nearest-neighbor interactions and nonconservative heat-bath dynamics [19–20]. The Hamiltonian for this model is Eq. (1) with all parameters except  $\Phi_{AA}^{(1)}$  and  $\bar{\mu}_A$  equal to zero.

Typical results for the time evolutions of the adsorbate coverage and the corresponding transient voltammetric current, which is proportional to the time derivative of the coverage, are shown in Fig. 3. Although the model is too simple to apply directly to a particular system, the similarity to the current transients recently obtained by Hölzle et al. [21] for UPD of Cu on Au(111) is striking. In particular, an early-time transient due to single-particle adsorption is clearly seen, followed by a second peak due to the irreversible growth

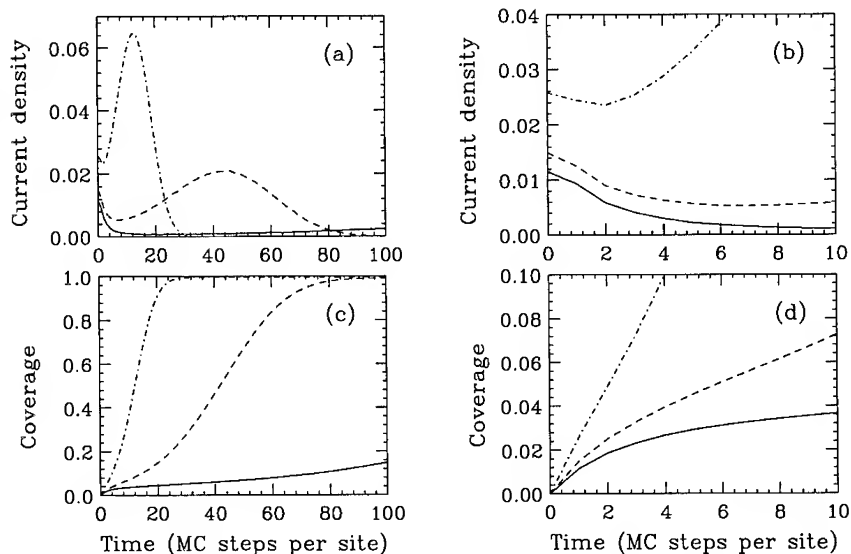


Figure 3: Current transients (a,b) and coverages (c,d) for a model UPD system driven through its first-order transition at a temperature 0.8 times its critical value. Assuming an experiment performed at 300K, this corresponds to  $\Phi_{AA}^{(1)} \approx 57\text{meV}$ . The overpotentials are approximately  $5.7\text{mV}/z_A$  (solid),  $11.4\text{mV}/z_A$  (dashed), and  $22.8\text{mV}/z_A$  (dot-dash).

of islands of the equilibrium phase. The early-time current maxima (see blow-up in Fig. 3b) correspond to the fast initial coverage increase, clearly seen in Fig. 3d. As is also observed in experiments, the maximum intensity of the early-time transient surpasses that of the late-time peak for sufficiently small potential steps.

Studies in which we combine kinetic simulations like the one reported here with the lattice-gas models of specific systems discussed in the first part of this paper are in progress.

## CONCLUSIONS

In this paper we have discussed a strategy for lattice-gas modeling of phase transitions in electrochemical submonolayer adsorption, illustrated by applications to two specific experimental systems. We also presented results from work in progress, which indicate that numerical simulation of *dynamic* lattice-gas models can contribute to the study of kinetic processes in such systems far from equilibrium.

## ACKNOWLEDGMENTS

Supported at Florida State University by the Center for Materials Research and Technology and the Supercomputer Computations Research Institute (DOE Contract No. DE-FC05-85-ER25000) and by NSF grant No. DMR-9315969, at Kyoto University by NSF Grant No. INT-9512679, and at The University of Illinois by NSF grant No. CHE-9411184 and the Frederick Seitz Materials Research Laboratory (DOE Contract No. DE-AC02-76-ER01198).



## REFERENCES

1. M. Gamboa-Aldeco, P. Mrozek, C.K. Rhee, A. Wieckowski, P.A. Rikvold, and Q. Wang, *Surf. Sci. Lett.* **297**, L135 (1993).
2. P.A. Rikvold, M. Gamboa-Aldeco, J. Zhang, M. Han, Q. Wang, H.L. Richards, and A. Wieckowski, *Surf. Sci.* **335**, 389 (1995).
3. P.A. Rikvold, J. Zhang, Y.-E. Sung, and A. Wieckowski, *Electrochim. Acta* **41**, 2175 (1996).
4. J. Zhang, Y.-E. Sung, P.A. Rikvold, and A. Wieckowski, *J. Chem. Phys.* **104**, 5699 (1996).
5. P.A. Rikvold, J.B. Collins, G.D. Hansen, and J.D. Gunton, *Surf. Sci.* **203**, 500 (1988).
6. D.A. Huckaby and L. Blum, *J. Electroanal. Chem.* **315**, 255 (1991).
7. L. Blum, D.A. Huckaby, and M. Legault, *Electrochim. Acta* **41**, 2207 (1996).
8. M. Rubel, C.K. Rhee, A. Wieckowski, and P.A. Rikvold, *J. Electroanal. Chem.* **315**, 301 (1991).
9. J.W. Schultze and D. Dickertmann, *Surf. Sci.* **54**, 489 (1976).
10. M. Zei, G. Qiao, G. Lempfuhr, and D.M. Kolb, *Ber. Bunsen Ges. Phys. Chem.* **91**, 3494 (1987).
11. P. Zelenay and A. Wieckowski, in *In Situ Studies of Electrochemical Interfaces: A Prospectus*, edited by H.D. Abruña (VCH Publishers, New York, 1991).
12. A. Peremans and A. Tadjeddine, *Phys. Rev. Lett.* **73**, 3010 (1994).
13. V. Climent, A. Rodes, J.M. Orts, J.M. Feliu, J.M. Pérez, and A. Aldaz, *Langmuir*, in press.
14. M.F. Toney, J.N. Howard, J. Richer, G.L. Borges, J.G. Gordon II, O.R. Melroy, D. Yee, and L.B. Sorenson, *Phys. Rev. Lett.* **75**, 4472 (1995).
15. Z. Shi and J. Lipkowski, *J. Electroanal. Chem.* **365**, 303 (1994).
16. Z. Shi, S. Wu, and J. Lipkowski, *Electrochim. Acta* **40**, 9 (1995).
17. M. Avrami, *J. Chem. Phys.* **7**, 1103 (1939); **8**, 212 (1940); **9**, 177 (1941).
18. E. Bosco and S.K. Rangarajan, *J. Chem. Soc. Faraday Trans. 1* **77**, 1673 (1981).
19. R.A. Ramos, P.A. Rikvold, and M.A. Novotny, in *Physical Phenomena at High Magnetic Fields II*, edited by Z. Fisk, L. Gor'kov, D. Meltzer, and R. Schrieffer (World Scientific, Singapore, 1996), p. 380.
20. R.A. Ramos, S.W. Sides, P.A. Rikvold, and M.A. Novotny, in preparation.
21. M.H. Hölzle, U. Retter, and D.M. Kolb, *J. Electroanal. Chem.* **371**, 101 (1994).
22. See numerous references in A.-L. Barabási and H.E. Stanley, *Fractal Concepts in Surface Growth* (Cambridge University Press, Cambridge, 1995).

## STM STUDY OF THE INFLUENCE OF ADSORPTION ON STEP DYNAMICS

T.P. MOFFAT

Materials Science and Engineering Laboratory  
National Institute of Standards and Technology  
Gaithersburg, Md 20899

### ABSTRACT

In situ STM has been used to examine the influence of anion adsorption and metal underpotential deposition on the structure and dynamics of steps on copper surfaces. Chloride is shown to form potential dependent adlayer structures on Cu(100) and Cu(111) which strongly affects the orientation of the surface steps. The adlayer acts as a template guiding step evolution during metal deposition and dissolution. Metal underpotential deposition (upd) exhibits similar effects on step structure. This is demonstrated for Pb upd on Cu(111). In this instance the Pb monolayer displaces chloride from the surface and leads to a reorientation of the steps and an alteration of the step dynamics.

### INTRODUCTION

Homoepitaxial film growth occurs by step propagation with the step density being determined by a combination of crystal miscut, two-dimensional cluster nucleation and the density of screw dislocations intersecting the free surface. Roughness development arises as a natural consequence of the relative rates of interlayer and intralayer surface processes as well as any surface site dependence of the reduction reaction. An understanding of the influence of adsorbates on the dynamics of step propagation is a subject of central importance to electrodeposition of metals. Recent developments in STM, along with other spectroscopic and scattering methods, provide a direct avenue for exploring these issues. For example, in situ STM studies characterizing the effect of substrate defects and organic additives on the heteroepitaxial deposition of copper on Au and Ag [1] have been reported.

In this report an in situ STM study of the impact of anion adsorption on the evolution of step morphology of copper surfaces will be described. The potential dependence of the adlayer structure and its sensitivity to different crystal faces will be highlighted by a brief comparison between chloride adsorption on Cu(100) and Cu(111). Similarly, the impact of metal upd, Pb on Cu(111), on step structure will be described.

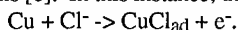
### EXPERIMENTAL DETAILS

Single crystal squares, 3 - 4 mm thick, were cut from 2.5 cm diameter cylindrical single crystal copper ingot which had been previously aligned by Laue X-ray diffraction. The crystals were mechanically polished to a 0.1  $\mu\text{m}$  diamond finish followed by electropolishing in 85 vol% phosphoric acid. After extensive rinsing with water the substrate was dried and transferred to either a conventional electrochemical cell for voltammetric studies or the STM electrochemical cell. The cell was filled with deaerated 0.01 mol/L HCl,  $\text{HClO}_4$ ,  $\text{H}_2\text{SO}_4$ ,  $\text{Pb}(\text{C}_2\text{H}_3\text{O}_2)_2$  or some mixture of these solutions which did not exceed a concentration of 0.011 mol/L. The conventional electrochemical cell was first deaerated and then blanketed with Ar gas during operation while the STM cell was exposed to the atmosphere. There was short time delay between filling the STM cell with electrolyte and turning on the potentiostat which results in slight etching of the substrate due to residual oxygen in the electrolyte. The STM experiments were performed using a Digital Instruments Nanoscope III. The STM cell incorporated a platinum counter electrode, an insulated tungsten tunneling probe and either a Ag/AgCl reference electrode or a Cu/Cu+ quasi-reference electrode. A saturated mercurous sulfate electrode was used for the voltammetric experiments in 0.01 mol/L  $\text{HClO}_4$  while a saturated calomel electrode was utilized for experiments performed in chloride media. All potentials in this paper are referenced to the saturated calomel electrode.

## RESULTS AND DISCUSSION

### *Voltammetry of Cu(111) and Cu(100) in Acid Chloride Media*

An overview of the electrochemical behavior of Cu(111) and Cu(100) in 0.01 mol/L HClO<sub>4</sub> with and without 0.001 mol/L HCl is shown in Fig 1 and 2. The redox reaction associated with halide adsorption and desorption is apparent at potentials between proton reduction and copper dissolution. Formation of a halide overlayer is congruent with several ex-situ surface analytical experiments which demonstrate specific adsorption of chloride at the potentials below  $E^0_{\text{Cu/Cu}^+}$  [2, 3]. This result is also consistent with the negative pzc reported for copper in KClO<sub>4</sub> solutions [4], work function data [5] as well as the well known tendency for underpotential reactions in Group IB-halide systems [6]. In this instance, the reaction may be viewed as



The adsorption process on Cu(111) is kinetically hindered as revealed by the separation between the adsorption and desorption waves which is also a strong function of sweep rate. The magnitude of the waves also appear to be asymmetric. This is presumably due to the superposition of the onset of proton reduction with the halide desorption process as well as the background current due to reduction of residual oxygen in the deaerated electrolyte. Integration and averaging the charge associated with the oxidative and reductive waves for a range of sweep rates yields a value of  $\sim 0.150 \text{ mC/cm}^2$  for Cu(111). Perhaps a more accurate assessment is obtained from the stripping wave measured at 0.1 V/s, where the background signal is minimized, yielding a value of  $0.135 \text{ mC/cm}^2$ . Assuming an electrosorption valency of unity this corresponds to the adsorption and desorption of a compressed  $(\sqrt{3} \times \sqrt{3})\text{R}30^\circ$  type chlorine adlattice ( $0.094 - 0.133 \text{ mC/cm}^2$ ). These results are in good agreement with a recently published LEED, AES and voltammetric study for Cu(111) in 0.001 mol/L HCl [3]. However, in addition to the main desorption peak there is a much smaller reduction wave center at  $-0.4 \text{ V}$  corresponding to a charge of  $\sim 0.020 \text{ mC/cm}^2$  which is roughly a tenth of a monolayer coverage of chloride. It is noteworthy that redox waves of this magnitude have recently been associated with significant structural transitions in anion-gold adlayers [6].

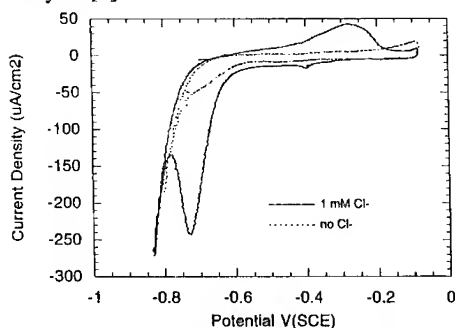


Fig 1. Cu(111), sweep rate = 0.1 V/s

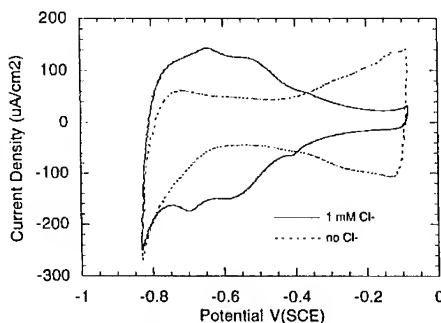


Fig. 2. Cu(100), sweep rate = 1 V/s

In contrast to Cu(111) the kinetics of the chloride adsorption process on Cu(100) are significantly more reversible as indicated by the symmetry of the redox waves with respect to the potential axis in Fig 2. Three peaks are visible with the separation between the corresponding anodic and cathodic peak potentials diminishing with sweep rate. As in the case of Cu(111) a residual d.c. offset of the voltammograms is apparent at slower sweep rates which may be attributed to proton reduction or reduction of residual oxygen. The broad nature of the peaks suggests a strong repulsive interaction exists between chloride ions. Prior LEED [2] and STM [7, 8] studies indicate the formation of a  $(\sqrt{2} \times \sqrt{2})\text{R}45^\circ \text{Cl}$  at potentials above  $-0.3 \text{ V}$ . Integration and averaging the redox waves yields a charge of  $\sim 0.070 \text{ mC/cm}^2$ . However, complete reduction of the  $(\sqrt{2} \times \sqrt{2})\text{R}45^\circ \text{Cl}$  structure, should correspond to  $0.123 \text{ mC/cm}^2$  for an electrosorption valency of unity. This difference indicates that only partial reduction of the halide adlattice occurs

prior to the onset of hydrogen evolution, while the multiple peaks are presumably associated with structural alterations occurring within the diminished adlayer. This assessment of the voltammetry compares reasonably well with an Auger study [2] of chloride coverage of emmersed electrodes.

#### *STM Results - Cu(100)*

A constant tunneling current image of a freshly prepared miscut Cu(100) electrode that had been held at -0.25 V for ~1 hr in 0.01 mol/L HCl reveals complete coverage of the terraces by a  $(\sqrt{2} \times \sqrt{2})R45^\circ$  structure [8]. This corresponds to a 0.5 monolayer coverage of oxidatively adsorbed chlorine in agreement with the results of prior AES-LEED [2] and STM studies for electrochemically etched Cu(100) [7] as well as UHV studies of chlorine and HCl dosed Cu(100) [2]. The spacing of the chlorine atoms in the adlayer corresponds to the van der Waals radius of chlorine [2, 6]. The most interesting consequence of the chlorine adlayer structure is the stabilization of the surface steps in the  $\langle 100 \rangle$  direction [7, 8]. The  $\langle 100 \rangle$  step orientation is in sharp contrast to the close packed  $\langle 110 \rangle$  orientation associated with an adsorbate-free copper surfaces in UHV systems [9]. The  $\langle 100 \rangle$  oriented step edge corresponds to the close packed direction of the commensurate chlorine adlattice yielding kink saturated  $\langle 100 \rangle$  metal steps beneath the overlayer. Thus, the chloride adlattice exerts a dominant influence on the step edge binding energy and the activation energy for diffusion of adatoms along the step edge and thereby controls the evolution of step morphology on Cu(100). Interestingly, the importance of enhanced step edge mobility relative to terrace mobility in defining step and island geometry has been recently noted for Cu atoms on clean Cu(100) in UHV [10]. Furthermore, it has been demonstrated that the chloride adlayer floats on the surface guiding step evolution in the  $\langle 100 \rangle$  direction during copper dissolution and deposition [7, 8].

In sharp contrast to the experiments performed in halide media, immersion of miscut Cu(100) in 0.01 mol/L HClO<sub>4</sub>, as well as limited investigation in 0.01 mol/L H<sub>2</sub>SO<sub>4</sub>, resulted in an ill-defined surface step structure and obtaining reliable atomically resolved images proved difficult. The recent observations [11] of the influence of chloride on the kinetic anisotropy of copper deposition compared to the isotropic nature of deposition from sulfate solution may be, at least partially, related to the anisotropy of steps induced by oxidative halide adsorption.

#### *Reductive Desorption of Chlorine Adlattice*

Voltammetry in combination with prior LEED and AES studies indicate that the oxidatively adsorbed chloride adlayer may be reductively desorbed. Consequently, the evolution of this reaction on Cu(100) was examined in 0.01 mol/L HCl. A series of topographic, constant current, images were collected, as shown in Fig 3, while the potential was repeatedly stepped between -0.250 V and -0.650 V over a period of time. These images exhibit several remarkable features. At -0.250 V the presence of the  $(\sqrt{2} \times \sqrt{2})R45^\circ$  chloride adlattice results in the steps adopting the  $\langle 100 \rangle$  orientation as noted earlier. Upon stepping the potential to -0.650 V, the  $\langle 100 \rangle$  oriented steps immediately become frizzy and tend to migrate rapidly away from the  $\langle 100 \rangle$  direction. The frizziness of the steps may be ascribed to the rapid movement of kinks on a time scale faster than the image acquisition rate. The connection between step frizziness and kink mobility has been previously noted in UHV studies of Cu(100) where the frizzy steps were ascribed to thermally-driven kink movement on the pristine surface [9]. In the current experiment the frizziness, or kink movement, derives from the partial desorption of the chloride adlattice which stabilizes the  $\langle 100 \rangle$  oriented kink saturated metal steps. The amplitude of the frizziness appears to scale with the kink concentration such that the amplitude is greatest for steps oriented in the  $\langle 100 \rangle$  direction and minimized for  $\langle 110 \rangle$  oriented steps. The close packed  $\langle 110 \rangle$  direction also corresponds to the low energy state for steps on pristine Cu(100) in UHV. Numerous attempts were made to obtain atomically resolved images of the terraces without success. The images were also found to be much noisier than images collected at -0.250 V. The streaking of the images being the most obvious signature of this perturbation. In vacuum studies similar streaking, often seen at elevated temperatures, has been associated with interactions between the scanning probe tip and the 2D adatom gas. These observation suggest that a highly mobile disordered chlorine adlayer exists at these potentials. This experiment was performed using both a constant imaging bias as well as a fixed tip potential with no apparent effect on the images obtained. At -0.250 V the surface is decorated with a variety of relatively small islands which dissolve back to the adatom state when the potential is lowered to -0.650 V. This effect in combination with the development of the curved

steps leads to an elevated adatom activity on the terraces. When the potential is stepped back to -0.250 V the ordered chloride adlattice reforms rapidly and the steps immediately adopt the  $\langle 100 \rangle$  orientation. Simultaneously, the elevated adatom concentration associated with the previously curved steps is quenched by nucleating a variety of small islands on the terraces. The surface structure then coarsens rapidly with time to reduce the total number of kinks.

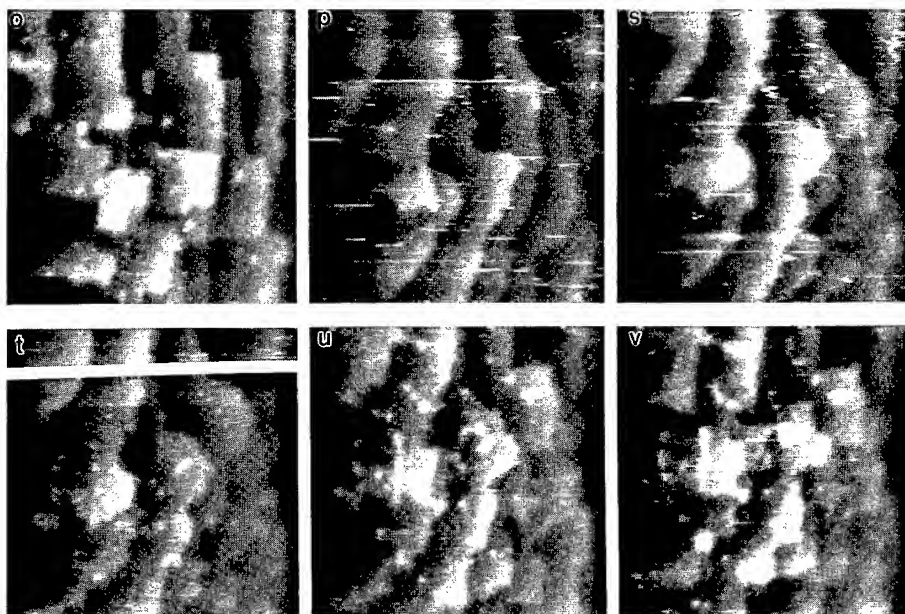


Fig. 3. A series of  $50 \times 50$  nm images revealing the effects of partial desorption of the  $(\sqrt{2} \times \sqrt{2})R45^\circ$  chlorine adlattice at negative potentials. The black horizontal line in image *p* corresponds to stepping the potential between -0.25 V and -0.65 V while the line in image *t* demarks stepping the potential back to -0.25 V (frame time of  $\sim 22$  s). The rapid movement and development of step curvature in images *p* and *s* corresponds to the reductive disruption and desorption of the chloride adlattice while the reordering of the steps in  $\langle 100 \rangle$  occurs rapidly with adsorption shown in *t-v*.

#### *Cu(111)*

Voltammetry indicates that chloride adsorption on Cu(111) is significantly different from adsorption on Cu(100). STM imaging at -0.25 V revealed the coexistence of two chloride adlayers as shown in Fig 4. Within the accuracy of our measurements the phase in the top half of the image corresponds to a higher order  $(6\sqrt{3} \times 6\sqrt{3})R30^\circ$  commensurate structure, although identification as an incommensurate structure with a nearest neighbor spacing on the order of  $0.39 \pm 0.2$  nm is also possible. In a manner analogous to the Cu(100) surface, chloride is found to stabilize the metal steps in the close packed direction of the adlattice. This corresponds to the metal steps being coincident with  $\langle 211 \rangle$  and thereby kink saturated as reported previously [12]. However, in contrast to Cu(100) the steps on Cu(111) were found to be remarkably frizzy as shown in Fig 5. The second adlayer phase shown in Fig 4, exhibits only two-fold symmetry. The  $(6\sqrt{3} \times 6\sqrt{3})R30^\circ$  structure has been previously reported for this system [12] while coexistence with the second lower symmetry phase has been noted for chlorine-dosed Cu(111) in vacuum [13].

It is interesting to speculate on the relative significance of commensurate versus incommensurate adlayers on the binding and activation energy of copper adatoms at steps. Similarly, the relative magnitude of the step edge barrier should strongly affect interlayer transport on the different surfaces. In the vacuum deposition literature, surfactants are being studied with the

hope of changing step edge barriers to favorably alter film growth. From this perspective a study of the influence of upd Pb on the step morphology of the copper surfaces has been initiated.

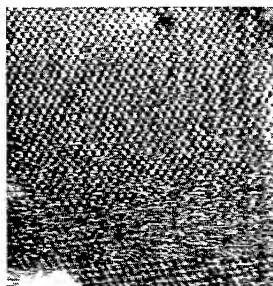


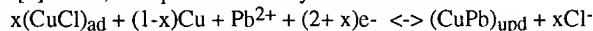
Fig. 4. Coexistence of two incommensurate halide adlayers on Cu(111). (15 x 15 nm)



Fig. 5. Frizzy <211> steps on Cu(111) (8.5 x 8.5 nm)

#### Pb upd on Cu(111)

A well-defined Pb upd wave is apparent on Cu(111) as shown in Fig. 6. RRDE studies combined with LEED and AES indicate that the upd Pb monolayer displaces chloride from the copper surface [3]. Thus, the upd reaction may be described as



where the stoichiometric number accounts for the fact that the deposition of one Pb atom does not necessarily accompany desorption of exactly one chlorine anion. LEED experiments indicate that

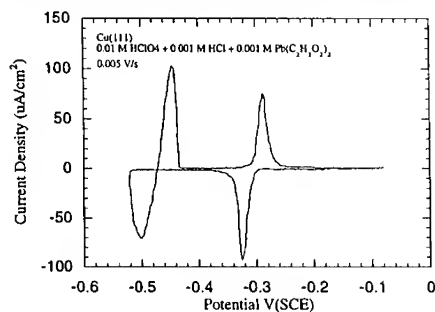


Fig. 6. Pb upd on Cu(111)

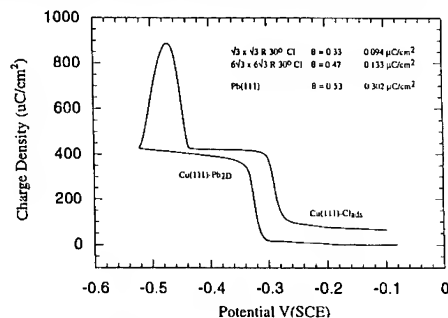


Fig 7. Coulometric analysis of Fig. 5.

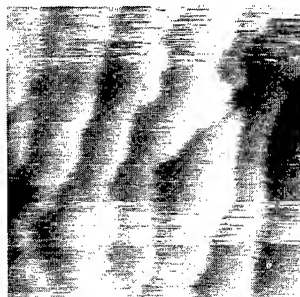
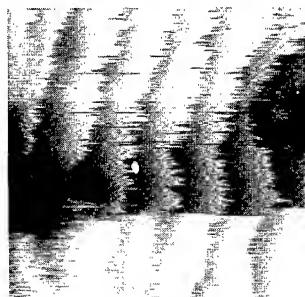


Fig 8. The influence of displacement of adsorbed Cl- (image A) by upd Pb (image B) on the step morphology of Cu(111) (27.5 nm x 27.5nm). Abscissa corresponds to <211> on Cu(111).

a close packed Pb monolayer is formed on Cu(111). The dimensions of the layer are identical with the (111) fcc plane of bulk lead while the close packed direction of the adlayer is coincident with the  $\langle 110 \rangle$  of Cu(111). Integration of the voltammetric upd wave yields a value in reasonable agreement with the theoretical value of 0.396-0.435 mC/cm<sup>2</sup> as shown in Fig 7. STM examination of the surface reveals the impact of the upd layer on step morphology, as shown in Fig 8. Displacement of the halide adlayer by upd Pb results in a rapid lowering of the kink density by step migration towards the coincident close packed  $\langle 110 \rangle$  orientation versus the  $\langle 211 \rangle$  step orientation which is stabilized by the close packed direction of the halide adlattice.

## CONCLUSIONS

Adsorbed anions and upd metals exerts a remarkable impact on the structure and dynamics of surface steps on copper surfaces. In the case of ordered chloride adsorption on Cu(100) and Cu(111) the metal steps adopt the close packed direction of the halide adlayer which corresponds to the metal step being kink saturated. The adlayer acts as a floating template guiding the morphological evolution of the surface during both copper deposition and dissolution. At negative potentials the adlayer may be reductively desorbed leading to rapid rearrangement of the destabilized kink saturated steps. This process is relevant to the dynamics of heteroepitaxial deposition of iron group metals on copper. The significance of halide adsorption on the electrochemical processing of copper is further highlighted by its ubiquitous presence as an additive in most commercial copper electroplating baths. Similarly, metal upd layers, which also impact step structure, are known to play an important role in the electrodeposition of metals and alloys.

## ACKNOWLEDGEMENTS

The author gratefully acknowledges the support of Gery Stafford and the NIST Nanostructural Initiative Program.

## REFERENCES

1. M. Dieterle, T. Will and D.M. Kolb, *Nanoscale Probes of the Solid/Liquid Interface*, eds. A.A. Gerwirth and H. Siegenthaler, Kluwer Academic Publishers, Boston (1995).
2. C.B. Ehlers, I Villegas and J.L. Stickney, *J. Electroanal. Chem.*, 284, 403 (1990) and ref. therein.
3. G.M. Brisard, E. Zenati, H.A. Gasteiger, N.M. Markovic and P.N. Ross, *Langmuir*, 11, 2221 (1995).
4. J. Lecoeur and J.P. Bellier, *Electrochimica Acta*, 30, 1027 (1985).
5. K. Giessen, F. Hage, J. Himpsel, J.H. Riess and W. Steinmann, *Phys. Rev. Lett.*, 55, 300 (1985) and ref. therein.
6. O.M. Magnussen, B.M. Ocko, R.R. Adzic and J.X. Wang, *Phys. Rev. B*, 51, 5510 (1995); O.M. Magnussen, B.M. Ocko, J.X. Wang and R.R. Adzic, *J. Phys. Chem.*, 100, 5500 (1996) and ref. therein.
7. D.W. Suggs and A.J. Bard, *J. Phys. Chem.*, 99, 8351 (1995).
8. T.P. Moffat, in *Nanostructured Materials in Electrochemistry*, eds. P. Searson and J. Meyer, PV 95-8, p. 225-237, The Electrochemical Society, Inc., Pennington, NJ (1995); T.P. Moffat, *Mat. Res. Soc. Symp. Proc. Vol. 404*, pg 3., MRS, Pittsburgh, PA (1996).
9. M. Poensgen, J.F. Wolf, J. Frohn, M. Giesen and H. Ibach, *Surf. Sci.*, 274, 430 (1992).
10. M. Breeman, G.T. Barkema, M.H. Langelaar and D.O. Boerma, *Thin Solid Films*, 272, 195 (1996).
11. D. Barkey, F. Oberholtzer, and Q. Wu, *Phys. Rev. Lett.*, 75, 16, 2980 (1995).
12. D.W. Suggs and A.J. Bard, *J. Amer. Chem. Soc.*, 116, 10725 (1994).
13. K. Motai, T. Hashizume, H. Lu, D. Jeon, T. Sakurai and H. Pickering, *Appl. Surface Science*, 67, 246 (1993).

## CHARACTERIZATION OF ETCHING PROCESSES ON CU SURFACES

C.Y. NAKAKURA\*, V.M. PHANSE\*\*, G. ZHENG\*\*, E.I. ALTMAN\*\*

\*Department of Applied Physics, \*\*Department of Chemical Engineering, Yale University, New Haven, CT 06520, eric.altman@yale.edu

### ABSTRACT

The etching of single crystal and polycrystalline Cu surfaces by halogens was studied using temperature programmed desorption (TPD), low energy electron diffraction (LEED), and scanning tunneling microscopy (STM). For Br<sub>2</sub> and Cl<sub>2</sub> on Cu(100) and polycrystalline Cu, the etching mechanism could be characterized as a two step process: 1) formation of a bulk Cu(I) halide, and 2) removal of the halide by sublimation. In all cases the first step was found to be adsorption rate limited. Halide formation was observed to consume Cu atoms from the step edge and thus etching can be considered the reverse of step flow growth. While STM showed that Cl<sub>2</sub> reacts isotropically with steps on Cu(100), the rate of CuBr formation was observed to be sensitive to the local adsorbate structure at the step edge. For Cl<sub>2</sub>, it was found that halide removal could be characterized as a simple bulk sublimation process independent of the structure of the underlying Cu. In contrast, a CuBr desorption peak at temperatures lower than anticipated from bulk vapor pressure data was observed. The presence of narrowly spaced steps on the Cu surface was observed to stabilize this low-temperature desorption peak.

### INTRODUCTION

Etching reactions of metals are used to define patterns for gates and interconnects in integrated circuits. Current fabrication techniques for interconnects involve blanketing the substrate with a metal film, then using photolithography to create a patterned polymer etch mask, and finally etching away the unmasked metal. Dry etching is required to obtain submicron features. The choice of the metal is limited to those that can be etched below approximately 420 K; higher temperatures degrade the etch mask. Aluminum can be etched by Cl near room temperature and is currently used as the interconnect material in virtually all integrated circuits. The speed of integrated circuits, however, will soon be limited by R-C (resistance-capacitance) time lags in Al interconnects; thus, lower resistance Cu interconnects are desired. The transition to Cu interconnects has been delayed by a lack of low-temperature dry etching processes for Cu [1]. Therefore, we have begun a project aimed at developing a detailed mechanistic model of the etching process based on microscopic observation of the atomic-scale processes that occur during etching. The goal of the project is to use the model to guide development of low-temperature dry etching processes for Cu. In this paper we focus on Cl<sub>2</sub> and Br<sub>2</sub> etching Cu surfaces.

There have been several previous studies of the interaction of halogens with Cu surfaces [2-4]. These studies have shown that both Cl<sub>2</sub> and Br<sub>2</sub> dissociatively adsorb on Cu with a high sticking coefficient. After saturation of the chemisorbed layer, continued halogen exposure results in the slow formation of the Cu (I) halide. The Cu (I) halide desorbs in the temperature range expected for sublimation of the bulk halide. Thus, halogen etching of Cu can be considered a two-step process: 1) formation of a Cu halide, and 2) removal of the halide by sublimation. Although plasma etching is commonly employed in industry, for metals it has been shown that the plasma inhibits etching [2]. Therefore, the relevant chemistry can be described by considering the interaction of neutral species with the Cu surface.



Our approach to studying the detailed etching mechanism is to characterize the macroscopic kinetics and structural changes involved in each of the reaction steps and then explain the macroscopic phenomena based on atomic and nanometer scale observations [5-7]. The kinetics are measured using TPD, and, for single crystals, macroscopic structural changes are monitored using LEED. *In situ* STM is used to characterize the structural changes on the atomic-scale. In this paper, halide formation and removal kinetics for  $\text{Cl}_2$  and  $\text{Br}_2$  on  $\text{Cu}(100)$  and polycrystalline Cu surfaces are compared, and STM data is presented that reveals the origin of differences in the  $\text{CuCl}$  and  $\text{CuBr}$  formation kinetics on  $\text{Cu}(100)$ .

## EXPERIMENTAL

Experiments were performed using an ultra-high vacuum (UHV) system equipped with an energy analyzer for Auger electron spectroscopy and ion scattering spectroscopy, LEED optics, a quadrupole mass spectrometer for TPD, an ion gun, halogen sources, and a high-speed variable-temperature scanning tunneling microscope. The microscope was designed and built at Yale and will be described in detail elsewhere [8]. Halogens were generated *in situ* using solid state electrochemical cells. The halogen dose is proportional to the electrochemical current times the exposure time, and thus doses are reported in units of  $\mu\text{A}\cdot\text{s}$ ; roughly  $80 \mu\text{A}\cdot\text{s}$  is equivalent to 1 Langmuir [5].

## RESULTS AND DISCUSSION

Temperature programmed desorption was used to measure the halide removal kinetics for  $\text{CuCl}$  and  $\text{CuBr}$  from both  $\text{Cu}(100)$  and polycrystalline Cu [5-7]. Figure 1 shows the TPD curves as a function of halogen exposure for these four cases. The Cu halides sublime as  $\text{Cu}_3\text{X}_3$ , the TPD curves in Figure 1 represent the sum of four mass traces in the  $\text{Cu}_3\text{X}_3$  cracking pattern; the ratio of the signals matches that obtained when the bulk Cu halide was sublimed towards the mass spectrometer. If halide removal is a simple sublimation process, then zero order desorption peaks are expected. For coverages in excess of a monolayer, zero order desorption results in increasing peak temperatures with increasing coverage and leading edges of the desorption curves that are proportional to the vapor pressure and, thus, independent of initial coverage. As shown in Figures 1.a and 1.b,  $\text{Cu}_3\text{Cl}_3$  desorption from both  $\text{Cu}(100)$  and polycrystalline Cu results in a single desorption peak consistent with a sublimation process. Further, for high  $\text{CuCl}$  coverages, when the leading edges of the desorption curves were plotted on an Arrhenius plot, the slope yielded the heat of sublimation of  $\text{CuCl}$  within experimental error [6].

The TPD results for  $\text{CuBr}$  are very different [5,7]. Rather than a single desorption peak, Figure 1.c shows that for  $\text{Cu}(100)$ , as many as three desorption peaks are observed depending on the coverage. Previously, we showed that the two higher temperature peaks can be accounted for by sublimation of a mixture of  $\alpha$  and  $\beta$ - $\text{CuBr}$  from the surface. The low temperature peak (at about 450 K) that is seen at low  $\text{CuBr}$  coverages on  $\text{Cu}(100)$ , however, occurs at a temperature lower than predicted based on the heat of sublimation and vapor pressure of all known bulk phases of  $\text{CuBr}$ . This result suggests that for  $\text{Br}_2$ , Cu etching temperatures may be reduced below those anticipated from bulk vapor pressure data.

Also different from  $\text{Cl}_2$ , comparison of the  $\text{Br}_2$  TPD results for  $\text{Cu}(100)$  (Figure 1.c) with those obtained for a polycrystalline Cu surface (Figure 1.d) shows that  $\text{Cu}_3\text{Br}_3$  desorption depends on the structure of the Cu surface. For  $\text{Cu}(100)$ , the low-temperature desorption peak shifts to higher temperatures and eventually disappears when the  $\text{Br}_2$  exposure is increased, while for the polycrystalline surface, the low-temperature desorption peak saturates but does not shift

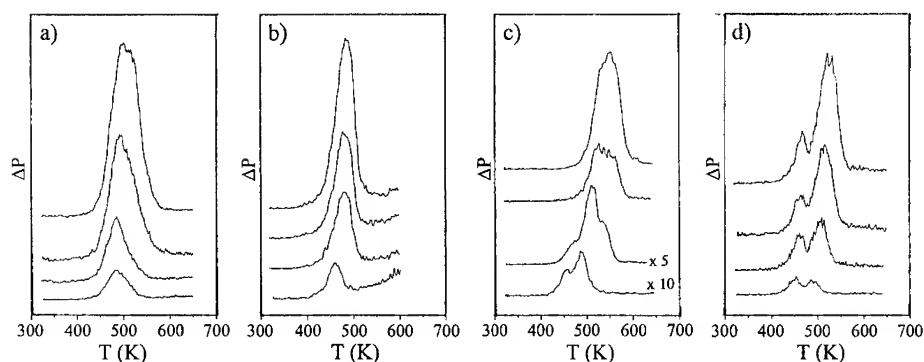


**Figure 1.** Temperature programmed desorption curves for varying exposures of  $\text{Cl}_2$  to (a) Cu(100) and (b) polycrystalline Cu, and  $\text{Br}_2$  to (a) Cu(100) and (b) polycrystalline Cu. Each desorption curve represents the sum of four mass traces in the  $\text{Cu}_3\text{X}_3$  cracking pattern [5,6]. The exposures vary between (a) 25,000 - 230,000  $\mu\text{A}\cdot\text{s}$ , (b) 3,800 - 15,800  $\mu\text{A}\cdot\text{s}$ , (c) 1,500 - 30,000  $\mu\text{A}\cdot\text{s}$ , and (d) 2,900 - 23,200  $\mu\text{A}\cdot\text{s}$ .

with increasing  $\text{Br}_2$  exposure. We have also found for the polycrystalline surface that the intensity of the low temperature desorption peak depends on the surface treatment prior to  $\text{Br}_2$  exposure [7]. The results in Figure 1.d are for a surface briefly annealed over 1000 K; both steady-state  $\text{Br}_2$  etching at 445 K and 500 eV  $\text{Ar}^+$  sputtering at 325 K reduce the low temperature Br desorption peak to a small shoulder. Scanning tunneling microscopy images of the surface after each of these treatments revealed that the annealed surface contains areas with bands of narrowly spaced steps (on average 3.5 nm apart), while neither the sputtered surface nor the etched surface display such features. The sputtered surface is characterized by circular mounds with no resolvable step-terrace structure. On the etched surface, large terraces (>100 nm wide) separated by multi-atom high steps were observed. These results suggest that the narrow terraces stabilize the low-temperature  $\text{Cu}_3\text{Br}_3$  desorption peak and that etching increases terrace widths by consuming Cu atoms at step edges. The step edges recede until they form a low index facet, leaving the observed multi-atom high steps. Because steady state etching removes the features responsible for the low-temperature desorption peak, this peak cannot be exploited to reduce etching temperatures unless the steps are regenerated during the etching process. We are currently exploring using brief, low energy ion bombardment to regenerate the steps. At this point it is unclear why a low-temperature desorption peak is observed for  $\text{Cu}_3\text{Br}_3$  but not  $\text{Cu}_3\text{Cl}_3$ , and why narrowly spaced terraces would stabilize such a desorption peak. More detailed STM studies are planned to investigate these issues.

By integrating the TPD curves the initial coverage can be obtained. Therefore, by measuring the TPD peak integrals as a function of exposure the halide formation rate can be obtained. These measurements have been performed for the reaction of  $\text{Cl}_2$  and  $\text{Br}_2$  with Cu(100) and the reaction of  $\text{Br}_2$  with polycrystalline Cu [5-7]. In all cases, the amount of halide formed increased linearly with exposure. As noted by Winters, this indicates that the reaction is adsorption rate limited [2]. Therefore, diffusional processes, including grain boundary diffusion, play no role in determining the halogenation rate. In fact, for  $\text{Br}_2$  a higher halogenation rate was observed for single crystal Cu(100) than for the polycrystalline sample [7].

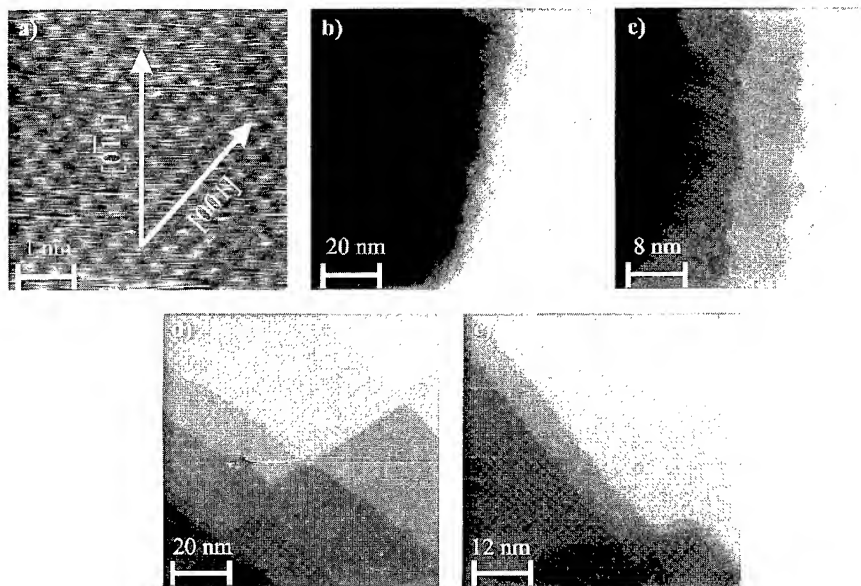


**Figure 2.** Scanning tunneling microscopy images of chemisorbed Cl and Br on Cu(100). (a) Atomically resolved image of the  $c(2 \times 2)$ -Br layer, the arrows show the crystallographic directions of the Cu. (b, c) Images showing formation of  $\{110\}$  step facets after saturating the Br (b) and Cl (c) chemisorbed layer at 325 K. (d, e) Images showing that annealing the  $c(2 \times 2)$  Br (d) and Cl (e) layers to 575 K removes most of the kinks seen in (b) and (c).

Two temperature dependent effects on the halogenation rate were observed [5-7]. For all the cases studied, between 300-385 K a decrease in the rate was observed with increasing reaction temperature. This decrease was *reversible*. In addition, an *irreversible increase*, by about a factor two, in the CuBr formation rate on Cu(100) was observed when a layer of chemisorbed Br atoms was annealed to 575 K prior to reaction to form CuBr. This annealing effect was only observed for Br on Cu(100).

Previous studies of the oxidation of Ni(100) indicate that such annealing effects can be due to irreversible structural changes in the surface due to the presence of the adsorbate [9]. To determine the nature of these structural changes and how and why they influence the bromination rate but not the chlorination rate, STM was used to study the structure of the Cu(100) surface as a function of halogen exposure and annealing temperature. Both LEED and STM indicate that Br<sub>2</sub> and Cl<sub>2</sub>, as well as O<sub>2</sub>, on Ni(100) [9], form a  $c(2 \times 2)$  chemisorbed layer on Cu(100). An STM picture of the  $c(2 \times 2)$  Br layer is provided in Figure 2.a. When the chemisorbed layer approaches saturation, a dramatic faceting of the Cu step edges occurs as shown in Figure 2.b for Br and Figure 2.c for Cl. For bare Cu(100),  $\{111\}$  steps oriented along a  $\langle 110 \rangle$  direction are favored; adsorption at room temperature creates many kinks in these steps resulting primarily in  $\{110\}$  steps oriented along  $\langle 100 \rangle$  directions. As shown in Figure 2.d (for Br) and 2.e (for Cl), annealing serves to remove many of the kinks and now there are long straight  $\{110\}$  steps oriented along  $\langle 100 \rangle$  directions. This step reorientation results in close-packed chains of halogen atoms at the step edge. In the previous study of Ni oxidation, this reorientation only occurred after annealing and differences between the reactivity of the different step orientations were shown to account for the differences in reactivity [9]. For Br on

Cu(100), however, the only noticeable change in the surface is the decrease in kink density. Since kinks are lower coordinated sites, one might expect the decrease in kink density to decrease the reactivity, not increase it. Thus it is apparent that step faceting alone is not responsible for the increase in reactivity after annealing.

To gain further insight into the increased reactivity toward Br induced by annealing the chemisorbed layer, STM images were recorded following halide formation. The results are shown in Figure 3.a for Br<sub>2</sub> and Figure 3.b for Cl<sub>2</sub>. Figure 3.a shows that Br<sub>2</sub> etches the {110} steps anisotropically creating step and vacancy peninsulas. The etching appears to stop when the step meets an ascending step and forms a {110} facet. The image in Figure 3.a is for an annealed c(2x2) layer, for a non-annealed surface the only noticeable difference is that less reaction appears to occur. In contrast, Figure 3.b shows that formation of CuCl neither changes the shapes of the steps nor creates etch pits suggesting that Cl<sub>2</sub> isotropically reacts with the step edges. As a result, the CuCl formation rate is not sensitive to annealing. For Cl<sub>2</sub>, the consumption of the step also appears to stop when the receding step meets an ascending step and forms a {110} facet, as evidenced by the appearance of multi-atom high steps following CuCl formation. These results reinforce the picture of etching as the reverse of step flow growth. The question that remains, however, is what is the structural variation across the step edge that creates the anisotropy in the reactivity towards Br<sub>2</sub>? In the c(2x2) Br and Cl structures, the adsorbate lies in every other four-fold hollow on the surface [10]. As a result, adsorbates can pack at {110} step edges in two distinct ways, occupying either the four-fold hollow at the step edge or the four-fold hollow one substrate atom back from the edge as shown in Figure 3.c. If the reaction of Br<sub>2</sub> with the step is sensitive to the packing at the edge, then the effect of annealing on the reaction rate can be understood in terms of annealing changing the local adsorbate packing at the step edges. Unfortunately, the adsorbate symmetry is the same for both adsorbate configurations at the step, therefore STM cannot readily distinguish the two.

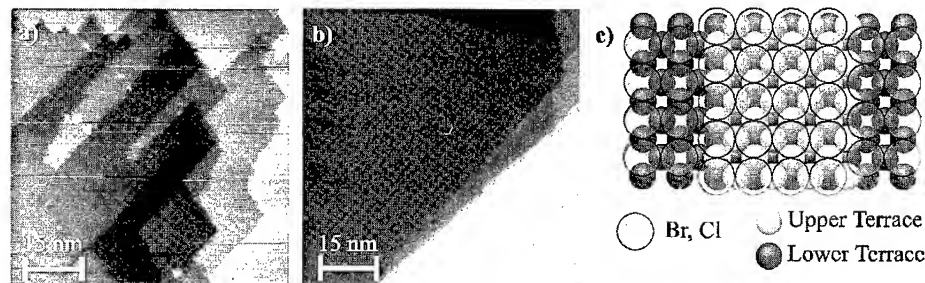


**Figure 3.** (a,b) Scanning tunneling microscope images after exposure of annealed c(2x2) halogen layers (see Figures 2.d and 2.e) to (a) 1.250  $\mu\text{A}\cdot\text{s}$  of Br<sub>2</sub> and (b) 25.000  $\mu\text{A}\cdot\text{s}$  of Cl<sub>2</sub> at 325 K. (c) Model of {110} steps on a (100) surface covered by a c(2x2) halogen layer showing the two possible adsorbate arrangements at the step edge. On the left the adsorbate occupies the adsorption sites at the edge, while on the right the adsorbate sits one atom from the edge.

Finally, Figure 3.a suggests that considerable reaction to form CuBr has occurred. While some clusters are evident in the image, these clusters cannot account for all the CuBr that is expected to form based on the number of Cu atoms withdrawn from the steps. We find, however, that other areas of the surface show a high density of halide clusters. Therefore, the reaction with the steps at room temperature produces a mobile Cu halide species that aggregates with other such species on the surface to form stable halide clusters. To date we

have observed no obvious correlation between the location of these clusters and the location where the reaction initially occurred.

## SUMMARY

The etching of Cu surfaces by halogens proceeds by the formation of Cu(I) halides at step edges and, thus, etching can be pictured as the reverse of step flow growth. For Cu(100), halogen adsorption creates {110} faceted steps. Chlorine reacts isotropically with these steps, and as CuCl is formed, the steps recede uniformly. In contrast, the Br<sub>2</sub> reaction rate depends on the local structure of the step edge, resulting in anisotropic step etching and sensitivity of the macroscopic halide formation rate to surface preparation conditions. The halide species formed at the steps are mobile and aggregate with other such species to form halide clusters. For Cl<sub>2</sub> etching, the desorption of these halide clusters can be described in terms of sublimation of bulk CuCl, independent of the structure of the Cu surface. For Br<sub>2</sub> etching, however, the halide clusters can desorb at temperatures lower than expected based on bulk vapor pressure data. The presence of narrowly spaced steps on the Cu surface stabilizes this low-temperature desorption. This demonstrates how etching temperatures can be reduced by controlling the surface structure.

## ACKNOWLEDGEMENTS

This work was supported by the National Science Foundation (DMR-9414404).

## REFERENCES

1. See MRS Bulletin **18** (1993) No. 6 and MRS Bulletin **19** (1994) No. 8, both issues devoted to Cu metallization.
2. H.F. Winters, J. Vac. Sci. Technol. **B3**, p.9 (1985); H.F. Winters, J. Vac. Sci. Technol. **A3**, p. 786 (1985); H.F. Winters and J.W. Coburn, J. Vac. Sci. Technol. **B3**, p. 1376 (1985).
3. S. Park, T.N. Rhodin and L.C. Rathbun, J. Vac. Sci. Technol. **A4**, p.168 (1986).
4. P.J. Goddard and R.M. Lambert, Surf. Sci. **67**, p. 180 (1977).
5. C.Y. Nakakura and E.I. Altman, Surf. Sci., in press.
6. C.Y. Nakakura, V.M. Phanse and E.I. Altman, Surf. Sci. Lett., in press.
7. C.Y. Nakakura and E.I. Altman, J. Vac. Sci. Technol., submitted for publication.
8. C.Y. Nakakura, V.M. Phanse, G. Zheng, G. Bannon and E.I. Altman, to be published.
9. E. Kopatzki and R.J. Behm, Phys. Rev. Lett. **74**, p. 1399 (1995).
10. P.H. Citrin, D.R. Hamann, L.F. Mattheis and J.E. Rowe, Phys. Rev. Lett. **49**, p. 1712 (1982).

## GROWTH, STRUCTURE AND CHARACTERIZATION OF ELECTRODEPOSITED Co/Cu ULTRATHIN FILMS AND MULTILAYERS

Y. JYOKO, S. KASHIWABARA, Y. HAYASHI

*Department of Materials Science & Engineering, Faculty of Engineering, Kyushu University,  
Fukuoka 812, Japan*

### ABSTRACT

Preparation of giant magnetoresistance Co/Cu multilayers by electrodeposition has been discussed on the basis of a nucleation- growth mechanism and experimental observations. Reflection electron microscopy (REM- RHEED) studies of electrodeposited Co,Cu/Pt(111) ultrathin layers and bilayers have revealed a simultaneous multinuclear multilayer growth (pseudo layer- by- layer growth). REM- RHEED observations have also suggested the formation of an additional (2×2) superstructure on an epitaxially grown Cu/Co/Pt(111) bilayer surface. "Giant" magnetoresistance and oscillatory antiferromagnetic interlayer coupling have been observed in a (111) textured Co/Cu multilayered nanostructure, prepared by electrodeposition under potential control in the presence of a very slight amount of CrO<sub>3</sub>. Such a multilayered structure containing a nominal nonmagnetic Cu spacer layer thickness of 3.2 nm exhibits a large saturation magnetoresistance of more than 18% at room temperature.

### INTRODUCTION

Since the discovery of giant magnetoresistance in antiferromagnetically coupled Fe/Cr, Co/Cu multilayers, and other metallic multilayer and heterogeneous alloy systems<sup>1-4</sup>, interest in magnetic multilayers has been greatly stimulated. Currently the development of new magnetic multilayered nanostructures has attracted considerable attention for potential applicability to magnetoresistive sensor devices. Most magnetic multilayers have been fabricated by sputtering or molecular beam epitaxy (MBE), which have proved to be the most suitable for the controlled preparation of high-quality multilayered structures on an atomic scale. Electrodeposition may also be a promising candidate for this purpose. It must be emphasized that the electrodeposition process does not require a vacuum system and can be carried out at room temperature, and hence will be more suitable than vapor- phase deposition techniques for producing multilayered nanostructures with a large area in an arbitrary shape. Very few papers directly addressing this subject, however, have been published to date, except for recently reported Co- Ni- Cu/Cu, Co- Cu/Cu compositionally modulated multilayered alloys<sup>5,6</sup>, Co/Cu multilayered nanowires<sup>7,8</sup>, and Co- Cu heterogeneous alloy films<sup>9</sup>. Recently we have presented the first evidence for composition modulation across successive layers in a Co/Pt nanometer- multilayered structure prepared by electrodeposition under potential control<sup>10</sup>. In this paper, we demonstrate the presence of oscillatory antiferromagnetic interlayer coupling and "giant" magnetoresistance in electrodeposited Co/Cu (111) textured multilayers, which are compositionally modulated over nanometer length scales with distinct ferromagnetic Co-Cu alloy and nonmagnetic Cu layers, especially effected by the addition of CrO<sub>3</sub>.

## EXPERIMENT

Multilayered Co/Cu thin films were grown on a clean and flat Pt(111) or Cu(111) single-crystal substrate from a single sulfate electrolyte containing 1.0 mol/L  $\text{Co}^{2+}$ ,  $10^{-2}$  mol/L  $\text{Cu}^{2+}$  and  $10^{-4}$  mol/L  $\text{CrO}_3$  or not, by repeatedly controlling the electrode (substrate) potentials for the alternate electrodeposition of both constituents of the multilayer from one to other. The electrode potentials were measured and quoted relative to a saturated Ag/AgCl reference electrode in a standard three-electrode electrolytic cell with separated compartments. Unless otherwise noted, all electrochemical experiments were performed in an atmosphere of purified nitrogen at ambient temperature. The microstructure and superlattice repeat length of the films were evaluated from cross-sectional transmission electron microscopy (TEM), X-ray diffraction, and magnetization measurements using a vibrating sample magnetometer. Resistance measurements were made with a standard low-frequency lock-in technique using a four in-line contact geometry. The magnetoresistance is measured with respect to the resistance in an applied high magnetic field. The saturation magnetoresistance is the highest resistance in the experimental field range normalized with respect to the resistance at the highest field used, as defined by  $\Delta R/R(\%) = (R(H) - R(H_{\max}))/R(H_{\max})$ .

## RESULTS AND DISCUSSION

### Growth of Electrodeposited Co,Cu/Pt(111) Ultrathin Layers and Bilayers

Monatomic steps on a Pt(111) surface have been directly imaged using a conventional transmission electron microscope in the reflection mode as in our previous report<sup>10</sup>. In Fig. 1(a) a typical reflection electron microscopy (REM) image obtained from a (111) surface of a Pt single-crystal sphere is shown together with the corresponding reflection electron diffraction (RHEED) pattern. The Bragg reflections are elongated into streaks perpendicular to the shadow edge indicating an atomically smooth crystal surface. The REM image was recorded with the intensity enhanced (444) specular Bragg reflection near the [110] azimuth. The contour lines seen in the image are monatomic height steps, and between these lines the surface is atomically flat<sup>11</sup>.

REM-RHEED observations of Co-rich and Cu-rich layers, and bilayers electrodeposited on the Pt(111) surface under potential control have shown a simultaneous multinuclear multilayer growth (pseudo layer-by-layer growth) as discussed in the previous paper<sup>10</sup> in a range from submonolayer up to some ten monolayer coverages, which has been dependent upon the deposition overpotential and the presence or absence of  $\text{CrO}_3$  in the electrolyte. The coverage was evaluated from the anodic stripping current-potential curves. Figure 1(b) shows a representative REM-RHEED picture obtained from the Pt(111) surface covered with 10 monolayers of a Co-rich layer electrodeposited under a relatively high overpotential, electrode potential of -1.1 V at a fast rate of approximately 10 monolayers per second in the absence of  $\text{CrO}_3$ . Besides the fundamental diffraction streaks, additional spots are observed together with a Debye-Scherrer ring pattern, which would be assigned to the formation of small, randomly oriented Co crystallites on the Pt(111) surface, leading to a three-dimensional island growth. On the other hand, for the surface with the same coverage of a Co-rich layer (10 monolayers) grown under similar electrodeposition conditions from the electrolyte containing  $10^{-4}$  mol/L  $\text{CrO}_3$ , as shown in Fig. 1(c), a good epitaxy of the Co-rich layer on the Pt(111) surface and a pseudo layer-by-layer growth are observed. In this case, it is probable that the Co deposition proceeds with the preceding formation of a hydrated complex oxide or a complex hydroxide, such as  $[\text{CoO} \cdot x\text{Cr}_2\text{O}_3 \cdot y\text{H}_2\text{O}]_{\text{ad}}$  or  $[\text{CoOH} \cdot n\text{Cr}(\text{OH})_3]_{\text{ad}}$ , as an adsorbed intermediate. The role of this adsorbed intermediate as an inhibitor not only for the nucleus growth

process but also for the dissolution of Co during Cu deposition onto the Co/Pt(111) layer is of great importance for the occurrence of a (111) textured Co/Cu multilayered nanostructure. Figure 1(d) shows a characteristic REM- RHEED picture obtained from a Cu/Co/Pt(111) ultrathin bilayer surface electrodeposited in the presence of  $\text{CrO}_3$ , composed of 10 monolayers of a Co-rich layer grown epitaxially on a Pt(111) surface and 7.5 monolayers of Cu further deposited on the Co-rich layer. As can be seen from the picture, a relatively good epitaxial and homogeneous Cu/Co bilayered structure is extending over some ten monolayers on the Pt(111) surface. The RHEED pattern also suggests the formation of an additional  $(2 \times 2)$  superstructure on the bilayer surface. Deposition of

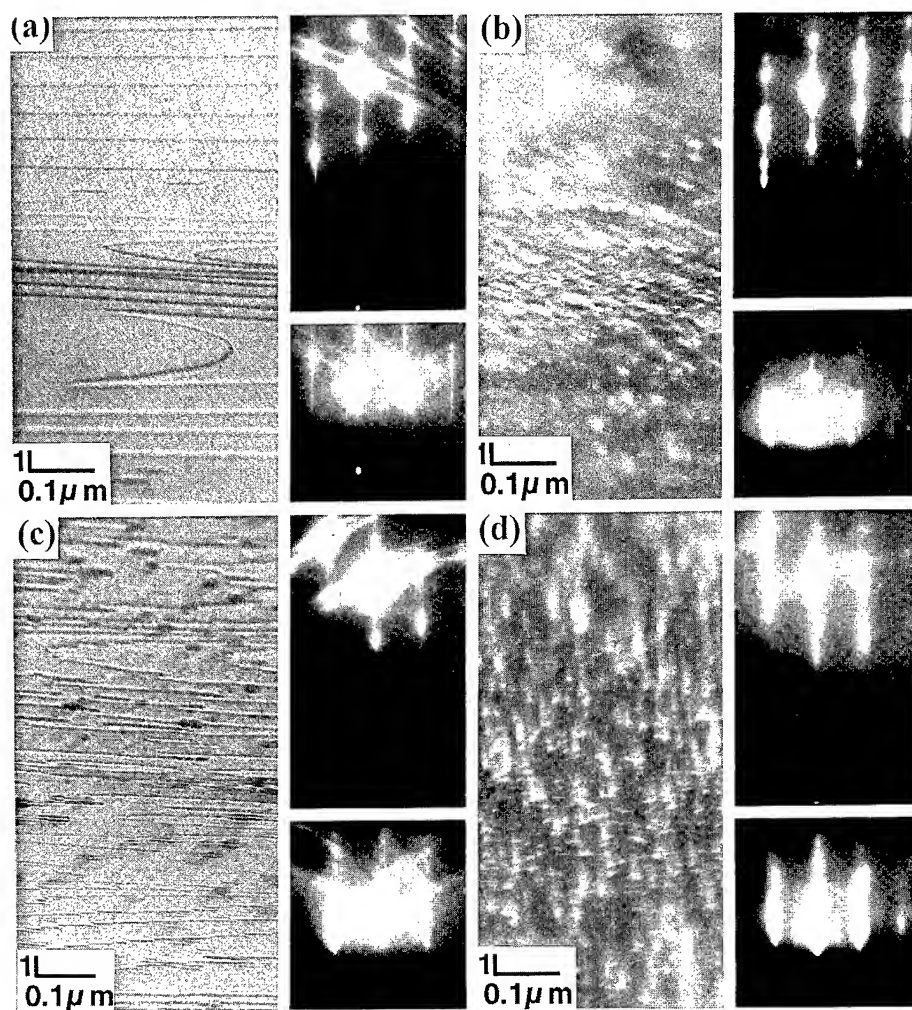


Fig. 1. Typical REM-RHEED pictures obtained from a clean Pt(111) surface (a), and the Pt(111) surfaces covered with 10 monolayers of Co (b,c) and a Cu(7.5 monolayers)/Co(10 monolayers) bilayer (d) electrodeposited in the presence (c,d) or absence (b) of  $\text{CrO}_3$ .



Cu onto the Co/Pt(111) layer leaves a rearranged surface, which indicates a more complicated deposition process for the monolayer than simple adsorption-desorption. Probably a place exchange between  $\text{Cr}(\text{OH})_{3\text{ad}}$  and  $\text{CuOH}_{\text{ad}}$  in the adsorbed intermediate occurs, which would also explain the inhibitory effect.

#### Structure and Magnetic Properties of Electrodeposited Co/Cu Multilayers

Figure 2(a) shows a typical cross-sectional TEM image obtained from a Co/Cu multilayered thin film comprising 20 repeats of alternating approximately 30 nm Co-rich layers (bright-contrast bands) and 30 nm Cu-rich layers (dark-contrast bands),  $[\text{Co}(30\text{nm})/\text{Cu}(30\text{nm})]_{30}$ , grown on a Cu(111) substrate under potentiostatic control. As can be seen from the image, a compositionally modulated Co/Cu multilayered structure has been prepared. The growth and microstructure of the multilayers have been dependent upon the deposition overpotential, the Co-rich and Cu-rich layer thicknesses, and the presence of  $\text{CrO}_3$  in the electrolyte, as assumed from the REM-RHEED studies described above. Figure 3(a) shows a series of X-ray diffraction profiles for Co/Cu multilayered thin films with repeat lengths down to several nanometers ( $[\text{Co}(2.0\text{nm})/\text{Cu}(t_{\text{Cu}}\text{nm})]_{300}$ ) fabricated by electrodeposition of the Co-rich and Cu-rich layers, respectively, at electrode potentials of -1.1 V and -0.40 V in the presence of  $\text{CrO}_3$ . Since the Cu deposition potential is much less negative than that of Co, deposits obtained at -1.1 V are predominantly Co layers with some traces of Cu while those at -0.40 V are almost pure Cu layers, with Co tending to dissolve at the latter electrode potential in the beginning of the Cu deposition on top of the precedently grown Co-rich layers in the absence of  $\text{CrO}_3$ . The X-ray diffraction data show that the electrodeposited Co/Cu nanometer-multilayered thin films are polycrystalline, and that for the films grown in the absence of  $\text{CrO}_3$ , the structure of the Co is a mixture of fcc Co, hcp Co and Co in stacking faults, while for those in the presence of  $\text{CrO}_3$ , with a thicker Cu layer thickness of more than 0.5 nm both the Co and Cu layers are mainly fcc with a (111) texture. As also characterized by the cross-sectional TEM image shown in Fig. 2(b), the film grown in the absence of  $\text{CrO}_3$  does not contain a multilayered structure but has rather a heterogeneous Co-Cu alloy consisting of Cu-rich particles (less than 10 nm in diameter) in a polycrystalline Co-rich matrix.

Typical room-temperature transverse magnetoresistance versus in-plane field data and the dependence of saturation magnetoresistance on the Cu spacer layer thickness,  $t_{\text{Cu}}$ , for the electrodeposited  $[\text{Co}(2.0\text{nm})/\text{Cu}(t_{\text{Cu}}\text{nm})]_{300}$  multilayered thin films shown in Fig. 3(a) are summarized in Fig. 3(b). As already discussed in sputtered polycrystalline Co/Cu multilayers<sup>2</sup> and MBE-grown highly oriented Co/Cu (111) superlattices<sup>3</sup>, oscillations in the saturation magnetoresistance as a function of the Cu layer thickness correspond to oscillations between antiferromagnetic and ferromagnetic interlayer coupling. No such oscillations in magnetoresistance nor large magnetoresistance values are evident for the films electrodeposited in the absence of  $\text{CrO}_3$ . This would also be confirmed by the magnetization curves, displaying incomplete antiferromagnetic coupling with large remanent magnetization in low fields of about 60-70% of the saturation magnetization. This suggests that a significant fraction of the films remains ferromagnetically coupled, which results from structural defects, for example, magnetic pinholes. Related observations have been recently reported for electrodeposited (100)- and (111)-oriented Co-Cu/Cu multilayers<sup>6</sup>. On the other hand, the (111) textured multilayered nanostructures grown in the presence of  $\text{CrO}_3$ , as shown in Fig. 3(b), exhibit the oscillations with a period of approximately 1.0 nm, and a large magnetoresistance with a much higher saturation field and a small remanent magnetization suggesting the presence of large antiferromagnetic coupling. Moreover, the (111) textured multilayered structure displays a substantial saturation magnetoresistance, exceeding 18% for a

nominal Cu layer thickness of 3.2 nm. However, for such sufficiently thick Cu layers, one is in the uncoupled regions rather than in the antiferromagnetically coupled regions<sup>2,3</sup>. The magnetoresistance in this case is related to the possibility of magnetic domains in neighboring Co-rich layers being aligned antiparallel to one another for certain field ranges. Indeed, the resistance of this structure is maximized close to the coercive field of the Co-rich layers where the net magnetization passes through zero and there is the greatest likelihood of antiparallel magnetic domains in successive Co-rich layers.

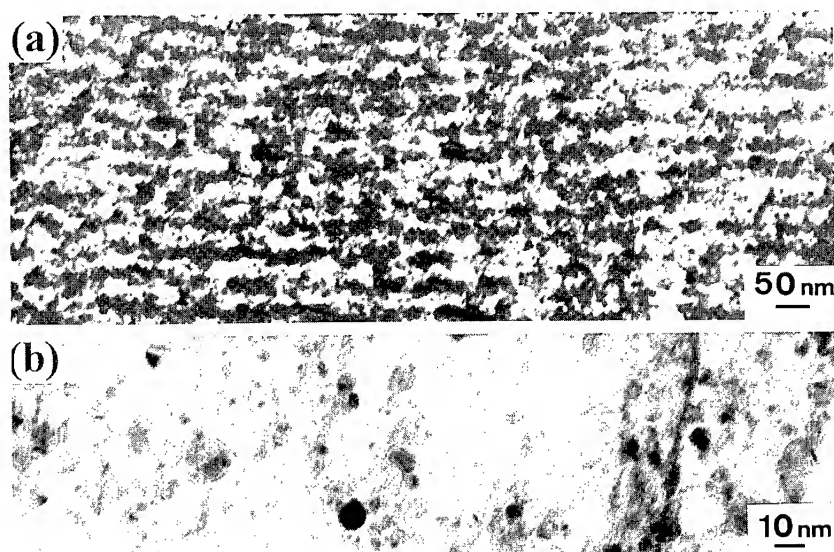


Fig. 2. Typical cross-sectional TEM images of Co/Cu multilayered thin films grown on a Cu(111) substrate by electrodeposition in the presence (a) or absence (b) of  $\text{CrO}_3$ .

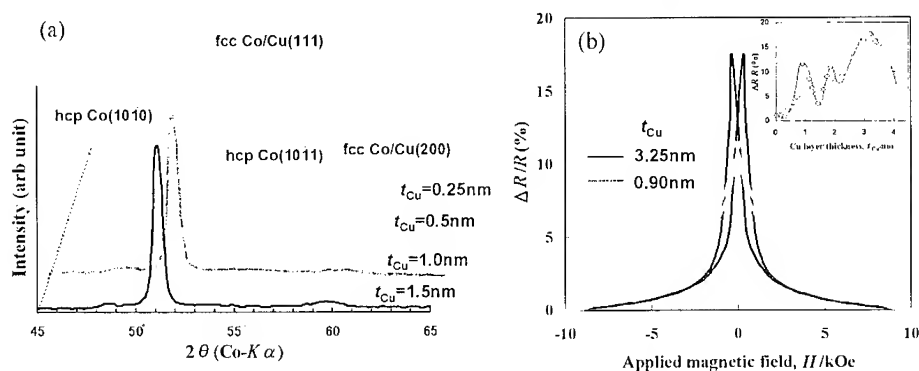


Fig. 3. A series of X-ray diffraction profiles (a) and room-temperature transverse magnetoresistance versus in-plane field curves (b) for  $[\text{Co}(2.0\text{nm})/\text{Cu}(t_{\text{Cu}}\text{nm})]_{300}$  multilayers prepared by electrodeposition in the presence of  $\text{CrO}_3$ . The inset shows the dependence of saturation magnetoresistance on the Cu spacer layer thickness.

## CONCLUSIONS

We have presented the first experimental evidence for oscillatory antiferromagnetic interlayer coupling and giant magnetoresistance in a (111) textured Co/Cu nanometer-multilayered structure grown by electrodeposition under potentiostatic control in the presence of a very slight amount of  $\text{CrO}_3$ . A large saturation magnetoresistance value of over 18% has been obtained at room temperature for such a multilayered nanostructure with a nominal Cu spacer layer thickness of 3.2 nm. This value is still low but substantial compared to those found for vapor-deposited multilayers. Given the simplicity of the apparatus required to produce the multilayers, our initial results reveal that electrodeposition will prove to be a highly competitive technique for the preparation of giant magnetoresistance multilayers. Further studies on the crystallization kinetics of nucleation and growth under precise overpotential control are necessary to obtain improved structural and magnetic qualities of the multilayers.

## ACKNOWLEDGMENTS

This study has been supported in part by a Grant-in-Aid for Scientific Research from the Ministry of Education, Science, Sports and Culture, Japan.

## REFERENCES

1. M. N. Baibich, J. M. Broto, A. Fert, F. Nguyen Van Dau, F. Petroff, P. Etienne, G. Creuset, A. Friederich and J. Chazelas, *Phys. Rev. Lett.* **61**, 2472 (1988).
2. D. H. Mosca, F. Petroff, A. Fert, P. A. Schroeder, W. P. Pratt Jr. and R. Laloce, *J. Magn. Magn. Mater.* **94**, L1 (1991).
3. S. S. P. Parkin, R. F. Marks, R. F. C. Farrow, G. P. Harp, Q. H. Lam and R. J. Savoy, *Phys. Rev. B* **46**, 9262 (1992).
4. A. E. Berkowitz, J. R. Mitchell, M. J. Carey, A. P. Young, S. Zhang, F. E. Spada, F. T. Parker, A. Hutten and G. Thomas, *Phys. Rev. Lett.* **68**, 3745 (1992); J. Q. Xiao, J. S. Jiang and C. L. Chien, *ibid.*, **68**, 3749 (1992).
5. S. Z. Hua, D. S. Lashmore, L. Salamanca-Riba, W. Schwarzacher, L. J. Swartzenruber, R. D. McMichael, L. H. Bennett and R. Hart, *J. Appl. Phys.* **76**, 6519 (1994).
6. S. K. J. Lenczowski, C. Schonenberger, M. A. M. Gijs and W. J. M. de Jonge, *J. Magn. Magn. Mater.* **148**, 455 (1995).
7. L. Piraux, J. M. George, J. F. Despres, C. Leroy, E. Ferain, R. Legras, K. Ounadjela and A. Fert, *Appl. Phys. Lett.* **65**, 2484 (1994).
8. A. Blondel, J. P. Meier, B. Doudin and J.-Ph. Ansermet, *Appl. Phys. Lett.* **65**, 3019 (1994).
9. H. J. Blythe and V. M. Fedosyuk, *J. Phys. Condens. Mater.* **7**, 3461 (1995).
10. Y. Jyoko, S. Kashiwabara and Y. Hayashi, *Mater. Res. Soc. Symp. Proc.* **382**, 167 (1995); *J. Magn. Magn. Mater.* **156**, 35 (1996).
11. Z. L. Wang, in *Reflection Electron Microscopy and Spectroscopy for Surface Analysis* (Cambridge University Press, New York, 1996), p.129.

## AN IN SITU SMALL ANGLE NEUTRON SCATTERING INVESTIGATION OF $\text{Ag}_{0.7}\text{Au}_{0.3}$ DEALLOYING UNDER POTENTIAL CONTROL

SEAN G. CORCORAN\*, DAVID G. WIESLER\*\*, AND KARL SIERADZKI\*\*\*

\*Hysitron, Inc., 2010 E. Hennepin Avenue, Minneapolis, MN 55413

\*\*Laboratory of Cardiac Energetics, National Heart, Lung, and Blood Institute, 4420 Rosedale Avenue, NIH Bldg. 10, Bethesda, MD 20892

\*\*\*Arizona State University, Department of Mechanical and Aerospace Engineering, Tempe, AZ 85287

### ABSTRACT

In situ small angle neutron scattering (SANS) was used to characterize the formation of the random 3-dimensional porous structure created during the dealloying of a  $\text{Ag}_{0.7}\text{Au}_{0.3}$  alloy under potential control. Using a model developed by N.F. Berk (Phys. Rev. Lett., **58** (1987) 2718) for the scattering properties of random porous media, we were able to characterize the average ligament width as a function of time during the dealloying process. We find that the coarsening of the average ligament width is strongly dependent upon the value of the applied potential. Our results represent the first in situ nanoscale characterization of the 3-dimensional formation of porosity in a dealloying system under potential control.

### INTRODUCTION

Alloy corrosion often leads to the production of a random porous network of the more noble element. This porous network exhibits a ductile-brittle transition[1] which is microstructurally controlled and is thought to be directly responsible for the stress corrosion cracking observed in many alloy systems[2]. Technologically there is interest in the production of these porous networks for their high surface to volume ratio, e.g. in the areas of biological sensors. The average pore size can be tailored typically in the range of 50 Å to 10 µm making them useful for specialized filtration needs where polymer filters are unstable. Despite the interest in porous metals, very little is known about the physical phenomena that cause the formation of these bicontinuous porous networks. The main difficulty has been in measuring the porosity of bulk samples at the nanometer size scale. To date no reliable in-situ or even ex-situ measurements exist for the pore size distributions of bulk dealloyed samples. Porosity has been typically analyzed using ex-situ techniques such as SEM and TEM. For SEM the dealloyed samples are first heat treated in order to coarsen the pores to a size that is observable. Exactly how these measurements relate back to the room temperature samples is unknown. TEM analysis requires the dealloying of foils which are extremely thin to allow for TEM imaging. However, the porosity observed on thin films will not be the same as that in a bulk specimen owing to differences in coarsening kinetics and dealloying rates. The only in-situ techniques that have been used to characterize dealloying have been ac-impedance[3] and more recently STM[4]. Neither technique is suitable for characterizing the morphology of the bicontinuous structure. Ac-impedance allows

for the measurement of surface area which can be used to determine an average porosity if the structure is known a priori. STM is of course limited to the alloy surface.

In this paper, we report on the use of SANS to characterize the 3-dimensional porosity created during the bulk dealloying of Ag-Au under potential control. Previously[5], we reported on the use of SANS to characterize the porosity of freely corroding Ag-Au in concentrated  $\text{HNO}_3$ . We find that the rate of coarsening of the nanoscale porosity is greatly influenced by the applied potential.

## EXPERIMENT

Samples were prepared by cutting 0.8" x 0.8" square sheets from a 0.005" thick foil of  $\text{Ag}_{0.7}\text{Au}_{0.3}$  which was previously annealed for 24 hours at 900 °C. The cut samples were then reannealed at 900 °C for 2 hours. A sample was placed vertically in a quartz electrochemical cell in transmission geometry. An electrolyte of 1 M  $\text{HClO}_4$  + 1 mM  $\text{Ag}^+$  was circulated through the cell from a 500 ml reservoir. A Ag wire reference electrode was used. The sample was dealloyed at 700 mV for 19 hours followed by 20 hours at 450 mV. SANS data was collected during the entire 39 hours.

The SANS measurements were performed using a 30 meter long SANS instrument at the National Institute of Standards and Technology 20 MW reactor. The neutron beam was pinhole collimated. A beam wavelength of 6 Å was used. The measurement range for the scattering vector,  $Q$ , was 0.003 to 0.11 Å<sup>-1</sup>, where  $Q$  is defined as:

$$Q = \frac{4\pi}{\lambda} \sin(\theta/2)$$

and  $\theta$  is the scattering angle. The absolute scattering was determined using a silica a2 standard.

## RESULTS

A selection of absolute scattering data are shown in Figs. 1 and 2 for applied potentials of 700 mV and 450 mV, respectively. The 700 mV applied potential is above the critical dealloying potential for this system ( $\cong$  640 mV) and gave a corresponding dealloying current of approximately 1 mA cm<sup>2</sup>. The 450 mV potential is below the critical potential. A very broad peak with weak intensity can be observed in Figure 1 after 15 hours of dealloying. Previously, we observed the formation of a scattering peak within minutes of placing a Ag-Au alloy in concentrated nitric acid[5]. The formation of a peak in the scattering intensity is indicative of a well-defined average pore size in the dealloyed structure. Immediately, after lowering the potential to 450 mV a well defined peak developed in the scattering data as shown in Figure 2. This peak continued to shift to lower values of  $Q$  with time indicating an increase in the average pore size. It is important to note that we are not increasing the depth of porosity at 450 mV; we are only changing the morphology of the porosity that was created during the 19 hours at 700 mV, i.e. the coarsening of the porosity is much more rapid at 450 mV than at the 700 mV dealloying potentials.

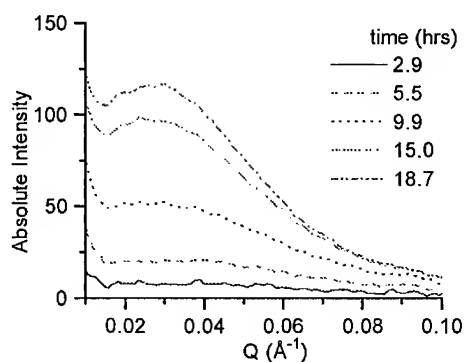


Figure 1: In-situ scattering data of  $\text{Ag}_{0.7}\text{Au}_{0.3}$  in 1 M  $\text{HClO}_4$  + 1 mM  $\text{Ag}^+$  at 700 mV (above the critical potential). The time at which each curve was taken following the application of the 700 mV potential is indicated in the figure.

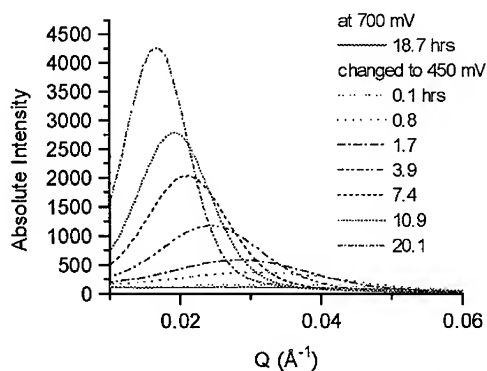


Figure 2: In-situ scattering data of  $\text{Ag}_{0.7}\text{Au}_{0.3}$  in 1 M  $\text{HClO}_4$  + 1 mM  $\text{Ag}^+$  at 700 and 450 mV. Note that the first curve on this plot (18.7 hrs at 700 mV) is the last curve taken at 700 mV as shown in figure 3. The applied potential was changed to 450 mV (below the critical potential) immediately after recording this curve.

## ANALYSIS AND DISCUSSION

The data was analyzed using the leveled wave method of N.F. Berk [6]. This method assumes that the bicontinuous pore morphology can be mathematically modeled as the two-dimensional continuous contours of a stochastic standing wave generated by summing a large

number of plane waves with random wavevector directions and phase constants but with defined wavevector magnitudes. The scattering from the mathematically modeled bicontinuous structure was determined and compared with the experiment. When a fit was found, a 3-dimensional image was created from the mathematical model. The image was analyzed to yield the average Au ligament size and ligament distribution. This model has been used previously to analyze the SANS from controlled pore glasses [7] and was found to agree with data obtained by other methods.

The data of Figure 1 can not be analyzed with this model since a well defined peak is not present in the data. The lack of a well defined peak is interesting because it is indicative of a very broad distribution of porosity which is "frozen" in its as dealloyed state, i.e. the porosity is not coarsening with time. However, after lowering the potential to 450 mV the porosity immediately begins to increase in size forming a well defined scattering peak which shifts to lower values of  $Q$  with time. Figure 3 shows the best fit to one of the normalized scattering curves in Figure 2 taken after 20 hours at 450 mV. Simulated TEM images (2-dimensional slices of the 3-d model) are shown in Figures 4 (A and B) after 1.7 hours and 20 hours at 450 mV respectively. The average ligament size represented in these images was found by making chord length measurements. Figure 5 shows the results for the average ligament width versus hold time at 450 mV.

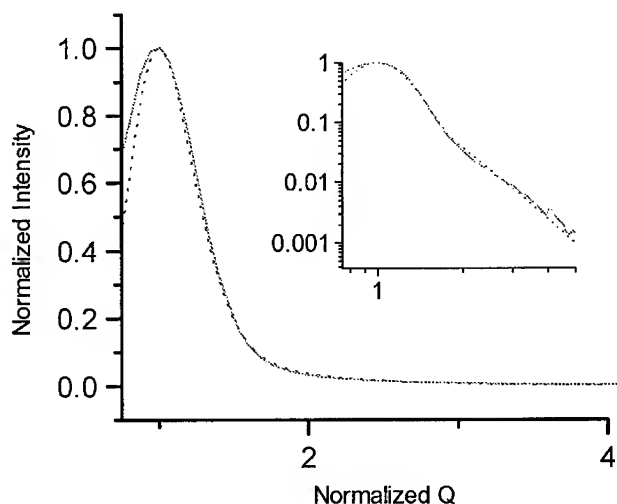


Figure 3: Best fit to normalized scattering curves. Fit is dotted line. Solid line is the normalized scattering curve taken after 20 hours at 450 mV.

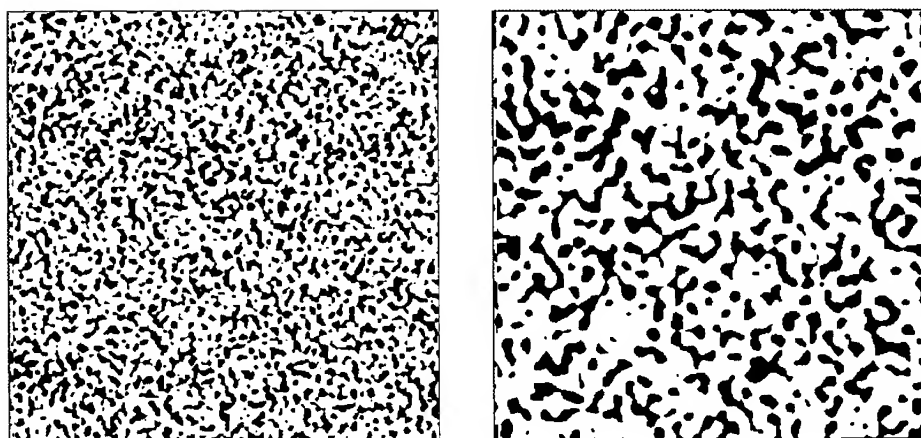


Figure 4: Simulated TEM images (768 nm x 768 nm) calculated from fits to the scattering data for (A) 1.7 hours and (B) 20 hours at 450 mV. The average ligament width calculated from the images is (A) 7.8 nm and (B) 15.0 nm.

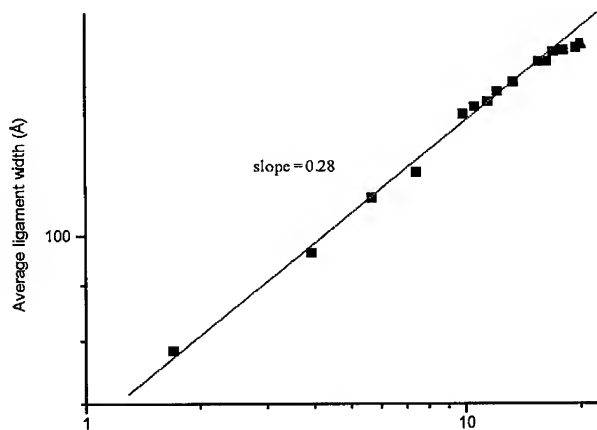


Figure 5: The calculated average ligament width versus time at 450 mV.



## CONCLUSIONS

In situ SANS was used for the first time to characterize the morphological evolution of the porosity created during the dealloying of a Ag-Au alloy under potentiostatic control. During the dealloying at 700 mV, the porosity did not coarsen. Immediately after lowering the potential to 450 mV, the porosity quickly coarsened and a well defined scattering peak became evident in the SANS data. After 1.7 hours at 450 mV, an average metal ligament size of 7.8 nm was measured. The average ligament size increased to a value of 15.0 nm after 20.1 hours at 450 mV.

## ACKNOWLEDGMENTS

We would like to acknowledge John Barker of NIST for his technical support on the SANS beam line. We are also grateful for the numerous discussions about SANS analysis with N.F. Berk and S. Trevino of NIST. We acknowledge support of this work by the U.S. Department of Energy, Division of Materials Sciences, Office of Basic Energy Sciences under Contract No. DE-FG02-90ER45421.

## REFERENCES

1. Rong Li and K. Sieradzki, Phys. Rev. Lett. **68**, 1168 (1992).
2. K. Sieradzki and R.C. Newman, J. Phys. Chem. Solids **48**, 1101 (1987).
3. R.G. Kelly, A.J. Young and R.C. Newman, in Electrochemical Impedance: Analysis and Interpretation, edited by J.R. Scully, D.C. Silverman and M.W. Kendig (ASTM, Philadelphia, 1993) pp. 94-112.
4. S.J. Chen, F. Sanz, D.F. Ogletree, V.M. Hallmark, T.M. Devine and M. Salmeron, Surf. Sci. **292**, 289 (1993); T.P. Moffat, F.F. Fan and A.J. Bard, J. Electrochem. Soc. **138**, 3224 (1991).
5. S.G. Corcoran, D.G. Wiesler, J. Barker, and K. Sieradzki, Mat. Res. Soc. Proc., **376**, (1994).
6. N.F. Berk, Phys. Rev. Lett. **58**, 2718 (1987); Phys. Rev. A **44**, 5069 (1991).
7. N.G. Berk, C.J. Glinka, W. Haller, and L.C. Sander, Mat. Res. Soc. Symp. Proc. **166**, 409 (1990).

## Structure of Monolayers of Silicotungstate Anions on Ag(111) and Au(111) Electrode Surfaces

Maohui Ge, Brian K. Niece, Craig G. Wall, Walter G. Klemperer,\* and Andrew A. Gewirth\*

Department of Chemistry, Frederick Seitz Materials Research Laboratory, and Beckman Institute for Advanced Science and Technology, University of Illinois at Urbana-Champaign, Urbana, IL 61801

\*Authors to whom correspondence should be addressed.

### ABSTRACT

$\alpha$ -Dodecatungstosilicate ( $\alpha$ -SiW<sub>12</sub>O<sub>40</sub><sup>4-</sup>) anions form ordered monolayers on Ag(111) and Au(111) surfaces. *In-situ* STM images reveal that the silicotungstate ion forms a square adlattice with an intermolecule spacing of  $10.2 \pm 0.5$  Å on both Ag and Au surfaces. Additional structures exhibiting either row or rhombic motifs are observed on Au electrodes. The structure of the adlattices can be modeled using a simple model which maximizes the coordination of the silicotungstate ion to the electrode while maintaining van der Waals contacts between terminal oxygens of adjacent silicotungstates.

### INTRODUCTION

There is much interest in understanding the adsorption of atoms and molecules at metal-solution interfaces. Such understanding will provide insight into the nature of technologically important processes including corrosion, electrodeposition, electrocatalysis, and electrode passivation. Implicit in this understanding is the development of appropriate structural models for the interaction of anions and other adsorbates with electrode surfaces.

Currently the most extensively studied adsorption systems at the metal-solution interface are those of small anions, specifically halides, bisulfate, and other small molecules. Iodide [1-7], bromide [7-9], and chloride [9] adsorption have been studied in situ on Au(111). Iodide adsorption has been studied on Pd(111) [10]. Bromide adsorption has been studied on Pt(111) [11]. Ordered overlayers have also been observed in the adsorption of iodide and bromide on Ag(111) [12]. These monatomic adsorbates all form closely packed arrays in registry or near-registry with the substrate. Adsorption of the more complex bisulfate ion has been studied on Au(111) [13,14], Pt(111) [15], and Rh(111) [16]. Cyanide adsorption has been studied on Pt(111) [17]. In addition, the superstructures formed from the electroreduction of Au(CN)<sub>2</sub><sup>-</sup> on Au(111) have been investigated [18].

Adsorption of polyoxometalates, such as  $\alpha$ -SiW<sub>12</sub>O<sub>40</sub><sup>4-</sup>, provide an interesting alternative to small anion adsorption for several reasons. They are much larger (ca. 10 Å or more across) than previously studied anionic adsorbates. They are highly symmetric, like sulfate, but they present a large number of terminal oxygens to the surface. They can be readily synthesized in a variety of shapes and valences with different core atoms [19]. They undergo reversible redox reactions themselves, and facilitate redox reactions in other molecules [20]. They have also been

observed to act as ligands for other small species [19]. Finally, they can be synthesized with a wide variety of functional groups attached, allowing for functionality to be tethered to the surface.

Heteropolyoxometalates have been found previously to adsorb to electrode surfaces. Electrochemical measurements on Hg electrodes indicate that the anions adsorb strongly to the surface and exhibit an inhibiting effect on reduction electrochemistry at the electrode [21]. Quartz crystal microbalance studies have shown that  $\alpha\text{-SiW}_{12}\text{O}_{40}^{4-}$  and other polyoxometalates adsorb strongly to Au electrodes [22]. Additionally, *in-situ* scanning probe microscope studies of polyoxometalate anions indicate that they form ordered adlayers on graphite substrates [23-29]. Moreover, in a previous paper we reported that  $\alpha\text{-SiW}_{12}\text{O}_{40}^{4-}$  anions self-assemble into passivating, ordered, monolayer arrays on Ag(111) surfaces [30].

The  $\alpha\text{-SiW}_{12}\text{O}_{40}^{4-}$  anion has tetrahedral symmetry. A model of the anion is shown in Fig. 1. The central Si atom is surrounded by twelve corner-sharing  $\text{WO}_6$  octahedra. The tetrahedral symmetry is clearly shown in Fig. 1A where the anion is viewed along a three-fold rotation axis. In Fig. 1B the anion is viewed along a two-fold rotation axis. In the latter view it can be seen that the cluster has four terminal oxygen atoms which form a rectangle in the plane normal to the two-fold axis.

In this paper we report that  $\alpha\text{-SiW}_{12}\text{O}_{40}^{4-}$  also forms monolayers on Au(111) electrode surfaces from acid solution. Three different adlayer lattices are observed: a square structure, a rhombic structure, and a row structure. These structures, and the one formed on Ag(111), can be rationalized using a simple model.

## EXPERIMENTAL

*In-situ* scanning tunneling microscope (STM) images were obtained using a NanoScope II electrochemical scanning tunneling microscope (ECSTM) equipped with a fluid cell made from Kel-F (Digital Instruments, Santa Barbara, CA). The tip was formed from a Pt/Ir wire coated except at the very tip with polyethylene to minimize the Faradaic background current. STM images were obtained on thin-film substrates comprised of 200 nm thick Ag(111) films obtained by evaporation of Ag onto V2 grade mica in a bell jar evaporator. Au(111) surfaces were prepared by annealing Au coated glass (Dirk Schröer, Berlin) in a  $\text{H}_2$  (99.999%) flame just prior to use [31]. STM images of either surface immersed in solutions containing either 0.1 M  $\text{HClO}_4$  or 0.1 M  $\text{H}_2\text{SO}_4$  revealed only the expected (111) hexagonal lattice structure of the underlying fcc metal surface and large (ca. 50 nm wide) terraces [32]. Solutions were prepared from purified water (Milli-Q UV plus, Millipore Inc., 18.2 M $\Omega$  cm) and the following chemicals:  $\text{HClO}_4$  (E. Merck, Suprapur),  $\text{H}_2\text{SO}_4$  (J.T. Baker, ULTREX Ultrapure Reagent), HF (E. Merck, Suprapur), and  $\text{H}_4\text{SiW}_{12}\text{O}_{40}$ .  $\text{H}_4\text{SiW}_{12}\text{O}_{40}$  was prepared following published procedures [33]. The concentration of  $\text{HClO}_4$  and  $\text{H}_2\text{SO}_4$  was 0.1 M, and the typical  $\text{H}_4\text{SiW}_{12}\text{O}_{40}$  concentration was  $10^{-4}$  M.

## RESULTS

### *Adsorption on Ag(111)*

Images obtained from acid solutions containing small quantities of silicotungstic acid yielded a completely different surface structure from the hexagonal Ag(111) adlattice. Fig. 2 shows a 28 nm  $\times$  28 nm STM image of a Ag(111) surface in an aqueous solution containing 0.1 M  $\text{HClO}_4$  and  $10^{-4}$  M  $\alpha\text{-H}_4\text{SiW}_{12}\text{O}_{40}$ . In contrast to the bare electrode surface, the electrode now exhibits domains of an approximately square lattice (angles  $90 \pm 5^\circ$ ) composed of spots

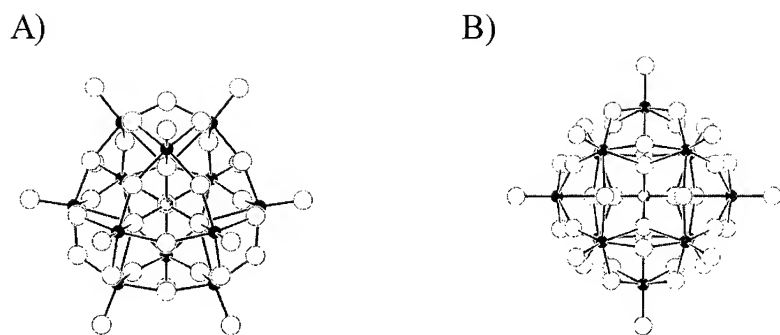


Figure 1. Structure of the  $\alpha\text{-SiW}_{12}\text{O}_{40}^{4-}$  ions observed in crystalline  $[\text{N}(\text{CH}_3)_4]\text{SiW}_{12}\text{O}_{40}$ . (A) viewed along a three-fold rotational symmetry axis of the  $T_d$ -symmetric molecular ion. (B) viewed along the two-fold rotational symmetry axis. Oxygen atoms are represented by large open circles, tungsten atoms by small filled circles, and silicon atoms by small shaded circles. Note that within the terminal plane normal to the two-fold symmetric axis there are four terminal oxygen atoms.

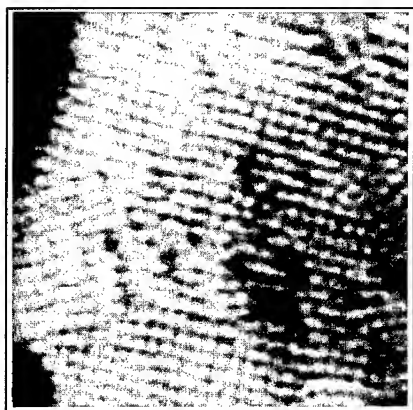


Figure 2. 28 nm  $\times$  28 nm STM image of a monolayer  $\text{SiW}_{12}\text{O}_{40}^{4-}$  on a Ag(111) surface in 0.1 M  $\text{HClO}_4$ .  $V_{\text{tip}}=100$  mV;  $i_{\text{tip}}=2.7$  nA.

which have a nearest neighbor distance of  $10.2 \pm 0.5 \text{ \AA}$ . This spacing matches the expected diameter of the  $\alpha\text{-SiW}_{12}\text{O}_{40}^{4-}$  ion (ca.  $10.5 \text{ \AA}$ ), and we associate each individual spot in the image with an adsorbed silicotungstate anion.

Monolayers of silicotungstic acid covering the entire Ag(111) surface could be observed following immersion of the electrode into perchloric acid electrolyte with silicotungstic acid concentrations ranging from  $\sim 10^{-3}$  to  $\sim 10^{-6}$  M. These images could be recovered following emersion of the surface, rinsing with water, and reimmersion into pure perchloric acid solution. This indicates that the silicotungstate is strongly bound to the Ag(111) surface.

#### *Adsorption onto Au(111)*

Fig. 3 consists of two *in-situ* STM images of Au(111) in a solution containing  $2 \times 10^{-4}$  M  $\alpha\text{-SiW}_{12}\text{O}_{40}^{4-}$  and 0.1 M  $\text{H}_2\text{SO}_4$  after about 4 hours immersion at open circuit potential. In Fig. 3A, the  $\alpha\text{-SiW}_{12}\text{O}_{40}^{4-}$  anion covers the entire Au surface except for a few defect sites. The two flat Au(111) terraces displayed in the image are separated by one  $2.5 \text{ \AA}$ -high step. This height is the expected value for a monatomically high Au(111) step. The anion evinces a different structure in this region of the Au(111) surface than is observed on the Ag(111) surface. The lattice is clearly rhombus shaped, with two different adlattice spacings. In one direction, the admolecule-admolecule spacing is  $10.2 \pm 0.7 \text{ \AA}$ , while in the other it is  $11.8 \pm 0.6 \text{ \AA}$ . The angle between the two directions is  $103 \pm 4^\circ$ .

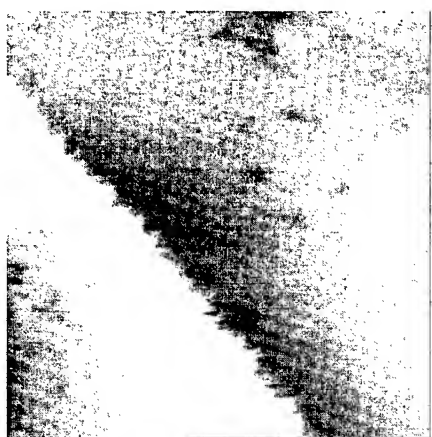
In another region of the same Au(111) electrode surface, two different structures are seen, as shown in Fig. 3B. On the right hand side of Figure 3B is a square lattice like that seen on the Ag(111) surface. The spacing between the anions is  $10.7 \pm 0.7 \text{ \AA}$  and the angle between the two row directions is observed to be  $90 \pm 2^\circ$ . Through comparison with images of the bare Au(111) surface obtained prior to the introduction of the silicotungstic acid, the rotation of one side of the square structure relative to the underlying Au(111) rows is found to be  $12 \pm 4^\circ$ . Several point defects in the adlattice are clearly visible. A row structure is visible in the upper left hand part of the image. While individual anions cannot be resolved along the row directions, the spacing between the rows is  $11.7 \pm 0.6 \text{ \AA}$ . The rows make an angle of  $45 \pm 5^\circ$  with respect to the diagonal of the square adlattice.

## DISCUSSION

The above results show that three different types of monolayer structures are formed by the  $\alpha\text{-SiW}_{12}\text{O}_{40}^{4-}$  anion on electrode surfaces, which we denote as the 'square', the 'rhomboid', and the 'row'. In what follows, we propose that each of these structures can be generated in a simple manner.

The  $\alpha\text{-SiW}_{12}\text{O}_{40}^{4-}$  anion has  $T_d$  symmetry, and, therefore, exhibits three-fold rotational symmetry which would be expected to dominate its interaction with the six-fold symmetric Au(111) surface. The matching symmetry of the molecule and surface leads to the expectation that the monolayers produced from their interaction would mimic this three-fold symmetry as the three terminal oxygen atoms in the plane normal to the  $C_3$  axis form a triangle which can be seated over three underlying Au atoms. Anions could then be placed in equivalent positions at multiples of  $60^\circ$  around the fixed anion. These simple symmetry ideas are also invoked in discussion of the orientation of the  $T_d$ -symmetric sulfate anion on Au(111) [13, 14]. However, our observation of rhombic or row structures on the Au(111) electrode and the square structure

A)



B)

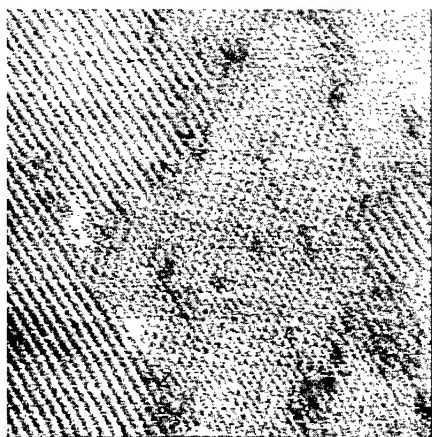


Fig. 3. A) 31 nm  $\times$  31 nm STM image of a monolayer  $\text{SiW}_{12}\text{O}_{40}^{4-}$  on Au(111) in 0.1 M  $\text{H}_2\text{SO}_4$ .  $V_{\text{tip}}=100$  mV;  $i_{\text{tip}}=2.7$  nA. This image shows the 'diamond' adlattice. B) 50 nm  $\times$  50 nm STM image of a monolayer  $\text{SiW}_{12}\text{O}_{40}^{4-}$  on Au(111) in 0.1 M  $\text{H}_2\text{SO}_4$ .  $V_{\text{tip}}=100$  mV;  $i_{\text{tip}}=2.7$  nA. This image shows both the 'square' (right) and 'row' (left) structures of the anion.

on both Au and Ag surfaces shows that this simple model must be reexamined.

Reorienting the  $\alpha\text{-SiW}_{12}\text{O}_{40}^{4-}$  anion so that the  $C_2$  axis is oriented normal to the surface now presents four terminal oxygens to the surface and these oxygens form a rectangle with sides of 5.0 Å and 5.5 Å. These distances correspond roughly to  $\sqrt{3}$  and 2 times the Au (2.88 Å) or Ag (2.89 Å) interatomic spacings, and allow the ion to sit over a rectangle of Au atoms, as shown in Fig. 4. The observed two-fold rather than three-fold symmetry of the overlayers imaged by STM leads to the conclusion that the  $\alpha\text{-SiW}_{12}\text{O}_{40}^{4-}$  anions bind to the electrode with the  $C_2$  axis normal to the surface.

After fixing the first anion on the surface over a rectangle of Au atoms, there are only a few positions near the first anion where additional anions can associate with their  $C_2$  axis normal to the surface. Fig. 5 shows possible lattice positions where an  $\alpha\text{-SiW}_{12}\text{O}_{40}^{4-}$  anion could pack relative to an anion fixed with a  $C_2$  axis normal to the surface. The figure shows 1/4 of the positions giving rise to intermolecular spacings between 9 Å and 12 Å. This pattern could be reflected across the horizontal and vertical axes of the fixed anion to give all of the possible positions. Table 1 lists the interatomic distances for the locations shown in Fig. 5 along with the closest contact distance between terminal oxygens on  $\alpha\text{-SiW}_{12}\text{O}_{40}^{4-}$  in that position and at the central position, X.

Positions A, B, G, and H all have oxygen-oxygen separations which are 2.6 Å or lower which is much less than the van der Waals contact between two oxygen atoms. Additional anions could thus not pack at these positions.

Table 1. Intermolecular spacing and closest nearest neighbor oxygen-oxygen contacts for possible positions of the  $\alpha\text{-SiW}_{12}\text{O}_{40}^{4-}$  anion on Au(111).

Position	Intermolecular Spacing	Nearest Neighbor O-O contact
A	11.5 Å	1.1 Å
B	10.4 Å	2.5 Å
C	13.9 Å	3.6 Å
D	10.0 Å	2.9 Å
E	10.4 Å	2.9 Å
F	11.5 Å	2.9 Å
G	10.4 Å	2.6 Å
H	10.0 Å	-0.4 Å
I	15.0 Å	4.6 Å

The next closest positions of approach are to positions D, E, and F. Each of these retains a nearest neighbor O-O contact greater than 2.8 Å (the sum of the van der Waals radii of two oxygen atoms) and can be associated with short (s), medium (m), and long (l) approach of the anions to each other. The observed spacings between the anions in the STM images can be generated from a combination of these possible distances of approach.

The square structure exhibits anion-anion spacings of  $10.2 \pm 0.5$  Å and this distance is in accord with a structure built up of anions placed at

positions E (10.4 Å) around the central anion, X. Equal spacings would give rise to the square structure observed. The rhomboid structure exhibits spacings at 10.2 and 11.8 Å. This structure can be built by placing one set of anions at positions E and another set at spacings corresponding to positions F (11.5 Å). Finally, the row structure can be generated by placing one set of anions at position D (10.0 Å) and the other at again at a spacing corresponding to position F. Note that in this structure, the anions are rotated  $15^\circ$  from the direction of the row of anions, allowing the terminal oxygen atoms to interdigitate. This allows for the smaller intermolecular spacing with the same oxygen-oxygen contact distance. This interdigitation could explain the lack of

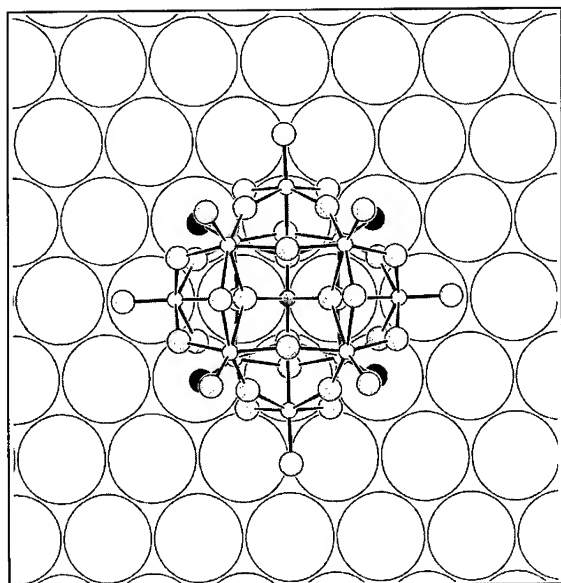


Fig. 4. Proposed model of the Au(111) or Ag(111) interaction with the  $\alpha\text{-SiW}_{12}\text{O}_{40}^{4-}$  anion viewed along the  $C_2$  axis normal to the Au surface. Note the near coincidence of the four terminal oxo groups on the surface with metal atoms on the surface.

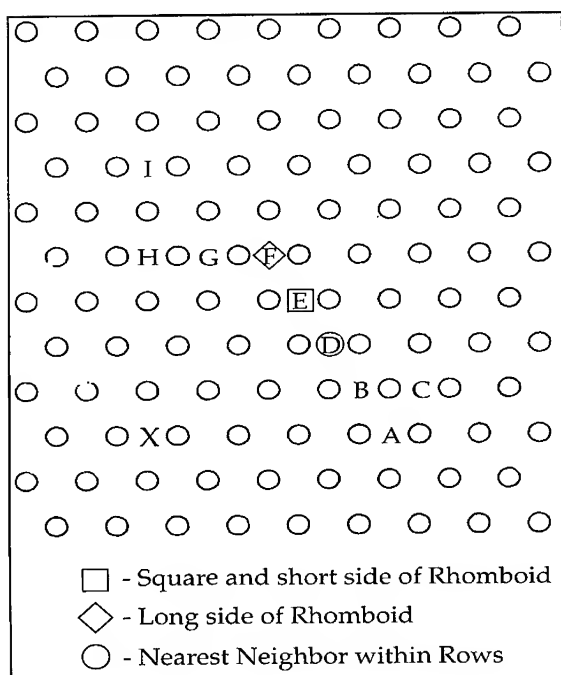


Fig. 5. Possible nearest neighbor positions for  $\alpha\text{-SiW}_{12}\text{O}_{40}^{4-}$  on Au(111) relative to an  $\alpha\text{-SiW}_{12}\text{O}_{40}^{4-}$  anion fixed in the registry shown in Fig. 4 and marked with an X. Only positions F, E, and D give the structures observed in the STM images.



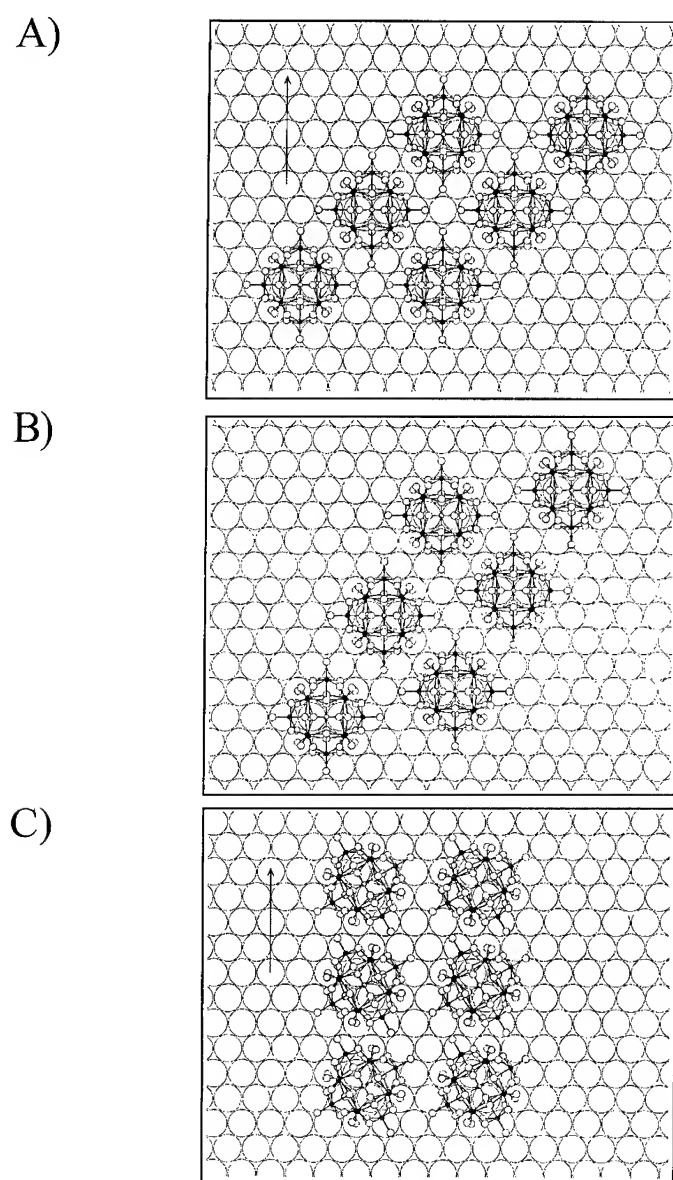


Fig. 6. Proposed models of the silicotungstate anion A) square, B) rhombic, and C) row adlattices on Au(111). The arrow denotes the  $\sqrt{3}$  direction on the square and row structures.

resolution along the rows observed in the STM image shown in fig. 3B as the molecules would simply be too close together to be distinguished. The proposed structures are shown in Fig. 6.

Positions C and I have intermolecular spacings of 13.9 Å and 15.0 Å respectively. These distances are too great to be close packed nearest neighbor distances. Position C is the site reached by performing the translation necessary to reach E followed by a reflection of the translation necessary to reach F. This is the position of the diagonal across the rhombic structure. Similarly, spot I is the position reached by following translation necessary to reach E twice, and is the position of the diagonal across the square structure.

The models for the square and row structures shown in Fig. 6 have two important features which help to support the proposed structures. First, the calculated misalignment between the square structure and the Au(111) rows is  $13.9^\circ$ , which correlates nicely with the  $12 \pm 4^\circ$  observed experimentally. Second, the row and square structures are related to each other by a  $45^\circ$  rotation; the row direction of the row structure is along the diagonal of the square structure. Examination of Fig. 6A shows that one of the diagonals of the square structure, marked with an arrow in Fig. 6A, is oriented along the  $\sqrt{3}$  direction of the underlying Au(111) lattice. From Fig. 6C, it is also apparent that the  $\sqrt{3}$  direction of the Au(111) lattice is the direction along which the rows propagate. Thus, the diagonal of the square and the row should be parallel to each other, as is observed experimentally.

## CONCLUSION

In this paper, we have demonstrated that  $\alpha\text{-SiW}_{12}\text{O}_{40}^{4-}$  anions adsorb in self-organized monolayers on Ag(111) and Au(111) surfaces in acidic aqueous solution. Three distinct structures of the anions on these surfaces are observed, all of which can be rationalized in a simple model which maximizes the coordination of the anion to the surface while maintaining appropriate van der Waals contacts between terminal oxo groups of neighboring anions. The rationalization of the structure of these anions on Ag(111) and Au(111) surfaces makes it possible to envision schemes where the structure of monolayer films of anions of different shape can be predicted and used to construct surfaces with novel structures and properties.

## ACKNOWLEDGMENT

Supported by Department of Energy grant DE-FG02-91ER45349 through the Materials Research Laboratory at the University of Illinois.

## REFERENCES

- [1] X. Gao and M. J. Weaver, *J. Am. Chem. Soc.* **114**, 8544 (1992).
- [2] B. M. Ocko, G. M. Watson, G. M., and J. Wang, *J. Phys. Chem.* **98**, 897 (1994).
- [3] R. L. McCarley and A. J. Bard, *J. Phys. Chem.* **98**, 9618 (1994).
- [4] T. Yamada, N. Batina, and K. Itaya, *J. Phys. Chem.* **99**, 8817 (1995).
- [5] T. Yamada, N. Batina, and K. Itaya, *Surf. Sci.* **335**, 204 (1995).
- [6] N. Batina, T. Yamada, and K. Itaya, *Langmuir* **11**, 4568 (1995).
- [7] N. J. Tao and S. M. Lindsay, *J. Phys. Chem.* **96**, 5213 (1992).

- [8] B. M. Ocko, O. M. Magnussen, R. R. Adzic, J. Wang, Z. Shi, and J. Lipkowski, *J. Electroanal. Chem.* **376**, 35 (1994).
- [9] O. M. Magnussen, B. M.; Ocko, R. R. Adzic, and J. X. Wang, *Phys. Rev. B* **51**, 5510-5513 (1995).
- [10] M. P. Soriaga, J. A. Schimpf, A. Carrasquillo, J. B. Abreu, W. Temesghen, R. J. Barriga, J. J. Jeng, K. Sashikata, and K. Itaya, *Surf. Sci.* **335**, 273 (1995).
- [11] S. Tanaka, S. Yau, and K. Itaya, *J. Electroanal. Chem.* **396**, 125 (1995).
- [12] D. D. Sneddon and A. A. Gewirth, *Surf. Sci.* **343**, 185 (1995).
- [13] O. M. Magnussen, J. Hageböck, J. Hotlos, and R. J. Behm, *Far. Disc.* **94**, 329 (1992).
- [14] G. J. Edens, X. Gao, and M. J. Weaver, *J. Electroanal. Chem.* **375**, 357 (1994).
- [15] A. M. Funtikov, U. Linke, U. Stimming, and R. Vogel, *Surf. Sci.* **324**, L343 (1995).
- [16] L. Wan, S. Yau, and K. Itaya, *J. Phys. Chem.* **99**, 9507 (1995).
- [17] C. Stuhlmann, I. Villegas, and M. J. Weaver, *Chem. Phys. Lett.* **219**, 319-324 (1994).
- [18] T. Sawaguchi, T. Yamada, Y. Okinaka, and K. Itaya, *J. Phys. Chem.* **99**, 14149 (1995).
- [19] M. T. Pope and A. Müller, *Angew. Chem. Int. Ed. Engl.* **30**, 34 (1991).
- [20] Pope, M. T. *Heteropoly and Isopoly Oxometalates*; Springer-Verlag: Berlin, 1983; pp. 101-165.
- [21] C. Rong and F. C. Anson, *Anal. Chem.* **66**, 3124-3130 (1994).
- [22] B. Keita, L. Nadjo, D. Belanger, C. P. Wilde, and M. Hilaire, *J. Electroanal. Chem.* **384**, 155 (1995).
- [23] L. Nadjo and B. Keita, *Journal de Physique IV* **4**, 329 (1994).
- [24] B. Keita, F. Chaveau, F. Theobald, D. Belanger, and L. Nadjo, *Surf. Sci.* **264**, 271 (1992).
- [25] B. Watson, M. A. Barteau, L. Haggerty, and A. M. Lenhoff, *Langmuir* **8**, 1145 (1992).
- [26] B. Zhang and E. Wang, *Electroanal. Chem.* **388**, 207 (1992).
- [27] M. S. Kaba, I. K. Song, and M. A. Barteau, *J. Phys. Chem.* **100**, 19577 (1996).
- [28] I. K. Song, M. S. Kaba, G. Coulston, K. Kourtakis, and M. A. Barteau, *Chem. Materials* **8**, 2352 (1996).
- [29] I. K. Song, M. S. Kaba, and M. A. Barteau, *J. Phys. Chem.*, **100**, 17528 (1996).
- [30] M. Ge, B. Zhong, W. G. Klemperer, and A. A. Gewirth, *J. Am. Chem. Soc.* **118**, 5812 (1996).
- [31] T. Will and D. M. Kolb in *Nanoscale Probes of the Solid-Liquid Interface*, Gewirth, A. A. and Siegenthaler, H., Eds. Kluwer: Dordrecht NATO-ASI V.I. **E288**, p. 137, (1995).
- [32] W. Obretenov, et. al. *J. Electrochem. Soc.* **140**, 692 (1993).
- [33] A. Tézé and G. Hervé, *Inorg. Syn.* **27**, 93 (1990).

# ENERGETICS OF EPITAXIAL MONOLAYERS DEPOSITED ON A (111) SURFACE OF AN FCC CRYSTAL: APPLICATION TO A Cu MONOLAYER ON Au(111)

F.R. ZYPMAN\*, L.F. FONSECA\*\*, AND L. BLUM\*\*.

\*Department of Physics and Electronics. University of Puerto Rico, Humacao, PR 00791-4300.

\*\*Department of Physics. University of Puerto Rico, P.O.Box 23343, San Juan, PR 00931-3343.

## ABSTRACT

We study a system in which a monolayer of atoms of one kind are deposited epitaxially onto a (111) surface of an FCC crystal using the Tight Binding approximation. First, we obtain an analytical expression for the energy spectrum of the system. This turns out to be an interesting result from the mathematical standpoint due to its simplicity, and to the fact that no artificial boundary conditions (like periodic or vanishing) were imposed on the wave functions. All the spectral information is shown to be contained in the roots of a quadratic polynomial. Then, for Cu on Au, we study the density of states and wave function decay out from the outer layer. This is done at zero and finite voltage applied between an electrode and bulk Gold, immersed in an electrolyte. This problem is of interest in electrochemistry.

## INTRODUCTION

The growth of films on single crystal surfaces is of considerable technological interest and has been discussed extensively in the literature. The occurrence of phase transitions in the adsorbed layers has been known for some time, but the studies, both experimental and theoretical, have been done in either dilute gas-solid interfaces, or vacuum-solid interfaces. The films adsorbed on single crystal surfaces do exhibit a rich variety of phase behavior, which also exists in liquid-solid interfaces. In electrochemistry these transitions can be easily observed by polarography which is surface sensitive, even for single planar surfaces, and which is capable of detecting the sudden formation of films at metallic electrodes. A well studied system is the underpotential deposition (UPD) of Copper onto Gold (111), where the phases and phase transitions are well known [1,2,3].

The voltamogram (closely related to the first derivative of the coverage with respect to the applied potential) first obtained by Kolb [1] shows two distinct peaks. The high voltage (first) peak shows a distinct foot, while the low voltage (second) peak is simple. The charge of the Copper in the first peak is not zero (probably 0.5) as shown by the near edge EXAFS experiments [3], while the second peak has presumably metallic, or nearly metallic Copper. The nature and geometry of the phases were discussed in previous work by one of the authors [4-8].

Metal ion adsorption onto metallic surfaces often involves sharing of the orbitals between the adsorbate and the substrate. The theory of adsorption, including UPD, must include the quantum aspects [9-19], and therefore a quantum statistical mechanics formulation is required. However, for the particular case of the Cu UPD onto Au (111) a number of questions regarding the metal surface has to be answered by semiempirical quantum mechanical calculations.

First, there is the interesting problem of the reconstruction and relaxation of surfaces immersed in electrolytes. Scanning Tunneling Microscopy pictures of Cu deposited on Au (111) in a sulfuric acid electrocell [20], show only half of the Copper atoms that are seen by other experimental and theoretical evidence. There is also the question of the charges of the adatom as

a function of the applied potential [5], that can be only addressed with a quantum mechanical calculation.

In this work a Tight Binding (TB) formalism is used to study the energetics of epitaxial monolayers deposited on a (111) surface of FCC crystals. Concretely, the eigenvalue problem of such kind of systems is solved analytically and a general solution is proposed. For the particular case of a Cu monolayer on Au (111) explicit results for the density of surface states and their contribution to the electronic density at the surface region are obtained numerically and their dependence on the applied voltage between an electrode and bulk Gold, immersed in an electrolyte.

#### ADLAYER ON (111) FCC PLANE.

We tag the atoms of an FCC material with the position vectors:  $\vec{m} = m_1\vec{e}_1 + m_2\vec{e}_2 + m_3\vec{e}_3$ , where  $\vec{e}_1 \equiv \frac{1}{2}(\hat{y} + \hat{z})$ ,  $\vec{e}_2 \equiv \frac{1}{2}(\hat{x} + \hat{z})$ ,  $\vec{e}_3 \equiv \frac{1}{2}(\hat{x} + \hat{y})$ . The planes (111) are expanded by the vectors  $\vec{e}_2 - \vec{e}_1$  and  $\vec{e}_3 - \vec{e}_1$ . We use the TB method to expand the electron wave functions in bulk

$$\Psi_B = \sum_{\vec{m}} e^{i\vec{m}\cdot\vec{\theta}} \Phi_{\vec{m}}$$

where  $\Phi_{\vec{m}}$  is the atomic wave function at atom  $\vec{m}$ ,  $\vec{\theta}$  is a dimensionless reciprocal lattice vector  $\vec{\theta} = \theta_1\vec{e}_{\theta_1} + \theta_2\vec{e}_{\theta_2} + \theta_3\vec{e}_{\theta_3}$  (the reciprocal lattice vector is obtained by just dividing  $\vec{\theta}$  by the lattice constant  $a$ ).

In the presence of the surface, the periodicity along the direction perpendicular to the free surface is lost, and the wave functions can be written as

$$\Psi_S = \sum_{\vec{m}_{||}, \vec{m}_T} e^{i\vec{m}_{||}\cdot\vec{\theta}} C_{\vec{m}_T} \Phi_{\vec{m}_{||}, \vec{m}_T};$$

where  $\vec{m}_{||} = M_1(\vec{e}_2 - \vec{e}_1) + M_2(\vec{e}_3 - \vec{e}_1)$ ,  $M_1, M_2$  integers. The transverse vector  $\vec{m}_T$  takes the following values at various depths (plane 0 is the surface, plane 1 is the second layer, or first layer of the host material, plane 2 is the third layer, etc...):

$$\begin{array}{ll} \text{plane 0} & , \vec{m}_T = 0 \\ \text{plane 1} & , \vec{m}_T = \vec{e}_1 \\ \text{plane 2} & , \vec{m}_T = \vec{e}_1 + \vec{e}_2 \\ \text{plane 3} & , \vec{m}_T = \vec{e}_1 + \vec{e}_2 + \vec{e}_3 \\ & \vdots \\ \text{plane } 3n & , \vec{m}_T = n\vec{e}_1 + n\vec{e}_2 + n\vec{e}_3 \end{array}$$

The Schrödinger equation  $H\Psi_S = E\Psi_S$  is projected on the basis of the atomic function  $\Phi_{\vec{m}}$  to obtain one equation per plane (and per coefficient). The equation for plane 0 is:

$$(\alpha_C - E)C_0 + \beta_{CC}FC_0 + \beta_{CA}LC_1 = 0,$$

where  $\alpha$  and  $\beta$  are the typical, on site and hopping, TB integrals. For concreteness, the subscripts stand for Cu or Au sites. For the next layers, the equations are similar. The partial matrix, in the basis of the truncated vector of the coefficients  $C_i$ ,

$$|C_0, C_1, C_2, C_3, C_4, C_5\rangle$$

is,

$$\begin{pmatrix} \alpha_C - E + \beta_{CC}F & \beta_{CA}L & 0 & 0 & 0 & 0 \\ \beta_{CA}L^* & \alpha_A - E + \beta_{SF} & \beta_{BJ} & 0 & 0 & 0 \\ 0 & \beta_{BJ}^* & \alpha_A - E + \beta_{BF} & \beta_{BM} & 0 & 0 \\ 0 & 0 & \beta_{BM}^* & \alpha_A - E + \beta_{BF} & \beta_{BL} & 0 \\ 0 & 0 & 0 & \beta_{BL}^* & \alpha_A - E + \beta_{BF} & \beta_{BJ} \\ 0 & 0 & 0 & 0 & \beta_{BJ}^* & \alpha_A - E + \beta_{BF} \end{pmatrix}$$

with the following definitions:  $F \equiv 2[\cos(\theta_1 - \theta_2) + \cos(\theta_2 - \theta_3) + \cos(\theta_3 - \theta_1)]$  ;

$$L \equiv 1 + e^{i(\theta_2 - \theta_1)} + e^{i(\theta_3 - \theta_1)} ; J \equiv 1 + e^{i(\theta_1 - \theta_2)} + e^{i(\theta_3 - \theta_2)} ; M \equiv 1 + e^{i(\theta_1 - \theta_3)} + e^{i(\theta_2 - \theta_3)} .$$

The complex matrix is infinite-dimensional and is obtained from the one above by simply repeating the bulk elements with period 3. This periodicity is a consequence of the fact that as one moves into an FCC bulk along (111) direction, the environment repeats itself each 3 layers.

Our next task is to obtain the energy spectrum of the system. In order to do that, we first introduce some definitions in order to simplify the notation:  $\gamma_1 \equiv \beta_{BJ}$  ;  $\gamma_2 \equiv \beta_{BM}$  ;  $\gamma_3 \equiv \beta_{BL}$  ;  $a_{11} \equiv \alpha_C - E + \beta_{CC}F$  ;  $a_{22} \equiv \alpha_A - E + \beta_{SF}$  ;  $a_{21} \equiv \beta_{CA}L^* = a_{12}^*$  ;  $\xi \equiv \alpha_A - E + \beta_{BF}$  .

The roots of the determinant of the following matrix, P, define the energy spectrum of the system,

$$P = \begin{pmatrix} a_{11} & a_{21} & 0 & 0 & 0 & 0 & 0 \\ a_{12} & a_{22} & \gamma_1 & 0 & 0 & 0 & 0 \\ 0 & \gamma_1^* & \xi & \gamma_2 & 0 & 0 & 0 \\ 0 & 0 & \gamma_2^* & \xi & \gamma_3 & 0 & 0 \\ 0 & 0 & 0 & \gamma_3^* & \xi & \gamma_1 & 0 \\ 0 & 0 & 0 & 0 & \gamma_1^* & \xi & \gamma_2 \\ 0 & 0 & 0 & 0 & 0 & \gamma_2^* & \xi \end{pmatrix}$$

Let  $\Delta_i(N)$  ( $i=1, 2, 3$  and  $N \times N$  the dimension of the matrix) be the determinant of

$$\begin{pmatrix} . & & & & & & \\ & . & & & & & \\ & & . & & & & \\ & & & . & & & \\ & & & & . & & \\ & & & & & . & \\ & & & & & & \xi & \gamma_i \\ & & & & & & \gamma_i^* & \xi \end{pmatrix}$$

As an example, P, without the dots, has a determinant  $\Delta_2(7)$ . The various determinants satisfy the following recurrences:

$$\Delta_3(N) = \xi \Delta_2(N-1) - \gamma^2 \Delta_1(N-2) ; \quad \Delta_2(N) = \xi \Delta_1(N-1) - \gamma^2 \Delta_3(N-2) ;$$

$$\Delta_1(N) = \xi \Delta_3(N-1) - \gamma^2 \Delta_2(N-2)$$

where  $\gamma^2 \equiv |\gamma_1|^2 = |\gamma_2|^2 = |\gamma_3|^2 = \beta_B^2(3 + F^2)$ .

In order to find the solution to the above recurrence, we introduce three extra variables:  
 $\Delta_4(N) = \Delta_1(N-1)$ ,  $\Delta_5(N) = \Delta_2(N-1)$ ,  $\Delta_6(N) = \Delta_3(N-1)$ , and the recurrences take the form:  
 $\Delta_1(N) = \xi\Delta_3(N-1) - \gamma^2\Delta_5(N-1)$  ;  $\Delta_2(N) = \xi\Delta_1(N-1) - \gamma^2\Delta_6(N-1)$  ;  
 $\Delta_3(N) = \xi\Delta_2(N-1) - \gamma^2\Delta_4(N-1)$  ;

or,  $\vec{v}_N = \Omega \vec{v}_{N-1}$ , with:

$$\vec{v}_N = \begin{pmatrix} \Delta_1(N) \\ \Delta_2(N) \\ \Delta_3(N) \\ \Delta_4(N) \\ \Delta_5(N) \\ \Delta_6(N) \end{pmatrix}, \text{ and } \Omega = \begin{pmatrix} 0 & 0 & \xi & 0 & \gamma^2 & 0 \\ \xi & 0 & 0 & 0 & 0 & \gamma^2 \\ 0 & \xi & 0 & \gamma^2 & 0 & 0 \\ 1 & 0 & 0 & 0 & 0 & 0 \\ 0 & 1 & 0 & 0 & 0 & 0 \\ 0 & 0 & 1 & 0 & 0 & 0 \end{pmatrix}.$$

The solution to this recurrence is  $\vec{v}_N = \Omega^{N-N_0} \cdot \vec{v}_{N_0}$  for any  $N > N_0 \geq 1$ .

### Energy Spectrum

We must impose  $\Delta_i(N \rightarrow \infty) \rightarrow 0$  in order to find the eigenenergies (which are those of a (111) surface-terminated bulk). This imposes  $\vec{v}_N \rightarrow 0$ . According to the solution to the recurrence written above, this is only possible if the eigenvalues of  $\Omega$ ,  $\lambda$ , lay within the complex unit circle. The bulk eigenvalues are thus obtained,

$$2\lambda^3 = \xi^3 - 3\xi\gamma^2 \pm \sqrt{(\xi^3 - 3\xi\gamma^2)^2 + 4\gamma^6}$$

and, the various bulk bands are given by  $|\lambda_i| < 1$ ,  $i = 1, 2, 3, 4, 5, 6$ .

Next, let us do a similar calculation, but taking into account explicitly the presence of the Cu monolayer. To do that, instead of letting the partial matrices to increase from the top left, we will let them increase from the bottom right, i.e., the last partial matrix will be the whole matrix. The determinant of the complete matrix will satisfy:

$$\text{DET} = a_{11} \left( a_{22}\Delta_2(N) - |\gamma_1|^2 \Delta_3(N-1) \right) - |a_{12}|^2 \Delta_2(N) = 0$$

We see that the recurrence relations are the same as in the case of a surface- terminated bulk. In order to solve the equation above, one need to evaluate  $\Delta_2(N)$  and  $\Delta_3(N-1) = \Delta_6(N)$ . Since the energy spectrum should be independent of  $N_0$ , then, when  $N \rightarrow \infty$ ,  $\Delta_1(N) \approx \Delta_2(N) \approx \Delta_3(N)$  and  $\Delta_1(N-1) \approx \Delta_2(N-1) \approx \Delta_3(N-1)$ , and are respectively, equal to:

$$\Delta(N-1) = \prod_{\vec{\theta}} [\alpha + 4\beta\Gamma(\theta_1, \theta_2, \theta_3)]$$

where,

$$\Gamma(\theta_1, \theta_2, \theta_3) \equiv \cos\left(\frac{-\theta_1+\theta_2+\theta_3}{2}\right) \left[ \cos\left(\frac{\theta_1-\theta_2+\theta_3}{2}\right) + \cos\left(\frac{\theta_1+\theta_2-\theta_3}{2}\right) \right] + \cos\left(\frac{\theta_1-\theta_2+\theta_3}{2}\right) \cos\left(\frac{\theta_1+\theta_2-\theta_3}{2}\right).$$

That is, the product of all the eigenenergies of the bulk. We notice:

$$\Delta(N) = [\alpha_A + 4\beta_B\Gamma] \cdot \Delta(N-1) .$$

Thus,

$$\text{DET} = \left\{ \left( a_{11}a_{22} - |a_{12}|^2 \right) \cdot [\alpha_A + 4\beta_B\Gamma] - a_{11}\gamma^2 \right\} \cdot \Delta(N-1) = 0 .$$

Substituting the definitions of the matrix elements, we obtain the spectrum of the monolayer-bulk system as the solution to the quadratic equation in E:

$$[(\alpha_C - E + \beta_{CC}F)(\alpha_A - E + \beta_S F) - \beta_{CA}^2] \cdot [\alpha_A + 4\beta_B F] - (\alpha_C - E + \beta_{CC}F)\beta_B^2 = 0$$

#### MONOLAYER OF COPPER ON (111) GOLD. NUMERICAL RESULTS.

Now we proceed to study the concrete case of a monolayer of Copper deposited on the (111) plane of Gold surface. Here again we use the basic TB equations to analyze the system but we will solve the corresponding eigenproblem numerically. We use,  $\alpha_C = 3.106\text{eV}$ ,  $\alpha_A = 1.410\text{eV}$ ,  $\beta_{CC} = -0.586\text{eV}$ ,  $\beta_B = -0.492\text{eV}$ ,  $\beta_{CA} = -0.539\text{eV}$ ,  $\beta_S = -0.492\text{eV}$ .

Since the surface states extend only a few layers into the bulk, their wave functions amplitudes are negligible far from the surface. We used the criterion that the surface states wave functions vanish at layer thirteen. Therefore in the TB approach, the eigenproblem is:  $P_{12 \times 12} \cdot V_{12} = 0$  where  $P_{12 \times 12}$  is the truncated P-matrix as defined above considering the first 12x12 elements and  $V_{12}$  is the vector of the C-coefficients truncated after the 12th element, as defined above.

Fig. 1 shows the normalized density of states (DOS) for the Copper on (111) Gold system calculating the energies of the surface states from the above expression. The dependence on the voltage is introduced by considering that only the first layer (the Copper adlayer) is affected by the electric field that decays to zero at interior layers. We find (Fig. 1) that DOS for the surface-bulk system is slightly dependent on voltage. They have a peak at about 1eV, high above Fermi energy ( $E_F$ ). Up to  $E_F$ , the DOS curve is higher at higher values of voltage (negative energies in Fig.1).

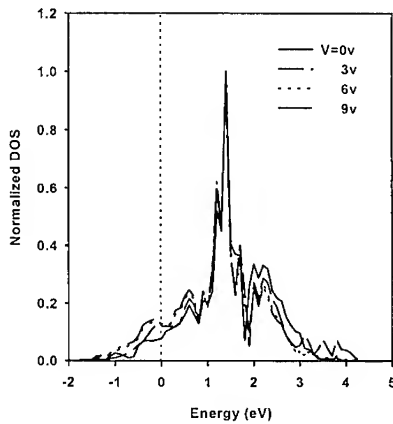


Figure 1. Surface DOS for different applied voltages. The vertical dotted line indicates the Fermi Energy.

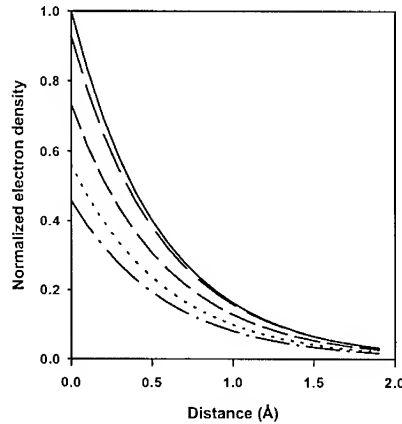


Figure 2. Decay of the electronic density for different applied voltages: 0V, 2V, 4V, 6V, and 8V. Upper curves correspond to lower voltages.

Fig. 2 shows the wave function amplitude on top of a Copper atom as a function of distance to the Copper plane. We see that, independently of the voltage, all the wavefunctions vanish at large distances as expected. At small distances however, the amplitude decreases with increasing



voltage. This is explained as follows. We evaluate the wave function amplitude as a non-coherent sum of amplitudes of TB eigenfunctions at energy  $E_F$ . We model the system as the Cu-Au system, electrically grounded, and an electrode at potential  $V$  in such a way that, when it is negative all the energy move up or, equivalently the surface Fermi energy is redefined to be  $E_F + eV$ . If  $V$  is positive, then  $E_F \rightarrow E_F - eV$ . This is in practice achieved by changing the TB parameter  $\alpha_C \rightarrow \alpha_C + eV$  or  $\alpha_C \rightarrow \alpha_C - eV$  and solve the corresponding eigenvalue problem. As the voltage is negatively increased, more and more surface levels reach the DOS peak and we see a significant increase in the value of the wave function. So the electron amplitude graph is almost a direct consequence of having more surface electrons populating states at  $E_F$ . This effect is measurable by electrochemistry means because the amplitude are not zero a distances above 1 Å.

A formalism based on the TB approach has been proposed to solve the quantum problem of electronic states at the surface of epitaxial monolayers deposited on FCC crystals. The method has analytical solutions and can be generalized for other substrate lattices. The surface states of a Cu monolayer on a Au (111) substrate has been studied as a function of the applied voltage. The system is easily solved with the method giving important information as local wavefunctions and density of states.

#### ACKNOWLEDGMENT

This work was supported by NSF OSR-94-52893. L. B. was also supported by ONR, and F.R. Z. by NASA-NAG8-1003. We appreciate useful conversations with Dr. Pablo Negrón.

#### REFERENCES

1. D.M. Kolb, K. Al Jaaf-Golze, and M.S. Zei, DEHEMA Monographien, **12**,53, Verlag Chemie Weinheim (1986); M. Zei, G. Qiao, G. Lehmppful and D.M. Kolb, Ber. Bunsenges, Phys. Chem. **91**, 3494 (1987).
2. L. Blum, H.D. Abruña, J.H. White, M.J. Albarelli, J.G. Gordon, G. L. Borges, M.G. Samant and O.R. Melroy, J. Chem. Phys. **85**, 6732 (1986).
3. L. Blum, Advances in Chemical Physics, S.A. Rice and I. Prigogine, Ed., J. Wiley, New York, **78**, 171 (1991).
4. D.A. Huckaby and L. Blum, J. Electroanal. Chem. **315**, 255 (1991).
5. L. Blum and D.A. Huckaby, J. Electroanal. Chem. **375**, 255 (1991).
6. L. Blum, D. A. Huckaby and M. Legault, Electrochimica Acta **41**, 2207 (1996).
7. M. Legault, L. Blum and D.A. Huckaby, J. Electroanal. Chem. **409**, 79 (1996).
8. M. Legault, D.A. Huckaby and L. Blum, J. Chem. Phys (in press).
9. S. Trassatti, J. Electroanal. Chem. **33**, 351 (1971).
10. J. Goodisman, Electrochemistry: Theoretical Foundations, Wiley and Sons, New York (1987)
11. W. Schmickler, J. Electroanal. Chem. **100**, 533 (1979).
12. A.A. Kornyshev and W. Schmickler, J. Electroanal. Chem. **185**, 253 (1985).
13. W. Schmickler, Chem. Phys. **141**, 95 (1990).
14. E. Leiva and W. Schmickler, Electrochimica Acta **40**, 37 (1995).
15. D. Price and J.W. Halley, Phys. Rev. **B23**, 12304 (1989).
16. L.A. Curtiss, J.W. Halley, J. Hautmann, N.C. Huang, Z. Nagy, Y.J. Ree and R.M. Yonco, J. Electrochem. Soc. **138**, 2033 (1991).
17. J. Ulstrup, Charge Transfer Processes in Condensed Media, Springer, Berlin (1979).
18. E.P.M. Leiva and W. Schmickler, Chem. Phys. Lett. **160**, 75 (1989).
19. E.P.M. Leiva, J. Electroanal. Chem. **350**, 1 (1993).
20. H. Honbo and K. Itaya, J. Chem. Phys. **88**, 1477 (1991).

## **SIMULATION OF DESORPTION KINETICS AT A LIQUID-SOLID INTERFACE**

T. W. SCOTT

Molecular Dynamics, Inc. Wharton, New Jersey 07885  
twscott@molydyn.com

### **ABSTRACT**

Molecular dynamics simulations are reported for the atomic motion of adsorbates at a liquid-solid interface. The rate for physical desorption is analyzed using the potential of mean force to describe adsorbate and transition state energies.

### **INTRODUCTION**

The behavior of fluids in contact with a solid surface remains an active area of research (1). It is widely accepted that liquid densities oscillate near a surface as the result of an external field superimposed on the fluid. The implications of these oscillations for interfacial chemical kinetics, however, have not been sufficiently explored. This work describes molecular dynamics simulations of atomic motion in the interphase and how this motion is influenced by temperature and the strength of the atom-surface interaction. While observed desorption kinetics can be described as a simple unimolecular decay, a deeper understanding of the activated process is provided by making a connection with the potential of mean force. This potential can be interpreted (2) as the free energy of the system as a function of the atom-surface separation. Regions with low values of this potential correspond to stable states (adsorption), while regions with high values can be attributed to barriers (3) on the pathway between states. Surface desorption of physically adsorbed atoms can then be interpreted as a unimolecular decay process with an activation energy determined by the difference in the potential of mean force. The potential itself can be determined directly from the structure in the simulated liquid density profile. It happens that the desorption rate constant shows an identical dependence on the potential of mean force regardless of whether the temperature or the atom-surface interaction is altered.

### **SIMULATION**

Simulations were performed using 1000 atoms with periodic boundary conditions applied to a rectangular simulation cell. A solid phase was placed at opposite ends of the cell. The cell length perpendicular to each surface was  $13.78\sigma$ , 25% longer than in the parallel directions. The simulation was carried out in the canonical ensemble (constant NVT).

Temperature was held constant by frequently rescaling the velocities. The equations of motion were solved by a finite difference method using a five term Gear predictor-corrector algorithm (4). The step size in reduced units was 0.0015. Using Xe as an example, each step would be 0.29fs and all desorption kinetics would reach 95% completion within 13ps.

### Interaction Potentials

The force exerted on an atom (i) near the surface is a combination of the force from all other liquid phase atoms ( $f_L^{ij}$ ) and the cumulative surface force ( $f_S^{ij}$ ) resulting from interaction with all atoms in the solid. Lennard-Jones 6-12 potentials were used for the atom-atom interactions

$$u_L(r_{ij}) = 4\epsilon_L \left[ \left( \frac{\sigma_L}{r_{ij}} \right)^{12} - \left( \frac{\sigma_L}{r_{ij}} \right)^6 \right] \quad (1)$$

The interaction energy of an atom and a solid surface is made up of the sum of its interactions with all atoms in the body. It is assumed here that the solid can be approximated as having a uniform number density (d). The mean field equation for the atom-surface potential (5) is then given by direct integration over all the atom-solid separations at a constant perpendicular distance from the surface (x)

$$u_S(x_i) = 2\pi\epsilon d \left[ \frac{2}{5} \left( \frac{\sigma}{x_i} \right)^{10} - \left( \frac{\sigma}{x_i} \right)^4 \right] \quad (2)$$

Equation 2 involves interactions between unlike atoms. The Lorentz-Bertheolt mixing rules (6) were used to express the potential depth ( $\epsilon$ ) and the distance from the surface where the potential is zero ( $\sigma$ )

$$\epsilon = \sqrt{\epsilon_L \cdot \epsilon_S} \quad (3a)$$

$$\sigma = \frac{\sigma_L + \sigma_S}{2} \quad (3b)$$

### Density Profile

The local density  $\rho(x)$  was calculated during each run by counting the number of atoms with any value of (y) or (z) in the simulation cell, but with (x) values lying only between (x) and (x+ $\Delta x$ )

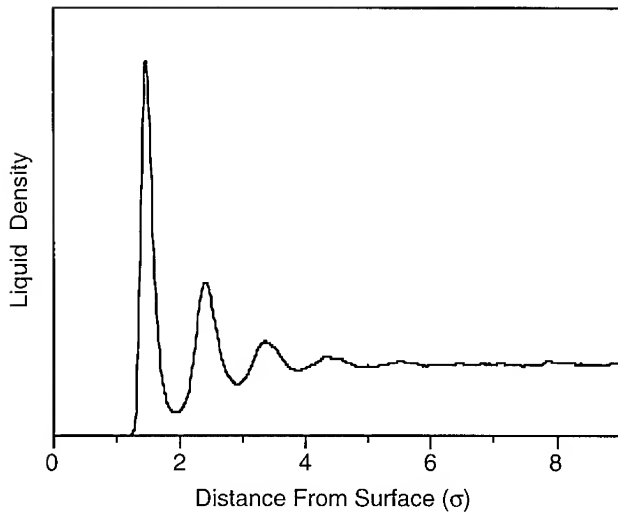


Figure 1 - Density profile of a Lennard-Jones liquid in contact with a smooth flat wall. Successive peaks show multilayer adsorption which gradually gives way to the bulk fluid density.

$$\rho(x) \approx \frac{1}{\Delta x} \sum_{i=1}^N \delta(x - x_i) \cdot \Delta x \quad (4)$$

Figure 1 shows the density profile at the reduced temperature  $T=2.0$  and using an atom-surface interaction strength of  $d=2.0$  with  $\varepsilon=1.15 \cdot \varepsilon_L$  and  $\sigma=1.5 \cdot \sigma_L$ . The multiple peaks arise from structuring of the liquid near the surface. These oscillations decay over several atomic layers. The peak closest to the surface is taken to represent the first layer of adsorbates. The constant density at large distances from the surface verifies that the second solid surface in the simulation did not alter the liquid properties near the first surface.

#### Potential of Mean Force

Of the vast number of interactions in a 1000 atom simulation, this work considers only the few degrees involved in atomic desorption. Desorption occurs under the influence of all the other degrees. Statistical mechanics (7) provides a means of expressing the average dependency of the degree of freedom of interest on the residual degrees of freedom: the potential of mean force  $\Delta V(x)$ .

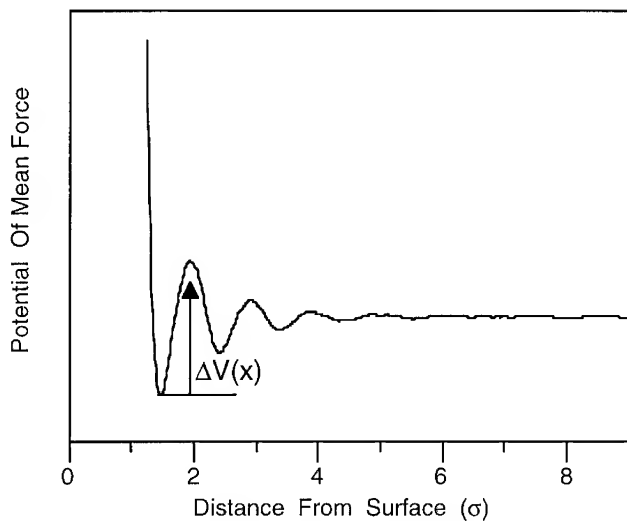


Figure 2 - Potential of mean force calculated from the density profile shown in Fig. 1. The vertical arrow indicates the energy barrier to desorption.

$$\Delta V(x) = -k_B T \cdot \ln \left( \frac{\rho(x_2)}{\rho(x_1)} \right) \quad (5)$$

Figure 2 shows the potential of mean force as a function of distance from the solid surface. In Eqn. 5  $\Delta V(x)$  is the free energy difference between  $(x_1)$  and  $(x_2)$ . This makes a natural connection with transition state theory for the desorption rate constant.

### Desorption Kinetics

After achieving equilibrium, the adsorbates at time zero were labeled. The loss of the initial adsorbates was then monitored at successive time delays. Desorption kinetics, neglecting readsorption of previously desorbed atoms, is described in this work as a single exponential decay

$$A(t) = A_0 \cdot \exp(-k t) \quad (6)$$

Figures 3 shows plots of  $\ln[A/A_0]$  verses time for different temperatures and surface forces. The slope in each case gives the desorption rate constant ( $k$ ) for specific values of ( $T$ ) and ( $d$ ).

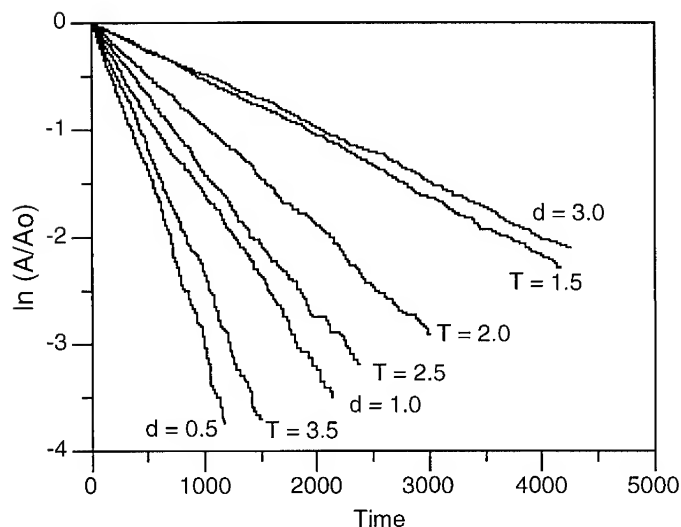


Figure 3 - Plot of the logarithm of the adsorbate number density versus time. Different reduced temperatures ( $T = 1.5, 2.0, 2.5, 3.5$ ) and surface forces ( $d = 3.0, 1.0, 0.5$ ) are displayed.

Assuming an Arrhenius equation for the form of the rate constant, where  $\Delta V$  is used as the activation energy, simulated rates should show a logarithmic relationship with the potential of mean force  $\Delta V(x)$ .

$$\ln\left(\frac{k_2}{k_1}\right) = -\left[\frac{\Delta V_2}{k_B T_2} - \frac{\Delta V_1}{k_B T_1}\right] \quad (7)$$

Properties which alter  $\Delta V$  should modify the desorption rate constant with exponential strength. This dependence has been tested as a function of temperature and atom-surface interaction strength. Figure 4 compares the simulation results with the linear plot expected for  $\ln(k_2/k_1)$  versus  $\Delta V$  at different temperatures and surface forces. Of the various ways of changing the surface interaction, we altered only the number density of atoms in the solid ( $d$ ).

## CONCLUSIONS

The potential of mean force correlates well with the logarithm of the desorption rate constant. Oscillations in the liquid density profile yield the energetics that control the desorption rate. Variations in either the temperature or atom-surface interaction strength give the same correlation curve when expressed in terms of the potential of mean force.

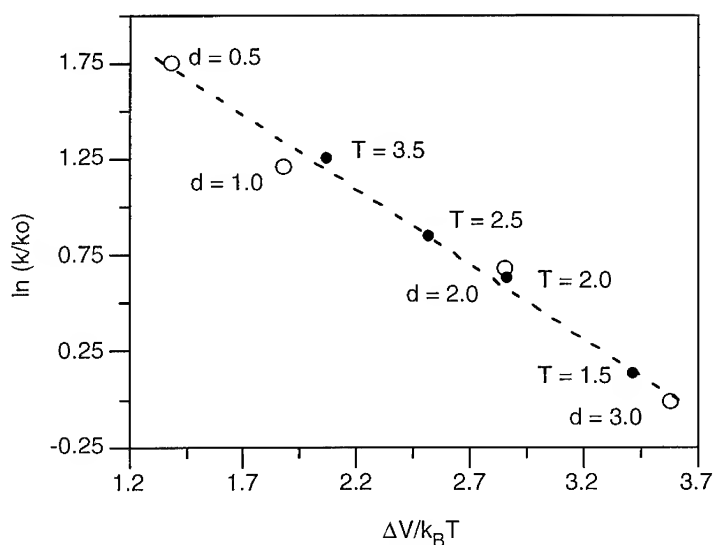


Figure 4 - Correlation between the rate constant ( $k$ ) and the potential of mean force at a series of temperatures ( $T=1.5, 2.0, 2.5, 3.5$ ) and surface forces ( $d=0.5, 1.0, 2.0, 3.0$ ). Notice that a single line fits both data sets.

## REFERENCES

1. M. Schoen, Computer Simulation of Condensed Phases in Complex Geometries, Springer-Verlog, Berlin, 1993.
2. T. C. Beutler and W. F. van Gunsteren, J. Chem. Phys. **100**, p.1492 (1994).
3. T. Lazardis, D. J. Tobias, C. L. Brooks III and M. E. Paulaitis, J. Chem. Phys. **95**, p.7612 (1991).
4. J.M. Haile, Molecular Dynamics Simulation, John Wiley, 1992, pp. 160-163.
5. J. N. Israelachvili, Intermolecular & Surface Forces, Academic Press, 1992, pp. 155-157.
6. M.P. Allen and D.J. Tildesley, Computer Simulation of Liquids, Clarendon Press, Oxford, 1994, p. 21.
7. D. Chandler, Modern Stastical Mechanics, , Oxford University Press, 1987, pp. 201-202.

**Part II**

**Pattern Formation During  
Film Growth**



## **ELECTROCHEMICAL SYNTHESIS AND PROCESSING OF MATERIALS: FROM FRACTAL ELECTRODES TO EPITAXIAL THIN FILMS**

FEREYDOON FAMILY

*Department of Physics, Emory University, Atlanta GA 30322*

### **ABSTRACT**

Electrochemical processes hold great promise as flexible and effective tools for synthesis and processing of a wide range of materials from fractal electrodes to epitaxial nanostructures. The key to successful application of electrochemical techniques is in understanding the kinetic processes which control the evolution and the morphology of the surface at the solid-liquid interface. This paper provides a review of recent advances made by different electrochemical communities in recent years in studies of the growth and modification of a wide variety of materials. The topics covered include studies of pattern formation and growth of dendritic and fractal structures in electrodeposition, kinetic roughening and dynamic scaling of surfaces fluctuations during electrochemical deposition and dissolution, as well as recent progress in electrochemical growth of epitaxial layers and nanostructures.

### **INTRODUCTION**

Electrochemical techniques are used to grow materials with a wide variety of structural properties ranging from fractal electrodes to epitaxial thin films, as well as to manipulate the surface morphology of materials by electropolishing and electrodedissolution. The rapid development and use of in-situ analytical probes have made it possible to directly study a variety of microscopic processes at the liquid-solid interface. This has added a new dimension to the range of methods that are available for characterization, analysis and control of electrochemical processes. In particular, in recent years, a number of research communities have independently used electrochemical techniques to grow a variety of novel materials and structures as well as to study various materials related issues. Since there has been little overlap among these communities, a unified language or approach for understanding materials synthesis and processing by electrochemical techniques has not yet emerged. This is in sharp contrast to the case of various vacuum deposition and sputtering techniques where considerable progress has been made in understanding many of the key issues through synthesis of experimental, theoretical and simulational efforts.

The aim of this review is to bring together the results of various investigations from different communities that have been studying materials related problems using electrochemical techniques. I hope that these discussions will promote interchange of ideas among different groups and promote further discussions which would eventually lead to the development of a unified framework for understanding the key mechanisms which control electrochemical processes at the solid-liquid interface.

For the sake of clarity I have divided the paper into three parts, along the lines of activities of different electrochemical materials communities. The first part is related to the general problem of the kinetics of aggregation and pattern formation [1-8 (for an early paper also see ref. 9)]. This part begins with a discussion of the growth of disordered patterns and structures in electrochemical deposition [10-28]. The main question of interest is understanding the structure of the variety

of dendritic and fractal [29] aggregates that form over a relatively large range of length scales from micrometers to centimeters. The second part discusses the problem of kinetic roughening [30,31] and dynamic scaling [32] of surface fluctuations during electrochemical deposition [33-37] and dissolution [38-41]. Understanding the dynamics of fluctuating surfaces and interfaces is a problem of central importance in a wide variety of fields [30,31], and studies of surface roughening in electrochemical processes [33-41] have been an integral part of the growing interest in this subject. The key questions here include the mechanisms that control the evolution and structure of fluctuating surfaces [30,31]. In the third part of the paper I discuss various efforts that have been made to grow epitaxial thin films and nanostructures using electrochemical techniques [42-61].

In order to make this review useful for experts in different fields, I have not necessarily followed a chronological order in the references. Instead I have included references that discuss key issues that could not have been discussed in detail in this short paper.

## DISORDERLY GROWTH AND PATTERN FORMATION

The spontaneous formation of random or regular patterns with special characteristics such as fractal geometry [29] and dendritic features is a common occurrence in many natural and industrial processes [1-6]. For this reason in the past decade there has been great interest in understanding the kinetics of aggregation [1-7] and the phenomenon of pattern formation [2,8] in the context of non-equilibrium growth phenomena. Electrochemical deposition generally leads to the growth of a metallic aggregate in an electrochemical cell filled with a solution of a salt of the metal, by imposing a potential difference and a finite current across the cell. It has been known for a long time that the morphology of the deposit can range from a forest of open tree-like structures to compact three dimensional aggregates. Thus, in recent years there has been great interest in understanding the mechanisms which give rise to these morphologies [10-28]. This effort parallels other studies in the fields of aggregation [1-7] and pattern formation [2,8], where the role of various physical and chemical processes in determining the evolution and the structure of patterns formed under far from equilibrium conditions have been studied. The richness of the patterns and the complexity of the microscopic kinetics that are present have made electrodeposition an ideal environment for sorting out the role of various processes on the growth of regular as well as random patterns.

From a technological point of view electrochemical processes play an important role in battery design, electroplating, and the production of metal powders. It is also a subject of considerable interest due to the important role of complex interfaces in many scientific and engineering problems [for example, see ref. 62 and references therein]. The reason is that many natural and industrial processes take place through surfaces or across interfaces between two media. These processes may involve both chemical and physical effects that are similar to those taking place in electrochemical deposition. Examples are mass and charge transport due to diffusion and drift in potential gradients. For example [62], the roots of a tree exchange water and inorganic salts with the earth through the surface of the roots. Oxygen in the air is exchanged with blood hemoglobin through the surface of the pulmonary alveoli. Similarly, the current supplied by a battery to a car flows through the interface between the electrode and the electrolyte. Thus, understanding the growth and the morphology of patterns in electrodeposition is of considerable interest.

In many applications it is advantageous to use electrodes with very large surface area [63]. Since many experimental conditions lead to the growth of open fractal structures, it is clear that it

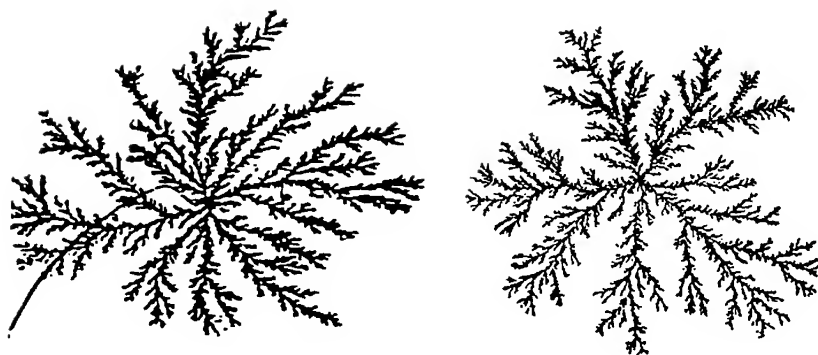


**Fig. 1:** The discovery [11] of the striking similarity between the fractal pattern of the two-dimensional electrodeposits, like the copper aggregate shown on the left, and the morphology of typical computer generated diffusion-limited aggregation (DLA) clusters, like the one shown on the right, led to considerable excitement and interest.

would be quite useful to use electrochemical deposition for growing macroscopically large electrodes [63]. However, electrodeposits are often quite fragile and can hardly be withdrawn from the solution without breaking apart [20]. Although some important progress has been made in this direction [63], a much deeper understanding of electrodeposition processes is needed for producing strong and robust electrodes that would be technologically useful.

The initial excitement (see Fig. 1) and interest in studies of pattern formation in electrochemical deposition was prompted by the pioneering works of Brady and Ball [10] and Matsushita et al. [11] who suggested that electrochemical deposits have a fractal geometry that are similar to the fractal patterns formed by diffusion-limited aggregation (DLA), which is a cluster growth process introduced by Witten and Sander [7]. The argument given in support of this conjecture was that in ideal electrochemical deposition, the potential controlling transport of the depositing species obeys the diffusion equation, which in the quasistatic approximation reduces to Laplace's equation,

$$\nabla^2 \phi = 0, \quad (1)$$

and therefore it was assumed that electrodeposition maps directly into the DLA problem [10,11]. This led to a number of studies of pattern formation in electrochemical deposition, particularly in quasi-two dimensional cells where at low voltage and concentrations, patterns such as the one in Figure 1 were obtained that had a spectacular similarity to the fractal structure of two-dimensional DLA clusters. Subsequent studies [12-28], however, found that a wide variety of other patterns, such as those shown in Figure 2, can be routinely formed by changing the experimental parameters such as cation concentration, applied potential difference, electrode separation, cell thickness and the presence of inert as well as chemically active electrolytes. Besides DLA-like patterns, dendritic

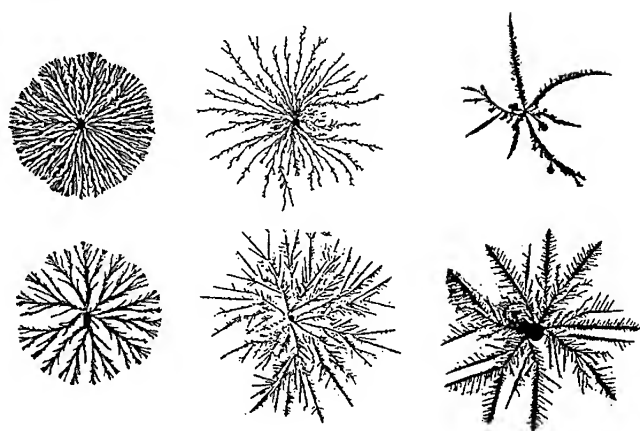


**Fig. 2:** Examples of some of the non-DLA like morphologies that are routinely observed in quasi-two dimensional electrodeposition.

[12] and dense radial morphologies [12-14], as well as unusual morphological transitions, such as the Hecker effect [64], were observed.

The growth of different patterns in electrodeposition presented a puzzle. If one assumes that the electrolyte is uniform and neutral everywhere (except in the double layer at the electrode surface that is less than 1 nm thick at high concentrations), then the static potential  $\phi$  must obey eq. 1. The fact that the morphological phase diagram in electrochemical deposition was found to be much richer than had been originally thought indicates that the full electrochemical equations must involve other parameters in addition to the potential  $\phi$ .

As a first attempt in developing a more realistic model of electrodeposition, Chazalviel [27] developed a theory involving some of the electrochemical aspects of the growth by taking into account the displacement of the ions in the solution due to both electric migration and diffusion. The results of Chazalviel [27] lead to the conclusion that the growth speed of the deposit is the speed at which the anions withdraw from the deposit. That is,  $v_a = -\mu_a \mathbf{E}_{bulk}$ , where  $\mu_a$  is the mobility of an anion and  $\mathbf{E}_{bulk}$  is the field in the electrolyte facing the branches. This was confirmed by a different independent theoretical analysis by Melrose, Hibbert and Ball [24]. Chazalviel's results also indicate that there must exist a large charged region near the cathode and the deposit. Measurements [25,26,65-68] of the potential in the vicinity of the deposit showed that a local and very sharp potential does indeed exist near the tips. By varying the electric field, the cell geometry and the salt, the growth speed was also shown to be quite accurately given by the recession speed of the anions [65-71].

Although Chazalviel's model [27] provided considerable insight into the complexities of electrochemical growth mechanisms, it was soon realized that measurements around actual branches were very different from the predictions of the model. A number of independent studies reached



**Fig. 3:** A typical shadowgraph shows the concentration gradients due to electroconvection near the tips of growing deposits [from ref. 70].

the conclusion that hydrodynamical convection must also be considered. Bruinsma and Alexander [72] noted that most experiments were performed at current densities far exceeding the diffusion limit of the Nernst theory, so that convection must be taken into account. In the presence of a flow field, spontaneous charge fluctuations are enhanced by the velocity gradients, which in turn generate gradients in the electrical force acting on the fluid body causing electroconvection. This positive feedback mechanism results in an instability as the applied electric field is increased. In fact, this could have been seen in the early work of Suter and Wong [18] who found that the current across the cell exhibited spontaneous oscillations in the regime of dendritic growth where the current density was high. This suggests the buildup and breakdown of space charge at the growth tips. The existence of electroconvection has been discussed by several groups [65-77] and direct evidence for it has been found through observations of concentration gradients and fluid motion near the deposit. Shadowgraphs like the one in Figure 3 taken near the tip of the deposits clearly show the concentration gradients due to electroconvection [70].

At higher concentrations shadowgraph studies have shown that natural convection dominates over electroconvection and both laminar and turbulent convection exists near the deposits at the cathode. This has led to the development of semi-quantitative models of convection-driven growth which show that the dynamics of electrodeposition at high velocities is distinctly different from diffusive growth.

More recently it has been found that gravity also induces convection in a thin cell geometry. The depletion of the electrolyte near the cathode induces a density difference of a few percent, which is enough to trigger motion of the electrolyte. Depending on the orientation of the cell, plumes or gravity currents can be observed [69,74-76]. In fact, natural convection exists at both electrodes since the density contrasts are similar. Recently an extension of Chazalviel's theory [27] which includes hydrodynamical effects has been worked out by Chazalviel and co-workers [77]. The results of this model are in reasonable agreement with experiments.

Although the importance of various bulk effects are now well established, the question of what role these effects play in determining the observed morphologies in electrochemical deposition is still not fully resolved. The reason is that the morphologies observed in the experiments are determined both by the dynamical processes in the bulk as well as surface kinetics, which have not been studied in as much detail as the bulk properties.

In general, four distinct classes of patterns have been observed in electrodeposits. These are (i) randomly branched DLA-type fractals, (ii) dense branching morphology which has a relatively

sharp front, (iii) regular dendritic crystal-like structures with well defined sidebranching which appear at a fixed angle with respect to the main part of the dendrite, and (iv) structures that are quite similar to Saffman-Taylor viscous fingering-type patterns observed in Hele-Shaw cells [78]. Clearly there are many crossover regimes in which a combination of any of these four types of patterns can be observed. However, depending on the experimental conditions and parameters, one can clearly distinguish between these four types of growth morphologies.

It should be emphasized that there still does not exist a unified answer to the basic question of what are the conditions that lead to the formation of each one of the four types of morphologies or what causes the type of morphological transitions that are observed in experiments. Perhaps the key to understanding the origin of various patterns must come from detailed studies of surface kinetics which is the subject of the next section.

## SURFACE ROUGHENING AND DYNAMIC SCALING

The study of the spatial and the temporal fluctuations of the surface in electrochemical processes is the second area in which there has been considerable activity in the past decade [33-41]. The goal of these studies is to determine processes which control the evolution and the roughening of the interface in electrochemical deposition and dissolution. In addition to the interest in understanding basic electrochemical processes, the main impetus behind these studies has been the development of dynamic scaling [32] concepts which have been extensively applied to studies of a wide variety of other surface growth phenomena [30,31]. Therefore I will begin this discussion by first presenting a brief introduction to dynamic scaling [32] before discussing various experimental and theoretical studies of surface fluctuations in electrochemical deposition [33-37] and dissolution [38-41].

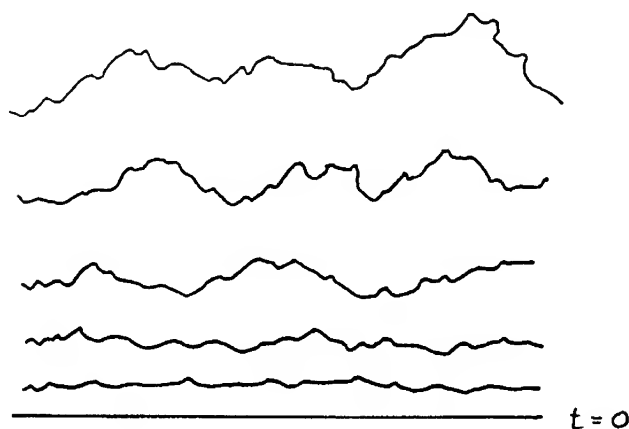


**Fig. 4:** Snapshots of a surface at different times show how a fluctuating surface wrinkles with time.

### Dynamic Scaling

Figure 4 shows snapshots of a dynamically evolving or growing surface at several different times after the surface began to roughen starting from an initially flat surface at time  $t = 0$ . It is important to note that the roughening process shown in Fig. 4 can be caused by either addition of new materials or by dissolution or erosion from an initially flat surface. Therefore, kinetic roughening is observed in both electrochemical deposition as well as electrochemical dissolution. In both cases the basic question is how can one characterize such a fluctuating surface? The dynamic scaling concept [32] is based on the assumption that since surface fluctuations occur over a wide range of length scales, it is possible that fluctuating surfaces may exhibit scale invariance. The basic physics of surface growth is the spread of fluctuations which roughen the surface and introduce correlations between different parts of the surface [30,31]. In particular, as surface fluctuations spread, the surface wrinkles both in the lateral direction parallel to the surface as well as in the direction perpendicular to the surface.

The basic assumption behind the dynamic scaling concept [32] is that there exist two different correlation lengths  $\xi_{\parallel}$  and  $\xi_{\perp}$  that characterize the spread of surface fluctuations in the two directions parallel and perpendicular to the surface, respectively. The length  $\xi_{\parallel}$  is a measure of the extent of a typical surface feature at time  $t$  and can be determined from the measurements of surface correlation functions or the structure function along the surface [30,31]. On the other hand,  $\xi_{\perp}$  is a measure of the surface roughness or the surface width and is often determined by calculating the root-mean-square of the surface height fluctuations [32,30,31].

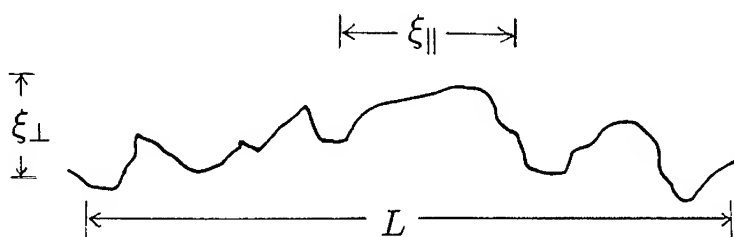


**Fig. 5:** The perpendicular correlation length  $\xi_{\perp}$  and the lateral correlation length  $\xi_{\parallel}$  are the two important characteristic lengths in the problem.  $L$  is the “window size” over which measurements are made.

Figure 5 shows a schematic picture of a typical rough surface and the two correlation lengths  $\xi_{\parallel}$  and  $\xi_{\perp}$  at some arbitrary time  $t$ . According to the dynamic scaling assumption [32] the correlation lengths  $\xi_{\parallel}$  and  $\xi_{\perp}$  diverge as a power-law in time. In particular, defining the *spreading exponent*  $n$  and the *growth exponent*  $\beta$  we can write,

$$\xi_{\parallel} \sim t^n \quad \text{and} \quad \xi_{\perp} \sim t^{\beta}. \quad (2)$$

This type of scaling behavior has been observed and used to characterize the dynamics of surfaces in a wide variety of theoretical and simulational models as well as different experiments [30,31].

Scaling relations (2) are quite general and can be used to study the dynamics of surfaces and interfaces irrespective of the morphology of the surface, i.e. these relations do not assume that the surface is geometrically scale-invariant or fractal. The values of the exponents  $\beta$  and  $n$  depend on the microscopic dynamical properties of the system, but recent studies have shown that it is possible to define a few broad universality classes to which a large number of different surface growth phenomena belong [30,31]. Thus the dynamic scaling approach [32] allows an elucidation of the physics of a particular system by studying its scaling behavior. In many problems there exists a relation between  $\beta$  and  $n$  so that only a single exponent is needed to describe the dynamics of the system.

The scaling relations (2) are analogous to the dynamic scaling expression in critical phenomena where the characteristic length scale in the system is assumed to grow as  $t^{1/z}$  where  $z$  is the *dynamic scaling exponent*. In surface growth literature [30,31] the dynamic scaling exponent is often defined by writing,  $\xi_{\parallel} \sim t^{1/z}$ , so that  $n = 1/z$ .

The scaling relations (2) imply that one can generally write,

$$\xi_{\perp} \sim \xi_{\parallel}^{\alpha} \quad \text{where} \quad \alpha = \frac{\beta}{n} = \beta z. \quad (3)$$

This relation expresses the fact that in general there exists a non-trivial scaling relation between the correlation lengths  $\xi_{\parallel}$  and  $\xi_{\perp}$ . This scaling relation implies that a rough surface may have a self-affine fractal geometry [5] which can be characterized by a *roughness exponent*  $\alpha$  [32]. The value of  $\alpha$  depends on the microscopic details of the system which defines the universality class to which the system belongs [30,31].

In studies of surface growth one typically concentrates on a part or a segment of the surface of length  $L$  (see Fig. 5). This implies that as surface fluctuations spread there exists a finite correlation time  $\tau$ , defined by  $\tau \sim L^z$ , at which the lateral correlation length  $\xi_{\parallel}$  becomes comparable to the length  $L$ . For  $t > \tau$  the surface roughness  $\xi_{\perp}$  cannot grow and it reaches a constant value that depends on  $L$ . In applications of dynamic scaling [32] one generally considers the scaling of the surface roughness or the width  $w(t, L)$  which is a measure of  $\xi_{\perp}$  and is defined as the root-mean-square of surface fluctuations. Then the dynamic scaling expression is written in its more familiar form [32],

$$w(L, t) = L^{\alpha} f(t/L^z) \quad (4)$$

where the scaling function  $f(x)$  goes to a constant for  $x \gg 1$  and  $f(x) \sim x^{\beta}$  for  $x \ll 1$ . The dynamic scaling expression (4) implies that plots of  $w(L, t)L^{-\alpha}$  against  $t/L^z$  for various  $L$  must all collapse onto a single curve [32]. This type of scaling has been verified in a wide variety of models as well as experimental systems [30,31].

The surface exponents  $\alpha$  and  $\beta$  can also be determined from various types of surface correlation functions [30,31]. As an example, consider the height difference correlation function  $c(r, t)$  which is defined by,

$$c(r, t) = [(\bar{h}(\mathbf{r}', t') - \bar{h}(\mathbf{r} + \mathbf{r}', t' + t))^2]_{\mathbf{r}', t'}^{1/2}, \quad (5)$$

where  $h(\mathbf{r}, t)$  is the height of a single-valued surface at position  $\mathbf{r}$  on a  $(d-1)$ -dimensional surface at time  $t$ ,  $\bar{h} = h - \bar{h}$  and  $\bar{h}$  is the average position of the interface. On the basis of the dynamic



scaling form (4), for  $r \ll L$  the correlation functions  $c(r, 0)$  should vary as,

$$c(r, 0) \sim r^\alpha, \quad \text{for } r \ll L, \quad (6)$$

and for fixed  $r$  and  $t \ll \tau$ ,  $c(0, t)$  scales as,

$$c(0, t) \sim t^\beta, \quad \text{for } t \ll \tau. \quad (7)$$

The scaling relations (6) and (7) persist as long as  $r \ll L$  and  $t \ll \tau$ . Beyond these limits the correlation functions  $c(r \rightarrow \infty, 0)$  and  $c(0, t \rightarrow \infty)$  saturate to constant values that depend on  $L$ . The scaling of these values can also be used to determine  $\alpha$  and  $\beta$ .

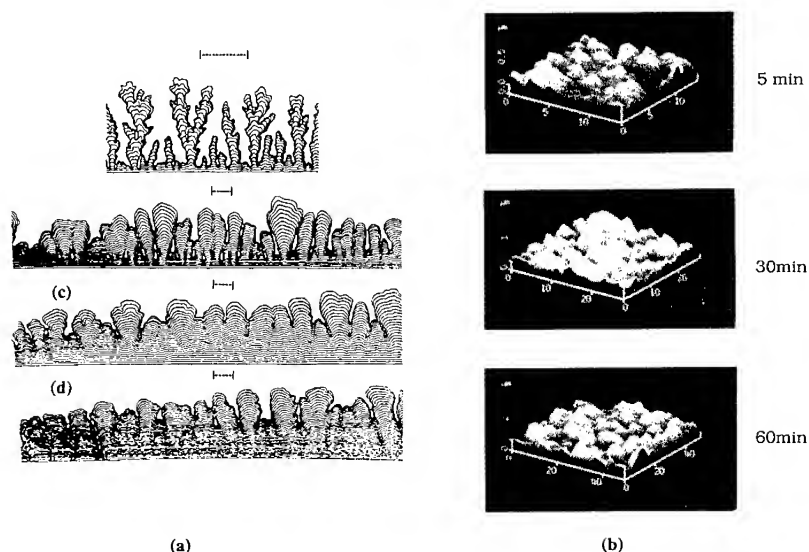


**Fig. 6:** (a) Surface evolution in slow electrochemical deposition of Cu from a line [From ref. 34] leads to the formation of columnar structures at late stages of the growth. Scale bar is 0.5 mm. (b) Atomic-force microscope images of the surface morphology of copper electrodeposited on a two-dimensional surface are shown after 5, 30 and 60 minutes [From ref. 36]. To demonstrate the self-similarity of the surface morphology, the vertical and the horizontal scales have been anisotropically changed according to the dynamic scaling.

#### *Kinetic Roughening in Electrodeposition*

The first experimental study of kinetic roughening in electrochemical deposition was carried out by Bursill, Julin and Xudong [33]. They studied the surface fluctuations of electrochemically deposited palladium hydride dendrites which were deposited on 3 mm discs cut from 25  $\mu\text{m}$  thick Pd

foil. They determined the roughness exponent  $\alpha$  of a number of different samples from calculations of both the correlation function and the width. A detailed study of their results shows that in the early stages of the growth the exponent  $\alpha$  is typically in the range  $\alpha \simeq 0.8 - 0.9$ . As already noted by Bursill et al [33], the interface morphology at later stages of the growth changes from a random pattern to a quasiperiodic cellular structure with a well defined characteristic wavelength. This can be clearly seen in Fig. 1 of their paper where the late stage patterns show clear periodic structures. They found that the roughness exponent for length scales smaller than this characteristic length is in the range  $\alpha \simeq 0.46 - 0.54$ . This is consistent with the value of  $\alpha = 0.55 \pm 0.06$  obtained by Kahanda et al. [34] for the roughness of columns in the late stages in the deposition of copper from  $\text{CuSO}_4$  solutions. Figure 6a shows some typical patterns obtained by Kahanda et al. [34]. As can be seen, at late stages of the growth these patterns have a characteristic columnar or periodic structure. These are similar to what was observed by Bursill et al. [33]. However, unlike Bursill et al. [33], Kahanda et al. [34] did not measure  $\alpha$  in the early stages of the growth.

The above experiments were both carried out in thin cells on quasi one-dimensional interfaces. More recently, Iwamoto, Yoshinobu and Iwasaki [36], and Iwasaki, Iwamoto, Sudoh and Yoshinobu [37] have used atomic force microscopy to study the two-dimensional morphology of copper deposits. Typical images of the two dimensional surface of the deposited copper obtained by Iwamoto et al. [36] are shown in Figure 6b. They have measured both  $\alpha$  and  $\beta$ . They find  $\alpha = 0.87 \pm 0.05$  and  $\beta = 0.45 \pm 0.05$ . These values do not belong in an obvious way in any of the universality classes for surface growth. In fact, both Bursill et al. [33] and Iwasaki et al. [37] have proposed that the origin of the discrepancy between their results and the standard surface growth models that are based on local dynamics is the presence of non-local effects due to the diffusion field [7]. This scenario would imply that at long-times and large length-scales surface instabilities would lead to a value of  $\alpha = 1$ . However, for finite times  $\alpha$  crosses over from  $1/2$  to  $1$ . Thus, the value of  $\alpha \simeq 0.8 - 0.9$  may be an intermediate value that is observed in the crossover region.

#### *Kinetic Roughening in Electrodeposition*

In addition to deposition, surface roughening due to electrochemical dissolution has also been investigated [38-41]. Processes involving removal of materials [38-41] from surfaces are important in a wide range of applications including etching, electropolishing, erosion, corrosion, passivation and battery technology. Despite their obvious technological importance, the morphological aspects of many of these processes had received little attention. However, there has been considerable interest over the years on the role of various kinetic mechanisms in chemical dissolution [79]. It is well known that dissolution is mainly controlled by surface reactions involving interfacial charge transfer. Surface dissolution occurs mainly at active sites where atoms are weakly bonded to the surface. The number of such sites is dependent on the structure and the morphology of the surface. Thus, dissolution rate is higher in rough surfaces which have a larger number of exposed surface sites. Therefore, studies of the roughening of the metal-electrolyte interface can provide valuable insight into the link between the evolution of the surface morphology and the kinetics of dissolution.

Fernandes, Latanision and Searson [38] studied the anodic dissolution of a metal-electrolyte interface. They used a simple cubic solid-on-solid (SOS) model with interactions limited to nearest-neighbors. The exposed surface was assumed to be a (001) surface. The SOS restriction requires that every surface occupied site be directly above another occupied site. Equilibrium properties of the SOS surface are well known [31]. In particular the surface undergoes a roughening transition at some finite temperature.

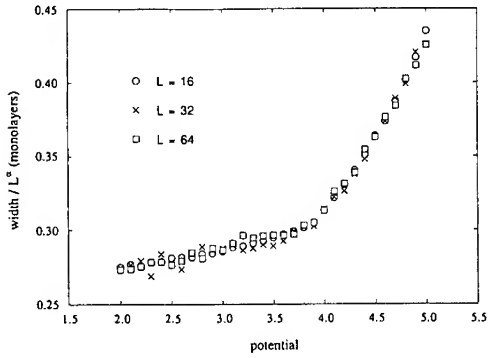


**Fig. 7:** Scaled width in the dissolution model is plotted as a function of the external potential  $\eta$ . The marked change in the behavior of the width at  $\eta \simeq 3.9$  indicates a change in the rate of dissolution of kink sites [From ref. 38].

Fernandes et al. [38] developed an activated hopping SOS model to simulate driven dissolution under the application of an anodic potential. They neglected surface diffusion and assumed a dissolution probability,

$$p_{diss} = \min[1, \exp(\Delta E)], \quad \text{with} \quad \Delta E = -z \frac{V}{k_B T} + \eta, \quad (8)$$

where  $z$  is the number of nearest-neighbor surface atoms,  $V$  is the nearest-neighbor bond strength, and  $\eta > 0$  is a dimensionless parameter that accounts for the applied anodic potential. Monte Carlo sampling was carried out with surface atoms chosen at random. The simulations [38] were carried out at a fixed temperature with  $V = 0.05$  eV such that  $V/k_B T = 1.95$ . The potential term was varied in the region  $2 < \eta < 5$ . Scaling of the data for the saturated width for different system sizes gave a value of  $\alpha = 0.28 \pm 0.02$ . As shown in Figure 7, however, an abrupt change was found in the slope in plots of  $w(L)/L^\alpha$  vs  $\eta$  at  $\eta \simeq 3.9$ . This implies that the surface is much more sensitive to changes in the applied potential for  $\eta \geq 3.9$ .

The nature of the transition can be qualitatively understood in terms of the rate of dissolution of different surface site configurations. In particular, Fernandes et al. [38] found that near the transition the number of atoms at kink sites, i.e. atoms with 3 nearest-neighbors dramatically increased and this was followed by a corresponding decrease in the number of atoms embedded in terraces, i.e. those having 5 nearest-neighbors. On the basis of this observation the authors have conjectured that there might be an analogy between this model and the height-conserved model studied by Sun, Guo and Grant [80]. However, further work is needed to fully understand the relation between the discrete dissolution model and the origin of the observed transition and the other models of surface roughening [30,31].

From an experimental point of view, Vela, Andreasen, Salvarezza, Hernández-Creus, and Arvia [41] used the dynamic scaling approach to study the evolution of the roughness during the electro dissolution of silver single-crystal surface domains in contact with aqueous 1M  $HClO_4$  derived from *in situ* sequential STM imaging. The electrochemical cell consisted of a small Kel-F cell ( $1.1 \times 2.0 \text{ cm}^2$ ) in which an annealed polycrystalline silver plate electrode, a large Pt counterelectrode, and a Pt reference electrode were lodged. The working electrode was mechanically polished first and then annealed. This resulted in Ag(111) surface consisting of smooth single crystal domains  $100 \text{ nm}^2$  in size. The constant current silver electro dissolution was carried out at current densities in the range  $4 \mu\text{A cm}^{-2} < j < 30 \mu\text{A cm}^{-2}$ . From STM images of the surface, Vela et al. [41] obtained  $\beta = 0.36 \pm 0.08$  and  $\alpha = 0.87 \pm 0.01$ . The values of  $\alpha$  and  $\beta$  found in the dissolution experiment are close to the values obtained by Iwamoto et al. [36] and Iwasaki et al. [37] in electrodeposition of Cu. This agreement suggests that the same processes that control surface growth may be responsible for surface dissolution. Clearly further experimental studies are needed to test this possibility.

Vela et al. [41] also used Monte Carlo simulations to model electro dissolution. They proposed two models, based on a site dependent detachment probability as well as surface diffusion and obtained values of the exponents similar to the Wolf-Villain model [81] which is known to exhibit a groove instability [82]. However, due to the presence of surface diffusion, this model is not in the same universality class as the model of Fernandes et al. [38].

#### *Future Work on Kinetic Roughening*

Despite the above efforts, many questions still remain. For example there still exists confusion regarding the definition of the dimensionality and its effect on the exponents. For example, Pastor and Rubio [83] measured the exponents for a one dimensional system, but compared their results with those of Iwamoto et al. [36], which was for a two-dimensional surface. However, their value of  $\alpha = 0.87 \pm 0.05$  is in fact in good agreement with the much earlier results of Bursill et al. [33] for a 1+1 dimensional system. In addition, further experimental work is necessary to determine the exponents for both deposition and dissolution more accurately. This will in turn help in the development of suitable models. In particular, an open question is the role of the instabilities, such as the Mullins-Skerka instability due to the Laplacian field [84] or the Ehrlich-Schwoebel step barrier [85], in later stages of growth or dissolution.

### **ELECTROCHEMICAL EPITAXY**

The formation of nanostructures, such as superlattices, is of great interest particularly for applications in optoelectronic devices. Techniques such as molecular-beam-epitaxy (MBE), metal-organic chemical vapor deposition (MOCVD), and liquid phase epitaxy (LPE) have been the predominant methods used for the epitaxial growth of these materials. Owing to the development of *in situ* techniques such as scanning tunneling microscopy (STM), atomic force microscopy, and x-ray reflectivity, it has become possible to characterize atomic processes on electrode surfaces. This has led to substantial progress in the study of solid-electrolyte interfaces. Through these advances, there has been considerable interest in electrochemical epitaxy, particularly of compound materials [42-61]. Besides the fundamental aspect of this rather unusual phenomenon, electrochemical processes offer convenient and inexpensive methods for the preparation of epitaxial materials. In fact, considerable effort has been made to grow well ordered nanostructures using electrochemical techniques [42-61].

One of the most promising routes for electrochemical deposition of epitaxial layers is the underpotential deposition (UPD) technique [42-47]. UPD is an electrochemical process in which a monolayer or submonolayer of a foreign adatom is deposited on a second element at a potential positive from the reversible Nernst potential. The UPD process on noble metal surfaces has attracted substantial attention over the past two decades because of its practical importance in growing epitaxial layers and its fundamental importance in understanding electrodeposition processes in general [86,87]. From a practical point of view, UPD-modified surfaces show increased resistance to poisoning from oxidation products, making these surfaces potentially attractive for use in fuel cells and in sensors.

As mentioned before, the development of analytical and, particularly, *in situ* measurements at the solid-liquid interface have played an important role in studies of electrochemical epitaxy. The structure of atomic layers formed by UPD have been studied using a wide variety of techniques [see 86,87 and references therein], including low-energy electron diffraction (LEED), scanning tunneling microscopy (STM), atomic force microscopy (AFM), and X-ray scattering, in addition to a host of less specific techniques. In particular, recent *in-situ* synchrotron x-ray scattering studies appear to provide an effective method for probing the structure of the epitaxial layers [60,61].

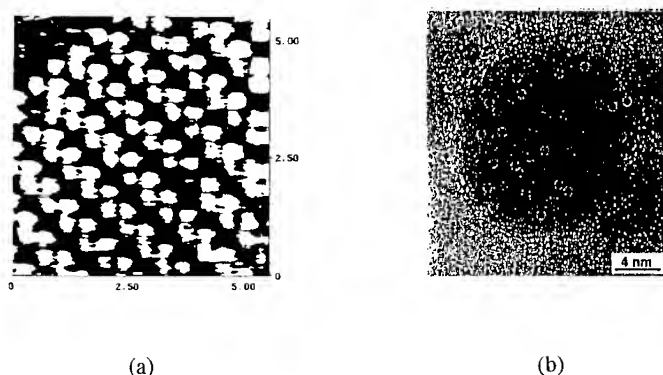


**Fig. 8:** (a) STM image shows the microstructure of CdTe on Au(100) surface [from ref. 52]. (b) High resolution electron microscope image of a single CdSe quantum dot [from ref. 53].

Through microscopic characterization of the atomic adlayer or submonolayer, a number of ordered phases have been observed in a wide variety of metal on metal UPD deposits. Most of these studies have involved noble metals (Pt, Au, Ag, Cu) because they are stable in aqueous solutions. For example, ordered phases have been found in UPD of Pb on Ag(*hkl*), Cu on Au(*hkl*) [44, 46, 47,61], Ag on Au(111) and Hg on Au(111) [60]. An interesting aspect of these studies is that some of the phases seen in UPD adlayers are phases which cannot be obtained by vacuum deposition methods. This indicates that through microscopic control of electrochemical epitaxy it might be possible to synthesize novel nanostructures with unusual electronic and optical properties.

In addition to studies of single metal deposition, there has been great interest in electrochemical deposition of epitaxial thin films of compounds [86,87], particularly semiconductors. The early work on compound electrodeposition was based on oxidation of a metal electrode [86], such as Cd, in a solution containing a chalcogenide ion, such as  $S^{2-}$ . This method resulted in the precipitation of CdS on the electrode surface. The quality of films produced by this method were quite poor and were limited in thickness.

Another method for deposition of compounds makes use of co-deposition of elements to form stoichiometric deposits [86]. It involves the use of solution containing precursors of the elements in the compound, such as group II and group VI elements. For example, CdTe was made from Te precursor,  $HTeO_2^+$  in a solution with a high concentration of  $Cd^{2+}$ . The potential was chosen high enough so that Cd UPD to occur on Te without bulk Cd deposition. The results of this technique were not satisfactory either since the deposits were polycrystalline and have a rough morphology.

More recently there has been increasing interest in electrochemical deposition of epitaxial compound materials. Homoepitaxial growth of compound materials has been achieved through growth of single crystals [48]. In particular, the groups at the University of Georgia [45,51,52,56,57] and the Weizmann Institute [50,53] have extended the UPD approach to deposition of epitaxial compound semiconductors. For example, Suggs and Stickney [51,52] have deposited structures formed by alternated UPD of Cd and Te on Au(*hkl*). A typical STM image of the CdTe layer deposited on Au(100) is shown in Figure 8a [52]. Similarly, Lister et al. [56] have grown Se on Au(*hkl*), which is the first step in the growth of such materials such as CdSe and ZnSe on Au(*hkl*). In their approach, Stickney's group [see ref. 86 for a recent review], developed an electrochemical analog of atomic layer epitaxy [87], in which atomic layers of the component elements are deposited alternately in a cycle. One cycle results in the formation of a monolayer of the compound. In the electrochemical deposition, UPD is used instead of the substrate temperature to limit the extent of an element's deposition to an atomic layer. Reductive UPD is used to deposit one of the elements, and oxidative UPD is used to deposit the other [86].

The Weizmann Institute group [50,53] has recently concentrated its efforts on electrodeposition of semiconductor quantum dots and nanoclusters. They used well characterized Au or Pd as the substrate and electrodeposited CdSe onto the substrates used as the cathode. They obtained nanocrystals of CdSe on single gold grains and used high resolution electron microscopy (HREM) and x-ray diffraction to demonstrate the crystalline nature of the CdSe aggregates [50,53]. They obtained crystalline quantum dots 5 nm in diameter on Au and amorphous quantum dots on Pd. A typical HREM of a single CdSe quantum dot is shown in Figure 8b [53]. In analogy with vacuum heteroepitaxy, they have discussed an epitaxial size-limiting mechanism based on the mismatch-induced strain energy as the size of the quantum dot increases [53]. They argue that using controlled electrodeposition techniques it may be possible to obtain "self-assembled" arrays of quantum dots, which would be of interest both scientifically and in technological applications.

A related area of considerable interest is the electrodeposition of nanoclusters of organic conductors [54,59]. The goal is manipulating electrodeposits at the molecular level to produce nanoscale materials with special electrical and optical properties. These low dimensional materials may have the potential to produce a new class of molecular-level devices with unusual optoelectronic properties. The best example of work in this area is that of Michael Ward's group in Minnesota [54,59], who have used electrodeposition to produce nanoclusters of organic salts with unusual geometrical properties. In particular, they have obtained radically different anisotropic orientations

of the molecules (with respect to the Au(111) substrate) by depositing different charge transfer salts, such as the quasi-one dimensional high conductor TTF-TCNQ. These organic nanoclusters may have interesting optoelectronic applications since the orientation of these types of molecules plays an important role in determining their metallic conductivity or superconductivity.

#### *The Role of Surface Diffusion in Electrodeposition*

It is now well recognized that the key parameter which controls the surface morphology and evolution is surface diffusion [see 81,88-91 and references therein]. Growth with enhanced surface diffusion leads to the formation of smooth surfaces through layer-by-layer growth mode. However, when surface diffusion is limited, three dimensional islands can form. The most dramatic illustration of this picture is the formation of mounds in multilayer MBE growth [see for example, ref. 88 and references therein]. It is now well established that the mound morphology arises from the instability due to the Ehrlich-Shwoebel step barrier [85] which hinders surface diffusion at descending steps and leads to the formation of three dimensional structures.

In order to develop a better understanding of electrochemical growth processes it is important to ask the question of whether the same processes that control the surface morphology in vacuum deposition are important in electrodeposition. A partial answer to this question was provided by the recent work of Corcoran, Chakarova and Sieradzki [89] who studied electrodeposition of Ag on Au(111) electrodes. They find that instead of a layer by layer growth, three dimensional islands form on the surface. They propose that due to the analogy with the vacuum deposition results, it is possible that the existence of a finite step barrier [85] may be responsible for the observed behavior. This is an example of the type of processes that control the surface morphology both in vacuum processes and the solid-liquid interface.

#### **CONCLUSIONS**

Electrochemical deposition holds great promise as an inexpensive, but controllable technique for synthesis and processing of a wide range of novel materials, from fractal electrodes to nanostructures and epitaxial thin films. This has been demonstrated by the type of experiments discussed above. The key question is understanding the parameters that control electrochemical deposition and dissolution, particularly in the growth of ordered layers. Clearly progress in this direction can only be made by close collaboration between experimental and theoretical groups. Unfortunately at the present time theoretical and computational efforts in this area are far more limited than the experimental efforts. Therefore future developments will require the sort of efforts made in theoretical and simulational studies of vacuum deposition techniques in the past decade. These efforts have led to significant advances in our understanding of MBE and other materials growth techniques. It is hoped that this review will provide an impetus and a starting point for the development of a unified approach for understanding some of the key issues in electrochemical synthesis and processing of materials.

#### **ACKNOWLEDGMENTS**

I would like to thank all the colleagues who kindly provided some of the figures for this paper. I also would like to thank Jacques Amar, George Hentschel and Peter Searson for their critical reading of the manuscript and their valuable comments. This work was supported by the National Science Foundation through grant number DMR-9520842 and by the Office of Naval Research.

## REFERENCES

1. F. Family and D. P. Landau, eds., *Kinetics of Aggregation and Gelation*, North-Holland, Amsterdam (1984).
2. H. E. Stanley and N. Ostrowsky, eds., *On Growth and Form: Fractal and Nonfractal Patterns in Physics*, Martinus Nijhof, Dordrecht (1986).
3. T. Vicsek, *Fractal Growth Phenomena*, World-Scientific, Singapore (1989).
4. D. Avnir, editor, *The Fractal Approach to Heterogeneous Chemistry*, Wiley, New York (1989).
5. A. Bunde and S. Havlin, editors, *Fractals and Disordered Systems*, Springer-Verlag, Berlin (1991).
6. F. Family, P. Meakin, B. Sapoval and R. Wool, eds., *Fractal Aspects of Materials*, Mat. Res. Soc., Pittsburgh (1993).
7. T. A. Witten and L. M. Sander, Phys. Rev. Lett. **47**, 1400 (1981).
8. J. S. Langer, Rev. Mod. Phys. **52**, 1 (1980); *ibid* Science **243**, 1150 (1989).
9. S. Sheldon and G. M. Downing, Phys. Rev. **1**, 51 (1893).
10. R. M. Brady and R. C. Ball, Nature **309**, 225 (1984).
11. M. Matsushita, M. Sano, Y. Hayakawa, H. Honjo and Y. Sawada, Phys. Rev. Lett. **53**, 286 (1984).
12. Y. Swada, A. Dougherty, and J. P. Gollub, Phys. Rev. Lett. **56**, 1260 (1986).
13. D. Grier, E. Ben-Jacob, R. Clarke and L. M. Sander, Phys. Rev. Lett. **56**, 1264 (1986).
14. L. M. Sander, in *The Physics of Structure Formation*, edited by W. Guttinger and G. Dangelmayr, Springer-Verlag, Berlin (1987), p. 257.
15. F. Argoul, A. Arneodo, G. Grasseau and H. L. Swinney, Phys. Rev. Lett. **61**, 2558 (1988).
16. J. R. Melrose and D. B. Hibbert, Phys. Rev. A **38**, 1036 (1988).
17. E. Ben-Jacob, P. Garik, T. Muller and D. Grier, Phys. Rev. A **38**, 1370 (1988).
18. R. M. Suter and P. Wong, Phys. Rev. B **39**, 4536 (1989).
19. D. B. Hibbert and J. R. Melrose, Proc. R. Soc. Lond. A **423**, 149 (1989).
20. G. L. M. K. S. Kahanda and M. Tomkiewicz, J. Electrochem. Soc. **136**, 1497 (1989).
21. P. Garik, D. P. Barkey, E. Ben-Jacob, E. Botchner, N. Broxholm, B. Miller, B. Orr and R. Zamir, Phys. Rev. Lett. **62**, 2703 (1989).
22. D. P. Barkey, R. H. Muller and C. W. Tobias, J. Electrochem. Soc. **136**, 2199 (1989).
23. D. P. Barkey, R. H. Muller and C. W. Tobias, J. Electrochem. Soc. **136**, 2207 (1989).
24. J. R. Melrose, D. B. Hibbert and R. C. Ball, Phys. Rev. Lett. **65**, 3009 (1990).
25. V. Fleury, J.-N. Chazalviel, M. Rosso and B. Sapoval, J. Electroanal. Chem. **290**, 249 (1990).
26. D. P. Barkey and D. P. LaPorte, J. Electrochem. Soc. **137**, 1655 (1990).
27. J.-N. Chazalviel, Phys. Rev. A **42**, 7355 (1990).
28. P. P. Trigueros, J. Claret, F. Mas, and F. Saguès, J. Electroanal. Chem. **312**, 219 (1991).
29. B. B. Mandelbrot, *The Fractal Geometry of Nature*, Freeman, San Francisco (1982).
30. F. Family and T. Vicsek, eds., *Dynamics of Fractal Surfaces*, World-Scientific, Singapore (1991).
31. A.-L. Barabási and H. E. Stanley, *Fractal Concepts in Surface Growth*, Cambridge Univ. Press, Cambridge (1995).
32. F. Family and T. Vicsek, J. Phys. A **18**, L75 (1985).
33. L. A. Bursill, P. Julin and F. Xudong, Int. J. Mod. Phys. B **5**, 1377 (1991).
34. G. L. M. K. S. Kahanda, X. Zou, R. Farrell and P. Wong, Phys. Rev. Lett. **68**, 3741 (1992).



35. H. Iwasaki and T. Yoshinobu, Phys. Rev. B **48**, 8282 (1993).
36. A. Iwamoto, T. Yoshinobu and H. Iwasaki, Phys. Rev. Lett. **72**, 4025 (1994).
37. H. Iwasaki, A. Iwamoto, K. Sudoh and T. Yoshinobu, in *Fractal Aspects of Materials*, F. Family, P. Meakin, B. Sapoval and R. Wool, eds., Mat. Res. Soc., Pittsburgh (1993), p. 159.
38. M. G. Fernandes and R. M. Latanision, and P. C. Searson, Phys. Rev. B **47**, 11749 (1993).
39. Wehrli, J. Colloid Int. Sci. **132**, 230 (1989).
40. K. Sieradzki, R. R. Corderman, K. Shukla and R. C. Newman, Philos. Mag. A **4**, 713 (1989).
41. M. E. Vela, G. Anderasen, R. C. Salvarezza, A. Hernández-Creus, and A. J. Arvia, Phys. Rev. B **53**, 10217 (1996).
42. D. M. Kolb, in *Advances in Electrochemistry and Eletrochemical Engineering*, Vol. II, H. Gerischer and C. W. Tobias, editors, Wiley, New York (1978), p. 125.
43. K. Jüttner and W. J. Lorenz, Z. Phys. Chem. **122**, 163 (1980).
44. O. M. Magnussen, J. Hotlos, R. J. Nichols, D. M. Kolb, and R. J. Behm, Phys. Rev. Lett. **64**, 2929 (1990).
45. D. W. Suggs and J. L. Stickney, J. Phys. Chem. **95**, 10056 (1991).
46. S. Manne, P. K. Hansma, J. Massie, V. B. Elings, and A. A. Gewirth, Science **251**, 133 (1991).
47. A. Tadjeddine, D. Guay, M. Ladouceur, and G. Tourillon, Phys. Rev. Lett. **66**, 2235 (1991).
48. J. A. Switzer, R. F. Raffaele, R. J. Phillips, C.-J. Hung and T. D. Golden, Science **258**, 1918 (1992).
49. B. E. Beryfogle, R. J. Phillips and J. A. Switzer, Chem. Mater. **4**, 1356 (1992).
50. Y. Golan, L. Margulis, I. Rubinstein and G. Hodes, Langmuir **8**, 749 (1992); Y. Golan, L. Margulis, G. Hodes, I. Rubinstein and J. L. Hutchison, Surf. Sci. **311**, L633 (1994).
51. D. W. Suggs and J. L. Stickney, Surf. Sci. **290**, 362 (1993).
52. D. W. Suggs and J. L. Stickney, Surf. Sci. **290**, 375 (1993).
53. Y. Golan, G. Hodes, I. Rubinstein, J. Phys. Chem. **100**, 2220 (1996).
54. J. H. Schott and M. D. Ward, J. of Am. Chem. Soc. **116**, 6806 (1994).
55. M. F. Toney, J. N. Howard, J. Richer, G. L. Borges, J. G. Gordon, O. R. Melroy, D. Yee, and L. B. Sorensen, Phys. Rev. Lett. **75**, 4472 (1995).
56. T. E. Lister, B. M. Huang, R. D. Herrick II, and J. L. Stickney, J. Vac. Sci. Technol. B **13**, 1268 (1995).
57. C. K. Rhee, B. M. Huang, E. M. Wilmer, S. Thomas and J. L. Stickney, Mat. Manuf. Processes **10**, 283 (1995).
58. E. E. Mola, A. G. Appignanessi, J. L. Vicente, L. Vazquez, R. C. Salvarezza and A. J. Avia, Surf. Rev. Lett. **2**, 489 (1995).
59. A. C. Hillier, J. H. Schott and M. D. Ward, Adv. Mater. **4**, 409 (1995).
60. J. Li, E. Herrero and H. Abruña, "UPD of Hg on Au(111): An In-situ Surface X-ray Scattering Study", CHESS meeting, Cornell (1996).
61. A. Finnefrock, J. D. Brock and H. Abruña, "In-situ Surface X-ray Scattering Study of UPD of Cu on Pt(111)", CHESS meeting, Cornell (1996).
62. B. Sapoval, in *Fractals and Disordered Systems*, A. Bunde and S. Havlin, eds., Springer-Verlag, New York (1991), p. 207.
63. Y. Huttel, E. Chassaing, M. Rosso, and B. Sapoval, in *Fractal Aspects of Materials*, F. Family, P. Meakin, B. Sapoval and R. Wool, eds., Mat. Res. Soc., Pittsburgh (1993), p. 177.

64. N. Hecker, D. G. Grier and L. M. Sander, in *Extended Abstracts: Fractal Aspects of Materials*, D. Weitz, L. M. Sander, and B. B. Mandelbrot, eds., Mat. Res. Soc., Pittsburgh (1988), p. 17.
65. D. P. Barkey, J. Electrochem. Soc. **138**, 2912 (1991).
66. V. Fleury, M. Rosso, J.-N. Chazalviel and B. Sapoval, Phys. Rev. A **44**, 6693 (1991).
67. D. P. Barkey and P. D. Laporte, J. Electrochem. Soc. **137**, 1655 (1990).
68. P. Trigueros, F. Saguès and J. Claret, Phys. Rev. E **49**, 4328 (1994).
69. M. Rosso, J.-N. Chazalviel, V. Fleury, E. Chassaing, Electrochimica Acta **39**, 507 (1994).
70. V. Fleury, M. Rosso, and J.-N. Chazalviel, Phys. Rev. Lett. **68**, 2492 (1992).
71. V. Fleury, J.-N. Chazalviel, and M. Rosso, Phys. Rev. E **48**, 1279 (1993).
72. R. Bruinsma and S. Alexander, J. Chem. Phys. **92**, 3074 (1990).
73. C. Livermore and P. Wong, Phys. Rev. Lett. **72**, 3847 (1994).
74. D. Barkey, D. Watt, Z. Liu, S. Raber, J. Electrochem. Soc. **141**, 1206 (1994).
75. J. M. Hutt, H. L. Swinney, W. D. McCormick, A. Kuhn and F. Argoul, Phys. Rev. E **51**, 3444 (1995).
76. F. Argoul and A. Kuhn, Physica A **213**, 209 (1995).
77. J.-N. Chazalviel, M. Rosso, E. Chassaing, V. Fleury, J. Electroanal. Chem. **407**, 61 (1996).
78. M.-Q. López-Salvans, P. P. Trigueros, S. Vallmitjana, J. Claret and F. Saguès, Phys. Rev. Lett. **76**, 4062 (1996).
79. K. J. Vetter, *Electrochemical Kinetics*, Academic Press, New York (1967).
80. T. Sun, H. Guo and M. Grant, Phys. Rev. A **40**, 6763 (1989).
81. D. E. Wolf and J. Villain, Europhys. Lett. **13**, 389 (1990).
82. J. G. Amar, P.-M. Lam, and F. Family, Phys. Rev. E **47**, 3242 (1993).
83. J. M. Pastor and M. A. Rubio, Phys. Rev. Lett. **76**, 1848 (1996).
84. J. Krug and P. Meakin, Phys. Rev. Lett. **66**, 703 (1991).
85. G. Ehrlich and F. Hudda, J. Chem. Phys. **44**, 1039 (1966); R. L. Schwoebel, J. Appl. Phys. **40**, 614 (1969).
86. M. B. Huang, T. E. Lister and J. L. Stickney, in *Handbook of Surface Imaging and Visualization*, edited by A. T. Hubbard, Chemical Rubber Company, Boca Raton (1995), Ch. 7, p. 75.
87. *Atomic Layer Epitaxy*, edited by S. Bedair, Elsevier, New York (1992); *Atomic Layer Growth and Processing*, edited by P. D. Dapkus and T. F. Kuech, Mat. Res. Soc. Proc. **222**, Materials Research Society, Pittsburgh (1991).
88. J. G. Amar and F. Family, Phys. Rev. B **54**, 14742 (1996).
89. S. G. Corcoran, G. S. Chakarova, and K. Sieradzki, Phys. Rev. Lett. **71**, 1585 (1993).
90. P. C. Searson, R. Li and K. Sieradzki, Phys. Rev. Lett. **74**, 1395 (1995).
91. J. D. Porter and T. O. Robinson, J. Phys. Chem. **97**, 6696 (1993).

## MORPHOLOGICAL PATTERNS DURING QUASI-TWO-DIMENSIONAL ELECTRODEPOSITION

JACOB JORNE, SEN-WEI WU

Department of Chemical Engineering, University of Rochester, Rochester, NY 14627,  
jorne@che.rochester.edu

### ABSTRACT

The quasi-two-dimensional electrodeposition of several metals (zinc, copper, silver and lithium) of varying levels of anisotropy has been investigated. The morphologies are very diverse for the different metals and the morphology selection depends on the degree of anisotropy. The fast propagation of the quasi-two-dimensional deposit is due to the lack of convection in the confined electrolyte. The velocity of the deposit is determined by the drift velocity of the anions, as the system is attempting to maintain electroneutrality and reduce the electric field in the space charge region. The effects of impurities and natural convection on the morphology are investigated as well.

### INTRODUCTION

In electrodeposition, as the electrolyte is confined to a thin layer, the electrodeposit becomes quasi-two-dimensional and some extraordinary patterns are observed. In contrast to the conventional three-dimensional electrodeposition, in which the ions are transported to the electrode surface where compact deposit is obtained, the quasi-two-dimensional deposit spreads out rapidly, well above the calculated limiting current, capturing the metal ions as it advances through the thin layer electrolyte. Furthermore, a rich variety of morphological patterns are observed, such as dense-branched, fractal, dendritic, stringy and needle-like morphologies (see examples in Refs. 1-11). In the present work, the reasons for the spreading mechanism are investigated and the factors affecting the morphology selection are identified.

### RESULTS AND DISCUSSION

Quasi-two-dimensional electro-deposition of four metals with different anisotropies (Zn, Cu, Ag and Li) is conducted under various concentrations, current densities, impurities and geometries. The morphologies are diverse for the four metals. For Zn, five morphologies are observed: ramified fractal-like, dense-branched, dendritic, stringy and needle-like. For Cu, only two morphologies are observed: ramified-fractal and dense-branched. For Ag, dendritic morphology dominates, while for Li, deposited from its perchlorate solution in propylene carbonate, only ramified or fractal morphology is obtained. Examples of the various morphologies are presented in Fig. 1. Ag is the most anisotropic, followed by Zn and Cu. Because Li is reactive with the solvent and is covered by a solid electrolyte interface, it is expected to be more isotropic, as observed experimentally in Fig. 1g. The important role of anisotropy in morphology selection has been discussed by Barkey et. al. (11).

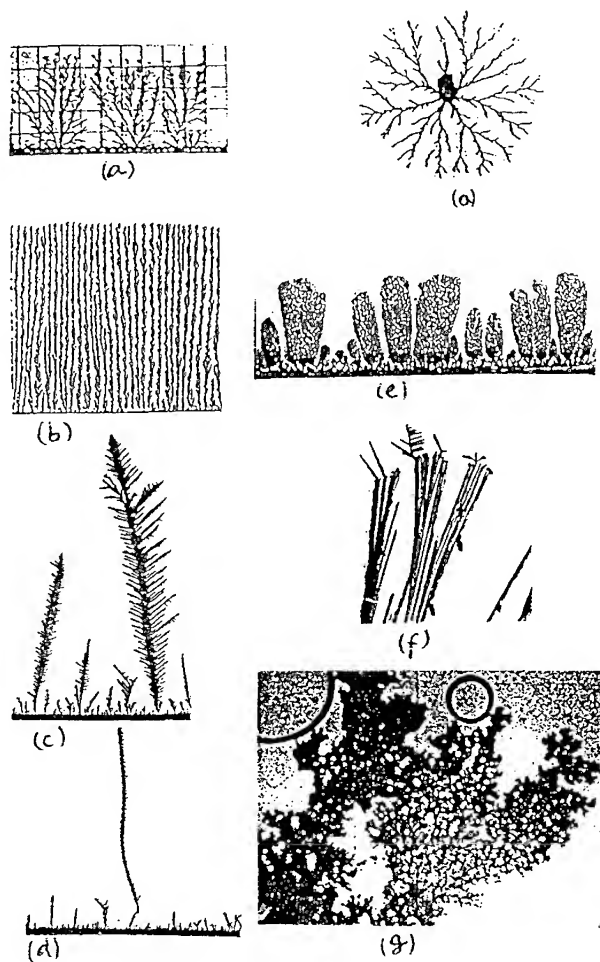


**Fig.1:** Various Morphological patterns of Zn, Cu, Ag and Li: (a)Fractal Zn. (b)Dense-branched Zn. (c)Dendritic Zn. (d)Needle Zn. (e)Mesh-like Cu. (f)Needle Ag. (g)Ramified-Fractal Li.

The fast propagation of the quasi-two-dimensional deposit originates from the confinement of the electrolyte and the lack of convection there. Consequently, the space-charge layer and the diffusion layer are sustained in front of the deposit. Starvation of adatoms occurs on the surface which triggers instability, bifurcation and self-organization. The velocity of the deposit is determined by the drift velocity of the anions away from the deposit, as the system is attempting to maintain electroneutrality and to reduce the electric field in the space-charge region. The growth velocity of the dense-branched morphology is proportional to  $(i/C)$ . Since the mobility of the common anion ( $\text{SO}_4^{2-}$ ) remains roughly the same, the results for both Cu and Zn coincide and agree with the theoretical prediction, as shown in Fig. 2.

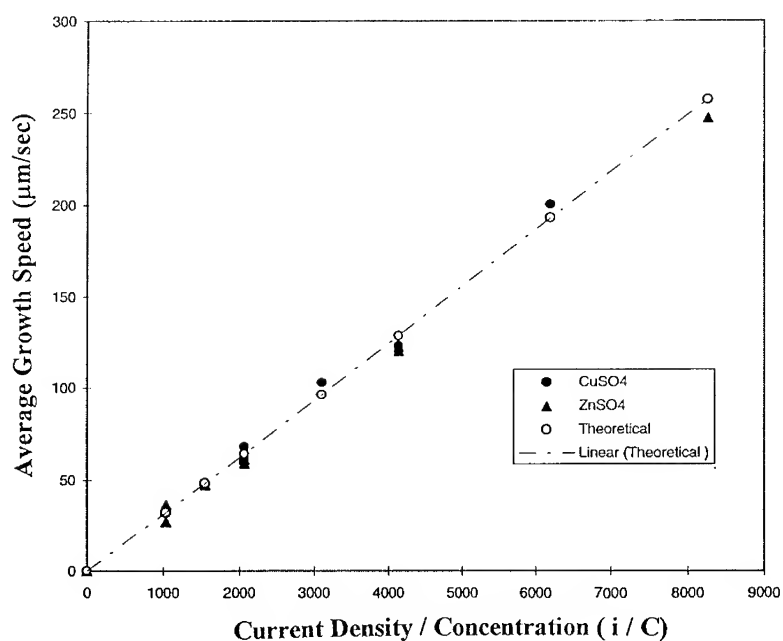
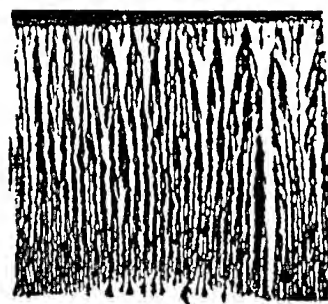


Fig. 2 Average growth speed vs. current density / concentration.

The effect of forced and natural convection on the morphology is presented in Fig. 3. In the absence of natural convection (cathode on top) dense-branched morphology is obtained. However, under identical conditions, except in the presence of natural convection (cathode at the bottom), dendrites are observed.

Sharp transition in the morphology, the so called Hecker effect (5), occurs when the growth front reaches a well-defined distance, which scales with the size of the cell. This relative position  $r$ , the distance from the cathode divided by the total distance between the cathode and the anode, depends only on the mobility ratio of the impurity and the anion:

$$r = (1 + \mu_i/\mu_a)^{-1}$$



(a)



(b)

Fig. 3 The morphology of electrodeposited zinc obtained from a vertical cell.  
(Electrode width = 2.54 cm, distance = 4 cm, thickness = 0.025 cm)  
0.05M ZnSO<sub>4</sub> at 24V  
(a) DBM pattern is observed when the cathode is on the top.  
(b) Dendritic structure is observed when the cathode is at the bottom.

Based on the mobilities of the various ions at infinite dilution, the relative positions of the transition in sulfate solutions for  $\text{H}^+$ ,  $\text{Li}^+$ ,  $\text{Na}^+$  and  $\text{K}^+$  are 0.19, 0.67, 0.61 and 0.52, respectively. Figs. 4 and 5 show transitions occurring in  $\text{CuSO}_4$  and  $\text{ZnSO}_4$  solutions, respectively. The first transitions occur due to the depletion of  $\text{H}^+$ , while the second transitions occur due to the depletion of the  $\text{Na}^+$  or  $\text{K}^+$  ions. The positions of the transition agree well with the values predicted above.

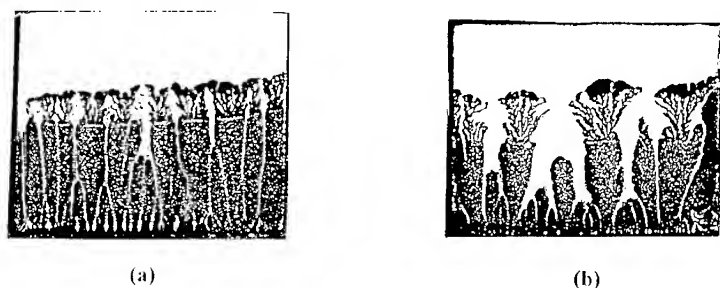


Fig. 4 The second transition occurred in the quasi-2D electrodeposited copper.  
 (a) 0.05M  $\text{CuSO}_4$  + 4 mM  $\text{Na}_2\text{SO}_4$  at 103.6  $\text{mA}/\text{cm}^2$ .  
 Transition occurred about 55% of the total length from the cathode.  
 (b) 0.05M  $\text{CuSO}_4$  + 4 mM  $\text{K}_2\text{SO}_4$  at 62.2  $\text{mA}/\text{cm}^2$ .  
 Transition occurred about 47% of the total length from the cathode.



Fig. 5 The second transition occurred in the quasi-2D electrodeposited zinc.  
 (a) 0.05M  $\text{ZnSO}_4$  + 0.5mM  $\text{Na}_2\text{SO}_4$  at 103.6  $\text{mA}/\text{cm}^2$ .  
 Transition occurred at about 55% of the total length from the cathode.  
 (b) 0.05M  $\text{ZnSO}_4$  + 0.5mM  $\text{K}_2\text{SO}_4$  at 103.6  $\text{mA}/\text{cm}^2$ .  
 Transition occurred at 43.75% of the total length from the cathode.

## CONCLUSIONS

Despite the existence of many morphologies, it is concluded that only dendritic growth occurs at the tips and the competition between dendritic growth and tip splitting determines the evolving morphology. Anisotropy plays an important role in the morphology selection. Highly anisotropic metals, such as Ag, exhibit dendritic growth, while less anisotropic metals, such as Zn and Cu, exhibit a variety of morphologies, varying from fractal, to ramified to dendritic. Li, which is covered by a solid electrolyte layer, exhibit only ramified fractal morphology.

## REFERENCES

1. S.-W. Wu, Morphological Pattern Formation During Quasi-Two-Dimensional Electrodeposition, Ph.D. Thesis, University of Rochester (1996).
2. R. M. Brady and R. C. Ball, *Nature*, 309, 225 (1984).
3. M. Matsushita, M. Sano, M. Hayakawa, Y. Hopjo and Y. Sawada, *Phys. Rev. Lett.*, 53, 286 (1984).
4. Y. Sawada, A. Dougherty and J. P. Gollub, *Phys. Rev. Lett.*, 56, 1260 (1986).
5. N. Hecker, D. G. Grier and L. M. Sander, in *Fractal Aspects of Materials*, R. B. Laibovitz, B. B. Mandelbrot and D. E. Passoja, eds., Materials Research Society (1985).
6. D. Grier, E. Ben-Jacob, R. Clarke and L. M. Sander, *Phys. Rev. Lett.*, 56, 1264 (1986).
7. R. F. Voss and M. J. Tomkiewicz, *J. Electrochem. Soc.*, 132, 371 (1985).
8. C.-P. Chen and J. Jorne, *J. Electrochem. Soc.*, 137, 2047 (1990).
9. D. Barkey, *J. Electrochem. Soc.*, 138, 2912 (1991).
10. D. Barkey, D. Watt, Z. Liu and S. Raber, *J. Electrochem. Soc.*, 141, 1206 (1994).
11. D. Barkey, F. Oberholtzer and Q. Wu, *Phys. Rev. Lett.*, 75, 2980 (1995).



## THE ROLE OF COULOMBIC FORCES IN QUASI-TWO DIMENSIONAL ELECTROCHEMICAL DEPOSITION

G. Marshall\*, P. Mocskos\*\*, F. Molina\*\* and S. Dengra\*\*

\* Universidad de Buenos Aires and Consejo Nacional de Investigaciones Cientificas

\*\* Universidad de Buenos Aires

### ABSTRACT

Recent work demonstrates the relevant influence of convection during growth pattern formation in thin-layer electrochemical deposition. Convection is driven mainly by coulombic forces due to local charges at the tip of the aggregation and by buoyancy forces due to concentration gradients. Here we study through physical experiments and numerical modeling the regime under which coulombic forces are important. In the experimental measurements fluid motion near the growing tips of the deposit is visualized with neutrally buoyant latex spheres and its speed measured with videomicroscope tracking techniques and image processing software. The numerical modeling consists in the solution of the 2D dimensionless Nernst-Planck equations for ion concentrations, the Poisson equation for the electric field and the Navier-Stokes equations for the fluid flow, and a stochastic growth rule for ion deposition. A new set of dimensionless numbers governing electroconvection dominated flows is introduced. Preliminary experimental measurements and numerical results indicate that in the electroconvection dominated regime coulombic forces increase with the applied voltage, and their influence over growth pattern formation can be assessed with the magnitude of the dimensionless electric Froude number. It is suggested that when this number decreases the deposit morphology changes from fractal to dense branching.

### INTRODUCTION

Electrochemical deposition (ECD) of ramified deposits in thin-layer cells, producing complex geometries of fractal or dendritic character and chaotic patterns [1]-[2], is a paradigmatic model for studying growth pattern formation. The electrolytic cell consists of two glass plates sandwiching two parallel electrodes and an electrolyte. A voltage difference applied between electrodes produces a tree-like deposit by reduction of the metal ions. The deposit structure ranging from fractal to dense branch morphology depends on many parameters such as cell geometry, solution concentration or voltage difference; its morphology variation has not yet been fully understood.

Recently, [3]-[6] demonstrated the importance of hydrodynamic motion in electrochemical transport processes in thin-layer cells in the vicinity of the electrodes. Fluid motion is mainly produced by electrical and buoyancy driven convection. When an electrolyte is subject to an electric field an electric or coulombic force acts on the fluid and a convective motion can be induced. During electrochemical growth chemical reactions deplete the electrolyte near the deposit front. The concentration gradients produce density gradients and a buoyant force that acts on the fluid inducing a convective motion. How is the resulting

morphology when the regime is electroconvection or buoyancy driven convection dominated is an interesting question. Reducing cell thickness and electrolyte concentration is the most direct way for minimizing buoyancy driven convection and enhancing electroconvection [5], [6]. Here we present a series of measurements of fluid motion focusing in the regime governed by electroconvection. Velocities are measured with particle tracking velocimetry under optical microscope following the technique developed in [6]. A similar technique was used in [7] to study the role of viscosity. Moreover, we construct a macroscopic model from first principles including all the relevant physical variables for the analysis of convection driven solely by coulombic forces and a mechanism that mimics the front growth following ideas developed in [8].

## THEORETICAL ANALYSIS

What follows is a three-dimensional model of ECD phenomena that is consistent with experimental observations and constitutes an extension of work in [3], [5], [6] and [8]. In an ECD experiment, when the circuit is closed the current starts flowing through the electrolyte. Because of ion depletion near the cathode and ion enhancement near the anode, zones with low concentration near the cathode and high concentration near the anode develop. These are separated by an initial concentration value zone. This unstable configuration generates a density current flow at both electrodes and two vortex tubes parallel to the electrodes, moving in opposite directions. During this initial period cation depletion at the cathode is supposed uniform.

Simultaneously, in a very narrow region near the cathode a local charge develops, giving rise to coulombic forces initially pointing towards the cathode. In an ideal situation, the resultant of coulombic and buoyant forces lie in a plane normal to the deposit thus conforming a stable configuration. However, in reality that symmetry is broken, and we suggest that this is due mainly to lateral wall-like effects (inside the vortex tube fluid rotates and translates in helicoidal trajectories), producing a vortex ring. In an idealized three-dimensional array of thin filaments each tip filament is crowned with a toroidal vortex ring produced by coulombic forces. The upper part of these vortices determines a surface in the form of spherical shells or domes with archs connecting neighbouring tips. Above this surface and near the tips a funnel is created and aggregation enhanced; below the surface aggregation is suppressed. The appearance of vortex rings triggers the deposit branching. The surface also determines a concentration front. Behind it the ion concentration is very small, above it, the concentration reaches the initial value. In the quasi-plane of the growth the previous three-dimensional picture reduces to the pair of counter rotating vortices and archs at the tips of each filament as described in [5].

The physical scenario just described can be studied with a macroscopic mathematical model based on first principles comprising the 3D Nernst-Planck equations for ions transport, the Poisson equation for the electric potential and the Navier-Stokes equations for the fluid written in dimensionless form. In a two-dimensional approximation, in the absence of buoyancy driven forces, the equations governing the system (in non dimensional form and in transport vorticity form) are:

$$\frac{\partial C}{\partial t} = \frac{1}{Pe_C} \nabla^2 C + \frac{1}{M_C} \left[ \frac{\partial}{\partial x} \left( C \frac{\partial \phi}{\partial x} \right) + \frac{\partial}{\partial y} \left( C \frac{\partial \phi}{\partial y} \right) \right] - \frac{\partial}{\partial x} (uC) - \frac{\partial}{\partial y} (vC) \quad (1)$$

$$\frac{\partial A}{\partial t} = \frac{1}{Pe_A} \nabla^2 A - \frac{1}{M_A} \left[ \frac{\partial}{\partial x} \left( A \frac{\partial \phi}{\partial x} \right) + \frac{\partial}{\partial y} \left( A \frac{\partial \phi}{\partial y} \right) \right] - \frac{\partial}{\partial x} (uA) - \frac{\partial}{\partial y} (vA) \quad (2)$$

$$\nabla^2 \phi = -\frac{1}{Po_C} C + \frac{1}{Po_A} A \quad (3)$$

$$\frac{\partial \omega}{\partial t} + u \frac{\partial \omega}{\partial x} + v \frac{\partial \omega}{\partial y} = \frac{1}{Re} \nabla^2 \omega + \frac{1}{Fr_C} \left( \frac{\partial C}{\partial y} \frac{\partial \phi}{\partial x} - \frac{\partial C}{\partial x} \frac{\partial \phi}{\partial y} \right) + \frac{1}{Fr_A} \left( \frac{\partial A}{\partial x} \frac{\partial \phi}{\partial y} - \frac{\partial A}{\partial y} \frac{\partial \phi}{\partial x} \right) \quad (4)$$

$$\nabla^2 \psi = -\omega \quad (5)$$

where  $Re = \frac{u_0 x_0}{\nu}$  is the electric Reynolds number,  $M_C(M_A) = \frac{\bar{\mu}}{\mu_C}$  is a migration number,  $Pe_C(Pe_A) = \frac{x_0 u_0}{D_C}$  is the electric Peclet number,  $Po_C(Po_A) = \frac{\epsilon \epsilon_0 E_0}{x_0 C_0 z_C e}$  is the Poisson number, and  $Fr_C(Fr_A) = \frac{\rho u_0^2}{\epsilon z_C C_0 \phi_0}$  is the electric Froude number. Using the following physical constants for copper sulphate in distilled water:  $z_C = z_A = 2$ ,  $T = 293K$ ,  $\mu_C = 5.37 \cdot 10^{-4} \frac{cm^2}{Vs}$ ,  $\mu_A = 8.29 \cdot 10^{-4} \frac{cm^2}{Vs}$ ,  $D_A = D_C = 10^{-5} \frac{cm^2}{s}$ ,  $\nu = 1 \cdot 10^{-2} \frac{cm^2}{s}$ ,  $\rho = 1 \frac{g}{cm^3}$ ,  $\phi_0 = 1V$ ,  $\bar{\mu} = 6.83 \cdot 10^{-4} \frac{cm^2}{Vs}$ , the dimensionless numbers become:  $Pe_C(Pe_A) = 68.3$ ,  $Re = 0.068$ ,  $Fr_C(Fr_A) = 5.094 \cdot 10^{-8}$ ,  $Po_C(Po_A) = 7.731 \cdot 10^{-6}$ ,  $M_C = 1.272$ ,  $M_A = 0.824$ , (here we have used  $C_0 = 6.022 \cdot 10^{18} \frac{1}{cm^3} (0.01M)$ ,  $x_0 = 6.889 \cdot 10^{-4} cm$ ,  $E_0 = 1.452 \cdot 10^3 \frac{V}{cm}$  and  $u_0 = 0.991 \frac{cm}{sec}$ ). A thorough discussion of the dimensionless numbers is given elsewhere.

To obtain numerical solutions of system (1-5) the computational model assumes an initial configuration and solves the equations, for each time step and in a fixed lattice, using finite differences and deterministic relaxation techniques. For the growth model approximation, the interface of the deposit moves at random with a stochastic rule (details in [8]).

## EXPERIMENTAL AND NUMERICAL RESULTS

The experimental setup consists in an electrolytic cell in an horizontal position with parallel copper wire electrodes of 0.07mm of diameter, CuSO<sub>4</sub> solution (0.01 M) in distilled water and a voltage difference between 5 and 10 Volts. These parameters correspond to a regime in which electroconvection is dominant [5]. Fluid flow is visualized with neutral fluorescent spheres (latex FluoSpheres, Carboxyl 0.966  $\mu$ , Molecular Probes Inc.) added to the electrolyte solution. A Leica DM RX microscope with an objective of 5x and 10x is used with a lateral illumination from a Foster 8375 lamp. Image is recorded with a Sony CCD camera. An IBM PC486 compatible with a Cardinal Snapplus frame grabber is used for digitizing the images with 256 grey levels at 5 frames/sec and a maximum of 0.6 pixel/ $\mu$  resolution. The National Institute of Health public domain software package, Image [9], is used to superimpose digital snapshots to produce composite streak images with a Mac emulator provided by Ardi Co. The evolution of the front is digitized with a sequence of 90 frames taken at different intervals during growth. After thresholding, approximately 1000 particles are left and a center-of-mass calculation is performed on the image. Figures 1a) and 1b) show a top

Table 1: Averaged velocities for  $V=10V$  and  $5V$ 

No. of part.	Average vel. $\frac{\mu m}{sec}$	time	No. of part.	Average vel. $\frac{\mu m}{sec}$	time
6 (10V)	87.24	1'30"	6(5V)	61.12	1'50"
5 (10V)	93.91	2'36"	5 (5V)	58.04	3'40"
5 (10V)	94.73	3'00"	5 (5V)	43.70	8'48"
5 (10V)	96.79	3'30"	6 (5V)	46.76	12'6"
Average	93.17(10V)		Average	52.40(5V)	

view of the experiment focusing in the quasi-plane of the growth, when a voltage difference of 5 volts and 10 Volts, respectively, is applied between electrodes. Figure 1a) is the result of adding 90 frames while figure 1b) of adding 20. Fluid motion in the second figure is much faster, due to the higher voltage used. An individual particle in the funnel is tracked and its speed measured in its trajectory towards the tip of the branch. Table I shows the velocities at the funnel estimated for 5 volts and 10 volts. The table shows average velocities of different particles inside the funnel for different times during growth. The first particles are near the cathode and the last ones near the anode. Table I (left) shows how the average velocity increases moving from cathode to anode. This is due to the increase in the electric field. Averaged velocities over several particles inside the funnel tracked on a 5 frame interval is larger for the 10 volt run. This shows that velocities are higher for higher coulombic forces.

In our experiments gravitoconvection is still noticeable, although its influence is greatly diminished, for we observe tracking particles in front of the deposit, ascending from the bottom following an almost straight line orbit (at 150x) inside a buoyancy driven vortex tube, collide with a vortex ring entering into its circular orbit and increase their velocity an order of magnitude, eventually sticking to the deposit or being trapped into another orbit. The center of the vortex ring acts as a basin of attraction. The appearance of a physical displacement may produce the repulsion of the particle. Physical displacements of the deposit are possible due to fluid advection and electrostatic interaction [3].

The nature of the three-dimensional electrohydrodynamic ion transport resulting in ramified deposits is briefly outlined here (more details are presented elsewhere). Vortex rings suck ions through their centers, acting like funnels, enriching the filament tip and simultaneously advecting the tip which deforms into a crater-like shape. Local charges generated at the crater cusp (which, to break symmetry, must be rugged) induce new coulombic forces and new vortex rings. In turn, each new vortex ring will replicate its predecessor's behaviour. In this way three-dimensional split and branching occurs. For higher Froude numbers (low growth speed) the split and branching is quite symmetric and the three-dimensional deposit looks fractal-like. For lower Froude numbers the more chaotic nature of the flow produces a relative displacement between the crater cusp and its crown of vortex rings, resulting in loss of symmetry and a lower survival branching rate. The resulting three-dimensional deposit has less branching and looks more parallel (dense branch morphology). Although not shown here, in our experiments higher coulombic forces produce thinner and more parallel branches.

In the following we present the numerical results obtained in the simulation of a small region near the tip of a filament surrounded by fluid. For numerical stability the dimensionless numbers used here correspond to voltage differences of 0.5V and 1V respectively, and a bulk concentration of  $C_0 = 1 \cdot 10^9 \frac{1}{cm^3}$ . The resulting dimensionless numbers for the 0.5V

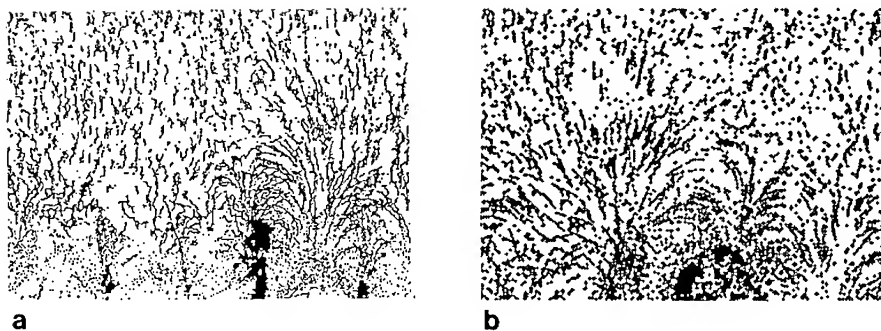


Figure 1. Electroconvection visualized with tracer particles. a) During 18 sec., 90 digital images are superposed to show the motion of the tracer particles in the flow, for a voltage difference of 5V. b) During 4 sec., 20 digital images are superposed, for a voltage difference of 10V.

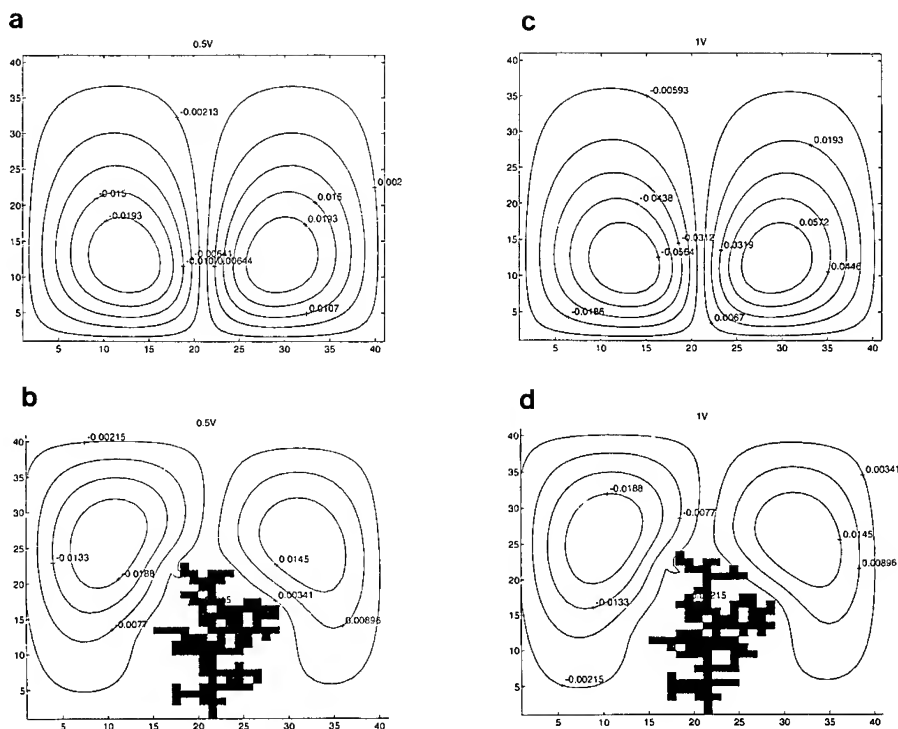


Figure 2. Numerical Simulations. a) Stream function around a spike for a voltage difference of 0.5V. b) Same result but with the growth model approximation. c) Stream function around a spike for voltage difference of 1V. d) Same result but with the growth model approximation.

(1V) are:  $Pe_C(Pe_A) = 34.5(68.3)$ ,  $Re = 0.034(0.068)$ ,  $Fr_C(Fr_A) = 1.168 \cdot 10^{-4}(9.2 \cdot 10^{-5})$ ,  $Po_C(Po_A) = 0.018(0.014)$ ,  $M_C = 1.272$ ,  $M_A = 0.824$ . Figure 2a) shows the stream function around a spike mimicking the deposit, obtained for  $(Fr_C(Fr_A) = 1.168 \cdot 10^{-4})$  and figure 2b) the same for the growth model approximation. Figure 2c) depicts the stream function around a spike for  $(Fr_C(Fr_A) = 9.2 \cdot 10^{-5})$  and figure 2d) the same for the growth model approximation. These results reveal that for higher coulombic forces, that is, lower electric Froude numbers, velocities (gradients of the stream function) increase at the tip, in agreement with experimental observations. More extensive results [8] suggest that a decrease in the Froude number produces deposits whose morphology changes from fractal to dense branching.

#### ACKNOWLEDGMENTS

G. M. thanks J. de Bruyn, J. N. Chazalviel, V. Fleury, S. Morris and M. Rosso for enlightening discussions and T. Molteno for the design of the electrolytic cell, and the hospitality of Memorial University, University of Toronto and Ecole Polytechnique-Palaiseau, where preliminary ECD experiments were made during a visit with a Thalmann Fellowship in 1995. P. M. acknowledges support of a UBA student research fellowship. This work was supported by UBA EX233/95.

#### REFERENCES

- [1] T. Vicssek, *Fractal Growth Phenomena 2nd. edn* (World Scientific, Singapore, 1992).
- [2] F. Argoul, J. Huth, P. Merzeau, A. Arneodo and H. L. Swinney, *Physica D* **62**, 170 (1993).
- [3] V. Fleury, J. Kaufman and B. Hibbert, *Nature* **367**, 435 (1994).
- [4] K. A. Linehan and J. R. de Bruyn, *Can. J. Phys.* **73**, 177, (1995).
- [5] V. Fleury, M. Rosso and J. N. Chazalviel in (*Mater. Res. Soc. Proc.* **367**, Pittsburg, PA, 1995)pp. 183-193.
- [6] J. Huth, H. Swinney, W. McCormick, A. Kuhn and F. Argoul, *Phys. Rev. E* **51**, 3444 (1995).
- [7] V. Fleury, G. Marshall et M. Rosso. Role de la viscosite dans la croissance electrochimique en cellule mince, to appear.
- [8] G. Marshall and P. Mocsos, *Phys. Rev. E* **55**, 1549 (1997).
- [9] The latest version of NIH-Image for Macintosh is available through Internet via anonymous ftp in directory /pub/image of zippy.nimh.nih.gov.

**Part III**

**Surface Modification and Characterization**

## SELF-ASSEMBLED ORGANIC MONOLAYER FILMS ON UNDERPOTENTIALLY DEPOSITED METAL LAYERS

G.K. JENNINGS, P.E. LAIBINIS

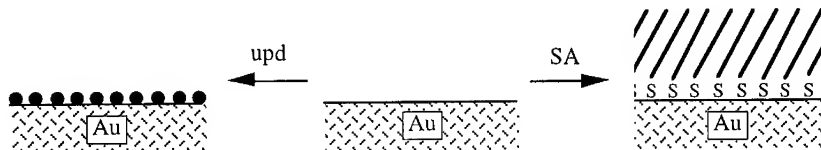
Dept. of Chemical Engineering, Massachusetts Institute of Technology, Cambridge, MA 02139

### ABSTRACT

This paper describes a new family of organized molecular assemblies that are produced by the spontaneous adsorption of alkanethiols onto gold surfaces that have been modified by the underpotential deposition of copper or silver. The system has the flexibility associated with the formation of self-assembled monolayers by the adsorption of thiols onto gold with the advantage of improved stability. The use of these systems as modified electrodes is also addressed.

### INTRODUCTION

Underpotential deposition (upd)<sup>1</sup> and self-assembly (SA)<sup>2</sup> represent two useful methods for modifying the surface of an electrode with up to one monolayer of material. In each case,



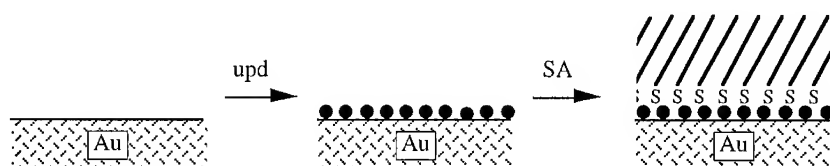
the monolayer formation is a self-limiting process and often produces epitaxial overlayers that have a high degree of structural order. The strengths of these methods are that the two processes differ in the type of adlayer that they produce -- metal (upd) and organic (SA) -- and they can provide a complementarity for the design and manipulation of organic/metal interfaces at atomic scales.

Self-assembled monolayers (SAMs) are a class of supported molecular films that form when organic molecules -- typically functionalized alkanes -- spontaneously adsorb onto a metal or metal oxide surface.<sup>2</sup> The formation of a SAM is driven by chemical interactions between the head groups of the organic adsorbates and active sites on the metal surface. The strength of these interactions typically governs the stability of the resulting SAM. The most popular and best characterized self-assembling system is the assembly of *n*-alkanethiols on gold, where the thiol head group binds to the gold surface and produces an ordered, densely-packed monolayer film.<sup>3-5</sup> Although these films have been proposed for numerous applications including sensors, thin-film optics, protection layers, surface coatings, and molecular adhesives,<sup>6,7</sup> they generally lack the long-term stability required for such applications. This lack of stability is especially pronounced at elevated temperatures and in aggressive environments where the S-Au bond that is responsible for the attachment may cleave and allow the components of the SAM to desorb from the surface.<sup>8</sup>

Upd offers the ability to tailor a metal surface with an atomic layer of a dissimilar metal by a straightforward electrochemical procedure.<sup>1</sup> The study of upd layers has provided much insight into the chemical structure and properties of metal/metal interfaces,<sup>9</sup> particularly for understanding adhesion and growth in electroplating processes. The ability to manipulate the chemical composition and constituency of a metal surface at the atomic level by this methodology provides the basis for our investigations into the properties of metal/organic interfaces and the use of this approach for improving the stability of SAMs.



To increase the stability of the thiols-on-gold system, we have developed a strategy that uses upd and SA in tandem. First, an upd adlayer of silver or copper is deposited on the gold electrode by cyclic voltammetry. The modified electrode is transferred from the electrochemical cell through air to a dilute solution of a thiol where a SAM is formed on the metal surface. In



this method, the upd metal is used as an interlayer between the gold surface and the adsorbing organic film and provides a flexible means of altering the surface chemistry of the support at the atomic level. If the thiol binds more strongly to the upd metal than to gold, then the presence of the upd metal would effect an increased adhesion between the organic layer and the electrode surface. We have focused our study on polycrystalline gold substrates modified by the upd of silver (Au/Ag(upd)) or copper (Au/Cu(upd)) because alkanethiols are known to form ordered SAMs on bulk silver and copper surfaces<sup>10</sup> and polycrystalline gold is widely used in device fabrication.

## EXPERIMENT

### Preparation of Assemblies

Gold substrates were prepared by the sequential evaporation of chromium (100 Å) and gold (1000 Å) onto silicon (100) wafers in a diffusion-pumped chamber with an operating pressure of  $2 \times 10^{-6}$  Torr. The gold-coated wafers were cut into  $1 \times 3$  cm<sup>2</sup> pieces and were used for upd and/or self-assembly within three days. Silver and copper were underpotentially deposited onto gold-coated wafers in a glass cell containing a gold-coated wafer as a counter electrode, a silver or copper wire as reference electrode, and a computer-controlled PAR Model 263A potentiostat. The exposed area of the working electrode was  $\sim 1$  cm<sup>2</sup>. The gold substrate was electrochemically cycled at 20 mV/s between 200 and 650 mV vs. reference for silver or between 50 and 550 mV vs. reference for copper in a 0.1 M H<sub>2</sub>SO<sub>4</sub>(aq) solution of 0.6 mM Ag<sub>2</sub>SO<sub>4</sub> or 1.0 mM CuSO<sub>4</sub>. On the second cathodic scan, the potential was held at a value just negative of the principal upd peak (460 mV for silver and 110 mV for copper). The electrode was emersed under controlled potential, rinsed with ethanol, blown dry in a stream of N<sub>2</sub>, and transferred rapidly through air to a 1 mM solution of an alkyl thiol in isooctane or ethanol for 1 h. The resulting SAMs were rinsed with hexane and ethanol and blown dry in a stream of N<sub>2</sub> prior to characterization.

### Thermal Desorption Studies

SAMs formed from *n*-C<sub>22</sub>H<sub>45</sub>SH on gold and Au/Ag(upd) (surface coverage,  $\phi_{Ag} = 0.6$ ) were exposed to decahydronaphthalene (DHN) at temperatures ranging from 70 - 103° C for various lengths of time. After removal from DHN, the samples were rinsed with hexane and ethanol and dried in a stream of N<sub>2</sub>. The thicknesses of the films were monitored *ex situ* by ellipsometry before and after exposure. The fractional SAM coverage was determined by normalizing these thickness measurements to the initial SAM thickness.

### Ellipsometry

SAM thicknesses were measured with a Gaertner LI 16A automatic ellipsometer equipped with a He-Ne laser at an incident angle of 70°. The refractive index of the SAMs was assumed

to be 1.46. Substrate values for upd assemblies were measured on unfunctionalized upd substrates within 2 min after emersion from the electrochemical cell. The reported thicknesses are the average of at least five independent experiments where each sample was characterized by ellipsometry at three different locations across the sample. The thickness for an independent experiment was the average of the measurements made at each of the three locations.

#### X-ray Photoelectron Spectroscopy (XPS)

XPS spectra were collected with a Surface Science Instruments Model X-100 spectrometer using a monochromatized Al K $\alpha$  x-ray source and a concentric hemispherical analyzer (pass energy = 150 eV). The detector angle with respect to the surface parallel was 35°. Peak positions were referenced to Au(4f<sub>7/2</sub>)=84.00 eV, and peaks were fit with 80% Gaussian/ 20% Lorentzian profiles and a Shirley background.

#### Electrochemistry

Cyclic voltammetry of SAMs formed from HS(CH<sub>2</sub>)<sub>10</sub>COC<sub>5</sub>H<sub>4</sub>FeC<sub>5</sub>H<sub>5</sub> on gold and Au/Ag(upd) was performed in a glass cell using a gold-coated silicon wafer as a counter electrode, a silver wire as a reference electrode, and a PAR Model 263A potentiostat. The SAM-coated working electrode was scanned at 100 mV/s in 0.1 M HClO<sub>4</sub> (aq). The amount of charge passed between the electrode and the monolayer was determined by averaging faradaic contributions to the anodic and cathodic peaks.

#### RESULTS

In preparing these assemblies, polycrystalline gold substrates were first atomically modified by upd of silver or copper, removed under potential control, rinsed with ethanol, and then, transferred through air to a 1 mM thiol-containing solution for at least 1 h. X-ray photoelectron spectroscopy (XPS) spectra of gold modified by upd of either silver or copper and functionalized with octanethiol are shown in Figure 1. Both spectra reveal the presence of the

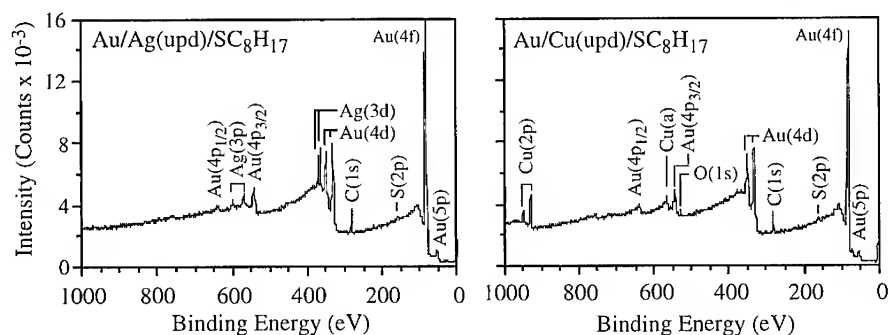


Figure 1. X-ray photoelectron spectra for SAMs of octanethiol on upd substrates.

expected elements: Au, Ag or Cu, S, and C. The spectrum for Au/Ag(upd)/SC<sub>8</sub> shows no oxygen signal although the sample was exposed to air during transfer to the thiol solution, suggesting that the Au/Ag(upd) substrate is not prone to oxidation or that any oxidation products are reduced by the thiol. The upd adlayers of silver are expected to be less prone to oxidation than bulk silver as the redox potential for Ag upd on gold is 510 mV positive of Ag<sup>+/0</sup>. For Au/Cu(upd), oxygen is detected for the functionalized sample by XPS; however, the level is lower than that typically observed for thiols adsorbed to bulk copper. Since the upd of copper

onto gold occurs at more reducing potentials than that of silver, the copper adlayer is expected to be more susceptible to oxidation than a silver adlayer, as was observed.

Table I displays the binding energies and coverages of Ag- and Cu-upd adlayers on gold, both before and after functionalization with an alkanethiol. The binding energy of each upd metal on gold is less than that of the corresponding bulk metal due to electronic equilibration with the gold substrate.<sup>11</sup> Adsorption of the alkanethiol induces a positive shift in the binding energy of each upd adlayer component, consistent with an oxidative addition process at the metal surface. This mechanism has been suggested for the assembly of thiols onto copper, silver, and gold, but has not been proven due to the inability to resolve the oxidized metal species at the interface from the bulk metal by XPS. As illustrated here, the upd/SAM system is a particularly convenient system for analyzing subtle binding energy changes arising from reactions at interfaces. The coverages of the Ag- and Cu-upd adlayers were submonolayer as indicated by XPS and coulometry<sup>12</sup> and exhibited no changes by XPS upon adsorption of an alkanethiol. These observations suggest that the upd metal remains at the sulfur/gold interface, is not displaced by the thiol, and does not diffuse into the gold.

Table I. XPS Binding Energies and Coverages for Ag and Cu Adlayers on Au

Sample	Ag		Cu	
	Binding Energy (eV) <sup>a</sup>	Coverage	Binding Energy (eV) <sup>a</sup>	Coverage <sup>c</sup>
bulk metal	368.0	-	932.0	-
Au/upd metal	367.4 <sup>b</sup>	0.64	931.3 <sup>b</sup>	0.92
Au/upd metal + C <sub>18</sub> H <sub>37</sub> SH	367.8 <sup>b</sup>	0.59	931.8 <sup>b</sup>	0.90

<sup>a</sup>Binding energies of Ag(3d<sub>5/2</sub>) and Cu(2p<sub>3/2</sub>) peaks. <sup>b</sup>Binding energies referenced to Au(4f<sub>7/2</sub>) at 84.0 eV. <sup>c</sup>Coverages are  $\pm 10\%$ .

We have found that the presence of a submonolayer amount of silver on the gold surface can increase the stability of adsorbed alkanethiolate films on gold.<sup>13</sup> A means of assessing this enhanced stability is to monitor the desorption rate of a SAM into a heated solvent.<sup>8,13</sup> The ellipsometry-monitored desorption of an n-docosanethiolate (C<sub>22</sub>H<sub>45</sub>S-) SAM from gold and Au/Ag(upd) ( $\phi_{\text{Ag}} = 0.6$ ) is shown in Figure 2 as a function of exposure time to a hydrocarbon solvent (DHN = decahydronaphthalene) at 103 °C. When adsorbed on gold, nearly 90% of the SAM desorbs within an hour while over 80% of the SAM remains on the Au/Ag(upd) ( $\phi_{\text{Ag}} = 0.6$ ) surface for an identical time of exposure. Data collected at temperatures between 70 and 103 °C indicate that SAMs bound to Au/Ag(upd) have desorption rate constants that are 5 to 12

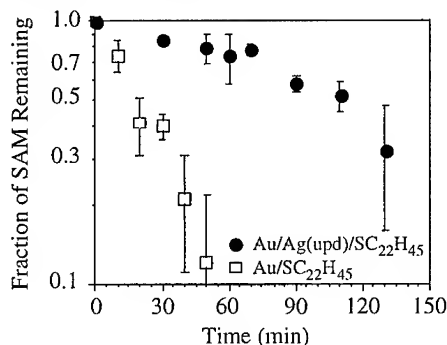


Figure 2. Ex situ ellipsometric coverages for n-docosanethiolate SAMs on Au and Au/Ag(upd) substrates as a function of exposure to decahydronaphthalene at 103 °C.

times smaller (slower) than those for SAMs bound to gold. This enhanced stability is a result of a stronger interaction between the sulfur head group and silver than to gold. As the coverage of Ag ( $\phi_{Ag}$ ) is increased (up to 85% of a monolayer), the stability of the SAM is improved further due to the formation of a greater number of stronger S-Ag bonds and fewer of the relatively weaker S-Au interactions.<sup>13</sup>

Like gold, the upd-modified substrates can accommodate thiol adsorbates with polar tail groups, such as -COOH or -OH, and substituted alkanethiols, such as those terminating in ferrocenyl groups ( $-C_5H_4FeC_5H_5$ ).<sup>14</sup> For example, electroactive SAMs prepared from  $HS(CH_2)_{10}COC_5H_4FeC_5H_5$  on Au/Ag(upd) exhibit reversible electrochemistry for the oxidation and reduction of ferrocene/ferrocenium as on a gold electrode (Figure 3). It is important to note

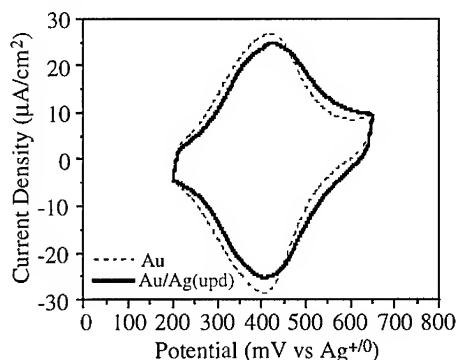


Figure 3. Cyclic voltammograms for Au and Au/Ag/upd substrates derivatized with  $HS(CH_2)_{10}COC_5H_4FeC_5H_5$

that the cyclic voltammogram shown in Figure 3 is not observed under normal conditions when the ferrocene-terminated adsorbate is bound to bulk silver, as the silver substrate would oxidize at  $\sim 0$  mV on the shown axis.<sup>15</sup> The Ag upd layer, which was deposited on gold at 510 mV, is stable to electrochemical cycling to at least 650 mV when a SAM is adsorbed on the Au/Ag(upd) substrate, as evidenced by XPS and cyclic voltammetry. The enhanced stability of the Ag adlayer to electrochemical oxidation after functionalization with an alkanethiol is attributed to the dielectric and physical screening of the upd metal by the SAM.

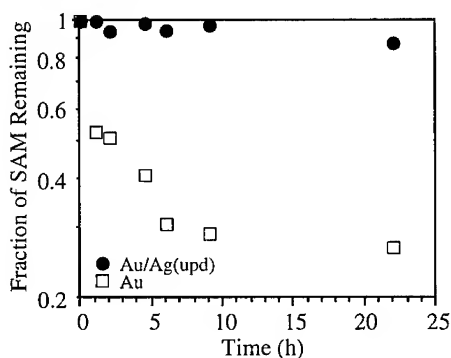


Figure 4. Replacement of  $C_5H_5FeC_5H_4CO(CH_2)_{10}S$ - SAMs on Au and Au/Ag(upd) substrates by exposure to  $C_{12}H_{25}SH$  (1 mM, ethanol). Coverages of the electroactive species were determined ex situ by cyclic voltammetry

As with unsubstituted *n*-alkanethiols, the ferrocene-terminated SAMs also exhibit greater stability when anchored to Au/Ag(upd), as compared with bare gold. For example, when exposed to a 1 mM solution of C<sub>12</sub>SH (ethanol), the electroactive SAM bound to gold exchanged rapidly with C<sub>12</sub>SH, but the SAM bound to Au/Ag(upd) did not exchange to any appreciable extent (Figure 4). These exchange studies represent another means of assessing the relative strength of an adsorbate/substrate bond. The slower exchange rates on Au/Ag(upd) suggest that the ferrocene-terminated thiolate is adsorbed more strongly and cannot be displaced from the surface by competing adsorbates.

## CONCLUSIONS

The self-assembly of alkanethiols onto gold surfaces provides a highly flexible means to prepare modified electrodes with potential chemical sensing applications. The use of underpotential deposition techniques can improve the stability of this class of molecular assemblies by incorporating an atomic interlayer at the gold/sulfur interface. Electroactive thiols that have been used as the components on gold for the construction of molecular sensors also self-assemble onto silver upd-modified gold surfaces and exhibit electrochemical signatures similar to those on gold electrodes with the advantage that the upd metal increases the stability of the adsorbed film. This behavior has been demonstrated for a thiol bearing an electroactive ferrocene tail group with a redox property ~400 mV positive of Ag<sup>+0</sup>.

## ACKNOWLEDGMENTS

We gratefully acknowledge the financial support of the Arnold and Mabel Beckman Foundation and the Office of Naval Research.

## REFERENCES

1. D.M. Kolb in *Advances in Electrochemistry and Electrochemical Engineering*, edited by H. Gerischer and C.W. Tobias, Wiley-Interscience, New York, 1978, Vol. 11, pp. 125-271.
2. A. Ulman, *An Introduction to Ultrathin Organic Films From Langmuir-Blodgett to Self-Assembly*, Academic Press, Boston, 1991, pp. 237-301.
3. A. Ulman, *Chem. Rev.* **96**, 1533 (1996).
4. L.H. Dubois and R.G. Nuzzo, *Ann. Rev. Phys. Chem.* **43**, 437 (1992).
5. E. Delamarche, B. Michel, H.A. Biebuyck, and C. Gerber, *Adv. Mater.* **8**, 719 (1996).
6. J.D. Swalen, D.L. Allara, H.D. Andrade, E.A. Chandross, S. Garoff, J. Israelachvili, T.J. McCarthy, R. Murray, R.F. Pease, J.F. Rabolt, K.J. Wynne, and H. Yu, *Langmuir* **3**, 932 (1987).
7. J.J. Hickman, D. Ofer, M.S. Wrighton, P.E. Laibinis, and G.M. Whitesides, *Science* **252**, 688 (1991).
8. C.D. Bain, E.B. Troughton, Y.-T. Tao, J. Evall, G.M. Whitesides, and R.G. Nuzzo, *J. Am. Chem. Soc.* **111**, 321 (1989).
9. S. Manne, P.K. Hansma, V.B. Elings, and A.A. Gewirth, *Science*, **251**, 183 (1991).
10. M.M. Walczak, C. Chung, S.M. Stole, C.A., Widrig, and M.D. Porter, *J. Am. Chem. Soc.* **113**, 2370 (1991); P.E. Laibinis, G.M. Whitesides, D.L. Allara, Y.T. Tao, A.N. Parikh, and R.G. Nuzzo, *ibid.* **113**, 7152 (1991).
11. D.M. Kolb and R.J. Michaelis, *J. Electroanal. Chem.* **284**, 507 (1990).
12. Coulometric coverages determined by averaging the cathodic and anodic charges for the upd peaks are 0.41 ± 0.05 for silver and 0.45 ± 0.05 for copper upd on gold.
13. G.K. Jennings and P.E. Laibinis, *Langmuir* **12**, 6173 (1996).
14. G.K. Jennings and P.E. Laibinis, submitted to *J. Am. Chem. Soc.*
15. L.S. Curtin, S.R. Peck, L.M. Tender, R.W. Murray, G.K. Rowe, and S.E. Creager, *Anal. Chem.* **65**, 386 (1993).

## ELECTROCHEMICAL HETEROEPITAXIAL GROWTH OF MOLECULAR FILMS ON ORDERED SUBSTRATES

Julie A. Last, Daniel E. Hooks, Christopher M. Yip, Michael D. Ward  
Department of Chemical Engineering and Materials Science, University of Minnesota,  
Minneapolis, MN 55455

### ABSTRACT

Electrocrystallization of the organic superconductor bis(ethylenedithio)tetrathiafulvalene triiodide,  $(\text{ET})_2\text{I}_3$ , on a highly ordered pyrolytic graphite (HOPG) substrate has been visualized using *in situ* atomic force microscopy (AFM). Previous studies have revealed the formation of a coincident epitaxial monolayer with a structure identical to that of a (001) layer of the superconducting beta phase of this material prior to bulk crystal growth. However, the symmetry of the HOPG substrate leads to domain boundary defects during self assembly of the separately growing domains. The number of defects is significantly reduced after an electrochemical annealing process in which the potential is cycled about the monolayer deposition potential. Annealing of these films is important if they are to be used in electronic devices as the defects may serve as barriers to electron transport in the two-dimensional layers.

In addition to  $(\text{ET})_2\text{I}_3$ , monolayer growth also has been visualized during electrocrystallization of  $(\text{ET})_2\text{ReO}_4$  on HOPG. The role of coincident epitaxy with HOPG in the monolayer formation and molecular orientation will be discussed.

Structurally modified substrates have also been investigated. Studies of the electrocrystallization of  $(\text{ET})_2\text{I}_3$  on HOPG, thermally treated to produce well-defined monolayer depth pit structures, have demonstrated that  $(\text{ET})_2\text{I}_3$  monolayer growth can occur inside the pit structures. The presence of monolayer domain boundaries within large pits indicates that multiple, independent nucleation events can occur in the pits, providing an opportunity to determine critical nucleation sizes by varying the pit dimensions. Recently we have discovered that  $\text{MoS}_2$  substrates can be electrochemically etched, giving rise to monolayer deep triangular pits.

### INTRODUCTION

There is increasing interest in the fabrication of crystalline molecular films for many electronic and optical technologies.<sup>1</sup> This interest stems from the ability to manipulate film structure and properties through the choice of molecular constituents and control over the molecular assembly on the substrate surface. This work focuses on the epitaxial growth of mono- and multilayer films of conducting organic charge transfer salts by electrocrystallization. Electrocrystallization is advantageous as compared to vapor phase and molecular beam techniques as growth can be performed in solution under ambient conditions. This allows growth to be viewed *in situ* and in real-time with the atomic force microscope (AFM).

Charge transfer salts typically exhibit layered structures with strong intralayer bonding and weak van der Waals bonding between layers.<sup>2</sup> This suggests that these materials can be used to fabricate robust, crystalline mono- and multilayer films. Studies conducted in our laboratory demonstrate that molecular films based on charge transfer salts exhibit structures identical to the bulk.<sup>3</sup> Analysis of these systems revealed that in all cases monolayer growth was governed by coincident epitaxy with the substrate surface. Coincidence exists when rows of overlayer sites are coincident with uniformly spaced rows of substrate sites corresponding to a specific lattice direction, such that one of the reciprocal lattice vectors of the overlayer has the same direction as the reciprocal lattice vector defined by the substrate rows (Figure 1).<sup>4</sup> An integral multiple relationship between the magnitudes of an overlayer reciprocal lattice vector and a substrate reciprocal lattice vector such that  $b_j^* = na_1^*$ , where  $n$  is an integer, but is not equal to zero. Consequently, commensurism exists with respect to these reciprocal lattice vectors ( $a_1^*$  and  $b_1^*$ ) while some overlayer sites are locally incommensurate along the vectors  $b_1$  and  $b_2$ . The degree of epitaxy therefore is weaker than in a truly commensurate structure. Coincidence also implies the existence of a non-primitive overlayer supercell, constructed from an integral number of

overlayer unit cells, whose perimeter is commensurate with the substrate. This is equivalent to stating that some overlayer positions (most commonly chosen to be the vertices of the supercell) coincide with substrate sites at periodic intervals, while other positions contained within the supercell are locally non-commensurate. For a given system the degree of epitaxy, and therefore the energetics, will improve as the number of primitive overlayer cells necessary to construct the non-primitive supercell decreases, as this leads to fewer non-commensurate overlayer sites.

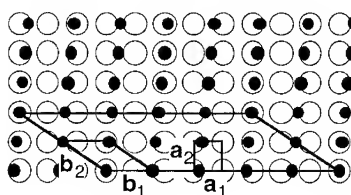


**Figure 1.** Schematic representation of a coincident overlayer with  $b_1 = 1.6a_1$ ,  $b_2 = 1.8a_2$  and  $\beta = 146.25^\circ$ . The  $5 \times 2$  non-primitive supercell having vertices which are commensurate with the substrate is depicted.

Molecular overlayers generally will comprise a large number of molecules assembled into low-symmetry two-dimensional lattices. The size and symmetry of these lattices will differ substantially from those of typical substrates, arguing against commensurate lattices in the absence of overlayer reconstruction. Consequently, any analysis of overlayer-substrate interfaces must consider the possibility of coincident overlayers.

The role of coincident epitaxy in the electrochemical growth of two organic overlayers on a highly ordered pyrolytic graphite substrate (HOPG) will be described herein:  $(\text{ET})_2\text{I}_3$  on HOPG and  $(\text{ET})_x(\text{ReO}_4)_y$  on HOPG. An electrochemical annealing process which reduces the number of grain boundaries will also be described. In addition, monolayer growth on modified substrates will be discussed.

## EXPERIMENT

Atomic force microscopy experiments were performed using a Digital Instruments, Inc. Nanoscope III scanning probe microscope and  $\text{Si}_3\text{N}_4$  tips (quoted spring constant of  $0.06 \text{ Nm}^{-1}$ ). A piezoelectric scanner with a maximum lateral scanning range of  $15 \mu\text{m} \times 15 \mu\text{m}$  was used for imaging. All images shown were obtained in lateral force mode, at tip scan rates ranging from 2 to 10 Hz. Electrodeposition of the monolayers was performed in acetonitrile solutions containing 0.5 mM ET (Aldrich) and 2 mM tetrabutylammonium triiodide or 0.1 M tetrabutylammonium perchlorate.

Electrodepositions were performed in an AFM fluid cell (Digital Instruments) equipped with ports for fluid entry and exit. Freshly cleaved highly oriented pyrolytic graphite (HOPG) was used as the substrate and working electrode, and platinum counter and quasi-reference electrodes were inserted through the outlet port of the fluid cell. Potential cycling was performed by applying a square wave with a homemade function generator. Potential limits were chosen based on the potential at which monolayer deposition and dissolution was observed in the scanning region. Typically, deposition first occurred at approximately 650 mV vs. Ag/AgCl, with the monolayer remaining stable at 620 mV. The potential was cycled approximately  $620 \pm 75$  mV, with the anodic potential held for approximately 20 seconds and the cathodic potential held for approximately 15 seconds.

Modified graphite substrates were prepared by placing freshly cleaved highly oriented pyrolytic graphite (HOPG) (Grade ZYH, Advanced Ceramics Corp. Cleveland, OH.  $\approx 1.2 \text{ cm} \times 1.2 \text{ cm} \times 0.2 \text{ cm}$ ) in a box furnace preheated to  $900^\circ\text{C}$ . The HOPG pieces were placed in ceramic crucibles prior to heating. The samples were heated for approximately 60 seconds, removed from the furnace and allowed to cool in the laboratory ambient. The density of pit coverage can be moderated by controlling both exposure time and temperature.

## RESULTS

### a) (ET)<sub>2</sub>I<sub>3</sub> on HOPG

Electrochemical oxidation of ET at 650 mV (vs. Ag/AgCl) in acetonitrile containing 2 mM n-Bu<sub>4</sub><sup>+</sup>N I<sub>3</sub><sup>-</sup> results in growth of a monolayer with lattice parameters (**b**<sub>1</sub> = 6.6 Å, **b**<sub>2</sub> = 9.1 Å, β = 110°) mimicking the (001) layer of β-(ET)<sub>2</sub>I<sub>3</sub> on an HOPG electrode, which can be observed directly in real-time by AFM (Figure 2).<sup>3c,3d</sup> Lateral force imaging, which relies on lateral twisting of the AFM cantilever due to friction between the tip and sample, revealed that complete monolayers actually formed by coalescence of separate growing domains. When imaging was performed such that the cantilever scan direction was perpendicular to the cantilever long axis (90° scanning mode) the domain boundaries were clearly revealed by large friction values compared to the domain interiors. The AFM data revealed identical heights (15.5 Å) and lattice parameters for all the domains,<sup>3c,3d</sup> although the monolayer lattices exhibited three different orientations at ±60°. This is consistent with the symmetry of the HOPG substrate and the epitaxy between the substrate and monolayer. AFM data and modeling of the interface<sup>3c,3d,5</sup> confirmed that epitaxy was achieved by coincidence at an azimuthal orientation of 19.8°, with the monolayer lattices vectors described by **b**<sub>1</sub> = 4.0**a**<sub>1</sub> + 2.0**a**<sub>2</sub> and **b**<sub>2</sub> = -4.0**a**<sub>1</sub> + 3.3**a**<sub>2</sub>, where **a**<sub>1</sub> and **a**<sub>2</sub> are the in-plane lattice vectors of HOPG. The enhanced friction at the domain boundaries can be attributed to disorder in these regions owing to orientational mismatch, which can lead to a decrease in the rigidity of the film at the boundaries. Previous studies have suggested that friction is greater for domains with lesser order and lower moduli due to greater penetration of the tip in softer phases.<sup>6,7</sup>

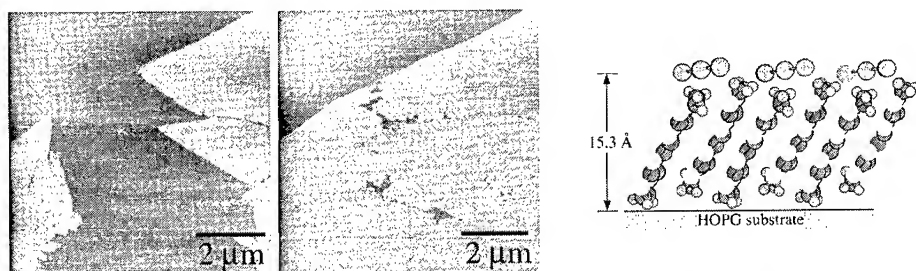


**Figure 2.** *In situ*, real-time AFM imaging of the electrocrystallization of (ET)<sub>2</sub>I<sub>3</sub> on HOPG revealed the formation of a monolayer 15 Å in height. Scan size = 8 × 8 μm. (a) t = 1 min, (b) t = 4 min. Also pictured is a schematic representation of a (001) layer of β-(ET)<sub>2</sub>I<sub>3</sub> on HOPG.

Real-time AFM revealed that application of a potential which was cathodic of the monolayer stripping potential (550 mV vs Ag/AgCl) resulted in film dissolution at the domain boundaries due to the higher free energy of the β-(ET)<sub>2</sub>I<sub>3</sub> monolayer at the domain boundaries.<sup>8</sup> Dissolution generally was more rapid at the boundaries of domains having larger perimeter-to-area ratios. Cycling the film potential between 550 mV and 675 mV vs Ag/AgCl, which is cathodic of the stripping potential and anodic of the deposition potential, respectively, resulted in progressive growth of the larger domains at the expense of smaller domains (Figure 3).<sup>9</sup> For example, the areas of domains 1, 2, and 3 in Figure 3 decrease upon potential cycling, while numerous domains in the center of the scanned region disappear completely. Domains 4, 5, and 6 increase in area, with domains 5 and 6 annealing into a single domain filling most of the scan area, resembling Ostwald ripening.<sup>1</sup> The result is an overall reduction of the total length of domain boundaries, with the data in Figures 3a, 3b, and 3c exhibiting total domain boundary lengths of 23.9, 18.7 and 14.3 μm, respectively. Additional experiments have demonstrated that incompletely dissolved domains regrow with the same orientation as the smaller domain, but growth from surrounding larger domains intrudes on the region previously occupied by the



domain. This results in a progressive movement of the domain boundary toward the center of the smaller domain until the annealing is complete. Secondary nucleation events in the dissolved regions were never observed.

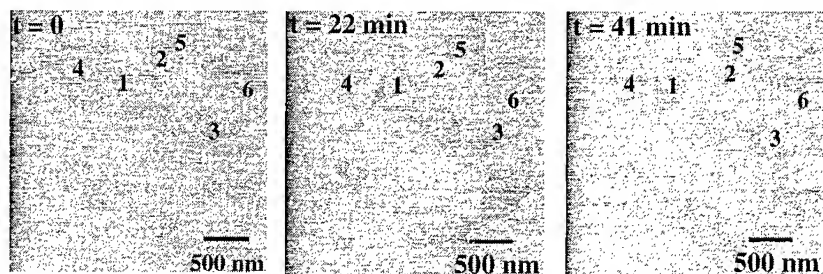


**Figure 3.** Sequence of AFM images illustrating the electrochemical annealing of a (001)  $\beta$ -(ET) $_2$ I $_3$  monolayer acquired in lateral force mode *in situ* during potential cycling between 550 and 650 mV (vs. Ag/AgCl) at (A)  $t = 0$ , (B)  $t = 22$  min., (C)  $t = 41$  min. The data was collected with the tip oriented at  $90^\circ$  with respect to the direction of tip motion. The number and the overall perimeter of the domain boundaries decrease with time. The domain boundaries are highlighted here with dashed lines for clarity. The numbered domains are discussed in the text.

#### (b) (ET) $_x$ (ReO $_4$ ) $_y$ on HOPG

Monolayer growth was also observed when ET was electrochemically oxidized in the presence of 0.1 M tetrabutylammonium perrhenate (Figure 4). The monolayer height is approximately 6.7 Å, suggesting that the ET molecules are arranged such that the sulfur atoms are in contact with the HOPG surface. Periodicities obtained by AFM gave 2-D lattice parameters ( $b_1 = 7.1$  Å,  $b_2 = 19.8$  Å,  $\beta = 103^\circ$ ) which are not consistent with any low index plane of known crystal structures. A theoretical analysis of the interface<sup>4</sup> using the experimentally determined lattice parameters indicate that the formation of this monolayer is governed by coincident epitaxy with the HOPG substrate. The azimuthal orientation obtained from the calculations is  $36.8^\circ$ , which agrees well with the experimentally determined angle of  $36^\circ$ .

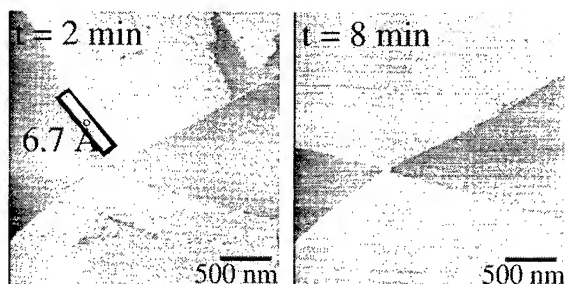


**Figure 4.** *In situ*, real-time AFM imaging of the electrocrystallization of (ET) $_x$ (ReO $_4$ ) $_y$  on HOPG revealed the formation of a monolayer 6.7 Å in height. (a)  $t = 2$  min, (b)  $t = 8$  min.

#### (c) (ET) $_2$ I $_3$ on structurally modified HOPG

While previous studies demonstrated that the formation of large  $\beta$ -(ET) $_2$ I $_3$  monolayer islands precedes bulk crystal growth, the critical nuclei radius remains unknown. Controlling the structure of the nucleating interface represents one means of addressing this issue. A route especially well-suited for examining such structural considerations involves thermal oxidation of cleaved highly oriented pyrolytic graphite (HOPG) that has been shown to afford well-defined

mono- and multilayer pits on the (0001) HOPG face.<sup>10,11</sup> The role of these "molecular corrals" in influencing both the rate and orientation of liquid crystal self-assembly recently was reported.<sup>12</sup> In contrast to these liquid crystal studies where the presence of a multilayer structure makes it difficult to extract the influence of the second and higher layers on orientation of the first monolayer in the corral or terrace, true monolayer growth would facilitate direct observation of independent nucleation and growth events within corrals and on the surrounding terraces. An estimate of critical nuclei dimensions may be acquired from a comparison of the relative rates of nucleation within the corrals and on adjoining larger terraces. Lateral interactions between monolayers may be assessed through comparison of the orientational mismatch or lack thereof between monolayers forming on the surrounding terraces and within the corrals.

While monolayer growth appeared to be largely suppressed in the "molecular corrals" when compared to nucleation rates on the surrounding terraces (Figure 5), the formation of grain boundaries within large, contiguous corrals suggested that, while independent nucleation events may occur within the corrals, a minimum island size must be attained in order for stable monolayer growth to occur (Figure 6). Close examination of the boundary between a monolayer covered terrace and its filled corral counterpart revealed that the monolayer orientations were independent, reflecting solely the orientation of the underlying graphite lattice (i.e. the monolayers were oriented at  $\pm 60^\circ$  to each other). Studies are underway to acquire statistical information on the nucleation of  $\beta$ -ET<sub>2</sub>I<sub>3</sub> inside corrals of various sizes.

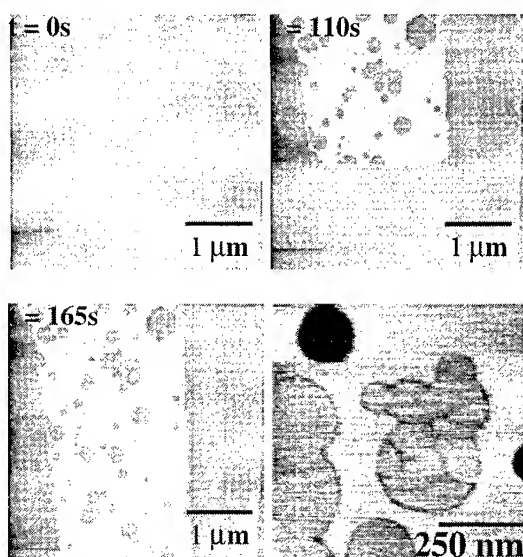


**Figure 5.** Real-time AFM solution contact mode images of ET<sub>2</sub>I<sub>3</sub> monolayer growth on topographically modified graphite revealing growth front progression on large contiguous terraces. Note how growth initiates on terraces and proceeds around pit structures. Frame size : 4  $\mu\text{m}$  x 4  $\mu\text{m}$ . Images collected at (a) 0 seconds ; (b) 110 seconds ; (c) 165 seconds. (d) Monolayers of (001) oriented  $\beta$ -(ET)<sub>2</sub>I<sub>3</sub> grown electrochemically in "Ignatz-like" etch pits on a thermally etched HOPG substrate.<sup>13</sup>

#### (d) Electrochemical modification of MoS<sub>2</sub>

We have discovered recently that MoS<sub>2</sub> can be etched electrochemically to produce small triangular, monolayer deep pits in the MoS<sub>2</sub> surface (Figure 6). Previous reports have described random etching of MoS<sub>2</sub> due to mechanical interaction with an AFM or STM tip.<sup>14</sup> Electrochemical etching is advantageous as the size and spatial distribution of the pits can be controlled easily by control of the etching potential and time. Etching occurs at potentials exceeding 1V vs. Pt. We have observed that etching just above 1V vs. Pt and for longer times (minutes) will result in a small number of large pits whereas at higher potentials and short times (seconds) numerous small pits are observed. Subsequent etching of the second layer yields triangular etch pits rotated by 180°, revealing the 2H stacking polytype of the MoS<sub>2</sub> crystal

(Figure 6). We are currently exploring electrochemical heteroepitaxial growth of molecular overlayers on MoS<sub>2</sub> substrates patterned in this manner.

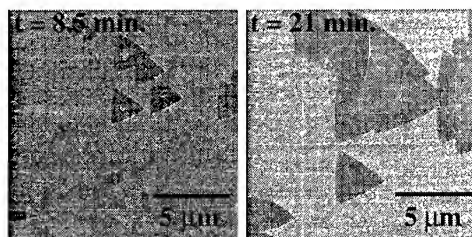


**Figure 6.** Real-time AFM imaging of the electrochemical etching of triangular, monolayer deep pits on a MoS<sub>2</sub> surface. The applied potential was 1.5 V (vs. Pt). Note that the second layer has a pit which is rotated by 180°.

## CONCLUSIONS

These observations illustrate that monolayer films with potentially novel electronic properties can be prepared by electrochemical routes, and that these films can be electrochemically annealed by simple potential cycling about the deposition and dissolution potentials. The ability to visualize these processes *in situ* and in real time with AFM enables elucidation of the role of epitaxy in domain formation and the influence of domain size on the dynamics of annealing. The combination of electrochemical growth and annealing can enable the fabrication of high quality redox-active molecular films on substrates with non-planar geometries.

## ACKNOWLEDGMENTS

The authors acknowledge the financial support of the Office of Naval Research and the University of Minnesota Graduate School.

## REFERENCES

- 1 (a) Molecular Electronic Devices, F. Carter, Ed. (Marcel Dekker, New York, 1982). (b) Molecular Electronics, G. Ashwell, Ed. (John Wiley and Sons, New York, 1992).
- 2 A. Uhlman, R.P. Scaringe, *Langmuir* **8**, 894 (1992).
- 3 (a) J. Hossick-Schott, M.D. Ward, *J. Am. Chem. Soc.* **116**, 6806 (1994). (b) J. Hossick-Schott, C.M. Yip, M.D. Ward, *Langmuir* **11**, 177 (1995). (c) A.C. Hillier, J.B. Maxson, M.D. Ward, *Chem. Mater.* **6**, 2222 (1994). (d) A.C. Hillier, J. Hossick-Schott, *Adv. Mater.* **7**, 409 (1995).
- 4 W. Unertl, in Scanning Tunneling Microscopy and Spectroscopy Theory, Techniques, and Applications, edited by D.A. Bonnell (VCH Publishers, Inc., New York, 1993), p. 115.
- 5 A.C. Hillier, M.D. Ward, *Phys. Rev. B*, in press.
- 6 R. M. Overney, E. Meyer, J. Frommer, H. J. Guntherodt, M. Fujihara, H. Takano, Y. Gotoh, *Langmuir* **10**, 1281 (1994).
- 7 X. Xiao, J. Hu, D.H. Charych, M. Salmeron, *Langmuir* **12**, 2359 (1996).
- 8 M. Ohring, The Materials Science of Thin Films (Academic Press, Inc., New York, 1992).
- 9 J.A. Last, M.D. Ward, *Advanced Materials* **8** (9), 730 (1996).
- 10 Evans, E.L.; Griffiths, R. J. M.; Thomas, J.M. *Science* **171**, 174 (1970).
- 11 Yang, R.T.; Wong, C. J. *Chem. Phys.* **75**(9), 4471 (1981).
- 12 Patrick, D.L.; Cee, V.J.; Beebe Jr., T.P. *Science* **265**, 231 (1994).
- 13 Ignatz was the brick-tossing sidekick of Krazy Kat, the subjects of a cartoon strip written by George Harriman and published daily between 1918 - 1941.
- 14 (a) Ed Delawski and B. A. Parkinson, *J. Am. Chem. Soc.* **114** 1661 (1992). (b) B. A. Parkinson, *J. Am. Chem. Soc.* **112** 7498 (1990).

## Epitaxial Growth of Organic Molecules on Vicinal Surfaces of Single Crystals

Toshihiro Shimada, Takafumi Sakurada and Atsushi Koma

Department of Chemistry, University of Tokyo, Bunkyo-ku, Tokyo 113, JAPAN

shimada@chem.s.u-tokyo.ac.jp

### ABSTRACT

Ultrathin film growth of vanadyl phthalocyanine was attempted on vicinal surfaces of hydrogen-terminated Si(111) in order to see the effect of regularly spaced steps to the growth feature. It has been observed that molecular arrangement was substantially affected when the terrace width was narrower than 2~4 times of the molecular lattice constants. This result is probably due to the weakness of molecular interaction in the material and it accounts for the reason why ordinary graphoepitaxy has not been successful for the organic thin films.

### INTRODUCTION

Organic ultrathin films grown on the surface of inorganic materials are of potential importance for the application to electrochemistry as well as to optoelectronic devices, and molecular ordering in the films is essential for some of the applications. Several methods have been established to achieve the ordering such as vapor phase epitaxy and self assembly, but the use of single crystalline substrates has been necessary. This is a limitation for the wide application of the organic thin films. Although the graphoepitaxy technique does not require single crystalline substrates, its application to the organic molecular materials has not been successful to the authors' knowledge. Graphoepitaxy utilizes array of  $\mu\text{m}$  scale grooves formed on amorphous substrates as the guides for the crystallographic arrangement in the films. We suspect that the effective range of the intermolecular force is too short to transfer the crystallographic information from guiding grooves separated by  $\mu\text{m}$  distance. In order to see how narrowly the guides should be separated to control the molecular orientation, we here attempted the use of miscut Si (111) wafers as substrates. By changing the miscut angle, we can in principle control the spacing of the atomic height steps. The surface of the substrates were hydrogen-terminated to get rid of the effect of chemical bonding on the surfaces. The grown molecule was vanadyl phthalocyanine (VOPc), which has a pyramid shape and is known to grow epitaxially on hydrogen-terminated Si (111) (H-Si(111)) [1].

## EXPERIMENTAL

The substrates used were n-type Si(111) wafers, with the surface tilted  $0^\circ$ ,  $2^\circ$ ,  $4^\circ$  and  $7^\circ$  toward  $\langle 11\bar{2} \rangle$ , all purchased as polished from vendors. Their surfaces were oxidized, etched and finally terminated with monohydride by using a wet process. The details of the substrate treatment are reported elsewhere [2,3]. After rinsing in distilled water and drying by  $N_2$  gas, they were introduced into a vacuum system with a base pressure of  $2 \times 10^{-7}$  Pa. The atomic structure of the surfaces were determined using reflection high energy electron diffraction (RHEED) with an acceleration energy of 15 kV. Purified VOPc powder was evaporated from Knudsen cells. The growth rate was about 1 monolayer (ML) per minute.

The molecular arrangement in the grown films was characterized by a new technique as briefly reported elsewhere [3]. It utilizes RHEED to obtain two dimensional reciprocal images similar to low energy electron diffraction (LEED). This technique was developed to reduce the electron bombardment effects and to enable the analysis of the growth on insulating substrate materials, both of which were made possible by making use of the shallow incident angle in RHEED. The procedure for the measurement is as follows (Fig.1). (1) RHEED patterns obtained with every  $2^\circ$  incident azimuth were recorded by a CCD video camera by rotating the sample around the surface normal. (2) The images were digitized into pixel data (8 bits each) using a video board installed in a personal computer. (3) A line parallel to the shadow edge with a constant reciprocal coordinate perpendicular to the surface was chosen in each image. (4) The intensity variation along the lines was accumulated in a two-dimensional plane, after being rotated by the angles corresponding to the incident azimuths. By repeating the process for  $180^\circ$  range of incident azimuth, the reciprocal image perpendicular to the surface is obtained. According to the kinematical analysis, the resulting image corresponds to the reciprocal image parallel to the surface plane after shifting the center of the reciprocal space (see APPENDIX).

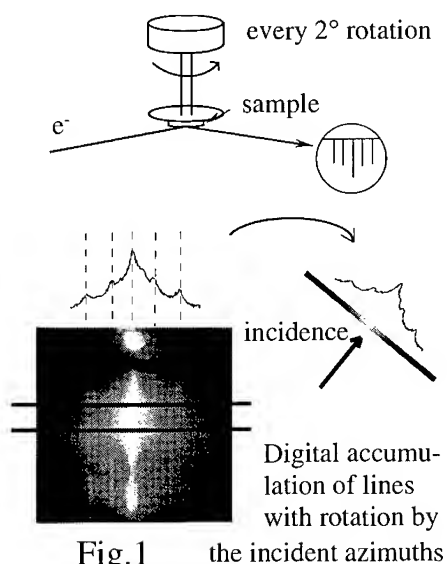


Fig.1

## RESULTS AND DISCUSSIONS

Figure 2 shows the RHEED pattern of the hydrogen-terminated 4°- off Si (111) with the incident from  $[1\bar{1}0]$ . It shows three pairs of narrow -spaced streaks. The wide spacing between the pairs corresponds to 0.333 nm, which is  $\sqrt{3/2}$  of the atomic spacing of Si(111) surfaces. The split, therefore, indicates the existence of the ordering and the period was estimated as  $4.0 \pm 0.5$  nm from the image. Since it is correspondent with the terrace width, the step height was calculated to be  $0.28 \pm 0.04$  nm by using the nominal miscut angle of 4°. It agrees with the height of monatomic steps (0.314 nm). It was also confirmed that the step height was monatomic in the cases of 2°- and 7°-off substrates.

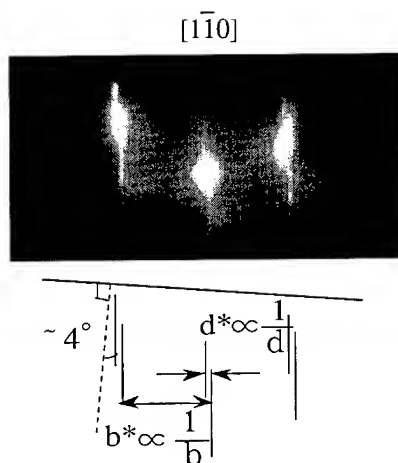


Fig. 2

RHEED patterns of the grown films showed streaks which indicates the flatness and crystallographic ordering of the film surface for all of the miscut angles of the substrates when the film was a few monolayer thick. Figure 3 shows the two dimensional reciprocal images (negative images; black portion has strong diffraction intensity) from the VOPc film grown on H-Si(111) with various miscut angles. The thickness was 1 ML for 2°, 4°, 7°-off substrates ((b)(c)(d)), and it was 30 ML for just-cut substrate ((a)). The center of the reciprocal space is indicated by white dots. The RHEED pattern for the film on the just-cut substrate (Fig. 3(a)) did not change substantially from 1ML thickness to 30 ML thickness. Fig. 3(a) shows 12-fold symmetry as expected from the difference in the symmetry between the molecular lattice (4-fold) and the substrate (6-fold). On the other hand, Fig. 3(d) shows lines along  $\langle 11\bar{2} \rangle$  (A-A', B-B' and C-C'), which is perpendicular to the direction of the steps, as well as broad spots  $\pm 15^\circ$ -off from  $\langle 1\bar{1}0 \rangle$ . Since the direction of the steps on this substrate is not parallel to that of the VOPc lattice on just-cut H-Si(111), there are two possibilities in the lattice orientation as illustrated in Fig. 4. In Fig. 4(a), the molecular lattice, which is shown by large dots and broken lines, changes the orientation to align to the steps, while in Fig. 4(b), the orientation is not changed from the optimum one on the just-cut substrate. The lines along  $\langle 11\bar{2} \rangle$  correspond to Fig. 4(a), because the molecules have ordering only along the steps. The broad spots correspond to Fig. 4 (b), although

the ordering is rather two dimensional, which indicates the span of the molecular ordering is across several terraces. The lack of other spots with 12-fold symmetry indicates that the domain orientation is influenced by the existence of the steps. The existence of the lattice like Fig.4 (a) indicates that the molecular lattice is actually affected by the steps when the miscut angle is  $7^\circ$ .

Since Fig. 3 (b) and (c) show only spot patterns similar to Fig. 3 (a) and do not show strong line patterns, it is concluded that the transition of the molecular lattice orientation occurs at the miscut angle between  $4^\circ$  and  $7^\circ$ . That range corresponds to

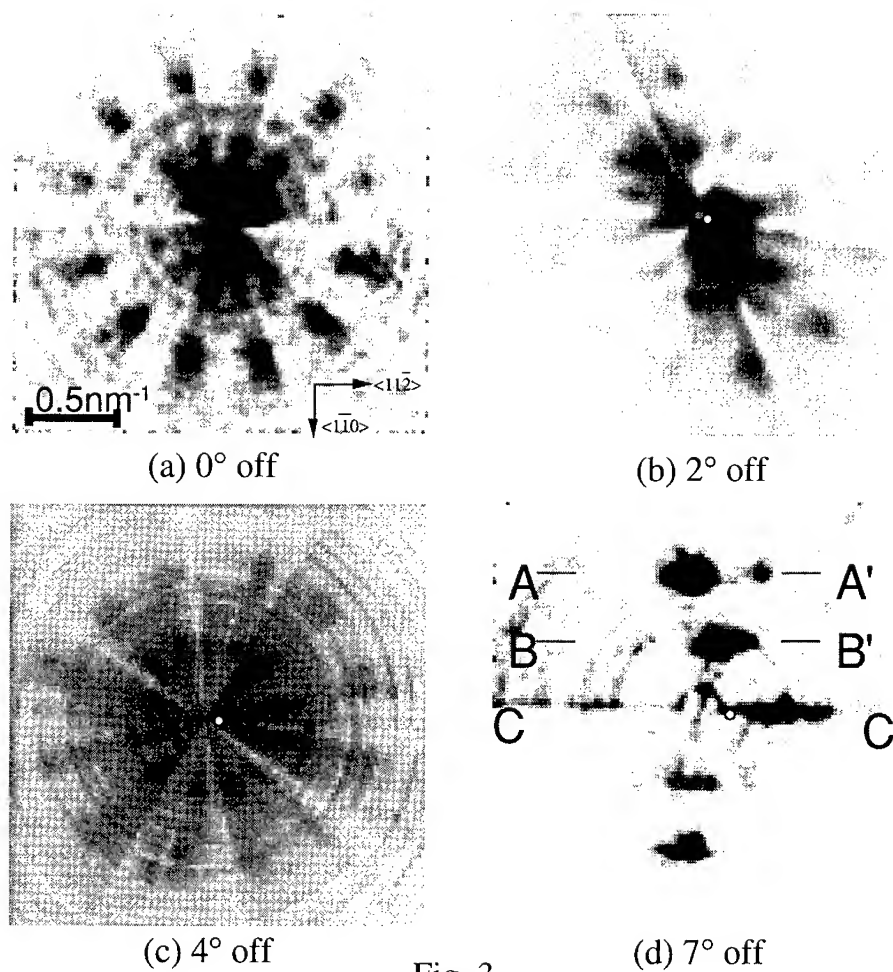
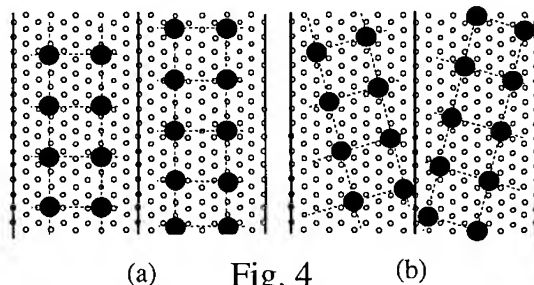


Fig. 3

the terrace width of 2~4 VOPc molecules ( $24\sim40\text{\AA}$ ). The weakness of the diffraction spots with higher indices in Fig. 3(b) and (c) shows that the Debye-Waller type factor is larger than in the case of just-cut substrates. Probably it is due to the orientation disorder of the molecules [3].



(a) Fig. 4 (b)

## CONCLUSION

We have examined the growth feature of an organic molecule VOPc on hydrogen terminated Si(111) with various miscut angles. The effect of the steps to the molecular lattice direction is observed only when the terrace width is narrower than 2~4 times of molecular lattice constant. It is therefore suggested that the guides for the crystal orientation in the graphoepitaxy must be of nm-scale for weak bonding organic molecules. Steps on vicinal surfaces of single crystals will be useful to modify the orientation of the molecular lattices.

## APPENDIX

Here we explain the detail of the construction of 2D reciprocal images from RHEED patterns of the films on vicinal surfaces. There are three approximations in

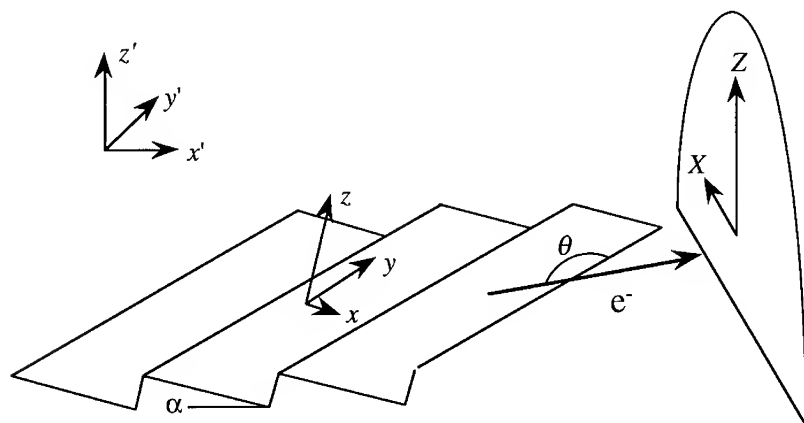


Fig. 5



our procedure: (1) The scattered electrons are not blocked by the terrace. This is valid when we do not treat very small takeoff angles. (2) The scattering is kinematical and multiple scattering by terraces can be ignored. This is valid because we use electrons with large kinetic energies. (3) The Ewald sphere can be approximated as a plane. This is valid because we are dealing with the scale of  $0.5\text{nm}^{-1}$ , and the wavelength of the electrons is of the order of  $100\text{nm}^{-1}$ . Let the miscut angle of the substrate  $\alpha$  and the azimuth of incident electron  $q$ , as illustrated in Fig. 5. Then we define the reciprocal Cartesian coordinate systems  $x^*y^*z^*$  (on a tilted terrace) and  $x'^*y'^*z'^*$  (on the surface plane),  $XYZ$  (RHEED screen) and  $k_xk_y$  in the resulting planar image (Fig.5;  $xyz$  and  $x'y'z'$  are corresponding real space coordinates.). We choose a line with  $Z=Z_0$  on the RHEED screen and rotate the sample by changing  $q$ . The relationship of the coordinates are

$$\begin{cases} x'^* = \cos \alpha \ x^* + \sin \alpha \ z^* \\ y'^* = y^* \\ z'^* = -\sin \alpha \ x^* + \cos \alpha \ z^* \end{cases} \quad \begin{cases} X = \cos \theta \ x'^* - \sin \theta \ y'^* \\ Y = \sin \theta \ x'^* + \cos \theta \ y'^* \\ Z = z'^* \end{cases} \quad \begin{cases} k_x = X \cos \theta \\ k_y = X \sin \theta \end{cases}$$

After a short arithmetic operation we obtain

$$\begin{cases} x^* = \cos \alpha \ k_x - \sin \alpha \ Z_0 \approx k_x - \sin \alpha \ Z_0 \\ y^* = -k_y \end{cases}$$

The approximation (" $\approx$ ") in the first equation is valid because  $\alpha$  was  $0\sim 7^\circ$  in the experiment, which means  $\cos \alpha$  was  $1\sim 0.9925$ . This result indicates that the 2D reciprocal image of the molecular lattice on the terrace is obtained from the accumulation of the line image with the rotation, followed by the shift of the origin and by flipping one coordinate parallel to the steps.

## REFERENCES

1. H. Tada, T. Kawaguchi and A. Koma, Appl. Phys. Lett. **61**, 2021 (1992).
2. G.S. Higashi, B.S. Becker, Y.J. Chabal and A.J. Becker, Appl. Phys. Lett. **58**, 1656 (1991).
3. T. Shimada, A. Suzuki, T. Sakurada and A.Koma, Appl. Phys. Lett. **68**, 2502 (1996).

## STM STUDIES OF ELECTRODE/ELECTROLYTE INTERFACES AND SILICON SURFACE REACTIONS IN CONTROLLED ATMOSPHERES

CHRISTOPHER P. WADE, HUIHONG LUO, WILLIAM L. DUNBAR, MATTHEW R. LINFORD, CHRISTOPHER E.D. CHIDSEY  
Department of Chemistry, Stanford University, Stanford, CA 94305-5080

### ABSTRACT

We have assembled a scanning tunneling microscope with an inverted sample that allows the sample surface to be contacted by fluid electrolytes in a controlled atmosphere. A hanging meniscus is formed between the sample and a small cup surrounding the tunneling tip. In-situ imaging of the electrode/electrolyte interface is conveniently achieved with clean samples under potentiostatic control. The functioning of the microscope is illustrated by the imaging of the electrodeposition of copper on gold. This microscope has been used to image hydrogen-terminated silicon surfaces and to demonstrate that islands, tentatively assigned as silicon oxide, are formed on rinsing in water but can be avoided if the surface is not rinsed on withdrawal from the ammonium fluoride etching solution. Finally, STM shows that the convenient, gas-phase photochlorination of H-Si(111) produces the simple Cl-Si(111)(1x1) structure with little or no etching of the silicon surface.

### INTRODUCTION

The scanning tunneling microscope (STM) is a powerful tool for the characterization of reactions at surfaces, particularly for providing information about how those reactions affect the distribution of physical features at the nanometer length scale. In the first part of this proceedings paper, we describe a novel design of an STM with an inverted sample and the capability to image the sample surface in a hanging meniscus of electrolyte under electrochemical control. The performance of the microscope is illustrated by imaging *in-situ* a well-understood system, the  $\sqrt{3} \times \sqrt{3} R30^\circ$  adlattice formed by underpotential deposition of copper on Au(111) from sulfuric acid [1]. The hanging-meniscus geometry employed in this microscope provides for convenient sample exchange and for operation in a well-controlled environment that is valuable for the characterization of reactions at air- and contaminant-sensitive surfaces.

As part of an effort to develop a molecular mechanistic understanding of the reactivity of hydrogen-terminated and other passivated silicon surfaces, we are employing this STM to complement the information obtained from spectroscopic methods that average over the entire silicon surface. A molecular understanding of the transformations of silicon surfaces is important both for the improvement of the wet and dry chemical methods used in current silicon device fabrication [2] as well as for the development of new devices with specific organic and biochemical molecular structures covalently bonded [3] to silicon. In this proceedings paper, we report two examples of the use of STM to complement other methods for studying transformations on silicon surfaces. The first example is the *ex-situ* tentative identification of the sites of oxidation of H-Si(111)(1x1) during rinsing with oxygenated water immediately following its formation in aqueous ammonium fluoride [4]. We find the sites of oxidation to be distributed across the Si(111) terraces. The second example is the characterization of the transformation from H-Si(111)(1x1) to another important surface, Cl-Si(111)(1x1), by a

convenient gas-phase photochlorination method [5]. In this case, STM establishes both the simple 1x1 nature of the resulting surface and the lack of silicon etching during the transformation. Future work will employ the STM described here to follow other transformations at the silicon surface, both in contact with gases and in contact with liquids, including electrolyte solutions under electrochemical control.

## MICROSCOPE

A simplified drawing of the scanning tunneling microscope is shown in Figure 1. The sample holder (or for larger samples the sample itself) rests on three static sample bearings at the top of the microscope base and faces down. The sample is clamped to the sample holder by sheet springs that engage grooves in the sides of the sample. The tunneling tip protrudes up toward the sample from a spring-loaded tip holder at the top of the piezoelectric scan tube. The scan tube is rigidly attached to the floor of the carriage which is held by a spring against four static carriage bearings in the bore in the microscope base. The carriage can be driven vertically by a loosely-coupled Burleigh Inchworm™ piezoelectric motor. When the tip is properly positioned, the motor can be reversed to decouple it from the carriage.

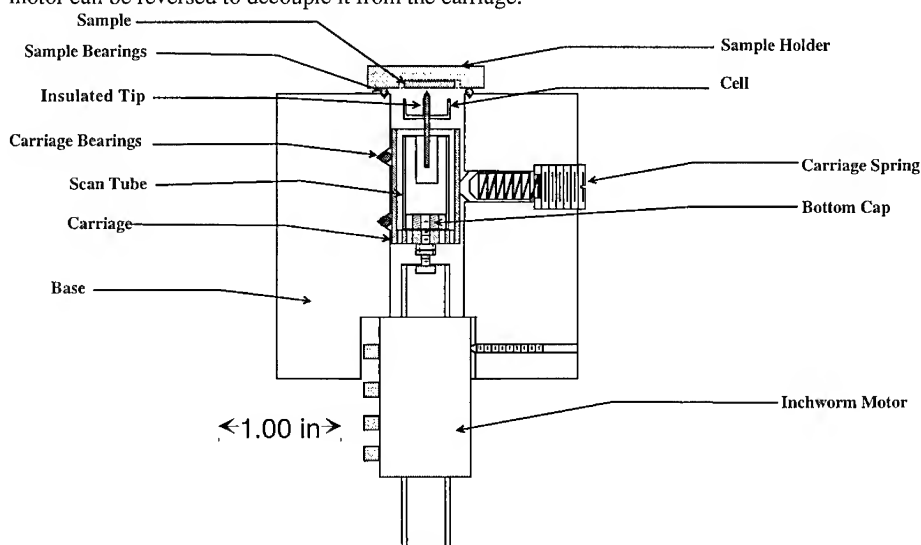


Figure 1 Diagram of the electrochemical STM.

Electrolytes or other liquids can be injected into the Teflon™ cell that encircles the insulated tip to form a hanging meniscus, which uniquely defines the electrode crystal face of interest. The counter and reference electrodes and Teflon™ liquid handling tubes are suspended from the base into the cell volume. The tip is sheathed in heat-shrink Teflon tubing and further insulated up to nearly its point by Apiezon wax. Because of surface tension effects, solution does not leak between the cell and the sheathed tip.

The tip current is transduced by a current-to-voltage converter (RHK Technology, Inc.). The potentials of the tip and the sample are independently controlled relative to the reference electrode with a bipotentiostat. Signals to drive the bipotentiostat as well as the vertical feedback

and horizontal scan signals are provided by a Nanoscope III™ controller and software (Digital Instruments).

The STM is mounted in a six-inch, six-way stainless steel cube that can be evacuated and/or filled with an inert gas. Liquids can be delivered hydrostatically from appropriate containers outside the chamber. Samples can be transferred from preparation or transfer chambers attached on top of the cube.

#### UNDERPOTENTIAL DEPOSITION OF COPPER ON Au(111)

The microscope has been tested on the well-known system of copper underpotential deposition (UPD) on a Au(111) electrode [6,7]. The electrolyte solution was 0.05 M H<sub>2</sub>SO<sub>4</sub>/1 mM Cu<sup>2+</sup>, prepared from concentrated H<sub>2</sub>SO<sub>4</sub> (suprapure, E. Merck), copper sulfate pentahydrate (E. Merck), and water from a 4-bowl Milli-Q purification system (Millipore). The Au(111) electrode was chemically cleaned by heating in nitric acid for 30 min. and hydrofluoric acid for 30 min. Then it was annealed for several minutes at 600°C in air immediately before transfer through air to the STM. The cell was cleaned by heating in suprapure H<sub>2</sub>SO<sub>4</sub> for 30 min. To verify proper solution and sample preparation, a cyclic voltammogram of the Au(111)/0.05 M H<sub>2</sub>SO<sub>4</sub>/1 mM Cu<sup>2+</sup> system was acquired in a glass electrochemical cell using the hanging-meniscus method with argon-saturated solution; the resulting current vs. potential plot was very similar to published results [6,7].

The STM tips were 0.040 inch-diameter tungsten rod electrochemically etched to a point in 2M NaOH solution and then insulated as described above. A tip was only used if it showed Faradaic current less than 100 pA between +20 and +300 mV vs. Cu/Cu<sup>2+</sup> in the deposition solution. The reference electrode was a gold wire (Aldrich, 99.999%) plated with copper, and the counter electrode was also a gold wire. All potentials are reported relative to the Cu/Cu<sup>2+</sup> couple in the same solution. For the images reported here, the solution was not de-oxygenated, and the STM was operated outside the stainless steel chamber.

Figures 2a and b show STM images of the Au(111)/0.05 M H<sub>2</sub>SO<sub>4</sub>/1 mM Cu<sup>2+</sup> system with the sample electrode potential at E<sub>s</sub> = +120 mV vs. Cu/Cu<sup>2+</sup> and the tip electrode potential at E<sub>t</sub> = +20 mV. This sample potential is between the two deposition peaks of the cyclic voltammogram, where the  $\sqrt{3} \times \sqrt{3}R30^\circ$  copper sulfate structure is known to exist. The ratio between the interatomic distances in Figure 2a and in an atomic resolution image of the underlying Au(111) substrate is approximately  $1.7 \approx \sqrt{3}$ . The angle between the closed-packed directions is approximately 30°. Thus, the lattice in Figure 2a can be assigned as the  $\sqrt{3} \times \sqrt{3}R30^\circ$  copper sulfate structure. It is now believed this structure is composed of sulfate molecules (1/3 monolayer) that form a  $\sqrt{3} \times \sqrt{3}R30^\circ$  structure on top of a  $\sqrt{3} \times \sqrt{3}R30^\circ$  honeycomb lattice of copper atoms (2/3 monolayer) bound to the Au(111) surface [8].

In addition to the surface structure, Figures 2a and b also reveal other spatial detail that aptly demonstrates the ability of *in-situ* STM to elucidate the spatial distribution of species at the nanometer level. Running down the middle of Figure 2a is a domain boundary; the closest-packed directions are not aligned across the boundary. During deposition, the copper sulfate adlattice nucleated at two different places on the gold terrace, with the two domains occupying different substrate crystallographic sites that are shifted relative to one another by a fraction of the adlayer unit cell. Figure 2b, on the other hand, shows atomic resolution of the  $\sqrt{3} \times \sqrt{3}R30^\circ$  copper sulfate structure across a step edge of the underlying Au(111) lattice. The large white structures in both Figures 2a and b are thought to be due to gold atoms that have been released

from the Au(111) reconstruction phase upon formation of the underpotential deposition layer[17].

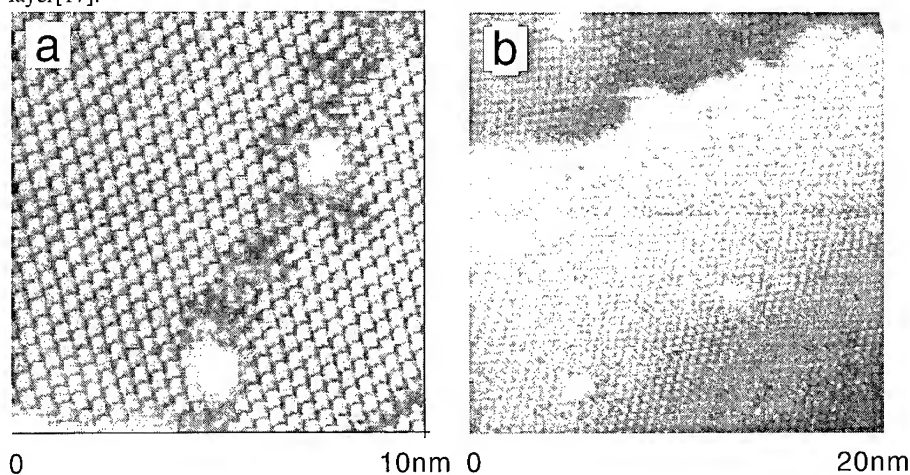


Figure 2 Constant-current STM images of a Au(111) electrode surface in 0.05 M  $\text{H}_2\text{SO}_4$ /1 mM  $\text{Cu}^{2+}$  solution: a) 10 nm x 10 nm region,  $E_s=+120$  mV,  $E_{\text{tip}}=+20$  mV, tunneling current = 8.0 nA, scan rate=8.0 Hz; b) 20 nm x 20 nm region,  $E_s=+130$  mV,  $E_{\text{tip}}=+20$  mV, tunneling current = 5.0 nA, scan rate=3.0 Hz.

#### HYDROGEN-TERMINATED Si(111)

As part of our broader agenda of understanding and developing the chemistry of the H-Si(111)(1x1) surface[4], we have sought to understand and minimize the formation of silicon oxides on the surface during handling in the laboratory atmosphere. Behm, *et al.*, have correlated the appearance of pits in the (111) terraces after a brief HF etch with the formation of oxide islands in humid air [9]. Here we compared x-ray photoelectron spectra (XPS) and STM images of H-Si(111) samples after rinsing with ultrapure water and immediately after withdrawal from an ammonium fluoride solution. It should be noted that because of the low surface energy of the H-Si(111) surface, it is hydrophobic and emerges dry from aqueous solutions.

Silicon wafers (n-type, 0.1-0.9  $\Omega\cdot\text{cm}$ , Siltec) were cleaned in 4 volumes  $\text{H}_2\text{SO}_4$ :1 volume 30%  $\text{H}_2\text{O}_2$ , for 10 minutes at 100°C, followed by 1 volume 30%  $\text{H}_2\text{O}_2$ : 1 volume conc.  $\text{HCl}$ :4 volumes  $\text{H}_2\text{O}$  for 10 minutes at 75°C, then another 10 minutes in 4 volumes  $\text{H}_2\text{SO}_4$ :1 volume 30%  $\text{H}_2\text{O}_2$  at 100°C. After rinsing with ultrapure water the wafers were etched for 15 minutes in 40% aqueous  $\text{NH}_4\text{F}$  in Teflon™ vials and were either (i) rinsed with ultrapure water or (ii) simply removed from the vials without a final water rinse.

The XPS data were acquired on a Surface Science Model 150 XPS spectrometer with an Al  $K_\alpha$  (1486eV) source, quartz monochromator, hemispherical analyzer and multichannel detector with a take-off angle of 35° and an angular acceptance of about 30°. The unrinsed sample was transferred to the XPS loadlock directly from the etch solution, and the loadlock was immediately evacuated. The STM chamber was pumped twice to less than 1 millitorr and then filled with a positive pressure of argon. The fresh H-Si(111) sample was transferred through air in less than 30 seconds to the STM under a flow of argon coming from the chamber. STM tips

were formed from 0.25 mm Pt/Ir wire soldered into stainless steel hypodermic tubing and electrochemically etched in calcium chloride solution. For the H-Si(111) surfaces, the bias at the sample was typically  $E_{\text{sample}} = -1.5$  V, with the tip held at ground. The tunneling current was on the order of 20-50 pA. These tunneling parameters were empirically determined and appeared to give the best images.

Figures 3a and b show the XPS survey spectra of the H-Si(111) with and without a 30 s water rinse. Note that the rinsed surface shows a reasonable amount of oxygen whereas the unrinsed surface shows only a barely detectable amount of oxygen. The calculated oxygen coverage in Figure 3a is about 7%, while the oxygen coverage in Figure 3b is 0.5% [30]. There was some variation in the oxygen coverage for several 30 second rinse trials, but the amount of oxygen in the rinsed samples was always at least several times greater than for the unrinsed samples. The presence of oxygen on the H-Si(111) surface after only a 30 second water rinse is not unknown. Gräf, *et al.*, have shown by high-resolution electron energy-loss spectroscopy (HREELS) that oxygen-related groups (OH and Si-O-Si) appear on the (111) surface after a 30

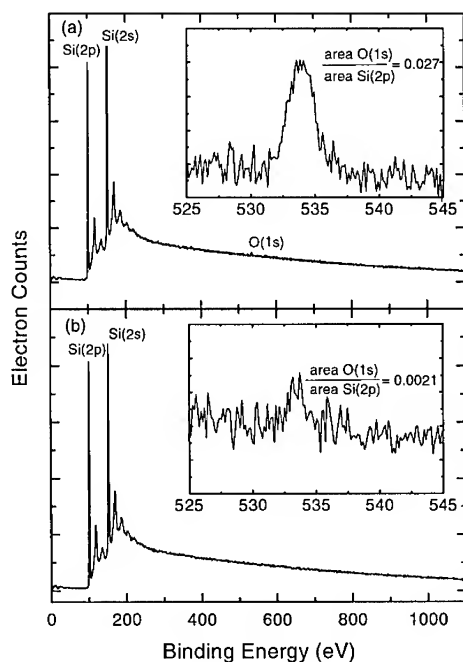


Figure 3 XPS survey spectra of H-Si(111) surfaces. Insets show narrow-scan spectra of the O 1s region. (a) Sample rinsed for 30s after removal from the ammonium fluoride solution. (b) Unrinsed sample placed directly into the loadlock of the XPS.

second water rinse [20]. In addition, the lack of fluorine on the unrinsed surface of Figure 3b is explained by (i) the hydrophobic nature of the H-Si(111) surface, which tends to repel dissolved species upon removal from solution, and (ii) by the extremely flat surface (100-200 nm wide

terraces) and very low step density obtained by this treatment, as can be seen in a 500 nm x 500 nm STM image of the unrinsed H-Si(111) surface (Figure 6a). Yasaka, *et al.*, have shown that very little fluorine is detected by XPS for Si(111) surfaces treated with fluoride solutions having a pH  $\geq 5$ ; fluorine is expected to be present primarily at step edges [21].

Figures 4a and b show STM images of the H-Si(111) surface with a range of 100 nm x 100 nm. In Figure 4a, the sample was rinsed for 30 seconds in water after the fluoride etch, while in Figure 4b the sample was not rinsed. Both images show two bilayers of the (111) silicon surface separated by the expected 0.31 nm high step edge. On the unrinsed surfaces, we found pits that were 1-2 nm in diameter and one bilayer deep. Their density was 10-20 per 100 nm x 100 nm area, resulting in a pit surface coverage of 1% of the total area. Pit positions and sizes were reproducible from image to image. The rinsed sample (Figure 4a) has small islands (20-30 in number) scattered homogeneously on the terraces that are approximately 5 nm in diameter and several tenths of a nanometer high, with an average coverage of approximately 4%. Although there was occasionally some variability in the island coverage from image to image, islands were always present. Additionally, the tip had difficulty tunneling over this surface, as seen by an increase in image noise. We repeatedly and consistently observed this result.

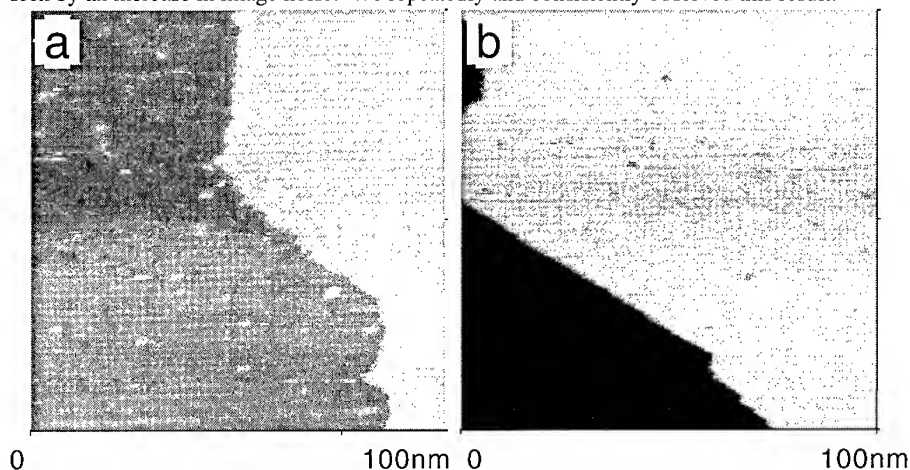


Figure 4 Constant-current STM images of H-Si(111) surfaces (100 nm x 100 nm) in an argon atmosphere: a) rinsed in water for 30 seconds after a 15 minute ammonium fluoride etch,  $E_s = -1.3V$ , tunneling current=15 pA, scan rate=1 Hz; b) unrinsed after the ammonium fluoride etch,  $E_s = -1.1V$ , tunneling current=20 pA, scan rate=1 Hz.

Based on the XPS results, we tentatively assign the islands as oxidized silicon formed during the water rinse. This assignment is supported by the increase in noise of the STM images relative to images of the unrinsed samples; it suggests an electronically non-homogeneous surface that would result from a partially oxidized silicon (111) surface. It might be postulated that oxidized areas of the silicon surface would show up as depressions in the STM images rather than protrusions due to a local decrease in the density of states. However, our assignment is not inconsistent with the literature; Ikegami, *et al.*, have reported that high spots (~2 nm in diameter)

observed on a Si(100) (2x1) surface exposed to molecular oxygen in UHV are indeed oxidized silicon, based on scanning tunneling spectroscopy (STS) measurements [18].

The presence of the pits on the (111) terraces for the unrinsed surfaces suggests that pit formation occurs during the ammonium fluoride etching process. Allongue, *et al.*, have assigned the oxidation of terrace sites to an electrochemical reaction with water [10]. However, we suspect that O<sub>2</sub> plays a significant role [22-25]. In XPS studies, Yano, *et al.*, have reported that Si(111) surfaces etched in 5% HF solutions containing a controlled amount of dissolved oxygen and then exposed to humid air in a cleanroom for 0.5-96 hours showed an increased rate of surface oxidation with increasing dissolved oxygen concentration [22]. Watanabe, *et al.*, found by FT-IR that the surface oxide concentration of H-Si(111) after immersion in water at 80°C depended on the amount of dissolved oxygen in the water, and they suggested that the Si-Si back bonds on (111) terraces are attacked by molecular oxygen in solution to form (SiO)<sub>3</sub>SiH groups [23]. In future experiments, we will examine the role of O<sub>2</sub> in the oxidation of H-Si(111) terraces.

#### CHLORINE-TERMINATED Si(111)

Chlorine-terminated silicon is another useful surface for the formation of organic monolayers [11,12] and may provide a useful passivation in silicon device fabrication. Moreover, photochlorination conditions similar to those used here have been used for the removal of metallic impurities [13]. The photochlorination procedure we are using has been shown to produce a saturated coverage of chlorine and no residual absorption due to the Si-H stretch in the infrared spectra [5]. When only room-light illumination is used, much lower coverages are observed. High resolution studies of the Si 2p photoemission features indicate that only monochlorinated silicon species are formed, and low energy electron diffraction shows only a 1x1 pattern characteristic of the substrate [14]. The present STM study was undertaken to determine whether or not the chlorine adlayer is disorganized or occupies the same 1x1 lattice as the substrate, and whether the surface is etched during the replacement of H by Cl. The only other example of the formation of this 1x1 surface of which we are aware requires the somewhat inconvenient annealing of the clean Si(111)(7x7) surface in the presence of chlorine gas at elevated temperature [15,16].

To produce the chlorine-terminated surface, a freshly-prepared, unrinsed H-Si(111) sample was placed in a fused silica cuvette and evacuated to  $< 6 \times 10^{-5}$  Torr on a glass vacuum line with a liquid N<sub>2</sub>-trapped diffusion pump. Chlorine gas (Matheson, 99.999%) was then admitted to the silicon sample. Pressure measurements were performed with an uncalibrated Granville-Phillips Convector gauge. Care was taken to minimize the exposure time of this gauge to Cl<sub>2</sub>. A broadband 350 nm lamp (Spectronics, MB-100, fluorescent flood lamp) with an average intensity of 6 mW/cm<sup>2</sup> at a distance of 6" over a 7" diameter was used for timed photoexposures. After UV exposure, the chlorine gas was pumped off, and the silica cuvette was backfilled with purified argon and sealed for sample transfer. Photochlorinated silicon samples were either (i) transferred directly from the sealed cuvette to the STM chamber through laboratory atmosphere in less than 30 seconds, or (ii) transferred directly from the cuvette into the XPS loadlock. Photoexposures from 3 Torr•s (the smallest convenient exposure) to 600 Torr•s gave samples with identical chlorine coverage as measured by XPS. The Cl-Si(111) surfaces were typically observed by STM with E<sub>sample</sub> = + 300 mV. The tunneling current was on the order of 20-50 pA. As in the case of the H-Si(111) surface, these parameters were empirically determined to give the best STM images.



Figure 5 is a XPS spectrum of the photochlorinated surface prepared with a 2 Torr  $\text{Cl}_2$  and 15 second UV light (30 Torr•s) exposure. Note that chlorine peaks are present and that there is almost no oxygen or any other contaminant. The peak area ratio of  $\text{Cl}_{2s}/\text{Si}_{2p}$  is 0.25. Almost identical spectra were obtained with photoexposures ranging from 3 Torr•s to 600 Torr•s. The fact that the chlorine signal does not change with photoexposure indicates a saturation coverage, which we have taken to be one monolayer. The saturated signal suggests that the silicon surface does not roughen, but it does not rule out step flow etching. To answer this question, we looked at the surface by STM.

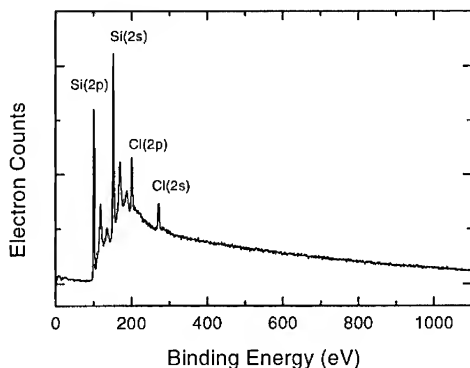


Figure 5 XPS survey spectrum of Cl-Si(111) surface prepared with 2 torr  $\text{Cl}_2$  and 15 second UV light exposure.

Figure 6a and b shows a comparison of 500 nm x 500 nm STM images of the H-Si(111) and Cl-Si(111) surfaces. The Cl-Si(111) surface in Figure 6b was prepared with a 2 torr  $\text{Cl}_2$  and 5 minute UV light exposure. There are large terraces 100-200 nm wide separated by bilayer-high step edges on both samples. It is clear that the two surfaces are very similar and that the photochlorination exposure has not disrupted the extremely flat (111) structure on this length scale.

Note that Figure 6a shows a few large islands of approximately 15-20 nm diameter. These islands are clearly distinct in size and distribution from the much smaller and more widely distributed islands of the rinsed H-Si(111) surfaces (Figure 4a) and are associated with step edge pinning, resulting in the triangular-shaped steps. It is likely that the islands are due to trace metal contamination that has been electrolessly plated onto the silicon [28,29]. On the other hand, the Cl-Si(111) surface in Figure 6b shows pits in similar locations as the islands in Figure 6a. It is possible that the photochlorination process has resulted in etching of the metallic impurities [13].

Higher resolution images of the Cl-Si(111) surface are shown in Figure 7a and b. Figure 7a shows that small pits are present, very similar to the unrinsed H-Si(111) in Figure 4b. We found the pits to be distributed over the surface homogeneously, averaging 10-20 pits of 2-4 nm diameter per 100 nm x 100 nm region and a pit surface coverage of  $2 \pm 1\%$  of the total area. Similar surfaces were observed for exposures of 0.2 torr  $\text{Cl}_2$  and 15 sec UV illumination and 2 torr  $\text{Cl}_2$  and 15 sec UV illumination.

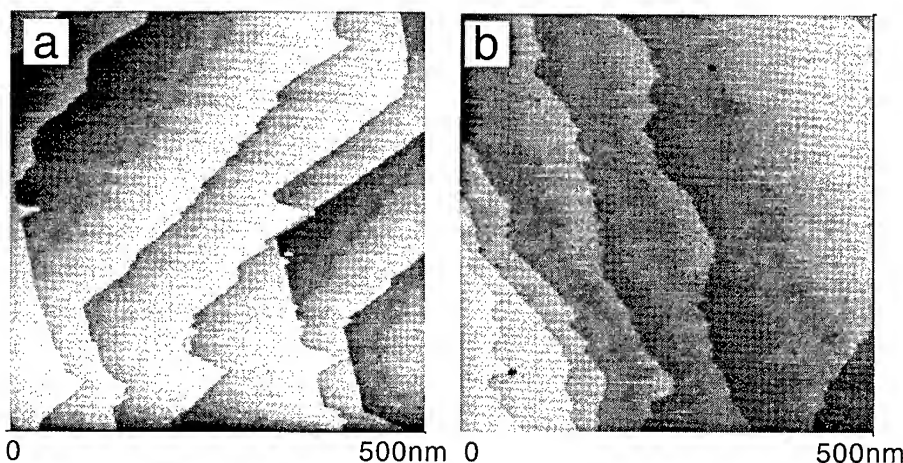


Figure 6 Constant-current STM images of the H-Si(111) and Cl-Si(111) surfaces in an argon atmosphere: a) 500 nm x 500 nm region of H-Si(111) with no final water rinse,  $E_s = -1.1$  V, tunneling current=20 pA, scan rate=1 Hz; b) 500 nm x 500 nm region of Cl-Si(111) prepared in 2 torr  $\text{Cl}_2$  gas and a 5 minute UV exposure,  $E_s = +300$  mV, tunneling current=50 pA, scan rate=1 Hz.

Figure 7b shows a 15 nm x 15 nm image of the photochlorinated surface showing that a simple 1x1 adlayer is observed. This hexagonal lattice has an interatomic spacing of 0.38 nm as determined by comparison with atomic resolution of highly ordered pyrolytic graphite taken with the same tip immediately after the image in Figure 7b. This spacing is the same as that seen for the H-Si(111)(1x1) surface from which it is made. The regularity of the corrugation observed is strong evidence that all the surface silicon atoms are bonded to chlorine, thus allowing us to assign the chlorinated surface as Cl-Si(111)(1x1). This structure is certainly viable from a steric point of view: assuming a Cl radius no more than the ionic radius of 1.81 Å [26], hexagonally packed chlorine atoms would require no more than 11.35 Å<sup>2</sup>/Cl, whereas, assuming a Si-Si distance of 2.35 Å [27], the total area available for each atom on the Si(111) surface is 12.77 Å<sup>2</sup>.

The presence of pits on the original H-Si(111) surfaces allows us to set an upper limit on the amount of etching of the silicon surface that accompanies the replacement of H by Cl. In no case did pit coverage exceed 3% of the surface, and we observed no clear statistical trend toward higher pit coverage with increased photoexposures up to 600 Torr•s. We conclude that the etching rate is very low or zero.

The difference in the bias used for the Cl-Si(111) surface relative to the H-Si(111) surface may arise from the surface dipole created by the more electronegative chlorine atoms, which leaves a partial positive charge at the silicon surface and may stabilize tunneling under the reverse bias conditions. Future experiments will compare the STS spectra of both surfaces for verification of this hypothesis.

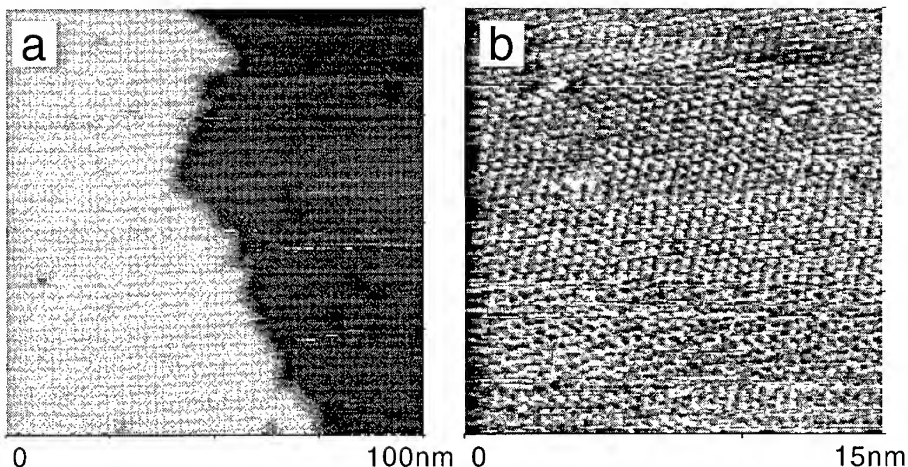


Figure 7 Constant-current STM images of the Cl-Si(111) surface in an argon atmosphere prepared in 2 torr  $\text{Cl}_2$  gas and a 5 minute UV exposure: a) 100 nm x 100 nm region,  $E_s = +300$  mV, tunneling current = 50 pA, scan rate = 1 Hz; b) 15 nm x 15 nm region,  $E_s = +300$  mV, tunneling current = 50 pA, scan rate = 3 Hz.

## ACKNOWLEDGMENTS

We thank Jeff Terry, Renyu Cao, Renee Mo and Piero Pianetta for valuable discussions about the photochlorination of H-Si(111). This work was partially supported by the Center for Environmentally Benign Semiconductor Manufacturing supported by NSF and the Semiconductor Research Corporation. W.L.D. was supported by a Partners in Science Fellowship from the Research Corporation. C.E.D.C. is a Camille and Henry Dreyfus Teacher Scholar. The XPS work has benefited from the facilities and equipment made available to Stanford University by the NSF-MRSEC program through the Center for Materials Research at Stanford University.

## REFERENCES

1. O.M. Magnussen, J. Hotlos, R.J. Nichols, D.M. Kolb and R.J. Behm, *Phys. Rev. Lett.* **64**, p. 2929 (1990).
2. C. E. D. Chidsey and M. R. Linford in *Cleaning Technology in Semiconductor Device Manufacturing IV*, edited by R.E. Novak and J. Ruzyllo (Electrochemical Soc. Proc. 95-20, Pennington, NJ 1996), p. 455-463.
3. M. R. Linford, P. Fenter, P. M. Eisenberger and C. E. D. Chidsey, *J. Am. Chem. Soc.* **117**, p. 3145 (1995).
4. G.S. Higashi, Y.J. Chabal, G.W. Trucks and K. Raghavachari, *Appl. Phys. Lett.* **56**, p. 2104 (1990).
5. M.R. Linford, Ph.D. Dissertation, Stanford University, 1996.
6. T. Will, M. Dietterle and D.M. Kolb in *Nanoscale Probes of the Solid-Liquid Interface*, (NATO ASI Series E 288 1995) p.137-162.
7. T. Hachiya, H. Honbo and K. Itaya, *J. Electroanal. Chem.* **315**, p. 275 (1991).

8. M.F. Toney, J.N. Howard, J. Richer, G.L. Borges, J.G. Gordon, O.R. Melroy, D. Yee and L.B. Sorensen, *Phys. Rev. Lett.* **75**, p. 4472 (1995).
9. U. Neuwald, H.E. Hessel, A. Feltz, U. Memmert and R.J. Behm, *Appl. Phys. Lett.* **60**, p. 1307 (1992).
10. P. Allongue, V. Kieling and H. Gerischer, *Electrochimica Acta* **40**, p. 1353 (1995).
11. A. Bansal, X. Li, I. Lauermaun, N.S. Lewis, S.I. Yi and W.H. Weinberg, *J. Am. Chem. Soc.* **118**, 7225 (1996).
12. J. Terry, M.R. Linford, C. Wigren, R. Cao, P. Pianetta and C.E.D. Chidsey, submitted to *Appl. Phys. Lett.*
13. A.S. Lawing, A.J. Muscat, H.H. Sawin, J. W. Butterbaugh, in Cleaning Technology in Semiconductor Device Manufacturing IV, edited by R.E. Novak and J. Ruzyllo (Electrochemical Soc.Proc. 95-20, Pennington, NJ 1996), p. 150.
14. J. Terry, M. R. Linford, C.E.D. Chidsey, R. Cao, P. Pianetta, unpublished results.
15. J.J. Boland and J.S. Villarrubia, *Phys. Rev. B*, **41**, p. 9865 (1990).
16. A. Feltz, U. Memmert and R.J. Behm, *Surf. Sci.* **307-309**, p. 216 (1994).
17. O. M. Magnussen, Ph.D. Dissertation, Universität Ulm, 1993; also private communication.
18. H. Ikegami, K. Ohmori, H. Ikeyda, H. Iwano, S. Zaima and Y. Yasuda, *Jpn. J. Appl. Phys.* Part I **35**, p. 1593 (1996).
19. H. Ogawa, K. Ishikawa, C. Inomata and S. Fujimura, *J. Appl Phys* **79**, p.472 (1996).
20. D. Gräf, M. Grunder and R. Schultz, *J. Vac. Sci. Technol. A* **7**, p. 808 (1988).
21. T. Yasaka, K. Kanda, K. Sawara, S. Miyazaki and M. Hirose, *Jap. J. Appl. Phys. Part I* **30**, p. 3567 (1991).
22. F. Yano, A. Hiraoka, T. Itoga, H. Kokima and K. Kanehori, *J. Vac. Sci. Technol. A* **13**, p. 2671 (1995).
23. S. Watanabe and Y. Sugita, *Surf. Sci.* **327**, p. 1 (1995).
24. K. Usuda, H. Kanaya, K. Yamada, T. Sato, T. Sueyoshi and M. Iwatsuki, *Appl. Phys. Lett.* **64**, p. 3240 (1994).
25. M. Morita, T. Ohmi, E. Hasegawa, M. Kawakimi and K. Suma, *Appl. Phys. Lett.* **55**, p. 562 (1989).
26. CRC Handbook of Chemistry and Physics, 73rd. ed., edited by D. R. Lide (CRC Press, Inc., Boca Raton, Florida, 1992) p. 12-8.
27. A. Kelly and G. W. Groves, Crystallography and Crystal Defects (Addison-Wesley Publishing Company, Inc., Herndon, VA, 1970), p. 411.
28. H. Moringa and T. Ohmi in Cleaning Technology in Semiconductor Device Manufacturing IV, edited by R.E. Novak and J. Ruzyllo (Electrochemical Soc.Proc. 95-20, Pennington, NJ 1996), p. 257-268.
29. O.M.R. Chyan, J.-J. Chen, H. Y. Chien, J. Sees and L. Hall, *J. Electrochem. Soc.* **143**, p. 92 (1996).
30. The oxygen coverage  $\Gamma_{O_2}$  determined from the XPS spectra was calculated by assuming that the coverage of chlorine on the Cl-Si(111) surface is 1 monolayer (Figure 5). That surface shows a  $Cl_{2s}/Si_{2p}$  peak area ratio of 0.25. We calculate the oxygen coverage on the rinsed and unrinsed H-Si(111) surfaces using the following equation:

$$\Gamma_{O_2} = \frac{O_{1s} / Si_{2p} \text{ peak area ratio}}{Cl_{2s} / Si_{2p} \text{ peak area ratio for Cl-Si(111)}} * \frac{a.s.f. \cdot c_{Cl_{2s}}}{a.s.f. \cdot c_{O_{1s}}},$$

where a.s.f. = the atomic sensitivity factors for the respective peaks. Using the atomic sensitivity factors given for our XPS as  $a.s.f. \cdot c_{Cl_{2s}} = 1.70$  and  $a.s.f. \cdot c_{O_{1s}} = 2.49$  (Surface Science Model 150 software), we calculate the oxygen coverage as 7% for Figure 3a and 0.5% for Figure 3b.

## MOLECULAR GRAFTING ON Si(111) SURFACES : AN ELECTROCHEMICAL APPROACH

C. Henry de Villeneuve <sup>a</sup>, J. Pinson <sup>b</sup>, F. Ozanam <sup>c</sup>,  
J. N. Chazalviel <sup>c</sup> and P. Allongue <sup>\*,a</sup>

<sup>a</sup> Laboratoire de Physique des Liquides et Électrochimie,  
CNRS - UPR 15, ESPCI, 10 rue Vauquelin, F-75005 Paris (France)

<sup>b</sup> Laboratoire d'Électrochimie Moléculaire,  
CNRS - URA 438, Université Paris 7, 2 Place Jussieu, F-75005 Paris (France)

<sup>c</sup> Laboratoire de Physique de la Matière Condensée,  
CNRS - UR 1254, École Polytechnique, F-91128 Palaiseau (France)

### ABSTRACT

This work addresses the question of the direct attachment of organic molecules on Si(111) by an electrochemical method. Anodic grafting of -OR group is demonstrated by *in-situ* STM and the LDOS characterized. The grafting of aryl groups, by reduction of aryl diazonium salts in aqueous solution, is also described. This approach leads to well ordered and close-packed thin molecular films with various functionality. Different chemical and structural characterizations conclude to a Si-C binding, between the Si surface and aryl groups. The stability of films is also investigated.

\* corresponding author : e-mail pa@ccr.jussieu.fr

### INTRODUCTION :

The formation and characterization of well defined organic thin films deposited on the surface of solids have been extensively studied over more than ten years [1]. A recent review [2] evidences however that most of the work concerned either clean metallic surfaces [3], oxidized metal or oxidized semiconductor surfaces [4]. Except for few publications, there has been no report aiming at the *direct* attachment of organic molecules on Si although applications of thin organic films should benefit from a direct coupling with an electronic material. Lindford and Chidsey [5,6] used a chain of radical reactions to graft robust (2x1) monolayers of alkyl chains on Si(111) with Si-OH groups on remaining sites. Though not performed on flat Si(111), the work of Chazalviel et al is quite interesting since it shows that electrochemistry is a powerful method for grafting molecules. Anodization of porous silicon layers in organic solvents leads indeed to the attachment of -OCH<sub>3</sub> [7] and -CH<sub>3</sub> [8] groups which stabilize the surface. No such work is however available on flat Si, except for a recent *in-situ* STM study showing that isolated -OCH(CH<sub>3</sub>)<sub>2</sub> groups bind to Si(111) from a mixture NaOH / IPA (isopropanol) [9]. More recently, a preliminary study showed that the electrochemical reduction of aryl diazonium salts enables the formation of thin aryl layers on flat Si(111) [10].

The present paper yields new insights into the characterization of the aryl layers, mainly by XPS, RBS and FTIR. Although we did not aim at growing monolayers of -OR groups, the first section presents STM images showing that -OCH(CH<sub>3</sub>)<sub>2</sub> grafting occurs during Si etching in a mixture NaOH / isopropanol (IPA). This is an illustration of an anodic process leading to molecular grafting. The electronic properties of the surface are also studied on the atomic scale.

#### EXPERIMENTAL :

Substrates were cut from 1  $\Omega$ .cm n-type Si(111) wafers and cleaned in hot trichlorethylene, acetone and methanol prior to stripping the oxide in 2% HF (1 min) and etching in 40% NH<sub>4</sub>F (6 min). Electrochemical measurements were conducted in a 3-electrode cell with a mercury sulfate electrode (SSE) as reference of potential and a Pt counter electrode. All potentials are quoted against SSE. Reagent chemicals and bidistilled water were used for solutions. XPS measurements were performed at ITODYS (Université Paris 6) with a SSX-100 spectrometer (monochromated AlK $\alpha$  source). The source was 30° off the surface plane and the take off angle was nominally 30° from the surface. RBS (Rutherford Backscattering) measurements were conducted with the 2 MeV Van Graaff accelerator of GPS (Groupe de Physique des Solides, Université Paris 7). Particles were detected at 165° from the incident <sup>4</sup>He<sup>+</sup> beam. FTIR was performed *ex-situ* within a multiple internal reflection geometry as exposed elsewhere [7]. The same sample was used throughout the process to ensure a quantitative comparison of spectra. STM images were acquired *in-situ* with the microscope described previously [11].

#### H-Si(111) SURFACES AND MOLECULAR GRAFTING : GENERAL CONSIDERATIONS

Ideally flat H-terminated Si(111) substrates can easily be prepared by wet chemical etching in fluoride solution [12]. They are therefore one of the best surface to obtain ordered organic layers, provided the process of grafting does not generate structural defects. Fig. 1 presents three large scale STM topviews of 1  $\Omega$ .cm n-type Si(111) surfaces with different miscut angles with respect to the (111) direction. The precisely oriented sample (Fig. 1a) displays wide terraces, atomically flat and separated by monoatomic steps (3.1 Å high). The two other surfaces have a nearly ideal staircase structure reminiscent of the initial miscut angle. Terraces become perfectly smooth with increasing tilt angle because the lateral flow of step edges becomes faster than the nucleation and grow rates of etch pits on the (111) planes [13,14,15].

The chemistry of the surfaces in Fig. 1 is unique with a more than 99% H-termination (atom density) [12,13], which is very much favorable for an homogeneous nucleation of any adlayer. The direct attachment of a molecular film on a covalent surface, such as the one of Si, is indeed not a simple adsorption stage but does involve the *substitution* of the H monolayer by the organic groups. A chemically homogeneous surface is thereby most necessary to achieve uniform nucleation. The fact that covalent bonds are created between Si and molecules has important implications regarding the maximum coverage obtainable. The layer structure is indeed necessarily in *registry* with the substrate since covalent bonds are rigid and highly directional. Reaching molecular close-packing will therefore depend not only on the size of the molecule with respect to the surface unit cell but also on the matching between the orientation of surface bonds out of the surface and the hybridization of the linking atom on the molecule.

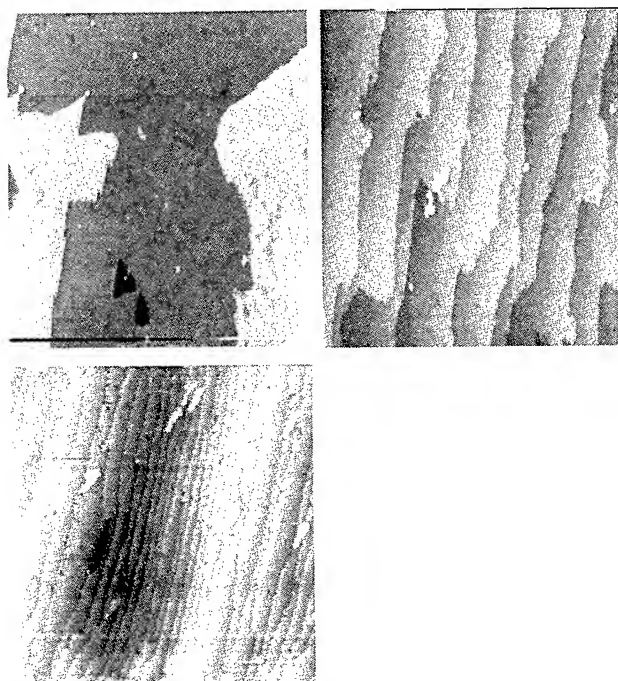


Fig. 1 : STM topviews of n-Si(111) after etching in 40%  $\text{NH}_4\text{F}$  (images taken in  $\text{NaOH}$ :  $i_t = 0.2 \text{ nA}$ ,  $U_s = -0.5 \text{ V / Pd-H}$  and  $U_t = +0.3 \text{ V / Pd-H}$ ). The tilt of the surface is  $<0.25^\circ$  (top left),  $0.4^\circ$  (top right) and  $2^\circ$  (bottom). Frames are  $2300 \times 2300 \text{ \AA}^2$ .

Figure 2 explains how electrochemistry offers an interesting alternative to derivative H-Si(111) terminated surfaces. On the molecular level the very initial steps of the dissolution (Fig. 2, top) and hydrogen evolution reaction - HER- (Fig. 2, bottom) routes involve the generation of an intermediate state  $\text{Si}^\bullet$ . This is a Si atom which has lost its H atom and bears an unpaired electron. This surface radical is likely to be the suitable precursor for molecular grafting.

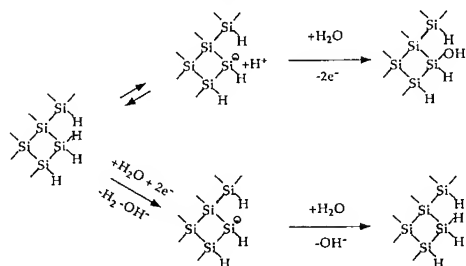


Fig. 2 : Molecular model focusing on the initial step of Si etching (top) and hydrogen evolution reactions (bottom). After [15].

#### ANODIC BINDING OF -OR GROUPS IN NaOH / IPA :

Figure 2 suggests that an anodic reaction involving H-OR instead of H<sub>2</sub>O molecules should lead to the binding of an -OR group. This has in fact been demonstrated by FTIR with porous Si layers anodized in dry methanol (with NaOCH<sub>3</sub> added) [7]. The mechanism proposed by the authors was very similar to the one accepted for Si etching in alkaline solutions [16]. The STM image in Fig. 3a provides a confirmation of the supposed reaction in the case of a mixture NaOH / IPA (isopropanol) where the image has been recorded. This solution is usually employed to obtain smooth Si(100) surface during anisotropic etching.

As in pure NaOH the Si surface is almost entirely H-terminated. The image in Fig. 3a evidences nevertheless some protrusions of well defined and reproducible dimensions and shape which can be attributed to OCH(CH<sub>3</sub>)<sub>2</sub> groups on the surface. In the absence of IPA (Fig. 3b), the inhomogeneities on the surface look indeed quite different. They present a depressed ring around, are also smaller and circular. These latter could be associated to ≡Si-OH groups generated during etching, by looking at their bias dependence [9].

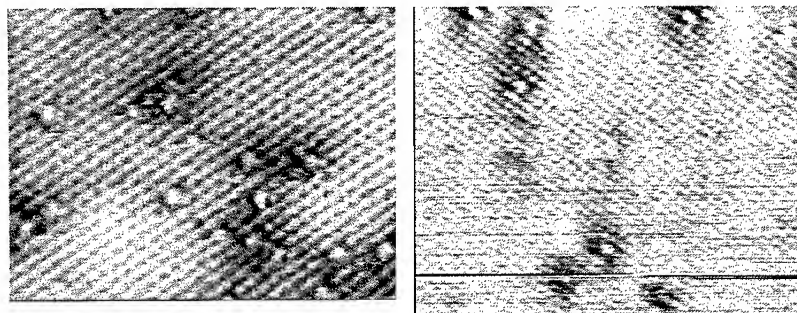


Fig. 3 : Atomically resolved *in-situ* STM images of n-Si(111) in NaOH / IPA (a : 99 x 72 Å<sup>2</sup>) and NaOH (b : 100 x 82 Å<sup>2</sup>). The sample has been shortly held at the rest bias and imaged nearly under the same conditions of Fig. 1 (after [9]).

A comparison between STM and hard sphere model contours (Fig. 4) for ≡Si-OR (R= H or -CH(CH<sub>3</sub>)<sub>2</sub>) is quite instructive to gain insights into the local electronic properties of the surface. The discrepancy is indeed striking between the heights derived from STM observations and molecular models. The OH looks higher in the STM image (Fig. 4b) than one expects from the molecular model (Fig. 4d). The -OCH(CH<sub>3</sub>)<sub>2</sub> entity is conversely shallower (Fig. 4a) than anticipated from Fig. 4c. This is direct evidence that the LDOS (local density of states) depends very much on the -OR group. An enhanced LDOS was anticipated at ≡Si-OH sites due to the large electronegativity difference between the Si atom and the OH. The Si is in fact partially positively charged as ≡Si<sup>+</sup><sub>δ</sub> and this charge is reduced with -OCH(CH<sub>3</sub>)<sub>2</sub> groups for two reasons. (i) The group is less electron attractor than the OH. (ii) The most stable configuration of the -OCH(CH<sub>3</sub>)<sub>2</sub> group is with the alkyl chain laterally positioned *above* the hollow site with no Si atom immediately underneath (Fig. 4c) because this pumps downward the electronic cloud. Both



reasons explain that the LDOS is not increased in this case. A confirmation of this interpretation is given by the absence of the dark rings around the protrusions in Fig. 3a. The ring around  $\equiv\text{Si}-\text{OH}$  (Fig. 3b) is indeed accounting for the potential distribution induced in the Si substrate by the charge  $+\delta$  on  $\equiv\text{Si}^{+\delta}$ . The absence of rings in Fig. 3a means a smaller  $\delta$  at  $\equiv\text{Si}^{+\delta}$ .

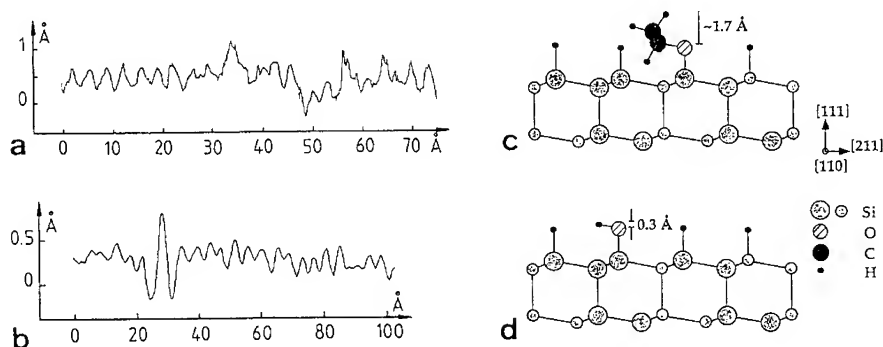
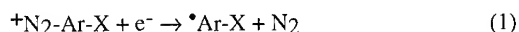


Fig. 4: (a) and (b) cross sections AA and BB of the STM images 2a and 2b respectively. (c,d) Ball and stick models of  $\text{Si}-\text{OCH}(\text{CH}_3)_2$  and  $\text{Si}-\text{OH}$  groups (side views).

To conclude this section, anodic grafting on  $\text{Si}(111)$  has been demonstrated. On the atomic scale the LDOS depends strongly on the molecule. From steric considerations, obtaining a full coverage of the surface seems possible with IPA. This would however require to work in an anhydrous solvent to avoid the (faster) dissolution of the material upon anodization. The size of the alcoholic molecule is certainly a critical parameter. IPA seems a better candidate than methanol since the reaction step in Fig. 2 (top), with ROH instead of  $\text{H}_2\text{O}$ , should stop for steric reasons after the attachment of the first  $-\text{OR}$  group on top of the  $\equiv\text{Si}$  (there is no access left to  $\text{Si}-\text{Si}$  back bonds). Experimentally, methanol leads to fast dissolution besides grafting since complete dissolution of porous layers is possible in dry methanol [7]. The smaller polarization of the  $\equiv\text{Si}^{+\delta}-\delta\text{OR}$  bond with IPA than with methanol is a further advantage.

#### CATHODIC GRAFTING OF CLOSE-PACKED PHENYL THIN LAYERS :

The method relies on the reduction of aryl diazonium salts either in acetonitrile or in acidic aqueous solution. Previously used by other to derivatize carbon surfaces [17,18,19], we recently extended this approach to H-terminated Si surfaces in a preliminary study [10]. The well accepted reaction of reduction of aryl diazonium is [20]:



where X is a substituent. The success of the method for modifying surfaces comes from the low cathodic overpotential necessary to reduce the  $^+\text{N}_2\text{-Ar-X}$  cation. This makes the aryl radical  $\cdot\text{Ar-X}$  long lived [21] and enables a reaction even with an inert surface such as that of HOPG (highly oriented pyrolytic graphite [17,18]).

The reaction of grafting is experimentally very simple to perform. Figure 5a shows the voltammetry of an H-Si(111) electrode (n-type) in a solution of  ${}^+\text{N}_2\text{-Ar-Br}$  in  $\text{H}_2\text{SO}_4$  (0.1 M) / HF (2 %). This supporting electrolyte was chosen to ensure that the surface remains free of oxide prior to the reaction. The reductive wave in Fig. 5a (bold line) corresponds to the generation of aryl radicals and to grafting. Upon further scanning (broken line) the disappearance of the wave is a signature of the surface modification. After careful rinsing in organic solvents (acetone and methanol) the modified surface was transferred into the supporting solution (no diazonium salt) for further electrochemical studies. Fig. 5b evidences that the treatment of the surface mainly results in a cathodic shift of the hydrogen evolution reaction (HER). Compare the dotted line (H-Si surface) and the bold line (as modified surface). Fig. 5b demonstrates further that the surface modification is quite robust and resists to a 2 min exposure to 40% HF (bold line) and to a 1 min dip in concentrated 10 M  $\text{NH}_4\text{F}$  (pH 4.5) (broken line) since the I-U curves remain nearly identical to that of the as-modified sample (bold line). More details are available in ref. [10].

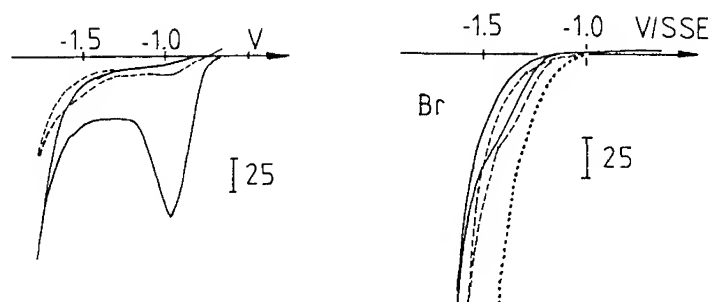


Fig. 5 : Left : Cyclic voltammograms of H-Si(111) in a solution of  ${}^+\text{N}_2\text{-Ar-Br}$  in  $\text{H}_2\text{SO}_4$  / HF(2%). First scan (bold line) and second scan (broken line). Right: Cyclic voltammogram of the -Ar-Br modified surface in  $\text{H}_2\text{SO}_4$  / HF(2%) : as prepared surface with or without exposure to 40% HF (bold line), same but exposed for 1 min to 10 M  $\text{NH}_4\text{F}$  pH 4.5 (broken line). H-terminated surface (dotted line). The bar is 25  $\mu\text{A}/\text{cm}^2$  in both cases.

XPS measurements confirm the derivatization of the surface after reduction of the diazonium salt. The different functional groups have indeed been identified by XPS [10] through the doublet Br3d3/2 and Br3d5/2 (respectively at 71.8 and 70.7 eV) for surfaces modified in  ${}^+\text{N}_4\text{-Ar-Br}$  solutions. In the case of Ar- $\text{NO}_2$  derivatization the N1s peak at 406 eV was consistent with the presence of nitro groups on the surface.

Focusing on the Si2p XPS peak (Fig. 6) yields insights into the nature of bonding and into the thickness of adlayers. All Si2p XPS peaks are centred on the  $\text{Si}^0$  ground state energy (99.8 eV). The asymmetry of peaks arises from spin-orbit coupling (the doublet Si2p1/2 and Si2p3/2 is resolved by curve fitting). The absence of noticeable chemical shift of the XPS Si2p, even under

experimental conditions where the signal is most surface sensitive (detector at grazing incidence), suggests the formation of  $\equiv\text{Si}-\text{Ar}$  bonds because the shift is  $\sim 1$  eV for  $\text{Me}_4\text{Si}$  and  $\text{Ph}_4\text{Si}$ , according to XPS tables. With a strongly electron attractor group like  $\text{NO}_2$ , the chemical shift should remain smaller than 1 eV. Moreover, in our case, the  $\equiv\text{Si}$  topmost atom is only once bound to a phenyl ring which reduces the charge  $\delta$  on  $\equiv\text{Si}^{+\delta}$  compared to a Si atom with 4 groups attached. We also note the absence of oxide or suboxide after modification. There is no satellite peak visible between the 99.5 eV ( $\text{Si}^0$ ) and 103.3 eV [22] (energy corresponding to  $\text{SiO}_2$ , Fig. 6b), even at grazing incidence.

Also instructive is to consider the attenuation of the  $\text{Si}2\text{p}$  peak. Expressing the XPS signal in Fig. 6c as  $I = I_0 \exp[-d/\lambda \sin(\theta)]$ , with  $I_0$  the intensity of the  $\text{Si}2\text{p}$  peak on the H-terminated surface,  $\theta=90^\circ$  (detector on the surface normal),  $d$  the film thickness and  $\lambda$  the escape depth, the experimental ratio  $I/I_0$  of 0.84 in Fig. 6 means a thickness  $d$  of  $7 \pm 0.8 \text{ \AA}$  for  $\lambda = 40 \pm 5 \text{ \AA}$  [23]. The same value is found with the Ar-Br derivatization. This result is a first element to state that aryl layers are one *monolayer* thick since  $7 \text{ \AA}$  is nearly equal to the vertical dimension of the Ar-X molecules used in this study.

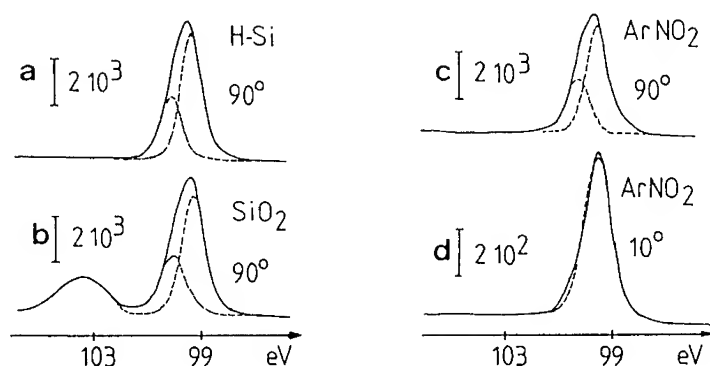


Fig. 6 : XPS  $\text{Si}2\text{p}$  peaks on different surfaces. H-terminated (a) and oxidized surfaces (b) with the detector on the surface normal. Ar- $\text{NO}_2$  modified surface: detector on the surface normal (c) and at grazing incidence (d) .

To gain further quantitative insights into the thickness and structure of layers RBS was used to dose the surface density of Br atoms. The technique could not be used in the case of Ar- $\text{NO}_2$  layers since N and O are lighter than the substrate (nuclear reaction analysis measurements are underway). Fig. 7 shows three RBS random spectra, before (a) and after (b,c) modification in the  $^+\text{N}_2\text{-Ar-Br}$  solution ( $U=-1$  V for 1 min). Provided one rasters the sample under the 1 MeV  $^4\text{He}^+$  beam, a linear dependency is observed between Br counts and the passed charge (see inset corresponding to curve b). The slope of the straight line yields  $\sim 4 \times 10^{14} \text{ BrAt/cm}^2$  on the surface after modification and rinse in organic solvents. Similar values were found after exposure of samples to HF and  $\text{NH}_4\text{F}$  as in Fig. 5 which confirmed the stability of organic films. Curve (c) evidences that the rinsing procedure is critical. Although the precursor molecule is soluble in wa-

ter, using water for washing the surface leaves physisorbed molecules. No Br is detected on the test H-Si(111) sample.

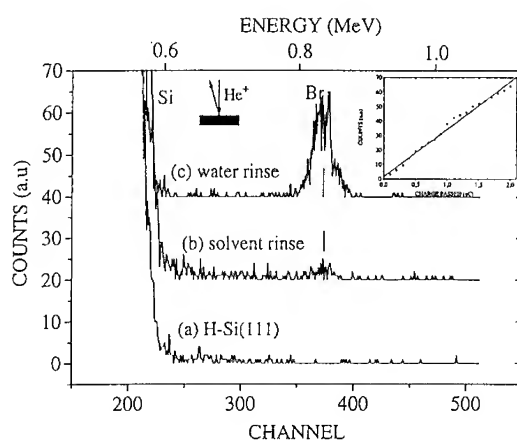


Fig. 7 : RBS spectra of H-terminated (a) and Ar-Br modified (b,c) Si(111) surfaces. The modified sample was rinsed either in organic solvents (b) or in water (c). The inset shows the variations, in case (b), of the Br counts as a function of the incident charge. The sample is rastered under the 1 MeV  $^4\text{He}^+$  beam to avoid Br losses.

Preliminary FTIR results (p-polarization) are shown in Fig. 8 for a sample modified by an Ar-NO<sub>2</sub> layer. The reference spectrum was that of the H-terminated surface, using the very same sample prior to modification. The sample was rinsed in acetone and methanol (spectrum a) and then exposed to 48% HF for 4 min (spectrum b). A number of positive peaks confirm the presence of Ar-NO<sub>2</sub> molecules on the surface. (i) The two absorption bands (1350 and 1525 cm<sup>-1</sup>) are related to symmetric and asymmetric νNO<sub>2</sub> modes groups. (ii) The prominent peak at 1605 cm<sup>-1</sup> and weaker ones at 1185 and 1115 cm<sup>-1</sup> are attributed to deformation modes of the ring. The first band is known to be enhanced by substituents like NO<sub>2</sub> [24]. The survival of NO<sub>2</sub> related IR bands, with *unchanged* intensity after the HF rinse, pertains to the excellent stability of the layer.

That Si-Ph bonding occurred is consistent with the two bands at 1435 and 1120 cm<sup>-1</sup> observed in spectrum (b) [24]. It was however impossible to look at the region 650-750 cm<sup>-1</sup> with our experimental set-up. That these two bands only appear after the HF rinse suggests that some physisorbed molecules were still present on the surface even after rinsing in methanol and acetone. They have probably been removed by HF as the disappearance of the broad band at 1040 cm<sup>-1</sup> suggests. This band is indeed attributed to trapped counterions BF<sub>4</sub><sup>-</sup> rather than to oxide because Si-O-Si vibrations should be polarization dependent, due to TO-LO splitting characteristic of the build-up of an (even incomplete) oxide layer. This effect is not observed here.

A last important issue concerns the Si-H related band around 2100 cm<sup>-1</sup>. The negative sharp peak at 2083 cm<sup>-1</sup> means that terrace Si monohydrides [12] have disappeared after molecular grafting. The positive broad band evidences however that some Si-H species are left on the surface after

the modification. Si hydrides from terrace edges have for instance probably not reacted for steric reasons (bands at  $2071\text{ cm}^{-1}$  and  $\sim 2090\text{--}2130\text{ cm}^{-1}$ ). Quantitatively, the integrated background appears nevertheless *larger* than on the initial H-Si(111) surface, which suggests either that terraces monohydrides remain in a rather large concentration (according to Fig. 9 below the (2x1) adlayer leaves 50% of initial terrace Si-H) or that drastic changes in the surface microstructure occurred upon grafting. We rather infer that the peak at  $2083\text{ cm}^{-1}$  associated to remaining terrace Si-H has broadened due to interactions between the organic moieties and vertical Si-H bonds. It is indeed well known that the local environment may strongly affect the  $\equiv\text{Si-H}$  stretch modes, as for instance when the surface is in contact with a liquid [7-8]. Deposition of Ag on H-Si(111) also enhances the IR response of terrace Si-H [25]. Work is nevertheless in progress to check that observations are not related to some surface roughening of the surface.

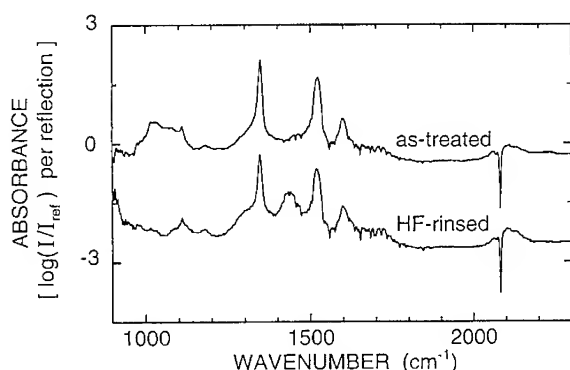
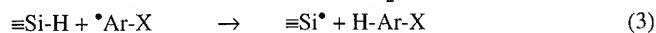
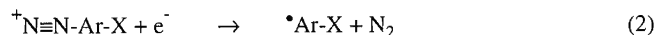


Fig. 8 : FTIR spectra of a surface modified by an Ar-NO<sub>2</sub> layer. The surface was rinsed in acetone and methanol (as treated sample) and then exposed to 48% HF (HF-rinsed). Spectra were obtained on the same sample at different stages of the preparation. The reference spectrum was that of the H-Si(111) surface.

The above results can be described according to the simplified reaction scheme :



where the generation of the aryl radical is given by reaction (2), which is identical to reaction (1). The aryl radicals then react with the Si surface. In a first step, a radical abstracts the H atom from the surface (reaction 3) and a second radical then binds on the surface radical  $\equiv\text{Si}\cdot$  to form a covalent bond  $\equiv\text{Si-Ar-X}$  (reaction 4). Within this description the formation of a second layer on top of the first one is unlikely from a (electro)chemical point of view. This is in agreement with XPS and RBS measurements (Figs. 6-7). The model is also consistent with FTIR results since Fig. 8 shows that Si-H species have disappeared from terraces.

On the molecular scale, it can be inferred that a (2x1) adlayer of Ar-X groups is formed on Si(111). A monolayer thickness is indeed consistent with XPS (Fig. 6) and RBS gives a Br coverage close to half of a monolayer (Fig. 7). This structure, which supposes that 50% of the initial vertical  $\equiv\text{Si-H}$  monohydrides are left on (111) planes is consistent with the FTIR results of Fig. 7 where  $\equiv\text{Si-H}$  species are clearly remaining on the surface. Fig. 9 shows a structure which has been derived from simulations [10]. Rings are aligned parallel to the  $\sqrt{3}$  direction to minimize Van der Waals interactions.

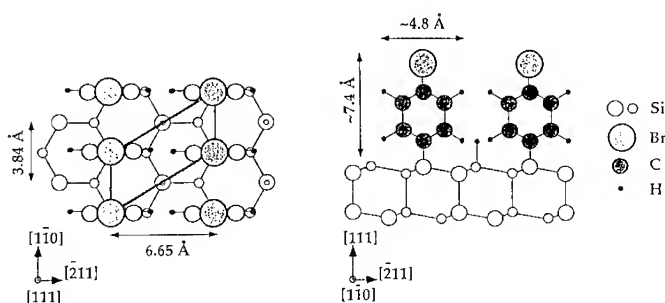


Fig. 9 : Molecular model of the Ar-Br layer on Si(111). Top (left) and side (right) views.

According to the model in Fig. 9, each molecule occupies  $\sim 25 \text{ \AA}^2$ , a value close to previous assumptions of  $21.8\text{-}25.2 \text{ \AA}^2$  [4] and previous simulations [17,18,19]. The good matching of the  $\text{sp}^3$  hybridisation, with one bond vertical, on Si atoms of (111) terraces and the  $\text{sp}^2$  hybridisation of the C on aryl groups is certainly critical to achieve this binding. Work is now in progress to characterize the structure layers by STM and X-ray techniques.

#### CONCLUSIONS :

Electrochemical molecular modification of Si surfaces has been demonstrated. The primary advantage of the method is its simplicity. The cathodic route, using aryl diazonium salts, seems most promising to achieve direct Si-C bonding in a very simple step even from an aqueous solution. Both the hydrophobic character of benzene rings and their large surface density make layers stable against chemicals like HF. The results presented in this paper should open to new opportunity to functionalize Si surfaces.

#### ACKNOWLEDGEMENTS :

We thank M. Leclerc for XPS measurements and M. Delamar for assistance in analysis of results and M. C. Bernard for RBS measurements. We are also grateful to Prof. Girault for molecular simulations. The surfaces shown in Fig. 1 have been prepared by R. Poetschke (University of Karlsruhe) during his stay at UPR 15.

## REFERENCES :

- [1] A. Ulman, in Ultrathin Organic Film. Academic Press, San Diego (1991).
- [2] A. Ulman, *Chem. Rev.*, **96** (1996) 1533
- [3] See, e.g., the Book of Abstracts of the ACS National Meeting in Chicago (1995), section Surface Science and Colloids.
- [4] A. Ulman, *Advanced Materials*, **2** (1990) 573
- [5] M. R. Lindford and C. E. D. Chidsey, *J. Am. Chem. Soc.*, **115** (1993) 12631.
- [6] M. R. Lindford, P. Fenter, P. M. Eisenberger and C. E. D. Chidsey, *J. Am. Chem. Soc.*, **117** (1995) 3145.
- [7] M. Warntjes, C. Veillard, F. Ozanam and J. N. Chazalviel, *J. Electrochem. Soc.*, **142**, 4138 (1995); C. Veillard, M. Warntjes, F. Ozanam and J. N. Chazalviel, *Proc. 4th Int. Symp. on Advanced Luminescent Materials*, D. J. Lockwood, P. M. Fauchet, N. Koshida and S. R. J. Brueck Eds., The Electrochemical Society Softbounds, PV 95-25 (1995) p250.[8]
- [8] T. Dubois, F. Ozanam and J. N. Chazalviel, Book of Abstracts of the 3rd European Workshop on Electrochemical Processing of Semiconductors (EWEPS '96), Meudon, Nov. 1996
- [9] P. Allongue, *Phys. Rev. Lett.*, **77** (1996) 1986.
- [10] C. Henry de Villeneuve, J. Pinson, M. C. Bernard and P. Allongue, *J. Phys. Chem.*, submitted
- [11] P. Allongue, V. Kielsing and H. Gerischer, *J. Electrochem. Soc.*, **140** (1993) 1008
- [12] For a review, see G. S. Higashi and Y. J. Chabal, in Handbook of Semiconductor Wafer Cleaning Technology. W. Kern, Ed., Noyes Publications, Park Ridge (1993).
- [13] P. Jakob and Y. J. Chabal, *J. Chem. Phys.*, **95** (1991) 2897.
- [14] G. J. Pietsch, U. Köhler and M. Henzler, *J. Appl. Phys.*, **73**, 4797 (1993) ; H. E. Hessel, A. Feltz, U. Memmert and R. J. Behm, *Chem. Phys. Lett.*, **186**, 275 (1991)
- [15] P. Allongue, V. Kielsing and H. Gerischer, *Electrochim. Acta*, **40** (1995) 1353.
- [16] P. Allongue, V. Costa-Kielsing and H. Gerischer, *J. Electrochem. Soc.*, **140** (1993) 1019.
- [17] M. Delamar, R. Hitmi, J. Pinson and J. M. Saveant, *J. Am. Chem. Soc.*, **114** (1992) 5883.
- [18] P. Allongue, M. Delamar, B. Desbat, O. Fagebaume, R. Hitmi, J. Pinson and J. M. Saveant, *J. Am. Chem. Soc.*, in press.
- [19] Y. C. Liu and R. L. Mc Crerry, *J. Am. Chem. Soc.*, **117** (1995) 11254.
- [20] J. P. Stradins and V. T. G. Glezer in Encyclopedia of the Elements, A. J. Bard and H. Lund Eds., Vol XII, p 78, Marcel Dekker, New York 1973
- [21] J. M. Savéant, *New J. Chem.*, **16** (1992) 131
- [22] M. Niwano, H. Katakura, Y. Takeda, Y. Takawura, N. Miyamoto, A. Hiraiwa and K. Kunhiro, *J. Vac. Sci. Technol.*, **A9** (1991) 195; M. Niwano, Y. Takeda, K. Kurita and N. Miyamoto, *J. Appl. Phys.*, **72** (1992) 2488.
- [23] This estimate assumes that  $\lambda$  is similar for aryl layers and alkylthiols. Values of  $\lambda = 42$  and  $34 \text{ \AA}$  have been reported for photoelectrons of kinetic energy of 1151 and 1402 eV respectively: see C. D. Bain and G. M. Whitesides, *J. Phys. Chem.*, **93** (1989) 1670.
- [24] L. J. Bellamy, in Infra Red Spectra of Complex Molecules, Methuen, London, 1958
- [25] M. Gruynters, Y. J. Chabal and P. Dumas, to be published

## Characterization of the Silicon / Fluoride Solution Interface by In-Situ Microwave Reflectivity

Arun Natarajan, Gerko Oskam, Douglas A. Oursler and Peter C. Searson  
Department of Materials Science and Engineering, The Johns Hopkins University, Baltimore,  
MD 21218.

### ABSTRACT

Etching of silicon in aqueous fluoride solutions can lead to almost atomically flat surfaces with a low density of surface states and recombination centers. The final quality of the surface, however, is strongly dependent on the solution composition and pH. We have performed electrochemical impedance spectroscopy in combination with potential modulated microwave reflectance spectroscopy (PMMRS) to elucidate the processes occurring at the surface during etching. PMMRS is a novel technique that only probes the free carriers in the conduction and valence bands and is, under certain conditions, not affected by processes involving electrically active surface states or charge transfer. This unique feature allows us to separate the energetics of the semiconductor from surface processes. Microwave reflectivity ( $\Delta R$ ) versus potential curves in HF solutions demonstrate the variation of the flatband potential as a function of pH. The  $\Delta R$  response in the narrow potential region around the flatband potential and at more negative potentials is also discussed.

### INTRODUCTION

In the semiconductor industry, the continuing decrease in feature sizes has resulted in increasing emphasis on surface properties [1]. Silicon wafers are routinely pretreated in HF solutions to remove residual  $\text{SiO}_2$  resulting in a hydrogen terminated surface of good electrical quality. Consequently, it is desirable to have *in situ* techniques which can be used to monitor the surface modifications of silicon in contact with HF solutions. For many years, electrochemical impedance spectroscopy (EIS) has been used to determine the charge and the potential distribution at the silicon/electrolyte interface by measuring the impedance as a function of potential [2-4]. However, the determination of the flatband potential and the doping density becomes complicated in the presence of surface states. In addition, at potentials more negative than the flatband potential the charge transfer impedance dominates the electrical response and studying the space charge layer becomes increasingly difficult. PMMRS is a novel *in situ* technique that allows the separation of the space charge and surface processes.

The microwave reflectivity,  $R$ , of a semiconductor is proportional to its conductivity,  $\sigma$ , hence, a change in conductivity,  $\Delta\sigma$ , result in a change in the microwave reflectivity,  $\Delta R$  [5,6]:



$$\Delta R = S \Delta \sigma \quad (1)$$

where  $S$  is the sensitivity factor which depends on the geometry of the sample.  $S$  can be determined by comparing the microwave response and the impedance response in the deep depletion regime.

Neglecting the contributions from minority carriers in an n-type silicon wafer, equation (1) can be rewritten as [7]:

$$\Delta R = S \mu_n e \Delta n \quad (2)$$

where  $\mu_n$  is the mobility of the electrons,  $e$  is the electronic charge, and  $\Delta n$  is the change in the mobile majority carrier concentration. Solving Poisson's equation and applying the small signal approximation in the depletion region [5,6] results in the following expression:

$$\Delta R = S \mu_n C_{sc} \Delta U / d \quad (3)$$

where  $d$  is the thickness of the sample,  $C_{sc}$  is the space charge layer capacitance, and  $\Delta U$  is the amplitude of the potential modulation.

From equations (2) and (3) we see that  $\Delta R$  is proportional to the change in the mobile electron concentration  $\Delta n$  and, hence, only relates to the space charge layer capacitance. For a sinusoidal potential modulation in the depletion region, the mobile charge carrier density increases as the applied potential is made more negative. Hence,  $\Delta R$ , will be  $180^\circ$  out of phase with the potential modulation. Due to the  $180^\circ$  phase shift of  $\Delta R$  with the modulating potential, in the complex plane the real component of  $\Delta R$  should have a negative value and the imaginary component of  $\Delta R$  is expected to be negligible. Note that the equilibration process of the mobile majority carriers in the space charge region of silicon is much faster than the frequency of the potential modulation so that the microwave response is independent of electron transport in the bulk of the material.

## EXPERIMENTAL

All the experiments were performed on  $25 \Omega \text{ cm}$ , n-type silicon (111), obtained from Semiconductor Processing Inc., MA. The wafers were cleaned with HF and rinsed with deionized water. The ohmic contact was made by rubbing in In-Ga along the circumference of the back of the wafer. The surface was again cleaned with HF just prior to each experiment.

A block diagram of the microwave system is shown in Figure 1. It is based on a rectangular X-band waveguide system [8] with a 60 mW, 9.33 GHz microwave source where the microwave field penetrates the back side of the silicon wafer. Typical amplitudes and frequencies

of the potential modulation for electrochemical impedance measurements (EIS) and PMMRS were 30 mV(rms) at 1 kHz in the deep depletion regime and 10 mV(rms) at 20 Hz in the surface state regime. PMMRS measurements at potentials negative of the flatband potential were performed at 30 mV(rms) and 20 Hz. All potentials were measured with respect to the saturated calomel electrode (SCE).

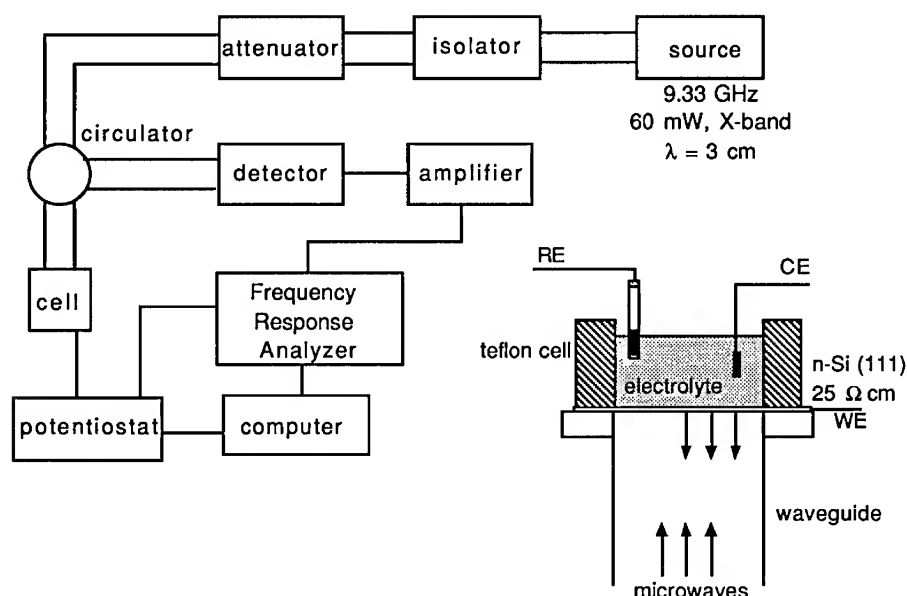


Figure 1: Block diagram of the experimental setup for PMMRS and EIS measurements.

## RESULTS AND DISCUSSION

PMMRS and EIS measurements were performed in 1 M HF (pH 2) and 0.01 M  $\text{NH}_4\text{F}$  (pH 6.8) with both solutions having the same fluoride ion concentration. Figure 2 shows a semi-logarithmic plot of  $\Delta R$ -real and  $|\Delta R|$  versus frequency in 0.01 M  $\text{NH}_4\text{F}$  in the deep depletion regime ( $U = +0.3$  V). The plot shows that  $\Delta R$  is virtually independent of frequency. The roll-off at frequencies close to  $10^5$  Hz is due to the response of the potentiostat. At frequencies below 10 Hz, there is some scattering in the microwave response. As expected, the magnitude of  $\Delta R$ -real is equal to  $|\Delta R|$  implying that  $\Delta R$ -imaginary is negligible. The anticipated  $180^\circ$  phase shift between the modulating potential and  $\Delta R$  is confirmed from the fact that  $\Delta R$ -real is negative

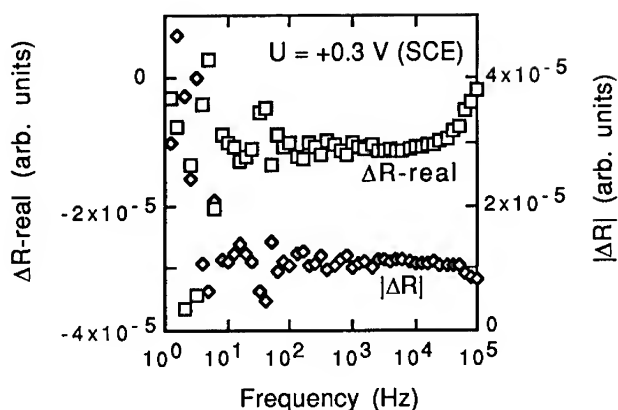


Figure 2: Bode plot of  $\Delta R$ -real and  $|\Delta R|$  versus frequency under depletion conditions in 0.01 M  $\text{NH}_4\text{F}$  (pH 6.8).

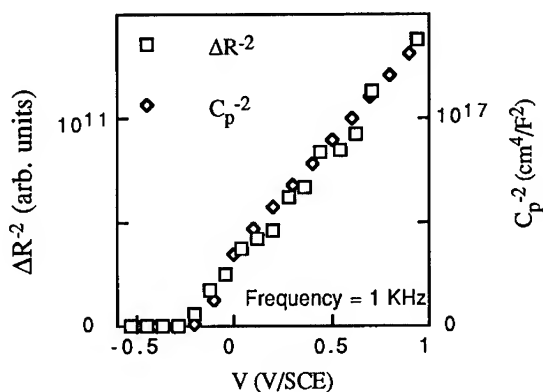


Figure 3:  $\Delta R^{-2}$  and  $C_p^{-2}$  versus potential plots in 1 M HF (pH 2).  $C_p$  is the parallel capacitance. The scan rate was 3 mVs<sup>-1</sup>.

Figure 3 shows typical Mott-Schottky plots of  $C^{-2}$  and  $\Delta R^{-2}$  versus potential in 1 M HF (pH 2). The flatband potential determined from these results was -0.30 V(SCE). The microwave response over the entire depletion regime compares remarkably well with the capacitance response showing that  $\Delta R$  is proportional to  $C_{sc}$  as was expected from equation (3) [8]. The value of the sensitivity factor  $S$  (equation (3)) was found to be 1.27. Similar plots in 0.01 M  $\text{NH}_4\text{F}$  (pH 6.8) yielded a flatband potential of -0.40 V (SCE) showing that the flatband potential shifts to more negative values with increasing pH [8].

Figure 4 shows the capacitance and  $\Delta R$  versus potential in a 0.01 M  $\text{NH}_4\text{F}$  solution (pH 6.8) in the potential regime where electrically active surface states dominate the impedance response

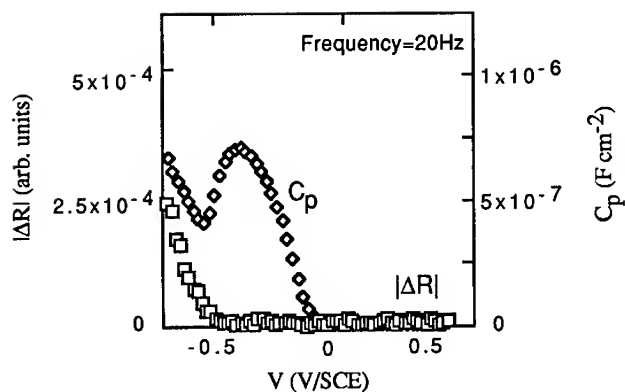


Figure 4:  $\Delta R$  and  $C_{p1}$  vs. potential in the surface state regime in 0.01 M  $\text{NH}_4\text{F}$  (pH 6.8). The scan rate was  $1 \text{ mVs}^{-1}$ .

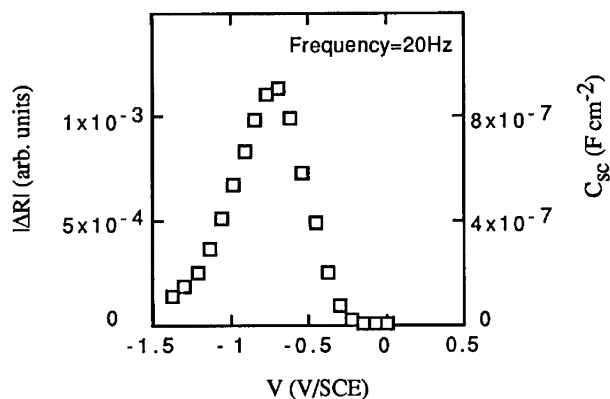


Figure 5:  $\Delta R$  and  $C_{sc}$  (calc.) vs  $V$  at negative potentials in 1M  $\text{HF}$  (pH 2). The magnitude of  $C_{sc}$  was determined from equation (3). The scan rate was  $3 \text{ mVs}^{-1}$ .

At potentials between  $-0.2 \text{ V}$  and  $-0.6 \text{ V}$ , the capacitance - potential curve shows a maximum and the capacitance is due to the filling and emptying of surface states [2]. The  $\Delta R$  curve, on the other hand, shows that the microwave reflectivity method only detects changes in the space charge capacitance and is not affected by the presence of surface states.

The surface state density can be calculated from the capacitance peak and was determined to be  $\approx 3.3 \times 10^{11} \text{ cm}^{-2}$  [2]. Assuming a Helmholtz layer capacitance  $C_H \approx 2 \times 10^{-6} \text{ F cm}^{-2}$ , the band edges shift by about  $26 \text{ mV}$  as the Fermi level moves through the surface states. These

results show that the band edges are essentially fixed as the Fermi level is increased from deep depletion to weak depletion.

The  $\Delta R$  response at potentials negative of the flatband potential was also investigated and the results obtained in 1 M HF (pH 2) are shown in Figure 5. The  $\Delta R$  curve goes through a maximum close to -0.6 V(SCE), and  $\Delta R$  subsequently decreases towards zero. This indicates that the modulated applied potential is mainly dropped over the Helmholtz layer at potentials more negative than -1 V. These results also confirm that the microwave response only detects a modulation of the free carrier concentration and is not affected by charge transfer processes. The increase in the  $\Delta R$  signal in the narrow potential region negative of the flatband potential (-0.3 V) is exponential with an inverse slope of 280 mV/decade. The expected potential dependence of the capacitance for an accumulation layer is 120 mV/decade [9] implying that the applied potential is partitioned over the accumulation layer and the Helmholtz layer in this region. These results show that PMMRS is a unique technique which allows us to probe the accumulation regime of the silicon / electrolyte interface.

## SUMMARY

PMMRS studies were conducted on silicon surfaces in contact with two solutions of different pH containing the same fluoride ion concentration. It was found that the flatband potential shifts more negative with increasing pH. It was further shown that in accordance with theory,  $\Delta R$  relates only to changes in the space charge layer and is not affected by the presence of electrically active surface states. Preliminary studies at negative potentials indicate that  $\Delta R$  is not influenced by charge transfer processes. Hence, PMMRS is an excellent technique to study the accumulation regime of the silicon / solution interface.

## ACKNOWLEDGMENTS

This work was supported, in part, by the U.S. Army Research Office DAAH04-95-2-0006.

## REFERENCES

1. The National Technology Roadmap for Semiconductors, Semiconductor Industry Association, San Jose, CA (1994).
2. G. Oskam, P. M. Hoffmann, J. C. Schmidt, and P. C. Searson, *J. Phys. Chem.* **100**, 1801 (1996).
3. M. J. Madou, B. H. Loo, K. W. Frese, S. R. Morrison, *Surf. Sci.* **108**, 135 (1981).
4. P. E. Laibinis, C. E. Stanton, N. S. Lewis, *J. Phys. Chem.* **98**, 8765 (1994).
5. M. Kunst and G. Beck, *J. Appl. Phys.* **60**, 3558 (1986); **63**, 1098 (1988).
6. G. Schlichthörl and H. Tributsch, *Electrochim. Acta* **37**, 919 (1992).
7. S. M. Sze, *Physics of Semiconductor Devices* (Wiley, NY, 1981).
8. G. Schlichthörl, and L. M. Peter, *J. Electrochem. Soc.* **141**, L171 (1994); *J. Electroanal. Chem.* **381**, 55-61 (1995).
9. S. R. Morrison, *Surf. Sci.* **15**, 363 (1969).

## IN-SITU CHARACTERIZATION OF THE SURFACE STATE DENSITY BY PHOTOLUMINESCENCE DURING ELECTROCHEMICAL TREATMENTS OF SILICON SURFACES

T. DITTRICH\*, V. Y. TIMOSHENKO\*\*, J. RAPPICH\*\*\*

\* Technische Universität München, Physik Department E16, D-85747 Garching, Germany

\*\* Physics Department, Moscow State University, 119899 Moscow, Russia

\*\*\* Hahn-Meitner-Institut, Abt. Photovoltaik, Rudower Chaussee 5, D-12489 Berlin, Germany

### ABSTRACT

The photoluminescence (PL) of c-Si is probed stroboscopically with single pulses of a  $N_2$  laser during electrochemical treatments (hydrogenation and anodic oxidation). The PL intensity of indirect semiconductors such as Si is controlled by the non-radiative surface and bulk recombination. By this reason the density of surface states can be estimated for unknown surfaces by using a calibrated standard. The surface state density of a hydrogenated Si surface increases by exchanging the electrolyte by gaseous  $N_2$  or water.

### INTRODUCTION

The in-situ characterization of the surface state density ( $N_s$ ) is not only important for the control of the passivation of Si-surfaces but also for studying surface related phenomena. They are of interest, for example, for the controlled creation of reactive surface sites in electrolytes. The value of  $N_s$  can be obtained from impedance measurements or via the determination of the surface recombination velocity  $v_s$ . The value of  $v_s$  is extremely low for Si surfaces in HF and the respective  $N_s$  was obtained to be lower than  $10^9 \text{ cm}^{-2}$  [1]. In-situ impedance measurements lead to values of  $N_s$  of about  $2 \cdot 10^{10} \text{ cm}^{-2}$  for Si surfaces in fluoride solution [2]. This value is very close to ex-situ measurements carried out with the pulsed surface photovoltage technique (SPV [3,4]) on electrochemically hydrogenated Si surfaces [5,6].

Changes in the surface recombination velocity can be observed also by measuring the change of the radiative band-band recombination of c-Si. For example, the PL of c-Si was excited with an Argon ion laser (cw) to study the oxidation of Si surfaces in air [7]. The PL excitation with an cw laser is not suitable for in-situ investigations in electrolytes due to the large net number of excess carriers ( $n_{exc}$ ) which may influence the chemical equilibria. The value of  $n_{exc}$  can be dramatically reduced for stroboscopic probing the PL with a pulsed  $N_2$  laser as proposed in this work. The duty cycle of this technique is given by the non-radiative recombination and by the laser repetition rate. However, a direct determination of  $v_s$  is complicated in our experiments due to one compromise we should make: For limiting the duty cycle and for excluding any influence of the back surface of the sample we chose Si samples with bulk lifetimes of about  $20 \mu\text{s}$  and thicknesses much larger than the diffusion length of the minority carriers of charge. By this reason we calibrate the time integrated PL intensity with SPV measurements. We demonstrate the stroboscopic in-situ PL probe for standard electrochemical treatments of p-type Si(100) surfaces in fluoride solutions (hydrogenation and anodic oxidation).

## EXPERIMENTAL

P-Type Si(100) wafers (FZ, resistivity 1  $\Omega\text{cm}$ , thickness 400  $\mu\text{m}$ ) are treated electrochemically in the potentiostatic regime in 0.1M  $\text{NH}_4\text{F}$  (pH from 2.5 to 4.5, adjusted by addition of  $\text{H}_2\text{SO}_4$ ). The samples are mounted into the center of a quartz tube and serve as working electrode. A Pt wire and a Ag/AgCl electrode are used as counter and reference electrodes, respectively. The electrolyte is pumped continuously through the quartz tube and can be quickly exchanged by  $\text{N}_2$  or water. The equipment is described in more detail in [8]. Anodic oxidation is carried out at potentials up to +10 V. The hydrogenation is reached after the current transient (at -0.4 V) levels out [9,10].

The PL is excited with a  $\text{N}_2$  laser (LTB-MSG200, pulse duration 0.5 ns, wavelength 337 nm, intensity from 0.1 to 5  $\text{mJ}/\text{cm}^2$ ). The repetition rate of the laser pulses is 1 Hz or less. The absorption length of the laser light in the c-Si is 10..20 nm. The PL signals are detected at 1.1  $\mu\text{m}$  wavelength with a prism monochromator and a Si photodiode in the time resolved (resolution time 1  $\mu\text{s}$ ) and in the time integrating (integration time 100  $\mu\text{s}$ ) regimes. The SPV measurements are carried out at a Si surface covered with a native oxide in the same manner as described in [5] which serves as reference.

## CALIBRATION OF THE SURFACE STATE DENSITY

The calibration is performed by the ratio of time integrated PL intensities of the investigated (I) and the reference ( $I_0$ ) samples which is given by:

$$I/I_0 = (\tau_b^{-1} + \tau_{so}^{-1}) / (\tau_b^{-1} + \tau_c^{-1})$$

where  $\tau_b$ ,  $\tau_s$  and  $\tau_{so}$  are the non-radiative lifetimes of the bulk and the investigated and calibrated surfaces, respectively. The value of  $\tau_{so}$  is given by  $\tau = \sigma \cdot v \cdot N_{so} / d$ , where  $\sigma$ ,  $v$ ,  $N_{so}$  and  $d$  are the capture cross section, the thermal velocity, the surface state density and the diffusion length of the minority carriers in the bulk.  $N_{so}$  can be obtained from the SPV measurements for a well stabilized Si surface by taking the interface state density in the minimum of their energy distribution. The values of  $\sigma$ ,  $v$  and  $d$  are  $10^{-15} \text{ cm}^2$ ,  $10^7 \text{ cm s}^{-1}$  and 170  $\mu\text{m}$ , respectively.

## RESULTS AND DISCUSSION

Fig.1 shows PL transients of a hydrogenated Si surface at the excitation intensities  $I_{exc} = 0.5, 1$  and 4  $\text{mJ}/\text{cm}^2$  (thick, medium and thin solid lines, respectively). The decay time is independent of  $I_{exc}$ . A peak is developing at the short times with increasing  $I_{exc}$  due to Auger recombination. PL transients of a hydrogenated Si surface and of a Si surface during electropolishing at +10V are shown in fig.2 ( $I_{exc} = 4 \text{ mJ}/\text{cm}^2$ ). The PL amplitude and decay time are strongly reduced during electropolishing. It should be mentioned that the decay times are not related directly to the surface non-radiative recombination rates since the PL transient includes the huge spatial redistribution of excess carriers in time. The PL amplitudes are more representative for the change of  $N_s$ . We remark that a detailed analysis of the excess carrier dynamics is not simple and out of the scope of this work. We focus our work on the stroboscopic probing of the time integrated PL signal. The transients from the figs.1 and 2 show that the duty cycle of the stroboscopic probe is about  $10^{-5}$  for 1 Hz repetition rate of the laser pulses.

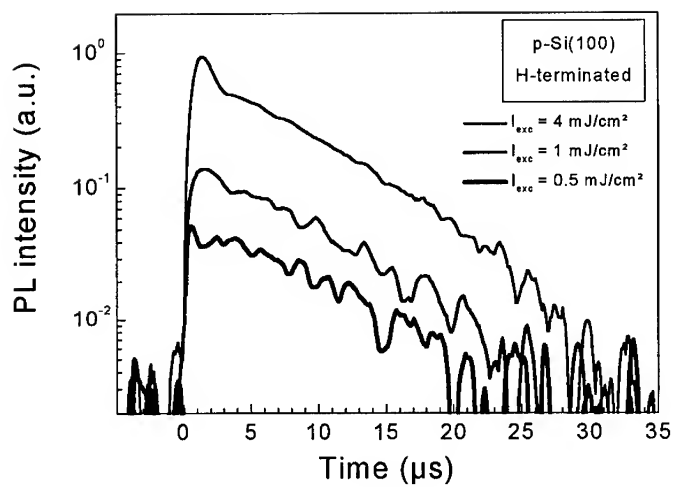


Fig. 1: PL transients of a hydrogenated p-Si(100) surface with  $I_{\text{exc}} = 0.5, 1$  and  $4 \text{ mJ/cm}^2$  (thick, medium and thin solid lines, respectively).

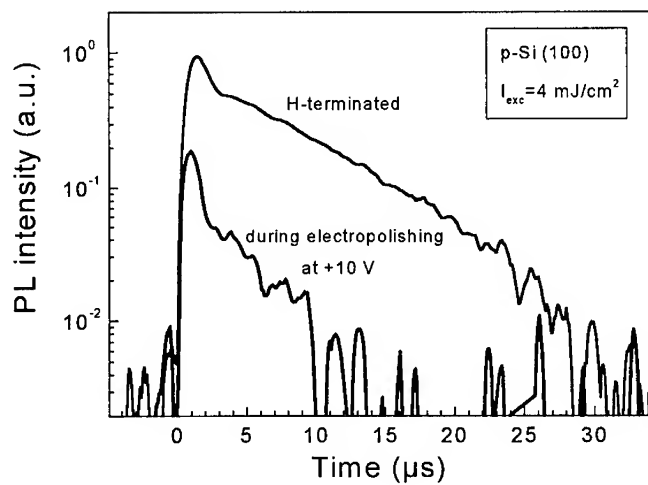


Fig. 2: PL transients of a hydrogenated p-Si(100) surface and of a p-Si(100) surface during electropolishing at  $+10 \text{ V}$  (thin and thick solid lines, respectively)



Fig.3 shows the potential scan with time (a) and the respective current and PL scans (b, solid line and circles, respectively). The potential is switched to a constant value of -0.4 V after 400 s. The current increases with increasing voltage up to about 140 s (nearly 2 V). The first increase of the PL intensity is due to a better passivation by hydrogenation, whereas the following decrease of the PL intensity should be connected with the roughening of the Si surface [11]. The PL intensity reaches a minimum when electropolishing starts (first current peak) and decreases slightly up to about the second current maximum. The current starts to oscillate at the higher potentials at about +4 V (after about 250 s). These current oscillations are well known from the literature [10]. The PL intensity anticorrelates to the current oscillations. This phenomenon was described recently [12] and is explained by the modification of the non-radiative recombination at the Si surface during the anodic oxidation (see also the dangling bond and center of reconstruction model in ref. [13]).

The thin anodic oxide is etched back after switching the potential from +10 V to -0.4 V and the current transient occurs [9]. The PL intensity starts to increase sharply at the maximum of the current transient and reaches a constant value when the transient levels out. This correlates well with ex-situ SPV measurements on n-type Si(111) surfaces [14], where the interface state density starts to decrease strongly when the maximum of the current transient was reached. A constant low value was observed when the current transient leveled out.

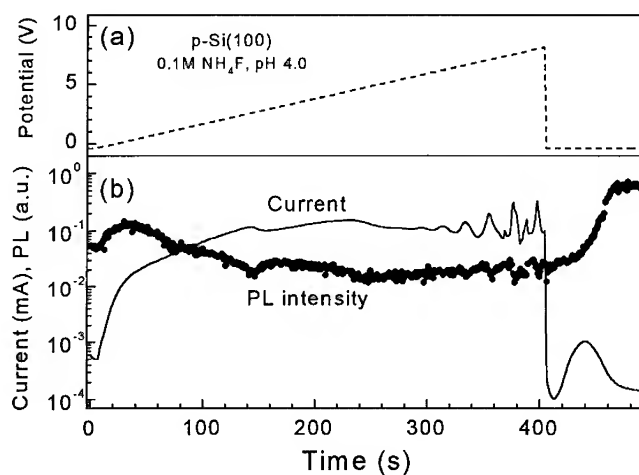


Fig.3: Potential scan with time (a) and respective current and PL scans (b, solid line and circles, respectively).

Another interesting question concerns the stability of the hydrogen passivated Si surfaces as a function of the former oxidation potential and after exchanging the electrolyte by  $N_2$  or  $H_2O$ . The PL intensity of the c-Si is shown in fig.4 by switching the potential between anodic oxidation and hydrogenation at -0.4 V. This figure shows further the PL intensities of the hydrogenated Si(100) surface after exchanging the electrolyte by gaseous  $N_2$

and  $\text{H}_2\text{O}$ , respectively. The fluctuations of the PL intensity during the anodic oxidation are a measure of the oscillation amplitudes. The mean PL intensity depends on the applied potential during the anodic oxidation while the PL intensity of the following hydrogenated Si surfaces is independent of the potential of the foregoing anodic oxidation. The PL intensity of the hydrogenated Si surface generally decreases after exchanging the electrolyte. The observed decrease of the PL intensity is not an optically induced effect since the PL intensity has the same low value after exchanging the gaseous  $\text{N}_2$  by  $\text{H}_2\text{O}$ . The general increase of the surface recombination velocity can be reduced by optimizing the parameters of interruption. This is a very important point and explains discrepancies between in-situ and ex-situ measurements.

The value of  $N_s$  obtained for the p-type Si(100) in the electrolyte is about  $5 \cdot 10^{10} \text{ cm}^{-2}$  while the ex-situ SPV or PL give  $8 \cdot 10^{10} \text{ cm}^{-2}$ . The partial depassivation of the Si surface by exchanging the electrolyte is, in principle, not surprising. There exist an equilibrium of the formation and passivation of nonradiative recombination surface defects at the Si/electrolyte interface which is distorted by the interruption process.

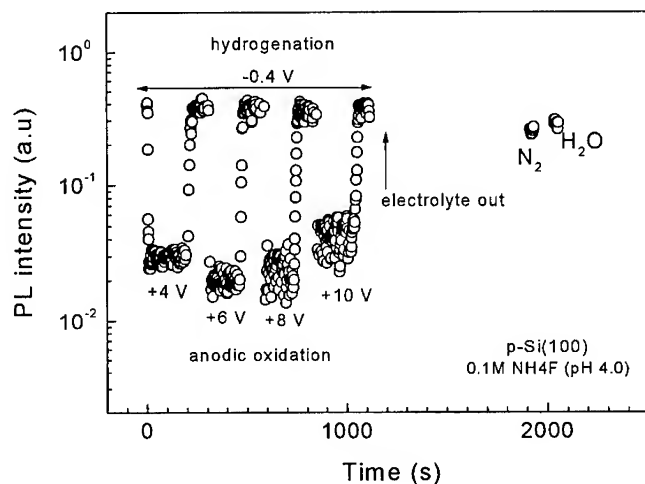


Fig.4: Dependence of the PL intensity on time during switching experiments between hydrogenation at  $-0.4 \text{ V}$  and anodic oxidation at different potentials and after exchanging the electrolyte by gaseous  $\text{N}_2$  and  $\text{H}_2\text{O}$ .

## CONCLUSIONS

Si surfaces were probed stroboscopically by PL during electrochemical treatments. We have shown that the change of the PL depends on the formation and passivation of non-radiative recombination centers, where the amount is defined by the type of the electrochemical reaction. Furthermore, we have presented a method to calibrate PL measurements. This offers a fast quality-check of the interface by photoluminescence techniques.

## REFERENCES

1. E. Yablonoich, D. L. Allara, C. C. Chang, T. Gmitter , and T. B. Bright, Phys. Rev. Lett. **27**, 249 (1986).
2. G. Oskam, P. M. Hoffmann, and P. C. Searson, Phys. Rev. Lett. **76**, 1521 (1996).
3. Y. W. Lam, J. Phys. D: Appl. Phys. **12**, 927 (1971).
4. K. Heilig, H. Flietner, and J. Reineke, J. Phys. D: Appl. Phys. **12**, 927 (1979).
5. Th. Dittrich, H. Angermann, H. Flietner, Th. Bitzer, and H. J. Lewerenz, J. Electrochem. Soc. **141**, 3595 (1994).
6. S. Rauscher, Th. Dittrich, M. Aggour, J. Rappich, H. Flietner, and H. J. Lewerenz, Appl. Phys. Lett. **66**, 3018 (1995).
7. T. Konishi, T. Yao, M. Tajima, H. Oshima, H. Ito, and T. Hattori, Jap. J. Appl. Phys. **31**, L1216 (1992).
8. J. Rappich, V. Yu. Timoshenko, Th. Dittrich, J. Electrochem. Soc., in press.
9. H. Gerischer, and M. Lübke, Ber. Bunsenges. Phys. Chem. **92**, 573 (1988).
10. F. Ozanam, J.-N. Chazalviel, A. Radi, and M. Etman, Ber. Bunsenges. Phys. Chem. **95**, 98 (1991).
11. D. J. Blackwood, A. Borazio, R. Greef, L. M. Peter, and J. Stumper, Electrochim. Acta **37**, 882 (1992).
12. J. Rappich, V. Yu. Timoshenko, Th. Dittrich, Ber. Bunsenges. Phys. Chem., in press.
13. H. Flietner in 7<sup>th</sup> Conf. Insulating Films on Semiconductors (INFOS) ed. By W. Eccleston and M. Uren (Hilger, Bristol 1991), p. 151-154
14. Th. Dittrich, S. Rauscher, Th. Bitzer, M. Aggour, H. Flietner, and H. J. Lewerenz, J. Electrochem. Soc. **142**, 2411 (1995).

## ELECTROLYTE ELECTROREFLECTANCE OF BORON PHOSPHIDE (BP)

E. SCHROTEN, A. GOOSSENS, J. SCHOONMAN

Laboratory for Applied Inorganic Chemistry, Delft University of Technology,  
P.O. Box 5045, 2600 GA Delft, The Netherlands, E.Schroten@stm.tudelft.nl

### ABSTRACT

An electrolyte electroreflectance study has been performed on boron phosphide thin films epitaxially grown on silicon (100) substrates. To our knowledge, this paper is the first report on the electrolyte electroreflectance spectrum of BP. All our boron phosphide of 1.5  $\mu\text{m}$  thick films show a pronounced peak at the energy 4.25 eV, indicating a critical point in the valence or conduction band of the semiconductor. Photoreflectance measurements confirm these results. The 4.25 eV energy level is much lower than previously reported direct bandgap values of BP. The electrolyte electroreflectance spectrum of much thinner layers shows, besides the 4.25 eV peak, some other features at still lower incident photon energies caused by interference effects.

### INTRODUCTION

Boron phosphide is a relatively unknown member of the III-V semiconductor family. The lattice parameter of this zinc-blende material is 4.53 Å, and its indirect bandgap is 2.0 eV. BP shows mechanical and chemical properties that classify it as a refractory material. Recently, we have investigated BP as a protecting optical window for silicon liquid junction solar cells<sup>1</sup>.

In this study, we focus on the fundamental properties of the semiconductor band structure. The few papers published on this matter report an indirect gap of 2.0 eV<sup>2</sup> and a direct gap of 6 eV<sup>3</sup>. These values are based on transmission spectra performed on polycrystalline samples. Much more sensitive methods to determine the energy structure of semiconductors are electrolyte electroreflectance (EER) and photoreflectance spectroscopy<sup>4</sup>. These are based on periodically perturbation of the electronic states of the material, and detection of the induced periodic change in optical reflection. As pointed out by Aspnes<sup>4</sup>, the resulting spectrum of the periodic change in reflection relative to the total reflection is a third derivative of the spectrum of the transition possibilities in the material.

### EXPERIMENT

Thin layers of boron phosphide have been epitaxially grown on Si (100) substrates using a conventional cold wall CVD reactor. After cleaning the silicon with acetone, HNO<sub>3</sub>, and HF, the substrates are heated to 950°C in a hydrogen flow at atmospheric pressure. After ten minutes the temperature is lowered to the deposition temperature (typically in the range of 870-930°C). The precursors, BBr<sub>3</sub> and PBr<sub>3</sub>, diluted in H<sub>2</sub>, are introduced into the reactor and BP starts to grow on the silicon with typical rates of 0.5  $\mu\text{m/hr}$ . The gas flows are 1800 ml/min with partial pressures of 0.3 and 3 Torr for BBr<sub>3</sub> and PBr<sub>3</sub>, respectively. In this study, samples of 450 nm and 1.5  $\mu\text{m}$  thickness have been studied.

Electrolyte electroreflectance measurements are performed in the so-called surface barrier configuration, in which the electrical field is perpendicular to the illuminated semiconductor

To perform the EER spectroscopy, the FRA is replaced by a lock-in amplifier, to provide the AC voltage (typically 70 Hz and 100 mV RMS) and the analysis of the modulated reflection. The probing light is provided by a 150 Watt Xe lamp and a grating monochromator with 2 mm slits, and has a spectral resolution of 5 nm. Spectra have been taken in the range from 2 to 5 eV, which is above the indirect bandgap of BP.

Photoreflectance spectra have been determined using the same light probing set-up. Now, the electronic structure of the semiconductor is perturbed by a periodic redistribution of charge carriers. The 2.3 eV laser photons are absorbed in both BP and Si. Experiments have been performed at room temperature, in air. The samples are mounted on a simple holder, and a small area is illuminated by a chopped HeNe laser beam of 543.5 nm light. Whereas the probing beam is directed almost perpendicular to the surface, the angle of incidence of the laser beam is large to reduce light scattering into the photomultiplier.

## RESULTS AND DISCUSSION

## Structural analysis

The as-grown BP layers are single crystalline in the same orientation as the silicon substrate, as has been determined with X-ray and electron diffraction. The thin layers exhibit very smooth surfaces, whereas the thicker samples tend to roughen. This phenomenon is common in the epitaxy of materials with lattice mismatch<sup>5</sup>, in which tensile (or, in other cases, compressive) strain causes the surface to roughen after a certain layer thickness. A dark field transmission electron micrograph of the silicon sublattice at the BP/Si interface is shown in Figure 2.

Although reconstruction of the silicon surface is desired to reduce anti phase boundaries, the observed roughening is extreme. Similar roughening is observed in the CVD grown epitaxial GaAs<sup>6</sup>. There the effect has been attributed to the interaction of the AsH<sub>3</sub> with the substrate prior to the epitaxial growth. During the heat treatment of the substrate just before layer growth, a similar process can take place induced by the phosphorus that is present in the alumina pedestal of the susceptor.

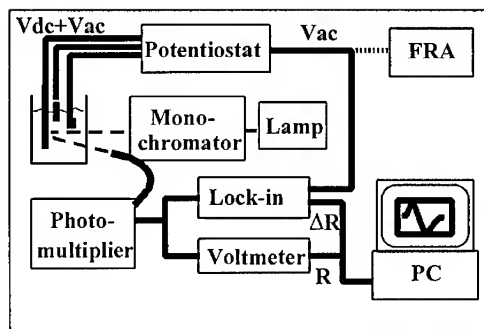


Figure 1. Schematic set-up for the electrochemical measurements. For the CV-profiling the Frequency Response Analyzer is used, for the electrolyte electroreflectance spectroscopy, the lock-in amplifier generates the AC-voltage.

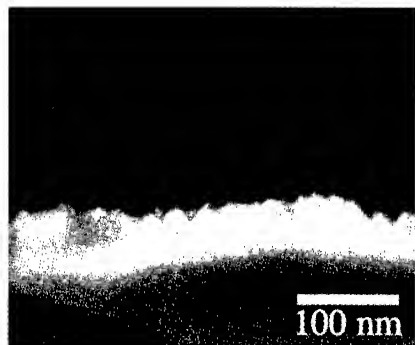


Figure 2. Dark field transmission electron micrograph, showing the silicon sublattice at the boron phosphide interface. The boron phosphide(top) is not visible, the white area is the silicon side of the interface. The contrast in the Si is caused by bending of the sample due to strain.

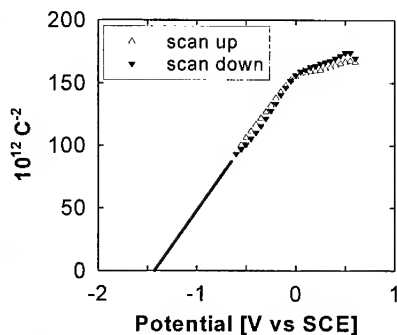


Figure 3. Mott-Schottky plot of the Si/BP/NaOH (0.1 M) cell. Measurements were performed at a frequency 10 kHz. The extrapolation shown indicates the flatband potential at -1.4 V vs SCE.

#### Electro-optical analysis

Prior to the electrolyte electroreflectance measurements, the system, consisting of both a heterojunction and a semiconductor/electrolyte junction, has been investigated by impedance spectroscopy. A CV-profile has been taken at a frequency of 10 kHz (see Figure 3), from which a donor concentration of  $8 \times 10^{18} \text{ cm}^{-3}$  and a flatband potential of -1.4 V vs SCE could be derived. As has been pointed out in previous work<sup>1</sup>, the potential drop takes place only at the BP/electrolyte interface.

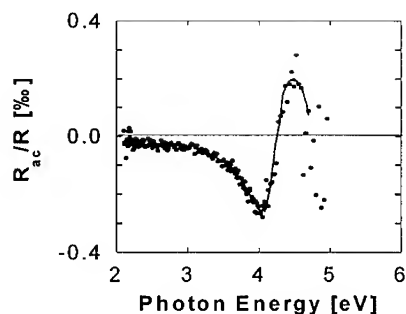


Figure 4. Electrolyte electroreflectance of a 1.5  $\mu\text{m}$  thick epitaxial layer of B. The typical EER oscillation is visible around the 4.25 eV. The polarization was -0.3 vs SCE, to which a AC voltage of 70 Hz 100mV RMS was added.

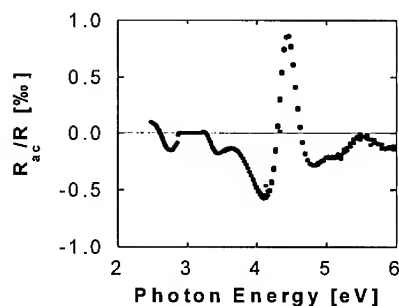


Figure 5. Electrolyte electroreflectance spectrum of a thin layer of epitaxial BP grown on Si(100). Note the difference in vertical scale with respect to Figure 4. The 4.25 eV critical energy is clearly visible. Other features are caused by interference.

Typical EER-spectra of 1.5  $\mu\text{m}$  and 400 nm samples, recorded at a polarization of -0.3 V vs SCE, are presented in Figure 4 and 5, respectively. The spectra scale with the amplitude of the perturbation voltage, and because the form is not dependent on the polarization of the electrode, the amplitude of the 4 eV peak can be plotted against the polarization to obtain the flatband potential at the cross-over voltage (See Figure 6).

From the spectra, at least one distinctive critical point can be extracted. The form of the spectrum around a critical energy obeys the relation

$$\frac{R_{ac}}{R} = \text{Re}\{(E_{ph} - E_c + i\Gamma)^{-n} C \exp(-i\theta)\} \quad (1),$$

in which  $R_{ac}$  represents the perturbed part of the reflectance signal  $R$ , the energies  $E_{ph}$  and  $E_c$  are those of the incident photons and the band separation at the critical point, respectively.  $\Gamma$  is the broadening parameter, and  $n$  depends on the dimension of the critical point ( $n=3$  and  $n=5/2$  for 2-dimensional and 3-dimensional critical points, respectively).  $C$  and  $\theta$  are amplitude and phase factors. The latter determines the asymmetry of the line shape. A non-linear least squares fit is performed on data around the largest feature in the spectrum of the thin (smoothest) layer. From this fit, a critical point at 4.25 eV is obtained. There are no previous experimental data available on this transition energy. Using data from theoretical band calculations<sup>7</sup>, we tentatively attribute this energy level to the first direct transition at the  $\Gamma$ -point in the reciprocal space.

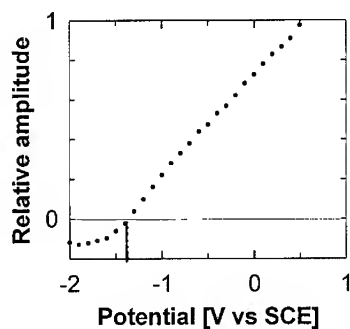


Figure 6. *Electrolyte electro-reflection voltammogram of epitaxial BP in 0.1 M NaOH. The change in relative amplitude of the 4 eV peak shows the flatband potential at -1.4 V vs SCE.*

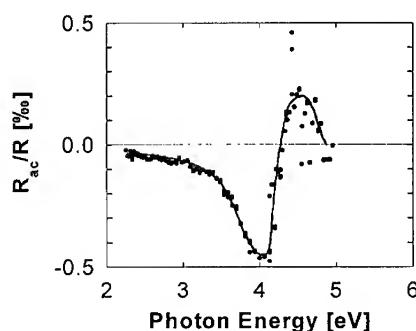


Figure 7. *Photoreflectance spectrum of epitaxial BP, confirming the critical energy of 4.25 eV.*

Figure 6 shows that a decrease in depletion layer thickness causes a decrease in the signal amplitude. Cross-over occurs when the electric surface field changes in sign, i.e., at the flatband potential. The flatband potential is revealed at -1.4 V vs SCE. This is the same value found by CV profiling (Figure 3).

To confirm the EER spectra, photoreflectance spectra have been recorded. The spectrum of Figure 7 is a typical result for both thick and thin epitaxial layers of boron phosphide. The scatter of the laser light into the photomultiplier caused a constant off-set on the AC reflection, and has

been subtracted. In combination with the low intensity of the probing beam at higher energies, the signal to noise ratio is rather poor. Although the photons of the laser beam will be absorbed in both the BP and Si, the latter does not introduce additional features in the spectrum. The reflected light of the probing beam is modulated by changes close to the material surface. The spectrum clearly confirms the existence of a critical energy of 4.25 eV.

## CONCLUSIONS

Both electrolyte electroreflectance and photorefectance spectra of boron phosphide, grown epitaxially on silicon (100) substrates, show a critical energy of 4.25 eV. This direct transition has not been observed before. Since only optical absorption and reflection experiments have been performed on BP, EER and PR data will contribute substantially to the fundamental understanding of the band structure of this unknown III-V semiconductor.

## ACKNOWLEDGMENTS

The TEM-analysis was performed at the National Center for HREM in Delft. This investigation was supported by the Netherlands Foundation for Chemical Research (SON) with financial aid from the Netherlands Organization for Scientific Research (NWO). A.G. wishes to thank the Royal Academy of Arts and Sciences (KNAW) for his fellowship.

## REFERENCES

- 1 Goossens, A, and J. Schoonman, J. Electrochem. Soc. **139**, 893 (1992).
- 2 Archer, R.J., R.Y. Koyama, E.E. Loebner, and R.C. Lucas, Phys. Rev. Lett. **12**, 538-540 (1964).
- 3 Stone, B., and D. Hill, Phys. Rev. Lett. **4**, 282-284, (1960).
- 4 Aspnes, D.E., Surface science **37**, 418-442 (1973).
- 5 See for a recent overview: Schowalter, L.J. (ed.), Material Research Bulletin april 1996, 18-49.
- 6 Fujita, K., and K. Asai, Applied Physics Letters **59** (26), 3458-3460 (1991)
- 7 For a recent report (and overview) see Wentzcovitch, R.M., K.J. Chang, and M.L. Cohen, Phys. Rev. B **34**, 1071-1079 (1986).



# Influence of a silicon cap on SiGe passivation by anodic oxidation

J. Rappich, I. Sieber, A. Schöpke and W. Füssel

Hahn-Meitner Institut, Abteilung Photovoltaik, Rudower Chaussee 5, D-12489 Berlin, Germany

M. Glück and J. Hersener

Daimler-Benz Forschungszentrum Ulm, Wilhelm-Runge-Str. 11, D-89081 Ulm, Germany

## Abstract

We applied electrochemical oxidation as a low thermal budget process for the passivation of thin SiGe epilayers on Si substrate and compared the results with those obtained on thermally oxidized layers. The use of a thin silicon cap on the SiGe layer reduces the electrochemical corrosion with dissolution of Ge during oxidation and leads to a higher amount of  $\text{GeO}_2$  in the oxidized SiGe layer than anodic oxidation without a Si cap. The protected SiGe layer shows a slight Ge enrichment at the interface which is different from the behavior of the non-protected SiGe layer. The highest Ge pile-up is achieved by the thermally oxidized samples where the oxide layer is formed by nearly pure  $\text{SiO}_2$ . Using photoluminescence spectroscopy we showed that the passivation and quality of the interface is best if no Ge enrichment occurs. The results suggest that electrochemical oxidation of SiGe layers is preferable to high temperature processing.

## Introduction

Thermal oxidation of SiGe leads to Ge segregation and enrichment at the oxide/semiconductor interface [1-3]. Therefore a low thermal budget process ( $T < 600^\circ\text{C}$ ) is of great interest for the technology of modern electronic devices like hetero-field-effect transistors which base on SiGe [4]. The Ge pile-up can be suppressed by carrying out the oxidation under high pressure (50-70 bar,  $550^\circ\text{C}$ ) [5], microwave ECR plasma [6], RF plasma [7] or ion beam deposition [8]. We used the anodic oxidation as a low thermal budget process and compared the results with those obtained on thermally oxidized SiGe layers. We investigated the thin oxide layers by Scanning Electron Microscopy (SEM), AUGER-, x-ray photoelectron (XP) and photoluminescence (PL) spectroscopy. Our investigations showed that the electrochemical oxidation without protection of the SiGe leads to no Ge enrichment at the interface. The oxidized samples have a PL signal comparable to the non-oxidized sample which implies good passivation and little damage of the interface.

## Experimental

Epitaxially grown samples of the structure p<sup>+</sup>-Si(100)/50 nm Si-buffer/46 nm Si<sub>0.7</sub>Ge<sub>0.3</sub>/5 nm Si cap were used for our investigations. Table 1 shows the preparation treatments of the samples studied.

Sample	Treatment
A	untreated layer with Si cap
B	dry rapid thermal oxidation at 1050°C, 3 min., with Si cap
C	electrochemical oxidation at +50V with Si cap
D	electrochemical oxidation at +50V without Si cap

Tab.1: Samples investigated in this study.

The electrochemical oxidation was performed in a solution of 0.04 M KNO<sub>3</sub>/ethylene glycol/0.4% H<sub>2</sub>O. These samples were then cleaned in a mixture of HCl-H<sub>2</sub>O<sub>2</sub>-H<sub>2</sub>O and dried at 400°C under nitrogen as applied for pure silicon [9]. Sample D was oxidized after removing the Si cap.

## Results

Fig.1 shows SEM images of samples A, C, D recorded at a 1 degree jewel to stretch the small distances of the different layers. The arrows in fig.1 mark the change of the position of the SiGe/oxide interface and the surface of the sample, respectively.

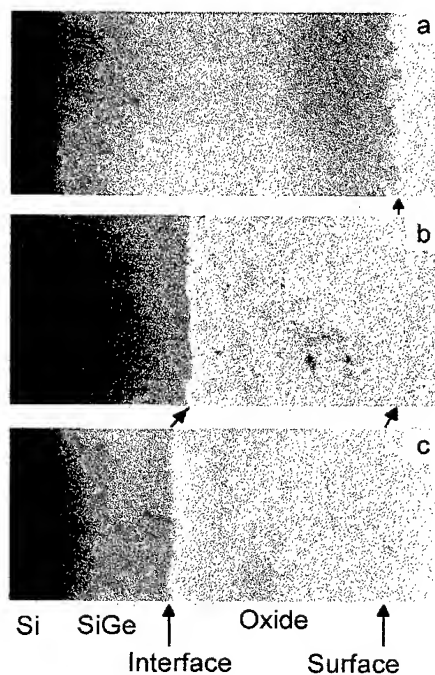
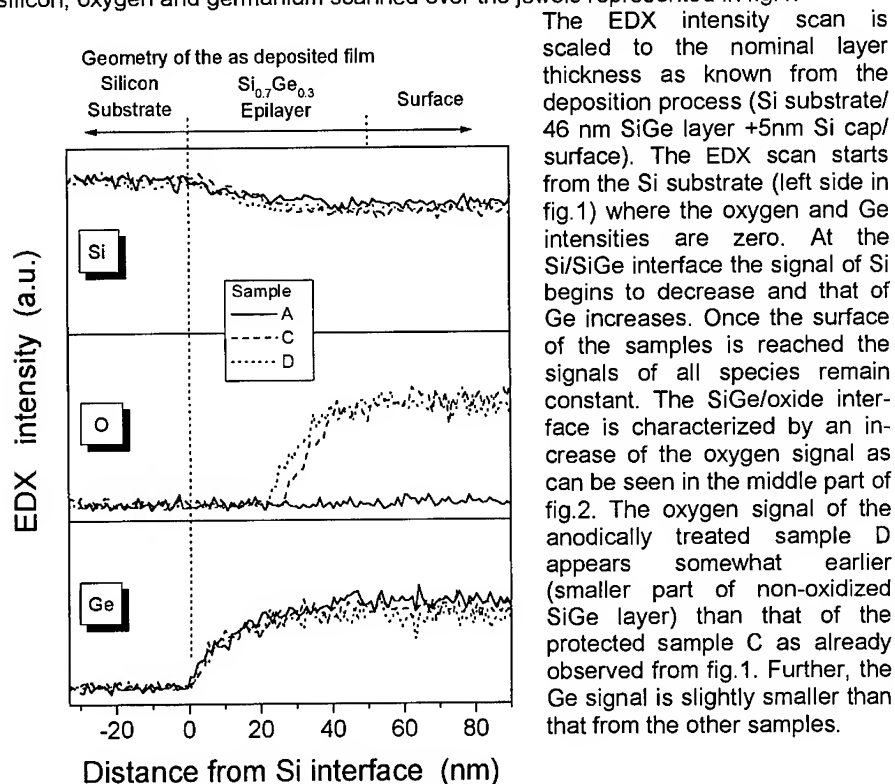


Fig.1 SEM images a,b,c of samples A, C, D (see tab.1), respectively. The photographs are taken at a 1 degree jewel.

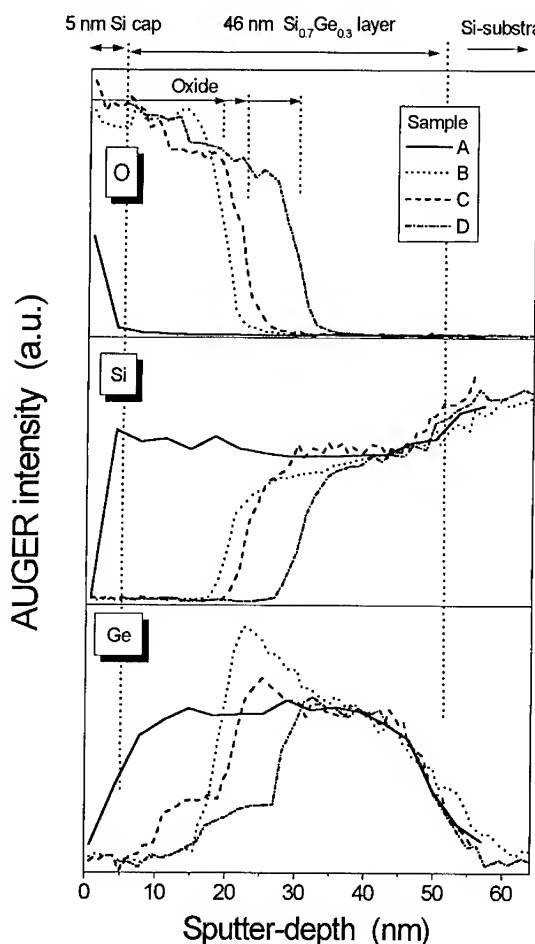
As seen from fig.1, the thickness of the non-oxidized SiGe layer is smaller for sample D (about 20 nm) than for sample C (about 28 nm), fig.1a represents the non-treated layer (46 nm SiGe + 5 nm Si cap). The decreasing thickness of the SiGe layer is accompanied by an increase of the thickness of the oxide. Taking into account that prior to the electrochemical oxidation of sample D the Si cap was removed we get a 3 nm thicker oxide for sample D. This finding points to a greater oxidation rate (about 10-15 %) when the SiGe layer is not protected by a Si cap. Fig.2 shows the EDX intensity of silicon, oxygen and germanium scanned over the jewels represented in fig.1.



The EDX intensity scan is scaled to the nominal layer thickness as known from the deposition process (Si substrate/ 46 nm SiGe layer +5nm Si cap/ surface). The EDX scan starts from the Si substrate (left side in fig.1) where the oxygen and Ge intensities are zero. At the Si/SiGe interface the signal of Si begins to decrease and that of Ge increases. Once the surface of the samples is reached the signals of all species remain constant. The SiGe/oxide interface is characterized by an increase of the oxygen signal as can be seen in the middle part of fig.2. The oxygen signal of the anodically treated sample D appears somewhat earlier (smaller part of non-oxidized SiGe layer) than that of the protected sample C as already observed from fig.1. Further, the Ge signal is slightly smaller than that from the other samples.

Fig.2 EDX intensities of silicon, oxygen and germanium scanned over the jewel represented in fig.1. The EDX intensity scan is scaled to the nominal layer thickness as known from the deposition process. EDX beam: 5 kV.

Ge enrichment cannot be seen neither for the electrochemically nor for the RTO processed samples, obviously due to the high penetration depth of the EDX beam ( $\approx 200$  nm at 5kV compared to the 50 nm layer thickness in our case). For a better resolution of the depth profiling, we applied AUGER spectroscopy after sputtering of small amounts of the layer system. The depth profile of the AUGER intensities of oxygen from  $\text{SiO}_2$ , elementary silicon and of all germanium species of samples A (solid line), B (dotted line), C (dashed line) and D (dash-dotted line) are plotted in figure 3.



The sputter-depth is scaled to the known layer thicknesses including the Si cap (note: The surface of sample D starts with a shift of about 5 nm due to the removed Si cap. This is performed to scale all samples at the Si/SiGe interface.). The oxygen AUGER intensities mark the thickness of the oxide layer, which is similar for the samples B and C. The oxide layer of sample D is slightly thicker (about 4-5 nm) which is in good agreement with the results obtained from the SEM images and EDX scans in figs. 1 and 2, respectively. The AUGER signal of the elementary Si starts to increase up to a constant level in the SiGe epilayer when the oxide/SiGe interface is reached. A second increase can be observed at the SiGe/bulk-Si interface where the Ge content starts to decrease.

Furthermore, the oxygen AUGER intensity of the non-treated sample shows a thin native oxide layer on the Si cap and the Ge distribution is quite homogeneous in the SiGe epilayer. The Ge content differs strongly for the different oxidation treatments.

Fig.3 Depth profile of the AUGER intensities of oxygen from  $\text{SiO}_2$ , elementary silicon and of all germanium species of samples A (solid line), B (dotted line), C (dashed line) and D (dash-dotted line). Note: The surface of sample D starts after removing the part of oxide which corresponds to the oxidized Si cap of about 5 nm).

The RTO processed sample B shows no significant Ge content in the oxide layer but a pile-up at the SiGe/oxide interface and the O-AUGER intensity is nearly constant in the oxide film. The Ge enrichment is suppressed by the electrochemical oxidation procedure for sample D but exists in a reduced manner for sample C. Inside the oxide, the Ge signal increases more slowly and reaches a lower constant value for sample D

(anodized without Si cap). Simultaneously, the O-AUGER intensity decreases slightly in the oxide film. Furthermore, the electrochemical oxidation leads to a significant Ge AUGER signal in the oxide layer. The lower intensity in comparison to the non-treated sample is due to the dilution of Ge in the SiGe layer by the incorporated oxygen. XP spectra of the non-treated and the anodically oxidized samples show the Ge(3d) peak when the Si cap is removed prior to the measurement. The anodized samples, after removing the part of oxide which corresponds to the oxidized Si cap, exhibits the GeO<sub>2</sub> but no Ge(3d) peak. The RTO samples consists mainly of pure SiO<sub>2</sub>. To characterize the interface quality of the oxidized SiGe layers we used the room temperature photoluminescence as plotted in figure 4. In general, the PL intensity of the band-band recombination of the SiGe layer is shifted to lower energy with respect to that of c-Si (upper curve in fig.4) as result of the reduced bandgap energy. All oxidation processes lead to a decrease of the PL intensity probably associated with dislocations, stress by bond angle mismatches or by the formation of dangling bonds. The PL intensity of the sample D (dashed line) is slightly decreased with respect to the non-treated sample A (solid line). The PL intensity of samples B and C is lower and nearly identical (dotted and dash-dotted lines).

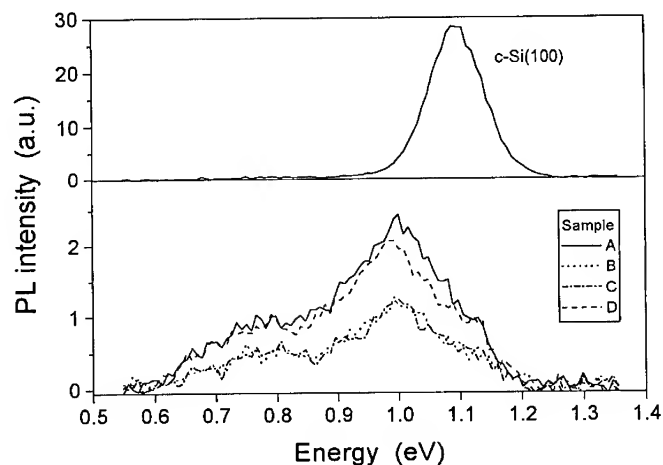


Fig.4 PL spectra of sample A (solid line), B (dotted line), C (dash-dotted line) and D (dashed line).

## Discussion

The SEM photographs, EDX scans and AUGER depth profiles suggest that a Si cap on the SiGe layer protects the Ge in the layer against anodic corrosion and dissolution. On the other hand, the anodically oxidized samples with a Si cap show Ge pile-up at the semiconductor/oxide interface. This is also observed for the thermally oxidized samples though considerably more pronounced. The anodic oxidation of the non-protected SiGe layer indicates some corrosion of Ge atoms in the top layer of about 10 nm thickness of the SiGe epilayer. A barrier of nearly pure SiO<sub>2</sub> is formed

against further corrosion of Ge. The dissolution of corroded Ge leads to a strongly decreased Ge pile-up at the interface due to less displacement of the Ge atoms. Oxygen ions ( $O^{2-}$ ) move from the electrolyte across the oxide to the interface during the oxidation process. The dissolution of Ge atoms opens new pathways for the diffusion of the oxygen ions and the Ge atoms/ions in the SiGe lattice. Obviously, this spatial dilution of Ge suppresses the Ge pile-up at the interface with a tendency to diffuse to the surface. This process may be electric field enhanced due to the positive charging of the interface (anodic oxidation) which could push the positively charged Ge species away from the interface. Furthermore, the Ge enrichment at the interface seems to build-up dislocations which could act as non-radiative recombination centers and decreases the radiative band-band recombination as seen from our PL measurement. The PL signal of the sample which was anodized without Si cap is slightly smaller than that of the non-treated SiGe epilayer, but is considerably higher than the PL spectra of the other oxidized samples. This behavior points to little damage of the oxide/SiGe interface and to better passivation.

## Conclusion

The anodic oxidation of SiGe layers on silicon can be used as a low thermal budget process ( $T < 500\text{ }^{\circ}\text{C}$ ) which reduces or suppresses the Ge enrichment at the interface which is always obtained for thermally oxidized layers. Anodization of non-protected SiGe layers shows no Ge pile-up at the interface and has the highest PL intensity from all oxidized samples in our investigation. Therefore, we conclude that Ge enrichment at the interface leads to a damage of the interface and has to be avoided for good device preparation.

## Acknowledgment

The authors thank Prof. Fuhs and Dr. Lange for critical reading of the manuscript and fruitful discussions, and Dr. Klein for measuring the XP spectra.

## References

1. F.K.LeGoues, R.Rosenberg, T.Nguyen, F.Himpsel and B.S.Meyerson; J. Appl. Phys. **65**(4), 1724 (1989)
2. D.K.Nayak, K.Kamjoo, J.S.Park, J.C.S. Woo and K.L.Wang; Appl. Phys. Lett. **57**, 369 (1990)
3. H.K.Liou, P.Mei, U.Gennser and E.S.Yang; Appl. Phys. Lett. **59**, 1200 (1991)
4. U. König and J. Hersener; Solid State Phenomena **47-48**, 17-32 (1996)
5. C.Caragianis, Y.Shigesato and D.C.Paine; J. Elec. Materials **23**, 883 (1994)
6. P.W.Li, H.K.Liou, E.S.Yang, S.S.Iyer, T.P.Smith and Z.Lu; Appl. Phys. Lett. **60**, 3265 (1992)
7. I.S.Goh, S.Hall, W.Eccleston, J.F.Zhang and K.Warner; Electron. Lett. **30**, 1988 (1994)
8. O. Vancuawenberghe, O.C. Hellman, N.Herbot and W.J.Tan; Appl. Phys. Lett. **59**, 2031 (1991)
9. G.Mende, H.Flietner and M.Deutscher; J. Electrochem. Soc. **140**, 188 (1993)

**Part IV**

**Electrodeposition and Etching of Compound  
Semiconductors and Electrodeposition  
of Metals on Semiconductors**

## CHEMICAL AND ELECTROCHEMICAL HETEROEPITAXIAL GROWTH OF CHALCOGENIDE SEMICONDUCTORS FROM SOLUTIONS

D. LINCOT\*, M. J. FURLONG\*, M. FROMENT\*\*, R. CORTES\*\*, M. C. BERNARD\*\*

\* Laboratoire d'Electrochimie et de Chimie Analytique (U.A. 216 du CNRS), Ecole Nationale Supérieure de Chimie de Paris, 11 rue Pierre et Marie Curie, 75231 Paris, France, lincot@ext.jussieu.fr

\*\*Physique des Liquides et Electrochimie (UPR15 du CNRS), Université Pierre et Marie Curie, 4 place Jussieu, 75232 Paris, France.

### ABSTRACT

Chalcogenide semiconductors have been deposited epitaxially from aqueous solutions either chemically or electrochemically at growth rates of up to  $0.7 \mu\text{mhr}^{-1}$ . After recalling the basic principles of these deposition processes, results are presented concerning chemically deposited CdS on InP, GaP and CuInSe<sub>2</sub> substrates, electrodeposited CdTe on InP, and CdS/InP heterostructures. Characterisation of these structures by RHEED, TEM, HRTEM, and glazing angle X ray diffraction allows to analyse the effects of substrate orientation, polarity, lattice match plus the influence of temperature on epitaxial growth. These results are discussed in terms of self organisation and a site selective growth mechanisms due to the free energy of formation of each compound.

### INTRODUCTION

Growth from aqueous solutions at low temperatures is attracting renewed attention as a versatile route for the preparation of materials for advanced applications. Such processes often take place near thermodynamic equilibrium allowing the remarkable growth of multi-element single crystals and organized structures as found in nature.

The deposition of chalcogenide compounds from chemical reactions between dissolved precursors in solutions, known as chemical bath deposition (CBD) is the liquid phase counterpart to gas phase chemical vapour deposition (CVD). Many sulfides and selenides have been deposited as thin films by CBD [1]. PbS layers are well established as infra-red detectors [2], CdS films are presently used in high efficiency (currently up to 18%) thin film solar cells [3] and are emerging as passivation layers in III-V devices [4]. Chalcogenide thin films may also be grown from the solution phase by electrodeposition (ED) [5], although this route has no equivalent in the vapour phase. Large area thin film solar cells are presently made with electrodeposited CdTe [6]. However, in most cases the deposited films are polycrystalline and the growth of high-quality epitaxial layers has received little attention. For the solution growth of epitaxial films few examples have been reported, i.e. PbS [7], Hg<sub>x</sub>Pb<sub>1-x</sub>S [8], ZnSe [9], CdS [10], and CdSe [11]. For electrodeposition, epitaxial growth has been only recently demonstrated for CdTe [12]. There is therefore a great interest to investigate in more detail these aspects concerning epitaxy from solutions both for basic reasons and for applications as has been recently pointed out [13].

In this paper, results will be presented for the epitaxial growth of CdS and CdTe by chemical and electrochemical routes. They then will be then discussed in the frame of more general considerations concerning the mechanisms of thin film growth.

### EXPERIMENTAL

*Substrates.* (111) and (100) InP single-crystal wafers were supplied by Applications Couches Minces Inc., France. (111) GaP wafers were kindly provided by Professor J. Kelly of the University of Utrecht, Netherlands. Prior to deposition the surface was rinsed in methanol followed by etching in a 1% solution of Br<sub>2</sub>/methanol for 30s and rinsed again. Surface oxides were removed by dipping in sulfuric acid (3 M) for 3 minutes.

*Chemical bath deposition.* CdS thin films were grown chemically in a sealed deposition cell from a freshly prepared solution (typically  $25 \text{ cm}^3$ ). The standard composition was cadmium acetate ( $10^{-3} \text{ M}$ ), ammonium acetate ( $10^{-2} \text{ M}$ ), ammonia (0.4 M), and thiourea ( $5 \times 10^{-3} \text{ M}$ ).



Samples were mounted on glass supports and immersed in the reaction mixture at room temperature, which was then heated to 85°C.

**Electrodeposition.** The deposition solution contained cadmium sulfate (1 M) and tellurium dioxide ( $5 \times 10^{-4}$  M) at pH=2 and 85°C. The pH of the acidified stock solutions were adjusted with potassium hydroxide. A pre-electrolysis of the cadmium sulfate solution was performed for purification [12]. N-type single crystal substrates (InP, InP/CdS) were back contacted by Ga-In eutectic and an active area of  $0.3 \text{ cm}^2$  was isolated using silicone rubber. The deposition potential was fixed over the range +5 mV to +50 mV with respect to the Cd/Cd<sup>2+</sup> reference potential in the same solution (-0.40 V vs SHE). Growth rate were about  $0.7 \text{ } \mu\text{mhr}^{-1}$

**Characterisation.** Film structure was characterised by reflection high energy electron diffraction (RHEED), transmission electron microscopy (TEM), high resolution TEM (HRTEM), and glazing angle X-ray diffraction using a five-circle goniometer specially designed for thin film studies. Full details of these methods have been given elsewhere [14].

## PRINCIPLES

### Chemical bath deposition of chalcogenides

For the equilibrium

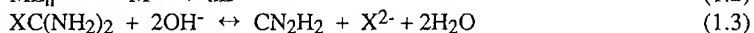


the precipitation of chalcogenide compounds such as MX (where M is a bivalent metal and X= S,Se,Te) occurs when the ionic product IP =  $[\text{M}^{2+}][\text{X}^{2-}]$  exceeds the solubility product  $K_s$ . Table 1 shows that the solubility products of chalcogenides are very low, indicating that precipitation takes place for a low concentration of free ions.

Compound	$\Delta G_f^\circ$ kJmol <sup>-1</sup>	$-\log K_s$	$-\Delta G_f^\circ/nF$ Volts	$E_0(\text{M}/\text{M}^{n+})$ V/SHE	$E_0(\text{MX})$ V/SHE	$E_0(\text{X}^{4+}/\text{X})$ V/SHE
CdTe	-98.4	42	0.5	-0.4	0.1	0.55
CdSe	-100.4	33.5	0.52	"	0.12	0.74
CdS	-140	24	0.73	"	0.33	0.45
ZnTe	-117.7	32	0.61	-0.76	-0.15	0.55
ZnSe	-137	31	0.71	"	-0.05	0.74
ZnS(cub.)	-193	27.5	1	"	0.24	0.45

Table I: Thermodynamic data for selected chalcogenide semiconductors at pH=0

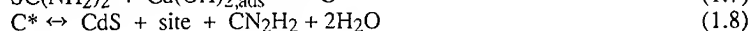
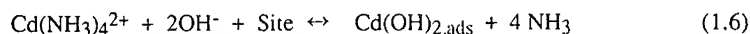
To ensure controlled growth from solution it is necessary to use complex ions or hydrolysable molecules such as thiourea (for CdS) and selenourea (for CdSe) that act as masking agents. The precipitation reaction is then controlled by three chemical reactions:



This series, known collectively as the dissociation mechanism, is generally presented to describe the deposition of various chalcogenides [1]. The advantage is clearly to illustrate the effect of changing the solution composition on the growth kinetics, for example the growth rate decreases by increasing or decreasing the concentrations of L or OH<sup>-</sup>, respectively. This enables the adjustment of IP close to  $K_s$ . For CdS deposition from ammonia-thiourea-cadmium solutions, according to the following reaction,



a further site-specific mechanism has recently been proposed [15] based on consecutive surface mediated steps :



This involves the formation of a surface intermediate species  $\text{C}^*$ . The growth is associated with an atom by atom mechanism which accounts quantitatively for experimental growth rates in conditions where bulk precipitation (homogeneous process) does not take place. In this case growth proceeds via the aggregation of colloids at the substrate surface. Figure 1 shows an example of the transition between the two mechanisms brought about by a change in the concentration of ammonia [15]. The boundary line corresponds to the bulk precipitation of cadmium hydroxide which is transformed into CdS according to reaction 1.7. Similar behavior has been observed for chemically grown CdSe layers [16].

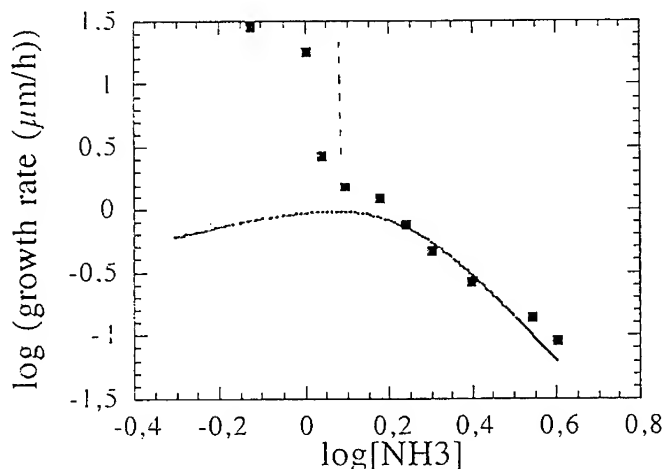
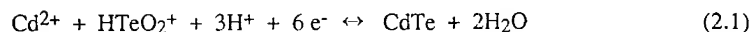


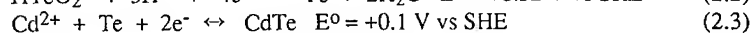
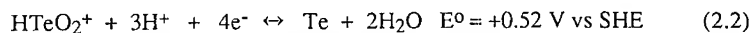
Figure 1: Influence of the ammonia concentration on the growth rate of CdS showing the transition between the atom by atom and colloidal growth modes. The solid line represents the calculated results. Conditions:  $[\text{CdSO}_4] = 0.014\text{ M}$ ,  $[\text{thiourea}] = 0.028\text{ M}$ ,  $T = 60^\circ\text{C}$ .

#### Electrodeposition of chalcogenide semiconductors.

The most popular method to grow selenide and telluride films is based on the use of chalcogenide precursors in the X(IV) oxidized state as the dissolved oxide  $\text{XO}_2$  in aqueous acidic solutions. The overall reaction for the electrochemical formation of CdTe is:



which can be expressed as two elementary reactions :



Since the deposition potential for CdTe is lower than that of elemental tellurium (table 1), reaction (2.1) corresponds to the thermodynamic formation of CdTe. The associated standard potential is more positive than that of elemental cadmium ( $\text{Cd}^{2+} + 2\text{e}^- \leftrightarrow \text{Cd}$ ,  $E^0 = -0.4\text{ V vs SHE}$ ) due to the effect of the free energy of formation of CdTe [17]. Figure 2 shows the theoretical shape of the

voltammogram assuming that the reduction of tellurium via reaction 2.2 is under diffusion control and that  $[Cd^{2+}] \gg [Te(IV)]$ . Compared with chemical deposition, no spontaneous phase formation can take place in the solution and deposition proceeds basically by an atom by atom mechanism.

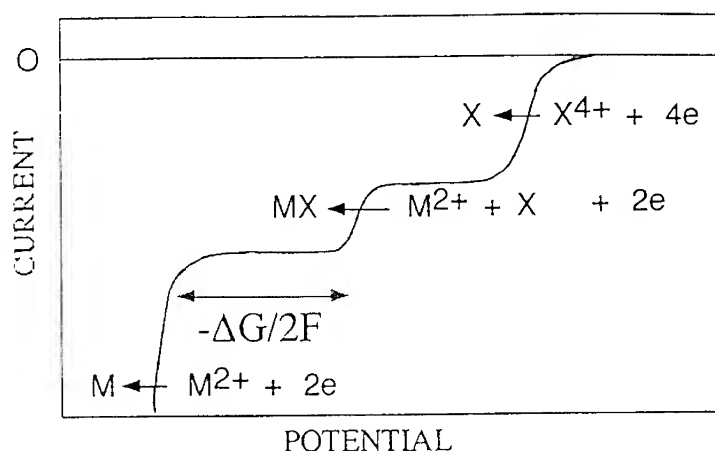


Figure 2: Theoretical I-V curve for the electrodeposition of CdTe with  $[Cd^{2+}] \gg [Te(IV)]$  in acidic solutions showing the effect of the free energy of formation of CdTe

## RESULTS

### Epitaxial growth of CdS films by CBD

Basic solutions containing cadmium ions and thiourea provide a wide range of conditions where the atom by atom growth mechanism is observed [15]. The use of single crystal substrates enables us to study in detail the conditions where epitaxial films are formed. Cadmium sulfide may form two crystallographic structures, one that is hexagonal ( $a = 0.413 \text{ nm}$ ,  $c = 0.671 \text{ nm}$ ) and the other fcc cubic ( $a = 0.582 \text{ nm}$ ). The hexagonal structure is slightly more stable than the cubic form. This explains why polycrystalline films grown by CBD can be hexagonal, cubic, or a mixture of the two [18].

The growth of CdS on InP illustrates the case where there is almost a perfect lattice match ( $\approx 0.3\%$ ). InP possesses the cubic fcc structure with  $a = 0.587 \text{ nm}$ , and the (111) face has a surface crystallographic structure identical to the (111) or (0002) planes of CdS. Epitaxial growth of CdS with the hexagonal structure is easily obtained on this substrate but only at the phosphorus terminated ( $\bar{1}\bar{1}\bar{1}$ ) surface [14]. On the In face only polycrystalline films are obtained. This indicates the important influence of surface chemical interactions during the initial stages of growth between atoms in the growing film and those at the polar InP faces. The stronger reactivity of this face may be related to the formation of P-Cd or In-S bonds by sulfide-phosphorus substitutions. Such chemical exchange reactions are known when InP surfaces are dipped in ammonium sulfide solutions. Recently reactions between thiourea and InP have been reported [4]. It can be mentioned that in the case of CdSe epitaxial growth on both (111) InP faces has been demonstrated.

The great significance of surface properties in governing the epitaxial growth is confirmed by the effect of substrate etching. In the absence of such chemical pre-treatments only polycrystalline growth is observed. One can indicate that ammonia is also an efficient etching agent for InP, enabling the removal of surface oxide layers. This leads to in-situ etching prior to the onset of film growth and may explain why epitaxial quality is improved when the sample is introduced in the solution at room temperature.

Using (100) InP allows to illustrate the effect of substrate orientation [19]. Figure 3 shows the glazing X ray diffraction (XRD) pattern for a 80 nm layer of CdS grown according to the standard method. The growth of CdS is epitaxial. The low value of the full width at half maximum (FWHM) of the (111) reflection peaks in CdS ( $0.6^\circ$  as compared to  $0.25^\circ$  for the InP substrate) and the low base line level demonstrates a good epitaxial quality. It is important to note that contrary to (111) substrates, the growth direction of CdS does not coincide with the preferred texture direction of CdS which is  $\langle 111 \rangle$  or  $\langle 0002 \rangle$ . The epilayer exhibits the cubic structure. This is explained by the fact that epitaxial matching on the (100) face is not possible for the hexagonal structure as it does not possess this plane. Thus, surface matching promotes the growth of the metastable form of CdS.

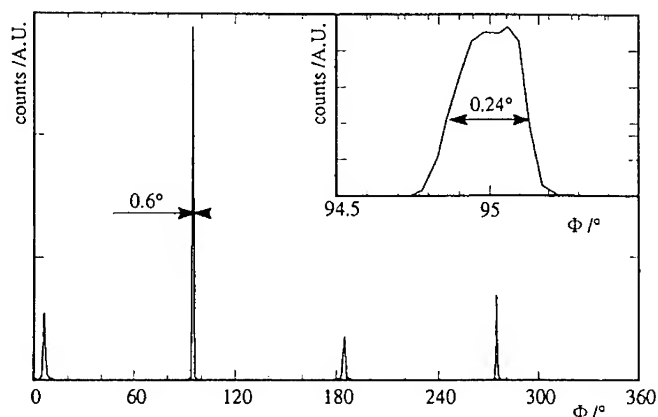


Figure 3: Glazing angle XRD diagrams of epitaxial CdS on InP (100) and InP (100) (Inset). The scans were obtained around an axis perpendicular to the surface. Glazing angles were  $0.6^\circ$  for CdS and  $6^\circ$  for InP.

Lattice mismatch is a very important parameter for heteroepitaxial growth. It is generally assumed that below a certain value ( $<10\%$ ) the mismatch can be accommodated in the epilayer. To test these effects in the case of CdS we have used  $(\bar{1}\bar{1}\bar{1})$  GaP substrates. GaP has a cubic fcc structure with  $a = 0.545$  nm. This leads to a 7% mismatch with CdS. By depositing CdS films on the P-face of GaP (which presents an identical chemical environment to the P-face of InP), we can assess the influence of the lattice parameter on epitaxy. Epitaxial films were formed which present both cubic and hexagonal phases in equivalent proportions. Cross sections observed by TEM reveals the presence of a polytype CdS structure [20]. This may be a consequence of the large lattice mismatch between the layers. The important conclusion is that CBD allows heteroepitaxy on large mismatched substrates.

In the above studies, the study of substrate effects on epitaxial growth has been made by maintaining the same "standard" deposition conditions for CdS (bath composition and temperature). However, it is evident that within the domain of the atom by atom growth mechanism the quality of the epitaxy should depends strongly on the deposition conditions at the solution side. Composition effects have been shown in [14] and are currently under investigation. In this work we will present the influence of temperature on the epitaxial growth of CdS on monocrystalline CuInSe<sub>2</sub> layers [21].

Figure 4 (a) shows the growth curve at  $85^\circ\text{C}$ . From the linear region a constant growth rate is determined. The influence of temperature on the growth rate is represented by an Arrhenius plot in figure 4 (b). The rate increases markedly with temperature with an activation energy of about  $85\text{ kJmol}^{-1}$ . This value is close to that determined for the formation of polycrystalline films grown under similar conditions [15] and indicates kinetic control, probably through reactions 1.7 or 1.8. RHEED experiments performed on a series of samples have revealed a transition temperature between polycrystalline and epitaxial growth close to  $70^\circ\text{C}$  under these conditions. For instance,

figures 4 (c) and 4 (d) show RHEED patterns obtained at 55°C (growth rate  $0.02 \mu\text{mhr}^{-1}$ ) and 93°C (growth rate  $0.6 \mu\text{mhr}^{-1}$ ). It is interesting to note that the improvement takes place despite that the growth rate is much higher. Under the standard solution composition, a temperature range between 75°C and 90°C is suitable for epitaxial growth.

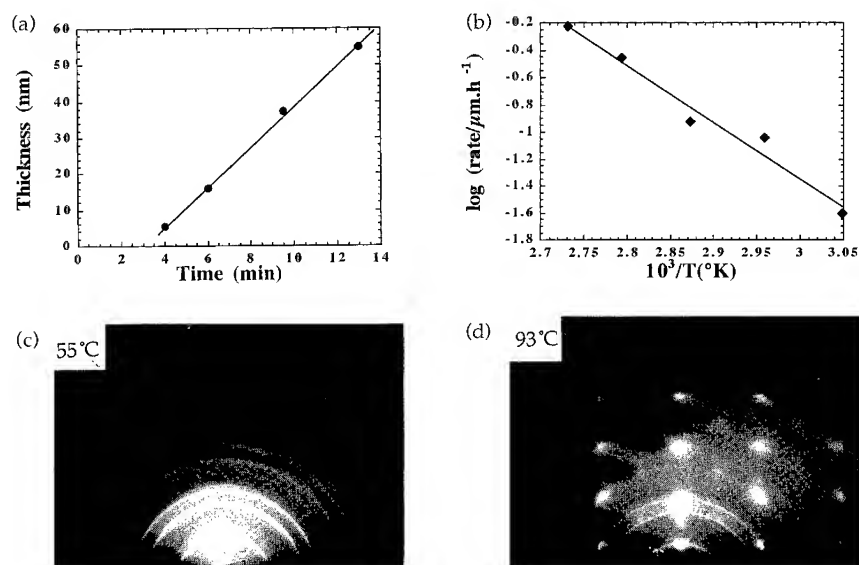


Figure 4: Effect of temperature on the epitaxial growth of CdS on CuInSe<sub>2</sub>. (a) growth curve at 85°C. (b) Arrhenius plot. (c) and (d) RHEED patterns along the  $[11\bar{2}]$  azimuth for films grown at 55°C and 93°C, respectively.

#### Epitaxial growth of CdTe by electrodeposition.

In contrary to the chemical bath route, growth of epitaxial thin films by one step electrodeposition has only been demonstrated recently for CdTe [12] and CdSe [22]. Using polycrystalline substrates we have previously observed that a potential domain exists that is close and positive to the cadmium reversible deposition potential where highly textured films can be grown [23]. Film growth was also found to be substrate dependent with the best results obtained on CdS as compared with sensitized tin oxide [24]. This led us to select the same deposition parameters for studies with single crystal substrates. CdTe presents the fcc structure with  $a = 0.649 \text{ nm}$ . A large lattice mismatch ( $\approx 9.5\%$ ) exists with InP or CdS.

RHEED patterns obtained for CdTe layers deposited on  $(\bar{1}\bar{1}\bar{1})$  InP and  $(\bar{1}\bar{1}\bar{1})$  InP covered by CBD CdS indicate that epitaxy takes place on these substrates despite the larger lattice mismatch [12]. However, in the case of bare InP, an important contribution of textured polycrystalline CdS is superimposed. Using CdS covered InP dramatically improves the epitaxial quality as confirmed by glazing-angle XRD patterns shown in figure 5.

Single crystal InP shows three fold symmetry around the  $\langle 111 \rangle$  direction. The detection of CdTe peaks proves the epitaxial relationship with the substrate. The low base line level relative to the peak height is a quantitative indication that the proportion of polycrystalline CdTe is very low. The presence of six peaks instead of the three expected is due to twinning in the layer, also observed in the RHEED patterns. Twinning is frequently observed in epilayers due to the fact that two

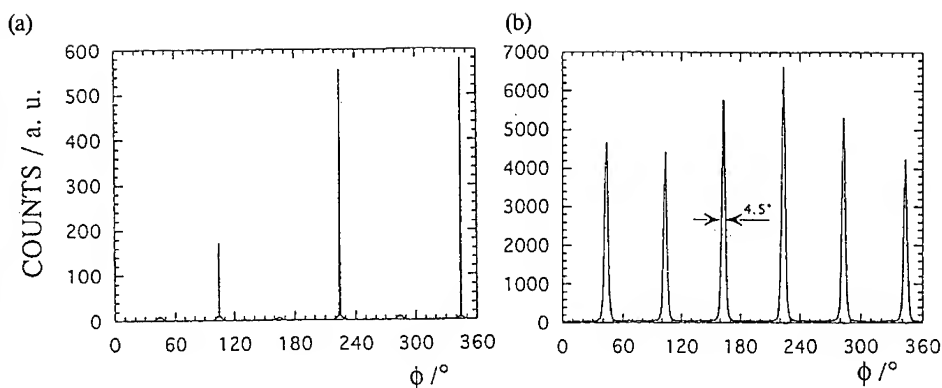


Figure 5: Glazing angle XRD diagrams of an epitaxial (111) CdTe film on (a) InP ( $\bar{1}\bar{1}\bar{1}$ ) and (b) CdS/InP ( $\bar{1}\bar{1}\bar{1}$ ) substrates.

equivalent possibilities exist for the relative position of the layer and the substrate (multipositioning). The FWHM of  $4.5^\circ$  indicates the presence of small angle grain boundaries in CdTe. This may be related to a rather low quality CdS layer which also presents also a rather large FWHM.

The structure of the layers have been studied by TEM and high resolution TEM (HRTEM) both in the plane and in cross section. Figure 6 shows in plane views, together with the corresponding diffraction diagrams (insets) for CdTe grown (a) directly on InP and (b) on InP/CdS. For the layer grown on InP the ring pattern confirms the textured growth. However the reinforcements around specific points still indicate preferential orientation with respect to the substrate. In the presence of CdS the dot pattern confirms the epitaxial growth. HRTEM views enable us to investigate film structure in more detail as shown in figures 6(c) and (d). Low angle grain boundaries, with a few degrees of misorientation, can be observed in the CdTe epilayer, in agreement with the value of the FWHM. For the textured layer, much larger misorientations are observed.

Figure 7 shows a cross section of the whole heterostructure CdTe/CdS/InP. At low magnification (a) all the three layers are observed. We see that the CdTe surface is faceted and that the corresponding pyramids are at the top of vertical columns, which probably correspond to the individual domains observed with in plane observations. It appears that the columns find their origin in the CdS itself. This indicates that the CdS growth proceeds via the formation and coalescence of 2D growth centers in epitaxial relationship with the substrate but which form, in the present case, slight misorientations with respect to one another. The size of these domains is about 30 nm. HRTEM observations (b) demonstrate the epitaxial relations over the whole structure by the prolongation of atomic rows associated with the (111) planes. The presence of sub-domains in CdTe is seen but without changes in the crystallographic direction. The continuation in CdS indicates that in this case it exhibits the cubic structure. The interface between CdTe and CdS is hardly visible. In some places it seems that the growth starts with a large number of stacking faults parallel to the substrate as is found for CdS on GaP, whereas over other regions the quality is much improved. It is important to note that no significant degradation of the epitaxial quality with the thickness of the CdTe layer has been observed. Layers of up to  $0.5\ \mu\text{m}$  have been characterised by RHEED. Preliminary studies on the effect of potential have been performed for values up to 50 mV more positive than the cadmium deposition potential. No significant degradation of the epitaxial quality is observed by RHEED on  $0.2\ \mu\text{m}$  thick films indicating that the potential window for deposition is rather large. Concerning the effect of temperature, studies are in progress. It is well documented that increasing the temperature increases the structural quality of polycrystalline CdTe layers. Similar trends are observed for epitaxial films.

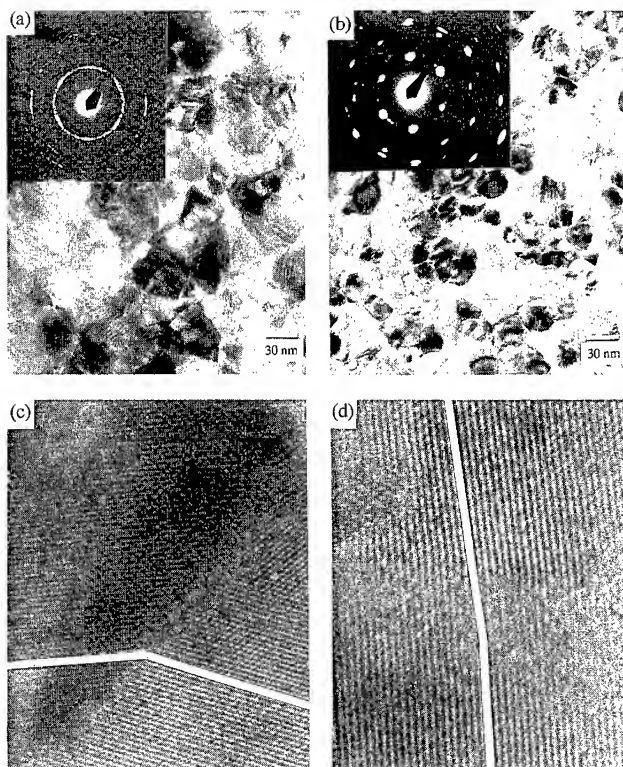


Figure 6: TEM and HRTEM in-plane views of electrodeposited CdTe films (a, c) directly on InP ( $\bar{1}\bar{1}\bar{1}$ ) and (b, d) on InP ( $\bar{1}\bar{1}\bar{1}$ ) covered with a CdS epitaxial layer. Insets: electron diffraction patterns.

## DISCUSSION

The results presented show that the epitaxial growth of thin chalcogenide films can be achieved directly from aqueous solutions, but depends critically on the precise control of experimental conditions. These conditions can be divided into two groups, one related to substrate effects and the second to the growth mechanism.

Substrate effects are mainly related to the level of surface quality. It must be structurally clean which points to the importance of proper etching procedures. In situ etching has been suggested as a very positive parameter in chemical bath deposition growth. Lattice matching does not seem to be as crucial since epitaxial growth has been obtained even when a large lattice mismatch exists (CdS on GaP, CdTe on CdS). On the contrary, the chemical reactivity between the substrate and the growing layer seems to be of great importance. The formation of strong surface bonds is well known to favor the epitaxial growth according to a layer by layer growth mode.

We now consider in more detail the conditions relating to the growth mechanism. The driving force for the self organization of multielement compounds is the free energy of formation  $\Delta G^0$ :



The more negative  $\Delta G^0$ , the more selective will be the compound formation with respect to secondary reactions. In table 1 thermodynamic data for important chalcogenide semiconductors are

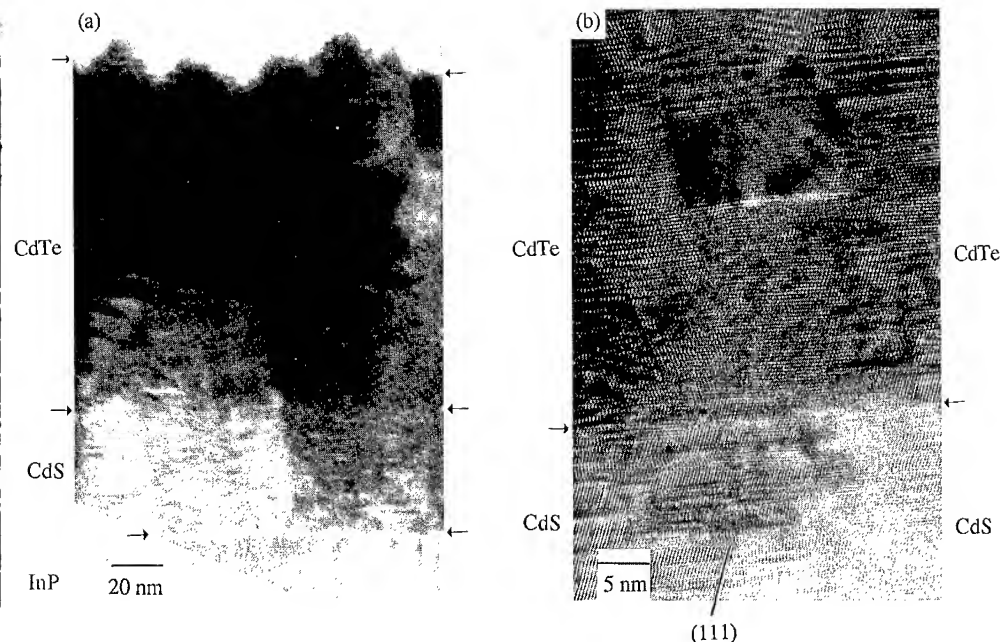


Figure 7: (a) TEM and (b) HRTEM cross section views of an electrodeposited epitaxial film of CdTe on CdS/InP.

presented. In chemical deposition and electrodeposition,  $\Delta G^0$  directly influences the solubility product and underpotential deposition, respectively.

In chemical bath deposition, the precipitation equilibrium has to be considered:



with  $K_S = [M^{2+}][X^{2-}] = \exp(\Delta G^0/RT) K_0$ . For CdS the term containing the free energy of formation  $\exp(\Delta G^0/RT)$  is about  $10^{-25}$  and is responsible for the low value of the solubility product.

For the electrodeposition of CdTe and parent MX compounds (listed in table 1), the standard potential of the main electrochemical reaction (2.3)



is given by  $E_{MX} = E_M - \Delta G^0/2F$  where  $F$  is the Faraday constant. As a consequence, the formation of the compound is displaced anodically by the amount  $-\Delta G^0/2F$  which is close to + 0.5 V for CdTe. This defines a potential domain where cadmium is selectively deposited on tellurium to form the compound (underpotential deposition) as shown in figure 2.

In chemical bath deposition, the growth of the compound corresponds to alternate deposition of one element on the other under  $\Delta G^0$  control through steps (1),(2) and (3). Due to the ionic nature of the precursors, repulsive electrostatic forces prevent the uptake of one element on the same element via steps (4) and (5). This means that a great site selectivity exists for an atom by atom mechanism. For the growth of CdS by CBD from non ionic precursors, adsorbed intermediates have to be considered as shown in reactions 1.6 to 1.8. Under non-optimized conditions, decomposition of these species may be incomplete leading to inclusions in the layer and a degradation of the epitaxy. This explains the presence of cadmium hydroxide and carbon-nitrogen species frequently reported in polycrystalline CBD CdS films [25]. High temperature is likely to enhance the decomposition steps, explaining the improvements obtained in film quality.



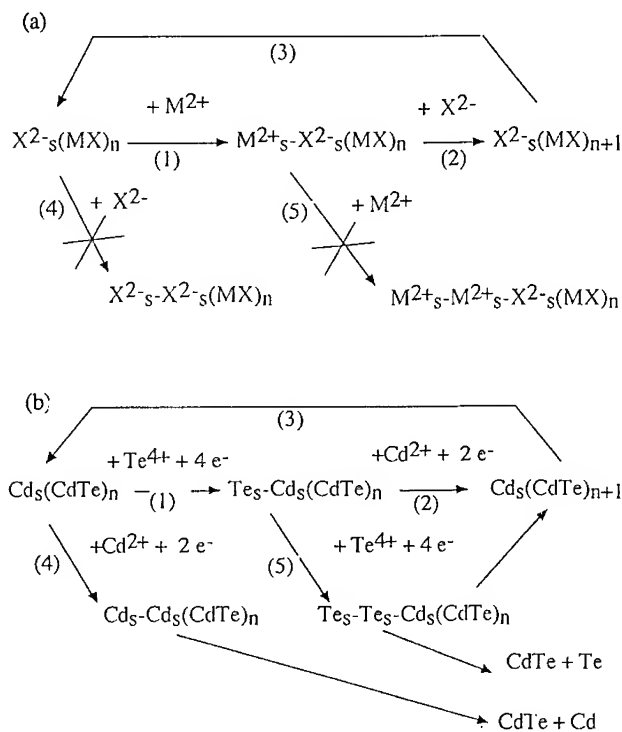


Figure 8: Reaction schemes for (a) chemical bath deposition (b) and electrodeposition of binary chalcogenides illustrating the site selective growth mechanism for epitaxial growth.

Similar trends have been reported for other solution and vapour phase growth processes.

For electrodeposition a similar scheme can be established. Steps (1), (2) and (3) represent the alternate deposition of one element on the other leading to stoichiometric compound formation.

Contrary to the previous scheme, only step (2) is under full  $\Delta G$  control and induces site selectivity. The deposition of tellurium is not under site selectivity since reaction (5) is also possible in parallel. This is because the deposition potential of elemental tellurium is higher than that of CdTe. The combination of steps (1),(2),(3) and (5) leads to the formation of tellurium rich CdTe. As tellurium has a very low solubility in CdTe, a tellurium excess will create inclusions interrupting the epitaxial growth of CdTe. As a consequence the achievement of epitaxial growth for CdTe imposes a precise control of the stoichiometry and thus a reduction in the rate of step (5). This is achieved by two means. Firstly, by using a much higher concentration of cadmium in the solution than tellurium, with ratios up to 1000 in some cases, thus leading to a relative increase in the rate of reaction (2). The second approach is to use more negative deposition potentials leading to an increase the rate of reaction (2) through the potential dependence of the rate constant, whereas the rate of reaction (5) is not modified since this reaction is under tellurium diffusion control. Competitive adsorption between  $\text{Te(IV)}$  and  $\text{Cd(II)}$  ions may also play a role [26]. The extension of the deposition potential is limited by the onset of reaction (4), corresponding to the deposition of elemental cadmium. As for tellurium, cadmium has a low solubility in CdTe and inclusion will be formed which tend to arrest epitaxial growth. These phenomena should be valid for polycrystalline growth, leading to a decrease in the grain size with the presence of inclusions. Figure 9 shows the effect of the deposition potential on the crystallinity and the composition of a CdTe film electrodeposited onto tin oxide coated glass which supports our arguments [23].

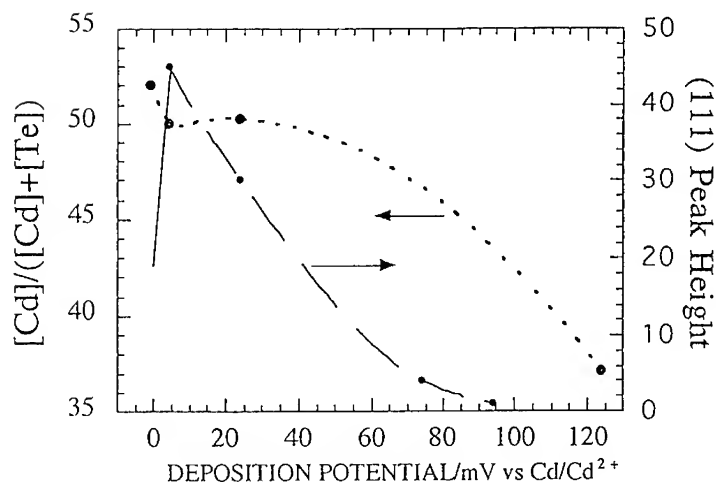


Figure 9: Relations between the crystalline quality and composition of electrodeposited CdTe on tin oxide substrates as a function of the applied potential. Data taken from [23].

The optimum crystallinity is obtained over a narrow range which coincides with the stoichiometric range, and is close to the deposition potential for cadmium. However, our results show that epitaxy is still observed at +50 mV indicating that the stoichiometric range is extended towards positive values as compared to the deposition on tin oxide. This indicates that the substrate has probably an influence on the stoichiometry as has been previously shown [24]. Theoretically, the stoichiometric range of CdTe films can be predicted by modeling the deposition mechanism on a thermodynamic basis [27].

## CONCLUSION

In this paper we have shown, by the examples of CdS and CdTe that chemical bath deposition and electrodeposition provide efficient routes for preparing epitaxial chalcogenide films at low temperature. The formation of epitaxial films has been discussed in a more general way in terms of growth mechanisms. CBD, which is directly derived from the concepts of heterogeneous precipitation, can more easily satisfy the conditions for epitaxy (atom by atom mechanism and great site selectivity). In the case of electrodeposition the existence of parallel electrochemical deposition reactions introduces some difficulties. These can be overcome by proper control of the electrodeposition conditions (precursor concentration, potential, temperature). Under optimal conditions the stoichiometric composition of the films is self-regulated by the sequential growth process resulting from the large free energy of formation of the compounds. A great margin exists to further improve these solution routes for heteroepitaxial growth of various chalcogenide semiconductors.

## ACKNOWLEDGEMENTS

One of us (M.J.F.) wishes to thank the Royal Society for a European Postdoctoral Fellowship Award. The European Union and ADEME/ECOTECH in France are acknowledged for financial support in research programs for photovoltaics.

## REFERENCES

1. K. L. Chopra, R.C. Kainthla, D. K. Pandya and A. P. Thakoor, *Phys. Thin Films* **12**, 167 (1982) and references therein.
2. J. Bloem, *Appl. Sci. Res. B* **6**, 92 (1956).
3. L. Stolt, J. Hedström, J. Kessler, M. Ruckh, K. O. Velthaus and H.W. Schock, *Appl. Phys. Lett.* **62**, 597 (1993).
4. K. Vaccaro, H. M. Dauplaise, A. Davis, S. M. Spaziani and J. P. Lorenzo, *Appl. Phys. Lett.* **67**, 527 (1995).
5. G. Hodes, Electrodeposition of II-VI Semiconductors, *Physical Electrochemistry*, edited by I. Rubinstein (M. Dekker Inc, New York, 1995), p. 515.
6. A. K. Turner, J. M. Woodcock, E. Özsan and J. G. Summers in *Proceedings of the 10th European Solar Energy Conference* (Harwood ed., 1991), p. 791.
7. M. Isshiki, T. Endo, K. Masumoto and Y. Usui, *J. Electrochem. Soc.* **137**, 2697 (1990).
8. N.C. Sharma, D. K. Pandhya, H. K. Sehgal and K. L. Chopra, *Thin Solid Films* **59**, 157 (1979).
9. G. N. Chaudary, S. N. Sardesai, S. D. Sathaye and V. J. Rao, *J. Mat. Sci.* **27**, 4647 (1992).
10. D. Lincot, R. Ortega-Borges, M. Froment, *Appl. Phys. Lett.* **64**, 569 (1994).
11. H. Cachet, R. Cortès, M. Froment, G. Maurin, N. Shramchenko, 190th Meeting of the Electrochem. Soc., (1995), in press.
12. D. Lincot, A. Kampmann, B. Mokili, J. Vedel, R. Cortès and M. Froment, *Appl. Phys. Lett.* **67**, 2355 (1995).
13. F. F. Lange, *Science* **273**, 903 (1996).
14. M. Froment, M. C. Bernard, R. Cortes, B. Mokili and D. Lincot, *J. Electrochem. Soc.* **142**, 2642 (1995).
15. R. Ortega-Borges and D. Lincot, *J. Electrochem. Soc.* **140**, 3464 (1993).
16. S. Gorér and G. Hodes, *J. Phys. Chem.* **98**, 5338 (1994).
17. F. A. Kröger, *J. Electrochem. Soc.* **125**, 2028 (1978).
18. I. Kaur, D. K. Pandya and K. L. Chopra, *ibid* **127**, 943 (1980).
19. R. Cortès, M. Froment, B. Mokili and D. Lincot, *Phil. Mag. Lett.* **73**, 209 (1996).
20. D. Lincot, B. Mokili, M. Froment., R. Cortès and M. C. Bernard, *Microscopy, Microstructures and Microanalyses* (1996), in press.
21. D. Lincot, M. J. Furlong, M. Froment, M. C. Bernard, R. Cortes, A. N. Tiwari, M. Krejci, H. Zogg in, *Proceedings of the 9th Photovoltaic Science and Engineering Conference*, Japan (1996), in press.
22. H. Cachet, G. Maurin, R. Cortès, and M. Froment, in preparation.
23. P. Cowache, D. Lincot and J. Vedel, *J. Electrochem. Soc.* **136**, 1646 (1989).
24. A. Kampmann, P. Cowache, B. Mokili, J. Vedel and D. Lincot, *J. Electroanal. Chem.* **387**, 53 (1995).
25. N. D. Betenkov, V. P. Medvedev and G. A. Kitaev, *Soviet Radiochem.* **20**, 369 (1978).
26. C. Sella, P. Boncorps and J. Vedel, *J. Electrochem. Soc.* **133**, 2043 (1986).
27. R. D. Engelken and T. P. Van Doren, *ibid* **132**, 2910 (1985).

### Thin Layer Electrochemical Studies of ZnS, ZnSe, and ZnTe Formation by Electrochemical Atomic Layer Epitaxy (ECALE)

Lisa P. Colletti, Sajan Thomas, Elvin M. Wilmer, and John L. Stickney\*  
Department of Chemistry, University of Georgia, Athens, Ga. 30602

#### Abstract

Thin-layer electrochemical studies of the underpotential deposition (UPD) of Zn, Te, Se, and S on polycrystalline Au substrates have been performed. These studies were initiated to investigate the electrodeposition of ZnTe, ZnSe, and ZnS by electrochemical ALE (ECALE). Zn UPD on Au begins at -0.5 V and results in a coverage of 0.47 monolayer (ML). Te and Se atomic layers were formed using a two step process where bulk chalcogenide was removed by reduction, leaving the atomic layer. The reduction of the last atomic layer of Te or Se was not observed, regardless of how negative the potential was scanned. Sulfur atomic layers were spontaneously deposited below -0.6 V from a sulfide solution. Thermodynamic effects are clearly evident during the first monolayer of deposition. Zinc deposition onto Te, Se, and S coated electrodes occurs at progressively more positive potentials as the stability of the zinc compounds increase.

This initial information was used to develop ECALE cycles for the compounds, and thin-films were formed by repeated application of the cycles. The dependence of the deposit coverage on the deposition potentials was examined and found to display the characteristic "S" curve of a surface limited process. In addition, the dependence of the coverage on the number of ECALE cycles performed was found to be near the ideal 0.5 ML per cycle for ZnSe and ZnS. The ZnTe coverage per cycle was less than expected indicating that further optimization of deposition conditions is needed.

#### Introduction

Compound semiconductor thin-film formation via electrodeposition may some day prove to be a simple, cost effective method relative to chemical vapor deposition (CVD) or molecular beam epitaxy (MBE). Possible advantages of an electrochemical deposition technique include deposition at or near equilibrium, a low deposition temperature, and the ability to deposit uniform films on large and irregularly shaped objects. In addition, environmental concerns over toxic organometallic chemicals are eliminated or reduced with the use of dilute aqueous solutions of ionic reactants [1]. A significant number of electrodeposition studies of II-VI compound semiconductors have been performed previously, primarily involving formation of the Cd based compounds, given their applicability to solar energy conversion. However, interest in zinc based II-VI compounds is increasing due to their use in phosphors, thin-film electroluminescent displays [2], and emerging optoelectronic technologies [3,4]. ZnSe, in particular, is being extensively studied due to applications such as solid state blue lasers and blue light emitting diodes [4].

Electrodeposition of the zinc based II-VI compounds has predominantly involved aqueous codeposition techniques to form zinc telluride [5], zinc selenide [6-14], and zinc sulfide [15-17] thin-films. X-ray diffraction (XRD) analysis [12,14-16] has shown the electrodeposited zinc chalcogenide films to be polycrystalline, while scanning electron microscopy (SEM) has shown discontinuous [16] or grainy films [5,12,15,17]. So far, only one study of ZnTe codeposition appears to have been reported [5]. Those were able to find conditions from which stoichiometric films could be formed; however, annealing was required to improve the optical properties of the film. Of the many ZnSe studies, two [12,14] have involved characterization of their films using techniques other than photoelectrochemistry. Natarajan et al. [12] concluded that an excess of Se in the films was unavoidable due to the complicated chemistry of Se. Vacuum annealing was required to produce stoichiometric ZnSe films. In contrast, Ohno et al. [14] found deposition conditions which formed stoichiometric ZnSe without annealing. For ZnS films, only Sanders and Kitai [16] determined the elemental stoichiometry. Auger spectroscopy analysis showed stoichiometric Zn:S ratios.

Work in our group presently involves development of an alternative electrochemical deposition technique, electrochemical ALE (ECALE) [18,19], the electrochemical analog of atomic layer epitaxy (ALE) [20-22]. In traditional vacuum-based ALE, control over deposit structure and stoichiometry is achieved using a cycle of surface limited reactions, to deposit atomic layers of the individual elements. In ECALE, underpotential deposition (UPD) [23], another name for a surface limited reaction, is used to deposit atomic layers of each element, again in a cycle. To form thin films, the cycle is repeated until the desired thickness is reached.

It appears that significantly more control is achieved over the deposition process using electrochemical ALE than with other electrodeposition methods. Ideally, stoichiometric and crystalline deposits will be formed without the need for post deposition heat treatments using ECALE. The present paper describes a series of studies performed to delineate conditions for the growth of Zn based II-VI compounds. The conditions determined here

then serve as a first approximation of those needed for the automated electrodeposition of zinc chalcogenide thin films [24,25].

### Experimental

Studies were performed in a static thin layer electrochemical cell (TLEC), described in detail elsewhere [18,26]. The TLEC consisted of an polished, annealed, polycrystalline Au cylinder in a fitted glass cavity with a solution gap of about 0.03 mm. Two holes were provided at the bottom (tip) of the TLEC to allow solution into and out of the cavity and for ionic conductivity. Solution aliquots were drawn in by capillary action and expelled by pressurizing the cell interior with  $N_2$  gas. The process of blowing out one aliquot of solution out and allowing another to wick in, is referred to as a rinse.

Other hardware consisted of a series of Pyrex glass "H-cells" that consist of two compartments divided by a fine glass frit [18].  $N_2$  gas was used to sparge all solutions prior to each experiment. Separate H-cells were used for each solution and the TLEC was carefully transferred between them for access to a given solution. The potentiostat was built in-house with a conventional op-amp based design. The reference electrode was Ag/AgCl, made with 1.0 M NaCl, and the auxiliary electrode was a Au wire. All solutions were made with 18 M-ohm water from a Nanopure water filtration system, fed from the house deionized water system. All experiments were performed at room temperature.

To assure surface cleanliness, each electrochemical experiment was preceded by at least three electrochemical cleaning cycles; each cycle consisted of ten rinses with fresh 1M  $H_2SO_4$  at 1.4 V, followed by 10 rinses at -0.5 V. A cyclic voltammogram, taken after three cleaning cycles, was used as a check of surface cleanliness (Figure 1A).

Experimental coverages are reported as the ratio of deposited atoms per substrate surface atom. A  $1.2\text{ cm}^2$  geometric surface area was determined and a roughness factor of 1.2 was assumed. A coverage of  $1.17 \times 10^{15}$  Au atoms/ $\text{cm}^2$  was used, corresponding to a Au(100) surface. The coverage of a Au(100) surface is intermediate between those of the other two low-index planes:  $1.35 \times 10^{15}$  atoms/ $\text{cm}^2$  for Au(111) and  $8.2 \times 10^{14}$  atoms/ $\text{cm}^2$  for Au(110). The assumption here is that a polycrystalline electrode can be represented as some average of all three low index planes.

### Results and Discussion

#### Zn Deposition

Zn electrodeposition on Ag [27], Au [28-31], and Pt [29,31-35] has been extensively investigated on both polycrystalline and single crystalline substrates. It is a complex system, consisting of an initial UPD process, alloy formation, and bulk deposition. To complicate matters, there are indications, via X-ray absorption spectroscopy (XAS), that alloying occurs between Au and Zn even within the UPD region [30].

A cyclic voltammogram of the clean gold electrode in the zinc blank solution, pH 5.7, is shown in Figure 1B. Gold oxidation begins above 0.8 V, with the corresponding gold reduction at 0.75 V. Hydrogen evolution slowly begins below -0.4 V. In Figure 1C, one aliquot of a  $ZnSO_4$  solution was rinsed into the TLE under open

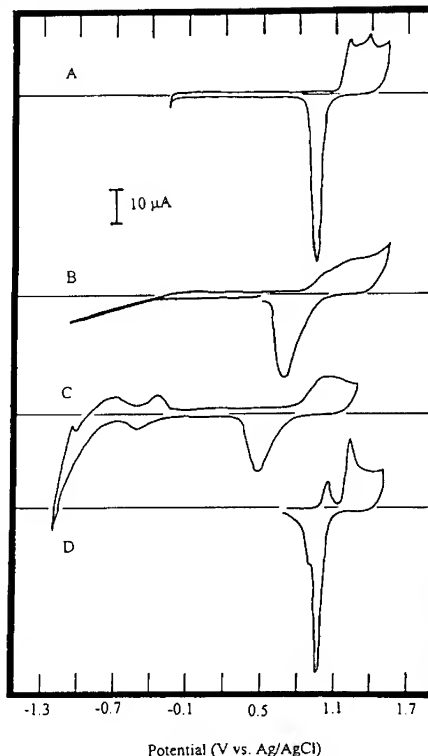


Figure 1: Cyclic voltammetry of a polycrystalline Au electrode in a thin-layer cell: (A) clean Au electrode in 1 M  $H_2SO_4$ ; (B) clean Au electrode in 0.5 M  $NaClO_4$  + 0.05 M  $HOCOC_6H_4COOK$  (KHP), pH 5.7; (C) clean Au electrode in 10 mM  $ZnSO_4$  + 5 M  $NaClO_4$  + 0.05 M KHP, pH=5.7; (D) Zn alloyed Au electrode in 1 M  $H_2SO_4$  after three cleaning cycles with an oxidation potential of 1.3 V. All scans were taken at  $5\text{ mVs}^{-1}$ .

circuit conditions and subsequently scanned negatively from the rest potential, -0.11 V. A small reductive Zn UPD peak is evident at -0.5 V resulting in a coverage of 0.47 monolayer (ML). Below -0.9 V, the reductive current begins to increase slowly, and on the subsequent positive going scan displays a small spike near -1.1 V. This small spike corresponds to bulk Zn stripping, indicating the formal potential for the  $\text{Zn}^{2+}/\text{Zn}$  couple in this solution is near -1.1 V. In addition to the currents for UPD and bulk deposition there appears to be other charge passed. For example, the net current at potentials below -0.9 V is cathodic, even on the positive going sweep. This could be attributed to hydrogen evolution, such as is evident in Figure 1B. However, there appears to be more current then expected on the negative going scan between -0.7 V and -1.1 V, possibly the result of a decreased hydrogen overpotential on the Zn modified surface. Alternatively, this current may be associated with the deposition of Zn, as there is a corresponding stripping feature between -1.0 V and -0.5 V, and hydrogen cannot be oxidized at these potentials. It is more likely that this extra charge is the formation of a Zn-Au alloy, as previously suggested by other workers [28-30]. Further evidence of alloying was observed during the subsequent cleaning procedure. When potentials less than 1.4 V were used as the positive limit in cleaning cycles, residual amounts of a Zn-Au alloy appeared to be present; indicated by a new feature at 0.95 V (Figure 1D) compared to the clean surface voltammetry (Figure 1A). A report by Tadjeddine and Torillon [30] supports this conclusion, as they found interactions between the zinc and gold in the alloy were so strong that high anodic potentials were required to oxidize the alloyed zinc. Finally, the UPD stripping feature is evident at -0.3 V, and is slightly larger (0.5 ML) then the corresponding deposition peak, which is understandable considering that it is probably superimposed on some of the Zn-Au alloy stripping current. Similar behavior appears to take place in the Cd-Au system [36,37].

#### Chalcogenide deposition

Figure 2 shows a series of thin-layer voltammograms for deposition of the chalcogenides on polycrystalline Au. Ideally, the chalcogenide atomic layers in an ECAL cycle would be formed directly by oxidative UPD, using a solution containing the element in a -2 oxidation state:  $\text{Te}^{2-}$ ,  $\text{Se}^{2-}$ , or  $\text{S}^{2-}$ . Unfortunately aqueous solutions of both  $\text{Te}^{2-}$  and  $\text{Se}^{2-}$  tend to be unstable; therefore,  $\text{HTeO}_2^+$  and  $\text{HSeO}_3^-$  solutions have been used as chalcogenide sources. Prior to each deposition, a clean voltammogram was obtained, similar to that shown in Figure 1A.

The clean TLEC was then immersed into the chosen chalcogenide solution and an aliquot rinsed in. Figure 2A is for an aliquot of  $\text{HTeO}_2^+$  solution. Two reversible couples at 0.20 V and 0.10 V correspond to Te UPD and bulk Te deposition, respectively. The bulk deposition feature is smaller than the UPD, since the amount of  $\text{HTeO}_2^+$  present in the aliquot was limited. The small bulk peak represents deposition of all the Te not already deposited during the UPD process. The peaks are fairly broad for several reasons. One is that the cleaning procedure consists of a sequence of oxidation and reduction cycles that can result in surface roughening of an already polycrystalline Au electrode [38-41]. In addition, the peaks are broadened by changes in the  $\text{HTeO}_2^+$  activity while the deposition is proceeding. There are also problems with IR drop due to the thin layer configuration. At potentials just below -1.0 V, another reversible couple is visible, corresponding to the reduction of bulk Te to  $\text{Te}^{2-}$ .

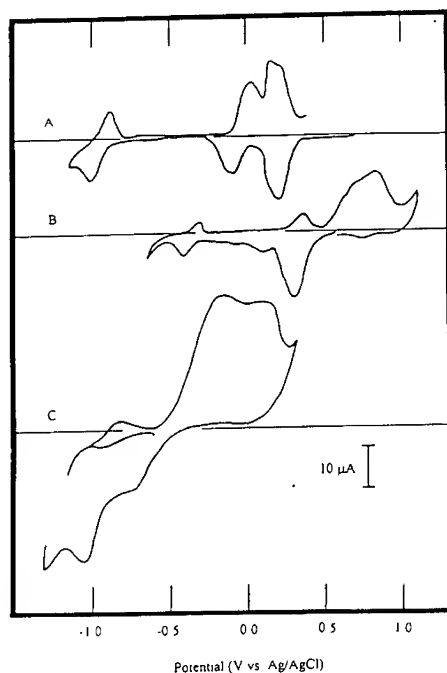
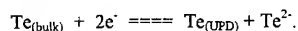


Figure 2: Cyclic voltammetry of the chalcogenides in a thin-layer cell: (A) clean Au electrode in 0.25 mM  $\text{TeO}_2$  + 0.5 M  $\text{Na}_2\text{SO}_4$  + 0.01M  $\text{Na}_2\text{B}_4\text{O}_7$ , pH 9.2; (B) clean Au electrode in 1.0 mM  $\text{SeO}_2$  + 0.5 M  $\text{NaClO}_4$  + 0.01M  $\text{Na}_2\text{B}_4\text{O}_7$ , pH 8.6; (C) clean Au electrode in 2.5 mM  $\text{Na}_2\text{S}$  + 0.5 M  $\text{NaClO}_4$ , pH 11.7. All scans were taken at 5 mVs<sup>-1</sup>.



{1}

As these experiments were performed with a trapped solution volume, in a TLEC, any  $\text{Te}^{2-}$  formed stayed in the cell and could be quantitatively reoxidize to Te during the anodic scan.

Figure 2B is a voltammogram for the corresponding deposition of Se from a solution of  $\text{HSeO}_3^-$ . The voltammograms in Figures 2A and B are very similar, with the main difference being the potentials needed to reduce bulk Se to  $\text{Se}^{2-}$  versus bulk Te to  $\text{Te}^{2-}$ . Selenium reduction occurs several hundred millivolts positive of the corresponding Te reduction feature. No features were observed for the reduction of UPD Se or Te, regardless of how negative the potential was scanned.

An atomic layer of Te or Se can be formed if the TLE is rinsed with pure supporting electrolyte after the UPD peak, at 0.05 V or at 0.14 V respectively. Alternatively, the whole aliquot can first be deposited, followed by the reaction in eq. 1 where excess Te or Se is reduced from the surface and rinsed away. While depositing a Te or Se UPD layer by the first method is relatively straight forward, it cannot be used in the formation of a second layer of a Zn chalcogenide. Zinc is clearly not stable on the surface at such potentials. Thus, the second, two step method, based on eq. 1, must be used for all but the first atomic layer of Te or Se.

Sulfide solutions are relatively stable compared with telluride and selenide solutions; thus, UPD of a S atomic layer is a more direct process. Figure 2C is the voltammetry of an aliquot of a sodium sulfide solution. It starts with a negative scan from -0.6 V to -1.2 V, displaying reductive stripping of a spontaneously formed S UPD layer [37,42-44]. Reversal of the scan at -1.2 V shows the UPD peak at -0.85 V. Continuation of the scan to 0.30 V reveals a very large peak, corresponding to oxidation of the remaining  $\text{S}^{2-}$  to bulk S. At 0.3 V, the current begins to increase again, as the deposited S starts to convert to sulfate [37]. A second reversal at this point, resulted in no current flow until -0.6 V, after which, reduction of sulfur to polysulfide occurred [37]. Below -1.2 V, solvent decomposition was the dominant process.

#### Zn Chalcogenide Formation

Figure 3 is a series of diagrams showing the deposition of Zn on atomic layers of Te, Se, and S. Comparing the voltammetry, there is a definite trend going up the periodic table. Zn is hardest to deposit on the Te atomic layer, not starting till -0.7 V. A well defined Zn UPD peak is visible for the Se atomic layer, beginning at -0.5 V. Finally, deposition of Zn on the S atomic layer begins near -0.3 V. The differences in the UPD potentials are consistent with differences in the free energies of formation of the compounds: -115.2, -173.6, -200.0 kJ/mol for ZnTe, ZnSe, and ZnS respectively [45].

The rest of this article describes TLEC studies of Zn chalcogenide electrodeposits. Each experiment involved formation of a deposit under a specific set of cycle conditions for a specified number of cycles. Coulometric stripping was then used to characterize elemental coverages per cycle as a function of the deposition potentials. These experiments proved very tedious but worthwhile. If 10 cycles were to be deposited under a specific set of conditions, then extreme care had to be taken as there were a minimum of 12 steps per cycle (Figure 4). Note that for the ECALE cycle diagrammed in Figure 4, each solution was in a separate H-cell. The TLEC, reference, and auxiliary electrodes were moved from H-cell to H-cell at each step. To prevent cross contamination of the separate solutions and the Au electrode, the TLEC exterior was rinsed with  $\text{H}_2\text{O}$  while pressurized with  $\text{N}_2$  (shown in Figure 4 as an  $\text{H}_2\text{O}$  solution block). Each cycle started with three rinses in the S blank at -1.0 V. This was done to condition the TLE, as the glass walls act as a reservoir for  $\text{H}^+$  ions from the more acidic Zn solutions. Then two aliquots of S were rinsed in at -1.0V. Before blowing out the second aliquot, the electrode was held at this potential for 30 seconds to deposit the S UPD layer. This was followed by

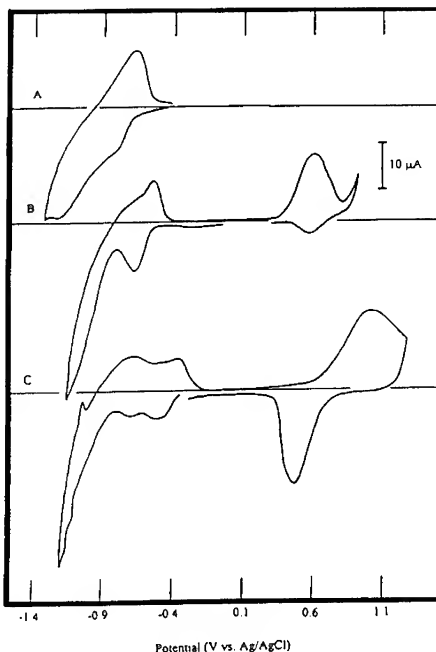


Figure 3: Cyclic voltammetry of an aliquot of 10 mM  $\text{ZnSO}_4$ : (A) with a Te coated electrode; (B) with a Se coated electrode; (C) with a S coated electrode.

Figure 4: Diagram of the sequence of steps used in an one complete ZnS ECALE cycle. See text for details

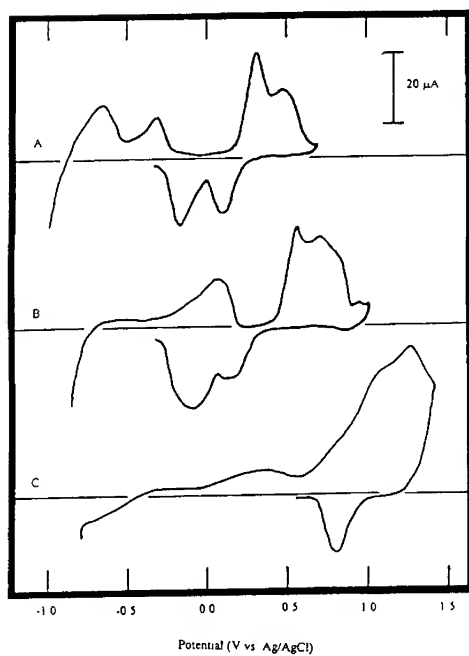
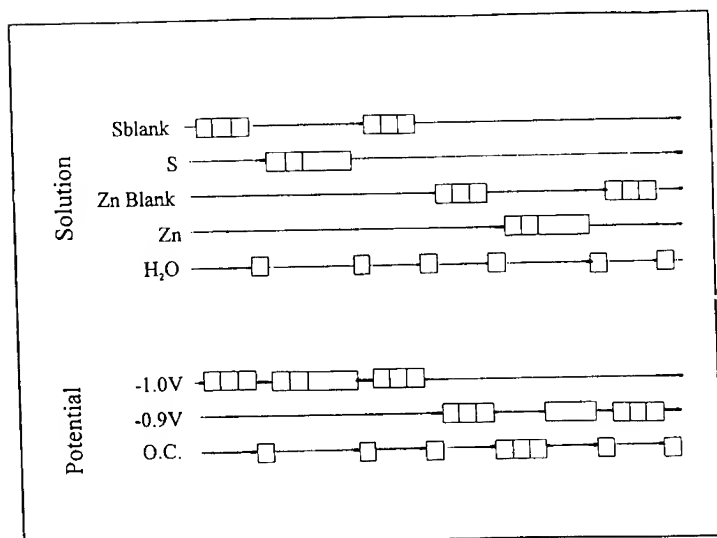


Figure 5: Stripping voltammetry taken at  $5 \text{ mVs}^{-1}$  of 4 ECALE cycles: (A) ZnTe in  $0.5 \text{ M Na}_2\text{SO}_4$ , pH 3; (B) ZnSe  $0.5 \text{ M NaClO}_4$ , pH 3; (C) ZnS in  $0.5 \text{ M NaClO}_4$ , pH 3.

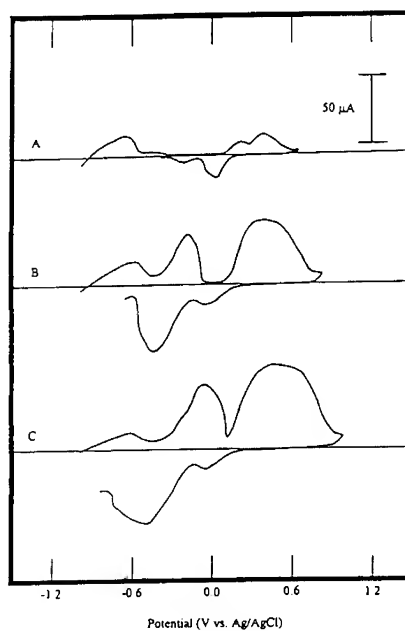


Figure 6: Stripping voltammetry taken at  $5 \text{ mVs}^{-1}$  of ZnTe in  $0.5 \text{ M Na}_2\text{SO}_4$ , pH 3: (A) 2 ECALE cycles; (B) 8 ECALE cycles; (C) 16 ECALE cycles.



three more rinses in the S blank at -1.0 V to remove any excess S species. The electrode was then removed, rinsed, and placed into the Zn blank solution at -0.9 V where three rinses were performed, conditioning the TLE for the more acidic environment. This was followed by two open circuit rinses of the Zn solution with the second aliquot of Zn held at -0.9 V to deposit a UPD layer. Three more rinses with the Zn blank were performed to remove any remaining  $\text{Zn}^{2+}$  ions.

Figure 5 consists of stripping curves for deposits resulting from four ECALE cycles of ZnTe (A), ZnSe (B), and ZnS (C). Several trends are evident. First, a trend similar to that seen during deposition of the initial Zn atomic layer (Figure 3) is observed: the Zn was easier to strip from the ZnTe then from ZnSe then from ZnS. From Figure 5, it also appears that there are generally two Zn stripping features in each scan. This is seen most demonstratively for ZnTe in Figure 5A, where the low potential peak, -0.7 V, grows in first but does not significantly increase in size after the second cycle (Figure 6). Instead the higher potential feature, -0.3 V, starts to grow. As the number of cycles is increased further, this second peak grows and shifts to still higher potentials. A simple explanation would be that the first peak represents the top layer of Zn atoms, those not completely coordinated to Te, while the second peak represents Zn from the interior of the compound.

In the next series of graphs, the number of monolayers of the elements deposited per cycle has been plotted as a function of the potential used to deposit one of the elements. The coverages should not be taken too literally at this stage. Theoretically, a coverage of 0.5 ML of each element per cycle should be optimal, as it takes 0.5 ML of each element to form 1 ML of the compound. However, the coverage measurements are made with a number of assumptions including the number of Au surface atoms and the background correction used in the coulometry.

Determination of the potentials needed to deposit atomic layers of Te and Se was straight forward. As mentioned above, they are formed by first depositing a few monolayers of the element and then reducing the surface at fairly negative potentials to remove the excess. The potentials at which Te and Se reduce are below -1.0 V for Te, and below -0.5 V for Se. Reduction of the last atomic layer of the chalcogenide was very difficult to achieve, as hydrogen evolution polarized the electrode potential, and obscured the reduction process before the atomic layers could be removed. Thus, any potential below -1.0 V for Te, or below -0.5 V for Se, should work for forming atomic layers.

The choice of conditions for formation of S atomic layers from sulfide solutions was less clear cut. Figure 7 is a graph of the monolayer/cycle for deposits formed after 3 cycles, as a function of the S deposition potential. The Zn deposition potential was -0.9 V for these studies. The resulting graphs of S and Zn coverage do not coincide well. Possible explanations include a problem in quantifying the voltammograms. In Figure 5, the Zn stripping feature overlaps significantly with the S oxidation feature after only four cycles. Regardless of the discrepancy between the Zn and S coverages, the trends appear valid.

ALE behavior is frequently indicated by an "S" curve. That is, for a given variable, at one extreme the

coverage is too high, while at the other the coverage is too low. In between, there is a plateau, where deposition is controlled by surface limited reactions alone, and one monolayer of the compound is formed per cycle [20-22]. In Figure 7, at the most negative S deposition potentials, below -1.1 V, insufficient S is deposited each cycle, and since Zn requires the presence of S, both coverages drop. At potentials above -0.9 V, both coverages increase, as bulk S begins to be incorporated into the deposits. That increase, however, starts to drop off at potentials above -0.7 V, as Zn no longer remains on the surface during the S deposition step. The

conclusion drawn from this study is that S should be deposited at potentials between -1.1 V and -0.9 V, where there is a small plateau, indicating probable surface limited control over the deposition.

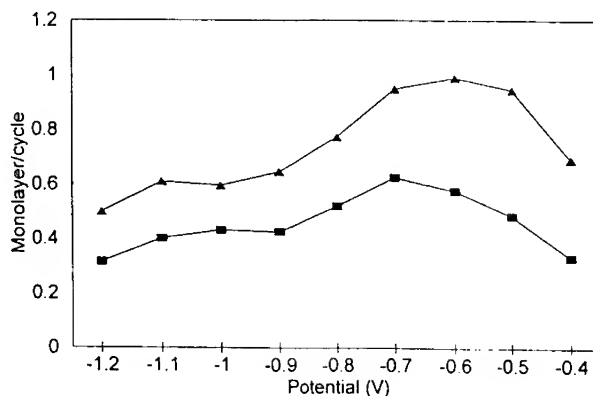


Figure 7: Graph of the coverages of Zn (□) and S (Δ) per ECALE cycle as a function of the potential used for S deposition.

From Figure 7, it was decided to proceed using -1.0 V for the deposition of S atomic layers. Figure 8 is then a graph of the coverages of Zn and S as a function of the Zn deposition potential, holding S deposition at -1.0 V. The dependence on the Zn potential is not dramatic, with only small changes in coverage/cycle as the potential is varied from -1.0 V to -0.5 V. As mentioned, -0.9 V was used as the Zn deposition potential in the studies shown in Figure 7. The difference in coverage between Zn and S are significant at -0.9 V and above in Figure 8, as they were in Figure 7. At -1.2 V, the Zn coverage is increasing, as bulk Zn deposition becomes important. At potentials more positive than -0.5 V, not enough Zn is being deposited and the coverages of both elements drop. The underpotential for Zn deposition appears to be negative of -0.5 V. A Zn deposition potential of -1.0 V appears optimal, as the coverages coincide well and are very close to the ideal 0.5 ML per cycle for each element. For this compound a cycle where both elements are deposited at -1.0 V looks to be the best starting point for further studies of ZnS deposition by ECALE.

Figure 9 is a similar graph of coverage/cycle, for the deposition of ZnSe as a function of the Zn deposition potential. Selenium deposition was carried out by first depositing several monolayers at -0.9 V, and then reducing off any excess at -0.9 V. The drop in the coverages above -0.8 V is due to decreasing Zn stability. A plateau in both the Zn and Se coverages is evident between -1.2 V and -0.9 V; however, it corresponds to Zn coverage/cycle of nearly 0.75 ML, while the Se coverage remains at 0.5 ML. Given the data in Figure 9, however, the optimal Zn potential appears to be between -0.9 V and -0.7 V, with -0.8 V looking best.

Figure 10 is the corresponding graph of coverage/cycle as a function of the Zn deposition potential in the formation of ZnTe. The Te was deposited by first forming a couple of monolayers at -0.8 V, and then reductively stripping the excess at -1.1 V. Under the conditions chosen, the Te coverage/cycle looks low at all potentials, about 0.33 ML per cycle. This is not the expected behavior, and indicates that the dependence of Te coverage on its deposition conditions needs more study. There is a plateau between -1.1 V and -1.0 V, similar to that seen in Figure 9 for ZnSe formation, where the Zn coverage is significantly higher than the corresponding chalcogenide, again. It is not clear what is causing this, besides maybe alloy formation between the Zn and Au [28-30]. Between -0.95 V and -0.8 V the coverages/cycle for Zn and Te coincide and correspond to about 0.33 ML/cycle. Positive of -0.8 V, the coverage of Zn falls off quickly, as expected. Given the data presented in Figure 10, a Zn deposition potential of -0.95 V would probably be optimal.

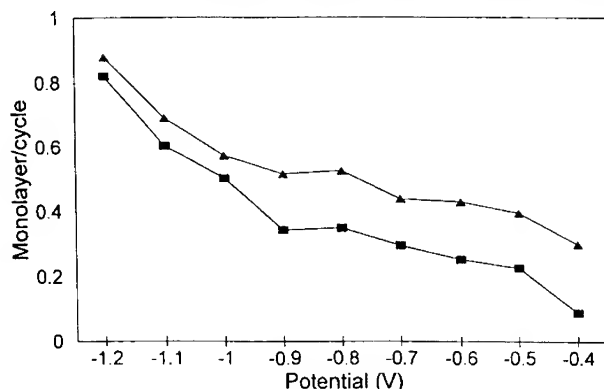


Figure 8: Graph of the coverages of Zn (□) and S (Δ) per ECALE cycle as a function of the potential used for Zn deposition.

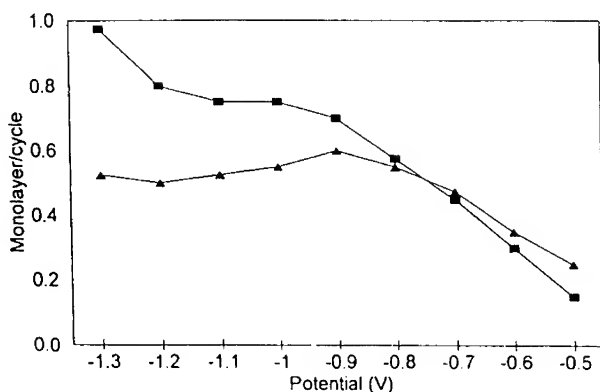


Figure 9: Graph of the coverages of Zn (□) and Se (Δ) per ECALE cycle as a function of the potential used for Zn deposition.

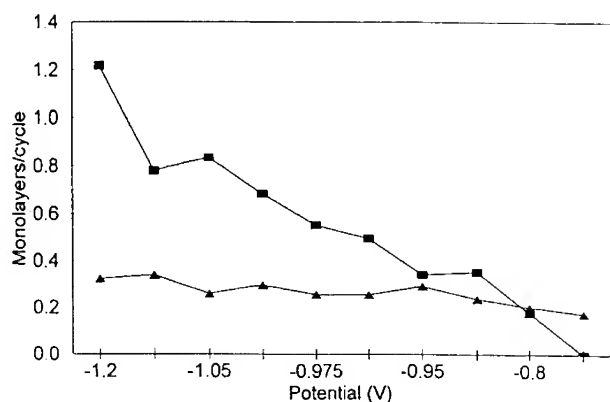


Figure 10: Graph of the coverages of Zn (□) and Te (Δ) per ECALE cycle as a function of the potential used for Zn deposition.

This may be a quantitation problem as the stripping peaks for the two elements start to overlap. In the present studies, clear problems were encountered after 16 cycles of ZnTe, 10 cycles of ZnSe, and only 4 cycles of ZnS, due to broadening of the Zn stripping peaks at higher potentials, as the coverage increases. They eventually run into the chalcogenide stripping features (e.g. Figure 5C), making it difficult to independently determine the coverages of the two elements. It may also be a problem with operator error, as each cycle involves 24 or more steps; therefore, as the number of cycles increase, there are more chances for mistakes, suggesting that the next step should be to use an automated system [24,25].

### Conclusion

Thin layer electrochemical cells have been used to study the conditions needed to deposit Zn chalcogenides by electrochemical ALE. It is fortuitous that the stripping voltammetry of deposited layers can be used to determine the coverages of both elements in the compound; however, it is limited to the first few cycles where the stripping features do not overlap. The studies presented here demonstrate behavior consistent with an ALE process. That is, deposit coverages increase linearly with the number of cycles, 0.5 ML deposits of each element are formed each cycle, and the characteristic "S" curve dependence of deposit coverages with various cycle variables are observed.

There are obvious discrepancies in the data presented. The sources are not all clear, however they do provide a good starting point for further studies. An automated deposition system has been constructed and will be used in subsequent studies. It will provide more reproducible results, and allow the formation of thicker deposits which can be studied using techniques such as electron probe microanalysis (EPMA) and X-ray diffraction (XRD). This will provide a better environment for optimization of deposition parameters.

### Acknowledgments

This work was supported in part by the National Science Foundation (NSF) under Grant No. DMR-9017431; The U.S. Navy, Office of the Chief of Naval Research, under Grant No. N00014-91-J-1919; and by the ARPA Phosphor Technology Center of Excellence. This financial assistance is gratefully acknowledged.

Finally, given the starting conditions determined from Figures 7-10, studies were performed investigating the dependence of the coverage on the number of cycles performed (Figure 11). A linear dependence is expected for an ALE process, and is evidenced in each of the graphs in Figure 11, given the error inherent in the measurements. The slopes in the case of ZnSe and ZnS formation are very close to the expected 0.5 ML per cycle. The slope is a little low in the case of ZnTe, in line with the need to better optimize the Te deposition. In all three graphs, there is a drop off in the coverages, at the highest number of

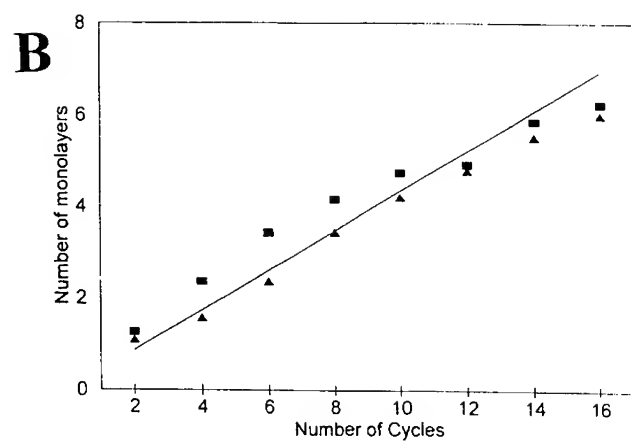
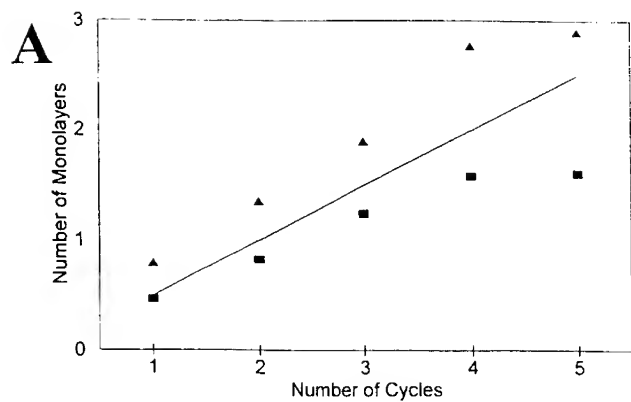
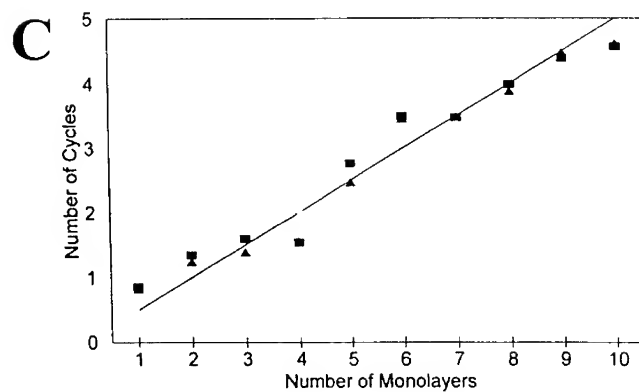


Figure 11: Graph of the coverage of the elements as a function of the number of ECALE cycles: (A) Zn (□) and S (Δ); (B) Zn (□) and Se (Δ); (C) Zn (□) and Te (Δ).



## References

- [1] K. Rajeshwar, *Advanced Materials*, **4**, 23 (1992).
- [2] R.N. Bhargava, *J. Crystal Growth*, **59**, 15 (1982).
- [3] W. Gebhart, *Materials Science and Engineering*, **B11**, 1 (1992).
- [4] R.N. Bhargava, *J. Crystal Growth*, **117**, 894 (1992).
- [5] M. Neumann-Spallart and C. Konigstein, *Thin Solid Films*, **265**, 33 (1995).
- [6] K. Singh and J.P. Rai, *J. Mat. Sci. Lett.*, **4**, 1401 (1985).
- [7] C.B. Roy, D.K. Nandi, and P.K. Mahapatra, *Electrochim. Acta*, **31**, 1227 (1986).
- [8] K. Singh and J.P. Rai, *Bull. Mater. Sci.*, **10**, 353 (1988).
- [9] K. Singh and J.P. Rai, *Ind. J. Chem.*, **28A**, 557 (1989).
- [10] J.P. Rai and K. Singh, *Ind. J. Chem.*, **32A**, 376 (1993).
- [11] J.P. Rai, *Sol. Eng. Mat. Sol. Cells*, **30**, 119 (1993).
- [12] I. Ohno, K. Wantanabe, and H. Numata, in *Electrochemically Deposited Thin Films*, M. Paunovic, I. Ohno, and Y. Miyoshi, Editors, **PV 93-26**, p. 108, The Electrochemical Society Proceedings Series, Pennington, NJ (1993).
- [13] K. Singh and R.K. Pathak, *Electrochim. Acta*, **39**, 2693 (1994).
- [14] C. Natarajan, M. Sharon, C. Levy-Clement, M. Neumann-Spallart, *Thin Solid Films*, **237**, 118 (1994).
- [15] C.D. Lokhande, M.S. Jadhav, S.H. Pawar, *J. Electrochem. Soc.*, **136**, 2756 (1989).
- [16] B.W. Sanders and A.H. Kitai, *J. Crystal Growth*, **100**, 405 (1990).
- [17] T. Mahalingam and C. Sanjeeviraja, *Phys. Stat. Sol. (A)*, **129**, K89 (1992).
- [18] B.W. Gregory, D.W. Suggs, and J.L. Stickney, *J. Electrochem. Soc.*, **138**, 1279 (1991).
- [19] B.W. Gregory and J.L. Stickney, *J. Electroanal. Chem.*, **300**, 543 (1991).
- [20] S. Bedair, *Atomic Layer Epitaxy*, Elsevier, Amsterdam, (1993).
- [21] T.F. Kuech, P.D. Dapkus, Y. Aoyagi, Atomic Layer Growth and Processing, Materials Research Society, Pittsburg (1991).
- [22] T. Suntola and J. Antson, U.S. Patent 4 058 430 (1977).
- [23] D.M. Kolb in *Advances in Electrochemistry and Electrochemical Engineering*, Vol. 11, H. Gerischer and C.W. Tobias, Editors, Wiley, New York, 1978, p. 125.
- [24] L.P. Colletti, R. Slaughter, and J.L. Stickney, *J. Soc. Inform. Disp.*, submitted.
- [25] L.P. Colletti and J.L. Stickney, in preparation.
- [26] A.T. Hubbard, *Crit. Rev. Anal. Chem.*, **3**, 201 (1973).
- [27] G. Adzic, J. McBreen, M.G. Chu, *J. Electrochem. Soc.*, **128**, 1691 (1981).
- [28] M.G. Chu, J. McBreen, G. Adzic, *J. Electrochem. Soc.*, **128**, 2281 (1981).
- [29] A.R. Despic, and M.G. Pavlovic, *Electrochim. Acta*, **27**, 1539 (1982). [45] A. Nasar and M. Shamsuddin, *Thermochim. Acta*, **205**, 157 (1992).
- [30] A. Tadjeddine and G. Tourillon, *Elektrokhimiya*, **29**, 63 (1993).
- [31] M.A. Quaiyyum, A. Aramata, S. Moniwa, S. Taguchi, and M. Enyo, *J. Electroanal. Chem.*, **373**, 61 (1994).
- [32] A. Aramata, M.A. Quaiyyum, W.A. Balais, T. Atoguchi, and M. Enyo, *J. Electroanal. Chem.*, **338**, 367 (1992).
- [33] S. Taguchi, A. Aramata, M.A. Quaiyyum, and M. Enyo, *J. Electroanal. Chem.*, **374**, 275 (1994).
- [34] S. Taguchi and A. Aramata, *J. Electroanal. Chem.*, **396**, 131 (1995).
- [35] A.A. El-Shafei, *J. Electroanal. Chem.*, **380**, 269 (1995).
- [36] J.W. Von Schultze, F.D. Koppitz, and M.M. Lohrengel, *Ber Bunsenges. Phys. Chem.*, **78**, 693 (1974).
- [37] L.P. Colletti, D. Teklay, and J.L. Stickney, *J. Electroanal. Chem.*, **369**, 145, (1994).
- [38] A. Hamelin, *J. Electroanal. Chem.*, **142**, 299 (1982).
- [39] D.M. Kolb and J. Schneider, *Electrochim. Acta*, **31**, 929 (1986).
- [40] J. Schneider and D.M. Kolb, *Surf. Sci.*, **193**, 579 (1988).
- [41] X. Gao, A. Hamelin, and M.J. Weaver, *Phys. Rev. Lett.*, **67**, 618 (1991).
- [42] A.N. Buckley, I.C. Hamilton, and R. Woods, *J. Electroanal. Chem.*, **216**, 213 (1987).
- [43] I.C. Hamilton and R. Woods, *J. Appl. Electrochem.*, **13**, 783, (1983).
- [44] X. Gao, Y. Zhang, and M.J. Weaver, *Langmuir*, **8**, 668 (1992).
- [45] A. Nasar and M. Shamsuddin, *Thermochim. Acta*, **205**, 157 (1992).

## UHV MODEL EXPERIMENTS OF ELECTROCHEMICAL ETCHING OF GaAs BY H<sub>2</sub>O/Br<sub>2</sub>

O. HENRION, A. KLEIN, C. PETTENKOFER, AND W. JAEGERMANN

Hahn-Meitner-Institut, Abteilung CG, Glienicker Straße 100, 14109 Berlin, Germany

### ABSTRACT

To investigate the initial steps of GaAs etching Br<sub>2</sub> and H<sub>2</sub>O were (co)adsorbed onto the (110) cleavage plane at 100 K and the interaction investigated by SXPS and LEED. H<sub>2</sub>O is dissociatively adsorbed at low temperatures and leads to Fermi level pinning close to midgap. Br<sub>2</sub> leads, depending on coverage, to the formation of bromides of different stoichiometries. During annealing to 290 K the bromides mostly evaporate from the surface (etching). Br<sub>2</sub> and H<sub>2</sub>O coadsorption leads to Ga-oxide remaining on the surface. For the reactive interfaces band bending is not observed. The results of the adsorption experiments are compared to electrochemically prepared surfaces.

### INTRODUCTION

Wet chemical and electrochemical etching and oxidation of semiconductor surfaces for device fabrication and epitaxy has been extensively studied in recent years [1,2]. Especially the III-V semiconductors were of particular interest (comp. Ref. [3] and references therein). The chemical composition of the interface after electrochemical treatment has been analyzed with surface science techniques in ex-situ experiments after emersion and transfer (see Ref. [4] and references therein). But a detailed knowledge of the involved chemical steps in electrochemical etching e. g. by H<sub>2</sub>O and Br<sub>2</sub> solutions can still not be given. Therefore we started to investigate etching of semiconductors by (co)adsorbing the reactive electrolyte components (H<sub>2</sub>O and Br<sub>2</sub>) onto the semiconductor surfaces in UHV to model the semiconductor/electrolyte interface [4]. The results on H<sub>2</sub>O adsorption have already been presented elsewhere [5]. The adsorption of Br<sub>2</sub> on GaAs cleavage plane has been investigated already previously to obtain detailed information on dry etching [6,7].

We will present here shortly our results on Br<sub>2</sub> interaction with vacuum cleaved n-doped GaAs (110) surfaces at 100 K and during heating to room temperature. The main focus of this paper will be the interactions which are observed during coadsorption of H<sub>2</sub>O and Br<sub>2</sub>. Chemical and electronic changes are monitored using synchrotron excited valence band and core level photoelectron spectroscopy (PES) and electron diffraction (LEED).

### EXPERIMENTAL

The experiments were performed in an ultra high vacuum system equipped with an angle resolving photoelectron spectrometer (VG ADES 500). The base pressure of the system was below  $1 \cdot 10^{-10}$  mbar. Photoelectron spectroscopy at the electron storage ring BESSY was used to characterize the samples. Cleavage of the samples was performed in a separate preparation chamber ( $p \leq 2 \cdot 10^{-10}$  mbar) at room temperature. N-type (Te,  $2 \cdot 10^{17} \text{ cm}^{-3}$ ) GaAs crystal bars were used. After transferring the samples to the measurement position the samples were cooled to  $T = 100 \text{ K}$  within one half hour. Deionized water and Br<sub>2</sub> (p.a) was cleaned via multiple vacuum distillations and dosed via a leak valve. The exposures are given in Langmuir [L] and were controlled by the uncorrected total pressure rise of the vacuum chamber. The gas cleanliness was controlled prior to adsorption by a mass spectrometer.

## RESULTS

For the discussion of the coadsorption experiments we will shortly summarize the results of  $\text{H}_2\text{O}$  adsorption [5].  $\text{H}_2\text{O}$  adsorbs dissociatively for low coverages and molecularly for high coverages. During annealing to room temperature a "Ga-Oxide" is formed which is not well defined. The Fermi level is pinned at  $E_F - E_V = 0.6$  eV for the dissociatively adsorbed  $\text{H}_2\text{O}$  and at  $E_F - E_V = 0.9$  eV for the Ga-oxide covered surface.

Fig. 1 shows a typical set of Ga and As core level spectra of the  $\text{Br}_2$  adsorption series recorded with  $h\nu = 60$  eV and 80 eV, respectively. At low  $\text{Br}_2$  exposures (up to 1 L),  $\text{Br}_2$  is evidently dissociatively adsorbed and binds to Ga and As as is evident from the core level shifts. At this stage the  $1 \times 1$  LEED pattern of the (110) cleavage plane remains unaffected. At increased dosages ( $> 3$  L)  $\text{GaBr}_3$  and  $\text{AsBr}_3$  are formed in good agreement to previous studies [7]. In our experiments we also find a weak feature which is attributed by Weaver et al. to the formation of  $\text{AsBr}_5$  at exposures exceeding 15 L. A strong Br 3d signal is detected which can be assigned to a superposition of  $\text{Br}^-$  species and molecularly adsorbed  $\text{Br}_2$ .

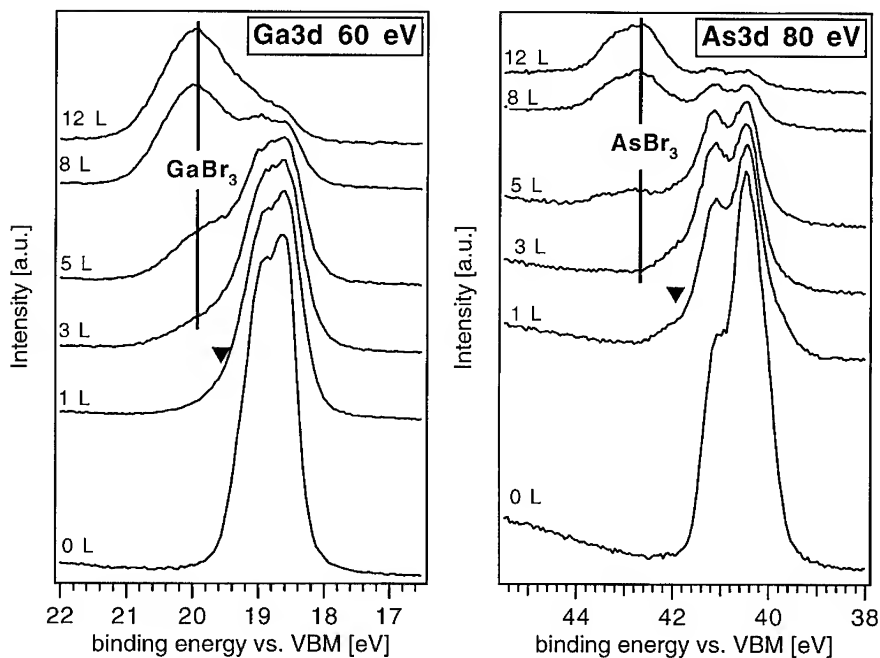


Fig. 1 Core level spectra ( $h\nu = 60$  eV and 80 eV) of n-type n-GaAs (110) with increasing bromine coverage. All spectra were taken at  $T = 100\text{K}$ . For exposures  $\leq 1\text{L}$  the surface core level shifts are removed and slight shoulders at the higher binding energy side indicate dissociative adsorption of bromine under formation of monobromides by saturating the dangling bonds of the substrate. At exposures  $\geq 3\text{L}$  the tribromides of Ga and As are formed by breaking backbonds (dry etching).

The chemical reaction is accompanied with the loss of the LEED pattern, indicating that no ordered reaction layer is formed. During annealing to room temperature (RT) the formed

Bromides evaporate from the surface ( $\text{GaBr}_3$  at around 290 K and  $\text{AsBr}_3$  at around 180 K). The Ga and As core level spectra obtained after annealing at RT are again comparable to the clean surface spectra, showing slight shoulders at higher binding energies, that are due to a small amount of residual (mono)bromides (compare Fig. 3). Also the weak Br 3d line together with the substrate core level lines indicates the presence of the monobromides with some remaining  $\text{GaBr}_x$  species. At this stage the (1x1) LEED pattern of the (110) cleavage plane reappears with a slightly increased diffuse background.

The changes of the Fermi level position (band bending) during the adsorption and annealing cycle is summarized in Fig. 2. Due to the dissociatively adsorbed  $\text{Br}_2$  acceptor states are introduced, which shift the Fermi level towards the valence band. This shift (0.4 eV) is slightly smaller than compared to previously published results [6,8]. We attribute this difference in part to the different exposures in the different experiments as well as to the influence of source induced surface photovoltage effects [9]. In addition dissociative adsorption merges very rapidly to the reactive stage. Interestingly with the onset of etching and the formation of the bromide compounds, the band bending is reduced again. Also after annealing and desorption of the bromides flat band potential is retained, indicating that etching is possible without introducing a high concentration of defects situated in the band gap.

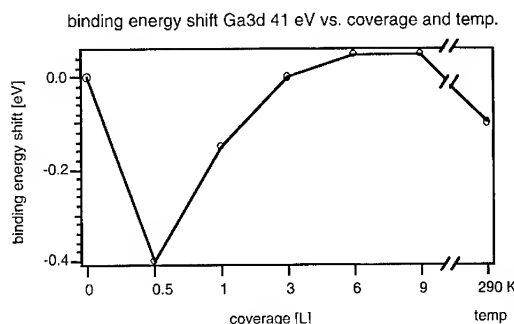


Fig. 2

Relative binding energy shift of the Ga3d substrate emission measured with 41 eV photon energy in dependence of the bromine exposure and after annealing to room temperature. The initial band bending is due to the mainly dissociative adsorbed bromine and is removed with increasing coverage due to surface etching. After annealing to room temperature a certain amount of the monobromides remains on the surface with a small concentration of  $\text{GaBr}_x$ .

The coadsorption series was performed similarly to the experiments described above in both possible sequences. As space does not allow to discuss the whole series we will only present results for the coadsorbates at low temperatures and after annealing to room temperature. In Fig. 3 the Ga 3d and As 3d core level spectra of the coadsorption experiments are shown in comparison to the cleaved sample and to the monoadsorbate covered surfaces. Coadsorption leads independently on the sequence to the formation of Ga-oxide ( $\text{Ga} + \text{III}$ ) and As-oxide ( $\text{As} + \text{III}$ ), with evidently minor contribution of hydroxide groups. The spectra still contain bromide species depending on the relative dosage of  $\text{H}_2\text{O}$  and  $\text{Br}_2$ . This is evident from Br 3d core level spectra and from the differing position of the chemically shifted emission lines, which are superpositions of -oxide and -bromide peaks. After annealing the As-oxide is lost. A small shoulder remains on the high binding energy side, which may be due to the formation of elemental As. We attribute this to the reaction of As-oxide with bulk GaAs resulting in As and Ga-oxide, which is known to proceed at the GaAs/oxygen interface [10]. The Ga-oxide remains adsorbed on the surface after annealing, even when its relative concentration is reduced. There is no principle difference in the behaviour for the different sequences. After annealing also for the coadsorbate system the 1x1 LEED pattern reappears very weakly, indicating that most of the reacted surface layer has been evaporated.



Interestingly the position of the Fermi level is not very much effected by the formation of the oxides. We observe its position to be almost at the flatband value.

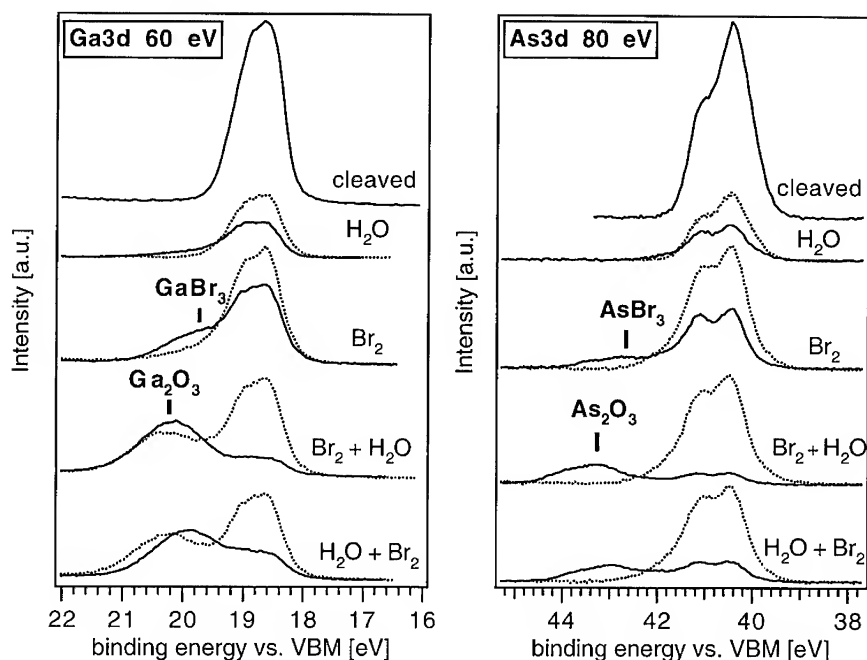


Fig. 3 Comparison of substrate core level lines of the different (co)adsorption experiments at low temperature (solid line) and after annealing to room temperature (dotted line). For the bromine adsorption the formed trivalent species are lost to vacuum, whereas in both coadsorption cases the formed Ga-oxide evidently remains on the surface and the As-species is transformed.

## CONCLUSIONS

In summary we have found a rather complex coadsorption behaviour of  $\text{Br}_2$  and  $\text{H}_2\text{O}/\text{Br}_2$  on cleaved GaAs (110) surfaces. We suggest the adsorption to proceed as follows: Initially  $\text{Br}_2$  is dissociatively adsorbed on the surface. Afterwards bromides are formed, which evaporate from the surface during room temperature annealing (dry etching). The dissociated species lead to acceptor states whereas the reacted surface and the annealed surface shows flatband position again. Coadsorption with  $\text{H}_2\text{O}$  leads to the formation of Ga(III)- and As(III)-oxides. During annealing the As-oxide is transformed whereas most of the Ga-oxide remains on the surface. Again the reacted surfaces do not show Fermi-level pinning. In contrast it can be expected that the Ga-oxides are dissolved in wet chemical etching. This has been proven by surface analysis after rinsing etched GaAs surfaces by deionized water [11,12]. It can thus be expected that nearly perfect and clean GaAs surfaces can be obtained. However, the interaction with water of the solvent may again produce pinning states, which deteriorates the electronic surface properties. The pinning of the Fermi level in aqueous solutions close to midgap has been proven for a number of

of different electrolyte solutions [13,14]. The pinning position may be assigned based on our experiments to be due to dissociatively adsorbed water. Interestingly in organic electrolytes GaAs (110) surfaces have shown flatband potential [15]. It is evidently possible to prepare GaAs surfaces free of surface states by reactive etching. But to study the electrochemical properties of these surfaces organic electrolytes must be used.

#### ACKNOWLEDGEMENTS

We would like to thank the Freiburger Elektronikwerkstoffe GmbH (FEW) and the Institut für Kristallzüchtung Berlin for providing us with the substrate material.

#### REFERENCES

- [1] S.D. Mukherjee and D.W. Woodard in: Gallium Arsenide: Materials, Devices, and Circuits, Eds. M. J. Howes and D. V. Morgan, John Wiley & Sons, Chichester, NY, 1985, p.119
- [2] A.M. Kaminska and M. Guziewicz, *Thin Solid Films* **254**, p. 194, (1995)
- [3] P.H.L. Notten, J.E.A.M. van den Meerakker and J.J. Kelly: Etching of III-V semiconductors: An electrochemical approach, Elsevier Advanced Technology, Oxford, 1991
- [4] W. Jaegermann in: Modern Aspects of Electrochemistry, Eds. J. O. Bockris, B. E. Conway and R. E. White, Plenum Press, New York, London, (in press)
- [5] O. Henrion, T. Löher, A. Klein, C. Pettenkofer and W. Jaegermann, *Surf. Sci. Lett.* **366**, L685, 1996
- [6] K. Cierocki, D. Troost, L. Koenders and W. Mönch, *Surf. Sci.* **264**, p. 23, 1992
- [7] C. Gu, Y. Chen, T.R. Ohno and J.H. Weaver, *Phys. Rev. B* **46**, p. 10197, 1992
- [8] W. Mönch, *J. Vac. Sci. Technol. B* **7**, p. 1216, 1989
- [9] M. Alonso, R. Cimino and K. Horn, *Phys. Rev. Lett.* **64**, p. 1947, 1990
- [10] C.W. Wilmsen, *J. Vac. Sci. Technol.* **19** (1981) 279.
- [11] Z.H. Lu, C. Lagarde, E. Sacher, J.F. Currie and A. Yelon, *J. Vac. Sci. Technol. A* **7**, p. 646, 1989
- [12] Y. Hirota, K. Sugii and Y. Homma, *J. Electrochem. Soc.* **138**, p. 799, 1991
- [13] P. Allongue and H. Cachet, *Surf. Sci.* **168**, p. 356, 1986
- [14] O. Savadogo, *Can. J. Chem.* **67**, p. 382, 1989
- [15] B. Ba, H. Cachet, B. Fotouhi and A. Gorochoy, *Semicond. Sci. Technol.* **9**, p. 1529, 1994

## SCANNING PROBE INVESTIGATIONS OF CLEAVED HETEROSTRUCTURE LAYERS

J. L. EBEL\*, T. E. SCHLESINGER\*\*, M. L. REED\*\*

\*Solid State Electronics Directorate, Wright Laboratory, Wright-Patterson AFB, OH 45433

ebel@el.wpafb.af.mil

\*\*Electrical and Computer Engineering, Carnegie Mellon University, Pittsburgh, PA 15213

### ABSTRACT

We present differential oxidation rate effects in cleaved heterostructures containing GaAs, AlGaAs, InGaP and InGaAs measured by atomic force microscopy (AFM). AFM images of the cleaved structures are presented, along with step height measurements at the different material interfaces. These height differences are the result of differences in oxidation rates of the heterostructure layers. The method used to extract the small step-height information from the images is also presented. Typical step heights range from about one to twenty angstroms for the structures measured. We have also observed steps which mimic the oxidation steps, but which are not related to the epitaxially grown material structure. However, in these cases images of both sides of the cleaved pieces show inverse (rather than similar) topographies. We also present results of digital etching techniques used to enhance the step heights based on the same differential oxidation mechanism.

### INTRODUCTION

AFM measurement of the topography of cleaved epitaxial material can be used in many cases to reveal the structure of the material. The number of applications for this type of measurement can be greatly increased if the topographic features related to the epitaxial structure are enhanced in a controlled manner. Many new scanning probe techniques are presently being developed to measure material properties in cleaved devices and epitaxially grown material. These techniques include scanning capacitance microscopy [1][2] (with both AFM and STM), scanning tunneling spectroscopy [3], kelvin probe force microscopy [4], and friction force microscopy [5]. All of these techniques have the capability of making simultaneous or subsequent topographical measurements of the area of interest. Properties of interest include, for example, doping concentrations, compositional variations, and electric potential. In many cases, it would be valuable if the samples could be processed so that the topographic data could be used to provide reference points in the material. Data from the specialized measurement could then be overlaid on the topographic data providing more useful information about the relative positions of the quantities of interest. The step heights required for this type of application should ideally be just large enough to be clearly identified by AFM or STM, on the order of 5 - 10 Å. The oxidation processes and digital etching processes investigated in this paper provide a means for enhancement of the topographic features which are directly related to the layer structure of the material.

The underlying idea of the measurements discussed here is shown schematically in figure 1. The epitaxial material is cleaved and mounted on edge. AFM measurements are taken on the cleaved surface across the epitaxial structure of the material. Differences in the oxidation rates for the materials in different layers result in measurable topography on the surface. For the simple case shown in figure 1, the AlGaAs layer oxidizes more rapidly than the GaAs layer and substrate. Some material structures will have measurable topographic features shortly after initial cleaving and exposure to air. However in many cases, the differences in oxidation rates are not sufficient to produce measurable steps after initial cleaving and oxidation in air. For such samples, the step edges can usually be enhanced by successively removing the oxide and allowing it to regrow a number of times. Successive oxide formation and removal can be used as a digital etching process on many materials because of the self-limiting nature of the oxide formation process [6][7]. When applied to cleaved epitaxial structures, this digital etching process will eventually produce good step edges between adjacent layers for even small differences in the oxidation rates. A greater differential in digital etch rates can be achieved if oxide is selectively removed from one material, for example GaAs and not AlGaAs.

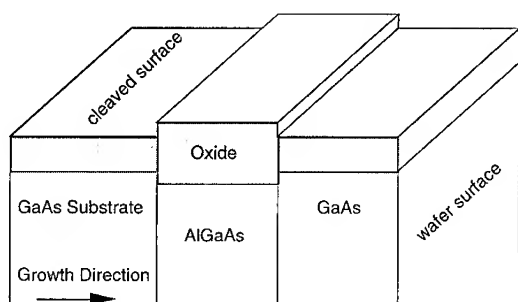


Figure 1. Example of a GaAs/AlGaAs structure after cleaving and oxidation.

Cleaving provides a simple means of cross-sectioning the material, however cleaving does not always produce good, flat surfaces. Often, the cleaving process produces steps on the surface which are not related to the epitaxial structure of the material. This problem seems to arise most often when attempting to cleave very small samples, perhaps due to the increased difficulty of applying even force to the sample, or due to measurement too close to the initiation point of the cleave. There are a few simple ways to identify these cleavage-induced steps. One method is to look at both halves of the cleaved piece. However, locating the exact corresponding spots on both pieces is difficult and time consuming. It is usually simpler to identify this type of step by measurement at different points along the cleaved edge. Cleavage-induced steps seldom run completely parallel to the layer structure of the material, so that the position of the step edges will change in relation to the layer structure or wafer surface. In addition, cleavage-induced steps will usually not change in height with successive digital etching cycles.

## EXPERIMENT AND RESULTS

The typical digital etching cycle used in these experiments consisted of (1) oxidation in air for 20 min. or more, (2) immersion in an acid solution of either hydrochloric acid (HCl) or buffered hydrofluoric acid (BOE) for 1 min., (3) rinse in deionized water (DI) for 1 min., and (4) an  $N_2$  blow dry and 5 min. oven bake at  $90^\circ\text{C}$ . The primary variation in this process for different samples was in the type and strength of the acid solution used for the oxide removal step, and in one case, we varied the oxidation step by immersion in a hydrogen peroxide solution to increase the oxidation rate. AFM images were collected using a Digital Instruments NanoScope II in contact mode with standard silicon nitride cantilevers. Images were processed using NanoScope III software. Offset and tilt were removed using a first order flatten routine. The cross section plots were produced by averaging scan lines across the image which greatly reduces the noise in the measurement.

One of the first samples we studied was the laser structure shown in figure 2. This sample had already been cleaved when we received it, and had been oxidizing for many months. The sample was not treated or processed in any way before imaging. Other measurements on similar laser structures showed the same general topography after one day of oxidation, but with smaller step heights. The regions of higher Al content are always the highest features. Regions of GaAs and InGaAs are seen as a dip in the topography. Subsequent experiments with digital etching indicate that steps like these are due primarily to differences in oxidation depth, rather than to differences in oxide composition or density. It is these differences in oxidation depth which result in topography enhancement after multiple digital etch cycles.

Topography enhancement through digital etching is demonstrated on the GaAs / InGaP structure shown in figure 3. The structure consists of alternating layers of GaAs and lattice-matched InGaP of varying thicknesses and was grown by MOCVD. The thicknesses of the InGaP layers varies from  $50\text{\AA}$  to  $500\text{\AA}$ . Upon initial cleaving and oxidation there was no measurable topography related to the epitaxial structure of the material. After six digital etch cycles

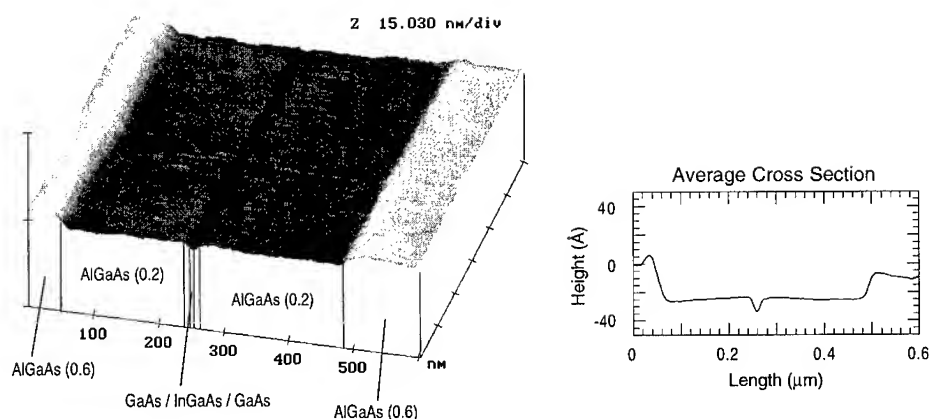


Figure 2. AlGaAs / GaAs / InGaAs laser structure after cleaving and oxidation.

the epitaxial structure of the material was clearly identifiable in AFM images. The digital etch cycle was performed using BOE:DI (1:100) for oxide removal. For this sample the digital etch rate for GaAs was slightly higher than the rate for InGaP and seemed to vary somewhat for different GaAs layers. The variation of etch rate between similar layers may have been caused by some anomaly in this particular sample, such as a slight lattice mismatch or by doping variation. We have not seen this problem in other material structures. The step heights for the image in figure 3 vary from about 5 Å to about 15 Å with the InGaP layers raised.

We performed a number of experiments on specialized GaAs / AlGaAs superlattice structures grown by MBE. The largest of these structures had ten periods of 2000 Å (1000 Å thick layers). Digital etch rate measurements of AlGaAs relative to GaAs were taken on four of these 2000 Å period structures with Al mole fractions of 0.10, 0.25, 0.50, and 0.75. The AFM image in figure 4 is an example of one of these measurements. For this sample the Al mole fraction was 0.50 and the measurement was taken after five digital etch cycles. The oxide removal step was performed using a mixture of HCl:DI (1:1000) for 1 minute. Step height measurements to establish relative digital etch rates were made to the center of adjacent layers as shown on the cross section plot in figure 4.

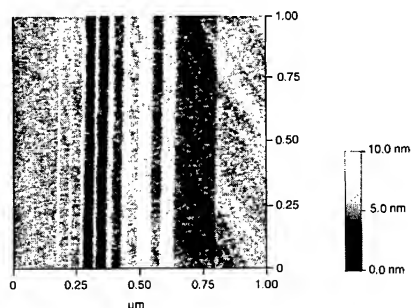


Figure 3. Digitally etched GaAs / InGaP structure. InGaP regions are raised.

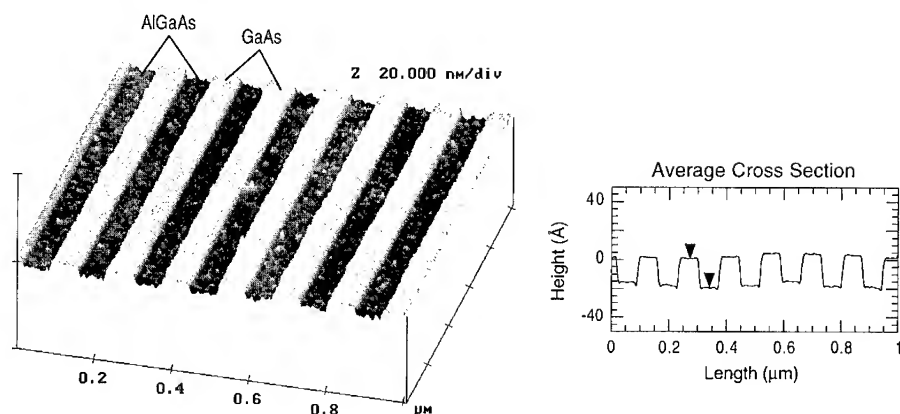


Figure 4. GaAs / AlGaAs (0.5) structure after five digital etching cycles.

The data in figure 5 were compiled from four of the  $2000\text{\AA}$  period structures with different Al mole fractions 0.10, 0.25, 0.50, and 0.75. Step heights between adjacent layers are plotted as a function of the number of digital etch cycles. The oxide removal step for all data in figure 5 was performed using pure deionized water for 2 minutes, and the rinse step was skipped. For the 0.10 and 0.25 Al mole fraction samples, the AlGaAs layers have a higher digital etch rate than the GaAs layers and the height of the AlGaAs layers becomes more negative with respect to the GaAs layers after each digital etch cycle. For the 0.50 and 0.75 Al mole fraction samples, the GaAs layers have a higher digital etch rate than the AlGaAs layers and the step to the AlGaAs layers becomes more

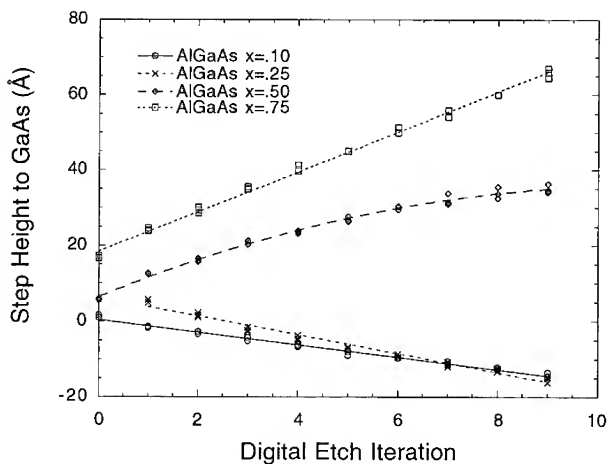


Figure 5. Digital etch rates for AlGaAs relative to GaAs .

positive with each cycle. The initial measurements (digital etch step 0) on these samples and other similar measurements [8] indicate that the oxidation rate for the AlGaAs layers is always greater than for the GaAs layers, and that the oxidation rate in AlGaAs increases monotonically with increasing Al mole fraction. The lower digital etch rate for the higher Al mole fraction samples in this case is explained by lower solubility of the oxides of Al in water than the oxides of Ga and As. In the case of the 0.50 mole fraction sample, after about six cycles the oxide on the AlGaAs layers begins to lose integrity and break down. This breakdown is reflected by the rolling-over of the curve in figure 3, and is explained by gradual removal of the Ga and As oxides from the oxide layer. The 0.75 mole fraction sample has a high enough concentration of Al oxides in the oxide layer for the layer to maintain its structure for nine etch cycles.

For material structures where the differential digital etch rates are small it would be desirable to decrease the number of cycles required and the cycle time by increasing the oxidation rate. One possible method of increasing the oxidation rate is by immersion in a hydrogen peroxide ( $H_2O_2$ ) solution.  $H_2O_2$  oxidation has been used successfully in digital etching of GaAs [6][7] with oxidation times of 1 min. and a digital etch rate around 16Å per cycle. Figure 6 shows a GaAs/AlGaAs HBT structure after treatment in a  $H_2O_2$  solution. The sample was cleaved in air and then immersed in a solution of  $H_2O_2$ :DI (1:50) for 3 min., followed by the normal rinse and dry steps. The bright bands in the image are regions containing AlGaAs and InGaAs. The  $H_2O_2$  treatment leads to significant roughening of the GaAs surface. We have consistently seen this type of surface roughening on cleaved GaAs surfaces after similar  $H_2O_2$  treatments of varying times and ratios. The rough surface greatly diminishes the usefulness of this type of treatment for quantitative measurements, or in conjunction with other types of scanning probe measurements.

## CONCLUSIONS

Different oxidation rates on the surface of cleaved heterostructure layers result in differences in oxide thickness which are directly related to the layer structure of the material. If the oxidation rates for adjacent layers are sufficiently different, the layer structure can be identified in AFM images shortly after the sample has been cleaved in air. For layers with nearly identical oxidation rates, it may not be possible to identify the layer structure after just cleaving the sample. Digital etching has been used to controllably enhance topographic differences between layers with similar oxidation rates. The digital etching process enhances the height differences between heterostructure layers primarily due to differences in oxidation depth of the layers. Topographic enhancement by the digital etching process can also result from variations in oxide solubility for different layers. AFM measurement of the heterostructure layers may be used directly to estimate layer thicknesses, or indirectly to provide reference points for other types of scanning

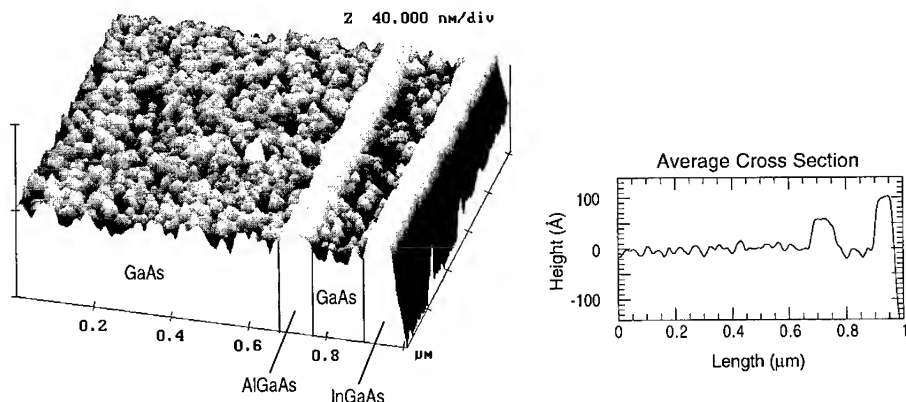


Figure 6. Effects of hydrogen peroxide on cleaved GaAs, AlGaAs, and InGaAs layers.

probe measurements. Cleaved heterostructures also allow for direct AFM measurement of the relative digital etch rates of adjacent layers. The relative digital etch rates are characteristic of the layer material and may be useful for compositional measurements.

#### ACKNOWLEDGMENTS

The authors would like to thank the following people for their support in providing samples and equipment, and for many helpful conversations: C. Bozada, J. Brown, C. Cerny, G. DeSalvo, R. Dettmer, J. Gillespie, C. Havasy, T. Jenkins, K. Nakano, C. Pettiford, T. Quach, J. Sewell, and D. Via. We would also like to thank J. Ehret for growth of the specialized GaAs / AlGaAs structures.

#### REFERENCES

1. J. A. Slinkman "Lateral Dopant Profiling in MOS Structures on a 100nm Scale Using Scanning Capacitance Microscopy" *IEEE International Electron Devices Meeting* 1990, 73.
2. A.N. Erickson, L. Sadwick, G. Neubauer, J. Kopanski, D. Adderton, M. Rodgers "Quantitative Scanning Capacitance Microscopy Analysis of Two-Dimensional Dopant Concentrations at Nanoscale Dimensions" *J. of Elec. Mat.* 1996, 25(2), 301.
3. R. M. Feenstra, E. T. Yu, J. M. Woodall, P. D. Kirchner, C. J. Lin, and G. D. Pettit "Cross-sectional imaging and spectroscopy of GaAs doping superlattices by scanning tunneling microscopy" *Appl. Phys. Lett.* 1992, 61(7), 795.
4. M. Arakawa, S. Kishimoto, T. Mizutani "Kelvin Probe Force Microscopy for Potential Distribution Measurement of Cleaved Surface of GaAs Devices" *Extended Abstracts of the 1996 International Conference on Solid State Devices and Materials, Yokohama* 1996, 100.
5. J. Tamayo, L. Gonzalez, Y. Gonzalez, R. Garcia "Compositional mapping of semiconductor structures by friction force microscopy" *Appl. Phys. Lett.* 1996, 68(16), 2297.
6. G. DeSalvo, J. Ebel, D. Look, C. Bozada, C. Cerny, R. Dettmer, J. Gillespie, C. Havasy, T. Jenkins, C. Pettiford, T. Quach, J. Sewell, and D. Via "Wet Chemical Digital Etching of GaAs at Room Temperature" submitted to the Journal of the Electrochemical Society.
7. G. DeSalvo, J. Ebel, C. Bozada, C. Cerny, R. Dettmer, J. Gillespie, C. Havasy, T. Jenkins, K. Nakano, C. Pettiford, T. Quach, J. Sewell, and G. D. Via "Controlled Digital Etching of GaAs for Precise Gate Recess Formation in MESFET, HEMT, and pHEMT Device Fabrication" *International Conference on GaAs Manufacturing Technology* 1996, 29.
8. F. Reinhardt, B. Dwir, and E. Kapon "Oxidation of GaAs/AlGaAs heterostructures studied by atomic force microscopy in air" *Appl. Phys. Lett.* 1996, 68(22), 3168.



## ELECTROCHEMICAL DEPOSITION OF METALS ON SEMICONDUCTORS

Gerko Oskam, John G. Long, Maria Nikolova, and Peter C. Searson  
Department of Materials Science and Engineering, The Johns Hopkins University  
Baltimore, MD 21218, gerko@jhunix.hcf.jhu.edu

### ABSTRACT

The general concepts governing the electrochemical deposition of metal films on semiconductors are discussed, and recent results on the fabrication of Schottky junctions consisting of silicon electrodeposited with platinum, copper and gold are presented. In order to obtain good adherent metal films, the density of nuclei should be high and the films should be grown at low current densities where the charge transfer process is rate limiting. This situation can be realized using potential controlled electrochemical deposition. For metal deposition on silicon, the surface should be pretreated in HF to dissolve the oxide layer. Furthermore, the surface should be stable during deposition which can be achieved by tailoring the deposition solutions and by using electrochemical deposition at negative potentials. It is shown that by using this approach, n-type silicon / Pt, Au, and Cu Schottky junctions can be fabricated of a quality comparable to that of junctions prepared by sputter and vapor deposition techniques.

### INTRODUCTION

Electrochemical deposition of metals and alloys onto metallic substrates plays an important role in many modern technologies. For example, in the electronics industry electrochemical and electroless deposition are widely used for applications such as copper printed circuit boards, through hole plating, multilayer read/write heads, and thin film magnetic recording media [1,2]. In contrast, the electrochemical deposition of metal films onto semiconductors has been largely overlooked despite the technological importance of metal / semiconductor contacts. Electrochemical deposition has several important advantages over other methods since it is an ambient pressure and temperature technique with low power requirements and can be used to deposit onto large areas and complex geometries.

The electrochemical deposition of metals on semiconductors generally follows a three dimensional nucleation and growth mechanism, resulting in the formation of metal islands with a density of  $10^8 - 10^{11} \text{ cm}^{-2}$  [3-5]. This feature has been exploited for electrocatalysis; for instance, platinum islands on p-InP and p-Si have been shown to enhance the hydrogen evolution rate and photoelectrochemical cells with efficiencies up to 12% have been fabricated [6-8]. Palladium islands have been shown to catalyze electroless nickel deposition onto  $\text{TiO}_2$  and silicon substrates [9,10].

In contrast, the electrochemical deposition of continuous metal films on silicon has received little attention. Various authors have shown that high quality Schottky diodes can be formed by

electrochemical deposition of metals onto II-VI and III-V semiconductors [11-14]. In many cases, the barrier heights of electrochemically fabricated Schottky junctions were found to be higher than those prepared by physical deposition techniques due to the presence of a thin interfacial layer.

In this paper, the electrochemical deposition of metal films on silicon is reported. A key feature for the fabrication of good quality, adherent metal films is the pretreatment of the silicon wafer, and the design of deposition solutions and conditions such that the formation of an oxide film is prevented.

## BACKGROUND

Figure 1 illustrates possible mechanisms for metal deposition on an n-type semiconductor. For convenience the metal ion is considered as an acceptor state in the Gerischer model where the temporal distribution of energy levels follows a Gaussian distribution [15,16]. The mid-point between the acceptor states and donor states (not shown) corresponds to the equilibrium potential. Figure 1a shows the situation for a metal / metal ion couple with a relatively negative equilibrium potential (e.g. a transition metal) that exhibits large overlap with the conduction band edge. In this case, if the electron concentration in the conduction band at the surface is sufficiently high, electrons can be transferred to the metal ion in solution resulting in deposition of the metal. For deposition on p-type substrates, illumination can be utilized to generate a sufficiently large density of electrons in the conduction band.

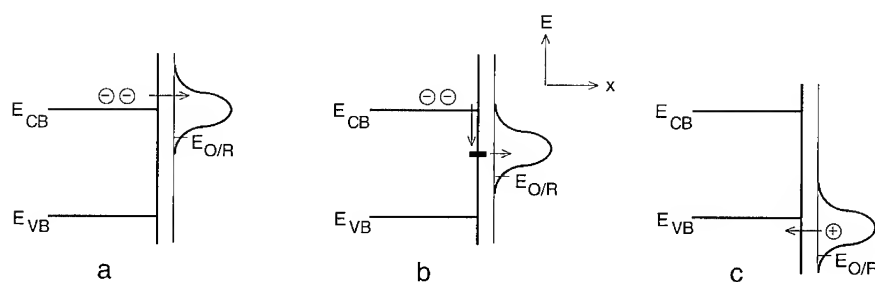


Figure 1. Energy band diagrams illustrating possible mechanisms for metal deposition on an n-type semiconductor. (a) Electron injection into a metal / metal ion couple with a negative equilibrium potential, (b) electron injection from surface states, and (c) hole injection from a metal / metal ion couple with a more positive equilibrium potential.

In Figure 1b, electrons are transferred to the metal ion from surface states in the bandgap of the semiconductor. Typical surface state densities for silicon are on the order of  $10^{10} - 10^{12} \text{ cm}^{-2}$  [17,18] which may be sufficiently large to influence the deposition process. Furthermore, several authors have suggested that metal islands can be treated in terms of surface states, thus explaining the catalytic properties of the islands [3,7,19,20]. As a consequence, the description of further deposition after the nucleation step may require the incorporation of the process shown in Figure

1b. The kinetics of charge transfer from surface states (which are in equilibrium with the conduction band) to the solution may be faster than direct transfer from the conduction band since the 'activation energy' for this process does not include the band bending in the semiconductor. Figure 1c shows the situation for a metal / metal ion couple with a positive equilibrium potential (e.g. a noble metal) where the acceptor state overlaps with the valence band of the semiconductor. In this case, holes can be injected directly into the valence band. Under open circuit conditions, the holes can be consumed by oxidation and / or etching of the semiconductor. This complicates the deposition process and often leads to poor quality films. For silicon noble metals such as gold and platinum can be deposited by this process, however, roughening of the silicon surface has been reported under these conditions [21].

When a metal film is formed on a semiconductor, the electronic properties of the semiconductor / metal contact strongly influence the electrochemical properties of the electrode. If a high-barrier Schottky junction on is formed on an n-type semiconductor, the metal layer cannot be dissolved in the dark as holes in the valence band are absent; the barrier for electron excitation from the metal into the conduction band is too high. If an ohmic or low barrier contact is formed, anodic polarization results in dissolution of the metal film; an example is the InP / In contact.

Many metals can be deposited from various complexes with different redox potentials. In general, the position of the band edges in aqueous solutions is mainly determined by the pH, usually following approximately 60 mV per pH unit. Hence, both the position of the band edges and the value of the redox couple potential can be varied which allows us to control the deposition process. For instance, gold can be either deposited from a  $\text{Au}^+$  solution at pH 2 ( $E_0 \approx 1.5$  V(SCE)) or from a  $\text{Au}(\text{CN})_2^-$  solution at pH 14 ( $E_0 = -0.85$  V(SCE)). In the first case, the valence band edge is at about 0.7 V(SCE) and hole injection is the dominant process, hence, electroless deposition can be achieved (Figure 1c). In the second solution, the electron acceptor levels of the  $\text{Au}(\text{CN})_2^-$  are just below the conduction band edge, which is at about -1.1 V(SCE), and electrons from the conduction band are needed for deposition (Figure 1a). Since both cases result in the same Schottky junction, it is clear that the process of nucleation and growth leads to a dramatic change in the energetics and kinetics of the semiconductor electrode. It has been shown previously that the presence of a metal layer on GaAs and InP electrodes influences the electrochemical properties, and that the relative rates of charge transfer between metal and solution, and between metal and semiconductor determine the overall energetics of the system [14,22].

The morphology of metal films on semiconductor surfaces is dependent on the mechanism of the nucleation process. Nucleation may be instantaneous or progressive, and the growth process can be kinetically or diffusion limited leading to many different deposition mechanisms. Mathematical treatments of specific cases have been reported although the complex three dimensional structure of the semiconductor / metal islands / solution system precludes analytical solutions from which quantitative information such as the nuclei density can be obtained [23].

## METAL DEPOSITION ON SILICON

Figure 2 shows a current - potential curve for (100) oriented n-type silicon ( $p = 4 \Omega \text{ cm}$ ) in 10 mM  $\text{KAu}(\text{CN})_2 + 1 \text{ M KCN}$  (pH 14) in the dark; the dotted line shows the current - potential curve

in 1 M KCN (pH 14). In the KCN solution, hydrogen evolution starts at about -1.7 V(SCE). In the  $\text{KAu}(\text{CN})_2$  solution, the current increases sharply at about -1.3 V(SCE) due to the nucleation and growth of gold on silicon. The current goes through a maximum as diffusion of  $\text{Au}(\text{CN})_2^-$  to the surface becomes rate limiting and at more negative potentials hydrogen evolution is observed. The reverse scan is markedly different and the current corresponding to gold deposition stops only at -1.0 V(SCE). Consequently, a nucleation barrier of about 0.3 V is observed.

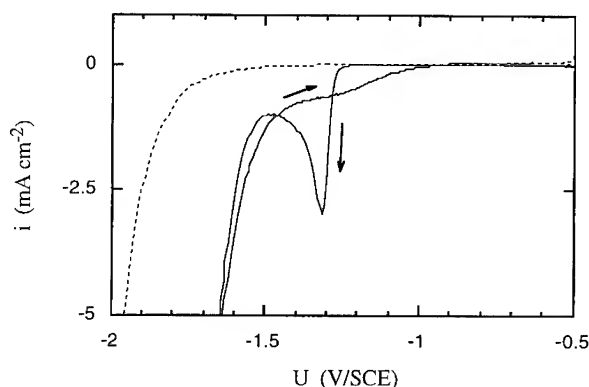


Figure 2: Current - potential curves of n-Si in 1 M KCN (pH 14) (dotted line) and in 10 mM  $\text{KAu}(\text{CN})_2$  + 1 M KCN (pH 14) (solid line); the sweep as started at -0.5 V(SCE) and the arrows show the scan direction. The scan rate was  $10 \text{ mV s}^{-1}$ .

The reverse scan does not show an anodic peak which confirms that electrochemical stripping of the gold layer cannot be achieved in the dark. This is due to the large barrier height of about 0.8 eV for an n-Si / Au junction: in order to dissolve the gold, electrons must be excited from the gold Fermi level into the conduction band which is extremely slow. In some cases, depending on the metal and the solution composition, the metal layer can be dissolved chemically. Scherb and Kolb [24] used reflectance spectroscopy in conjunction with electrochemical measurements to show that an electrodeposited copper layer on n-GaAs is chemically dissolved in a chloride solution while this does not occur in a sulfate solution. For the work reported here, this effect is not expected and we did not observe any chemical dissolution of deposited metal layers. In the dark, gold cannot be deposited from this solution onto p-type silicon but under illumination gold deposition is realized. These results confirm that deposition proceeds through electron transfer from the conduction band (or via surface states), which agrees with expectations as the redox potential of the  $\text{Au}(\text{CN})_2^- / \text{Au}$  couple is situated close to the energy of the conduction band edge at the surface ( $\approx -1.1 \text{ V(SCE)}$ ). Although a gold layer is present on the surface after several potential sweeps, as shown in Figure 2, the adhesion was generally poor. In order to obtain continuous, adherent films, special care must be taken to ensure a large density of nuclei and a kinetically limited deposition rate for the growth of the film.

Figure 3 shows a series of current transients for potential steps from -1.1 V(SCE), where no

deposition occurs on a bare silicon surface, to potentials in the range -1.45 V(SCE) to -1.70 V(SCE). The transients show a charging peak at  $t < 1$  ms which is followed by the nucleation and growth current. For clarity, the charging peaks are not shown in the Figure. For deposition potentials in the range from -1.30 V(SCE) to -1.55 V(SCE) the current at  $t > 1$  s is limited by diffusion of  $\text{Au}(\text{CN})_2^-$  to the surface, while at potentials more negative than -1.55 V(SCE) an additional current due to hydrogen evolution is observed. After nucleation, the current corresponding to gold deposition is kinetically limited in the potential range from -1.10 V(SCE) to -1.25 V(SCE). Qualitatively, the transients compare well with a model in which three dimensional diffusion to small, isolated gold nuclei is followed by one dimensional diffusion limited growth [25].

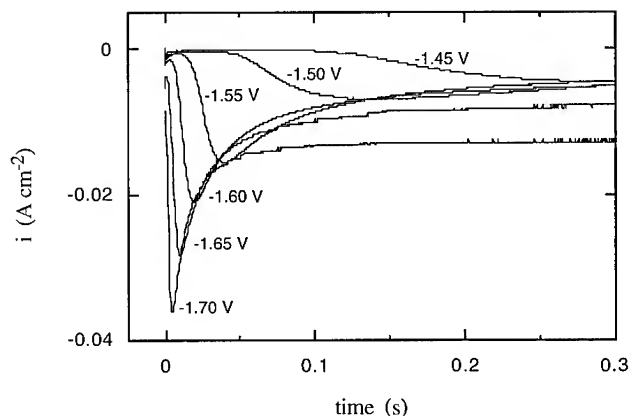


Figure 3: Current - time transients as a function of the applied potential step for bare silicon electrodes in 10 mM  $\text{KAu}(\text{CN})_2$  + 1 M KCN (pH 14). The silicon electrode was first polarized at -1.1 V(SCE) where no gold deposition occurs.

The shape of the transients can be used to distinguish between instantaneous and progressive nucleation. A convenient way to analyze the data is to plot the transients using the reduced dimensionless parameters ( $i^2 / i_{\text{max}}^2$ ) versus ( $t / t_{\text{max}}$ ). Scharifker and Hills [25,26] calculated the transient response to a potential pulse for both instantaneous and progressive nucleation for a diffusion controlled growth mechanism and they obtained the following expressions:

for instantaneous nucleation:

$$\frac{i^2}{i_{\text{max}}^2} = 1.9542 \left( \frac{t_{\text{max}}}{t} \right) \left[ 1 - \exp \left( -1.2564 \frac{t}{t_{\text{max}}} \right) \right]^2 \quad \{1\}$$

and for progressive nucleation:

deposition at open circuit can be achieved (Figure 1c). Since the films deposited under open circuit conditions were poor, we employed the electrochemical method described above which resulted in the formation of dense, adherent platinum layers. This is probably due to slow kinetics for hole injection since the redox potential of the  $\text{Pt} / \text{PtCl}_6^{2-}$  couple is close to the valence band edge at the surface. As a consequence, electrochemical deposition at negative potentials may occur either directly or through surface states if the density of electrons at the surface is sufficiently high. In this case, injected holes are likely to recombine with electrons from the conduction band thus stabilizing the silicon surface. Figure 3 shows a cross-sectional SEM picture of an n-Si / Pt junction fabricated using the double potential pulse method as described above. It can be concluded that a dense, 10  $\mu\text{m}$  thick platinum film was formed with good adhesion to the silicon substrate.

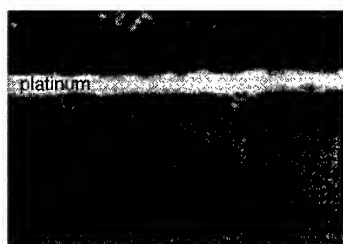


Figure 4. SEM cross-section of a 10  $\mu\text{m}$  thick electrochemically deposited platinum film on n-type silicon.

#### CHARACTERIZATION OF Si / METAL JUNCTIONS

The three metals used to prepare continuous, adherent films on n-type silicon all resulted in the formation of a Schottky junction with a high barrier. The electrical properties of Schottky junctions are dependent on the quality of the interface and on the presence of any interfacial layer. Impedance spectroscopy in the reverse bias regime in conjunction with current - voltage measurements in the forward regime are generally used to determine the barrier height of the junction. The forward current - voltage curve also gives information on the ideality of the interface as the current should increase by 60 mV per decade. In the reverse bias regime, the capacitance of the semiconductor is related to the applied potential according to the Mott-Schottky relation [27]:

$$C_{sc}^{-2} = \frac{2}{e \epsilon \epsilon_0 N_D} \left( U - U_{fb} - \frac{k T}{e} \right) \quad \{3\}$$

where  $C_{sc}$  is the capacitance of the space charge layer,  $e$  is the electronic charge,  $N_D$  is the donor density,  $U$  is the applied potential and  $U_{fb}$  is the flat band potential. The barrier height can be obtained from the flat band potential by correcting for the energy difference between the conduction band edge and the Fermi level of the silicon. Applying thermionic emission theory, the current - voltage curve is described by:

$$\frac{i^2}{i_{\max}^2} = 1.2254 \left( \frac{t_{\max}}{t} \right) \left[ 1 - \exp \left( -2.3367 \frac{t^2}{t_{\max}^2} \right) \right]^2 \quad \{2\}$$

where  $i_{\max}$  and  $t_{\max}$  are the current and the time at the maximum, respectively. For the assumptions underlying these theoretical expressions the reader is referred to refs. 25 and 26.

Equations {1} and {2} are plotted in Figure 5, and three transients from Figure 3 re-plotted in reduced form are included. It is clear that the nucleation of gold onto silicon follows a progressive nucleation mechanism in the  $\text{KAu(CN)}_2 + \text{KCN}$  solution. From the maxima in the transients shown in Figure 5 the diffusion coefficient of  $\text{Au(CN)}_2^-$  was determined to be about  $3 \times 10^{-5} \text{ cm}^2 \text{ s}^{-1}$  [25,26]. In the framework of this model, the observation that the time to reach the maximum becomes increasingly smaller upon applying more negative potentials is indicative of an increasing density of nuclei, which is commonly observed (see [24]).

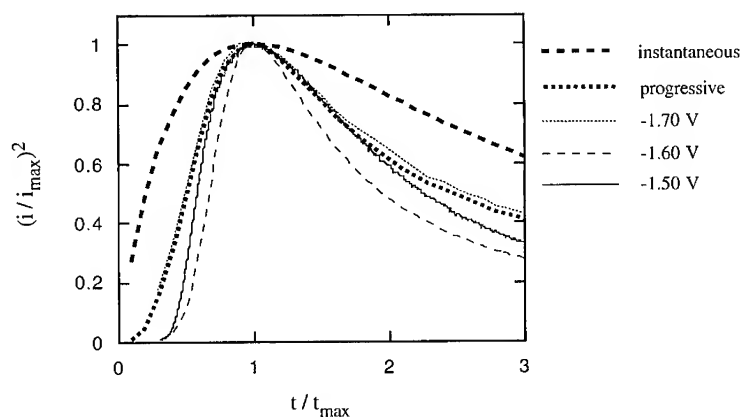


Figure 5: Analysis of the current - time transients shown in Figure 3 using reduced dimensionless parameters (see equations {1} and {2}).

## FILM FORMATION

Metal films were electrochemically deposited onto (100) oriented n-type silicon ( $\rho = 4 \Omega \text{ cm}$ ) using a double potential step method: first, the potential was stepped from a potential where no metal deposition occurs and where the silicon surface is stable (i.e. generally slightly negative of the open circuit potential) to a potential where a high density of nuclei is formed and, second, the potential was stepped to a potential where the growth rate is kinetically limited. The first pulse was generally around 30 ms and the second pulse lasted for about 500 s (depending on the concentration of the metal ion).

Platinum and copper layers were prepared by a similar method. The case of platinum deposition is more complicated since  $\text{PtCl}_6^{2-}$  injects holes into the valence band and electroless

$$j = -j_0 \exp\left(-\frac{eU}{nkT}\right) \left\{ 1 - \exp\left(\frac{eU}{kT}\right) \right\} \quad \text{with:} \quad j_0 = A^* T^2 \exp\left(\frac{-\phi_B}{kT}\right) \quad \{4\}$$

where  $j$  is the current density,  $j_0$  is the saturation current density,  $n$  is the ideality factor,  $A^*$  is the reduced Richardson constant, and  $\phi_B$  is the barrier height.

Good Schottky junctions must have an ideality factor of  $n = 1.0 - 1.2$ , and the current at positive bias should not be much larger than the saturation current density as obtained from extrapolation of the forward current - voltage curve to a bias of 0 V. These characteristics provide an opportunity to determine the electronic properties of the junctions prepared by electrochemical deposition.

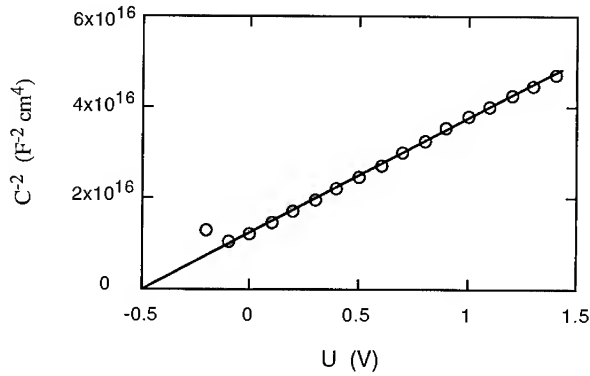


Figure 6: Mott-Schottky plot of an electrochemically fabricated n-Si / Pt contact. The modulation frequency shown is 10 kHz

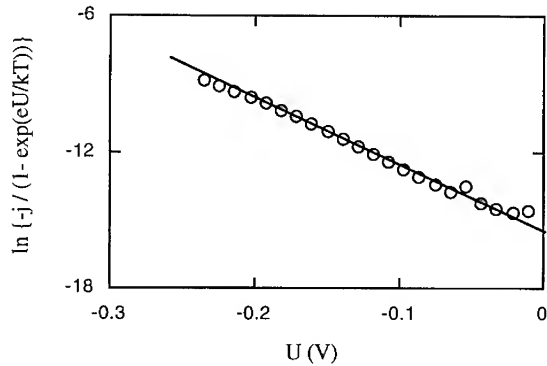


Figure 7: Forward current - voltage curve in a semilogarithmic plot (see equation {4}) for the same n-Si / Pt junction as used for Figure 4a.



Figures 6 and 7 show the results of impedance and current measurements as a function of the bias of an electrochemically fabricated n-Si / Pt contact. Figure 6 shows that  $C^{-2}$  versus  $U$  is linear with a slope corresponding to the donor density (equation {3}), and from the intercept with the potential axis and the donor density a barrier height of 0.81 eV is obtained. This value is in good agreement with values reported for junctions fabricated by vapor deposition of the platinum layer [27]. Figure 7 shows the forward current - voltage curve in a semi-logarithmic plot and it is seen that a straight line with an inverse slope of 67 mV per decade is obtained which leads to an ideality factor of 1.12. The intercept at zero bias gives the saturation current density and by using equation {4} a barrier height of 0.82 eV is found, which is in good agreement with the value obtained from the impedance measurements. The current in the reverse bias regime (not shown) was within a factor 2 of the saturation current density up to a voltage of 1.5 V, indicating that the interface is of good electronic quality. Similar results were obtained on n-Si / Au and n-Si / Cu contacts prepared by electrochemical deposition.

## CONCLUSIONS

It has been shown that Schottky junctions of high quality can be prepared using electrochemical deposition of thick metal films on silicon. In order to obtain good adherent films, a large density of metal nuclei is needed and the film should be grown at a rate where the charge transfer kinetics are limiting. Using this method, gold, copper, and platinum films were successfully electro-deposited onto n-type silicon.

## ACKNOWLEDGEMENTS

This work was supported in part by the National Science Foundation under grant DMR-9202645. JGL acknowledges support from the Undergraduate Research Opportunities program provided by the Whiting School of Engineering at The Johns Hopkins University.

## REFERENCES

1. L. T. Romankiw and T. A. Palumbo, in: "Electrodeposition Technology, Theory and Practice", Eds. L. T. Romankiw and D. R. Turner, Electrochemical Society, Pennington, NJ (1988) p.13.
2. P. C. Searson and T. P. Moffat, "Electrochemical Surface Modification and Materials Processing", *Critical Reviews in Surface Chemistry*, **3**, 171 (1994).
3. P. Allongue and E. Souteyrand, *J. Electroanal. Chem.* **269**, 361 (1989).
4. P. Allongue and E. Souteyrand, *J. Electroanal. Chem.* **286**, 217 (1990).
5. P. Allongue and E. Souteyrand, *J. Electroanal. Chem.* **362**, 79 (1993).
6. A. Heller, E. Aharon-Shalom, W. A. Bonner, and B. Miller, *J. Am. Chem. Soc.* **104**, 6942 (1982).
7. Y. Nakato, K. Ueda, H. Yano, and H. Tsubomura, *J. Phys. Chem.* **92**, 2316 (1988).
8. M. Szklarczyk and J. O'M. Bockris, *J. Phys. Chem.* **88**, 1808 (1984).

9. J. W. M. Jacobs, *J. Phys. Chem.* **90**, 6507 (1986).
10. A. T. M. van der Putten, J. W. G. de Bakker, and L. G. J. Fokkink, *J. Electrochem. Soc.* **139**, 3475 (1992).
11. P. Bindra, H. Gerischer, and D. M. Kolb, *J. Electrochem. Soc.* **124**, 1012 (1977).
12. R. Reineke and R. Memming, *Surf. Sci.* **192**, 66 (1987).
13. P. Allongue and E. Souteyrand, *J. Vac. Sci. Technol.* **B 5**, 1644 (1987).
14. G. Oskam, L. Bart, D. Vanmaekelbergh, and J. J. Kelly, *J. Appl. Phys.* **74**, 3238 (1993).
15. H. Gerischer, in: "Physical Chemistry: An Advanced Treatise", Vol. 9A, Ed. H. Eyring, Academic Press, New York (1970), p. 463.
16. H. Gerischer, *Electrochim. Acta* **35**, 1677 (1990).
17. G. Oskam, P. M. Hoffmann, and P. C. Searson, *Phys. Rev. Lett.* **76**, 1521 (1996).
18. G. Oskam, P. M. Hoffmann, J. C. Schmidt, and P. C. Searson, *J. Phys. Chem.* **100**, 1801 (1996).
19. G. Oskam, D. Vanmaekelbergh, and J. J. Kelly, *Electrochim. Acta* **38**, 301 (1993).
20. J.-N. Chazalviel and M. Stefenel, *Surf. Sci.* **134**, 865 (1983).
21. P. Gorostiza, J. Servat, J. R. Morante, and F. Sanz, *Thin Solid Films* **275**, 12 (1996).
22. G. Oskam, D. Vanmaekelbergh, and J. J. Kelly, *Electrochim. Acta* **38**, 1115 (1993).
23. see e.g.: "Instrumental Methods in Electrochemistry", Southampton Electrochemistry Group, Ellis Horwood Series in Physical Chemistry (1990), Chapter 9.
24. G. Scherb and D. M. Kolb, *J. Electroanal. Chem.* **396**, 151 (1995).
25. G. Gunawardena, G. Hills, I. Montenegro, and B. Scharifker, *J. Electroanal. Chem.* **138**, 225 (1982).
26. B. R. Scharifker and G. J. Hills, *Electrochim. Acta* **28**, 879 (1983).
27. E. H. Rhoderick and R. H. Williams, "Metal-Semiconductor Contacts", Oxford Science Publications, Clarendon Press, Oxford (1988).

## DISCRETE METAL DEPOSITION ON HYDROGEN TERMINATED SILICON SURFACES: KINETICS, MORPHOLOGIES AND SENSOR APPLICATIONS

Oliver Chyan\*, Jin-Jian Chen, Junjun Wu, Steve Chien, Min Liu,  
Department of Chemistry, University of North Texas, Denton, TX 76203,  
\* E-mail: Chyan@CAS1.UNT.EDU

### ABSTRACT

The presence of ultra-trace (as low as  $10^{10}$  -  $10^{13}$  atoms/cm<sup>2</sup>) quantities of metal contaminants on silicon substrates is well known to adversely affect the electrical properties of the silicon based microelectronic devices. In this paper, we report our most recent experimental findings on the trace metal deposition mechanisms and its interplays with silicon substrate surface properties at specific chemical environments. The emphases were on the deposition kinetics and morphology, especially at the early stage of metal out-plating process. For instance, our atomic force microscopy results revealed that the Cu deposition on H-Si(100) surface was dominated by nucleation of nanometer-sized Cu nuclei at the initial stage (less than 60 seconds). The growth of the existing Cu nuclei was suppressed for the initial nucleation period until all the nucleation sites were consumed. The number of nucleation sites were found to closely relate to wafer intrinsic properties and solution compositions. A novel sensor which provides direct detection of part-per-trillion level of metal ion impurities in wet cleaning solutions will also be presented.

### INTRODUCTION

Wet chemical cleaning process<sup>1</sup> involved various acids/bases and oxidants is generally the critical first step to prepare ultra-clean silicon wafers for the fabrication of Ultra Large Scale Integrated (ULSI) silicon circuits, such as 256-megabit DRAM devices. Although microelectronic industries have made tremendous efforts to minimize the contamination by carefully selecting and configuring the fabrication process, in reality, identification and elimination of potential contamination sources still receive the top priority in the quality control to ensure the device performance, reliability and product yield. In the past, efforts of contamination control have been mainly directed on reducing the metallic levels across the board in process chemicals and wafer handling components. However, this method may not be effective due to the fact that wide variety of chemicals were used to perform different tasks of etching, cleaning and passivation in the microfabrication processes. For example, Fe impurity is the main concern in the highly alkaline and oxidative cleaning solutions ( $\text{H}_2\text{O}_2/\text{NH}_4\text{OH}/\text{H}_2\text{O}$ ) used in removing adsorbed organics from silicon wafer surfaces. In comparison, all the noble metal ions like  $\text{Ag}^{+1}$ ,  $\text{Cu}^{+2}$ ,  $\text{Au}^{+3}$ ,  $\text{Pt}^{+2}$ , and  $\text{Pd}^{+2}$  etc. will deposit on silicon wafer surface when submerged in HF solution. Therefore, understanding the deposition mechanisms of various metal contaminants and their interplays with silicon substrate surface properties at specific chemical environments have received a lot of research attention lately.

HF solution is widely used to remove the surface oxide layer before the critical thermal gate oxide growth step. The HF treated Si surface has been shown to terminate by Hydrogen and exhibit surprisingly stability toward air oxidation<sup>2,3</sup>. Graf et al.<sup>3</sup> have demonstrated that a monolayer coverage of oxygen ( $7 \times 10^{14}$  atom/cm<sup>2</sup>) is barely reached after seven days of storage in air. However, the chemical stability of the HF-etched Si surface can be abruptly eliminated by a trace amount of metal ion impurities, like Ag<sup>+</sup>, Cu<sup>2+</sup>, Au<sup>3+</sup>, Pt<sup>2+</sup>, and Pd<sup>2+</sup> etc., present in HF-related etching solutions.<sup>1</sup> For example, at  $10^{11}$  -  $10^{13}$  atoms/cm<sup>2</sup> level, degradation of the gate oxide integrity as well as crystal defects has been observed.<sup>4,5</sup> Although the freshly replenished chemical baths are generally very pure, as the device fabrication process proceeded, the purity of chemicals will inevitably degrade due to the accumulation of contamination from wafer handling equipments, wafers itself and chemical containers, etc. This imposes a challenging problem on the overall microfabrication process control. Therefore, the development of a practical sensor for on-line monitoring ultra-trace metallic contaminants in the processing chemicals is highly desirable to ensure the highest purity of the processing chemicals at the point of use.

In the present work, we report a time dependent study of the interaction between Cu<sup>2+</sup> ions and HF-treated silicon surfaces using atomic force microscope (AFM). The relatively short deposition durations (10 to 100 seconds) were purposely selected to reveal the nucleation and growth of Cu deposits at the initial stage of the deposition process. We utilized an AFM volume-integration approach to demonstrate that the metal out-plating kinetics can be extracted directly from the AFM topographical images of Cu deposits on HF-etched silicon surfaces. Furthermore, we also investigated the electrochemical potential developed in the metal deposited Si wafer/HF solution interface and demonstrated a novel sensor for extremely low level of metal ion impurities in HF using a silicon based sensing electrode. A unique feature of this sensor is that part-per-trillion detecting sensitivity can be achieved via the use of a sensing electrode derived directly from the regular silicon wafer. Thereby, the new Si-based sensing methodology described here can have an important advantage to be made completely compatible and incorporated into the actual silicon device fabrication sequences.

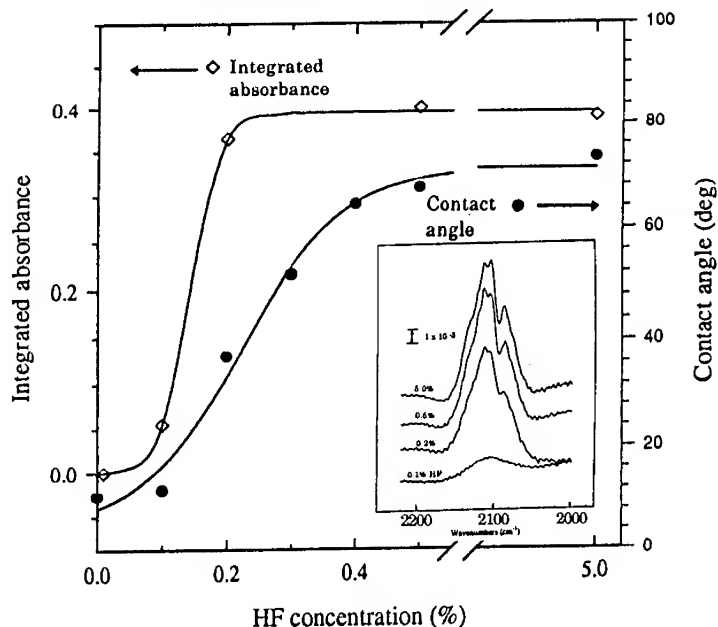
## EXPERIMENTAL

The silicon wafer samples (boron doped, Texas Instruments) were cleaned in H<sub>2</sub>O:NH<sub>4</sub>OH:H<sub>2</sub>O<sub>2</sub> = 5:1:1 and then HF etched by dipping into low particulate, electronic grade hydrofluoric acid (5.0 wt. %) for 60 seconds. The multiple internal reflection FTIR spectra from the HF-treated silicon surface were measured using a Bruker EQUINOX 55 spectrometer with a MCT detector (High D\*, narrow band, EG&G). Following several rinses with ultra-pure water and air dry, the hydrophobic Si samples were placed into 5.10 ppm Cu<sup>2+</sup> (CuSO<sub>4</sub>·5H<sub>2</sub>O, 99.999%, AESAR)/5.0% HF solution at 25° C for various deposition times. The Cu<sup>2+</sup>/HF treated silicon samples were characterized by the AFM (Nanoscope III, Digital Instruments). The Cu contents per surface area were determined by inductively coupled plasma mass spectroscopy (ICP/MS, Fisons PQS model) and graphite furnace atomic absorption spectroscopy (GFAAS, Varian SpectraAA 330/400). The electrical contact of

silicon sensing electrode was made to the backside of the silicon chip using Ga/In eutectic (99.99%, AESAR). The open circuit potential of the silicon electrode was measured with respect to a double junction standard Ag/AgCl reference electrode using a computer interfaced, high input impedance potentiometer under normal room light condition. The  $\text{Ag}^+$  content in the prepared solutions were independently verified by ICP/MS and GFAAS. Preceding each sample preparation, all Teflon labware was boiled in fresh 10%  $\text{HNO}_3$  (aq) three times for 30 minutes, followed by thorough rinsing with ultra-pure water.

## RESULTS AND DISCUSSION

**Hydrogen termination on Si(100) surface.**-- Silicon surface is easily oxidized when exposed to air to form a layer of thin silicon oxide (30~50 Å). HF etching effectively removes surface oxide and terminate the silicon surface with hydrogen. The extent of hydrogen termination can be monitored by either water contact angle and FTIR measurements.<sup>6</sup> Figure 1 show the effects of HF concentrations to the measured water contact angles and integrated silicon hydride absorbance from silicon surface after one minute HF etching. The integrated absorbance represents the total infrared absorbance contributed from the silicon dihydride and silicon monohydride on silicon surface as shown in the Figure 1 insert. The leveling of both water contact angle and integrated absorbance indicated the completion of the hydrogen passivation. For all the following experiments, the completely hydrogen terminated silicon surface [H-Si(100)] with large contact angle of  $68 \pm 3^\circ$  was used as the standard substrate for the discrete metal deposition studies.



**Discrete nanoscale Cu deposition on H-Si(100) surface.**-- The HF-etched Si(100) surface is not atomic smooth with a mean roughness of ca 0.15 nm as measured by the atomic force microscopy. The H-Si(100) surface without metal contamination is featureless. However, subsequent dipping into  $\text{Cu}^{2+}/\text{HF}$  solution produces rougher terrains which are covered by predominantly segregated nanometer-sized Cu nuclei deposits.<sup>7</sup> Further AFM topographical analyses reveal that the number of Cu nuclei initially increases rapidly with deposition time up to 60 seconds, as illustrated in Figure 2, after which it reaches a constant plateau at about  $1.1 \times 10^{10}$  nuclei/cm<sup>2</sup>.

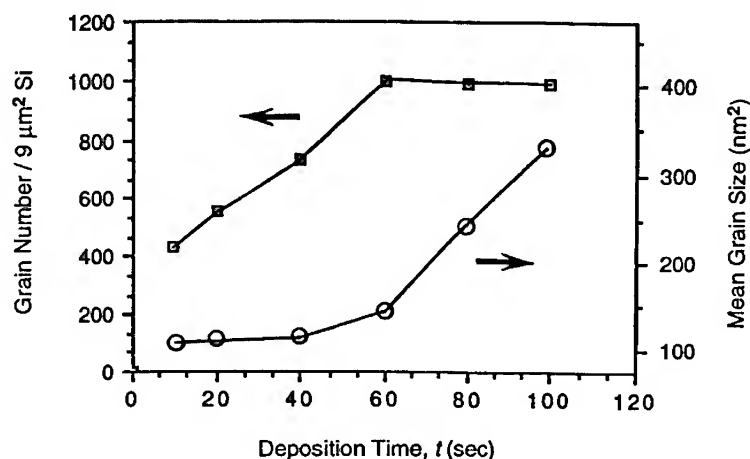


Figure 2: Cu deposits nucleation number and size vs. deposition time.

Analyses of the deposited Cu nuclei size distribution also reveal that the silicon surfaces was initially (10-40 seconds) covered mostly by smaller Cu deposits (diameter < 15 nm). After 60 seconds of deposition time, a noticeable size increase of Cu deposits is observed. The AFM results indicate the nucleation process dominates the initial stage (< 60 seconds) of Cu deposition and that nucleation preferentially originates from a finite number of nucleation sites on the HF treated silicon wafer surfaces. Consequently, the growth of the existing Cu nuclei is suppressed for the initial nucleation period until all the nucleation sites are consumed.

**Deposition kinetics.** -- Next, we explored the deposition kinetics of the  $\text{Cu}^{2+}/\text{H-Si}(100)$  system through two different approaches. First approach relies on the relationship of the AFM integrated volume ( $V_{\text{Cu}}$ ) of Cu nanodeposits with respect to the deposition time ( $t$ ). Second approach measures the mass of Cu nanodeposits ( $M_{\text{Cu}}$ ) directly by dissolving in ultrapure  $\text{HNO}_3$  solution and analyzing by ICP/MS and GFAAS. As shown in Figure 3, both  $V_{\text{Cu}}$  and  $M_{\text{Cu}}$  are found to be linearly proportional to  $t^{1/2}$ . These results are consistent with the Cottrell type diffusion-control reaction kinetics, which are frequently

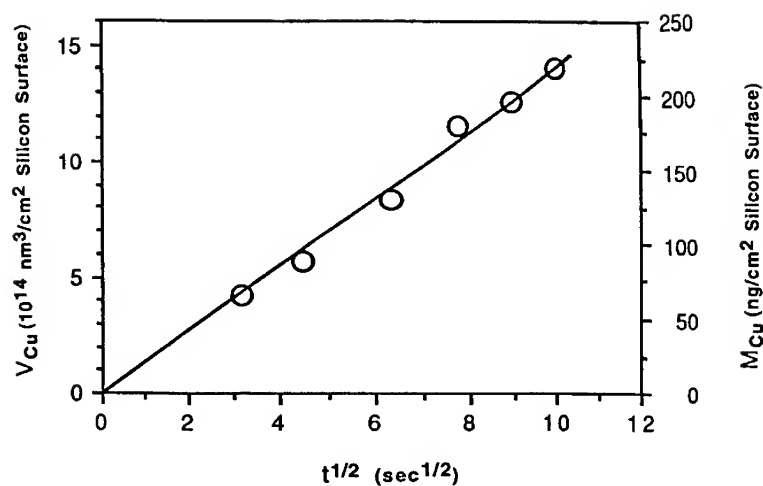


Figure 3: Cu deposition on H-Si(100) is diffusion limited.

encountered in large-amplitude potential step electrochemical experiments.<sup>8</sup> In the present case, the heterogeneous electron-transfer reaction takes place at the interface between the HF treated Si surface and  $Cu^{2+}$  ions from the HF solution. The diffusion limited deposition kinetics indicates the direct displacement reaction of silicon by  $Cu^{2+}$  in  $HF_{(aq)}$  is thermodynamically favorable. According to our ICP/MS and GFAAS results, up to several monolayers of surface silicon atoms were oxidized and etched away by the HF solution during the first 100 seconds of this  $Cu^{2+}$ /Si redox reaction. Concurrently, the equivalent amount of  $Cu^{2+}$  was reduced and deposited on a finite number of nucleation sites on the silicon surface. The silicon removal was found to proceed non-uniformly, which resulted in the increase of the silicon wafer microroughness as demonstrated by the separate AFM studies. Furthermore, if the Cu deposition is extended over several minutes, the continue localized silicon etching can cause pits formation on the silicon wafer surface. We have also observed using AFM a preferential Cu deposition from HF solution on scratches and cracks which are deliberately generated on the silicon surface. These observations suggest that the inherent structural imperfections on the silicon wafer surfaces may function as the localized cathodic sites to electrochemically attract and chemically reduce  $Cu^{2+}$  ions from HF solution. Separate experiments also show the same deposition mechanism is applicable to the noble metal ions include  $Ag^{+1}$ ,  $Au^{+3}$ ,  $Pt^{+2}$ , and  $Pd^{+2}$ .

**Potentiometric responses of H-Si(100) electrodes to metallic ions in HF solution,**

-- We further investigated the electrochemical potential developed in the metal deposited H-Si(100)/HF solution interface. Figure 4 shows the measured potentiometric responses of HF-etched n-Si(100) electrodes in contact with various level of  $Ag^{+}$  impurities in HF solutions. Before each detection run, all

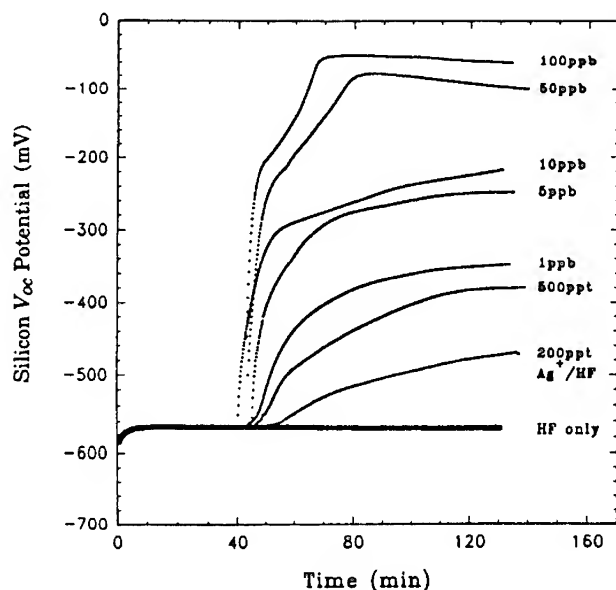


Figure 4: Potentiometric responses of Si-based sensing electrode to  $\text{Ag}^+$  in HF.

the silicon electrodes were pre-etched in 0.49% HF for 10 minutes to remove any surface oxides. After an ultrapure water rinse, each sensing electrode was first allowed to establish a stable potential baseline in pure 0.01% HF solutions for 40 minutes and then immersed in various trace level of (200 ppt to 100 ppb)  $\text{Ag}^+$  spiked 0.01% HF solutions. As depicted in Figure 4, the  $V_{oc}$  of the silicon electrode were found to shift increasingly positive as the concentration of  $\text{Ag}^+$  contaminants in the HF solutions increased. Most significantly, the relatively simple, direct silicon open circuit potential measurements can easily detect  $\text{Ag}^+$  ion in HF below ppb levels which is in the detection sensitivity range required by microelectronic applications. For example, 200 ppt of  $\text{Ag}^+$  ion in HF solution is capable of depositing sufficient Ag on silicon electrode to shift the  $V_{oc}$  90 mV more positive. Plotting  $\log [\text{Ag}^+]$  versus the silicon  $V_{oc}$  potentials recorded at the end of 90 minute detection runs shows a linear calibration curve. The detecting sensitivity of the n-Si(100) sensing electrode toward  $\text{Ag}^+$  ion in HF solution is ca. 150 mV per decade change of  $[\text{Ag}^+]$ . The sensing sensitivity is more than twice that of an electrochemical sensor<sup>9</sup> which relies solely on the Nernstian equilibrium (59 mV per decade concentration change) at the analyte/sensor interface.

The ultra-sensitive detection capability makes the sensor very useful in monitoring the metal contamination onset and assuring the chemical purity at the point of use. However, one potential drawback is the sensor's lacking of the selectivity to identify individual metal contaminants. From the microelectronic application standpoint, we would argue that the contamination onset detection and overall purity monitoring will be more



useful than the identification of the individual metal impurities.

Furthermore, by using the silicon wafer itself as the sensing element, the sensor was designed to selectively response only to the contaminants which will react with the silicon wafer surfaces. Recently, we have completed an off-line testing of our sensors in a Texas Instruments' wafer fab. During the off-line testing, the sensor was used to monitor and assure the purity of the HF bath during its complete life cycle. In addition, we have applied this silicon based sensor to evaluate the relative purity level of the HF solutions from different suppliers. Our sensor successfully identified the HF solution with the higher purity, which was later shown to consistently provide significant improvement in gate oxide integrity (i.e. enhanced breakdown field strength) and lower wafer scrap rate.

## CONCLUSIONS

We have demonstrated that the rate of Cu deposition on hydrogen terminated Si(100) surface is limited by the diffusion. AFM results indicate that the nanoscale Cu deposition on H-Si(100) surface follows nucleation and growth process. The simple and direct open circuit potential measurements on silicon electrodes provide a sensitive method for detecting ultratrace part per trillion level of metal ion impurities in HF solution. The silicon based sensor could find practical applications in the on-line monitoring of ultra-trace metallic impurities during microelectronic chemical processing.

**ACKNOWLEDGEMENT:** This work has been supported by grants from the Robert A. Welch Foundation and Texas Instruments. The valuable discussions and technical assistances from Dr. Lindsey Hall, Dr. Jennifer Sees and Bud Schmidt (all from Texas Instruments) are greatly acknowledged.

## REFERENCES

1. a) *Handbook of Semiconductor Wafer Cleaning Technology*, W. Kern ed.; Noyes Publications, Park Ridge, New Jersey, 1993. b) W. Kern, *RCA Review*, Part I: **31**, 207(1970).; Part II: **31**, 234(1970).; Part III: **32**, 64(1971).
2. M.C. Thornton and R. H. Williams, *Physica Scripta*, **41**, 1047(1990).
3. D.Graf, M. Grundner, R. Schulz and L. Muhlhoff, *J. Appl. Phys.*, **68**, 5155 (1990).
4. D. Riley, and R. Carbonell, *Proc. of The Institute of Enviromental Sciences Ann. Tech, Mtg.*, pp 224-228, New Orleans, LA(1990).
5. W. Kern, *J. Electrochem. Soc.*, **137**, 1887 (1990).
6. O.M.R. Chyan, J. Wu and J. Chen, submitted for publication in *Applied Spectroscopy*.
7. O. M.R, Chyan; J.J., Chen; H.Y., Chien ; J. Sees and L. Hall; *J. Electrochem Soc.*, **143**, 92 (1996).
8. A. J. Bard and L. R. Faulkner; *Electrochemical Methods: Fundamentals and Application*, ; John Wiley & Sons: New York; 1980; chapter 5.
9. H.D. Wiemhofer and K. Cammann in *Sensors: A comprehensive Survey*; W. Gopel, J. Hesse and J.N. Zemel, ed.; VCH:Weinheim, 1991, vol. 2, chapter 5.

## MODIFICATION OF THE SILICON SURFACE BY ELECTROLESS DEPOSITION OF PLATINUM FROM HF SOLUTIONS

P. GOROSTIZA, J. SERVAT, R. DIAZ, F. SANZ<sup>1</sup>\*, J.R. MORANTE\*\*

\* Departament de Química Física, Universitat de Barcelona

\*\* Departament de Física Aplicada i Electrònica, Universitat de Barcelona  
Av Diagonal, 647. E-08028 Barcelona (Spain)

### ABSTRACT

Platinum electroless deposition on Si(100) from HF solutions is hindered on n+ substrates as compared to p-substrates defining an induction period and displaying a more local behavior. The results are discussed in terms of a global electrochemical process. Platinum reduces injecting holes to the silicon valence band and silicon atoms oxidizes. The final morphological situation is a porous silicon layer which contains platinum nuclei formed by filling pits originated in the first stages of the deposition process.

### INTRODUCTION

Electroless Metal Deposition (EMD) was introduced in 1946 by Brenner and Riddell [1] and has been widely studied ever since. Its principles and behavior are well established [2] but many contributions, patents and reviews are still published every year [3]. EMD develops by a reduction of a metal ion present in the solution through a chemical reducing agent which usually is also in solution. However, previous activation of the surface is often a key step for many properties of the electroless coating: adhesion, resistivity of the contact, selectivity of the deposit... Activation is usually achieved by depositing small amounts of palladium on the surface from solutions containing HF or other acids [4,5]. Pd nuclei act as charge exchange and hydrogen evolution centers, thus initiating the massif electroless coating.

These kind of solutions, ionic metals in HF, have drawn interest recently either due to the described activation role in EMD processes on semiconductors [6-12], or to understand the effect of metallic contaminants in wet cleaning processes for the microelectronics industry [13,14]. Additionally, they have also been extensively used to reveal dislocations and lattice defects in silicon surfaces [15]. EMD from HF solutions is an electrochemical redox reaction in which both anodic and cathodic processes occur simultaneously at the Si surface while the charge may be exchanged through the substrate. Fluoride ions in acid solutions serve not only to prevent the formation of silicon oxide but also to solubilize the silicon material as  $\text{SiF}_6^{2-}$  complexes. The global chemical reaction does not inform about the detailed mechanism of the deposition process, and the electrons in the half-cell equations can have different thermodynamic potential because the electron transfer could be through a different interphase, that is, platinum-solution or silicon-solution interphases. Thus, in the case of p substrates the metallic ions reduce and deposit on the surface forming nuclei while the silicon substrate is oxidized and etched away helped by HF, promoting an increase of surface roughness and pitting. In the case of platinum the electrochemical reaction produces highly pure, polycrystalline nuclei and in the beginning of the process, it seems plausible to compete with a direct chemical reaction between the platinum ions and silicon atoms: XPS

---

<sup>1</sup>Corresponding Author. e-mail: f.sanz@dept.qf.ub.es

measurements on similar samples demonstrated the plausibility of a spontaneous room-temperature silicidation [15]. The effect of pH has also been analyzed [16]: An increase of pH to a value of 3 where fluoride ions constitutes the majority carriers in solution promotes Si etching rather than  $\text{SiO}_2$  dissolution. The ratio between metallic platinum and platinum silicide now present in the silicon samples by XPS changes and metal nuclei get nailed into the etched substrate.

Of course, EMD rate depends on the defect concentration of the substrate, as it was demonstrated by the increase of the EMD coverage on samples previously damaged with different Ar ion doses: crystal and surface defects in Si are revealed in this way by using EMD-like solutions [14]. It seems also evident that since the electric charge is transferred through the substrate the electric properties of silicon will play a role on the deposition mechanism and may be different for differently doped samples. In comparison with p samples, deposition is initially hindered on n+ substrates. In n+ samples deposition and subsequent etching occurs more locally, the nuclei grow in the bottom of pits and gather around the pits on the surface, forming a buried platinum layer. The lack of holes in the n+ substrates seem to be the cause, the only sources for holes being injection of metal ions from the solution or photogenerated holes. In the case of p-substrate nucleation develops on the surface and the rate of the process seems to be controlled by the etching of silicon [17].

Luminescent Porous silicon (PS) layers are usually produced by anodic etching of Si in a fluoride solution. Control over the HF concentration, applied potential and the current passing through the electrode allows to select between Si electropolishing and PS formation conditions. This procedure requires the n-type samples to be illuminated and in general produce layers of high porosity, sponge-like or deeply pitted.

In an alternate method which require no application of bias to the sample, Si is etched in  $\text{HF}:\text{HNO}_3:\text{H}_2\text{O}$  solutions (stain etch) producing  $0.5\ \mu\text{m}$  thick layers of amorphous material that show visible photoluminescence [18, 19]. In any case, good metallic contacts with PS layers are difficult to achieve due to its own porous nature, and in some cases metal deposition has been reported to cause quenching of the Photoluminescence [20].

In this contribution, we are reporting the formation of a PS layer during the electroless deposition of Platinum on Si(100) substrates.

## EXPERIMENTAL

All solutions were prepared with p.a. grade reagents and triply-distilled water (18 M $\Omega$  resistivity), which was also used for all water rinses. Etching solutions were freshly-prepared from 40% HF "Suprapur" grade supplied by Merck and low conductivity water. The substrates used in this study were 2 inches diameter CZ silicon (100) wafers supplied by Crysteco Co in isolated boxes with quality control signature. N-type samples have a resistivity ranging between 0.01 and 0.02  $\Omega\text{cm}$ . Previous to each deposition experiment the native oxide layer was etched in an aqueous HF solution (the 40% HF solution was diluted ten times, the final pH of the solution being less than 2) during a few seconds, until the sample showed a hydrophobic behavior.

Plating solutions were obtained by dissolving small amounts of a metal salt in the aqueous HF etching solution. Sodium or Potassium hexachloroplatinate (IV),  $\text{Na}_2\text{PtCl}_6 \cdot 6\text{H}_2\text{O}$  or  $\text{K}_2\text{PtCl}_6 \cdot 6\text{H}_2\text{O}$  (Johnson Matthey GmbH) were used to yield a final platinum concentration in solution of 1.0 mM. Immediately after removal of the protective oxide layer, samples were immersed in the solution and held vertically during deposition. Typical deposition times ranged between 1 minute and 60 minutes. All depositions were carried out under controlled ambient and lighting conditions.

Morphological characterization of the deposited samples was carried out by TEM

in a Philips CM30 (300 KeV) TEM equipped with an Q2300 Link EDX. X-ray diffraction measurements were recorded with a Philips MRD diffractometer working in high resolution mode using monochromatic  $K_{\alpha 1}$  radiation obtained with a primary Bartels monochromator (Ge 220). Photoluminescence measurements were performed illuminating the samples with a 6 W coherent Ar laser working in single-line mode at a wavelength of 457 nm (blue).

## RESULTS

Controlled convection of the solution flowing in the perpendicular direction of the sample surface resulted in better homogeneity of the deposits. After immersion in the solution for times between 1 and 60 minutes, films are brown-yellow for non-coalescent Platinum deposits, and color turn to grey for a complete Platinum film. Darkness or illumination conditions did not affect the deposition process on p-doped samples but deposition on n-doped samples in darkness produced less regular layers [17].

A cross-section of a sample where platinum was deposited for 30 minutes was imaged by TEM (figure 1), clearly showing the distribution of the nuclei underneath the silicon surface. These nuclei are not just nailed or inlaid within the substrate as a result of the enhanced silicon etching which was reported previously in the case of p type samples. Instead, the nuclei seem to have grown under the surface, most probably as a consequence of the electrical potential reached at the bottom of pits formed by silicon corrosion. It is well known that electrical potential can drop by several hundred of millivolts between the sample surface and the bottom of a pit during pitting corrosion of metallic electrodes, and also that in the case of the electrochemical etching of metals current lines converge into the surface pits [21]. Outside and around the pits small nuclei of platinum are starting to grow and to form the film.

Figure 2 shows a cross section of the same sample where we can observe how a platinum nucleus is filling the pit and entering almost  $1\mu\text{m}$  on the silicon substrate. Just this thickness corresponds to the modified layer of silicon which has a different grey tone than the silicon bulk. High resolution imaging on the modified layer and on the silicon bulk makes evident that the modified layer implies a modification of the bulk structure exhibiting crystalline domains of some nm in size. The layer formation is not due to the high concentration of platinum nuclei because a cross section of a sample electrodeposited only during 10 minutes also develops an incipient modified layer due to the electrochemical nature of the process. Fig. 3 shows the corresponding TEM image. Now the density of nuclei in the surface is rather low, the surface roughness is mainly the value at the bare silicon sample and a layer between the nuclei is also observed with a thickness of  $0.5\mu\text{m}$ .

X-ray diffraction rocking curves were recorded from (004) reflection on the Si substrate deposited for 30 min. (fig. 4) The narrow intense peak corresponds to the substrate. The (top) layer contribution consists on a broad weak peak very close to the substrate peak ( $\Delta\theta \sim 0.021^\circ$ ). The peak position shift corresponds to a lattice mismatch of  $a_L / a_{Si} = 1 + 5.3 \cdot 10^{-4}$ . Thus, the PS layer is mostly crystalline but somehow rearranged thus confirming HRTEM results.

Laser irradiation of the as-deposited silicon samples show visible photoluminescence with a maximum ranging between 1.7 and 1.8 eV (figure 5). Photoluminescence could not be clearly detected on samples deposited for more than 60 min, most likely due to the coalescence of the Pt layer.

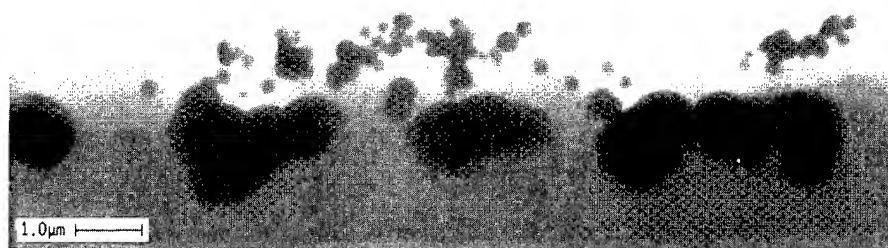


Fig. 1: TEM image of a cross section of a Si sample deposited for 30 min. showing the distribution of nuclei underneath the silicon surface.

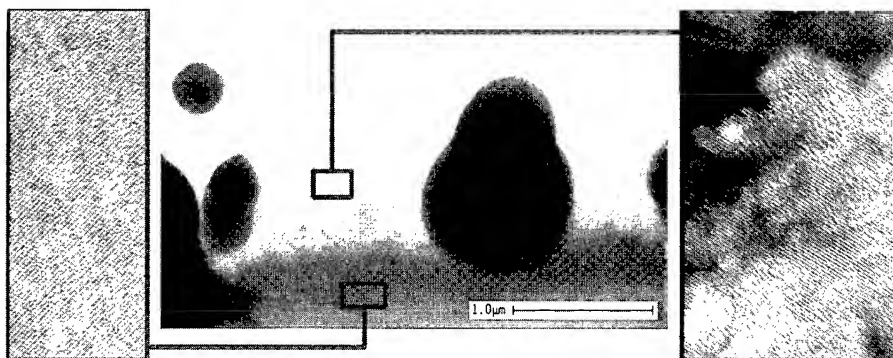


Fig.2: Detailed TEM image showing the top layer of the sample in fig.1. High resolution imaging on the modified layer (right) and on the silicon bulk (left) demonstrates that the modified layer implies a modification of the bulk structure exhibiting crystalline domains of some nm in size.

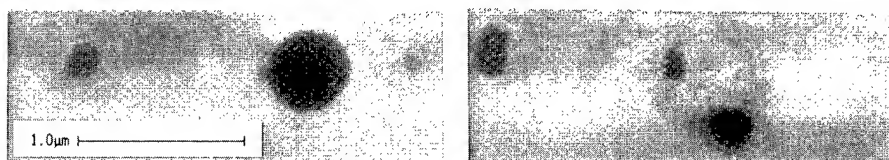


Fig.3: Detailed TEM image of buried Pt nuclei in a Si sample deposited during 10 min. Although nuclei are small and distant from each other, the topmost Si layer has been modified on the entire interface exposed to the solution and not only on the nuclei surroundings.

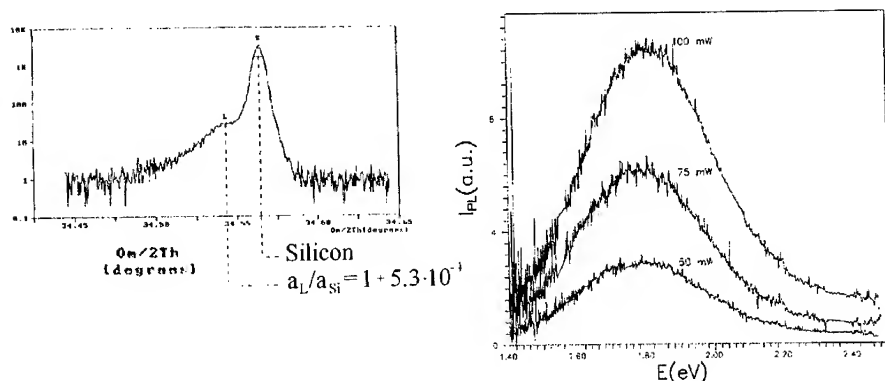


Fig.4 (left): X-ray diffraction rocking curve of the Si substrate deposited for 30 min. The narrow intense peak corresponds to the substrate. The (top) layer contribution consists on a broad weak peak very close to the substrate peak ( $\Delta\theta \sim 0.021^\circ$ ). The peak position shift corresponds to a lattice mismatch of  $a_L / a_{Si} = 1 + 5.3 \cdot 10^{-4}$  indicating that the PS layer is mostly crystalline but somehow rearranged.  
Fig. 5 (right): Photoluminescence spectra of a silicon sample deposited for 30 min.

## CONCLUSIONS

The formation of a PS layer during electroless Pt deposition from HF solutions on n-Si(100) has been reported. Visible photoluminescence has been measured in non-coalescent samples. Preliminary morphological characterization of the samples indicate that a PS layer is present on the surface. The layer is mostly crystalline but it has undergone some kind of rearrangement, so that domains of a few nanometers are detected. PS formation in these samples has been explained in terms of the electrochemical corrosion of Silicon which is induced by the injection of holes to the substrate from Platinum ions in solution. Electroless platinum deposition in fluoride media provides simultaneous platinum nuclei deposition and the formation of a luminescent PS layer.

## ACKNOWLEDGEMENTS

The authors gratefully acknowledge J. M. Bassas, A. Santiago and Y. Maniette of the Serveis Científic-Tècnics (Universitat de Barcelona) for XRD, SEM and TEM measurements respectively. This work was financially supported by the contract MAT94-1338 of the Comisión Interministerial de Ciencia y Tecnología (CICYT).

## REFERENCES

1. A. Brenner and G.E. Riddell, J. Res. Natl. Bur. Stan. **37**, p. 31(1946).
2. See, for example, Modern Electroplating, edited by F.A. Lowenheim, John Wiley & Sons Inc., New York (1974).
3. See, for example, M. Paunovic, T. Nguyen, R. Mukherjee, C. Sambucetti and L. T. Romankiw, a) J. Electrochem. Soc. **142**, p. 1,495 (1995) and b) C.Y. Mak, MRS Bulletin

- XIX (8), p. 55 (1994).
4. See, for example, A. F. Arnold, U. S. Pat. 3,857,733 (1974) or the recipes in references 2,3.
5. C. Longo, P. T. A. Sumodjo, F. Sanz, J. Electrochem. Soc., submitted.
6. G. Stremsdoerfer, H. Perrot, J. R. Martin and P. Cléchet, J. Electrochem. Soc., **135**, p. 2881 (1988).
7. L.A. Nagahara, T. Ohmori, K. Hashimoto and A. Fujishima, J. Electroanal. Chem., **333**, p. 363 (1992).
8. L.A. Nagahara, T. Ohmori, K. Hashimoto and A. Fujishima, J. Vac. Sci. Technol. A, **11**, p. 763 (1993).
9. K. K. Yoneshige, H. G. Parks, S. Raghavan, J. B. Hiskey, P. J. Resnick, J. Electrochem. Soc., **142**, 671 (1995).
10. O.M.R.Chyan, J.J.Chen, H.Y.Chien, J.Sees and L.Hall, J. Electrochem. Soc., **143**, p. 92 (1996).
11. P. Gorostiza, J. Servat, J. R. Morante and F. Sanz, Thin Solid Films, **275**, p. 12 (1996).
12. T. Ohmi, T. Imaoka, I. Sugiyama and T. Kezuka, J. Electrochem. Soc., **139**, p. 3,317 (1992).
13. H. Morinaga, M. Suyama and T. Ohmi, J. Electrochem. Soc., **141**, p. 2834 (1994).
14. P. Gorostiza, J. Servat, F. Sanz and J. R. Morante, in Defect Recognition and Image Processing in Semiconductors, edited by A. R. Mickelson, (Institute of Physics Publishing Ltd. Bristol, UK 1996), p. 293 and references therein.
15. P. Gorostiza, R. Díaz, J. Servat, F. Sanz and J. R. Morante, J. Electrochem. Soc., in press.
16. P. Gorostiza, J. Servat, J.R.Morante and F. Sanz, in Silicide Thin Films Fabrication, Properties and Applications, edited by R. Tung, K. Maex, P. W. Pellegrini and L. H. Allen, (Mater. Res.Soc. Proc. 402, Pittsburgh, PA 1996), p. 611.
17. P. Gorostiza, R. Diaz, J. R. Morante and F. Sanz, J. Electrochem. Soc., submitted.
18. R.W. Fathauer, T. George, A. Ksendzov and R.P. Vasquez, Appl. Phys. Lett **60**, p. 995,(1992)
19. P. Allongue, in *Advances in Electrochemical Science and Engineering*, Vol.4, H. Gerischer, C. W. Tobias, Editors, p.42, VCH Verlagsgesellschaft GmbH, Weinheim (1995).
20. D. Andsager, J. Hilliard, J.M. Hetrick, L.H. AbuHassan, M. Plisch and M.H. Nayfeh, J. Appl. Phys **74**, p. 4,783 (1993)
21. D. Pletcher, F. C. Walsh, Industrial Electrochemistry, 2nd. ed., Chapman and Hall, University Press, Cambridge (1990).

**Part V**

**Electrodeposition and Modification  
of Oxide Electrodes**



## ELECTRODEPOSITION OF COPPER / CUPROUS OXIDE NANOCOMPOSITES

JAY A. SWITZER, ERIC W. BOHANNAN, TERESA D. GOLDEN, CHEN-JEN HUNG,  
LING-YUANG HUANG, AND MARK SHUMSKY

Department of Chemistry and Materials Research Center, University of Missouri - Rolla,  
Rolla, MO 65409-1170, USA, switzer@umr.edu.

### ABSTRACT

Nanocomposite films of copper metal and cuprous oxide were electrodeposited at room temperature from an alkaline copper(II) lactate solution. The electrode potential oscillated spontaneously during constant-current deposition of the composites. The oscillations were periodic in a stirred solution, but became chaotic in unstirred solution. For a given current density the phase composition was a strong function of solution pH. As the pH was increased, the cuprous oxide content increased. At pH 12, no oscillations were observed, and pure cuprous oxide was deposited. At pH 9, the phase composition varied from pure cuprous oxide at current densities below 0.1 mA/cm<sup>2</sup> to 96 mole percent copper at 2.5 mA/cm<sup>2</sup>.

### INTRODUCTION

Cuprous oxide, Cu<sub>2</sub>O, is a relatively non-toxic, p-type semiconductor with a bandgap of approximately 2 eV. Interest in the semiconducting properties of the material began as early as 1926, when Grondahl produced the Cu/Cu<sub>2</sub>O rectifier [1]. Cuprous oxide is also a textbook example of a Wannier-Mott excitonic solid [2]. Up to 10 hydrogen-like exciton lines can be seen in the absorption spectrum of Cu<sub>2</sub>O at low temperatures [3-5]. Unbound excitons in Cu<sub>2</sub>O have a binding energy of 150 meV, and a radius of 0.7 nm. The physics community is presently very excited about the excitonic properties of Cu<sub>2</sub>O, since there is evidence that Bose-Einstein condensation of excitons can occur in the material [6]. Since the effective mass is close to that of a free electron, the de Broglie wavelength is large, and condensation can be observed at relatively high temperatures. Because excitons, like photons, are bosons, they can be made to propagate through a solid coherently [7]. Studies of Bose-Einstein condensation of excitons in Cu<sub>2</sub>O have all been on single crystals. We undertook the present study in order to prepare Cu<sub>2</sub>O crystallites with dimensions comparable to the exciton de Broglie wavelength.

We have previously shown that both compositional [8-11] and defect chemistry [12] superlattices of metal oxide semiconductors can be grown by pulsing either the applied potential or current during electrodeposition. The materials in our previous work were highly-conducting degenerate semiconductors [13]. A fascinating aspect of the present system is that the potential oscillates *spontaneously* if a constant current density is applied to the cell. The Cu/Cu<sub>2</sub>O nanocomposites are only produced when oscillations of the potential are observed.

### EXPERIMENTAL

All solutions were made from reagent-grade chemicals dissolved in HPLC grade water from Aldrich. To prepare the deposition solution, 90g of copper sulfate was added to 150 mL of 85% lactic acid with stirring. Over a period of a few minutes, 450 mL of 5M NaOH was added in 50-100 mL increments. The solution was stirred overnight, and then the pH was adjusted to the final value in the 9-12 range with the addition of 5M NaOH. Deposition currents were controlled with

an EG&G Model 273A potentiostat/galvanostat, and the potential oscillations were recorded on a Nicolet Pro 10 oscilloscope. A constant temperature of 30 °C was maintained during deposition. Phase analysis was done by Rietveld analysis of powder x-ray diffraction patterns obtained on a Scintag 2000 diffractometer with Cu K $\alpha$  radiation. Crystallite sizes were estimated from the broadening of the diffraction lines using both a simple Scherrer analysis of the [200] reflection of Cu and the [111] reflection of Cu<sub>2</sub>O, and a Williamson-Hall analysis of the entire XRD pattern.

## RESULTS AND DISCUSSION

Potential oscillations are observed at pH 9 when the current density is greater than about 0.1 mA/cm<sup>2</sup>. At current densities below that value, highly oriented films of red Cu<sub>2</sub>O are deposited [14], and at higher current densities nanocomposites are deposited, with a color and phase composition which depend on the applied current density [15]. The color of the films deposited at pH 9 varies from red at a current density of 0.05 mA/cm<sup>2</sup>, to green at a current density of 0.5 mA/cm<sup>2</sup>, to metallic gold at a current density of 2.5 mA/cm<sup>2</sup>. An example of potential oscillations is shown in fig. 1 for an applied current density of 0.5 mA/cm<sup>2</sup> from a stirred solution of 0.6 M Cu(II), 3M lactate acid, and a pH of 9. Notice that the time axis runs from 5000 to 6000 seconds. We have observed that these oscillations persist in a stirred solution for days. In an unstirred solution, however, the oscillation become chaotic with time, and “ring out” at a time which depends on the applied current density. Examples of oscillations in unstirred solution are shown in fig. 2.

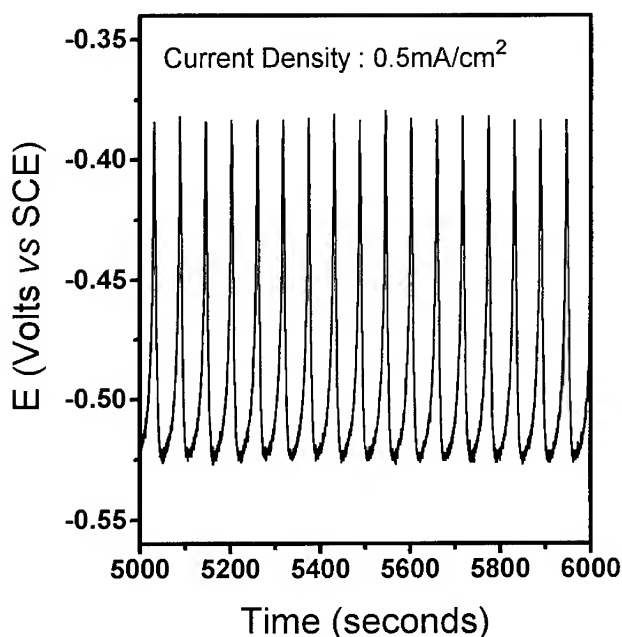


Figure 1. Potential oscillations in a stirred solution at pH 9 and a current density of 0.5 mA/cm<sup>2</sup>.

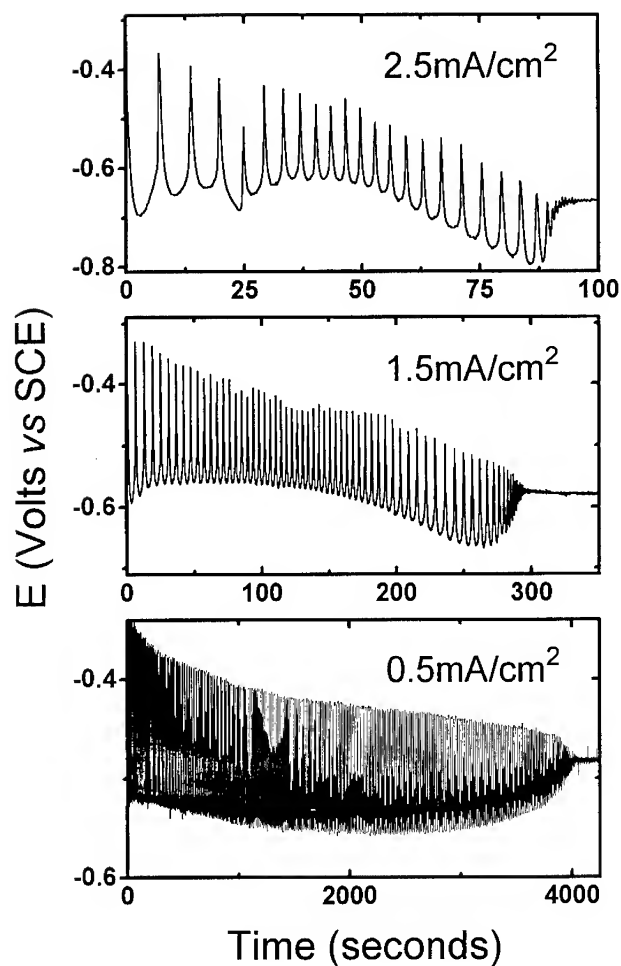


Figure 2. Potential oscillations in an unstirred solution at pH 9.

The phase composition can be controlled by varying the applied cathodic current density used to deposit the films. Our phase analysis was done on films grown from a stirred solution at pH 9. At current densities below  $0.1 \text{ mA/cm}^2$  the films are pure  $\text{Cu}_2\text{O}$  with a strong [100] preferred orientation. As the current density is increased, the Cu content increases from 37 mole percent at  $0.25 \text{ mA/cm}^2$  to 98 mole percent at  $2.5 \text{ mA/cm}^2$ . All of the films in which oscillations were observed had a near random orientation. The simple control of the phase composition is a key feature of the electrochemical method. The crystallite radii for both Cu and  $\text{Cu}_2\text{O}$  decrease as the current density is increased. The phase composition and crystallite radii for both Cu and  $\text{Cu}_2\text{O}$  as a function of applied current density is shown in Table I. At current densities greater than  $0.5 \text{ mA/cm}^2$ , the crystallite radii for both Cu and  $\text{Cu}_2\text{O}$  are less than 10 nm.

Table I. Phase composition and crystallite radii as a function of current density for Cu/Cu<sub>2</sub>O nanocomposites electrodeposited at pH 9 from a stirred solution.

J (mA/cm <sup>2</sup> )	Mol% Cu	Cu <sub>2</sub> O Radius (nm)	Cu Radius (nm)
0.175	30	44	---
0.25	37	20	10
0.375	44	12	6
0.5	60	9	7
0.75	76	8	5
1.0	89	3	5
1.5	89	3	4
2.5	98	---	4

The phase composition at a given current density is a strong function of the solution pH. The composition of composites as a function of current density for a series of solution pH's is shown in fig. 3. As the pH is increased the Cu content in the films decreases. At pH 12, the films are pure, textured Cu<sub>2</sub>O for current densities up to 1.5 mA/cm<sup>2</sup>, while for pH 8, the films are nearly pure Cu at 1.5 mA/cm<sup>2</sup>. Potential oscillations were not observed at pH 12.

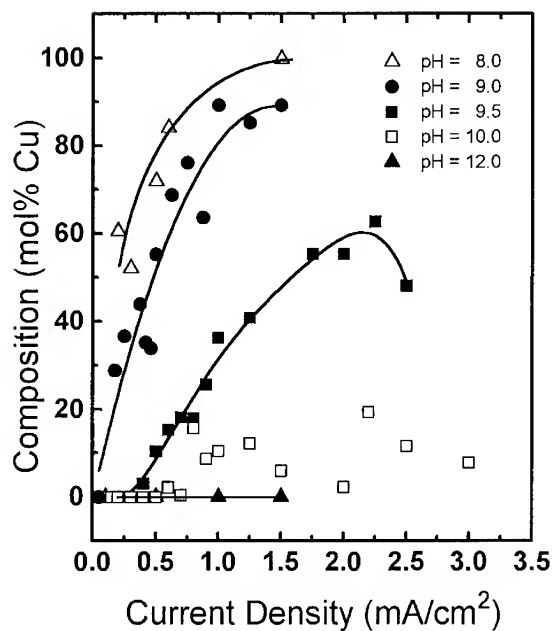


Figure 3. Phase composition as a function of current density for solutions of pH 8 through 12

Potential and current oscillations are quite common in electrodeposition [16-18]. The oscillations are often caused by the adsorption and dissolution of an insoluble layer. Electrochemical oscillations that are particularly relevant to the present work are those observed during the anodic dissolution of copper metal in solutions containing acetate ion. Dewald *et al.* attribute these oscillations to the deposition and dissolution of passivating films of basic copper acetate [18]. Since we do not observe oscillations at pH 12, we believe the oscillations observed at lower pH may be caused by the precipitation of a neutral Cu(II) lactate complex produced by the reduced local pH at the electrode surface during oxide formation at higher current densities. Electrochemical quartz microbalance studies are presently in progress to follow the deposition process in real time.

The potential oscillations observed during the deposition of all of the composites would suggest that these materials are modulated. For example, the period in the potential oscillations in fig. 1 of 58 second would correspond to the modulation wavelength of approximately 20 nm. Microstructural analysis by cross-sectional TEM is presently in progress to determine if these materials are multilayers or granular nanocomposites. We are also interested in comparing the microstructure of nanocomposites grown with periodic oscillations to those grown with quasi-periodic or chaotic oscillations.

#### ACKNOWLEDGMENTS

This work was supported by National Science Foundation grant DMR-9202872, Office of Naval Research grants N00014-96-1-0984 and N00014-94-1-0917, and the University of Missouri Research Board.

#### REFERENCES

1. L. O. Grondahl, *Science* **64**, 306 (1926).
2. C. Kittel, *Introduction to Solid State Physics*, Wiley, New York, ed. 6, 1986, chap. 11.
3. P. W. Baumeister, *Phys. Rev.* **121**, 359 (1961).
4. D. Fröhlich, R. Kenkies, Ch. Uihlien, and C. Schwab, *Phys. Rev. Lett.* **43**, 1260 (1979).
5. V. T. Agekyan, *Phys. Status Solidi (A)* **43**, 11 (1977).
6. J. L. Lin and J. P. Wolfe, *Phys. Rev. Lett.* **71**, 1222 (1993).
7. A. Mysyrowicz, E. Benson, and E. Fortin, *Phys. Rev. Lett.* **77**, 896 (1996).
8. J. A. Switzer, M. J. Shane, and R. J. Phillips, *Science* **247**, 444 (1990).
9. J. A. Switzer and T. D. Golden, *Advanced Materials* **5**, 474 (1993).
10. J. A. Switzer, R. P. Raffaele, R. J. Phillips, C.-J. Hung, and T. D. Golden, *Science* **258**, 1918 (1992).

11. J. A. Switzer, R. J. Phillips, and T. D. Golden, *Appl. Phys. Lett.* **66**, 819 (1995).
12. J. A. Switzer, C.-J. Hung, B. E. Breyfogle, M. G. Shumsky, R. Van Leeuwen, and T. Golden, *Science* **264**, 1573 (1994).
13. R. A. Van Leeuwen, C. -J. Hung, D. R. Kammler, and J. A. Switzer, *J. Phys. Chem.* **99**, 15247 (1995).
14. T. D. Golden, M. G. Shumsky, Y. Zhou, R. A. VanderWerf, R. A. Van Leeuwen, and J. A. Switzer, *Chem. Mater.* **8**, 2499 (1996).
15. J. A. Switzer, C.-J. Hung, E. W. Bohannon, M. G. Shumsky, T. D. Golden, and R. C. Van Aken, *Advanced Materials*, submitted.
16. B. Rush and J. Newman, *J. Electrochem. Soc.* **142**, 3770 (1995).
17. W. Wolf, K. Krischer, M. Lübke, M. Eiswirth, and G. Ertl, *J. Electroanal. Chem.* **385**, 85 (1995).
18. H. D. Dewald, P. Rarmananda, and R. W. Rollins, *J. Electrochem. Soc.* **140**, 1969 (1993).

## Microelectrochemical Characterization and Modification of Semiconductor Surfaces with Polycrystalline Ti/TiO<sub>2</sub> as an Example

A. Michaelis, S. Kudelka, J.W. Schultze

Institut für Physikalische Chemie und Elektrochemie, Heinrich-Heine-Universität  
Düsseldorf, 40225 Düsseldorf, Germany

### Abstract

Different new micro-methods such as anisotropy micro-ellipsometry (AME), photoresist micro-electrochemistry, micro-photocurrent spectroscopy, and UV-laser scanning were performed simultaneously to characterize and modify heterogeneous semiconductor surfaces. All measurements were carried out on single grains with the Ti/TiO<sub>2</sub> system as an example. The crystallographic orientations of the substrate grains were determined in-situ by AME. It is shown that both the electronic and the optical properties of the semiconducting TiO<sub>2</sub> films sensitively depend on the substrate texture. Film properties such as layer thickness and defect state concentration vary with the substrate orientation in a systematic manner.

The TiO<sub>2</sub> films were modified at high local resolution by means of focused UV-laser illumination. Both a thickening (writing) or thinning (erasing) of the films could be realized depending on the potential applied during the illumination. Therefore, the anodic potential could be used to control the layer thickness and to generate semiconducting structures with thickness gradients.

## 1 Introduction

Electrochemical methods show an excellent vertical resolution for the investigation of semiconductor surfaces but often their application is limited because of the poor lateral resolution to the mm<sup>2</sup>-range. In order to enable a deeper insight into important local electrode reactions, in-situ micro-methods must be developed and applied which feature both high lateral and vertical resolution. In this study, the combined application of different new methods are presented which, depending on the input/output signals, can be divided into three different classes: 1) optical/optical where the exciting and measured signal is the light beam, 2) optical/electrical (measured signal is an electric current  $i_{ph}$ ) and 3) electrical/electrical, i.e. standard electrochemical methods. Fig. 1 summarizes the intercorrelation of these methods and indicates which quantities are measured and which corresponding parameters can be derived. All methods allow to characterize or/and modify semiconductor surfaces at high lateral resolution which only is limited by refraction of light to about 1  $\mu\text{m}$ . This is demonstrated with the polycrystalline Ti/TiO<sub>2</sub>-system as an example. All experiments were carried out on single Ti-grains. As optical/optical method micro-ellipsometry was chosen which allows for determination of both the optical parameters of the system and the film thickness  $d_f$ . Moreover, the new method of Anisotropy Micro-Ellipsometry (AME) was applied which allows to determine crystallographic properties such as the orientation of substrate grains, recrystallization of the semiconducting films, and epitaxy. Furthermore, the combination of AME with the new method of photoresist microelectrochemistry (electrical/electrical) allows to correlate the electronic film parameters with the substrate texture elucidating the growth mechanisms. This photoresist method allows to perform all kinds of electrochemical

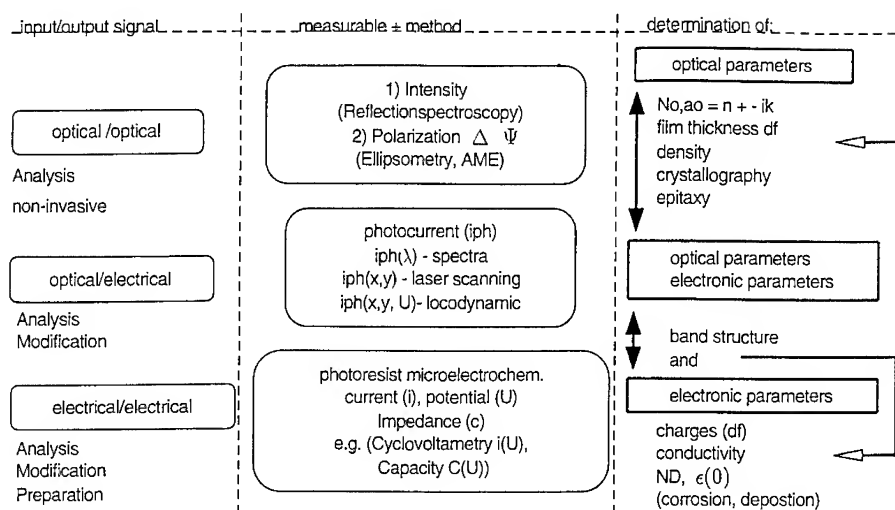


Figure 1: Correlation between the different method classes applied in this study. The measurable and corresponding methods as well as the evaluable quantities are specified. The lateral resolution of all methods is some  $\mu\text{m}$ .

measurements in a droplet of nl-volume e.g. on single substrate grains. Additionally, optical/electrical methods such as micro-photocurrent spectroscopy and UV-laser scanning were applied which allow for both characterization and modification of the semiconducting layers.

## 2 Experimental

For all experiments Ti high purity (99.98 %) samples with a coarse grain texture were used (grain diameter  $> 600 \mu\text{m}$ ) enabling to carry out several independent experiments on each single grain. In order to prepare samples with open grain boundaries the surfaces were electropolished applying a procedure given in [1]. As the electrolyte 0.5 M  $\text{H}_2\text{SO}_4$  was chosen. Potentials are given with respect to the standard hydrogen electrode (SHE).

Microellipsometry was performed using a rotating analyser configuration with a HeNe laser (632.8 nm) as the light source. AME requires rotation of the sample around the surface normal. In order to enable this sample rotation, a particular in-situ cell was constructed. For this, the cell windows were mounted on the ellipsometer arms using an alignable connector and simply dipped into the electrolyte. Therefore, rotation of the entire cell containing the sample in three electrode configuration was possible without affecting the window alignment. The details of AME are described in [2, 3].

The photoresist microelectrodes were prepared by standard mask-photolithography. An electrolyte droplet was dispensed onto the microelectrodes by means of a microcapillary which was connected to a nanopipette and a miniaturized reference electrode. As the counter electrode a Pt-wire (50  $\mu\text{m}$  diameter) was used which was bent to a loop and dipped into the droplet. Measurements and preparation were performed under microscopic control. The



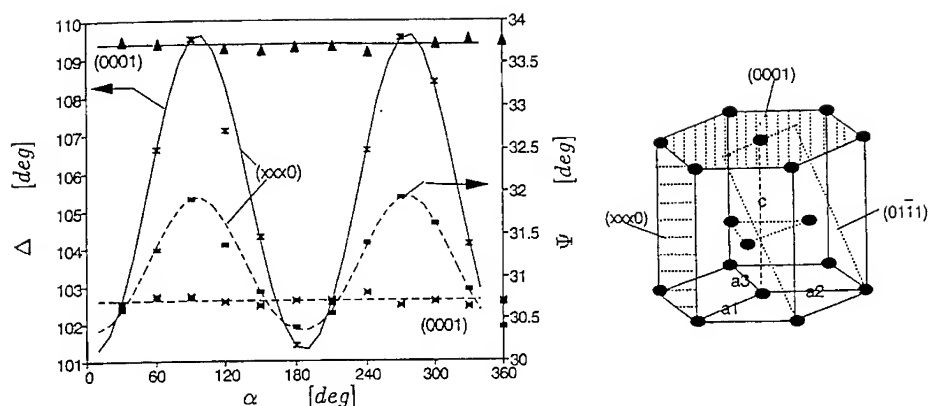


Figure 2: Anisotropy Micro-Ellipsometry (AME) on two different Ti grains. The determined crystallographic orientations are illustrated in the displayed Ti-Bravais lattice

details of this new method are described in [4, 5].

For photoelectrochemical experiments at high local resolution, an in-situ laser scanning apparatus was developed [6, 7]. The light of a frequency doubled  $\text{Ar}^+$ -laser ( $\lambda = 257$  nm, i.e. 4.8 eV) was focused onto the sample surface by means of the same microscope which was used for the photoresist microelectrochemistry. A minimum spot radius of about  $1 \mu\text{m}$  was achieved yielding power densities up to some  $\text{kW cm}^{-2}$ . The sample/cell configuration could be scanned normal to the light beam using a computerized x, y - stage (step size =  $1 \mu\text{m}$ ). For the detection of photocurrent spectra, the laser was substituted by a standard 1kW Xe high pressure arc lamp and a monochromator. In this case the lateral resolution was about  $50 \mu\text{m}$ . The whole set-up is based on a modular concept, i.e. all measurements could be performed simultaneously under microscopic control and further tools such as reflection-spectroscopy or video-microscopy could be added.

### 3 Results

#### 3.1 Determination of substrate grain orientation by AME

In order to determine the crystallographic orientation of single Ti grains, the new AME method was applied. The fundamentals of this method and its application for the determination of crystal orientations of optically anisotropic systems (Ti crystallizes in the hcp-lattice) are described in a recent publication [3]. AME yields the angle  $\varphi$  between the surface normal and the optical axis (c-axis). For this, the ellipsometric measurables  $\Delta$  and

$\Psi$  are measured as a function of the angle  $\alpha$  which describes rotation of the sample around the surface normal. The corresponding experimental curves are shown in fig. 2 for the example of two different Ti-grains. The grains are covered by anodically formed 4V TiO<sub>2</sub> layers which themselves are amorphous and therefore do not contribute to the  $\Delta(\alpha)$  and  $\Psi(\alpha)$  variation. The quantitative analysis of these curves yields the indicated orientations which are illustrated in the shown Ti-Bravais lattice. The (0001)-surface ( $\varphi=0$  deg) is the closest packed surface with  $1.15 \text{ \AA}^{-2}$  ( $a = 0.2951 \text{ nm}$ ,  $c = 0.4679 \text{ nm}$ ), (xxx0) refers to any plane perpendicular to the c-axis ( $\varphi = 90$  deg).

### 3.2 Anodic TiO<sub>2</sub>-film formation on single Ti grains

The semiconducting TiO<sub>2</sub> layers were formed potentiodynamically at a sweep rate of 50 mV/s in 0.5 M H<sub>2</sub>SO<sub>4</sub> on single Ti substrate grains. The corresponding cyclovoltammograms and capacity measurements during formation of an 8 V layer are shown in Fig 3a and b) for the example of three different Ti surfaces. The orientations were determined applying AME as explained above. The curves significantly vary from grain to grain. For example, the oxygen formation starting at 3 V decreases with increasing angle of the optical axis and reaches a maximum for the (0001) orientation. This correlates with the micro-ellipsometrically determined TiO<sub>2</sub> formation factor. The corresponding measurements are shown in fig 4a. In the coulometrically evaluable potential range between 0 and 3V a formation factor of 2 nm/V for all orientations is found by both coulometric and ellipsometric evaluations. The formation factor remains constant for the (xxx0) surface which showed no oxygen formation but decreases to 0.7 nm/V for the (0001) surface in the potential region above 3V. Due to the different onset potentials for layer growth the layer thicknesses and coulometrically determined charges  $q$  are different over the entire potential range with increasing tendency at the potential of 3V. The different film thicknesses can be explained by the different electronic TiO<sub>2</sub> film parameters such as the defect state concentration  $N_D$  and permittivity number  $\epsilon(0)$  which were determined by the shown capacity measurements using the Schottky-Mott and condensor model.  $\epsilon(0)$  varies between 34 for the (xxx0) and 40 for the (0001) surface. The  $N_D$ -values are highest for (xxx0) and lowest for (0001) (see fig 4b discussed below). Subsequently, the extension of space charge layer ( $d_{sc}$ ) at a given anodic potential is smallest for the TiO<sub>2</sub> film on the (0001) orientation. Since the Ti-ion migration is limited to the scl this results in a thinner TiO<sub>2</sub> layer. The results are summarized in fig. 4b correlating the measured orientation angle  $\varphi$  with  $N_D$  and the determined charge in the coulometrically evaluable potential region. Charges, i.e. layer thicknesses and donor densities vary with  $\varphi$  in a systematic manner proofing that the oxide layer properties depend sensitively on the underlying substrate grain orientation. On the closest packed surfaces films with the highest defect state concentration occur which might be attributed to the high lattice mismatch between Ti and TiO<sub>2</sub>. This mismatch is smaller for the low angle  $\varphi$  substrate grains resulting in thicker layers. For a further check of the structure of the TiO<sub>2</sub> layers micro-photocurrent spectra were taken.

### 3.3 Photocurrent spectra

Illumination of anodically polarized n-type semiconducting TiO<sub>2</sub> layers with photon energies above the band gap energy results in electron/hole pair formation. These charges are separated within the space charge layer (scl) causing a photocurrent  $i_{ph}$ . Micro-photocurrent

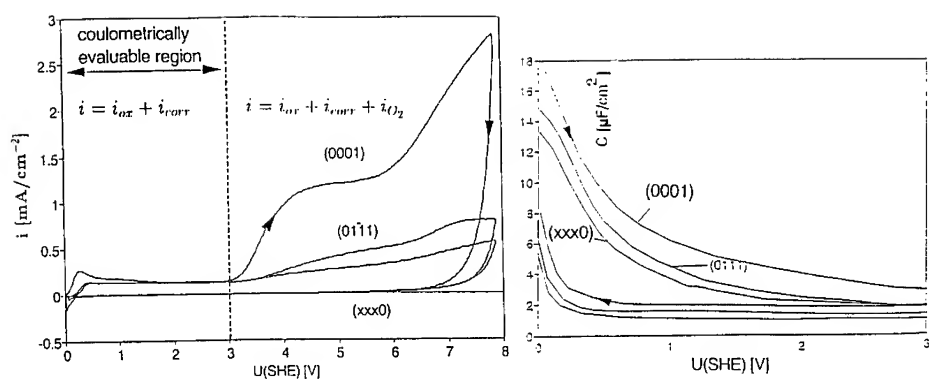


Figure 3: a)  $\text{TiO}_2$  layer formation cyclic voltammograms on different Ti crystal surfaces, sweep rate 50 mV/s, 0.5 M  $\text{H}_2\text{SO}_4$ . b) Corresponding capacity measurements.

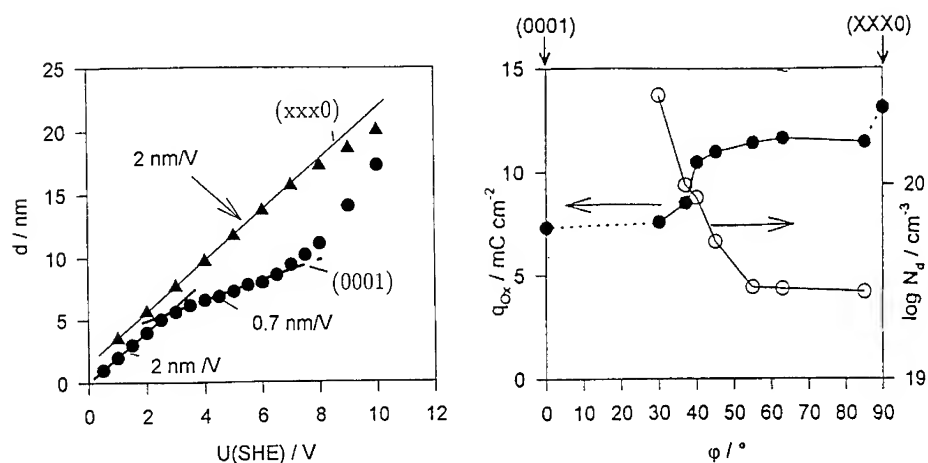


Figure 4: a) Micro-ellipsometrically determined  $\text{TiO}_2$  film thickness  $d_f$  as a function of the formation potential b) Coulometrically evaluated  $\text{TiO}_2$  formation charge  $q_{\text{Ox}}$  (potential range between 0 and 3 V) and defect state concentration  $N_D$  as a function of the Ti substrate orientation angle  $\varphi$ .

spectra, (quantum yield  $Q$ ) taken on different oriented single Ti grains in 0.5 M  $H_2SO_4$  are shown in fig. 5. Before the experiments were carried out at a constant anodic potential of 1 V,  $TiO_2$  layers were formed potentiodynamically in same solution at the indicated formation potentials (2 V up to 20 V) yielding different  $TiO_2$  film thicknesses. Evaluation of the  $Q^2$  and  $Q^{0.5}$ -curves allows determination of the direct and indirect bandgap energies.  $E_{dir}$  varies between 3.7 and 3.4 eV for the different orientations and shows a slight decay in dependence on  $d_f$ . The same holds for  $E_{indir}$  which varies between 3.3 and 3 eV. Below the band gap energy an Urbach tail can be found with a constant slope of 120 meV for the disorder energy. This is an important result because it proves the amorphizity of the  $TiO_2$  layers. Subsequently, the terminus band gap has to be substituted by mobility gap. It shall be mentioned that the mobility gap energies are similar to the band gap energies of the  $TiO_2$  modification anatase therefore indicating a relation between this modification and the amorphous  $TiO_2$  layers found here (near order). The variation of  $i_{ph}$  with the Ti surface orientation confirms again that despite of the amorphous character of the formed  $TiO_2$ -layers, their properties depend sensitively on the substrate texture.

In order to explain the variation of  $i_{ph}$  with the film thickness  $d_f$  (up to 10 V  $i_{ph}$  increases, thereafter  $i_{ph}$  decreases) for each grain and to evaluate the  $i_{ph}$ -curves in terms of the optical and electronic layer parameters, a quantitative photocurrent model must be applied. As described in a recent publication [8] this model can be divided into three different parts:

1. The classical Gärtner part describing the effect of the extension of the space charge layer  $d_{sc}$  which itself depends on the electronic properties  $\epsilon(0)$  and  $N_D$ .
2. The exact optical model describing multiple internal reflection which are important for thin films where the penetration depth of the light is larger than the layer thickness. Due to this part  $i_{ph}$  depends on the layer thickness and the optical constants of both substrate and layer. This optical part mainly explains the observed  $i_{ph}(d_f)$  variation found in the photocurrent spectra [9, 10, 11].
3. The third part describes the electron/hole pair recombination efficiency  $r(E)$  which causes a further dependence of  $i_{ph}$  on the layer thickness for very thin films or high potentials ( $d_{sc} = d_f$ ) and superimposes to the thickness dependence due to the optical part [12, 13].

The application of this model for determination of both electronic and optical film properties which up to date were only obtainable by evaluation of pure optical and pure electronic methods are discussed in [11, 8]. The corresponding results show an excellent agreement with the parameters ( $N_D$ ,  $\epsilon(0)$ , complex refractive index  $N = n + ik$ ) determined and discussed in the previous sections by capacity measurements and ellipsometry therefore confirming these results. However, in the following the modification of the semiconducting  $TiO_2$  films by means of photocurrent experiments will be emphasized.

### 3.4 Microscopic modification of the $TiO_2$ layers by means of laser scanning

The migration of holes to the oxide/electrolyte interface leads to an accumulation of positive charge at the surface which causes a change of the potential distribution within the oxide namely the photopotential. Under potentiostatic conditions, the potential drop in the Helmholtz layer will be increased accordingly enhancing the charge transfer of oxygen

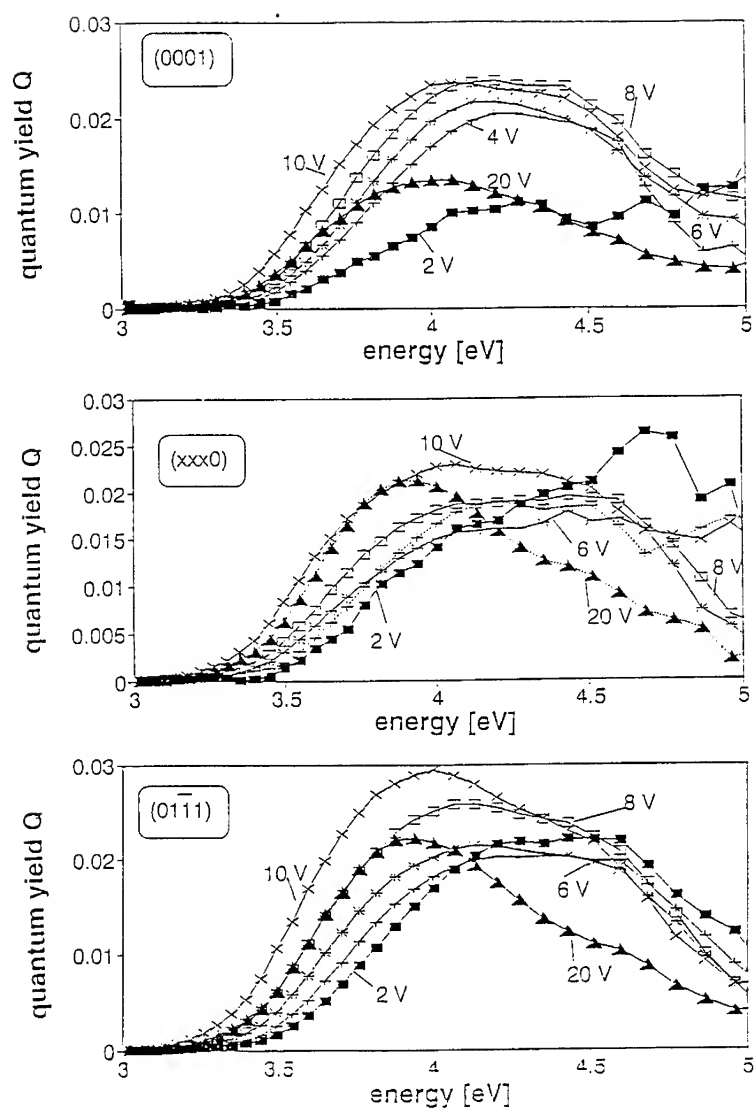
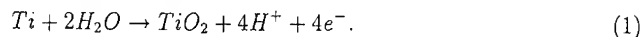


Figure 5: Photocurrent spectra (quantum yield  $Q$ ) of  $\text{TiO}_2$  films formed at different formation potentials (different thicknesses). The measurements were carried out on three different oriented Ti single grains. Electrolyte 0.5 M  $\text{H}_2\text{SO}_4$ , anodic potential 1 V, Xe-arc lamp.

through the oxide/electrolyte interface. This affects the film formation which itself is a simple anodic ion transfer reaction without direct contribution of holes as:



On the other hand, the holes are directly involved in two reactions, oxygen formation and photo-corrosion as:



As will be shown below, at high anodic potentials reaction (1) dominates resulting in a light induced modification of the surfaces namely laser induced film growth. This is demonstrated in fig. 6 where the results of so called locodynamic experiments across grain boundaries between single Ti grains of known orientation are shown. For this, the illuminated sample was scanned in  $\mu m$  steps normal to the laser beam while the electrode potential was increased as in a common cyclovoltamogram. The advantage of this procedure is that the ray always hits an almost fresh surface area allowing to investigate the potential dependence of the photo-reactions without previous modification of the initial semiconducting films. Fig. 6a shows micrographs of the resulting modified Ti surfaces on four substrate grains. The surface orientations and the grain boundaries between the single grains are indicated. The locodynamic experiments were performed on anodic  $TiO_2$  films formed potentiodynamically at 20 V. The UV-laser power was  $50 \text{ kW/cm}^2$ , the applied potential  $U_{loco}$  during illumination was cycled between 0 V and 3 V. The lateral dimensions of the laser modified line (parallel to the grain boundaries) extends the illuminated area (spot radius  $2\mu m$ ) significantly indicating lateral transport mechanisms like hole diffusion beyond the laser focus. The color of the laser traces varies with the applied anodic potential  $U_{loco}$  indicating formation of a gradient in the film thickness.

### 3.5 Characterization of the modified $TiO_2$ films

#### 3.5.1 Laser scanning analysis

For a quantitative analysis of the laser modified films, laser scanning experiments normal to the laser traces and across the grain boundaries were carried out using reduced laser power below the threshold of modification ( $50 \mu W$ ). The results ( $i_{ph}(x, y)$ ) are shown in fig 6b. The scale of the x-axis holds for both micrograph and the corresponding  $i_{ph}(x)$ -curve. These curves give a sectional profile of the laser modified site corresponding to the potential  $U_{loco}$  applied in the locodynamic experiment before. From the x-scan the lateral dimensions of the laser induced modification can be evaluated. Scanning of the surface  $i_{ph} = f(x, y)$  in both dimensions allows an imaging of the entire potential dependence  $i_{ph} = f(x, y = U_{loco})$  of the laser induced modification. The photocurrent fluctuations on the unmodified crystal surfaces are below 1 %. Crossing from one crystal surface to the other (scan across the grain boundary) yields an immediate  $i_{ph}$  change of about a factor of 2 due to the dependence of  $i_{ph}$  on the texture as discussed previously. From the decay of this sudden change, the lateral resolution of the method can be estimated to be about  $2\mu m$  which agrees well with the laser focus. Hence, it can be concluded that laser scanning allows imaging of passive layer properties at heterogeneties like grain boundaries. For instance, in case of the (0001)/(xxx0) sample, the fringed structure of the grain boundary which is visible in the micrograph can be imaged accurately by the  $i_{ph}(x, y)$ -curves.

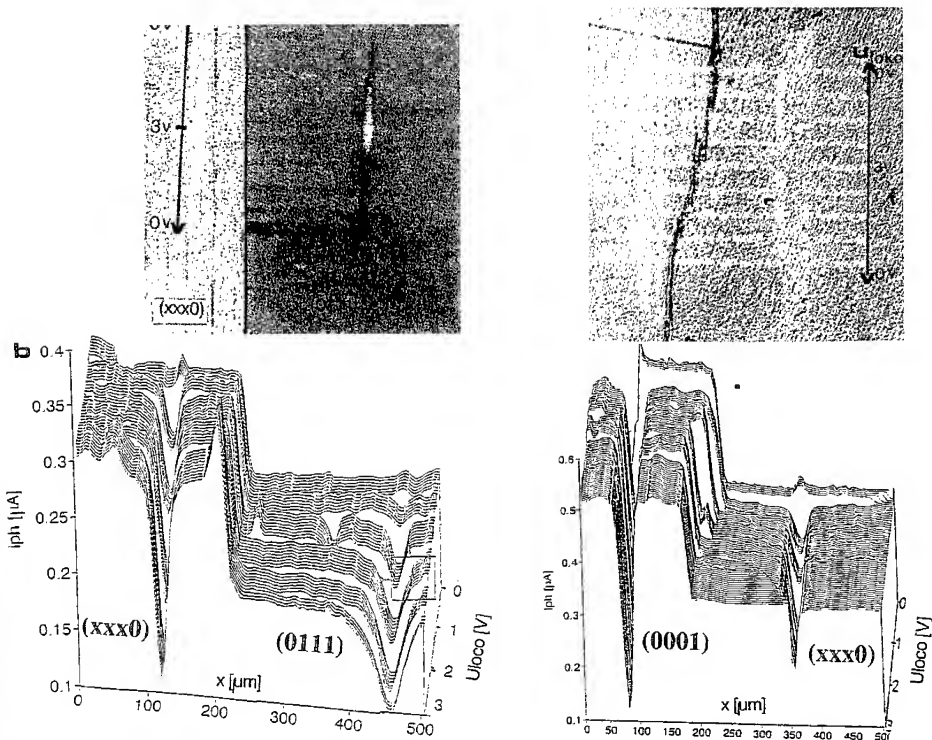


Figure 6: a) Micrographs of the (0001)/(xxx0) and (0111)/(0001) grains (anodic 20 V TiO<sub>2</sub> films). The applied locodynamic potential  $U_{locc}$  was cycled between 0 and 3V, laser power = 50 kW cm<sup>-2</sup>. The visible laser traces indicate formation of a gradient in the TiO<sub>2</sub> film thickness. b) Laser scanning analysis across the laser traces and the grain boundaries (imaging of film properties).

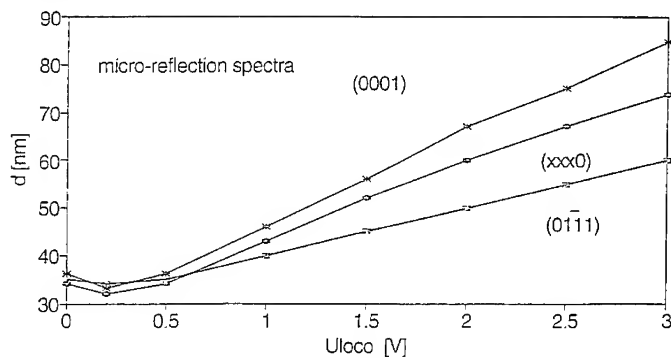


Figure 7: Micro reflection spectroscopically determined film thickness of the UV-laser generated TiO<sub>2</sub> gradients as a function of  $U_{locc}$ .

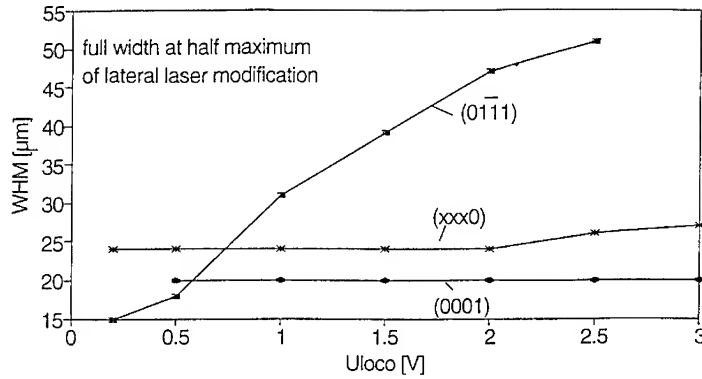


Figure 8: Lateral extension (full width at half maximum) of the  $\text{TiO}_2$  gradients as a function of  $U_{loco}$ . The focus spot diameter during illumination was  $2 \mu\text{m}$ .

### 3.5.2 Micro-reflection spectroscopy

Fig. 7 shows the film thickness measured on top of the modified region by means of micro-reflection spectroscopy applying averaged optical constants which were determined with ellipsometry before. Above locodynamic potentials of  $0.25 \text{ V}$  clearly an increase of the film thickness is observed proving reaction (1) to be dominant in this potential regime. However, below  $0.25 \text{ V}$  a thinning of  $d_f$  took place which can be attributed to photocorrosion, i.e. reaction (3). This leads to the important conclusion that UV-laser illumination can be used for both a thickening (writing) or thinning (erasing) of semiconducting films. The applied potential ( $U_{loco}$ ) determines which reaction dominates and therefore can be used to control the layer thickness. Hence, this method can be applied for preparation of special semiconducting structures such as thickness gradients which easily can be realized by means of locodynamic illumination of the sample surface.

Additionally,  $d_f$  as well as the lateral extension of the laser modified films depend on the substrate orientation which therefore must be known. For this, AME can be applied in-situ. For all substrate orientations it was found that the lateral extension of the modified regions exceeds the illuminated site significantly. In the case of the (0001) and (xxx0) orientation, the lateral extension of the modified site is almost independent of  $U_{loco}$ . In contrast, the (0111) surface shows a significant dependence of the laser line extension on  $U_{loco}$ . This is quantified in fig. 8 showing the full width at half maximum of the normal laser scans as a function of  $U_{loco}$ . This behaviour roughly correlates with the  $d_f(U_{loco})$ -curves in fig 7, i.e. the laser induced oxides are vertical thicker but less extended for the (0001) and (xxx0) than for the (0111) orientation. This suggests that the amount of the laser induced oxide is determined by the number of generated electron/hole pairs and is almost constant for the different orientations. The difference in the lateral and vertical extension of the laser modified region for the different grains is due to the different electronic properties of the original semiconducting films which determine the lateral hole diffusion.



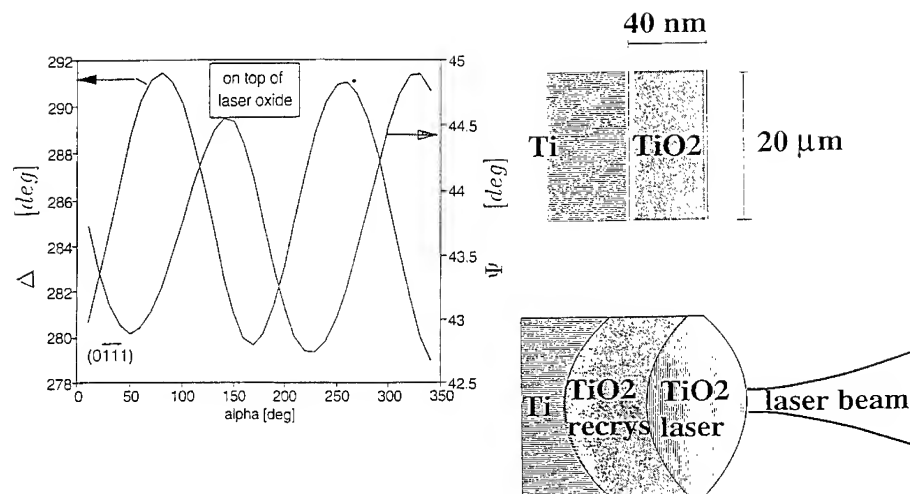


Figure 9: AME measurement performed on top of the UV-laser modified  $\text{TiO}_2$ -film,  $U_{\text{loco}}$  during formation was 2 V. Additionally, a cartoon of the formed film system is shown.

### 3.5.3 AME analysis of the modified films

In order to analyze the structure of the UV laser modified semiconducting  $\text{TiO}_2$  films, AME was performed on top of the modified area ( $U_{\text{loco}} = 2$  V). The resulting AME-curves  $\Delta(\alpha)$  and  $\Psi(\alpha)$  are shown for the example of the (0111) surface in fig. 9. In comparison to fig. 2 now a change in amplitude, phase and average value of the  $\Delta(\alpha)$  and  $\Psi(\alpha)$ -curves was measured. The shift of the average  $\Delta$  and  $\Psi$  curves towards higher average values can be attributed to the increased layer thickness but the alteration of both phase and amplitude indicates a structure change of the  $\text{TiO}_2$  film. The quantitative evaluation of these curves yielded a two layer model as is illustrated in fig. 9, too. Interestingly, it was found that the initial films (metal/oxide interface) recrystallized to anatase (ordinary and extraordinary optical parameters  $n_o = 2.55$ ,  $n_{ao} = 2.48$ ). On top of this layer a very amorphous one was found exhibiting a low density of about  $3 \text{ g cm}^{-3}$  (estimated by analysis of the determined optical constants [14]). Therefore, these oxides can clearly be distinguished from each other and from the original anodic layers.

## 4 Conclusions

In order to characterize and modify heterogeneous semiconducting surfaces, several in-situ micro methods were applied simultaneously under microscopic control. All measurements were carried out on single grains with the Ti/ $\text{TiO}_2$  system as an example. It is shown that the properties of the semiconducting  $\text{TiO}_2$  films sensitively depend on the substrate texture. The new AME-method was used for in-situ determination of the substrate grain orientation.

The electronic and optical film parameters were determined by means of photoresist micro-electrochemistry and micro-ellipsometry. The layer properties such as film thickness and defect state concentration vary with the substrate orientation in a systematic manner. For instance, on the densest packed surface (i.e. (0001)) the highest defect state concentration and lowest film thickness was found. The electronic and optical film parameters were confirmed by photocurrent measurements. The anodic TiO<sub>2</sub> films were found to be amorphous with mobility gap energies close to the one of the TiO<sub>2</sub> modification anatase.

The TiO<sub>2</sub> films were modified at high local resolution by means of focused UV-laser illumination. Both a thickening (writing) or thinning (erasing) of the films could be realized depending on the applied potential ( $U_{loc}$ ) which could be used to control the layer thickness. This allows preparation of singular structures such as semiconducting films with thickness gradients. AME was applied to characterize the modified area and a two layer system (see fig 8b) was found. The original anodic layers, which were amorphous before, showed a recrystallization to anatase. The films on top of the recrystallized ones were amorphous with a low density of about 3 g cm<sup>-3</sup>.

#### Acknowledgement

The financial support of the Deutsche Forschungsgemeinschaft DFG is gratefully acknowledged.

#### References:

1. Lj. D. Arsov: *Electrochim. Acta*, 30 (1985) 1645
2. A. Michaelis, J.W. Schultze: *Thin Solid Films* 233 (1993) 86
3. A. Michaelis, J.W. Schultze: *Thin Solid Films* 274 (1996) 82
4. St. Kudelka, A. Michaelis, J.W. Schultze: *Electrochim. Acta*, 40 (1995)
5. St. Kudelka, A. Michaelis; J.W. Schultze: *Ber. Bunsenges. Phys. Chem.* 99 (1995) 1020
6. J.W. Schultze, K. Bade, A. Michaelis: *Ber. Bunsenges. Phys. Chem.* 95 (1991) 1349
7. K. Bade, O. Karstens, A. Michaelis, J.W. Schultze: *Faraday Disc.* 94 (1992) 45
8. A. Michaelis, J.W. Schultze: *Electrochim Acta*, accepted for publication 9. J.P.H. Sukamto, W.H. Smyrl, C.S. McMillan, M.R. Kozlowski: *J. Electrochem. Soc.* 130 (1992) 265
10. J.P.H. Sukamto, C.S. McMillan, W.H. Smyrl: *Electrochimica Acta* 38, (1993) 15
11. A. Michaelis, J.W. Schultze, *Applied Surface Science* (1996) in press
12. F. Di. Quarto, S. Piazza, C. Sunseri: *Ber. Bunsenges. Phys. Chem.* 91, (1987) 437
13. F. Di. Quarto, S. Piazza, C. Sunseri: *J. Chem. Soc. Faraday Trans. I*, 85, (1989), 3309
14. A. Michaelis, J.L. Delplancke; J.W. Schultze: *Materials Science Forum*, 471 (1995) 185

## IN SITU INVESTIGATION OF WORKING BATTERY ELECTRODES USING SYNCHROTRON X-RAY DIFFRACTION

N.M. JISRAWI<sup>\*</sup>, T.R. THURSTON<sup>\*\*</sup>, X.Q. YANG<sup>+</sup>, S. MUKERJEE<sup>+</sup>, J. MCBREEN<sup>+</sup>,  
M.L. DAROUX<sup>++</sup>, X.K. XING<sup>++</sup>

<sup>\*</sup> Dept. of Physics, Birzeit University, P.O.Box 14, West Bank.

<sup>\*\*</sup>Dept. of Physics, Brookhaven National Laboratory, Upton, NY 11973, USA.

<sup>+</sup>Dept. of Applied Science, Brookhaven National Laboratory, Upton, NY 11973, USA.

<sup>++</sup>Gould Electronics, Eastlake, OH 44095, USA.

### ABSTRACT

The results of an *in situ* investigation of the structural changes that occur during the operation of working battery electrodes using synchrotron radiation are presented. Two types of electrodes were investigated: an AB<sub>2</sub>-type *Laves* phase alloy anode with the composition Zr<sub>x</sub>Ti<sub>1-x</sub>M<sub>2</sub> and a proprietary cell based on a Li<sub>x</sub>Mn<sub>2</sub>O<sub>4</sub> spinel compound cathode made by Gould electronics. For the *Laves* phase alloy compositions with x=0.25 and 0.5 and M=V<sub>0.5</sub>Ni<sub>1.1</sub>Mn<sub>0.2</sub>Fe<sub>0.2</sub> were examined. Cells made from two different batches of Li<sub>x</sub>Mn<sub>2</sub>O<sub>4</sub> material were investigated. The relationships between battery performance and structural changes will be discussed. In the later case, we also discuss the role of over-discharging on the Li<sub>x</sub>Mn<sub>2</sub>O<sub>4</sub> structure and on battery operation.

### INTRODUCTION

Considerable research efforts have devoted to the development of stable, low cost, reproducible battery materials.[1,2] Two of the more important families of materials are hydrogen-absorbing alloys and spinel-type *Li* insertion electrodes. The importance of these two families of batteries cannot be over-emphasized. Metal-hydride batteries have been widely studied, but systematic *in situ* studies of batteries in operation remain to be done.[3] In situ structural studies on operating battery electrodes can provide guidance in optimizing alloy compositions with desirable performance characteristics. However, it is difficult to investigate operating batteries because it is necessary for the probing radiation to penetrate not only the cell walls and electrolyte, but also through the electrode itself, if changes that occur in the bulk of the electrode are to be monitored.

Li insertion electrodes with the spinel structure have been studied extensively since Hunter [4] showed that the spinel can be a Li insertion compound. The so-called "rocking chair" batteries used as secondary(rechargeable) cells have generated much commercial interest because of their relative safety ( no free Li is being used ). In these batteries, an intercalation compound other than Li is used for the anode and the battery voltage depends on the difference between the chemical potential of Li in the two electrodes. Ohzuku *et al.* Did the first systematic *in situ* study in which some of the phases that occur during Li intercalation were identified. [5] However, LiMn<sub>2</sub>O<sub>4</sub> exhibits many different structural properties depending on the initial processing conditions, and Ohzuku *et al* examined LiMn<sub>2</sub>O<sub>4</sub> processed under only one set of conditions. In this investigation, we

report on an *in situ* investigation in which hard x-rays from a synchrotron source were used to probe the bulk of the operating electrode for  $\text{LiMn}_2\text{O}_4$  processed differently from Ohzuku *et al.*

## EXPERIMENTAL DETAILS

The experiments as described elsewhere[6], were performed at beamline X-27A at the National Synchrotron Light Source. X-rays with energy  $\sim 24.5\text{KeV}$  ( $\lambda \sim 0.505\text{\AA}$ ) were used. White light from the synchrotron was monochromatized using a bent  $\text{Si}(111)$  crystal of the type used by the medical group at the NSLS.[7] The samples, consisting of a specially made cell in the case of the nickel-hydride and a proprietary cell for the  $\text{Li}_x\text{Mn}_2\text{O}_4$ , were placed in a transmission geometry in a two circle goniometer. An  $\text{LiF}(200)$  crystal was used as an analyzer. The construction of the nickel-metal hydride cell has been described in detail in Ref. [6] and [8]. The thickness of the metal-nickel-hydride anode was  $\sim 0.5\text{ nm}$  and both anode and carbon cathode were immersed in a 6 molar  $\text{KOH}$  solution. The  $\text{Li}_x\text{Mn}_2\text{O}_4$  cells were manufactured by Gould electronics for the purposes of this experiment as  $2\text{cm} \times 5\text{cm} \times 0.5\text{mm}$  cells, but were otherwise similar in construction to their commercial cells. The cells contained a carbon anode and nonaqueous electrolyte. They were factory sealed in a plastic casing with a fixed amount of  $\text{Li}$  available for intercalation into the cathode so that  $x$  was always less than 1. Different charging cycles were applied to each set of electrodes while x-ray data was continuously taken. A custom-made cycler was used to control the charging state of the  $\text{Li}_x\text{Mn}_2\text{O}_4$  - battery while in situ cycling of the  $\text{AB}_2$  cell was done using standard cyclic voltammetry apparatus.

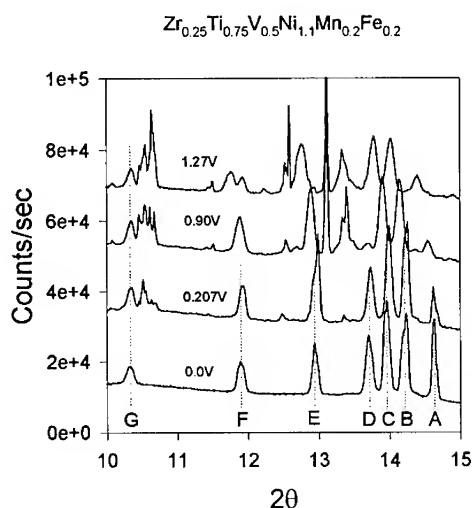
## RESULTS

### The Laves Phase $\text{AB}_2$ Material:

Two  $\text{AB}_2$  compositions were studied in this investigation. First, a cell with an anode made of  $\text{Zr}_{0.5}\text{Ti}_{0.5}\text{V}_{0.5}\text{Ni}_{1.1}\text{Mn}_{0.2}\text{Fe}_{0.2}$  was prepared and *activated* by cycling more than ten times. The cell was then charged to a voltage  $\sim 1.4\text{V}$  and moved to the synchrotron beam line where it was allowed to discharge through an external resistor. The structural changes that occur during the discharge process were observed directly via x-ray diffraction. This demonstration experiment was done to show the utility of the method. The changes that occur during the discharge process are discussed in some detail in Ref. 6. In Fig. 1 we show results obtained on another alloy with a more complex structure. The alloy used here is  $\text{Zr}_{0.25}\text{Ti}_{0.75}\text{V}_{0.5}\text{Ni}_{1.1}\text{Mn}_{0.2}\text{Fe}_{0.2}$  which is a mixture of two phases in its unhydrided state. The figure shows a set of x-ray  $\theta$ - $2\theta$  scans taken after the electrode with the above composition was activated then charged to a voltage of  $1.4\text{V}$ . The cell was then taken to the beam line and discharged while x-ray scans were taken. The data in figure 1 show that peaks with intensities up to 20,000/sec can be obtained readily with this technique, even though the x-rays had to penetrate through electrolyte, binding materials, all casings, and the electrodes themselves. The first scan shown corresponds to a cell

voltage of 1.27V which is considered an intermediate state. The other scans also show the complicated intermediate behavior of this alloy.

**Figure 1:** X-ray  $\theta$ - $2\theta$  scans for the  $AB_2$  material with the composition  $Zr_{0.2}Ti_{0.75}M_2$  (see text). The unhydrided material is a mixture of a b.c.c. phase (~13%) and a C14 *Laves* phase (87%). In addition binder material peaks are also visible (feature G). The figure shows the complicated behavior of the material during the intermediate states of partial hydrogen charging. Such states cannot be studied easily using ex-situ methods. In the figure we have also indexed peaks belonging to the C14 *Laves* phase for the unhydrided material. There are: F:(110), E:(103), D:(200), C:(112), B:(201), and A:(004).



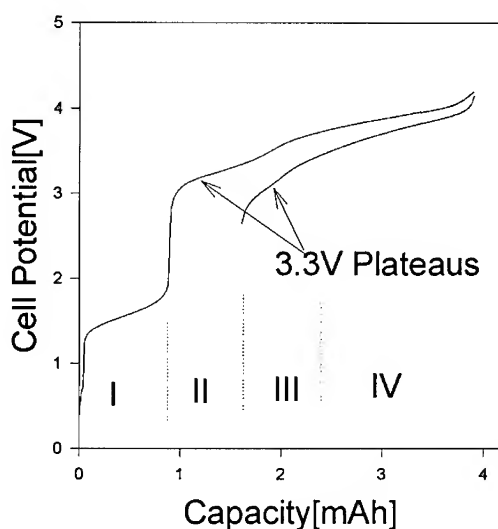
#### $Li_xMn_2O_4$ Cathodes:

Fresh cells of this type were obtained from Gould electronics. The x-ray diffraction experiments were performed while the cells were connected to a cycler. Fig. 2 is a plot of the voltage versus capacity for one such cell where the following experiments were done:

1) An initial charging cycle was done where the cell was charged from 0 to 4.2 V. The charging current used was 200 $\mu$ A. The voltage-capacity (V-C) curve for this initial charge can be divided into 4 distinct regions, each associated with special structural changes as explained in detail in Ref. 9. We discuss here briefly the main features of this cycle. Region I is characterized by irreversible changes where a multiphase  $LiMn_2O_4$  material converts into single phase material at a constant voltage of ~1.5V. As discussed in Ref. 9, the existence of this plateau seems to be dependent on the preparation conditions for the  $Li_xMn_2O_4$  material. This result is of practical importance because it could be used as a method for discerning batches of  $LiMn_2O_4$  with favorable properties. Another plateau at 3.3 V (region II) is where Li is intercalated into the carbon anode while the  $Li_xMn_2O_4$  lattice contracts as Li is removed. In this region the  $Li_xMn_2O_4$  is single phase. In region III, two cubic phases coexist with distinct lattice constants, while single phase behavior is recovered in region IV which extends up to 4.3V.

## $\text{Li}_x\text{Mn}_2\text{O}_4$

**Figure 2:**  $\text{Li}_x\text{Mn}_2\text{O}_4$  cell potential plotted against cell capacity for the initial charging cycle. Four distinct regions are seen in the plot as detailed in the text. The figure also shows data for the first discharge cycle. Note that the 3.3V plateau loses much of its capacity during the first cycle.



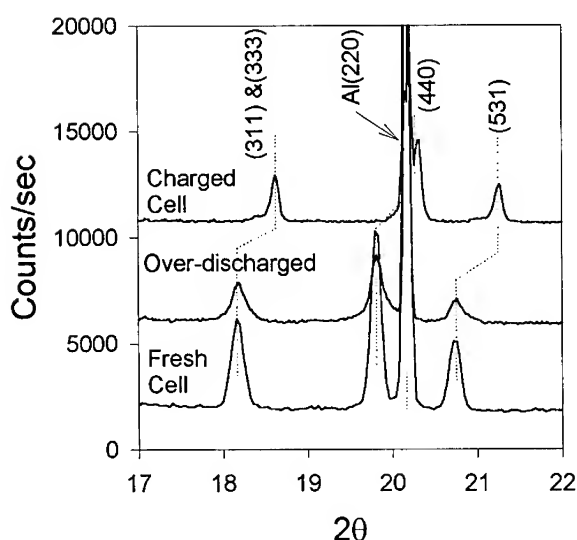
2) The cell was then discharged slowly to a voltage higher than 2.2 V, held and then recycled between 2.2V and 4.3V. This relatively fast procedure was designed to study changes that occur during the *activation* process. While the two-phase coexistence region is retained over the appropriate voltage range, that plateau voltages changed during the discharge process. The capacity of the battery in the region of the 3.3V plateau was extremely reduced.

3) The cell is finally *over-discharged* while x-ray scans are done to study the structural changes during this final phase. As will be shown below the  $\text{Li}_x\text{Mn}_2\text{O}_4$  lattice is permanently deformed and will not charge again as before.

Figure 3 compares x-ray  $\theta$ - $2\theta$  scans for the cell when it was fresh, over-discharged, and fully charged to a voltage of 4.2V. The peaks for the over-discharged cell are broad and diffuse compared to those of the fresh cell. Other x-ray data shows that when charged again, the peaks will not sharpen as in the initial cycle. Instead, damage to the cell seems to be permanent.

### Li<sub>x</sub>Mn<sub>2</sub>O<sub>4</sub>-Carbon Cell, $\lambda = .505 \text{ \AA}$

**Figure 3:**  $\theta$ - $2\theta$  scans for the Li<sub>x</sub>Mn<sub>2</sub>O<sub>4</sub> electrode. Three scans are shown which compare between the cell when it was fresh, fully charged, and over-discharged. The x-ray peaks for the over-discharged cell are permanently deformed.



## RESULTS AND DISCUSSION

The structural and microstructural changes that occur during the operation of battery cells are very important because they have a direct affect on their performance. We have discussed in other publications that synchrotron hard x-rays provide a powerful technique by which these changes can be monitored, and that differences in battery performance due to sample preparation can readily be correlated with these structural changes.[6,8] Data shown here provide two more examples of the power of this method.

Firstly, the data on AB<sub>2</sub> compounds shows that the technique can be applied to many types of systems. In this case the example is the mixed phase material Zr<sub>0.25</sub>Ti<sub>0.75</sub>M<sub>2</sub>. In its unhydrided state this material is a mixture of a b.c.c. phase (13%) and the cubic *Laves* phase C14 (87%). In this preliminary experiment, the cell was charged to a voltage of 1.4V and then disconnected from the charger and brought to the beamline in its charged state. Figure 1 shows  $\theta$ - $2\theta$  scans for the unhydrided cell and three scans taken during the discharge process. All three scans illustrate the complex behavior during intermediate charging states of alloy. Peaks belonging to both phases and also to the binder material are visible in the scans. In this first experiment on this alloy, our goal was only to demonstrate the capabilities of the method in looking at such complex behavior. In future experiments, we plan to study this behavior in detail by doing the charging and discharging *in situ* and by tracing the various phases and their behavior as the cells are charged and discharged.

Second, we have the data on the “rocking chair”  $\text{Li}_x\text{Mn}_2\text{O}_4$ -carbon cell. The changes that occur in these cells during the first charging cycle were discussed in another publication.[9] There it was shown that irreversible changes occur during this cycle that were different depending on the batch of material used in each battery and its preparation conditions. These batteries can be operated at two different plateau voltages. At 3.9V a “*lever rule*” situation occurs as conversion occurs between two coexisting cubic phase with different lattice constants. The other plateau is at 4.1V when Li insertion or extraction is reflected as an expansion (contraction) of the  $\text{Li}_x\text{Mn}_2\text{O}_4$  lattice. It is known that these batteries should be operated between these voltages and never to be over-discharged below a nominal voltage of 2.0V. In this study we have deliberately over-discharged batteries below that voltage while observing changes to the crystal structure of the underlying  $\text{Li}_x\text{Mn}_2\text{O}_4$  lattice. It is shown in Fig. 3 that the spinel peaks are broadened and their intensity reduced, due to damage done to the lattice. Later attempts to charge the cell after over-discharging have failed showing that this damage is permanent. We believe that this experiment is of importance because it may help identify the reasons behind this damage. Further work is planned where the goal is to identify the critical voltages beyond which permanent damage occurs and hence to help battery manufacturers identify the proper operating limits for their batteries.

## ACKNOWLEDGMENTS

This work was supported by the U.S. Department of Energy under contract No. DE-AC02-76CH00016.

## REFERENCES

1. J.M. Tarascon, E. Wang, F. K. Shokoohi, W.R. McKinnon, and S. Colson, J. Electrochem. Soc. **138**, 2859(1991); J. M. Tarascon and D. Guyomard, *ibid.*, 2864(1991).
2. M. M. Thackery, A.de Kock, and W.I. David, Mat. Res. Bull., **28**, 1041-1049(1993).
3. J. Huot, E. Akiba, T. Ogura, and Y. Ishido, J. Alloys and Compounds, **218**, 101-109(1995).
4. J.C. Hunter, J. Solid State Chem., **39**, 142(1981).
5. T. Ohzuku, M. Kitagawa, and T. Hirai, J. Electrochem. Soc. **137**, 769(1990).
6. T.R. Thurston, N.M. Jisrawi, S. Mukerjee, X.Q. Yang, J. McBreen, M.L. Daraoux, and X.K. Xing, Appl. Phys. Lett., **69**, 194(1996).
7. P. Suortti, W. Thomlinson, D. Chapman, N. Gmur, D.P. Siddons, and C. Schulze, Nucl. Instrum. Methods A, **336**, 304(1993).
8. S. Mukerjee, J. McBreen, J.J. Reilly, J.R. Johnson, G. Adzik, K. Petrov, M.P.S. Kumar, W. Zhang, and S. Srinivasan, J. Electrochem. Soc. **142**, 2278(1995).
9. N. M. Jisrawi, X.Q. Yang, S. Mukerjee, T.R. Thurston, J. McBreen, M.L. Daraoux, and X.K. Xing, *submitted to J. Electrochem. Soc.*



## PREPARATION AND STUDY OF CONDUCTIVE POLYMER / HIGH- $T_c$ SUPERCONDUCTOR ASSEMBLIES

J.T. MCDEVITT\*, J. E. RITCHIE\*, C. T. JONES\*, A. D. WELLS\*, C. A. MIRKIN\*\*, F. XU\*\*

\*Department of Chemistry, The University of Texas, Austin, TX, 78712, USA

\*\*Department of Chemistry, Northwestern University, Evanston, IL 60208, USA

### ABSTRACT

In this report, a monolayer of N-(3-aminopropyl) pyrrole is used as a template layer for the controlled growth of polypyrrole on polycrystalline and oriented films of the high temperature superconductor,  $YBa_2Cu_3O_7$ . Large increases in the growth rate and smoothness of the polymer layer are obtained with the use of the monolayer template as compared with the bare superconductor electrodes. Observation of the electrochemical growth characteristics as well as polymer morphological properties allows for an evaluation of the local surface conductive properties of superconductor-based ceramic and thin film samples. The use of the amine substituted pyrrole self-assembled monolayer serves to drastically alter the polymer growth characteristics and the surface adhesion properties.

### INTRODUCTION

Of the four classes of extensively explored electronic materials (i.e. insulators, semiconductors, metals, and superconductors) methods have been developed for chemically modifying all but the last category. For example, the spontaneous adsorption of monolayer films has been demonstrated for a large number of adsorbate molecules with varying functional groups onto a range of different substrates. This chemistry has been shown to include: thiols, disulfides, sulfides, and phosphines on Au, carboxylic acids on metal oxides, trichloro- and trialkoxysilanes on oxide surfaces, phosphonates on metal phosphonate surfaces, thiols on GaAs, CdSe, CdS, Cu, and Ag, and thiols, olefins, and isonitriles on Pt.<sup>1</sup> Such monolayer films have been used in the design of interfaces for chemical sensing applications, nonlinear optical materials, methodology for photopatterning of surfaces, optically sensitive interfaces for proof-of-concept molecule-based actinometers, and high density memory devices. In addition, self-assembled monolayer films have been used to study fundamental processes involving interfacial electron transfer, adhesion, and surface wetting.

Following the discovery of high temperature superconductivity by Bednorz and Müller in 1986, there has been a tremendous amount of excitement in the scientific and industrial communities. This excitement is related to the fundamental studies of these remarkable compounds and their practical utilization. Unfortunately, the poor materials properties exhibited by these brittle and reactive ceramic materials has slowed progress in high- $T_c$  research and development. Many of the envisioned technological applications for cuprate-based compounds rely on a firm understanding of the fundamental surface structure of high temperature superconductors (HTSC), and methods that can be used to control the interfacial properties of High- $T_c$  materials. Furthermore, the interpretations of fundamental measurements on HTSCs are often conflicting due to a poor understanding of HTSC surface structure and chemical composition. The inherent reactivity of these materials towards environmental reagents (i.e.  $H_2O$ ,  $CO_2$ , CO, etc.) often yields a surface composition that differs substantially from the bulk.<sup>2</sup> For example, under ambient conditions,  $YBa_2Cu_3O_7$  reacts with atmospheric  $H_2O$  and  $CO_2$  to form a surface passivating layer of the corrosion product,  $BaCO_3$ . It is surprising that given the importance of HTSC systems, very little information is currently available for the chemical modification of high- $T_c$  surfaces.

Only recently have methods been developed for the spontaneous adsorption of monolayer reagents onto high- $T_c$  surfaces.<sup>3-6</sup> Information regarding the surface modification of the cuprate

systems has been obtained from studies of the surface coordination chemistry of  $\text{YBa}_2\text{Cu}_3\text{O}_7$  using a series of redox-active ligands containing alkylamine, arylamine, thiol, phosphine, amide, and alcohol functionalities.<sup>4</sup> Using a series of redox-active ligands, detailed studies of the chemical adsorption properties of  $\text{YBa}_2\text{Cu}_3\text{O}_7$  have been completed using electrochemical procedures. It has been determined from these studies that the spontaneous adsorption process occurs for the amine and thiol containing molecules. These molecules have been shown to adsorb onto surfaces of epoxy encapsulated polycrystalline  $\text{YBa}_2\text{Cu}_3\text{O}_7$  electrodes as well as thin film electrodes of  $\text{YBa}_2\text{Cu}_3\text{O}_7$  prepared by the laser ablation method.

Of the six compounds studied, the alkylamine reagents consistently yielded the largest surface coverages and the most persistent electrochemical response (i.e. after 30 cycles at 200 mV/sec, there was very little noticeable loss in electroactivity). The  $\text{YBa}_2\text{Cu}_3\text{O}_7$  electrode modified with a redox active arylamine exhibited similar behavior, but with significantly lower surface coverages. In contrast, monolayer films based on alkylthiol modified surfaces of  $\text{YBa}_2\text{Cu}_3\text{O}_7$  thin films exhibit a slow, but steady loss in electroactivity.

The spontaneous adsorption of molecular assemblies onto the surfaces of superconductors provides an effective and simple method for controlling the interfacial properties of high- $T_c$  structures and devices.<sup>3,4,7</sup> Here, we show that electroactive self-assembled monolayers (i.e. SAMs) based on alkylamine substituted pyrrole functionalities can be used to alter the growth of polypyrrole onto c-axis oriented films of  $\text{YBa}_2\text{Cu}_3\text{O}_7$  as well as on ceramic electrodes prepared from the same material. Information relevant to the mechanism of polymerization is explored by varying the deposition times and the applied potential biases.<sup>5</sup>

## EXPERIMENTAL

Polycrystalline pellets of  $\text{YBa}_2\text{Cu}_3\text{O}_7$  were synthesized using a solid-state technique, incorporating three 900°C sintering steps with intermediate grinding, followed by a 550°C annealing step completed in flowing oxygen. The pellets were characterized by powder x-ray diffraction (XRD) and resistivity versus temperature measurements. The ceramic pellets were used to fashion epoxy encapsulated electrodes using a previously described procedure.<sup>8</sup> The surface of the electrodes were sanded immediately prior to use to expose areas of fresh superconductor.

Thin film samples of  $\text{YBa}_2\text{Cu}_3\text{O}_7$ , having c-axis orientations, were deposited onto MgO (100) substrates by the pulsed laser ablation technique.<sup>9</sup> Films with thickness values of  $\sim 1500\text{\AA}$  were utilized for the described studies. When characterized by XRD, these films produced only the (00 $\ell$ ) reflections of the superconductor. These films were electrically contacted using alligator clips and suspended in solution for the electrochemical measurements.

The synthesis of N-(3-aminopropyl) pyrrole was performed as described previously.<sup>5</sup> The aminopyrrole reagent was adsorbed onto  $\text{YBa}_2\text{Cu}_3\text{O}_7$  by soaking the fresh cuprate surface in a 1mM acetonitrile solution of the adsorbate molecule for a period of 24 hours.<sup>4</sup> Polypyrrole was deposited onto  $\text{YBa}_2\text{Cu}_3\text{O}_7$  electrodes using a 1.4V potential step (vs. Ag wire) from a 1% solution of pyrrole monomer in 0.1M  $\text{Bu}_4\text{NBF}_4/\text{acetonitrile}$ .<sup>10</sup> Electrochemical depositions were carried out in a nitrogen filled inert atmosphere glove box, using acetonitrile distilled from  $\text{P}_2\text{O}_5$ . Pyrrole (Aldrich) was purified by passing the monomer over activated alumina immediately prior to use. Tetrabutylammonium tetrafluoroborate (Fluka) was twice recrystallized, dried under reduced pressure, and stored under an inert atmosphere.

## RESULTS

The lattice structure of  $\text{YBa}_2\text{Cu}_3\text{O}_7$  and related cuprate compounds possess two dimensional characteristics in which high electrical conductivity is achieved within the a-b plane and poor conductivity perpendicular to this direction. As illustrated in Figure 1, the  $\text{YBa}_2\text{Cu}_3\text{O}_7$  lattice can be broken down into four different types of layers, i.e. Cu(2) O, Cu(1) O, Ba-O and an oxygen deficient Y sheet. As shown previously, each of these layers are receptive to various

cation substitutions.<sup>11,12</sup> Certain formulations such as  $\text{Y}_{0.6}\text{Ca}_{0.4}\text{Ba}_{1.6}\text{La}_{0.4}\text{Cu}_3\text{O}_{7.8}$  have been shown to exhibit good superconducting properties while exhibiting excellent resistance to corrosion. To minimize complications associated with surface damage to the high- $T_c$  material, this cation substituted compound is utilized for some of the studies described below, along with similar experiments completed with the parent compound,  $\text{YBa}_2\text{Cu}_3\text{O}_7$ .

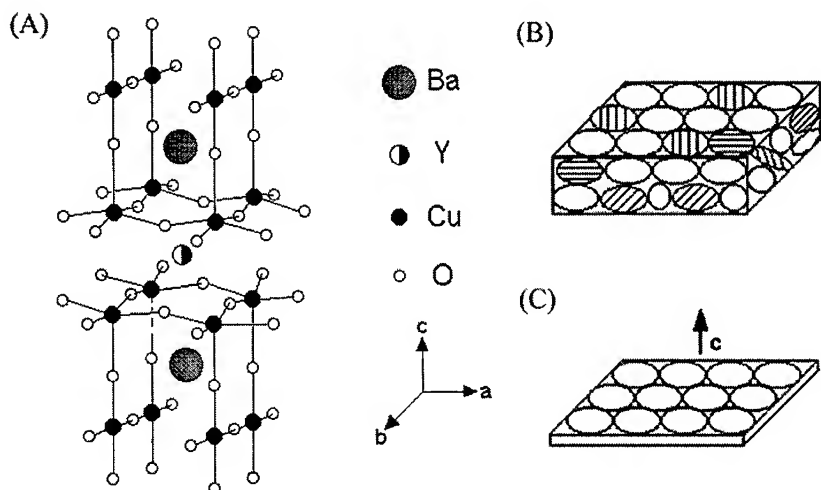


**Figure 1:**

(A) The unit cell of  $\text{YBa}_2\text{Cu}_3\text{O}_7$  is shown along with (B) a schematic of a polycrystalline pellet and (C) a c-axis oriented thin film sample.

In order to better study the polymer growth behavior onto the high- $T_c$  surfaces, both polycrystalline (Figure 1b) and c-axis oriented thin film samples (Figure 1c) were studied. Many of the unusual features associated with these remarkable compounds can be traced to the anisotropic structures associated with these materials. The superconducting coherence length within the popular high- $T_c$  compound,  $\text{YBa}_2\text{Cu}_3\text{O}_7$ , has been reported to be a factor of  $\sim 5$  times larger within the copper oxide sheets as compared to the perpendicular direction ( $\xi_{ab} \sim 30 \text{ \AA}$ ,  $\xi_c \sim 6 \text{ \AA}$ ). Similarly, the normal state electrical resistivity of  $\text{YBa}_2\text{Cu}_3\text{O}_7$  exhibits quasi 2-dimensional properties ( $\rho_{ab} \sim 3 \times 10^{-4} \Omega \text{ cm}$ ,  $\rho_c \sim 2 \times 10^{-2} \Omega \text{ cm}$ ).<sup>13</sup> Polycrystalline ceramic samples possess randomly oriented grains which contribute to poor intergrain electrical contact. Samples of this type are unoriented and expose multiple sample orientations to the electrolytic solution.

Important information related to the local surface electroactivity and conductivity properties of the high- $T_c$  superconductors are obtained through an evaluation of the electrochemical growth of polypyrrole onto the surfaces of cuprate samples. For the polymer growth studies, both potential step and cyclic voltammetric scanning procedures are used. These procedures utilize acetonitrile containing 1% pyrrole monomer (by volume) with 0.1M  $\text{Bu}_4\text{NBF}_4$  supporting electrolyte. Various potentials and polymerization times are employed so that polymer growth behavior, both for the nucleation and latter stages of polymer growth, can be evaluated. Moreover, high- $T_c$  samples are investigated with and without the pyrrole-terminated alkyl amine reagent, N-(3-aminopropyl) pyrrole.

Electrochemical deposition of polypyrrole onto bare ceramic electrodes occurs in such a

manner that the polymer layer's morphological features resemble those obtained for similar electrodes such as Pt and Au as illustrated in the scanning electron micrograph (SEM) of Figure 2a. Here, polymer nodules of ~5-10 $\mu$ m diameter are obtained. The polymer layers appearance shown here differs drastically from that observed for the underlying ceramic electrode (not shown).

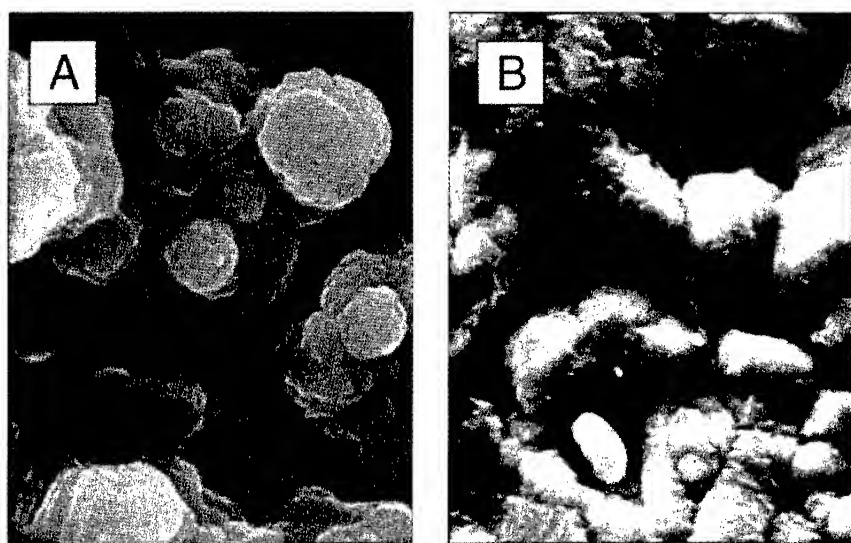


**Figure 2:**

Scanning electron micrographs showing layers of electrochemically deposited polypyrrole onto (A) bare and (B) N-(3-aminopropyl) pyrrole modified polycrystalline superconductor electrodes. The polypyrrole was deposited from a 1% solution of pyrrole in acetonitrile using a 1.4V vs. Ag wire potential step for a period of 10 sec.

Interestingly, polypyrrole layers grown on YBa<sub>2</sub>Cu<sub>3</sub>O<sub>7</sub> pellets modified with N-(3-aminopropyl) pyrrole produce morphological properties that differ from those observed for the unmodified samples. In this case, uniform films which nicely follow the topology of the polycrystalline surface are obtained, as shown in Figure 2b. This behavior suggests rapid nucleation occurs over a large portion of the exposed superconductor surface (*vide infra*).

The adhesion properties for these films were evaluated by applying adhesive tape to the sample, removing the tape, and imaging the sample before and after the adhesive tape tear. Under these conditions, it is noted that the polymer layer tears nearly completely away from the bare superconductor. The superconductor modified with the pyrrole amine reagent displays a more complex behavior. Here it is noted that on the modified YBa<sub>2</sub>Cu<sub>3</sub>O<sub>7</sub> sample, a much larger portion of polymer adheres to the cuprate surface. From such studies it is clear that the presence of the electroactive monolayer serves to improve, in a significant manner, the adhesion of polymer to the superconductor surface.

Furthermore, the large changes in polymer growth morphology on the polycrystalline samples suggest that the inclusion of the pyrrole monolayer serves to alter the polymer nucleation/growth behavior in a significant manner. Shown in Figure 3 are proposed sequence of steps that lead to the deposition of polymer onto the SAM-modified sample. (A) In the initial step, the N-(3-aminopropyl) pyrrole monolayer is adsorbed onto the high-T<sub>c</sub> surface. (B) Upon oxidative treatment of the modified surface, the surface localized reagents are oxidized. Because of the presence of the amine anchor, the oxidized pyrrole reagent must remain in close proximity to

the electrode surface where it can serve as a nucleation site for subsequent polymer growth. (C) On a slower time scale, additional solution dissolved monomer diffuses to the electrode surface where it can be oxidized. (D) Because the oligomers are oxidized more readily than the monomers, some fraction of the solution dissolved monomer couples to the surface localized pyrrole reagent where they foster further polymer growth.

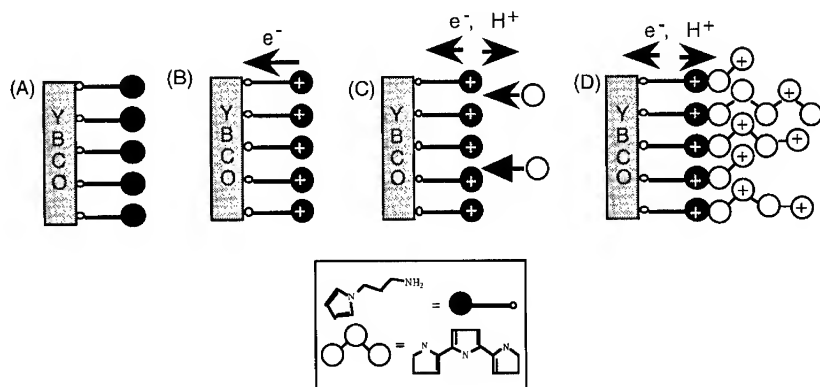


**Figure 3:**

Schematic illustration showing the proposed sequence of steps which may occur at the cuprate surface that are coated with an electroactive monolayer during their electrochemical coating with polypyrrole. (A) In the initial step, the amine-tagged pyrrole monolayer is adsorbed to the cuprate surface. (B) Upon oxidative cycling of the electrode, the adsorbed reagent is rapidly oxidized.<sup>18</sup> (C) On a more gradual time scale, solution dissolved monomer diffuses to the electrode surface. (D) Upon reaching the electrode surface, oxidation of the monomer occurs commensurate with proton loss and coupling of the monomer to the electrode confined template layer whereby growth of the oligomer ensues.

Polymers grown onto the bare cuprate surfaces are expected to couple to the oxide surface in a different manner as detailed in Figure 4. (A) Here, the initial step involves a diffusion of the electroactive monomer to the surface of the electrode. (B) Once the pyrrole molecules reach the surface, it is oxidized to the radical cation. (C) Two oxidized monomers units can couple to each other, and in the process lose two protons to form a neutral oligomeric compound. This oligomer is more readily oxidized than the isolated monomer units, and again becomes oxidized. In addition, an oxidized monomer can also couple to an oxidized oligomer. (D) The oxidation and coupling steps continue to occur in the solution phase in the region of the electrode until the solubility limit of the organic oligomer is exceeded. At this stage, polymer nodules begin to collect on the electrode surface at localized spots. (E) Continued electrochemical growth results in a further expansion of the size of the polymer nodules.<sup>14</sup>

It should be emphasized that polypyrrole growth onto bare electrodes proceeds through an electrode deposition method in which the growing polymer structures couple to the metal surface only after the solubility of the oligomeric compounds is exceeded, as shown in Figure 4. Under such circumstances, polymer solubility characteristics and precipitation dynamics play an important role in dictating the morphology of the as grown polymer layer. Large polymer nodules noted in Figure 2 and their similarity to layers grown on noble metal electrodes suggest this mode of coupling to the surface is occurring. However, the change in morphology noted for the SAM coated ceramic samples suggest more rapid and frequent nucleation occurs for the modified electrodes. The direct coupling of the polymer chains to the electrode surface is also consistent with

an increase in polymer to superconductor adhesion, as noted in above describe adhesion tests.

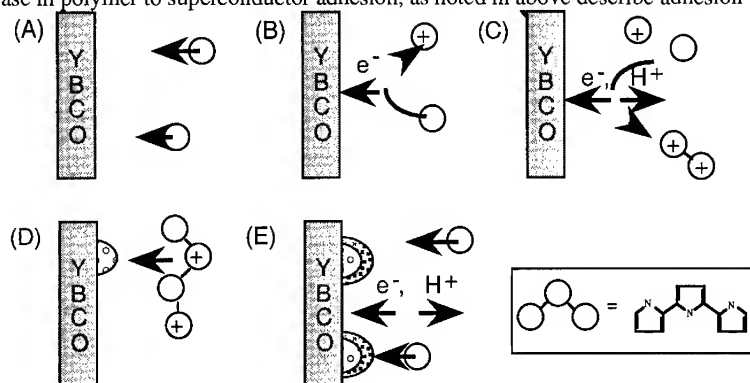


**Figure 4:**

Proposed sequence of steps which may occur at the bare superconductor electrode surface during their coating with an electrochemically deposited layer of polypyrrole. (A) In the first step, neutral monomer diffuses to the electrode surface. (B) Then oxidative treatment of the electrode serves to oxidize monomer molecules which are close to the electrode surface. (C) Once oxidized, the reactive monomers can couple to other pyrrole units, with simultaneous proton loss, to produce soluble oligomer compounds. (D) The growth of the length of the oligomer continues until the solubility limit is exceeded at which time the oligomer precipitates onto the superconductor surface. (E) Further growth of the polymer can occur at these nucleation sites.

To explore whether or not superconductor sample orientation influences the polymer growth behavior, electrochemical growth studies were evaluated on  $\text{YBa}_2\text{Cu}_3\text{O}_7$  films, with and without pyrrole monolayer templates. Here, the initial stages of polymer growth were investigated using a 5 sec potential step to the modest potential of 1.4V vs. Ag quasi-reference electrode.

Interestingly, AFM and SEM images of polypyrrole layers grown under identical conditions onto films of c-axis  $\text{YBa}_2\text{Cu}_3\text{O}_7$ , with and without the pyrrole self-assembled monolayer, reveal that the SAM modified surface produces thicker, more uniform, and more strongly adhered polymer layers. These differences are remarkable, as illustrated in the AFM images provided in Figure 5. The polymer layers grown onto N-(3-aminopropyl) pyrrole-tagged  $\text{YBa}_2\text{Cu}_3\text{O}_7$  compare favorably with the smoothest layers of polypyrrole, on any substrate, reported in the literature.<sup>15</sup> The observation that ultra-smooth polymer layers are obtained with SAM modified  $\text{YBa}_2\text{Cu}_3\text{O}_7$  is consistent with the conclusion that polymer growth proceeds through rapid and uniform nucleation on the modified superconductor surface.<sup>16</sup>

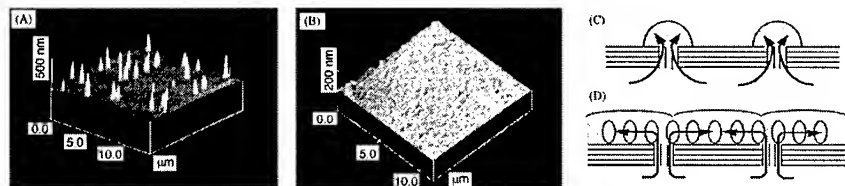


**Figure 5:**

Images acquired by AFM for c-axis oriented films of  $\text{YBa}_2\text{Cu}_3\text{O}_7$  on  $\text{MgO}$  (100) (1500Å superconductor thickness) onto which polypyrrole layers were grown via a potential step

procedure. Conditions were the same as those used to generate the data supplied in Figure 2. Images are provided for (A) untreated  $\text{YBa}_2\text{Cu}_3\text{O}_7$ , and (B) SAM-modified  $\text{YBa}_2\text{Cu}_3\text{O}_7$ . Also included are (C) a schematic drawing showing localized polymer growth which occurs at defect sites for uncoated superconductor, and (D) a similar schematic illustrating how more uniform nucleation of polymer layer can be accomplished through the influence of a surface localized electroactive adsorbed monolayer. Here the ovals represent the adsorbed pyrrole monolayer. This figure has been adapted with permission from Reference 5.

Polypyrrole grown onto the modified superconductor is observed to have >98% surface coverage with feature sizes of approximately 0.20 to 0.25  $\mu\text{m}$  width and a surface roughness of <0.05  $\mu\text{m}$ . However, polymer grown directly onto bare  $\text{YBa}_2\text{Cu}_3\text{O}_7$  leads to the creation of remotely spaced polymer nodules. Here, polymer nodules 0.4  $\mu\text{m}$  - 0.6  $\mu\text{m}$  in width and 0.3  $\mu\text{m}$  - 0.5  $\mu\text{m}$  high are observed to cover approximately 4% of the surface.<sup>5</sup>

It should be emphasized that the use of c-axis oriented films of  $\text{YBa}_2\text{Cu}_3\text{O}_7$  serves to expose the poorly conductive crystallographic direction of this anisotropic conductor to the electrolytic solution.<sup>13</sup> While the uniform, highly conductive Au films studied previously foster rapid and uniform polypyrrole growth, untreated, c-axis oriented  $\text{YBa}_2\text{Cu}_3\text{O}_7$  surfaces yield only sporadic growth at remotely spaced areas, which we term "electroactive hot spots". These "hot spots" correspond to the polymer growth features found in Figure 5a. This behavior is consistent with prior studies reporting that electrochemically deposited polymer structures on c-axis  $\text{YBa}_2\text{Cu}_3\text{O}_7$  nucleate primarily at defect sites, which comprise a small fraction of the overall surface area of the material.<sup>10,17</sup> Polypyrrole grown directly onto unmodified c-axis  $\text{YBa}_2\text{Cu}_3\text{O}_7$  thin films leads to the creation of remotely spaced polymer nodules. The presence of alternative crystallographic orientations of the  $\text{YBa}_2\text{Cu}_3\text{O}_7$  lattice at localized defect sites in laser ablated high- $T_c$  films has been noted previously.<sup>7</sup> Accordingly, it is reasonable to conjecture that exposure of such high conductivity sites to the electrolytic solution dominate the polymer growth dynamics at early polymerization time, Figure 5c.

## CONCLUSIONS

In summary, an electrochemical method was used to explore the growth of conductive polymer layers of polypyrrole onto anisotropic superconductor surfaces of  $\text{YBa}_2\text{Cu}_3\text{O}_7$ . Analysis of the morphological features has provided useful information regarding the local surface conductivity and electroactivity properties of oriented thin film and polycrystalline samples. Clearly, polymer growth occurs more rapidly and over a larger portion of the exposed surface for the ceramic samples as compared to the c-axis oriented films. However, a monolayer of N-(3-aminopropyl) pyrrole is found to alter the growth rate, and nucleation properties for the electrochemically deposited films. Large increases in the polymer growth rates and radically smoother polymer layers are obtained using this adsorbed monolayer. Moreover, dramatic improvements in the polymer to superconductor adhesion properties are observed.

## ACKNOWLEDGMENTS

CAM and JTM acknowledge the AFOSR, NSF, and ONR for support of this work. Allen J. Bard and Stephen E. Webber are thanked for use of their equipment and helpful discussions.

## REFERENCES

- (1) Dubois, L. H.; Nuzzo, R. G. *Annu. Rev. Phys. Chem.* **1992**, *43*, 437-463.
- (2) Barkatt, A.; Hojaji, H.; Amarakoon, V. R. W.; Fagan, J. G. *MRS Bulletin* **1993**, *18*, 45-52.
- (3) Chen, K.; Xu, F.; Mirkin, C. A.; Lo, R.-K.; Nanjundaswamy, K. S.; Zhou, J.-P.; McDevitt, J. T. *Langmuir* **1996**, *12*, 2622-2624.
- (4) Chen, K.; Mirkin, C. A.; Lo, R.-K.; Zhao, J.; McDevitt, J. T. *J. Am. Chem. Soc.* **1995**,

117, 6374-6375.

- (5) Lo, R.-K.; Ritchie, J. E.; Zhou, J.-P.; Zhao, J.; McDevitt, J. T. *J. Am. Chem. Soc.* **1996**, *118*, 11295-11296.
- (6) Clevenger, M. B.; Zhao, J.; McDevitt, J. T. *Chem. Mater.* **1996**, *8*, 2693-2696.
- (7) McDevitt, J. T.; Lo, R.-K.; Zhou, J.; Haupt, S. G.; Zhao, J.; Jurbergs, D. C.; Chen, K.; Mirkin, C. A. *Chem. Mater.* **1996**, *8*, 811-813.
- (8) McDevitt, J. T.; Haupt, S. G. In *Electroanalytical Chemistry Series*; A. J. Bard, Ed.; Marcel Dekker: 1996; Vol. 19; pp 355-481.
- (9) Allmen, M. V. *Laser Beam Interactions with Materials: Physical Principles and Applications*; Springer-Verlag: Berlin, 1987.
- (10) Haupt, S. G.; Riley, D. R.; Grassi, J. H.; Lo, R.-K.; Zhao, J.; Zhou, J.-P.; McDevitt, J. T. *J. Am. Chem. Soc.* **1994**, *116*, 9979-9986.
- (11) Zhou, J.-P.; Savoy, S. M.; Zhao, J.; Riley, D. R.; Zhu, Y. T.; Manthiram, A.; Lo, R.-K.; Borich, D.; McDevitt, J. T. *J. Am. Chem. Soc.* **1994**, *116*, 9389-9390.
- (12) Zhou, J.-P.; Savoy, S. M.; Lo, R.-K.; Zhao, J.; Arendt, M.; Zhu, Y. T.; Manthiram, A.; McDevitt, J. T. *Appl. Phys. Lett.* **1995**, *66*, 2900-2902.
- (13) Poole, C. P.; Farach, H. A.; Creswick, R. J. *Superconductivity*; Academic Press: San Diego, 1995.
- (14) Diaz, A. F.; Bargon, J. In *Handbook of Conducting Polymers*; T. A. Skotheim, Ed.; Marcel Dekker: New York, 1986; Vol. 1; pp 81.
- (15) Willicut, R. J.; McCarley, R. L. *Langmuir* **1995**, *11*, 296-301.
- (16) MacDonald, D. D. In *Transient Techniques in Electrochemistry*; Plenum: 1977; pp 273-307.
- (17) McDevitt, J. T.; Haupt, S. G.; Clevenger, M. B. In *Handbook of Conducting Polymers*; T. Skotheim, J. Reynolds and R. Elsenbaumer, Eds.; Marcel Dekker: New York, 1996, accepted.
- (18) In the schematic, coupling between the surface localized monolayer reagents is ignored. Some proton loss and coupling may actually occur, but experimental evidence has yet to be obtained to support the occurrence of such a process in this system



## ELECTROCHEMICAL MODIFICATION OF $\text{La}_2\text{CuO}_4$ : THE ROLE PLAYED BY MICROSTRUCTURE

E.J. WILLIAMS<sup>1,2</sup>, A. DARIDON<sup>1,3</sup>, F. ARROUY<sup>1</sup>, J. FOMPEYRINE<sup>1,3</sup>, E. MÄCHLER<sup>1</sup>,  
H. SIEGENTHALER<sup>3</sup> and J.-P. LOCQUET<sup>1</sup>

<sup>1</sup>IBM Research Division, Zurich Research Laboratory, CH-8803 Rüschlikon, Switzerland

<sup>2</sup>DPMC, Université de Genève, CH-1211 Genève, Switzerland

<sup>3</sup>Institut für Anorganische Chemie, Universität Bern, CH-3012 Bern, Switzerland

### ABSTRACT

Using electrochemical oxidation as a probe technique for the mechanisms by which oxidation occurs in *c*-axis  $\text{La}_2\text{CuO}_4$  films, the vital role played by specific through-film microstructural defects has been observed using transmission electron microscopy. These defects are namely the large through-film precipitates sometimes found in these films and {111} planar faults. Two high-oxygen-content phases are formed; one locally and with a superstructure, the other of reduced orthorhombicity and larger *c*-axis than as-grown material. Some films were found not to oxidize, and the defects in these films were compared with those in the oxidizable films.

### INTRODUCTION

The properties of most high-temperature superconducting oxides are extremely sensitive to oxygen content and the homogeneity of its distribution. These oxides are also layered compounds with highly anisotropic physical and mechanical properties, including the oxygen diffusion coefficients. For example, in the  $\text{La}_2\text{CuO}_{4-\delta}$  system (LCO, orthorhombic Fmmm with  $a = 0.53556$  nm,  $b = 0.54011$  nm,  $c = 1.3149$  nm [JCPDS 38-709]), at 775 K the diffusion coefficient in the *a*-*b* plane is  $10^{-8}$  cm<sup>2</sup>/s, whereas that parallel to the *c*-axis, i.e. across the layers, is only  $10^{-11}$  cm<sup>2</sup>/s [1]. As the properties of LCO vary from those of a semiconductor at  $\delta \approx 0$ , to those of a superconductor of increasing transition temperature (up to ~42 K) as  $\delta$  increases to ~0.09, it is vitally important to be able to ensure adequate oxygenation and sufficient homogenization. This problem becomes most marked for films grown with the *c*-axis orientation, i.e. with the slow diffusion direction parallel to the growth direction; this was discussed together with the strain relaxation mechanisms in these materials [2]. Generally, thin oxide films are oxygenated post-deposition but still in-situ by holding them at a temperature a little below their growth temperature in an oxygen-rich atmosphere for some hours and then allowing them to cool to room temperature. However, a further method has been used recently and that is electrochemical oxidation. This technique has been used to reach oxidation levels in bulk LCO not normally attained by thermal oxidation [3], it has been used to oxidize thin films both over a wide area [4,5] and locally (by masking) [6], and here as a probe technique to help understand the oxidation routes and mechanisms which enable *c*-axis films to be oxidized to an adequate level and with sufficient speed. These mechanisms will also apply to a certain extent to the Sr (and Ba) doped material, e.g.  $\text{La}_{2-x}\text{Sr}_x\text{CuO}_4$ .

As the oxygen content of LCO increases, its orthorhombicity decreases to a minimum at  $\delta \approx 0.05$  and then increases again, whereas the *c*-parameter increases until  $\delta \approx 0.06$ –0.07 and then saturates at a value of ~1.321 nm. Meanwhile the transition temperature increases from ~32 K for  $\delta \approx 0.06$  to ~42 K for  $\delta \approx 0.09$ , at which oxygen contents well-ordered phases exist in the bulk materials [7].

As previous experiments involving electrochemical oxidation of *c*-axis LCO films revealed a plateau in the current versus potential curve during initial oxidation [5], it was mooted that this was due to an initial stage in the oxidation process by which certain microstructural defects within the

films were filled, or activated, only after which a full oxidation of the film could occur. In this paper we aim to link the microstructure of these thin films, determined using transmission electron microscopy (TEM), with their properties post-oxidation.

## METHOD

Thin films of LCO were deposited in a 'block-by-block' [8] sequence using molecular beam epitaxy. Films (100 nm thick) were grown initially on (001)SrTiO<sub>3</sub> substrates, but subsequently also on (110)NdGaO<sub>3</sub> (NGO), R-plane LaAlO<sub>3</sub> (LAO) and (001)SrLaAlO<sub>4</sub> (SLAO) [9,10]. They were electrochemically oxidized in 1M KOH at room temperature against an Hg/HgO reference electrode with a platinum foil as counter electrode at 650 mV [5]. Prior to and post-electrochemical processing, the films' resistance versus temperature behaviour and *c*-lattice parameter (x-rays) were investigated, as was the microstructure using TEM; a JEOL 2010 was used for this. Some films were found to oxidize, whereas others, even when subjected to a potential higher than the standard 650 mV, did not. These two sets of specimens will be compared.

## RESULTS

### Oxidizable Films

A 100-nm-thick LCO film on (001)STO was examined using TEM before and after electrochemical treatment. Figure 1a is from a plan-view specimen of material prior to electrochemistry. This dark-field image clearly shows the twin boundaries, marked 'T' and running vertically in this region, and the deviation of the moiré fringes (arising from interference between the 200<sub>STO</sub> reflexion and the two 220<sub>LCO</sub> reflexions) as they intersect the twin boundaries indicating a significant degree of orthorhombicity in this as-grown specimen. This correlates with this film's semiconducting behaviour and relatively small *c*-parameter of 1.314 nm. Planar faults may also be observed, marked 'F'; these generally lie on {111}<sub>ortho</sub> planes [10,11], although they have also been observed occasionally on {110} and {100}<sub>ortho</sub> planes. Figure 1b shows an image of the same film under similar diffraction conditions but after electrochemical processing. In this case the moiré fringes can be seen to no longer deviate on intersection with twin boundaries, indicating a considerable reduction in orthorhombicity. All that remains now of the twin boundaries themselves are streaks of strain-like contrast, which is also observed in oxide thin films in which the orthorhombicity has been reduced thermally, e.g. reduced YBa<sub>2</sub>Cu<sub>3</sub>O<sub>7-δ</sub> [12]. This reduced orthorhombicity links with the observed increase in the *c*-parameter (1.3215 nm) and the change in the materials' electrical properties, as the film had become metallic with a superconductive transition temperature *T*<sub>c0</sub> of 42 K. This transition temperature is rather higher than might be expected from comparison with bulk material observed to have such a reduced orthorhombicity and a *c*-parameter of that magnitude (suggestive more of the 32 K phase); at present this phenomenon is not understood. The resistivity curve also showed some signs of the film containing a second local superconducting phase of higher *T*<sub>c</sub>.

Comparison of the two inset diffraction patterns reveals that the electrochemically processed material generates extra reflexions. These reflexions do not correlate with any Cu–O or La–O compound, neither was any K (from the electrolyte) observed, hence there is little danger that we are observing the results of a degradation reaction, which would also appear unlikely from the resistivity and x-ray data. When these reflexions are used to image, it is found that specific regions of the specimen are illuminated. Figure 2 is a dark-field image of the LCO film alone (no substrate) taken using the 220<sub>LCO</sub> and surrounding reflexions. This figure shows two faults (indicated by 'F') with adjacent bright regions containing moiré fringes. The spacing and orientations of these fringes correlate with an interference between the 220<sub>LCO</sub> reflexion (orthorhombicity has now been reduced) and the two new reflexions, indicating that there is a sheet of a new electrochemically modified phase coexisting with the matrix (although itself modified to a lower orthorhombicity and longer *c*-axis than before oxidation) LCO. Further, a zone close to the right-hand fault can be seen to be

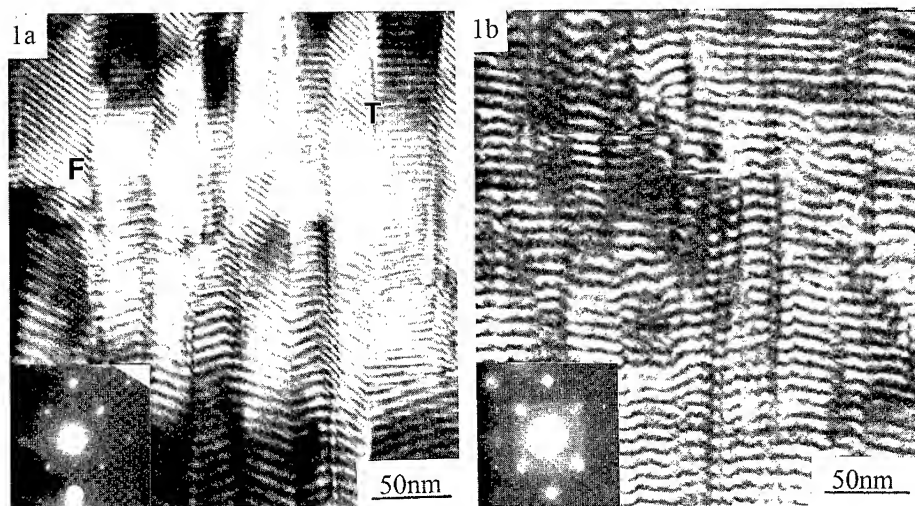


Figure 1. (a) Dark-field image with corresponding diffraction pattern inset of a plan-view specimen of as-grown LCO/(001)STO, taken using the  $200_{\text{STO}}$  and  $220_{\text{LCO}}$  reflexions. Twin boundaries are marked 'T' and the moiré fringes can be seen to deviate as they cross the boundaries. Faults are indicated with an 'F'. (b) Image taken under the same conditions of the same film but after electrochemical processing. Only strain-like contrast remains of the twin boundaries and the moiré fringes no longer deviate, indicating a reduced orthorhombicity.

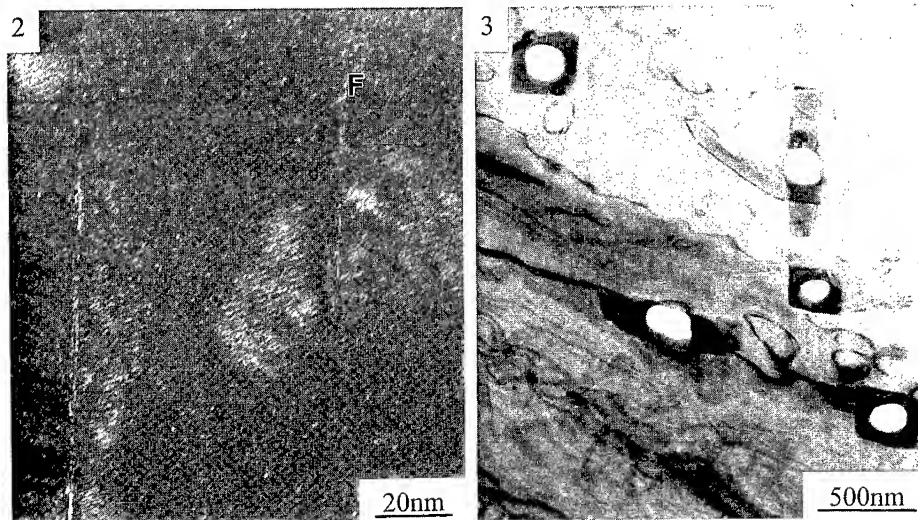


Figure 2.  $220_{\text{LCO}}$  (and surrounding superstructure reflexions) dark field of a region of specimen containing only the film. Here faults are indicated with an 'F' and bright regions containing fine moiré fringes are seen to surround them. A moiré-denuded zone is to be seen just left of the right-hand fault.

Figure 3. Bright-field image of oxidized LCO/STO showing the remnants of large Cu-O through-film precipitates.

denuded of moiré fringes. This could be interpreted as a region from which some of the extra oxygen incorporated has been lost via the fault, linking with the gradual reduction in  $T_c$  observed with time [5]. When the specimen is tilted within the microscope a whole series of related extra reflexions are revealed, indicating that a superstructure is introduced during oxidation. These superstructure reflexions correlate with those observed in bulk material for  $\delta \approx 0.09$ .

Figure 3 shows an overview of the film after oxidation. From this bright-field image we can see what remains of large, diamond-shaped Cu–O precipitates (La–O precipitates were also observed in this film), their centres appear to have been etched away. In fact, x-ray data for this film showed no change regarding the precipitates pre- and post-electrochemical processing, suggesting that the precipitate/film interface was sufficiently weakened during the process so that the precipitates were removed during TEM specimen preparation. However, other films were seen by scanning electron microscopy to have lost their precipitates during the electrochemical process.

Both these data suggest that second phase precipitates and faults may be possible entry routes for oxygen into these *c*-axis films. Similar observations have been made for *c*-axis films with faults and precipitates grown on NGO, SLAO and LAO [10].

#### Non-oxidizable Films

Not all films, however, were found to be oxidizable. This could be due to the formation of a surface corrosion layer. However, it is unlikely that such a layer would appear in only a few samples as all films undergo essentially the same processes of growth and electrochemical oxidation. Hence, the origin is more likely to be related to differences in microstructure. Two sets of phenomena were observed relating to non-oxidizable films, the first is shown in Fig. 4. In this  $110_{\text{LCO}}$  dark-field image of the film alone (from a specimen grown on SLAO), neither planar faults nor through-film precipitates are observed but only threading dislocations and small precipitates embedded within the film. In this case the only defects passing through the full film thickness are the dislocations, these are assumed to provide insufficiently substantial diffusion channels for significant oxygen ingress. The second, and perhaps more subtle, phenomenon observed is illustrated in Fig. 5.

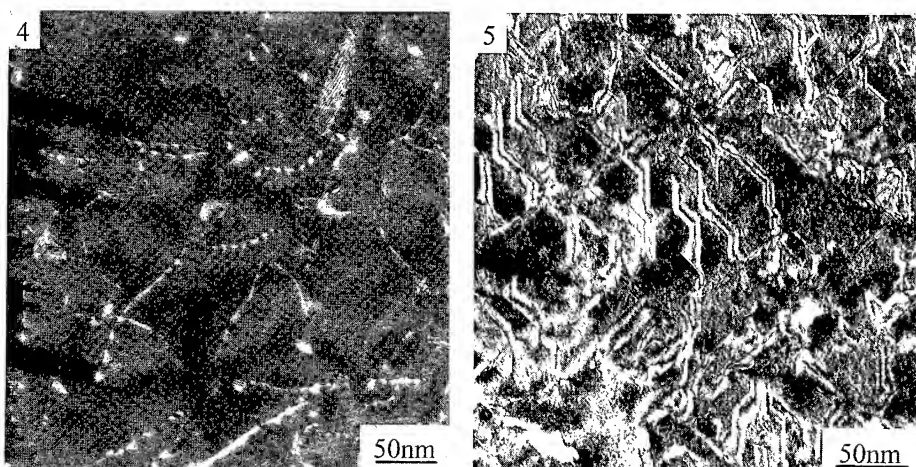


Figure 4. Only threading dislocations and small embedded precipitates were observed in this non-oxidizable LCO film grown on SLAO, as can be seen in this  $110_{\text{LCO}}$  dark-field image of a region of a plan-view specimen containing only the film.

Figure 5. APBs, which do not act as oxygen diffusion channels, are observed to result from slow cooling post-deposition in this  $020_{\text{LCO}}$  dark-field image.

Although this specimen (LCO/(001)STO) does contain faults, they are of different types or lie on different planes from those observed previously. This  $020_{\text{LCO}}$  dark field shows vertical bands with symmetrical top-bottom contrast characteristic of anti-phase domain boundaries (APBs) and inclined on the  $\{401\}$  planes.

These APBs are joined to faults lying on the  $\{111\}$  or  $\{110\}$  planes (the same fault planes as observed previously) although these are seen to have reacted destructively during electrochemical treatment. The fact that the two sets of faults are joined indicates that a subtly different mechanism has operated during their formation. This is very probable as this specimen underwent a very slow cooling, rather than the normal initial rapid cool to the annealing temperature. This in turn suggests that their atomistic structure is different and hence that very specific bonding arrangements are required within a fault for it to operate as an effective oxygen channel.

## CONCLUSIONS

Whilst it is still not possible to state categorically by which mechanism (or mechanisms) oxygen enters into *c*-axis grown LCO films, it is clear that microstructural defects play a vital role in the process. It is also clear that two phases are formed; the matrix phase of low orthorhombicity and long *c*-parameter, which probably relates to the 42 K  $T_{\text{c0}}$  observed, and the more localized phase related to the superstructure reflexions and possibly having a higher  $T_{\text{c}}$ . It appears that specific faults (on  $\{111\}$  planes) and through film Cu-O (and possibly also La-O) precipitates could play the role of oxygen channels. The first by virtue of a specific bonding, or oxygen arrangement at that fault surface, this being one of the more stable crystal faces in this material [13]. The second possibly by a valence exchange reaction occurring at the Cu-O/LCO-film interface. Hence, if this oxidation technique is to be applied on a very local scale, attention must be paid to the density and magnitude of the defects involved.

## ACKNOWLEDGMENTS

The authors thank the Swiss National Science Foundation for their financial support and the IBM Research Laboratory, Rüschlikon, for provision of laboratory facilities.

## REFERENCES

1. E.J. Opila, H.L. Tulle, and B.J. Wuensch, *J. Am. Ceram. Soc.* **76**, 236 (1993).
2. J.-P. Locquet and E.J. Williams, *Acta. Physica. Polonica A* (1996) in press.
3. A. Wattiaux, J.C. Park, J.C. Grenier and M. Pouchard, *C. R. Acad. Sci. Paris* **310**(II), 1047 (1990).
4. J.-P. Locquet, C. Gerber, A. Cretton, Y. Jaccard, E.J. Williams and E. Mächler, *Appl. Phys. A* **57**, 211 (1993).
5. F. Arrouy, J.-P. Locquet, E.J. Williams, E. Mächler, R. Berger, C. Gerber, C. Monroux, J.-C. Grenier and A. Wattiaux, *Phys. Rev. B* **54**, 7512 (1996).
6. J.-P. Locquet, F. Arrouy, E. Mächler, M. Despont, P. Bauer and E.J. Williams, *Appl. Phys. Lett.* **68**, 1999 (1996).
7. C. Monroux, Ph.D. Thesis, Bordeaux University, France, 1996.
8. J.-P. Locquet and E. Mächler, *MRS. Bulletin* **19**, 39 (1994).
9. A. Daridon, H. Siegenthaler, F. Arrouy, E.J. Williams, E. Mächler and J.-P. Locquet, *Proc. E-MRS '96, J. Alloys & Compounds* (1996) in press.

10. E.J. Williams, A. Daridon, F. Arrouy, J. Perret, Y. Jaccard, J.-P. Locquet, E. Mächler, H. Siegenthaler, P. Martinoli and Ø. Fischer, Proc. E-MRS '96, J. Alloys & Compounds (1996) in press.
11. E.J. Williams, J.-P. Locquet, E. Mächler, Y. Jaccard, A. Cretton, R.F. Broom, C. Gerber, T. Schneider, P. Martinoli and Ø. Fischer, Proc. EMAG '94, Inst. Phys. Conf. Ser. **138**, 329 (1994).
12. E.J. Williams and W.M. Stobbs, Phil. Mag. A **68**, 1 (1993).
13. C.F. Woensdregt, private communication.

Current address of E.J. Williams is IBM Research Division, Zurich Research Laboratory, CH-8803 Rüschlikon, Switzerland. E-mail: [EWI@ZURICH.IBM.COM](mailto:EWI@ZURICH.IBM.COM); and of F. Arrouy is Essilor, Usine des Battants, F-55550 Ligny en Banois, France.

## ELECTRODEPOSITED WO<sub>3</sub> THIN FILMS

E.A. Meulenka, R.J.J. de Groot and J.M.L. de Vries,  
Philips Research Laboratories, Prof. Holstlaan 4 (WA13), 5656 AA Eindhoven, The Netherlands,  
meulenk@natlab.research.philips.com

### ABSTRACT

The electrodeposition of WO<sub>3</sub> thin films from peroxy-tungstate solution is discussed. The emphasis is on the feasibility of this deposition technique for production of electrochromic devices. Therefore, the influence of deposition parameters (solution composition, electrodeposition potential, mass transport, etc.) on the properties of WO<sub>3</sub> was studied. Furthermore, it was investigated whether electrodeposition of WO<sub>3</sub> offers unique possibilities as compared to WO<sub>3</sub> deposition by other techniques.

### INTRODUCTION

Intercalation materials are of considerable commercial interest in view of their application in e.g. batteries and electrochromic devices. Their actual use requires a low-cost and reproducible production method. Wet-chemical deposition may be such a method. Indeed, electrochromic WO<sub>3</sub> layers have been successfully prepared by sol-gel technology and electrodeposition [1].

We studied parameters that influence WO<sub>3</sub> electrodeposition from peroxy-tungstate solution, as first described by Yamanaka [2]. The results are discussed with a view to possible use of this deposition method for production of electrochromic devices. Special attention is paid to features which distinguish this method, and the layers produced by it, from other deposition techniques.

### EXPERIMENTAL

Peroxy-tungstate solutions were prepared according to [3]. W powder was dissolved in 30% H<sub>2</sub>O<sub>2</sub>. After a clear solution had been obtained, excess H<sub>2</sub>O<sub>2</sub> was removed by decomposition at a Pt sheet. A 50 mM W solution was obtained by dilution with isopropanol/H<sub>2</sub>O 30/70 (V/V) [3]. This was stored at 4 °C. The total peroxide content was determined iodometrically.

A classical three-electrode setup was used for electrodeposition. WO<sub>3</sub> deposition was carried out at rotating and stationary Sn-doped indium oxide (ITO) electrodes with a sheet resistance of 30 Ω or 100 Ω. Film characterization included thickness, electrochromic coloration, morphology, and homogeneity. W content was determined by Inductively Coupled Plasma Optical Emission Spectrometry (ICP-OES).

### RESULTS

Initial experiments showed that the quality of the electrodeposited WO<sub>3</sub> films was comparable to that of WO<sub>3</sub> obtained by other physical or chemical deposition techniques, in accordance with earlier work [1-3]. For example, the coloration efficiency (H<sup>+</sup> intercalation) at 620 nm was about 50 cm<sup>2</sup>/C, a typical value for WO<sub>3</sub> [1]. Up to a thickness of 1.0-1.5 μm good adhesion to the substrate was observed. Furthermore, after a moderate thermal anneal, reasonably

stable optical switching behaviour was found, at a fast switching speed. Thus, electrodeposited  $\text{WO}_3$  can meet the requirements of the active layer in an electrochromic device.

In order to evaluate the influence of deposition parameters on  $\text{WO}_3$  film growth, two aspects of electrodeposited  $\text{WO}_3$  were studied: current efficiency and porosity. The first was defined as the amount of W (moles) deposited per Coulomb deposition charge. The second was defined as (1-measured density/theoretical density). The measured density was calculated from the W content, assuming  $\text{WO}_3$  stoichiometry, and the known dimensions of the film. The theoretical density was taken equal to that of crystalline  $\text{WO}_3$  ( $7.16 \text{ g.cm}^{-3}$  [1]). We will discuss the effects of peroxide concentration, deposition potential and mass transport.

The composition of the deposition solution varies with time since the total peroxidic oxygen content, denoted  $[\text{O}_2^{2-}]$ , decreases slowly during a period of several weeks. This leads to a marked variation of deposition efficiency and also affects film properties, see figure 1. After preparation,  $[\text{O}_2^{2-}]$  was about 50 mM, yielding an  $[\text{O}_2^{2-}]/\text{W}$  ratio of about 1.0. A small deposition current efficiency was found. This increased at lower  $[\text{O}_2^{2-}]$ . However, for very small  $[\text{O}_2^{2-}]$  (typically  $[\text{O}_2^{2-}] < 5 \text{ mM}$ ) a small efficiency was again obtained. The peroxide content also affected the porosity of the  $\text{WO}_3$  films. It showed a small maximum in an intermediate concentration range.

Current efficiency and porosity are also a function of the deposition potential. Figure 2 shows both parameters for the case of  $[\text{O}_2^{2-}] \approx 25 \text{ mM}$ . Analogous to the results shown in figure 1, a large variation of current efficiency was found, up to factor of four, in combination with a relatively small change in porosity. Furthermore, figure 3 shows that the electrochromic properties of the as-deposited film also depend on the deposition potential. It shows the (de)intercalation (i-E) curve, measured in 0.1 M  $\text{H}_2\text{SO}_4$ , for three deposition potentials. Clearly, the amount of intercalated charge at a particular potential is influenced by deposition conditions. This indicates that the amount of sites available for intercalation and, hence, the structure of the films, can vary.

Figure 4 shows the effect of mass transport on the deposition characteristics. This was studied by using a rotating disk electrode. The absolute  $\text{WO}_3$  growth rate ( $\text{mole.s}^{-1}$ ) is, to a first approximation, independent of rotation rate. However, the current efficiency decreases markedly with increasing rotation rate. This is due to an additional reduction reaction, which is under (partial) diffusion control, and does not contribute to film growth.

The above observations can be explained by taking into account electrochemical reduction of three species which can be present in solution. (i) Free  $\text{H}_2\text{O}_2$  is present because of equilibria between tungstate species with various degrees of coordination by peroxidic oxygen [4]; (ii) bound  $\text{O}_2^{2-}$  is present in the form of peroxy-tungstates; (iii) poly-tungstate is present when the tungsten atom is coordinated solely by oxidic oxygen. The relative concentrations and the reduction rates of these three species depend on  $[\text{O}_2^{2-}]$  and on potential.

Reduction of bound  $\text{O}_2^{2-}$  has been shown to be responsible for film growth [5]. Reduction of free  $\text{H}_2\text{O}_2$  and poly-tungstate can be considered 'parasitic' side reactions. Thus, the results shown in figures 1,2 and 4, with regard to current efficiency, can be explained as follows. In a fresh peroxy-tungstate solution, the concentration of free  $\text{H}_2\text{O}_2$  is high. Therefore, the current efficiency is low. In aged solutions (low  $[\text{O}_2^{2-}]$ ), poly-tungstate is thought to be the main tungsten species and the efficiency is again low. Reduction of free  $\text{H}_2\text{O}_2$  and polytungstate is under mixed kinetic-diffusion control [5]. Since these reactions do not contribute to film growth, current efficiency is low at high rotation rates, see figure 4. The effect of the deposition potential is more complicated. At positive potential, the reduction rate of bound  $\text{O}_2^{2-}$  is relatively small compared to that of free  $\text{H}_2\text{O}_2$  and polytungstate. Thus, the efficiency is low. When the potential is chosen



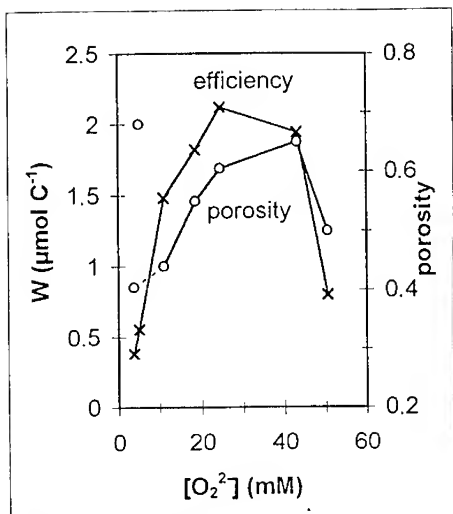


Figure 1. Dependence of current efficiency and porosity on the total concentration of peroxidic oxygen. Deposition was carried out at stationary electrodes at -0.5 V.

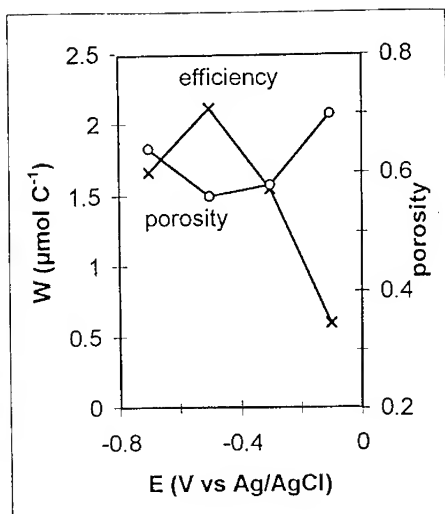


Figure 2. Dependence of current efficiency and porosity on deposition potential. Deposition was carried out at stationary electrodes from a 25 mM [O<sub>2</sub><sup>2-</sup>] solution.

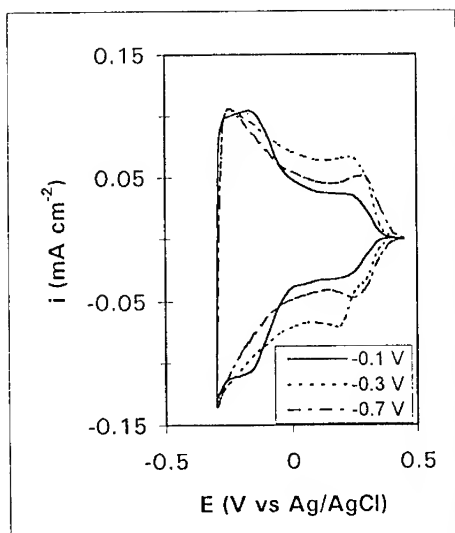


Figure 3. (De-)intercalation current-potential curves of WO<sub>3</sub> films deposited at three potentials. Layer thickness was roughly equal. The (i-E) curves were obtained in deoxygenated 0.1 M H<sub>2</sub>SO<sub>4</sub> at 5 mV/s.

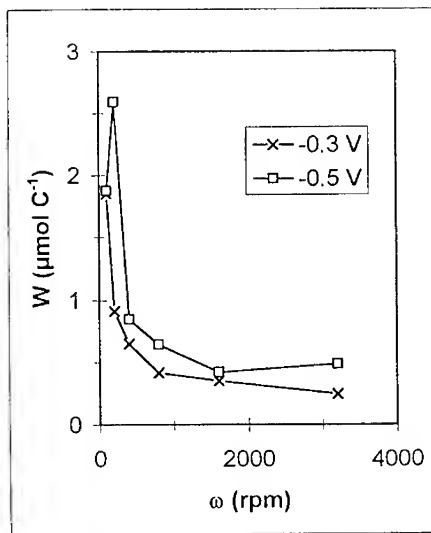


Figure 4. Effect of rotation rate  $\omega$  (revolutions per min) on current efficiency at two deposition potentials ([O<sub>2</sub><sup>2-</sup>]  $\approx$  40 mM).

more negative, the efficiency increases because the reduction of bound  $O_2^{2-}$  shows a more pronounced potential dependence. This is due to the (partial) diffusion limitation of the 'parasitic' reactions. The efficiency decreases again at  $E \leq -0.7$  V due to  $H_2$  evolution.

The observed variations of the porosity of the electrodeposited films is considered to be caused by variations in the nature of the predominant tungsten species in solution and by the degree of condensation of  $WO_6$  octahedra in the deposited film. Tungsten shows rather complex aqueous chemistry [6], because of slow hydrolysis and condensation of monomeric species into oligomers at low pH. The additional presence of hydrogen peroxide gives rise to a possible continuous variation of the degree of oligomerization and the (average) number of peroxide groups per tungsten atom. The concentration of each species will depend on  $[O_2^{2-}]$ ; each species can also show slightly different redox properties, as the electronic properties are influenced by polymerization and by the presence of peroxidic oxygen.

The length and the degree of 'branching' of  $WO_3$  chains in the film can be expected to reflect the solution chemistry and electrochemical properties. Thus, the porosity (density) of the films and the intercalation (electro-)chemistry can vary. Unfortunately, there is too little knowledge of the detailed nature of the dominant tungsten species as well as of the mechanism of film formation at a *molecular* level, to interpret the variations depicted in figures 1-3 in terms of particular structures of the electrodeposited film. Note, for example, that although figure 1 suggests that porosity increases with increasing efficiency, such a relationship is contradicted by figure 2.

The observed dependence of electrodeposition on solution composition makes this technique quite unattractive for applications. The small but significant effects of mass transport and potential add further difficulties if, for example, large areas have to be coated. However, electrodeposition does offer some special features which could prove to be important for certain applications. Figures 1 and 2 illustrate the low density of electrodeposited  $WO_3$ , which is very hard to obtain by other deposition techniques. Consequently, fast (de-)intercalation kinetics are found, the main requirement for display applications. Also, low density implies a small refractive index, which can be important in view of reflection losses in an electrochromic device. The results of figures 1-3 point out that fine-tuning of deposition conditions for a particular application is feasible as well.

We have studied two other possible attractive features of electrodeposition. First, it was tried to deposit  $WO_3$  on a patterned substrate. This consisted of a thin patterned non-conducting  $SiO_2$  film on a continuous ITO substrate. The pattern in the  $SiO_2$  film ( $\approx 30$  nm thickness) was made by photolithography.  $WO_3$  was electrodeposited at the stationary electrode at  $-0.5$  V from a solution with  $[O_2^{2-}]/W \approx 0.7$ . The SEM picture shown in figure 5 shows a detail of the obtained pattern. The dark area, e.g. at the lower left corner, is the  $SiO_2$  film. The light area in the upper right hand corner is  $WO_3$ . Clearly, small-size islands of  $WO_3$  can be deposited, with very good edge definition. There is no evidence for overgrowth on the  $SiO_2$ -covered areas. Higher amplification reveals some roughness (perpendicular to the substrate) at the edges, as compared to areas away from the  $WO_3/SiO_2$  edge.

A useful aspect of any deposition technique is that more than one type of material can be deposited. In the case of electrodeposition from peroxide-containing solutions, growth of  $MoO_3$  [7]  $TiO_2$  [8] and mixed  $MoO_3/WO_3$  [9] layers has been demonstrated. Such combinations of oxides may lead to improved stability or colour neutrality [1]. Therefore, it was investigated whether the range of suitable early transition metals could be extended.

Electrodeposition of  $Nb_2O_5$  or  $Nb_2O_5/WO_3$  layers from peroxide-containing solution was not possible. In the former case, no film growth was observed. No niobium could be detected in

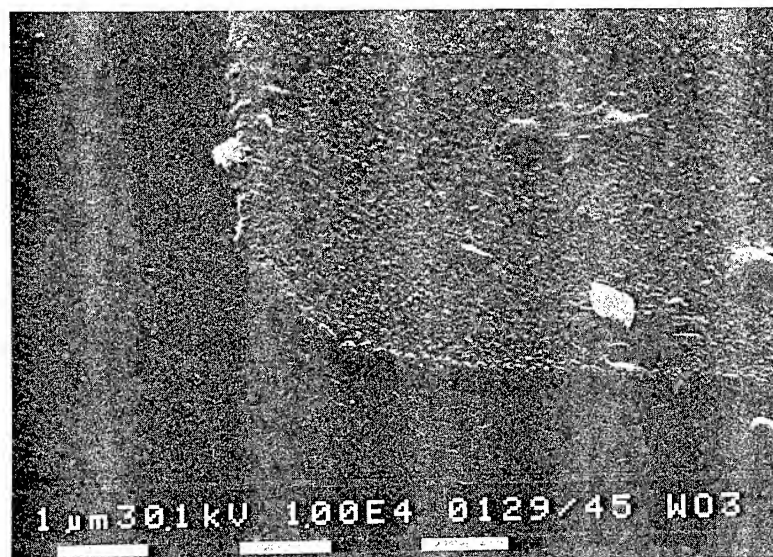


Figure 5. SEM micrograph of a  $\text{WO}_3$  pattern electrodeposited on ITO. Upper right is  $\text{WO}_3$ ; the rest is  $\text{SiO}_2$ .

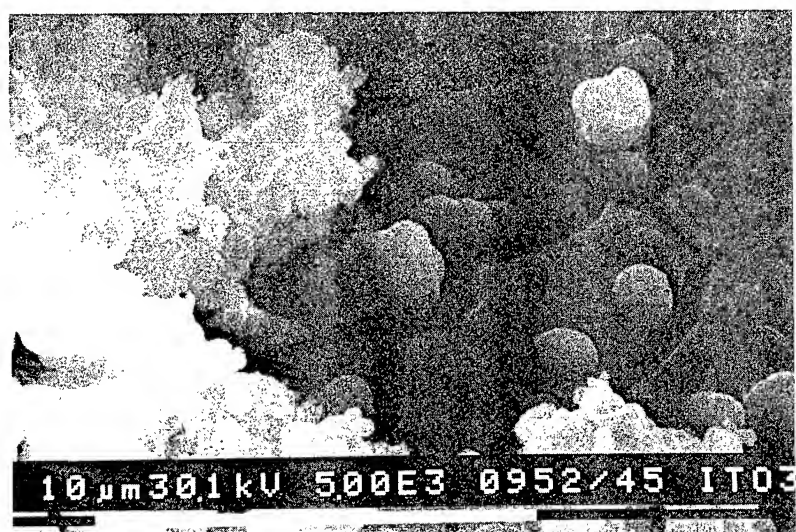


Figure 6. SEM micrograph of a mixed  $\text{V}_2\text{O}_5 / \text{WO}_3$  film.

the 'mixed' oxide layers. It was also attempted to (co-)deposit  $V_2O_5$ . The results were very poorly reproducible. Sometimes, transparent mixed  $WO_3/V_2O_5$  layers could be deposited but often poorly adherent, opaque films were obtained. Variation in the color of such films pointed to the presence of a varying degree of reduced  $V^{IV}$ . An example of the morphology of a mixed oxide film is given in figure 6. Two layers can be discerned. The cracked inner layer resembles that of a pure  $WO_3$  film. The cracks are due to build-up of stress in the film during drying and concomitant loss of water. The granular outer layer has a very rough structure, similar to pure  $V_2O_5$  films. Elemental analysis, however, indicated no substantial difference between the vanadium content of both layers.

## CONCLUSIONS

Electrodeposition is capable of providing good quality electrochromic  $WO_3$  layers. However, actual use of this deposition technique is expected to be limited mainly because unavoidable variations of the composition of the deposition solution have a marked effect on current efficiency and on the properties of the  $WO_3$  film. Mass transport and deposition potential also have to be controlled carefully in order to grow  $WO_3$  reproducibly.

Electrodeposition does offer several unique features. Low density material can be obtained. This has the advantage of fast (de-)intercalation kinetics. Growth onto patterned substrates was shown to be straightforward. Deposition of mixed oxide films seems to be limited to  $MoO_3$  [8] and  $TiO_2$  [9] since attempts to deposit  $Nb_2O_5$  and  $V_2O_5$  were not successful.

## ACKNOWLEDGEMENTS

We would like to thank Ms. S. van der Putten and Ms. W. de Laat for tungsten analysis.

## REFERENCES

1. C.G. Granqvist, Handbook of Inorganic Electrochromic Materials, Elsevier, Amsterdam, 1995, pp. 29-144.
2. K. Yamanaka, Jap. J. Appl. Phys. **26**, 1884 (1987).
3. P.K. Shen, J. Syed-Bokhari and A.C.C. Tseung, J. Electrochem. Soc. **138**, 2778 (1991).
4. M.T. Pope, Prog. Inorg. Chem. **39**, 181 (1991).
5. E.A. Meulen Kamp, J. Electrochem. Soc. (submitted).
6. C.F. Baes, Jr. and R.E. Mesmer, The Hydrolysis of Cations, John Wiley & Sons, New York, 1976, pp. 257-260.
7. A. Guerfi, R.W. Paynter and L.H. Dao, J. Electrochem. Soc. **142**, 3457 (1995)
8. A. Pennisi, F. Simone and C.M. Lampert, Sol. Energy Mater. Solar Cells **28**, 233 (1992)
9. A. Zhitomirsky, L. Gal-or, A. Kohn and H.W. Henniscke, J. Mater. Sci. **30**, 5307 (1995)

## BULK RESTRUCTURING OF AMORPHOUS TUNGSTEN TRIOXIDE FILMS DUE TO HYDRATION OF THE FILM/ELECTROLYTE INTERFACE

I. V. SHIYANOVSKAYA\*

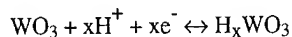
Institute of Physics, Ukrainian Academy of Science, Kiev-22, Pr.Nauki 46, 252022, Ukraine

### ABSTRACT

The influence of film/electrolyte interface on structure and electrochromic properties of amorphous  $\text{WO}_3$  (a- $\text{WO}_3$ ) films has been studied using cyclic voltammetry, optical electrochemistry and vibrational spectroscopy.

### INTRODUCTION

During two past decades, electrochromic phenomena in transition metal oxides have been very widely studied. The unique effect of electrically induced reversible coloration and charge storage in the thin films has diverse applications that range from high-contrast information displays with a wide view angle, automobile rearview mirrors, which automatically control the reflectance to "smart" windows allowing regulation of solar energy passing through them [1-2]. A number of inorganic and organic materials with electrochromic properties has been studied in recent years, but until now thin films of tungsten trioxide, by far show the best results. Coloration into the deep blue color is achieved by cathodic polarization of the tungsten trioxide film in an electrolyte medium. Coloration remains for various lengths of time, even after the external electric field is removed. Reverse polarization causes the bleaching of the film to the initial colorless state. It is now well known that electrochromic coloration of  $\text{WO}_3$  films results from the injection of electrons from a conductive substrate and protons (or small cations) from the electrolyte. In some sense the material behaves like a super-ionic conductor. The reaction proceeds with the general mechanism:



Several models of electrochromic coloration have been proposed. The models of intervalence charge transfer and small polaron are the most widely accepted [3-4]. According to these models the injected electron is localized at a  $\text{W}^{6+}$  site, perturbing the surrounding lattice and forming a  $\text{W}^{5+}$  color center. Light absorption proceeds by electron transfer between two neighboring tungsten sites  $\text{W}^{5+} \rightarrow \text{W}^{6+}$ . In these models, inserted protons essentially play a passive role whereby they compensate the negative charge of the injected electrons while being situated at interstices in the host matrix.

Despite numerous investigations  $\text{WO}_3$ -based electrochromic displays are not yet commercially viable. The main difficulty is the short device lifetime due to rapid film degradation in the electrolyte media. Aqueous  $\text{H}_2\text{SO}_4$  solutions are the widely used in electrochromic cells due to the fast coloration associated with high proton mobility.

\*Present address: Department of Chemistry, State University of New York at Potsdam, Potsdam, NY, 13676, E-mail: shiyaniv@potsdam.edu.

It is now known that the chemical stability of  $\alpha$ - $\text{WO}_3$  in aqueous electrolytes is far from perfect and electrochromic properties are gradually lost during storage due to dissolution and physical erosion [5]. However, the rapid loss of electrochromic efficiency in electrolyte (40 hours) compared to the slow dissolution rate (4 nm/day) suggests that an additional degradation mechanism must exist.

The objective of this work was to elucidate the influence of film/electrolyte interface on structure and electrochromic properties of amorphous tungsten trioxide films. The structural and optical properties of as-deposited  $\text{WO}_3$  films were examined as a function of aging in the electrolyte.

## EXPERIMENT

Thin films of the  $\text{WO}_3$  with thickness of 0,5  $\mu\text{m}$  were deposited by thermal evaporation at the different deposition rates on Si and conductive glass substrates. After deposition part of the films was stored in 0.5 M  $\text{H}_2\text{SO}_4$  at room temperature. The as-deposited films were confirmed to be amorphous by using a TEM, UEMB-100. The film morphology was examined with a SEM, JSM-35. Cyclic voltammograms were measured in a classical three-electrode electrochemical cell with a Pt counter-electrode and a saturated calomel reference electrode. Optical measurements were performed in an electrochemical cell with a KSVU-12 Spectrometer in the 200-1400 nm wavelength range, for colored and bleached films. IR transmittance spectra were measured using a IFS-88 Spectrometer in the range of 400-4000  $\text{cm}^{-1}$  with a spectral resolution 2  $\text{cm}^{-1}$ . Raman spectra measurements were performed using a Spex Ramalog Spectrometer with Ar laser excitation (wavelength - 488 nm). To prevent sample crystallization the laser power did not exceed 10mW.

## RESULTS

The morphology and structure of the amorphous tungsten trioxide films undergo drastic changes after storage in the electrolyte for 40 hours. Electron diffraction and SEM show that the amorphous structure of the freshly deposited  $\text{WO}_3$  film transforms into a polycrystalline structure [6]. Further identification of devitrified structure was performed using vibrational spectroscopy. In Fig.1 the changes in the IR transmittance spectra associated with storage in the electrolyte are given. Curve 1 corresponds to the freshly deposited film, while curve 4 corresponds to the crystallized film. Crystallization leads to the appearance of the characteristic stretching bands of the double bond of terminal oxygen atoms  $\text{W}=\text{O}_t$  at 950  $\text{cm}^{-1}$  and 1010  $\text{cm}^{-1}$ . Similarly, Fig.2 shows the changes in the stretching vibrations of the O-H bonds associated with storage in the electrolyte. The increasing intensity and splitting of the O-H stretching vibration band into three bands (symmetrical and antisymmetrical stretching vibrations, and overtone of bending mode) reflects the formation of strong hydrogen bonds associated with structural water molecules.

These observations indicate that amorphous films crystallize forming hydrates of tungsten trioxide.

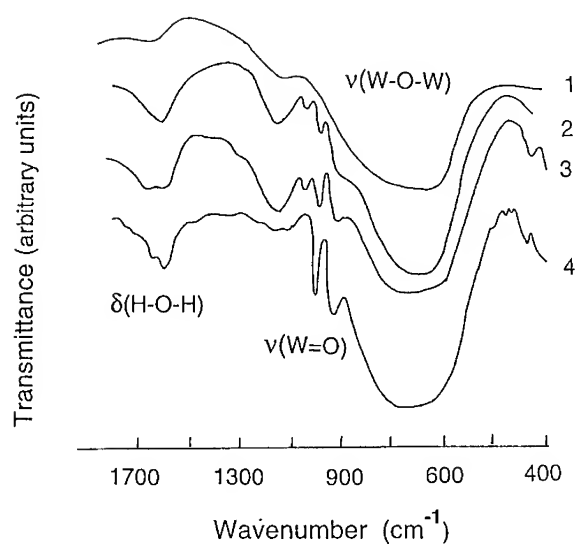


Fig.1. IR spectra in the stretching vibration range of W-O bonds for freshly deposited a-WO<sub>3</sub> film (curve 1) and the same film after storage in 0.5 M H<sub>2</sub>SO<sub>4</sub> at room temperature (curve 2 - after 12 hours, curve 3 - after 24 hours, and curve 4 - after 40 hours).

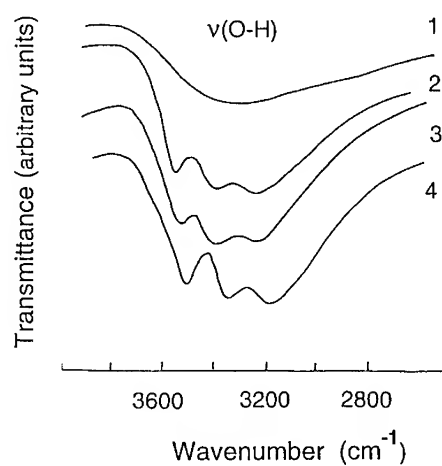


Fig.2. IR spectra in the stretching vibration range of the O-H bonds for freshly deposited a-WO<sub>3</sub> film (curve 1) and the same film after storage in 0.5 M H<sub>2</sub>SO<sub>4</sub> at room temperature (curve 2 - after 12 hours, curve 3 - after 24 hours, and curve 4 - after 40 hours).

Raman spectra measurements demonstrate that the deposition rate during film growth strongly affects the water content and structure of the crystalline hydrates of tungsten trioxide formed electrochemically. Specifically, the deposition rate determines the film density and porosity.

It is turn out, that rapidly deposited films (5 nm/s) have a higher density and transform into  $\text{WO}_3 \cdot 1/3(\text{H}_2\text{O})$ , while slowly deposited films (0.5 nm/s) have a lower density and transform into  $\text{WO}_3 \cdot 2(\text{H}_2\text{O})$ . Crystalline hydrates of tungsten trioxide are stable in electrolyte media, as no further changes of structural or property alterations have been observed.

Cyclic voltammograms (Fig.3) demonstrate that both the cathodic current (associated with coloration process) and anodic current (associated with bleaching) became lower with formation crystalline hydrates, since the devitrified structure is denser than the amorphous precursor (i.e. crystallization hampers proton diffusion). The peak potentials of anodic and cathodic waves are also shifted in the negative direction.

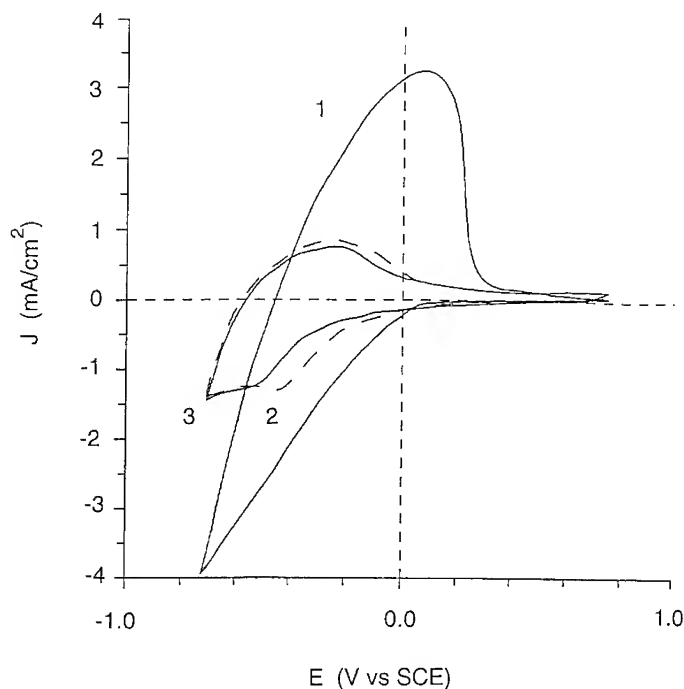


Fig.3. Cyclic voltammograms (at 30 mV/s scan rate in 0.5 M  $\text{H}_2\text{SO}_4$  electrolyte) of the  $\text{WO}_3$  films (solid curve 1) and films transformed with storage in electrolyte during 40 hours:  $\text{WO}_3 \cdot 2(\text{H}_2\text{O})$  (dashed curve 2) and  $\text{WO}_3 \cdot 1/3(\text{H}_2\text{O})$  (solid curve 3).

The impact of hydration and crystallization on the optical response is clearly revealed in Figure 4. As shown in the transmission spectra, the initial amorphous film is colorless due to the transparency in all visible region (dashed curve). Charge injection into this film leads to strong



absorption in the red region of spectrum (solid curve) and results in blue coloration. In the case of crystalline hydrates the main changes in transmission spectra due to charge injection occur in the near IR region.

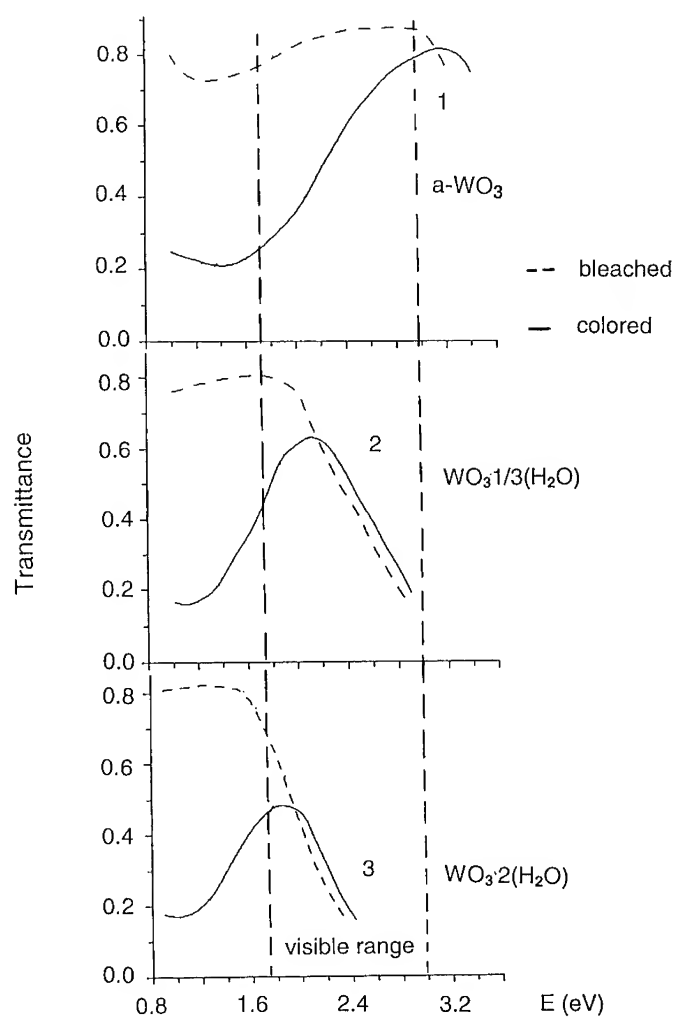


Fig.4. Optical transmittance spectra of electrochemical colored and bleached a-WO<sub>3</sub> film (curves 1) and crystalline hydrates WO<sub>3</sub>·1/3(H<sub>2</sub>O) (curves 2) and WO<sub>3</sub>·2(H<sub>2</sub>O) (curves 3). The dashed and solid curves represent the bleached and colored states, respectively.

Thus, the decrease of electrochromic efficiency of  $\alpha$ - $\text{WO}_3$  in the visible spectral range with storage in the electrolyte is caused by strong red shift of induced absorption band of the crystalline hydrates.

Nevertheless, the electrochromic efficiency (a ratio of induced optical density to the injected charge) is high at the maximum of induced absorption band ( $80 \text{ cm}^2/\text{C}$ ). Taking into account the high stability of crystalline hydrates in aqueous electrolytes they are very promising electrochromic materials for application in the near IR range.

## CONCLUSIONS

1. Hydration of the  $\alpha$ - $\text{WO}_3$  film in aqueous electrolytes induces a transformation of initial amorphous structure to the crystalline state.

2. Water molecules penetrate into the amorphous  $\text{WO}_3$  framework and form the crystalline hydrates  $\text{WO}_3 \cdot n(\text{H}_2\text{O})$ . Inserted water molecules form hydrogen and coordinating bonds with tungsten-oxygen octahedra.

3. Water content in the crystalline hydrates depends on a density and porosity of the initial film which are a function of the deposition rate.

4. The decrease of the electrochromic efficiency of the amorphous  $\text{WO}_3$  films in the visible spectral range with the storage in the electrolyte is due to a red shift of the electrochemically induced absorption band of the crystalline hydrates.

5. Due to high electrochromic efficiency and high stability in the aqueous electrolytes the crystalline hydrates may be used for application in the near IR range.

## REFERENCES

1. S.K.Deb, Sol. Ener. Mat. Sol. Cell, **25**, 327 (1992).
2. C.G.Granquist, Thin Solid Films, **193/194**, 730 (1990).
3. B.W.Faughnan, P.S.Crandall, and P.M.Heyman, RCA Rev., **36**, 177 (1975).
4. O.F.Shrimer, V.Wittwer, B.Baur, and G.Brandt, J.Electrochem.Soc., **124**, 749 (1977).
5. J.P.Randin, J.Electron. Mat. **7**, 47 (1978).
6. T.A.Gavrilko, V.I.Stepkin, and I.V.Shiyanovskaya, J.Mol.Struct., **218**, 411 (1990).

## Electroless Deposition of $\text{La}_{1-x}\text{Sr}_x\text{MnO}_3$ Perovskite Film on Yttria Stabilized Zirconia Substrate

T. Sasaki\* and Y. Matsumoto\*\*

\*National Institute of Materials and Chemical Research (NIMC), Agency of Industrial Science and Technology, MITI, 1-1 Higashi, Tsukuba, Ibaraki 305, Japan.

\*\*Department of Applied Chemistry and Biochemistry, Faculty of Engineering, Kumamoto University, 2-39-1 Kurokami, Kumamoto 860, Japan.

### ABSTRACT

A  $\text{LaMnO}_3$  precursor was electrolessly deposited on a YSZ substrate in a solution containing  $\text{Mn}^{2+}$ ,  $\text{La}^{3+}$ , an oxidizing agent and some additives. Peroxydisulfate was used as the oxidizing agent. The  $\text{LaMnO}_3$  precursor was an amorphous and hydrous  $\text{MnO}_2$  which contained  $\text{La}^{3+}$  ions. The incorporation of  $\text{La}^{3+}$  ions into the precursor oxide film was based on the ion-exchange reaction, where  $\text{La}^{3+}$  ions in the solution were exchanged for  $\text{H}^+$  ions on the deposited amorphous and hydrous  $\text{MnO}_2$ . A  $\text{La}_{1-x}\text{Sr}_x\text{MnO}_3$  precursor was also prepared from the  $\text{LaMnO}_3$  precursor by the ion-exchange reaction of some of the  $\text{La}^{3+}$  ions in the  $\text{LaMnO}_3$  precursor for  $\text{Sr}^{2+}$  ions in the solution.  $(\text{La}_{0.5}\text{Sr}_{0.5})_{0.75}\text{MnO}_3$  perovskite film was obtained from the precursor films on Pt substrate by heat-treatment at 800 °C.

### INTRODUCTION

Some complex oxide films can be prepared using electrochemical oxidation. We have electrochemically synthesized perovskite oxides,  $\text{La}_{1-x}\text{Sr}_x\text{MnO}_3$  [1-3] and  $\text{LaCoO}_3$  [4], where metal cations such as  $\text{Mn}^{2+}$  and  $\text{Co}^{2+}$  ion are electrochemically oxidized in a solution containing  $\text{La}^{3+}$  ions, followed by some chemical reactions with  $\text{H}_2\text{O}$  and  $\text{La}^{3+}$  ions. The process using electrochemical oxidation is much more useful for preparing complex oxide films than other methods such as CVD, sputtering etc., since the film can be easily prepared using a simple apparatus and under simple conditions. However, the substrate is restricted to a conductor, because of the necessity for an external electrical current to the electrode substrate.

Some metal oxide films such as  $\text{PbO}_2$  [5],  $\text{MnO}_2$  [6],  $\text{Ti}_2\text{O}_3$  [6] and  $\text{NiO}$  [7] have been electrolessly deposited on a glass in solutions containing metal cations, where they are oxidized in a heterogeneous reaction by an oxidizing agent, peroxydisulfate. In such cases, metal oxide films are also formed by electrochemical reactions similar to those in the anodic oxidation. Therefore a complex oxide film can be electrolessly deposited on a dielectric substrate, if the solution contains other metal cations and a suitable oxidizing agent. From this point of view we have prepared  $\text{LaMnO}_3$  perovskite film using electroless deposition in a solution containing  $\text{La}^{3+}$ ,  $\text{Mn}^{2+}$  and  $\text{S}_2\text{O}_8^{2-}$  [8].

$\text{La}_{1-x}\text{Sr}_x\text{MnO}_3$  is suitable as an air electrode material for high temperature solid oxide fuel cells (SOFC), because of its chemical stability at high temperature, electrocatalytic properties, high electron conductivity and thermal expansion allowance with the solid oxide electrolyte, yttria stabilized zirconia (YSZ) [9]. In addition,  $\text{La}_{1-x}\text{Sr}_x\text{MnO}_3$  is more preferable to  $\text{LaMnO}_3$  as an oxygen electrode material, because of its higher conductivity.

In this paper, we report on the preparation of a  $\text{LaMnO}_3$  precursor and a mechanism for incorporating  $\text{La}^{3+}$  ions into the precursor. We also demonstrate the preparation of  $\text{La}_{1-x}\text{Sr}_x\text{MnO}_3$  perovskite films on YSZ using  $\text{LaMnO}_3$  precursor as a starting material.

### EXPERIMENT

3 mol%  $\text{Y}_2\text{O}_3$ - $\text{ZrO}_2$  disks (14 mm $\phi$  and 0.5 mm thick) and Pt (10 mm square and 0.2 mm thick) plates were used as substrates. YSZ substrates were soaked in 46% HF for 5 min to clean

and etch their surfaces. After rinsing with water, these substrates were sensitized in 10 g/l SnCl<sub>2</sub> + 40 ml/l HCl solution for 5 min, followed by activation in 2 g/l PdCl<sub>2</sub> + 20 ml/l HCl solution for 3 min. The sensitization and activation were necessary for the deposition of the oxide film on YSZ. Pt substrates, on the other hand, were polished with 0.5 μm alumina powder and soaked in aqua regia for 30 sec. After these treatments, these substrates were vertically immersed in the mixed solution of La(NO<sub>3</sub>)<sub>3</sub>, Mn(NO<sub>3</sub>)<sub>2</sub>, and (NH<sub>4</sub>)<sub>2</sub>S<sub>2</sub>O<sub>8</sub>. CH<sub>3</sub>COONa and AgNO<sub>3</sub> were added to the solution as a supporting electrolyte and catalyst for the reactions, respectively. Table I shows a typical composition of the solution for the electroless deposition of the LaMnO<sub>3</sub> precursor. The pH of the solution was adjusted by 0.01M NaOH titration. After several hours, the solution gradually turned brown, and after 24 hr a compact and continuous oxide film was precipitated on the substrate. The induction time for the electroless deposition of oxide film was usually 24 hr. It should be noted that no precipitation of the oxide in the solution containing acetate ions was observed, and

**Table I** Typical solution for electroless deposition of LaMnO<sub>3</sub> precursor.

Electrolyte	Concentration ( <i>M</i> ; mol/l)
Mn(NO <sub>3</sub> ) <sub>2</sub>	$5 \times 10^{-4}$
La(NO <sub>3</sub> ) <sub>3</sub>	0.5
(NH <sub>4</sub> ) <sub>2</sub> S <sub>2</sub> O <sub>8</sub>	0.167
CH <sub>3</sub> COONa	0.5
AgNO <sub>3</sub>	$5 \times 10^{-6}$
pH	6.0

the color of the solution remained clear brown even after several days. The deposited oxide films were immersed in distilled water at pH=7 and diluted nitric acid at pH=2 in order to evaluate the adsorption of La<sup>3+</sup> ions on the films.

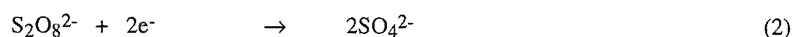
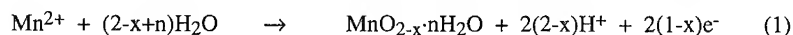
A La<sub>1-x</sub>Sr<sub>x</sub>MnO<sub>3</sub> precursor could not be directly deposited from the mixed solutions of La(NO<sub>3</sub>)<sub>3</sub>, Mn(NO<sub>3</sub>)<sub>2</sub>, Sr(NO<sub>3</sub>)<sub>2</sub> and (NH<sub>4</sub>)<sub>2</sub>S<sub>2</sub>O<sub>8</sub>, because white precipitate was observed even in the solutions that contained additives. Thus, the La<sub>1-x</sub>Sr<sub>x</sub>MnO<sub>3</sub> precursor was prepared by immersing the LaMnO<sub>3</sub> precursor in a solution of 0.5 *M* Sr(NO<sub>3</sub>)<sub>2</sub> at pH=6.

The as-deposited oxide films prepared on the substrates were washed by immersion in distilled water for 1 min, then dried at room temperature. All the samples were heated in air at 800 °C for 5 hr for the purpose of crystallization, since the as-deposited oxide films were always amorphous. The structures of the oxide films after the heat-treatment were examined by X-ray diffraction analysis (XRD) using CuKα radiation. The precursor films were dissolved in HCl and the amounts of metallic components in the precursor films were analyzed by inductively coupled plasma atomic emission spectroscopy (ICP-AES). Morphological observations of the oxide films were carried out with a scanning electron microscope (SEM).

## RESULTS AND DISCUSSION

### *Preparation of LaMnO<sub>3</sub>*

La<sub>1-x</sub>MnO<sub>3</sub> precursor films were deposited on YSZ from the solution (Table I). The precursor films were formed by the following anodic and cathodic partial reactions, respectively,



with the adsorption of La<sup>3+</sup> ions onto the oxide, as stated in ref. [8]. A mixed potential of these

electrochemical reactions was observed in the potential range of 800 mV to 950 mV vs. Ag/AgCl for all the solutions used in the experiments.

It should be noted that the solution containing  $\text{CH}_3\text{COONa}$  changed in color from colorless to clear brown without the precipitation of the oxide during the electroless deposition. It is very important for the electroless deposition of films that no precipitate is formed in the solutions, because some precipitates can cause defects in the deposited films. In our solution,  $\text{CH}_3\text{COONa}$  played a very important role in the inhibition of oxide precipitates in the solutions. In the solutions containing  $\text{CH}_3\text{COONa}$ , other anodic partial reactions to form highly oxidized manganese complex ions might also have existed during the electroless deposition. It is probable that ligands such as  $\text{CH}_3\text{COO}^-$ ,  $\text{NO}_3^-$ ,  $\text{S}_2\text{O}_8^{2-}$ , and  $\text{SO}_4^{2-}$  in the solution contributed to the formation of the complex ions, resulting in no precipitate.

A precursor film with a La/Mn atomic ratio of 0.85 on YSZ was obtained after 24 hr in the solution, as shown in Table I [8]. We studied the ion exchange behavior of this precursor film. Figures 1 and 2 show the La/Mn atomic ratio and the amounts of La and Mn in the precursor films on YSZ as a function of immersion time in the distilled water at pH=7 and in diluted nitric acid at

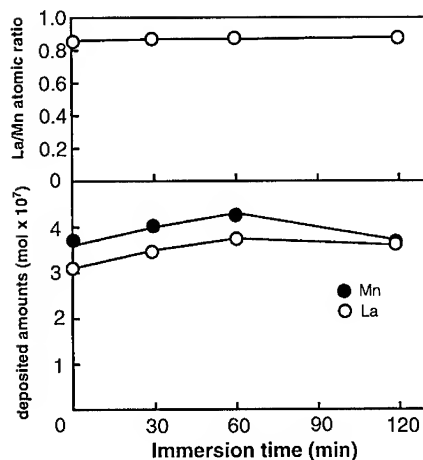


**Fig. 1** The La/Mn atomic ratio and deposited amounts of Mn and La in the precursor film on YSZ as a function of immersion time in distilled water at pH=7.

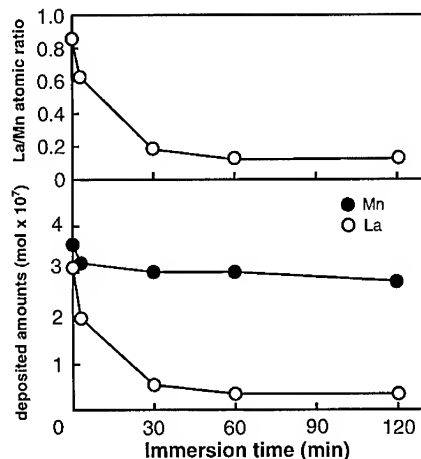
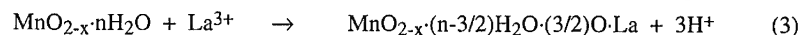


**Fig. 2** The La/Mn atomic ratio and deposited amounts of Mn and La in the precursor film on YSZ as a function of immersion time in diluted nitric acid at pH=2.

pH=2, respectively. As shown in Fig. 1, the La/Mn atomic ratio was constant in the distilled water, indicating that  $\text{La}^{3+}$  ions in the precursor were not eluted in the distilled water. In contrast, the La/Mn atomic ratio decreased with time in diluted nitric acid at pH=2, indicating that  $\text{La}^{3+}$  ions in the precursor were easily eluted in diluted nitric acid at pH=2. It is well known that manganese dioxide has a cation-exchange property, in which some metal cations are exchanged for  $\text{H}^+$  ions on the  $\text{MnO}_2$  [10,11]. The adsorbed metal cations on  $\text{MnO}_2$  can be easily eluted from  $\text{MnO}_2$  in an acidic solution, as well as in our case, as shown in Fig. 2. The precursor film after the elution of  $\text{La}^{3+}$  ions was immersed in a 2 M  $\text{La}(\text{NO}_3)_3$  solution at pH=6 for 12 hr, causing the La/Mn atomic ratio in the

film to increase from 0.17 to 0.83. These data indicate that the incorporation of  $\text{La}^{3+}$  ions into the oxide film was based on the ion-exchange reaction, where  $\text{La}^{3+}$  ions in the solution were exchanged for  $\text{H}^+$  ions on the deposited  $\text{MnO}_2$ .

Consequently, the formation of a  $\text{LaMnO}_3$  precursor on YSZ will occur through the following two steps. The first step is the formation of hydrous  $\text{MnO}_2$  resulting from the oxidation of  $\text{Mn}^{2+}$  by peroxydisulfate, i.e. reactions (1) and (2) proceed. The second step is the incorporation of  $\text{La}^{3+}$  ions into the amorphous and hydrous  $\text{MnO}_2$  by the ion-exchange reaction as follows.



We have developed another solution for the electroless deposition of a  $\text{La}_{1-x}\text{MnO}_3$  precursor film to improve long deposition time for the precursor film on YSZ in the solution shown in Table I. An oxide film with a La/Mn atomic ratio of 0.86 was deposited on YSZ in a solution of 0.01 M  $\text{Mn}(\text{NO}_3)_2$  - 0.2 M  $\text{La}(\text{CH}_3\text{COO})_3$  - 0.167 M  $(\text{NH}_4)_2\text{S}_2\text{O}_8$  - 0.5 M  $\text{CH}_3\text{COONa}$  -  $5 \times 10^{-6}$  M  $\text{AgNO}_3$  at pH=6.5 for 60 min.  $\text{La}_{0.86}\text{MnO}_3$  perovskite film was also obtained after the heat-treatment at 800 °C.

#### Preparation of $\text{La}_{1-x}\text{Sr}_x\text{MnO}_3$

In the mixed solution of  $\text{La}(\text{NO}_3)_3$ ,  $\text{Mn}(\text{NO}_3)_2$ ,  $\text{Sr}(\text{NO}_3)_2$  and  $(\text{NH}_4)_2\text{S}_2\text{O}_8$ , white precipitate was observed in the solution even after the addition of additives that are effective for  $\text{LaMnO}_3$  precursor preparation. Since a  $\text{La}_{1-x}\text{Sr}_x\text{MnO}_3$  precursor could not be directly deposited from these mixed solutions, it was prepared using an ion exchange reaction between  $\text{Sr}^{2+}$  ions in a solution and  $\text{La}^{3+}$  ions in  $\text{La}_{0.86}\text{MnO}_3$  precursor film. The precursor film, deposited on YSZ and Pt substrates

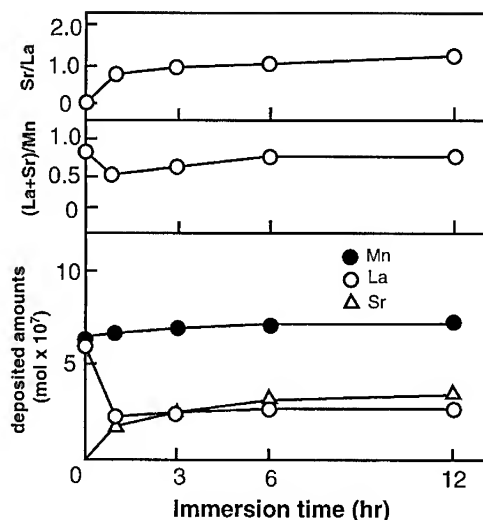


**Fig. 3** The Sr/Mn and (La+Sr)/Mn atomic ratio and deposited amounts of Mn, La and Sr in the oxide film on YSZ as a function of immersion time in a solution of 0.5 M  $\text{Sr}(\text{NO}_3)_2$  at pH=6. The oxide films used for this figure were deposited on YSZ in a solution of 0.01 M  $\text{Mn}(\text{NO}_3)_2$  - 0.2 M  $\text{La}(\text{CH}_3\text{COO})_3$  - 0.167 M  $(\text{NH}_4)_2\text{S}_2\text{O}_8$  - 0.5 M  $\text{CH}_3\text{COONa}$  -  $5 \times 10^{-6}$  M  $\text{AgNO}_3$  at pH=6.5 for 60 min.

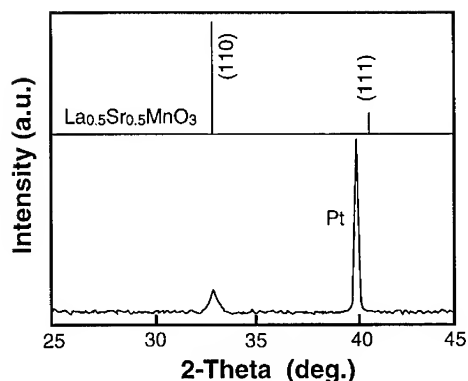


Fig. 4 X-ray diffraction patterns of the heated  $(\text{La}_{0.5}\text{Sr}_{0.5})_{0.75}\text{MnO}_3$  precursor film on Pt substrate at 800 °C for 5 hr in air and  $\text{La}_{0.5}\text{Sr}_{0.5}\text{MnO}_3$  perovskite .

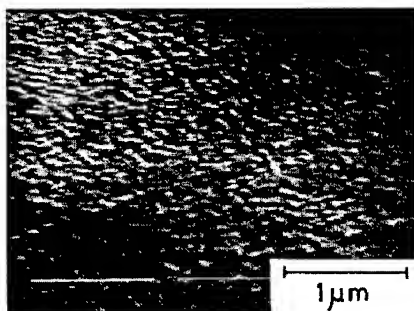


Fig. 5 A SEM photograph of the heated  $(\text{La}_{0.5}\text{Sr}_{0.5})_{0.75}\text{MnO}_3$  precursor film on Pt substrate at 800 °C for 5 hr in air .

in a solution of 0.01 M  $\text{Mn}(\text{NO}_3)_2$  - 0.2 M  $\text{La}(\text{CH}_3\text{COO})_3$  - 0.167 M  $(\text{NH}_4)_2\text{S}_2\text{O}_8$  - 0.5 M  $\text{CH}_3\text{COONa}$  -  $5 \times 10^{-6}$  M  $\text{AgNO}_3$  at pH=6.5 for 60 min, was immersed in a solution of 0.5 M  $\text{Sr}(\text{NO}_3)_2$ , at pH=6. Figure 3 shows the Sr/La and (La+Sr)/Mn atomic ratios and the amounts of La, Mn and Sr in the oxide films. Oxide films with (La+Sr)/Mn and Sr/La atomic ratios of 0.5 to 0.86 and 0 to 1 were obtained after immersion in a solution of 0.5 M  $\text{Sr}(\text{NO}_3)_2$  at pH=6. The composition of precursor films can be expressed as  $(\text{La}_{1-x}\text{Sr}_x)_{1-y}\text{MnO}_3$ , since the atomic ratio of (La+Sr)/Mn remained almost constant during the ion exchange process.  $(\text{La}_{0.5}\text{Sr}_{0.5})_{0.75}\text{MnO}_3$  precursor films were obtained on Pt and YSZ substrates after immersion in a solution of 0.5 M  $\text{Sr}(\text{NO}_3)_2$  at pH=6 for 6 hr.

Figure 4 shows X-ray diffraction patterns of the heated  $(\text{La}_{0.5}\text{Sr}_{0.5})_{0.75}\text{MnO}_3$  precursor film on Pt substrate at 800 °C for 5 hr in air, where the diffraction pattern of  $\text{La}_{0.5}\text{Sr}_{0.5}\text{MnO}_3$  is also indicated. Except for the peaks of the substrate of Pt, only one diffraction peak was observed at 32.9 deg, which corresponds to the diffraction peak from the perovskite structure. In the film on

YSZ substrate, no obvious diffraction peak was observed except for the peaks of YSZ substrate after the heat-treatment, because the oxide film may react with the substrate of YSZ. A SEM photograph of the heated  $(\text{La}_{0.5}\text{Sr}_{0.5})_{0.75}\text{MnO}_3$  precursor film on Pt substrate at 800 °C for 5 hr in air is shown in Fig. 5.  $(\text{La}_{0.5}\text{Sr}_{0.5})_{0.75}\text{MnO}_3$  perovskite film on Pt was uniform and consisted of small grains of ca. 0.1  $\mu\text{m}$  in diameter.

## CONCLUSIONS

A  $\text{LaMnO}_3$  precursor was electrolessly deposited on YSZ substrate in a solution containing  $\text{Mn}^{2+}$ ,  $\text{La}^{3+}$ , an oxidizing agent and some additives. Peroxydisulfate was used as the oxidizing agent. The  $\text{LaMnO}_3$  precursor was an amorphous and hydrous  $\text{MnO}_2$  which contained  $\text{La}^{3+}$  ions. The incorporation of  $\text{La}^{3+}$  ions into the precursor oxide film was based on the ion-exchange reaction, where  $\text{La}^{3+}$  ions in the solution were exchanged for  $\text{H}^+$  ions on the deposited amorphous and hydrous  $\text{MnO}_2$ . A  $\text{La}_{1-x}\text{Sr}_x\text{MnO}_3$  precursor was also prepared from the  $\text{LaMnO}_3$  precursor, where some  $\text{La}^{3+}$  ions were exchanged for  $\text{Sr}^{2+}$  ions in the solution.  $(\text{La}_{0.5}\text{Sr}_{0.5})_{0.75}\text{MnO}_3$  perovskite film was obtained from the precursor films on Pt substrate by heat-treatment at 800 °C. This technique is very useful for preparing  $\text{La}_{1-x}\text{Sr}_x\text{MnO}_3$  perovskite film on substrates such as YSZ.

## REFERENCES

1. T. Sasaki, Y. Matsumoto, J. Hombo, and Y. Ogawa, *J. Solid State Chem.* **91**, 61 (1991).
2. T. Sasaki, T. Morikawa, J. Hombo, and Y. Matsumoto, *Denki Kagaku* **58**, 567 (1990).
3. Y. Matsumoto, T. Sasaki, and J. Hombo, *J. Electrochem. Soc.* **138**, 1259 (1991).
4. Y. Matsumoto, T. Sasaki, and J. Hombo, *Inorg. Chem.* **31**, 738 (1992).
5. W. Mindt, *J. Electrochem. Soc.* **117**, 615 (1970).
6. W. Mindt, *J. Electrochem. Soc.* **118**, 93 (1971).
7. P. Pramanik and S. Bhattacharya, *J. Electrochem. Soc.* **137**, 3869 (1990).
8. T. Sasaki, Y. Matsumoto, J. Hombo, and M. Nagata, *J. Solid State Chem.* **105**, 255 (1993).
9. A. Hammouche, E. Siebert, and A. Hammou, *Mater. Res. Bull.* **24**, 367 (1989).
10. A. Kozawa, *J. Electrochem. Soc.* **106**, 552 (1959).
11. M. Tsuji and M. Abe, *Bull. Chem. Soc. Jpn.* **58**, 1109 (1985).



**Part VI**

**Electrodeposition of Metals and Alloys  
for Magnetic and Electronic Applications I**

## FABRICATION AND CHARACTERIZATION OF NiFe THIN FILM COMPOSITION MODULATED ALLOYS

S.D. LEITH and D.T. SCHWARTZ

University of Washington, Department of Chemical Engineering, Box 351750, Seattle, WA 98195-1750

### ABSTRACT

Described are results showing that an oscillating flow-field can induce spatially periodic composition variations in electrodeposited NiFe films. Flow-induced NiFe composition modulated alloys (CMA's) were deposited on the disk of a rotating disk electrode by oscillating the disk rotation rate during galvanostatic plating. Deposit composition and structure were investigated using potentiostatic stripping voltammetry and scanning probe microscopy. Results illustrate a linear relationship between the composition modulation wavelength and the flow oscillation period. CMA's with wavelengths less than 10 nm can be fabricated when plating with a disk rotation rate oscillation period less than 3 seconds.

### INTRODUCTION

The production of electronic, magnetic and optical devices hinges on the ability to fabricate thin films with highly reproducible properties. A common aspect in all thin film manufacturing processes is the need to understand the relationship between process conditions and the resulting structure and properties of the deposit. NiFe thin films are used throughout the magnetic data storage industry [1-3] and are commonly electrodeposited in a paddle cell in which the electrolyte flow field oscillates periodically. Theory suggests that plating in an oscillating electrolyte flow will induce spatially periodic composition modulations through an alloy deposit provided at least one species is mass-transfer limited, one species is kinetics limited, and the flow oscillation period is longer than the concentration field relaxation time [4-5]. All of these conditions are satisfied by NiFe plating with electrolyte flow fields with oscillation periods greater than 1 second. It therefore seems likely that NiFe films plated in such an oscillating flow would exhibit spatially periodic composition modulations.

Presented here are experimental results describing the fabrication and characterization of flow-induced NiFe composition modulated alloys (CMA's) electrodeposited in an oscillating electrolyte flow. Studies are described which explore the processing/structure relationship in NiFe thin films electrodeposited in the flow generated by a rotating disk electrode with an oscillating rotation rate. Film composition profiles and structural characteristics are analyzed using stripping voltammetry and scanning probe microscopy. These techniques illustrate relationships between the processing environment and the resulting structure of the deposit in terms of the composition modulation repeat length (the wavelength,  $\Lambda$ ) and the variation in iron composition between layers (the modulation amplitude,  $\Delta X_{Fe}$ ).

### EXPERIMENTAL

Flow-induced NiFe CMA's were deposited onto a platinum disk electrode by oscillating the disk rotation rate during plating. A Pine Instruments model MSRX rotator and a Wavetek function generator were used to control the oscillating rotation rate of the disk electrode. During deposition, the rotation rate of the disk was oscillated in a square wave having maximum and minimum values of 400 and 3400 rpm with electrodeposition terminated at the end of the 400 rpm leg. Oscillation periods investigated ranged from 3 to 100 seconds. Aside from the time-periodic flow induced by the oscillating disk electrode, all deposition parameters were held constant in time. Electrodeposited CMA's were plated either onto the disk of a Pine Instruments rotating disk electrode (RDE with a removable platinum electrode disk of radius  $r_1 = 0.25$  cm) or onto the disk of a Pine Instruments rotating ring-disk electrode (RRDE with a platinum disk of radius  $r_1 = 0.2286$  cm and a platinum ring with inner ring radius  $r_2 = 0.2464$  and outer ring radius  $r_3 = 0.2692$ ). For all investigations, the rotating disk, a large area platinum mesh counter electrode and a saturated calomel reference electrode (SCE) were used in a 200 ml single chambered electroplating vessel. Films were plated galvanostatically at room temperature from a

pH controlled, chloride-based bath to a total depth of 1.0 to 3.5  $\mu\text{m}$ . A number of different film growth rates ranging from 0.04 to 0.79  $\mu\text{m}/\text{min}$  (-5 to -40  $\text{mA}/\text{cm}^2$ ) were investigated. During deposition using the RRDE, the ring potential was set to +800 mV vs. SCE to prevent plating on the ring. Current and potential in the cell were controlled by a Pine Instruments model AFRDE5 Bi-Potentiostat which was interfaced to a Macintosh Centris 650 computer using a National Instruments 12-bit multi-function I/O board. Acquisition of ring and disk current data was controlled by custom software written in LABVIEW 2.2.1.

NiFe CMA's plated onto the disk of the RRDE were analyzed using stripping voltammetry. After the CMA was deposited, the RRDE was immersed and slowly rotated in deionized water to remove residual plating bath components. The RRDE was then steadily rotated (at 2500 rpm) in a HCl/NaCl stripping bath in which the NiFe film was oxidized potentiostatically at a disk potential of 0.0 mV vs. SCE. Stripping at this potential ensured that the oxidation products liberated from the film were  $\text{Ni}^{+2}$  and  $\text{Fe}^{+2}$ . The ring potential during stripping was set to +800 mV vs. SCE to further oxidize the liberated ferrous ions to ferric ions. All stripping voltammetry experiments were carried out in a 200 ml electrochemical cell with a platinum mesh counter electrode and SCE reference. Continuous monitoring of the disk and ring currents during stripping allowed determination of the average wavelength and amplitude of NiFe CMA's [6].

Films deposited onto the removable disk of the RDE were studied in cross section using atomic force microscopy. After deposition of the CMA, a nickel overlayer was plated on top of the film to a depth of roughly 175  $\mu\text{m}$ . The disk was then removed and cut into cross sections using a diamond wafering blade. After sectioning, the samples were polished using a hand lapping tool with a series of sandpaper grades from 800 to 2400 grit. Diamond paste (6 and 1  $\mu\text{m}$ ) was used in the final polishing step. Upon completion of polishing, the sample cross sections were anodically etched in a HCl/NaCl stripping bath identical in composition to that used in the stripping voltammetry experiments. In cross section, the NiFe CMA films etch anisotropically due to the difference in reduction potential between iron-enriched and iron-depleted layers. Using potentiostatic etching, areas of Fe-enriched film are preferentially removed, resulting in a corrugated sample surface corresponding to regions of different iron composition. Topographical studies of the etched cross sections were used to determine local CMA wavelengths. The cross section samples were studied using a Nanoscope II scanning probe microscope.

## RESULTS AND DISCUSSION

Characteristic wavelengths of electrodeposited NiFe CMA's were determined using stripping voltammetry and AFM analysis. While stripping voltammetry allowed a measure of the average wavelength throughout the deposit, the higher resolution microscopy technique provided a means to investigate the wavelength at specific locations in the film. Of the characterization techniques discussed here, however, stripping voltammetry was the only method capable of measuring the modulation amplitude in the films.

Figure 1 shows typical stripping voltammetry results for NiFe CMA's electrodeposited at 0.79  $\mu\text{m}/\text{min}$  (-40  $\text{mA}/\text{cm}^2$ ) in a time-periodic electrolyte flow. The left side of the figure shows the disk (dashed curve) and ring (solid curve) currents measured during stripping and the right side shows the corresponding composition profile of the film. Using potentiostatic stripping conditions, oscillations in the disk and ring currents are clearly seen. The disk current oscillates due to the enhanced oxidation rate of iron-enriched layers and the ring current responds in tandem as  $\text{Fe}^{+2}$  liberated from the disk is oxidized to  $\text{Fe}^{+3}$ . Figure 1 shows that the square wave rotation rate oscillation used during plating results in the deposition of a NiFe CMA.

Two interesting aspects of potentiostatic stripping voltammetry are illustrated in Figure 1. First, the figure shows that near the end of stripping, the apparent iron content of the alloy rises abruptly. This feature of the composition profile is always present, since the ring current response lags behind the disk current by the transit time across the disk-ring gap. Therefore, when the disk current drops to zero at the end of stripping, the ring still measures a finite current, leading to an apparent iron mole fraction in excess of unity [6]. Second, the disk and ring currents in Figure 1 are seen to gradually fall as stripping is completed. For a deposit of uniform thickness that is also stripped uniformly, it is expected that the disk and ring currents will exhibit a sharp drop off at the point where the film is completely removed. The deviation of our data

from this type of profile is likely due to well documented non-uniformities in the plating and stripping current distributions on the disk electrode [7]. While these non-uniformities are an issue when using stripping voltammetry, it is still possible to determine the average CMA wavelength and amplitude over the deposit depth provided that the non-uniformities in plating and stripping are of similar magnitude [6].

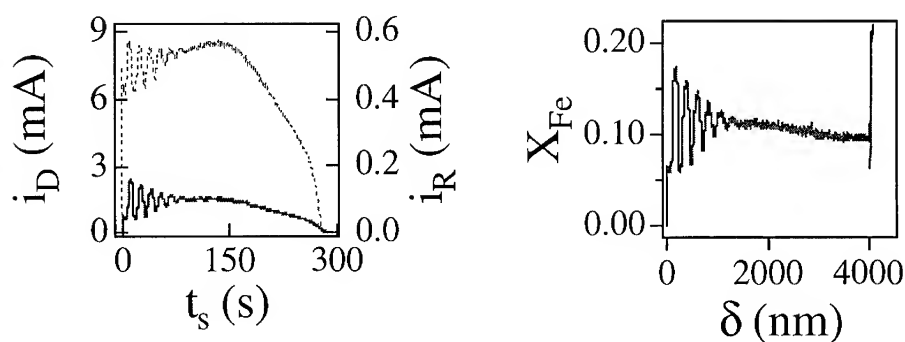


Figure 1. Potentiostatic stripping curves for a NiFe CMA plated galvanostatically in an oscillating electrolyte flow. Left hand plot shows the disk (----) and ring (—) currents as a function of strip time. Right hand plot illustrates the corresponding composition profile.

Figure 1 shows that the peak-to-peak composition modulation amplitude appears to decline as etching progresses throughout the deposit. Normally, one expects the CMA to have well defined lamellae near the substrate, with progressively less defined layers as the deposit grows and the growth front becomes rougher. The decline in the amplitude shown here is due to the non-uniform current distribution during stripping, since the further stripping progresses, the more the etch front becomes distorted. Therefore, we use the very first modulation in each stripping curve to estimate the amplitude of the CMA throughout the alloy, keeping in mind that this likely represents a lower limit for the alloy as a whole. Using stripping voltammetry, we have been able to measure composition modulation amplitudes ranging from 8 to 15 mol% in flow-induced NiFe CMA's.

Theoretically, one expects a flow-induced NiFe CMA to have a modulation wavelength ( $\Lambda$ ) that follows the relationship

$$\Lambda = \left( \frac{\hat{V}_{\text{NiFe}}}{2F} \right) \eta j T, \quad (1)$$

where  $\hat{V}_{\text{NiFe}}$  is the mean molar volume of the alloy,  $\eta$  is the plating current efficiency,  $j$  is the plating current density,  $F$  is Faraday's constant, and  $T$  is the flow oscillation period. The relationship between the measured CMA wavelengths and the rotation rate oscillation periods of flow-induced CMA's made in our laboratory is summarized in Figure 2. Figure 2 shows that  $\Lambda$  has the expected linear dependence on  $T$ ; an increase in the oscillation period results in a CMA with longer wavelength. Note that the CMA's made at the smallest oscillation periods are characterized by nanometer-scale modulation wavelengths. For example, films plated using an oscillation period of 3.33 seconds can exhibit composition modulation wavelengths of roughly 7 nm.

The modulation wavelength of NiFe CMA's was also measured by investigating the topographical characteristics of electrochemically etched cross sections. Figure 3 is an AFM

image of a typical NiFe CMA plated onto a removable platinum disk electrode. The film was deposited at a rate of  $0.79 \mu\text{m}/\text{min}$  using a disk rotation oscillation period of 16.67 seconds. After sectioning and polishing, the film was etched potentiostatically at 0 mV vs. SCE until a total charge of approximately 0.05 mC had passed. When viewed with the AFM, the film, platinum substrate and nickel overlayer are all easily identified. The contrast in the CMA region represents corrugations in the surface of the cross section caused by preferential oxidation of iron-enriched areas of the film. The *local* modulation wavelength can be determined from this image visually or electronically and its value, 160 nm, is within 20% of the average wavelength determined using stripping voltammetry. Note that to better distinguish between the three layers in the AFM cross section image, the platinum substrate region was uniformly darkened and the nickel overlayer region was uniformly brightened.

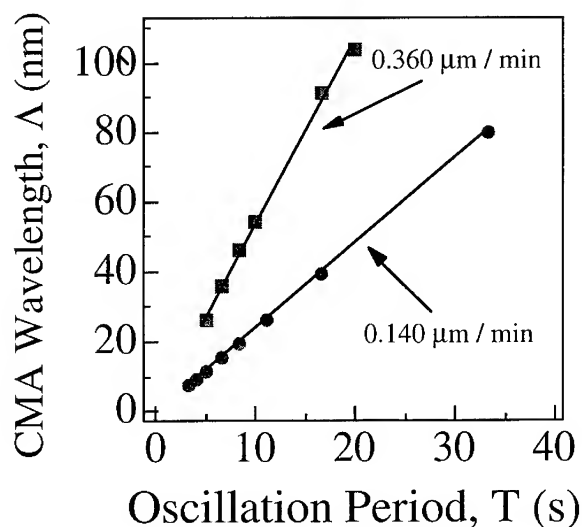


Figure 2. Relationship between the measured wavelength and disk rotation rate oscillation period for flow-induced NiFe CMA's electrodeposited at different rates. The CMA wavelength is shown to be a linear function of oscillation period, as predicted by theory. CMA's with wavelengths less than 10 nm can be fabricated using the oscillating flow technique.

## CONCLUSIONS

We have illustrated that electrodeposited NiFe CMA's can be fabricated over a range of film growth rates when the electrolyte flow-field is subjected to oscillation periods greater than one second. NiFe alloys (e.g. permalloy) used in magnetic data storage devices are commonly electrodeposited in a paddle cell under very similar conditions to those used in the present study. It is entirely possible, therefore, that industrially manufactured NiFe films exhibit nanometer-scale composition modulations. We have begun to investigate the relationship between the processing environment and the structure of NiFe CMA's, but it remains to be seen what effect the structure of these alloys has on material properties. Future work will focus on continued exploration of the processing/structure relationships in NiFe CMA's as well as systematic studies of the structure/property relationships in these materials.

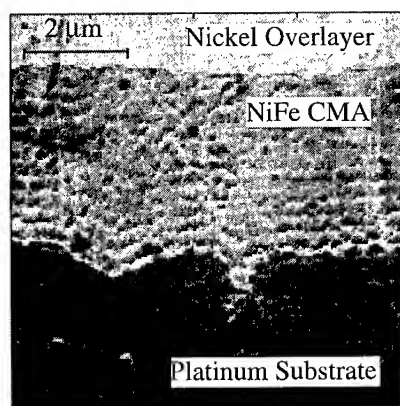


Figure 3. AFM image of an electrochemically etched NiFe CMA cross section. Using potentiostatic stripping, areas of Fe-enriched film are preferentially removed, resulting in a corrugated sample surface. The wavelength of this CMA is measured to be 160 nm.

#### ACKNOWLEDGMENTS

Support for this research was provided by the National Science Foundation through grant number CTS-9210637 and the Young Investigator program (CTS-9457097). We thank Mike Garrison at the University of Washington for assistance with the AFM studies.

#### REFERENCES

1. J.H. Judy, MRS Bull., **15**, 63 (1990).
2. P.C. Andricacos and L.T. Romankiw, in *Advances in Electrochemical Science and Engineering*, edited by H. Gerischer and C.W. Tobias, (VCH Publishers, New York, 1994), Vol. 3, pp. 227.
3. T. Jagielinski, MRS Bull., **15**, 36 (1990).
4. D.T. Schwartz, J. Electrochem. Soc., **136**, 53C (1989).
5. D.T. Schwartz, P. Stroeve, and B.G. Higgins, AIChE J., **35**, 1315 (1989).
6. S.D. Leith and D.T. Schwartz, J. Electrochem. Soc., **143**, 873 (1996).
7. J. Newman, J. Electrochem. Soc., **113**, 1235 (1966).

## ELECTRODEPOSITED MAGNETIC MULTILAYERS

W. SCHWARZACHER\*, M. ALPER\*\*, R. HART\*, G. NABIYOUNI\*, I. BAKONYI\*\*\*  
AND E. TOTH - KADAR\*\*\*

\* H. H. Wills Physics Laboratory, Tyndall Avenue, Bristol BS8 1TL, United Kingdom.

\*\* Current address: Bursa Uludag Üniversitesi, Fizik Bölümü, Bursa 16059, Turkey.

\*\*\* Research Institute for Solid State Physics, H-1525 Budapest, P.O.B. 49, Hungary.

### ABSTRACT

Electrodeposited magnetic multilayer films consisting of alternating layers of a ferromagnetic and a non-magnetic metal may exhibit giant magnetoresistance (GMR), but the effect is very sensitive to whether deposition is carried out under potentiostatic or galvanostatic control, and the choice of substrate. The texture of Co-Ni-Cu/Cu superlattices grown on polycrystalline (100)-textured Cu plates and (110)-textured Cu foil under potentiostatic control depended on that of the substrate, while comparable superlattices grown under galvanostatic control had a predominantly (111) texture. The films grown under galvanostatic control generally exhibit AMR or smaller GMR. The magnetic and magnetotransport properties of Co-Ni-Cu/Cu superlattices and a single-layer Co-Ni-Cu film electrodeposited directly onto n-GaAs (100) are also described, and evidence is presented for an in-plane magnetic anisotropy in these samples.

### INTRODUCTION

The discovery of giant magnetoresistance (GMR) in Fe/Cr/Fe 'sandwich' films<sup>1</sup> and Fe/Cr superlattices<sup>2</sup> prepared by molecular beam epitaxy (MBE) stimulated much research into magnetic multilayer films. Shortly after the initial discovery, other metal/metal systems were found which showed GMR, and sputtering was shown to be an excellent method of preparing such films<sup>3,4</sup>. Since the equipment required for electrodeposition is much simpler and less costly than required for either sputtering or MBE, and since it had been shown that high-quality short-period metal/metal superlattices could be electrodeposited from a single electrolyte<sup>5,6</sup>, attempts were made to prepare films showing GMR by this method. The first electrodeposited films for which significant GMR was reported were Co-Ni-Cu/Cu alloy superlattices<sup>7</sup>, and GMR was later found in electrodeposited Co-Cu/Cu<sup>8,9</sup>, Ni-Cu/Cu<sup>8,10</sup> and Fe-Ni-Cu/Cu<sup>11</sup> superlattices, as well as in electrodeposited Co-Cu heterogeneous alloy films<sup>12,13</sup>. It was also shown that magnetic metal/metal superlattices could be deposited in pores having a diameter of a few tens of nm and a length of several  $\mu\text{m}$  to create wire-like samples suitable for current perpendicular to plane GMR measurements<sup>14,15</sup>. GMR in electrodeposited films has been the subject of a recent review article<sup>16</sup>.

The GMR observed in electrodeposited films can be changed significantly by altering details of the growth process. For example, for Co-Ni-Cu/Cu superlattices with fixed Co-Ni-Cu and Cu layer thicknesses grown on polycrystalline Cu substrates,

the GMR was found to be very sensitive to the electrolyte pH<sup>17</sup>. Co-Ni-Cu(20Å)/Cu(8Å) superlattices electrodeposited from a sulphamate electrolyte at pH=1.8 exhibited GMR of ~ 10%, while superlattices with the same layer thicknesses grown from a similar electrolyte at pH=3.3 exhibited predominantly anisotropic magnetoresistance (AMR)<sup>18</sup>. AMR is a phenomenon also found in bulk ferromagnets, whereby the magnetoresistance depends on the angle between the film magnetization and the direction of current flow, in contrast to GMR which is independent of the direction of (in-plane) current flow. For films showing AMR, the longitudinal magnetoresistance (MR) (measured with the current parallel to the applied field) has a minimum close to zero applied field, while the transverse MR (measured with the current perpendicular to the applied field) has a maximum. For films showing GMR, however, both the longitudinal and the transverse MR have a maximum close to zero applied field. It appears that for the Co-Ni-Cu/Cu superlattices electrodeposited at higher pH there is more Co dissolution during the deposition of the Cu layers, which could give rise to rough interfaces that would favour ferromagnetic coupling of the magnetic layers and destroy the GMR.

Here we show that the magnitude of the GMR measured for electrodeposited Co-Ni-Cu/Cu superlattices also depends on whether they are grown potentiostatically (controlled potential) or galvanostatically (controlled current) and on the texture of the polycrystalline Cu substrate. We also present magnetic and magnetotransport results for Co-Ni-Cu/Cu superlattices and a single Co-Ni-Cu alloy layer electrodeposited directly onto n-GaAs to illustrate the presence of a uniaxial magnetic anisotropy in such samples.

#### A COMPARISON OF Co-Ni-Cu/Cu SUPERLATTICES GROWN UNDER POTENTIOSTATIC AND GALVANOSTATIC CONTROL

Co-Ni-Cu/Cu superlattices for this study were deposited from an electrolyte containing 2.3 mol Ni sulphamate ( $\text{Ni}(\text{SO}_3\text{NH}_2)_2$ ), 0.41 mol Co sulphate ( $\text{CoSO}_4$ ), ~0.05 mol Cu sulphate ( $\text{CuSO}_4$ ), and 0.5 mol boric acid ( $\text{H}_3\text{BO}_3$ ) per litre of  $\text{H}_2\text{O}$ . Superlattices grown under potentiostatic control were prepared in a 3-electrode cell (in Bristol) with deposition potentials of -1.6V and -0.2V, relative to a standard calomel electrode placed ~ 4cm from the cathode, used to deposit Co-Ni-Cu and Cu respectively. Superlattices grown under galvanostatic control were prepared in a 2-electrode cell (in Budapest) with current densities of 50 mA cm<sup>-2</sup> and 1.3 mA cm<sup>-2</sup> used to deposit the Co-Ni-Cu and the Cu. These current densities were chosen to be close to the average current densities during the potentiostatic deposition of Co-Ni-Cu and Cu. Films were grown with 100 or 1000 repeats on two types of polycrystalline Cu substrate; foils with a predominantly (110) texture, and plates with a predominantly (100) texture. The nominal Co-Ni-Cu layer thickness (ie the thickness calculated assuming 100% current efficiency) was fixed at 30Å, while the nominal Cu layer thickness was varied between 10 and 30 Å. The real Co-Ni-Cu and Cu layer thicknesses are respectively ~60% and ~90% of the nominal thicknesses.



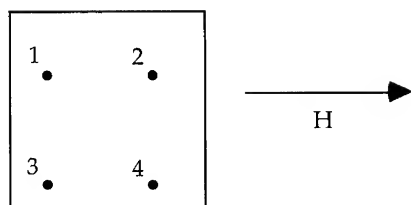


**Figure 1:** Experimental configuration used for magnetotransport measurements.

Magnetoresistance (MR) measurements were made using 4 spring-loaded point probes arranged in a square to make pressure contacts to the film, as shown in figure 1. The ratio of the potential difference between contacts 1 and 2 to the current flowing between contacts 3 and 4 will subsequently be referred to as the 'longitudinal' MR, while the ratio of the potential difference between contacts 1 and 3 to the current flowing between contacts 2 and 4 will be referred to as the 'transverse' MR. Although the 'longitudinal' and 'transverse' MR defined in this way are convenient to measure, the percentage changes in these quantities are not in general the same as the percentage changes in the true longitudinal and transverse MR<sup>16</sup>.

Figures 2a and 2b show the 'longitudinal' MR for 1000 x (nominally) 30Å Co-Ni-Cu/15Å Cu superlattices electrodeposited on (110)-textured Cu foil under potentiostatic and galvanostatic control respectively. The 'longitudinal' MR reaches a maximum close to zero applied field for the potentiostatically grown film, while it reaches a minimum for the galvanostatically grown film. This is clear evidence that although the potentiostatically grown film exhibits GMR, the galvanostatically grown film exhibits predominantly AMR.

Measurements on other samples showed that in general potentiostatic deposition favoured GMR, while galvanostatic deposition favoured either a smaller GMR or AMR, but that the choice of substrate was also important. Figures 3a and 3b again show the 'longitudinal' MR for 1000 x (nominally) 30Å Co-Ni-Cu/15Å Cu superlattices electrodeposited respectively under potentiostatic and galvanostatic control, but this time using (100)-textured Cu plates as the substrates. Although the magnitude of the MR for the galvanostatically grown film is much less than for the potentiostatically grown one, it is clear that on this substrate material both growth methods give films showing GMR.

X-ray diffraction (XRD) studies show that there are also significant structural differences between potentiostatically and galvanostatically grown superlattices<sup>19</sup>. The potentiostatically grown superlattices gave X-ray patterns similar to those of the substrates, whether (110) or (100), while galvanostatically grown films tended to grow with a (111) texture on both the (100) and (110) textured substrates. Transmission electron microscopy (TEM) studies showed heavy twinning in a galvanostatically grown superlattice on a (100)-textured substrate, and a 'nanocrystalline' structure for such a superlattice grown on a (110)-textured foil<sup>20</sup>. Twinning defects and the disruption to the layering found in the 'nanocrystalline' sample could both lower the GMR.

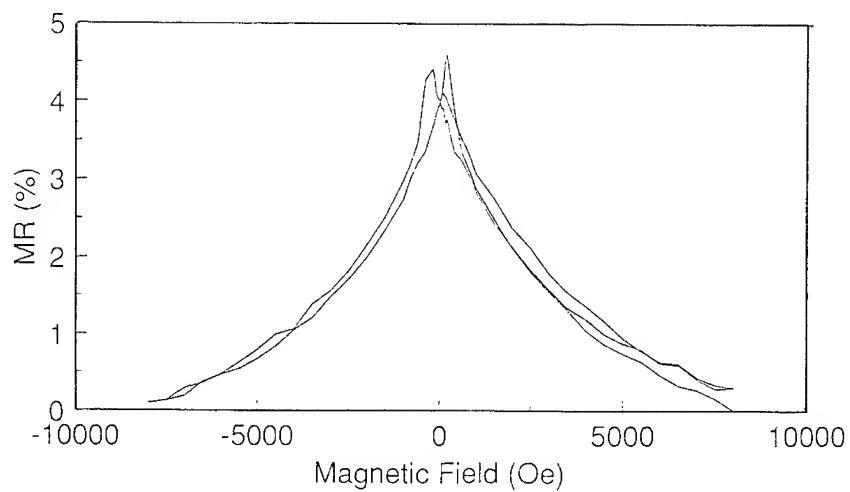


**Figure 2a:** Percentage change in the 'longitudinal' MR for a 1000 x (nominally) 30 Å Co-Ni-Cu/15 Å Cu superlattice electrodeposited on (110)-textured Cu foil under potentiostatic control.

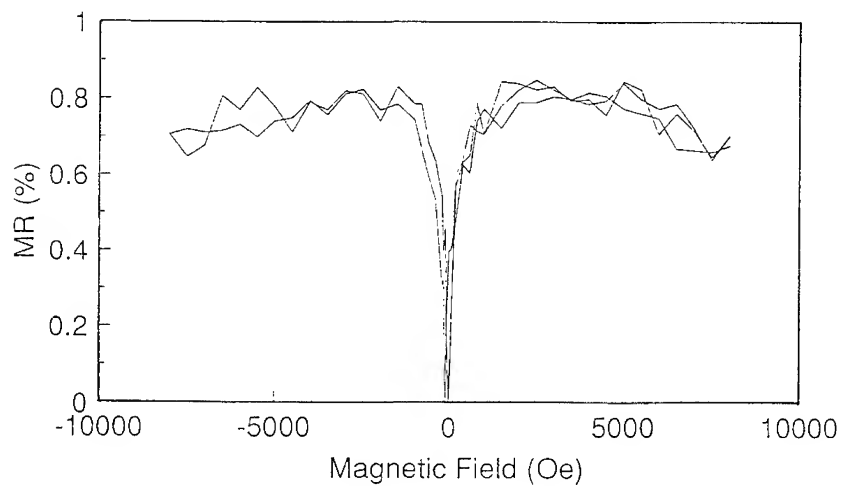


**Figure 2b:** Percentage change in the 'longitudinal' MR for a 1000 x (nominally) 30 Å Co-Ni-Cu/15 Å Cu superlattice electrodeposited on (110)-textured Cu foil under galvanostatic control.

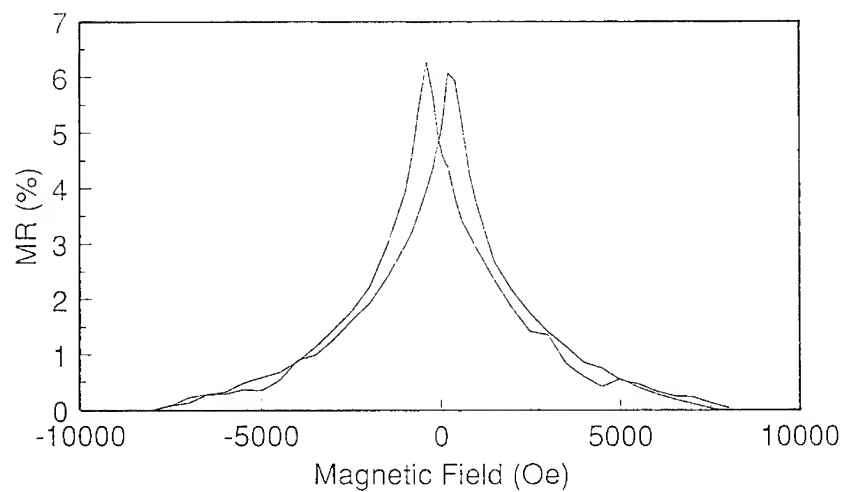


Figure 3a: Percentage change in the 'longitudinal' MR for a 1000 x (nominally) 30Å Co-Ni-Cu/15Å Cu superlattice electrodeposited on (100)-textured Cu plate under potentiostatic control.

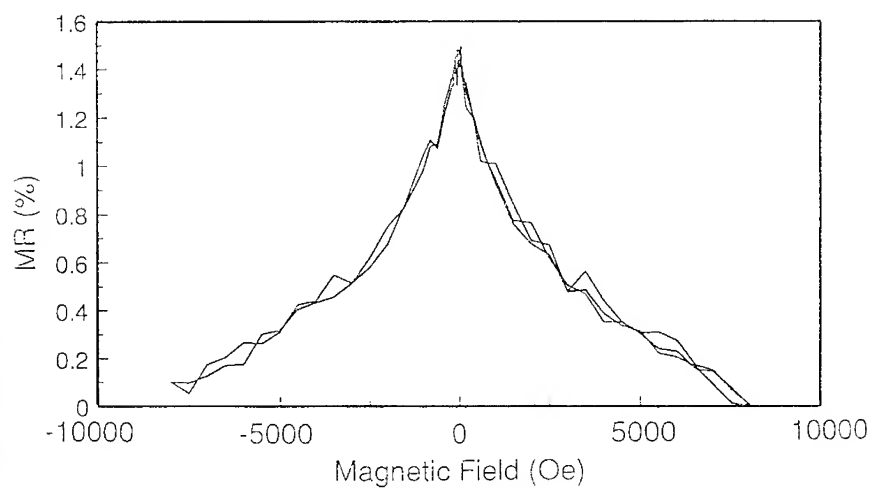


Figure 3b: Percentage change in the 'longitudinal' MR for a 1000 x (nominally) 30Å Co-Ni-Cu/15Å Cu superlattice electrodeposited on (100)-textured Cu plate under galvanostatic control.

## Co-Ni-Cu/Cu SUPERLATTICES AND SINGLE-LAYER FILMS ELECTRODEPOSITED ON n-GaAs

One disadvantage of electrodepositing GMR multilayers on Cu is that the substrates have a very low resistance and must be removed before making magnetotransport measurements in order to avoid short-circuiting the films. As removing the substrates is a laborious process, some Co-Ni-Cu/Cu superlattices were electrodeposited directly onto (100) oriented single-crystal n-type GaAs. With these samples it was possible to make MR measurements without removing the substrates.

The Co-Ni-Cu/Cu superlattices were electrodeposited from a sulphamate electrolyte similar to that used for the superlattices on Cu, but containing proportionately less Co and having a higher pH. Back contacts to the GaAs were fabricated by the galvanostatic deposition of Cu from an alkaline pyrophosphate solution. Electrodeposition was carried out in a 3-electrode cell with the sample held vertical.

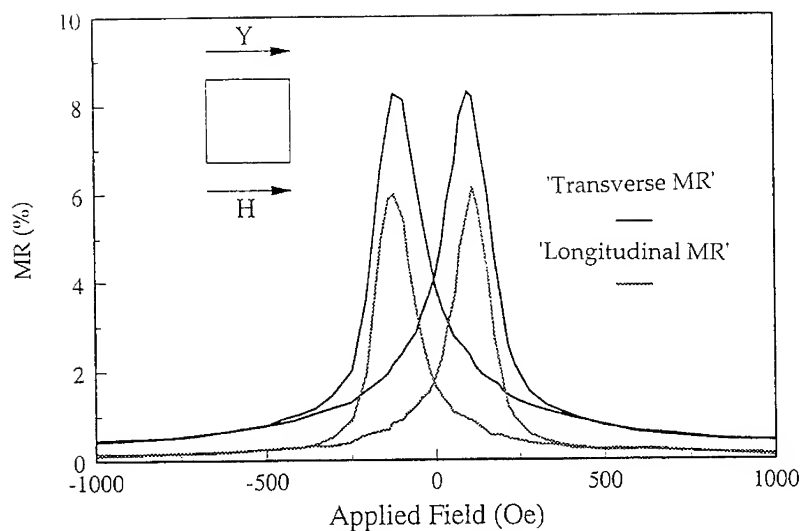
As was done for the superlattices grown on Cu, MR measurements were made using 4 spring-loaded point contacts in a square configuration. The GMR was found to be small for superlattices with very thin Cu layers (less than  $\sim 20\text{\AA}$ ), possibly due to ferromagnetic coupling of the magnetic layers caused by interface roughness or pinholes in the Cu layers. Some films showed sensitivities of over 0.05% change in MR per Oe<sup>21</sup>.

Figure 4a shows the measured 'transverse' and 'longitudinal' MR for a superlattice consisting of 200 repeats of nominally 50Å Co-Ni-Cu/50Å Cu (real thickness  $\sim 30\text{\AA}$  Co-Ni-Cu/37Å Cu). The differences between the two MR curves are due to AMR. Both MR curves show peaks at applied fields close to the coercivity, as is typical for multilayers in which the magnetizations of successive magnetic layers are not strongly coupled. For this measurement, the direction in the sample plane which was vertical during deposition of the film (denoted by 'Y') was parallel to the direction of the applied field, as shown in the inset.

Figure 4b shows the measured 'transverse' and 'longitudinal' MR for the same sample, but rotated by 90° about the normal to the film plane, so that direction 'Y' was perpendicular to the applied field. If the multilayer were isotropic, this rotation would not make a difference to the MR, but it is clear from the figure that in fact the difference between the 'transverse' and the 'longitudinal' MR is greater than before, suggesting that for some reason rotating the sample increases the AMR.

In order to study the AMR without the complication of the GMR introduced by the multilayer structure of the film, a single-layer Co-Ni-Cu film with a nominal thickness of 500Å was electrodeposited and its magnetic and magnetotransport properties measured. Figures 5a and 5b show the 'transverse' MR for this film with direction 'Y' respectively parallel and perpendicular to the applied magnetic field. It is immediately apparent that the 'transverse' MR is greatly increased when 'Y' is perpendicular to the applied field. A similar effect is seen in the 'longitudinal' MR, confirming the conclusion drawn from the comparison of figures 4a and 4b that the AMR increases significantly when 'Y' is perpendicular to H.

Figures 6a and 6b suggest a possible reason for the increase in the AMR when the sample is rotated. They show the film magnetization measured using a vibrating



**Figure 4a:** Percentage change in the 'transverse' and 'longitudinal' MR for a 200 x (nominally) 50Å Co-Ni-Cu/50Å Cu superlattice electrodeposited on n-GaAs. The inset shows the relationship between the direction in the sample plane which was vertical during deposition of the film (denoted by 'Y') and the direction of the applied field.

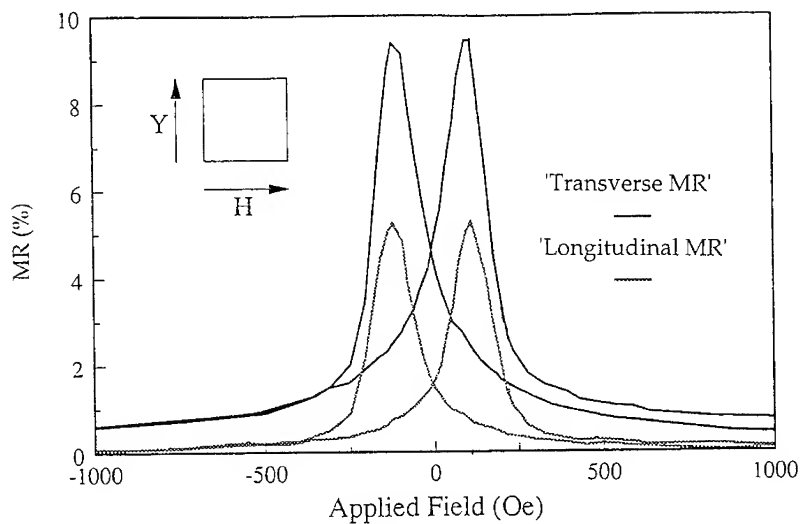


**Figure 4b:** Percentage change in the 'transverse' and 'longitudinal' MR for the same sample, but rotated by 90° about the normal to the film plane, so that direction 'Y' is perpendicular to the applied field.

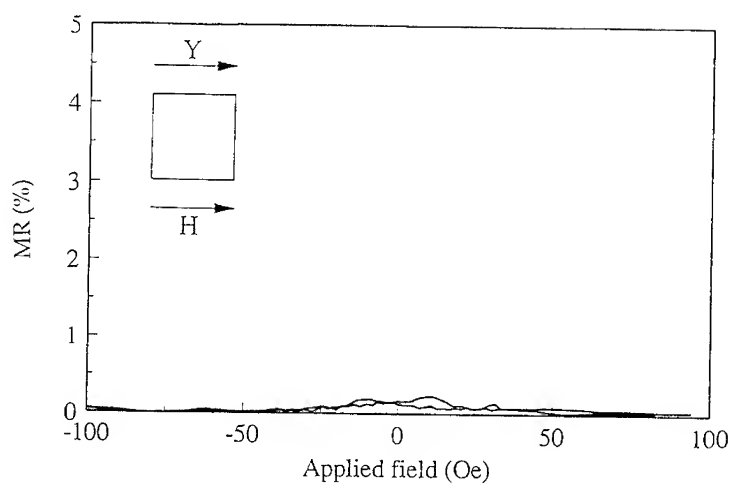


Figure 5a: Percentage change in the 'transverse' MR for a nominally 500Å thick Co-Ni-Cu single-layer film electrodeposited on n-GaAs. The inset shows the relationship between the direction in the sample plane which was vertical during deposition of the film (denoted by 'Y') and the direction of the applied field.

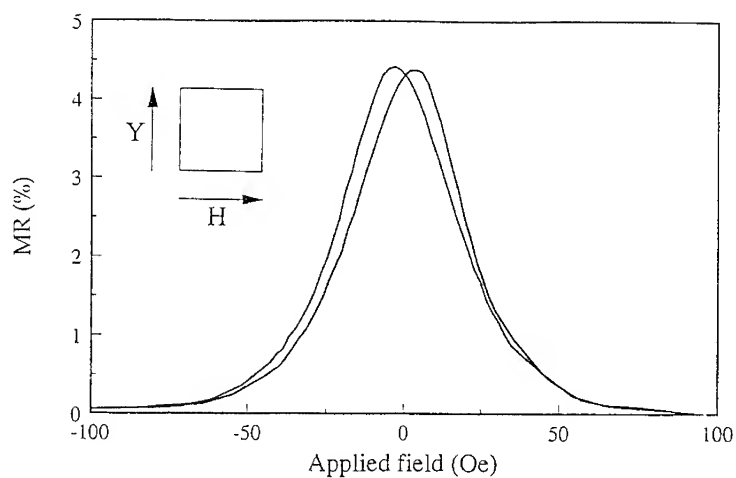
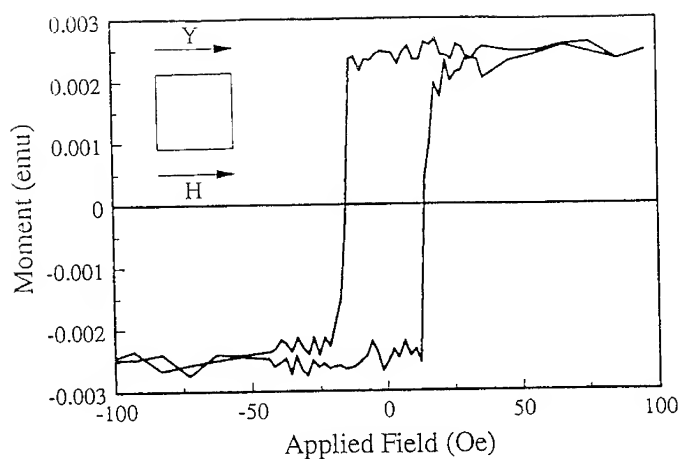
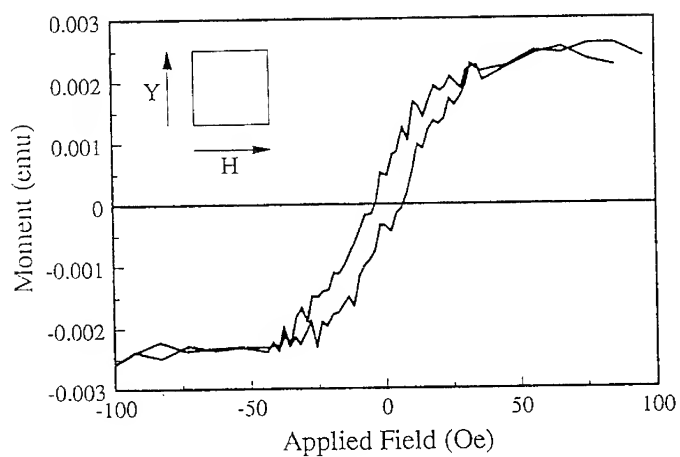


Figure 5b: Percentage change in the 'transverse' MR for the same sample rotated by 90° about the normal to the film plane, so that direction 'Y' is perpendicular to the applied field.



**Figure 6a:** Magnetic hysteresis loop from the nominally 500Å thick Co-Ni-Cu single-layer film electrodeposited on n-GaAs. The inset shows the relationship between the direction in the sample plane which was vertical during deposition of the film (denoted by 'Y') and the direction of the applied field.



**Figure 6b:** Magnetic hysteresis loop for the same sample rotated by 90° about the normal to the film plane, so that direction 'Y' is perpendicular to the applied field.

sample magnetometer with direction 'Y' respectively parallel and perpendicular to the applied field. When the applied field is parallel to 'Y', there is a large remanence, whereas when the applied field is perpendicular to 'Y' the remanence is small. This suggests that the electrodeposited Co-Ni-Cu film possesses a uniaxial anisotropy, with 'Y' being an easy axis for the magnetization.

When the magnetization direction of a uniaxial film is reversed by applying a field parallel to the easy axis, the magnetization reversal is likely to take place predominantly by domain wall motion. During this process, although the sense of the magnetization reverses, its direction remains parallel to the easy axis, and therefore at a fixed angle relative to the direction of current flow. Since AMR is only observed when the angle between the magnetization direction and the current flow changes, very little AMR will be observed, as is the case in figure 5a. When the magnetization direction of a uniaxial film is reversed by applying a field perpendicular to the easy axis, however, it will rotate to be parallel to the easy axis at small applied fields. The change in angle between the magnetization direction and the current flow gives rise to a significant AMR, as is the case in figure 5b.

The cause of the uniaxial anisotropy remains unclear, especially as TEM studies showed no visible structural anisotropy, but it could be that vertical concentration gradients due to natural convection during film growth led to compositional variations in the direction which was vertical during growth (the Y direction).

## CONCLUSIONS

The results presented here show the variety of factors which may affect the MR of electrodeposited metal/metal superlattices. Potentiostatic deposition was shown to be better suited to achieving GMR in Co-Ni-Cu/Cu superlattices electrodeposited on Cu than galvanostatic deposition, although it was shown that the substrate texture is also important. Results for Co-Ni-Cu/Cu superlattices and a Co-Ni-Cu thin film electrodeposited on GaAs provide evidence for a growth induced magnetic anisotropy, which also affects the MR.

## ACKNOWLEDGEMENTS

We are grateful to the EPSRC (UK) and the British Council for financial support.

## REFERENCES

- 1.) G. Binasch, P. Grünberg, F. Saurenbach, and W. Zinn, *Phys. Rev. B* **39**, 4828 (1989).
- 2.) M. N. Baibich, J. M. Broto, A. Fert, F. Nguyen Van Dau, F. Petroff, P. Etienne, G. Creuzet, A. Friederich, and J. Chazelas, *Phys. Rev. Lett.* **61**, 2472 (1988).
- 3.) S. S. P. Parkin, Z. G. Li and D. J. Smith, *Appl. Phys. Lett.* **58**, 2710 (1991).
- 4.) D. H. Mosca, F. Petroff, A. Fert, P. A. Schroeder, W. P. Pratt Jr. and R. Laloe, *J. Magn. Magn. Mat.* **94**, L1 (1991).
- 5.) J. Yahalom and O. Zadok, *J. Mater. Sci.* **22**, 499 (1987); J. Yahalom and O. Zadok, U.S. Patent No. 4,652,348 (1987).
- 6.) D. M. Tench and J. T. White, *Metall. Trans. A* **15A**, 2039 (1984).



- 7.) M. Alper, K. Attenborough, R. Hart, S. J. Lane, D. S. Lashmore, C. Younes and W. Schwarzacher, *Appl. Phys. Lett.* **63**, 2144 (1993).
- 8.) K. D. Bird and M. Schlesinger, *J. Electrochem. Soc.* **142**, L65 (1995).
- 9.) S. K. J. Lenczowski, C. Schönenberger, M. A. M. Gijs, and W. J. M. de Jonge, *J. Magn. Magn. Mat.* **148**, 455 (1995).
- 10.) D. S. Lashmore, Y. Zhang, S. Hua, M. P. Dariel, L. Swartzendruber and L. Salamanca-Riba, *Proceedings of 3rd International Symposium on Magnetic Materials, Processes and Devices, Electrochem. Soc. Proc. Vol. 94-6*, 205 (1994).
- 11.) K. Attenborough, R. Hart, S. J. Lane, M. Alper and W. Schwarzacher, *J. Magn. Magn. Mat.* **148**, 335 (1995).
- 12.) Y. Ueda and M. Ito, *Jpn. J. Appl. Phys. Part 2* **33**, L1403 (1994).
- 13.) H. J. Blythe and V. M. Fedosyuk, *J. Phys. Condens. Matt.* **7**, 3461 (1995).
- 14.) L. Piraux, J. M. George, J. F. Despres, C. Leroy, E. Ferain, R. Legras, K. Ounadjela and A. Fert, *Appl. Phys. Lett.* **65**, 2484 (1994).
- 15.) A. Blondel, J. P. Meier, B. Doudin and J.-Ph. Ansermet, *Appl. Phys. Lett.* **65**, 3019 (1994).
- 16.) W. Schwarzacher and D. S. Lashmore, *IEEE Trans. Magnet.* **32**, 3133 (1996).
- 17.) M. Alper, PhD thesis, University of Bristol, 1995; M. Alper, S. J. Lane and W. Schwarzacher (submitted to *J. Electrochem. Soc.*).
- 18.) T. R. McGuire and R. I. Potter, *IEEE Trans. Magnet.* **MAG-11**, 1018 (1975).
- 19.) G. Nabiyouni, W. Schwarzacher, I. Bakonyi and E. Tóth-Kádár (unpublished).
- 20.) A. Cziráki, G. Nabiyouni, W. Schwarzacher, J. G. Zheng, A. Michel, E. Tóth-Kádár and I. Bakonyi (unpublished).
- 21.) R. Hart, PhD thesis, University of Bristol 1996; R. Hart, M. Alper, K. Attenborough and W. Schwarzacher, *Proceedings of 3rd International Symposium on Magnetic Materials, Processes and Devices, Electrochem. Soc. Proc. Vol. 94-6*, 215 (1994).

## NANOWIRES GROWN ELECTROCHEMICALLY IN POROUS TEMPLATES

C. SCHÖNENBERGER \*, B. M. I. VAN DER ZANDE \*\*, and L. G. J. FOKKINK \*\*,

\*University of Basel, Department of Physics and Astronomy, Klingelbergstrasse 82, CH-4056 Basel, Switzerland. \*\* Philips Research Laboratories, Prof. Holstlaan 4, NL-5656 AA Eindhoven, The Netherlands.

### ABSTRACT

Metallic nanowires are synthesized by electrochemical growth in nanopores of either track-etched polycarbonate membranes or anodized aluminum films. The potentiostatic growth is systematically investigated for track-etched membranes with nominal pore diameters  $d_N$  between 10 and 80 nm. For this model system, the cross-section of the metallic wires is found to vary: the wire diameter, which is argued to directly reflect the pore diameter, is observed to be substantially larger in the middle than at both ends. Therefore, the pores are not cylindrical with constant cross-section, but appear to be 'cigar-like'. Inside the membranes, the pores are wider by up to a factor 3.

The aluminum oxide template has successfully been used to prepare a colloidal suspension of gold needles (anisotropic metallic colloid) by growing Au wires in the pores, dissolving the aluminum oxide and finally stabilizing and dispersing the 'nano-rods' in water. Visible near-infrared absorption spectroscopy reveal two absorption maxima caused by the anisotropy of these scatterers. The maxima can be assigned to a longitudinal and transversal plasma resonance.

### INTRODUCTION

Template synthesis is an elegant chemical approach for the fabrication of nanostructures, in particular for different kinds of nanowires.<sup>1</sup> It can be considered an alternative to conventional lithography-methods. Arrays of nanowires are obtained by filling a porous template that contains a large number of straight cylindrical holes with a narrow size distribution. Filling proceeds in solution by electrochemical deposition<sup>1-4</sup> or other chemical methods,<sup>1</sup> e.g. polymerization reactions. Useful templates for nanowires are: alumite membranes (anodized aluminum films)<sup>5</sup> or track-etched membranes,<sup>6</sup> and nanochannel array-glass,<sup>7</sup> or mesoporous channel hosts.<sup>8</sup> The first two are commercially available.

Templates filled with Co, Ni or Fe are magnetic nanocomposites that have a strong perpendicular magnetic anisotropy suitable for perpendicular recording.<sup>9</sup> Penner and Martin demonstrated the successful synthesis of conducting polymers (pyrrole and polythiophene) from commercial screen membranes, which are polycarbonate foils with pores obtained by etching nuclear damage-tracks.<sup>4,10</sup> For small pore diameters, the conductivity of these polymeric fibrils was found to be almost an order of magnitude higher than in bulk polymers prepared by the same method. This has been attributed to polymer chains with an enhanced order having less defects due to the unidirectional growth imposed by the confined geometry. In addition, pores have successfully been filled with two different materials which were stacked alternately to form multilayers.<sup>11</sup>

In this paper, we present recent results of our work on template-synthesis, which is conducted in two directions: In the first place, we study the potentiostatic growth in track-etched polycarbonate membranes and investigate the morphology of the wires. Secondly, we have successfully been using template-synthesis to fabricate a strongly anisotropic colloid in

which the nano-rods, initially grown in alumite films, are dispersed and stabilized in water.

## EXPERIMENTAL

For the electrochemical growth studies, polycarbonate screen membranes (overall diameter 13 mm) from Poretics are used with nominal pore diameters  $d_N = 10, 30, 80$  nm specified by the manufacturer. These membranes have a thickness of  $L = 6 \mu\text{m}$ . A metallic layer serving as back electrode is electron-beam evaporated onto one side of the membrane. This gold layer is sufficiently thick ( $\approx 1 \mu\text{m}$ ) to cover the pores completely. Before mounting the prefixed membrane into the electrochemical cell, it is immersed in deionized water under ultrasonic agitation during 2 min. This step is essential to ensure homogeneous pore wetting. Alumite membranes are prepared on  $14 \times 14 \text{ mm}^2$  Si substrates which are covered successively with a 10 nm Ti-adhesion layer, 100 nm Pt, and  $1 \mu\text{m}$  Al. The aluminum is converted into porous aluminum oxide by anodization at a constant voltage of 15 V in 15 v/v %  $\text{H}_2\text{SO}_4$ . The resulting porous alumite film has a thickness of  $1.5 \mu\text{m}$ , a pore density of  $\approx 8 \cdot 10^{14} \text{ m}^{-2}$ , and an average pore diameter equal to 12 nm.

Electroplating in the pores is done in a teflon cell with the substrate (membrane) facing upwards. There is no separate compartment for the counter electrode which is a Pt plate of about  $10 \text{ cm}^2$ , nor is there any agitation (stirring) or heating. A saturated-calomel electrode (SCE) was used as reference for the applied potential. This electrode is placed  $\approx 7$  mm above the substrate. Using a conventional potentiostat, the current is measured during electroplating at a fixed potential versus SCE, referred to as  $V_{\text{SCE}}$ . The growth in pores has been studied for Ni, Co, Cu, Au deposits, for which the following aqueous electrolytes (concentrations in the range of 0.3...1 M) have been used: Ni-solution: 515 g/l  $\text{Ni}(\text{H}_2\text{NSO}_3)_2 \cdot 4\text{H}_2\text{O}$  + 20 g/l  $\text{NiCl}_2 \cdot 6\text{H}_2\text{O}$  + 20 g/l  $\text{H}_3\text{BO}_3$ ; Co-solution: 400 g/l  $\text{CoSO}_4 \cdot 7\text{H}_2\text{O}$  + 40 g/l  $\text{H}_3\text{BO}_3$ ; Au-solution: 0.32 M gold(I)cyanide + 0.26 M citric acid and 0.65 M KOH ( $\text{pH} = 5...6$ ); Cu-solution: 125 g/l  $\text{CuSO}_4 \cdot 5\text{H}_2\text{O}$  +  $\text{H}_2\text{SO}_4$  such that  $\text{pH} = 1$ ; Typical deposition voltages are  $-1.2$ ,  $-1.1$ ,  $-1.0$ , and  $-0.2$ , for Ni, Co, Au, and Cu, respectively.

In order to measure the diameter and the shape of the wires using scanning-electron microscopy (SEM), the polycarbonate membrane is dissolved in  $40^\circ\text{C}$  dichloromethane ( $\text{Cl}_2\text{CH}_2$ ), rinsed in fresh dichloromethane, chloroform and ethanol. In case of the aluminum-oxide model system, the oxide is dissolved in a 1.25 M NaOH solution containing 0.1 mM polyvinylpyrrolidone (PVP,  $M = 40,000$ ).

## RESULTS AND DISCUSSION

### Growth in Polycarbonate Membranes

In the following, we will focus our attention to one pore-diameter ( $d_N = 80$  nm). At the end of this chapter, the results for smaller pores are briefly discussed. Figure 1a shows a potentiostatic electric current  $I$  versus time  $t$  characteristic ( $I$ - $t$  characteristic) for the reduction of  $\text{Ni}^{2+}$  on track-etched polycarbonate membranes. In the same figure, two pores are schematically drawn in cross-section at three different stages of the growth process. During the first stage (left schematics labeled I) the metal (shown hatched) is growing in the pores while the reduction current takes on a value of  $\approx 2 \text{ mA}$  (the variation in the current will be discussed below). Growth proceeds in the pores until they are filled up to the top surface of the membrane (middle schematics). Beyond this, growth can continue in three dimensions: hemispherical caps form on top of the wires (see Figure 2 left and

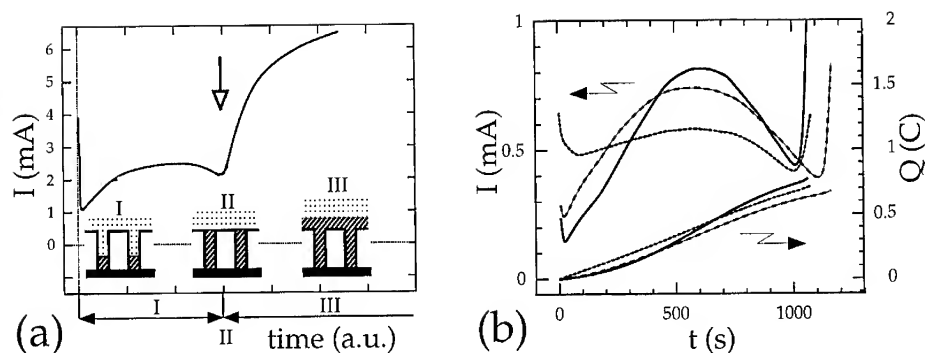


Fig. 1 (a) Electrochemical reduction current  $I(t)$  as a function of time  $t$  for the potentiostatic plating of Ni in pores of polycarbonate membranes with  $d_N = 80$  nm. The schematics displays three different stages of the growth process. (b) Three detailed characteristics of  $I(t)$  and the charge  $Q(t)$  for Ni growth at  $-1.0 V_{SCE}$ .

middle) which grow in size until coalescence on the membrane surface occurs. This is the transition region (labeled II), which starts at the position of the arrow in Figure 1a. Since the effective electrode area increases rapidly during this stage, the electrochemical current increases. Once growth proceeds on the whole membrane surface (right schematics labeled III), the current approaches an asymptotic value. This value corresponds to the current measured on a metallic electrode of the same overall area and for the same applied voltage.

In the following, the apparent wire diameter  $d_a$  deduced from SEM images (similar to Figure 2) will be compared to the electrochemically derived effective wire diameter  $d_e$ . The latter is obtained from the charge  $Q_t$  transferred during potentiostatic growth up to the point of transition.<sup>12</sup> From  $\approx 50$  samples (Ni and Co deposits), where the growth covered the whole exposed area, we obtain  $Q_t = 0.7 \pm 0.13$  C. Using this value, an effective electrochemical diameter  $d_e = 161 \pm 10$  nm is deduced. Similar, from SEM images we obtain an apparent average diameter  $d_a = 180 \pm 40$  nm. These values for the diameter are in good agreement with the result of Chlebny et al.<sup>13</sup> who studied the diameter of similar wires with transmission-electron microscopy and found a value of  $d_a = 164 \pm 10$  nm. Both from electron microscopy images of nanowires and from the electrochemically transferred charge, a considerable (factor two) larger wire diameter is found as compared to the nominal pore diameter  $d_N$ . Data obtained for Cu and Au deposition are in full agreement with the Co and Ni data.

In region I (Figure 1a) where electroplating proceeds in the pores, the observed electrochemical current is not constant. Details of the  $I$ - $t$  characteristic during this growing period are shown in Figure 1b where three representative  $I(t)$  curves are displayed. Growth proceeds in the pores up to  $t \approx 1000$ – $1200$  s when the rapid current increase signals the transition to bulk growth. Starting growth in the pores, the current first increases with time, approaches a maximum after  $\approx 1/2$  of the period needed to fill the pores up to the top membrane surface, and then starts to decrease significantly before the transition to bulk growth. To a first approximation, the length  $l$  of the wires can be assumed to be proportional to the time  $t$ , that has elapsed after growth was initiated. Hence, we observe a deposition current, which can be up to factor of 6 larger than the initial current, when the wires have

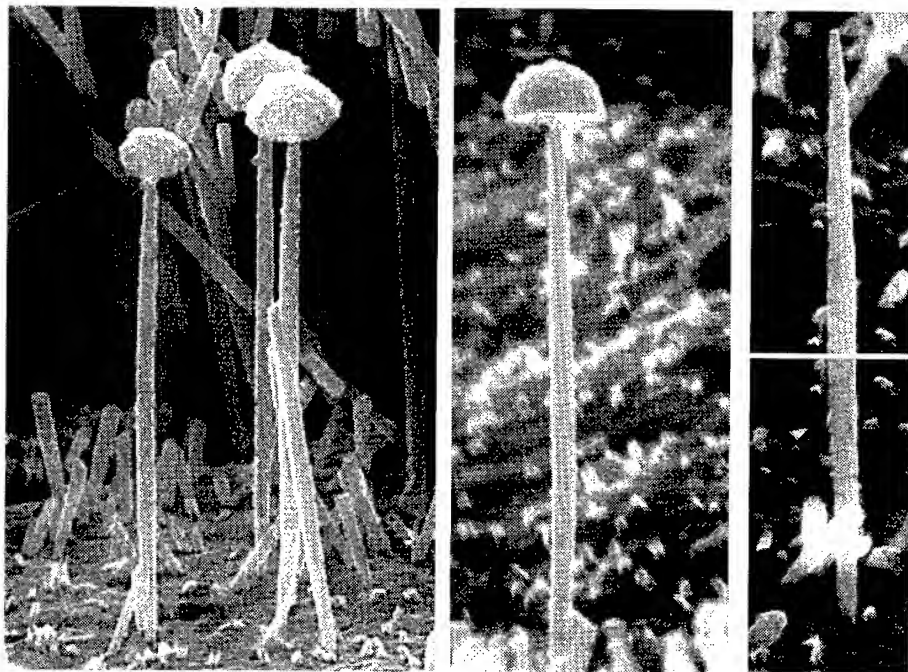


Fig. 2 SEM images of Ni wires grown in  $d_N = 80$  nm polycarbonate membranes. The total length of a wire is  $\approx 6 \mu\text{m}$ . The right most image shows the top and bottom  $2 \mu\text{m}$  of one and the same wire.

been grown to a length  $\approx 1/2$  of the total pore length of  $L \approx 6 \mu\text{m}$ . The decreasing reduction current with progressive growth is quite unexpected: the electrochemical current is determined by the applied voltage and, if mass transport has to be considered, by the diffusion of ions. Since the reference electrode is located in the bulk electrolyte (reservoir) above the membrane, there may be a voltage drop along the electrolyte in the pores which would result in a reduced electrochemical current. With progressive growth, this voltage drop should decrease however, since the wires are approaching the reservoir. Hence, the current is predicted to increase. A similar conclusion is reached if mass-transport limitation is considered. The surprising current drop in the  $I$ - $t$ -behaviour is also observed for all the other electrochemical systems studied (Ni, Co, Au, and Cu). These systems correspond to a wide range of deposition voltages.

The current maximum is due to an increased wire diameter in the middle section of the nanowires, as will be demonstrated. Figure 2 shows high-resolution SEM images of Ni wires viewed from a direction almost perpendicular to the wires. The wire diameter is observed to be larger in the middle than at the bottom (where growth started first) and top immediately underneath the caps. This effect is most pronounced in the example displayed in the right most image of Figure 2, which shows the top and bottom part of one and the same wire. The diameters are 100 and 75 nm close to bottom and top, and 210 nm around the middle section. The wires are observed to be up to a factor of 2.5 wider in the middle than at the

base or top end. This increase in diameter, which amounts to a factor of  $\approx 6$  increase in area, is consistent with the  $I$ - $t$  behaviour of Figure 1b. The observed dimensions are also in agreement with the average of the effective electrochemical pore diameter of about 160 nm.

We think that the metallic nanowires replicate the pore geometry. Hence, the pores are not cylindrical with a constant cross-section, but rather appear to be 'cigar-like' in shape.

The observed current maxima in Figure 1b directly reflects the shape of the pores. We mention, that a similar maximum is observed in case of  $d_N = 200$  nm membranes, while for thinner diameters the  $I$ - $t$  dependence is different.<sup>12</sup> With decreasing pore diameter, the current is found to adapt a time dependence with a current increase with progressive growth. This observation is caused by a diffusion coefficient for the metal ions, which effectively decreases for smaller pore diameters. However, regarding the shape of the obtained nanowires, the measured wire diameters (either  $d_e$  or  $d_a$ ) are consistently larger by up to a factor 4 similar to the case discussed before. These results are discussed in detail in Ref. 12.

#### Aqueous Anisotropic Colloids using Growth in Aluminum Oxide Membranes

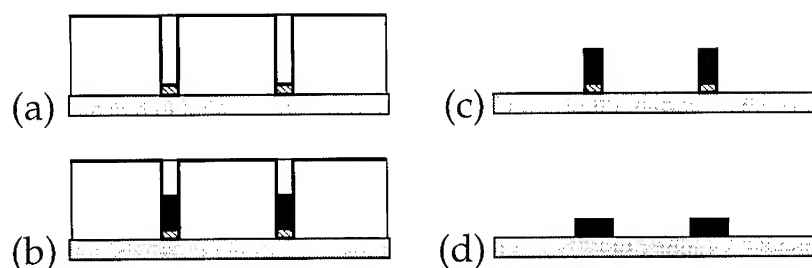


Fig. 3 Schematic synthesis route for obtaining an anisotropic colloid of metallic rods dispersed in water. (a) Porous alumite with grown copper layer (hatched), (b) gold deposition (filled black), (c) dissolution of the aluminum oxide, and (d) selective dissolution of the copper base to release the Au rods.

In Figure 3 the synthesis route from the electrodeposition of gold nanowires to an anisotropic colloid of Au-rods dispersed in water is schematically presented. Electrodeposition of gold in porous aluminum oxide is preceded by electrodeposition of a small amount of copper of length  $\approx 30$  nm (Figure 3a). Gold is then deposited in the pores on top of the copper to a predetermined length (80 – 200 nm) controlled via the deposition time (Figure 3b). Next, the aluminum oxide is dissolved (Figure 3c), and finally, we selectively dissolve the Cu, cleaving off the Au rods from the substrate (Figure 3d). It is found that most of the rods are lying flat on the substrate after this step. Collecting several identical samples, the rods are dispersed into demineralized water with the aid of ultrasonic agitation.

This method has been successful and stable anisotropic colloids have been obtained. This new preparation route has the advantage that both the rod diameter  $d$  and the length  $L$  can be controlled. In the examples discussed in this paper, the rod diameter is 12 nm and the aspect ratio  $L/d$  has been varied between 4 and 13. The short-rod ( $L/d = 4$ ) sol appears optically greyish and the long-rod solution ( $L/d = 13$ ) is pink like. The respective volume fractions are  $43 \cdot 10^{-6} \%$  and  $69 \cdot 10^{-6} \%$ .

The optical properties of the prepared monodisperse colloidal solution of gold rods have been investigated with VIS/NIR spectroscopy (shown in Figure 4) and compared with a sol

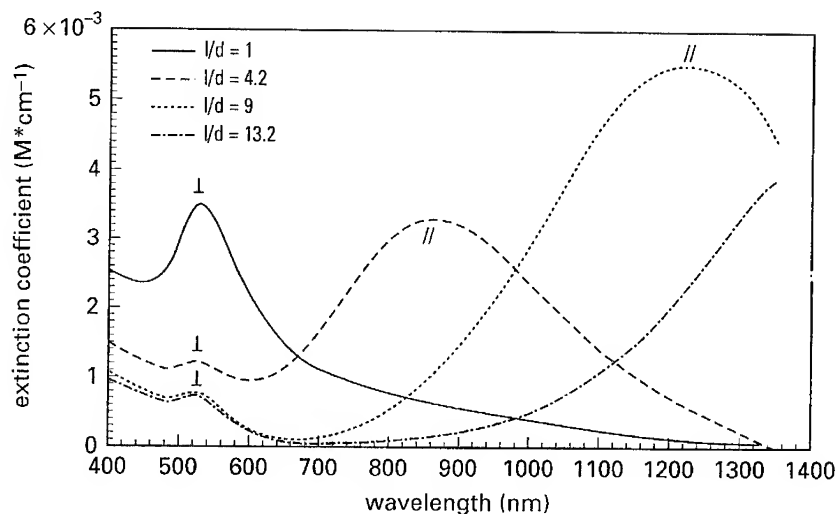


Fig. 4 Normalized VIS/NIR adsorption spectra of Au-rod dispersions with aspect ratio  $L/d = 1$  (spherical gold sol),  $L/d = 4.2$ ,  $L/d = 9$ , and  $L/d = 13.2$ .

consisting of spherical particles of the same diameter. As is clear from Figure 4, the optical properties of the dispersion change markedly with increasing aspect ratio. Instead of one adsorption maximum as for spherical gold sols, two maxima exist for the rods. The maximum for the rods in the visible regime is attributed to the transverse plasmon resonance ( $\perp$ ), for which the particle orientation is such that the incident optical wave has an electric-field component perpendicular to the rod axis. With increasing aspect ratio, this resonance shifts (slightly) to shorter wavelength and is damped. This effect has been observed before<sup>14</sup> in an optical study of the extinction of light through an alumite membrane containing metallic rods (not dispersed in solution). In our colloidal system, the most pronounced optical effect caused by the anisotropy of the rods is the presence of a second peak in the near infrared, attributed to the longitudinal plasmon resonance ( $\parallel$ ) which is excited by an electric-field component parallel to the rod axis. This second absorption maximum shifts strongly to longer wavelengths with increasing aspect ratio.

Anisotropic colloidal solutions of this kind offer several attractive possibilities for future studies. The rods can be aligned with an electric field, or – if magnetic rods are grown – with a magnetic field enabling to change the extinction by electronic means, for example.

## REFERENCES

1. For a review see: (a) C. R. Martin, *Science* **1994**, *266*, 196, and (b) C. J. Brumlik, V. P. Menon and C. R. Martin, *J. Mater. Res.* **1994**, *9*, 1174.
2. G. E. Possin, *Rev. Sci. Instrum.* **1970**, *41*, 772.
3. W. D. Williams and N. Giordano, *Rev. Sci. Instrum.* **1984**, *55*, 410.

4. R. M. Penner and C. R. Martin, *J. Electrochem. Soc.* **1986**, *133*, 2206.
5. R. C. Furneaux, W. R. Rigby, and A. P. Davidson, *Nature* **1989**, *337*, 147.
6. R. L. Fleisher, P. B. Price, and R. M. Walker, *Nuclear Tracks in Solids*, Univ. of California Press, Berkley (1975).
7. R. J. Tonucci, B. L. Justus, A. J. Campillo, and C. E. Ford, *Science* **1992**, *258*, 783.
8. Chun-Guey Wu and Thomas Bein, *Science* **1994**, *264*, 1757.
9. S. Kawai and R. Ueda, *J. Electrochem. Soc.* **1975**, *121*, 32.
10. Z. Cai and C. R. Martin, *J. Am. Chem. Soc.* **1989**, *111*, 4138.
11. A. Blondel, J. P. Meier, B. Doudin, and J.-Ph. Ansermet, *Appl. Phys. Lett.* **1994**, *65*, 3019; L. Piraux, J. M. George, J. F. Despres, C. Leroy, E. Ferain, R. Legras, K. Ounadjela, and A. Fert, *Appl. Phys. Lett.* **1994**, *65*, 2484.
12. C. Schönenberger, B. M. I. van der Zande, L. G. J. Fokkink, M. Henny, C. Schmid, M. Krüger, A. Bachtold, R. Huber, and U. Staufer, submitted to *J. Phys. Chem.*
13. I. Chlebny, B. Doudin, and J.-Ph. Ansermet, *Nano-Structured Materials* **1993**, *2*, 637.
14. C. A. Foss, G. L. Hornyak, J. A. Stockert, and C. Martin, *J. Phys. Chem.* **1994**, *98*, 2963.



## ELECTROCHEMICAL FABRICATION OF THE NANO-WIRE ARRAYS: TEMPLATE, MATERIALS AND APPLICATIONS

DMITRI ROUTKEVITCH<sup>†\*</sup>, JIMMY CHAN<sup>†</sup>, DMITRI DAVYDOV<sup>†</sup>, IVAN  
AVRUTSKY<sup>‡</sup>, J. M. XU<sup>‡</sup>, M. J. YACAMAN<sup>#</sup>, AND MARTIN MOSKOVITS<sup>†</sup>

<sup>†</sup> Department of Chemistry and <sup>‡</sup> Department of Electrical Engineering, University of  
Toronto, Toronto, Ontario, Canada

<sup>#</sup> Univ. Nacl. Autonoma Mexico, Inst. Fis., Mexico City, Mexico

\*drutkevi@chem.utoronto.ca

### ABSTRACT

Anodic aluminum oxide (AAO) may be used as a template for electrochemically fabricating metal and semiconductor nano-wires. We assess the seminal factors involved in each step in this fabrication process with an aim at producing device-quality semiconductor nano-arrays. This includes an analysis of the electrochemical factors, the structural effects resulting from the templating, the crystallinity of the nano-wires, their anisotropy and their suitability for device applications.

### INTRODUCTION

Anodic aluminum oxide (AAO) is known to have relatively uniform parallel pores when produced in certain electrolytes<sup>1</sup>. AAO films electrochemically loaded with metal particles have been used as corrosion resistant and decorative coatings. Magnetic materials based on the highly anisotropic coercivity of ferromagnetic metal wires deposited in AAO were first fabricated in the mid seventies<sup>2</sup>. Nevertheless, a full recognition of the potential of AAO a template for nano-fabrication only developed in the last few years. Other porous materials such as polymer nuclear track membranes<sup>3</sup> and zeolites<sup>4</sup> are also actively used for nano-templating.

Despite such recent advances in templated nanofabrication, as the electrodeposition of arrays of semiconductor micro-<sup>5</sup> and nanowires<sup>6</sup>, the fabrication of multilayered nanowires for GMR sensors<sup>7</sup>, the generation of nanoelectrode arrays<sup>8</sup>, ion-selective switchable membranes<sup>9</sup>, and AAO with highly symmetrical hexagonally close packed pores<sup>10</sup>, an overall analysis of the potential and the limitations of the AAO-based approach as a tool for the nano-technology has not been reported. Device-suitable nanoarrays require a high level of template integrity and dimensional uniformity, as well as control over the structure and composition of the nanowires. One of the main issues is the ability to modify the AAO technology to produce templates with pore diameters below 10 nm while maintaining the high quality of the template and a narrow size distribution. Another very important problem is increasing the quality of the nanowire structure and decreasing the number of defects. These challenges are vital to ensure that the response of quantum devices based on arrays of nano-wires reflect the characteristics of the individual nano-structure.

In this paper, we evaluate our recent accomplishments with AAO-templated electrochemical nano-fabrication in terms of the suitability of this technology for creating and manipulating device-quality nano-arrays.

## RESULTS AND DISCUSSION

### TEMPLATE

The primary challenge in nano-technology is the creation of nanometer-scale objects with as narrow a size distribution as possible about a controllable value of the mean size and shape, and with as perfect a crystal structure as possible. In order to accomplish this goal with templated electrodeposition, the first requirement is the ability to fabricate as perfect a template as possible with a narrow distribution of pore diameters and with mean diameters controllable down to as low a value as desired. Pore sizes small enough to ensure the observation of quantum size effects in the deposited structures are not available with commercial anodic aluminum oxide membranes. The smallest nominal diameter of AAO filters sold by Wattman is 20 nm<sup>11</sup>. Recently, nuclear track polycarbonate membranes with the nominal pore diameter of 10 nm have become available from Poretics and other companies and have been used for the fabrication of nanoelectrode ensembles<sup>12</sup>. However, direct measurements of the diameter distribution of the metallic wires deposited into those templates<sup>13</sup> found the mean pore diameter of the “10 nm” and “30 nm” membranes to be 36±3 nm and 57±3 nm respectively. The nominal size specified for these membranes, apparently, corresponds to the low cut-off value of the pore diameter rather than to the mean. Additionally, the nuclear track pores are not parallel, and the pore density (6×10<sup>8</sup> cm<sup>-2</sup>) is substantially lower than that of AAO films (10<sup>9</sup>-10<sup>11</sup>). The pore diameters and densities of AAO can be easily varied by changing anodization parameters such as the electrolyte, its concentration, and the anodizing voltage,  $U_a$ . The standard deviation of the pore diameter typically does not exceed 10% of its mean, and much smaller when highly organized domains of hexagonally close packed pores are formed on pure Al with low concentration of crystal structure defects under specific anodization conditions.<sup>10</sup> In addition to variations in the pore size, one must also control the overall integrity of the porous structure, that is the straightness and the roundness of the pores and the degree of the pore branching and merging. Using high resolution scanning electron microscopy equipped with a field emission electron source we were able to examine directly the structure of cleaved AAO with nanometer resolution without using a conductive coating (Figure 1). Samples are cleaved by simply bending a film against a sharp blade. These micrographs present high-quality direct information on the fine structure of templates, eliminating artifacts often created by microtoming and other sample preparation procedures.

The structure of AAO obtained in the three most commonly used electrolytes (H<sub>3</sub>PO<sub>4</sub>, H<sub>2</sub>C<sub>2</sub>O<sub>4</sub>, and H<sub>2</sub>SO<sub>4</sub>) differ significantly even under similar electrochemical conditions. Films anodized in phosphoric acid have a more disordered structure than those anodized in oxalic or sulphuric acids. Consequently, they are not good candidates for nano-fabrication. Likewise the pore diameters,  $d_p$ , which is almost linear function<sup>14</sup> of the anodization voltage and electrolyte concentration, depends on the nature of the electrolyte, the mean diameter decreasing in the following sequence:

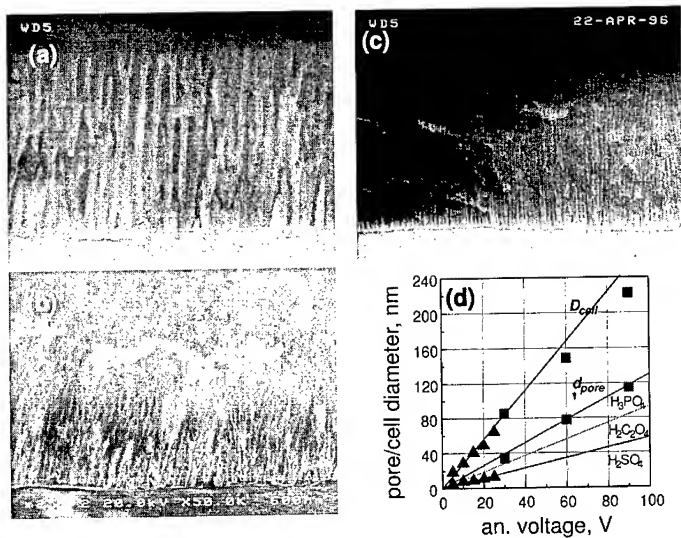
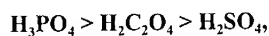


Figure 1. SEM of a cleaved edge of AAO grown in (a,b) 0.9 M H<sub>3</sub>PO<sub>4</sub>, U<sub>a</sub>=30V(a), 10V(b); (c) 1.2 M H<sub>2</sub>SO<sub>4</sub>. (d) Pore/cell diameter as a function of the anodization voltage



while the cell diameter,  $D_c$ , where cell is the portion of the film with one pore, remains the same for different electrolytes and depends only on  $U_a$ <sup>14</sup> (Figure 1c). And although the linear dependence of the ratio  $d_p/D_p$  on  $U_a$  might suggest that pores of very small diameters could be obtained at appropriately low anodization voltages, the degradation of the porous structure at low  $U_a$  (Figure 1a,b) makes it difficult to achieve small pore diameters in this way. This observation is qualitatively explained in terms of the generally accepted mechanism of the growth of porous structure. The integrity of the porous network is determined by the ratio of the lateral and normal propagation rates of the reaction front at the bottom of the pore. (Lateral and normal refer to the plane of the substrate.) Propagation in the normal direction is determined by the dynamic equilibrium between the oxidation of the Al and the field-assisted dissolution of the alumina, which depend on the electric field strength at the interface. The lateral pore growth is governed by the homogeneous and inhomogeneous disturbance of the hemispherical reaction front, which, in contrast to growth in the normal direction, is determined by the temperature and by the concentration of crystal structure defects of the Al substrate and is independent on the electric field.

Hence the question of the lowest pore diameter achievable in a given electrolyte for a desired nano-technological goal must be answered in conjunction with the question of the quality or integrity of the template.

As an alternative to decreasing  $U_a$ , in order to reduce the pore diameter, the anodization temperature,  $T_a$ , could be varied. This would have an advantage over varying the anodizing voltage since one might expect that changing the temperature would not affect the electric field strength at the growth interface, and, therefore, the normal/lateral

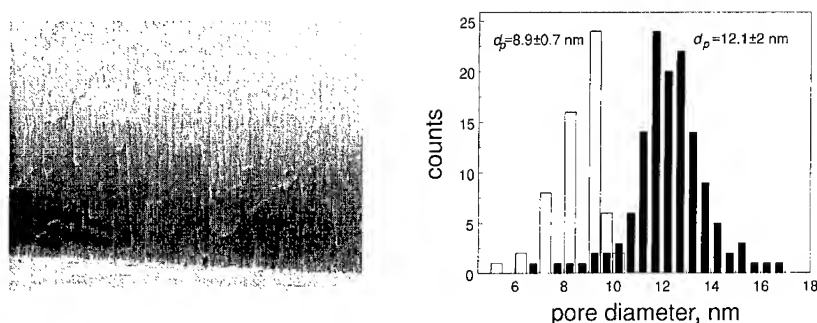


Figure 2. SEM of the cleaved edge of an AAO film produced in 1.2 M  $\text{H}_2\text{SO}_4$  /  $\text{CH}_3\text{OH}$  at  $-10^\circ\text{C}$ . Size distribution of the pore diameter before and after pore widening

rates ratio, sufficiently to affect the template integrity. At the same time, the electric field distribution may be changed enough to affect the geometry of the growth front. Hence, the pore diameter might be changed without adversely affecting the template quality. A number of contradictory results are reported in the literature in this regard. Ebihara<sup>15</sup> reported that varying  $T_a$  of an oxalic acid electrolyte in the range 0 to  $40^\circ\text{C}$  did not affect the pore diameter of the resulting AAO. More recently,<sup>16</sup> Debuyck and co-authors demonstrated that decreasing the temperature from 28 to  $0^\circ\text{C}$  reduces the porosity of films anodized in sulphuric acid by 20-35%. The porosity depends both on the *size* of the pores and the pore *density*, but data on the pore morphology were not reported.

In order to create very small pores one should anodize at as low a temperature as possible. A low temperature anodizing apparatus was constructed for the purpose with which the effect of anodizing temperature on the pore diameter and overall AAO structure was investigated.<sup>17</sup> Anodizing temperatures as low as  $-90^\circ\text{C}$  were achieved. In order to maintain the electrolyte liquid, methanol/water mixtures of concentrations up to 75% methanol (v/v) were used as the base of the electrolyte. A thorough discussion of these results will be reported elsewhere for anodization in the range  $+20$  to  $-80^\circ\text{C}$ .<sup>17</sup> Briefly, the pore diameter was found to decrease with decreasing  $T_a$ , while the cell diameter increased and, therefore, the pore density decreased with decreasing  $T_a$ . The growth rate of the AAO films decreases markedly as the temperature is reduced, some films requiring several hours to grow. The smallest AAO pore diameter achieved so far in this way is 3.6 nm at  $-40^\circ\text{C}$ . In contrast to low voltage anodization, low temperature anodization achieves small pore diameters without compromising the template integrity (Figure 2). A narrower size distribution from the low diameter anodization could be achieved by prepatterning the Al under conditions where uniform and highly ordered relatively large pores develop.<sup>18]</sup>

This influence on the pore morphology by the temperature is the result of the activation response of the many electrochemical processes contributing to the dynamic equilibria at the growth front, including field assisted AAO dissolution, Al oxidation,  $\text{Al}(3+)$  and  $\text{O}(2-)$  migration through the dense oxide barrier layer (BL) separating the Al and oxide/electrolyte interface. A preliminary attempt to describe the observed behaviour using the model developed by Parkhutić<sup>19</sup> failed to provide correct prediction. The model predicts an increase in both the pore and the cell diameters with decreasing temperature.

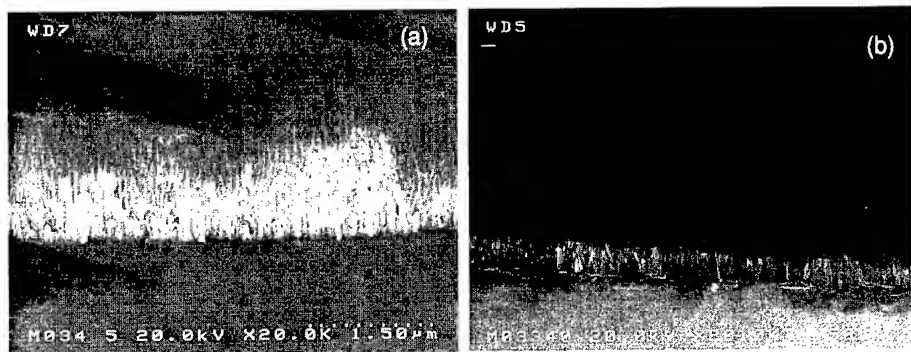


Figure 3. Cleaved cross-section of AAO with Ag nano-wires deposited from (a) aqueous electrolyte and (b) non-aqueous electrolyte.

This failure is probably due to the simplified assumption regarding the potential distribution across the metal/oxide/electrolyte interface used in the model.

As a general observation, instability of the reaction front presents the major obstacle for creating an ideal template. Minimizing that instability requires a low-noise environment with maximal voltage, temperature, and hydrodynamic stability combined with a high-purity annealed<sup>20</sup> Al substrate. Aluminum films on Si substrate are good candidates for making nano-arrays for devices.

## DEPOSITION and MATERIALS

Although electrochemical processing of materials has not been a popular approach in the device community until recently, it is gradually becoming a feasible alternative for a number of applications, such as interconnects, magnetic head arrays, LIGA components, etc. For our applications electrodeposition is the only practical tool for filling the pores of a template fabricated on a conductive substrate from the bottom up. When using templates for EC deposition of nanostructures, one must take into account the template's chemical stability in the electrolyte. Polymer nuclear truck membranes<sup>3</sup> work well in aqueous electrolytes, except for strong bases, while AAO templates work well in moderately acidic or basic electrolytes and are ideal in non-aqueous electrolytes. The main constraint in using porous alumina films directly after anodization is the insulating, dense BL which prohibits the use of dc electrodeposition to fill the pores. However, the inherent rectifying properties of the BL allow the pores to be filled uniformly by ac electrolysis without simultaneously depositing material on the surface or into macroscopic defects of the film, as happens with dc electrodeposition (Figure 3 a,b). Nevertheless, if necessary, AAO film can be processed to provide direct access by the electrolyte to the electrode surface.

In some aqueous electrolytes, though, the aluminum/anodic alumina substrate is prone to a number of side reactions, which affect the template's morphology and compete with the electrodeposition. Among these reactions are reanodization, Al/AAO pit corrosion, especially in the Cl<sup>-</sup>-containing media, BL breakdown, and water electrolysis. High

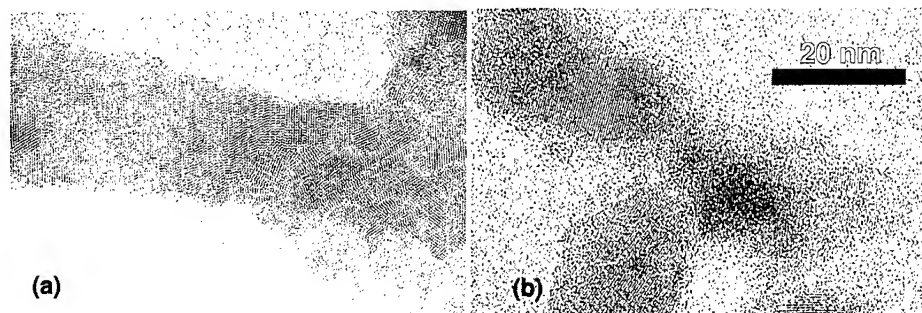


**Figure 4.** HR TEM microphotographs of (a) as deposited and (b) annealed (500°C, 1 hr, N<sub>2</sub>) fragments of CdS nanowires after AAO matrix has been dissolved away. Note the increased long-range order in the crystallites.

deposition voltages, often required to deposit certain materials, promote side reactions due to their high limiting current density, resulting in the formation of nano-wires of non-uniform lengths (Figure 3 a) as well as in the development of defects in the film. It is also difficult to fill pores with the diameters smaller than 10 nm using high-voltage deposition. Non-aqueous solvents, with their increased range of solvent stability and low corrosivity, are the ultimate alternative for avoiding these problems. Well known electrolytes based on solvents such as PC, EG, PG, DMF, DMSO, which are perfectly compatible with AIAAO, lower the deposition voltage and expand the range of materials for deposition. Thus, CdS nanowires have been successfully electrodeposited from DMSO<sup>6</sup>, while aqueous electrolytes, developed for the deposition of CdS films, have failed. Much better uniformity of pore filling and improved deposition into the smallest pores have been achieved with non-aqueous electrolysis (Figure 3) as compared with aqueous ones.

Good quality crystal structure of the nano-wires, control of the chemical composition and the doping level are essential for the observation of quantum confinement effects and anisotropy and, ultimately, for potential device applications. Conditions for the nucleation and growth on the surface of the amorphous or polycrystalline alumina are unfavorable for the formation of high quality epitaxial nano-structures. However, using relatively high deposition temperature in non-aqueous electrolytes together with post-deposition annealing may partially offset the disordering effect of the substrate (Figure 4). Moreover, the confinement of the growth direction and the uniform diffusion front inside the pore may be used to advantage by tuning the overpotential so that only one crystallite would be formed in the pore, thereby stimulating long-range coherent growth along the wire. We have also found an additional effect of the confined growth conditions on the crystalline orientation of the wire. Nanowires of CdS<sup>6</sup> and other A<sup>II</sup>B<sup>VI</sup> semiconductors showed a significant degree of orientation with the hexagonal c-axis aligned along the pore, whereas deposition on the flat metal electrode in the same conditions produced no preferential orientation.

The size of the pores has been found to affect crystallite dimensions when the latter become comparable with the former. Two types of strain, accumulating during nano-wire growth, has been identified in the CdS nanowire system. One, which was eliminated by annealing, becomes more pronounced with increasing pore size, and is typical for

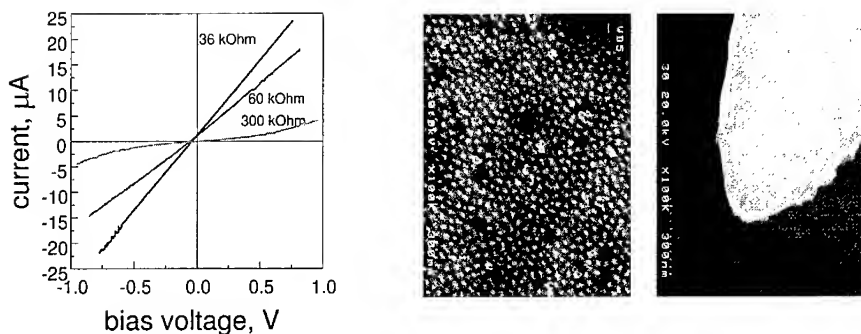


Figure 5. I-V characteristics observed during a close approach of an STM tip to a Ni nano-wire array. Note transition from non-linear tunneling to linear behavior when ohmic contact is established. Insert: SEM of the STM tip and AAO embedded nanowire array.

electrodeposited polycrystalline films due to the non-equilibrium phase formation. The other, appearing when the characteristic crystallite size approaches the pore diameter, is imposed by the spatial constrain of the crystallites growth.

In addition to electron microscopy and X-ray diffraction, resonance Raman<sup>21</sup> (RR) and luminescence spectroscopy were used to characterize the crystal quality as well as the extent of the confinement and anisotropy in the A<sup>II</sup>B<sup>VI</sup> nanowires. The exciton energy in CdS nanowires with diameters from 9 to 25 nm was calculated by fitting ratios of the RR overtones to their analytical expression.<sup>21</sup> A small blue shift with decreasing size indicated the onset of quantum confinement effects. The RR spectra showed no anisotropy, however, which was likely due to the low aspect ratio of the nano-crystallites composing the nanowire. Annealing (up to 625°C) improved the signal-to-noise ratio of the RR spectra by a factor of 20, increased the intensity and the number of observed overtones, and increased the intensity of room- and low-temperature band-to-band luminescence, suggesting an improved crystallinity and a reduced level of defects. Nevertheless, the linewidth of the Raman (60-85 meV) and luminescence (40-75 meV) peaks indicated that the lifetime of the exciton is considerably shorter than in bulk or in CdS nano-crystals obtained by other methods,<sup>22</sup> possibly due to the interaction at the CdS/oxide interface or with neighboring crystallites within the nanowire as well as due to the scattering at the remaining crystal structural imperfections. This is supported by the observation that the intensity of the CdS nanowire luminescence increases with increasing diameter. The shift in the location of the band-to-band luminescence peak by 15-30 meV to the lower energy, may be attributed to the significant level of disorder even in annealed nanowires, while the intense and broad luminescence in the near IR indicates defect-induced transitions. It should be noted, however, that no special care was taken to eliminate impurities in those samples. Using higher-purity materials in the electrodeposition should improve the quality of the nanowires.

A significant degree of crystalline disorder was also implied by the results of resistivity measurements of Ni nanowires (diameter 10 nm, length 1 μm) using an STM tip as a contacting probe (Figure 5). The resistance of a single nanowire before annealing was found to be at least an order of magnitude higher than expected for a polycrystalline Ni wire of the same dimensions based on bulk conductivity values.

## PROCESSING, DEVICES

AAO is optically transparent, has a high dielectric constant, possesses superior mechanical and thermal stability and allows the inexpensive, large-scale fabrication of conveniently assembled electrically or optically accessible arrays of 1- and 2-D nanostructures with a high degree of integrated circuit compatibility.

Furthermore, prepackaged arrays can, in principle, yield signal throughputs comparable to

conventional devices while possessing properties determined by the individual nanostructure. Magnetic, transport and optical measurements

on the of AAO based nano-arrays from the standpoint of device applications are reviewed elsewhere.<sup>23</sup> Here we briefly examine key processing steps for nano-wire arrays.

**1. Etching AAO.** Providing electrical/optical access to one or both ends the nanowires is a first step after depositing nano-array of desired quality. The structure of the AAO oxide is inhomogeneous; the inner walls of the pore are composed of amorphous alumina while the honeycomb porous skeleton is composed of polycrystalline alumina.<sup>24</sup> This structure dissolves in the basic or acidic solutions very anisotropically,<sup>25</sup> which is useful in the lithographic fabrication of nano-array domains.<sup>26</sup> At the same time it complicates the uniform etching of the porous AAO surface when the pores are not filled with deposit. If the length of the wires is not uniform they can be made so by cutting the exposed wires flush with the surface by polishing with 50 nm alumina powder, removing the exposed ends of the wires while leaving the AAO unaffected.

**2. Etching the Al and the BL.** Making direct contact to the end of the nanowire at the bottom of the pore requires consecutive removal of the Al and the BL. Several etching solutions have been suggested in the literature:  $\text{CH}_3\text{OH}/5\%\text{Br}_2$ ,  $\text{Hg}_2\text{Cl}_2(\text{sat})/\text{H}_2\text{O}$ . The best results in terms of the rate of etching, selectivity, defect formation and handling are obtained with  $\text{CuCl}_2(0.1\text{M}) \setminus 20\%\text{HCl}$ . Using this solution large thicknesses of Al can be removed in several minutes without undercutting the masked area and without any noticeable dissolution of the BL. The BL could be then gradually etched, and the process could be easily monitored by imposing a potential waveform of small amplitude ( $\pm 5\text{mV}$ ) followed by measuring the polarization resistance (Figure 6).<sup>27</sup> A view of the nanowire array exposed from the BL side is presented in the Figure 5 (insert). Free-standing AAO films with nanowires can be prepared using this method.

Some of the possible future device designs based on these processing steps, were discussed elsewhere.<sup>23a</sup>

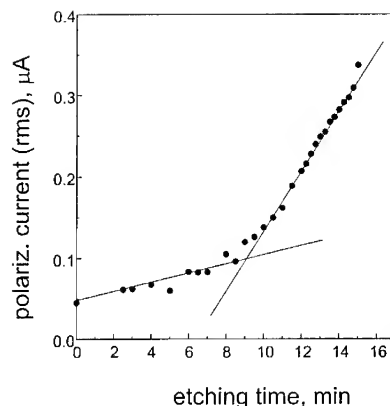


Figure 6. Polarization current (lock-in output) as a function of the etching time.



## CONCLUSIONS

A strategy was described for the non-lithographic templated nano-fabrication of metal and semiconductor nano-wires with significant potential for creating a variety of nano-structures and quantum devices. While these nano-structures can not yet be obtained in the form of single crystalline or epitaxial forms, unless the template is attached to the single crystal substrate, there are, in principle, no insurmountable obstacles to realizing templates with narrow size distribution and excellent integrity. Likewise it is possible to obtain high quality deposits of polycrystalline nano-wires with controllable doping. The processing and packaging of the nano-arrays are compatible with current lithographic technology and provide a route for incorporation into more conventional devices.

## ACKNOWLEDGMENTS

This work was supported by NSERC.

## REFERENCES

- <sup>1</sup>. S. Wernick, R. Pinner, P. G. Sheasby, The Surface Treatment and Finishing of Aluminum and its Alloys, Finishing Publ.: Teddington, 1987; vol. 1.
- <sup>2</sup>. (a) S. Kawai, in Proc. Symp. Electroch. Techn. Electronics, edited by L. T. Romankiw, and T. Osaka, Electroch. Soc., Pennington, NJ, PV 88-23, 389 (1987); (b) D. AlMawlawi, N. Coombs, M. Moskovits, *J. Appl. Phys.*, 70, 4421 (1991); (c) D. J. Dunlop, S. Xu, O. Ordemir, D. AlMawlawi, M. Moskovits, *Phys. Earth Planet. Inter.*, 76, 113 (1993).
- <sup>3</sup>. (a) C. R. Martin, *Science*, 266, 1961 (1994); (b) T. M. Whitney, J. S. Jiang, P. C. Searson, C. L. Chien, *Science*, 261, 1316 (1993).
- <sup>4</sup>. G. Ozin, *Adv. Mater.*, 4, 612-648 (1992)
- <sup>5</sup>. J.D. Klein, R.D. Herrik, II, D. Palmer, M. Sailor, C.J. Brumlik, and C. Martin, *Chem. Mater.*, 5, 902-904 (1993).
- <sup>6</sup>. D. Routkevitch, T. Bigioni, M. Moskovits, and J. M. Xu, *J. Phys. Chem.*, 100, 14037-14047 (1996).
- <sup>7</sup>. B. Doudin, A. Blondel, J.-Ph. Ansermet, *J. Appl. Phys.*, 79(8), 6090-6094 (1996).
- <sup>8</sup>. V.P. Menon, C.R. Martin, *Anal. Chem.*, 67, 1920-1928 (1995).
- <sup>9</sup>. M. Nishizawa, V.P. Menon, C.R. Martin, *Science*, 268, 700-702 (1995).
- <sup>10</sup>. H. Masuda, K. Fukuda, *Science*, 268, 1466-1468 (1995)
- <sup>11</sup>. Wattman technical support (private communication)
- <sup>12</sup>. V. P. Menon, C. R. Martin, *Anal. Chem.* 1995, 67, 1920.
- <sup>13</sup>. I. Chlebny, B. Doudin, J.-Ph. Ansermet, *Nanostr. Mater.*, 2, 637 (1993).
- <sup>14</sup>. see, for example, an overview in J. Randon, P. P. Mardilovich, A. N. Goviadinov, and R. Paterson, *J. Coll. Sci. Techn.*, 169, 335-341 (1995).
- <sup>15</sup>. K. Ebihara, H. Takahashi, M. Nagayama, *J. Met. Finish. Soc. Jap.*, 34, 548-553 (1983)
- <sup>16</sup>. F. Debuyck, M. Moors, A. P. Van Peteghem, *Mater. Chem. Phys.*, 36, 146-149 (1993).
- <sup>17</sup>. D. Routkevitch, J. Chan, J. M. Xu and M. Moskovits, in preparation.
- <sup>18</sup>. D. Routkevitch, M. Moskovits, unpublished recent result.
- <sup>19</sup>. V. P. Parkhucic, V. I. Shershulsky, *J. Phys. D: Appl. Phys.*, 25, 1258-1263 (1992).

- <sup>20</sup> Mardilovich, modelling paper with regular structure
- <sup>21</sup> D. Routkevitch, T. L. Haslett, L. Ryan, T. Bigioni, C. Doiketis, and M. Moskovits, Chem. Phys., 210, 343-352 (1996).
- <sup>22</sup> J.J. Shiang, S. H. Risbud, and A. P. Alivisatos, J. Chem. Phys., 98, 8432 (1993).
- <sup>23</sup> (a) D.Routkevich, A. Tager, J. Haruyama, D. Al-Mawlawi, M. Moskovits and J. M. Xu, IEEE Trans. Electron Dev., 43(10), 1646-1658 (1996), (b) A. Tager, D. Routkevich, J. Haruyama, D. Al-Mawlawi, L. Ryan, M. Moskovits and J. M. Xu, Future Trends in Microelectronics: Reflection on the Road to Nanotechnology, edited by S. Luryi, J.M. Xu, and A. Zaslavsky (Proc. NATO Adv. Res. Worksh.) NATO ASI Ser. E , Vol. 323, Kluwer Acad. Publ., Dordrecht, 1996, pp. 171-185.
- <sup>24</sup> P.P. Mardilovich, A.N. Govyadinov, N.I. Mazurenko, R. Paterson, J. Membr. Sci., 98(1-2), 143-155 (1995).
- <sup>25</sup> (a) D. Routkevitch, M. Moskovits, unpublished recent results; (b) reference 24.
- <sup>26</sup> V. Sorganov, IEEE Trans. Comp. Pack. Manuf. Techn., B, 17(2), 197-200 (1994).
- <sup>27</sup> D. Routkevitch, D. Davydov, J. Chan, M. Moskovits, in preparation.

## HETEROJUNCTIONS IN NANOWIRES BY ELECTROCHEMICAL PROCESSING

G. REDMOND, S. GILBERT, B. DOUDIN, J.-PH. ANSERMET

*Institut de Physique Expérimentale, Ecole Polytechnique Fédérale de Lausanne,  
PHB-Ecublens, CH-1015 Lausanne*

Nanowires, 100 nm in diameter and 6  $\mu\text{m}$  in length, with an oxide barrier intercalated between two ferromagnets, were produced via an electrochemical route. Non ohmic behavior was found. The magnetoresistance of Ni/NiO/Co heterostructures abruptly change by more than 7% at the switching field of the ferromagnets.

### Introduction

The purpose of our work is to show that samples consisting of two ferromagnets separated by an insulating barrier can be obtained by electrochemical techniques. Large changes of the resistance with applied field are interpreted as tunneling magnetoresistance (TMR). The synthesis of heterogeneous nanowires of this type allow us to study samples of a surface area as small as  $10^{-10} \text{ cm}^2$ ,

The studies of spin dependent transport have been mainly motivated by the occurrence of giant magnetoresistance (GMR) in samples where the magnetic alignment can be controlled at a nanometer scale [1]. Magnetic multilayers, separated by non magnetic metal layers, were the most extensively studied type of samples. It has been recently shown that electrodeposition can be an alternative technique to produce these samples [2]. In particular, the fabrication of multilayered metallic nanowires allowed the control of the sample morphology in the nanometer range in three dimensions [3]. Thus large GMR values were obtained [4]. However, GMR occurred with large field changes (typically a few kOe), limiting the field sensitivity of these samples.

Tunneling current occurring between two ferromagnets separated by an insulating barrier can be shown to vary with the relative magnetic alignment of the two ferromagnets [5,6,7,8]. In this paper, we present our technique for the fabrication of wires with heterogeneous junctions. To our knowledge, this is the first report of metal-insulator-metal structures made by electrochemical techniques. The major difficulty to overcome was the cathodic reduction of the oxide when electrodepositing the metal. We show that the use of water-free electrolyte is the solution of choice. Nanowires of Ni/NiO/Co were obtained, with magnetoresistance change of typically 10%, larger than the values reported for Ni/NiO/Co vacuum-made samples [6,9]

### Fabrication technique

The synthesis of metallic nanowires has been achieved through the method of pore template electrodeposition [10]. Briefly, a porous polymer membrane with a conductive backing

previously deposited, is used as the working electrode in an electrodeposition cell. Metal ions of choice are reduced inside the pores of the polymer membrane at a suitable applied potential, thus forming wires of diameters corresponding to that of the pores.

Ni nanowires were electrodeposited into the pores of a commercially available filtration membrane [11]. Plating was terminated when the pores were approximately half filled, i.e., after the wires had grown to roughly 3.5  $\mu\text{m}$  in length.

Following this procedure, the membrane was withdrawn from the plating bath, washed thoroughly with deionised water, dried in air and placed into a deaerated boric acid-sodium borate solution (pH 8.34). Anodisation in this electrolyte solution for 15 minutes at an applied potential of 0.0 V (Vs. Ag/AgCl) resulted in the formation of a NiO passive layer on the surface of the Ni nanowires. Following this step, the membrane was withdrawn from the anodising bath, washed thoroughly with deionised water and allowed to dry in air. Electrodeposition of Co nanowires on top of the NiO-covered Ni nanowires in the membrane pores produced as follows. Thoroughly dried membranes with anodised nanowires were placed into a 0.1 M solution of  $\text{CoCl}_2$  in dimethylformamide. Co was electrodeposited from this solution at an applied potential of -1.3 V (Vs. Ag/AgCl). The water-free nonaqueous medium protected the NiO passive layer from cathodic reduction. Plating of Co was terminated when a few nanowires reached the outer surface of the template membrane. This was observed as an increase in plating current. Following removal from the plating bath, the membrane was washed sequentially with acetone and deionised water, finally left in air to dry. The electrical connection to heterojunction nanowires was effected by attachment of thin gold wires to the front and back surfaces of the template membrane with silver epoxy conducting glue.

## Results

The resistance measurements were performed by DC methods, at temperatures between 10 and 300 K under an applied field in the range  $\pm 70$  KOe. Samples with resistances in the range of  $10^5$ - $10^7 \Omega$  were studied. The resistance of our samples increased (by typically 10-30%) when cooling down from 300K to 10 K. At temperatures below typically 100 K, non linear current versus voltage characteristics appear (Fig. 1). The conductance near zero bias corresponds to that of a tunnel junction in that it is nearly parabolic at small bias, as expected of tunneling barriers (cf. Fig. 1b). By applying Simmons's theory [12] to the parabolic fit, we found a barrier thickness of 2.7 nm and a barrier height of 0.26 eV. However, the nature of the dominant conduction mechanism has yet to be ascertained.

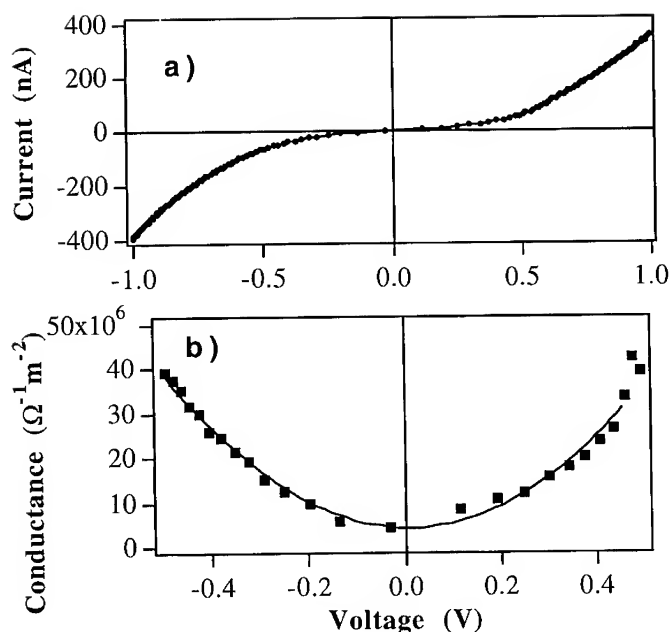


Figure 1. (a) Current versus voltage of a Ni/NiO/Co heterogeneous nanowire measured at a temperature of 10K. (b) Conductance curve (squares) derived from data in curve a. Solid line is parabolic fit. Note that voltage scales are different. The wire diameter is approximately 100 nm.

Large magnetoresistance jumps are observed at low temperatures (Fig. 2). We limited our measurements to the low bias regions (with a voltage smaller than 10 mV). The magnetoresistance was found to decrease with increasing temperature. No effects larger than 1% were observed at temperatures above 80 K. From measurements of the hysteresis curves, the jump of the magnetoresistance was found to correspond to the coercive field of the sample (Fig. 3). Note that the magnetization is measured on samples made from typically  $10^6$  wires, but only a few wires (presumably one) are connected for the resistance measurement. No evidence of anti-parallel alignment of the Ni and Co can be deduced from magnetization measurements. Therefore we can only infer from our data that the resistance changed abruptly at the most probable switching field of the magnetization,

From Julliere's expressions of the differences of conductances between parallel and anti-parallel ferromagnets [5,6], assuming typical values of the spin polarizations in the ferromagnets [13], one can infer a relative change of 7.8% for a Ni/Co heterostructure. It corresponds to our observations. However, determining the basic mechanism of our magnetoresistance needs further investigation.

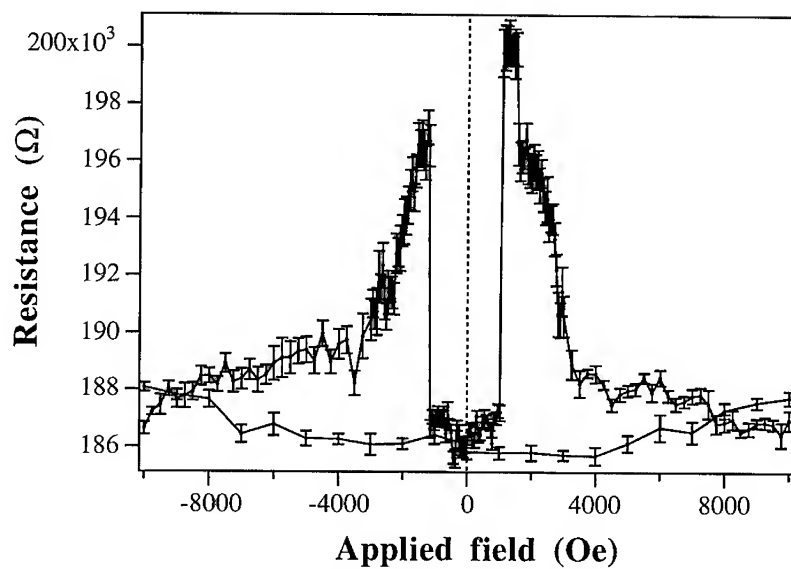


Figure 2. Resistance versus applied field measured at a temperature of 20K.

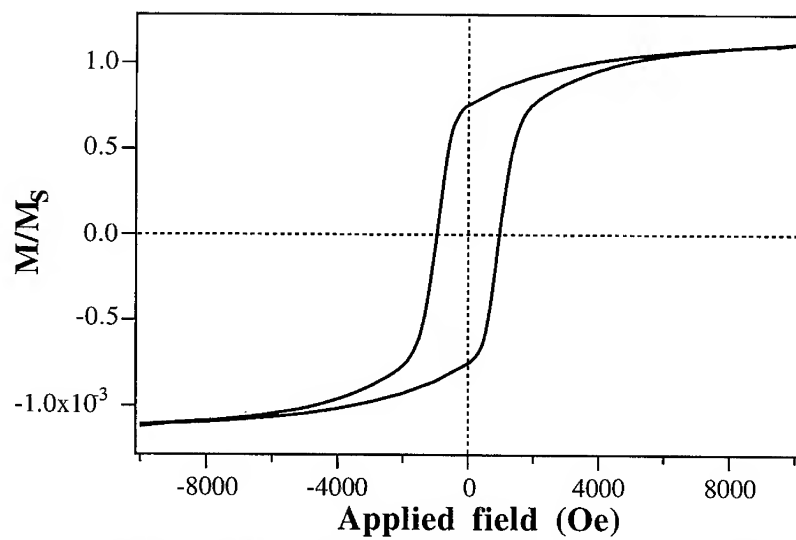


Figure 3. Magnetization curve of an assembly of Ni/NiO/Co wires, 50 nm in radius, measured at 20K.

## Conclusions

We have successfully demonstrated that giant magnetoresistive effects can be found in a ferromagnet-insulator-ferromagnet structure made by electrochemical techniques. Magnetoresistances of up to 10% are found for Ni/NiO/Co wires, 100 nm in diameter, at low temperatures. The use of small area samples was mainly motivated by the desired limitation of defects in the insulator. It opens the way to open surface heterostructures made by electrochemical route, which could be competitive with the vacuum made samples for applications.

This work was supported by the Brite-Euram program BR2-0546 and the MINAST Swiss Priority Program (ELECPRO 7.08),

- 
- [1] review: Levy, P.M., Solid State Physics Series, vol. 47 (1994) 367
  - [2] review: W. Schwarzacher and D. S. Lashmore, IEEE Trans. Magn. 32, 3133 (1996)
  - [3] B. Doudin and J.-Ph. Ansermet Nanostructured Mater. 6, 521 (1995).
  - [4] A. Blondel, J.P. Meier, B. Doudin, J-Ph Ansermet, Appl. Phys. Lett. 65,3019(1994), L. Piraux, J.M. George, J.F. Despres, C. Leroy, E. Ferain, R. Legras, K. Ounadjela, A. Fert, Appl. Phys. Lett. 65, 2488(1994), K. Liu, K. Nagodawithana, P.C. Searson, C.L. Chien, Phys. Rev. B51, 7381(1995)
  - [5] M. Julliere Pys. Lett. 54A, 225 (1975).
  - [6] S. Maekawa & U. Gafvert, IEEE Trans. Magn. 18, 707 (1982).
  - [7] J. S. Moodera, L. R. Kinder, T. M. Wong and R. Meservey, Phys. Rev. Lett. 74, 3273 (1996).
  - [8] C. L. Platt, B. Dieny and A. E. Berkowitz, Appl. Phys. Lett 69, 2291 (1996)
  - [9] Y. Suezawa and Y. Gondo, Proc. Int. Symp. Physics of Magnetic Materials, Sendai, MAG-18, 303 (1987).
  - [10] C. Martin, Science 266 (1994) 1961
  - [11] Poretics Corp., 111 Lindbergh Av., Livermore, CA 94550-9520.
  - [12] Simmon's paper
  - [13] P. M. Tedrow and R. Meservey, Phys. Rev. B 7, 318 (1973).

## PRODUCTION OF MAGNETIC NANOPOWDERS BY PULSED SONOELECTROCHEMISTRY

J.-L. DELPLANCKE\*\*, O. BOUESNARD\*\*, J. REISSE\* and R. WINAND\*\*

\* Chimie organique, CP 165, ULB, 50 Avenue F.D. Roosevelt, B1050 Bruxelles, Belgium

\*\* Métallurgie-Electrochimie, CP 165, ULB, 50 Avenue F.D. Roosevelt, B1050 Bruxelles, Belgium, jdelpla@ulb.ac.be

### ABSTRACT

Sonoelectrochemistry, or pulsed electrodeposition at high current density in presence of high intensity ultrasound, is used to produce magnetic powders with a mean diameter in the range of 100 nm. Pure iron, cobalt and nickel powders are produced together with their binary and ternary alloys. The powders are crystalline and homogeneous as observed by scanning and transmission electron microscopy, electron diffraction and X-ray fluorescence. The compositions of the binary and ternary alloy powders reproduce strictly the iron, nickel and cobalt compositions of the starting electrolytes except for the nickel-cobalt alloys.

### INTRODUCTION

Metal powders are used in enamels, anti-corrosion paints, thermal spray coatings and formings, claddings, overlays and hardfacing applications. The corresponding selected markets present a growing rate of 25 to 30% annually. The availability of ultrafine (less than 20 microns) as well as nano-sized metal powders is opening up many exciting new applications like the production of nanomaterials with new mechanical, optical, magnetic, electric,... properties.

Magnetic metal powders with a diameter ranging from 100 to 50 micrometers are currently produced by electrolysis at high current density in aqueous electrolytes. A lot of work is then devoted to produce by electrolysis and with a high yield, ultrafine metal powders. Two main trends are presently developed : strong electrolyte stirring and pulsed currents. By these two techniques, higher current densities may be used. Accordingly, higher nucleation rates and smaller nuclei diameters may be obtained. Stirring is performed mechanically, by air injection or by ultrasound.

Recently, a new technique has been developed [1-3] and patented [4] for the production of nano-sized metal powders. This new technique is based on the use of a pulsed electrical current density and a pulsed pressure wave, the two irradiation periods being out-of-phase. The home-made ultrasound generator triggered by a commercial pulsed potentiostat works in the 20 kHz range in order to obtain strong mechanical effects at the surface of the sonoelectrode.

The purpose of this paper is to describe the results obtained for the production of pure or alloyed iron, nickel and cobalt nanopowders by sonoelectrochemistry.



## EXPERIMENTS

The sonoelectrochemical cell is described in a previous paper [1]. As shown in Figure 1, out-of-phase electric and ultrasound pulses are sent to the titanium sonoelectrode. During the electric pulses, the electrode potential is shifted from +56 mV/NHE to -1.84 V/NHE. This potential is more cathodic than the thermodynamic potentials for the iron, nickel and cobalt depositions in the selected electrolytes. The duration of the electrodeposition pulses is 600 ms. A 400 ms rest periode follows each deposition pulse. During this rest periode, a 300 ms pulse of 20 kHz ultrasound is sent to the titanium horn. The ultrasound intensity is above the cavitation threshold and produces erosion of the electrode surface with projection of the metal nuclei in the electrolyte, together with intense agitation of the electrolyte with replenishment of the diffusion layer with the metal cations.

The electrolyte composition is obtained from Aotani [5] :

- 0.48 mol/l  $\text{NH}_4\text{Cl}$
- 0.48 mol/l  $\text{H}_3\text{BO}_3$
- 0.01 mol/l citric acid
- 0.017 mol/l  $\text{NaOH}$  (pH = 3.8)
- 0.27 mol/l metal cations ( $\text{Fe}^{2+}$ ,  $\text{Ni}^{2+}$  or  $\text{Co}^{2+}$  as sulphates)
- temperature 60°C

For the alloy depositions, the total concentration in metal cations is kept constant, the concentration in each metal being equal.

The powders are filtered under nitrogen on 0.1  $\mu\text{m}$  Millipore filters, slightly washed with degassed water and dried at room temperature. It has to be noted that the pure iron powder only is too reactive to be obtained by this procedure.

The morphology of the powders is examined by scanning electron microscopy and transmission electron microscopy respectively with a JEOL JSM 820 and a PHILIPS CM 20 apparatus. Their crystallinity is analysed by X-ray and electron diffraction with a SIEMENS D5000 and a PHILIPS CM 20 equipment respectively. Their composition is studied by X-ray fluorescence in the scanning electron microscope with a TRACOR NORTHERN 5525 apparatus or, after powder dissolution in nitric acid, by atomic absorption with a PERKIN ELMER 2380 apparatus.

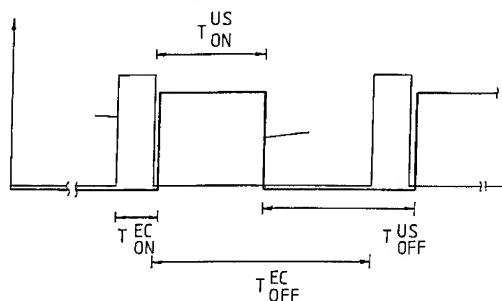


Figure 1 : Electrochemical  
(EC) and Ultrasound (US)  
Pulses

## RESULTS

Figure 2 shows the morphology of pure nickel powder and of binary and ternary alloys, as observed by SEM. Aggregates of fine crystals with a sharp distribution and a mean diameter ranging from 50 to 100 nm are observed. This ultrafine structure is confirmed by the transmission electron microscopies (see Figure 3), except for the Co-Ni alloys for which a dendritic structure is observed.

For pure nickel and cobalt powders only traces of chloride contamination are detected. Titanium (coming from the cathode erosion) is not detected in all the produced powders. The compositions of binary and ternary alloy powders are compared in Table 1 with electrolyte compositions (as far as the metal cations are concerned) and with the compositions of the alloys obtained by electrodeposition at -1.84 V/NHE constant potential in the same electrolytes.

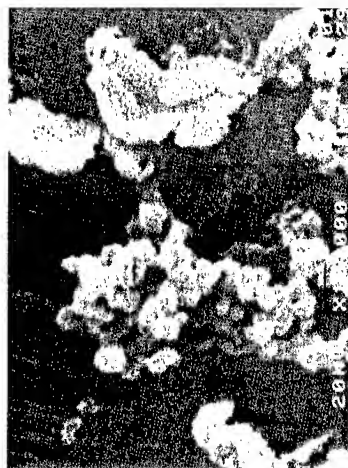
Alloy Type	Powder Composition (at%)	Current Yield (%)	Electrolyte Composition (at%)	Deposit Composition (at%)
Co-Ni	87 - 13	49	50 - 50	50 - 50
Fe-Ni	50 - 50	34	50 - 50	60 - 40
Fe-Co	50 - 50	31	50 - 50	50 - 50
Fe-Ni-Co	33 - 33 - 33	40	33 - 33 - 33	40 - 20 - 40

Table 1 : Comparison of the powders compositions with the electrolytes compositions and with the compositions of deposits obtained at constant potential in the same electrolytes

A high concentration of chloride ions is detected in the Co-Ni powders (may be as cobalt chloride). The dendritic structure of these powders could be responsible for a bad cleaning and washing of the produced powders and then for electrolyte incorporation, chloride contamination and anomalous powder composition. For the other alloys, the powder composition is similar to the electrolyte composition and is different from the composition of the corresponding deposits. Indeed, during constant potential deposition, macroscopic diffusion gradients could take place and influence the final composition of the alloys either via the diffusion coefficients of the different cations or via the diffusion overpotentials. On the contrary, during pulsed electrodeposition, transient behaviours are observed. The pulse duration is short and only the cations contained close to the electrode surface are consumed until their concentrations reach approximately zero.  $H^+$  cations are also reduced during the pulses, as proved by the medium values of the current yields (see Table 1). This could explain the correlation between the powder compositions and the electrolyte compositions.

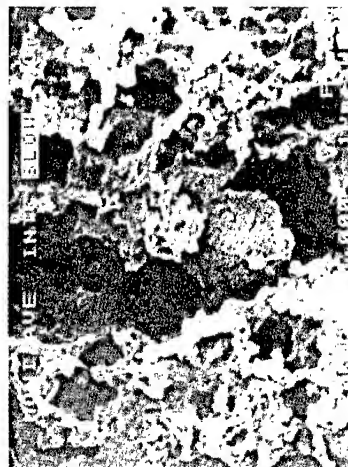


Fe-Ni-Co alloy

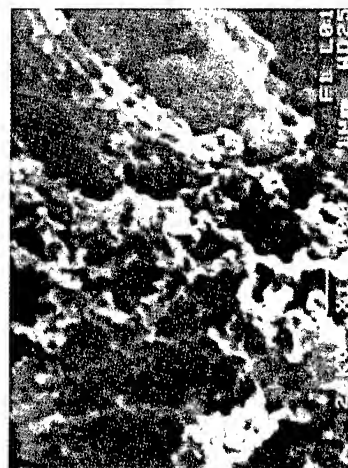


Co-Ni alloy

1  $\mu\text{m}$



Fe-Ni alloy



Fe-Co alloy

Figure 2 : Morphology of the alloy powders

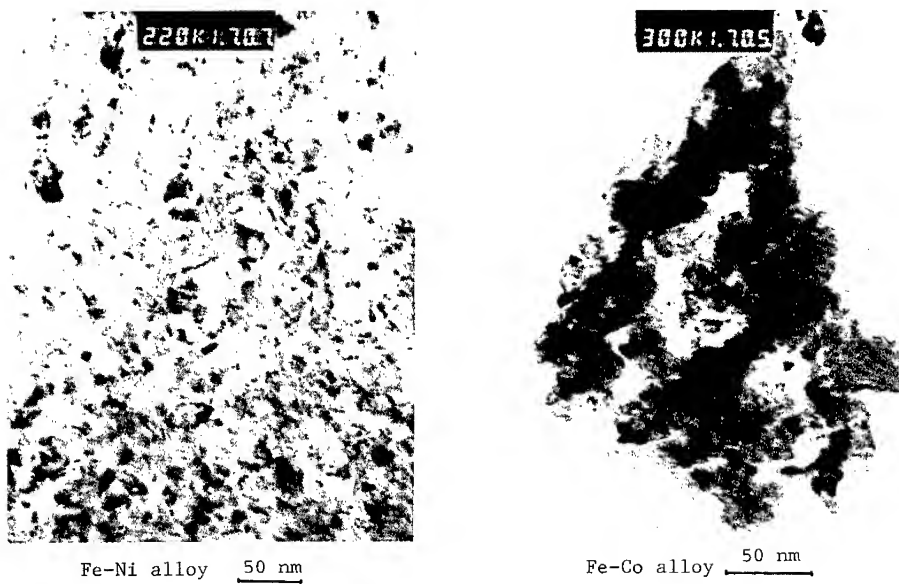


Figure 3 : TEM pictures of alloy powders

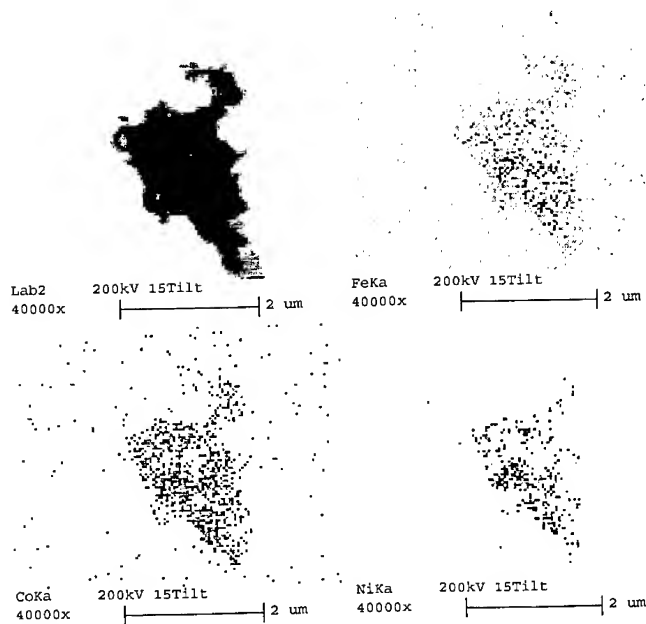


Figure 4 : Composition distribution of Fe-Ni-Co aggregate

The alloy powders present a homogeneous composition as proved by energy dispersive X-ray analysis in the transmission electron microscope (see Figure 4).

The powders are crystalline. The fine analysis of the X-ray diffraction patterns or of the electron diffraction rings is extremely difficult mainly due to the very close values of the repetition distances of the lattice planes in cubic iron, cubic cobalt and cubic nickel.

For pure cobalt powders, hexagonal cobalt is observed. For pure nickel powders, cubic nickel is observed. For alloys, only peaks corresponding to cubic structure(s) are observed. These structures could be related to the structures observed in the phase diagrams.

Experiments are under way to measure and to quantify the magnetic properties of the produced powders.

## CONCLUSIONS

Magnetic nanopowders of iron, nickel, cobalt and their alloys may be produced by sonoelectrochemistry. These powders are homogeneous and crystalline. Their compositions seem to be directly connected with the composition of the electrolyte when their shape is rounded. More experiments have to be performed in order to confirm this hypothesis.

The crystallographic structure of the produced binary and ternary alloys is exclusively cubic, even when a high concentration of cobalt is present in the alloy. More experiments are under way to evaluate their magnetic properties.

## ACKNOWLEDGMENTS

One of the authors (J-L. D.) is indebted to the National Fund for Scientific Research of Belgium for financial support.

## REFERENCES

- [1] J. Reisse, H. François, J. Vandercammen, O. Fabre, A. Kirsch-De Mesmaeker, C. Maerschalk and J-L. Delplancke, *Electrochimica Acta*, **39**(1), 37-39, 1994
- [2] J-L. Delplancke, V. Di Bella, J. Reisse and R. Winand, *Mat. Res. Soc. Symp. Proc.*, **372**, (1995), 75-81
- [3] A. Durant, J-L. Delplancke, R. Winand and J. Reisse, *Tetrahedron Letters*, **36**(24), (1995), 4257-4260
- [4] "Dispositif pour la production de poudres ultrafines", R. Winand, J. Reisse et J-L. Delplancke (1994), Belgian and PCT Patents WO 95/33871
- [5] K. Aotani, *J. Electrochem. Soc. Japan*, **20**, (1952), 31-34

## **Electrodeposition for HI-MEMS with Special Reference to Fabrication of a Magnetic Mini-Motor**

E.J. O'Sullivan, E.I. Cooper, L.T. Romankiw, J. Horkans and K.T. Kwietniak

IBM Research Division  
Thomas J. Watson Research Center  
Yorktown Heights, NY 10598

### **ABSTRACT**

Electrodeposition through photoresist masks is a critical, enabling technology for fabrication of the thick structures (of up to several hundred microns) involved in HI-MEMS. Process integration is an important issue in HI-MEMS. The electrodeposited structure is influenced by the choice of optical or X-ray lithography. Thickness uniformity of the deposit on the wafer scale can be optimized by the use of an auxiliary cathode. On the device or feature scales, thickness uniformity can be improved by the thoughtful design of the pattern to be plated.

A variable reluctance, planar, integrated mini-motor with a 6 mm diameter rotor has been fabricated using lithography, electrodeposition and dielectric planarization processes. The rotors were fabricated separately, released from the substrate, and slipped on the shaft, which was plated up as part of the stator fabrication.

### **INTRODUCTION**

MEMS - an acronym for micro electromechanical systems - encompasses the design and fabrication of miniature structures and systems ranging from sensors, actuators, controllers and pumps in applications from aerospace technology to biotechnology. MEMS uses processing common in integrated microelectronics, but MEMS devices are 3-dimensional devices with high aspect ratios and large structural heights, in contrast to the essentially 2-dimensional microelectronic devices. The first major commercial MEMS success was the Si-based pressure sensor in automobile airbags. It is anticipated that MEMS revenues will grow from ca. US\$2 billion in 1996 to about \$10 billion by 2000, according to a recent market study by Semiconductor Equipment and Materials Intl. (SEMI) (1).

A variety of technologies are used in MEMS fabrication. It is common to form Si structures through the use of bulk Si machining using wet or dry processes or through surface micromachining of Si. Metallic "micromolding" techniques are also commonly used for fabrication of MEMS structures.

The most common micromolding technologies are photolithographic processes. Molds are created in polymer films, usually photoresist, on planar surfaces. The molds are then filled with metal using electrodeposition. The rapidly-emerging field known as HI-MEMS is an important subset of the MEMS field. HI-MEMS uses X-ray lithography to create deep trenches, of up to 1 mm, in PMMA resist on an electroplating base (called as seed layer). Electrodeposition of magnetic materials has enabled the important class of magnetically-actuated devices in HI-MEMS and other areas of MEMS.

In this paper we provide an overview of key aspects of electrodeposition technology for HI-MEMS fabrication. A description of the fabrication of a magnetic minimotor is also given, with emphasis on the electrodeposition. The reader is referred to two other articles (2, 3) for a discussion of aspects of non-electrodeposition fabrication processes that have been employed by our group at IBM.

## ELECTRODEPOSITION FOR HI-MEMS

Electrodeposition through a resist mask is a critical technology for HI-MEMS. Physical vapor deposition (PVD) techniques, such as evaporation or sputtering, are less suitable for building these thick, high-aspect ratio structures because of the lower deposition rates and the inability to fill features selectively. If the metal is deposited by PVD as a blanket and chemically etched, it is difficult to control the pattern within tight tolerances because of undercutting and roughening of the features (4). Patterning by sputter etching, ion milling, and lift-off also have disadvantages compared to deposition through a photoresist mask (4).

Deposition through a mask can be accomplished by either electroless (autocatalytic) deposition or electroplating. Electroless deposition is too slow for convenient use in MEMS and requires much effort in controlling the chemistry. It is also impossible, at present, to obtain pure Ni deposits from practical electroless Ni baths. Thus, electrodeposition is the most viable method for obtaining the thick deposits required in HI-MEMS structures. Pioneering work in this field was carried out by Romankiw and his co-workers at IBM in the seventies (5, 6) during the development of thin film recording heads. Thin film head fabrication employs electroplating in forming the Permalloy cores and pole tips and the Cu coils, and it requires the integration of electroplating with other processing.

A typical technique employed is as follows (Fig. 1): sputter deposition of a blanket seed layer of e.g. Cr/Cu, on the substrate; application and patterning of photoresist; electrodeposition of the metal or alloy; removal of resist; and removal of the plating base and adhesion layers from between the plated features.

In lithographic processes the electrodeposited sidewall angles are determined by the photoresist. In positive resists a substantial deviation from a wall angle of  $90^\circ$ , to as low as  $75^\circ$ , may occur. Negative-working resists exhibit wall angles closer to  $90^\circ$ , which tend to be biased to values higher than  $90^\circ$ . Negative resist, however, are generally very difficult to remove cleanly following electrodeposition, especially in multilayer structures where organic materials are employed as dielectrics.

The problem of wall angle becomes more acute as resist thickness is increased, and this imposes a constraint on the design rules of the device. In tall features plated in positive resists, the top separator may be so small that removal of the resist and seed layers becomes very difficult. Device designs should thus not be finalized until a working knowledge of the optically-exposed resist has been acquired.

X-ray lithography, in contrast to optical lithography, routinely produces vertical sidewalls in the PMMA X-ray resist. Features up to 1 mm in thickness can be produced (7,8). This explains the interest in X-ray lithography for HI-MEMS device fabrication. Depending on factors such as the thickness of the PMMA, the masks for X-ray lithography may require up to 15 microns or more of Au X-rays absorber. An early success of electrodeposition through resist technology was the fabrication of good

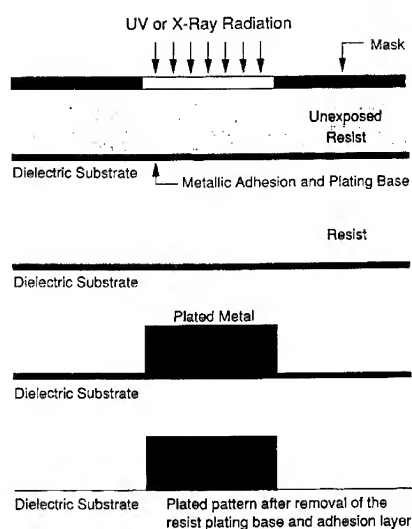


Fig. 1. Schematic representation of process steps used in electrodeposition through resist masks.

X-ray masks (8). The electrodeposition of Au continues to be a key component of X-ray mask fabrication.

Electrodeposited Cu and Ni have generally been the metallic materials of choice in MEMS, the latter often for magnetic as well as structural uses. More recently, Permalloy (Ni(80wt%)/Fe) has been replacing Ni as the magnetic material of choice because of its higher saturation magnetization (10K Gauss for 80:20 NiFe compared to 6 K Gauss for Ni). Experimental conditions for electrodeposition have been described elsewhere (9) and will not be discussed here.

#### **Current Density Uniformity in Electrodeposition in HI-MEMS**

In electrodeposition, deposit thickness and alloy composition are determined by local conditions of current density and mass transport. When current density varies across a substrate and may cause thickness non-uniformities on the scales of the substrate, the pattern, or the individual feature. When electrodeposition is followed by planarization, many of the issues of uniformity are not of major concern for single element deposition. The situation is more complex when depositing an alloy, since alloy composition may be a strong function of current density. This is particularly true for alloys of Fe, Co and Zn with Ni. The magnetic properties are strongly dependent on alloy composition and other current-density dependent properties such as grain size, structure and crystal orientation. If there is no planarization step, there may be areas where high current density results in plating beyond the surface of the resist, making removal of the seed layer difficult in these localities.

#### ***Across-Substrate, Current Density Uniformity***

The boundary between a conductor to which current is applied and a non-insulator causes a nonuniformity in the potential field. The consequent nonuniformity in plating current is evidenced by nonuniformity in the deposit thickness. Redistribution of current from a uniform planar distribution is often called "current crowding". On the substrate scale, the current crowding at the substrate edge can cause substantially higher thickness there. The difference in thickness across a substrate can be as much as 50% and can extend a significant distance from the edge. Independently-powered, auxiliary electrodes, often known as "thieves", which surround and are coplanar with the cathode, are employed to diminish this edge effect, and to achieve deposits with much improved, across-the-wafer uniformity. This problem has been studied by a number of groups. It has been modeled extensively by Mehdizadeh et al. (10), studied the situation which applies in a paddle cell (11), which in its simplest form is a rectangular cell containing a reciprocating paddle that sweeps to and fro at a controlled distance of a few millimetres above the horizontal cathode surface at speeds up to 60 hertz. The rectangular anode is placed parallel to, and above, the cathode and auxiliary, and the reciprocating paddle. The walls of the cell are adjacent to the outer edges of the auxiliary and anode electrodes and hence ensure that current lines are contained within the rectangular region encompassing the electrodes.

Figure 2, taken from ref. (10), shows the effect of auxiliary electrode current on the secondary current distribution at the cathode. When no current is applied to the auxiliary electrode, there is major current density non-uniformity at the cathode extending a considerable distance from its edge. Application of increasing currents to the auxiliary electrode - shown in Fig. 2 as  $I$ , the ratio of auxiliary current to cathode current - increases the cathode current density uniformity until an essentially uniform current density is obtained for  $I = 2.5$ . Further increases in  $I$  lower the current density near the edge of the cathode. An optimum value of  $I$  needs to be established for each cathode/auxiliary electrode case.



### Local Current Distribution Uniformity

In electrodeposition on photoresist-patterned substrates, the resist pattern may strongly influence deposit thickness uniformity. The pattern scale (the current distribution caused by the spacing of the device or groups of devices) and the feature scale (the current distribution within a pattern) need to be considered in assessing the thickness distribution when plating through resist. Practical experience and modeling have demonstrated that significant, local non-uniformity in deposit thickness can occur (12).

### Device-Scale Uniformity

In MEMS, several devices are typically on a single Si wafer. The active plating area density may differ in each device, resulting in device-to-device variations in deposit thickness. Additionally, the devices are separated by insulating areas where no plating occurs. The resulting higher current density at the device edge causes an across-device thickness and composition nonuniformity.

The device-scale nonuniformities encountered in the fabrication of the IBM magnetic mini-motor resulted mainly from the parallel fabrication of motors with different stator sizes. Device-scale nonuniformities were also introduced by the layout of devices on the wafer.

The thickness variation between groups of features in electrodeposition has been studied by Mehdizadeh et al. (13,14). Using potential theory these authors modeled the behavior expected for electrodeposition with a secondary current distribution, where there is essentially no mass transport control (13). They verified their modeling results experimentally using resist-patterned substrates (14). Good agreement was obtained between the model prediction and the electrodeposit thicknesses. The results indicate that when mass transfer control is not significant, a patterned area can be characterized completely by its overall active electrochemical area and modeled effectively.

The authors (14) also found that the active area current density is generally higher where the active plating area density is lower. Thus thicker deposits may be expected in regions where there is a low plating area density, i.e. where much of the seed layer is covered by resist. This variation of deposit thickness uniformity between regions of varying active plating area, or photoresist density, may be exacerbated by low Wagner numbers (14). Thus, among other things, the choice of an appropriate plating solution, e.g. of high conductivity, may help to improve uniformity.

A tertiary current distribution case, or where there is significant mass transfer control of deposition, may apply in certain electrodeposition solutions. Mehdizadeh et al. (14) extended their model to include the effects of mass transfer control and tested it experimentally. Whereas reasonable agreement was obtained between theory and experiment for 10 micron wide lines, the agreement was less at line widths much greater than the diffusion layer thickness, possibly because of enhancement effects of transverse convection. Interestingly, mass-transfer rate control in electrodeposition at resist-patterned wafers may either attenuate or amplify the nonuniformity relative to the case where there is negligible mass transfer control (14).

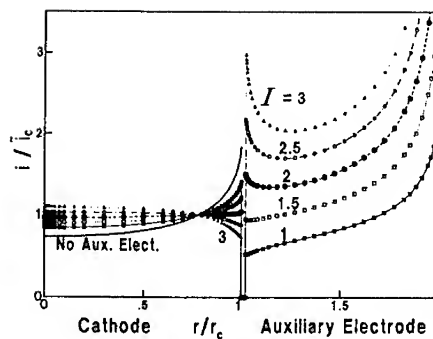


Fig. 2. Normalized secondary current distributions at the cathode and auxiliary electrode with Tafel-type polarization for different  $I$  values, the ratio of auxiliary electrode current to cathode current density (Ref. 10).  $i_c$  = average current density on cathode;  $r$  = radial position on cathode;  $r_c$  = radius of cathode.

The modeling illustrates that an understanding of deposit thickness uniformity can be obtained, but it should be kept in mind that the relatively simple case of an additive-free Cu solution was treated (14). It remains difficult to model features much larger than the diffusion layer thickness, probably due to intra-feature, lateral convection (14). It is yet more difficult to model plating in baths with one or more additives, or in baths involving alloy deposition, especially for materials like Permalloy, for which anomalous deposition rates for one component are observed (9). Finally, the resist employed in HI-MEMS may be an order of magnitude thicker than those employed by Mehdizadeh et al. (14). Thus, alloy composition at the bottom of deep features may differ from the composition near the top of the deposit because the mass transport conditions vary continuously during filling of the deep feature.

#### Feature-Scale Uniformity

The discrete device usually consists of a large number of features. The features that make up an electrochemically-active pattern are not all the same size and are not uniformly spaced. Uniformity of deposition is governed both by the size of the individual features and by their location. Feature-scale uniformity has been discussed at some length by Romankiw (12).

Thickness nonuniformity is greatest for isolated features because of "current crowding." Large features may be thicker at their edges, especially if at a distance from other active features. Small isolated lines will be thicker than more closely spaced small lines. The situation is worsened in the tertiary current distribution region since radial, or nonplanar diffusion amplifies the nonuniformity.

The IBM magnetic mini-motor was subject to feature-scale variations of various types. The most extreme case was the alignment mark for the photolithography, which is isolated and very much smaller than any of the other features to be plated; its thickness was thus much greater than the deposit thickness at any other point. Another example of an extreme variation in feature size on this device is the row of small vias parallel to the large-area magnetic core. It is possible to design the mask with extra, redundant features in strategic areas, such as at certain edges of large features and adjacent to edge features in arrays, to control nonuniformity. When it was not possible to utilize dummy plating patterns, vias that plated only slightly faster than adjacent, large-area magnetic cores plated at almost double the rate when the core regions were covered by photoresist.

#### **HI-MEMS Mask Design and Electrodeposition Considerations**

The foregoing discussion suggests a number of guidelines that may profitably be followed in mask design for HI-MEMS electrodeposition:

- ♦ A uniformly distributed resist pattern is the ideal situation, but it is often impractical;
- ♦ The placing of "dummy" active plating areas in certain regions of the mask to diminish current crowding at edges of large features, and features located at edges of arrays, is desirable (only if they do not interfere with device operation, or if they can be removed later);
- ♦ Isolated features should be avoided;
- ♦ The judicious use of bare margin, i.e. resist-free seed layer region, on a wafer may be employed to prevent the current density in the patterned region from concentrating at the periphery of the electrochemically-active devices;
- ♦ Finally, resist pattern-related non-uniformities tend to be less severe when the electrodeposition rate is low and the bath is highly conductive. Here it may be noted that electrodeposition from high-acidity, Cu baths enjoys an advantage over Ni or Permalloy baths, because of the very high proton conductivity of the Cu solutions.

### Examples of Electrodeposits Obtained Using Thick Resists

Figure 3(a) is an SEM picture of studs electroplated at IBM through PMMA resist with Permalloy (80at% Ni) to a height of ca. 150 microns. The bottom region of the stud on the extreme left shows evidence of a defect, possibly related to incomplete removal of PMMA resist during the development step. The Permalloy was deposited using a solution typically used in thin film head manufacture (15,16). At IBM, we have electrodeposited Permalloy (80at%Ni) up to thicknesses of 250 microns, as shown in the SEM in Fig. 3(b), part of a minimotor rotor plated in a PMMA resist stencil provided by MCNC and CAMD. On the right of this picture is shown the hole for the motor pin bearing; the other openings are used to facilitate solution release of the rotor from the substrate. Around the openings, the Permalloy is slightly thicker than the main body of the rotor because of current crowding.

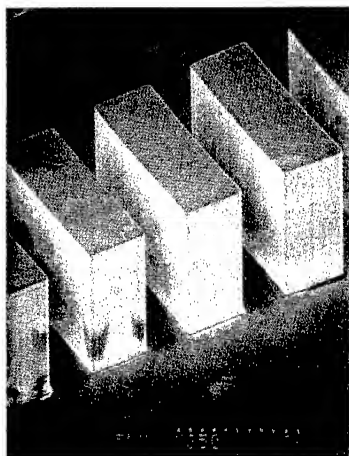


Fig. 3(a). SEM of Permalloy studs electrodeposited using X-ray exposed PMMA resist which was then removed.

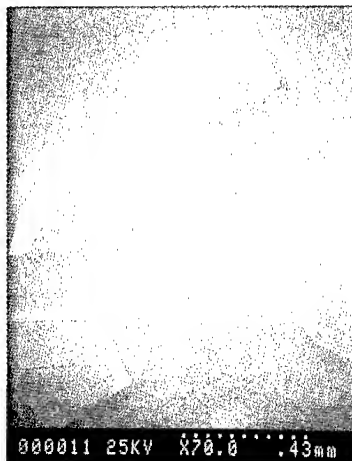


Fig. 3(b). SEM of part of a Permalloy mini-motor rotor electrodeposited using X-ray exposed PMMA resist which was then removed

In MEMS, copper is mainly used in devices requiring good electrical conductors. Displayed in Fig. 4(a) is an SEM of 60 micron thick and 60 micron wide Cu conductors electrodeposited through X-ray-exposed PMMA, which was then removed. As expected for such resists, the walls are vertical, and there is negligible underplating, indicating good adhesion of PMMA to the Ti/Cu/Ti seed layer. Copper lines with the same dimensions, electrodeposited through a positive resist exposed optically (Fig. 4(b)) have walls with angles (ca. 82-85 degrees) significantly less than those observed in the X-ray exposed part. It is generally difficult to approach 90° wall angles with these optical positive resists. Although negative resists are much better in this regard, they are, as mentioned earlier, difficult to remove following electrodeposition.

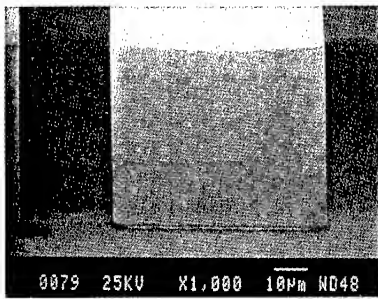


Fig. 4(a). SEM of mini-motor Cu conductors, 70 microns thick, that were electrodeposited through X-ray exposed PMMA resist, which was then removed.

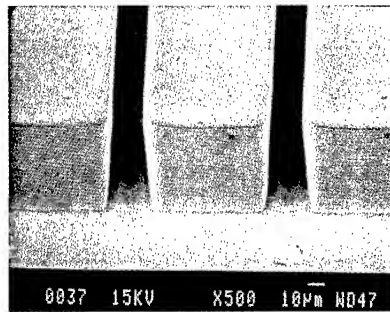


Fig. 4(b). SEM of mini-motor Cu conductors, 58 microns thick, that were electrodeposited through Shipley SJR 3740 positive resist, which was then removed.

The results shown in Fig. 4(b) are very good for positive resist; and we have obtained resist patterns in excess of 100 microns in thickness having similar wall angles. We have successfully combined the use of positive resist and with X-ray exposed PMMA for multilevel structure fabrication (in association with CAMD and MCNC). In such hybrid cases, the PMMA resist process is used for tall structures, especially those in which tolerances are important.

#### FABRICATION OF A MAGNETIC MINI-MOTOR

Small-size, high-efficiency motors, with torque in the range  $10^{-5}$  to  $10^{-4}$  N-m, fabricated using low-cost, batch techniques, are expected to have applications in future data storage, automotive, medical and other fields. We shall briefly describe here the fabrication of an experimental, variable-reluctance, magnetic minimotor using high-aspect-ratio, optical lithography and electrodeposition. A schematic representation of the mini-motor is shown in Fig. 5. The motor, which is 17 mm in diameter, consists of six horseshoe-shaped magnets surrounding a rotor. Helical coils of Cu conductors are wound around the magnets, as shown in Fig. 5. Key physical parameters of the motor are given in Table I.

**TABLE 1**

**MINI-MOTOR PARAMETERS**

Motor size as diam.	Rotor radius	Core width	Coil width	Gap between coil	Air gap between rotor and stator	Coil turns (per core)
(mm)	( $\mu\text{m}$ )	( $\mu\text{m}$ )	( $\mu\text{m}$ )	( $\mu\text{m}$ )	( $\mu\text{m}$ )	
17	2976	700	60	30	5-20	108

The mini-motor design (17) and magnetic field modeling (18) have been described elsewhere.

#### *Fabrication Overview*

The stator and the rotor were fabricated separately. The stator fabrication sequence is summarized in Fig. 6. Five photomasks were used. The motor, in essence, consisted of the following levels:

- Bottom-level Cu conductors;
- Bottom conductor - magnetic core polymer insulation layer;
- Magnetic core, via, pin bearing;
- Magnetic core - top conductor polymer insulation level;
- Top-level Cu conductors.

The fabrication process for the stator was initiated by sputtering a Ti/Cu/Ti seed layer on an oxidized Si wafer, lithographically forming the plate-through mask for the bottom part of the Cu conductor windings, removing the upper Ti film, and electrodepositing Cu. Following removal of resist and seed layer, a dielectric was applied, and the surface was planarized, leaving the top surfaces of the plated Cu features exposed. A

photo-patterned dielectric layer was then formed on top of the Cu conductors to insulate them from the magnetic core, leaving the end of each Cu bar exposed to permit coil formation in subsequent steps. A Ti/Cu/Ti seed layer was then deposited; photoresist was applied and patterned; the upper Ti film was etched away; and the magnetic horseshoe core, rotor pin bearing and coil vias were fabricated in one Permalloy

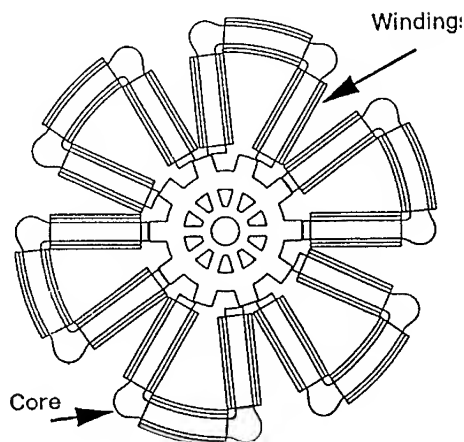


Fig. 5. Schematic representation of the mini-motor.

electrodeposition step. The resist and seed layer were removed; dielectric was applied, cured and polished back to the top of the Permalloy features, leaving a planar surface. A second photo-patterned dielectric layer was formed over the core regions, leaving the vias exposed. Once again, seed layer was

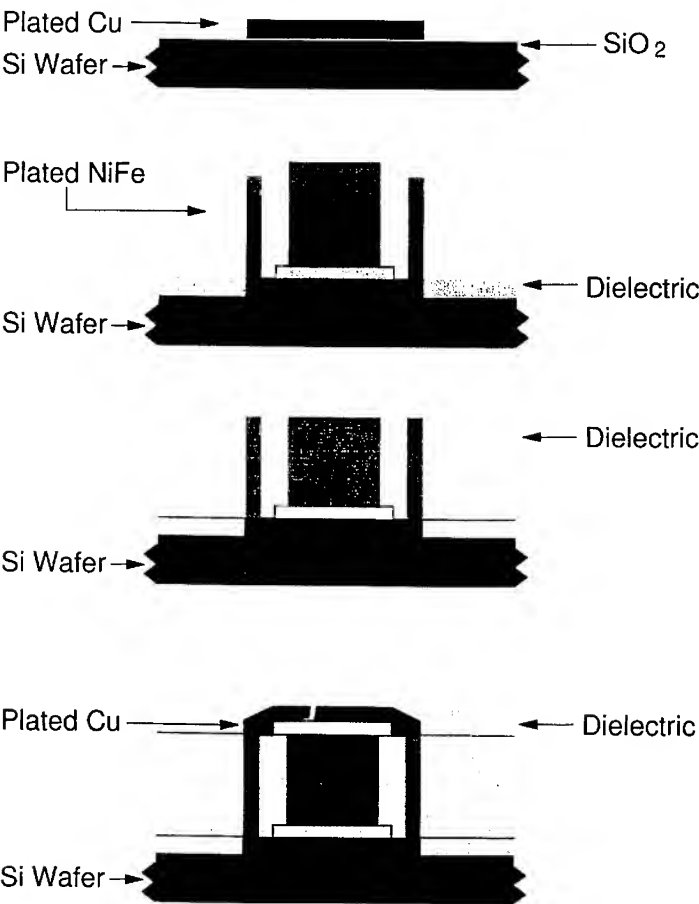


Fig. 6. Schematic representation of the fabrication flow for the mini-motor stator. Seed layers are not shown for clarity.

deposited; resist was applied and patterned; and the top Cu conductor level was electrodeposited to complete the conductor coils. The structure could then be encapsulated by a final dielectric application, if desired. The rotor cavity was opened by reactive ion etching (RIE) of the dielectric following masking of the other regions of the stator.

The rotor was fabricated by through-mask electrodeposition of Permalloy on a separate oxidized Si substrate that was precoated with a thick, sacrificial layer of Cu. The rotor was detached by a chemical release method that selectively dissolves Cu and slipped onto the pin bearing located in the center of the stator.

#### ***Permalloy Electrodeposition***

The soft magnetic material in the horseshoe-shaped cores and rotors was Permalloy (Ni(80 at%)/Fe). Deposition was carried out in a horizontal paddle cell (11), with the paddle between electrodes travelling at a distance of about 3 mm above the cathode surface, and a frequency of 1 hertz. The plating cell was connected to a larger plating solution reservoir, and the solution (15,16) was continuously recirculated and filtered using 0.2 micron Millipore filters. The temperature in the reservoir was maintained at  $27 \pm 0.1^\circ\text{C}$ . Solution pH was controlled at  $3 \pm 0.1$  through automatic addition of dilute HCl solution as needed. Using a Brinkmann Dosimat, the ferrous ion concentration was kept constant by adding a pH=2 solution of ferrous sulfate at a rate calculated to match the rate of iron consumption. A nickel plate served as the anode. A stainless-steel plate - generally coated with a plated layer of Permalloy - surrounding the cathode and served as an auxiliary electrode, or "thief" (10).

The current densities used were in the 5-12.5 mA/cm<sup>2</sup> range, based on the active area of the wafer. Auxiliary electrode current densities were set at 1.1-1.2 times the superficial, or geometric, device wafer current densities (10), thus ensuring uniform deposit thickness across the wafer. Individual features, however, did exhibit higher thickness at the Permalloy-resist boundary, caused by "current crowding", especially when features, or areas of features, were surrounded by a large area of resist, as is the stator pin bearing. This behavior is consistent with the earlier discussion of feature-scale uniformity. In general, Permalloy deposits were smooth and faithfully reproduced the lithographic patterns.

#### ***Copper Electrodeposition***

Copper was deposited in a paddle cell (10) using a commercially available acid-Cu plating solution operated at the conditions recommended by the vendor. At the target current density, the deposition rate was 20  $\mu\text{m/hr}$ . An annulus around the periphery of the wafer, left bare of photoresist, served as an on-wafer "thief electrode". Although this on-wafer thief was not powered independently, good thickness uniformity was achieved, across-wafer thickness variation was typically about 3%. The thickness uniformity depended primarily on the layout of the photoresist pattern. Since the current efficiency of Cu deposition was 100%, the deposit thickness was easily controlled once the active area of the photoresist pattern was accurately known.

#### ***Rotor Release***

Sacrificial Cu release layers were employed to facilitate rotor release. A thin seed layer was sputtered on the oxidized Si wafer, and a blanket Cu film 1.0  $\mu\text{m}$  thick was electroplated. The photolithography and rotor plating were completed on the Cu-coated substrate. Rotor release was accomplished by selective dissolution of the Cu in a near-neutral, ammonium persulfate solution.

### ***Process Integration and Completion of the Mini-motor Structure***

Several stators were completed with 30-34 micron-thick Cu conductors and 40-45 micron-thick Permalloy cores using optical lithography. Since the final structure requires five mask levels (excluding the masking required for RIE of the rotor cavity) and three levels of electrodeposited metal, it is important to limit the layer thicknesses in order to limit the thickness of the final motor. The torque of the minimotor is proportional to the thickness of the Permalloy core, and thus the Permalloy layer is required to be thick. The Cu layer need only be thick enough to carry the current without undue heating. The Cu thickness was thus kept fairly low to reduce the stresses that build up in thick structures.

The rotor cavity in the stator was opened using RIE with masking to ensure selectivity; dielectric removal rates were ca. 0.5 microns per minute. The RIE tool, a Leybold Z401 model, employed a water-cooled stage, and thermally-conductive compound was used between the sample and the stage. To avoid excessive heating and structural damage, runs were interrupted periodically.

### ***Minimotor Operation***

The characteristics of an operational mini-motor was presented elsewhere (19). With no designed-in feedback sensor for rotor position, the motor was driven open-loop. The rotor levitation threshold was 60 mA. The motor torque, as determined from the angular dependence of inductance, was  $2.3 \times 10^{-7}$  N-m. at 100 mA 0-pk for a 43 micron thick Permalloy core. In the open-loop configuration, the maximum rpm (880) was limited by the undamped resonance of the rotor.

The modest torque is the result of using optical lithography to fabricate the stator. The rotor was fabricated using X-ray lithography. the sidewall angle produced by optical lithography in positive photoresist resulted in large clearances between the stator and rotor pole tips and between the pen and rotor, thus lowering the efficiency of the motor. The friction caused by the a few microns of eccentricity in the rotor - pin interface further lowered the torque. The mini-motor has been redesigned for greater ease of fabrication and better flux saturation properties. The fabrication, using X-ray lithography, and the evaluation of this new mini-motor will be described in a future paper (20).

## **CONCLUSIONS**

Electrodeposition plays a pivotal role in HI-MEMS fabrication; there is no serious alternative metal deposition process for these devices. The success of electrodeposition is linked to good process integration. Among the requirements for process integration are the following: 1) high quality, adherent layers; 2) good photoresist technology yielding strongly adherent and pore-free, photoresist with clean development in the patterns; 3) patterns with relatively uniformly spaced lines, and no excessive variation in feature size; 4) electroplating technology giving high-quality deposits from solutions with compositions that can be easily monitored and controlled; 5) plating tools that provide good uniformity and control of the current density and mass transport; and 6) reliable methods of removing photoresist and seed layers without leaving residues.

The integration of electrodeposition and other fabrication processes has allowed us to build and evaluate a preliminary design of a variable-reluctance mini-motor.



## REFERENCES

1. See *Micromachine Devices*, (Cahners Publishing Co.), **1** (1996) 1.
2. I.V. Babich, T. Chainer, E.I. Cooper, S. Hegde, J. Horkans, C. Jahnes, S. Krongelb, K.T. Kwietniak, N.C. LaBianca, E.J. M. O'Sullivan, L.T. Romankiw, J.A. Tornello and P. Trouilloud, in *ECS Proc. Fourth Intl. Symp. on Magnetic Materials, Processes, and Devices (1995)*, L.T. Romankiw and D. Herman Editors, **95-18** (1996) 505.
3. E.J. O'Sullivan, E.I. Cooper, L.T. Romankiw, J. Horkans, K.T. Kwietniak, J.A. Tornello, C. Jahnes, I.V. Babich, N.C. LaBianca, S. Krongelb, S. Hegde, J.M. Cotte and P. Trouilloud, to be published in *IBM J. Res. and Develop.*
4. L.T. Romankiw, *Etching for Pattern Definition*, Pub. by the The Electrochemical Society, Inc., (1976) 161-193.
5. L.T. Romankiw, S. Krongelb, E.E. Castellani, J. Powers, A.T. Pfeiffer and B. Stoeber, in *Proc. Intl. Conf. on Magnetism ICM-73*, Moscow, USSR, **6** (1973) 104.
6. L.T. Romankiw, I.M. Croll and M. Hatzakis, *IEEE Trans. Mag-6*, **4** (1970) 729.
7. E.W. Becker, W. Ehrfeld, P. Hagman, A. Maner and D. Munchmeyer, *Microelectron. Eng.* **4** (1986) 35.
8. E. Spiller, R. Feder, J. Topalian, E.E. Castellani, L.T. Romankiw and M. Heritage, *Solid State Technol.*, April (1976) 62.
9. For Permalloy, see P.C. Andricacos and L.T. Romankiw, *Adv. in Electrochem. Sci. and Eng.*, H. Gerischer and C. W. Tobias Editors, **3** (1994) 225-321.
10. S. Mehdizadeh, J. Dukovic, P.C. Andricacos and L.T. Romankiw, *J. Electrochem. Soc.*, **137** (1990) 110.
11. J.V. Powers and L.T. Romankiw, *U.S. Pat.* 3,652,442 (1972).
12. L.T. Romankiw, in *Ref. 2*, p. 253.
13. S. Mehdizadeh, J. Dukovic, P.C. Andricacos, L.T. Romankiw and H.Y. Cheh, *J. Electrochem. Soc.*, **139** (1992) 78.
14. S. Mehdizadeh, J. Dukovic, P.C. Andricacos, L.T. Romankiw and H.Y. Cheh, *J. Electrochem. Soc.*, **140** (1993) 3497.
15. E.E. Castellani, J.V. Powers and L.T. Romankiw, *U.S. Pat.* 4,102,756 (1978).
16. N.C. Anderson and C.R. Grover, Jr., *U.S. Pat.* 3,652, 442 (1972).
17. T. Chainer and L.T. Romankiw, in *Ref. 2*, p. 482.
18. P.L. Trouilloud, *ibid*, p. 493.
19. I.V. Babich, T. Chainer, E.I. Cooper, S. Hegde, J. Horkans, C. Jahnes, S. Krongelb, K.T. Kwietniak, N.C. LaBianca, E.J. M. O'Sullivan, L.T. Romankiw, J.A. Tornello and P. Trouilloud, to appear in *IEEE Trans. Mag.*, Sept. 1997.
20. L.T. Romankiw et al., paper to appear in proceedings of *Harmst '97* (Worldwide Liga Forum), June 20-21, 1997.

## ACKNOWLEDGMENTS

This work was supported in part by ARPA under Technology Reinvestment Project Development Agreement MDA972-94-3-0043. The authors gratefully acknowledge the receipt of X-ray patterned PMMA samples from R. Wood (MCNC), and C. Khan Malek, Z. Ling and Y. Vladimirovsky (CAMD). The authors are grateful to S. Roux for mask creation. Finally, the authors wish to acknowledge useful discussions with T. Chainer, R. Acosta, L. Shi, D. Rath, D. Herman, J. Gelorme and J. Dukovic.

## ELECTRODEPOSITION OF HIGH- $T_c$ SUPERCONDUCTOR MATERIAL FOR MICROSENSOR FABRICATION

A. NATARAJAN \*, W. WANG \*, E. MA \*, R.N. BHATTACHARYA \*\*,  
C. KHAN-MALEK \*\*\*, M. PARANTHAMAN \*\*\*\*, P.M. MARTIN \*\*\*\*

\*Microsystems Engineering Team ( $\mu$ -SET), Department of Mechanical Engineering, Louisiana State University, Baton Rouge, LA 70803

\*\*National Renewable Energy Laboratory, 1617 Cole Boulevard, Golden, CO 80401

\*\*\*Center for Advanced Microstructures and Devices, Louisiana State University, Baton Rouge, LA 70803

\*\*\*\*Oak Ridge National Laboratory, Oak Ridge, TN 37831

### ABSTRACT

Thin-films of  $\text{YBa}_2\text{Cu}_3\text{O}_7$  (YBCO) superconductor precursor were synthesized using an electrodeposition process. The YBCO precursor thin films were deposited on Ag foils using pulsed potential deposition conditions of 10 s at -4 V and 10 s at -1 V (versus Ag reference electrode). The post-annealed films showed zero electrical resistance at 60 K. The procedures for the fabrication of a high precision micro-sensor using YBCO superconductor for measurement of weak magnetic fields are outlined. The micro-sensor templates were patterned using X-rays and precursor films were deposited into the features.

### INTRODUCTION

It has been demonstrated recently that electrodeposition can be used to fabricate high temperature superconductors [1-6]. This process has tremendous practical potential in the fabrication of planar and non-planar electronic devices and micro-sensors. Electrodeposition is a low-cost process and has the ability to deposit conductors or conductor-coated insulators of any shape. It is also an integral processing step in LIGA microfabrication, which involves lithography, electroforming and plastic molding. The short coherence lengths, anisotropy of electronic structures and low carrier densities of high- $T_c$  oxide superconductors have not made them suitable for conventional superconducting electronic devices. However, these properties have been utilized to fabricate other devices such as magnetic field sensors. The abrupt increase in electrical resistance with the application of a weak magnetic field in high- $T_c$  superconductors has been reported [7-8]. This property has been utilized in the fabrication of a bulk magnetoresistive sensor using YBCO superconductor by Nojima et al. [9]. These sensors were reported to exhibit a much higher sensitivity as compared with the traditional Hall Effect or semiconductor sensors and a magnetic field resolution of  $2 \times 10^{-6}$  G/(Hz) at 100 Hz in the 0.1 - 100 G range.

We are in the process of developing a microfabricated YBCO based superconductor microsensor for detection of weak magnetic fields. The LIGA process is being employed to achieve low cost, batch fabrication and integration with on-chip signal processing circuits. In this paper we report the electrochemical synthesis of YBCO thin film superconductors deposited from a single bath solution under pulsed plating conditions. Preliminary results of post-deposition annealing,  $T_c$  measurements, and electrodeposition into microfabricated template patterns will also be reported.

## EXPERIMENTAL

The precursors of YBCO superconductor were obtained by co-electrodeposition of the constituent metals using nitrate salts dissolved in dimethyl sulfoxide (DMSO). A typical electrolyte bath for YBCO films consisted of 0.07 M  $\text{Y}(\text{NO}_3)_3 \cdot 5\text{H}_2\text{O}$ , 0.180 M  $\text{Ba}(\text{NO}_3)_2$ , 0.07 M  $\text{Cu}(\text{NO}_3)_2 \cdot 5\text{H}_2\text{O}$  and 0.003 M  $\text{Ag}(\text{NO}_3)$  dissolved in 250 ml of (DMSO) solvent. All chemicals were of Analar or Puratronic grade and were used as received. A conventional three electrode cell was employed. The substrates (working electrode) were commercial-grade 0.125 mm thick Ag foils. The reference electrode was Ag (pseudo-reference) and the counter electrode was Pt gauze. Two opposed Pt gauze counter electrodes on either side of the working electrode were employed to deposit a stoichiometric film on both sides of the Ag substrate. A pulsed potentiostatic mode was employed to deposit the films and potential cycle was 10 s at -4.0 V followed by 10 s at -1.0 V. Film depositions were performed at room temperature with minimal stirring, thus assuring the process occurred in the diffusion-limited regime. A Princeton Applied Research potentiostat/galvanostat Model 273A with an IBM PC AT computer interface was used for controlling the pulsed-potential electrolysis and to monitor the current and voltage profiles.

A number of electrodeposition runs were conducted with different electrolyte compositions to optimize the composition of the as-deposited film. Inductively coupled plasma (ICP) spectrometry was used to analyze the composition of the electrolyte and the electrodeposited films. A ternary diagram showing how the electrolyte compositions were adjusted to reach the desired film composition is presented in Fig. 1. The films were annealed in air for 16 hours at 920° C. They were then annealed at 600° C for 4 hours and 400° C for 4 hours and very slowly cooled down to room temperature, while maintaining oxygen gas flow during these steps. X-ray diffraction analysis was carried out on the post-annealed films. The post-annealed film compositions were also measured using electron probe microanalysis (EPMA) and SEM images were taken to reveal the microstructure of the films. The superconducting transition temperature of the films was determined by the resistivity-temperature (R-T) measurement at a constant current in a four-point probe configuration.

## RESULTS AND DISCUSSION

### YBCO SYNTHESIS AND PROPERTIES

The electrolyte bath composition was optimized to produce YBCO precursor of the desired ratio. The composition of the optimized electrolyte bath as measured by ICP analysis was 0.077 M  $\text{Y}(\text{NO}_3)_3 \cdot 5\text{H}_2\text{O}$ , 0.184 M  $\text{Ba}(\text{NO}_3)_2$ , 0.072 M  $\text{Cu}(\text{NO}_3)_2 \cdot 5\text{H}_2\text{O}$  and 0.003 M  $\text{Ag}(\text{NO}_3)$  dissolved in 250 ml of (DMSO) solvent. The composition of the precursor films deposited from this bath (in terms of the ratio of the constituent elements Y/Ba/Cu) was 0.861/2.026/3.114. Ag content in the film was about 1% . A deposition rate of  $\sim 0.25 \mu\text{m}/\text{minute}$  was observed with the reported bath.

A series of samples was produced from the same bath with nearly the same composition each time and it showed that the electrodeposition process was very reproducible. DMSO was found to be an effective solvent to electrodeposit elements like yttrium and barium with very high negative reduction potentials. Interpreting the individual rate of co-deposition of the cations is very complex and depends on the mass transfer to the electrode, various surface effects, kinetic variables and the required overpotential. The most significant stand-alone parameter is the extra bias potential applied to the individual elements Y, Ba and Cu during the co-deposition process. The extra bias potential ( the applied potential minus the reduction potential) for Cu is therefore significantly higher than for Y or Ba. At -1.0 V, the loosely bound materials are stripped off the

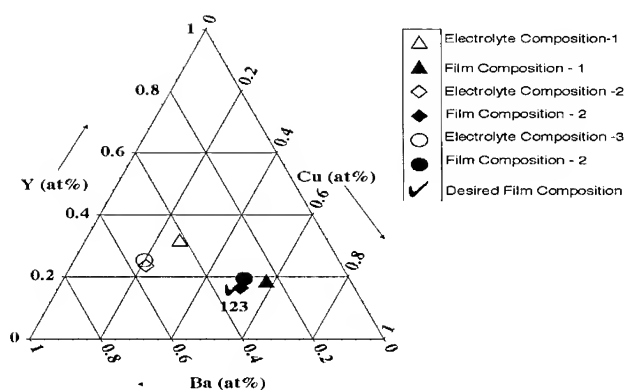


Figure 1. A ternary diagram showing the electrolyte composition map to the film composition. The deposition bath contains 3 mM  $\text{Ag}(\text{NO}_3)$ .

substrate and Cu is deposited to maintain the conductivity of the deposited layer which then results in a significantly higher rate of deposition of Cu than Y or Ba. Addition of Ag during the deposition process as a co-deposited element was found to improve the uniformity of the deposit. Ag is believed to mitigate the weak-link problems associated with the superconducting films. Ag is also known to lower the melting point of all the oxide superconductors and influence the phase development and reaction process during the post-deposition annealing [10].

The X-ray diffraction pattern of the post-annealed film presented in Fig. 2 showed the c-axis textured orthorhombic superconducting  $\text{YBa}_2\text{Cu}_3\text{O}_7$  phase. XRD peaks detected for Ag are from the substrate. The SEM of a post-annealed film is presented in Fig. 3. The resistivity - temperature (R-T) measurement was carried out in a four-point probe configuration and the superconducting transition is shown in Fig. 4. The post-annealed films showed reproducible zero resistance at about 60 K. The low value of the transition temperature ( $T_c$ ) for this superconductor film suggests a low critical current density ( $J_c$ ). However we believe this may not be detrimental to our intended application of fabricating a magnetoresistive sensor, where a suppression of the critical current in the film in its superconducting state at low magnetic fields is essential to exhibit a sharp jump in the resistance with the application of a weak magnetic field.

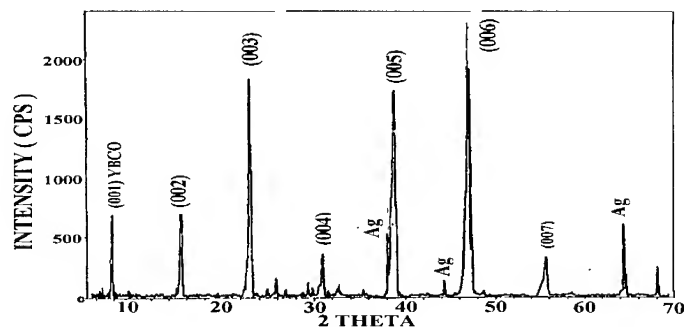


Figure 2. XRD spectra of an electrodeposited YBCO film on Ag annealed at 920°C for 16 hours.

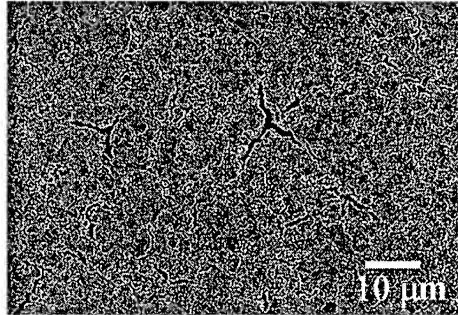


Figure 3. SEM micrograph of a post-annealed electrodeposited YBCO film, 4 microns thick, on Ag substrate.

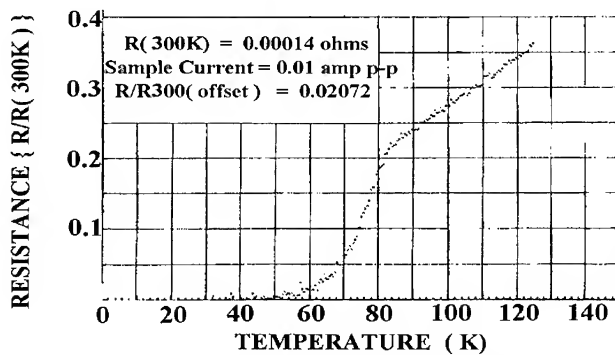


Figure 4. Resistance vs. temperature for electrodeposited YBCO films on Ag substrate.

#### Microsensor Device Fabrication

The schematic design of the magnetic field microsensor is illustrated in Fig. 5. The microsensor device fabrication sequence is presented in Fig. 6. In this sequence, an oxidized Si

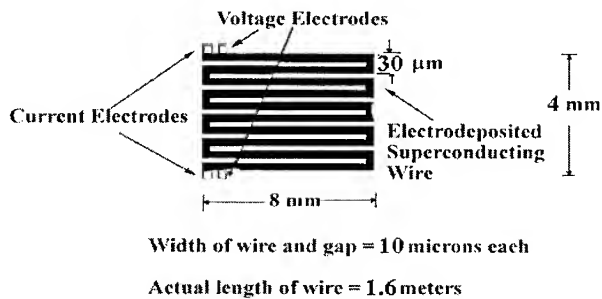


Figure 5. Schematic design of the microsensor. The meandered shape of the sensor is designed to increase its magnetoresistive sensitivity.

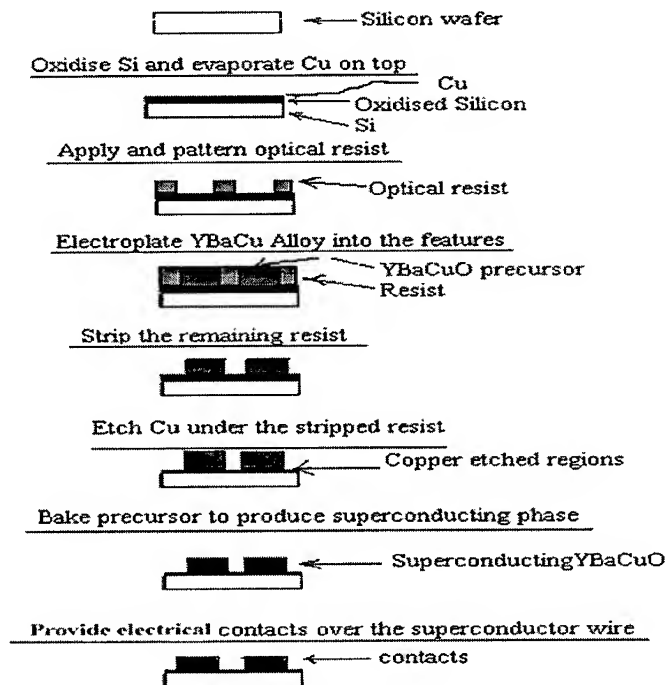


Figure 6. Fabrication sequence for the superconductor based microsensor

wafer is evaporated with a thin layer of 200Å of Cu or Ag as a plating base for depositing the YBCO precursor. Poly-methyl-methacrylate (PMMA), a positive photoresist, is spun coat onto the wafer to a thickness of about 3.0  $\mu\text{m}$ . The resist is then patterned using X-rays, employing an X-ray mask, to produce the desired template. The patterned microsensor template is presented in Fig. 7. The patterns reveal well-defined features with the grooves and the resist walls, each 10 microns wide.

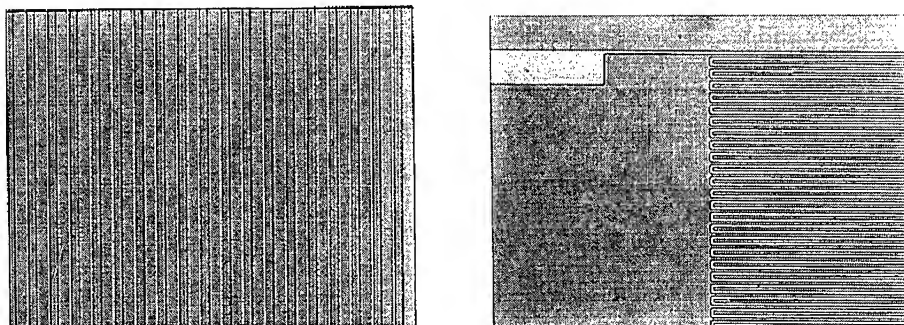


Figure 7. Patterned microsensor templates using an X-ray lithography technique.

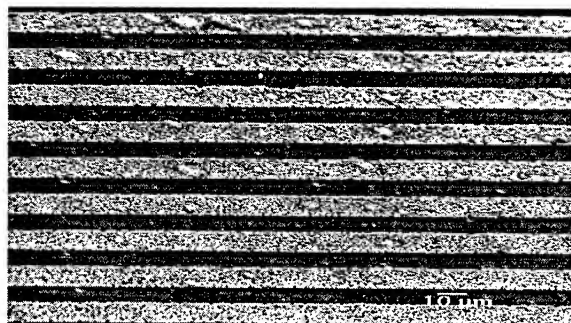


Figure 8. YBCO precursor deposited into the patterned grooves to produce a meandered wire.

The precursor films are subsequently electrodeposited into the patterned grooves to produce the meandered wire shape that is desired for our microsensor. An example is shown in Fig. 8. The composition of this precursor deposited into the patterns is being optimized. The effect of the Cu/Ag plating base and silica substrate on the superconducting properties of the post-annealed YBCO precursor is to be investigated and the sensor is to be calibrated for magnetoresistive applications.

## CONCLUSIONS

We have electrodeposited YBCO precursor films with the desired elemental ratio on Ag substrates. Post-deposition annealing produced the orthorhombic superconducting  $\text{YBa}_2\text{Cu}_3\text{O}_7$  phase. Resistivity - temperature measurements revealed superconducting behaviour with a  $T_c$  of 60 K. The fabrication of a weak magnetic field microsensor is being investigated. Preliminary results demonstrate the feasibility of electrodeposition as a processing technique in the fabrication of the sensor. The simplicity and low cost of the electrodeposition process, combined with the capability of batch fabricating microfeatures with superior geometry and functionality using the LIGA microfabrication technique, have the potential to open up a new realm in the field of microsystems technology.

This work is supported by the Louisiana Board of Regents, LEQSF Program (1995-98)-RD-A-13. Part of the research conducted at Oak Ridge National Lab was managed by Lockheed Martin Energy Research Corporation, for the US D.O.E under the contract DE-AC05-96-OR 22464.

## REFERENCES

1. D.J. Zurawski, P.J. Kulesza and A. Wiekowski, *J. Electrochem. Soc.* **135**, 1607 (1988).
2. M. Maxfield, H. Eckhardt, Z. Iqbal, F. Reidinger and R.H. Baughman, *Appl. Phys. Lett.* **54**, 1932 (1989).
3. P. Slezak and A. Wiekowski, *J. Electrochem. Soc.* **138**, 1038 (1991).
4. R.N. Bhattacharya, P.A. Parilla, A. Mason, L.L. Roybal, R.K. Ahrenkiel, R. Noufi, R.P. Hellmer, J.F. Kwak and D.S. Ginley, *J. Mater. Res.* **6**, 1389 (1991).
5. R.N. Bhattacharya, P.A. Parilla, R. Noufi, P. Arendt and N. Elliot, *J. Electrochem. Soc.* **139**, 67 (1992).
6. R.N. Bhattacharya, A. Duda, D.S. Ginley, J.A. DeLuca, Z.F. Ren, C.A. Wang, J.H. Wang, *Physica C* **229**, 145-151 (1994).
7. H. Nojima, S. Tsuchimoto and S. Kataoka, *Japan Journal Of Applied Physics* **27**, 746 (1988).
8. J.M. Rowell, *IEEE Trans. on Magn.* **25**, 759 (1989).
9. H. Nojima, H. Shintaku, M. Nagata and S. Kataoka, *IEE Trans. on Electron Devices*, **139**, 576-580 (1992).
10. R.N. Bhattacharya, P.A. Parilla and R.D. Blaugher, *Physica C* **211**, 475 (1993).

## STRUCTURE AND MAGNETIC PROPERTIES OF ELECTRODEPOSITED COBALT/PLATINUM MULTILAYERS

S. KASHIWABARA, Y. JYOKO AND Y. HAYASHI

*Department of Materials Science & Engineering,*

*Faculty of Engineering, Kyushu University, Fukuoka 812, Japan*

Qhu@zaiko.kyushu-u.ac.jp

### ABSTRACT

The electrodeposition of Co/Pt multilayers have been carried out under potential control. The influence of the deposition potential on the structure of the multilayers is investigated. Deposition of the Pt layers at an electrode potential in the Co dissolution region gives rise to the destruction of the compositionally modulated structure and a large internal stress. The structure and magnetic properties of electrodeposited Co/Pt multilayers are discussed in connection with the dissolution of Co during Pt deposition.

### INTRODUCTION

Many interesting magnetic properties, such as perpendicular magnetic anisotropy and giant magnetoresistance, have been reported in metallic multilayers[1]. Most of the multilayered films have been prepared by physical vapor deposition (PVD). In recent years, however, there has been renewal of interest in preparation and characterization of electrodeposited metallic multilayers[2-5]. Although a number of studies have been done on the preparation and characterization of electrodeposited multilayers, little are attempted on the control of structures by the deposition conditions.

We have reported reflection electron microscopic (REM) observations on the initial stage of electrodeposition of Co on Pt (111) surface[6], and discussed the possibility of the formation of Co/Pt multilayers which have attracted attention as new materials for magnetic and magneto-optical recording media[7]. We have also focused on the feasibility of controlling the layered structure by applying potentials in the overpotential region for Co deposition [8]. On the other hand, it is suspected that the deposition potential of the Pt layers affects the interface structure. The difference in equilibrium potentials between Co and Pt allows Co to dissolve during Pt deposition. The dissolution of Co is considered to affect the structure and magnetic properties of the multilayers. In other words, the Pt deposition potential is also an important factor to obtain the well-ordered layered structure. In this paper, we were concerned with the influence of the Pt deposition potential on the structure and magnetic properties of the multilayers.

### EXPERIMENT

The Co/Pt multilayers were prepared by electrodeposition using dual cells. Pt or Co layers were electrodeposited from each cell, and the substrate was transferred alternatively to obtain a multilayered structure. A 1-mm thick polycrystalline Cu sheet was used as a substrate. Pt and Co layers were electrodeposited in each electrolytic cell under potential control. All the electrode potentials were measured and quoted relative to a saturated silver-silver chloride (Ag/AgCl) reference electrode. Electrolytes, 0.5 M H<sub>2</sub>SO<sub>4</sub> containing 0.1 M CoSO<sub>4</sub> or 10<sup>-2</sup> M H<sub>2</sub>PtCl<sub>6</sub>, were prepared with analytical grade reagents and distilled water. The growth rate of Co was determined



from the relation between the deposition time and the Co coverage which was estimated by the anodic stripping curve. The thickness of the Pt layers was controlled by the electrical charge  $Q_{Pt}$  passed during time  $T_{Pt}$ , taking into account the current efficiency. The layers of Co were deposited at a constant electrode potential, -1.5V and the Pt layers were deposited at two different electrode potentials, -0.30 V (Co dissolution region) and -0.65 V (no Co dissolution region). Evaluated growth rate of Co was 0.2nm/s. Pt growth rate were 0.3nm/s at -0.30V and 0.1nm/s at -0.65V, respectively.

The periodicity of the composition modulation and the crystallographic structures of the multilayers were investigated by low and high angle X-ray diffraction (XRD) using Co- $K\alpha$  radiation. Cross-sectional transmission electron microscopy (TEM) was also used to examine the structure of the multilayer films. The magnetization at room temperature was measured using a vibrating sample magnetometer (VSM) with an applied field up to 10kOe. The effective perpendicular magnetic anisotropy energy was calculated from the magnetization curves measured with the applied field perpendicular and parallel to the film surface.

## RESULTS AND DISCUSSION

Figs.1 (A) and (B) show cross-sectional TEM images for Co(2nm)/Pt(8nm) multilayers, prepared at the different deposition potentials of the Pt layers, (A) -0.30V and (B) -0.65V, respectively. In both specimens, Co layer was deposited at the same potential -1.5V. The specimen shows a periodic structure. Since the diffraction pattern (unlisted) shows ring pattern, there is no preferred orientation in this multilayer. The Co/Pt multilayers prepared by PVD have a texture and column boundaries along the growth direction[9]. But the Co/Pt multilayers prepared by electrodeposition dose not have a texture and column boundaries. It is said that the structure of electrodeposited multilayer is different from that prepared by PVD. In Fig.1(A), the layered structure is unclear, and the layer stacking is partially destroyed. The deposition potential of Pt,  $E_{Pt}$  = -0.30V, is in the region of Co dissolution. Therefore, it is considered that the contrast of the Co layers is unclear and a destroyed stacking structure is observed because of the dissolution of Co during Pt deposition. Moreover, it is suspected that the Co layer will be a Co-Pt alloy layer, especially when the Co thickness is so small as shown in this case. On the other hands, as shown in Fig.1(B), the contrast of the Co layers is clearly observed. Though the roughness of the interface becomes larger than that shown in Fig.1(A), it is said that the improvement of the layered structure is done by changing the Pt deposition potential. The deposition potential of Pt,  $E_{Pt}$  = -0.65V, is not in the region of Co dissolution, and the sharp interface is obtained in this condition.

Fig. 2 (A) shows low angle X-ray diffraction profile for typical electrodeposited Co/Pt multilayers prepared at  $E_{Pt}$  = -0.30V (Co dissolution region). The designed Co and Pt layer thicknesses,  $t_{Co}$  and  $t_{Pt}$ , are; (a)  $t_{Co}$  = 3.5nm (b)  $t_{Co}$  = 2.0nm and (c)  $t_{Co}$  = 0.5nm, respectively, and  $t_{Pt}$  = 2nm, and the layer pairs  $n$  = 30 being fixed. In the samples (a) and (b), a multilayered structure is proved by the presence of the first Bragg peak. The bilayer periods,  $A$ , calculated from the observed first Bragg peak positions, (a)  $A$  = 5.8nm and (b)  $A$  = 3.9nm, respectively, are relatively in good agreement with the designed periods. But these Bragg peaks are broad and the intensities are much lower than that might be expected for the multilayer with the well-defined interface. In the case of the sample (c), no diffraction peak is observed. It seems that it is difficult to obtain a compositionally modulated structure with a small Co thickness ( $t_{Co}$  < 1nm) under this experimental condition, and the film is almost Co-Pt alloy in such a small Co thickness.

Fig. 2 (B) shows low angle X-ray diffraction profiles of the multilayers electrodeposited at  $E_{Pt}$  = -0.65V (no Co dissolution region). The designed thickness are; (a)  $t_{Co}$  = 3.4nm (b)  $t_{Co}$  = 2.1 nm and (c)  $t_{Co}$  = 0.8 nm, respectively, while the Pt layer thickness and the layer pairs are the same as

those shown in Fig 2 (A). The periodic structure is confirmed by the first Bragg peak. In contrast to Fig 2(A), these peaks are sharp and the intensities are high. And the first Bragg peak of layered structure is observed even for the specimen with a thinner Co layer thickness  $t_{Co}=0.8\text{nm}$ . As mentioned above, the Pt deposition potential is related to the Co layer dissolution. In case the Pt layers are deposited at potentials in the region of Co dissolution interface mixing and a destruction of the compositionally modulated structure will be suspected to occur. Accordingly, it is said that great care must be taken to avoid the Co dissolution when the Pt deposition potential is set up.

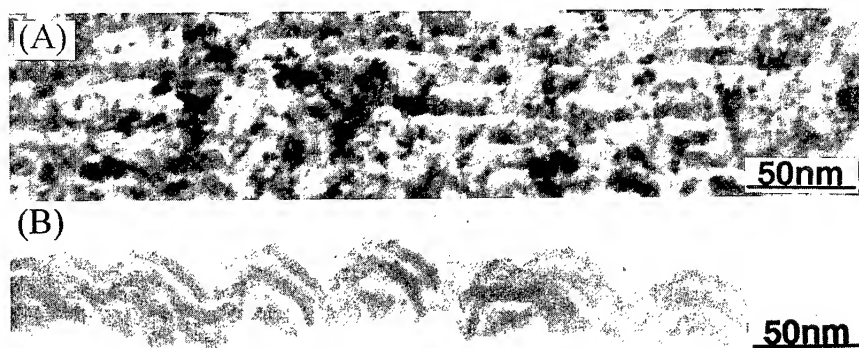


Fig. 1 Cross-sectional TEM images of electrodeposited [Co(2nm)/Pt(8nm)] multilayers. The Pt deposition potentials of the Pt layers are -0.30V(A) (Co dissolution region) and -0.65V(B) ( no Co dissolution region),respectively.

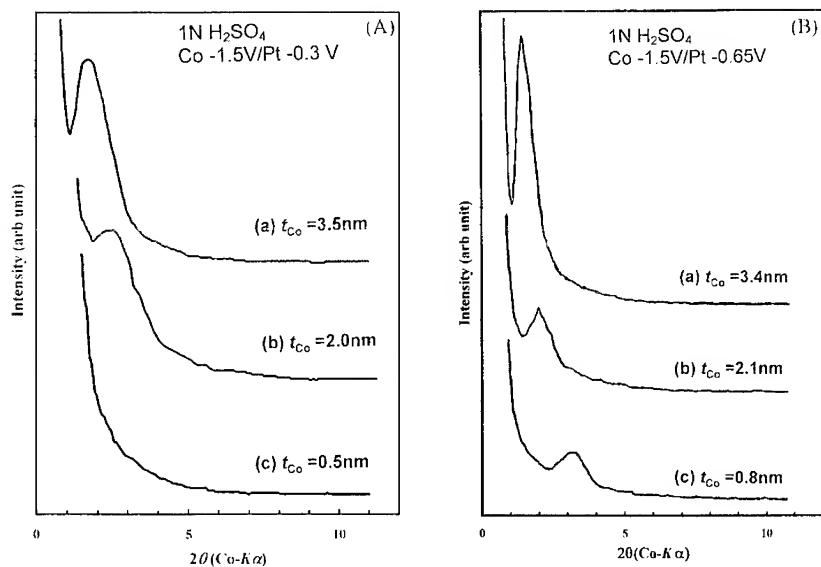


Fig. 2 Low angle X-ray diffraction profiles for electrodeposited Co/Pt multilayers with 2nm Pt-layers and varying Co-layer thickness. The Pt deposition potentials are -0.30V(A) (Co dissolution region) -0.65V(B) ( no Co dissolution region),respectively.

The magnetic anisotropy of Co/Pt multilayers prepared by PVD is very sensitive to the Co-layer thickness [10]. To make clear the dependence of magnetic properties of the electrodeposited multilayers on the Co-layer thickness, the magnetization curves were measured applying magnetic field parallel and perpendicular to the film surface for the specimens with 2nm Pt layers and varying Co layer thickness. The coercivity of the electrodeposited Co/Pt multilayers is always less than 150Oe and the easy magnetization axis lay in plane, regardless of the Co-layer thickness. It seems that the small coercivity is due to the fine grains of the magnetic layer, and the in-plane anisotropy is caused by no coherency at the interface and no preferred orientation. Lee et al [11], reported that the perpendicular anisotropy of Co/Pt multilayers are dependent on crystallographic orientations. Since there is no preferred orientation in these films, the easy axis is in the plane

For the relation between magnetic anisotropy energy ( $K_{eff}$ ) and Co-layer thickness it is known by the following equation

$$K_{eff} t_{Co} = 2K_s + K_v t_{Co} \quad (1)$$

where  $K_s$  and  $K_v$  are the surface and volume anisotropy energy, respectively. To make clear the dependence of the magnetic anisotropy on the Co layer thickness, values of  $K_{eff} t_{Co}$  obtained for the electrodeposited multilayers are plotted against  $t_{Co}$  in Fig.3. The anisotropy energies were determined from the magnetization curves for perpendicular and parallel fields. The electrodeposited Co/Pt multilayers show all in-plane magnetization for every  $t_{Co}$ . The values of  $K_s$  and  $K_v$  obtained from the plot are  $K_s = -0.10[\text{mJ/m}^2]$  and  $K_v = -0.27[\text{MJ/m}^3]$  for the multilayers deposited at  $E_{Pt} = -0.30\text{V}$ , and  $K_s = 0.05[\text{mJ/m}^2]$  and  $K_v = -0.46[\text{MJ/m}^3]$  for those at  $E_{Pt} = -0.65\text{V}$ .

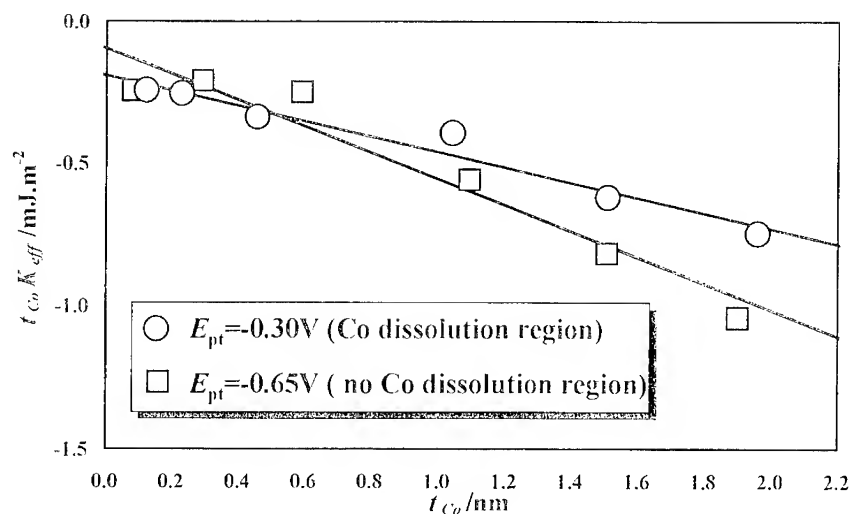


Fig. 3. Effective anisotropy energy,  $t_{Co}K_{eff}$  versus Co layer thickness,  $t_{Co}$  for electrodeposited Co/Pt multilayers.

Note the small values of the surface anisotropy energy and volume anisotropy energy. Both  $K_s$  and  $K_v$  of the multilayers prepared in the region of Co dissolution are smaller than that of the

multilayers prepared in no Co layer dissolution. Usually surface anisotropy energy takes a positive value in the Co/Pt multilayers prepared by PVD. Diffuse interfaces introduce randomness in magnetic pair bonds according to Néel's model, which obviously reduces the surface anisotropy energy  $K_s$ . From the structural properties of the electrodeposited Co/Pt multilayers, it seems that incoherence of the interface contributes to the negative value of the surface anisotropy energy. And the difference of  $K_s$  between two Pt deposition potential suggests the difference of the layered structural quality due to the Co dissolution. The reason of the small value of the volume anisotropy energy  $K_v$  is the contribution of the magnetoelastic anisotropy and shape anisotropy attributable to the peculiar structure (no orientation, fine grains and mixing interfaces) of the electrodeposited multilayers.

In order to explain the small value of volume anisotropy  $K_v$ , internal stress of the electrodeposited multilayers was examined. Internal stress measurement was done by XRD using  $\sin^2\psi$ - $d_{\psi}$  method. Fig. 4 shows the stress  $\sigma$  of electrodeposited  $\text{Co}(t_{\text{Co}}, \text{nm})/\text{Pt}(2\text{nm})$  multilayers. Regardless Pt deposition potentials, the stress increases as  $t_{\text{Co}}$  decreases, and the sign of stress is always negative. It is clearly observed that  $\sigma$  of the multilayers with Pt deposited at  $E_{\text{Pt}} = -0.30\text{V}$  are larger than that deposited at  $E_{\text{Pt}} = -0.65\text{V}$ . Therefore, it is considered that the dissolution of Co during Pt deposition leads to a large internal stress.

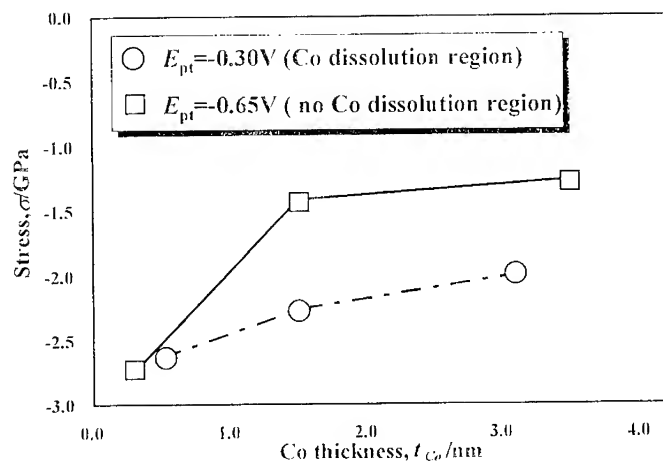


Fig. 4. Stress versus Co layer thickness  $t_{\text{Co}}$  in electrodeposited  $[\text{Co}(t_{\text{Co}}, \text{nm})/\text{Pt}(2\text{nm})]_{30}$  multilayers.

The stress of the magnetic multilayers has the effect on magnetoelastic anisotropy energy  $K_{\text{ME}}$ , which is given by

$$K_{\text{ME}} = -\frac{3}{2}\lambda\sigma \quad (2)$$

where  $\lambda$  is a magnetostriction constant. In case of polycrystalline, a mean magnetostriction constant  $\bar{\lambda}$  is expressed as

$$\bar{\lambda} = \frac{2}{5}\lambda_{100} + \frac{3}{5}\lambda_{111} \quad (3)$$

where  $\lambda_{100}$  and  $\lambda_{111}$  are magnetostriction constants in [100] and [111] directions, respectively. For Co/Pt multilayer,  $\bar{\lambda}$  becomes positive value. Because  $\sigma$  of the electrodeposited multilayer is a negative value,  $K_{ME}$  becomes a positive value. Positive value of  $K_{ME}$  leads to small volume anisotropy energy  $K_v$ . Then, it is considered that the obtained small value of  $K_v$  for the electrodeposited multilayers is attributed to large compressive internal stress. The difference of  $K_v$  for films with different Pt deposition potentials is explained in a similar way.

Although we have not obtain a large perpendicular magnetic anisotropy, electrodeposited multilayers have a potential to exhibit unusual properties unavailable by conventional preparation techniques.

## SUMMARY

The influence of the Pt deposition potential on the structure and magnetic properties of electrodeposited Co/Pt multilayers was investigated. TEM observations and low angle X-ray diffraction measurements showed that the electrodeposited multilayers had a mixing interface when the Pt layers were deposited at the potential of Co dissolution. The interface mixing was caused by the electrochemical reaction during the Pt-layer deposition. The magnetic properties of the multilayers were affected by the Pt deposition potential. The large internal stress was observed when the Pt deposition potential was in the Co dissolution region. From a consideration of the magnetoelastic anisotropy, it is suggested that the obtained small values of volume magnetic anisotropy energy may be caused by the large compressive internal stress.

## ACKNOWLEDGMENTS

The authors would like to acknowledge the support and advice of HVEM Laboratory of Kyushu University for TEM observation. This study was supported in part by a Grant-in-Aid for Scientific Research from the Ministry of Education, Science and Culture.

## REFERENCES

1. P. F. Carcia, J. Appl. Phys. **63**, 5066 (1988); M. N. Baibich, J. M. Broto, A. Fert, F. Nguyen Van Dau, F. Petroff, P. Etienne, G. Greuzet, A. Friendrich and J. Chazelas, Phys. Rev. Lett. **61**, 2472 (1988).
2. M. Alper, K. Attenborough, R. Hart, S. Lane, D.S. Lashmore, C. Younes and W. Schwarzacher, Appl. Phys. Lett. **63**, 2144 (1993).
3. L. Piraux, J.M. Geprge, J.F. Despres, C. Leroy, E. Ferain, R. Legras, K. Ounadjela and A. Fert, Appl. Phys. Lett. **65**, 2484 (1994).
4. T.P. Moffat, J. Electrochem. Soc. **142**, 3767 (1995).
5. G. Nabiyouni and W. Schwarzacher, J. Magn. Magn. Mater. **156**, 355 (1996).
6. Y. Jyoko, S. Kashiwabara and Y. Hayashi, Mater. Trans., JIM. **33**, 1149 (1992).
7. Y. Jyoko, S. Kashiwabara and Y. Hayashi, Mater. Trans., JIM. **34**, 946 (1993).
8. Y. Jyoko, S. Kashiwabara and Y. Hayashi, J. Magn. Magn. Mater. **126**, 52 (1993).
9. G.A. Bertero and R. Sinclair, J. Magn. Magn. Mater. **134**, 173 (1994).
10. C.-J. Lin, G.L. Gorman, C. H. Lee, R.F.C. Farrow, E.E. Marinero, H.V. Do, H. Notarys and C.J. Chien, J. Magn. Magn. Mater. **93**, 194 (1991).
11. C.H. Lee, R.F.C. Farrow, R.F. Marks, W.F. Bennett, E.E. Marinero and C. J. Chien, J. Magn. Magn. Mater. **93**, 592 (1991).

## ELECTRODEPOSITION OF STRAINED-LAYER SUPERLATTICES

T.P. MOFFAT

Materials Science and Engineering Laboratory  
National Institute of Standards and Technology  
Gaithersburg, Md 20899

### ABSTRACT

A variety of Cu/(Ni, Co) multilayers have been grown on Cu single crystals by pulse plating from an alloy electroplating bath. Copper is deposited under mass transport control while the iron group metal is deposited under interfacial charge transfer control. The structural evolution of these films is influenced by the morphological instability of the mass transport limited copper deposition reaction and the development of growth twins during iron-group metal deposition. Specular films have been obtained for growth on Cu(100) while rough, defective films were typically obtained for growth on Cu(111) and Cu(110).

### INTRODUCTION

Over the last ten years a large effort has been focused on the synthesis and characterization of compositionally modulated alloys [1]. These materials offer several interesting properties ranging from enhanced hardness to giant magnetoresistance. In this paper, the growth and structure of Cu/Ni and Cu/Co multilayers will be examined. Superlattices of Cu/Ni represent a model system for understanding dislocation dynamics in compositionally modulated solids. This follows from Cu and Ni having the same fcc crystal structure and similar lattice parameters (~ 2.6 % misfit). From a different perspective, the magnetic properties of Cu/Co multilayers have received much attention and GMR values as high as 60% at room temperature have been reported. In fact, there are several reports describing the interesting mechanical and magnetic properties of these materials [2-6]. Unfortunately, relatively little attention has been given to correlating the processing parameters with the resulting microstructures. In this paper a selection of experiments addressing this issue will be presented.

### EXPERIMENTAL DETAILS

Single crystal Cu (100), (110) and (111) disks were cut from 2.5 cm diameter cylindrical single crystal ingots. Each crystal was mechanically polished to a 0.1  $\mu\text{m}$  diamond finish followed by electropolishing in 85 vol% phosphoric acid [7]. The orientation was verified by Laue X-ray diffraction. After extensive rinsing with water the substrate was transferred to the electrochemical cell. The cell was comprised of a Pyrex glass cylinder with the working and counter electrodes mounted in glass-reinforced PTFE blocks located at opposite ends of the cylinder. The Pt mesh counterelectrode was separated from the main compartment by a Nafion membrane. A saturated mercurous sulfate (SSE) or saturated calomel electrode (SCE = SSE + 0.400 V) was located in an external cell which was connected to the working electrode compartment via a Luggin capillary. The capillary terminated as a fine hole drilled in the side of the working electrode compartment PTFE cylinder such that the tip was < 1mm from the electrode. For depositing Cu/Ni multilayers the electrolyte was 1.5 mol/L  $\text{Ni}(\text{SO}_3\text{NH}_2)_2$  (Fluka), 0.5 mol/L  $\text{H}_3\text{BO}_3$  and 0.009 mol/L  $\text{CuSO}_4$  with a pH of 3.5. In the case of Cu/Co multilayers the electrolyte was 1.5 mol/L  $\text{CoSO}_4$ , 0.5 mol/L  $\text{H}_3\text{BO}_3$  and 0.008 mol/L  $\text{CuSO}_4$  with a pH of 3.5. The kinetics of nickel and cobalt deposition were initially investigated in copper-free electrolytes. The electrochemical cell was deaerated for ~ 1/2 hour immediately prior to immersion of the copper substrate. Following immersion of the substrate, the cell was sealed and the gas flow terminated such that film growth occurred under stagnant conditions. The films were grown under potentiostatic control with a programmed coulometer used to toggle the potential between appropriate values.

## RESULTS AND DISCUSSION

Nickel and cobalt were deposited under charge transfer control from a sulfamate and sulfate electrolyte, respectively. Consideration of the conductivity of the electrolytes (0.0597 and 0.0464 S/cm) indicates that for practical current densities of 5-50 mA/cm<sup>2</sup>, a significant iR drop will exist in the electrolyte. This will lead to spatial dispersion of the deposition rate, i.e. film thickness, across the sample unless appropriate cell design measures are implemented. In this study a uniform current distribution was assured by using a tubular recessed electrode template, with an aspect ratio, length/diameter  $\approx 3$  [8]. It is interesting to note that electrodeposition of multilayer wires has benefited, either knowingly or unknowingly, from the uniform primary current distribution associated with the high aspect ratio of the porous polycarbonate or alumina membranes used as wire templates [5].

Deposition of nickel and cobalt exhibit many similarities although the chemical reversibility of the respective reactions differ greatly. Anodic dissolution of nickel is inhibited in chloride-free media by the formation of a hydrated nickel oxide film as indicated in Fig. 1. In order to prevent nickel oxide from being incorporated into the multilayer film, the potential of freshly deposited nickel should not be raised above  $\sim -0.250$  V SCE. In contrast to nickel, significant cobalt dissolution may occur at positive potentials as revealed by the deposition and stripping of cobalt shown in Fig. 2. In order to avoid significant dissolution the potential of freshly deposited cobalt should not be raised above  $-0.960$  V SSE. The chief consequence of these potential limits is

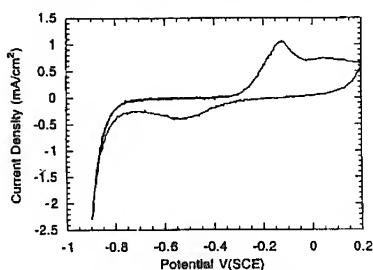


Fig. 1. Voltammetry revealing passivation of freshly electrodeposited nickel on a copper substrate, sweep rate was 0.1 V/s

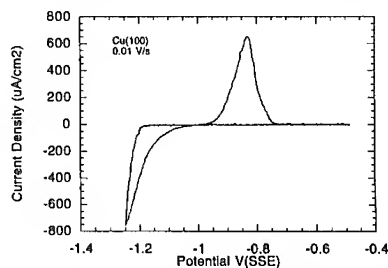


Fig. 2. Voltammetry of freshly deposited cobalt on Cu(100), Sweep rate was 0.01 V/s.

that copper deposition from an electrolyte containing a millimolar concentration of Cu<sup>++</sup> occurs under transport control. This is shown in Fig 3. where the potential of the freshly prepared electrode is stepped from  $-0.384$  to  $-0.960$  V and the current decay is monitored. The Cu<sup>++</sup> concentration at the interface goes to zero immediately and the current decreases following a  $t^{-1/2}$  relationship until a steady-state deposition rate of 1/3 of a monolayer of copper per second is reached. This corresponds to an average boundary layer thickness of  $\sim 360$   $\mu\text{m}$ . A typical

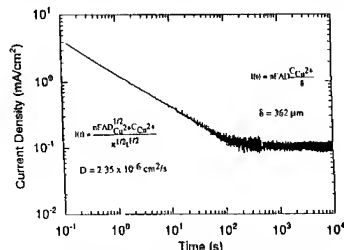


Fig. 3. Initial current transient for copper deposition on Cu(100).

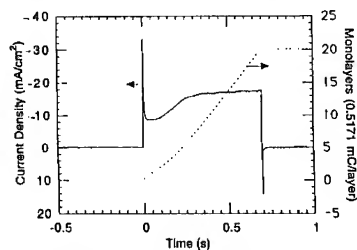


Fig. 4. Current transients for the nickel deposition during growth of a Cu/Ni multilayer.

growth cycle begins with copper being deposited under steady-state conditions until a specific charge has accumulated. The potential is then stepped to a more negative value where nickel or cobalt is deposited. A typical transient is shown in Fig 4. for nickel deposition. The background current associated with copper is constant which makes estimating the copper contamination of the nickel layer straightforward and typically amounts to  $\sim 1$  at%. The current transients indicate that on the order of five equivalent monolayers of nickel are deposited prior to reaching a steady-state growth rate. The simplest interpretation of this heteroepitaxial current transient would be that it takes on the order of five monolayers to completely cover the copper substrate under these conditions [9]. A closer and more thorough analysis of these transients will help determine the shortest wavelength that can be grown while maintaining a pin-hole-free multilayer geometry. The transients also provide a useful measure of the stability of film growth. During growth of an ideally laminated multilayer, the transients should be of the same shape and magnitude between successive bilayer cycles. This is observed to be case for Cu/Ni and Cu/Co multilayer growth on Cu(100). However, monitoring the transients for Co deposition during Cu/Co growth on Cu(111) reveals a change in the shape of the transients during film growth as shown in Fig 5. This reflects a change in the character of the periodic heteroepitaxial growth interface. There appears to be a one to one correlation between the reproducibility of sequential heteroepitaxial nickel or cobalt current

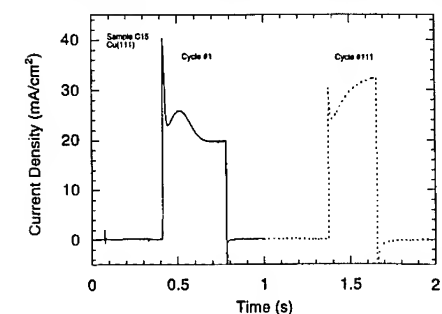


Fig. 5. Current transients for cobalt deposition on Cu(111) during multilayer growth.

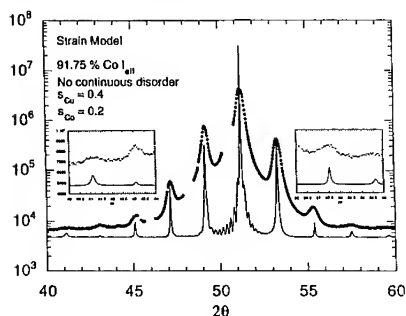


Fig 6. High angle X-ray diffraction for a  $[\text{Co}(2.29 \text{ nm})/\text{Cu}(2.46 \text{ nm})]_{112}$  multilayer grown on Cu(100).

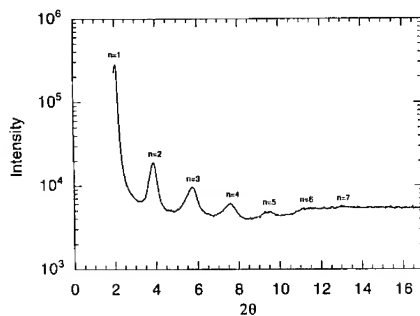


Fig 7. Low angle X-ray diffraction for a  $[\text{Co}(2.29 \text{ nm})/\text{Cu}(2.46 \text{ nm})]_{112}$  multilayer grown on Cu(100).

**Interfacial Roughness** - It is usually observed that the width of the growth interface scales with film thickness. Evolution of roughness may be associated with both homoepitaxial and heteroepitaxial processes. Kinetic roughening (e.g. step edge barriers), twinning, and instability of mass transport limited reactions are examples of the former, while strain-induced islanding may be associated with the latter. The implication of these roughening processes is that the roughness per interface in a multilayer will typically increase with an increasing number of bilayers. However, in some



instances a deposited layer can "heal" or level the roughness associated with the previous layer. In this instance roughness depends more strongly on the constituent layer thickness than on the total film thickness. Consequently, roughness evolution during multilayer growth can be described as either correlated or uncorrelated, cumulative or otherwise[10]. Depending on the specific conditions, any of the above description may be applicable to multilayer growth.

**Morphological Instability During Mass Transport Limited Reactions** - The linear stability of a mass transport limited process is a generic problem that is relevant to several different processing technologies. The stability of a solid surface may be evaluated by monitoring the amplification or attenuation of a small perturbation randomly imposed on the growing interface. The electrochemical problem was first developed in the early 1980's [11, 12]. Applying this treatment to mass transport limited copper deposition from a 0.008 mol/L  $\text{Cu}^{++}$  solution yields the curve shown in Fig 8. The low wavelength cut-off is a consequence of the stabilizing influence of surface tension and the facile nature of surface diffusion as reflected in the product of the surface diffusion coefficient and the adatom concentration. The parameters used in the model are listed in the figure. The diffusion coefficient is two orders of magnitude above that observed for Cu(100) in vacuum [13]. This is congruent with the observation of enhanced surface diffusion of copper in the presence of halide [14], which is a likely trace contaminant in the present study. The diffusion coefficient is also consistent with one possible interpretation of recent STM data obtained for copper deposition on Cu(100) in halide media[15]. The stability model indicates that perturbations should develop on the surface, with a dominant wavelength on the order 0.4-0.5  $\mu\text{m}$ . The reciprocal of the amplification factor may be viewed as the induction time for a given wavelength to develop. This yields an induction period on the order of 2500 seconds which corresponds to the deposition of 150 nm of copper. An SEM image of a 280 nm thick copper film deposited under mass transport control at -0.960 V SSE is shown in Fig 9. The dominant wavelength of the roughness is on the order of  $\sim 0.4 \mu\text{m}$ . It is interesting to note that electrodeposition of "one dimensional" wire structures with nanometer cross-sections [5] will probably not be susceptible to the linear stability problem outlined above since the diffusion fields associated with copper deposition in the neighboring pores of the plating template will be independent of each other and the dimensions of the pores are often below the cut-off for amplification of a perturbation.

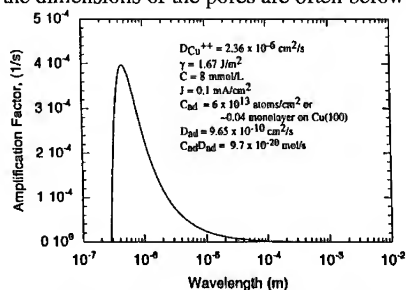


Fig. 8. Amplification factor versus the spatial frequency of the perturbation.

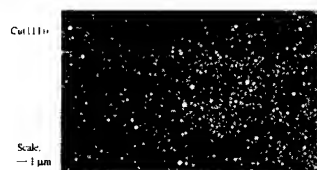


Fig 9. An SEM image of a  $\sim 280 \text{ nm}$  thick copper film grown under mass transport control on Cu(111).

A key question is whether or not such roughness is propagated in a cumulative manner through a multilayered film. This was investigated by growing a series of Cu/Co multilayers with fixed modulation wavelength and film thickness but with variable thickness of the constituents comprising the bilayers. For Cu/Co multilayers grown on Cu(100), with a 4.7 nm wavelength, the roughness is observed to increase as the copper content is increased. As shown in the SEM images, Figs. 10-12., roughness with a characteristic length scale  $\sim 0.5 \mu\text{m}$  is dominant. Growth of similar films on Cu(111) and Cu(110) reveals a much larger roughness amplitude as shown in Fig 13-14. The increased roughness compared to films grown on Cu(100) suggests that a degree of leveling occurs during cobalt deposition on Cu(100). Thus, increasing the cobalt thickness in a bilayer enables thicker films to be grown for a given roughness. In contrast, roughness associated with the morphological instability of copper deposition appears to be cumulative during multilayer

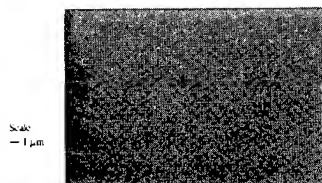


Fig 10. [Co(3.05 nm)/Cu(1.64 nm)]<sub>112</sub>  
Cumulative copper thickness is ~184 nm.  
Cu(100) substrate

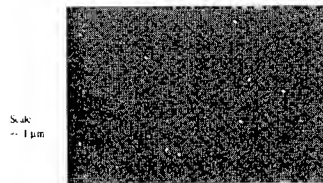


Fig 11. [Co(2.29 nm)/Cu(2.46 nm)]<sub>112</sub>  
Cumulative copper thickness is ~276 nm.  
Cu(100) substrate

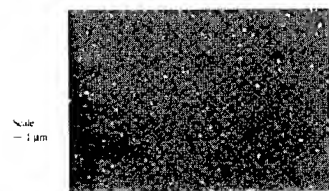


Fig 12. [Co(1.53 nm)/Cu(3.28 nm)]<sub>112</sub>  
Cumulative copper thickness is ~367 nm  
grown on Cu(100)

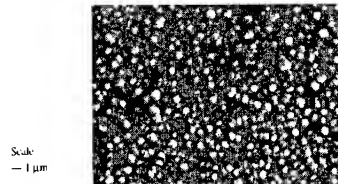


Fig 13. [Co(2.65 nm)/Cu(2.89 nm)]<sub>112</sub>  
Cumulative copper thickness ~324 nm  
grown on Cu(110)

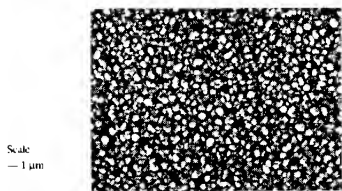


Fig 14. [Co(2.65 nm)/Cu(2.89 nm)]<sub>112</sub>  
Cumulative copper thickness ~ 324 nm  
grown on Cu(111).

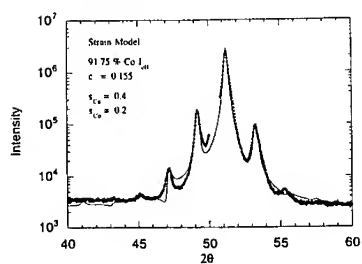


Fig 15. High angle X-ray diffraction for a  
[Co(2.29 nm)/Cu(2.46 nm)]<sub>112</sub> multilayer  
grown on Cu(100)

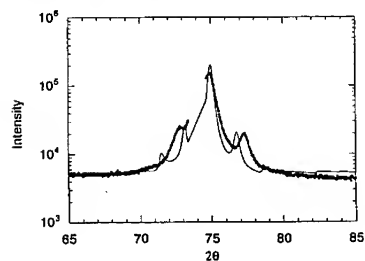


Fig 16. High angle X-ray diffraction for a  
[Co(2.65 nm)/Cu(2.89 nm)]<sub>112</sub> multilayer  
grown on Cu(110)

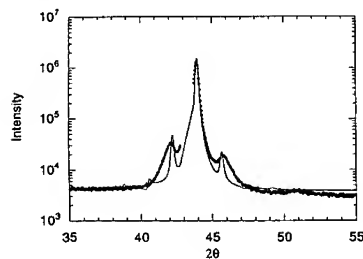


Fig 17. High angle X-ray diffraction for a  
[Co(2.65 nm)/Cu(2.89 nm)]<sub>112</sub> multilayer  
grown on Cu(111)

growth on Cu(110) and Cu(111). Other factors, such as growth twins and polymorphism of cobalt combined with different surface tension and mobility parameters for copper on Cu(111) and Cu(110) may also contribute to roughness evolution. The structural dispersion associated with these defective multilayered films is clearly revealed by high angle X-ray scattering as shown in Figs. 15-17. The solid lines in the figure represent simulations based on the fitting parameters used for the multilayer film grown on Cu(100). This includes parameters such as the discrete and continuous errors [16] associated with the growth of each successive Cu or Co layer. It is clear that the significant change in roughness with film thickness will lead to significant variation in the wavelength through the film resulting in the broad satellite structure shown for Cu(110). In contrast to the dominant influence of the mass transport deposition reaction on the evolution of roughness of Co/Cu multilayers, twinning is observed to be the dominant defect in Cu/Ni multilayers investigated to date [17].

## CONCLUSIONS

The single electrolyte method of multilayer deposition may be generalized to systems incorporating chemically reversible reactions such as cobalt deposition and dissolution. However, close consideration of the morphological stability of the process is required. High quality strained-layer superlattices of Cu/Ni and Cu/Co may be grown on Cu(100). In contrast, the microstructure of multilayers grown on Cu(110) and Cu(111) are highly defective and deviate significantly from the desired layer structure. This arises from twinning during growth of the iron group metal and/or instability of the growing interface associated with the mass transport limited copper deposition reaction.

## ACKNOWLEDGMENTS

The author gratefully acknowledges the support of Gery Stafford and the NIST Nanostructural Initiative Program

## REFERENCES

1. Structure and Properties of Multilayer Thin Films, eds. T. Nguyen, B. Larson, B. Clemens, S.-C. Shin and K. Sato, V382, MRS, Pittsburgh (1995).
2. S.S. Parkin, *Annu. Rev. Mater. Sci.*, 25, 357 (1995).
3. S.K.J. Lenczowski, M.A.M. Gijs, J.B. Giesbers, R.J.M. van de Veerdonk and W.J.M. de Jonge, *Phys. Rev. B*, 50, 9982 (1994); S.K.J. Lenczowski, C. Schonenberger, M.A. M. Gijs and W.J.M. de Jonge, *J. Magn. Magn. Mater.*, 148, 455 (1995).
4. M. Alper, P.S. Aplin, K. Attenborough, D.J. Dingley, R. Hart, S.J. Lane, D.S. Lashmore and W. Schwarzacher, *J. Magn. Magn. Mater.*, 126, 8 (1993).
5. K. Liu, K. Nagodawithana, P.C. Searson and C.L. Chien, *Phys. Rev. B*, 51, 7381 (1995); and ref. therein.
6. D. Tench and J. White, *Met. Trans.*, 15A, 2039 (1984).
7. R. Vidal and A.C. West, *J. Electrochem. Soc.*, 142, 2682 (1995); *ibid* 142, 2689 (1995).
8. A. West and J. Newman, *J. Electrochem. Soc.*, 138, 1620 (1991).
9. J.A. Harrison and H.A. Thirsk, *Electroanalytical Chemistry*, 5, 67 (1971).
10. E.E. Fullerton, J. Pearson, C.H. Sowers, S.D. Bader, X.Z. Wu, and S.K. Sinha, *Phys. Rev. B* 48, 17432 (1993).
11. R. Aogaki, K. Kitazawa, Y. Kose and K. Fueki, *Electrochimica Acta*, 25, 965 (1980).
12. R. Aogaki and T. Makino, *J. Electrochem. Soc.*, 131, 40 (1984).
13. J.J. De Miguel, A. Sanchez, A. Cebollada, J.M. Gallego, J. Ferron and S. Ferrer, *Surf. Sci.*, 189/190, 1062 (1987).
14. G.E. Rhead, *Surf. Sci.*, 47, 207 (1975).
15. T.P. Moffat, *In Situ Electron and Tunneling Microscopy of Dynamic Processes*, V-404, eds. R. Sharma, P. Gai, L. Whitman, M. Josifovska, and R. Sinclair, MRS, Pittsburgh, PA (1996).
16. E.E. Fullerton, I.K. Schuller, H. Vanderstraeten and Y. Bruynseraede, *Phys. Rev. B*, 45, 9292 (1992).
17. T.P. Moffat, *J. Electrochem. Soc.*, 142, 3767 (1995).

## MAGNETORESISTIVE PROPERTIES OF QUASIPERIODIC METALLIC MULTILAYERS

M. Shima\*, L. Salamanca-Riba\*, and L. J. Swartzendruber\*\*

\*Department of Materials and Nuclear Engineering, University of Maryland, College Park, MD 20742

\*\*National Institute of Standards and Technology, Gaithersburg, MD 20899

### ABSTRACT

Fibonacci Ni/Cu multilayers were fabricated by electrodeposition for the first time. The deposition of these quasiperiodic as well as periodic multilayers was fully controlled by a computer. X-ray diffraction spectra from a quasiperiodic multilayer built up from blocks of Ni(8ML)/Cu(4.5ML) and Ni(8ML)/Cu(9ML) indicate that the multilayer is of good quality. Since a Fibonacci multilayer has a quasiperiodic nature, the magnetoresistance effect in this system is expected to give more information about the mechanism for magnetic interlayer coupling in the GMR effect. The magnetic and magnetoresistive properties of the quasiperiodic multilayer were compared with those of two periodic multilayers having the equivalent layer thicknesses as the blocks composing the quasiperiodic multilayer. The magnetic and electrical properties of the quasiperiodic multilayer are not the weighted average of the two periodic multilayers.

### INTRODUCTION

Metallic multilayers have been extensively studied for decades because of their potential importance for various technological applications. The Giant Magnetoresistance (GMR) effect has been observed in many metallic multilayers consisting of alternating magnetic and nonmagnetic (or spacer) layers such as Co/Cu and Ni/Cu systems. In many of such multilayers, an oscillatory dependence of the magnetoresistance on the spacer layer thickness has been observed[1]. The oscillatory dependence has been observed and is due to an oscillatory change in the magnetic coupling between the magnetic layers from antiferromagnetic to ferromagnetic with increasing spacer layer thickness. The oscillatory dependence of GMR can be explained by the RKKY mechanism, first proposed for nuclear spins and transition metal magnetic impurity systems[1][2]. The long-period RKKY-like oscillatory behavior in multilayers can be explained fairly well if structural information such as the lattice periodicity is considered[2]. This model predicts an oscillation in GMR as the separation between the magnetic layers is increased. However, at the present time there is still some controversy as far as whether or not the interfaces between the layers play a role in GMR. It is also not well known if long range interactions are important in the magnetic properties of these materials.

Since the discovery of a quasicrystalline phase in metallic alloys[3], quasicrystals and quasiperiodic metallic systems have gained considerable attention. Moreover, owing to recent developments in thin film preparation techniques, it is now possible to prepare one-dimensional (1D) quasiperiodic multilayers. The two best-known examples of 1D quasiperiodic structures are the Fibonacci and the Thue-Morse sequences[4]. The Fibonacci sequence can be produced by repeated application of the substitution rule;  $A \rightarrow AB$  and  $B \rightarrow A$ . Most of the experimental work has focused on Fibonacci sequence superlattices except for a few studies on Thue-Morse sequences[5].

Since a quasiperiodic structure can be regarded as an intermediate between periodic and disordered structures, it is expected to give more information on the oscillating coupling mechanism in these materials. The role of interfaces could also be investigated if the interaction between adjacent interfaces is important for the GMR effect. Although there have been extensive studies on the magnetic properties of Ni/Cu multilayers[6][7][8][9], to our knowledge no systematic work has been done on the magnetoresistive properties of quasiperiodic multilayers.

The Fibonacci sequence can be obtained by repeated applications of the concurrent substitution rules for blocks A and B, namely,  $A \rightarrow AB$  and  $B \rightarrow A$ . The successive application of these rules gives the following sequence,  $A \Rightarrow AB \Rightarrow ABA \Rightarrow ABAAB \Rightarrow ABAABABA \Rightarrow \dots$ , etc.[9]. The ratio of the two incommensurate intervals approaches the golden mean  $\tau = (1+\sqrt{5})/2$ . By starting with two building blocks A and B, each composed of Cu and Ni, for example, to ensure that a Cu layer is always above a Ni layer and vice versa, one can fabricate a Fibonacci sequence where the n-th order string of A and B is composed of strings from two previous orders. This is illustrated in Fig. 1, along with the structures of the blocks A and B. The blocks A and B consist of x monolayers (ML) of Ni and y ML of Cu, and x ML of Ni and z ML of Cu, respectively. If the thicknesses, D, of blocks A and B are in the ratio of the golden mean  $\tau$ , i.e.,  $D_A / D_B = (1+\sqrt{5})/2 = \tau$ , stronger satellite peaks in the X-ray spectra are observed as explained below.

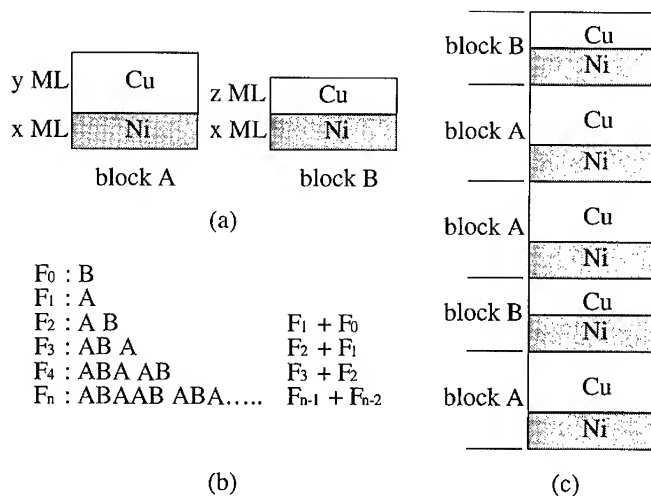


Fig. 1 Schematic diagrams of a Fibonacci sequence multilayer.  
 (a) The two building blocks consisting of Ni and Cu layers.  
 (b) Fibonacci sequence. (c) The stack of the quasiperiodic multilayer.

The multilayers defined above have two different modes. One corresponds to the average reciprocal lattice vector of the crystal,  $K_0$ , and the other has a wave vector that depends on the nature of the superlattice,  $K_S$ . For a periodic superlattice,

$$K_S(m) = 2\pi m D^{-1} \quad (1-a)$$

where  $m$  is an integer,  
and

$$D = D_A + D_B. \quad (1-b)$$

is the period of the superlattice with  $D_A$  and  $D_B$ , the thicknesses of the A and B layers, respectively. For a quasiperiodic superlattice,

$$K_S(m, n) = 2\pi(m+n\tau)D^{-1} \quad \text{or} \quad K_S(n, p) = 2\pi D^{-1} n \tau^p \quad (2-a)$$

and

$$D = \tau D_A + D_B. \quad (2-b)$$

Satellites in the X-ray diffraction spectra can be observed when  $m$ ,  $n$ , and  $p$  are integers.

In this work, the magnetic and magnetoresistive properties of Fibonacci sequence multilayers are compared to those of periodic multilayers having equivalent layer thicknesses, i.e., two multilayers with different Cu layer thicknesses and the same Ni layer thickness.

## EXPERIMENTAL DETAILS

A Ni/Cu Fibonacci sequence multilayer and two periodic multilayers were prepared by the electrodeposition technique. The multilayers were deposited onto an annealed polycrystalline (100) textured copper substrate using a very high speed coulometer interfaced with a personal computer in which the measured current is digitally integrated. The substrate was polished electrochemically before deposition to obtain a clean and flat surface. The electrodeposition of the multilayers was carried out in a single cell containing Ni and a very dilute amount of Cu ions. The electrolyte composition was 90 g/l Ni as metal (Ni-sulfamate), 0.9 g/l Cu as metal (Cu-sulfate pentahydrate), and 30 g/l boric acid. The potential was alternated between -0.2 V and -1.6 V to obtain sequential deposition of Cu and Ni. At the low potential, only the more noble Cu metal is deposited. When the potential is set at a value corresponding to the less noble metal, then both metals are reduced at a rate limited by the relative concentrations in the solution. The result is a layered structure of Cu alternating with Ni having a low (<5%) Cu content. The individual layer thicknesses of a periodic multilayer P1 were chosen to be  $x = 11$  ML and  $y = 9$  ML and those of multilayer P2 were  $x = 11$  ML and  $z = 5$  ML. The quasiperiodic multilayer Q was designed to have 233 bilayers to complete the 12th Fibonacci sequence which consists of 144 bilayers of A blocks and 89 bilayers of B blocks. The designed layer thicknesses in block A were the same as those in multilayer P1, namely,  $x = 11$  ML and  $y = 9$  ML, while those in block B were the same as those in multilayer P2, namely,  $x = 11$  ML and  $z = 5$  ML. The layered structures were studied by x-ray diffraction  $\theta$ - $2\theta$  scans carried out with the scanning vector normal to the film surface. The magnetization of the electrodeposited samples was studied utilizing vibrating sample magnetometry. The magnetoresistance measurements were carried out using a conventional four point probe technique with a lock-in amplifier. All data were obtained on free standing films after etching the substrate away with a solution of 15 ml  $H_2SO_4$  and 500 g/l  $CrO_3$ .

## RESULTS AND DISCUSSION

The X-ray spectra of the Ni/Cu multilayers are shown in Fig. 2. Satellite peaks associated with the quasiperiodicity are observed on both sides of the main (200) Bragg reflection indicating that the quasiperiodic multilayer is of good quality. Clear superlattice satellite peaks are observed in the

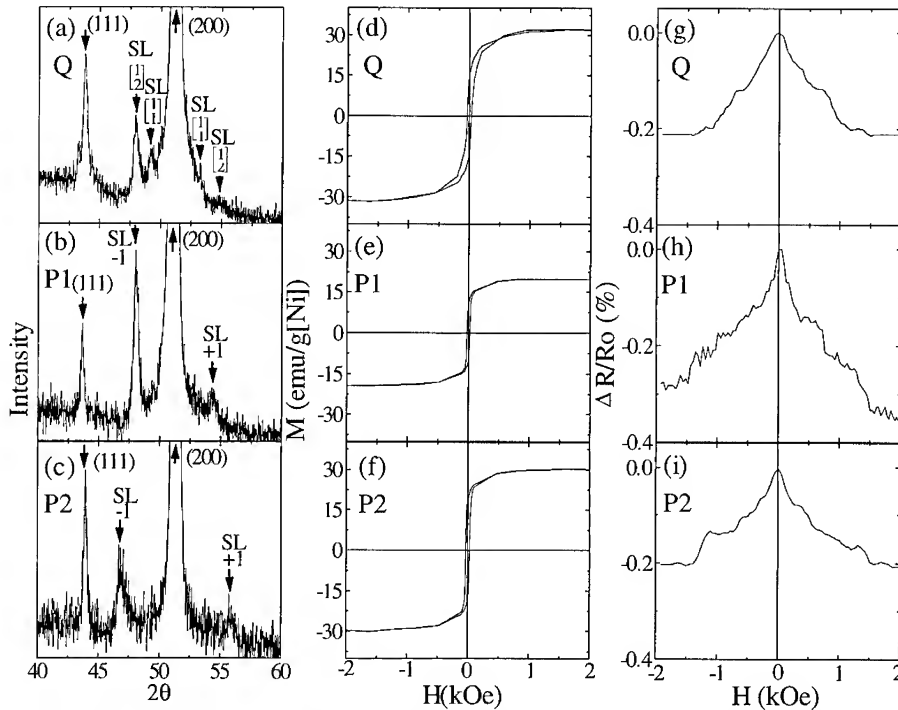


Fig. 2  $\theta$ -2 $\theta$  X-ray diffraction spectra for (a) Q, (b) P1 and (c) P2; hysteresis loops for (d) Q, (e) P1 and (f) P2 and magnetoresistance curves for (g) Q, (h) P1 and (i) P2.

spectra of both periodic multilayers, P1 and P2 as shown in Figs.2(b) and 2(c), respectively. The (111) Bragg reflection is observed because the Cu substrates were polycrystalline with (100) texture but had some (111) oriented grains which were reproduced in the multilayer. Using eq.(1-a) and the satellite peak positions in the X-ray spectra, the modulation wavelengths of P1 and P2 are calculated to be  $D = 31 \text{ \AA}$  and  $22 \text{ \AA}$ , respectively. The asymmetry of the intensity of the satellite peaks indicates that the multilayers are strained. For example, the out-of-plane components of the lattice strain are estimated to be  $\epsilon_{Cu} \approx -0.016$  and  $\epsilon_{Ni} \approx 0.01$  for the Cu and Ni layers, respectively. However, a lower strain is expected to occur in (100)-textured

electrodeposited Ni/Cu multilayers due to the incorporation of Cu in the Ni layers[10] which is about 5%. It is, therefore, assumed that the multilayer (200) peak position,  $\theta_{ML}$ , is not affected by lattice distortion but linearly determined by the relative concentrations of Ni and Cu in the multilayer, and the peak positions of pure Ni and Cu,  $\theta_{Ni}$  and  $\theta_{Cu}$ . Namely,  $\theta_{ML} = (1-\alpha)\theta_{Ni} + \alpha\theta_{Cu}$ , where  $\alpha$  is the relative concentration of Cu in the multilayer. The individual layer thickness is estimated such that  $D = (1-\alpha)d_{Ni} + \alpha d_{Cu}$  where  $d_{Ni}$  and  $d_{Cu}$  are the Ni and Cu layer thicknesses, respectively. The results are shown in Table I. The thicknesses of the Cu layers agree fairly well with the designed values, however, those of the Ni layers are slightly smaller than the designed values. This difference is due to a slight dissolution of Ni during the Cu deposition. Using the estimated thicknesses of the Cu and Ni layers, we estimated the peak positions in the X-ray spectrum from the Fibonacci multilayer and obtained good agreement with the satellite positions in the X-ray spectrum shown in Fig. 2(a).

The hysteresis loops from samples Q, P1 and P2 were obtained in a magnetic field of up to 2 kOe as shown in Figs.2(d), (e) and (f), respectively. The obtained values of the saturation magnetization,  $M_s$ , coercive field,  $H_c$ , and saturation field,  $H_s$ , are summarized in Table I.

Table I Experimental data for Ni/Cu multilayers.

Sample	Type	Total thickness ( $\mu\text{m}$ )	Cu layer thickness (ML)	Ni layer thickness (ML)	$M_s$ (emu/g(Ni))	$H_c$ (Oe)	$H_s$ (Oe)	$\Delta R/R_0$ (%)
Q	Fibonacci	0.6	block-A : 9 block-B : 4.5	block-A : 8 block-B : 8	32	36	950	-0.21
P1	periodic	0.6	9	8	20	24	700	-0.36
P2	periodic	0.7	4.5	8	30	31	750	-0.20

Figs.2(g), (h) and (i) show the transverse magnetoresistance  $\Delta R/R_0 = (R(H)-R_0)/R_0$  curves for samples Q, P1 and P2, respectively.  $R(H)$  and  $R_0$  are the resistance in a magnetic field  $H$  and that in  $H = 0$ , respectively. All of the multilayers show negative magnetoresistance effect, though the resistivities saturate at  $H \approx 1.0$  kOe, 1.5 kOe and 1.4 kOe for samples Q, P1 and P2, respectively. These values are larger than the saturation fields,  $H_s$ , obtained from the hysteresis loops probably due to other scattering contributions. Comparing the absolute values of the MR in the Fibonacci and periodic multilayers we can see that  $|\Delta R/R_0(Q)| = 0.21\%$  is smaller than  $|\Delta R/R_0(P1)| = 0.36\%$  and rather close to  $|\Delta R/R_0(P2)| = 0.20\%$ . The sensitivity, which is defined as  $(\Delta R/R_0)/(H_0-H_s)$ , where  $H_0$  is zero field, in Q is  $0.22\%/kOe$ , which is smaller than  $0.51\%/kOe$  in P1 and rather close to  $0.27\%/kOe$  in P2. It is interesting to note that multilayer Q behaves more like P2 even though it has more A blocks (like P1) than B blocks (like P2). Moreover,  $H_c(Q) = 36$  Oe is larger than  $H_c(P1) = 24$  Oe and  $H_c(P2) = 31$  Oe, indicating that the mechanism of the magnetic interlayer coupling in the quasiperiodic multilayer may be different from that in the periodic multilayers. Thus, the magnetic and electric properties of the quasiperiodic multilayer are not the weighted average of the two periodic multilayers. The results presented here suggested that next nearest neighbor interactions might be important in these materials. The exact nature of the MR behavior in these quasiperiodic multilayers still needs further investigation.



## CONCLUSIONS

We presented the first magnetoresistance studies in quasiperiodic Fibonacci multilayers in the Ni/Cu system. We compared these results to those of equivalent periodic multilayers. The magnetic and electric properties of the quasiperiodic multilayer are not the weighted average of the two periodic multilayers. Further investigation is required to understand the GMR effect in these multilayers.

## ACKNOWLEDGMENTS

The work was supported by the National Science Foundation Contract No. DMR9111516.

## REFERENCES

1. T. Shinjo and T. Tanaka, Editors, *Metallic Superlattices Artificially Structured Materials* (Elsevier, Amsterdam, 1987).
2. K.B. Hathaway, *Ultrathin Magnetic Structures II* ed. by B. Heinrich and J. A. C. Bland (Springer-Verlag, Berlin, Heidelberg, 1994) p.60.
3. D. Shechtman, I. Blech, D. Gratias and J. W. Cahn, *Phys. Rev. Lett.* **53**, 1951 (1984).
4. R. Merlin, *IEEE J. Quantum Electron.* **24**, 1791 (1988).
5. Z. Cheng, R. Savit and R. Merlin, *Phys. Rev. B* **37**, 4375 (1988).
6. Y. Zhang, "Giant Magnetoresistance of Electrochemically Produced Copper-Nickel Multilayers," Thesis submitted to the University of Maryland, (1994).
7. L.H. Bennett, L. J. Swartzendruber, D. S. Lashmore, R. Oberle, U. Atzmony, M. P. Dariel and R. E. Watson, *Phys. Rev. B* **40**, 4633 (1989).
8. K. D. Bird and M. Schlesinger, *J. Electrochem. Soc.* **142**, L65 (1995).
9. K. Kyuno, T. Kaneko, M. Sakuda, Sun Tianfu and R. Yamamoto, *J. Magn. Magn. Mater.* **126**, 158 (1993).
10. D. van Heerden, E. Zolotoyabko and D. Shechtman, *J. Mater. Res.* **11**, 2825 (1996).

## **ELECTROCHEMICAL STUDY ON THE GROWTH OF MULTILAYER FILM ELECTRODES OF THE CONDUCTING POLYMERS PPP, POT AND OF THE COPOLYMER OF PPP AND POT**

C. KVARNSTRÖM, R.-M. LATONEN, A. IVASKA

Åbo Akademi University, Laboratory of Analytical Chemistry, Biskopsgatan 8, FIN-20500 Åbo-Turku, Finland

### **ABSTRACT**

Multilayer polymer film electrodes were prepared from the electrochemically synthesized conducting polymers poly(paraphenylene), PPP, poly(3-octylthiophene), POT and from the electrochemically synthesized copolymer of PPP and POT. The electrochemical behavior of the multilayer film electrodes made from PPP and POT is compared with the response of a copolymer layer. The structure of the copolymer film could be changed by varying the polymerization potential and the concentration as well as the ratio of the concentration of the two starting materials. Due to the slightly lower (0.15 V) oxidation potential of the POT monomer in comparison to the oxidation potential of biphenyl, POT is usually present to a higher extent than PPP in the electrochemically produced copolymer. The copolymer electrodes, the single polymer film layers and the multilayer polymer film electrodes showed different electrochemical response of the charging-discharging cycle.

### **INTRODUCTION**

Multilayer and bilayer combinations of electroactive polymers were first reported by Murray et al. [1]. Since the introduction of the bilayer concept studies on different combinations of polymers have been reported. Among the more recent results presented on bilayer are the bilayers of polypyrrole(polystyrenesulfonate) combined with poly(3-octylthiophene) [2] and with poly(vinylferrocene) [3], polypyrrole with poly(N-methylpyrrole) [4] and polybithiophene with polyxylylviologen [5]. Potential applications for electroactive polymers in bilayer structures are in electronic devices [6], charge storage [7] and display devices [8]. Combining conducting polymers having separate redox processes also make them work as electrochemically controllable ion-transport membranes. The electrochemical switching of electrically conducting polymers between their neutral and their conducting states involves transfer of anions, cations and solvent in and out of the film. For ideal bi- or multilayer films of conducting polymers the interface between the polymer layers has to be well separated. This means that the deposition of the different polymers has to result in films with even and smooth surfaces. In cases where the film-film interface is ill defined the two polymers have mixed forming a thin layer of an undefined structure between the actual layers.

In this work the electrochemical behavior of bilayers of poly(paraphenylene), PPP and poly(3-octylthiophene), POT are compared with bilayers of POT or PPP combined with the copolymer made from POT and PPP.

### **EXPERIMENTAL**

Polymer films were prepared by galvanostatic polymerization or by potential cycling. The electrolyte in all experiments was (0.1 M) TBABF<sub>4</sub> (TBA=tetrabutylammonium, Fluka) in

acetonitrile (Aldrich, anhydrous 99+%). Biphenyl (99% Aldrich) was used as starting material for PPP and in the case of POT, 3-octylthiophene (Neste Oy Research Centre, FIN-06850 Kulloo, Finland) was used. All solutions were deaerated with nitrogen prior to measurements and the measurements were performed in nitrogen atmosphere. A conventional three-electrode electrochemical cell was used where the working electrode was a 0.07 cm<sup>2</sup> Pt-disk or ITO-glass and the auxiliary electrode was a glassy carbon rod. All potentials reported in this work are measured vs a Ag/AgCl/KCl (3M) reference electrode used in combination with a salt bridge filled with the electrolyte solution used in the experiment. The chemically made PPP was synthesized from the route of Kovacic et al. [9] and the chemically synthesized POT was obtained from Neste Oy.

## RESULTS

The film electrodes studied and the polymer structures are shown schematically in figure 1. Earlier studies have been reported on the bilayer combination of PPP/POT and POT/PPP [10,11] and therefore these bilayers will not be treated as thoroughly as the ones with the copolymer.

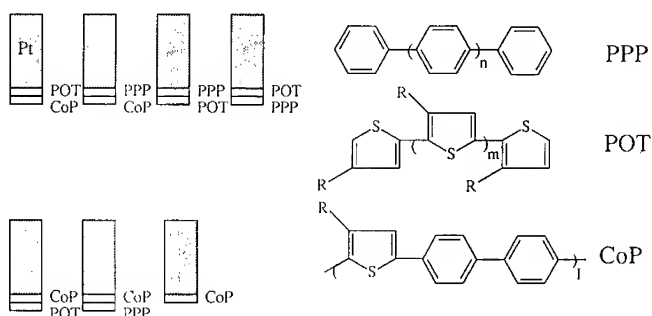


Figure 1. The different polymer film combinations studied. PPP indicates poly(paraphenylene), POT poly(3-octylthiophene) and CoP the copolymer made from 3-octylthiophene and biphenyl. The structure showing the CoP is the ideal structure with alternating units of both starting materials.

The peak potential for a single PPP film is around 0.8 V [12] and for a single POT film at around 1 V [13]. The charge involved in the redox response of a PPP film is only a fifth of the response of a POT film of similar thickness. From the studies of the Pt/PPP/POT bilayers it was found that the POT layer can act as an ion blocker in its semiconducting state [10,11]. In this way the redox response of the whole bilayer is controlled by the POT layer. This results in that only a single oxidation peak is observed in the redox response of a Pt/PPP/POT bilayer, i.e. at the potential where a single POT film is oxidized. An other effect that was found with this bilayer was that the PPP layer, when used as inner layer can be charged to a higher extent than when charged as a single layer [10]. This was explained to be due to further polymerization and cross linking reactions taking place in the PPP film during the polymerization of the POT layer on top of the PPP film.

In order to study if the characteristic behavior of PPP and POT in bilayers can be transferred to the copolymer material of the two polymers the copolymer was electrosynthesized and studied in bilayers. The structure of the copolymer is highly dependent on the polymerization parameters and the sequence of the two starting materials in the resulting copolymer can highly vary. The oxidation potential of the starting material for POT; 3-OT is approximately 150-200 mV lower than for the starting material for PPP; biphenyl. This leads to a faster polymerization of POT in synthesis routes where both starting materials are present. In order to control the growth of POT the concentration of 3-octylthiophene was kept much lower than the concentration of biphenyl. Also the potential at which the copolymer film is made (when made potentiostatically, end potential when made by potential cycling) highly determines the content and sequence of the two starting materials in the copolymer. Besides the electrochemical parameters also the color of the copolymer film was used as indicator of the degree of copolymerization. Single PPP films are to their color pale yellow to brownish depending on the thickness of the film. POT films again gold to red colored. In Table I the influence of the 3-octylthiophene concentration on the resulting copolymer can be seen. At the lowest concentration of 3-octylthiophene the highest value of charge involved in the redox reaction,  $q$ , as well as of peak currents,  $i$ , for oxidation and reduction of the film was obtained. At this combination of concentration of the starting materials the color of the resulting film was gold-brownish, which would indicate that a mixed material has been formed.

Table I. The influence of the concentration of the starting material of POT; 3-octylthiophene on the redox behavior of the resulting copolymer film. The film electrode is cycled in the potential range 0-1.2 V in (0.1 M) TBABF<sub>4</sub> -acetonitrile solution.  $q$  denotes the charge involved in the redox reaction of the film (obtained by integrating the area of the cv).  $i_{ox}$  and  $i_{red}$  are the peak currents for the oxidation and the reduction of the film, and  $E_{ox}$  and  $E_{red}$  denotes the peak potentials.

Table 1

3-OT [M]	Biphenyl [M]	$q$ [mC]	$i_{ox}$ [μA]	$i_{red}$ [μA]	$E_{ox}$ [V]	$E_{red}$ [V]	$\Delta E$ [mV]
0.03	0.1	0.68	94	70	1.00	0.92	80
0.05	0.1	0.59	85	76	1.00	0.95	50
0.08	0.1	0.48	76	48	1.05	0.95	100
0.1	0.1	0.45	59	39	1.08	1.00	80

The electropolymerization of the copolymer is shown in figure 2a. The polymerization is made by cycling between 0 and 1.8 V (vs Ag/AgCl) in (0.03 M) 3-octylthiophene-(0.1M) biphenyl solved in acetonitrile containing 0.1 M TBABF<sub>4</sub>. During the first cycles the oxidation of the formed material takes place in a broad potential range (0.7 V-1.1 V) indicating that the material formed undergoes many redox reactions obviously due to that the material is of copolymer type. High linearity was obtained when the charge used for polymerization vs the charge obtained from the adsorbed material during one potential cycle was plotted. This indicates a continuous growth of the copolymer material. In figure 2b the redox response of the resulting copolymer film from the polymerization in figure 2a can be seen. A very stable response is obtained where the redox peak potentials are the same as for a pure POT film but the peak currents are lower and the peaks

are broader. The redox response of a similar film but made from a solution containing 0.1 M 3-octylthiophene and 0.1 M biphenyl gives an almost identical cv-response as a pure POT film.

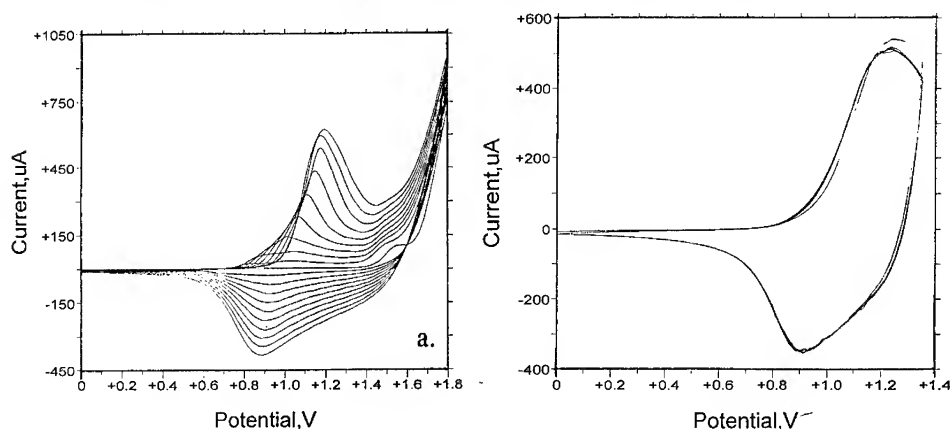


Figure 2a. The polymerization of a copolymer film by potential cycling at a scan rate of 100 mV/s. The film is made in (0.03M) 3-octylthiophene and (0.1 M) biphenyl solution, the electrolyte was (0.1 M) TBABF<sub>4</sub> in acetonitrile. 2b. The redox response of a copolymer film of PPP and POT made as in 2a, scan rate 100 mV/s.

The polymers POT and PPP were also chemically synthesized, dissolved and mixed in tetrahydrofuran after which films were solution casted on ITO electrodes. Chemically made POT is fully soluble in THF but in the case of PPP only the shorter oligomers are soluble in this solvent. The resulting film material is of composite character and consists of long POT chains mixed with PPP-oligomers. The film was electrochemically doped and the redox behavior of this material is shown in figure 3.

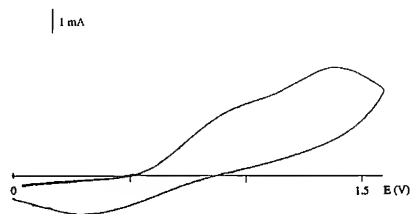


Figure 3. The cyclic voltammetric response of a solution casted film on a 1.2 cm<sup>2</sup> ITO electrode. The solution consists of chemically synthesized POT and PPP which are dissolved in THF. Potential cycling is made in acetonitrile containing (0.1 M) TBABF<sub>4</sub>. Scan rate is 100 mV/s.

Two oxidation peaks can easily be observed in the voltammogram the first peak is from the PPP-oligomers and is at a slightly lower potential as a pure PPP film, the second oxidation peak is from the POT chains in the film. By comparing the film of the composite type with the copolymer

film a clear difference in their redox response can be seen indicating that a real copolymer structure is built up during copolymerization.

Copolymer films were made as described in figure 2a, the total current used for polymerization was between 3 mC-16 mC. Bilayer electrodes were made by combining the copolymer with POT and PPP films. In figure 4a. the redox response of the bilayers Pt/PPP/CoP and Pt/POT/CoP is shown. The charge used for polymerization of the POT and the PPP layer was 10 mC. In both cases a single oxidation peak can be observed at a potential where the copolymer is oxidized at around 1.1 V. In the bilayer combination Pt/POT/CoP the oxidation peaks for both polymers when cycled as single layers coincide and the oxidation potential of the bilayer remains unchanged. However, in the Pt/PPP/CoP bilayer combination the oxidation potential of the PPP film should be approximately 200 mV lower than for the copolymer but only one broad oxidation peak is observed. This means that at least some of the ion blocking effect of the semiconducting pure POT film has been transferred to the copolymer structure. The ion blocking effect of the copolymer means that the inner PPP layer cannot become conducting before the outer copolymer layer is fully charged and permits transport of anions from the solution through itself to the inner PPP layer. In figure 4a it can also be seen that the charge involved in the Pt/PPP/CoP bilayer is higher than for the Pt/POT/CoP bilayer. This takes place despite that the charge of a single PPP layer is much lower than for a single POT layer of the same thickness. The same effect was observed in the Pt/PPP/POT bilayer [10] and was interpreted to be due to changes in the structure of PPP taking place during polymerization of the outer layer.

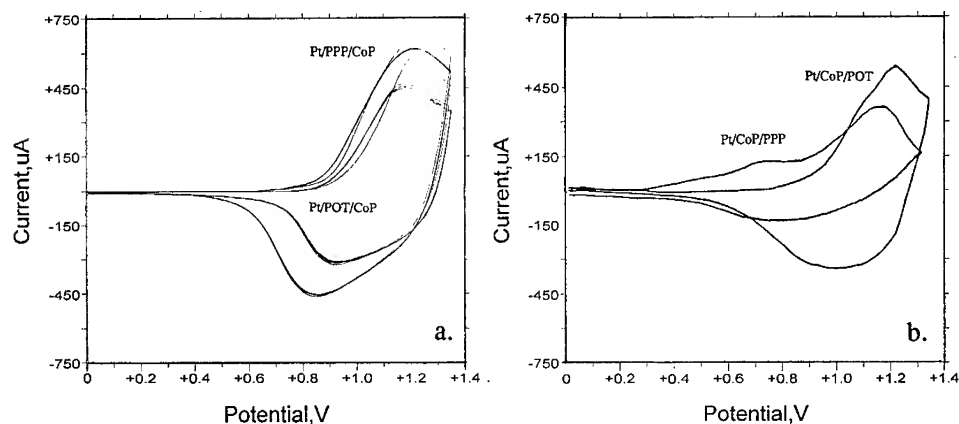


Figure 4a. The bilayer electrodes Pt/PPP(10mC)/CoP and Pt/POT(10mC)/CoP (the copolymer layer is made by 10 potential cycles between 0 and 1.8 V) cycled in (0.1 M) TBABF<sub>4</sub>-acetonitrile solution. 4b. shows the bilayers Pt/CoP/POT and Pt/CoP/PPP. The layers are polymerized in the same way as in 4a. Scan rate 100 mV/s.

In figure 4b the redox responses of the bilayer combinations Pt/CoP/PPP and Pt/CoP/POT are shown. A similar broad oxidation peak is seen in the Pt/CoP/POT electrode as for the bilayer where the copolymer was placed as outer layer. However, the charge involved in the bilayer combination Pt/CoP/POT is slightly higher than for the Pt/POT/CoP bilayer. This indicates that the polymer chains in the inner copolymer layer undergo further reactions upon polymerization of

the outer layer. The phenylene units inside the copolymer might undergo crosslinking reactions between the chains thus extending the conjugation between phenylene units. When the copolymer is cycled with a PPP layer as outer layer two distinct oxidation peaks are visible. In this bilayer combination the oxidation potential is lower for the outer film than for the inner film and therefore no ion blocking takes place. The inner copolymer film permits electron transfer through itself also in its semiconducting state and the outer PPP film can become oxidized at its "normal" potential, before the copolymer film. In figure 4b the oxidation peak at the lower potential (0.7 V) is interpreted to be from the PPP film and the peak at around 1.1 V from the copolymer layer. The reduction response of this bilayer is weak, which can be partly explained with that the PPP layer is slowly relaxing [10].

## CONCLUSIONS

The characteristic behavior of both POT and PPP when combined in bilayer structures has been shown to be transferred to the copolymer material made of the two polymers. The new copolymer material is easily polymerized and shows a stable redox response. The redox response of the copolymer differs clearly from the response of the material where the two polymers are mixed together forming a composite material. In bilayer combinations with POT and PPP films the copolymer film shows the ion blocking effect of POT and the increased charging effect of PPP. The mixed film characteristics of the new material shows that it is a real copolymer structure that has been synthesized.

## REFERENCES

1. H. D. Abruna, P. Denisevich, M. Umana, T.J. Meyer and R. W. Murray, *J. Am. Chem. Soc.*, 103, 1 (1981).
2. S. Demoustier-Champagne, J.R. Reynolds and M. Pomeranz, *Chem. Mater.* 7, 277 (1995).
3. M. Pyo and J.R. Reynolds, *J. Phys. Chem.* 99, 8249 (1995).
4. K. Maksymiuk, *J. Electroanal. Chem.*, 373, 97 (1994).
5. A. R. Hillman and A. Glidle, *J. Electroanal. Chem.*, 379, 365 (1994).
6. P.G. Pickup, W. Kutner, C.R. Leidner and R.W. Murray, *J. Am. Chem. Soc.*, 106, 1991 (1984).
7. Y. Morishima, Y. Fufushima and S. Nozakura, *Chem. Commun.*, 912 (1985).
8. P. Denisevich, K.W. Willman and R.W. Murray, *J. Am. Chem. Soc.* 103, 1427 (1981).
9. P. Kovacic, J. Oziomek, *J. Org. Chem.* 29, 100 (1964).
10. C. Kvarnström and A. Ivaska, *J. Electroanal. Chem.*, accepted.
11. C. Kvarnström and A. Ivaska, *Synth. Met.*, accepted.
12. C. Kvarnström and A. Ivaska, *Synth. Met.*, 41-43, 2917 (1991)
13. J. Bobacka, Z. Gao and A. Ivaska, *Synth. Met.* 55-57, 1453 (1993).

**Part VII**

**Electrodeposition of Metals and Alloys  
for Magnetic and Electronic Applications II**



## DEFECT STRUCTURE AND CRYSTALLOGRAPHIC TEXTURE OF POLYCRYSTALLINE ELECTRODEPOSITS

H. D. Merchant\* and O. B. Girin\*\*

\* Gould Electronics, Eastlake, Ohio 44095

\*\* State Metallurgical Academy of Ukraine, Prospekt Gagarina 4,  
Dnepropetrovsk 320635, Ukraine

### Abstract

The polycrystalline electrodeposits of metals and alloys are characterized by exceptionally fine, equiaxed grain structure; the grain sizes two to four orders of magnitude smaller than those encountered in the bulk metals are generally obtained. Under the conditions of high cation discharge rate, twins accommodate interface growth; elongated grains and columnar morphology then become the common features. The dislocation density can be very high; the dislocations reside primarily as complex substructural configurations which are inherently unstable to thermal or mechanical stimuli. Vacancies, microvoids and vacancy/impurity complexes are endemic to deposits. The defect structure infrastructure (dislocation density and configuration, twinning frequency and hydrogen bubbles) is controlled by the deposition overpotential which also determines the preferred crystallographic texture. When the texture axis is parallel to the twin plane, anisotropic grain structure and columnar morphology are promoted; when the texture axis is perpendicular to the twin plane, a layered structure forms. The textured electrodeposit generates a duplex grain and subgrain structure. The random grains are small and defect saturated; the oriented grains are much larger and relatively free from crystal defects. The incidence of random grains, their size and defect concentration also depend upon the melting temperature of the metal.

### Introduction

Three types of crystallographic defects occur in the polycrystalline electrodeposits: vacancies, dislocations and twins. The vacancies, vacancy clusters and vacancy-impurity complexes are endemic to deposits; they reside primarily in the grain and morphological boundaries.<sup>1</sup> The dislocations form a variety of substructural arrays on a scale much finer than the grain size;<sup>2</sup> unless stabilized (by additive to the electrolyte), these arrays are basically unstable to the thermal or mechanical stimuli. The coherent twins help accommodate interface growth when the adions arrive rapidly at the growing interface. The twins thread across the grain as parallel lamellae within the confines of the high angle boundaries. For a textured deposit, when the texture axis is parallel to (or makes a small angle with) the twin plane, vertical traces, corresponding to multiple twinning, appear in the deposit transverse cross-section.<sup>3</sup> Further, if considerable twinning has permeated the microstructure, the twinning promotes z-direction growth such that the grains become elongated along the twin plane.

These and other aspects of the electrodeposit microstructure have been discussed at length in recent reviews.<sup>2,4,5</sup> Figure 1 illustrates the mid-thickness planar view of a fine-grained (0.05-0.5  $\mu\text{m}$ , average 0.18  $\mu\text{m}$  grain size) 12  $\mu\text{m}$  thick copper deposit. Twinning has been suppressed by a surfactant addition to the electrolyte; the addition also eliminates a preferential z-direction growth and the grain size anisotropy. In view of the very fine grain structure, the substructural features are either absent or are difficult to discern. Figure 2 shows the defect saturated microstructure of a 35  $\mu\text{m}$  thick copper deposit. Twinning has been promoted by a catalyst addition (which enhances the cation discharge rate) to the electrolyte. Low density morphology boundaries (which contain several grains) (Figure 2a), twin lamellae traversing the grains (Figure 2b) and twin traces and columnar morphology in the transverse cross-section (Figure 2c) can be observed. Profusion of twinning obliterates the substructural details. Figure 3 shows the substructure of

nickel electrodeposit.<sup>6</sup> Coarse grains contain open portions of subgrain boundaries as well as broken and diffuse boundaries. For example, a large grain delineated by ABCD is comprised of subgrains slightly rotated with respect to each other and having boundaries which vary in sharpness. Subgrains 1 and 4 are separated by a broken diffuse boundary. Open portions of subboundaries in subgrains 2, 4, 5, and 6 are made by the dislocation pileups.

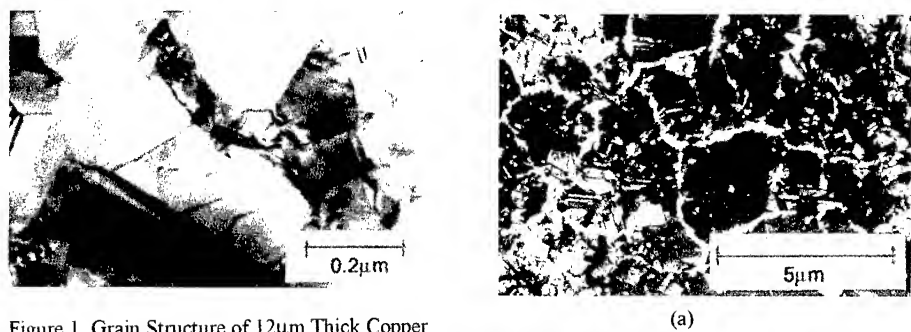


Figure 1. Grain Structure of 12μm Thick Copper Deposit, TEM Mid-thickness Planar View

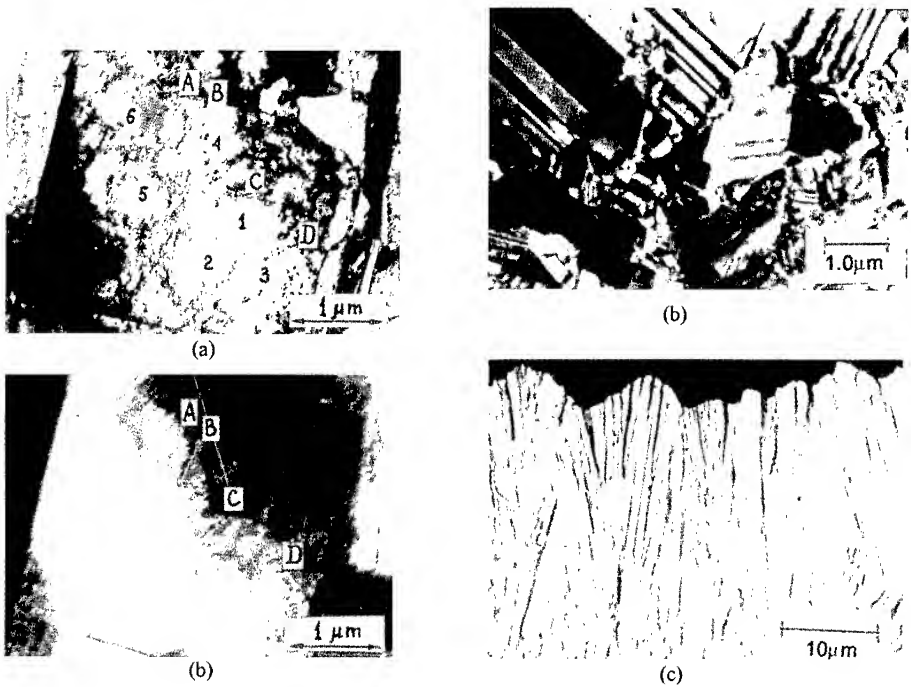


Figure 2. Defect saturated 35mm thick copper deposit  
(a) Morphology Boundaries, TEM  
(b) Twin Lamellae Transversing Grains, TEM  
(c) Twin Traces and Columnar Morphology, Optical

Figure 3. Electron Micrographs of Nickel Electrodeposit; 50 °C, 2.5 A/dm<sup>2</sup>  
a: Bright Field Image  
b: Dark Field Image ({020} Reflex Illumination)<sup>(6)</sup>

It is not uncommon to encounter 0.1 - 1% volume (point) defects, 0.05 - 10  $\mu\text{m}$  grain size, 0.03 - 0.1  $\mu\text{m}$  subgrain size, 0.01 - 0.1  $\mu\text{m}$  coherent domain size (diffraction line broadening analysis),  $10^8 - 10^{12} \text{ cm}^{-2}$  dislocation density and 0.05 - 0.5  $\mu\text{m}$  twin spacing (line asymmetry analysis).<sup>7</sup> When the grain size is less than 1  $\mu\text{m}$ , the low angle subgrain boundaries consist of unusual and complex dislocation configurations<sup>2</sup> which can be justified by invoking the presence of disclinations (rotational defects).<sup>9</sup> When the grain size is less than 0.1  $\mu\text{m}$ , the grains (or crystallites), subgrains and coherent domains (or mosaic blocks) tend to become identical and are delineated by large angle boundaries.<sup>7</sup> For grain size less than 10 nm, the grain boundary triple junctions (which have the structural character of disclinations<sup>10</sup>), make a significant contribution to the defect structure.<sup>11</sup> Grain sizes as low as 1-10 nm have been reported.<sup>12, 13</sup>

### Defect Generation

The deposition overpotential, the difference between the deposition and equilibrium potentials, is the driving force for defect generation<sup>14</sup>. Increasing current density and decreasing electrolyte temperature, cation concentration, pH or flow rate have the effect of enhancing the overpotential. For a given set of deposition parameters, the surface active additives to the electrolyte, often added in ppm quantities, have a profound impact on the adion attachment kinetics. The additive may increase or decrease the overpotential, depending upon its growth inhibiting or enhancing (catalytic) effect on the cathode surface.<sup>15</sup>

Figure 4 illustrates the effect of polyacrylamide (PAA) on the incidence of twinning, coherent domain size and dislocation density in the copper deposit.<sup>16, 17</sup> With increasing PAA, the domain (as well as the grain<sup>16</sup>) size decreases and the dislocation density increases, indicating an increasing overpotential; further, the twinning probability decreases, indicating the suppression of twinning promoted growth. Since the dislocations in electrodeposits are generated by incoherent nucleation on top of the impurity adsorbents,<sup>18</sup> any addition which hinders nucleation will enhance deposition overpotential as well as the dislocation density. As the degree of incoherent nucleation (cathode surface coverage by PAA) and the overpotential increase, the twins should disappear and the substructure should become more imperfect, displaying increasing subgrain misalignment.<sup>19, 20</sup> At sufficient PAA level, the deposit becomes free of twins and the fine subgrains are bounded by relatively high misorientation angles.<sup>16, 17</sup> In effect, the surfactant

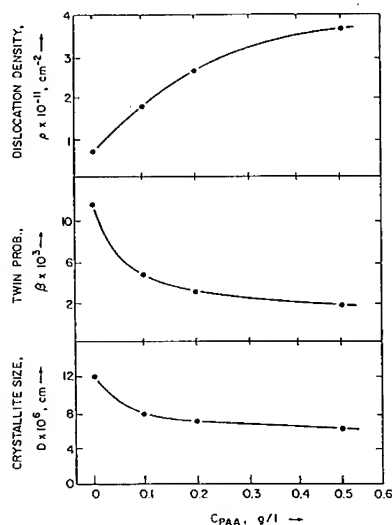


Figure 4. Influence of Polyacrylamide Concentration on the Dislocation Density  $\rho$ , Relative Growth Twin Concentration  $\beta$ , and Crystallite Size  $D$  in Copper Deposits (Adapted After Trofimenko and Kozlov<sup>(16,17)</sup>)

adsorption reduces the surface energy and therefore the work of nucleation; the nucleation probability increases accordingly. Hence the density of grain and subgrain boundaries, and with it that of dislocations, also increases. The predominant influence of adsorption, however, is the reduction in growth of adatom clusters developing on the cathode. While lowering the rate of growth process, and raising the deposition overpotential, the surfactant has no important influence on the step of cation discharge.

The enhanced cation discharge rate, however, is critical for the incidence of coherent growth twins in electrodeposits. The twinning is common for the FCC metals and for the metallic alloys in which the solute reduces the stacking fault energy (SFE) of the solvent.<sup>21</sup> The deposition conditions (reduced nucleation, catalytic impurity or additive, high electrolyte temperature) which enhance the deposit interface growth rate also promote twinning. Given the conditions conducive to twinning, increasing overpotential increases the frequency of twins (more closely spaced twin lamellae). This is illustrated in Figure 5 for copper deposited from the chloride (catalyst) containing electrolyte.<sup>3</sup> It should be emphasized that the incidence of packing defects (twinning) appears unrelated to the linear (dislocations) and surface (grain and subgrain boundaries) defects; except that given the right conditions, all defects should increase simultaneously with the increasing overpotential. A correlation between grain size and twin spacing is illustrated in Figure 6.

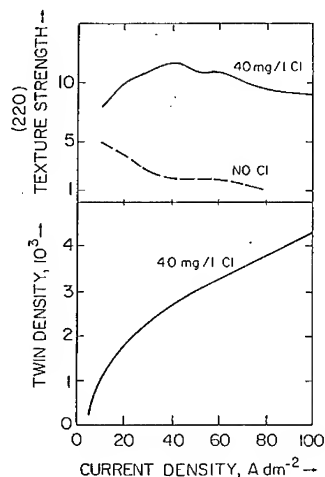


Figure 5. Effect of Current Density and Chloride on (220) Texture Strength and Twin Density in Copper Electrodeposit (After Schmidt<sup>3</sup>)

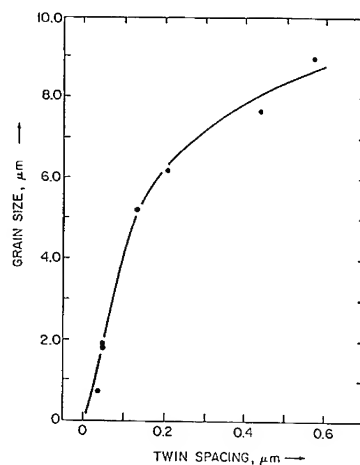


Figure 6. Relation Between Grain Size and Twin Spacing for 35mm Copper Deposit (Courtesy: S.K. Chiang, Gould Electronics)

The twinning is the most likely means of preferential grain growth in the direction of twinning planes (which for the FCC metals are the {111} or equivalent planes). With [110] texture, a large part of the twins subtend an angle of 90° to the deposit plane and the grains become elongated in the vertical direction 1:1.4 due to preferential growth in that direction.<sup>22</sup> The elongated grains compose the columnar morphology<sup>23,24</sup> with the column axis nearly parallel to the twin planes (that is, perpendicular to the substrate) (see Figures 2 and 5). However, when the texture axis makes close to 90° with the twinning plane, as for nickel with [111] texture,<sup>22</sup> the columnar grain axis is parallel to the substrate and a layer structure is promoted.<sup>25,26</sup>

Note that the bulk of the work on the defect structure of electrodeposits has focused on the FCC metals; in particular, nickel, copper and silver. Nickel with the highest SFE is most prone to form the smallest grains and subgrains, the narrowest twin spacing and the highest defect related microstrain; under correct conditions, it is also most likely to form extensive stacking faults.<sup>27</sup> Silver, with the lowest SFE, infrequently forms stacking faults but widely spaced twins appear readily.<sup>28, 29</sup> The defect concentration is intermediate for copper with moderate SFE; the stacking faults appear at high overpotentials<sup>30</sup> and in the presence of impurities and additives.<sup>14</sup> The twinning in copper deposit can be suppressed at low overpotentials,<sup>31</sup> low electrolyte temperature and in the presence of growth inhibiting surfactant.<sup>17</sup> (Figure 4)

For the non-FCC metals, a limited defect structure characterization has been reported for cobalt,<sup>32-34</sup> chromium,<sup>35, 36</sup> iron,<sup>37</sup> zinc<sup>38</sup> and cadmium.<sup>39</sup> Except for cobalt, the planar defect (twins and stacking faults) formation is apparently suppressed for these metals. The defect structure of cathodically deposited alloys has been investigated for the Fe, Ni, Co binaries and ternaries,<sup>21, 40-44</sup> Bi-Sb<sup>45</sup> and Al-Ti<sup>24</sup>, the last of these with deposition from the melt (rather than the aqueous solution). The results have been discussed in the earlier review.<sup>4</sup> Exceptionally small grain size, profuse planar defects and solute clustering are the salient features of the electrodeposited alloys.

### **Deposit Growth**

Given a single crystal substrate and sufficiently small current density (or overpotential), the deposit will also be monocrystalline, largely replicating the substrate orientation.<sup>46</sup> At sufficiently large current density and/or deposit thickness, a transition occurs from the epitaxial single crystal to the polycrystalline structure.<sup>47, 48</sup> The transition is accompanied by twinning; purity and defect structure of the substrate determine the critical epitaxial layer thickness (at a given current density) above which the transition to polycrystallinity may occur. Above the critical deposit thickness, defect structure and texture of the deposit become independent of the substrate, but are determined by the deposition parameters. If the substrate were amorphous or polycrystalline, the epitaxial layer would be polycrystalline; the transition from the epitaxial to the dominant texture would occur by twinning.<sup>49</sup>

During the early stages of growth, paracrystalline adatom clusters, with the icosahedral and decahedral structures and a five-fold symmetry, often form near the substrate where the local overpotential is enhanced.<sup>50</sup> Upon growth to a critical size, the clusters are transformed into twinned or multiple twinned particles such that the initial five-fold symmetry of the clusters is roughly preserved. For the FCC metals, the multiple twinned particles can be regarded as an assembly of tetragonal single-crystal subgrains bounded by {111} faces, each twinned in relationship to its neighbors. The twin planes contain the growth direction and in the planar TEM examination the twins appear as five lines meeting at a point, being the intersection with the plane of sample by the growth direction common to all of them.<sup>51</sup>

Deriving from the multiple twinning process, a nearly spherical shape of the growing particle, with a radial organization and high faceting, may be expected.<sup>52</sup> The spheroidal surface growth, aided by multiple twinning, has been examined at length by Mamontov and coworkers.<sup>53</sup> The conditions which promote limited initial active sites and zones of "excluded nucleation" are particularly conducive to the spherulitic growth.<sup>53</sup> With increasing thickness, the multiple twin density rises to a broad maximum and then falls gradually.<sup>54</sup> The density of grains and subgrains, however, decreases (grain and subgrain sizes increase) uniformly. This is illustrated in Figure 7 for the polycrystalline nickel deposit.<sup>55</sup>

The conditions conducive to the spherulitic growth also promote morphological instability and columnar configuration during deposit growth. The "column" consists of an aggregation of stacked elongated grains, often with elongated subgrains or coherent domains as well. The grains

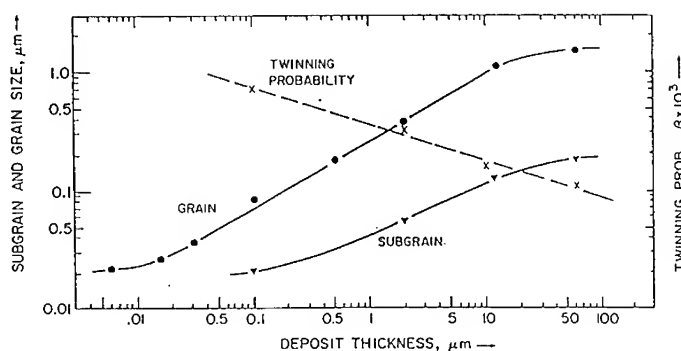


Figure 7. Effect of Nickel Deposit Thickness on Grain and Subgrain Size and Twinning Probability (Data after Atanasov<sup>(35)</sup>)

developing into the columnar structure often become wider with increasing distance from the substrate,<sup>24, 56</sup> the grains growing outward and joining laterally, and the grain size becomes larger with the deposit thickness.<sup>57</sup> The column boundaries are low density regions, often populated by minrovoids, impurities, oxides and hydroxides.

### Crystallographic Texture and Substructure

As the deposition overpotential is a driver for defect generation, it also determines the crystallographic texture (grain/subgrain orientation) perpendicular to the substrate. For the copper deposit, as the overpotential increases, the texture evolves as:  $\langle 110 \rangle \rightarrow \langle 111 \rangle \rightarrow \langle 100 \rangle \rightarrow \langle 311 \rangle \rightarrow$  random. Specific to a texture is a characteristic twin type, manifested as disturbances (twin traces) in the cross-section microstructure. The texture transition occurs by twinning:<sup>3</sup>

Texture:  $\langle 110 \rangle \rightarrow \langle 110 \rangle + \langle 111 \rangle \rightarrow \langle 111 \rangle \rightarrow \langle 100 \rangle \rightarrow \langle 100 \rangle + \langle 311 \rangle \rightarrow$  Random

Twin:  $\langle 411 \rangle \rightarrow \langle 411 \rangle + \langle 877 \rangle \rightarrow \langle 511 \rangle \rightarrow \langle 221 \rangle \rightarrow \langle 221 \rangle \rightarrow$  None

The twinning accommodates the reorientation of grains in a new crystallographic direction.<sup>58, 59</sup> At sufficiently high overpotential, the grain orientation becomes random and the twin trace features in the cross-section microstructure disappear; the deposit growth apparently occurs without significant twinning. This particular scheme for copper deposit is valid for a reasonable purity electrolyte. Impurities or additives in the electrolyte may stabilize a particular mix of twin defects and texture.<sup>3</sup>

Inevitably, there is a connection between the texture and the defect structure. The electrodeposits of the FCC metals (in particular nickel, copper and silver) exhibit a strong microstructural inhomogeneity, coupled with a large spread in grain size and non-uniform distribution of defects within the grains. Large and small grains are found together and the defect saturated grains often occur in close proximity to the perfect grains.<sup>2</sup> A typical textured electrodeposit shows a mix of fine and coarse grains; the fine grains (subgrains, coherent domains or mosaic blocks) are random and defect saturated whereas the coarse grains are oriented and have a significantly lower defect concentration.<sup>60</sup> The oriented grains are essentially free from twins and have a relatively low dislocation density; the random grains are heavily twinned and are characterized by a much larger dislocation density. The net effect is an anisotropy in the coherent domain size:<sup>61</sup> larger size ( $D_1$ ) for the oriented grains and smaller size ( $D_2$ ) for the random grains.

The average mosaic block (coherent domain) size  $D = \eta D_1 + \epsilon D_2$ , where  $\eta$  is the oriented grain fraction and  $\epsilon$  is the random grain fraction, shows a sharp peak with change in the (diffraction goniometer) tilt angle. The extent of domain size anisotropy  $n = (D_1 - D_2) / D_2$ , however, depends upon the melting temperature ( $T_m$ ) of the metal, as shown in Figure 8.<sup>62</sup> For chromium deposit, the anisotropy is high; for copper (and lower  $T_m$  metals), it is virtually nonexistent.

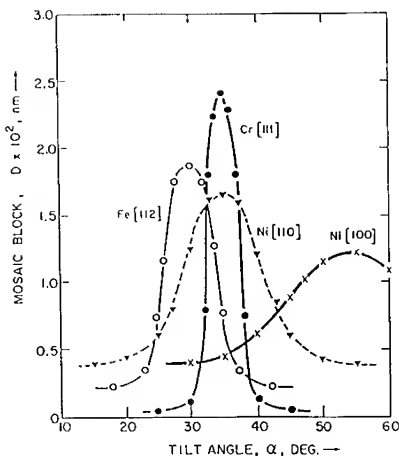


Figure 8. Mosaic Block Anisotropy Around the Electrodeposit Texture Axis<sup>62</sup>

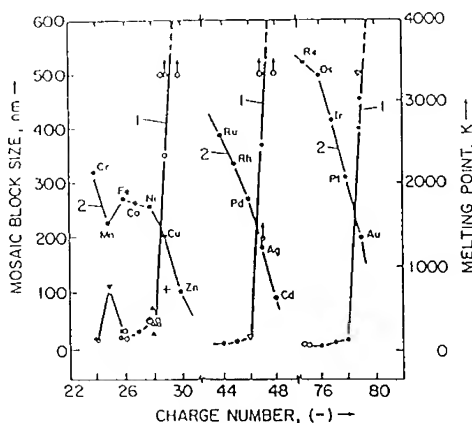


Figure 9. Variation of Melting Temperature and Mosaic Block Size With Atomic Number<sup>63</sup>

The variation of melting temperature with atomic number  $z$  for metals belonging to periods 4, 5, and 6 in Groups I, II, VI, VII and VIII of the periodic table of elements is shown in Figure 9.<sup>63</sup> Also shown in the figure is the variation of available mosaic block size with atomic number. Here the quantitative characteristics of substructure associated with the random component is used for deposits from addition-free aqueous solution of pure salt at the smallest current density and the highest electrolyte temperature (that is, at the minimum threshold overpotential for the respective metal). Periodic changes in the melting temperature and in the mosaic block size are observed: for each period, melting temperature decreases and the subgrain size  $D$  increases with increasing atomic number.

The trend of  $D$  versus  $z$  is similar for all periods, displaying a gradual 2-2.5 fold rise in  $D$ ; this gives way to an increase by about an order of magnitude in transition from Group VIII to I. Groups I and II metals have low concentration of crystal defects when deposited at the threshold overpotential; hence the  $D$  values are large, marked by an arrow in the figure. The substructure coarsening begins with smaller  $D$  in periods with greater number (from 20-30 nm in period 4 and 10-12 nm in period 5). An abrupt change from fine (5-50 nm) to coarse (>500nm) is more marked at greater period numbers.

An inverse relationship between  $D$  and supercooling  $\Delta T = T_m - T$ , where  $T$  is the electrolyte temperature, is indicated. The  $D$  vs.  $\Delta T$  is plotted in Figure 10 and fits the relation  $D^{-1} = 6.6 \times 10^{-5} (\Delta T - 1010)$ .<sup>64</sup> For  $\Delta T \leq 1025$  (Ag, Al, Au, Bi, Cd, Cu, Pb, Sn and Zn in Groups IB, IIB, IIIA, IVA and VA), it is possible to produce deposits with relatively small concentration of defects using the threshold overpotential; provided that the substructure refinement is eliminated

through an appropriate selection of electrodeposition conditions, precluding high current density, low electrolyte temperature and additions to electrolyte. For  $\Delta T \geq 3090$  (Re, W in period 6), it is possible to produce amorphous structure with the threshold deposition overpotential. The D vs.  $\Delta T$  relation also permits prediction of substructure for the electrodeposited metals not covered in the literature: Co (30-45 nm), Ti (20-35 nm), Pt and Zr (15-25 nm), Rh and V (15-20 nm), Hf, Ru and Ir (10-15 nm) and Mo, Os and Ta (5-10 nm).

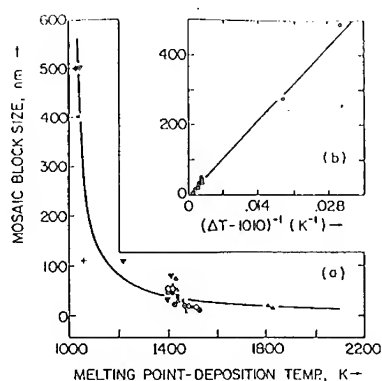


Figure 10. Mosaic Block Size vs. Difference DT Between the Melting Point and the Temperature of Electrodeposition (a) and vs.  $(\Delta T - 1010)^{-1}$  (b). Open Circles Correspond to Experimental Data; Other Symbols Denote Results From the Literature.<sup>(64)</sup>

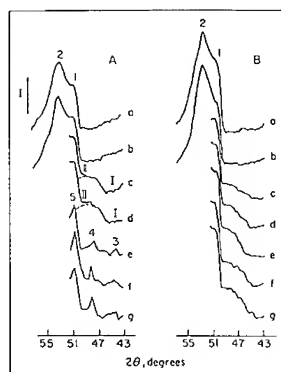


Figure 11. X-Ray Diffraction Patterns Obtained Directly During Re Electrodeposition on a Graphite Cathode at 100 (A) and 15 A/dm<sup>2</sup> (B); 1 and 2: (10.0) and (10.1) Diffraction Peaks of Graphite, 3, 4, and 5: (10.0), (00.2), and (10.1) Diffraction Peaks if Re. Co-K $\alpha$  Radiation, Sulfuric Electrolyte, 293K.<sup>(65,67)</sup>

Figure 11 depicts the diffraction patterns obtained at various stages of electrocrystallization of rhodium on a graphite cathode.<sup>65,67</sup> The halo effect on patterns c and d deposited at the high current density apparently represents the paracrystalline or amorphous phase which eventually transforms to the crystalline state (patterns e, f, and g) due to the high stored energy of lattice defects. For deposition at the low current density, the amorphous phase remains frozen in (patterns c to g); there is no diffraction evidence of crystallinity. The amorphous to crystalline phase transformation apparently occurs continuously in microregions on the cathode surface during electrodeposition, except for large  $\Delta T$  when the transformation is suppressed and a stable amorphous structure is obtained. The metallic, or the metallic solvent and non-metallic solute, alloys are especially prone to form a stable amorphous electrodeposit.<sup>13, 68-71</sup>

As a general rule, with increasing current density, (i) subgrain size (d), (ii) fraction of random grains ( $\epsilon$ ) and (iii) scatter angle ( $\alpha$ , see Figure 8) around the D vs. (tilt angle)  $\alpha$  peak increase and (iv) fraction of oriented grains ( $\eta$ ) decreases. However, due to the coarse/fine duplex grain structure, there are notable exceptions. For the chromium deposit with [111] texture, the size of oriented subgrains slowly increases with the current density; the random subgrain size, however, decreases sharply so that the overall effect is a large refinement of subgrain structure with the current density.<sup>72</sup> The effect of current density is especially acute for the low electrolyte temperature; when the temperature approaches 60°C, the effect becomes very small or non-existent, the fraction of oriented grains increases and the scatter angle decreases to a small value.<sup>73, 74</sup> At 60°C, a very strong texture, with close to 100% oriented grains, persists.



The electrodeposited silver displays two texture types [111] and [100], each stable over a partially overlapping current density range.<sup>75</sup> For the [100] texture, there is an intermediate current density at which the fraction of oriented grains is maximum and the scatter angle minimum. The effect of current density on the texture and substructure parameters becomes especially complicated for the nickel deposit with [100] texture, as shown in Figure 12.<sup>76</sup> The fraction of random grains is minimum, and of oriented grains is maximum, at an intermediate current density at which  $\alpha$  is minimum and the anisotropy factor  $n$  is maximum. A sharp differentiation between the defect saturated ( $D_1$ ) and low defect density grains ( $D_2$ ) occurs at this optimum current density, and is conducive to the formation of a strong crystallographic texture.

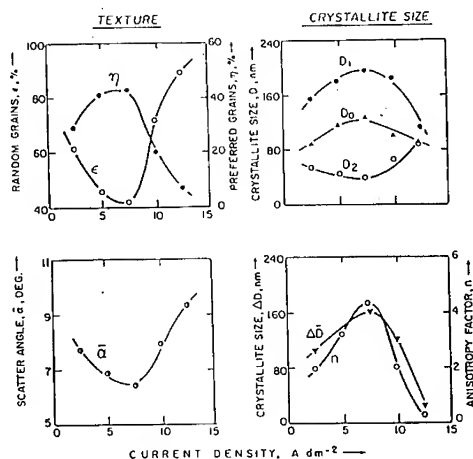


Figure 12. Effect of Current Density on Texture and Crystallite Size Parameters in Electrodeposited Nickel.<sup>(76)</sup>  
 $[\Delta D = D_1 - D_2, D = \eta D_1 + \epsilon D_2, n = \Delta D / D_2]$

Figure 13 shows the TEM microstructure, and the corresponding electron diffraction patterns, of [100] and [221] axial texture components and of randomly oriented grains in nickel deposited at  $7.5\ A\ dm^{-2}$  current density.<sup>60</sup> The largest grains, 1 to  $2\ \mu m$ , have low defect concentration (Figure 13a) and are associated with the preferred axial component [100] ( $\alpha = 6.41^\circ$ ,  $\eta = 0.44$ ) of the texture (Figure 13b). Smaller grains, 0.4 to  $0.7\ \mu m$ , with high defect concentration (Figure 13c), correspond to the minor axial component [221] ( $\alpha = 9.17^\circ$ ,  $\eta = 0.14$ ) of the texture (Figure 13d). Fine crystallites with sizes in the range of  $0.05 - 0.20\ \mu m$  and a finely divided substructure (Figure 13e) are randomly oriented ( $\epsilon = 0.42$ ) (Figure 13f).

Quantitative characterization of substructure in relation to the texture of electrodeposited nickel has shown that increasing the electrolyte temperature from  $20^\circ$  to  $80^\circ C$  at  $2-5\ A\ dm^{-2}$  current density first leads to a nearly three-fold increase in the mosaic block size at  $50^\circ C$  from the initial  $47\ nm$ ; this, however, is followed by a 40%+ decline.<sup>77</sup> If the substructure is characterized without regard to its anisotropy in the [100], [221], [210], [211] and [110] axial components, one may mistakenly conclude that the average block size in nickel increases with the electrolyte temperature.

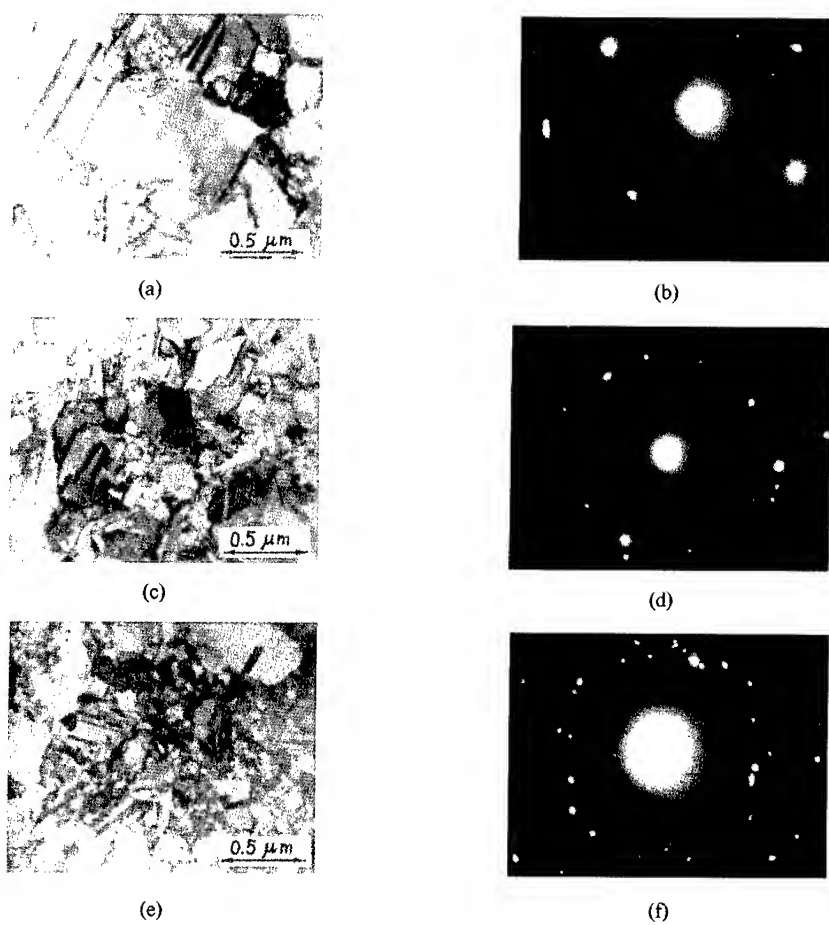


Figure 13. Electron Micrographs (a,c,e) and corresponding electron diffraction pattern (b,d,f) of nickel electrodeposit having a [100] + [221] duplex texture; temperature 65 °C, cathode current density 7.5 A/dm<sup>2</sup>.<sup>(60)</sup>

## References

- (1) S. Nakahara, *Thin Solid Films* **45** (1977), 421.
- (2) A. A. Vikarchuk, *Soviet Electroch.* **26** (1990), 883.
- (3) C. Schmidt, *Galvanotechnik* **82** (1991), 3800.
- (4) H. D. Merchant, "Defect Structure of Electrodeposits" in Defect Structure, Morphology and Properties of Deposits, The Minerals, Metals and Materials Society, 1995, 1-59.
- (5) T. R. Bergstresser and H. D. Merchant, "Surface Morphology of Electrodeposits" in Defect Structure, Morphology and Properties of Deposits, The Minerals, Metals and Materials Society, 1995, 115-167.
- (6) O. B. Girin, "Texture Development and Texture/Property Relations in Electrodeposits", in Defect Structure, Morphology and Properties of Deposits, The Minerals, Metals and Materials Society, 1995, 103-114.
- (7) A. A. Vikarchuk, *Soviet Electrochem.* **28** (1992), 805.
- (8) A. A. Vikarchuk and A. A. Vinogradov, "Defects with Rotation Symmetry in Galvanic FCC Metals and their Behavior under Load" in Strength of Materials, Japan Institute of Metals, 1994, 223-226.
- (9) A. A. Vikarchuk, A. P. Volenko and S. A. Yurchenkova, *Soviet Electroch.* **27** (1991), 535.
- (10) W. Bollmann, *Mater. Sci. Eng. A* **113** (1989), 129.
- (11) L. Wong et al, "Mechanical Properties of Nanocrystalline Ni-P Alloys", in Nanophase and Nanocrystalline Structures, TMS, 1993, 85.
- (12) G. D. Hughes et al, *Scripta Metall.* **20** (1986), 93.
- (13) G. McMahon and U. Erb, *Microstr. Sci.* **17** (1989), 447.
- (14) Y. D. Gamburg et al, *Soviet Electroch.* **10** (1974), 278; 1420.
- (15) R. K. Astakhova et al, *J. Appl. Chem. USSR* **22** (1990), 930.
- (16) V. V. Trofimenko et al, *Soviet Electroch.* **11** (1975), 1761.
- (17) V. M. Kozlov et al, *Soviet Electroch.* **25** (1989), 1067.
- (18) V. M. Kozlov, *Soviet Electroch.* **17** (1981), 1083.
- (19) V. M. Kozlov and O. I. Lyubchik, *Soviet Electroch.* **25** (1989), 845.
- (20) V. M. Kozlov, *Soviet Electroch.* **23** (1987), 808.
- (21) V. V. Povetkin and I. M. Kovenskii, *Russian Metall.* (2) (1983), 91.
- (22) A. V. Boltushkin and T. A. Tochitskii, *Soviet Electroch.* **26** (1990), 437.
- (23) H. J. Choi and R. Weil, *Plating and Surface Finishing* **68** (May, 1981), 110.
- (24) G. M. Janowski and G. R. Stafford, *Metall. Trans. A* **23A** (1992), 2715.
- (25) T. A. Tochitskii and A. V. Boltushkin, *Soviet Electroch.* **25** (1989), 430.
- (26) T. Watanabe and T. Kanayama, *Nippon Kinzoku Gakkaishi* **58** (1994), 132.
- (27) Y. M. Polukarov and Z. V. Semenova, *Soviet Electroch.* **12** (1976), 1059.
- (28) R. W. Hinton, L. H. Schwartz and J. B. Cohen, *J. Electrochem. Soc.* **110** (1963), 103.
- (29) E. A. Mamontov, L. A. Kurbatova and S. B. Tolstonogova, *Soviet Electrochem.* **16** (1980), 1450.
- (30) T. G. Stoebe, F. H. Hammand and M. J. Rudec, *Electrochem. Acta* **9** (1964), 925.
- (31) W. A. Schultze, *J. Crystal Growth* **13/14** (1972), 421.
- (32) S. Nakahara and S. Mahajan, *J. Electroch. Soc.* **127** (1980), 283.
- (33) I. G. Zhikhareva and A. I. Zhikharev, *Soviet Electroch.* **18** (1982), 971.
- (34) V. V. Povetkin and I. M. Kovenskii, *Soviet Electroch.* **22** (1986), 1101.
- (35) A. G. Mokhov and A. A. Proskurnikov, *Soviet Electroch.* **11** (1975), 774.
- (36) M. K. Kazakbaev, *Tr. Przheval'skogo Ped. Inst., Ser. Fiz.-Met.* (9) (1963), 43.
- (37) E. A. Mamontov and V. M. Kozlov, *Soviet Electroch.* **5** (1969), 1096.
- (38) E. A. Mamontov, V. M. Kozlov and V. M. Azovskii, *Soviet Electrochem.* **15** (1979), 1497.
- (39) V. V. Povetkin and N. A. Ermakova, *Soviet Electroch.* **18** (1982), 1484.
- (40) Y. M. Polukarov and Z. V. Semenova, *Soviet Electroch.* **10** (1974), 141.
- (41) V. V. Povetkin, *Soviet Electroch.* **15** (1979), 618; *Russian Metall.* (4) (1980), 213.
- (42) I. G. Zhikhareva and A. I. Zhikharev, *Soviet Electroch.* **18** (1982), 876.
- (43) I. M. Kovenskii and V. V. Povetkin, *Soviet Electroch.* **25** (1989), 1271; *Russian Metall.* (1) (1990), 116; *Hyperfine Interactions* **52** (1989), 367.
- (44) V. V. Povetkin and I. M. Kovenskii, *Soviet Electroch.* **27** (1991), 802; *Russian Metall.* (3) (1987), 136.
- (45) V. V. Povetkin, T. G. Shibleva and I. M. Kovenskii, *Soviet Electroch.* **26** (1990), 1616.

- (46) U. Bertocci and C. Bertocci, *J. Electroch. Soc.* **118** (1971), 1287.
- (47) J. Bebezuk de Cusminsky, *Electroch. Acta* **15** (1970), 73.
- (48) J. Bebezuk de Cusminsky, *J. Crystal Growth* **41** (1977), 330.
- (49) M. Froment and G. Maurin, *J. Microsc. Spectrosc. Electron.* **22** (1986), 589.
- (50) G. Maurin, in *Growth and Properties of Metal Clusters*, J. Bourdon, ed., Elsevier (1980), 101.
- (51) E. A. Mamontov, V. M. Kozlov, and L. A. Kurbatov, *Soviet Electroch.* **12** (1976), 377; **15** (1979), 217.
- (52) J. Amblard et al, *Electroch. Acta* **28** (1983), 909.
- (53) E. A. Mamontov, L. A. Kurbatova and A. P. Volenko, *Soviet Electroch.* **19** (1983), 1383; **22** (1986), 589; **23** (1987), 166.
- (54) C. R. Hall and S. A. H. Fawzi, *Philos. Mag.* **A54** (1986), 805.
- (55) N. Atanassov, S. Vitoka and S. Rashkov, *Surf. Tech.* **13** (1981), 215.
- (56) V. G. Shadrow, A. V. Boltushkin and T. A. Tochitskii, *Russian Metall.* (4) (1970), 61.
- (57) A. N. Barboshkin et al, *Soviet Electroch.* **14** (1978), 6.
- (58) S. Rashkov, D. S. Stoichev and I. Timov, *Electroch. Acta* **17** (1972), 1955.
- (59) S. Rashkov and D. S. Stoichev, *Surf. Tech.* **6** (1978), 155.
- (60) O. B. Girin and V. P. Khlyntsev, *Russian Metall.* (6) (1990), 151.
- (61) O. B. Girin, *Indus. Lab.* **49** (1983), 55.
- (62) O. B. Girin, *Russian Metall.* (5) (1988), 122.
- (63) O. B. Girin and G. M. Vorob'ev, *Russian Metall.* (3) (1987), 140.
- (64) O. B. Girin and G. M. Vorob'ev, *Russian Metall.* (4) (1987), 148.
- (65) O. B. Girin and G. M. Vorob'ev, *Zh. Fizicheskoi Khimii* **62** (5) (1988), 1347.
- (66) O. B. Girin, V. P. Khlyntsev and S. V. Kalichevskii, *Fizika Neuporyadochennykh Sistem* (8) (1986) 81.
- (67) O. B. Girin et al, *Electronnaya Obrabotka Materialov* (1) (1990), 84.
- (68) F. I. Danilov, O. B. Girin and E. R. Popov, *Zaschita Metallov* **29** (6) (1993), 942.
- (69) T. Watanabe and Y. Tanabe, "Preparation and Physical Properties of Fe-W and Co-W Amorphous Alloys by Electroplating Method" in *Rapidly Quenched Metals*, Elsevier (1985), 127-131.
- (70) A. Narita, T. Watanabe and Y. Tanabe, "Preparation of Ni-S Amorphous Alloy by Electroplating Method", in *Rapidly Quenched Metals*, Elsevier (1985), 133-137.
- (71) H. Bestgen, "Microstructures of Amorphous and Microcrystalline Electrodeposited Co-P, Ni-P and Fe-P", in *Rapidly Quenched Metals*, Elsevier (1985), 443-446.
- (72) O. B. Girin, *Russian Metall.* (4) (1990), 128.
- (73) O. B. Girin and G. M. Vorob'ev, *Russian Metall.* (2) (1983), 129.
- (74) O. B. Girin, *Russian Metall.* (2) (1986), 174.
- (75) O. B. Girin, *Russian Metall.* (1), (1990), 179.
- (76) O. B. Girin, *Russian Metall.* (5) (1990), 109.
- (77) O. B. Girin, *Russian Metall.* (5) (1990), 113.

## ATOMIC FORCE MICROSCOPY STUDY OF SURFACE EVOLUTION DURING ELECTROCRYSTALLIZATION OF ZINC-IRON ALLOYS

F. CZERWINSKI <sup>1)</sup>, K. KONDO <sup>2)</sup> AND J.A. SZPUNAR <sup>1)</sup>

<sup>1)</sup>Department of Metallurgical Engineering, McGill University, Montreal, Canada, H3A 2A7

<sup>2)</sup>Department of Materials Science and Engineering, Hokkaido University, Sapporo, 060 Japan

### ABSTRACT

Zn-Fe alloys, composed of  $\eta$  (h.c.p.) phase, were electrolytically deposited on cold rolled steel substrates from sulfate electrolytes. Deposits, which initially exhibited a morphology of approximately 20 nm thick platelets inclined 10-20 deg to the substrate surface, subsequently evolved either into triangular pyramids or hexagonal columnar crystals depending on the deposition conditions. A combination of X-ray texture measurements and AFM topographical analysis was used to characterize the growth surface of Zn-Fe alloys. For the morphology of hexagonal columnar crystals, the (00·1) basal planes were aligned perpendicular to the growth direction. For the morphology of the triangular pyramids, the (10·0) and (00·1) planes of  $\eta$  phase were tilted to the growth direction and surrounded the growth surface. For both morphologies the micro- and nanosize steps of growth were identified.

### INTRODUCTION

Characterization of the growth surface of coatings formed during electrocrystallization from aqueous solutions requires both the crystallographic and topographic data. While the crystallographic texture of a deposit can easily be measured by X-ray diffractometers, until recently there was no accurate technique for precise analysis of the topography of the rough surfaces. This gap was filled by development of scanning probe microscopes [1]. The new atomic force microscope (AFM) complements the common technique of surface observations, i.e. SEM, in different respects. While in SEM, the information is a mixture of chemical composition and topography and the image tends to emphasize sharp edges, AFM is superior in the analysis of steps of small heights on flat surfaces [1]. Moreover, the three-dimensional digital images can easily be analyzed by powerful software packages.

In this paper we present an application of AFM and X-ray diffraction to describe an evolution of the surface topography of alloy electrodeposits. The Zn-Fe binary alloys were chosen for analysis because of their application as protective coatings in the automotive industry [2,3]. According to the recent findings [4,5] there are possibilities for improving corrosion resistance of  $\eta$  phase by controlling its crystallographic texture and morphology.

### EXPERIMENTAL

The electrodeposition of Zn-Fe alloys marked as A and B was conducted from an electrolyte containing:  $\text{FeSO}_4 \cdot 0.85 \times 10^3$ ,  $\text{ZnSO}_4 \cdot 0.76 \times 10^3$ ,  $\text{Na}_2\text{SO}_4 \cdot 0.99 \times 10^3$  (mol/m<sup>3</sup>). pH of electrolyte was kept constant at a level of 1.5, temperature at 50 °C and current density at a level of 8000 A/m<sup>2</sup>. During the deposition of alloy A a 1.0 ppm of  $\text{SnSO}_4$  was added to the electrolyte.

The substrate material was a commercial low carbon steel after cold rolling. Prior to deposition, the steel specimens were mechanically polished, degreased in acetone with an ultrasonic cleaner, etched in 10 vol% sulphuric acid and rinsed in deionized water. The growth morphology of deposits was examined using SEM and AFM techniques. The AFM, a Digital Instruments Nanoscope III, was operated in contact mode using a  $\text{Si}_3\text{N}_4$  cantilever. Three-dimensional digital images, stored in the computer's memory, were subsequently analyzed by AFM software to assess the geometry of cross-sectional features and parameters of surface roughness. Phase composition of alloys was derived using an X-ray Rigaku diffractometer with a rotating anode ( $\text{Cu}_{K\alpha}$  radiation). Texture analysis was conducted using a Siemens D-500 X-ray goniometer. Pole figures were measured using the reflection technique, tilting the specimen to a maximum of 80 deg in 5 deg polar and angular intervals. The pole figures were normalized within the available interval of distribution of crystallographic planes, and the intensity on the pole figures is shown using multiples of intensities from a random specimen. In order to analyze the chemical composition using inductively coupled plasma emission spectroscopy, the deposits were dissolved in 10 vol% hydrochloric acid with an inhibitor to prevent dissolution of the steel substrate.

## RESULTS AND DISCUSSION

### Phase composition and texture

Alloys A and B, obtained under conditions of this experiment, contained 96.6 and 88.8 at% of Zn respectively, and were composed almost entirely of  $\eta$  phase. In alloy A some traces of  $\Gamma$  phase in addition to the essential  $\eta$  matrix were detected. The major difference between the X-ray diffraction patterns of both alloys was a drastic change in intensities of (00·1) and (10·1) peaks suggesting a texture (Fig. 1). Therefore, the pole figures of selected peaks of  $\eta$  phase were measured.

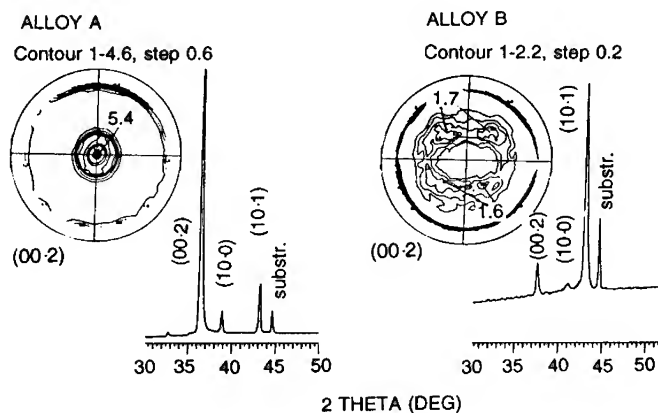


Fig. 1. X-ray diffraction patterns and (00·2) pole figures of alloys A and B. The angle locations of peaks are shifted due to the differences in lattice parameter caused by iron content [2,3].

The pole figure of alloy A shows that the basal planes of  $\eta$  phase are aligned perpendicular to the growth direction. This is expressed by  $\langle 00\cdot1 \rangle$  fibre texture with a maximum intensity of 5.4 times random. The second texture component, not shown in this pole figure, a  $\langle 10\cdot0 \rangle$  fibre with intensity of 1.2 times random, is relatively weak. An essentially different texture was detected in alloy B (Fig. 1). In this case the basal planes ( $00\cdot1$ ) of  $\eta$  phase are inclined about 30-45 deg to the growth direction. Similarly to alloy A, the contribution of  $\langle 10\cdot0 \rangle$  component is negligible.

#### Surface morphology

The resolution of SEM was not sufficient to distinguish the details of the morphology of deposit formed during the early stages. However, the AFM revealed that at this stage the deposit was composed of small platelets and was relatively uniform in thickness (Fig. 2). Although some features with heights up to 360 nm are present, the roughness of the regions between them expressed by a standard deviation *rms* [6] did not exceed 7 nm. According to the cross sectional analysis, the platelets had thicknesses of up to 20 nm and lengths of up to 100 nm, and were inclined 10-20 deg to the substrate surface. It is believed that such a morphology was formed from fish scale like platelets, observed during the very initial stages and described in detail elsewhere [4,5]. An arrangement of platelets indicates that there was an influence of crystallographic orientation of substrate grains, and as a result the morphology changed slightly from grain to grain of the substrate.

Different deposition conditions caused at a steady stage of growth, the alloys A and B to exhibit the essentially different morphologies. While the surface of alloy A was covered with the hexagonal columnar crystals (Fig. 3a), the surface of alloy B showed a morphology of triangular pyramids (Fig. 3b).

The deposit with a morphology of hexagonal crystals was characterized by relatively high roughness parameters. For alloy electrodeposited for 60 seconds, the *rms* parameter measured 638 nm. Moreover, some individual crystals extended up to 3127 nm above the surface. The planar size of crystals was up to 2000 nm and their shape imaged by AFM was in agreement with SEM observations. The top planes of the crystals were oriented perpendicularly to the growth direction and were covered with micro- and nano-size steps of growth (Fig. 4a). In particular, AFM revealed the presence of fish-scale like morphology, very similar to that observed previously during the very early stages of electrocrystallization of Zn-Fe alloys on steel substrate [4,5].

The morphology of triangular pyramids (Fig. 4b) exhibited markedly lower roughness parameters than that found for hexagonal grains. After 60 seconds of deposition, according to AFM measurements *rms* was 130 nm and maximum heights  $R_{max}$  was 715 nm. It should be emphasized that SEM and AFM images at low magnifications were in good agreement. This agreement is of special importance for AFM imaging of rough surfaces, since it is a first indicator of artifacts introduced by cantilever-surface interaction [7].

#### Growth morphology-texture relationship

The combination of crystallographic X-ray measurements and topographical SEM/AFM analysis allowed us to describe the growth surface of Zn-Fe deposits. A simple comparison of results obtained by both techniques indicates on the existing correlation between texture and

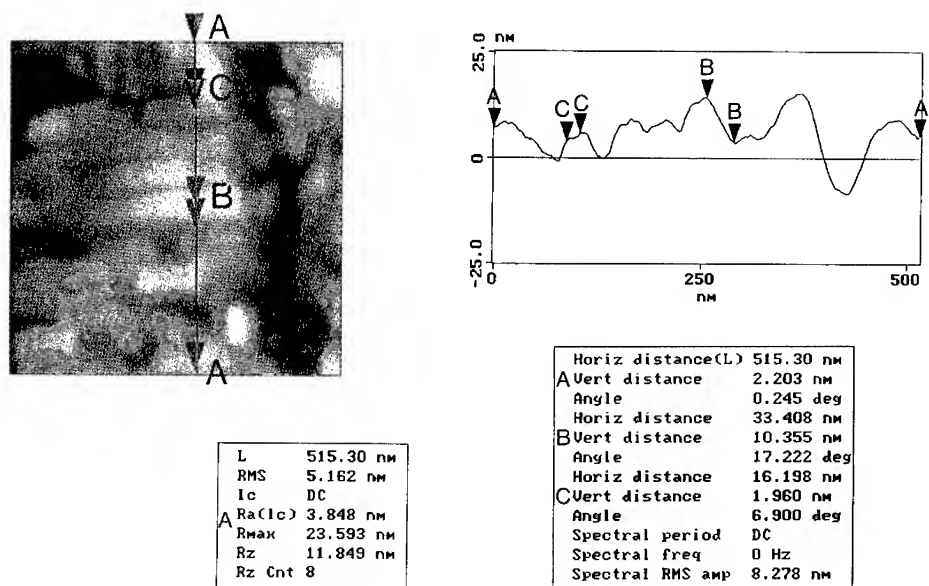


Fig. 2. Top view and cross-sectional analysis of the platelets morphology formed during the early stages. The values of topographical parameters corresponding to individual markers are given in the tables.

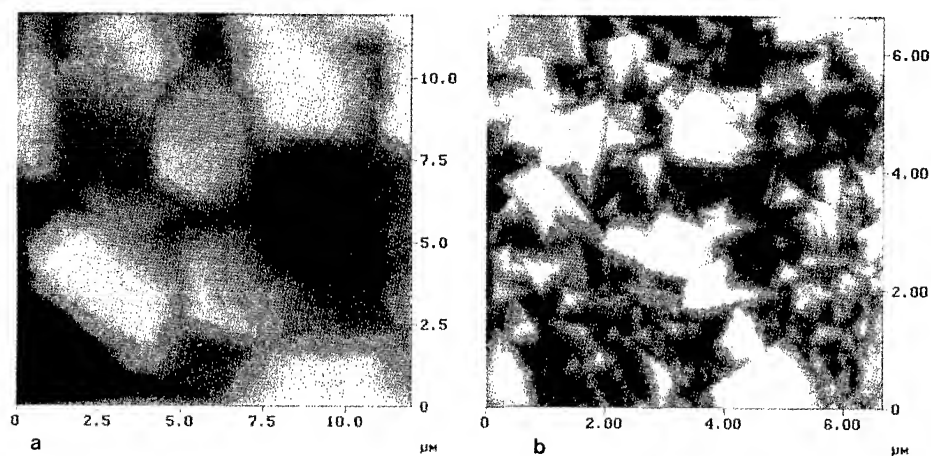


Fig. 3. Top view of morphology of hexagonal columnar grains (a) and triangular pyramids (b), imaged by AFM.



surface morphology. A strong fibre  $\langle 00\cdot1 \rangle$  texture is attributed to the morphology of hexagonal columnar crystals. This indicates that the hexagonal plates were aligned roughly perpendicular to the growth direction consisting of  $(00\cdot1)$  planes of  $\eta$  phase. The presence of steps and fish scale-like morphology on this surface proves that the hexagonal crystals grow laterally along their  $\langle 00\cdot1 \rangle$  direction.

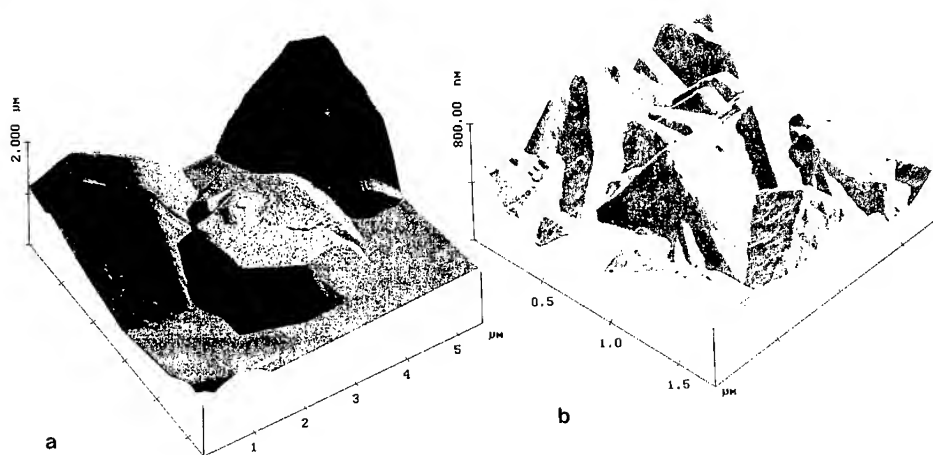


Fig. 4. Three dimensional AFM images of the morphology of hexagonal columnar grains (a) and triangular pyramids (b).

Conversely, the pole figure of alloy B with a morphology of triangular pyramids shows that the basal plane of  $\eta$  phase is inclined to the growth direction. AFM cross-sectional analysis indicates, that the triangular pyramids are, in fact, the hexagonal columnar crystals with a basal plane inclined to the growth direction, as proposed previously [2,3]. This implies that the pyramids are surrounded by the  $(00\cdot1)$  and  $(10\cdot0)$  planes of  $\eta$  phase. Moreover, a high magnification AFM imaging shows that these pyramids consist of the stacking of hexagonal thin plates which grow along  $\langle 00\cdot1 \rangle$  direction.

## CONCLUSIONS

Electrocrystallization of Zn-Fe alloys from sulfate electrolytes, under conditions of this experiment, starts from the form of nanosized platelets inclined to the growth direction. During growth, this morphology evolves either to the hexagonal columnar crystals or to triangular pyramids, depending on the deposition conditions. The morphology of hexagonal columnar crystals is accompanied by a  $\langle 00\cdot1 \rangle$  fibre texture. In this morphology, the basal planes are aligned perpendicular to the growth direction and are covered with micro- and nanosized steps of growth. The morphology of triangular pyramids is accompanied by a fibre texture with  $(00\cdot1)$  basal planes inclined to the growth direction. In this morphology the walls of the pyramids are surrounded by  $(00\cdot1)$  and  $(10\cdot0)$  planes of  $\eta$  phase.

#### ACKNOWLEDGMENT

Part of this research was supported by an ISIJ Research Promotion Grant.

#### REFERENCES

1. G. Binning, C.F. Quate, and Ch. Gerber, *Phys. Rev. Lett.*, **56**, 930 (1986).
2. K. Kondo, M. Yokoyama, and K. Shinohara, *J. Electroch. Soc.*, **142**, 2256 (1995).
3. K. Kondo, T. Murakami and K. Shinohara, *J. Electroch. Soc. Lett.*, **143**, L75 (1996).
4. H. Park, F. Czerwinski, and J.A. Szpunar, in Electrochemically Deposited Thin Films II, editor M. Paunovic (The Electrochemical Society, Pennington, NJ), 146 (1994).
5. H. Park, F. Czerwinski, and J.A. Szpunar, *Materials Science Forum*, **204-206**, 703 (1996).
6. J.M. Bennett and L. Mattsson, Surface Roughness and Scattering, Optical Society of America, Washington D.C. (1989).
7. P. Niederman and O. Fisher, *J. Microscopy*, **152**, 93 (1988).

## STUDY OF NUCLEATION OF ELECTROLESS Cu DEPOSITION ON Pd

R. AMSTER, B. JOHNSON, AND L. S. VANASUPA  
DEPARTMENT OF MATERIALS ENGINEERING, CAL POLY, CA 93407

### ABSTRACT

We studied the nucleation of Cu deposited by an electroless bath. A Pd seed layer was sputtered onto a (100) Si substrate and analyzed with GIX, STM, and AFM. The seed layer was then placed in varying ED-Cu bath conditions and also analyzed using GIX, STM, and AFM. GIX analysis results show a (111) texture for the Pd seed layer as well as the ED-Cu layer. The seed layer's influence on the deposited Cu grain's texture was found to be inconclusive.

### INTRODUCTION

Shrinking dimensions associated with ultra large scale integrated circuits place greater demands on interconnect materials [1-4]. Attention has focused on copper as the future material for interconnects [5]. Copper is predicted to outperform Aluminum metallization in electromigration resistance [4,6,7], electrical conductivity and reliability of multilevel metallization [6].

It is becoming increasingly important to understand the structural nature of the deposited metal films. We've chosen to focus our attention on the growth of copper by electroless deposition (ED-Cu). In this paper we present the results of the grain nucleation and film characterization of electroless copper deposited on a sputtered Pd seed layer.

### EXPERIMENTAL

A seed layer for ED-Cu was created by sputtering a Pd film onto a 4 in. (100) Si wafer and plasma etching the Pd layer back to 0.1  $\mu\text{m}$  thickness. The electroless copper solution was composed of: 1l : deionized  $\text{H}_2\text{O}$ , 7.5g:  $\text{CuSO}_4 \cdot 5\text{H}_2\text{O}$ , 25g : EDTA, 10ml :  $\text{CHOCOOH}$  (Glyoxylic acid-50wt%), NaOH to regulate pH, 14mg : KCN, 2.25g :  $(\text{NH}_4)\text{HF}_2$ , and 2.3ml : of a 5 ml RHODAFAC RE-610 (Formerly GAFAC RE-610) diluted into 95ml of deionized  $\text{H}_2\text{O}$ , following the chemistry recommended by Cho et al. [1], with glyoxylic acid substituting for formaldehyde [8,9]. The deposition conditions used in this study are summarized in Table 1. The films were analyzed with a Topometrix Explorer atomic force microscope (AFM), a Burleigh instructional scanning tunneling microscope (STM), and grazing incident X-ray (GIX) analysis using a Siemens D5000 X-ray diffractometer.

**Table 1.** Range of Electroless Cu Bath conditions used for deposition

pH range:	10.5 - 12.5
Temperature Range:	40 - 70°C
Bath Concentration:	1 - 1/20 standard concentration
Time of Exposure to ED-Cu:	1 - 300 sec.

## Seed Pd Layer Characterization

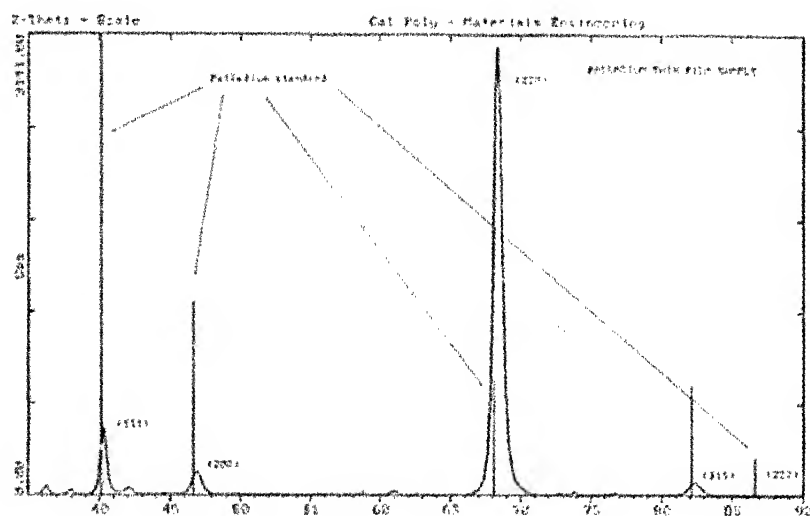


Fig. 1 GIX spectrum of a sputtered Pd thin film on a (100) Si substrate. The Pd served as the seed layer for the ED-Cu. The incident angle used was  $2^\circ$ , with a divergence slit of  $.05^\circ$ . The spectrum shows a large (220) diffraction peak. This peak indicates a (111) texture of the sputtered Pd.

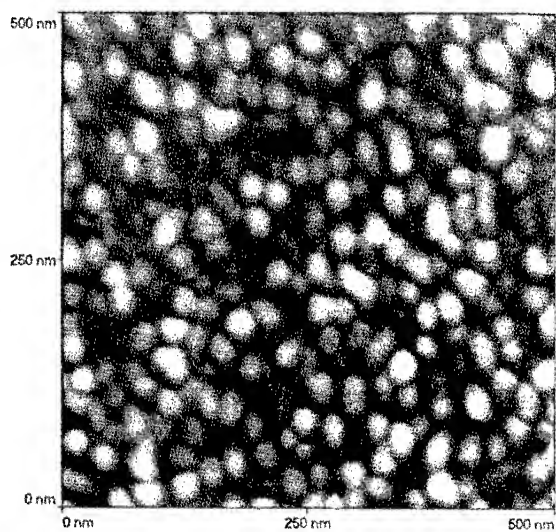


Fig. 2 AFM image of sputtered Pd on a (100) Si substrate. A contact-mode image acquisition showed the highly regular size distribution of the Pd grains (on the order of 30nm in diameter) and the uniform spacing of the grains.

### ED -Cu Grain Nucleation

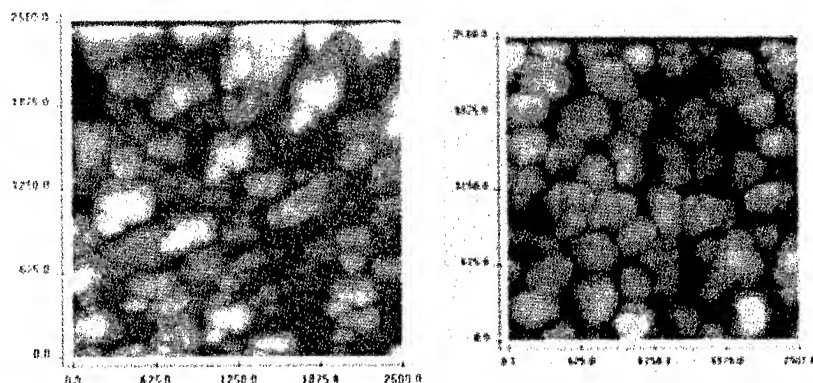


Fig. 3 STM images showing a) nucleation of ED-Cu grains at multiple sites in the grain boundaries of the Pd seed layer. The Cu grains as small as 5nm in diameter are observed along with other larger Cu grains. The large grain size variation present is not characteristic of Pd grain images. The sample was exposed to a 1:20 concentration bath strength (electroless solution to DI water) for 2 sec at a temperature of 45°C and a pH measured to be 10.5; and b) Pd sputtered onto a (100) Si substrate used for a comparison of grain size and distribution.

### ED-Cu Growth

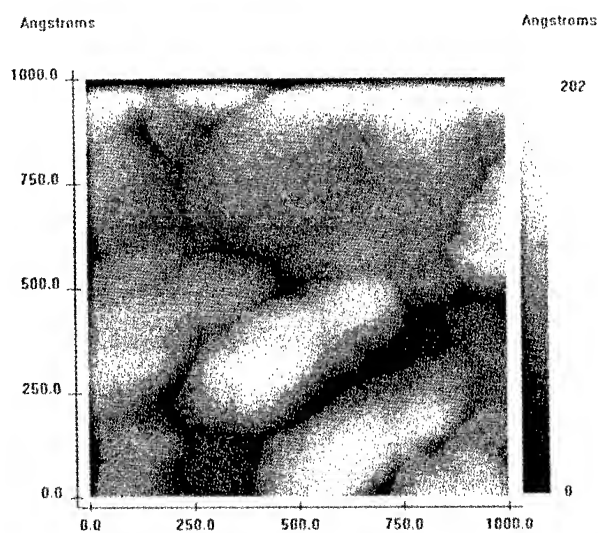


Fig. 4 STM images of Cu grains coalescing together to form row like structures. This sample was dipped into a 1:20 (electroless solution to DI water) concentration bath at 45°C for 1 sec. with a pH of 10.5.

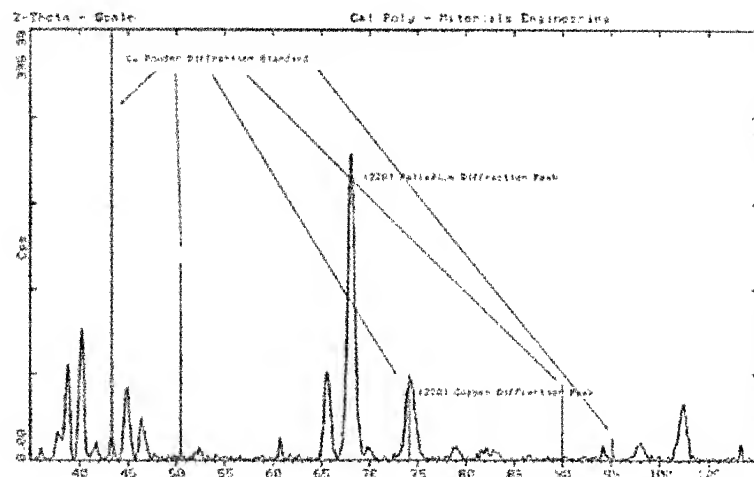


Fig. 5 GIX spectrum of the Electroless Cu plated on a Pd seed layer overlaid with the Cu JCPD library standard. The incident angle used was  $2^\circ$  with a divergence slit of  $.05^\circ$ . The Cu thin film spectrum shows a (220) diffraction peak indicating a (111) texture with some random grain textures present.

## DISCUSSION

The sputtered Pd demonstrated a preferential growth direction which is not unexpected for these types of metallic film growths. The GIX showed this preferential growth direction to be (111) direction. The same GIX analysis was made of a ED-Cu sample allowed to plate for a much longer time than those used in the AFM and STM analysis, in order to plate enough material that a high enough intensity could be achieved for such a spectrum. The results demonstrated a similar (111) texture for the ED-Cu. The results are inconclusive whether the Cu film's orientation was determined by the Pd seed layer.

The uniform grain size and shape of the Pd seed layer allowed for the comparison of the nucleating Cu grains imaged after exposure to the ED-Cu bath. The distinct difference in surface morphology indicated that Cu had indeed been deposited. In Figure 3 a), the range of grain sizes, 5nm to 50nm and possibly larger, and variance of shape from spherical to very elliptical, are a strong departure from the 30-50nm spherical shape of the sputtered Pd morphology visible in Figure 3 b). Due to the AFM's and STM's inability to record spectroscopic information it was not possible to analyze the observed grains for material information. The ED-Cu films were analyzed over a range of bath conditions that allowed for the capturing in STM images the first nucleating grains within the resolution capabilities of our system. The surface roughness was a limiting condition on being able to image below 100x100nm.

## CONCLUSIONS

GIX analysis of the sputtered Pd seed layer indicated a (111) texture. The Pd grains were shown to have a regular distribution with a typical grain diameter of 30nm. STM images showed the ED-Cu grains had multiple nucleation sites in the grain boundaries. The grains then grew together to form rowed structures. The ED-Cu grains were determined to have a (111) texture, the seed layer's role in the deposited grains' texture is inconclusive.

## ACKNOWLEDGMENTS

Research was made possible by the National Science Foundation RUI Grant #: NSF-ECS#9322083.

## REFERENCES

1. J.S.H. Cho, H. Kang, S.S. Wong and Y. Shacham-Diamand, MRS Bulletin, June, 31 (1993).
2. C.Y. Mak, B. Miller, L.C. Feldman, B.E. Weir, G.S. Higashi, E.A. Fitzgerald, T. Boone, C.J. Doherty and R.B. van Dover, Appl. Phys. Lett. **59**, 3449 (1991).
3. S. Lakshminarayanan, J. Steigerwald, D. Price, M. Bourgeois, T.P. Chow, R.J. Gutmann, S.P. Murarka, 1994 VMIC Conf. Proc., June 7-8, 49 (1994).
4. D.C. Edelstein, 1995 VMIC Conf. Proc., June 27-29, 301 (1995).
5. J. Li, R. Blewer and J.W. Mayer, MRS Bulletin, June, 18 (1993).
6. J.M.E. Harper, E.G. Colgan, C-K. Hu, J.P. Hummel, L.P. Buchwalter and C.E. Uzoh, MRS Bulletin, August, 23 (1994).
7. K-N. Tu and J. Mayer, *Electronic Thin Film Science*, New York: Macmillan, 1992.
8. J. Darken, Printed Circuit World Convention 5, June 12-15, B 6/2-3 (1990).
9. H. Honma and T. Kobayashi, J. Electrochem. Soc. **141**, 730 (1994).

## Influence of Nucleation on the Crystallization Behavior of Electroless Nickel-Phosphorous Alloys

Robert Oberle

Enthone-OMI, New Haven CT\*

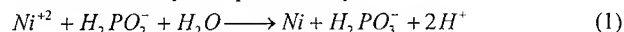
### Abstract:

The production of amorphous electroless nickel (EN) deposits from hypophosphite ( $\text{H}_2\text{PO}_2^-$ ) containing solutions is well known<sup>1,2</sup>. The crystallization of the deposits has been studied by differential scanning calorimetry (DSC) and the changes in crystallization behavior with deposit thickness have been attributed to chemical effects<sup>3</sup>. In this work, DSC results from deposits initiated by use of a noble metal catalyst are compared to those from a conventional zincate.

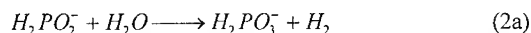
The implication of the DSC data is that the bulk structure of the EN deposit is determined to a large degree by the mechanism of deposit initiation. This is in contrast to the conventional view that solution chemistry is the dominant factor that determines the properties of the deposit.

### Introduction:

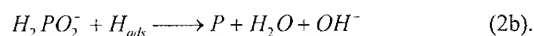
Hypereutectic electroless nickel phosphorous alloys (11.0-13.0 percent phosphorous) are widely used in the hard disk drive industry as substrates for magnetic recording media. The requirement is for a paramagnetic, smooth deposit that is thermally stable relative to the downstream processes, such as sputtering of the magnetic media and CVD of diamond like carbon. The alloy is typically deposited on an aluminum alloy substrate from a metastable solution of nickel sulfate ( $\text{Ni}_2\text{SO}_4$ ), a reducing agent (typically sodium hypophosphite,  $\text{NaH}_2\text{PO}_2$ ), and a proprietary blend of additives and stabilizers. The general assumption of additive plating baths is that the solution chemistry determines the structure and composition of the deposit. The exact deposition mechanism is controversial<sup>2</sup> but the overall reaction may be represented by



coupled with

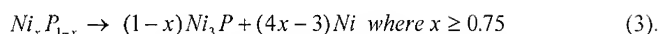


and



The partition between reactions 1, 2a and 2b is governed by the plating bath chemistry and operating parameters. In the conventional process an immersion zinc film is applied to the surface of the part to be plated (zincating). This film dissolves in the EN plating solution and the EN deposition proceeds on the aluminum substrate. The deposits are generally considered to be amorphous though this has been challenged<sup>2</sup>. The alloy crystallizes at approx. 300°C according to the reaction





Although there have been studies of thermomagnetic stability, no systematic study of the effect of operating parameters on the crystallization of the deposit has been attempted.

#### Experimental:

Deposits were obtained using a commercial product, Enplate® ADP-300 (Enthone-OMI, New Haven CT), operated at 80 °C at pH = 3.8. The substrate was commercially available Al 5586D (Kobe Precision, Hayward CA) which is widely used for rigid memory disk applications. Deposit initiation for a standard commercial cycle was done using a double zincate process, Alumon® EN (Enthone-OMI, New Haven CT). A novel alkaline palladium activation process[details are proprietary to Enthone-OMI] was used to initiate deposition without the zincate process. Deposition ran for 80 minutes resulting in a nominal deposit thickness of 5 microns. The plated disks were sectioned and the substrate dissolved in 30% by volume hydrochloric acid (HCl). The resulting free standing films were mechanically punched for DSC analysis (Perkin-Elmer DSC-7). The typical sample weight was 10mg. Heating rates were typically 1-100 K/min. Peak area and position were determined using the onboard Perkin-Elmer software without baseline subtraction. Composition of the deposits was determined by wet chemical analysis.

#### Results and discussion:

A DSC scan for an as plated sample using the alkaline palladium activation cycle is shown in figure. 1. There is a very slight kink in the slope at ~ 150°C and a very strong exotherm at 352°C. Both features are irreversible. A similar DSC scan for a deposit obtained using a normal zincate procedure is shown in figure 2. This scan shows a kink at ~ 175°C and a large exotherm at ~ 370°C. There are two smaller exotherms at ~ 360°C and 370°C. In all cases, the combined specific enthalpy from figure 2 is approximately equal to that of the single large exotherm in figure 1.

Kissinger analysis of the activation energy for the large exotherm in Figure 1 gives an activation energy of 2.31 eV/atom. Earlier work with a lower phosphorous alloy (5.76 % P) gave a value of 2.24 eV/atom<sup>4</sup>. Kissinger plots for both data sets are shown in figure 3. Both results are consistent with other measurements (2.25 eV<sup>5</sup>, 2.40 eV<sup>3</sup>) using a similar technique. Analysis from isothermal data<sup>6</sup> results in somewhat higher values 2.90-3.73 eV/atom. The kink in the initial scans presumably arises from a thermally activated structural relaxation. The precision of the data did not allow for accurate determination of an activation energy. The activation energy for the large exotherm in Figure 2 is 2.00 eV/atom. and the second (highest temperature) exotherm is 0.74 eV/atom. . Kissinger plots for these two processes are shown in fig 4. A reliable assignment was not made for the intermediate peak owing to difficulty of determining the peak position.

Isothermal transformation kinetics are modeled by the Johnson-Mehl-Avrami-Kolmogorov (JMAK) relation<sup>7</sup>,

$$X(t) = 1 - \exp[-K(t - t_0)^n] \quad (4),$$

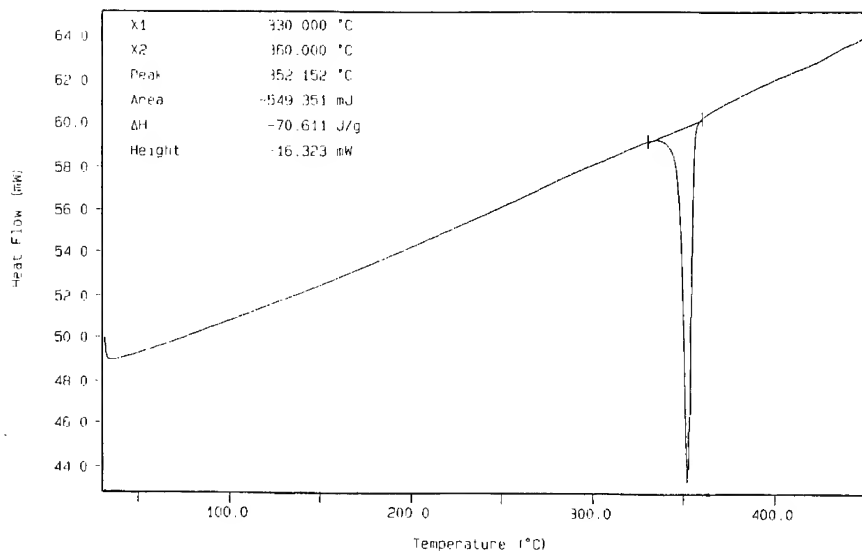


**Figure 1:** DSC signature from a film prepared using the noble metal catalysis process. The heating rate is 10K/min

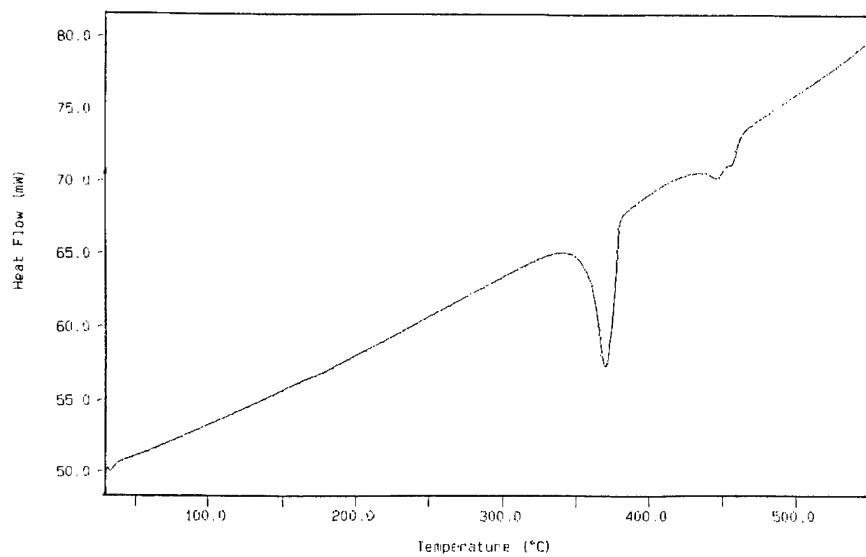


**Figure 2:** DSC signature from a film prepared using the conventional zincate process. The heating rate is 20K/min

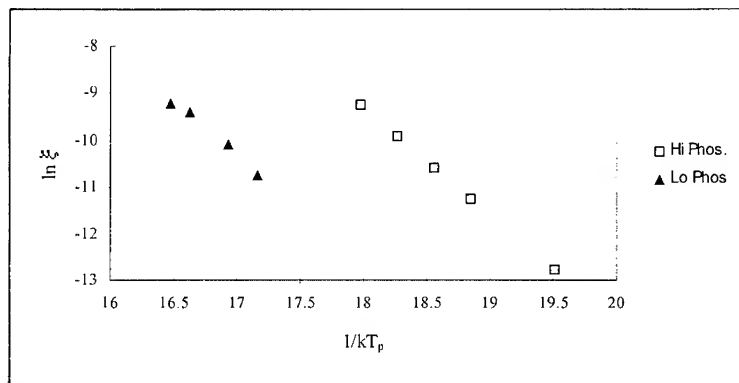


Fig. 3: Kissinger plot for palladium activated EN deposited on aluminum  $\xi = \frac{1}{T_p^2} \frac{dT}{dt}$

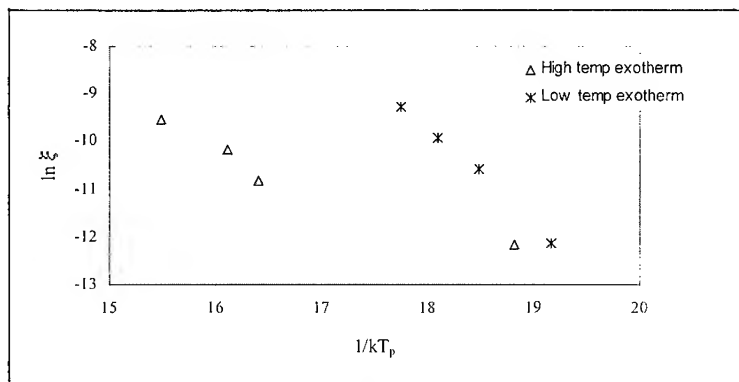


Fig. 4: Kissinger plot for zincate activated EN deposited on aluminum  $\xi = \frac{1}{T_p^2} \frac{dT}{dt}$

Where  $X(t)$  is the volume fraction transformed at time  $t$ ,  $t_0$  is the induction time,  $K$  is a kinetic parameter, and  $n$  is the Avrami exponent that characterizes the crystallization process.

A local Avrami exponent may be defined as<sup>8</sup>

$$n(X) = \partial [\ln - \ln(1 - X)] / \partial \ln(t - t_0) \quad (5),$$

i.e. the slope of the standard Avrami plot as a function of the volume transformed. The intent is to determine the change of crystallization mode as a function of volume transformed. An Avrami plot for isothermal crystallization at 300°C is shown in figure 5a and the local Avrami exponent is plotted as a function of transformation volume in figure 5b.

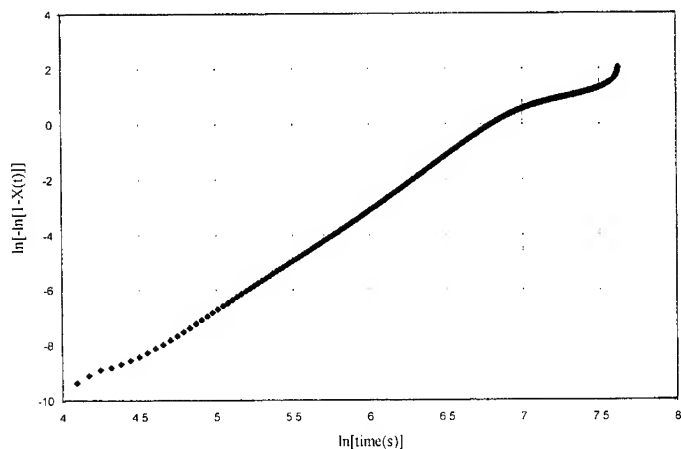


**Fig 5a:** Avrami plot for crystallization at 300°C, for Ni<sub>0.88</sub> P<sub>0.12</sub> from EN on aluminum using a zincate process.

The exponent rises almost instantaneously to 4 and gradually drops off as the transformation proceeds. At the end of the transformation the exponent once again rises. This appears to arise from interaction between the first process and the succeeding processes that give rise to the minor peaks in figure 2. The implication is that the nucleation rate is immediately saturated and decreases throughout the transformation. Growth is three dimensional and thus unlikely to proceed from the surface as has been postulated in other work<sup>3,8</sup>.

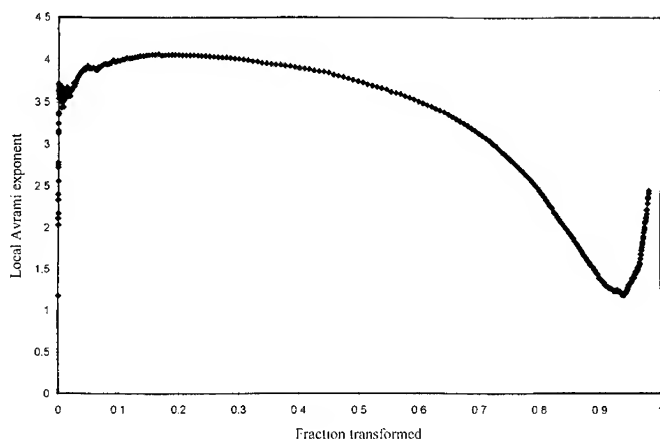


**Fig 5b:** Local Avrami exponent for crystallization at 300°C, data from figure 5a

#### Conclusion:

Differential Scanning Calorimetry shows a distinct difference between the crystallization behavior of deposits initiated from conventional zincate and noble metal catalyzed processes. The crystallization pathway for a film plated using the zincate process is multi-step and the thermal signature is less reproducible than that in the noble metal catalyzed process. It is postulated that the degree of short range order of the latter films is greater than the former, owing to the presence of a single well defined peak.

DSC results indicate that the solid state crystallization does not start at the surface and then sweep through the film, rather it appears to be a volume transformation. The implication is that the average local atomic environment is set during initiation. This is contrary to the assumption of additive plating processes, that the structure and composition of the deposit is determined by the chemistry of the plating solution.

#### References:

1. see for example the review in G.O. Mallory and J.B. Haydu, *Electroless Plating: Fundamentals and Applications*, American Electroplaters and Surface Finishers Society, Orlando FL(1990) and the references therein
2. W. Riedel, *Electroless Nickel Plating*, ASM International, Metals Park OH(1991)
3. L.T. Shi and E.J.M O'Sullivan, IBM Research Report #92A005444
4. R.Oberle, unpublished
5. S.C. Mehta, D.A. Smith and U. Erb, *Materials Sci. and Eng.* **A204**, 227(1995)
6. K. Lu and J.T.Wang, *Materials Sci. and Eng.* **A133**, 500(1991)
7. M. Avrami, *J. Chem. Phys.* **7**,1103(1939); **8**,212(1940);**9**,177(1941)
8. K. Lu and J.T.Wang, *J. Non-crystall. Solids* **117/118**, 716(1990)

# ELECTROLESS CoWP BARRIER/PROTECTION LAYER DEPOSITION FOR Cu METALLIZATION

S. LOPATIN, Y. SHACHAM-DIAMAND, V. DUBIN\*,

P. K. VASUDEV\*\*, J. PELLERIN\*\*, B. ZHAO\*\*,

School of Electrical Engineering and the Cornell Nanofabrication Facility, Cornell University, Ithaca, NY 14853-5401, slopatin@ee.cornell.edu, Tel. 607-255-1438, Fax. 607-254-4565

\* AMD, One AMD Place, P.O. Box 3453, Sunnyvale, CA 94008

\*\* SEMATECH, 2706 Montopolis Drive, Austin, TX 78741

## Abstract

A fully encapsulated copper interconnect with CoWP barrier and protection layer can be produced by conformal electroless CoWP barrier layer deposition at the bottom and on the sidewalls of trenches and selective electroless CoWP deposition on in-laid Cu lines. The electroless CoWP deposition is an autocatalytic reaction with activation energy of about 0.985 eV. Deposition rate of about 10 nm/min at 80°C and average surface roughness of 5 nm for 200 nm thick films were measured. CoWP layer with resistivity of 25  $\mu\text{Ohms}\cdot\text{cm}$  was obtained. Resistivity of electroless CoWP films was decreased from 25  $\mu\text{Ohms}\cdot\text{cm}$  to 20  $\mu\text{Ohms}\cdot\text{cm}$  after annealing in vacuum with  $10^{-7}$  torr at 400°C for 30 min. The RBS spectra of the Cu/CoWP/Co/Si structure formed by electroless CoWP barrier and Cu deposition and annealed at 400°C for 60 min in vacuum  $10^{-7}$  torr showed no interdiffusion in deposited films.

## Introduction

Copper, because of its low resistivity (1.67  $\mu\Omega\cdot\text{cm}$ ) and enhanced resistance to electromigration, is an excellent choice for ULSI metallization [1, 2]. Copper films have been deposited successfully by a number of methods including PVD, laser-induced reflow, CVD, electroplating and electroless deposition. Among them, CVD and electroless deposition are two of more promising because of its ability to deposit highly selective and conformal films [3]. Conformal deposition of barrier layer and copper is critical for filling high-aspect ratio trenches and vias. The need for conformal films becomes very important for the deep submicron interconnect features, where the aspect ratio of interconnects is expected to exceed 3:1 [4, 5]. The formation of encapsulated copper lines and vias at low temperatures is highly desirable, because copper diffuses into Si and  $\text{SiO}_2$  and reacts with most metals and silicides, such as Al, Ti,  $\text{CoSi}_2$  and  $\text{TiSi}_2$ , which are commonly used in microelectronic devices.

Electroless Cu deposition from aqueous solution is appealing because of its low cost, low processing temperature and ability to integrate electroless Cu with electroless barrier deposition [6]. Table 1 shows the ternary and binary alloys which can be synthesized by an electroless process for barrier layer applications.

Table 1. Catalytic properties of alloy metals for reduction.

Reducing agent	Catalytic metal	Noncatalytic metal	Co-deposition component
$\text{NaH}_2\text{PO}_2$	Ni, Co, Fe, Rh, Pd, Cu, Au	W, Re, Zn, Cd, Hg, V, Cr, Ag, Sn, Mn, Mo, Ti	P
$\text{NaBH}_4$	Ni, Co, Fe, Rh, Pd, Pt, Cu, Au, Ag, Ru	W, Re, Zn, Cd, Hg, V, Cr, Sn, Mn, Mo, Ti	B
HCHO	Cu, Ag, Pd, Pt, Au	Cd, Ni, Co, Pb, Sn, Bi, Sb, Zn	---
$\text{N}_2\text{H}_4\cdot\text{H}_2\text{O}$	Ni, Co, Fe, Rh, Pd, Pt, Ag, Au, Ru	W, Re, Zn, Hg, Sn, Cr, V, Mn, Mo	---

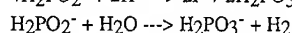
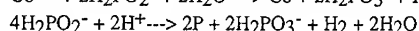
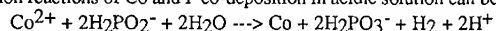
In this paper, we focus on electroless Cu line and CoWP barrier/protection layer depositions with emphasis on copper encapsulation at low temperature for on-chip wiring of very high aspect ratio. We present a profile study of seed layers covered with thin (~100 nm) electroless barrier films by SEM cross sections and step coverage in trenches and vias as a function of aspect ratio. This paper also describes electroless CoWP deposition mechanism, electroless CoWP chemistry for thin (50-100 nm) film deposition and the properties of thin electroless CoWP films. The electroless CoWP deposition on sputtered cobalt for barrier fabrication and on electroless Cu lines for protection layer formation have been studied.

## Electroless CoWP deposition mechanism

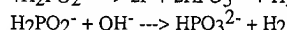
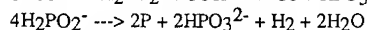
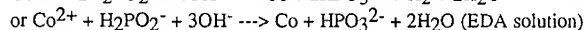
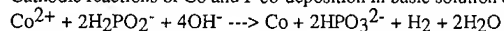
Electroless Co(P,B)-W alloys can be deposited from aqueous solutions using hypophosphite and borane dimethylamine as reducing agents. The deposition rate of the electroless Co(P,B)-W alloy with borane

dimethylamine is higher than that with hypophosphite but solution stability with borane dimethylamine as reducing agent is very low.

Mechanism of electroless CoWP deposition can be described by a set of electrochemical oxidation-reduction reactions. It is very complicated system due to different catalytic activities of the co-deposited metals. Cathodic reduction reactions of Co and P co-deposition in acidic solution can be described as:

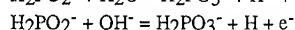
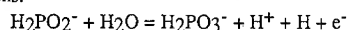


Cathodic reactions of Co and P co-deposition in basic solution can be described as:

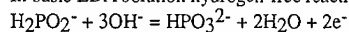


Tungsten is co-deposited with Co-P in small amount, (0.2 - 4) % of composition, and is not catalytically active for the reduction reaction. The exact mechanism is unclear.

Anodic oxidation of hypophosphite in the both acidic and basic solutions occurs according to the following reactions:



In basic EDA solution hydrogen-free reaction may occur as following:



Anodic oxidation reactions lead to the formation of electrons which are consumed in the cathodic part of the electrochemical reaction (metal ion reduction).

## Experiment and results

CoWP alloy was deposited from the solution that is described in Table 2.

Table 2. Electroless CoWP deposition solution.

Chemicals	Concentrations
(NH <sub>4</sub> ) <sub>2</sub> WO <sub>4</sub>	10 g/l
CoCl <sub>2</sub> 6H <sub>2</sub> O	30 g/l
Na <sub>3</sub> C <sub>6</sub> H <sub>4</sub> O <sub>7</sub> 2H <sub>2</sub> O	80 g/l
Na <sub>2</sub> H <sub>2</sub> PO <sub>2</sub>	20 g/l
RE 610	0.05 g/l

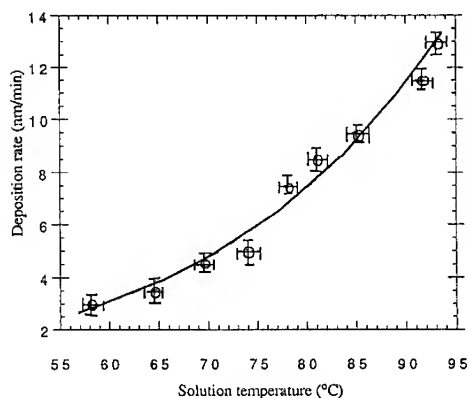


Fig. 1. CoWP deposition rate versus solution temperature

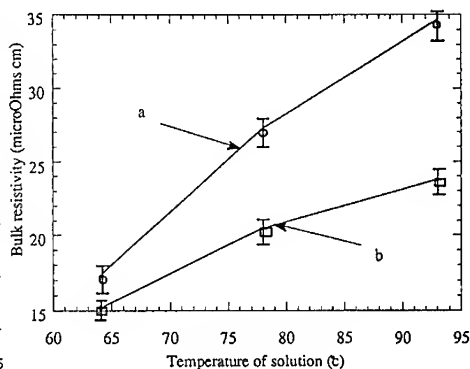
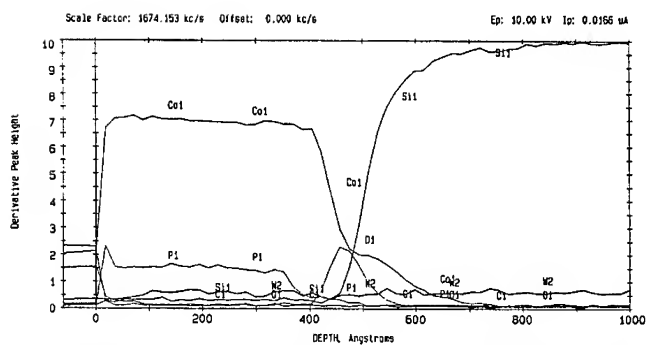
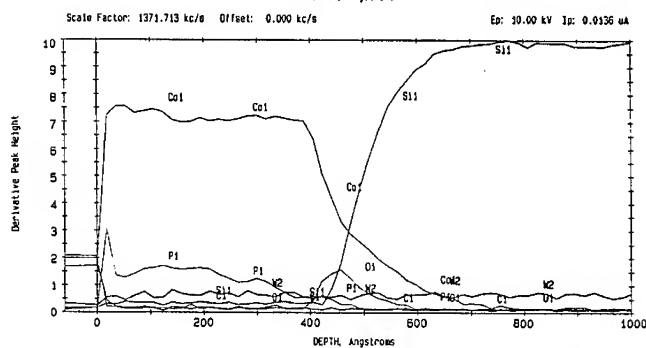


Fig. 2. CoWP film resistivity versus solution temperature: (a) before anneal, (b) after anneal at 400 °C.



(a)



(b)

Fig. 3. Auger electron spectroscopy profiles of the CoWP/Co/Si structure: (a) before anneal, (b) after anneal at 400°C for 30 min in vacuum.

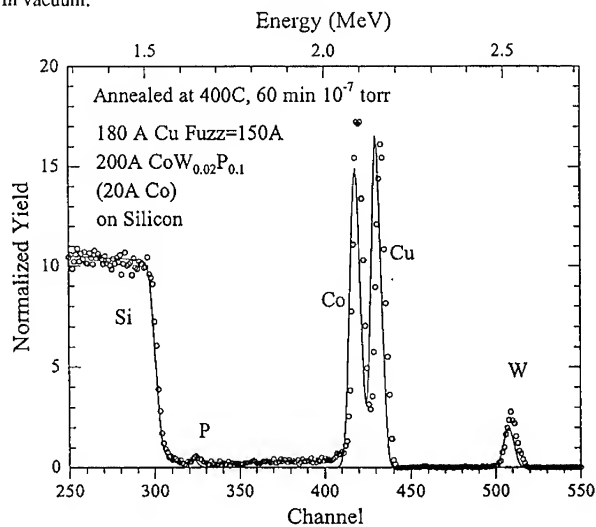


Fig. 4. RBS spectrum of the Cu/CoWP/Co/Si structure formed by electroless CoWP barrier / Cu depositions and annealed at 400 °C for 60 min in vacuum  $10^{-7}$  torr and a simulation of this spectrum using RUMP.



Electroless CoWP deposition is initiated by dry and wet activation processes. In-situ electroless CoWP deposition at 90°C on either sputtered Cu or electroless Cu surfaces resulted in an uniform deposition on both surfaces.

Using a Co seed layer allowed a decrease in the deposition temperature. We assume that this is because the Co surface is more catalytically active for electroless CoWP deposition than the Cu surface. The Co surface also oxidizes more slowly than that of Cu surface. Auger spectra of the Co seed layer after annealing at 300°C and 400°C in vacuum showed no oxide formation on the Co surface. However, the spectra showed oxide formation after annealing at 700°C. Auger spectra of the Co seed layer with Al protection layer showed an oxide formation on the Al surface after annealing at 400°C.

#### Dry activation. CoWP barrier layer deposition

A sputtered thin Co layer was used as a seed layer for electroless CoWP barrier deposition. CoWP deposition is an autocatalytic reaction with activation energy of about 0.985 eV.

Figure 1 illustrates how the deposition rate depends on the solution temperature, T. When the solution temperature increases from 75°C to 85°C the deposition rate increases by a factor of 2, from 5 nm/min to 10 nm/min. The deposition rate also increases with increasing pH in the range from 9 to 9.5.

The pH depends on the solution temperature, T. The pH value increases significantly for solution temperatures between 92°C and 94°C. This jump in pH value shows that there is a threshold temperature that above it the solution decomposes spontaneously. A stable electroless CoWP deposition can be achieved at deposition temperatures in the range of 75 - 85°C.

Figure 2 shows that the resistivity of electroless CoWP deposits depends on the solution temperature. When the deposition temperature decreases from 85°C to 70°C the resistivity of electroless CoWP deposits decreases from 27-30  $\mu\Omega\cdot\text{cm}$  to 15-20  $\mu\Omega\cdot\text{cm}$ . Figure 2 shows that the bulk resistivity of electroless CoWP deposits depends on the anneal. Annealing at a temperature of 400°C for 30 min in vacuum decreases the bulk resistivity from 27  $\mu\Omega\cdot\text{cm}$  to 20  $\mu\Omega\cdot\text{cm}$  for a deposition temperature of 75°C. Annealing at 300°C for 30 min in vacuum reproduced a similar change in bulk resistivity.

The average surface roughness does not depend on deposition rate and is approximately 5 nm for 30 nm thick CoWP films.

#### Thermostability of electroless CoWP / sputtered Co structure on Si

The Auger spectrum of the CoWP/Co/Si structure formed by electroless CoWP barrier deposition is shown in Figure 3(a). The Auger spectrum of the CoWP/Co/Si structure annealed at 400°C for 30 min in vacuum ( $10^{-7}$  torr) is shown in Figure 3(b). A comparison of the two spectra shows that the anneal results in some redistribution of P and Co in the CoWP/Co and Co/Si interfaces without a deep interdiffusion of the elements.

#### Electroless Cu deposition on electroless CoWP barrier. Thermostability of electroless Cu / electroless CoWP structure

The process flow for electroless CoWP barrier and Cu deposition included:

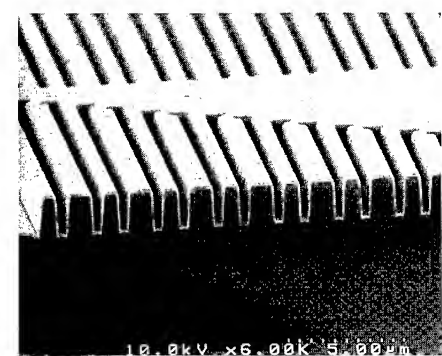
- preparing the Si wafers;
- in-situ ion-beam cleaning of the Si surface and RF (or DC) sputtering of a thin Co seed layer;
- electroless CoWP deposition, rinsing in de-ionized water and drying in N<sub>2</sub> flow;
- anneal at 300°C for 30 min in vacuum ( $10^{-7}$  torr);
- electroless Cu deposition, rinsing in de-ionized water and drying in N<sub>2</sub> flow (Cu was deposited on electroless CoWP without any activation);
- anneal at 400°C for 60 min in vacuum  $10^{-7}$  torr.

The RBS spectrum of the Cu/CoWP/Co/Si structure formed by electroless CoWP barrier / Cu deposition and annealed at 400°C for 60 min in vacuum  $10^{-7}$  torr and a simulation of this spectrum are shown in Figure 4. No interdiffusion in deposited films and no oxidation of the Cu surface were observed. The thicknesses of the Co, CoWP, and Cu films were approximately 20 Å, 200 Å and 200 Å, respectively.

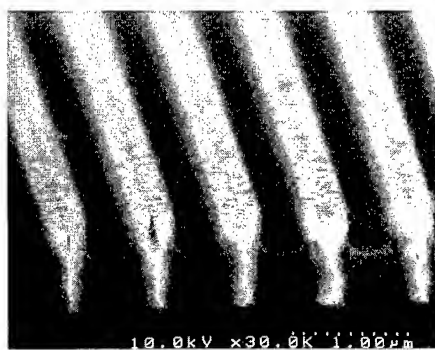
#### SEM cross sectional analysis of CoWP layer in narrow trenches

In this section we present a profile study of seed layers covered with thin electroless CoWP films in sub-half micron trenches by SEM cross sections. We also present step coverage in trenches as a function of size and aspect ratio.

The CoWP alloy was deposited from heated aqueous solution with addition of ductility promoter and surfactant RE 610. Typical CoWP structures made by covering trenches using this solution are presented in Figures 5 (a), (b), (c). The seed layer of the sample shown in Figures 5 (a), (b), (c) is collimated sputtered Co with thickness measured on the field of 30 nm. The 335 - 350 nm wide trenches with an aspect ratio of 5:1 are covered with a thin



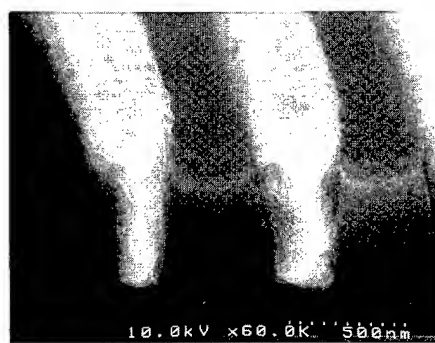
(a)



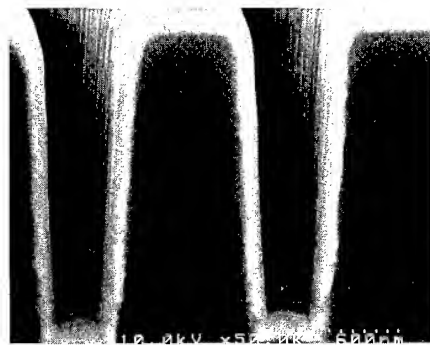
(d)



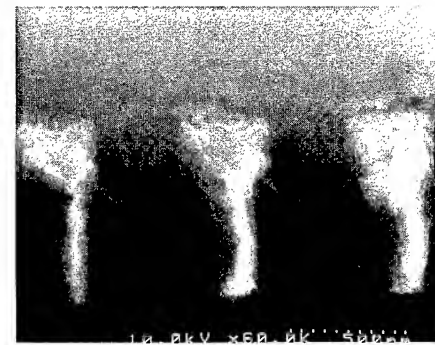
(b)



(e)



(c)



(f)

Fig. 5. SEM cross sections of the electroless CoWP films in the damascene process: (a), (b), (c) - conformal CoWP films in 0.3 - 0.4 wide trenches with aspect ratio of 5:1, (d), (e), (f) - selective CoWP films on in-laid Cu lines.

(thickness ~ 50 nm) electroless CoWP film. Conformal electroless CoWP deposition in such narrow trenches was observed. Similar results were observed for trenches greater than 350 nm wide with aspect ratio <4:1.

Figure 5 (c) demonstrates an ability of the electroless ternary alloy deposition to cover vertical sidewalls in the narrow trenches with high aspect ratio. The thickness and surface roughness of the electroless CoWP at top edges, lower sidewalls and bottom of the trenches play an important role in the following Cu deposition onto CoWP. Very uniform, shiny and smooth thin barrier CoWP films are electrolessly deposited. This leads to a void/seam-free Cu filling of sub-half micron trenches with very high aspect ratios and vertical sidewalls.

#### Damascene process, Wet activation, Selective CoWP protection layer deposition

The key technologies in the damascene process are Cu deposition and Cu CMP. The damascene process avoids copper oxidation and diffusion because the sidewalls and the bottom surfaces of copper interconnects are already covered by CoWP barrier/adhesion layer. The top surface of the Cu interconnect has to be protected to prevent corrosion.

An important advantage of electroless CoWP deposition is its selectivity, which is achieved by the activation of the patterned Cu lines versus the non-activated silicon dioxide surface.

An activation step is needed to initiate selective electroless CoWP deposition and start the autocatalytic reaction. PdCl<sub>2</sub> in a HF solution was used as the activation solution. The substrate is first placed in the activation solution for a short period of time, during which Pd nucleates on the Cu surface. The sample is then placed in the CoWP plating solution, where CoWP is deposited on the Pd sites. Once there is a CoWP layer formed the autocatalytic reaction takes over.

We found that the amount of activation is controlled by the Pd and HF concentrations, and the activation time. Increasing the HF concentration and activation time led to removal of the Cu lines from the trenches, since the silicon dioxide was etched along the sidewalls.

HF concentrations in the range of 20-100 ml/l with 3 sec of activation resulted in nonuniform Co deposits. The Cu is usually covered with a layer of copper oxide that is removed in the activation solution by HF. Also CMP process modifies the silicon dioxide surface that is etched in diluted HF. Therefore, optimizing the HF concentration is critical to CoWP uniformity and selectivity.

Selective and uniform growth of electroless CoWP on Cu lines was observed after activation for 2-3 sec with 150-200 ml/l HF concentrations. Optimized HF concentration and activation time are about 200 ml/l ( pH = 3 ) and 2 sec, respectively.

Figures 5 (d), (e), (f) show that optimized Pd activation resulted in selective CoWP deposition on Cu line surfaces at 65 °C.

Three critical steps are involved in this process: 1) removal of the copper oxide on Cu lines and etching of the modified layer on silicon dioxide surface among Cu lines with HF, 2) surface activation with a high density of Pd particles on Cu line surfaces and 3) uniform initiation of the autocatalytic electroless CoWP deposition only on the Cu lines.

#### **Conclusions**

A possibility of Cu interconnect encapsulation by an electroless ternary alloy deposition at temperatures of 65 - 75 °C is demonstrated.

Fully encapsulated copper interconnects with CoWP barrier and protection layer can be produced by two processes:

1) conformal electroless CoWP barrier layer deposition onto sputtered Co seed at the bottom and on the sidewalls of trenches.

2) selective electroless CoWP deposition onto Pd activated in-laid Cu lines.

SEM cross sections showed conformal 50 nm thick CoWP film in 0.3 - 0.4 µm wide trenches with aspect ratio of 5:1 and selective CoWP film on in-laid Cu lines separated by 0.5 µm wide silicon dioxide.

The RBS and Auger spectra showed no interdiffusion in deposited electroless Cu and CoWP thin films after anneal at 400 °C for 60 min.

#### **References**

1. P.L. Pai and C.H. Ting, IEEE Electron. Device Lett. 10, 423 (1989).
2. Y. Shacham-Diamand, V.M. Dubin, M. Angyal, Thin Solid Films 262, 93 (1995).
3. Y. Shacham-Diamand, S. Lopatin, V. Dubin, P.K. Vasudev, B. Zhao, J. Pellerin, U.S. Patent (Cornell Univ., submitted 3 September 1996).
4. S. Lopatin, Y. Shacham-Diamand, V. Dubin, J. Pellerin, B. Zhao, P. K. Vasudev, "Conformal Electroless Copper Deposition for Sub - 0.5 µm Interconnect Wiring of Very High Aspect Ratio", in Proc. 190th Meeting of The Electrochemical Society, Inc., ed. by The Electrochemical Society, Inc. (San Antonio, Texas 1996) pap. 330.
5. S. Lopatin, Y. Shacham-Diamand, V. Dubin, J. Pellerin, B. Zhao, P. K. Vasudev, "Profile Improving in Electroless Cu Metallization of Narrow Trenches", in Proc. Advanced Metallization Conf., (Boston, MA 1996).
6. Y. Shacham-Diamand and S. Lopatin, in Proc. of the SRC Topical Research Conf. on Copper Interconnect Technology, Troy, NY, 1996.

## **ELECTROCHEMICAL PROCESSING OF LAYERED COMPOSITE COATINGS OF NICKEL - ALUMINUM - ALUMINA / ALUMINA - YTTRIA STABILIZED ZIRCONIA**

K. BARMAK, S. W. BANOVIC, H. M. CHAN, L. E. FRIEDERSDORF, M. P. HARMER, A. R. MARDER, C. M. PETRONIS, D. G. PUERTA AND D. F. SUSAN  
Department of Materials Science and Engineering, Lehigh University, Bethlehem, PA 18015

### **ABSTRACT**

Multilayered coatings of single and dual particle metal matrix composites, with or without ceramic overlayers, have been produced by a novel combination of electrochemical deposition (electroplating and electrophoretic deposition) and reaction bonding. The coatings contain the following layers in a variety of combinations deposited on Ni substrates: (i) electroplated composites of Ni with Al and/or alumina particles, (ii) precursor Al + Al<sub>2</sub>O<sub>3</sub> + yttria stabilized ZrO<sub>2</sub> transformed into Al<sub>2</sub>O<sub>3</sub> + yttria stabilized ZrO<sub>2</sub> by the reaction bonding method, and (iii) yttria stabilized ZrO<sub>2</sub>. In order to determine the appropriate processing parameters for the multilayered coatings, uniform one-layer coatings were deposited and characterized. We find that in the dual particle Ni-Al-Al<sub>2</sub>O<sub>3</sub> coatings the volume percent of the particles does not show a dependence on deposition current density. However, volume percent alumina in these coatings has a strong dependence on the amount of this particle in the plating bath, while the volume percent Al shows only a weak dependence on its bath content. Comparison of the deposition behavior of these dual particle with single particle coatings, containing Al or alumina only, reveals that the presence of Al in the bath interferes with the codeposition of alumina. This interference, however, is not reciprocal. When coatings containing Al are annealed, Ni and Al react to form a solid solution of Al in Ni ( $\gamma$ ) or a two phase mixture of this solid solution and the intermetallic, Ni<sub>3</sub>Al, ( $\gamma$ - $\gamma'$ ) depending on the annealing temperature. Finally, we find that the formation of the reaction bonded alumina plus yttria stabilized zirconia layer requires the oxidation resistance afforded by aluminum in the underlying electroplated layer.

### **INTRODUCTION**

The aim of the present work is to investigate the use of electrochemical methods to fabricate metal/ceramic thermal barrier coatings (TBCs) for advanced gas turbine systems. Electrochemical methods, by which we mean electroplating and electrophoretic deposition, were chosen because of their versatility, ability to coat complex shapes and low cost, which make them attractive alternatives to other coating techniques. By adding particles to the plating bath, composite coatings of the plated metal and the codeposited particles are easily formed, for example see reference [1]. The volume fraction of codeposited particles depends on many parameters. These include the nature of the electrolytic bath, the current density and the type (metallic, ceramic, etc.), size, shape and amount of particles. Here we briefly present the effect of two parameters, namely bath particle content and current density, on the deposition of Ni-Al-Al<sub>2</sub>O<sub>3</sub>, where Ni is the electroplated matrix and aluminum and/or alumina are the codeposited particles. The effect of particle shape on the codeposition has been reported elsewhere [2].

In the fabrication of the ceramic layers we made use of a combination of electrophoretic deposition and reaction bonding of metal oxides. Typically, the reaction bonding of metal oxides (RBMO) [3-7], utilizes precursor powders of aluminum plus alumina, with or without other ceramic particles, e.g., yttria stabilized zirconia (YSZ), in order to form monolithic ceramic bodies. During the heat-treatment procedure, two processes occur: a) oxidation of the aluminum metal to alumina, and b) sintering of the alumina and the additional ceramic powders to give a monolithic ceramic. In this paper, we present the first report of reaction bonded composites of alumina and YSZ made as coatings.

## EXPERIMENT

The details of our metal-matrix electrodeposition process are given in a longer publication [8]. Here we give a brief summary. The substrate for all the coatings was pure Ni 200 plate. The electrodeposition bath was of the sulfamate type and contained 400 g/l of nickel sulfamate tetrahydrate, 30 g/l boric acid, 5 g/l nickel chloride hexahydrate, 0.5 g/l sodium lauryl sulfate and 0.1 g/l Coumarin. For most experiments,  $\alpha$ -alumina powder, with an average size of 0.6-0.8  $\mu\text{m}$ , and Al powder, with majority of the particles in the 1-4  $\mu\text{m}$  size range, were added to the electrolytic bath for codeposition with Ni. In some experiments large nickel aluminide particles (with average size 7.1  $\mu\text{m}$ ) were used to study the effect of particle shape and size on the codeposition process. The bath was sonicated prior to the deposition run and was mechanically agitated during the run. The starting pH of the electrolyte was  $4 \pm 0.2$  and the bath temperature was maintained at  $50 \pm 2^\circ\text{C}$ . The vol.% of the incorporated particles was measured through quantitative image analysis of the polished cross sections on a LECO 2001 image analyzer.

The RBMO coatings were formed by electrophoretic deposition, oxidation, and sintering on metallic substrates. The substrates were pure Ni 200 plate on which Ni-Al or Ni-Al-Al<sub>2</sub>O<sub>3</sub>, or bilayers of Ni-Al plus Ni-Al-Al<sub>2</sub>O<sub>3</sub>, composite coatings had been electrodeposited, as discussed above. Samples were prepared from a solution of 17 wt.% powder with a composition of 45 vol.% Al, 45 vol.% Al<sub>2</sub>O<sub>3</sub>, and 10 vol.% YSZ which was suspended in ethanol and mechanically stirred. A potential of 100 V was applied for 5 seconds resulting in a film of approximately 25  $\mu\text{m}$  in thickness. The samples were then heat treated in air, to both oxidize and sinter. The samples were heated to a temperature of up to 1350°C at a heating and cooling rate of 1°C/min and held at the maximum temperature for 3 hours. The final YSZ layer was also electrophoretically deposited onto three-layered Ni-Al/Ni-Al-Al<sub>2</sub>O<sub>3</sub>/precursor-RBMO coatings to yield four layers overall.

## RESULTS

When alumina was codeposited with Ni as a single particle, an enhanced deposition of alumina was seen at lower current densities (1 or 2 A/dm<sup>2</sup>) and the amount of alumina in the coating increased with increasing amounts in the bath [8]. In the two particle case, the increased volume percent was seen with increasing amounts in the bath, but the effect of current density was no longer seen, as shown in Fig. 1a. This figure is a plot of volume percent alumina in the coating as a function of its volume percent in the bath for three current densities of 1, 5, and 15 A/dm<sup>2</sup> and three different Al bath contents. In effect, the presence of Al in the bath eliminated the enhanced codeposition of alumina at lower current densities. From this we conclude that Al

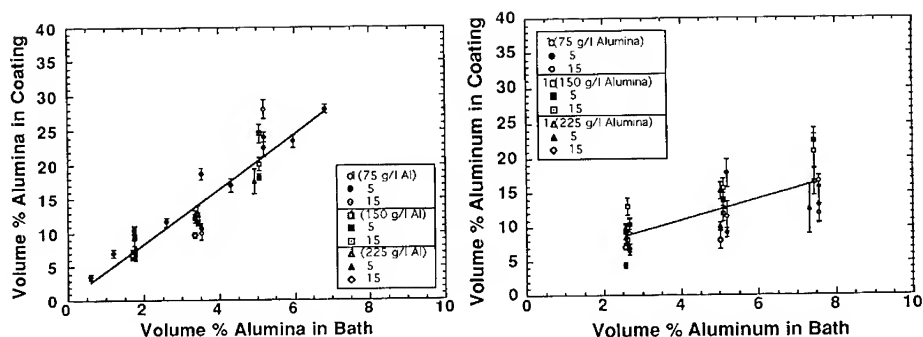


Fig. 1 - Volume percent (a) Al<sub>2</sub>O<sub>3</sub> (b) Al in dual particle Ni-Al-Al<sub>2</sub>O<sub>3</sub> coatings as a function of particle volume percent in the bath for three current densities of 1, 5 and 15 A/dm<sup>2</sup>. The amount of the second particle in the bath is given as the mass per liter of liquid.

interfered with the deposition of alumina. The nature of this interference is not yet clear, but may be related to the distortion of the field lines around the codepositing Al particles [8,9].

For the deposition of Al, however, very little difference was seen in the single or dual particle systems. Figure 1b shows the volume percent of aluminum in the dual particle coating as a function of its volume percent in the bath for the same current densities as above and three different alumina bath loadings. As can be seen in this figure, the amount of aluminum in the coating increased with increasing bath loading, but not as strongly as for alumina. In addition, there was no apparent dependence of Al codeposition on the current density or alumina loading. Thus, while Al (the electrically conducting particle) interfered with the deposition of Al<sub>2</sub>O<sub>3</sub> (the insulating particle), this interference was not reciprocated by alumina. This leads us to believe that the electrical properties of the particles, as well as particle-particle interactions, must be playing a role in the electrodeposition process. Since none of the existing theories take these properties or interactions into account, there is a need for further studies and theoretical developments in this area.

Figures 1a and b, and similar ones for the codeposition of single particles, provided us with appropriate processing parameters for the deposition of layered coatings of Ni-Al-Al<sub>2</sub>O<sub>3</sub>. These coatings were produced by varying the bath particle type and content at a fixed current density of 5 A/dm<sup>2</sup>. Light optical micrographs of one such coating are shown in Figs. 2a and b. Figure 2a shows the as-deposited coating with the three layers in the coating containing approximately 12-0, 9-16, and 9-24 Al vol.-%-Al<sub>2</sub>O<sub>3</sub> vol.%, respectively. Figure 2b shows the coating as in Fig. 2a which has been annealed at 635°C for 1 hour. When coatings containing Al were annealed, the reaction of the two elements resulted in the formation of either a solid solution of Al in Ni ( $\gamma$ ) phase or a two phase mixture of  $\gamma$ - $\gamma'$ , where  $\gamma'$  is the Ni<sub>3</sub>Al intermetallic phase. Electron probe

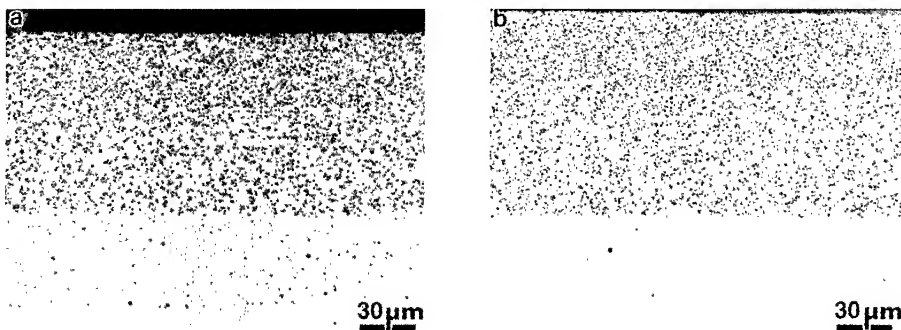


Fig. 2- Light optical micrographs of a Ni-Al-Al<sub>2</sub>O<sub>3</sub> coating. (a) From bottom to top, the three layers in the coating contain approximately 12-0, 9-16, 9-24 vol.%Al-vol.%Al<sub>2</sub>O<sub>3</sub>, respectively. (b) Same coating as in (a) annealed at 635°C for 1 hr.

microanalysis (EPMA) revealed that the composition of the solid solution and the ratio of  $\gamma$  to  $\gamma'$  were in agreement with the equilibrium phase diagram, thereby indicating that the samples had reached equilibrium during annealing. The metal matrix of the sample in Fig. 2b, was a two phase mixture of  $\gamma$  -  $\gamma'$ , with the alumina particles residing in  $\gamma$  the phase.

The RBMO layers were electrophoretically deposited onto single-layer Ni-Al or two-layer Ni-Al/Ni-Al-Al<sub>2</sub>O<sub>3</sub> coatings. The as deposited RBMO layer, or the "green" state of this coating, is gray due to the high aluminum content, as can be seen in Fig. 3a, which was deposited onto an electrodeposited Ni-Al layer containing approximately 12 vol.% Al. Figure 3b shows the coating after oxidizing and sintering to 1050°C in air for 3 hours. As can be seen in this figure, the coating has been completely oxidized as is apparent by its color change to white. We found that the oxidation resistance rendered to the substrate by the presence of Al in the Ni-Al layer was necessary in order to maintain adherence of the RBMO layer. In other words, the excessive oxidation of Ni substrates, when bare Ni substrates were used, resulted in the spallation of RBMO/NiO during heat treatment. The cross section of a sample with a RBMO coating, which was heat treated to 1250°C, is shown in Fig. 3c. The central regions are a uniform thickness of ~25  $\mu$ m, but the edges are approximately 100  $\mu$ m in thickness. The variation in the thickness around the edges can be controlled by processing parameters such as electrophoretic cell

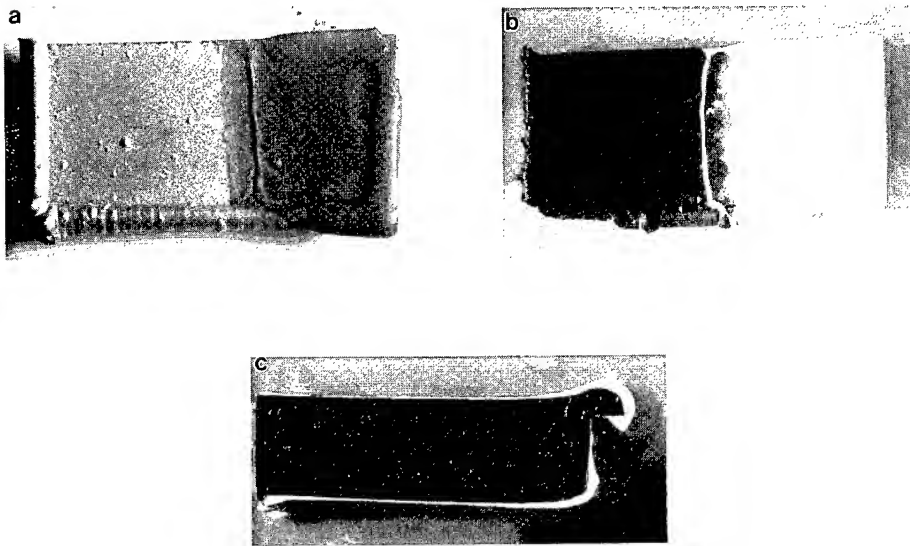


Fig. 3 - Light optical micrographs of the RBMO coating on Ni-Al coated Ni substrates (a) plan view, as-deposited, (b) plan view, after oxidation and sintering to 1050°C for 3 hrs, (c) cross section, similar coating to (b) but heat treated to 1250°C.

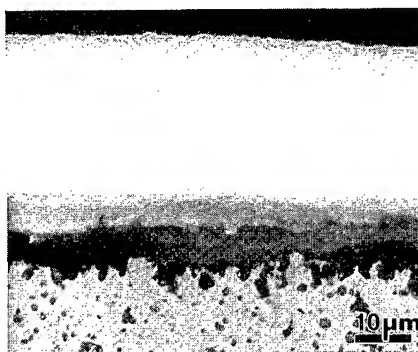


Fig. 4 - Light optical micrograph of the cross section of a four layered Ni-Al/Ni-Al-Al<sub>2</sub>O<sub>3</sub>/RBMO/YSZ coating heat treated to 1100°C for 3 hrs. The Ni-Al layer is not shown. The substrate is Ni.



geometry, solution viscosity, stirring conditions, etc. Figure 4 shows a four layered coating of Ni-Al/Ni-Al-Al<sub>2</sub>O<sub>3</sub>/RBMO/YSZ formed by oxidizing and sintering in air to 1100°C for 3 hours. The YSZ layer in this coating was electrophoretically deposited directly onto the precursor RBMO layer and the entire structure was then heat treated.

## SUMMARY AND CONCLUSIONS

Composite coatings of Ni with Al and Al<sub>2</sub>O<sub>3</sub> second phase particulates were produced by electrodeposition from a sulfamate type bath. The effects of current density and bath particle content on the volume percent particles in the coatings were investigated. The presence of aluminum particles in the bath was seen to influence the alumina codeposition, but the reverse was not true. Reaction bonded metal oxides (RBMO) were successfully deposited onto the above Ni-matrix composite layers, oxidized and sintered. Yttria-stabilized zirconia (YSZ) layers were deposited on the RBMO films, to yield four layer coatings of Ni-Al/Ni-Al-Al<sub>2</sub>O<sub>3</sub>/RBMO/YSZ. This paper demonstrates the versatility of electrochemical processing for the fabrication of multilayer composite coatings of both metals and ceramics that will be needed to produce thermal barrier coatings (TBCs) for advanced turbine systems. Although the utility of the coatings reported here as TBCs remains to be seen, the success of electrochemical processing in producing the desired architecture is noteworthy.

This work was made possible by the research subcontract DE-FC21-92MC29061 sponsored by the U.S. Department of Energy - Morgantown Energy Technology Center through a cooperative agreement with the South Carolina Energy Research Development Center at Clemson University. The authors thank NSF for financial support of S.W. Banovic and C. M. Petronis through Graduate Traineeships in Materials Science and Engineering, DMR-9256332. The authors respectfully acknowledge A.O. Benscoter for his help with metallography and microscopy. X.M. Ding, Professor B. Ilschner and Professor Rachman Chaim are gratefully acknowledged for helpful discussions.

## REFERENCES

1. X. M. Ding, N. Merk, and B. Ilschner, *FGM '94, Proc. 3rd International Symp. on Structural and Functional Gradient Materials*, Ed. B. Ilschner and N. Cheradi, (Presses Polytechnique et Universitaires Romandes), 365 (1995).
2. K. Barnak, S.W. Banovic, H.M. Chan, L.E. Friedersdorf, M.P. Harner, A.R. Marder, C.M. Petronis, D.G. Puerta, and D.F. Susan, *FGM '96, Proc. 4th International Symp. on Functionally Graded Materials*, Tsukuba, Japan Oct. 21-24, 1996.
3. N. Claussen, T. Le, and S. Wu, *J. Europ. Ceram. Soc.* **5**, 29 (1989).
4. N. Claussen, N.A. Travitzky, and S. Wu, *Ceram. Eng. Proc.* **11**, 806 (1990).
5. S. Wu, A. Gesing, N.A. Travitzky, and N. Claussen, *J. Europ. Ceram. Soc.* **7**, 277 (1991).
6. D. Holtz, S. Wu, S. Scheppokat, and N. Claussen, *J. Amer. Ceramic. Soc.* **77**, 2509 (1994).
7. S. Wu and N. Claussen, *J. Amer. Ceram. Soc.* **74**, 2460 (1991).
8. K. Barnak, S.W. Banovic, C.M. Petronis, D.F. Susan and A.R. Marder, *J. Micros.*, in press.
9. R. Bazzard and P.J. Boden, *Trans. Inst. Met. Finish.* **50**, 63 (1972).

## Investigation of the Codeposition of Polymer Lattices With Copper on a Rotating Disk Electrode

J. FRANSAER & J.P. CELIS

Dept. MTM, KU. Leuven, de Croylaan2, 3001 Heverlee, Belgium, jan@sunmtm.kuleuven.ac.be

### ABSTRACT

This article involves the study of the electrodeposition of composite coatings that form when colloidal particles deposit onto an electrode at which metal electrodeposition simultaneously occurs. The codeposition process of polystyrene (PS) and polymethylmethacrylate (PMMA) particles from a copper plating bath on a rotating disk electrode (rde) was investigated both theoretically and experimentally. The influence of the fluid flow velocity, density, mean size and zeta-potential of the particles, viscosity and temperature of the plating bath on the deposition rate of particles is studied using the theoretical model. The predictions of the model are compared with experimental results.

### THEORY

The codeposition of particles can be separated in two, nearly independent sub-processes: the reduction of metal ions and the concurrent deposition of particles. The amount of codeposited particles is given by the rate of depositing particles divided by the total deposition rate of particles and metal. Hence, in order to predict the amount of particles in a composite coating, the mass transport of both particles and metal ions to the electrode surface is required.

The mass transfer of metal ions was obtained from the transport equations which account for diffusion and hydrodynamic convection. It was assumed that the electrodeposition reaction of the metal cations can be described by Butler-Volmer kinetics. Furthermore, it is assumed that the deposition of metal is not influenced by the presence of particles in solution.

The mass transport of particles in the vicinity of the electrode surface, was obtained from a trajectory analysis [1, 2]. Based on all the forces and torques acting on a particle, Newton's second law yields the trajectories taken by individual particles in the electrolyte. Two types of forces were taken into account: forces of fluid mechanical origin and external forces. As the Reynold number associated with the flow around a particle is much smaller than one, the fluid forces are readily obtained from the creeping flow equations. The external forces consist of forces that only operate in the immediate vicinity of the electrode and long range forces. Gravity, buoyancy and the electrophoretic force were considered as long range forces. The short range forces consist of the dispersion and double-layer force. The dispersion force was calculated from the spectral constants of the particle and electrode. As such, the model does not contain adjustable parameters. Taking into account all the forces mentioned above, the number of particles that make contact with the electrode was calculated. This number is given by the sum of all particles whose trajectories fall within the limiting particle trajectory, defined as the particle trajectory that divides incoming particles with terminal contact from those which pass by. The number of particles  $j_p$  colliding with the disk per unit time is given by:

$$j_p = \pi \rho_{limit}^2 c_p V_z \quad (1)$$

where  $c_p$  is the volume concentration of particles in the bath,  $V_z$  and  $\rho_{limit}$  are resp. the fluid flow velocity and the radial distance of the limiting trajectory at the axial distance where the particle trajectories coincide with the undisturbed streamlines. In this work this distance was ten particle radii.

Before venturing further, it will be assumed that all the particles that reach the electrode, codeposit. This is known as the perfect sink condition. We will investigate how well the perfect sink boundary condition describes the codeposition of particles. Therefore, we will momentarily disregard the simultaneous deposition of metal and focus on the trajectory equations.

### MODEL PREDICTIONS

The trajectory equations were used to simulate the effect of the variation of several variables on the incident rate of particles with the rde. This yields information about the sensitivity of the model to its input variables. For each simulation, the incident rate of particles with a diameter of 5, 10 and 20  $\mu\text{m}$  is

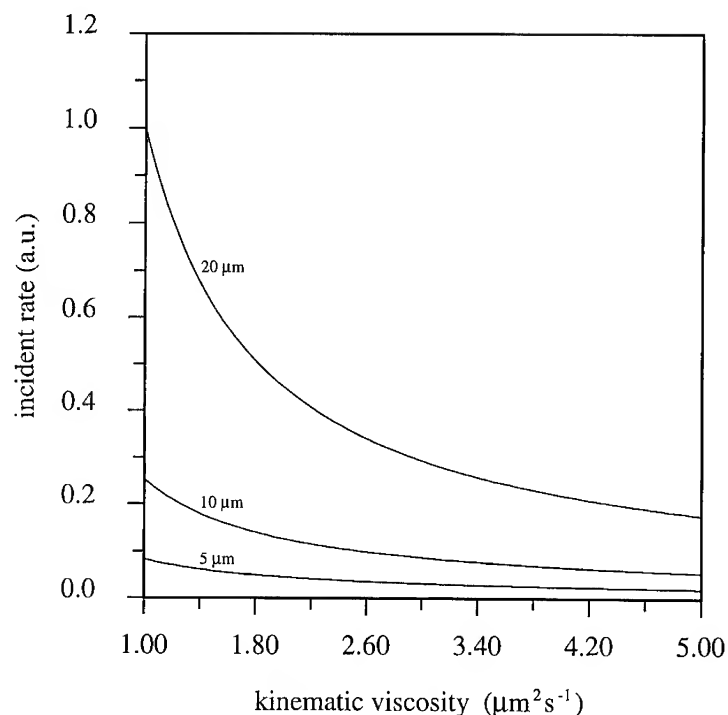


Figure 1: Dimensionless incident rate of polystyrene particles on a copper rde rotating at 200 rpm, as a function of the viscosity of the suspending electrolyte.

computed. In view of the use of the rde in the experimental section, the system parameters correspond to polystyrene particles that codeposit with copper on a 3 cm diameter rde rotating at 200 rpm, from an electrolyte consisting of  $200 \text{ gl}^{-1} \text{ CuSO}_4 \cdot 5\text{H}_2\text{O}$  and  $20 \text{ gl}^{-1} \text{ H}_2\text{SO}_4$ . The density, viscosity and the diffusion coefficients of such an electrolyte, were obtained from literature.

The effect of the rotation speed of the rde on the number of incident particles was studied. With increasing rotation speed, the incident rate increases. The increase is more pronounced for the bigger particles, that respond much more to the fluid flow field. This result indicates that, under the perfect sink conditions, it is advantageous to work with the highest possible rotation speed. Within the perfect sink model, however, the concomitant increase in the tangential fluid forces was neglected, which will offset part of the increase, by tearing away the particles from the surface. The increase in the codeposition with rotation speed of the rde has been observed in the codeposition of SiC with Ni [3]. In her thesis [3], Anne Lavanant reports an increase in the codeposition of SiC between 100 and 1000 rpm, followed by a decline in codeposition at higher rotation speeds.

If it were possible to change only the viscosity of the suspending electrolyte, the trajectory model with perfect sink conditions predicts a monotonous decrease of the incident rate with increasing viscosity (fig. 1). This drop is due to the increased hindrance to drain the fluid from between the particle and the electrode. As such, the particles tend to stay away from the surface, and the codeposition efficiency drops. This finding is in contradiction with the experimental observation of Anne Lavanant. In her thesis, she studied the effect of the addition of a rheological compound (xanthane gum) on the codeposition of SiC particles with nickel. The rheological compound increased the viscosity of the electrolyte, and led to a spectacular increase in the codeposition of SiC particles. It might be that the compound attaches itself to the particle and thus contributes to an increase of the adhesion force between the particle and the electrode. Moreover, it needs to be said that the addition of the compound also modified the structure, morphology and texture

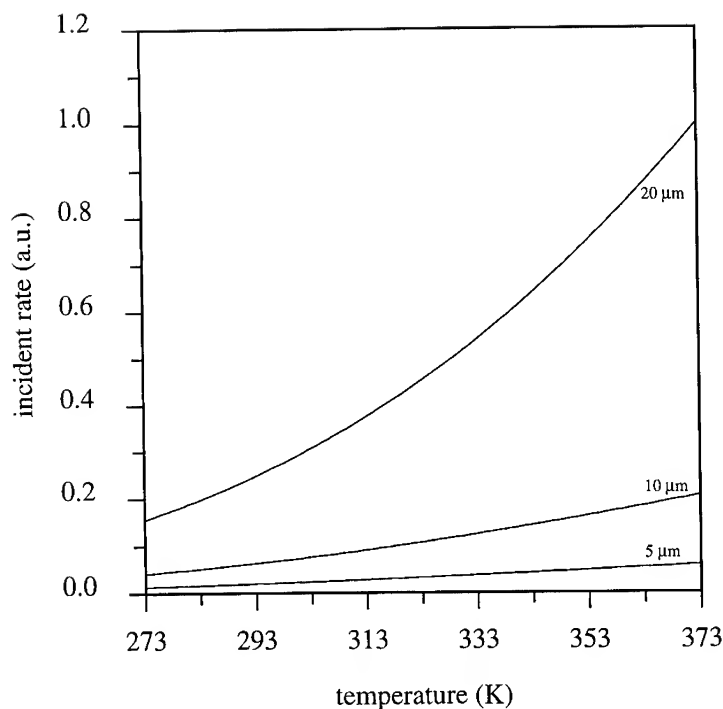


Figure 2: Dimensionless incident rate of polystyrene particles on a copper rde as a function of the temperature of a  $200 \text{ g l}^{-1} \text{ CuSO}_4 \cdot 5\text{H}_2\text{O} - 20 \text{ g l}^{-1} \text{ H}_2\text{SO}_4$ , when the rotation speed is 200 rpm.

of the deposit. Our calculations point out that the reason for the increase is not due to the increase of the viscosity. However, some caution is in order, since the rheological compound turned the electrolyte into a non-Newtonian fluid, while the trajectory equations were derived for a Newtonian fluid.

The predicted influence of temperature on the incident rate, is depicted in fig. 2. The change of the conductivity, density and viscosity of the electrolyte with temperature are explicitly taken into account in the trajectory model. The minor effect of temperature on the dielectric spectra, and thus on the dispersion force, or the change of the surface and  $\zeta$ -potentials of the particles and electrode with temperature, is not taken into account. Neither is the (unknown) effect on the solvation force. Some articles in literature point out that the hydration force might be substantially reduced when the temperature is increased. The softening of the polystyrene particles with temperature (the glass transition temperature of polystyrene is  $100^\circ\text{C}$ ) should increase the contact radius of the particles, and hence promote the adhesion of the particles to the electrode. From numerical experiments, it was found that the increase in the incident rate with temperature (seen in fig. 2) can largely be ascribed to the reduction of the viscosity.

It is seen in fig. 3 that the codeposition becomes zero if the density is larger than  $1.24 \text{ kg/dm}^3$ . Particles heavier than this, no longer reach the electrode. This can be explained as follows. Far from the electrode, the fluid velocities are large enough to transport the particles towards the electrode. As the particle nears the electrode, the fluid velocities die out, due to the evanescence of the fluid velocities on the plane of the electrode. In the immediate vicinity of the electrode, the dispersion force is large enough to attract the particle towards the electrode. In between these two extremes, gravity, which is directed away from the electrode for particles heavier than the electrolyte, can be larger than any of the two aforementioned forces. Within this region, the particle is too far from the electrode for the dispersion forces to be felt, and the particle is too close to the electrode for the fluid forces to operate. This creates a so-called *forbidden region*, delineated by an upper and a lower branch, marking the point where gravity just balances the sum of the

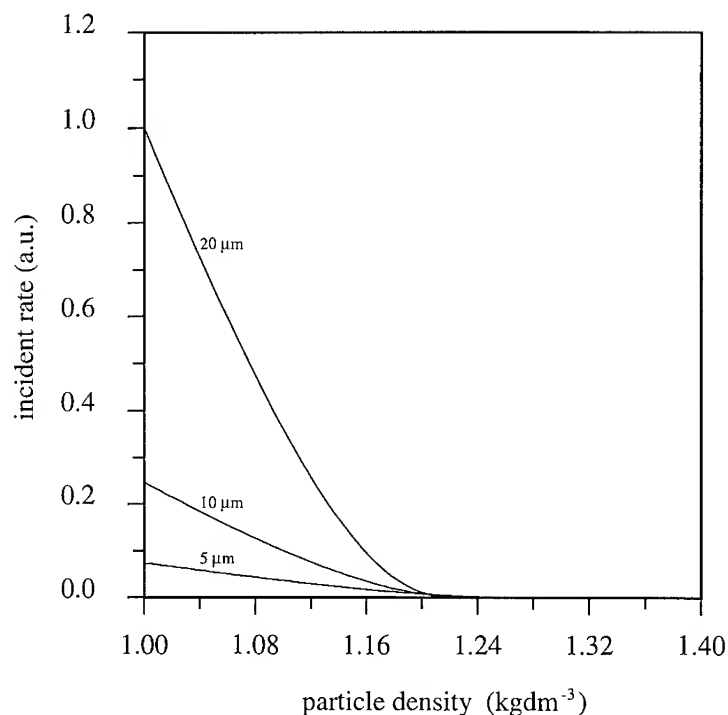


Figure 3: Dimensionless incident rate of polystyrene particles on a copper rde (rotating at 200 rpm) as a function of the specific density of the suspended particles. The density of the suspending fluid corresponds with a  $200 \text{ g l}^{-1} \text{ CuSO}_4 \cdot 5\text{H}_2\text{O} - 20 \text{ g l}^{-1} \text{ H}_2\text{SO}_4$ , at  $20^\circ\text{C}$ .

dispersion and the fluid forces. Particles that are brought up by the fluid convection instigated by the rotation of the electrode must traverse this region before they can reach the electrode. But, particles that would enter this region, sediment away from the electrode since gravity dominates in this region.

The importance of gravity was already mentioned by a number of researchers. However, in practice it is observed that micron sized particles heavier than the critical density of  $1.24 \text{ kg/dm}^3$  e.g. SiC with a specific density of  $3.22 \text{ kg/dm}^3$  codeposit on a rde. How can this be explained? The width of the region is of the order of the size of the particle. Near the lower branch of the *forbidden region*, particles will accumulate, while new particles are constantly arriving from below. It is therefore plausible, almost inevitable that, due to particle-particle interactions, some of the particles residing near the lower branch of the *forbidden region* get enough momentum to traverse the region and reach the electrode. Near the center of the rde, an approaching particle does not push a particle towards the electrode. On the contrary, the newly arriving particle lowers the hydrodynamic force on the particles already there. Further from the center the situation becomes different since the particles do no longer interact head-on but the approach can be sideways. This might explain why Anne Lavanant, in her thesis, observed a drop in the concentration of SiC particles codeposited with Ni, near the center of the rde.

An invariant in all of the cases above, is the lower incident rate predicted by the trajectory model for small particles (cf. fig. 4). The difference lies in the particle-electrode interactions and fluid forces that scale with the size of the particle. Small particles tend to follow the fluid streamlines, while big particles leave the streamlines when close to the electrode. These findings are again in accord with the results of Anne Lavanant. In her study of the codeposition of SiC with Ni, she compared the codeposition behaviour of SiC with different sizes. Much to her surprise, and contrary to popular belief, she found that the codeposition of SiC increased with increasing particle diameter. It's only for very large particles ( $> 10 \mu\text{m}$ ) that the

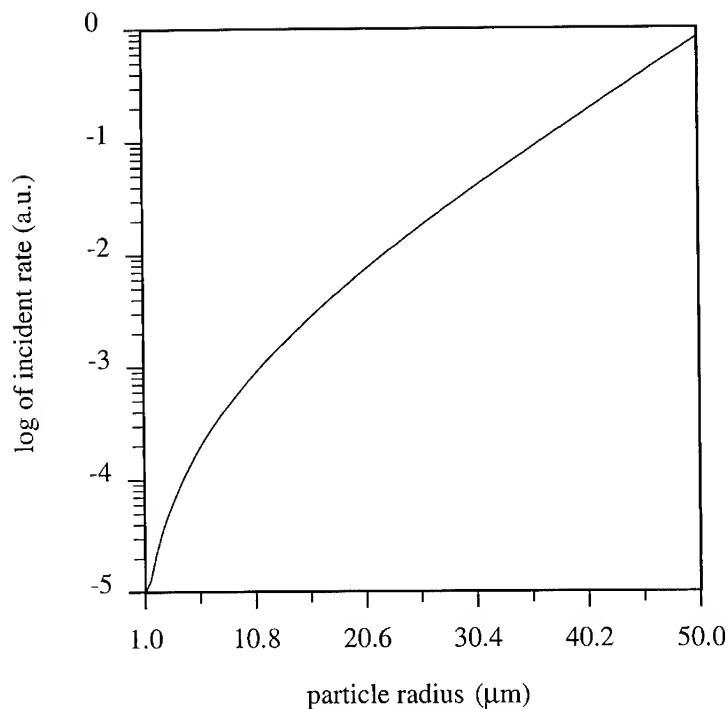


Figure 4: Dimensionless incident rate of polystyrene particles on a copper rde (rotating at 200 rpm) as a function of the radius of the suspended particles. The particles are suspended in a  $200 \text{ gl}^{-1} \text{ CuSO}_4 \cdot 5\text{H}_2\text{O}$ - $20 \text{ gl}^{-1} \text{ H}_2\text{SO}_4$ , at  $20^\circ\text{C}$ .

codeposition decreased. Might this explain why some studies report a decrease in codeposition efficiency when the size of the particles drops below  $1 \mu\text{m}$ ? We believe not. Particles that are smaller than  $1 \mu\text{m}$  tend to leave the fluid streamlines due to Brownian diffusion. Therefore, one must be careful to extrapolate the results of the trajectory analysis beyond the realm of the micron-sized particles.

## EXPERIMENTS

To test the validity of the trajectory analysis in the study of electrolytic codeposition, the model predictions are compared with experimental results obtained on the codeposition of latex model particles with copper on a rde. Electrolytic codeposition experiments were conducted, in which polydisperse spherical polystyrene particles were codeposited with copper on a rde. From the modeling point of view, this represents a less refractory problem, while manifesting all the complications of real electro-deposition of particles.

The experiments involved the codeposition of PS or PMMA particles from a copper plating bath containing  $200 \text{ gl}^{-1} \text{ CuSO}_4 \cdot 5\text{H}_2\text{O}$  (analytical grade) and  $20 \text{ gl}^{-1} \text{ H}_2\text{SO}_4$ . Deposition was carried out from a double walled, 1 liter pyrex un baffled cell, thermostated at  $21^\circ\text{C}$ , with a counter electrode of electrolytic copper mounted in the bottom. The rotating disk electrode was an interchangeable degreased brass electrode, with an active radius of 1.5 cm, mounted in a PTFE holder. The PS and PMMA particles were prepared by adding a 5–10% (w/v) PS and/or PMMA solution in methylenedichloride, to an aqueous solution containing 1% (w/v) gelatin as protective colloid, under vigorous stirring with a double bladed, or vortex stirrer. The resulting suspension is slowly heated, to evaporate the organic solvent ( $\text{CH}_2\text{Cl}_2$ , b.p.  $40^\circ\text{C}$ ), whereupon the particles are collected by sedimentation or centrifugation and repeatedly washed to remove the protective

$T$ (°C)	exper. (QIA)	theor.	viscosity ( $\mu\text{m}^2\text{s}^{-1}$ )	exper. (QIA)	theor.
0	1.00	1.00	1.45	1.00	1.00
10	1.21	1.26	1.87	0.85	0.72
20	1.28	1.58	2.36	0.72	0.54
30	1.38	1.94	2.72	0.70	0.45
40	1.76	2.35	3.30	0.67	0.36
			3.92	0.63	0.30

Table 1: Comparison between the observed and predicted codeposition of polystyrene particles with copper from a  $200\text{ g l}^{-1}\text{ CuSO}_4 \cdot 5\text{H}_2\text{O} - 20\text{ g l}^{-1}\text{ H}_2\text{SO}_4$  electrolyte, on a disk electrode rotating at 200 rpm as a function of resp. the temperature and the viscosity of the electrolyte.

colloid. The surface coverage of the rde by codeposited particles was obtained by quantitative image analysis (QIA) techniques of scanning electron micrographs. The volume percentage of codeposited particles is proportional to the surface concentration with proportionality constant equal to 0.80.

The size distribution of the particles was measured with a Coulter Electronics Inc. LS100 laser diffraction instrument. The  $\zeta$ -potential of the polystyrene particles in the plating bath was determined using a Zetasizer IIc of Malvern Instruments Limited. A positive  $\zeta$ -potential of  $13.5 \pm 0.5\text{ mV}$  was measured. In order to establish the sign of the charge of the copper electrode near rest potential, the  $\zeta$ -potential of very fine copper powder ( $\approx 1\text{ }\mu\text{m}$ ) prepared by the polyol method [4], was measured. A  $\zeta$ -potential of  $6.4\text{ mV}$  was found.

As a first test, we studied the influence of the temperature and the viscosity on the amount of codeposition of polystyrene particles from an acid copper sulphate bath. In these experiments, either the viscosity of the electrolyte was varied through the addition of ethyleenglycol and the temperature kept constant at  $20^\circ\text{C}$ , or the temperature was varied between  $0$  and  $40^\circ\text{C}$ . The experimental codeposition values found in table 1 are measured in the center of a rde, rotating at 200 rpm. As we are interested in the variation of the amount of codeposition, the values in table 1 were scaled to make the first item equal to 1. The data in this table shows that the trajectory model with perfect sink conditions predicts the increase in the codeposition with increasing temperature and the drop in codeposition with increasing viscosity.

## CONCLUSIONS

Assuming that all the particles contacting the electrode codeposit (also known as perfect sink conditions), the mass transport of metal and particles was used to predict the concentration of particles in the deposit. The experiments confirm the effect of the size of the particles and the effect of temperature and viscosity of the electrolyte on the volume content of particles in the center of the coating on a rotating disk electrode. It was found that the rate at which particles are brought to the surface of the cathode is governed almost entirely by the convection instigated by the rotating disk at large distances from the disk and by the dispersion force close to the disk. The agreement between theory and experiments indicates that the essential physics of codeposition on a rotating disk electrode is captured in the model.

## References

- [1] J. Fransaer, J.P. Celis & J.R. Roos, *J. Electrochem. Soc.*, **139**, 413–425 (1992).
- [2] J. Fransaer, Behaviour of particles in the vicinity of electrodes, Ph.D. Thesis, KULeuven, (1994).
- [3] A. Lavanant, *Contribution à l'étude du mécanisme d'incorporation de particules solides dans un dépôt électrolytique*, doctorat de l'université Pierre et Marie Curie, Paris 6 (1991).
- [4] F. Fievet, J.P. Lagier & M. Figlarz, Preparing monodisperse metal powders in micrometer and submicrometer sizes by the polyol process, *MRS Bulletin*, **14**, 29–34 (1989).

## ACKNOWLEDGEMENTS

J.F. wishes to thank the NFWO for the financial support through a post-doctoral grant.

## COMPOSITE FILMS OF COPPER / BORON NITRIDE AND NICKEL / BORON NITRIDE

Maria Hepel, Tania Tannahill, Christopher Baxter and Richard Stephenson

*Department of Chemistry, State University of New York, Potsdam,  
New York 13676*

### Abstract

The formation and characterization of composite films of copper/boron nitride (Cu/BN) and nickel/boron nitride (Ni/BN) are described. Composite Cu/BN and Ni/BN films were synthesized by a metal electrodeposition from suspensions of boron nitride particles on carbon steel substrates. The effects of concentration of boron nitride in the solution, temperature, potential and various additives on the morphology of composite films have been investigated. The morphology of these films was examined using Scanning Electron Microscopy. The elemental analysis for boron, nitrogen, copper and nickel was performed using Energy Dispersive X-ray Spectroscopy (EDS), and a Microprobe X-ray Analyzer. The Vickers hardness of Cu/BN and Ni/BN films prepared under different conditions was also investigated. It has been found that the composite Cu/BN and Ni/BN films have an increased microhardness as compared to the respective pure metal films. The effects of deposition potential, temperature, concentration of BN and presence of various additives on the microhardness of Cu/BN and Ni/BN films have been investigated.

### Introduction

Recently, there has been a growing interest in the dispersion-strengthened composite materials [1-4]. Metal films formed by electrodeposition from solutions containing suspended solid lubricant can function as hard and wear-resistant coatings, and also as heat-resistant coatings [5-10]. The use of boron nitride (BN) for nickel coating has been suggested by Bapu [7], Pushpavanam and Natarayan [8], and Hepel et al. [10]. An improvement in corrosion resistance of Cu/BN films [10] and Ni/BN films [7, 10] in comparison to their metal counterparts has also been reported.

In this paper, we report on the preparation and properties of Cu/BN and Ni/BN electrocomposites formed under different conditions on a carbon steel C-1018 substrate. The electrodeposited films were characterized using electrochemical methods, SEM, Energy Dispersive X-ray Analysis and microhardness tests.

### Experimental

**Chemicals.** All chemicals were of reagent grade purity (Aldrich) and were used without further purification.

**Instrumentation.** A Model PS-605 Precision Potentiostat/Galvanostat (ELCHEMA, Potsdam, NY) was used in measurements. The program waveform was generated by VOLTSCAN Real-Time Data Acquisition System (ELCHEMA). All electrochemical measurements were performed using a double-junction saturated (KCl) calomel electrode (SCE) as the reference electrode and a Pt wire was used as the counter electrode. Disk-shaped C-1018 carbon steel electrodes mounted in a Working Electrode Assembly (ELCHEMA) were used as substrates for deposition of electrocomposite films. The active geometric surface area of the substrates was 1.2 cm<sup>2</sup>. Scanning Electron Micrographs were



taken using a Model JSM-6300 SEM (JEOL) equipped with an Energy Dispersive X-ray unit for elemental analysis and a Noran Voyager X-Ray Microanalyzer. Vickers microhardness was measured using a Leco Microhardness Tester, Model M-400, with a standard 50 mN load.

**Procedures.** Electrodepositions of Cu/BN films were carried out from suspensions of boron nitride particles in acidified copper sulfate solutions. The Ni/BN films were obtained by electrodeposition from suspensions of boron nitride particles in Watt's bath solution. The average size of BN particles used was 1  $\mu\text{m}$ . The suspension density was from 0 to 50 g/L (BN). Films were deposited on carbon steel C-1018 substrates. They were degreased with propanol, polished with 0.05  $\mu\text{m}$  alumina powder, rinsed with distilled water and ethanol, and assembled in a demountable working electrode. The solution and suspensions were deoxygenated by nitrogen bubbling prior to the experiments. Constant hydrodynamic conditions during the deposition process were maintained by stirring with a constant rate of 600 r.p.m. The measurements were performed at room temperature, 22°C.

## Results and Discussion

### Formation of Cu/BN Films

The electrodeposition of Cu in the presence and absence of boron nitride particles in the solution was investigated for various conditions. Typical current transients recorded during the electrodeposition are presented in Figure 1, curves 1 and 2. These current-time transients were obtained for the same macro-hydrodynamic conditions from a solution containing 0.25 M  $\text{CuSO}_4$  + 2.5 M  $\text{H}_2\text{SO}_4$ , at a constant potential  $E = -800$  mV vs. SCE in the presence of 30 g/L BN (curve 2) and in its absence (curve 1).

In the presence of BN particles forming suspension, a significant increase in the deposition current was observed. This increase can be attributed to the increased mass transport associated with micro-stirring introduced by the translational and rotational movement of BN particles in the suspension. Thus, the change in micro-hydrodynamic conditions in the solution caused by the presence of BN particles is directly responsible for the increase in the copper electrodeposition rate.

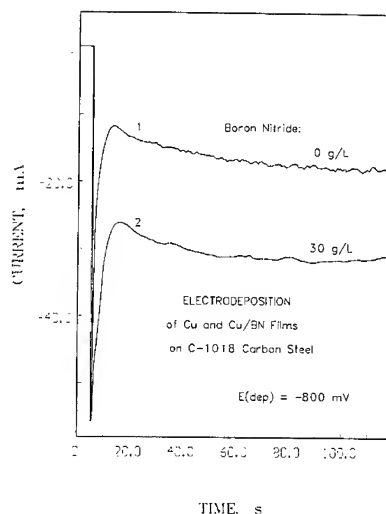


Figure 1. Current-time transient recorded during electrodeposition of Cu/BN film at a constant potential,  $E_{\text{dep}} = -800$  mV vs. SCE from a solution containing 0.25 M  $\text{CuSO}_4$  + 2.5 M  $\text{H}_2\text{SO}_4$  (1) in the absence of BN, (2) with 30 g/L BN.

### Morphology of Cu/BN Films

The effects of various deposition conditions on the morphology of Cu/BN composite films were investigated using a Scanning Electron Microscopy. The morphology of a composite Cu/BN film deposited from a solution containing 10 mM CuSO<sub>4</sub> + 0.1 M H<sub>2</sub>SO<sub>4</sub> + 10 g/L BN, at a constant deposition potential  $E_{\text{dep}} = -600\text{mV}$  vs. SCE, is presented in Figure 2. Several round disk-like BN particles embedded in the copper film are visible in this Figure.

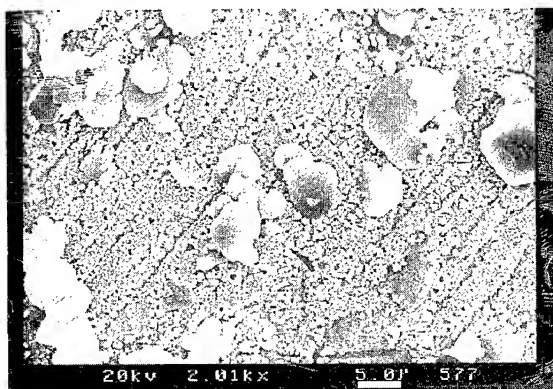


Figure 2. SEM image of the surface of Cu/BN film electrodeposited on carbon steel substrates at a constant potential,  $E_{\text{dep}} = -600\text{ mV}$  vs. SCE, with  $t_{\text{dep}} = 480\text{ s}$ , at  $T = 22^\circ\text{C}$ , from a 0.01 M CuSO<sub>4</sub> + 0.1 M H<sub>2</sub>SO<sub>4</sub> solution with suspended BN particles; suspension density: 10 g/L.

Many different variables can affect the morphology of Cu/BN films. The effects of the electrodeposition potential and additives were previously reported [10]. The effect of BN particles in the suspension on the morphology of Cu/BN films is illustrated in Figure 3 and 4. The size of electrodeposited copper clusters decreases with increasing concentration of BN particle in the solution and, as a consequence, the formation of smoother copper films is observed. The electrodeposition of copper from a solution containing 0.01M CuSO<sub>4</sub> + 0.1 M H<sub>2</sub>SO<sub>4</sub>, without BN, was carried out at a constant deposition potential  $E_{\text{dep}} = -600\text{mV}$  vs. SCE. The SEM micrograph of the deposit obtained is presented in Figure 3. Hemispherical, rounded copper crystallites with an average size of 0.3  $\mu\text{m}$  are visible in this Figure. In the presence of 20 g/L BN in the solution, the average size of copper crystallites decreases and is equal to approximately 0.1  $\mu\text{m}$ . Some larger copper crystals are also formed as a result of the secondary nucleation and growth. In the right corner of the SEM micrograph presented in Figure 4 a BN particle is also visible.

### Energy Dispersive X-Ray Analysis of Cu/BN Films

The presence of BN particles in copper films deposited from boron nitride suspensions was confirmed by an EDS analysis which was performed for films prepared under different deposition conditions. The X-ray intensities of K $\alpha$  line for boron, nitrogen, and copper were monitored.

A gray image and X-ray maps of a composite Cu/BN film obtained by electrodeposition on a Pt substrate, at a constant potential  $E_{\text{dep}} = -200\text{mV}$ , from a solution containing 0.01M CuSO<sub>4</sub> + 0.1 M H<sub>2</sub>SO<sub>4</sub> and 30g/L BN, was recorded. The Cu\_L and Cu\_K $\alpha$  intensities show voids in copper signals in place where a BN particle is seen on the gray image of the film. Signals from boron B\_K $\alpha$  and nitrogen N\_K $\alpha$  show enhancements in the area where a BN particle is present. The presence of very small BN particles, not visible under a scanning electron microscope, was also confirmed by EDS analysis.

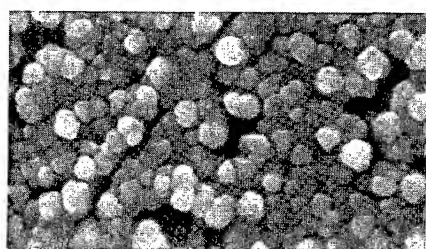


Figure 3. SEM image of the surface of Cu/BN film electrodeposited on carbon steel substrates at a constant potential,  $E_{\text{dep}} = -600\text{mV vs. SCE}$ , with  $t_{\text{dep}} = 120\text{ s}$ , at  $T = 22^\circ\text{C}$ , from a  $0.25\text{ M CuSO}_4 + 2.5\text{ M H}_2\text{SO}_4$  solution with no suspended BN particles. Magnification 10kx.

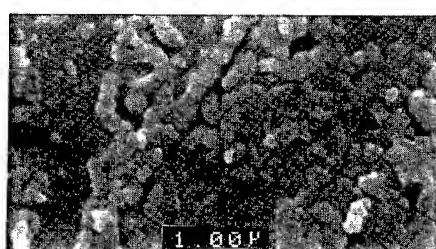


Figure 4. SEM image of the surface of Cu/BN film electrodeposited on carbon steel substrates at a constant potential  $E_{\text{dep}} = -600\text{ mV vs. SCE}$ , with  $t_{\text{dep}} = 480\text{ s}$ , at  $T = 22^\circ\text{C}$ , from a  $0.01\text{ M CuSO}_4 + 0.1\text{ M H}_2\text{SO}_4$  solution with suspended BN particles; suspension density:  $50\text{ g/L}$ . Magnification 10kx.

### Vickers Microhardness Test of Cu/BN Films

The microhardness test for films prepared under different conditions were performed using a maximum load of  $50\text{ mN}$  and for a load time of 15 seconds. The average from five measurements for each sample was calculated and is presented in Table I, Table II, Table III and Table IV. The composite Cu/BN films show a significant improvement in microhardness in comparison to the respective pure metal films.

**Table I. Effect of Deposition Potential on Microhardness of Cu/BN Films**

Deposition Potential [mV]	Vickers Microhardness [VHN <sub>50</sub> ]	Concentration of BN in Solution [g/L]	Temperature °C
-400	273.0	30	22°
-800	326.0	30	22°
-1000	437.9	30	22°

The data presented in Table I were obtained for Cu/BN films prepared from a solution containing  $0.25\text{M CuSO}_4 + 2.5\text{ M H}_2\text{SO}_4$  and  $30\text{g/L BN}$ , at room a temperature and for a constant deposition time of 120 seconds. The microhardness tests were performed for films deposited at the following constant potentials  $E_{\text{dep}} = -400, -800$  and  $-1000\text{ mV}$ .

As shown in Table I, the microhardness of Cu/BN films increases when more negative potential is applied.

In our previous studies [10], we have demonstrated that the morphology of Cu/BN films changes significantly with the deposition potential. The size of copper nuclei decreases when more negative potential is applied, but number of nucleation sites increases.

The microhardness of Cu/BN films is strongly affected by changes in the film microstructure which, in turn, is reflected in the changing morphology of the film surface.

**Table II. Effect of Temperature on Microhardness of Cu/BN Films**

Temperature °C	Vickers Microhardness [VHN <sub>50</sub> ]	Concentration of BN in Solution [g/L]	Deposition Potential [mV]
22°	273.0	30	-400
45°	356.0	30	-400
60°	354.2	30	-400

The data presented in Table II were obtained for Cu/BN films prepared from solutions with the same composition as for Table I. The results obtained indicate that the microhardness of Cu/BN films increases when temperature is raised from 22°C to 45°C.

**Table III. Effect of Concentration of BN in Suspension on Microhardness of Cu/BN Films**

Concentration of BN in Solution [g/L]	Vickers Microhardness [VHN <sub>50</sub> ]	Temperature °C	Deposition Potential [mV]
0	208.3	22°	-600
5	245.6	22°	-600
10	299.9	22°	-600
30	315.5	22°	-600
50	387.2	22°	-600

Cu/BN films of Table III were prepared from a solution containing 0.25M CuSO<sub>4</sub> + 2.5 M H<sub>2</sub>SO<sub>4</sub> and variable concentration of BN particles in the suspension. The results obtained confirm that the microhardness of Cu/BN films increases when concentration of BN in suspension increases.

**Table IV. Effects of Additives on the Microhardness of Cu/BN Films**

Concentration Additive of [mM]	Vicker Microhardness [VHN <sub>50</sub> ]	Concentration of BN in Solution [g/L]	Deposition Potential [mV]	Temperature °C
no additives	326.0	30	-800	22°
10 mM NaCl	429.0	30	-800	22°
1 mM Thiourea	456.7	30	-800	22°
10 mM EDTA	417.0	30	-800	22°
10 mM Coumarin	399.9	30	-800	22°
0.1 mM CTAB	332.7	30	-800	22°

In these experiments, the Cu/BN samples were prepared from a solution containing 0.25M  $\text{CuSO}_4$  + 2.5 M  $\text{H}_2\text{SO}_4$  + 30 g/L BN and varying concentration of different additives. It is seen that the microhardness of Cu/BN films increases when additives are present during the plating process. It is known that most of organic additives adsorb on the electrode surface and inhibit the electrodeposition of metals. Organic additives also change significantly the morphology of electrodeposited metals [11].

### Electrodeposition and Characterization of Ni/BN Films

The electrodeposition of Ni is only slightly dependent on hydrodynamic conditions at lower overvoltage and completely independent of any changes in hydrodynamic conditions at higher cathodic overvoltage. The effects of the concentration of BN particles in a suspension and the deposition potential on the current-time transients recorded during the formation of Ni/BN films were reported previously [10]. It has been found that, at a low overvoltage, both the effect of changes in the micro-hydrodynamics due to the movement of BN particles, as well as the effect of BN entrapment on the nucleation and growth processes of nickel itself, played an important role in the film formation process. At higher cathodic overvoltage, the micro-hydrodynamic effects were negligible and surface blocking effect due to the entrapment of nonconductive BN particles became dominant.

In this paper, we have studied the effects of the deposition potential, concentration of BN particles, temperature, and various additives on the morphology and microhardness of Ni/BN films.

In Figure 5, a SEM micrograph of a Ni/BN film prepared at room temperature, at  $E_{\text{dep}} = -1300$  mV vs. SCE on a steel substrate, from a solution containing 0.85 M  $\text{NiSO}_4$  + 0.15 M  $\text{NiCl}_2$  + 0.1 M boric acid + 5 g/L BN, is presented. Several BN particles embedded in the smooth nickel film are visible. In order to confirm the presence of BN particles in nickel films, the EDS analysis was performed for films obtained under different deposition conditions. The X-ray intensities of  $K_{\alpha}$  for boron, nitrogen and nickel were monitored.

In Figure 6, a gray image and X-ray maps of a composite Ni/BN film obtained by electrodeposition at  $E_{\text{dep}} = -1200$  mV vs. SCE, from a solution containing 0.85 M  $\text{NiSO}_4$  + 0.15 M  $\text{NiCl}_2$  + 0.1 M boric acid and 5 g/L BN, are presented.

The gray image shows a BN particles on the surface of a nickel film. Both the  $\text{Ni}_{K_{\alpha}}$  and  $\text{Ni}_{L}$  lines show voids in nickel signal in areas where BN particles are seen on the gray image of the surface. Strong enhancements in the  $\text{B}_{K_{\alpha}}$  and nitrogen  $\text{N}_{K_{\alpha}}$  lines in the areas of BN particles are observed confirming the presence of BN particles in the film.

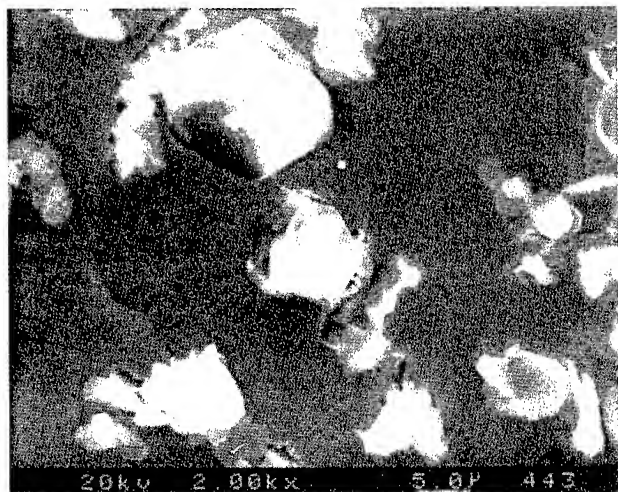


Figure 5. SEM image of the surface of Ni/BN film electrodeposited on carbon steel substrates at a constant potential,  $E_{\text{dep}} = -1300$  mV vs. SCE, with  $t_{\text{dep}} = 120$  s, at  $T = 22^\circ\text{C}$ , from a 0.85 M  $\text{NiSO}_4 + 0.15$  M  $\text{NiCl}_2 + 0.1$  M boric acid solution with suspended BN particles; suspension density: 5 g/L.

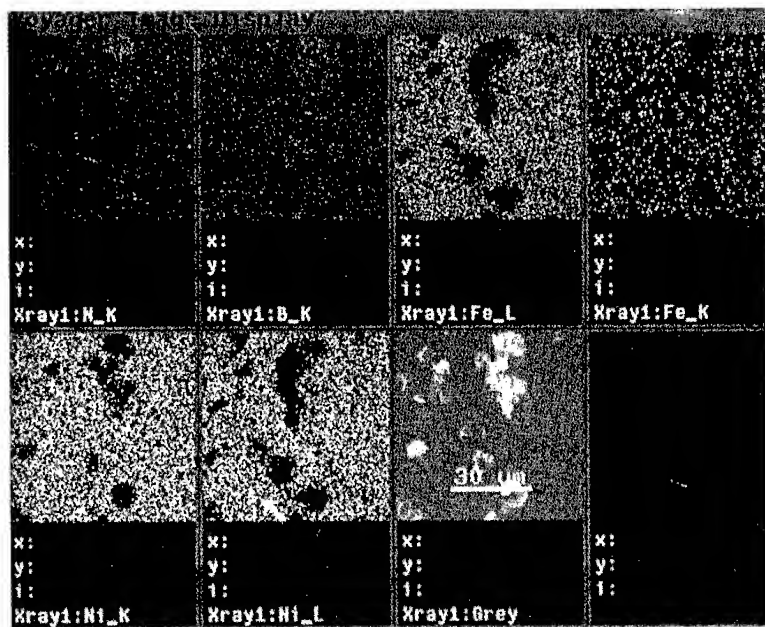


Figure 6. X-ray map and gray image of Ni/BN film electrodeposited on carbon steel substrates at a constant potential,  $E_{\text{dep}} = -1200$  mV vs. SCE, with  $t_{\text{dep}} = 120$  s, at  $T = 22^\circ\text{C}$ , from a 0.85 M  $\text{NiSO}_4 + 0.15$  M  $\text{NiCl}_2 + 0.1$  M boric acid solution with suspended BN particles; suspension density: 5 g/L.

**Table V. Microhardness of Ni/BN Films**

Vickers Microhardness [VHN <sub>50</sub> ]	Deposition Potential [mV]	Temperature °C	Concentration of BN in Solution [g/L]
328.0	-1000	22	5
337.9	-1200	22	5
355.6	-1300	22	5
332.2	-1000	45	5
359.1	-1200	45	5
502.7	-1300	45	5
387.8	-1000	45	30
462.9	-1200	45	30
514.1	-1300	45	30
190.0	-1000	22	0
210.0	-1200	22	0
324.0	-1300	22	0

The microhardness of Ni/BN films increases when the deposition potential changes from  $E_{\text{dep}} = -1000$  mV to  $E_{\text{dep}} = -1300$  mV vs. SCE. The increase in the bath temperature from 22°C to 45°C results in an increase in the microhardness, especially at high cathodic overvoltage. The microhardness of composite Ni/BN films in comparison to pure nickel film is considerably higher.

## References

1. A. Hovestad and L.J.J. Janssen, *J. Appl. Electrochem.*, **25**, 519 (1995).
2. B.J. Hwang and C.S. Hwang, *J. Electrochem.Soc.*, **140**, 979 (1993).
3. N. Guglielmi, *J. Electrochem.Soc.*, **119**, 1009 (1972).
4. J.P. Celis, J.R. Roos and C. Buelens, *J. Electrochem.Soc.*, **134**, 1402 (1987).
5. V. Bhalla, C. Ramasamy, N. Singh, and M. Pushpavanam, *Plating Surf. Fin.*, **11**, 58 (1995).
6. P.J. Sonneveld, W. Visscher, F. Panneflek, E. Barendrecht, and M.A.J. Michels, *J. Appl. Electrochem.*, **22**, 935 (1992).
7. G.N.K. Bapu, *Plating Surf. Fin.*, **7**, 70 (1995).
8. M. Pushpavanam, S.R. Natarayan, *Met. Fin.*, **93(6)**, 97 (1995).
9. G.N.K. Bapu, M.M. Yusuf, *Mat. Chem. Phys.*, **36**, 134 (1993).
10. M. Hepel, T. Tannahill and C. Baxter, in the *Proceeding of the Electrochemical Society "Electrodeposited Thin Films III"*, (Ed) M. Paunovic, The Electrochemical Society (1996) Pennington, NJ.
11. M. Hepel, Y.M. Chen and L. Adams in the *Proceedings of the SUR/FIN '95 Technical Conference of the American Electroplaters and Surface Finishers Society*, June 26-29, 1995, Baltimore, MD, pp. 709-720

## Acknowledgment

This work was partially supported by the Chema Technology Inc. Grant.

## CHARACTERIZATION OF HIGH STRENGTH Cu/Ag MULTILAYERED COMPOSITES

Qing Zhai, Dan Kong, Augusto Morrone, and Fereshteh Ebrahimi  
Materials Science & Engineering Department  
University of Florida, Gainesville, FL 32611

### ABSTRACT

In this study, electrodeposition was employed to produce Cu-Ag multilayered nanocomposites using a single-bath cyanide solution. The silver and the copper layers were applied by electroless deposition and galvanostatic electrodeposition methods, respectively. The as-deposited composite showed a very high strength, which was increased upon annealing at 104°C. Annealing at 149°C caused the strength to drop to a level comparable to the strength of electrodeposited pure copper specimens. In this paper, the effect of heat treatment on the mechanical properties and structure of Cu-Ag multilayered nanocomposites is discussed.

### INTRODUCTION

Nanocomposites, which have extraordinary high strength, have been the subject of many recent investigations [1-5]. Electrodeposition has been used to make layered nanocomposites [2,3]. The advantages of this method when compared with other deposition techniques, such as sputtering, are low deposition temperature, ease of control, and that no vacuum is needed. Cu-Ag nanocomposites have been made and investigated by Tench and White [6], who have reported an ultimate tensile stress of 898MPa for a composite with an average bilayer thickness (Cu+Ag) of 50nm. High temperature annealing of this composite resulted in spheroidization of silver layers and hence the ultimate tensile stress dropped to 40MPa [7]. Low temperature annealing is expected to cause recovery and perhaps recrystallization of the copper layers without a major modification of silver layers. The objective of this study has been to investigate the effect of low temperature annealing on tensile properties and microstructure of a Cu-Ag nanocomposite.

### EXPERIMENTAL PROCEDURES

Following the deposition method used by Tench and White [6], a cyanide solution was used for deposition of Cu-Ag nanocomposites. The composition of the solution was 60g/l CuCN, 102g/l KCN, 15g/l K<sub>2</sub>CO<sub>3</sub>, 15g/l KOH, 15g/l potassium sodium tartrate (Rochelle salt), and 34mg/l AgCN. The substrate was pure copper disk of 35mm in diameter, which was electropolished before plating. Copper was plated using the galvanostatic technique at a constant current density of 3.5 mA/cm<sup>2</sup>. Silver was deposited by the electroless displacement process, which occurs without polarization. Therefore, the silver concentration was kept very low and the solution was replenished periodically by addition of silver ions. The working electrode was rotated at a speed of 750 rpm during the silver deposition; and during copper deposition the working electrode was still. Between silver plating and copper plating, there were 10 seconds for the flow to rest. The plating was proceeded in an isothermal bath at 60 ± 0.2°C. Before plating, the solution was degassed by pure nitrogen flow for one hour, while during plating, a nitrogen



blanket was kept above the solution. The periods of copper plating and silver plating were 180 seconds and 60 seconds, respectively, and 85 cycles were repeated for each sample. The copper substrate was removed by chromic acid with 10% sulfuric acid [2]. The deposited composite sample had an approximate thickness of  $28\mu\text{m}$ , which means the thickness of a Cu-Ag layer is about  $329\text{nm}$ . Tensile specimens with a gauge length of  $12\text{mm}$  were prepared from each composite disk using a grinding method. Pure copper specimens were electroplated at the same conditions as the Cu-Ag composites were made except that there were no silver ions in the solution.

Heat treatment was performed in silicon oil for six hours at  $104\pm 2^\circ\text{C}$  and  $149\pm 2^\circ\text{C}$ , respectively. Tensile testing was conducted at a strain rate of  $1.8 \times 10^{-4} (\text{sec}^{-1})$  at room temperature. Two specimens were tested for each condition. Fracture surfaces of tensile specimens were studied by SEM (Scanning Electron Microscopy). Cross-sectional thin foils for TEM (Transmission Electron Microscopy) were prepared using the ion milling technique. A cold stage was used to minimize the possible damage from the ion milling process. A 200CX JOEL electron microscope was used at  $200\text{KV}$  for the analysis of the foils.

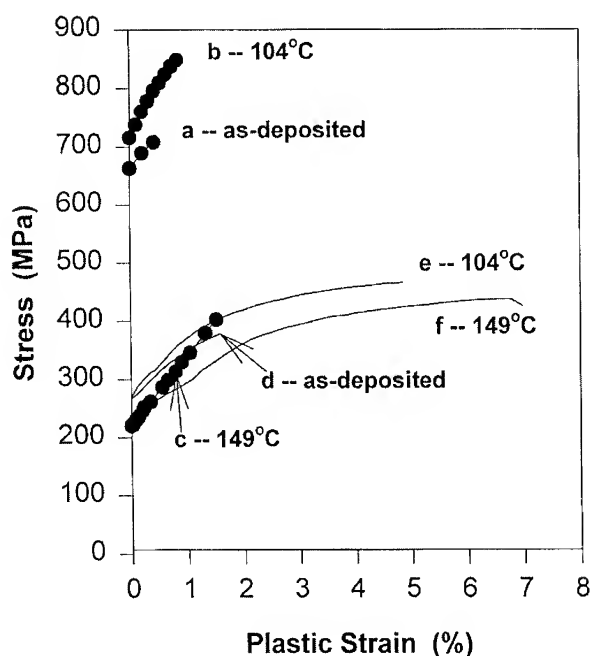


Fig. 1 The tensile data for as deposited and heat treated composite samples (a,b &c) and pure copper samples (d,e & f)

## RESULTS AND DISCUSSIONS

Tensile stress-strain curves for as-deposited and heat treated Cu-Ag nanocomposites and pure copper specimens are shown in Figure 1. Consistent tensile data were obtained by testing two specimens for each condition. The as-deposited composite showed a much higher strength (708MPa) and a lower ductility than the as-deposited pure copper specimen (378MPa) did. Heat treatment at 104°C improved both ductility and strength of the composite as well as those of the pure copper samples. Heat treatment at 149°C resulted in a drastic drop of composite strength (about 446MPa) to a level comparable to its pure copper counterpart. However, the strength of the pure copper was reduced only by 41MPa. The composite specimens showed a higher strain hardening rate than the pure copper counterparts did. It is interesting to note that the 149°C heat treated composite specimen showed a high strain hardening rate in spite of its low strength. Furthermore, its ductility is lower than its pure copper counterpart although the composite specimen has a similar yield strength and a higher strain hardening rate.

Figure 2 presents SEM fractographs of the composite specimens. There is a significant change in the fracture behavior with annealing temperature. The fracture surface of the as-deposited and 104°C annealed specimens showed distinct layered structures. The number of layers was 85, consistent with the number of cycles applied during deposition. No layered structure was observed on the fracture surface of the 149°C annealed specimen, which fractured by a microvoid coalescence mechanism similar to the pure copper specimens. The observation of layers on the fracture surface can be attributed to the delamination of Cu/Ag interface. It is suggested that the fracture proceeds first by delamination of the interfaces, then the subsequent necking of each copper layer, and finally the copper layers fracture individually. The absence of a layered structure in the 149°C annealed specimen suggests that: (1) the Cu/Ag interface has become stronger, (2) the deformation between layers has become more compatible and hence triaxial stresses that lead to delamination have not developed, and/or (3) the silver layer has spheroidized upon annealing at 149°C for 6 hours.

Figures 3 and 4 present TEM micrographs of the 104°C and 149°C annealed specimens. The estimated layer thickness from TEM micrographs is consistent with the value calculated based on the total thickness. As shown in Figure 3a, the copper layer is heavily defected and contains a high density of twins. It was difficult to distinguish copper grain boundaries, except for isolated regions where showed grain growth as depicted in Figure 3b. Heat treatment at 149°C resulted in recrystallization of copper layers and removal of most of defects and twins as shown in Figure 4a. Figure 4b shows a dark field image which demonstrates that grains on adjacent layers can have similar crystallographic orientation. The silver layer appears to have a non-uniform thickness with a minimum thickness of approximately 6nm. Since silver layer is deposited by a displacement technique, it is expected to be only a few nanometers in thickness, and the variation in thickness is a result of the angle of silver layer relative to the deposition front.

Assuming that the plastic deformation is controlled by motion of dislocation in the specimens studied in this investigation, it is expected that both grain boundaries and interface act as barriers to dislocation motion. The large difference in strength of the as-deposited pure copper and the composite specimens suggests that the silver layer plays an important role during plastic deformation. It is reported [6] that for an as-deposited Cu-Ag composite with an average layer thickness of about 50nm, the ultimate tensile strength is around 898MPa [6]. The lower strength of the composite produced in this study is believed to be associated with a large layer thickness (329nm). Since the motion of dislocation is interrupted at the Cu/Ag interface, a decrease of the

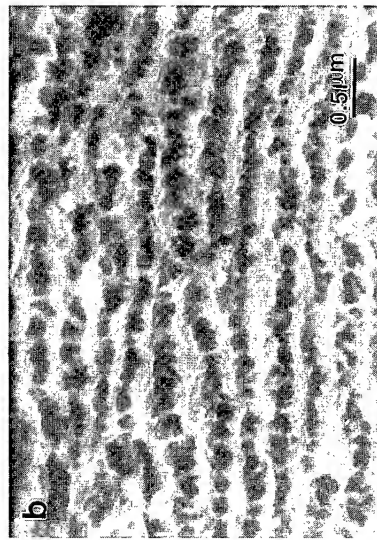
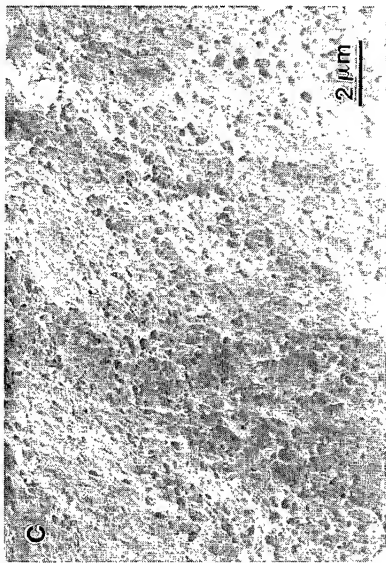


Fig. 2 SEM picture of fracture surface of Cu-Ag composite specimens

- (a) As-deposited
- (b) Heat treated at 104°C
- (c) Heat treated at 149°C

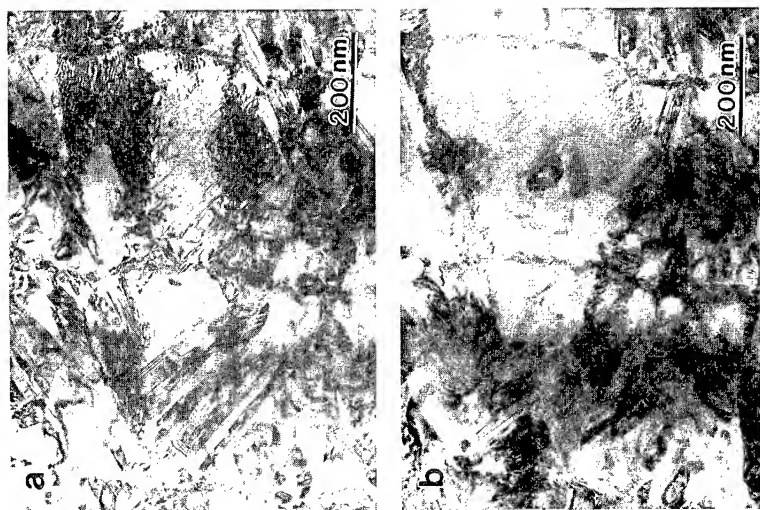


Fig. 3 TEM micrographs of the 104°C annealed composites specimen showing (a) highly defected copper grains and (b) a recrystallized region

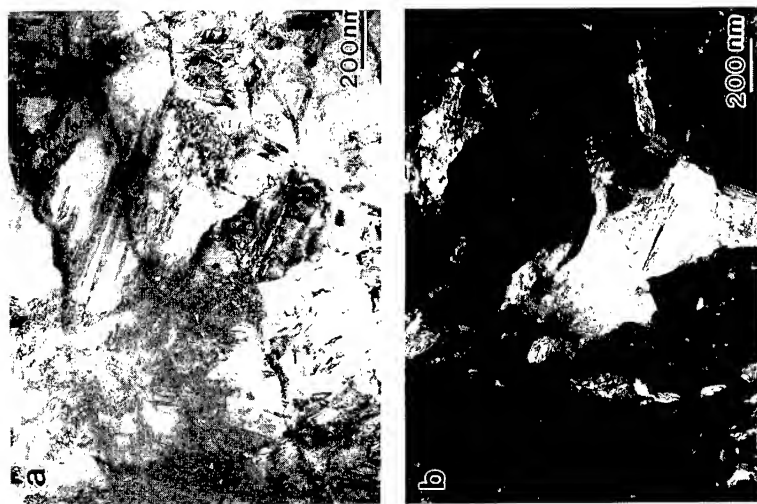


Fig. 4 TEM micrographs of the 149°C annealed composite specimen (a) bright field image (b) dark field image

copper layer thickness may effectively lead to high strength. The increase in the strength of both pure copper and composites upon heat treatment at 104°C is suggested to be due to the recovery of the microstructure and release of internal stresses by modification and relaxation of the grain boundary structure and interfaces to lower energy state as well as the reduction in density of the bulk defect structure [8]. Also, since hydrogen was produced together with copper during plating, hydrogen embrittlement can not be neglected. Annealing at 104°C for 6 hours is expected to eliminate most of hydrogen and to contribute to both higher fracture strength and higher ductility of the composites as well as the pure copper specimens.

The drastic decrease in the strength of composite with a change in annealing temperature from 104°C to 149°C is attributed to the ease of transmission of dislocations across silver layers, from one copper layer to another copper layer. As a result, the whole composite specimen deformed and fractured in the same way as the pure copper specimens did. The continuity of the silver layers in the 149°C annealed specimen (see figure 4a) suggests that spheroidization of silver layers has not occurred in this specimen and hence can not be the reason for its low strength. Further work is needed to investigate the silver layer and its role as a barrier to dislocation motion.

## CONCLUSIONS

The results of this study suggest that the very high strength of the as-deposited Cu-Ag nanocomposites produced by electrodeposition in comparison to its pure copper counterpart is mainly owing to the presence of the silver layers. However, the sharp drop in the composite strength due to annealing at 149°C for 6 hours suggests that the structures of the silver layer and its interface with copper play important roles in the deformation of Cu-Ag nanocomposites.

## ACKNOWLEDGMENTS

This research was supported by the national Science foundation under the contract number DMR-9527624. The authors wish to thank Prof. A. Brajter-Toth for discussions regarding electrodeposition techniques.

## REFERENCES

- [1] J. E. Hillard *et al*, *J. Appl. Phys.* **57** (4), 1076 (1985)
- [2] D. S. Lashmore, M. P. Dariel, *J. electrochem. Soc.* **135** (5) 1218 (1988)
- [3] D. M. Tench, J. T. White, *Microcomposites and Nanophase materials*, edited by D. C. Van Aken, *et al*, (The minerals, metals & Materials Society, 1991) 53
- [4] H. Gleiter, *Progress in Materials Science*, **33** (1989) 223
- [5] R. W. Siegel *et al*, *Nanostructured materials*, **1** (1992) 185
- [6] D. M. Tench, J. T. White, *J. Electrochem. Soc.*, **139**, (2), P. 443 (1992)
- [7] D. M. Tench, J. T. White, *J. Mater. Sci.* **27** 5286 (1992)
- [8] J. R. Weertman *et al*, *Solid State Phenomena* **35** (30) 249 (1994)

## ELECTROCHEMICAL PREPARATION OF AMORPHOUS FeB FILMS CONTAINING A LARGE QUANTITY OF PLASTICS

P. B. LIM<sup>1</sup>, N. FUJITA<sup>2</sup>, P. T. SQUIRE<sup>3</sup>, M. INOUE<sup>1</sup>, and T. FUJII<sup>1</sup>

<sup>1</sup>Department of Electrical & Electronic Engineering, Toyohashi University of Technology,  
Toyohashi 441, Japan, inouem@eee.tut.ac.jp

<sup>2</sup>Department of Electronics and Computer Sciences, Osaka Prefectural College of Technology,  
Neyagawa 572, Japan, fujita@ipc.osaka-pct.ac.jp

<sup>3</sup>Department of Physics, University of Bath, Bath BA2 7AY, UK, P.T.Squire@bath.ac.uk

### ABSTRACT

Amorphous Fe<sub>80</sub>B<sub>20</sub> alloy films with a large quantity of plastics (polymethyl methacrylate: PMMA) are prepared using a combined technique of electrochemical plating and spin coating. The embedding of amorphous alloys into PMMA plastics is expected to reduce the effective conductivities of alloy films, and hence to improve their magnetomechanical coupling coefficients at high frequency by reducing effective eddy-current losses. Preparation conditions for obtaining Fe<sub>100-X</sub>B<sub>X</sub> (X=20±5at%) films with amorphous structure are determined, and the composite films are formed in accordance with the plating conditions. The resultant composite films are studied by examining their surface states and magnetic properties.

### INTRODUCTION

Iron-based amorphous alloys, such as Fe<sub>80</sub>B<sub>20</sub> and Fe<sub>78</sub>Si<sub>10</sub>B<sub>12</sub>, have been expected as useful materials for various magnetoacoustic applications [1]. This is because these alloys exhibit large electro- (magneto-) mechanical coupling coefficient  $k_m^2$ , originating from their extreme magnetic properties of large magnetostriction and high magnetic permeability[2]. However, with increasing operation frequency, the eminent magnetoacoustic properties of alloys are deteriorated due to eddy-current losses, which unfavorably causes the reduction of their  $k_m^2$ -values [3]. Then, to employ these alloys in high frequency magnetoacoustic devices, reduction of their conductivities is indispensable without losing the inherent magnetoacoustic properties of the alloys.

In this article, preparation of amorphous Fe<sub>80</sub>B<sub>20</sub> alloy films containing a large quantity of plastics (polymethyl methacrylate: PMMA, hereafter) is described and their fundamental properties for use in high frequency magnetoacoustic devices are examined. The embedding of amorphous Fe-B alloys into PMMA plastics is expected to be effective for reducing eddy-current losses by reducing the conductivities of the alloy films, and hence to improve their magnetomechanical coupling characteristics at high frequency. The composite films were formed using a combined technique of electrochemical deposition and spin coating. The electrochemical method was employed, because it enables us to form the alloy films at low temperature without causing any damage to the plastic ingredient. To materialize the composite films with good magnetoacoustic properties, the key is whether the amorphous Fe<sub>80</sub>B<sub>20</sub> alloy film can be obtained electrochemically. Thus, to begin with, electrochemical preparation of Fe-B alloy films was examined in detail and plating conditions for obtaining the alloy films with good reproducibility were clarified. Then, in accordance with the plating conditions, the composite films consisting of amorphous Fe<sub>80</sub>B<sub>20</sub> alloys and PMMA plastics were formed and their magnetic properties were studied.

## EXPERIMENTAL

The Fe-B alloy films were formed using plating baths composed of iron sulfate ( $\text{FeSO}_4 \cdot 7\text{H}_2\text{O}$ ) 71.9mM, potassium borohydride ( $\text{KBH}_4$ ) 0~400mM, sodium hydroxide ( $\text{NaOH}$ ) 100~400 mM, and potassium sodium tartrate ( $\text{C}_4\text{H}_4\text{KNaO}_6 \cdot 4\text{H}_2\text{O}$ ) 50~318.9mM. The plating bath was prepared as the following: First,  $\text{C}_4\text{H}_4\text{KNaO}_6 \cdot 4\text{H}_2\text{O}$  as a complexing agent was dissolved in distilled water, whose temperature was about  $25^\circ\text{C}$ . The amount of distilled water was more than 60% of that of the resultant plating bath. Then,  $\text{FeSO}_4 \cdot 7\text{H}_2\text{O}$  as an iron supplier was dissolved. After stirring the solution sufficiently,  $\text{NaOH}$  solution as a pH control agent and  $\text{KBH}_4$  as a boron supplier and a reducing agent were mixed. The preparation procedure of plating bath as well as the amount and the temperature of distilled water in which  $\text{C}_4\text{H}_4\text{KNaO}_6 \cdot 4\text{H}_2\text{O}$  was dissolved were found to be very important for preventing the precipitation of iron hydroxide. The bath temperature during the film deposition was maintained from  $25^\circ\text{C}$  to  $55^\circ\text{C}$  with  $\pm 2^\circ\text{C}$  accuracy. The film samples were formed on 0.1mm-thick copper plates with the dimension of 15mm wide and 50mm long, using current densities ranging from  $0.67\text{A}/\text{dm}^2$  to  $3.33\text{A}/\text{dm}^2$ . To determine plating conditions for obtaining amorphous  $\text{Fe}_{80}\text{B}_{20}$  alloy film, film samples were formed under above various conditions and their compositions and crystallographic structures were studied in detail with ICP spectrochemical analysis and XRD measurements, respectively.

The composite film samples consisting of amorphous  $\text{Fe}_{80}\text{B}_{20}$  alloys and PMMA plastics were fabricated by means of a combined technique of electrochemical plating and spin coating as the following: A toluene solution of PMMA with an appropriate viscosity was spin coated on the copper plate and was dried rapidly in a vacuum desiccator. The toluene was evacuated during the solidification process and the resultant PMMA thin film had a porous structure with a large number of irregular pits reaching to the substrate surface. The PMMA film sample was then immersed into the plating bath and the  $\text{Fe}_{80}\text{B}_{20}$  alloy film was deposited. As illustrated in Fig.1 (a), the Fe-B alloy invaded the pits of the PMMA porous film, and the resultant alloy film contained a large quantity of PMMA plastics. These processes were repeated until the film thickness reached to desired thickness as shown in Fig.1 (b). To examine the effect of embedding of Fe-B alloys into PMMA plastics, surface states of the resultant composite films were evaluated from SEM pictures. Magnetic properties of the composite films and the Fe-B alloy films were studied using VSM, where the film samples were subject to successive annealings up to  $350^\circ\text{C}$  for 1 hour in the presence of a dc magnetic field of 100Oe.

## RESULTS AND DISCUSSION

### Electrochemically Deposited Fe-B Alloy Films

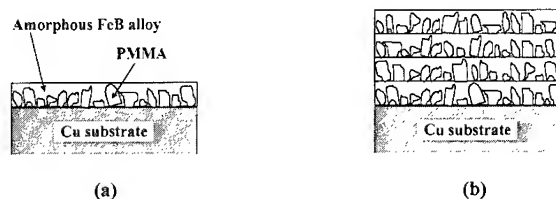


Fig. 1 Schematic drawings showing the film structures: (a) single-layer film and (b) four-layer film.

Prior to fabricating the composite films, Fe-B films were formed under various plating conditions in order to determine the conditions for obtaining amorphous  $\text{Fe}_{80}\text{B}_{20}$  films.

Figure 2 shows film compositions as a function of  $\text{KBH}_4$  concentration of the plating bath. As seen in the figure, boron content in films increases monotonically with increasing the concentration of  $\text{KBH}_4$  in the bath. This situation is similar to the case of Ni-P films of Brenner et al. [4], suggesting that the film composition can be controlled by changing the concentration of the reducing agent.

Figure 3 shows XRD patterns of the films in Fig.2. No apparent peak except the peaks from Cu substrate is seen, and then these films are considered to have X-ray amorphous structure.

Figure 4 shows film compositions as a function of NaOH concentration of the plating bath. In this case, boron content in films decreases monotonically with increasing the concentration of NaOH in the bath. This is due to the reduction of reducing power of  $\text{KBH}_4$  associated with heightening alkalinity of the bath, and coincides with the experimental rule of Brenner et al. [4] showing that the phosphorus content in Ni-P films decreases with increasing pH-value of the bath. Crystallographic structures of the films in Fig.4 were identified as X-ray amorphous from XRD measurements.

Figure 5 shows film compositions as a function of  $\text{KNaC}_4\text{H}_4\text{O}_6$  concentration of the bath. When  $\text{KNaC}_4\text{H}_4\text{O}_6=50\text{mM}$ , boron content of the film was 56at%, but other films prepared with  $\text{KNaC}_4\text{H}_4\text{O}_6=100\sim 318.9\text{mM}$  had boron content of 20~28at%. This indicates that the reduction of iron complex being formed in the plating bath with lower concentration of  $\text{KNaC}_4\text{H}_4\text{O}_6$  is weakly taken place. From XRD measurements, films in Fig.5 had X-ray amorphous structure except the film with 56at% B showing the existence of polycrystalline  $\alpha\text{-Fe}$  phase.

Bath temperature was found to be another significant parameter which governed the resultant film structures. Figure 6 shows bath temperature dependence of the film deposition rate (film weight vs. bath temperature), where each sample

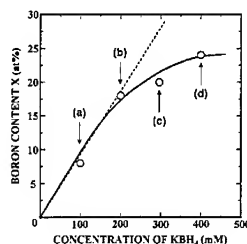


Fig. 2 Film composition versus  $\text{KBH}_4$  concentration in bath, where  $\text{FeSO}_4=71.9\text{mM}$ ,  $\text{KNaC}_4\text{H}_4\text{O}_6=318.9\text{mM}$ ,  $\text{NaOH}=400\text{mM}$ ,  $T_b$  (bath temperature)  $=40^\circ\text{C}$ , and  $i$  (current density)  $=3.33\text{A/dm}^2$ .

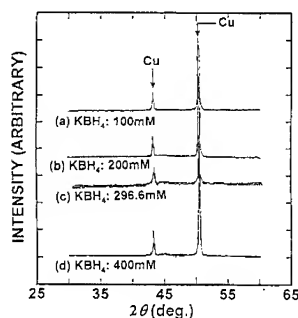


Fig.3 X-ray diffraction patterns of films (a), (b), (c) and (d) shown in Fig.2.

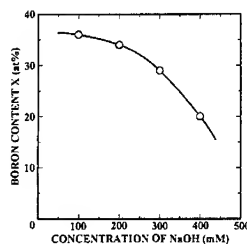


Fig. 4 Film composition versus NaOH concentration in bath, where  $\text{FeSO}_4=71.9\text{mM}$ ,  $\text{KNaC}_4\text{H}_4\text{O}_6=318.9\text{mM}$ ,  $\text{KBH}_4=296.6\text{mM}$ ,  $T_b=40^\circ\text{C}$ , and  $i=3.33\text{A/dm}^2$ .



was formed for 20mins. in the bath being held at respective temperature. For comparison, results of Fe films formed in the bath without having  $\text{KBH}_4$  are also plotted by  $\triangle$  and  $\circ$ . At  $T_b=30^\circ\text{C}$  for  $i=0.67\text{A/dm}^2$  and  $T_b=35^\circ\text{C}$  for  $i=3.33\text{A/dm}^2$ , the deposition rates of Fe-B films apparently change from those of Fe films. This is presumably due to the fact that the reducing power of  $\text{KBH}_4$  is markedly strengthened when the bath temperature is higher than the above critical temperature, and iron cations in such a bath is reduced by the combination of the reducing agent ( $\text{KBH}_4$ ) and the currents. In fact, when  $T_b \leq 30^\circ\text{C}$  for  $i=0.67\text{A/dm}^2$  and  $T_b \leq 35^\circ\text{C}$  for  $i=3.33\text{A/dm}^2$ , the deposition rates of Fe-B films are exactly the same as those of Fe films which were formed only by the reduction power of currents. These changes in film deposition mechanism depending on the bath temperature affect strongly the crystallographic structures of resultant films. This is clearly seen in Figs. 7 and 8 showing the XRD patterns of film samples in Fig.6. When  $i=3.33\text{A/dm}^2$  (Fig.7), the film samples showed X-ray amorphous structure irrespective to the bath temperature. On the other hand, when  $i=0.67\text{A/dm}^2$  (Fig.8), the film samples formed at  $T_b \geq 38^\circ\text{C}$  had polycrystalline structures of  $\alpha\text{-Fe}$  phase, suggesting that Fe-B films with amorphous structure cannot be obtained whenever the reducing power of  $\text{KBH}_4$  is enhanced due to high bath temperature overcoming the reducing power of currents.

From these results, therefore, it is concluded that amorphous  $\text{Fe}_{80}\text{B}_{20}$  alloy films are electro-

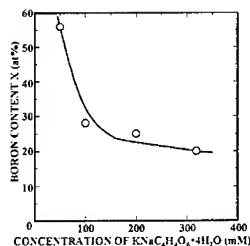


Fig. 5 Film composition versus  $\text{KNaC}_4\text{H}_4\text{O}_6$  concentration in bath, where  $\text{FeSO}_4=71.9\text{mM}$ ,  $\text{KBH}_4=296.6\text{mM}$ ,  $\text{NaOH}=400\text{mM}$ ,  $T_b=40^\circ\text{C}$ , and  $i=3.33\text{A/dm}^2$ .

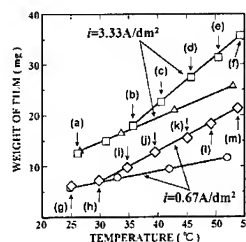


Fig. 6 Film weight versus bath temperature  $T_b$ , where the current density  $i$  is taken as a parameter. The deposition time of each film was 20mins. and the bath composition was  $\text{FeSO}_4=71.9\text{mM}$ ,  $\text{KBH}_4=296.6\text{mM}$ ,  $\text{NaOH}=400\text{mM}$ , and  $\text{KNaC}_4\text{H}_4\text{O}_6=318.9\text{mM}$ . Marks  $\triangle$  and  $\circ$  in the figure denote the weights of Fe films formed in the bath without having  $\text{KBH}_4$ .

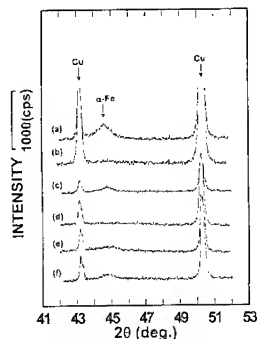


Fig.7 XRD patterns of film samples in Fig.6 formed with  $i=3.33\text{A/dm}^2$ .

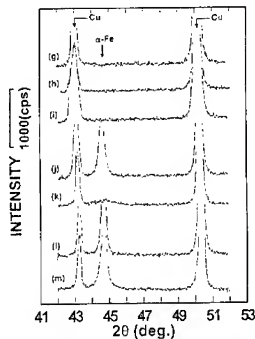


Fig.8 XRD patterns of film samples in Fig.6 formed with  $i=0.67\text{A/dm}^2$ .

chemically obtainable by using the plating bath composed of  $\text{FeSO}_4 \cdot 7\text{H}_2\text{O} = 71.9\text{mM}$ ,  $\text{KBH}_4 = 296.6\text{mM}$ ,  $\text{NaOH} = 400\text{mM}$ , and  $\text{C}_4\text{H}_4\text{KNaO}_6 \cdot 4\text{H}_2\text{O} = 318.9\text{mM}$ , and by maintaining the bath temperature below  $30^\circ\text{C}$  during film deposition.

#### Amorphous $\text{Fe}_{80}\text{B}_{20}$ films with PMMA Plastics

In accordance with the above conditions, amorphous  $\text{Fe}_{80}\text{B}_{20}$  films containing PMMA plastics were prepared by introducing spin coating process for fabricating PMMA porous films. Average thickness of the spin coated PMMA film was estimated to be less than  $1\mu\text{m}$ . As a matter of course, the thickness depends on the viscosity and the coating speed of toluene solution of PMMA. The PMMA porous film and the  $\text{Fe}_{80}\text{B}_{20}$  alloy film ( $1.6\mu\text{m}$ -thick) were deposited alternatively so as to form a thick composite film with (PMMA/FeB)  $\times 5$  structure. The film surface was further covered with a  $3.2\mu\text{m}$ -thick  $\text{Fe}_{80}\text{B}_{20}$  alloy film, and hence the total thickness of the composite film was approximately  $15\mu\text{m}$ .

Figures 9 and 10 show SEM pictures of film surfaces, where the samples were  $2.4\mu\text{m}$ -thick  $\text{Fe}_{80}\text{B}_{20}$  single-layer film and the composite film, respectively. In both cases, the films are composed of many circular grains with different sizes. The average grain size of the composite film is larger than that of the Fe-B single film. This is likely due to the difference in growing times of grains in respective films; the top Fe-B layer ( $4.8\mu\text{m}$ -thick) of the composite film was formed by 30mins. deposition while the Fe-B single film ( $2.4\mu\text{m}$ -thick) was formed by 15mins. deposition.

The film samples were annealed in nitrogen atmosphere for 1 hour in the presence of a dc magnetic field of 100Oe, and the changes of their coercivities  $H_c$  were evaluated as a function of the annealing temperature. For comparison, amorphous alloy ribbon (2605S2) was also annealed with the same conditions. The results are summarized in Fig.11. As-prepared composite film showed the coercivity of 20Oe, while other as-prepared Fe-B single films showed the coercivities ranging from 21Oe to 63Oe depending on their compositions. After annealing, magnetic softening

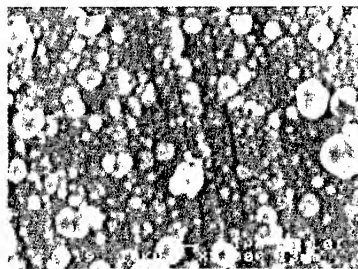


Fig.9 SEM picture showing the surface state of amorphous  $\text{Fe}_{80}\text{B}_{20}$  single-layer film.

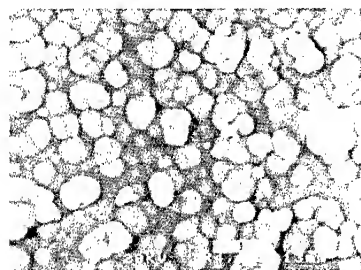


Fig.10 SEM picture showing the surface state of composite film, where the film is composed of 6 layers of amorphous Fe-B alloy films and 5 layers of PMMA porous films.

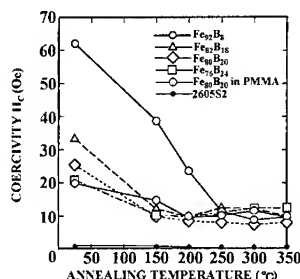


Fig. 11 Changes in coercivities of the composite film due to successive annealing in a dc magnetic field. In the figure, changes in coercivities of amorphous Fe-B plated films with different compositions and amorphous ribbon (2605S2) are also shown for comparison.

was proceeded for all film samples mainly due to relief of internal stresses, and the coercivity of the composite film was reduced to 9Oe after the annealing at 350°C. In comparison with the amorphous ribbon, however, this value of  $H_c$  is about 18 times higher than that of the ribbon ( $H_c \sim 0.5$ Oe after 350°C annealing). Then, further magnetic softening of the composite film is needed for use in magnetoacoustic applications. The relatively hard magnetic property of the composite film chiefly arises from hard properties of electrochemically deposited  $Fe_{80}B_{20}$  amorphous alloys, although the alloy films can possess very soft magnetization and very high magnetostriction simultaneously when they are prepared by sputtering. The magnetic properties of films are closely related to microscopic ordering of Fe and B atoms, and thus the microscopic ordering of atoms in electrochemically deposited film is considered to be different from that of the sputtered film.

#### CONCLUDING REMARKS

Plating conditions for obtaining amorphous  $Fe_{80}B_{20}$  alloy film were determined, and the alloy films with a large quantity of PMMA plastics were prepared by the combination of electrochemical deposition and spin coating. Although the composite films with considerably flat surfaces and metallic luster were obtained, magnetic softening of the films is still necessary for use in high frequency magnetoacoustic devices. To proceed with this, further investigations of electrochemical preparation of Fe-B alloy films are now under progress by introducing thiourea and sodium ascorbate in plating bath as magnetic softening agents.

#### ACKNOWLEDGMENTS

The work was supported in part by the Casio Science Promotion Foundation. P. B. Lim expresses her sincere thanks to MRS symposium organizers for their financial support to attend the symposium.

#### REFERENCES

1. M. Inoue, S. Tanaka, T. Yoshimine, and T. Fujii, Elsevier Studies in Applied Electromagnetics in Materials, **4**, 127 (1994), *ibid.*, **4**, 137 (1994).
2. K. I. Arai, N. Tsuya, and M. Yamada, IEEE Trans. Magn., **MAG-12**, 936 (1976).
3. M. Inoue, Y. Tsuboi, A. Makita, N. Fujita, T. Miyama, and T. Fujii, Jpn. J. Appl. Phys., **25**, S25-1, 157 (1986).
4. A. Brenner, D. E. Couch, and E. K. Williams, J. Research of National Bureau of Standards, **44**, 109 (1950).

## THERMAL STABILITY OF ELECTRODEPOSITED NANOCRYSTALLINE Ni-45%Fe ALLOYS

F. CZERWINSKI, H. LI, F. MEGRET, and J.A. SZPUNAR

Department of Metallurgical Engineering, McGill University, Montreal, PQ H3A 2A7 Canada  
D.G. CLARK and U. ERB

Department of Materials and Metallurgical Engineering, Queen's University, Kingston, Ont.,  
K7L 3N6, Canada

### ABSTRACT

Electrolytically deposited nanocrystalline Ni-45%Fe alloys, composed of  $\gamma$  (f.c.c.) phase, were annealed at 573 and 673 K for time periods up to 20 h in an inert atmosphere of argon. The evolutions of crystallographic texture, grain size, and microhardness were analyzed as a function of annealing parameters. The initial grains, approximately 5 nm in size increased after annealing up to 10-20 nm, however, the growth kinetics and the final grain size depended on the temperature. A correlation was found between the grain size and alloy microhardness. The phase composition was unstable and during annealing the  $\alpha$  (b.c.c.) phase was detected to precipitate from the  $\gamma$  matrix. The texture of  $\gamma$  phase, consisted of two fibre components of  $\langle 111 \rangle$  and  $\langle 200 \rangle$ , and evolved at high temperatures. Although the detailed changes depended on the annealing temperature, in general, the  $\langle 111 \rangle$  component became stronger at the expense of the  $\langle 200 \rangle$  component.

### INTRODUCTION

Nanocrystalline materials represent a new generation of solids with different properties than their counterparts having a significantly larger grain size. Due to a specific structure, their physical properties are unique and very useful in some applications [1]. Among a wide range of techniques used for manufacturing of nanocrystals, a relatively simple and effective way is by electrodeposition. It has many advantages over other nanoprocessing techniques, including the potentially large number of materials which can be obtained with grain size smaller than 100 nm and high effectiveness when applied at the commercial scale [2].

The study of thermal stability of nanocrystalline materials is of great importance for the general assessment of potential technological applications. Because of high electrode polarization, usually used during electrodeposition, the nanocrystalline materials are not in the state of equilibrium [3]. This implies, that at elevated temperatures, the electrodeposits will recrystallize very fast, similarly as is the case for highly deformed metal. The structural factors which will evolve during annealing are: the phase composition, crystallographic texture and grain size. In this paper we follow the evolution of those structural parameters for nanocrystalline alloy of Ni-45%Fe.

## EXPERIMENTAL

The electroplating solution used for electrodeposition was a modified Watts nickel bath containing the iron chloride as a source of iron, sodium citrate as a complexing agent, and saccharin as stress reliever and grain refinement agent [4]. The cathode was titanium and the anode was electrolytic nickel. Deposition was carried out at temperature of 323 K and at a current density of 200 mA/cm<sup>2</sup>. No bath agitation was applied. Electrodeposits of size 10x10 mm and the thickness of 300  $\mu$ m were stripped from the titanium cathode. The annealing was performed in quartz tube furnace in flowing argon atmosphere at the temperature of 573 and 673 K for time periods up to 20 h. Phase composition was analyzed using an X-ray Rigaku diffractometer with a rotating anode. Texture was measured using a Siemens D-500 X-ray goniometer. Pole figures were measured using the reflection technique, tilting the specimen to a maximum of 80 deg in 5 deg polar and angular intervals. The pole figures were normalized within the available interval of distribution of crystallographic planes, and the intensity on the pole figures is shown using multiples of intensities from a random specimen. The calculation of the grain size was accomplished by considering the broadening of the diffraction peaks [5]. Microhardness was measured using a Vickers indenter under a load of 200 g. The result is an average of at least 10 measurements conducted on different areas of the sample.

## RESULTS AND DISCUSSION

### Phase composition

According to the phase diagram [6], the Ni-45%Fe alloy should contain both  $\alpha$  and  $\gamma$  phases. After deposition, however, the X-ray diffraction revealed the presence of  $\gamma$  (f.c.c.) phase only. A deviation of the phase composition of electrolytic alloys from an equilibrium is frequently observed. For example Iwase and Nasu [7] reported the coexistence of  $\alpha$  and  $\gamma$  phases in the range 14-58% Ni, Marshak and Stepanow [8] in the range 30-50% Ni and Aotani [9] between 8 and 62% Ni.

Short-term annealing at 573 K did not affect the phase composition of deposit. However, after 20 h period at 573 K, the relatively weak (110) peak of  $\alpha$  phase was formed on diffraction pattern. At 673 K, a time of 0.5 h was necessary to show the presence of  $\alpha$  phase. In both cases, however, the amount of  $\alpha$  phase, estimated from X-ray diffraction pattern was of the order of a few percent. Thus, the essential component of alloys discussed below is the  $\gamma$  phase being a solid solution of Fe in Ni.

### Texture

The electrodeposited alloys were characterized by the presence of texture. After deposition, texture consisted of two major components,  $\langle 100 \rangle$  fibre and  $\langle 111 \rangle$  fibre. Annealing did not change the fibre texture but affected only the intensities of both components (Fig. 1). Annealing at 573 K resulted in an increase of intensity of  $\langle 111 \rangle$  component on the expense of  $\langle 200 \rangle$  component (Fig. 2). At 673 K the intensity of  $\langle 111 \rangle$  fibre increases even stronger than observed at 573 K. However, for times longer than 7 h a tendency to decrease intensity of  $\langle 111 \rangle$  was observed. The  $\langle 200 \rangle$  fibre showed small changes for times shorter than 7 h, and a tendency to decrease for longer times.

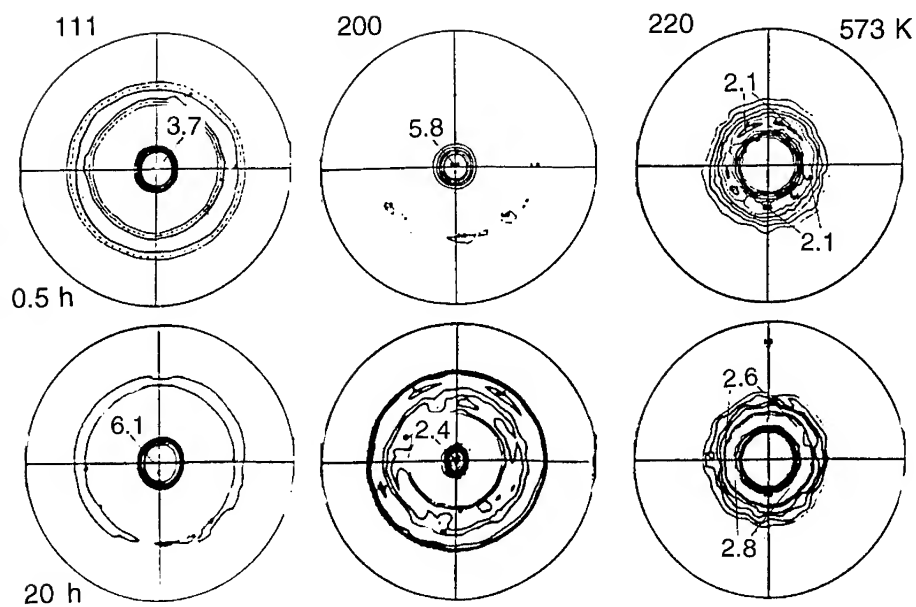


Fig. 1. Pole figures of Ni-45%Fe deposit after annealing at 573 K for 0.5 and 20 h.

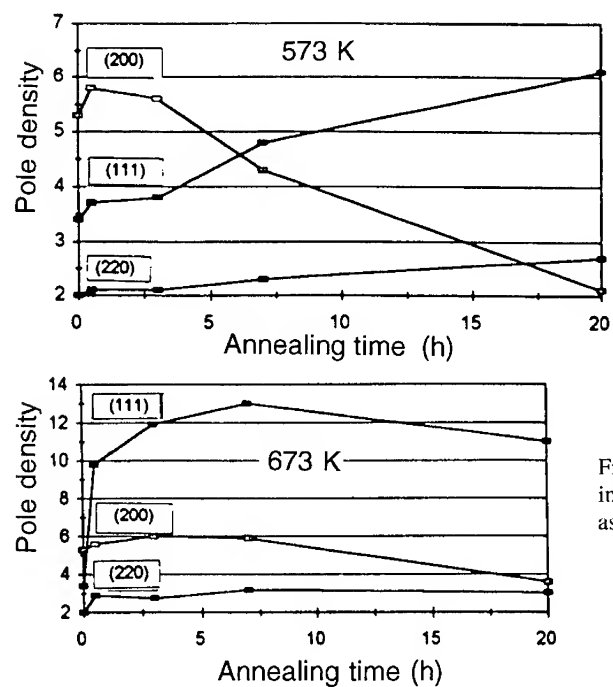


Fig. 2. Plots of pole density in the center of pole figures as a function of annealing time.

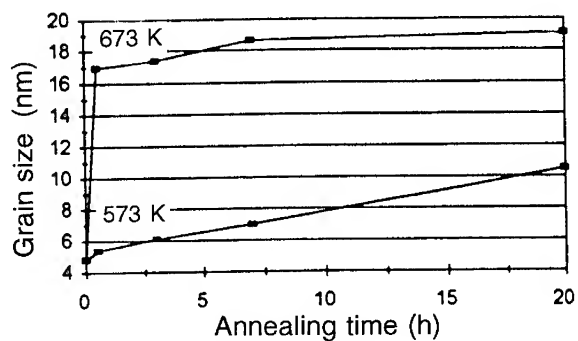


Fig. 3. Evolution of grain size during annealing plotted as a function of time for temperatures of 573 and 673 K.

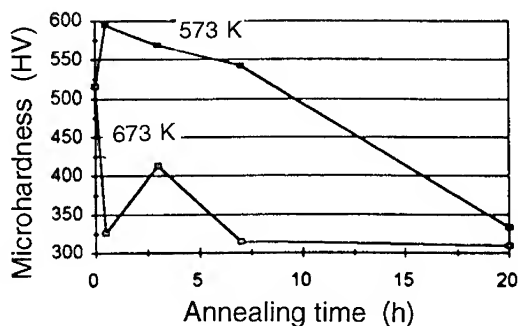


Fig. 4. Evolution of microhardness during annealing as a function of annealing time for temperatures of 573 K and 673 K.

#### Grain size

The evolution of deposit grain size determined on the basis of X-ray diffraction patterns is shown in Fig. 3. It is seen that annealing at 573 K caused a gradual increase in grain size up to approximately 10 nm after 20 h. During annealing at 673 K, the rapid grain growth up to 17 nm was observed during the first 0.5 h of annealing. Further annealing caused only small grain growth up to about 20 nm after 20 h.

#### Microhardness

A relatively high microhardness of alloy after deposition, of 515 HV, should be attributed to the small grain size and the higher density of structural defects. Annealing at 573 K caused gradual decrease of microhardness to a level of 330 HV after 20 h. Annealing at 673 K led to drastic reduction of hardness to a level of 320 HV after 0.5 h. The data collected in Figs. 3 and

4 can be used to analyze a correlation between the grain size and microhardness of nanocrystalline alloys.

## CONCLUSIONS

After deposition the Ni-45%Fe alloys are composed exclusively of  $\gamma$  phase. The small amounts of  $\alpha$  phase are formed after 20 h annealing at 573 K or after 0.5 h at 673 K. The texture of deposit composed of two fibres  $\langle 111 \rangle$  and  $\langle 200 \rangle$  evolves during annealing. In general, the intensity of  $\langle 111 \rangle$  component increases at the expense of  $\langle 200 \rangle$  component. The initial grain of 5 nm grows up to 10-20 nm after annealing at temperatures 573 and 673 K, respectively. The grain growth is accompanied by reduction of the microhardness of the deposit.

## ACKNOWLEDGEMENT

This research was financially supported by the Natural Sciences and Engineering Research Council of Canada.

## REFERENCES

1. H. Gleiter, *Progr. Mater. Sci.*, 33, 223 (1989).
2. A.M. El-Sherik and U. Erb., *J. Mater. Sci.*, 30, 5743 (1995).
3. C. Cheung, F. Djuanda, U. Erb, and G. Palumbo, to be published.
4. A. Brenner, *Electrodeposition of Alloys*, Academic Press, New York (1963).
5. B.D. Cullity, *Elements of X-ray Diffraction*, Addison-Wesley, Reading (1978).
6. E. Schurman and J. Brauckmann, *Arch. Eisenhüttenwes.*, 48, 3 (1977).
7. K. Iwase and N. Nasu, *Bull. Chem. Soc. Japan*, 7, 305 (1932).
8. F. Marshak and D. Stepanow, *Z. Elektroch.*, 41, 599 (1935).
9. K. Aotani, *J. Japan Inst. Met.*, B14, 55 (1950).



## ELECTRODEPOSITION OF METALS ON CONDUCTIVE POLYMER FILMS

Maria Hepel, Laura Adams, and Cynthia Rice-Belrose

*Department of Chemistry, State University of New York at Potsdam,  
Potsdam, New York 13676*

### ABSTRACT

The electrodeposition of copper on composite conductive polymer polypyrrole/polystyrenesulfonate PPy(PSS) has been studied. The morphology of copper deposits was investigated in the presence of thiourea and other additives. It has been found that in the presence of thiourea in the solution, the rate of copper deposition on a PPy(PSS) substrate is slightly inhibited but the rate of copper stripping is faster than in its absence. The Electrochemical Quartz Crystal Microbalance (EQCM) technique allowed us to simultaneously monitor voltamperometric and resonance frequency vs. potential or time characteristics. The amount of electrodeposited copper was controlled by monitoring the EQCM resonant frequency. Composite PPy(PSS) films functioning as cation-exchange membranes were used as substrate materials for metal deposition. They allowed us to electrodeposit copper not only on the surface of the conductive polymer but also inside the polymer matrix. The size of copper nanocrystals formed inside the polymer was controlled by the applied electrode potential. Copper crystals as small as 20 nm were detected with Transmission Electron Microscopy (TEM).

### INTRODUCTION

A few papers appeared in the literature dealing with metallization of conductive polymer films [1-10]. Among the variety of methods used in polymer metallization, electrodeposition from aqueous solutions is the most promising. The electrodeposition of copper on a polypyrrole precoat formed by chemical polymerization on an insulating substrate, with potential applications for metallization of printed circuit boards, has been reported [2]. The electrodeposition of various metals on polypyrrole carried out from typical industrial plating baths was examined by cyclic voltammetry by Tan *et al.* [3]. The electrodeposition of palladium, platinum, lead and ruthenium on polypyrrole film was reported by Pletcher *et al.* [4]. The electroplating of nickel on polypyrrole in the presence and absence of additives has been investigated using the EQCM technique [5]. The effect of the composition of polypyrrole substrate on the electrodeposition of copper and nickel has been found [6]. The formation of Pt nanoclusters in conductive polymer matrix and electrocatalytic effect for methanol oxidation reaction has also been described [10]. The electrodeposition of copper is a process of great practical importance, particularly in the electronics industry. However, the deposition process is mechanistically very complex and the final quality of copper electrodeposit depends on many interlinking factors, including bath composition, convection, temperature, current density and the presence of additives used as brightening and levelling agents [10-17]. The presence of organic compounds in

an electrochemical system causes significant changes that affect the nucleation process and growth of metal nuclei. For this reason, many additives are used to optimize industrial electrochemical plating processes. The most desired properties of deposits are mirror-brightness, high-levelling, low internal stress of the coatings, as well as stability during use. Even trace levels of additives present in electroplating baths can change the properties of electrodeposits. In most cases, these additives act as inhibitors in the electrodeposition process.

In this work, we report on the electrodeposition of copper inside the composite polypyrrole (PPy(PSS)) matrix and on the surface of the conductive polymer. The composite PPy/PSS films were coated on Au piezoelectrodes. Using the EQCM technique, we were able to follow changes in the electrode mass by measuring the oscillation frequency of these piezoelectrodes, in addition to the simultaneously recorded voltammetric and current transient characteristics.

## EXPERIMENTAL

**Chemicals.** All chemicals were of reagent grade purity (Aldrich) and were used without further purification. Solutions were prepared using water deionized with a Millipore Milli-Q purification system. All tests reported here were performed at room temperature, 22 °C.

**Instrumentation.** Voltamperometric and microelectrogravimetric measurements were performed using Model PS-605 Precision Potentiostat/Galvanostat (ELCHEMA, Potsdam, NY) and Model EQCN-700 Electrochemical Quartz Crystal Nanobalance (ELCHEMA). The program waveform was generated by VOLTSCAN Real-Time Data Acquisition System (Intellect Software, Potsdam, NY). All electrochemical measurements were performed using a double-junction Ag/AgCl electrode as the reference electrode. Scanning Electron Micrographs were taken using a Model JSM-6300 SEM (JEOL) equipped with an Energy Dispersive X-ray unit for elemental analysis and a Noran Voyager X-Ray Microanalyzer. A Transmission Electron Microscope Model JM-1200-ES (JEOL) was used to determine the size of electrodeposited copper clusters.

**Film Preparation.** The electropolymerization of pyrrole was carried out on gold piezoelectrodes from aqueous solutions containing 20-70 mM pyrrole, an organic dopant, e.g. poly(styrenesulfonate) (PSS), and a supporting electrolyte, at a constant potential  $E = +650$  mV vs. SCE. Films with thicknesses below 1  $\mu\text{m}$  were typically grown. The geometric surface area of the electrode was 0.25  $\text{cm}^2$ .

## RESULTS AND DISCUSSION

### Electrodeposition of Copper without and with Additives

Effects of various additives have been studied. In this paper, we limit our discussion to the effect of thiourea. The deposition of copper from 0.1 M  $\text{H}_2\text{SO}_4$  solution without any additives usually begins in the potential range from +100 to -100 mV vs.

SCE. In this potential range, the composite PPy(PSS) film electrode remains highly conductive and, thus, copper can be readily deposited on such a film substrate.

In Figure 1, typical voltammetric and microelectrogravimetric characteristics obtained for a PPy(PSS) modified Au-EQCM electrode in 10 mM Cu(II) + 0.1 M H<sub>2</sub>SO<sub>4</sub> solution, are presented. The increase in cathodic current observed during the negative potential scan, at potentials less than E = -100 mV, is accompanied by a simultaneous mass increase manifested on the microelectrogravimetric curve. The cathodic peak potential is E<sub>p,c</sub> = -140 mV and coincides with the highest rate of mass increase on the *m*-*E* curve. During the reverse potential scan, the copper stripping begins at the potential, E = 0 mV, as demonstrated by the onset of the anodic current on the *i*-*E* curve and the beginning of the mass decrease on the *m*-*E* characteristic. The anodic peak potential E<sub>p,a</sub> = +100 mV. The total mass increase, Δ*m* = 3270 ng, due to the copper deposition, corresponds to approximately 82.5 mono-layers of copper, assuming that smooth deposit is being formed and the mean monolayer mass of copper is:  $m_{mono} = M^{1/3} N^{-1/3} d^{2/3} = 201.7$  ng/cm<sup>2</sup>, where *M* is the atomic mass of copper, *N* is the Avogadro number, and *d* is the density of copper metal (*d* = 8.96 g/cm<sup>3</sup>). As seen in Figure 1, the mass change in one potential cycle is not well balanced, *i.e.* the final mass does not return to the initial level. The current stripping peak also shows a long tail indicating incompleteness of the stripping process. All this is caused by some degree of the system's irreversibility.

In Figure 2a, the results of three repeated chronoamperometric experiments performed on PPy(PSS) modified Au-EQCM electrode in 10 mM Cu(II) + 0.1 M H<sub>2</sub>SO<sub>4</sub> solution, are presented. In experiments of Figure 2a, the electrode potential was stepped between E = -800 mV (deposition) and E = +400 mV (stripping). Thus, the potential for copper stripping was the same as the anodic potential limit E<sub>an</sub> in experiments of Figure 1. The pulse duration for deposition was *t*<sub>dep</sub> = 30 s, and for stripping was *t*<sub>diss</sub> = 370 s. As seen in Figure 2a, the longer dissolution time is more than sufficient to allow all deposited copper to be removed from the electrode surface. As expected, the amount of copper deposited is strongly dependent on the presence of additives. This is confirmed by a gravimetric characteristic presented in Figure 2b, obtained for the same potential steps from E = +400 mV to E = -800 mV. The mass of copper in the presence of thiourea, for *t*<sub>dep</sub> = 30 s, is 4700 ng, *versus* 6700 ng for copper deposited at the same potential but without any additives. The conductivity of polypyrrole is decreased at potentials more negative than E = -500 mV. It is interesting to note that it does not inhibit the copper electrodeposition process.

The effects of various additives on copper deposition on metal substrates have been studied for long time and in many cases the mechanisms have been elucidated. The major role in the metal nucleation process play the adsorption of metal atoms, coadsorption of additives, surface diffusion of adatoms, interaction of metal complexes with the electrode surface, and the charge transfer mechanism. Since the properties of the substrate used in this work differ substantially from metal substrates used in other studies, we can not assume that the mechanism will remain unaffected. In fact, all the processes listed above are very sensitive to the state of the substrate and it is not unreasonable to expect that even the well known mechanisms of action of various additives on the nucleation of copper on metal substrates can be different in the case of the nucleation of copper on a conductive polymer substrate. Significant effects of different polymer substrates on

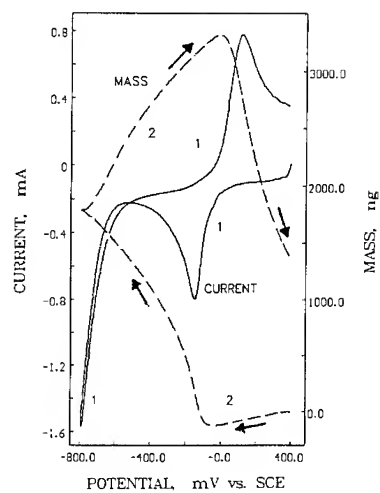


**Figure 1.** Linear potential scan current vs. potential and mass vs. potential characteristics for copper deposition on PPy(PSS) modified Au-EQCM electrode obtained in 10 mM Cu(II) + 0.1 M H<sub>2</sub>SO<sub>4</sub> solution without additives, at scan rate  $v = 50$  mV/s.

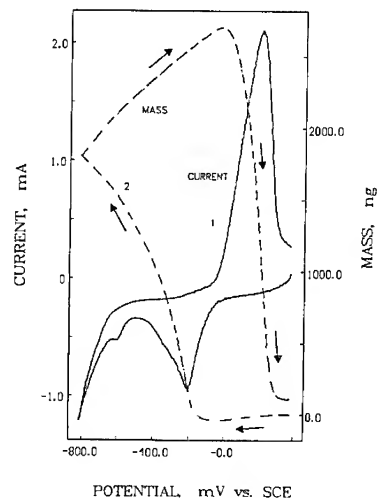


**Figure 3.** Linear potential scan current vs. potential and mass vs. potential characteristics for copper deposition on PPy(PSS) modified Au-EQCM electrode obtained in 10 mM Cu(II) + 0.1 M H<sub>2</sub>SO<sub>4</sub> + 5.3 mM thiourea solution, at scan rate  $v = 50$  mV/s.

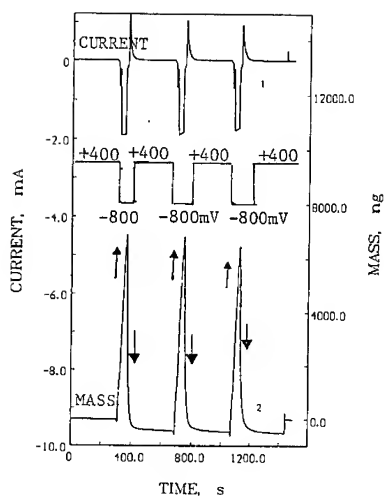


**Figure 2 (a).** Current and mass transients for sequential copper deposition and stripping obtained on a Au-EQCM electrode in 10 mM Cu(II) + 0.1 M H<sub>2</sub>SO<sub>4</sub> solution without additives for potential steps from  $E = +400$  mV to  $E = -800$  mV and pulse duration  $t_{\text{dep}} = 30$  s.

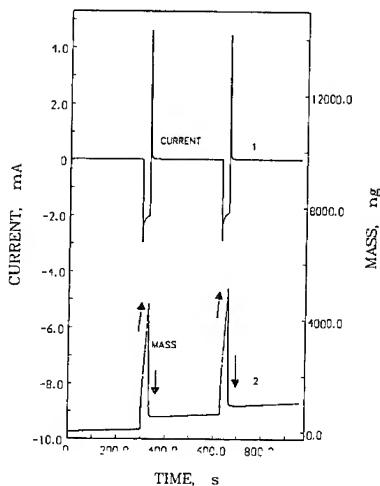


**Figure 2 (b).** Current and mass transients for sequential copper deposition and stripping obtained on a Au-EQCM electrode in 10 mM Cu(II) + 0.1 M H<sub>2</sub>SO<sub>4</sub> + 5.3 mM thiourea solution for potential steps from  $E = +400$  mV to  $E = -800$  mV and pulse duration  $t_{\text{dep}} = 30$  s.

copper plating have already been reposted [6].

Thiourea is probably the most commonly used additive for copper plating. In spite of the long history of its utilization and numerous research studies performed [15-17], the detailed mechanism of the brightening action of this additive is still not well understood. In Figure 3, a typical voltammetric and microelectrogravimetric characteristics obtained for a PPy(PSS) modified Au-EQCM electrode in 10 mM Cu(II) + 0.1 M H<sub>2</sub>SO<sub>4</sub> + 5.3 mM thiourea solution, are presented. The increase in cathodic current observed during the negative potential scan, at potentials less than E = -100 mV, is accompanied by a mass increase manifested on the microelectrogravimetric curve. During the reverse potential scan, the copper stripping begins at the same potential, E = -100 mV, as demonstrated by the onset of the anodic current on the *i*-E curve and the beginning of the mass decrease on the *m*-E characteristic. The total mass increase,  $\Delta m = 2600$  ng, due to the copper deposition, corresponds to approximately 66 monolayers of copper, assuming that a smooth deposit is being formed. As seen in Figure 3, the mass change in one potential cycle is well balanced, *i.e.* the final mass returns to the initial level. This is indicative of the high degree of the system reversibility due to the complexing ability of thiourea. The experiments performed on the same PPy(PSS) film electrode, under the same conditions, but in the absence of thiourea (Figure 1), show a faster copper deposition process, larger amount of copper deposited (3300 ng), and a faster initial rate of dissolution. However, in the absence of thiourea, the copper stripping peak has a more sluggish falling branch (a longer *tail*) and, as a result, a rather large amount of copper (1300 ng) remains undissolved at the end of the potential cycle.

### Morphology of PPy/PSS/Cu Films

The surface morphology of a copper film deposited on a PPy(PSS) substrate, at a potential E = -650 mV vs. SCE, for 600 seconds, from a solution containing 10 mM Cu(II) + 0.1 M H<sub>2</sub>SO<sub>4</sub> is presented in Figure 4a. Hemispherical copper clusters with sizes ranging from 0.1  $\mu$ m to 1  $\mu$ m are formed under these conditions. The morphology of electrodeposited copper under the same conditions as in Figure 4a but in the presence of  $5 \times 10^{-3}$  M thiourea, is presented in Figure 4b. Very pronounced smoothing effect of thiourea on the morphology of copper film is visible in this Figure.

### Energy Dispersive X-Ray Analysis of Composite PPy/PSS/Cu Films

In order to confirm the presence of copper in conductive polymer, the Energy Dispersive X-ray Analysis (EDS) was performed for films obtained under different deposition conditions. The X-ray intensities of K $_{\alpha}$  lines for copper were monitored. The grey image and X-ray map of copper film electrodeposited from 10 mM CuSO<sub>4</sub> + 0.1 M H<sub>2</sub>SO<sub>4</sub> solution, at E = -650 mV, for  $t_{dep} = 200$  s, on a PPy/PSS substrate were also obtained. Strong signals of K $_{\alpha}$  copper were observed. They coincided with the areas on the grey image showing copper clusters.

Another evidence for the formation of copper nuclei was obtained from EDS

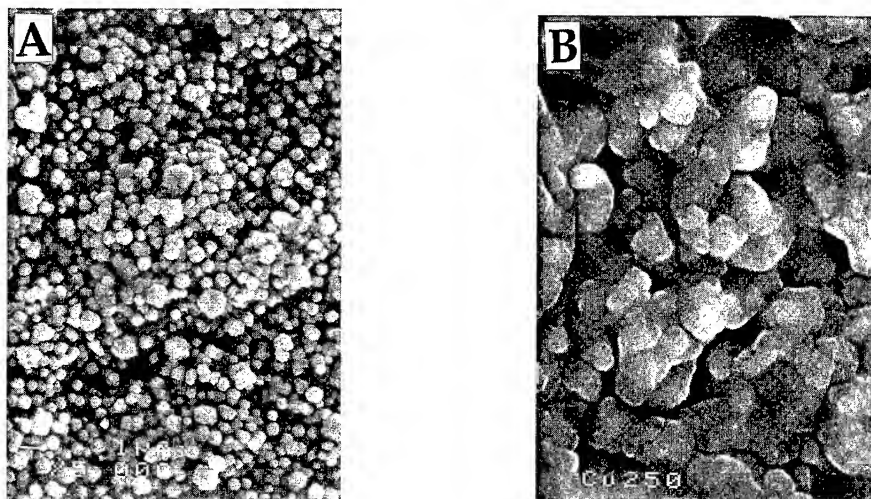


**Figure 4.** SEM micrograph of Cu deposited on PPy/PSS/Au-modified EQCM electrode at  $E_{\text{dep}} = -650$  mV,  $\tau_{\text{dep}} = 660$  sec, from solution containing 10 mM  $\text{CuSO}_4 + 0.1$  M  $\text{H}_2\text{SO}_4$  without thiourea (a), and with 5 mM thiourea (b).

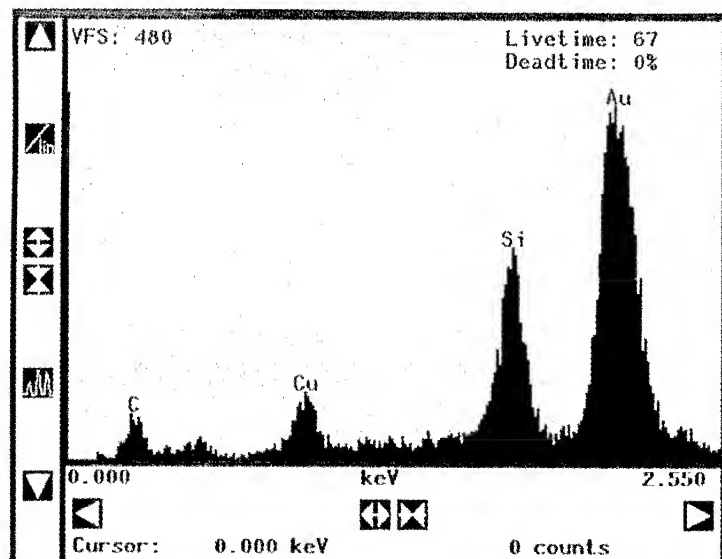


**Figure 5.** Intensities of X-ray as function of energy taken for a composite PPy/PSS/Cu film deposited on a gold-coated quartz crystal substrate.

spectra of X-ray intensities as a function of energy for composite PPy/PSS/Cu films. In Figure 5, a typical spectrum is presented. Intensities of  $K_{\alpha}$  lines for Au, Si, Cu, and C can be readily identified. The additional signals for Au and Si originate from the gold underlayer and quartz substrate, respectively.

### Transmission Electron Microscopy

By incorporating large immobile  $PSS^{-}$  anions into polypyrrole films during the electropolymerization process, the ion dynamics in these films was changed. Films with predominantly cationic dynamics were obtained. Copper(II) cations were incorporated into these films as counterions and they were reduced subsequently to the metallic copper when a negative enough potential was applied. In this way, copper was deposited inside the matrix of the conductive polymer and also on its surface. This procedure allowed us to obtain films with 3D-copper clusters distributed uniformly inside the polymer matrix. A transmission electron micrograph obtained for the composite PPy/PSS/Cu film is presented in Figure 6. In this film, copper was deposited at a constant potential  $E = -300$  mV vs. SCE, from a 10 mM  $CuSO_4$  + 0.1 M  $H_2SO_4$  solution. The amount of copper deposited was controlled by monitoring frequency changes of the piezoelectrode. For the film of Figure 6, the total frequency change recorded during the copper electrodeposition was 5,000 Hz and this corresponds to 5,765 ng of the mass increase. The size of individual metallic clusters ranged from 20 to 60 nm. The cluster size was controlled by changing the electrode potential applied for copper electrodeposition.

### CONCLUSIONS

The experiments performed show that copper can be readily deposited on the composite PPy(PSS) polymer surface and its morphology can be controlled with organic additives. The main difference between the copper deposition on gold (and other metal substrates) and on the PPy(PSS) surface lies in different interaction of the latter substrate surface with additives and with the copper deposit. Thus the initial stage of the copper nucleation process is mostly affected by the presence of the PPy(PSS) film. An increased reversibility of the copper deposition and stripping process was observed in the presence of thiourea.

For short deposition times, small individual copper nuclei were formed. The presence of these copper nuclei was confirmed by EDS analysis and TEM micrographs. The use of composite PPy/PSS films with cation dynamics allowed us to form copper nanocrystals inside the polymer matrix. The copper nanocrystals were uniformly distributed with sizes ranging from 20 to 60 nm.

### ACKNOWLEDGEMENTS

This work was partially supported by the State University of New York at Potsdam Grant F-USRP and Chema Technology Grant.



**Figure 6.** TEM micrograph of a composite PPy/PSS/Cu<sup>0</sup> film electrodeposited on a gold-coated quartz substrate. The PPy/PSS film was formed by electropolymerization at  $E = +650$  mV ( $\Delta f = 10,000$  Hz). Copper was deposited potentiostatically at  $E = -200$  mV vs. SCE ( $\Delta f = 5,000$  Hz) from a solution of 50 mM CuSO<sub>4</sub> + 0.1 M H<sub>2</sub>SO<sub>4</sub>. Scale bar: 34 nm; magnification: 50,000.

## REFERENCES

1. A. Leone, W. Marino, and B. R. Scharifker, *J. Electrochem. Soc.*, **139**, 438 (1992).
2. S. Gottesfeld, F. A. Uribe, and S. P. Armes, *J. Electrochem. Soc.*, **139**, L14 (1992).
3. J. Y. Lee and T. C. Tan, *J. Electrochem. Soc.*, **137**, 1402 (1990).
4. G. K. Chandler and D. Pletcher, *J. Appl. Electrochem.*, **16**, 62 (1986).
5. M. Hepel and R. Stephenson, *Proc. of Int. Tech. Conf. SURFIN'94*, Indianapolis, IN, June 20-23, 1994, Am. Electroplaters and Surf. Fin. Soc., 1994, pp. 51-67.
6. M. Hepel, M. Chen and R. Stephenson, *J. Electrochem. Soc.*, **143** [2], 498 (1996).
7. G. Tourillon and F. Garnier, *J. Phys. Chem.*, **88**, 5281 (1984).
8. S. Holdcroft and B. L. Funt, *J. Electroanal. Chem.*, **240**, 89 (1988).
9. R. Kostecki, M. Ulmann, J. Augustynski, D. J. Strike, and M. Koudelka-Hep, *J. Phys. Chem.*, **97**, 8113 (1993).
10. M. Hepel, *Proceedings of the Electrochem. Soc. Meeting*, Los Angeles, CA May 6-10, 1996, (Eds.) A. Wieckowski and K. Itaya, Electrochemical Society, Pennington, NJ, Vol. 96-8, 1996, pp. 456-480.
11. J.P. Healy, D. Pletcher and M. Goodenough, *J. Electroanal. Chem.*, **338**, 155 (1992).
12. M.J. Armstrong and R.H. Muller, *J. Electrochem. Soc.*, **138**, 2303 (1991).
13. D. Stoychev, I. Vitanova, R. Buynklev, N. Petkova, I. Popova and I. Pojarliev, *J. Appl. Electrochem.*, **22**, 987 (1992).
14. H. S. Jennings and F. E. Rizzo, *Met. Trans.*, **4**, 921 (1973).
15. A. Szymaszek, J. Biernat and L. Pajdowski, *Electrochim. Acta*, **22**, 359 (1977).
16. A. Szymaszek, L. Pajdowski and J. Biernat, *Electrochim. Acta*, **25**, 985 (1980).
17. D.F. Suarez, F.A. Olson, *J. Appl. Electrochem.*, **22**, 1002 (1992).



## ETCHING OF POLYMERS BY PHOTO-MATERIAL PROCESSING USING AN EXCIMER LAMP

Noritaka TAKEZOE\*, Atsushi YOKOTANI\*, Kou KUROSAWA\*, Wataru SASAKI\*,  
Kunio YOSHIDA\*\*, Tatsushi IGARASHI\*\*\*, Hiromitsu MATSUNO\*\*\*

\* Department of Electrical and Electronic Engineering, Faculty of Engineering, Miyazaki University, 1-1, Gakuenkibanadai Nishi, Miyazaki, 889-21, Japan.

\*\* Department of Electronic Engineering, Osaka Institute of Technology, 5-16-1, Omiya, Asahi-Ku, Osaka, 535, Japan.

\*\*\*Research and Development Center, USIO Inc., 1194, Sazuchi, Bessho-Cho, Himeji, 671-02, Japan.

### ABSTRACT

An excimer lamp is a new light source which can produce shorter wavelength of vacuum ultraviolet radiation than conventional ArF excimer lasers. We have tried to use the excimer lamp for photo-etching of polymers such as polymethylmetacrylic and polyimidic resins. We have found that the etching process was including the chemical and the quantum processes. We also applied this technique for etching of some single crystalline organic materials which were very important to opt-electronic applications.

### INTRODUCTION

Recently, various kinds of excimer lamps have been developed as a new light source in the vacuum ultra-violet (VUV) region[1-4], which can produce shorter wavelengths than conventional ArF excimer lasers. In particular, the excimer lamps, in which the dielectric barrier discharge has been utilized, are very compact and have a high efficiency. These characteristics make them a promising light source for photo-material processing[3-5]. An Xe excimer lamp produces radiation at a wavelength of 172 nm, which corresponds to photon energy of 7.2 eV. Energy of this level is higher than bonding energy of many covalent bonds, such as C-H (4.3 eV), N-H (4.1 eV), O-H (4.8 eV), C-C (3.5 eV), C-N (3.4 eV), C-O (3.9 eV), C=C (6.4 eV) and C=N (6.7 eV), which are the principal components in most organic materials. Furthermore, stronger bondings such as C=O (7.9 eV), C≡C (8.7 eV), etc. can be broken if we use an Ar excimer lamp which produces 126 nm (9.8 eV) radiation. Therefore, most bonding in organic materials is completely broken by using these lamps. In addition, unlike lasers, because the lamp produces incoherent radiation, uniform processing over a large sample area without speckling or interference

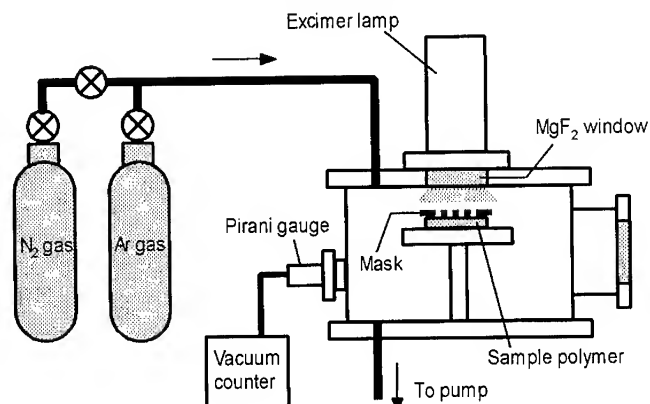


Fig. 1. A schematic drawing of the experimental setup.

fringes can be performed[8]. Besides, because the peak power of the light from the lamp is significantly lower than that of excimer lasers, effective quantum effects and photochemical effects without thermal effects can be observed[5,8]. In this paper, we adopted the dielectric barrier discharge excimer lamps as a light source of photo-etching of some organic optical materials which potentially had good characteristics for opt-electronic applications and observed the change of surface morphologies of them.

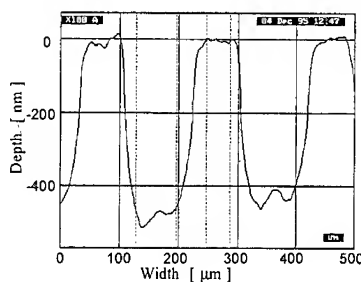
## EXPERIMENT

Fig. 1 shows the schematic drawing of the experimental setup for the etching experiment. We used head-on type Xe and Ar excimer lamps (USHIO Inc., UER20H-172 and UER20H-126). The input electric power was 20 W (20 kHz, 20 kV). The VUV radiation from the lamp was introduced into a vacuum chamber made of stainless steel through a  $\text{MgF}_2$  window of 2 mm thick. Polymers such as polymethylmethacrylic and polyimide resins were used as samples. The sample was placed 25 mm below the window and intensity of light at the surface of samples was approximately  $12 \text{ mW/cm}^2$ . A metal mask with slits of  $100 \mu\text{m}$  wide was used. The pressure of the gas in the chamber was monitored and regulated by using a combination of a rotary vacuum pump and a pirani vacuum gauge. Either the air,  $\text{N}_2$ , or Ar were used as an ambient gas. The irradiation period was varied from 10 to 60 min., in order to estimate the etching rate. The etched samples were characterized by the Talystep surface-roughness-meter, a scanning electron microscope (SEM) and an Atomic force microscope (AFM). We also applied this technique to single crystalline organic opt-electric materials such as l-arginine phosphate monohydrate (LAP)[6] and l-histidine tetrafluoroborate (LHBF)[7], 2-methyl-4-nitroaniline (MNA), *meta*-nitroaniline (*m*-NA), 2-( $\alpha$ -methylbenzylamino)-*s*-nitro-pyridine (MBANP), amino-benzophenone (ABP), and 2-(*N,N*-dimethylamino)-5-nitroacetoanilide (DAN).

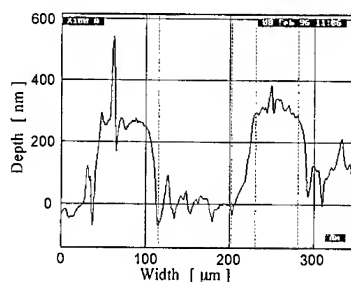
## RESULTS AND DISCUSSION

### ETCHING OF POLYMERS

Fig. 2 shows the typical results which were obtained by measuring the surfaces etched with the mask by means of surface roughnessmeter. Etched pattern corresponding to the mask pattern has been observed. We could easily measure the etch depth from these results. Changing the irradiation period, gas species and pressure, we estimated the etch rate from the etch depth. The results are shown in Fig. 3. In the case of air and  $\text{N}_2$ , the etch rates of both



(a)



(b)

Fig. 2. Typical results which were obtained by measuring the surfaces etched with the mask by means of surface roughnessmeter.

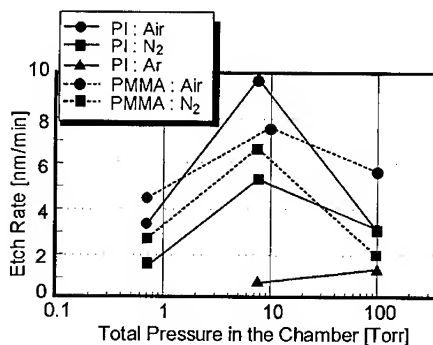


Fig. 3. The etch rate vs. the pressure in the chamber.

polymers became the maximums at a pressure around 10 Torr. The etch rate become smaller when the pressure became both larger and smaller than around 10 Torr. From these results, we concluded that the radicals of gases[4] which was excited by VUV radiation should play an important role in the photo-etching process. When the pressure less than 1 Torr, and/or in the case of Ar gas, the etch rate was a few nm/min. Under these conditions, because the number of radicals created was small, we concluded that an etch rate of this level was mainly due to a quantum process, where the energies of the photon directly broke the covalent bond in the polymers. The smaller etch rates at 100 Torr. in the air and  $N_2$  is probably due to the too strong absorption of the ambient gases.

Fig. 4(a) and (b) show AFM images of PMMA before and after etching of 5 hrs. with Xe excimer lamp at 10 Torr. in air, respectively. The surface was slightly roughen by etching. This roughening is considered to be caused by degree of crystallization in the PMMA bulk. However, as the roughness after etching was approximately 30 nm rms, the light scattering on the etched surface is almost negligible. As almost the same results has been obtained in the case of Ar excimer lamp in the same ambient condition, these results agree with the results mentioned above: etching in air, 10 Torr. is the chemical processs involving the radicals. Fig. 5(a) and (b) shows AFM images of surface of PMMA etched with Xe and Ar excimer lamps in Ar ambient, respectively. In Fig. 5(a), particle-like structure was observed, whereas no such structure was observed in Fig. 5(b). This agrees with the results that etching in Ar ambient is more quantumn, where the energies of the photon directly broke the covalent bond in the polymers, as also mentioned above. Because absorption coefficient of PMMA for 126 nm is much larger than that for 172 nm, only the bonds very near the surface are considered to be broken effectively by the 126 nm radiation. The structure observed in Fig. 5(a) should be made by a process in which the photon from the Xe excimer lamp had broken the bonds in many places in certain region near the surface.

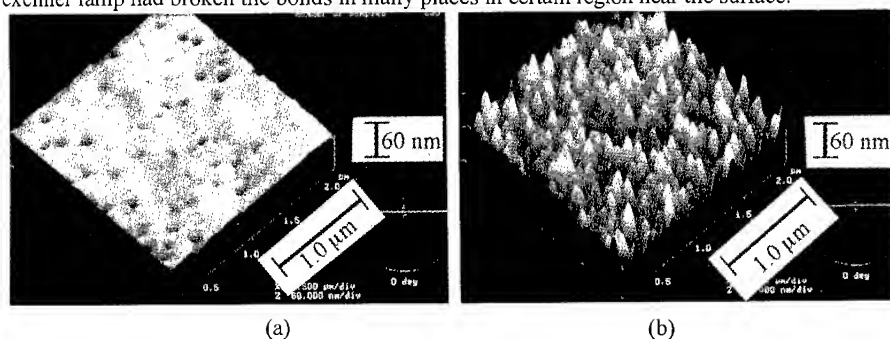


Fig. 4. AFM images of PMMA (a) before and (b) after etching of 5 hrs. with Xe excimer lamp at 10 Torr. in air.

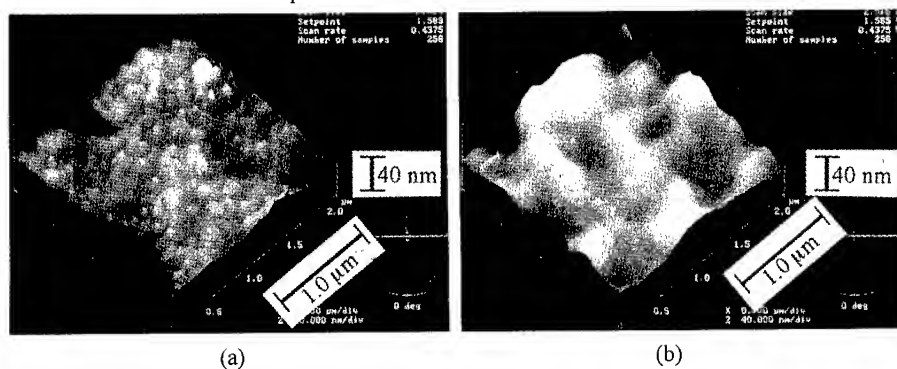


Fig. 5. AFM images of PMMA etched with (a) Xe and (b) Ar excimer lamp at 10 Torr. in air.

## ETCHING OF SINGLE CRYSTALLINE ORGANIC OPTICAL MATERIAL

Figs. 6 (a) and (b) show optical micrographs of LAP and LHBF which have been etched by the Xe excimer lamp with the mask, in the air at a pressure of 10 Torr. The successful etching of these materials can be seen by observing the pattern of the mask on the surface. In the LHBF sample, wrinkle-like pattern and brownish discoloration were observed on the surface of the etched parts. In the LAP crystal, similar pattern was observed soon after the etching had been completed. However the pattern disappeared after leaving in the air for a few days as shown in Fig. 6 (a). The reason of these phenomena might be that LAP contains phosphate group which has low evaporation pressure and very high deliquescency. An AFM image of the etched LAP was shown in Fig. 7. The profile of cross section of these crystals estimated from AFM images were schematically summarized in Fig. 8(a)-(c). In Fig. 8(a), the LAP sample, the upheaval part was observed near the edge of the mask. This upheaval should be probably due to some cohesion of the residual inorganic group. In the case of LHBF crystal, no such cohesion has been observed as shown in Fig. 8(b). Because the evaporation pressure of  $\text{BF}_4$  group is high, it is easy to evaporate and removed from the etched surface. Fig. 8(c) shows a surface profile of LAP etched with Ar excimer lamp in Ar ambient. Because the chemical process is very weak and photon energy of 126 nm radiation is sufficiently higher than the bonding energy of phosphate group, no cohesion has been observed in contrast with the case in Fig. 8(a).

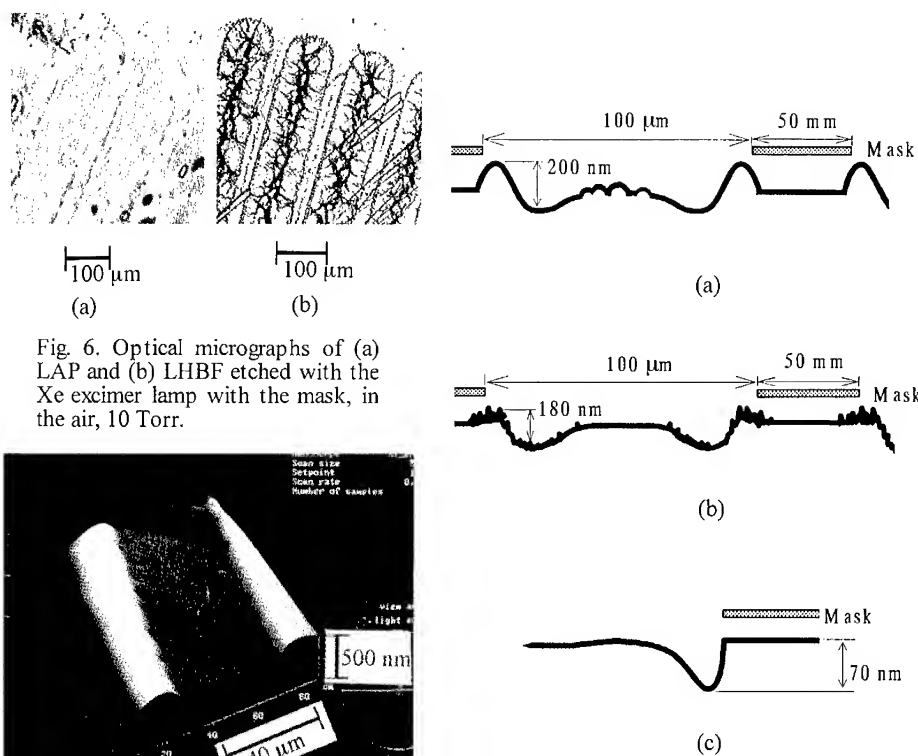


Fig. 6. Optical micrographs of (a) LAP and (b) LHBF etched with the Xe excimer lamp with the mask, in the air, 10 Torr.



Fig. 7. AFM image of the LAP crystal etched with the Xe excimer lamp with the mask, in the air, 10 Torr.

Fig. 8. The profiles of cross section of the crystals. (a) LAP and (b) LHBF crystals etched with Xe excimer lamp in the air, 10 Torr., and (c) LAP crystal etched with Ar excimer lamp in the Ar ambient, 10 Torr.

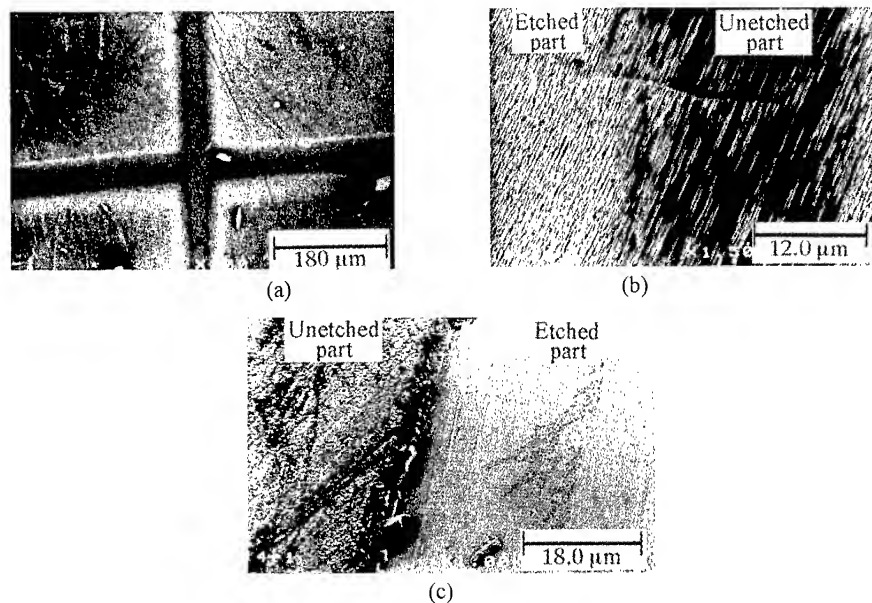


Fig. 9 Typical SEM images of an etched (a) DAN (b) MBANP and (c) ABP crystals.

Similarly, organic nonlinear optical crystals such as MNA, *m*-NA, MBANP, ABP, and DAN has been etched by the Xe and Ar excimer lamp with the mesh like metal mask in various conditions. Fig. 9(a) shows a typical SEM image of an etched sample. Clear mesh pattern has been observed on the etched surface. Fig. 9(b) shows surface of MBANP after etching. The etched surface was found to become smoother. However, in some samples, the etched surface had a tendency to have a more rough surface which was reflecting the structure of the crystals as shown in Fig. 9(c). The results of the observation of etched surface of these crystals were summarized in Table I. The smooth etched surfaces were obtained only for MBANP. At this moment, we

Table I. Summary of the results of etching experiment of organic crystals with Xe and Ar excimer lamps.

	Xe excimer lamp (172 nm, 7.2 eV)		Ar excimer lamp (126 nm, 9.8 eV)	
	Air (10 Torr.)	Ar (10 Torr.)	Air (10 Torr.)	Ar (10 Torr.)
MNA	Rough	Rough	Rough	Rough
<i>m</i> -NA	Rough	NC	NC	Rough
ABP	Rough	NC	Rough	NC
DAN	Rough	NC	NC	NC
MBANP	Smooth	NC	NC	Smooth

NC: Roughness not changed.

consider the cause of this difference may be due to anisotropy of the crystals. Because MBANP has the smallest anisotropy among these crystals and it is much easier to grow the bulk crystals of several cm comparing with all other crystals.

## SUMMARY AND CONCLUSION

The dielectric barrier discharge Xe and Ar excimer lamps have been used for etching of some polymers (PMMA and PI), semi-organic crystals (LAP and LHBf) and organic crystals (MNA, *m*-NA, MBANP, ABP, and DAN). The surface structures of these materials were modified by the irradiation. The mechanism of the modification can be divided into two kinds of processes, *i.e.*, the chemical process and the quantum process. The chemical processes were enhanced when the radicals of the ambient gases were effectively produced. The quantum processes were mainly observed in the rare gas and/or low pressure ambient.

The surface of the polymers and the semi-organic crystals tended to have optically smooth surface after the irradiation, whereas that of most of the organic crystals had more rough surfaces. This difference is considered to be due to very strong anisotropy of the organic crystals.

From these results we can conclude that the incoherent VUV radiation produced from the excimer lamps is very useful and promising as a light source for fine photo-material processing of organic materials in which potentially have good characteristics for opt-electronic applications.

## ACKNOWLEDGMENTS

Authors gratefully acknowledge Prof. T.Sasaki, Faculty of Engineering, Osaka University, Japan for supplying LAP crystals and helpful discussion. Authors also gratefully acknowledge Prof. J. N. Sherwood, Faculty of Science, University of Strathclyde, UK for supplying the organic crystals and helpful discussion.

## REFERENCES

1. H. Kumagai and M. Obara, Appl. Phys. Lett., **54**(26), 2619-2621 (1989).
2. H. Kumagai and M. Obara, Appl. Phys. Lett., **55**(15), 1583-1584 (1989).
3. T. Igarashi, The Review of Laser Eng., Laser Soc. Jpn., **23**(12), 1051-1055 (1995).
4. H. Esrom and U. Kogelschatz, Thin Solid Films, **218**, 231-246 (1992).
5. A. Yokotani, N. Takezoe, K. Kurosawa, H. Matsuno, and T. Igarashi, Appl. Phys. Lett., **69**(10), 1399-1401 (1996).
6. A. Yokotani, T. Sasaki, K. Yoshida, and S. Nakai, Appl. Phys. Lett., **55**(26), 2692-2693 (1989).
7. H. O. Marcy, M. J. Rosker, L. F. Warren, C. A. Thomas, L. A. Deroach, S. P. Veisko, C. A. Ebberts, J. H. Liao, and M. G. Kanatzidis, Opt. Lett., **20**(3), 252-254 (1995).
8. A. Yokotani, N. Takezoe, K. Kurosawa, W. Sasaki, K. Yoshida, T. Sasaki, H. Matsuno, and T. Igarashi, Proc. 11th Int. Symp. Gas and Chemical Lasers, Edinburgh, UK, Aug., 1996. SPIE, in press.

# HIGH RESOLUTION DISPLACEMENT OF FUNCTIONAL GROUPS ONTO FLUOROCARBON RESIN SURFACE BY USING ArF EXCIMER LASER

T.SHIMIZU and M.MURAHARA

Faculty of Engineering, Tokai University, 1117 Kitakaname, Hiratsuka, Kanagawa  
259-12, JAPAN

## ABSTRACT

A Fluorocarbon resin surface was selectively modified by irradiation with a ArF laser beam through a thin layer of  $\text{NaAlO}_2$ ,  $\text{B(OH)}_3$ , or  $\text{H}_2\text{O}$  solution to give a hydrophilic property. As a result, with low fluence, the surface was most effectively modified with the  $\text{NaAlO}_2$  solution among the three solutions. However, the contact angle in this case changed by 10 degrees as the fluence changed only  $1\text{mJ/cm}^2$ . When modifying a large area of the surface, high resolution displacement could not be achieved because the laser beam was not uniform in displacing functional groups. Thus, the laser fluence was successfully made uniform by homogenizing the laser beam; the functional groups were replaced on the fluorocarbon resin surface with high resolution, which was successfully modified to be hydrophilic by distributing the laser fluence uniformly.

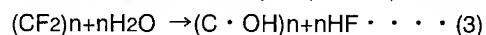
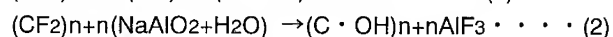
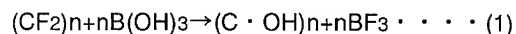
## INTRODUCTION

The Fluorocarbon resin has excellent properties such as heat or chemical resistance. These excellent properties, on the other hand, make its surface modification difficult. Surface modification methods used on fluorocarbon resins to increase the adhesive property, there are laser ablation with high fluence and chemical treatment [1,2]. These methods, however, deform the surface. If the surface can be photochemically modified into hydrophilic or oleophilic, it enables the modified surface to adhere to different materials. We have previously reported an ArF laser induced photochemical modification without deforming the surface to be hydrophilic or oleophilic, and Si or Cu film was deposited on the sample surface[3-7]. However, the substitution efficiency in this method highly depends on the laser fluence or shot number irradiated. Since a laser fluence of the ordinary ArF laser beam is inhomogeneous, functional groups are not replaced uniformly when modifying a large area of the surface. Therefore, we have homogenized the laser fluence of the ArF laser beam and substituted the functional groups on the fluorocarbon

resin surface with high resolution by the homogeneous ArF laser beam irradiation through a thin layer of NaAlO<sub>2</sub>, B(OH)<sub>3</sub>, or H<sub>2</sub>O solution.

### **PHOTOCHEMICAL REACTION**

Fluorocarbon resin is composed of C-F bonds, whose bond energy is 128 kcal/mol. To modify this surface photochemically, the F atoms should firstly be removed from the surface. We previously reported that the fluorocarbon resin surface was irradiated with the ArF excimer laser in the atmosphere of B, Al, or H atoms to pull out the F atoms, and successfully modified into hydrophilic by substituting the OH radicals for the F atoms[3,5]. In this study, the NaAlO<sub>2</sub>, B(OH)<sub>3</sub> or H<sub>2</sub>O solution are employed as they contain defluorination atoms or OH radicals[4,5]. The photochemical reactions take place in the following formulae:



### **EXPERIMENTAL SET UP**

Fig.1 shows the experimental set up. The desired solution (the NaAlO<sub>2</sub>, B(OH)<sub>3</sub>, or H<sub>2</sub>O solution) was sandwiched between the fluorocarbon resin surface and fused silica window. The ArF excimer laser beam irradiated the surface through the solution from a vertical direction.

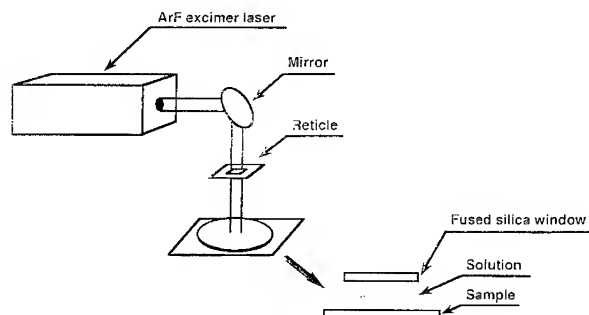


Fig.1 Schematic Diagram of Experimental Set up



## RESULTS AND DISCUSSION

The surfaces modified by the above mentioned methods were evaluated. For evaluating a hydrophilic property, a contact angle with water is generally measured. The contact angle with water of the untreated sample surface is 110 degrees, and the purpose of this study is to achieve the contact angle of the modified surface less than 30 degrees.

As exhibited in Fig. 2, with a shot number of 3,000, the contact angle with water are 20 degrees at the laser fluence of  $12\text{mJ/cm}^2$  with the  $\text{NaAlO}_2$  solution of 0.45% concentration, 32 degrees at  $16\text{mJ/cm}^2$  with the  $\text{B(OH)}_3$  solution of 0.8%, and 41 degrees at  $16\text{mJ/cm}^2$  with the  $\text{H}_2\text{O}$ . The surface modification was most effective with the  $\text{NaAlO}_2$  solution at the low laser fluence (8-  
 $16\text{mJ/cm}^2$ ).

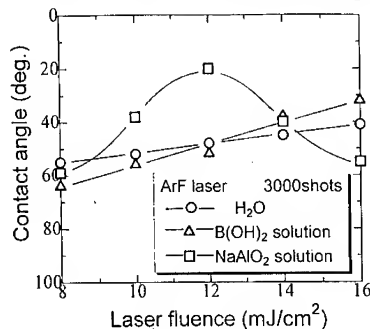


Fig.2 Laser Fluence Dependence of the Contact Angle with Water of the Sample Surface

Fig. 3 exhibits the contact angles with water of the surface before and after the treatment, showing that the  $\text{NaAlO}_2$  solution is the most effective solution at the low fluence. The contact angle with water changed by 10 degrees as the fluence changed only  $1\text{mJ/cm}^2$ .

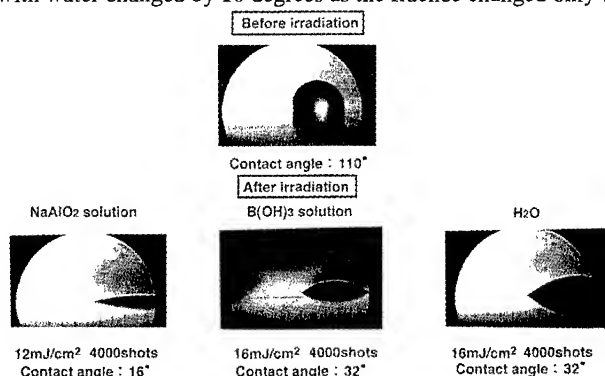
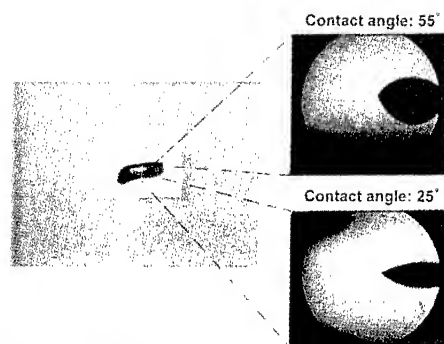


Fig.3 Photograph of the Contact Angle with Water of the Sample Surface

Consequently, the modified surface lacked uniformity (Fig. 4) because the laser fluence was inhomogeneous. In order to modify the surface uniformly, it is required to homogenize the laser fluence.



**Fig.4 Photograph of the Sample Surface Modified to be Hydrophilic Property in Ununiformity with the Ordinary ArF Laser Beam (laser fluence:12 mJ/cm<sup>2</sup>, shot number:3,000shots) and NaAlO<sub>2</sub> solution (concentration:0.45%)**

We, accordingly, homogenized the ArF laser beam with the regular a polyhedron prism that has 25 planes (Fig. 5) and successfully substituted the functional groups uniformly on the surface with the uniform ArF laser through a thin layer of NaAlO<sub>2</sub>, B(OH)<sub>3</sub>, or H<sub>2</sub>O solution.

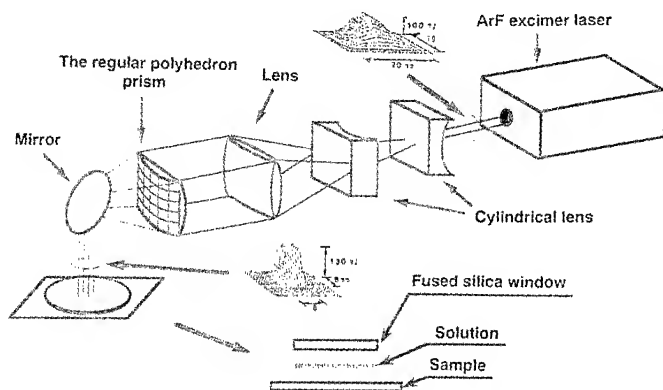


**Fig.5 Schematic Diagram of Experimental Set up with the Beam Homogenizer**

Fig.6 displays the photograph of the uniformly modified surface. Water attached itself to the only area irradiated of the surface; the contact angle with water on the modified surface was examined at every spot and was confirmed almost the same.

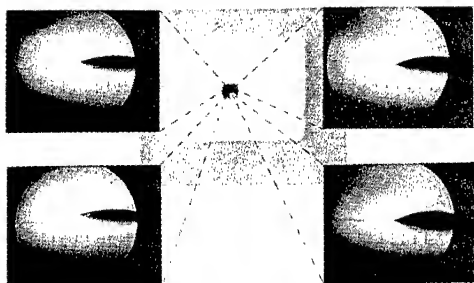


**Fig.6 Photograph of the Sample Surface Modified to be Hydrophilic Property in uniformity by using the Homogenized ArF Laser with the Beam Homogenizer (laser fluence:12 mJ/cm<sup>2</sup>, shot number:4,000shots) and NaAlO<sub>2</sub> solution (concentration:0.45%)**

## **CONCLUSION**

The thin layer of NaAlO<sub>2</sub>, B(OH)<sub>3</sub>, or H<sub>2</sub>O solution was formed on the fluorocarbon resin surface by a capillary phenomenon, which was then irradiated with a ArF excimer laser to selectively modify the surface into hydrophilic. The most effective modification was formed with the NaAlO<sub>2</sub> solution. From the dependence of the contact angle with water upon the laser fluence, it was found that the change of the fluence had a big effect on the contact angle with water in the case of the NaAlO<sub>2</sub> solution. When modifying the large area of the surface with an ArF laser, accordingly, it is required for its laser fluence to be homogenized. By using a homogenized ArF excimer laser, the OH radicals were widely replaced on the surface with high resolution and the large area of fluorocarbon resin was uniformly modified to have a hydrophilic property.

## **REFERENCES**

1. Peter R.Herman, Boyi Chen and Davud J.Moore, Mat.Res.Soc.Symp.Proc.vol.285, 163-168(1992)
2. D.L.Gong, Q.J.Xue and H.G.Wang: J.Appl.poly.sci., 40, 1141(1990)
3. M.Okoshi, M.Murahara and K.Toyoda: J.Mater.Res., 7, No.7, (1992)
4. M.Okoshi, H.Kashiura, T.Miyokawa, K.Toyoda and M.Murahara, Mat.Res.soc.symp.proc.vol.279, 737-742(1992)
5. M.Murahara and K.Toyoda, J.Adhesion.Sci.Tech., 9, 1601(1995)
6. M.Okoshi, K.Toyoda and M.Murahara, Mat.Res.Soc.Symp.Proc.Vol.236, 377-382(1991)
7. M.Okoshi, K.Toyoda and M.Murahara, Mat.Res.Soc.Symp.Proc.Vol.397, 655-660(1995)

## DEVELOPMENT OF A CONTINUOUS SURFACE MODIFICATION SYSTEM OF FLUOROCARBON RESIN FOR STRONG ADHESION

K. Hatao, K. Toyoda\* and M. Murahara

Faculty of Engineering, Tokai University, 1117 Kitakaname, Hiratsuka,  
Kanagawa 259-12, Japan

\*Applied Electronics Science University of Tokyo, 2641 Yamazaki, Noda, Chiba  
278, Japan

### ABSTRACT

Large area surface modification of fluorocarbon resin was performed by ArF laser beam irradiation, and water or  $B(OH)_3$  solution for its practical application. To complete treatment in a short time and keep its cost lower, the total amount of photons that induce reactions was reduced by decreasing the laser fluence as well as shot number. Water or  $B(OH)_3$  was sandwiched between a fused silica glass and a fluorocarbon resin film to form a thin layer using a capillary phenomenon. The substrate was perpendicularly irradiated with ArF excimer laser through a cylindrical lens. By moving horizontally, the surface was continuously modified. The extensively modified sample was mounted to stainless steel with epoxy resin, and the tensile strength was measured. As a result, the adhesive strengths of the sample modified with water and the one with  $B(OH)_3$  solution improved 275 and 490 times that of the untreated sample respectively.

### INTRODUCTION

Fluorocarbon resin is the most chemically stable material among engineering plastics. Its stable property, however, makes it show poor affinity for other materials. If the material surface is modified to add new functional properties, it can be applied for materials such as high voltage resistance compound material and high frequency print basis[1-2]. We have studied the photochemical surface modification by using ArF excimer laser, aiming at its practical application [3-4]. A purpose of this study is to photochemically modify a large area of the fluorocarbon resin surface. We successfully demonstrated a large area modification of fluorocarbon resin surface into a hydrophilic one without surface deformation. The modification was performed by using ArF excimer laser light ( $\lambda=193\text{nm}$ ) and water or  $B(OH)_3$  solution. In order to evaluate its hydrophilic property, the modified surface was checked by measuring contact angles with water. The minimum contact angle was 30deg, whereas a non-treated fluorocarbon resin surface has a contact angle of about 120deg. The surface was then analyzed by FTIR measurement and XPS analysis; the OH group peak appeared at 3300 $\text{cm}^{-1}$  and fluorine was removed from the fluorocarbon resin surface. As a result, the adhesion strength with epoxy resin improved about

275 times with water and about 490 times with  $B(OH)_3$  solution in comparison with that of a non-treated surface.

## PHOTOCHEMICAL REACTION

In order to dissociate C-F bonds, the composition of fluorocarbon resin, it is essential to use a light source whose photon energy is greater than 128kcal/mol. ArF excimer laser satisfies this condition and has 147kcal photon energy. Furthermore, to prevent C-F rebonding, B or H atoms are employed to defluorinate due to their higher bonding energies as compared to F atom's. Replacing with desired functional groups produced from treatment solutions, the surface is selectively modified to have a hydrophilic property [5].

## EXPERIMENTAL SETUP

The experimental set up is shown in Fig. 1. Water or  $B(OH)_3$  solution was placed between a fused silica glass and a fluorocarbon resin film to form a thin layer by a capillary phenomenon [6]. Then, ArF excimer laser ( $\lambda = 193\text{nm}$ ) beam irradiated perpendicular to the substrate through a cylindrical lens. Moving horizontally, the fluorocarbon resin surface was continuously modified.

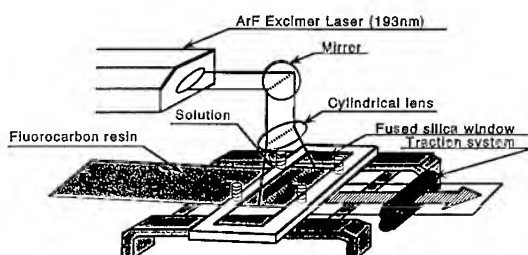


Fig. 1 Schematic Diagram of Experimental Setup

## RESULTS AND DISCUSSION

This study is aimed at industrialization. In order to achieve it, displacement efficiency per unit area should be improved with less total photons. The type of solution used and its density, therefore, are important. Fig. 2 shows the measurement of the contact angles with water of the modified fluorocarbon resin surface. The experimental conditions were the ArF excimer laser fluence of  $20\text{mJ}/\text{cm}^2$ , the 1.2%  $B(OH)_3$  solution and the shot number of 1000, 1500, 2000, 2500, 3000, 3500 or 4000. As seen in the figure, the  $B(OH)_3$  solution modifies the fluorocarbon resin surface to be hydrophilic more efficiently than water; when the shot number is 1000, the contact angle with water becomes 34deg. Fig. 3 exhibits the changes of the contact angles with the laser fluence of  $20\text{mJ}/\text{cm}^2$  and with increasing a density of  $B(OH)_3$  solution and shot number from 0.5 to 1.5% and from 1000 to 3000, respectively. The modification efficiency of 0.8% improved by three times than that of 1.2%. As shown in Fig.4, when  $B(OH)_3$  solution is 1.2% and shot number changes from 0 to 1000, the contact angle decreases to 50deg with 200 shots. When the

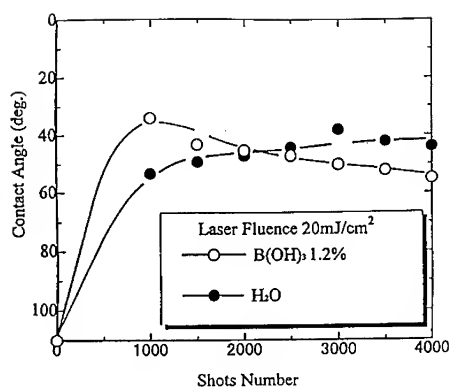


Fig. 2 Dependence between contact angle with water and shot number, with the laser fluence of 20mJ/cm<sup>2</sup> and H<sub>2</sub>O or 1.2% B(OH)<sub>3</sub>

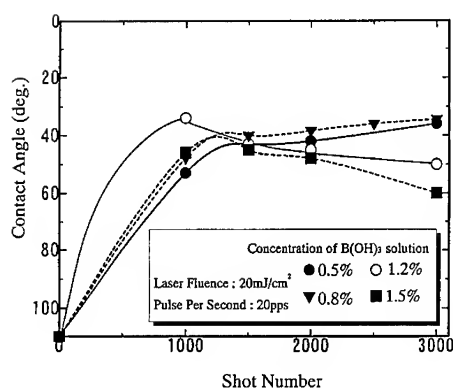


Fig. 3 Dependence between contact angle with water and density of B(OH)<sub>3</sub> solution, with the laser fluence of 20mJ/cm<sup>2</sup> and at the shot number of 1000, 1500, 2000, 2500 or 3000

laser fluence changes from 20mJ/cm<sup>2</sup> to 30mJ/cm<sup>2</sup>, the minimum contact angle with water is 30deg at 30mJ/cm<sup>2</sup>, as indicated in Fig. 5. In order to examine that the fluorocarbon resin surface was defluorinated, XPS measurements were conducted (Fig. 6). F1s peak decreased

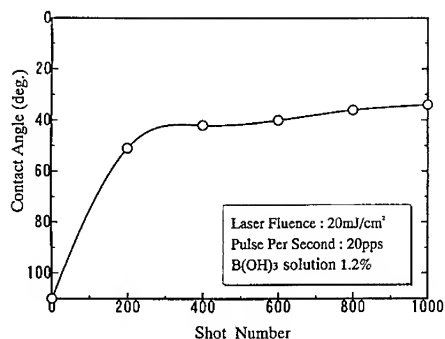


Fig. 4 Dependence between contact angle with water and shot number, with the laser fluence of 20mJ/cm<sup>2</sup> and 1.2% B(OH)<sub>3</sub> solution

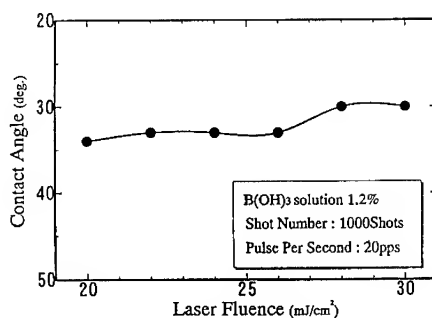


Fig. 5 Dependence between contact angle with water and laser fluence, with 1.2% B(OH)<sub>3</sub> solution and at the shot number of 1000

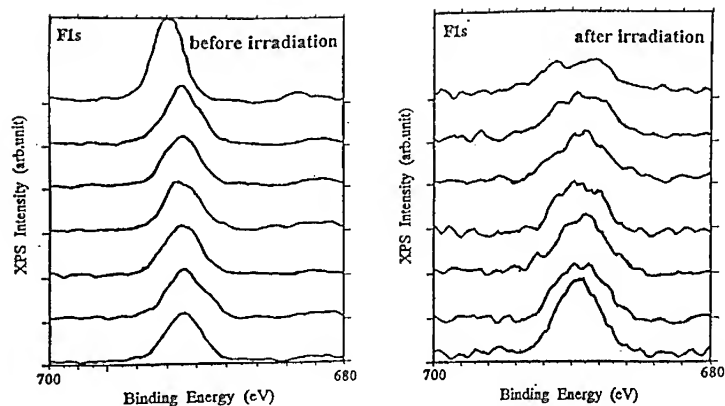


Fig. 6 Results of XPS measurement of the modified surface

compared with the untreated surface; thus, it is apparent that defluorination of the surface took place. Furthermore, the modified surface was evaluated by ART-FTIR. The measurement of spectra are exhibited in Fig. 7(a) with  $B(OH)_3$  solution and (b) with water. Compared with the untreated surface, the peak of OH group appeared in the vicinity of  $3300\text{cm}^{-1}$  in both cases. It was confirmed that substitution of the OH groups took place more effectively with  $B(OH)_3$  than with water as the peak of (a) was higher than that of (b). From the results shown in Fig. 6 and 7, it is clear that the modified surface was defluorinated and replaced with the OH group.

The sample whose surface was modified under the above mentioned conditions was epoxied to stainless steel; tensile strength was determined. As shown in Fig. 8, tensile strength of the modified samples with water and  $B(OH)_3$  increased by 275 times ( $55\text{kgf/cm}^2$ ) and 490 times ( $98\text{kgf/cm}^2$ ) that of the untreated sample ( $0.2\text{kgf/cm}^2$ ), respectively.

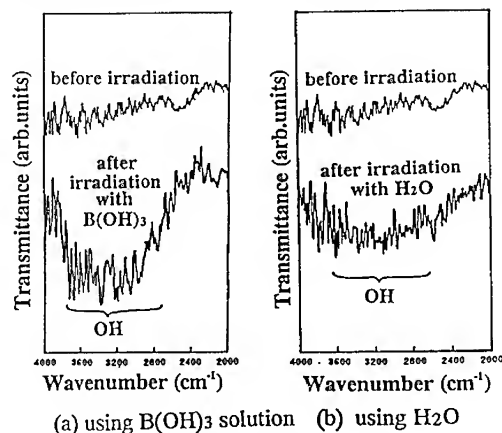


Fig. 7 Results of ATR-FTIR measurement spectra of the modified surface

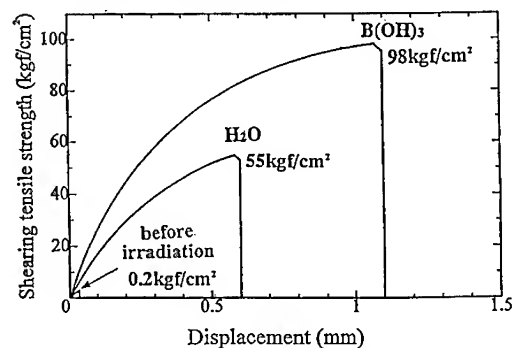


Fig. 8 Results of shearing tensile strength measurement

## CONCLUSION

Large area surface modification in a short time is indispensable for its practical application. We successfully demonstrated the extensive surface modification of fluorocarbon resin by horizontally moving the substrate at a uniform rate which was irradiated with the ArF excimer laser beam through a cylindrical lens. As a reaction solution, water and  $B(OH)_3$  solution were employed for defluorination atom and substitution group in the open air treatment.

With  $B(OH)_3$  solution, the density was changed from 0.5% to 1.5%; the hydrophilic property improved approximately three times with a density change from that of 0.8% to 1.2%. The surface modified in large area was, then, evaluated at various spots. The contact angle with water was 50deg with a solution of 1.2%, a laser fluence of 20mJ/cm<sup>2</sup> and a shot number of 500; it decreased to 30deg when the laser fluence was changed to 30mJ/cm<sup>2</sup>. The XPS measurement revealed that the of F atom peak decreased compared with that of the untreated sample, and the OH peak was equally observed in the vicinity of 3300cm<sup>-1</sup> at various spots by ATR-FTIR measurement. The extensively modified sample was glued to stainless steel with epoxy resin, and the tensile strength was measured. The sample modified with water and the one with  $B(OH)_3$  improved 275 times and 490 times the untreated sample, respectively, in terms of tensile strength.

## REFERENCES

1. H.Nino and A.Yabe : Appl. Phys. Lett. 60 (1992) 2697
2. H.Nino and A.Yabe : Appl. Phys. Lett. 63 (1993) 3527
3. M.Okoshi, M.Murahara, and K.Toyoda: J.Mater. Res., 7 No.7, (1992) 1912
4. M.Murahara and K.Toyoda: Jadhesis Sci. Tec., 9 1601 (1995).
5. M.Okoshi, H.Kashiura, T. Miyokawa, K.Toyoda, and M.Murahara: Mater. Res. Soc. Symp. Proc., Vol.279, 737 (1993)
6. T.Okamoto, K.Hatao, T.Shimizu, M.Aoike and M.Murahara: Mat. Res. Soc. Symp. Proc. Vol. 397 , 555-559



## OPEN AIR FABRICATION OF $\text{Al}_2\text{O}_3$ THIN FILMS AT ROOM TEMPERATURE

T. Okamoto, K. Toyoda\* and M. Murahara  
Faculty of Electrical Engineering, Tokai University  
1117 Kitakaname, Hiratsuka, Kanagawa, 259-12, JAPAN  
\*Applied Electronics, Science University of Tokyo  
2641 Yamazaki, Noda, Chiba, 278, JAPAN

### ABSTRACT

A thin layer of water or hydrogen peroxide solution, which was formed on a pure aluminum substrate, was photodissociated by ArF excimer laser ( $\lambda = 193\text{nm}$ ) or  $\text{Xe}_2^*$  excimer lamp ( $\lambda = 172\text{nm}$ ) light to photochemically oxidize the surface of aluminum substrate. The layer was formed by a capillary phenomenon between the substrate and a fused silica glass as an entrance window of ultraviolet light. Then, the layer was photodissociated by the excimer laser or the excimer lamp light irradiation to generate active oxygen; the surface oxidation was performed by the photo-induced active oxygen. The surface before and after modification was evaluated by the XPS analysis; the high densified photo-oxidation film was confirmed on the modified surface, compared with a natural oxidation film. Furthermore, the contact angle with water became remarkably small, and it is seen that the treated surface was quite densely oxidized.

### INTRODUCTION

In electronic field, pure aluminum and its compounds are widely used as conductive or dielectric materials. Anodic oxidation, plasma oxidation and chemical treatments have been extensively studied in order to fabricate  $\text{Al}_2\text{O}_3$  films [1-3]. It is difficult, however, to selectively form oxidized films by conventional methods. Therefore, the studies on aluminum deposited by photo-CVD method [4] or aluminum oxide deposited by electron beam evaporation [5] and the like have been reported, but no experiments to apply this in the semiconductor processing were reported yet. If the surface can be simply oxidized with low energy and in the air, it leads to a simplification of the modification process and the function of the surface improves further. To give functional properties, we have reported the methods by substituting functional groups on polymer materials with low energy [6-8] and by replacing it with Si semiconductor on a teflon surface [9]. In this study, as a new fabrication method, we successfully formed photo-oxidation films by photodissociating water or hydrogen peroxide with the excimer laser or excimer lamp irradiation, and having active oxygen generated and pure aluminum interact. The fabrication of  $\text{Al}_2\text{O}_3$  films was confirmed on the modified surface by the XPS analysis and measurement of the contact angle with water. Furthermore, the dependence of the photoreaction on the surface upon the excited wavelength was investigated by  $\text{Xe}_2^*$  excimer lamp or ArF excimer laser to compare. It was confirmed that the production amount of active oxygen that were photodissociated from water or hydrogen peroxide by the excimer laser or excimer lamp irradiation varied, resulting in the change of oxide film formation. Thus, photo-induced  $\text{Al}_2\text{O}_3$  thin films were fabricated at the interface between the surface and the reaction solution. In this paper, we report on successful performance of the aluminum surface oxidation at room temperature for use as dielectric materials.

## PHOTOCHEMICAL REACTIONS

Water or hydrogen peroxide solution has the absorption band in 220 nm below, 300nm below respectively [Fig. 1], its layer was formed between a fused silica window and a pure aluminum substrate. The layer was irradiated with the ArF excimer laser or Xe<sub>2</sub>\* excimer lamp, and the solution was photodissociated to react as follows:

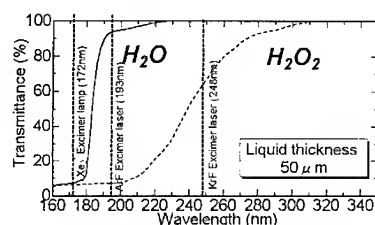


Fig.1 VUV and UV absorption spectra of H<sub>2</sub>O<sub>2</sub> and H<sub>2</sub>O

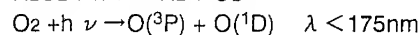
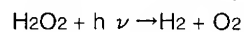
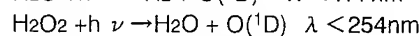
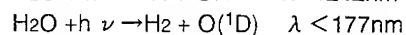
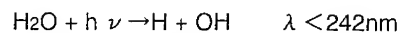


Photo-induced oxidation of the pure aluminum surface was attributed to the active oxygen O(<sup>1</sup>D) generated from water through these reactions. Especially, as aluminum has high reflectance in the range of ArF excimer laser light or Xe<sub>2</sub>\* excimer lamp light, the light not participated in photodissociating water reflected on the surface and re-entered into the water that was again photodissociated. Consequently, this process photodissociated the interface of pure aluminum effectively and improved the oxidation efficiency. There are  $1.67 \times 10^{20}$  water molecules in an area of  $1\text{cm}^2 \times$  approximately  $50\text{ }\mu\text{m}$  for the ArF laser fluence of  $50\text{ mJ/cm}^2$  (photon number =  $4.66 \times 10^{16}$  number/cm<sup>2</sup>); assuming 1% of water to be photodissociated when the water is irradiated with the ArF laser light (photon number =  $4.66 \times 10^{16}$  number/cm<sup>2</sup>),  $1.67 \times 10^{18}$  water molecules are to be photodissociated. If a reflectance of the aluminum at the interface is estimated 70%,  $4.657 \times 10^{16}$  photons not participated in photodissociating water reflect on the aluminum surface and photo-dissociate  $1.65 \times 10^{20}$  water molecules which are left. Thus, it is expected that the surface oxidation will be efficiently performed at the interface between the thin layer and the surface.

## EXPERIMENTAL PROCEDURE

### Experimental Setup

Fig. 2 shows the experimental setup. Solution, water or hydrogen peroxide water, was sandwiched between a pure aluminum substrate and a fused silica window to form an approximately  $50\text{ }\mu\text{m}$  thin layer by a capillary phenomenon. The ArF excimer laser or Xe<sub>2</sub>\* excimer lamp light vertically irradiated the aluminum surface through the window. The layer was photodissociated, and the surface was photo-excited to oxidize. The experimental conditions were as follows: the thickness of the thin layer was approximately  $50\text{ }\mu\text{m}$ , the ArF excimer laser fluence was  $0\text{--}50\text{ mJ/cm}^2$ , and shot number was  $0\text{--}4000$ .

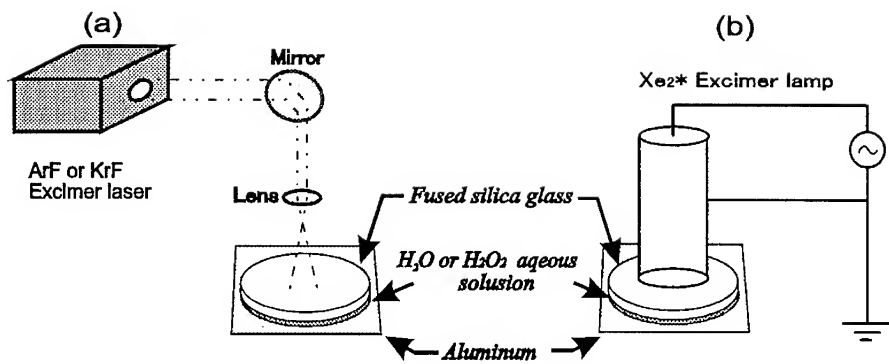


Fig.2 Schematic Diagram of Experimental Setup

(a) using ArF or KrF Excimer laser

(b) using Xe<sub>2</sub>\* excimer lamp

#### Evaluation of surface modification

Oxidation process of the pure aluminum surface was observed by the XPS analysis, and the photo-induced oxidation film was compared with that of naturally oxidized. Moreover, the contact angle with water of the sample surface was measured to confirm if the photo-induced oxidation of the surface took place.

## RESULTS AND DISCUSSION

To photochemically oxidize a pure aluminum, the photo-excited O<sub>2</sub>, H<sub>2</sub>O and H<sub>2</sub>O<sub>2</sub> were used as oxidizers. It is then needed to efficiently photo-dissociate them on the surface in order to generate a large amount of active oxygen. Therefore, interdependence of a wavelength and oxide film formation was measured in the presence of each oxidizer by using three excitation light sources of different wavelengths: KrF laser ( $\lambda=248\text{nm}$ ), ArF laser ( $\lambda=193\text{nm}$ ) and Xe<sub>2</sub>\* excimer lamp ( $\lambda=172\text{nm}$ ). In general, pure aluminum is spontaneously oxidized in the air and the contact angle with water of the surface changes from 60 deg. to 50 deg for a few hours. Moreover, as the simplest evaluation method of oxide fabrication, the contact angle with water was measured. When the oxidizers were photodissociated on the surface by the three excitation light sources, the changes in contact angle with water were inspected.

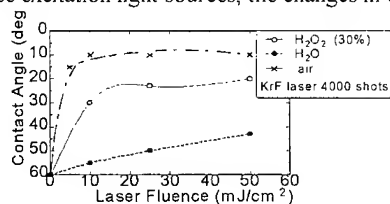


Fig.3 Dependence of KrF laser fluence upon the Contact angle

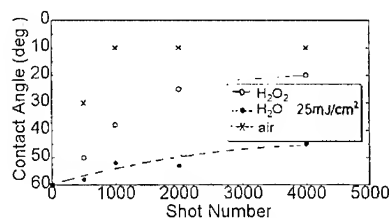


Fig.4 Dependence of KrF shot number upon the Contact angle

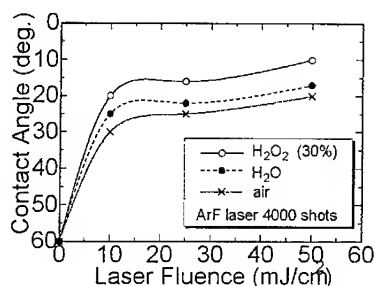


Fig. 5 Dependence of ArF laser fluence upon contact angle

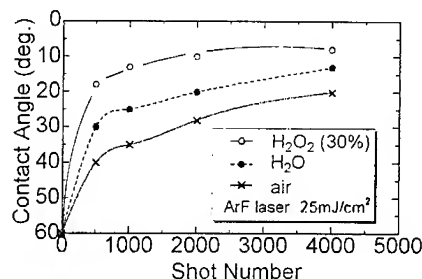


Fig. 6 Dependence of ArF laser shot number upon contact angle

inspected. Fig. 3 shows the dependence of laser fluence upon the contact angle, with KrF laser irradiation. The close oxide film was formed at the laser fluence of  $25\text{mJ/cm}^2$  when the contact angle was smallest. The dependence of shot number at the same laser fluence is investigated, as shown in Fig. 4. In the same manner, with ArF laser irradiation, the dependence of laser fluence and shot number are examined and shown in Fig. 5 and 6, respectively.

Moreover, Fig. 7 shows the dependence of irradiation time, with  $\text{Xe}_2^*$  excimer lamp that has photochemically high photon energy and effectively generates active oxygen atoms. From the comparison of Fig. 3 through 7, by inducing the photochemical reactions with the excimer laser and the excimer lamp, it was apparent that the photo-induced oxidation was performed more effectively in a shorter time relative to the spontaneous oxidation.

As indicated in Fig. 5 and 6, specially, the ArF laser irradiation effectively photo-dissociates the three oxidizers to induce surface reactions, which results in the smaller contact angle. It was due to the photo-induced oxidation of the pure aluminum. When the aluminum was irradiated with the  $\text{Xe}_2^*$  excimer lamp of short wavelength for 6 minutes, the contact angle became approximately 15 deg. and the oxidation efficiency was remarkable.

On the other hand, as to the change of the contact angle [Fig. 3 and 4] with KrF laser irradiation in the air, hydrogen peroxide solution was photodissociated with the wavelength of about  $248\text{nm}$ , while oxygen and water were not photodissociated, as given in the above equations of photodissociation. Fig. 10 shows that the formation efficiency of  $\text{Al}_2\text{O}_3$  is lower by using the KrF laser than the ArF laser; consequently, the related contact angle is large, as exhibited in Fig. 4 and 6. As the modified surface was inspected with SEM, a lot of micro-cracks, which could not be confirmed by ArF laser and  $\text{Xe}_2^*$  excimer lamp irradiation, were observed on the surface. The XPS spectra of the surface

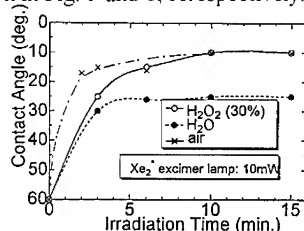


Fig. 7 Dependence of irradiation time upon contact angle

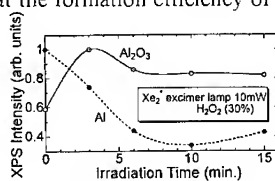


Fig. 8 XPS intensity of modified surface with  $\text{Xe}_2^*$  lamp irradiation

indicated that the oxide films were closely formed by the ArF laser and Xe<sub>2</sub>\* excimer lamp but roughly produced by the KrF laser. It was considered that the micro-cracks physically made the contact angle small.

From the above-mentioned results, it was found that hydrogen peroxide solution was the most effective oxidizer. By using the hydrogen peroxide solution, the surface was photo-oxidized with the KrF laser, ArF laser and Xe<sub>2</sub>\* lamp; the respective XPS intensity of Al<sub>2</sub>O<sub>3</sub> and Al are shown in Fig. 8, 9-(a) and 9-(b).

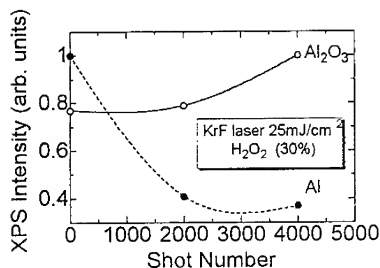


Fig. 9-(a) XPS intensity of the modified surface with H<sub>2</sub>O<sub>2</sub> and KrF laser

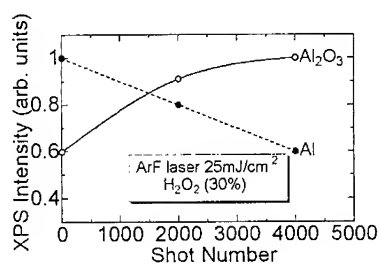


Fig. 9-(b) XPS intensity of the modified surface with H<sub>2</sub>O<sub>2</sub> and ArF laser

With the Xe<sub>2</sub>\* lamp irradiation, the XPS intensity of Al<sub>2</sub>O<sub>3</sub> increased as irradiation time increased, being saturated; however, the intensity of Al decreased as irradiation time increased. A similar behavior was observed with the ArF laser irradiation. That is, the hydrogen peroxide solution was photodissociated with the excimer lamp irradiation to generate active oxygen (O(<sup>1</sup>D), O(<sup>3</sup>P)); which promoted the photochemical surface reaction and effectively oxidized the surface. Furthermore, when using the ArF laser, the oxide film required less time with the increase of shot number for its formation because the ArF laser light has more photons than Xe<sub>2</sub>\* lamp. In the case of using the ArF laser, XPS intensity was Al<sub>2</sub>O<sub>3</sub>/Al > 1, while in the case of the natural oxidation film, the intensity was Al<sub>2</sub>O<sub>3</sub>/Al < 1, as indicated in Fig. 10. As the result, it was clear that the surface was effectively photo-oxidized with hydrogen peroxide solution by using ArF excimer laser or Xe<sub>2</sub>\* excimer lamp.

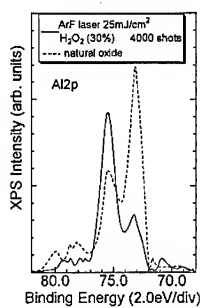


Fig. 10 XPS spectrum of natural oxide and photo-induced oxidation film

## CONCLUSION

The photo-induced oxidation of pure aluminum surface was successfully demonstrated by KrF, ArF excimer laser or Xe<sub>2</sub>\* excimer lamp irradiation through water or hydrogen peroxide

solution. From the measurement of contact angle of the sample before and after modification, it was found that the photo-induced oxidization took place more effectively with the hydrogen peroxide solution than with water; the surface modification was achieved at the low laser fluence and with the low shot number. Moreover, the results of XPS analysis revealed that the surface was effectively photo-oxidized with hydrogen peroxide solution as an oxidizer and ArF excimer laser or Xe<sub>2</sub>\* excimer lamp as a light source. As a result, it was clear that the photo-induced oxidization was controlled by the difference in type and amount of the active oxygen produced.

## REFERENCES

1. J. C. W. Kruishoop, Philips Technical Review, Vol. 29, No.2, 37 (1968)
2. G. J. Tibol and R. W. Holl, J. Electrochem. Soc. Vol.111, No.12, 1368 (1964)
3. H. Bohni, H. Uhling, J. Electrochem. Soc., 116, 906 (1969)
4. M. Hanabusa and K. Sahara, Mat. Res. Soc. Symp. Proc., Vol. 201, 607 (1991)
5. W. Frbansen, T. Tetreault, W. Kosik, W. Groft and J. K. Hirvonen, Mat. Res. Soc. Proc. Vol. 279, 825 (1993)
6. M. Murahara and M. Okoshi, J. Adhesion Sci. Technol., Vol.9, No.12, 1593 (1995)
7. M. Okoshi, H. Kashiura, T. Miyokawa, K. Toyoda and M. Murahara, Mat. Rec. Soc. Symp. Proc., Vol.279, 737 (1993)
8. M. Murahara, M. Okoshi and K. Toyoda, SPIE, Vol.2207, 577 (1994)
9. T. Miyokawa, M. Okoshi, K. Toyoda and M. Murahara, Mat. Res. Soc. Symp. Proc. Vol. 334, 87 (1994)

**Part VIII**  
**Corrosion**

## CORROSION OF ELECTRONIC AND MAGNETIC DEVICES AND MATERIALS

GERALD S. FRANKEL

The Fontana Corrosion Center, The Ohio State University, 477 Watts Hall, 2041 College Rd.,  
Columbus, OH 43210, frankel.10@osu.edu

### ABSTRACT

Corrosion of thin film structures commonly used in electronic and magnetic devices is discussed. Typical failure modes are presented, and galvanic corrosion is discussed in some detail since it is one common problem with such devices. A graphical explanation for the determination of the ohmic potential drop during galvanic corrosion is presented. The corrosion problem of thin film disks is shown to have changed during the past ten years owing to changes in disk structure. The corrosion susceptibility of two antiferromagnetic alloys used for exchange coupling to soft magnetic layers is discussed.

### INTRODUCTION

Corrosion is one common electrochemical modification of materials that is usually unwanted and deleterious to the material performance. Almost all metals tend to corrode because the corroded state is thermodynamically more stable. By corroding, metals often revert to a state that is similar to the ores in which they are found in nature; the effort and cost of refining the ores are simply lost as a result of the corrosive action.

This paper will focus on the corrosion of thin film structures, since this is the emphasis of the rest of this symposium. Thin film structures, such as are commonly found in electronic and magnetic devices are often very susceptible to corrosion for many reasons:

1. The materials used in electronic and magnetic devices are designed for properties other than corrosion resistance, and thus may be very susceptible to corrosion.
2. The structures often contain multilayers of electrochemically-incompatible thin films. This can result in large driving forces for galvanic corrosion that will accelerate the rate of corrosion of the least-noble layer.
3. The shrinking dimensions of devices results in extremely small allowable losses of metal to corrosion.
4. Electronic components are often biased with a high voltage (a few volts is large in electrochemical terms) at small distances, resulting in very large applied fields.
5. Whereas operating environments for computers and other electronics are often rather benign, there are some process steps that can be quite aggressive.
6. Electronic devices are increasingly being used in more-aggressive and less-controlled environments.

Some of these factors will be discussed in detail below.

### FAILURE MODES

Metals are deposited onto chips to act as conductive pathways for electric signals. For any metallization to corrode, the metal needs to be exposed to an aqueous environment. Metals covered with a deposited passivation layer (not to be confused with thin, naturally-formed oxides called passive films in the corrosion literature) will not corrode if the passivation is fully covering. However, such deposited layers often contain defects such as cracks, pinholes, and inadequate step coverage, and underlying metals are thus susceptible to corrosive attack. Polymers are, in general, permeable to water and other contaminants. Metallic structures under organic coatings, such as in plastic packages, can corrode if a continuous water layer forms at the metal surface.

Failure of electronic metallization resulting from corrosion typically can be characterized as one of a few different modes [1].

One common failure mode is electrolytic dissolution of a positively-biased structure leading to an open. Al metallization will fail in this mode in the presence of chloride contamination, which tends to cause localized corrosion in Al and Al alloys.



Owing to its amphoteric nature, Al can also suffer cathodic corrosion. In this case, the negatively-biased structure will corrode despite the negative bias to result in an open. This mode will occur if chloride contamination is absent, but some other type of contamination exists to provide a conductive electrolyte. The use of phosphosilicate glass as a top passivation layer promotes cathodic corrosion. The cathodic reaction at the negatively-biased electrode causes a local increase in pH. Al will dissolve in alkaline environments even if a cathodic bias is applied.

Electrolytic migration is often the cause of failure for Ag, Sn, Au, and Cu, which are all conductive metals used extensively in electronic applications. This phenomenon should not be confused with electromigration, which is purely physical in nature. During electrolytic migration, metallic ions dissolved from the positively-biased structure are transported by migration and diffusion through the electrolyte, and deposit at the negatively-biased structure with a dendritic morphology. Deposition under transport-limited conditions often promotes the stability of dendrites. These dendrites grow from the cathode toward the anode, resulting in failure by a short in a time that is much less than that required for failure by an open at the anode.

Galvanic corrosion, the final failure mode, can occur even in the powered-off condition. Galvanic corrosion will be discussed below in some detail.

The primary technological components in magnetic storage devices, the heads and disks, were once made from ceramic materials. In advanced disk drives, both heads and disks now have important metallic components, and are thus susceptible to corrosion. Furthermore, the materials with the best magnetic properties are very susceptible to corrosion. The primary mode of corrosion in both heads and disks is galvanic corrosion. Ultimately, however, the corrosion failures that occur are from a head crash or other tribological problem resulting from the voluminous corrosion product existing at the head/disk interface. Heads are flying increasingly closer to disks, (now on the order of tens of nm) so the allowable extent of interface contamination by corrosion product is becoming less and less. Corrosion of magnetic materials will be addressed below in more detail.

## GALVANIC CORROSION

Microfabrication processing techniques allow the construction of complex miniature structures. Layers of different metals or alloys are often used for their individual characteristics: electronic conductivity, adhesion, bondability, diffusion barrier nature, tribological properties, or magnetic properties. As a result, the devices are often multilayers of several different metals with varying electrochemical properties. Depending on the details of the structure that is exposed to the environment, severe galvanic corrosion can result, even under unbiased conditions. Galvanic corrosion is described in any textbook on corrosion. The fundamentals will be reviewed presently, with an added insight to explain the concept of solution ohmic potential drop.

Galvanic corrosion will occur when three conditions are met: (a) dissimilar metals must be (b) in electrical contact and (c) ionic contact, i.e. in the same electrolyte. The less-noble metal will suffer accelerated corrosion, and the more-noble metal will corrode at a slower rate. The driving force for galvanic corrosion is the difference in open circuit potentials of the different metals that would be measured in the environment if they were electrically isolated. As a result of the galvanic action, the structure will polarize to a mixed potential between the individual open circuit potentials. The extent of galvanic corrosion will depend on the polarization kinetics of the metals, the cathode/anode area ratio, and the ohmic resistance in the environment. In a galvanically-corroding structure, charge is conserved, so the net current flowing must be zero. In other words, the sum of the anodic currents equals the sum of the cathodic currents. If only two metals are connected, the anodic current, which flows primarily from the less-noble metal, must equal the cathodic current, which originates primarily from the more-noble metal:

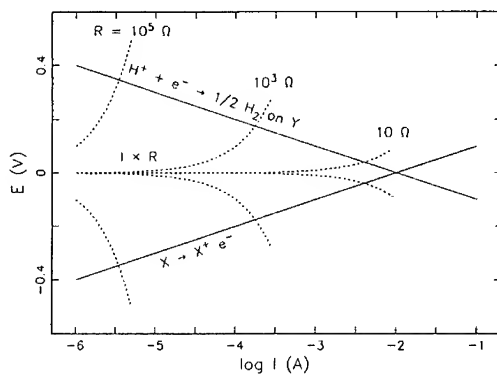
$$I_a = I_c \quad (1)$$

Since corrosion rate is expressed in terms of current density,  $i = I/A$ , the following expression, which highlights the importance of the cathode/anode area ratio, can be determined:

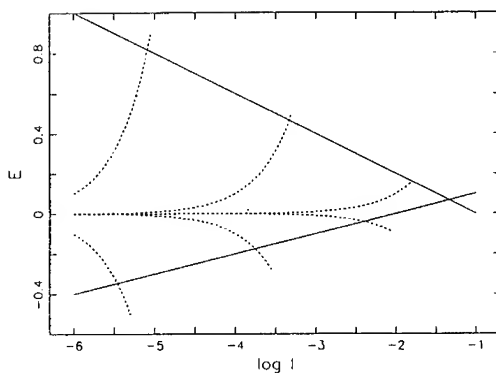
$$i_a = i_c (A_c/A_a) \quad (2)$$

The rate of galvanic corrosion of the less-noble metal is thus more intense when its exposed area is small compared to that of the cathodic, more-noble metal.

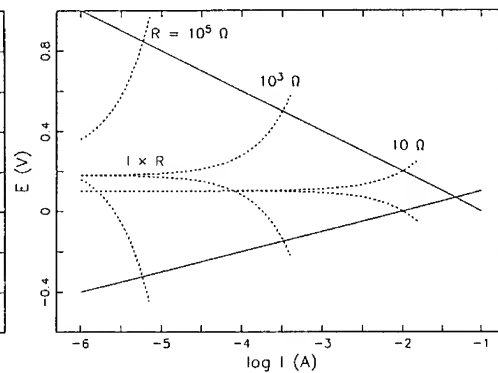
Since the galvanic circuit is completed by current flowing through the electrolyte of finite conductivity, an ohmic potential drop will exist with a magnitude that depends on the magnitude of the current flowing, the electrolyte conductivity, and the current distribution in the electrolyte. As a result of this ohmic potential drop, the anode and cathode will not be at the same mixed potential; instead, they will be separated by an amount equal to the ohmic potential drop, with the potential of the anode being lower than that of the cathode. The galvanic current flowing, and thus the corrosion rate, will be lower than what would happen in the case of an infinitely high solution conductivity. Textbooks typically do not explain clearly how the galvanic current and electrode potentials are determined in a system with finite electrolyte conductivity. In Figure 1, a graphical explanation for the determination of ohmic potential drop is shown.



a)



b)



c)

Figure 1. Schematic representation of ohmic potential drop during galvanic corrosion: a) equal Tafel slopes for anodic and cathodic reactions, b) unequal Tafel slopes, but improper positioning of line representing ohmic potential drop line, c) unequal Tafel slopes with ohmic potential drop line centered halfway between the anodic and cathodic polarization curves.

In these semilog plots, the polarization curves for the dissolution of some metal X and for the cathodic reaction on a more noble metal Y (assumed to be hydrogen evolution for convenience) are straight lines. This assumes that both reactions are under pure activation control. The actual shape of those curves is not critical to this discussion. The galvanic corrosion potential of both metal X and Y would be the intersection of these curves, 0 V for the case shown in Fig. 1a, if the ohmic potential drop were insignificant. The dashed lines in the plots represent the ohmic potential drop,  $\Delta V_{\Omega} = I \times R$ , where I is the galvanic current flowing in the electrolyte with an effective resistance R. In the semilog plot,  $I \times R$  has an exponential shape. The magnitude of  $\Delta V_{\Omega}$  obviously depends on the value of R, and three different values are given. In Fig. 1a, the Tafel slopes of the anodic and cathodic curves are both equal to 0.1 V/dec. It is clear that ohmic potential drop increases with current, and where the lines for  $\Delta V_{\Omega}$  intersect the polarization curves, the difference in potential at the two electrodes is equal to the ohmic potential drop for that R. The potentials at each electrode and the galvanic current are given by the two intersection points.

Fig. 1b shows the case of different Tafel slopes for the two reactions. As drawn, the curves representing  $\Delta V_{\Omega}$  intersect the two polarization curves at different current. There is obviously a problem here since the same galvanic current must pass at each electrode. This problem is remedied in Fig. 1c after realizing that the curve representing the ohmic potential drop should not be centered at 0 V. The ohmic potential drop is a potential difference, with no connection to the reference electrode scale used to plot the polarization curves. The ohmic potential drop curve must be centered along the line bisecting the two polarization curves, as shown in Fig. 1c. Now the galvanic current flowing at each electrode is equal, and again the respective potential of the two electrodes during galvanic corrosion may be determined from the intersection points.

#### THIN FILM DISK CORROSION

The hard drives of all computers made today utilize a thin film metallic disk medium for storage of information. Most thin film disks have an Al alloy substrate covered by a thick NiP base layer. This NiP layer is polished flat, then intentionally roughened in a controlled fashion ("textured") to prevent adhesion ("stiction") of the smooth head to the disk on startup. This texture is the cause of most disk corrosion problems because the layers on top of the rough NiP include a Co alloy magnetic layer and a thin C overcoat, which is applied for improved tribology between the head and disk. If the C overcoat could completely cover the underlying metallic layers, corrosion would not be a problem. However, owing to the roughness induced by texturing, the Co-based magnetic layer may be exposed at small sites through the thin C overcoat. Carbon films are, in general, noble to Co-based alloys used in thin film disks, so galvanic corrosion of the magnetic layer will occur. The galvanic corrosion is exacerbated as a result of the small anode/cathode area ratio.

The continual increase in recording density has forced disk drive designers to make certain modifications over the past decade. Recording density can increase as the separation of the magnetic medium and the sensor in the head decreases. In order to bring the head and disk closer, the carbon overcoat thickness has decreased, and the head is flying closer to the disk. In order to fly closer, the disk roughness has decreased. A decrease in carbon thickness is potentially deleterious to corrosion resistance because it is harder to cover the magnetic layer with a very thin carbon overcoat. Conversely, the trend toward smoother disks is beneficial to corrosion resistance because the mag layer can be more-easily covered by carbon. Figure 2 shows the trends in carbon overcoat thickness and average roughness, as well as the ratio of the two. The ratio of carbon thickness to disk roughness has increased over the last 9 years, indicating that corrosion should be less of a problem now than in the past. This trend will apparently continue.

Figure 3 shows polarization curves for disk materials and structures in a droplet of water. The water droplet technique has been shown to be useful for comparing the corrosion resistance of materials like disk materials in a mild environment that simulates atmospheric corrosion [2]. First note the two curves from full disk structures. One is from a lubed disk, the other is from an unlubed disk. The lube decreases the current only slightly. The anodic current flowing at a given potential from the unlubed disk is about 100x less than that of the blanket magnetic layer on glass. It is clear that the magnetic layer is rather well covered by carbon. However, the anodic signal is not coming only from the small amount of uncovered magnetic layer because a blanket layer of C

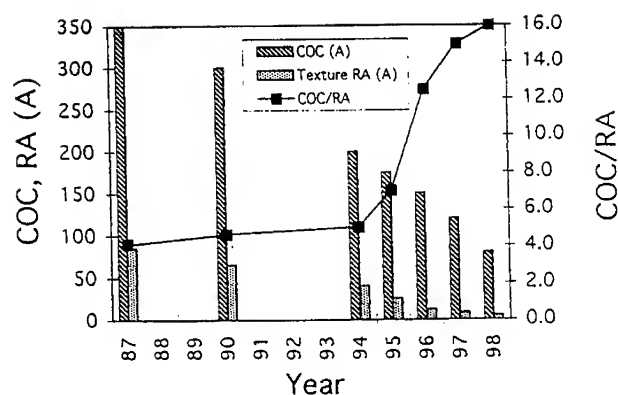


Figure 2. Trend of carbon overcoat (COC) thickness and average disk roughness (RA) with time. Also shown, with right axis, is the ratio of COC/RA. Data from HMT Technology, Inc.

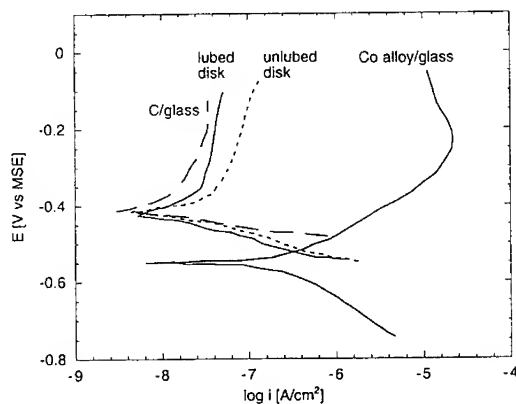


Figure 3. Polarization curves in a water droplet for a lubed and unlubed disk as well as a blanket magnetic layer and carbon layer on glass.

(unlubed) on glass exhibits an electrochemical signal that is a large fraction (about half as large) of the signal measured on the unlubed disk. Carbon is not really an extremely noble material. It is more that the oxidation of C is kinetically hindered. Carbon can, in fact oxidize to form various species, such as carbonyl, carboxyl, phenol, quinone or lactone [3]. The polarization curve for carbon is similar to that of a spontaneously passive metal. It supports a reasonable amount of cathodic current, which is the cause of galvanic corrosion. At anodic potentials, there is some steady-state oxidation current, which is likely associated with a low rate of C oxidation. From the polarization curves, it could be suggested that the difference in current between the unlubed disk and the C blanket is the corrosion current of the magnetic layer. The finding that carbon oxidation is now a significant fraction of the total current flowing to a thin film disk is reasonable given the trend of increasing carbon thickness to disk roughness ratio. However, small areas of magnetic

layer are still exposed. Therefore, corrosion will still occur if the disks are exposed to aggressive environments (such as chloride) or if problems in disk texture control occur.

Another example of disk corrosion is given in Fig. 4 for a different disk. In the water droplet environment, the corrosion rate of the blanket magnetic layer is seen to be about the same as that for the disk shown in Fig. 3, despite being a different alloy. The carbon film deposited on glass in Fig. 4, however, exhibits extremely low currents that are probably artifactual in nature. This carbon has a high hydrogen content and is essentially nonconductive. Nonetheless, the full disk structure (lubed disk) still provides an electrochemical response. Here, the current from the disk likely flows only from the uncovered, exposed areas of Co alloy. The corrosion potential for the disk structure in Fig. 4 is ennobled compared to the blanket magnetic layer, despite the expectation that galvanic corrosion by the nonconductive COC will not occur. The corrosion rate is lower than that of the lubed disk in Fig. 3. The reason for this difference may be a combination of improved coverage and decreased galvanic interaction with the COC.

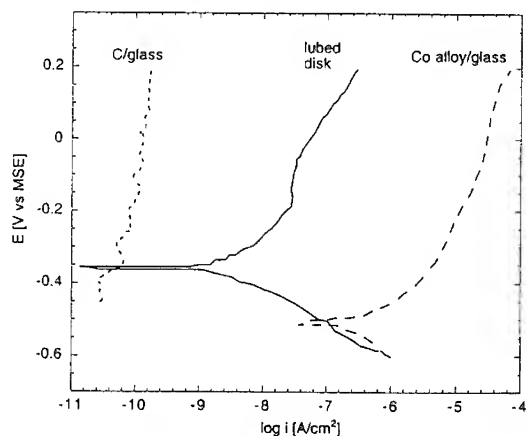


Figure 4. Polarization curves in a water droplet for a blanket magnetic layer and hydrogenated carbon layer on glass, and a lubed disk made with the same magnetic and carbon layers.

#### CORROSION OF ANTIFERROMAGNETIC LAYERS

Magnetoresistive sensors that are the read elements in advanced magnetic heads may contain antiferromagnetic layers to pin the domains of adjacent soft magnetic layers by exchange coupling. Spin valve heads that take advantage of the giant magnetoresistive effect also use antiferromagnetic layers. An example of one such head was recently reported [4]. A commonly used antiferromagnetic layer is MnFe, with about 50% of each element. This alloy is extremely corrodible as is seen in Figure 5, where the polarization curve for MnFe in 0.1 N Na<sub>2</sub>SO<sub>4</sub> exhibits only active dissolution. Sulfate is a neutral-pH solution that is not very aggressive to most metals. In a buffered borate solution of higher pH, MnFe forms a protective passive film at high potentials after a rather large active peak, Figure 6. The corrosion rate, peak current density, and passive current density all decrease with increasing pH. These results are interesting because of the possibility for environment control in certain process steps that might otherwise be aggressive. One example is lapping, a process used to expose the device and make the head surface very flat. Lapping is potentially very aggressive because the sample is abraded in an aqueous environment. The exposed cross-section is typically a multilayer stack of different materials, and fresh metal area is continually exposed. If the material does not spontaneously passivate in the lapping environment, severe corrosion can result.

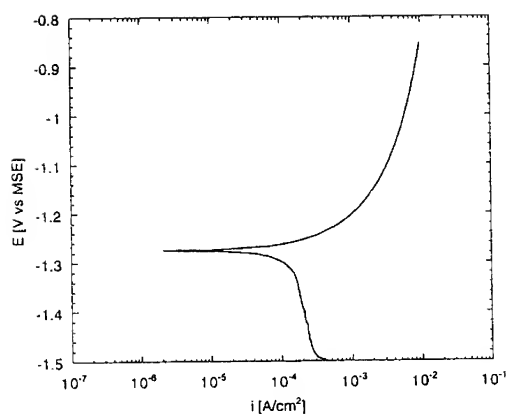


Figure 5. Polarization curve for MnFe in stagnant, air-exposed 0.1 N  $\text{Na}_2\text{SO}_4$ .

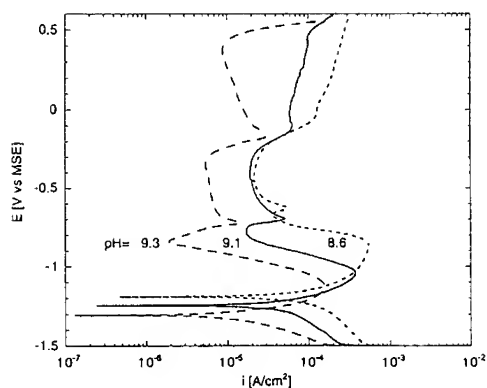


Figure 6. Polarization curves for MnFe in stagnant, air-exposed borate buffer solutions with varying pH.

Another possible antiferromagnetic layer is MnIr, with about 20 at. % Ir. In sulfate solution MnIr is as corrodible as MnFe, and dissolves rapidly. In borate buffer solution, the behavior is found to be different from that of MnFe, Figure 7. There is very little change in polarization behavior with pH. It is possible that dealloying of the Mn, leaving an Ir-rich surface layer, occurs at each pH. The mechanism of passivation may thus involve enrichment of the noble Ir, as opposed to the formation of an oxide as in the case of MnFe. The corrosion rate of MnIr is also higher than that of MnFe at each pH.

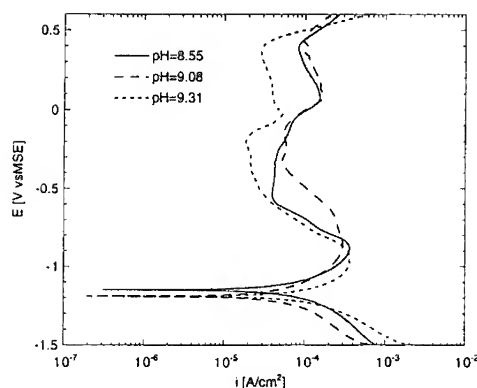


Figure 7. Polarization curves for MnIr in stagnant, air-exposed borate buffer solutions with varying pH.

## CONCLUSIONS

Corrosion is an unwanted electrochemical modification of materials. It is especially a problem in multilayer thin-film structures where galvanic interactions can lead to accelerated attack. Corrosion must be considered in the design of such structures to prevent severe problems from arising.

In this paper a number of failure modes for thin film structures in electronic and magnetic applications were described. Galvanic corrosion is one common mode of corrosion for multilayer structures containing electrochemically-incompatible metals. A graphical explanation for the determination of the magnitude of ohmic potential drop and galvanic current is given. The corrosion of thin film disk structures is discussed. The ratio of carbon overcoat thickness to disk roughness induced during texturing has increased over the past 9 years, and will continue to do so. As a result, corrosion should be less of a concern. However, as long as some area of magnetic alloy is exposed, corrosion will continue to be a concern, even for the case of a poorly-conducting overcoat. The ferromagnetic alloys MnFe and MnIr are shown to be very corrodible, but passivate in slightly alkaline environments. MnIr corrodes at a higher rate, however, and probably passivates by a different mechanism.

## ACKNOWLEDGMENTS

The author is indebted to S. Hauert and Z. Xia for performing the experimental. Collaborations with HMT Technology, Inc., Read-Rite Corp., and Hoya USA are greatly appreciated.

## REFERENCES

1. G. S. Frankel, in *Corrosion Mechanisms in Theory and Practice*, edited by P. Marcus and J. Oudar, Marcel Dekker, New York, 1995, pp. 547-580.
2. V. Brusic, M. Russak, R. Schad, G. Frankel, A. Selius, and D. DiMilia, *J. Electrochem. Soc.*, **136**, pp. 42-46 (1989).
3. K. Kinoshita, *Carbon, Electrochemical and Physiochemical Properties*, John Wiley and Sons, New York, 1988, pp. 86-93.
4. J. A. Brug, T. C. Anthony, and J. H. Nickel, *MRS Bulletin*, **21**, pp23-27, (1996).

## ELECTROCHEMICAL ATOMIC FORCE MICROSCOPY STUDY OF THE DISSOLUTION KINETICS OF 304 STAINLESS STEEL

T. J. MCKRELL AND J. M. GALLIGAN

Department of Metallurgy and Materials Engineering, University of Connecticut, Storrs,  
Connecticut, 06269-3136

### ABSTRACT

An electrochemical atomic force microscope (ECAFM) has been employed to observe, *in situ*, the topographical and electrical changes that occur on 304 stainless steel as a function of an electrical potential. The concurrent acquisition of a polarization curve and topographical data allows direct correlation of variations in the surface roughness with the electrochemical characteristics of the passivation process. Also, the large AFM scan size, employed in this study, allows for the delineation and determination of the interdependence of the surface kinetics at various regions of the surface. Simultaneous measurements of topographical and electrical changes at these regions have established a correspondence of the competing kinetics between the reactions of dissolution and passivation. This provides a way to relate chemical surface reactions to surface topography.

### INTRODUCTION

Passivation of metals is a long-standing process which is poorly understood [1]; this is especially true of any direct, dynamic observation(s) of the passivation process itself. That is there are few experiments which observe the surface topography, while a metal is passivated. Such *in situ* observations are reported here for the case of stainless steel in HCl. In particular these direct observations of the passivation process provide information on the:

- i. uniformity of the passivation and
- ii. the roughness - local and widespread - during passivation.

These experiments, described below, exploit the capabilities of an electrochemical atomic force microscope (ECAFM). This instrument has the unique ability of simultaneously operating as a potentiostat and as a microscope capable of attaining quantitative, three-dimensional images of surfaces while the material is subject to a particular surface treatment. This provides quantitative electrical and topographical measurements of the passivation process. This capability of the ECAFM has been exploited by a few groups [2,3]; however not at the large scan sizes which are necessary for the correlation of polarization and surface roughness measurements of industrial grade alloys. Nor has it been applied in the context here, that is simultaneous studies of surface topography and of electrochemical characteristics.

In the study reported here we expose industrial grade 304 stainless steel to hydrochloric acid, under potential control, and measure the resulting surface roughness and electrochemical behavior. While the material is exposed to HCl AFM images of a 150 X 150  $\mu\text{m}^2$  area are obtained. Such large scan sizes are necessary due to the heterogeneous reaction kinetics which result from the polycrystalline and impure nature of industrial grade 304 stainless steel. Possible regions responsible for the heterogeneous reaction kinetics include: grains; grain boundaries; and inclusions. Thus, the present experiments measure, and correlate,



the electrochemical behavior with the associated surface roughness measurements. The method and results of such experiments are described below.

## EXPERIMENT

The industrial grade 304 stainless steel was mechanically polished to a mirror finish with 0.05  $\mu\text{m}$  alumina, ultrasonically cleaned, coated with a lacquer leaving an exposed area of 3.4  $\text{mm}^2$ , and then exposed to air for 24 hours. This coating was carried out in order to obtain current density measurements which were commensurate with the area imaged by the ECAFM. The 304 stainless steel was exposed to a 0.25 M aqueous HCl solution prepared from research grade HCl and distilled water. A saturated calomel electrode (SCE) was employed with a liquid bridge to the ECAFM cell for standardized potential measurements. The sample and solution were loaded into a Digital Instruments NanoScope II ECAFM and the procedure for anodic polarization experiments, as outlined in ASTM designation G5-82, followed.

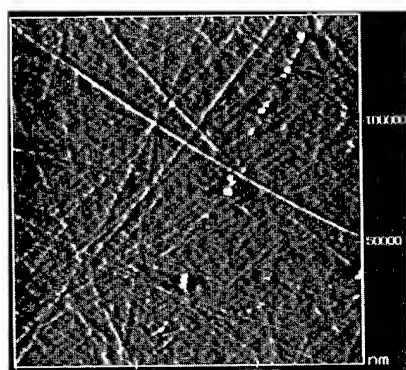
Spatially fixed 150 X 150  $\mu\text{m}^2$  images were taken prior to and consecutively after addition of the 0.25 M HCl solution. The electrochemical cell was allowed to equilibrate for one to two hours before a potential ramp of 0.1 mV/sec was applied; this was continued until oxygen evolution was observed. The average surface roughness,  $R_a$ , current density,  $I_a$ , and potential,  $E$ , were measured simultaneously while the potential was increased linearly with time. Once oxygen evolution occurred the potentiostat was open circuited and allowed to equilibrate for approximately one hour. Each experiment lasted  $\approx$  220 minutes, while AFM images were being acquired at a time interval of every three minutes.

## RESULTS AND DISCUSSION

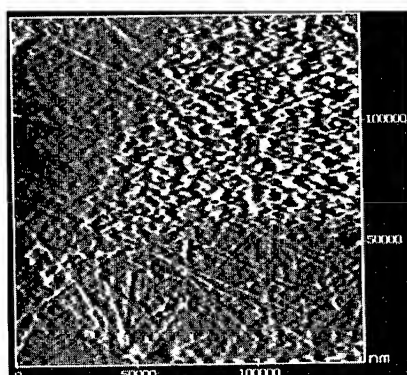
### Observations

The behavior of the stainless steel surface, when exposed to hydrochloric acid has been previously described [4]. The present results are largely in agreement with these previous observations. A number of interesting and very revealing things happen when the potential is anodically ramped. For example, the observed surface roughness as a function of time varies as shown in both AFM images, Fig. 1, and graphically as  $R_a$  values, Fig. 2a. Fig. 2a shows the roughening behavior of two regions - that of the top right quarter of the images which includes the second region which falls completely within a single grain. These regions show that the variation of the surface roughness has at least three obvious characteristics: First, the surface roughness, resulting from the electrochemical reactions, is very non-uniform, Fig. 1. Second, the surface roughness is significantly non-monotonic; Fig. 2a shows this variation as a function of exposure time to an electrochemical potential. Third, the non-monotonic behavior of the surface roughness, for the single grain, corresponds, in a one to one way, with the corresponding non-monotonic behavior of the polarization curve, Fig 2. These observations show that the surface roughness and the passivation behavior are interconnected.

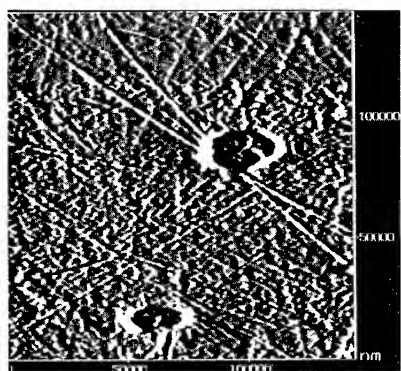
Consider now the roughening characteristics within a single grain. In this case there is a one to one correspondence of the non-monotonic behavior of the polarization curve, Fig. 2b, and of the surface roughness within a single grain, Fig 2a. As Fig. 2a shows both regions initially dissolve at a slow rate, however once the potential is applied and increased the roughness of both regions increases dramatically and both show a maximum and minimum. That is the roughness then drops precipitously, but then rises until the passivation potential,  $E_p$ ,



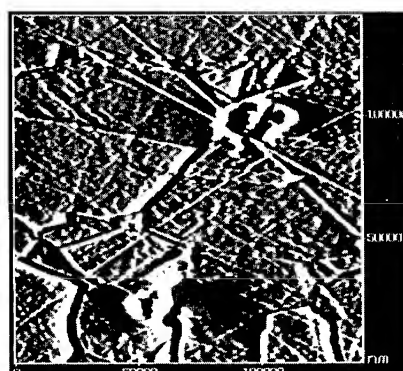
a



b

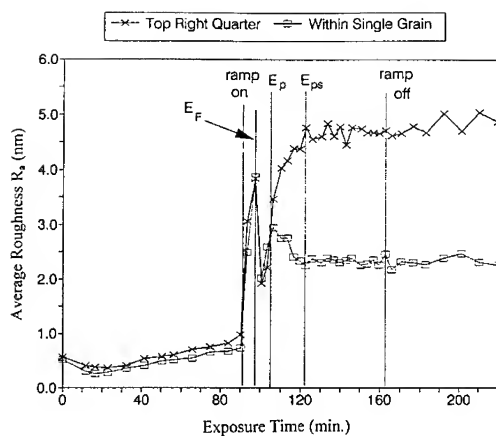


c

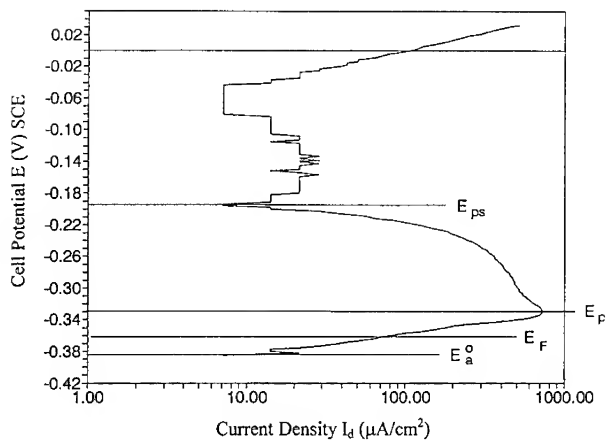


d

Fig. 1. Sequential *in situ* EAFM images, 150 X 150  $\mu\text{m}$  scan size with 40 nm height range, of the surface of 304 stainless steel exposed to 0.25M HCl and an anodic potential ramp. The exposure time and potential of each image are as follows: a) 90 minutes and  $E_a^0$ , b) 97 minutes and  $E_F$ , c) 106 minutes and  $E_p$  and d) 131 minutes and beyond  $E_{ps}$ .



a



b

Fig. 2. Roughening behavior of the surface of 304 stainless steel with exposure time, (a), and anodic polarization behavior of the surface during an applied potential ramp, (b). Notice that in (a) the potential was applied between 90 and 170 minutes of exposure, and also that the occurrence of significant potential events are labeled on both figures. It is clear that at  $E_p$  both  $I_d$  and  $R_a$ , within a single grain, experience a maximum.

is reached at which point the two curves then diverge. This divergence corresponds to the potential at which the current is a maximum, Fig. 2b. As shown in Fig. 2a once the complete passivation potential is reached,  $E_{ps}$ , the average roughness remains relatively constant.

### Discussion

The results described above show that the surface roughening is non-uniform. Second, they show that when a maximum roughness is attained within a grain, then the material also shows a maximum in the current density, that is the material is at the onset of passivation at this point.

Consider now the one to one correspondence of the roughness inside a single grain, Fig. 2a, with the electrochemical behavior of the surface, Fig. 2b. These figures show that the roughness results are in excellent agreement with the corresponding electrochemical behavior of the surface. To illustrate, the surface behavior will be described in conjunction with the increase in the potential as it is ramped from the equilibrium potential,  $E_a^0$ . The portion of the polarization curve from  $E_a^0$  to the Flade potential,  $E_F$ , corresponds to active dissolution of the alloy and is expected to coincide with an increase in surface roughness and current density [5]. At  $E_F$  the formation of a protective oxide is thermodynamically possible; thus at this point two competitive reactions exist [5]: the dissolution reaction and the passivation reaction which results in the formation of a protective oxide film, thereby insulating the surface and reducing the current density. The reduction in roughness at  $E_F$  results from the dissolution of the previous corrosion product. The solubility of the corrosion product is apparent by the unchanging morphology of the string of spires, evident in Fig. 1; these distinctive features provide a fiduciary mark for the roughening sequence and most likely are preexisting oxide features.

Continuing along the potential ramp, at  $E_p$  continued acceleration of the metal dissolution reaction no longer occurs due to the accelerated rate of the passivation reaction. This point then represents the maximum in the dissolution rate and of the current density, Fig. 2b, and correspondingly a maximum in  $R_a$  within the single grain, Fig. 2a. The common maxima in the roughness, within the single grain, and of the current at  $E_p$  shows that the passivation reaction is becoming the dominant surface reaction and identifies this peak in roughness with the passivation reaction. After passing  $E_p$  patches of the protective oxide spread until the entire surface is covered by a continuous protective oxide film, that is a passive film, thus lowering both the roughness and current density. The continued decrease in  $R_a$  and  $I_a$  after  $E_p$  shows this spread of the passive film within the single grain, again Fig. 2. While the continued increase in roughness experienced by the top right quarter of the images, Fig. 2a, beyond  $E_p$  shows the continued reactivity of certain microstructural features. Beyond  $E_{ps}$  the anodic current density and  $R_a$  are almost independent of the potential, Fig. 2. This supports the electrochemical theory which states that complete coverage of the surface occurs at  $E_{ps}$ . This model presents a self-consistent treatment of the passivation process, based on combined roughening experiments and electrochemical measurements of the passivating surface.

Some relevant studies which relate to these experiments have been carried out by Olefjord et. Al. [6]. These studies investigated the composition and thickness of the passive film formed, under anodic polarization, on an austenitic stainless steel in chloride containing solutions using X-ray photoelectron spectroscopy. This investigation showed that beyond the Flade potential the formation of a 10-15 Å thick duplex passive film occurs. These findings are

in agreement with the observed roughness changes which occur after  $E_p$  for the single grain region, Fig. 2a. This result further supports the conclusion that the passivation reaction is becoming the dominant reaction at potentials above  $E_p$ .

## CONCLUSIONS

- I. Various microstructural regions react at varying rates, leading to heterogeneous surface roughening, Fig. 1.
- II. Different regions form passive films at different rates; in all regions the formation of the passive film was shown to protect the surface from further corrosion attack, Fig. 2a.
- III. The observed maximum in the average roughness within a single grain occurs at the same potential,  $E_p$ , as the current density maximum of the polarization curve, Fig. 2. This correlation of the topographical and the electrochemical measurements establishes a correspondence between the competing reactions of dissolution and passivation. This provides a way to relate chemical surface reactions to surface topography.

## REFERENCES

1. Mars G. Fontana, Corrosion Engineering, 3<sup>rd</sup> ed. (McGraw-Hill, Inc., New York, 1986), pp. 469-481.
2. R. M. Rynders, C. Paik, R. Ke and R. C. Alkire, J. Electrochem. Soc. **141**, 1439 (1994).
3. M. G. Walls, A. Ponthieux, B. Rondot and R. A. Owen, J. Vac. Sci. Technol. A, **14**, 1362 (1996).
4. Thomas J. M<sup>c</sup>Krell and James M. Galligan in In Situ Electron and Tunneling Microscopy of Dynamic Processes, edited by Renu, Pratibha Gai, Marja Gajdardziska-Josifoska, Robert Sinclair and Loyd Whitman (Mater. Res. Soc. Proc. **404**, Pittsburgh, PA, 1995) pp. 199-204.
5. N. D. Tomashov and G. P. Chernova, Passivity and Protection of Metals Against Corrosion, (Plenum Press, New York, 1967), p. 40.
6. I. Olefjord, B. Brox, and U. Jelvestam, J. Electrochem. Soc. **132**, 2854 (1995).

## ELECTROCHEMICAL REACTIONS OF MOLYBDENUM NITRIDE ELECTRODES IN $\text{H}_2\text{SO}_4$ ELECTROLYTE

S.L. Roberson\*, D. Finello\*\*, R.F. Davis  
Department of Materials Science and Engineering, North Carolina State University, Box 7907  
Raleigh, NC 27695-7907

\* U.S. Air Force Palace Knight student attending North Carolina State University  
\*\* U.S. Air Force, WL/MNMF, Eglin AFB, FL 32542

### ABSTRACT

The electrochemical reaction of polycrystalline  $\text{Mo}_x\text{N}$  ( $x=1$  or  $2$ ) thin film electrodes in  $4.4 \text{ M H}_2\text{SO}_4$  electrolyte has been investigated. The films were prepared by a temperature programmed procedure involving the reaction of  $\text{MoO}_3$  and  $\text{NH}_3$ . The electrochemical voltage stability of these films in the electrolyte, referenced to a standard hydrogen electrode (SHE), was  $+0.70 \text{ V}$  ( $-0.01$  to  $+0.69$ ). Below  $+0.69 \text{ V}$ , cyclic voltammetry and AC impedance spectroscopy indicated that  $\text{Mo}_x\text{N}$  electrodes were capacitive. However, above this value an electrochemical reaction of the  $\text{Mo}_x\text{N}$  films was observed. The formation of an amorphous phase in the reacted  $\text{Mo}_x\text{N}$  films was indicated by X-ray diffraction (XRD) patterns. Secondary ion mass spectroscopy (SIMS) detected the presence of hydrogen, oxygen, and sulfur. The voltage bias ( $+$  or  $-$ ) applied to the electrodes influenced the chemical composition of the reacted  $\text{Mo}_x\text{N}$  films.

### INTRODUCTION

The potential applications of high surface area (HSA)  $\text{Mo}_x\text{N}$  powders as catalysts for CO hydrogenation [1], hydrodenitrogenation [1], and hydrosulfurization [2] have recently been demonstrated. Films of  $\text{Mo}_x\text{N}$  having a small grain size ( $\leq 20 \text{ nm}$ ) also show promise as potential electrode materials for high energy density double layer capacitor storage devices due to their high electrical conductivity ( $1/\rho = 10^{-4} \text{ ohm}^{-1}\text{cm}^{-1}$ ) and high surface area. Several techniques have been used to deposit  $\text{Mo}_x\text{N}$  films [3-5]; however, they have not yielded a small grain sized or high surface area material. By contrast,  $\text{Mo}_x\text{N}$  films with grain sizes  $\leq 20 \text{ nm}$  have recently been achieved in the authors' laboratories [6]. The availability of these films in the form of electrodes has allowed the determination of the electrochemical stability and reaction products of  $\text{Mo}_x\text{N}$  electrodes in  $\text{H}_2\text{SO}_4$ .

In the research described below, we have observed that  $\text{Mo}_x\text{N}$  thin film electrodes are capacitively and electrochemically stable in  $4.4 \text{ M H}_2\text{SO}_4$  electrolyte between  $-0.01$  and  $+0.69 \text{ V}$ . Below and above these values, electrochemical reaction resulted in the formation of an amorphous material as shown by X-ray diffraction (XRD). The crystalline phases of  $\text{MoO}_3$  or  $\text{MoS}_3$  were not observed in the reacted  $\text{Mo}_x\text{N}$  films. The voltage bias ( $+$  or  $-$ ) applied to the  $\text{Mo}_x\text{N}$  electrodes influenced their chemical composition.

### EXPERIMENTAL

The details of the preparation of the  $\text{Mo}_x\text{N}$  films on nitrided titanium substrates used in these studies have been presented elsewhere [6]. Briefly, the  $\text{Mo}_x\text{N}$  films were prepared by a temperature programmed procedure involving the reaction of  $\text{MoO}_3$  films and  $\text{NH}_3$ . The former were prepared by spray pyrolysis of an  $\text{MoCl}_5$ /methanol mixture in air at  $500^\circ \text{C}$ .

The structural, chemical, and surface microstructural properties of the  $\text{Mo}_x\text{N}$  films were analyzed prior to and after electrochemical reaction using several techniques. X-ray diffraction (Rigaku Model A) was used to determine the bulk phases present. Secondary ion mass spectroscopy (Cameca ims - 3F) depth profiling was employed to determine the presence of

elements in low concentrations. An  $\text{Mo}_x\text{N}$  film calibrated for H, Mo, N, O, and S via ion implantation was used as a standard for SIMS. Scanning electron microscopy (SEM) (JEOL 6400FE) at 5 kV was used to determine the effects of the electrochemical reaction on the surface of the films.

The electrochemical evaluation of  $\text{Mo}_x\text{N}$  electrodes in  $\text{H}_2\text{SO}_4$  was conducted using cyclic voltammetry and AC impedance spectroscopy in 4.4 M  $\text{H}_2\text{SO}_4$ . The former measurements were taken with a standard hydrogen reference electrode, a platinum counter electrode, and an EEG Model 173 potentiostat in tandem with an EEG Model 175 programmer. A Solotron 1250 frequency analyzer and an EEG Model 273 potentiostat were used for the latter studies.

## RESULTS AND DISCUSSION

The successful fabrication in this research [6] of  $\text{Mo}_x\text{N}$  films with very low oxygen concentrations has been paramount to the investigation of the electrochemical stability and any resultant reaction products of these films when exposed to 4.4 M  $\text{H}_2\text{SO}_4$ . This is due to the instability of molybdenum oxides in  $\text{H}_2\text{SO}_4$ . A representative XRD pattern of these films prior to electrochemical reaction is shown in Figure 1a. The films consisted of  $\approx 60\%$   $\gamma\text{-Mo}_2\text{N}$  and  $\approx 40\%$   $\delta\text{-MoN}$ . The peak broadening is due to the very small ( $\leq 20$  nm) calculated average grain size. The effects of electrochemical reactions on the films are shown in Figures 1b and 1c. These patterns indicate the formation of an amorphous product phase. However, there was more amorphous formation in the (+) biased electrode than in the (-) biased electrode.

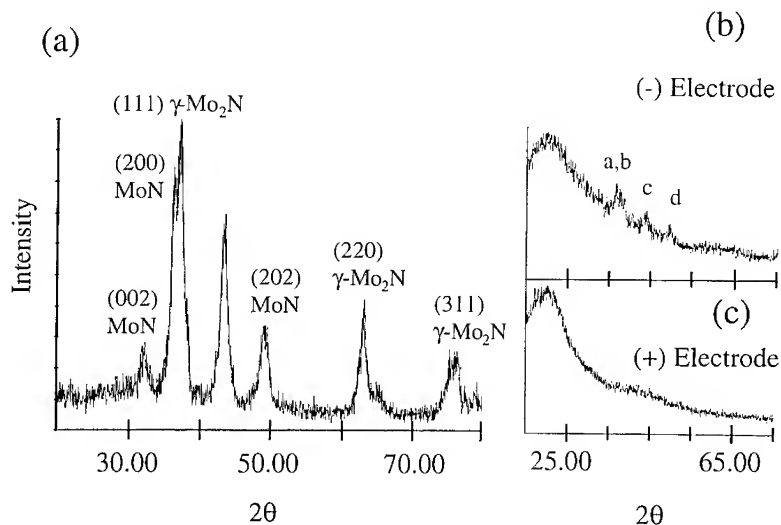


Figure 1. X-ray diffraction patterns of a (a)  $\text{Mo}_x\text{N}$  film prior to electrochemical reaction in 4.4 M  $\text{H}_2\text{SO}_4$ , (b) (-) biased reacted  $\text{Mo}_x\text{N}$  electrode, and (c) (+) biased reacted  $\text{Mo}_x\text{N}$  electrode. The peaks in (b) are indexed as follows: (a) - (200) MoN, (b) - (111)  $\gamma\text{-Mo}_2\text{N}$ , (c) - (200)  $\gamma\text{-Mo}_2\text{N}$ , and (d) - (202) MoN.

The results of chemical analyses via SIMS depth profiling of the  $\text{Mo}_x\text{N}$  films prior to an after exposure to  $\text{H}_2\text{SO}_4$  at + 0.70 V are shown Table I. There was considerably less nitrogen in the exposed  $\text{Mo}_x\text{N}$  electrodes than in the non-exposed  $\text{Mo}_x\text{N}$  electrodes. There was also less nitrogen present in the electrodes which were positively biased compared to those which were negatively biased. The oxygen, hydrogen, and sulfur levels were highest in the (+) biased electrodes. This indicates that the exposure of these electrodes to  $\text{H}_2\text{SO}_4$  above + 0.69 V resulted in the possible production of  $\text{Mo}(\text{OH})_x$ ,  $\text{MoO}_x$ , and  $\text{MoS}_x$ . Elemental hydrogen and sulfur were also detected in the (-) biased electrodes, but the concentrations were considerably lower than those found in the (+) biased electrodes. This indicates that nitrogen/oxygen exchange was the principal reaction product in these electrodes. The relatively high concentrations of sulfur, hydrogen, and oxygen and the low concentrations of nitrogen in the positively biased electrodes indicate that  $\text{Mo}_x\text{N}$  is more susceptible to  $\text{SO}_3^-$  attack than  $\text{H}_3\text{O}^+$ . It should be noted that the concentrations of elements in non-exposed and exposed electrodes during depth profiling did not vary appreciably and were very reproducible; however, all electrodes had slightly greater (< 1%) oxygen and hydrogen concentrations on the surface. This is most likely due to the physical adsorption of water and the cleaning of the surface of the films with methanol.

An low magnification SEM micrograph of a typical  $\text{Mo}_x\text{N}$  film prior to and after electrochemical exposure between -0.01 and +0.69 V is shown in Figure 2a. Large cracks visible on the surface were also observed throughout the film. These cracks were due to the increase in density of the individual grains during their conversion from  $\text{MoO}_3$  to  $\text{Mo}_x\text{N}$ . Representative SEM micrographs of electrochemically reacted  $\text{Mo}_x\text{N}$  films are shown in Figures 2b and 2c. The (+) biased electrode shows that the cracks around the islands of material became substantially larger as a result of the etching of these higher surface energy areas. The micrograph of the (-) biased  $\text{Mo}_x\text{N}$  in Figure 2c shows that a crack structure similar to that of the unexposed electrode was present after the electrochemical reaction.

Representative cyclic voltammogram (CV) curves determined for 1 and 50 cycles for an  $\text{Mo}_x\text{N}$  film biased at (a) + 0.70 volts and (b) + 0.69 volts are shown in Figure 3. The splitting of the lines between cycles 1 and 50 in (a) indicate a reduction in capacitance which is directly related to a decrease in film thickness due to an electrochemical reaction and resultant etching. In contrast, the overlapping lines of cycles 1 and 50 in (b) indicate that  $\text{Mo}_x\text{N}$  films are electrochemically stable in 4.4 M  $\text{H}_2\text{SO}_4$  below + 0.69 volts. The rectangular shape of the CV curves indicates that the  $\text{Mo}_x\text{N}$  films are capacitive.

The electrochemical characteristics of  $\text{Mo}_x\text{N}$  films determined using constant potential AC impedance spectroscopy are shown in Figure 4. The two lines in this figure represent  $\text{Mo}_x\text{N}$  films biased at (a) + 0.70 volts and (b) + 0.65 volts. At frequencies lower than 1 Hz, the slope of lines (a) and (b) is -1 which is typical of small grain sized porous films with a capacitive response. Above 1 Hz, the slope of lines (a) and (b) approaches 0 because the electrolyte can not respond to the high frequency signal and, as a result, the films become resistive. The second and more rapid change in the slope of line (a) at very low frequencies was due to the above mentioned electrochemical reaction.

Transition metal hydroxides are usually predicted by Pourbaix diagrams to be the reaction products when their associated metal nitrides are exposed to  $\text{H}_2\text{SO}_4$  in an *unbiased* cell. Although Pourbaix diagrams of molybdenum nitride are not available, the most likely reaction product of *unbiased*  $\text{Mo}_x\text{N}$  electrodes in  $\text{H}_2\text{SO}_4$  is  $\text{Mo}(\text{OH})_x$ . However,  $\text{Mo}(\text{OH})_x$  is not electrochemically stable at the voltages employed in the cyclic voltammetry and AC impedance spectroscopy studies used in this research. As shown in Figure 3, there is a reduction in capacitance between cycles 1 and 50 of electrodes biased at + 0.70. However, after 50 cycles the electrodes remain capacitive. This indicates that a conductive  $\text{MoO}_x$  phase is most likely formed on the surface of the electrodes. Molybdenum dioxide is electrically conductive and electrochemically stable in  $\text{H}_2\text{SO}_4$  below + 0.70 volts. However, above this voltage this phase is unstable and is etched from the surface of the film (i.e., the thickness and capacitance decreases). This explains the decrease in the capacitance between cycles 1 and 50. The (-) biased electrodes have higher levels of nitrogen and some polycrystalline  $\text{Mo}_x\text{N}$  phases present after 50 cycles. This indicates that  $\text{Mo}_x\text{N}$  is less susceptible to  $\text{H}_3\text{O}^+$  attack when (-) biased than  $\text{SO}_3^-$  attack when (+) biased.



Table I. Secondary Ion Mass Spectroscopy data of  $\text{Mo}_x\text{N}$  films prior to and after electrochemical reaction during exposure to  $\text{H}_2\text{SO}_4$  at a constant potential of + 0.70 V.

Elements	Approximate Atomic Concentration Percentages		
	Standard	(-) Electrode	(+) Electrode
Mo	60.02	59.97	59.96
N	39.48	12.00	2.04
O	0.30	26.45	31.97
H	0.10	1.55	2.59
S	0.10	0.03	3.44

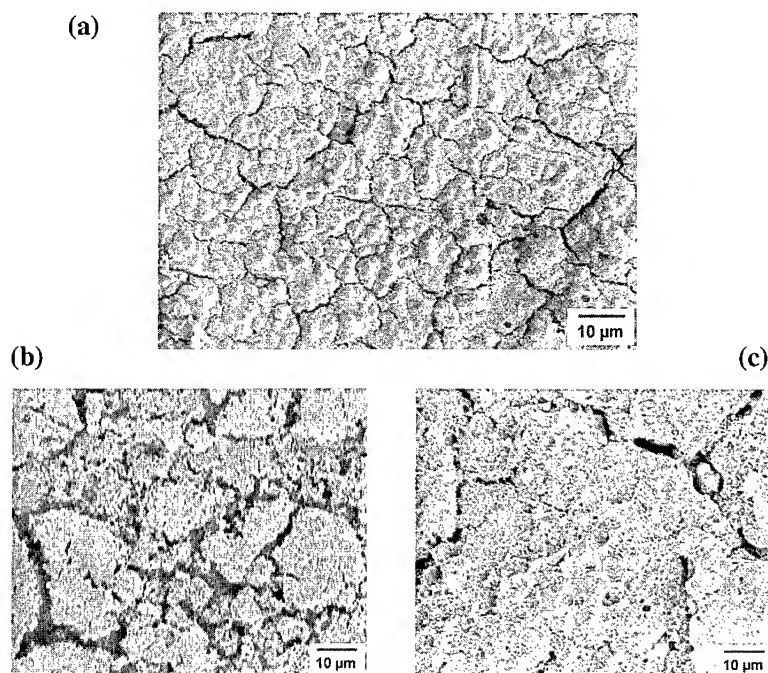


Figure 2. Scanning electron micrographs of (a) an  $\text{Mo}_x\text{N}$  film prior to reaction, (b) a (+) biased electrochemically reacted  $\text{Mo}_x\text{N}$  electrode, and (c) a (-) biased electrochemically reacted  $\text{Mo}_x\text{N}$  electrode.

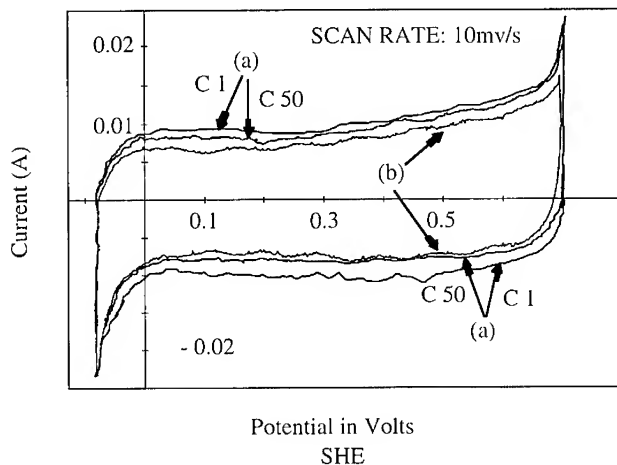


Figure 3. Cyclic voltammogram for 1 and 50 cycles for  $\text{Mo}_x\text{N}$  electrodes in deaerated 4.4 M  $\text{H}_2\text{SO}_4$  biased at (a) +0.70 volts and (b) +0.69 volts. The splitting of the cycle lines in (a) indicates an electrochemical reaction. The upper line is cycle 1 and the lower line is cycle 50 in (a). In (b) the lines for both numbered cycles overlap. The rectangular shape indicates a capacitive electrode.

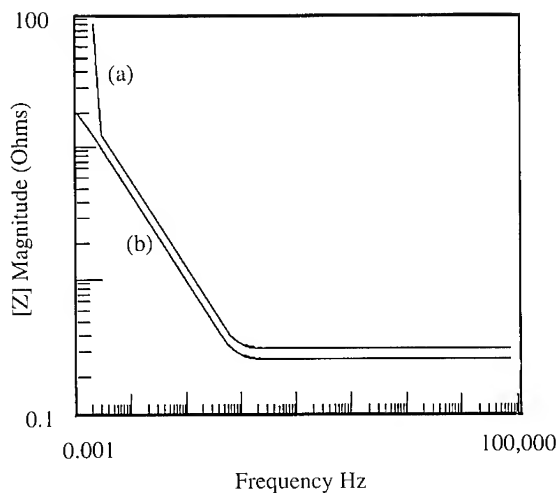


Figure 4. AC impedance spectroscopy of  $\text{Mo}_x\text{N}$  electrodes in 4.4 M  $\text{H}_2\text{SO}_4$  biased at (a) +0.70 volts and (b) +0.65 volts. The second change in slope of curve (a) at the lowest frequencies indicates an electrochemical reaction.

## CONCLUSIONS

The electrochemical voltage stability of  $\text{Mo}_x\text{N}$  ( $x=1$  or  $2$ ) electrodes in a  $4.4 \text{ M H}_2\text{SO}_4$  electrolyte has been determined to be  $0.70 \text{ volts}$  ( $-0.01$  to  $+0.69$ ). At voltages lower than  $+0.69$ , cyclic voltammetry and AC impedance spectroscopy showed that  $\text{Mo}_x\text{N}$  electrodes were capacitive. However, above  $+0.69 \text{ volts}$ , electrochemical reaction of the films was observed. X-ray diffraction patterns of reacted films indicated that an amorphous phase was formed. Chemical analysis via SIMS indicated that the amorphous phase of the (+) and (-) biased electrodes contained mostly  $\text{MoO}_x$ . Scanning electron micrographs showed that the non-reacted (polycrystalline) and reacted electrodes (amorphous) had similar surface morphologies.

## ACKNOWLEDGMENTS

The authors wish to express their appreciation to John Miller and Todd Zeigler of JME, Inc., Shaker Heights Ohio for the AC impedance and cyclic voltammetry data and to Dr. A.D. Batchelor, Dr. Deiter Griffis, and David Ricks at North Carolina State University for the analysis of the films. One of the authors (SLR) acknowledges the continuing support via U.S. Air Force Palace Knight Program.

## REFERENCES

1. J. C. Schlatter, S. T. Oyama, J. E. Metcalf and J. M. Lambert, *Ind. Eng. Chem. Res.*, **27**, p. 1648 (1988).
2. E. J. Markel and J. W. V. Zee, *J. Catal.*, **126**, p. 643 (1990).
3. V. P. Anitha, S. Major, D. Chandrashekharam and M. Bhatnagar, *Surface Coatings and Technology*, **79**, p. 50 (1996).
4. P. J. Rudnik, M. E. Graham and W. D. Sproul, *Surface Coatings and Technology*, **49**, p. 293 (1991).
5. J. G. Choi, D. Choi and L. T. Thompson, *J. Mater. Res.*, **7**, p. 374 (1992).
6. S. L. Roberson, D. Finello and R. F. Davis, *MRS Soc. Symp. Proc.*, Fall 1996 (To be published in the Proceedings of Symp. V), **457**.

## AC AND DC POLARIZATION AND CYCLIC VOLTAMMETRIC BEHAVIOR OF BORON-DOPED CVD DIAMOND IN 0.5M NaCl SOLUTION

R. Ramesham\* and M. F. Rose  
Space Power Institute, 231 Leach Center, Auburn University, Auburn, AL 36849-5320

### ABSTRACT

Boron-doped diamond has been deposited over a Mo substrate by microwave plasma CVD using methane and hydrogen. Boron doping of diamond has been achieved *in situ* by using a solid boron source while growing the diamond. Impedance spectroscopy of diamond in 0.5 M NaCl solution has been studied. We have observed two time constants at the diamond/solution interface. Solution resistance was found to be constant irrespective of the electrode in the same electrolyte. DC polarization techniques such as linear and Tafel polarization have been used to evaluate the doped diamond/Mo and Mo for corrosion resistance characteristics in terms of charge-transfer coefficients and corrosion rate. Cyclic voltammetry has been used to evaluate the doped diamond/Mo to study the background current response and the redox kinetics of ferri/ferrocyanide in 0.5M NaCl solution.

### INTRODUCTION

Diamond is a unique material for innumerable applications because of its unusual combination of physical and chemical properties. Therefore, several potential applications can be anticipated in electronics, optics, protective corrosion resistant coatings, and electroanalytical chemistry. There have been some reports on the characterization of diamond films by electrochemical techniques. Natishan and Morrish [1] have reported the electrochemical behavior of diamond/Mo using potentiostatic polarization in 0.5M NaCl solution. Ramesham et al., [2] have demonstrated the diamond growth over glassy carbon and graphite electrode materials for various electrochemical applications. Pleskov et al., [3] have reported photoelectrochemical properties of undoped poly-diamond films. Tenne et al., [4] have reported the use of conducting diamond for electrosynthesis of ammonia from nitrate solution by reduction process. Swain [5] has reported the effect of potential cycling over the impedance data of diamond electrode in HNO<sub>3</sub> solution. Miller et al., [6] have reported the cyclic voltammetric behavior of ferri/ferrocyanide at cobalt ion implanted diamond electrode. Swain and Ramesham [7], Martin et al., [8], Alehashem et al., [9] have reported the cyclic voltammetric behavior of ferri/ferrocyanide at boron-doped diamond in various electrolytes. Ramesham and Rose have reported the electrochemical behavior of undoped and doped diamond deposited by hot-filament and microwave plasma techniques [10-11] in 0.5 M NaCl solution.

Diamond films are chemically inert in a variety of environments including strong acids, bases, fluoride and chloride environments and therefore might have significant use in corrosion resistance applications. Boron-doped diamond films are electrically conducting and therefore corrosion measurements are of practical interest. We are reporting in this paper, evaluation of doped diamond films for corrosion resistant applications and cyclic voltammetric behavior of doped diamond and the redox kinetics of ferri/ferrocyanide redox couple for electroanalytical applications.

### EXPERIMENTAL DETAILS

Surface damaging is a necessary process to nucleate the CVD diamond on non-diamond substrates. Mo substrates have been mechanically pretreated with 0.25 - 60  $\mu$ m diamond paste and washed with tap water, acetone, methanol, and deionized water. Microwave plasma (2.45 GHz) assisted CVD system (ASTeX, MA) has been used to grow diamond films. A schematic diagram of the diamond deposition system and the deposition parameters were described earlier. Boron doping of diamond was achieved by using a solid disk source consisting of B<sub>2</sub>O<sub>3</sub> and more details were provided in earlier publications.[10,11,12]

A 0.5 M NaCl solution was prepared using analytical grade salt in deionized water. Background cyclic voltammogram has been obtained at a scan rate of 100 mV/sec. The area of the diamond electrode is 0.7122 cm<sup>2</sup> (The true area corrected for surface roughness is 0.819 cm<sup>2</sup>) [8]. All the experiments have been carried out using a single compartment electrochemical cell. A simple three electrode (test, counter, reference) electrochemical cell has been used in this study. A reference electrode of Hg/Hg<sub>2</sub>Cl<sub>2</sub>, Cl<sup>-</sup> (0.5 M NaCl) ( $E_{R,E} = 0.3$  V vs. NHE) and a Pt mesh counter electrode has been used. Impedance spectroscopy of doped diamond/Mo has been carried out in a wide frequency range of 65,000 - 0.001 Hz with an AC excitation signal of 10 mV (rms) under 0 mV DC polarization conditions. All the electrochemical experiments were conducted at room temperature, 25°C and the solution was stirred with a magnetic bit except during cyclic voltammetry experiments. The solution was not purged but exposed to air during electrochemical measurements.

## RESULTS AND DISCUSSION

The morphology of the doped diamond films is very well faceted. The films grown by microwave plasma CVD under similar conditions has been analyzed by Raman earlier [12].

We have employed an AC excitation signal of 10 mV (rms) in impedance spectroscopy since as-deposited diamond is electrically conducting. An electrode/solution interface undergoing an electrochemical reaction is typically analogous to an electronic circuit consisting of a specific combination of resistors and capacitors. Electrochemical impedance that describes the response of such a circuit to an alternating current or voltage as a function of frequency. An electrode/solution interface has been modeled as a Randles Cell, [13]  $R_{\Omega}$  is the ohmic resistance of the solution between the working and reference electrode.  $R_t$  is the polarization resistance at the electrode/solution interface.  $C_{dl}$  is the double-layer capacitance at the interface. It is possible to calculate the electrochemical reaction rates, provided the data on  $R_t$  is available. An equivalent circuit that include additional circuit elements (film capacitance,  $C_{film}$  and the film resistance,  $R_{film}$ ) were proposed for a corroding metal coated with a porous, non-conductive film. [14]

Figure 1 shows the complex impedance plane plot of the as-deposited doped diamond in 0.5 M NaCl solution for various immersion periods. (Open square: 10 min, Open circle: 30 min, Filled circle: 45 minutes, Filled square: 16.25 hours, and Open diamond: 77 hours). The experimental data has been fit for semicircle fit. We noticed that at high frequencies the impedance of the diamond electrode/solution interface is almost entirely due to the ohmic resistance of the electrolyte solution,  $R_{\Omega}$ . The solution resistance was found to be 141  $\Omega$ -cm<sup>2</sup> which is evaluated from the Nyquist plot. This is the first report in isolating the solution resistance for a diamond electrode/solution interface that is an acceptable value and comparable to the value (150.7  $\Omega$ -cm<sup>2</sup>) obtained with molybdenum electrode/solution interface. The observed  $R_{\Omega}$  is independent of test electrode in the same electrolyte solution. The next step is to determine the overall ohmic resistance of the diamond electrode/solution interface at very low frequencies. The experiment duration will be too long to obtain the semicircle to draw useful conclusions and therefore the observed experimental data was fit for semicircle (Figure 1) and the overall ohmic resistance ( $R_{\Omega} + R_{film} + R_t$ ) of the diamond electrode/solution interface was determined. The overall resistance value of the diamond electrode/solution interface has been found to be  $2.1 \times 10^6 \Omega$ -cm<sup>2</sup>. This polarization resistance value is 30 times higher than the pure Mo electrode/solution interface. This observation qualitatively indicates the diamond/Mo electrode will have proportionately long useful life in the test environment compared with Mo. The double-layer capacitance is calculated using the frequency corresponding to the top of the semicircle,  $\omega(q=\max)$ , and  $R_f + R_t$  that is known from the low frequency data and the observed value is in the range of 3.7 to 48  $\mu$ F/cm<sup>2</sup>. The observed double layer capacitance is substantially lower than the pure Mo electrode/solution which indicates diamond's robustness. The

experimental data corresponding to 45 minutes of immersion of doped diamond electrode in 0.5M NaCl solution was obtained by using an AC excitation signal of 100 mV and found that the double-layer parameters are comparable to the values obtained with 10 mV AC signal. The observed double layer capacitance was  $100 \mu\text{F}/\text{cm}^2$ .

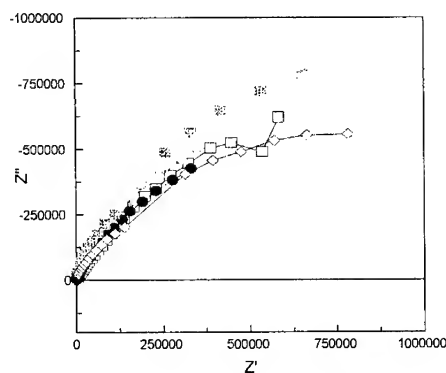


**Figure 1:** Complex Impedance plane plot of B-doped diamond in 0.5 M NaCl solution at the corrosion potential (OCP). AC signal: 10mV. Frequency range: 65,000 Hz - 0.001 Hz. Complete frequency range. (Square open : 10 min, Open circle: 30 min, Filled circle: 45 minutes, Filled Square: 16.25 hours, and Open diamond: 77 hours)

The experimental data shown in figure 1 has also been plotted in a Bode format as figure 2 [a: Impedance vs. log (frequency) and b: Phase shift vs. log (frequency)]. We could identify a straight line region in the medium frequency regime and the experimental data was linear fit and extrapolated to 0.16 Hz (1 radian/sec). The capacitance was calculated to be  $\approx 5.1$  to  $25.6 \mu\text{F}/\text{cm}^2$  which is very close to the value obtained by using large semicircle data (complex impedance plot) corresponding to low frequency data (Figure 1). We could also identify the a straight line region in the high frequency regime and the experimental data was linear fit and extrapolated to determine the intercept on the Y-axis. The determined intercept is about  $168 - 188 \Omega\text{-cm}^2$  on the Y-axis which is equal to the solution resistance  $R_\Omega$ . No linear portion has been observed in the low frequency regime of the Bode plot to evaluate  $R_\Omega + R_t$ . Phase shift

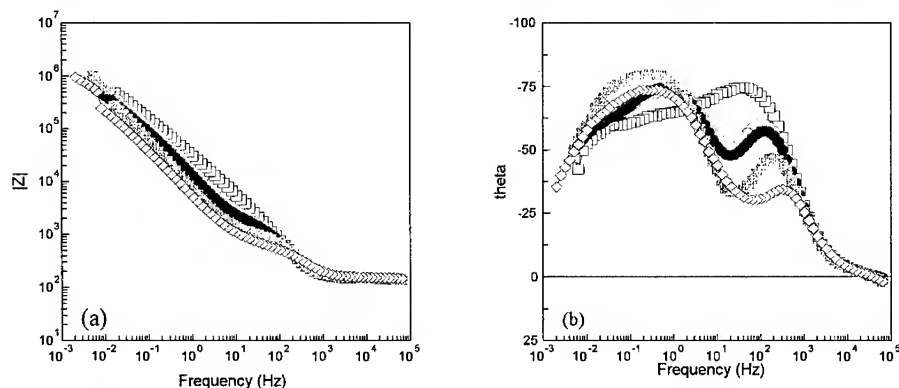


**Figure 2:** Bode plot of B-doped diamond in 0.5 M NaCl solution at the corrosion potential [a: Impedance vs. log (frequency) and b: Phase shift vs. log (frequency)]. AC signal: 10 mV. Frequency range: 65,000 Hz - 0.001 Hz. (Square open :10 min, Open circle: 30 min, Filled circle: 45 minutes, Filled square: 16.25 hours, and Open diamond: 77 hours)

will provide information about the electrode/solution interface. At the high frequency range the interface is completely an ohmic type and phase shift was tending to  $0^\circ$  and in the medium frequency range phase shift started increasing and that shows the occurrence of the double layer capacitance. At low frequencies the phase shift started decreasing, indicating that the interface will act as purely resistive type.

We have made an important observation in this study that there is a formation of a secondary semicircle as a function of immersion time of doped diamond electrode in 0.5M NaCl solution in the high frequency regime. Figure 3 clearly shows the progressive formation of the semicircle in the high frequency region.  $R_t'$  corresponding to this semicircle decreases as the immersion period increases ( $3.7 \times 10^3 \Omega\text{-cm}^2$ ) and the double layer capacitance varies from  $6.8\text{--}2.7 \mu\text{F/cm}^2$ . This could be due to the doping of diamond with boron. It is difficult to identify the two semicircles in figure 1 but it is quite clear in figure 3 that there are two humps in phase shift vs log (frequency) data. Two time constants exist at the doped diamond electrode/solution interface. Formation of second time constant as a function of immersion time in figure 2 is clearly noticeable.

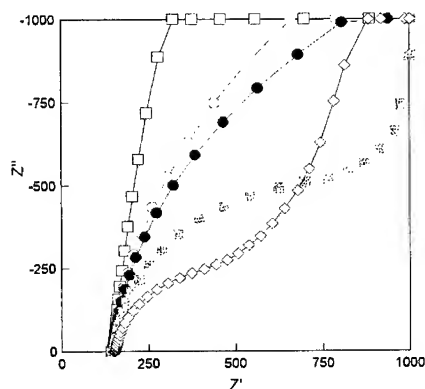


**Figure 3:** Complex impedance plane plot of B-doped diamond in 0.5 M NaCl solution at the corrosion potential (OCP) in the high frequency regime. AC signal: 10mV. (Square open : 10 min, Open circle: 30 min, Filled circle: 45 minutes, Filled Square: 16.25 hours, and Open diamond: 77 hours)

The polarization resistance determined from the slope is approximately  $9.2 \times 10^3 \Omega\text{-cm}^2$  for doped diamond in 0.5M NaCl solution. This value is almost equal to the value evaluated ( $3.7 \times 10^3 \Omega\text{-cm}^2$ ) from the first semicircle in figure 3. The electrochemical technique of polarization resistance is used to measure corrosion rate. DC polarization provides no details on the solution resistance whereas AC polarization will provide such information. Corrosion rate may be determined using the Faradays laws of electrolysis, the corrosion current, and physical properties of the materials. But usually polarization resistance will provide qualitatively the corrosion resistance characteristics of the electrode/solution interface.

Tafel polarization plots for doped diamond/Mo and bare Mo are shown in figure 4. The corrosion rate of diamond/Mo substrate is significantly lower by 2 - 4 orders of magnitude. The electrode area and the employed reference electrode are same for both the systems tested.

In the case of Mo we have observed a linear polarization regime in the cathodic direction of corrosion potential. We obtained a cathodic Tafel constant ( $b_c = -0.440\text{V/decade of current}$ ) from the slope of linear portion of the curve. Active, passive, and transpassive regions were observed in the anodic direction of polarization. We did not observe any linear polarization region within +250 mV polarization from the corrosion potential ( $E_{\text{corr}} = -0.491 \text{ V vs., R.E.}$ ). Anodic Tafel constant is difficult to determine from the observed experimental data. The evaluated corrosion current from the Tafel plot is in the range of  $3.8 \times 10^{-6} \text{ Amp/cm}^2$ .

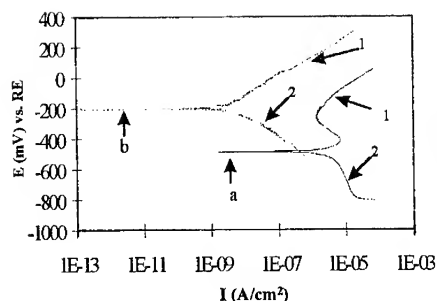


**Figure 4:** Tafel polarization of (a)Molybdenum and (b)Boron-doped diamond coated Molybdenum in 0.5 M NaCl solution. (1) anodic and(2) cathodic. Scan rate: 0.166 mV/sec.

We have observed a linear polarization regime for doped diamond coated molybdenum substrate in anodic and cathodic direction of corrosion potential ( $E_{\text{corr}} = -0.204 \text{ V vs., R.E}$ ). We were able to determine the Tafel constant for anodic and cathodic chemical reactions during the polarization ( $b_a = 0.123 \text{ V/decade of current}$ ,  $b_c = -0.156 \text{ V/decade of current}$ ). These constants support qualitatively the involvement of two electrons in the charge-transfer reactions at the electrode/solution interface. The evaluated corrosion current from the Tafel plot is in the range of  $1.8 \times 10^{-9} \text{ Amp/cm}^2$ . It is quite clear from the Tafel plots that the doped diamond/Mo is significantly superior to the bare Mo in 0.5M NaCl solution. We have not observed active, passive or transpassive regions that are observed in the case of Mo substrates. The efficacy of diamond coating as a corrosion resistant material over the Mo substrate is  $\approx 2000$  ( $I_{\text{corr}}$  for Mo/ $i_{\text{corr}}$  for doped diamond/Mo).

Background cyclic voltammogram corrected for IR compensation for doped diamond electrode immersed in 0.5M NaCl solution is shown in Figure 5. From figure 5 it is clear that the doped diamond electrode is stable over a broader potential range where an insignificant water decomposition occurred. The potential range without the water decomposition on the doped diamond electrode extended approximately from +1.25 to -1.5 V vs. NHE. The diamond is stable over a wide potential range since there are no features associated with any electrochemical process and therefore it should have significant application in electroanalytical chemistry, From our unreported experimental data it is clear that the diamond is more stable than the Pt and Mo in the potential range investigated.

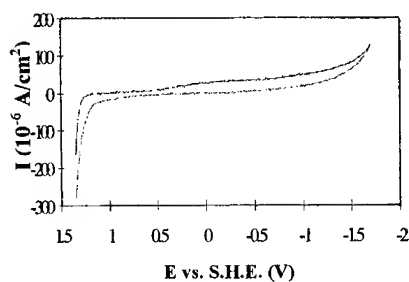


**Figure 5:** Cyclic voltammetric behavior of boron-doped diamond (resistivity= 0.01 - 0.001 Ohm-cm) in 0.5 M NaCl over a wide potential range. Scan rate:100 mV/sec.

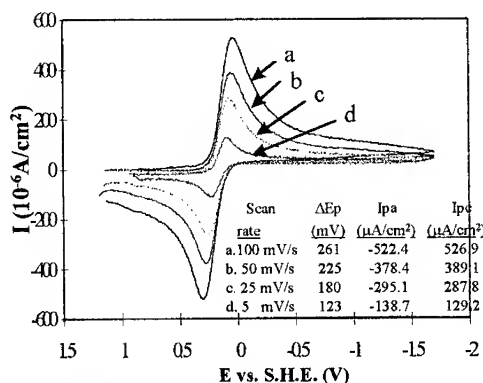


**Figure 6:** Cyclic voltammetric behavior of highly conducting (resistivity = 0.01 - 0.001 Ohm-cm) boron-doped diamond in 4mM  $\text{K}_3\text{Fe}(\text{CN})_6$  in 0.5 M NaCl at scan rates of (a) 100, (b) 50, (c) 25 , and (d) 5 mV/sec.



Figure 6 show the cyclic voltammetric behavior of  $\text{Fe}(\text{CN})_6^{3-}/\text{Fe}(\text{CN})_6^{4-}$  in 0.5M NaCl solution at boron-doped diamond electrode/solution interface at various scan rates. The resistivity ( $\rho$ ) of boron-doped diamond is  $\sim 0.001 \Omega\text{-cm}$  according to four point probe technique. We have not stirred the solution during the experiments performed in figure 6. The data reported in figure 5 & 6 is corrected for IR compensation and subtracted for background current. The peak separation ( $\Delta E_p$ ) for boron-doped diamond was found to be 123 mV at a scan rate of 5mV/sec. The redox reaction is quite reversible at the diamond electrode. The reaction rate at the diamond electrode/solution interface may be considered sluggish and our future research work will address this in detail by improving the over all electrode kinetics.

## CONCLUSIONS

We have reported the growth of doped diamond over the Mo substrate by microwave plasma CVD using hydrogen and methane. The lumped interfacial resistance of the doped diamond electrode/solution interface is in the range of  $10^6 \Omega\text{-cm}^2$ . This indicates the faradaic reaction rate at the interface is negligible and therefore, one may predict the corrosion rate of diamond in the 0.5 M NaCl solution is insignificant. Corrosion rate determined from the Tafel plot is in the range of  $1.8\text{nA/cm}^2$  for doped-diamond/Mo and  $\approx 3.77 \mu\text{A/cm}^2$  for bare Mo. We have determined the charge-transfer coefficients of the anodic and cathodic reactions to predict the corrosion rate accurately. Charge-transfer coefficients will generally be obtained using Tafel polarization measurements. Cyclic voltammogram showed that the diamond electrode material is stable over a wide potential range (+1.25 V to -1.5 V) for the decomposition of  $\text{H}_2\text{O}$  to occur to evolve hydrogen and oxygen during and anodic polarization, respectively. We have successfully shown that the coating of doped diamond over the Mo substrate substantially improved the corrosion characteristics of Mo in aggressive NaCl chemical environment.

Acknowledgments: The reported research work is carried out at the SPI of Auburn University and was supported by the NSF under Grant No. 9509842. Authors thank Mr. B.F. Crowe, Mr. J.A. Nichols, and Mr. J.R. Scott for their assistance in this research work. NSF is greatly appreciated for the support of undergraduate students in this research project.

## REFERENCES

1. P.M. Natishan and A. Morrish, *Materials Letters*, 8 (1989) 269.
2. R. Ramesham, R.F. Askew, M.F. Rose, B.H. Loo, *J. Electrochem. Soc.*, 140 (1993) 3018.
3. Yu.V. Pleskov, A.Ya. Sakharova and M.D. Krotova, L.L. Bouilov, and B.V. Spitsyn, *J. Electroanal. Chem.*, 228 (1987) 19.
4. R. Tenne, K. Patel, K. Hashimoto, A. Fujishima, *J. Electroanal. Chem.*, 347 (1993) 409.
5. G.M. Swain, *J. Electrochem. Soc.*, 141 (1994) 3382.
6. B. Miller, R. Kalish, L.C. Feldman, A. Katz, N. Moriya, K. Short, and A.E. White, *J. Electrochem. Soc.*, 141 (1994) L41.
7. G.M. Swain and R. Ramesham, *Anal. Chem.*, 65 (1993) 345.
8. H.B. Martin, A. Argoitia, U. Landau, A.B. Anderson, J.C. Angus, *J. Electrochem. Soc.*, 143 (1996) L133.
9. S. Alehashem, F. Chambers, J. Strojek, G.M. Swain, and R. Ramesham, *Anal. Chem.* 67 (1995) 2812.
10. R. Ramesham and M.F. Rose, *Thin Solid Films*, Accepted Nov 1996.
11. R. Ramesham and M.F. Rose, *Diamond and Related Materials*. Accepted Oct 1996.
12. R. Ramesham, *Thin Solid Films*, 229 (1993) 44.
13. A.J. Bard and L.R. Faulkner, in *Electrochemical Methods: Fundamentals and Applications*, John Wiley & Sons, Inc., New York (1980).
14. F. Mansfeld, M.W. Kendig, and S. Tsai, *Corrosion*, 38 (1982) 478.

## THE EFFECTS OF CARBONATE-BICARBONATE CONCENTRATION ON EMPIRICAL CORROSION DIAGRAM OF MILD STEEL AS A MATERIAL OF GEOLOGICAL DISPOSAL PACKAGE FOR HIGH LEVEL NUCLEAR WASTES

Guen Nakayama, Yuichi Fukaya, and Masatsune Akashi  
Research Institute, Ishikawajima-Harima Heavy Industries Co., Ltd. 3-1-15 Toyosu, Koto-ku  
Tokyo 135 Japan, guen@rimat.ty.ihl.co.jp

### ABSTRACT

In the scheme for geological disposal of high level radioactive nuclear wastes, the burial pit is to be isolated from the sphere of human life by a multiple-barrier system, which consists of an artificial barrier, composed of a canister, an overpack and a bentonite cushioning layer, and a natural barrier, which is essentially the bedrock. As the greatest as well as essentially the sole detriment to its integrity would be corrosion by groundwater. The groundwater comes to it seeping through the bentonite zone, thereby attaining conceivably the  $pH$  of transition from general corrosion to passivity,  $pH_d$ , the behaviors of mild steel in such a groundwater environment have been examined. It has been shown that the  $pH_d$  is lowered (enlargement of the passivity domain) with rising temperature and carbonate-bicarbonate concentration, while it is raised (enlargement of the general corrosion region) with increasing concentrations of chloride and sulfate ions.

### PRESUMPTION OF WORK ENVIRONMENT

The high level radioactive nuclear wastes<sup>(1)</sup> will diminish fast, and with it much of the heat of nuclide decay will have dissipated away during the 30 to 50 years of intermediate storage for cooling-down. Therefore, the intended practice of executing the disposal work when the overpack attains a surface temperature of lower than 100°C appears to be quite feasible. As the natural temperature of the disposal pit deep underground, say at 1,000m, should be 55°C or thereabout because of the geothermy, the service temperature would be somewhere between 55°C and 100°C.

The work environment that such a groundwater creates for the overpack can be considered as a neutral natural water environment. Moreover, as such a water must have been deprived of its oxygen, it can only be a reducing atmosphere. In the early stage of the construction of the geological disposal pit, however, the water can be an oxidizing environment because some air will inevitably be drawn into the pit from the surface.

Figure 1 depicts an empirically determined corrosion phase diagram of mild steel in an aqueous solution of 1 mMol/L [ $HCO_3^- + CO_3^{2-}$ ] + 10 ppm [ $Cl^-$ ] held at 20°C. Now, here we find a transition boundary, shown by a dotted line, existing at  $pH = 9.4$  or thereabout to indicate the corrosion mode of the steel to change from general corrosion (i.e., an active phase) over to passivity (a passive phase). This is the critical transition  $pH$ ,  $pH_d$ , and in the domain beyond this, mild steels are passivated in much the same way as stainless steels do.

As the general corrosion is of the uniform attrition, at least macroscopically so even though there can be numerous microscopical irregularities, provision of an ample enough corrosion margin will suffice to ensure the projected service life. When the corrosion environment has a  $pH$  higher than  $pH_d$ , on the other hand, it is in the domain of passivity, where occurrence of localized corrosion, i.e., pitting, crevice corrosion, or stress-corrosion cracking, is likely. As the rate of localized corrosion can be many times faster, however, use of a material on presumption of localized corrosion is an unpardonable practice: it must be

designed on a material/environment combination that will never allow localized corrosion to occur.

In the case at hand, a bentonite layer is to be laid as a shock-absorber between the disposal package and the bedrock, so that groundwater that gets in contact with the overpack must come seeping through the bentonite, likely dissolving rock salt on its way. This means that it is the composition and the *pH* of the groundwater as it has been filtered through a layer of bentonite that determine if the mild steel is in the general corrosion domain or in the passivity / localized corrosion domain.

It is well known that carbon steels are susceptible to chloride-induced type SCC in the passivation domain. As for the effects of carbonate-bicarbonate, on the other hand, *Parkins*<sup>(2)</sup> described the SCC range around  $\text{Fe}_3\text{O}_4/\text{FeCO}_3$  zone in 2Mol/L  $[\text{HCO}_3^- + \text{CO}_3^{2-}]$ . *Kasahara et al.*<sup>(3)</sup> have shown that SCC can take place only in a range of 2N  $[\text{NaHCO}_3]$  (*pH* = 8.3) to 1.75 N  $[\text{Na}_2\text{CO}_3] + 0.25\text{N} [\text{NaHCO}_3]$  (*pH* = 10.0), that it does not occur when  $[\text{Na}_2\text{CO}_3]$  is present and that the SCC potential is confined to a range of - 650 to - 850 mV vs.  $\text{Cu}/\text{CuSO}_4$ .

## **EXPERIMENTAL**

### **1. Determination of *pH<sub>d</sub>***

There are two reliable methods for determining *pH<sub>d</sub>*. One is the anodic polarization method, while the other is the free immersion potential method. The tests were conducted as follows:

#### **a. The anodic polarization method**

The specimen was a plate of JIS SM400 mild steel with its testing surface finished to 10 x 10 mm area. A X Mol/L  $[\text{HCO}_3^- + \text{CO}_3^{2-}] + \text{Y ppm} [\text{Cl}^-] + \text{Z Mol/L} [\text{SO}_4^{2-}]$  testing solution was made at 20°C. The *pH* was varied by a step of 0.25 or 0.5, with  $\text{Na}_2\text{CO}_3$  or  $\text{NaOH}$  as the need may be. The anodic polarization test was conducted starting from the free immersion potential at a scan rate of 10 mV/min while keep deaerating the testing solution by blowing nitrogen gas into it.

#### **b. The free immersion potential method**

Here, the same solution was used as the starting testing solution without adjusting *pH*, and the test proceeded as follows: after a sufficiently long time of immersion to stabilize *pH* under continuous aeration, the potential was determined by an electrometer; then the *pH* was changed by a step of 0.25 to 0.5; the solution was left standing for 4 to 48 hours to make the potential stabilize, then the potential and *pH* were determined; then the *pH* was changed again appropriately; this procedure was repeated until a reversal in the trend of potential change was observed.

### **2. Determination of Susceptibility to SCC Examined by the SSRT Test**

The specimen with a gauge section of 4 (φ) x 20 (L) mm were machined off. The SSRT test was conducted in 90°C, 2 Mol/L  $[\text{HCO}_3^- + \text{CO}_3^{2-}]$  at a tensile rate of 0.0001 mm/min (i.e.,  $8.3 \times 10^{-8} \text{ s}^{-1}$  as the strain rate), and carry it out to a strain of 5 %. The occurrence of SCC is examined after completion of test by visual inspection.

## RESULTS AND DISCUSSION

### 1. Determination of $pH_d$

The effects of  $pH$  on the anodic polarization curve are summarized in Fig. 2 in 20C, 1 *m* Mol/L [ $HCO_3^- + CO_3^{2-}$ ] + 0.12 Mol/L [ $SO_4^{2-}$ ],  $pH$  adjusted by NaOH. The potential vs. current (in logarithm) feature curve takes on a convex shape in the free corrosion domain because the current increases rapidly as the potential is raised from the free corrosion level. Against this, the trend of corrosion current in the passivation domain is such that the passivation holding current is attained, following appearance of a protrusion, or a mound, while the applied potential is yet low. If there are chloride or sulfate are present plentifully enough, they may induce pitting corrosion when the potential has been raised to the critical pitting corrosion potential. For yet higher  $pH$ 's, furthermore, the oxygen generation potential can be reached, where the state of perfect passivation.

In the region around  $pH_d$ , on the other hand, unequivocal determination whether it is still the free corrosion domain or already the passivation domain where some localized corrosion is taking place is difficult, because passivation is incomplete while the critical potential for occurrence of localized corrosion is low. Therefore, we have decided in this study on a criterion based on the principle of setting the passivation domain downwards beyond  $pH_d$ : when a somewhat concave change is seen in otherwise convex trend in the potential-current diagram, it is regarded as lying in the passivation domain. Thus, taking the potential at which the convex protrusion is observed as the pitting potential, we have been able to construct a  $pH$ -pitting potential diagram, which is shown in Fig. 3. The  $pH$  vs. free corrosion potential diagram as determined by the aerated free immersion test is also presented in Fig. 3. While the specimen stays in the general corrosion domain, the immersion potential decreases with a rate of -0.059  $pH$ , but as it enters the passivation domain, the potential starts increasing. The transition point is taken as the  $pH_d$ . We notice in the figure that the ennoblement of  $pH$  is insufficient in the transition  $pH$  range. Actually, several experimental difficulties were recognized in this observation. Namely, where stabilization of free corrosion potential at room temperature takes a long time in the order of thousand hours, the potentials actually measured in the experiments, in which the time that could be spared for potential stabilization for each  $pH$  was two full days at the most, represent only some intermediate stage toward the state of effective passivation. Therefore, the practice of raising the  $pH$  from the free corrosion domain to determine  $pH_d$  cannot escape from an intrinsic problem of making the transition  $pH$  obscure. When the  $pH$  is high enough to accomplish stable passivation, on the other hand, the time needed to establish stabilization can be short enough to be practical, whereby sufficiently noble potential can be attained with relative ease. However, the practice of lowering  $pH$  by adding an acid is met with a difficulty that there is no suitable acid available: the use of hydrochloric acid or sulfuric acid, for example, will change the quality of the testing solution by introducing additional [ $Cl^-$ ] and [ $SO_4^{2-}$ ], respectively, both seemingly reducing the immersion potential by making the occurrence of localized corrosion easier. As such debasement of potential will render an original passivation region to be regarded erroneously as part of free corrosion domain, there arises a danger of underestimating the extent of the passivation domain. For these reasons, we have elected to take that  $pH$  at which the  $pH$ -dependent decreasing trend of potential turns an increasing trend on gradually increasing the  $pH$  from neutral the transition  $pH$ ,  $pH_d$ .

It turned out that both the anodic polarization method and the free immersion potential method showed the corrosion behavior of mild steel to change at  $pH = 9.4$ . We conclude therefore that the critical  $pH$  of transition between free corrosion and passivation is  $pH_d = 9.4$  for 1 *m* Mol/L [ $HCO_3^- + CO_3^{2-}$ ] + 10 ppm [ $Cl^-$ ] solution held at 20C.

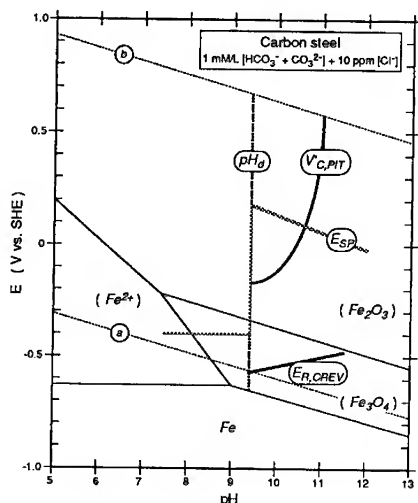


Fig. 1 Empirically drawn corrosion diagram or mild steel in aqueous solution of 1 mMol/L  $[HCO_3^- + CO_3^{2-}]$  held at 20 C.

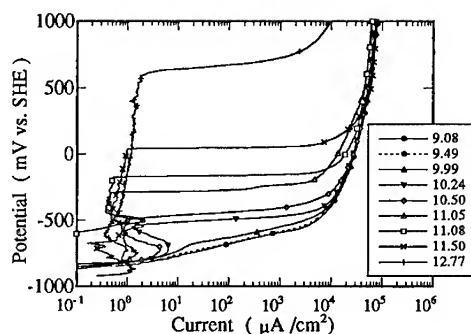


Fig. 2 Effects of pH on the anodic polarization curve for 0.01 mol/L  $[HCO_3^- + CO_3^{2-}]$  + 0.12 mol/L  $[SO_4^{2-}]$  environment.

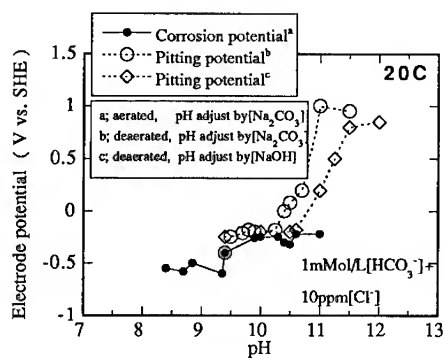


Fig. 3 Effects of pH on the critical pitting corrosion initiation potential as determined by the anodic polarization test conducted on pH-controlled and deaerated solutions and those on the free immersion potential as determined for aerated solutions.

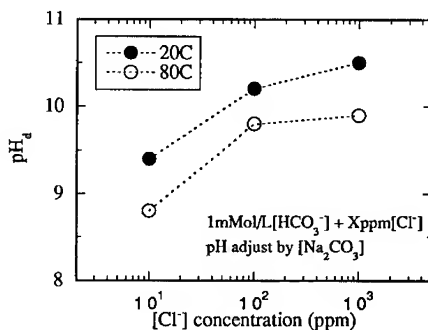


Fig. 4 Effects of temperature and chloride ion concentration on  $pH_d$ .

## 2. Effects of Temperature, Carbonate-Bicarbonate and Other Ions on $pH_d$

Figure 4 summarizes the effects of chloride concentration and temperature on  $pH_d$  determined as described above together with the results of previous investigation<sup>(4)</sup>, which was conducted at 80°C. We observe that  $pH_d$  is raised with increasing chloride concentration, thereby enlarging the domain of free corrosion, whereas it is lowered on raising the temperature from 20 to 80°C, enlarging the passivation domain.

In the determination of  $pH_d$  reported above, the concentration of carbonate-bicarbonate was allowed to change as  $Na_2CO_3$  was used to control the  $pH$  of the initially 1mM/L [ $HCO_3^- + CO_3^{2-}$ ] + 10 ppm [Cl<sup>-</sup>] solution. Now, as may be seen in Fig. 3 with regard to the pitting potential diagram (which was determined by the anodic polarization test with the  $pH$  altered with NaOH), both  $pH_d$  and the pitting potential are essentially the same whether the  $pH$ -adjusting agent is NaOH or  $Na_2CO_3$  as long as the environment remains slightly alkaline, whereas when the concentration is higher, the practice of  $pH$  adjustment with  $Na_2CO_3$  gives rise to nobler pitting potential. For these observations, following two facts may be cited as rational reasons: that the carbonate ion works to promote passivation, and that as  $pH$  adjustment with  $Na_2CO_3$  calls for a greater mass than with NaOH, the initiation of pitting by chloride has been prevented by a mass effect of augmented anion population.

The effects of carbonate-bicarbonate on  $pH_d$  thus determined in this study are shown in Fig. 5 together with the results due to Fukuda et. al.<sup>(5)</sup>. The  $pH_d$ , which is 9.4 or thereabout when the [ $HCO_3^- + CO_3^{2-}$ ] is  $10^{-3}$  Mol/L whichever the  $pH$ -adjusting agent is, is shifted toward acidic side with increasing concentration, so much so that when it is  $10^{-2}$  Mol/L, passivation is attained without adjusting the  $pH$ . It is well to remember, however, that, as part of Fukuda's tests was conducted by lowering  $pH$  with sulfuric acid from high  $pH$  side, their  $pH_d$ 's are intrinsically subject to influences of [ $SO_4^{2-}$ ]. With regard to this, Fig. 6 shows the effects of [ $SO_4^{2-}$ ] on  $pH_d$ . We observe here that  $pH_d$  is raised with rising [ $SO_4^{2-}$ ], right contrarily to the effect of [ $HCO_3^- + CO_3^{2-}$ ]. Table 1 summarizes these observations.

## 3. Effects of Carbonate-Bicarbonate on Susceptibility to SCC

SCC does occur at 90°C in an environment of 1Mol/L [ $HCO_3^- + CO_3^{2-}$ ] solution with its  $pH$  left unadjusted at  $pH = 8.8$ . The holding potential was - 0.65 V vs. SCE, which was a potential situated on the anodic polarization curve right after the small mound indicating formation of  $Fe_3O_4$  was passed through and just before the passivation potential was reached.

## CONCLUSIONS

If, for geological disposal of high-level nuclear wastes, a mild steel is to be used for the package in conjunction with the use of bentonite as a buffer to stand between the packages and the hostrock;

- 1) One has to take the occurrence of localized corrosion into consideration because mild steels will passivated if the environment  $pH$  is over 9.4, which is the critical  $pH$  for the general corrosion-to-passivity transition,  $pH_d$ , and in much of the passivity domain.
- 2) The effect of temperature on  $pH_d$  is to lower it; that of carbonate-bicarbonate ion, to lower it; that of chloride, to raise it; and that of sulfate, to raise it.
- 3) Mild steels are susceptible to carbonate-induced type stress-corrosion cracking in environments of high carbonate-bicarbonate concentrations.

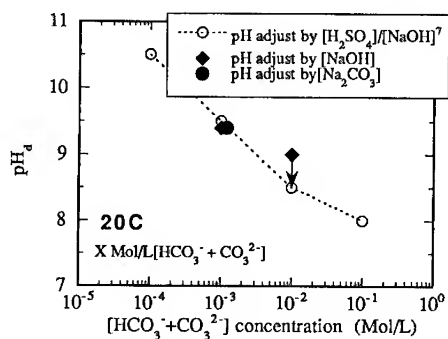


Fig. 5 Effects of carbonate-bicarbonate ion concentration on  $pH_d$ .

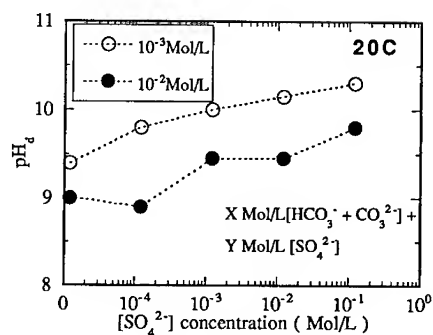


Fig. 6 Effects of sulfate ion concentration on  $pH_d$ .

Table 1. Effects of temperature and dissolved ions on  $pH_d$ .

Parameter	Range	Effects
Temperature, C	20 ~ 80	To lower
[Cl <sup>-</sup> ], ppm	10 ~ 10 <sup>3</sup>	To raise
[HCO <sub>3</sub> <sup>-</sup> + CO <sub>3</sub> <sup>2-</sup> ], mol/L	10 <sup>-4</sup> ~ 10 <sup>-1</sup>	To lower
[SO <sub>4</sub> <sup>2-</sup> ], mol/L	0 ~ 10 <sup>-1</sup>	To lower

## REFERENCES

- (1) *Disposal of Radioactive Waste: Review of Safety Assessment Method*, OECD/NEA, p. 19 (1991).
- (2) R.N. Parkins; *Corrosion Science*, 20, 147 (1980).
- (3) K. Kasahara and H. Adachi, *Tetsu-to-Hagané*, 69 (1983) 100.
- (4) G. Nakayama and M. Akashi, *Mat. Res. Soc. Symp. Proc.*, Vol. 294 (1992).
- (5) T. Fukuda and R. Staehle, *Preprints to 39th Lecture Meeting on Corrosion and Corrosion Prevention*, JSCE (1993).

## CORROSION PROTECTION OF PARTICULATE ALUMINUM-MATRIX COMPOSITES BY ANODIZATION

JIANGYUAN HOU, D.D.L. CHUNG

Composite Materials Research Laboratory, State University of New York at Buffalo,  
Buffalo, NY 14260-4400

### ABSTRACT

Anodization is effective for improving the corrosion resistance of aluminum-matrix composites. For SiC particle filled aluminum, anodization was performed successfully in sulfuric acid electrolyte, as usual. However, for AlN particle filled aluminum, anodization needed to be performed in an alkaline (0.7 N NaOH) electrolyte, because NaOH reduced the reaction between AlN and water, whereas an acid enhanced this reaction. The concentration of NaOH in the electrolyte was critical; too high a concentration caused the dissolution of the anodizing product ( $\text{Al}_2\text{O}_3$ ) by the NaOH, whereas too low a concentration did not provide enough ions for the electrochemical process. The corrosion properties and anodization characteristic of pure aluminum, Al/AlN and Al/SiC were compared. Without anodization, pure Al had better corrosion resistance than the composites and Al/SiC had better corrosion resistance than Al/AlN. After anodization, the corrosion resistance of Al/AlN was better than Al/SiC and both composites were better than pure Al without anodization, but still not as good as the anodized pure Al.

### INTRODUCTION

Metal-matrix composites (MMCs) with lightweight aluminum alloy matrices and high modulus SiC or AlN particle reinforcements offer low thermal expansion and excellent mechanical properties. SiC reinforced MMC is more common than AlN reinforced MMC, but AlN reinforced MMC exhibits better mechanical properties at elevated temperatures or after heating due to the lack of a reaction between Al and AlN, in contrast to the reaction between Al and SiC [1]. Though both MMCs are promising, addition of a second phase could degrade the corrosion resistance.

Corrosion is diminished by chemical passivation [2], polymer [3] and/or anodized coatings [4]. The anodization of an aluminum alloy is an electrochemical method of converting aluminum to aluminum oxide ( $\text{Al}_2\text{O}_3$ ) by applying an electric current in the presence of an electrolyte. The most widely used electrolyte is an acid, such as sulfuric acid. There are two types of sulfuric acid anodizing: (1) conventional anodizing, which is performed at room temperature and provides a hard oxide film about 10  $\mu\text{m}$  thick; (2) hard anodizing, which is performed at 0°C and provides a hard oxide film about 50  $\mu\text{m}$  thick. The structure of the porous anodization layer was described [5] as a close packed array of columnar hexagonal cells, such that each cell contains a central columnar pore normal to the substrate surface. The porous layer has to be sealed in order to improve the corrosion resistance after anodizing. Through sealing, anodic coatings are partly converted to more voluminous boehmite ( $\text{Al}_2\text{O}_3 \cdot n\text{H}_2\text{O}$ ), which plugs the pores [6].

The conventional anodizing method is less effective for the corrosion protection of Al MMCs than for aluminum alloys due to the presence of the reinforcement phase, which hinders the initiation and growth of the oxide film [7,8].



The hard anodization method is usually used for high foreign content alloys and MMCs. Several works [3, 7-12] have been reported on the effect of anodization on SiC reinforced Al, but all of them are restricted to acid anodizing. It is commonly concluded that anodizing improves the corrosion resistance of all kinds of SiC reinforced aluminum, though the effectiveness depends on the alloy used as the matrix. For example [11], the corrosion potential (higher for better corrosion resistance) of pure aluminum, Al alloy 6061 and their corresponding MMCs was increased by about 140 mV for samples with a hard coating; hard anodizing did not improve the corrosion resistance of the 2024 Al alloy, but increased the corrosion potential of the MMC by up to 200 mV. In addition to the similar conclusion drawn regarding the effect of sulfuric acid anodizing on a SiC reinforced aluminum, it is reported in the present work that sulfuric acid anodization shows little, if any, effect on AlN reinforced pure aluminum. Anodizing in an alkaline solution was used in this work to solve this problem. AlN reinforced Al anodized in 0.7 N NaOH solution showed good corrosion resistance. Though there has been some work done on alkaline solution anodizing of metals like iron or copper [13], no report has yet been made on aluminum anodizing in an alkaline solution.

Various techniques have been used to evaluate corrosion resistance. These include salt-spray test as well as measurements of reflectivity, abrasion resistance and electrical breakdown voltage [7]. Electrochemical test methods are particularly useful in understanding and controlling corrosion, because they relate to the thermodynamics and kinetics of corrosion reactions; the electrochemical potential is equivalent to the driving force for the reaction; the current is equivalent to the reaction rate. The anodic polarization tests were used in this work to study the corrosion properties of Al and Al-matrix composites.

## EXPERIMENT

Three kinds of material were used, namely (1) pure aluminum (170.1), with composition 99.77% Al, 0.16% Fe and 0.07% Si, as supplied by Roth Brothers Smelting Corp., (2) pure aluminum matrix with 59 vol.% AlN particle (Advanced Refractory Technologies Inc., Buffalo, NY, AlN<sub>el</sub> grade A-100) reinforcement (Al/AlN), and (3) pure aluminum matrix with 58 vol.% SiC particle (Electro Abrasives Corp., Lackawana, NY, #1200-W) reinforcement (Al/SiC).

The AlN particle size ranged from 2 to 7  $\mu\text{m}$ , with a mean of 3.7  $\mu\text{m}$ . The composition of AlN was 66.0% Al, 33.0% N, 0.07% C, 1.0% O, 0.005% Fe and 0.005% Si. The SiC particle size ranged from 1 to 10  $\mu\text{m}$ , with a mean of 2  $\mu\text{m}$ . The composition of SiC was 98.5% SiC, 0.5% SiO<sub>2</sub>, 0.3% Si, 0.08% Fe, 0.1% Al, 0.3% C.

AlN and SiC composites were fabricated by liquid metal infiltration [15], with argon (UN1600) as the pressurizing gas. The reinforcement preform was baked (200°C for 8 h for AlN and 550°C for 2 h for SiC) and then furnace cooled.

All the materials were anodized in an electrolyte at 0°C, with a pure Al plate as the cathode. Pure aluminum was etched in 10% NaOH at 40°C, electrochemically polished in 50% HNO<sub>3</sub> at room temperature and then anodized in 10 vol.% H<sub>2</sub>SO<sub>4</sub> for 0.5 h. Al/AlN and Al/SiC were ground, mechanically polished and then rinsed in water and methanol before anodization in both 10 vol.% H<sub>2</sub>SO<sub>4</sub> and 0.7 N NaOH for 1 h. The composites were not etched, because there was negligible native oxide film on their surface. Additionally, the high reinforcement content of the composite surface made etching very preferential, and there was essentially no aluminum left on the composite surface after etching. Anodization applied on the etched Al/AlN

and Al/SiC resulted in no anodization film.

The current density during anodization was 25 mA/mm<sup>2</sup>. Pure Al and the Al/SiC composite were sealed in distilled water at 90-100°C for 30 min after anodization. The corrosion potential of H<sub>2</sub>SO<sub>4</sub> anodized Al/AlN without sealing was -660 mV, and that with sealing was -670 mV; in contrast, the corrosion potential of H<sub>2</sub>SO<sub>4</sub> anodized Al/SiC without sealing was -590 mV, and that with sealing was -510 mV [16]. Since sealing had no positive effect on anodized Al/AlN, sealing was applied only to Al/SiC after anodization.

Electrochemical polarization resistance measurement and potentiodynamic scan testing were used to study corrosion in 0.5 N NaCl. The CMS105 DC Corrosion Test System of Gamry Instruments (Willow Grove, PA) was used, with a saturated calomel electrode as the reference electrode and platinum as the counter electrode.

The corrosion current is the current when the tested sample is in a freely corroding open circuit condition. The corrosion potential is the open-circuit potential. In the polarization experiment, the potential was scanned from 20 mV below to 20 mV above the corrosion potential. As the same time, the current flowing from the test sample to the counter electrode was measured.

Anodic polarization experiments were started after a steady open-circuit potential was achieved. The scan rate was 5 mV/s. The current vs. voltage curve was roughly linear. An applied potential that is more positive than the corrosion potential results in an anodic current, whereas a potential that is more negative than the corrosion potential results in a cathodic current. A linear fit of the data to a standard model yields an estimate of the polarization resistance ( $R_p$ ).

Anodic polarization diagrams (potentiodynamic test) were generated to identify the corrosion mechanisms. The potential was scanned from 200 mV below the corrosion potential to 1.5 V at 0.15 mV/s.

The volume resistivity of each composite was measured by using the four-probe method. Silver paint electrical contacts were applied circumferentially in four planes perpendicular to the current direction in order to form the four probes.

## RESULTS

Table 1 shows the polarization resistance results of pure Al, Al/AlN and Al/SiC without any surface treatment. The corrosion current density of pure Al was lower than those of both Al/AlN and Al/SiC. This is because the high volume fraction of either reinforcement degraded the uniformity of the native oxide film on

Table 1 Corrosion properties of Al and its composites

	Corrosion potential (mV, $\pm 5$ mV)	Corrosion current density (A/cm <sup>2</sup> )	Polarization resistance ( $\Omega$ .cm <sup>2</sup> )
Pure Al	-760	$2.4 \times 10^{-8} \pm 5 \times 10^{-9}$	$1.1 \times 10^6 \pm 5 \times 10^5$
Al/AlN	-680	$1.4 \times 10^{-6} \pm 5 \times 10^{-7}$	$3.5 \times 10^4 \pm 5 \times 10^3$
Al/SiC	-610	$1.2 \times 10^{-6} \pm 5 \times 10^{-7}$	$5.7 \times 10^4 \pm 5 \times 10^3$

Table 2 Corrosion potential (mV,  $\pm 5$  mV) of Al/AlN under different conditions

Without anodization	-680
Anodized in 0.3 N NaOH	-690
Anodized in 0.7 N NaOH	-440
Anodized in 1.0 N NaOH	-700

the surface and thus decreased the corrosion resistance of the composites. Because both AlN and SiC are not electrically conductive, the corrosion potential of the two composites were less negative than pure Al, even though the corrosion rates (corrosion current densities) of the composites were higher than that of pure Al.

Comparison of the corrosion potential, corrosion current density and polarization resistance of Al/AlN and Al/SiC shows that the corrosion resistance of Al/SiC was a little better than that of Al/AlN. The electrical resistivity of Al/AlN ( $(1.8 \pm 0.05) \times 10^{-4} \Omega \cdot \text{cm}$ ) was only a little lower than that of Al/SiC ( $(2.2 \pm 0.05) \times 10^{-4} \Omega \cdot \text{cm}$ ). The main reason that Al/SiC exhibited better corrosion resistance than Al/AlN is that AlN reacts with water ( $\text{AlN} + 3\text{H}_2\text{O} = \text{Al}(\text{OH})_3 + \text{NH}_3$ ), while SiC does not. The corrosion resistance of Al/SiC is better than that of Al/AlN when no surface treatment is involved.

Table 2 shows the corrosion potential of Al/AlN anodized in NaOH. With an appropriate NaOH concentration, the corrosion resistance was improved greatly. The concentration of NaOH was critical; only the concentration of 0.7 N gave a less negative corrosion potential than the case without anodization. Concentrations of 0.9 and 0.3 N did not give any satisfactory result. During the anodization of Al/AlN in NaOH, the  $\text{OH}^-$  ions provided by NaOH reduced the reaction between AlN and water and thus enhanced the growth rate of the  $\text{Al}_2\text{O}_3$  film. If the concentration of the NaOH is too low, the NaOH will not be effective, because there are not enough  $\text{OH}^-$  ions to reduce the reaction between AlN and water. Too high a concentration of NaOH is not effective for enhancing the growth rate of the oxide film either, because NaOH at a high enough concentration dissolves  $\text{Al}_2\text{O}_3$  and Al.

Table 3 shows the corrosion properties of Al/AlN.  $\text{H}_2\text{SO}_4$  anodization hardly had any effect on the corrosion resistance of the composite, but NaOH anodization greatly improved the corrosion resistance. After NaOH anodization, the corrosion potential increased, the corrosion current density decreased, while the polarization resistance increased. Because an acid solution enhanced the reaction between water

Table 3 Corrosion properties of Al/AlN

	Corrosion potential (mV, $\pm 5$ mV)	Corrosion current density (A/cm <sup>2</sup> )	Polarization resistance ( $\Omega \cdot \text{cm}^2$ )
Without anodization	-680	$1.4 \times 10^{-6} \pm 5 \times 10^{-7}$	$3.5 \times 10^4 \pm 5 \times 10^3$
$\text{H}_2\text{SO}_4$	-540	$1.0 \times 10^{-6} \pm 5 \times 10^{-7}$	$5.4 \times 10^5 \pm 5 \times 10^4$
NaOH	-440	$3.0 \times 10^{-10} \pm 5 \times 10^{-11}$	$1.4 \times 10^8 \pm 5 \times 10^7$

Table 4 Corrosion properties of Al/SiC

	Corrosion potential (mV, $\pm 5$ mV)	Corrosion current density (A/cm <sup>2</sup> )	Polarization resistance ( $\Omega$ .cm <sup>2</sup> )
Without anodization	-610	$1.2 \times 10^{-6} \pm 5 \times 10^{-7}$	$5.7 \times 10^4 \pm 5 \times 10^3$
H <sub>2</sub> SO <sub>4</sub>	-510	$1.4 \times 10^{-9} \pm 5 \times 10^{-10}$	$6.8 \times 10^7 \pm 5 \times 10^6$
NaOH anodized	-680	$4.5 \times 10^{-7} \pm 5 \times 10^{-8}$	$5.9 \times 10^4 \pm 5 \times 10^3$

and AlN (Eq. (2)), it was difficult to obtain a uniform and continuous film by acid anodization. By anodizing in NaOH, the corrosion resistance was improved. This is because NaOH reduced the reaction between water and AlN, so that a more compact and continuous coating was formed. It should be noted that Al(OH)<sub>3</sub> formed by this reaction is equivalent to Al<sub>2</sub>O<sub>3</sub>.nH<sub>2</sub>O, which is akin to the anodized film itself, thereby enhancing the smoothness of the film.

Table 4 shows the corrosion properties of Al/SiC. NaOH anodization had little effect on the corrosion resistance, because the positive effect of NaOH mentioned above for Al/AlN is not applicable to Al/SiC. Because the interface between SiC and pure Al is not as good as that between AlN and pure Al, Al/AlN was a better composite for anodization. Due to the poor interface between SiC particles and the anodization film, the anodized film had to grow around the SiC particles, leaving small gaps between SiC particles and anodized film both around and above the particles. The effect of a poor interface was particularly significant in the case of NaOH anodization, as the film growth rate was much lower and the resulting film was thinner for NaOH anodization than H<sub>2</sub>SO<sub>4</sub> anodization. However, H<sub>2</sub>SO<sub>4</sub> anodization decreased the corrosion current density of Al/SiC, increased the polarization resistance and increased the corrosion potential. The incompatible interface problem still existed in H<sub>2</sub>SO<sub>4</sub> anodization, but was not as dominating as in NaOH anodization, because the film growth was more rapid, and the ultimate film thickness was larger for a film anodized in an acid solution than that anodized in an alkaline solution. Therefore, acid anodization plus sealing still improved the corrosion resistance of Al/SiC, whereas alkaline anodization had little effect.

Table 5 shows the corrosion properties of pure Al with and without anodization. Acid anodization decreased the corrosion current density of pure Al, increased the polarization resistance and increased the corrosion potential.

Comparison of Tables 2, 3 and 4 shows that pure Al after anodization had the best corrosion resistance. This is due to the superior quality of the anodization film

Table 5 Corrosion properties of pure Al

	Corrosion potential (mV, $\pm 5$ mV)	Corrosion current density (A/cm <sup>2</sup> )	Polarization resistance ( $\Omega$ .cm <sup>2</sup> )
Without anodization	-760	$2.4 \times 10^{-8} \pm 5 \times 10^{-9}$	$1.1 \times 10^6 \pm 5 \times 10^5$
H <sub>2</sub> SO <sub>4</sub>	-400	$2.5 \times 10^{-12} \pm 5 \times 10^{-13}$	$6.8 \times 10^{10} \pm 5 \times 10^9$

on pure Al compared to that of the anodization film on Al/AlN or Al/SiC.

The corrosion resistance of Al/AlN was not as good as Al/SiC before anodization, but was better than Al/SiC after anodization with the appropriate electrolyte (alkaline for Al/AlN and acid for Al/SiC). This is partly due to the difference in the anodization coating morphology between the two composites. As shown by microscopy and dielectric constant measurement, the anodization film on Al/AlN was more compact and continuous than that on Al/SiC.

#### REFERENCES

1. Shy-Wen Lai and D.D.L. Chung, *J. Mater. Sci.* **29**, 6181 (1994).
2. A. Turnbull, NPL Report DMM(A), **15**, 1990.
3. S. Lin and H. Greene, *Corrosion* **48**, 61 (1992).
4. F. Mansfeld and S. Lin, *Corrosion* **45**, 615 (1989).
5. F. Keller, M.S. Hunter and O.L. Robinson, *J. Electrochem. Soc.* **100**, 411 (1983).
6. S. Tajima, in Advances in Corrosion Sci. and Tech. **1**, 1970, Plenum Press, New York, NY, p. 229.
7. P.P. Trzaskoma and E. McCafferty, in Proc. Symp. on Aluminum Surface Treatment Tech. **86**, 1986, p. 171.
8. F. Mansfeld and S.L. Jeanjaquet, in Adv. Localized Corros., Int. Corros. Conf. Ser., NACE-9, 1990, p. 343.
9. P.P. Trzaskoma, *Corrosion (Houston)* **46**, 401 (1990).
10. E. McCafferty and P.P. Trzaskoma, *J. Electrochem Soc.* **130**, 1804 (1983).
11. E. McCafferty and P.P. Trzaskoma, in Adv. Localized Corros., Int. Corros. Conf. Ser., NACE-9, 1990, p. 181-190.
12. E. Mansfeld and S.L. Jeanjaquet, *Corros. Sci.* **29**, 727 (1986).
13. M.R. Generro de Chialvo and J.O. Zerbini, *J. Appl. Electrochem.* **16**, 517 (1986).
14. R.K. Dhir, M.R. Jones and M.J. McCarthy, *Cem. Concr. Res.* **23**, 1443 (1993).
15. Jiangyu Yang and D.D.L. Chung, *J. Mater. Sci.* **24**, 3605 (1989).
16. Jiangyuan Hou and D.D.L. Chung, in Electronic Packaging Materials Science VII (Mat. Res. Soc. Symp. Proc. **390**, Pittsburgh, PA, 1995), pp. 129-134.

# In-Situ Characterization of Oxide Films on Liquid Alkali Metals Using Second Harmonic Generation (SHG)

H. Tostmann\*, D. Nattland\*\* and W. Freyland\*\*

\*Division of Engineering and Applied Sciences, Harvard University, Cambridge, MA 02138

\*\*Institut für Physikalische Chemie und Elektrochemie, Universität Karlsruhe, 76128 Karlsruhe, Germany

## Abstract

The experiments described in this paper clearly show that Second Harmonic Generation (SHG) may be used as a sensitive tool for detecting oxide impurities at interfaces not accessible for usual surface characterization methods. As a striking feature, one peak in the temperature dependent SH intensity is observed for liquid potassium and five peaks for liquid cesium. The occurrence of these peaks cannot be understood in terms of the nonlinear optical properties of the pure metal. By varying the oxygen content present in the melt it can be shown that these peaks must be attributed to the presence of oxide impurities segregating at the interface. In addition it is shown that the presence of oxides at the interface inert sapphire – molten alkali metal significantly alters the structure of the sapphire surface finally leading to corrosion visible even by the eye.

## Introduction

Both the surface of solid metals [1] and the bulk phase of liquid metals [2] have been the subject of numerous studies during the past years and are comparatively well understood. This is not true for the surface of liquid metals and for processes that might occur at these surfaces (like e.g. surface induced ordering, premelting, surface segregation or wetting phenomena [3]). Knowledge about these and similar processes is not only of interest for a general understanding of liquid metals but also of particular importance for many metallurgical processes involving liquid metals.

The investigation of the surface of liquid metals is generally restricted to UHV conditions for the following reasons. First of all, liquid metals tend to oxidize much faster than the corresponding solid phase and it is therefore not possible to probe the bare metal surface if the liquid metal is exposed to even small amounts of oxygen. Second of all, most methods to study or characterize surfaces are only applicable under UHV conditions [1]. This holds in particular for liquid alkali metals at elevated temperatures. In this case the pertinent vapor pressure is so high (e.g.  $10^{-5}$  Torr for Cs at  $75^\circ\text{C}$ ) that the liquid metal has to be contained in a vacuum tight cell. This restricts the access to the surface of interest even more. Apart from these experimental problems, knowledge about the surface properties of liquid alkali metals is highly desirable because they represent the most simple and ideal metals (as opposed to e.g. liquid Hg or Ga which have been investigated more thoroughly [4]). The high reactivity of alkali metals against oxygen is well known [5] and liquid alkali metals are among the strongest oxygen getters. In order to perform any surface sensitive investigation

on liquid alkali metals it is therefore of crucial importance to know the extent of the surface segregation of the oxides which form in the melt. As will be shown in this paper, the nonlinear optical method of Second Harmonic Generation (SHG) is well suited to probe the extent of surface contamination of liquid metals enclosed in an inert vacuum tight cell.

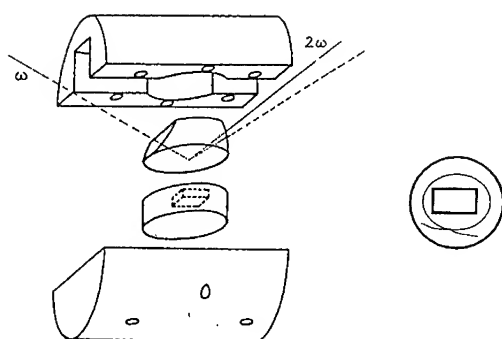


Figure 1: Schematic draw of the sapphire cell holding the liquid alkali metal. Left: sapphire plates with stainless steel brackets. Right: top view on reservoir sapphire with tantalum wire sealing.

## Experimental

If the inert cell is made of transparent sapphire ( $\text{Al}_2\text{O}_3$ ), any optical method is suited to probe the interface between the sapphire and the molten metal. Using intense laser pulses, not only photons of the fundamental laser wavelength will be reflected at the sapphire – liquid metal interface (depicted as  $\omega$  in Fig. 1) but also higher harmonics will be generated [6]. The most intense of these harmonics is the Second Harmonic (SH) depicted as  $2\omega$  in Fig. 1. Strong laser pulses are the prerequisite for SHG because the harmonic (nonlinear) output generated at the interface sapphire–liquid metal is orders of magnitudes less intense than the reflected fundamental beam. The advantage of this nonlinear optical method — compared to linear optical experiments like reflectivity spectroscopy — is based on the fact that SHG is surface sensitive and specific. For symmetry reasons, SHG is forbidden *inside* media with inversion symmetry but allowed at the interface *between* two media with inversion symmetry (like e.g. the interface sapphire–liquid metal). The inversion symmetry is only broken in the immediate vicinity of the interface which extends about a few Å [7].

The experimental setup is described in more detail in [8]. The sapphire cell is shown schematically in Fig. 1: the reservoir plate holds the liquid metal whereas the covering prism allows to probe the interface sapphire–liquid metal. A  $50\text{ }\mu\text{m}$  thick tantalum wire of high ductility in between the two sapphire plates ensures that the cell will be vacuum tight over the whole temperature range [5].

A Q-switched Nd:YAG laser is used as a high intensity light source (12 mJ per 4 ns pulse; repetition rate 5 Hz). The fundamental laser pulses (dashed line in Fig. 1) enter the sapphire prism and are reflected specularly at the interface sapphire prism – liquid metal. A small amount of the 1064 nm radiation is converted into SH radiation at 532 nm.

Due to the dispersion of the refractive index of the sapphire, the low intensity harmonic beam can be separated geometrically from the high intensity fundamental beam. Because of the comparatively low intensity of the SH output, a sensitive detection unit with photon counting ability is essential.

For the SH output  $I(2\omega)$  from isotropic surfaces, the following expression holds [6]:

$$I(2\omega) = \frac{32\pi^3\omega^2 \sec^2 \Theta_{2\omega}}{c^3 \epsilon_1(\omega) \epsilon_1^{1/2}(2\omega)} |e_{2\omega} \chi_{s,eff}^{(2)} e_{\omega} e_{\omega}|^2 I(\omega)^2 \quad (1)$$

with  $\Theta_{2\omega}$ : angle of the reflected SH output against the surface normal,  $\epsilon_1(\omega)$  and  $\epsilon_1(2\omega)$ : real part of the dielectric constant of the fundamental and the harmonic beam. The expressions  $\epsilon_{\Omega}$  contain the polarization of the light and the Fresnel factor for the field. Finally,  $I(\omega)$  is the intensity of the incoming laser field. All these quantities remain unchanged during heating up the liquid metal. The same should hold for the effective nonlinear susceptibility  $\chi_{s,eff}^{(2)}$  of the surface. In the case of liquid metals, the main contribution to  $\chi_{s,eff}^{(2)}$  is originating from the free electron gas. The nonlinear susceptibility of the free electron gas should only vary slightly and monotonically with temperature (neither the number nor the nature of the free electrons change considerably in the temperature range of interest, separated far enough from the gas-liquid critical point and the metal-nonmetal transition). Any drastic change in  $I(2\omega)$  has to be attributed to a change in  $\chi_{s,eff}^{(2)}$ . This can only be understood if another component of the melt segregates at the surface.

## Results and Discussion

The assumption of a monotonically varying SH output as a function of temperature is corroborated by experimental results obtained for liquid Ga and liquid Bi [8]. As expected, the SH output originating from the free electron gas only varies continuously with temperature (in the case of liquid Ga, the SH intensity decreases slowly and monotonically in the temperature range from the melting point to 800° C).

In a very pronounced contrast to these findings, the temperature dependent SH output found for liquid alkali metals shows a drastic variation of the SH intensity in a very close temperature range. In the case of liquid potassium, a prominent peak in the SH intensity is found in the vicinity of 450° C (see Fig. 2).

The occurrence of this peak is reproduced in several experiments. A less pronounced peak is found in some experiments in the vicinity of 250° C.

In the case of liquid Cs at least five different peaks are discernible and reproduced in several experiments (see Fig. 3), the first occurring at 250° C and the others at 370° C, 500° C, 610° C and 690° C respectively.

This behavior found for K and Cs is highly surprising because the alkali metals are supposed to be perfect or ideal free electron metals and the occurrence of those peaks is not consistent with the nonlinear response of a free electron gas. So it has to be assumed that the surface SHG measured in the case of liquid alkali metals is not the SH intensity emerging from the surface of a liquid free electron metal.

A striking difference between e.g. Ga and Bi on the one hand and alkali metals like Cs and K on the other hand is the very strong affinity of the latter for oxygen. The alkali metals employed here have a purity of 99.85 % at best (cf. 99.99999% for Ga). In addition, we can not exclude a slight contamination of the sample with oxygen during the filling procedure



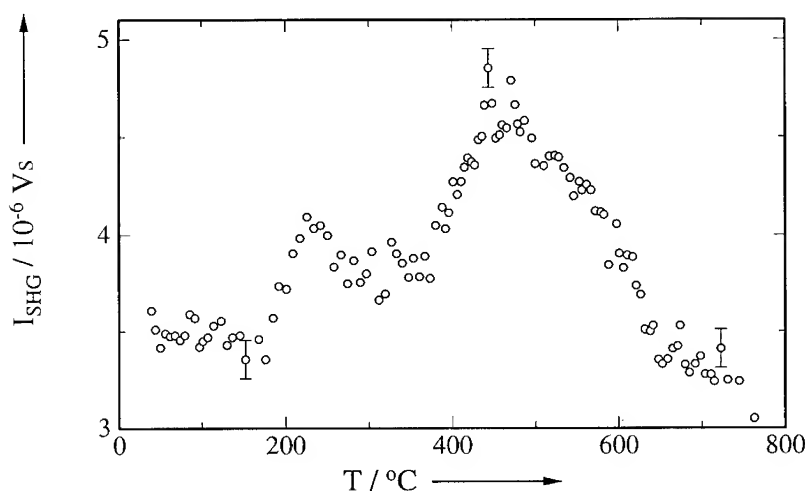


Figure 2: Temperature dependent SH output from the interface sapphire–liquid potassium (p-polarized light in, p-polarized light out). Typical error bars are shown.

even under the high purity conditions of an argon glove box (1–2 ppm oxygen). Even if the molten alkali metal is treated with extra care, some oxygen dissolves in the liquid and forms the pertinent alkali metal oxide. These oxides tend to segregate at the high energy sapphire surface and eventually react with the sapphire. This is proven experimentally as follows. In a first experiment, liquid potassium is heated up to 150° C and held in contact with pyrophorous titanium powder. Ti is known to be a better oxygen getter than K at elevated temperatures (i.e. the Ti oxide is thermodynamically more stable than the K oxide)[5]. Using this purification method, the peak vanishes almost completely after 24h of purification [8].

In a second experiment, a very small amount of  $\text{KO}_2$  ( $x_{\text{KO}_2} \leq 0.01$ ) has been added to the liquid K. As can be seen in Fig.4 (filled circles), this leads to a threefold increase in the SH intensity at the peak position of 450° C. Obviously, the K oxide indeed segregates at the surface and leads to an enhanced SH signal at the interface sapphire–melt. Three basic questions arise which cannot be answered directly or unambiguously using the experimental data collected so far. First of all: what mechanism is responsible for the fact that the peaks reproducibly occur at the same temperature? This might be explained by the interplay between the different forces of adhesion (sapphire–oxide anions vs. sapphire–free electron gas) and cohesion. Obviously it is energetically favorable for a film containing oxide anions to intrude between the high energy sapphire surface and the homogeneous melt at 450° C. Second of all: why are the peaks so sharp (cf. to the peak at 450° C in the case of the K melt with a small amount of  $\text{KO}_2$  as shown in Fig.4)? Any oxide anion (like e.g.  $\text{O}^{2-}$ ) is highly polarizable and should yield a strong SH output as the SH intensity scales roughly with the linear polarizability [6]. This signal from highly polarizable ions may very well be higher than the output from the free electron gas. As a matter of fact, monolayers of highly polarizable molecules yield a much stronger SH signal than a liquid metal surface in

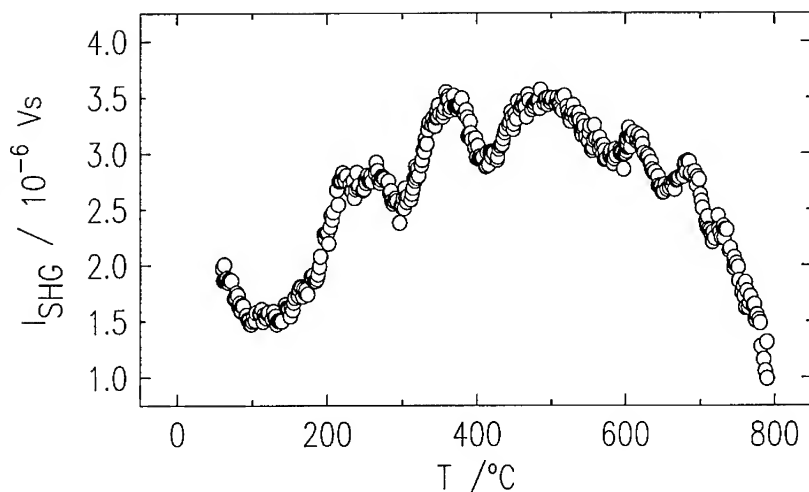


Figure 3: Temperature dependent SH output from the interface sapphire-liquid cesium (p-polarized light in, p-polarized light out).

this geometry [8]. In this case, a well oriented monolayer of oxide anions may be formed in the beginning which is destroyed with increasing oxygen segregation (both with time and temperature). Subsequent layers may destroy this orientation or have an opposite orientation. The third question concerns the occurrence of only one peak in the case of liquid K whereas several SH peaks are found in liquid Cs. It is compelling to associate these surface features with the bulk phase chemistry: in liquid K only one oxide should be thermodynamically stable, whereas a rich (sub)oxide chemistry is known for the bulk phase of Cs [10]. In this case, different species may be stable at different temperatures. But the connection between bulk oxide chemistry and surface segregation is not clear yet.

The last point to discuss concerns the corrosion of the sapphire. Because of the symmetry properties of the  $\chi_{s,eff}^{(2)}$  tensor, the combination of both incoming and detected light being polarized parallel to the plane of incidence (p-polarized) only probes the isotropic components of this tensor. On the other hand, any combination containing s-polarized light (polarized perpendicular to the plane of incidence) measures the anisotropic components of the  $\chi_{s,eff}^{(2)}$  tensor. For this it is by no means surprising that only the p/p combination yields a detectable SH output if the isotropic interface of a liquid is probed. The SH output for the s/p combination can hardly be discriminated from the background noise in this case. For liquid K with  $KO_2$  added however this s/p output drastically increases in the vicinity of 450° C (see open circles in Fig. 4), the temperature of the prominent peak in the p/p SH output (see filled circles in Fig. 4). After the drastic increase the s/p signal remains on this high level in contrast to the p/p SH intensity decreasing steadily towards the former SH intensity. The very same behavior is found for liquid Cs: the s/p SH signal raises from the background noise level to a strong signal in the vicinity of 250° C, the temperature where the first peak in the p/p SH signal is observed. The fact that the s/p signal must be due to anisotropic structures and that the raise of this s/p signal is irreversible leads to the

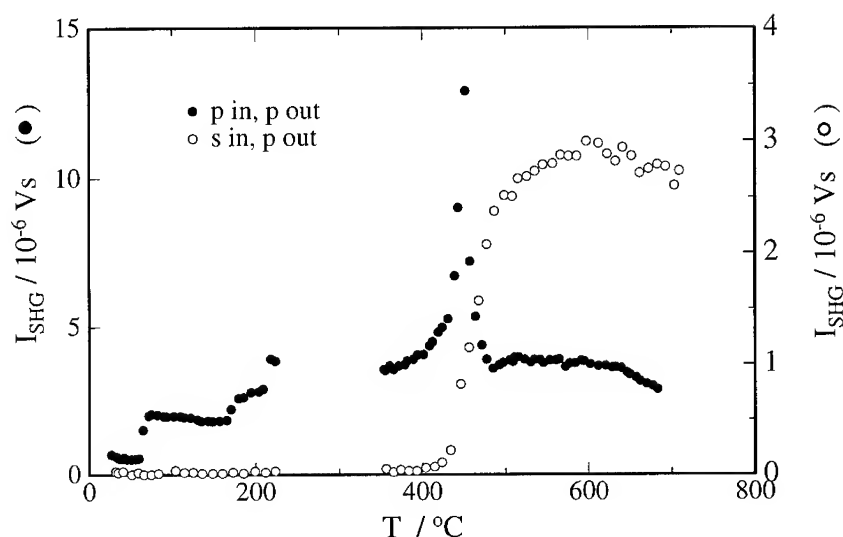


Figure 4: Temperature dependent SH output from the interface sapphire–liquid potassium with a small amount of  $\text{KO}_2$  added (combination of polarization: see key).

conclusion that the s/p SH output probes corrosion processes altering the structure of the  $\text{Al}_2\text{O}_3$ . If the alkali metal is not purified using titanium powder, this corrosion is visible by the eye at higher temperatures (about  $600^\circ\text{C}$ ).

## Acknowledgements

The authors gratefully acknowledge financial support of this work by the Deutsche Forschungsgemeinschaft and the Fonds der Chemischen Industrie

## References

1. A.W.Adamson, *Physical Chemistry of Surfaces*, 5th ed., (Wiley, New York, 1990).
2. N.H.March, *Liquid Metals, Concepts and Theory*, (The University Press, Cambridge, 1990).
3. Proceedings of the 9th International Conference on Liquid and Amorphous Metals, J.Non-Cryst.Solids, 1997.
4. M.J.Regan et al, Phys.Rev.Lett **75**, 2498 (1995).
5. D.Nattland, H.Heyer and W.Freyland, Z.Phys.Chemie NF **149**, 1 (1986).
6. Y.R.Shen, *The Principles of Nonlinear Optics*, (Wiley, New York, 1984).
7. G.L.Richmond, J.M.Robinson and V.L.Shannon, Progr.Surf.Sc. **28**, 1 (1988).
8. H.Tostmann, D.Nattland and W.Freyland, J.Chem.Phys. **104**, 8777 (1996).
9. B.U.Felderhof et al., J.Opt.Soc.Am. **B 10**, 1824 (1993).
10. A.Simon, J.Solid State Chem. **27**, 87 (1979).

## AUTHOR INDEX

- Abruña, H.D., 49  
 Adams, Laura, 507  
 Akashi, Masatsune, 567  
 Allongue, P., 185  
 Alper, M., 347  
 Altman, E.I., 81  
 Amster, R., 451  
 Ansermet, J-Ph., 377  
 Arrouy, F., 315  
 Avrutsky, Ivan, 367  
  
 Bakonyi, I., 347  
 Banovic, S.W., 469  
 Barmak, K., 469  
 Baxter, Christopher, 481  
 Behm, R.J., 43  
 Bernard, M.C., 223  
 Bhattacharya, R.N., 401  
 Blum, L., 109  
 Bohannan, Eric W., 283  
 Bouesnard, O., 383  
 Brock, J.D., 49  
 Brunt, T.A., 37  
 Buller, L.J., 49  
  
 Celis, J.P., 475  
 Chan, H.M., 469  
 Chan, Jimmy, 367  
 Chazalviel, J.N., 185  
 Chen, Jin-Jian, 267  
 Chidsey, Christopher E.D., 173  
 Chien, Steve, 267  
 Chung, D.D.L., 573  
 Chyan, Oliver, 267  
 Clark, D.G., 501  
 Colletti, Lisa P., 235  
 Cooper, E.I., 389  
 Corcoran, Sean G., 31, 93  
 Cortes, R., 223  
 Czerwinski, F., 445, 501  
  
 Daridon, A., 315  
 Daroux, M.L., 301  
 Davis, R.F., 555  
 Davydov, Dmitri, 367  
 de Groot, R.J.J., 321  
 de Villeneuve, C. Henry, 185  
 de Vries, J.M.L., 321  
 Delplancke, J-L., 383  
 Dengra, S., 147  
 Diaz, R., 275  
 Dietterle, M., 9  
 Dittrich, T., 203  
 Doudin, B., 377  
 Dubin, V., 463  
 Dunbar, William L., 173  
  
 Ebel, J.L., 251  
 Ebrahimi, Fereshteh, 489  
 Erb, U., 501  
  
 Family, Fereydoon, 123  
 Finello, D., 555  
 Finnefrock, A.C., 49  
 Fokkink, L.G.J., 359  
 Pompeyrine, J., 315  
 Fonseca, L.F., 109  
 Frankel, Gerald S., 541  
 Fransaer, J., 475  
 Freyland, W., 579  
 Friedersdorf, L.E., 469  
 Froment, M., 223  
 Fujii, T., 495  
 Fujita, N., 495  
 Fukaya, Yuichi, 567  
 Furlong, M.J., 223  
 Füssel, W., 215  
  
 Galligan, J.M., 549  
 Ge, Maohui, 99  
 Gewirth, Andrew A., 99  
 Giesen, M., 9  
 Gilbert, S., 377  
 Girin, O.B., 433  
 Glück, M., 215  
 Golden, Teresa D., 283  
 Goossens, A., 209  
 Gorostiza, P., 275  
  
 Haftel, Michael I., 31  
 Harmer, M.P., 469  
 Hart, R., 347  
 Hatao, K., 527  
 Hayashi, Y., 87, 407  
 Henrion, O., 245  
 Hepel, Maria, 481, 507  
 Hersener, J., 215  
 Hooks, Daniel E., 161  
 Horkans, J., 389  
 Hou, Jiangyuan, 573  
 Huang, Ling-Yuang, 283  
 Hung, Chen-Jen, 283  
  
 Ibach, H., 9  
 Igarashi, Tatsushi, 515  
 Inoue, M., 495  
 Ip, W.F., 37  
 Ivaska, A., 425  
  
 Jaegermann, W., 245  
 Jennings, G.K., 155  
 Jisrawi, N.M., 301  
 Johnson, B., 451

Jones, C.T., 307  
 Jorne, Jacob, 141  
 Jyoko, Y., 87, 407  
  
 Kashiwabara, S., 87, 407  
 Khan-Malek, C., 401  
 Klein, A., 245  
 Klemperer, Walter G., 99  
 Kolb, D.M., 9, 19  
 Koma, Atsushi, 167  
 Kondo, K., 445  
 Kong, Dan, 489  
 Kudelka, S., 289  
 Kurosawa, Kou, 515  
 Kvarnström, C., 425  
 Kwietniak, K.T., 389  
  
 Lachenwitzer, A., 43  
 Laibinis, P.E., 155  
 Last, Julie A., 161  
 Latonen, R-M., 425  
 Leith, S.D., 341  
 Li, H., 501  
 Lim, P.B., 495  
 Lincot, D., 223  
 Linford, Matthew R., 173  
 Liu, Min, 267  
 Locquet, J-P., 315  
 Long, John G., 257  
 Lopatin, S., 463  
 Luo, Huihong, 173  
  
 Ma, E., 401  
 Mächler, E., 315  
 Magnussen, O.M., 43  
 Marder, A.R., 469  
 Marshall, G., 147  
 Martin, P.M., 401  
 Matsumoto, Y., 333  
 Matsuno, Hiromitsu, 515  
 McBreen, J., 501  
 McDevitt, J.T., 307  
 McKrell, T.J., 549  
 Megret, F., 501  
 Merchant, H.D., 433  
 Meulenkamp, E.A., 321  
 Michaelis, A., 289  
 Mirkin, C.A., 307  
 Mocskos, P., 147  
 Moffat, T.P., 75, 413  
 Mokerov, V.G., 3  
 Molina, F., 147  
 Möller, F.A., 43  
 Morante, J.R., 275  
 Morrone, Augusto, 489  
 Moskovits, Martin, 367  
 Mukerjee, S., 301  
 Murahara, M., 521, 527, 533  
  
 Nabiyouni, G., 347  
 Nakakura, C.Y., 81  
 Nakayama, Guen, 567  
  
 Natarajan, A. 401  
 Natarajan, Arun, 197  
 Nattland, D., 579  
 Niece, Brian K., 99  
 Nikolova, Maria, 257  
  
 Oberle, Robert, 457  
 Ocko, B.M., 55  
 Okamoto, T., 533  
 O'Shea, S.J., 37  
 Oskam, Gerko, 197, 257  
 O'Sullivan, E.J., 389  
 Oursler, Douglas A., 197  
 Ozanam, F., 185  
  
 Paranthaman, M., 401  
 Pellerin, J., 463  
 Petronis, C.M., 469  
 Pettenkofer, C., 245  
 Phanse, V.M., 81  
 Pinson, J., 185  
 Puerta, D.G., 469  
  
 Ramankiw, L.T., 389  
 Ramesham, R., 561  
 Ramos, Raphael A., 69  
 Randler, R.J., 19  
 Rappich, J., 203, 215  
 Rayment, T., 37  
 Redmond, G., 377  
 Reed, M.L., 251  
 Reisse, J., 383  
 Rice-Belrose, Cynthia, 507  
 Rikvold, Per Arne, 69  
 Ringland, K.L., 49  
 Ritchie, J.E., 307  
 Roberson, S.L., 555  
 Rose, M.F., 561  
 Rosen, Mervine, 31  
 Routkevitch, Dmitri, 367  
  
 Sakurada, Takafumi, 167  
 Salamanca-Riba, L., 419  
 Sanz, F., 275  
 Sasaki, T., 333  
 Sasaki, Wataru, 515  
 Schlesinger, T.E., 251  
 Schönenberger, C., 359  
 Schoonman, J., 209  
 Schöpke, A., 215  
 Schrotten, E., 209  
 Schultze, J.W., 289  
 Schwartz, D.T., 341  
 Schwarzacher, W., 347  
 Scott, T.W., 115  
 Searson, Peter C., 197, 257  
 Servat, J., 275  
 Shacham-Diamand, Y., 463  
 Shima, M., 419  
 Shimada, Toshihiro, 167  
 Shimizu, T., 521  
 Shiyonovskaya, I.V., 327

Shumsky, Mark, 283  
Shumyankov, A.G., 3  
Sieber, I., 215  
Siegenthaler, H., 315  
Sieradzki, Karl, 93  
Squire, P.T., 495  
Stapel, D., 9  
Stephenson, Richard, 481  
Stickney, John L., 235  
Susan, D.F., 469  
Swartzendruber, L.J., 419  
Switzer, Jay A., 283  
Szpunar, J.A., 445, 501

Takezoe, Noritaka, 515  
Tannahill, Tania, 481  
Thomas, Sajan, 235  
Thurston, T.R., 301  
Timoshenko, V.Y., 203  
Ting, P.D., 49  
Tostmann, H., 579  
Toth-Kadar, E., 347  
Toyoda, K., 527, 533  
Trofimov, V.I., 3

van der Zande, B.M.I., 359  
Vanasupa, L.S., 451  
Vasudev, P.K., 463

Wade, Christopher P., 173  
Wall, Craig G., 99

Wandlowski, Th., 55  
Wang, W., 401  
Ward, Michael D., 161  
Welland, M.E., 37  
Wells, A.D., 307  
Wieckowski, Andrzej, 69  
Wielgosz, R.I., 19  
Wiesler, David G., 93  
Williams, E.J., 315  
Wilmer, Elvin M., 235  
Winand, R., 383  
Wu, Junjun, 267  
Wu, Sen-Wei, 141

Xing, X.K., 301  
Xu, F., 307  
Xu, J.M., 367

Yacaman, M.J., 367  
Yang, X.Q., 301  
Yip, Christopher M., 161  
Yokotani, Atsushi, 515  
Yoshida, Kunio, 515

Zhai, Qing, 489  
Zhao, B., 463  
Zheng, G., 81  
Ziegler, J.C., 19  
Zypman, F.R., 109

## SUBJECT INDEX

- AB<sub>2</sub>-type Laves planes, 301
- adhesive strengths, 527
- adlattice structure, 99
- adlayer, 55
- alkanethiols, 155
- aluminum, 533, 573
  - nitride, 573
- amorphous
  - Fe-B film, 495
  - WO<sub>3</sub>, 327
- anion adsorbates, 75
- anisotropy micro-ellipsometry (AME), 289
- annealing, 161
- anodic
  - aluminum oxide, 367
  - oxidation, 215
- anodization, 573
- antiferromagnetic
  - alloys, 541
  - interlayer coupling, 87
- ArF excimer laser, 521, 527, 533
- atomic force microscopy, 161, 451, 549
- B(OH)<sub>3</sub> solution, 527
- bentonite, 567
- boron(-)
  - doped CVD diamond, 561
  - phosphide thin films, 209
- Br<sub>2</sub>, 81
- carbonate-bicarbonate concentration, 567
- ceramic overlayers, 469
- chalcogenides, 223
- chemical deposition, 223
- Cl<sub>2</sub>, 81
- cleaved heterostructures, 251
- Cl-Si(111) (1 × 1), 173
- CMA's, 341
- Co dissolution, 407
- Co/Cu multilayers, 87
- codeposition, 475
- colloidal particles, 475
- composite films
  - Cu/boron nitride and Ni/boron nitride, 481
- composites, 573
  - coatings, 469, 475
  - Cu/cuprous oxide, 283
  - films, 481, 495
  - mechanical properties, 489
  - structure, 489
  - superconductor, 307
- conductive polymers, 307
- Co-Ni-Cu/Cu, 347
- contact angle, 521
- contamination control, 267
- copper(-), 19, 81, 141, 155, 257
  - boron nitride, 481
  - Cu(100), 75
  - Cu(111), 75
  - Cu/cuprous oxide nanocomposites, 283
  - Cu metallization, 463
  - Cu/(Ni, Co) multilayers, 413
  - deposition, 507
  - monolayer, 109
  - Ni deposition on Cu(100), 43
  - nucleation, 451
  - single crystal, 413
- Co/Pt multilayers, 407
  - structure and magnetic properties, 407
- corrosion, 93, 541, 549, 573, 579
- CoWP, 463
- crystallization
  - nickel alloy, 457
- crystallographic texture, 433
- cyclic voltammetry, 327, 555
  - background current response, 561
- dealloying, 93
- defect structure, 433
- digital etching, 251
- dissolution, 549
- domain boundaries, 161
- electrochemical
  - adsorption, 69
  - atomic layer epitaxy, (ECALE), 235
  - deposition, 147, 495
  - etching - model experiments, 245
  - fabrication, 367
  - impedance spectroscopy (EIS), 197
  - kinetics, 549
  - modification, 315
  - oxidation, 315
  - processing, 377
  - synthesis, 123
  - transport, 147
  - treatments, 203
- electrochromic
  - devices, 321
  - phenomena, 327
- electroconvection, 147
- electrocrystallization, 445
- electrodeposit 347, 433
- electrodeposition, 19, 37, 223, 321, 383
  - Ag, 141
  - Ag on Au(111), 31
  - Co/Cu, 87
  - Co/Pt multilayers, 407
  - Cu, 141, 283
  - on conductive polymers, 507

- from suspensions, 481
- HI-MEMS, 389
- in situ* STM, 43
- Li, 141
- metal on semiconductors, 257
- morphology of, 507
- multilayers, 87, 419
- nanocomposites, 283
- Ni on Au(111), 43
- ordering in, 49
- polymers, 307
- superconductors, 401
- Zn, 141
- electroless deposition, 463
  - amorphous nickel, 457
  - Cu, 451
  - nickel-phosphorous alloys, 457
  - on yttria-stabilized zirconia, 333
  - Pt, 275
- electrolyte electroreflectance, 209
- electron diffraction - LEED, 245
- embedded atom model (AEM), 31
- epitaxial
  - growth, 167
  - thin films, 123
- epitaxially-grown materials, 251
- epitaxy, 223
- etching, 81
- excimer lamp, 515
- excitons, 283
- fabrication of  $\text{Al}_2\text{O}_3$  thin films, 533
- ferri/ferrocyanide, 561
- Fibonacci Ni/Cu multilayers, 419
- fluorocarbon resin, 521, 527
- fractal electrodes, 123
- giant magnetoresistance, 347
- gold, 257
  - Au(111), 99, 109
  - Ni deposition
    - on Au(100), 43
    - on Au(111), 43
  - porous, 93
  - single crystal, 19, 55
  - thiol(s)
    - monolayers on, 37
    - on, 155
- grain structure, 433
- graphoepitaxy, 167
- groundwater, 567
- growth
  - layer by layer, 3
  - Stranski-Krastanov, 31
  - 2d nucleation, 3
- halide electroadsorption, 55
- heteroepitaxy, 161
- HF solutions, 275
- HI-MEMS, 389
- homoepitaxial growth, 3
- H-Si(111), 167, 173, 267
- impedance spectroscopy, 555
- in situ* STM, 43
- interdiffusion, 463
- interface, 115
- $\text{La}_2\text{CuO}_4$ , 315
- $\text{La}_{1-x}\text{Sr}_x\text{MnO}_3$ , 333
- lattice-gas models, 69
- layer-by-layer growth, 3
- Li, 141
- $\text{Li}_x\text{Mn}_2\text{O}_4$  material battery, 301
- liquid metals, 579
- lithography, 389
- localized corrosion, 567
- magnetic
  - anisotropy, 347
  - devices, 541
  - mini-motor, 389
  - multilayer, 347
  - nanopowders, 383
  - properties of multilayers, 407
- magnetoacoustic devices, 495
- magnetoresistance, 87, 377, 419
- magnetostrictive material, 495
- mass transport control, 413
- mechanical properties 489
- metal
  - contaminations, 267
  - hydride batteries, 301
- microhardness, 501
- micromechanical stress sensors, 37
- micro-photocurrent spectroscopy, 289
- microsensors
  - magnetic fields, 401
- microvoids, 433
- microwave
  - plasma CVD, 561
  - reflectivity, 197
- mild steel, 567
- molecular
  - dynamics, 115
  - films, 161
- molten alkali metal, 579
- molybdenum nitride electrodes, 555
- monolayers, 99
- morphological
  - instability, 413
  - patterns, 141
- multilayers
  - Co/Cu, 87
  - Co/Pt, 407
  - Cu/Ag, 489
  - Ni/Cu, 419
  - polymer film, 425
- $\text{NaAlO}_2$ , 521
- nanocomposites, 283, 489
- nanocrystalline, 501
- nanowires, 367, 377
- n-GaAs(100), 347



- nickel
  - electrodeposition of, 43
  - Ni-Al-Al<sub>2</sub>O<sub>3</sub>, 469
  - Ni/Cu multilayers, 419
  - Ni-45%Fe alloys, 501
  - Ni/boron nitride, 481
  - NiFe composition modulated alloys, 341
- nucleation, 457
- optical electrochemistry, 327
- organic
  - molecules, 167
  - monolayers
    - self-assembled, 155
    - thiols on Au, 37
  - thin films, 185
- oxidation, 251
  - microstructure effects, 315
- oxide barriers, 377
- passivation, 549
- passivity, 567
- pattern formation, 147
- Pd seed layer, 451
- peroxide, 533
- peroxy-tungstate, 321
- phase transitions, 69
- photochlorination, 173
- photoelectron spectroscopy (PES), 245
- photoetching, 515
- photoluminescence, 203
- photorefectance, 209
- photoresist microelectrochemistry, 289
- phthalocyanine, 167
- physically adsorbed, 115
- platinum electroless deposition, 275
- polycrystalline Mo<sub>x</sub>N thin film
  - electrodes, 555
- polymer, 515
  - electrochemically synthesized, 425
  - electrodeposition, 307
  - multilayers, 425
- poly(3-octylthiophene), 425
- poly(paraphenylene), 425
- polypyrrole/polystyrenesulfonate, 507
- porous
  - aluminum oxide, 367
  - gold, 93
  - media, 93
  - silicon, 275
- POT, 425
- potential of mean force, 115
- PPP, 425
- Pt, 257
- Pt(111)-Cu deposition on, 49
- pulsed potential deposition, 401
- reaction bonding, 469
- reflective electron microscopy, 87
- RHEED, 3
- rotating disk electrode, 475
- scanning(-)
  - probe microscopy, 251, 341
  - tunneling microscopy, 19, 75, 81, 173, 185, 451
    - Ag deposition, 9
    - of step fluctuations, 9
- Schottky junctions, 257
- second-harmonic generation, 579
- self-assembled, 307
  - organic monolayers 155
- semiconductor, 185
  - band structure, 209
  - electrochemistry, 185
  - electrolyte interface, 245
  - surface structure, 185
  - III/V, 209
- sensor applications, 267
- SiGe passivation, 215
- silicon, 19, 173, 197, 257
  - cap, 215
  - carbide, 573
  - Si(100), 275
  - surfaces, 203
- silicotungstate 99
- silver, 55, 141, 155
  - Ag(111), 9, 99
- simulations, 69, 115
- small-angle neutron scattering, 93
- sonoelectrochemistry, 383
- space charge layer capacitance, 197
- spinel Li insertion compound, 301
- stainless steel, 549
- step
  - dynamics, 75
  - flow, 81
  - fluctuations, 9
- strained layer superlattices, 413
- Stranski-Krastanov growth, 31
- stress corrosion cracking, 93
- structural evolution, 413
- superconductor, 315
  - composites, 307
  - thin films, 401
- surface(-)
  - modification, 527
  - morphology, 3
  - properties, 579
  - segregation, 579
  - state(s), 197
    - density, 203
  - stress, 31, 37
  - structure, 185
- texture, 501
- thermal stability, 501
- thermostability, 463
- thin film(s), 223
  - disks, 541
  - NiFe, 341
- thin-layer electrochemical studies, 235
- tight binding approximation 109

Ti/TiO<sub>2</sub>, 289  
 trajectory analysis, 475  
 twins, 433  
 2d nucleation, 3  
  
 ultrasound, 383  
 underpotential deposition, 69, 109, 235  
   Ag on Au(111), 31  
   Cu on Pt, 49  
   on Au, 155  
   Pb, 75  
   x-ray scattering, 49  
 unimolecular, 115  
  
 vacuum uv radiation, 515  
 vibrational spectroscopy, 327  
 vicinal surfaces, 167  
 voltammetry, 341  
  
 wet chemical cleaning, 267  
 WO<sub>3</sub>, 321  
   amorphous, 327  
   properties, 321  
  
 x-ray  
   scattering, 49, 55  
   texture measurements, 445  
  
 yttria-stabilized zirconia, 333  
  
 zinc, 141  
   Fe alloys, 445  
   morphology of Fe alloys, 445  
 ZnS, 235  
 ZnSe, 235  
 ZnTe, 235